



# Lightning Electromagnetics

Edited by Vernon Cooray

**IET POWER AND ENERGY SERIES 62**

# **Lightning Electromagnetics**

## **Other volumes in this series:**

- Volume 1   **Power circuit breaker theory and design** C.H. Flursheim (Editor)  
Volume 4   **Industrial microwave heating** A.C. Metaxas and R.J. Meredith  
Volume 7   **Insulators for high voltages** J.S.T. Looms  
Volume 8   **Variable frequency AC motor drive systems** D. Finney  
Volume 10   **SF<sub>6</sub> switchgear** H.M. Ryan and G.R. Jones  
Volume 11   **Conduction and induction heating** E.J. Davies  
Volume 13   **Statistical techniques for high voltage engineering** W. Hauschild and W. Mosch  
Volume 14   **Uninterruptible power supplies** J. Platts and J.D. St Aubyn (Editors)  
Volume 15   **Digital protection for power systems** A.T. Johns and S.K. Salman  
Volume 16   **Electricity economics and planning** T.W. Berrie  
Volume 18   **Vacuum switchgear** A. Greenwood  
Volume 19   **Electrical safety: a guide to causes and prevention of hazards** J. Maxwell Adams  
Volume 21   **Electricity distribution network design, 2nd edition** E. Lakervi and E.J. Holmes  
Volume 22   **Artificial intelligence techniques in power systems** K. Warwick, A.O. Ekwue and R. Aggarwal (Editors)  
Volume 24   **Power system commissioning and maintenance practice** K. Harker  
Volume 25   **Engineers' handbook of industrial microwave heating** R.J. Meredith  
Volume 26   **Small electric motors** H. Moczala *et al.*  
Volume 27   **AC-DC power system analysis** J. Arrillaga and B.C. Smith  
Volume 29   **High voltage direct current transmission, 2nd edition** J. Arrillaga  
Volume 30   **Flexible AC transmission systems (facts)** Y-H. Song (Editor)  
Volume 31   **Embedded generation** N. Jenkins *et al.*  
Volume 32   **High voltage engineering and testing, 2nd edition** H.M. Ryan (Editor)  
Volume 33   **Overvoltage protection of low-voltage systems, revised edition** P. Hasse  
Volume 34   **The lightning flash** V. Cooray  
Volume 36   **Voltage quality in electrical power systems** J. Schlabbach *et al.*  
Volume 37   **Electrical steels for rotating machines** P. Beckley  
Volume 38   **The electric car: development and future of battery, hybrid and fuel-cell cars** M. Westbrook  
Volume 39   **Power systems electromagnetic transients simulation** J. Arrillaga and N. Watson  
Volume 40   **Advances in high voltage engineering** M. Haddad and D. Warne  
Volume 41   **Electrical operation of electrostatic precipitators** K. Parker  
Volume 43   **Thermal power plant simulation and control** D. Flynn  
Volume 44   **Economic evaluation of projects in the electricity supply industry** H. Khatib  
Volume 45   **Propulsion systems for hybrid vehicles** J. Miller  
Volume 46   **Distribution switchgear** S. Stewart  
Volume 47   **Protection of electricity distribution networks, 2nd edition** J. Gers and E. Holmes  
Volume 48   **Wood pole overhead lines** B. Wareing  
Volume 49   **Electric fuses, 3rd edition** A. Wright and G. Newbery  
Volume 50   **Wind power integration: connection and system operational aspects**  
              B. Fox *et al.*  
Volume 51   **Short circuit currents** J. Schlabbach  
Volume 52   **Nuclear power** J. Wood  
Volume 53   **Condition assessment of high voltage insulation in power system equipment** R.E. James and Q. Su  
Volume 55   **Local energy: distributed generation of heat and power** J. Wood  
Volume 56   **Condition monitoring of rotating electrical machines** P. Tavner, L. Ran, J. Penman and H. Sedding  
Volume 57   **The control techniques drives and controls handbook, 2nd edition** B. Drury  
Volume 58   **Lightning protection** V. Cooray (Editor)  
Volume 59   **Ultradcapacitor applications** J.M. Miller  
Volume 63   **Energy storage for power systems, 2nd edition** A. Ter-Gazarian  
Volume 65   **Protection of electrical distribution networks, 3rd edition** J. Gers  
Volume 905   **Power system protection, 4 volumes**

# Lightning Electromagnetics

Edited by Vernon Cooray

The Institution of Engineering and Technology

Published by The Institution of Engineering and Technology, London, United Kingdom

The Institution of Engineering and Technology is registered as a Charity in England & Wales (no. 211014) and Scotland (no. SC038698).

© 2012 The Institution of Engineering and Technology

First published 2012

This publication is copyright under the Berne Convention and the Universal Copyright Convention. All rights reserved. Apart from any fair dealing for the purposes of research or private study, or criticism or review, as permitted under the Copyright, Designs and Patents Act 1988, this publication may be reproduced, stored or transmitted, in any form or by any means, only with the prior permission in writing of the publishers, or in the case of reprographic reproduction in accordance with the terms of licences issued by the Copyright Licensing Agency. Enquiries concerning reproduction outside those terms should be sent to the publisher at the undermentioned address:

The Institution of Engineering and Technology  
Michael Faraday House  
Six Hills Way, Stevenage  
Herts, SG1 2AY, United Kingdom

[www.theiet.org](http://www.theiet.org)

While the author and publisher believe that the information and guidance given in this work are correct, all parties must rely upon their own skill and judgement when making use of them. Neither the author nor the publisher assumes any liability to anyone for any loss or damage caused by any error or omission in the work, whether such an error or omission is the result of negligence or any other cause. Any and all such liability is disclaimed.

The moral rights of the author to be identified as author of this work have been asserted by him in accordance with the Copyright, Designs and Patents Act 1988.

#### **British Library Cataloguing in Publication Data**

A catalogue record for this product is available from the British Library

**ISBN 978-1-84919-215-6 (hardback)**

**ISBN 978-1-84919-216-3 (PDF)**

Typeset in India by MPS Limited

Printed and bound in the UK by CPI Group (UK) Ltd, Croydon, CR40 4YY

*'In appreciation of the work of a merciful God'*

---

## Acknowledgements

---

First of all I wish to thank all my colleagues who have spent a good deal of their free time to write the chapters of this book. My special thanks to Prof. Farhad Rachidi and Prof. Carlo Alberto Nucci who helped me in numerous ways, as both friends and colleagues, in compiling the material for this and the previous lightning books published by the IET.

I wish to express my sincere thanks to Ms. Helen Langley and Ms. Lisa Reading of the IET publishing department who were at all times prepared to listen to my suggestions and accommodate submission delays and last-minute changes without complaint.

My thanks to the donation fund from B. John and Svea Andersson to Uppsala University and to the Swedish Natural Science Research Council (Vetenskapsrådet) for supporting my research over the past 30 years at Uppsala University; without this support I would not be in a position to be the editor of this book.

Finally, I express my gratitude to my mother, Dorothy Cooray, who taught me the value of knowledge, to my wife, Ruby Cooray, who provided me with encouragement and ensured that I had ample time to gain knowledge through my research activities, to my sons, Gerald and Charith, and their respective wives, Shamara and Anna, who were always there to share this knowledge and to my granddaughters, Sanduni Cooray and Ella Cooray, who, with their curious young minds, convinced me of the value of documenting the knowledge gathered for the future generations. The work I have done in this book is dedicated to my father, the late Gerard Cooray.

---

# Contents

---

<b>1</b>	<b>Basic electromagnetic theory – A summary</b>	<b>1</b>
1.1	Introduction	1
1.2	The nomenclature	1
1.3	Coordinate systems	2
1.4	Important vector relationships	2
1.4.1	The scalar product of two vectors	2
1.4.2	The vector product of two vectors	4
1.4.3	Vector field	5
1.4.4	The nabla operator and its operations	5
1.4.4.1	The gradient of a scalar function	5
1.4.4.2	The divergence of a vector field	6
1.4.4.3	The curl of a vector field	7
1.4.5	Important vector identities	8
1.4.6	Relationship between the curl of a vector field and the line integral of that vector field around a closed path	8
1.4.7	The flux of a vector field through a surface	8
1.4.8	Relationship between the divergence of a vector field and the flux of that vector field through a closed surface	9
1.4.9	Divergence theorem	9
1.4.10	Stokes theorem	10
1.5	Static electric fields	10
1.5.1	Coulomb's law	10
1.5.2	Electric field produced by static charges is a conservative field	12
1.5.3	Gauss's law	13
1.5.4	Electric scalar potential	14
1.5.5	Poisson and Laplace equations	15
1.5.6	Concept of images	16
1.5.7	Electrostatic boundary conditions	17
1.6	Static magnetic fields	19
1.6.1	Electric current	19
1.6.2	Conservation of electric charge	20
1.6.3	Re-distribution of excess charge placed inside a conducting body	22
1.6.4	Magnetic field produced by a current element – Biot–Savart's law	22

1.6.5	Gauss's law for magnetic fields	23
1.6.6	Ampere's law	24
1.6.7	Boundary conditions for the static magnetic field	25
1.6.8	Vector potential	26
1.6.8.1	Vector potential of a current distribution	27
1.6.8.2	Vector potential due to a current element $\mathbf{d}\mathbf{l}$	28
1.6.9	Force on a charged particle	29
1.7	Energy density of an electric field	29
1.8	Electrodynamics – Time-varying electric and magnetic fields	30
1.8.1	Faraday's law	31
1.8.2	Maxwell's modification of Ampere's law – the displacement current term	33
1.8.3	Energy density in a magnetic field	34
1.9	Summary of the laws of electricity	35
1.10	Wave equation	36
1.11	Maxwell's prediction of electromagnetic waves	37
1.12	Plane wave solution	39
1.12.1	The electric field of the plane wave	39
1.12.2	The magnetic field of the plane wave	39
1.12.3	Energy transported by a plane wave – Poynting's theorem	41
1.13	Maxwell's equations and plane waves in different media (summary)	42
1.13.1	Vacuum	42
1.13.2	Isotropic and linear dielectric and magnetic media	43
1.13.3	Conducting media	44
1.14	Retarded potentials	46
1.14.1	Vector potential of a current element	48
1.15	Electromagnetic fields of a current element – Electric dipole	48
1.16	Electromagnetic fields of a lightning return stroke	51
	Further reading	53
<b>2</b>	<b>Application of electromagnetic fields of an accelerating charge to obtain the electromagnetic fields of a propagating current pulse</b>	<b>55</b>
2.1	Introduction	55
2.2	Electromagnetic fields of a moving charge	55
2.3	Basic equations pertinent to the radiation and velocity field of a propagating current pulse	56
2.4	Electromagnetic fields generated by a current pulse propagating with uniform velocity and without attenuation	57
2.4.1	The electric radiation field generated by the initiation of the current	58
2.4.2	The electric radiation field generated by the termination of the current	58

2.4.3	The static field generated by the accumulation of charge at the point of current initiation	58
2.4.4	The static field generated by the accumulation of charge at the point of current termination	58
2.4.5	The velocity field generated by the propagating current pulse	59
2.4.6	The magnetic radiation field generated by the initiation of the current	59
2.4.7	The magnetic radiation field generated by the termination of the current	59
2.4.8	Magnetic velocity field generated by the current pulse	59
2.5	Electromagnetic fields generated by a current pulse propagating with non-uniform velocity and with attenuation	60
2.5.1	The electric radiation field generated by the initiation of the current	61
2.5.2	The electric radiation field generated by the termination of the current	61
2.5.3	The static field generated by the accumulation of charge at the point of current initiation	61
2.5.4	The static field generated by the accumulation of charge at the point of current termination	61
2.5.5	The velocity field generated as the current pulse propagates along the channel element	61
2.5.6	The magnetic radiation field generated by the initiation of the current	62
2.5.7	The magnetic radiation field generated by the termination of the current	62
2.5.8	Magnetic velocity field generated as the current pulse propagates along the channel element	62
2.5.9	Electric radiation field generated due to the attenuation of the current along the channel	62
2.5.10	Magnetic radiation field generated due to the attenuation of the current along the channel	63
2.5.11	Static field generated by the charge deposited along the channel by the current pulse	63
2.5.12	Electric radiation field generated due to the variation of current velocity along the channel	64
2.5.13	Magnetic radiation field generated due to the variation of current velocity along the channel	64
2.6	Concluding remarks	65
	References	65
<b>3</b>	<b>Basic discharge processes in the atmosphere</b>	<b>67</b>
3.1	Introduction	67
3.2	Electron avalanche	68

3.3	Streamer discharges	70
3.4	Corona discharges	75
3.5	Thermalization or heating of air by a discharge	76
3.6	Low-pressure electrical discharges	77
3.7	Leader discharges	77
3.8	Some features of mathematical modelling of positive leader discharges	79
	References	84
<b>4</b>	<b>Numerical simulations of non-thermal electrical discharges in air</b>	<b>87</b>
4.1	Introduction	87
4.2	Outline of electrophysical processes in gaseous medium under electric fields	87
4.2.1	Generation of charged species in gas	88
4.2.2	Losses of charged species in gas	89
4.2.3	Dynamics of densities of charge carriers in discharge plasma	90
4.2.4	Concepts of electron avalanche and streamer	90
4.3	Hydrodynamic description of gas discharge plasma	92
4.4	Solving gas discharge problems	96
4.4.1	Simulations of corona in air	96
4.4.2	Computer implementation of corona model	97
4.4.3	Study case: positive corona between coaxial cylinders	107
4.4.4	Study case: positive corona in rod–plane electrode system	112
4.5	Simulations of streamer discharges in air	116
4.5.1	Study case: positive streamer in a weak homogeneous background field	124
4.5.2	Study case: negative streamer in weak homogeneous background fields	130
	References	134
<b>5</b>	<b>Modelling of charging processes in clouds</b>	<b>139</b>
5.1	Introduction	139
5.2	Definitions of some model descriptors	140
5.2.1	Basic terminology	140
5.2.2	Terms related to microphysics	142
5.2.3	Categories of electrification mechanisms	146
5.2.4	Other categorizations of cloud models	147
5.3	Brief history of electrification modelling	149
5.4	Parameterization of electrical processes	153
5.4.1	Calculating the electric field	153
5.4.2	Charge continuity	156
5.4.3	The non-inductive graupel–ice collision mechanism	158
5.4.3.1	Parameterized laboratory results	158
5.4.3.2	General formulation	165

5.4.4	The inductive charging mechanism	167
5.4.5	Small ion processes	170
5.5	Lightning parameterizations	174
5.5.1	Stochastic lightning model	176
5.5.2	Pseudo-fractal lightning	179
5.6	Some applications of models	180
5.6.1	Ion and inductive mechanisms	180
5.6.2	Non-inductive graupel–ice sensitivity	181
5.6.3	Charge structure and lightning type	182
5.6.4	Concluding remarks	186
	References	187
<b>6</b>	<b>The physics of lightning flash development</b>	<b>193</b>
6.1	Introduction	193
6.2	Definitions and attributes of lightning processes	194
6.3	The composition of a lightning flash	196
6.3.1	The nature of ‘recoil streamers’ and dart leaders	196
6.3.2	Intracloud flashes	198
6.3.3	Cloud-to-ground flashes	201
6.4	Continuing current as an indicator of a developing leader	203
6.5	Spider lightning	204
6.6	The analytical relationship between the electrical structure of a cloud and lightning parameters	205
6.6.1	Physical model of the development of intracloud and cloud-to-ground leaders	206
6.7	Current cut-off in developing lightning flashes	208
6.7.1	Current cut-off and recoil leaders	211
6.8	The remaining puzzle of positive cloud-to-ground flashes	212
6.9	Upward lightning	215
6.10	M-component	218
6.11	The electrostatic model of M-events	221
6.12	Summary	226
	References	227
<b>7</b>	<b>Return stroke models for engineering applications</b>	<b>231</b>
7.1	Introduction	231
7.2	Current propagation models (CP models)	232
7.2.1	Basic concept	232
7.2.2	Most general description	234
7.3	Current generation models (CG models)	236
7.3.1	Basic concept	236
7.3.2	Mathematical background	238
7.3.2.1	Evaluate $I_b(t)$ , given $\rho(z)$ , $\tau(z)$ and $v(z)$	238
7.3.2.2	Evaluate $\tau(z)$ , given $I_b(t)$ , $\rho(z)$ and $v(z)$	239
7.3.2.3	Evaluate $\rho(z)$ , given $I_b(t)$ , $\tau(z)$ and $v(z)$	240
7.3.2.4	Evaluate $v(z)$ , given $I_b(t)$ , $\rho(z)$ and $\tau(z)$	240

7.3.3	CG models in practice	241
7.3.3.1	Model of Wagner	241
7.3.3.2	Model of Heidler	241
7.3.3.3	Model of Hubert	242
7.3.3.4	Model of Cooray	242
7.3.3.5	Model of Diendorfer and Uman	244
7.3.3.6	First modification of the Diendorfer and Uman model by Thottappillil <i>et al.</i>	245
7.3.3.7	Second modification of the Diendorfer and Uman model by Thottappillil and Uman	246
7.3.3.8	Model of Cooray	247
7.3.3.9	Model of Cooray and Rakov	248
7.3.3.10	Model of Cooray, Rakov and Montano	248
7.4	Current dissipation models (CD models)	249
7.4.1	General description	249
7.4.2	Mathematical background	251
7.4.3	Cooray and Rakov model – a combination of current dissipation and current propagation models	252
7.5	Generalization of any model to current generation type	253
7.6	Generalization of any model to a current dissipation type model	255
7.7	Current dissipation models and the modified transmission line models	256
7.8	Effect of ground conductivity	257
7.9	Concluding remarks	259
	References	259
<b>8</b>	<b>Electromagnetic models of lightning return strokes</b>	<b>263</b>
8.1	Introduction	263
8.2	General approach to finding the current distribution along a vertical perfectly conducting wire above ground	265
8.2.1	Current distribution along a vertical perfectly conducting wire above ground	265
8.2.2	Mechanism of attenuation of current wave in the absence of ohmic losses	266
8.3	Representation of the lightning return-stroke channel	268
8.3.1	Type 1: a perfectly conducting/resistive wire in air above ground	269
8.3.2	Type 2: a wire loaded by additional distributed series inductance in air above ground	269
8.3.3	Type 3: a wire embedded in a dielectric (other than air) above ground	274
8.3.4	Type 4: a wire coated by a dielectric material in air above ground	276

8.3.5	Type 5: a wire coated by a fictitious material having high relative permittivity and high relative permeability in air above ground	276
8.3.6	Type 6: two wires having additional distributed shunt capacitance in air	276
8.4	Comparison of model-predicted current distributions and electromagnetic fields for different channel representations	277
8.4.1	Comparison of distributions of current for different channel representations	277
8.4.2	Comparison of model-predicted electric and magnetic fields with measurements	280
8.5	Excitations used in electromagnetic models of the lightning return stroke	283
8.5.1	Closing a charged vertical conducting wire at its bottom end with a specified circuit	286
8.5.2	Lumped voltage source	287
8.5.3	Lumped current source	287
8.5.4	Comparison of current distributions along a vertical perfectly conducting wire excited by different sources	287
8.6	Numerical procedures used in electromagnetic models of the lightning return stroke	290
8.6.1	Methods of moments (MoMs) in the time and frequency domains	290
8.6.1.1	MoM in the time domain	290
8.6.1.2	MoM in the frequency domain	292
8.6.2	Finite-difference time-domain (FDTD) method	292
8.6.3	Comparison of current distributions along a vertical perfectly conducting wire calculated using different numerical procedures with those predicted by Chen's analytical equation	294
8.7	Applications of electromagnetic models of the lightning return stroke	294
8.7.1	Strikes to flat ground	295
8.7.2	Strikes to free-standing tall object	300
8.7.3	Strikes to overhead power transmission lines	304
8.7.4	Strikes to wire-mesh-like structures	305
8.8	Summary	305
	References	307
<b>9</b>	<b>Antenna models of lightning return-stroke: an integral approach based on the method of moments</b>	<b>315</b>
9.1	Introduction	315
9.2	General formulation	318
9.2.1	Time-domain formulation	319
9.2.2	Frequency-domain formulation	323

9.3	Numerical treatment	327
9.3.1	Method of moments	327
9.3.2	Time-domain formulation	328
9.3.3	Frequency-domain formulation	331
9.3.4	Lossy half-space problem	335
9.4	Various AT models	338
9.4.1	Time-domain AT model	339
9.4.2	Time-domain AT model with inductive loading	341
9.4.3	Time-domain AT model with non-linear loading	346
9.4.4	Frequency-domain AT model	349
9.5	Numerical results	350
9.5.1	AT Model	350
9.5.1.1	Current profiles	350
9.5.1.2	Line charge density profiles	352
9.5.1.3	Electromagnetic fields	353
9.5.2	ATIL Model	356
9.5.2.1	Current profiles	356
9.5.2.2	Current dispersion	359
9.5.2.3	Current wave propagation speed	359
9.5.2.4	Electromagnetic fields	360
9.5.3	AT model with non-linear loading	364
9.5.3.1	Current profiles	364
9.5.3.2	Current peak and current rise time	365
9.5.3.3	Electromagnetic fields	367
9.5.3.4	Current wave propagation speed	372
9.5.4	Frequency-domain AT model	372
9.5.4.1	Current profiles	372
9.5.4.2	Electromagnetic fields	373
9.5.4.3	Electromagnetic fields above lossy half-space	374
9.6	Summary	381
	References	383
<b>10</b>	<b>Transmission line models of lightning return stroke</b>	<b>389</b>
10.1	Introduction	389
10.2	Overview of transmission line models of lightning return stroke	392
10.2.1	Discharge-type models	393
10.2.2	Lumped-excitation models	395
10.3	Calculation of channel parameters per unit length	398
10.3.1	Channel inductance and capacitance	399
10.3.2	Effect of corona on the calculation of channel parameters	401
10.3.2.1	Leader and return stroke channels in the presence of corona	402
10.3.2.2	Transmission line equations in the presence of corona	407

10.3.3	Calculation of channel resistance	409
10.3.3.1	Strong-shock approximation	411
10.3.3.2	Toeppler's arc resistance equation	412
10.3.3.3	Computation of the channel resistance	412
10.4	Computed results	414
10.4.1	Channel currents	414
10.4.1.1	Lossless non-uniform channel	414
10.4.1.2	Lossy non-uniform channel	416
10.4.1.3	Lossy non-uniform channel with corona	418
10.4.2	Predicted electromagnetic fields	419
10.5	Summary and conclusion	421
	References	422
<b>11</b>	<b>On the various approximations to calculate lightning return stroke-generated electric and magnetic fields over finitely conducting ground</b>	<b>427</b>
11.1	Introduction	427
11.2	Exact expressions for the electromagnetic fields of a dipole located over finitely conducting ground and their extension to return stroke fields	428
11.2.1	Exact expressions for the vector potential of a dipole over finitely conducting ground	428
11.2.2	The exact expressions for the electromagnetic fields of a dipole over finitely conducting ground	430
11.2.2.1	Vertical electric field in air and underground	430
11.2.2.2	The azimuthal magnetic field in air and underground	430
11.2.2.3	Horizontal electric field in air and underground	431
11.2.3	Electromagnetic fields of return strokes	432
11.3	Return stroke models utilized in testing the approximate expressions	433
11.4	Summary of exact propagation effects in the vicinity of the channel	434
11.5	Simplified procedures to calculate electric and magnetic fields over finitely conducting ground	438
11.5.1	Norton and Bannister's approximations	438
11.5.1.1	Comparison of Norton's and Bannister's approximate expressions for the vertical electric field with exact calculations	439
11.5.2	Simplified expressions derived by Cooray and Lundquist and Cooray to calculate vertical electric field and horizontal magnetic field over finitely conducting ground	440
11.5.2.1	Approximation 1	442
11.5.2.2	Approximation 2	443

11.5.3	Simplified expressions to calculate the horizontal electric field	448
11.5.3.1	Quasi-static expression to calculate horizontal electric field close to the lightning channel	449
11.5.3.2	Surface impedance expression	449
11.5.3.3	Comparison of the predictions of the quasi-static approximation and predictions of surface impedance expression with exact calculations	449
11.5.4	Barbosa and Paulino expression to calculate the horizontal electric field	456
11.5.5	Approximate time domain expressions to calculate underground electric fields	458
11.5.5.1	Vertical electric field at the surface and at different depths below the ground	459
11.5.5.2	Azimuthal magnetic field at the surface and at different depths below the ground	461
11.5.5.3	Horizontal electric field at the surface and at different depths below the ground	461
11.6	Propagation over vertically stratified ground	464
11.6.1	Expressions for the attenuation function for a dipole at ground level	464
11.6.2	Simplified expression for the electromagnetic fields from lightning over vertically stratified ground	466
11.6.3	Validation of the simplified expression	466
11.6.4	Some interesting effects of vertically stratified ground on radiation fields as described by Cooray and Cummins	466
11.6.4.1	Sea gain effects	466
11.6.4.2	Reciprocity	468
11.6.4.3	Equivalent conductivity	470
11.7	Propagation effects over horizontally stratified ground	471
11.7.1	Wait's simplified expressions for the attenuation function for a dipole at ground level	471
11.7.2	Simplified expression for the electromagnetic fields from lightning over vertically stratified ground	473
11.7.3	Validity of simplified expression	473
11.7.4	Some interesting effects of horizontally stratified ground on radiation fields as presented by Cooray and Cummins	473
11.7.4.1	Stratified ground with two layers – field enhancement caused by stratified ground	473
11.7.4.2	Continuously stratified ground	475
11.8	Future studies	481
	References	482

<b>12 Propagation effects on electromagnetic fields generated by lightning return strokes: Review of simplified formulas and their validity assessment</b>	<b>485</b>
12.1 Introduction	485
12.2 Basic assumptions	485
12.2.1 Formulation of the electromagnetic fields above a perfect ground in the time domain	486
12.2.2 Using the electromagnetic fields above a perfect ground as the input for calculating the fields above a lossy ground	488
12.3 Propagation along a homogeneous lossy ground	489
12.3.1 Vertical electric and azimuthal magnetic fields	490
12.3.2 Horizontal electric field	491
12.4 Propagation along a horizontally stratified ground	493
12.4.1 Simplified formulations for the lightning electromagnetic fields above a two-layer horizontally stratified ground	493
12.4.2 Test and validation of the simplified formulas	495
12.5 Propagation along a vertically stratified ground	500
12.5.1 Simplified approaches for the lightning far field above a vertically stratified ground	501
12.5.1.1 Formulations	501
12.5.1.2 Numerical results	503
12.5.2 Test and validation of the simplified formulae	504
12.6 Summary	505
References	508
<b>13 Lightning electromagnetic field calculations in presence of a conducting ground: the numerical treatment of Sommerfeld's integrals</b>	<b>515</b>
13.1 Introduction	515
13.2 Lightning electromagnetic field calculation in presence of a lossy ground with constant electrical parameters	516
13.2.1 Overground electromagnetic field	517
13.2.1.1 Overview on Green's functions theory	517
13.2.1.2 Derivation of the Green's functions for the overground electromagnetic field	518
13.2.1.3 Derivation of the lightning return stroke overground electromagnetic field	522
13.2.1.4 Evaluation of the Sommerfeld's integrals	523
13.2.1.5 The vertical component of the electric field	527
13.2.1.6 The radial component of the electric field	530
13.2.1.7 The azimuthal component of the magnetic field	532
13.2.2 Underground electromagnetic field	533

13.2.3	Validation of the simplified approaches	535
13.2.3.1	Overground electromagnetic field	535
13.2.3.2	Underground electromagnetic field	537
13.3	Lightning electromagnetic field calculation in presence of a lossy ground with frequency-dependent electrical parameters	542
13.3.1	The dependence of soil conductivity and permittivity on the frequency	543
13.3.2	Numerical simulation of overground and underground lightning electromagnetic field	545
13.4	Lightning electromagnetic field calculation in presence of a lossy and horizontally stratified ground	548
13.4.1	Statement of the problem and derivation of the Green's functions for the electromagnetic field	549
13.4.2	Derivation of the lightning electromagnetic field	553
13.4.3	The reflection coefficient $R$	554
13.4.4	The effect of the stratified soil on the overground electromagnetic field	557
13.5	Conclusions	561
	References	561
<b>14</b>	<b>Measurements of lightning-generated electromagnetic fields</b>	<b>567</b>
14.1	Introduction	567
14.2	Electric field mill or generating voltmeter	567
14.3	Plate or whip antenna	568
14.3.1	Measurement of electric field	568
14.3.2	Measurement of the derivative of the electric field	573
14.4	Measurements of the three electric field components in space	574
14.5	Crossed loop antennas to measure the magnetic field	576
14.6	Magnetic field measurements using anisotropic magnetoresistive (AMR) sensors	578
14.7	Narrowband measurements	578
	References	580
<b>15</b>	<b>The Schumann resonances</b>	<b>583</b>
15.1	Introduction	583
15.2	Theoretical background	584
15.3	SR measurements	587
15.4	SR background observations of global lightning activity	588
15.5	SR transient measurements of global lightning activity	591
15.6	Using SR as a climate research tool	592
15.7	SR in transient luminous events (TLE) research	595
15.8	SR in extraterrestrial lightning research	597
15.9	Summary	598
	Acknowledgements	599
	References	599

<b>16</b>	<b>Lightning effects in the mesosphere and ionosphere</b>	<b>611</b>
16.1	Introduction	611
16.2	General phenomenology of TLEs	613
16.2.1	Phenomenology of sprites	613
16.2.2	Phenomenology of blue jets	614
16.2.3	Phenomenology of elves	615
16.3	General consideration of physical mechanisms and modellings	615
16.3.1	High-altitude electric fields induced by a lightning discharge	616
16.3.1.1	Electromagnetic pulse	617
16.3.1.2	Quasi-electrostatic fields	618
16.3.2	Heating of the ionosphere and neutral atmosphere	620
16.4	Physical mechanism of sprites	621
16.4.1	Thermal ionization and QE mechanism	621
16.4.2	Runaway mechanism	624
16.5	Elves and sprites	626
16.5.1	Blue jets	627
16.6	Unsolved problems	628
16.6.1	Polarity problem	629
16.6.2	Morphological changes of sprites	631
16.6.3	Lateral shift of a sprite from its parent lightning	634
16.6.4	Time delay effect	635
16.6.5	Fine structure of sprites	639
	References	640
<b>17</b>	<b>The effects of lightning on the ionosphere/magnetosphere</b>	<b>647</b>
17.1	Introduction	647
17.2	Lightning-induced whistlers in the ionosphere/magnetosphere	647
17.2.1	General description of whistlers	647
17.2.2	Theoretical background	649
17.2.2.1	Characterization of the ionosphere and magnetosphere	649
17.2.2.2	General equations	650
17.2.2.3	Special cases of longitudinal and perpendicular propagation and general oblique propagation	655
17.2.2.4	Whistler propagation, dispersion relation and the use of whistlers as a diagnostic tool of magnetospheric plasma	659
17.3	IAR	661
17.3.1	Brief history and general introduction	661
17.3.2	Observations and data processing	663
17.3.3	Seasonal and diurnal variations of the SRS parameters	666
17.3.4	SRS IAR and geomagnetic activity	669
17.3.5	Summary of observations at middle latitudes	671

17.3.6	Former generation mechanisms of IAR	671
17.3.7	Excitation of IAR by nearly thunderstorms	673
17.4	Summary of lightning effects onto the ionosphere/ magnetosphere	680
	References	681
<b>18</b>	<b>Interaction of lightning-generated electromagnetic fields with overhead and underground cables</b>	<b>687</b>
18.1	Introduction	687
18.2	Transmission line theory	688
18.3	Electromagnetic field interaction with overhead lines	690
18.3.1	Single-wire line above a perfectly conducting ground	690
18.3.2	Taylor, Satterwhite and Harrison model	690
18.3.3	Agrawal, Price and Gurbaxani model	691
18.3.4	Rachidi model	693
18.3.5	Inclusion of losses	694
18.3.6	Multiconductor lines	695
18.3.7	Coupling to complex networks	698
18.3.8	Frequency-domain solutions	698
18.3.9	Time-domain solutions	700
18.3.10	Application to lightning-induced voltages	702
18.3.10.1	Effect of Ground Losses on O vervoltages Due to a Direct Strike	702
18.3.10.2	Effect of Ground Losses on Induced O vervoltages	705
18.4	Electromagnetic field interaction with buried cables	707
18.4.1	Field-to-buried cables coupling equations	707
18.4.2	Frequency-domain solutions	710
18.4.3	Time-domain solutions	711
18.4.4	Lightning-induced disturbances in a buried cable	711
18.5	Conclusions	713
	Acknowledgements	714
	References	714
<b>19</b>	<b>Scale models and their application to the study of lightning transients in power systems</b>	<b>719</b>
19.1	Introduction	719
19.2	Basis of scale modelling	721
19.3	Simulation of the electromagnetic environment	723
19.3.1	Return stroke channel	724
19.3.2	Ground	727
19.3.3	Overhead lines	727
19.3.4	Transformers	728
19.3.5	Surge arresters	730
19.3.6	Buildings	733

19.4	Evaluation of lightning surges in power lines	733
19.4.1	Surges associated with direct strokes	735
19.4.2	Surges associated with indirect strokes	738
19.4.2.1	Validation of theoretical models	739
19.4.2.2	Analysis of complex situations	749
19.5	Conclusions	755
	Acknowledgements	756
	References	756
<b>20</b>	<b>Attachment of lightning flashes to grounded structures</b>	<b>765</b>
20.1	Introduction	765
20.2	Striking distance	767
20.3	Leader inception models	769
20.3.1	Critical radius and critical streamer length concepts	769
20.3.2	Rizk's generalized leader inception equation	770
20.3.3	Lalande's stabilization field equation	770
20.3.4	Leader inception model of Becerra and Cooray (SLIM)	771
20.4	Leader progression and attachment models	771
20.5	The potential of the stepped leader channel and the striking distance	774
20.5.1	Armstrong and Whitehead	774
20.5.2	Leader potential extracted from the charge neutralized by the return stroke	774
20.5.3	Striking distance based on the leader tip potential	776
20.6	Comparison of EGM against SLIM	777
20.7	Points where more investigations are needed	780
20.7.1	Orientation of the stepped leader	780
20.7.2	The orientation of the connecting leader	782
20.7.3	The connection between the leader potential and the return stroke current	782
20.7.4	Inclination of the leader channel	784
20.7.5	Main assumptions of SLIM	784
20.8	Concluding remarks	785
	References	785
<b>21</b>	<b>On the NO<sub>x</sub> generation in corona, streamer and low-pressure electrical discharges</b>	<b>789</b>
21.1	Introduction	789
21.2	Testing the theory using corona discharges	791
21.3	NO <sub>x</sub> generation in electron avalanches and its relationship to energy dissipation	791
21.4	NO <sub>x</sub> production in streamer discharges	792
21.5	Discussion and conclusions	794
	References	796

<b>22 On the NO<sub>x</sub> production by laboratory electrical discharges and lightning</b>	<b>799</b>
22.1 Introduction	799
22.2 NO <sub>x</sub> production by laboratory sparks	800
22.2.1 Radius of spark channels	800
22.2.2 The volume of air heated in a spark channel and its internal energy	802
22.2.3 NO <sub>x</sub> production in spark channels	803
22.2.4 Efficiency of NO <sub>x</sub> production in sparks with different current wave-shapes	804
22.2.5 NO <sub>x</sub> production in sparks as a function of energy	806
22.3 NO <sub>x</sub> production in discharges containing long-duration currents	808
22.4 NO <sub>x</sub> production in streamer discharges	808
22.5 NO <sub>x</sub> production in ground lightning flashes	809
22.5.1 The model of a ground lightning flash	809
22.5.2 NO <sub>x</sub> production in different processes in ground flashes	810
22.5.2.1 Leaders	810
22.5.2.2 Return strokes	814
22.5.2.3 M components and K processes	815
22.5.2.4 Continuing currents	816
22.5.2.5 NO <sub>x</sub> production in a typical negative ground flash	817
22.6 NO <sub>x</sub> production by cloud flashes	818
22.7 Global production of NO <sub>x</sub> by lightning flashes	820
22.8 Conclusions	822
Appendix 1	823
References	824
<b>23 High energetic radiation from thunderstorms and lightning</b>	<b>831</b>
23.1 Introduction	831
23.2 Observations	832
23.3 Runaway electrons	835
23.4 Monte Carlo simulations	837
23.5 Energy spectrum	842
23.6 RREA parameters from Monte Carlo simulations	844
23.7 Relativistic feedback	844
23.8 Theory and observations	846
23.9 Summary	848
Acknowledgements	849
References	849
<b>24 Excitation of visual sensory experiences by electromagnetic fields of lightning</b>	<b>855</b>
24.1 Introduction	855
24.2 Features of ball lightning	856
24.3 Alternative explanations	857

24.3.1	Visual sensations produced by the magnetic fields generated by lightning	857
24.3.2	Visual sensations produced by the epileptic seizures of the occipital lobe	858
24.3.2.1	Possible association with thunderstorms	860
24.4	Visual effects produced by energetic radiation	862
24.4.1	Induction of phosphenes by the energetic radiation of lightning and thunderstorms	864
24.4.1.1	Energetic electrons generated by leader steps	864
24.4.1.2	X-ray bursts from lightning	865
24.4.1.3	Terrestrial gamma rays	865
24.4.1.4	Possible effects inside airplanes	866
24.4.2	Concluding remarks concerning the possibility of phosphenes stimulation by energetic radiation of lightning and thunderstorms	866
24.5	Stimulation of phosphenes by Corona currents	866
24.6	Concluding remarks	867
	References	868
<b>25</b>	<b>Modelling lightning strikes to tall towers</b>	<b>873</b>
25.1	Introduction	873
25.2	Modelling lightning strikes to tall structures	873
25.2.1	Engineering models	874
25.2.1.1	Extension of engineering models based on a distributed source representation	874
25.2.1.2	Extension of engineering models based on a lumped series voltage source	876
25.2.1.3	On the representation of the elevated strike object	876
25.2.1.4	Current distribution along the channel as predicted by engineering models	877
25.2.1.5	Determination of reflection coefficients at the top and the bottom of the strike object	878
25.2.2	Electromagnetic models	880
25.2.3	Hybrid electromagnetic model	881
25.3	Electromagnetic field computation	881
25.3.1	Electromagnetic field expressions for a perfectly conducting ground	882
25.3.1.1	Turn-on term	884
25.3.1.2	Comparison between different engineering models	885
25.3.1.3	Effect of the tower	888
25.3.2	Electromagnetic field computation for a finitely conducting ground	888
25.3.2.1	Dedicated algorithms	888
25.3.2.2	Simplified approaches	889
25.3.2.3	Numerical methods	890

25.4	Review of lightning current data and associated electromagnetic fields	891
25.4.1	Experimental data	892
25.4.2	Data from short towers	893
25.4.3	Summary of Berger's data	894
25.4.4	Other data obtained using short towers ( $\leq 100$ m)	895
25.4.5	Data from tall towers	898
25.5	Summary	904
References		908
<b>Index</b>		<b>917</b>

---

## *Chapter 1*

# **Basic electromagnetic theory – A summary**

*Vernon Cooray<sup>1</sup>, Pasan Hettiarachchi<sup>1</sup> and Gerald Cooray<sup>2</sup>*

---

## **1.1 Introduction**

The goal of this chapter is to provide a summary of the basic concepts of electromagnetic theory as a complement to the subject matter, most of which is related to electromagnetism, discussed in this book. The chapter covers only the concepts that are necessary to understand the electromagnetics of lightning flashes.

## **1.2 The nomenclature**

**I** – Current, unit: Amperes (A)

**J** – Current density, unit: Amperes/metre<sup>2</sup> (A/m<sup>2</sup>)

**E** – Electric field intensity, unit: Volts/metre (V/m) (In this chapter this quantity is referred to as E-field.)

**D** – Electric flux density, unit: Coulombs/metre<sup>2</sup> (C/m<sup>2</sup>) (In this chapter this quantity is referred to as D-field.)

**H** – Magnetic field intensity, unit: Amperes/metre (A/m) (In this chapter this quantity is referred to as H-field.)

**B** – Magnetic flux density, unit: Tesla (T) or Webers/metre<sup>2</sup> (Wb/m<sup>2</sup>)  
(In this chapter this quantity is referred to as B-field.)

$\sigma$  – Conductivity, unit: Siemens/metre (S/m)

$\phi$  – Scalar potential, unit: Volts

**A** – Vector potential, unit: Tesla metre (Tm) or Webers/metre (Wb/m)

$\epsilon_0$  – Electrical permittivity of vacuum, unit: Farads/metre (F/m)

$\mu_0$  – Magnetic permeability of vacuum, unit: Henrys/metre (H/m)

$\epsilon_r$  – Relative dielectric constant, a ratio; no units

$\mu_r$  – Relative magnetic permeability, a ratio; no units

In this chapter, we consider homogeneous (no spatial variation in properties), isotropic (properties are rotation invariant) and linear mediums. If the medium is

<sup>1</sup>Uppsala University, Uppsala, Sweden

<sup>2</sup>Department of Clinical Neuroscience, Karolinska Institute, Stockholm, Sweden

## 2 Lightning electromagnetics

isotropic and linear, then one can write

$$\mathbf{D} = \epsilon_0 \epsilon_r \mathbf{E} \quad (1.1)$$

In a similar manner,  $\mathbf{B}$  and  $\mathbf{H}$  in an isotropic and linear medium is related by

$$\mathbf{B} = \mu_0 \mu_r \mathbf{H} \quad (1.2)$$

### 1.3 Coordinate systems

Electromagnetic theory is frequently described either in Cartesian, spherical or cylindrical coordinate systems. These systems together with the relevant three coordinates are shown in Figure 1.1. Unit vectors (vectors whose magnitude is unity; see the next section for definition) associated with these coordinates are denoted in this chapter by  $\mathbf{a}_x$ ,  $\mathbf{a}_y$  and  $\mathbf{a}_z$  in Cartesian coordinates;  $\mathbf{a}_r$ ,  $\mathbf{a}_\theta$  and  $\mathbf{a}_\phi$  in cylindrical coordinates and  $\mathbf{a}_r$ ,  $\mathbf{a}_\theta$  and  $\mathbf{a}_\phi$  in spherical coordinate system. In this chapter we will be using mainly the Cartesian coordinate system.

### 1.4 Important vector relationships

In electromagnetic theory, electric and magnetic fields are represented by vectors. The most important vector relationships are referred to in the following. As mentioned above, in this chapter unit vectors in the direction of  $x$ -,  $y$ - and  $z$ -axes are denoted by  $\mathbf{a}_x$ ,  $\mathbf{a}_y$  and  $\mathbf{a}_z$ . Thus, any three-dimensional vector, say  $\mathbf{P}$ , is defined by the equation

$$\mathbf{P} = p_x \mathbf{a}_x + p_y \mathbf{a}_y + p_z \mathbf{a}_z \quad (1.3)$$

where  $p_x$ ,  $p_y$  and  $p_z$  are the magnitudes of the component of the vector in  $x$ -,  $y$ - and  $z$ -directions. The magnitude of this vector is

$$|P| = \sqrt{p_x^2 + p_y^2 + p_z^2} \quad (1.4)$$

A unit vector in the direction of  $\mathbf{P}$  is then given by

$$\mathbf{a}_P = \frac{\mathbf{P}}{\sqrt{p_x^2 + p_y^2 + p_z^2}} \quad (1.5)$$

Note that the magnitude of  $\mathbf{a}_P$ , i.e.  $|\mathbf{a}_P| = 1$ .

#### 1.4.1 The scalar product of two vectors

The scalar product of two vectors are given by

$$\mathbf{P} \cdot \mathbf{Q} = |P||Q|\cos \theta_{PQ} \quad (1.6)$$

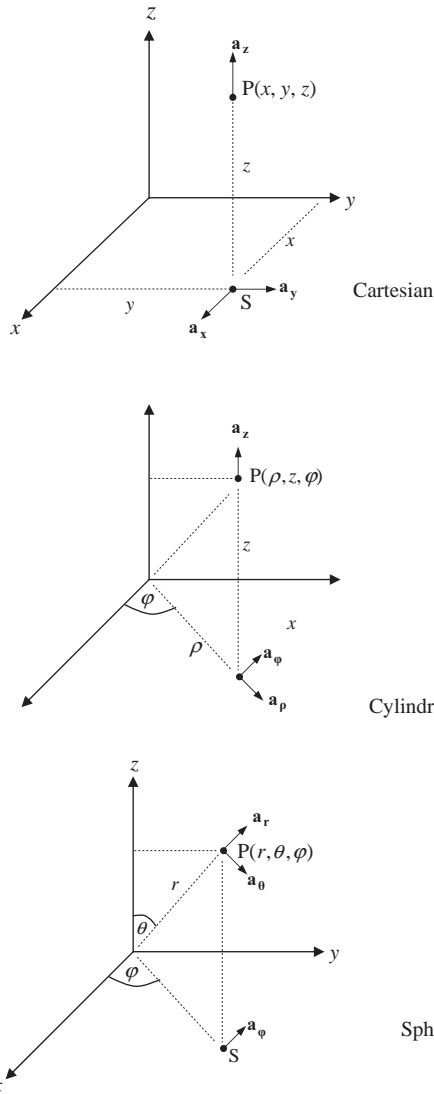


Figure 1.1 Pictorial definition of unit vectors and coordinates in different coordinate systems

where  $\theta_{PQ}$  is the angle between them. Thus, it follows that

$$\mathbf{P} \cdot \mathbf{Q} = \mathbf{Q} \cdot \mathbf{P} \quad (1.7)$$

Let us now resolve the two vectors into its components in the  $x$ -,  $y$ - and  $z$ -directions and perform the scalar product. The result would be the following:

$$\mathbf{P} \cdot \mathbf{Q} = (p_x \mathbf{a}_x + p_y \mathbf{a}_y + p_z \mathbf{a}_z) \cdot (q_x \mathbf{a}_x + q_y \mathbf{a}_y + q_z \mathbf{a}_z) \quad (1.8)$$

## 4 Lightning electromagnetics

Performing the scalar product term by term and noting that  $\mathbf{a}_x \cdot \mathbf{a}_y = 0$ ,  $\mathbf{a}_x \cdot \mathbf{a}_z = 0$  and  $\mathbf{a}_y \cdot \mathbf{a}_z = 0$  (because the angle between these vectors is equal to  $90^\circ$ ), one obtains

$$\mathbf{P} \cdot \mathbf{Q} = p_x q_x + p_y q_y + p_z q_z \quad (1.9)$$

Note also that

$$\mathbf{P} \cdot \mathbf{P} = |P|^2 \quad (1.10)$$

One can use the scalar product to find the component of a vector in a given direction. For example, the component of vector  $\mathbf{P}$  in the direction specified by the unit vector  $\mathbf{a}$  is

$$\mathbf{P} \cdot \mathbf{a} = |P| |a| \cos \theta_{Pa} = |P| \cos \theta_{Pa} \quad (1.11)$$

where  $\theta_{Pa}$  is the smaller of the two angles between  $\mathbf{P}$  and  $\mathbf{a}$ .

### 1.4.2 The vector product of two vectors

The vector product of two vectors are defined by the equation:

$$\mathbf{P} \times \mathbf{Q} = |P| |Q| \sin \theta_{PQ} \mathbf{a}_n \quad (1.12)$$

In the above equation,  $\theta_{PQ}$  is the small angle between  $\mathbf{P}$  and  $\mathbf{Q}$  and  $\mathbf{a}_n$  is a vector that is perpendicular to both  $\mathbf{P}$  and  $\mathbf{Q}$ . The direction of  $\mathbf{a}_n$  is given by the right-handed screw rule. Namely, rotate a right-handed screw from  $\mathbf{P}$  to  $\mathbf{Q}$  around the angle  $\theta_{PQ}$  the direction of motion of the screw defines the positive direction of  $\mathbf{a}_n$ .

Let us now take the vector product of the two vectors resolved into its components in the direction of  $x$ ,  $y$  and  $z$ . We can then write

$$\mathbf{P} \times \mathbf{Q} = (p_x \mathbf{a}_x + p_y \mathbf{a}_y + p_z \mathbf{a}_z) \times (q_x \mathbf{a}_x + q_y \mathbf{a}_y + q_z \mathbf{a}_z) \quad (1.13)$$

After taking the vector product of each individual term, we find

$$\begin{aligned} \mathbf{P} \times \mathbf{Q} = & p_x q_x (\mathbf{a}_x \times \mathbf{a}_x) + p_x q_y (\mathbf{a}_x \times \mathbf{a}_y) + p_x q_z (\mathbf{a}_x \times \mathbf{a}_z) + p_y q_x (\mathbf{a}_y \times \mathbf{a}_x) + p_y q_y (\mathbf{a}_y \times \mathbf{a}_y) \\ & + p_y q_z (\mathbf{a}_y \times \mathbf{a}_z) + p_z q_x (\mathbf{a}_z \times \mathbf{a}_x) + p_z q_y (\mathbf{a}_z \times \mathbf{a}_y) + p_z q_z (\mathbf{a}_z \times \mathbf{a}_z) \end{aligned} \quad (1.14)$$

Noting that  $\mathbf{a}_x \times \mathbf{a}_x = 0$ ,  $\mathbf{a}_y \times \mathbf{a}_y = 0$  and  $\mathbf{a}_z \times \mathbf{a}_z = 0$  (because the angle between them is zero), one obtains

$$\mathbf{P} \times \mathbf{Q} = (p_y q_z - p_z q_y) \mathbf{a}_x + (p_z q_x - p_x q_z) \mathbf{a}_y + (p_x q_y - p_y q_x) \mathbf{a}_z \quad (1.15)$$

This can be obtained by the determinant of the following matrix:

$$\mathbf{P} \times \mathbf{Q} = \begin{vmatrix} \mathbf{a}_x & \mathbf{a}_y & \mathbf{a}_z \\ p_x & p_y & p_z \\ q_x & q_y & q_z \end{vmatrix} \quad (1.16)$$

### 1.4.3 Vector field

In a vector field, every point in space is associated with the field under consideration. The field can be either electric or magnetic in our case. Since the field is defined by a vector, we have to define the value of this vector in every point in space. The field at any general point  $(x, y, z)$  is given by

$$\mathbf{F} = f_x(x, y, z)\mathbf{a}_x + f_y(x, y, z)\mathbf{a}_y + f_z(x, y, z)\mathbf{a}_z \quad (1.17)$$

This is called a vector field. As one can see  $\mathbf{F}$  defines the field at every point in space and how it varies from one point to another depends on the functions  $f_x, f_y$  and  $f_z$ .

### 1.4.4 The nabla operator and its operations

The nabla operator is defined in Cartesian coordinates by

$$\nabla = \mathbf{a}_x \frac{\partial}{\partial x} + \mathbf{a}_y \frac{\partial}{\partial y} + \mathbf{a}_z \frac{\partial}{\partial z} \quad (1.18)$$

In cylindrical and spherical coordinates it is given by

$$\nabla = \mathbf{a}_\rho \frac{\partial}{\partial \rho} + \mathbf{a}_\phi \frac{1}{\rho} \frac{\partial}{\partial \phi} + \mathbf{a}_z \frac{\partial}{\partial z} \quad (1.19)$$

and

$$\nabla = \mathbf{a}_r \frac{\partial}{\partial r} + \mathbf{a}_\theta \frac{1}{r} \frac{\partial}{\partial \theta} + \mathbf{a}_\phi \frac{1}{r \sin \theta} \frac{\partial}{\partial \phi} \quad (1.20)$$

respectively. The nabla operator can operate on either a scalar function or a vector function. In the later case it could operate as either a scalar product or a vector product.

#### 1.4.4.1 The gradient of a scalar function

Let us consider a scalar function  $S(x, y, z)$ . Consider the operation:

$$\nabla S(x, y, z) = \mathbf{a}_x \frac{\partial}{\partial x} S(x, y, z) + \mathbf{a}_y \frac{\partial}{\partial y} S(x, y, z) + \mathbf{a}_z \frac{\partial}{\partial z} S(x, y, z) \quad (1.21)$$

Observe that when the nabla operator operates on a scalar function it gives rise to a vector. The resulting vector is called the gradient of the scalar function  $S(x, y, z)$  and is denoted by  $\text{Grad } S$ . We can also define the same scalar function either in cylindrical or in spherical coordinate systems. In cylindrical coordinates  $\text{Grad } S$  is given by

$$\nabla S(\rho, \varphi, z) = \mathbf{a}_\rho \frac{\partial}{\partial \rho} S(\rho, \varphi, z) + \mathbf{a}_\phi \frac{1}{\rho} \frac{\partial}{\partial \varphi} S(\rho, \varphi, z) + \mathbf{a}_z \frac{\partial}{\partial z} S(\rho, \varphi, z) \quad (1.22)$$

## 6 Lightning electromagnetics

and in the spherical coordinates it is given by

$$\nabla S(r, \theta, \varphi) = \mathbf{a}_r \frac{\partial}{\partial r} S(r, \theta, \varphi) + \mathbf{a}_\theta \frac{1}{r} \frac{\partial}{\partial \theta} S(r, \theta, \varphi) + \mathbf{a}_\varphi \frac{1}{r \sin \theta} \frac{\partial}{\partial \varphi} S(r, \theta, \varphi) \quad (1.23)$$

### 1.4.4.2 The divergence of a vector field

The scalar product of the nabla vector with a vector field  $\mathbf{F}$  is defined as the divergence of that vector field. In Cartesian coordinates it becomes

$$\nabla \cdot \mathbf{F} = \frac{\partial}{\partial x} f_x(x, y, z) + \frac{\partial}{\partial y} f_y(x, y, z) + \frac{\partial}{\partial z} f_z(x, y, z) \quad (1.24)$$

Note that this operation results in a scalar function and it is denoted by  $\text{Div } \mathbf{F}$ .

Now if we take the divergence of the vector field given by (1.21) (i.e.  $\text{Grad } S$ ), we obtain

$$\nabla \cdot \nabla S(x, y, z) = \frac{\partial^2}{\partial x^2} S(x, y, z) + \frac{\partial^2}{\partial y^2} S(x, y, z) + \frac{\partial^2}{\partial z^2} S(x, y, z) \quad (1.25)$$

This is denoted by  $\nabla^2 S(x, y, z)$ . This is called the Laplacian of the scalar function  $S$ . One can also perform the operation  $(\nabla \cdot \nabla) \mathbf{F}$ . This results in

$$\nabla^2 \mathbf{F}(x, y, z) = \frac{\partial^2}{\partial x^2} \mathbf{F}(x, y, z) + \frac{\partial^2}{\partial y^2} \mathbf{F}(x, y, z) + \frac{\partial^2}{\partial z^2} \mathbf{F}(x, y, z) \quad (1.26)$$

This is called the Laplacian of the vector field  $\mathbf{F}$ . The divergence and the Laplacian in cylindrical coordinates are given by

$$\nabla \cdot \mathbf{F} = \frac{1}{\rho} \frac{\partial}{\partial \rho} \rho f_\rho(\rho, \varphi, z) + \frac{1}{\rho} \frac{\partial}{\partial \varphi} f_\varphi(\rho, \varphi, z) + \frac{\partial}{\partial z} f_z(\rho, \varphi, z) \quad (1.27)$$

$$\nabla \cdot \nabla S(\rho, \varphi, z) = \frac{1}{\rho} \frac{\partial}{\partial \rho} \left\{ \rho \frac{\partial S(\rho, \varphi, z)}{\partial \rho} \right\} + \frac{1}{\rho^2} \frac{\partial^2}{\partial \varphi^2} S(\rho, \varphi, z) + \frac{\partial^2}{\partial z^2} S(\rho, \varphi, z) \quad (1.28)$$

and in spherical coordinates they are given by

$$\nabla \cdot \mathbf{F} = \frac{1}{r^2} \frac{\partial}{\partial r} r^2 f_r(r, \theta, \varphi) + \frac{1}{r \sin \theta} \frac{\partial}{\partial \theta} \sin \theta f_\theta(r, \theta, \varphi) + \frac{1}{r \sin \theta} \frac{\partial}{\partial \varphi} f_\varphi(r, \theta, \varphi) \quad (1.29)$$

$$\begin{aligned} \nabla \cdot \nabla S(r, \theta, \varphi) &= \frac{1}{r^2} \frac{\partial}{\partial r} \left\{ r^2 \frac{\partial S(r, \theta, \varphi)}{\partial r} \right\} + \frac{1}{r^2 \sin \theta} \frac{\partial}{\partial \theta} \left\{ \sin \theta \frac{\partial S(r, \theta, \varphi)}{\partial \theta} \right\} \\ &\quad + \frac{1}{r^2 \sin^2 \theta} \frac{\partial^2 S(r, \theta, \varphi)}{\partial \varphi^2} \end{aligned} \quad (1.30)$$

In the above equations  $f_\rho, f_\varphi, f_z$  and  $f_r, f_\theta, f_\varphi$  are, respectively, the components of  $\mathbf{F}$  in cylindrical and spherical coordinate systems.

#### 1.4.4.3 The curl of a vector field

The vector product of the nabla operator with another vector or a vector field, say  $\mathbf{F}$ , is called the curl of that vector field. It is denoted by  $\text{Curl } \mathbf{F}$ . Using the technique described previously to obtain the vector product,  $\text{Curl } \mathbf{F}$  in Cartesian coordinates is given by

$$\text{Curl } \mathbf{F} = \nabla \times \mathbf{F} = \begin{vmatrix} \mathbf{a}_x & \mathbf{a}_y & \mathbf{a}_z \\ \frac{\partial}{\partial x} & \frac{\partial}{\partial y} & \frac{\partial}{\partial z} \\ f_x & f_y & f_z \end{vmatrix} \quad (1.31)$$

After expanding the above, we obtain

$$\text{Curl } \mathbf{F} = \mathbf{a}_x \left[ \frac{\partial f_z}{\partial y} - \frac{\partial f_y}{\partial z} \right] + \mathbf{a}_y \left[ \frac{\partial f_x}{\partial z} - \frac{\partial f_z}{\partial x} \right] + \mathbf{a}_z \left[ \frac{\partial f_y}{\partial x} - \frac{\partial f_x}{\partial y} \right] \quad (1.32)$$

In cylindrical coordinates it is given by

$$\text{Curl } \mathbf{F} = \nabla \times \mathbf{F} = \frac{1}{\rho} \begin{vmatrix} \mathbf{a}_\rho & \rho \mathbf{a}_\varphi & \mathbf{a}_z \\ \frac{\partial}{\partial \rho} & \frac{\partial}{\partial \varphi} & \frac{\partial}{\partial z} \\ f_\rho & f_\varphi & f_z \end{vmatrix} \quad (1.33)$$

after expanding the matrix, we obtain

$$\text{Curl } \mathbf{F} = \mathbf{a}_\rho \frac{1}{\rho} \left[ \frac{\partial f_z}{\partial \varphi} - \frac{\partial f_\varphi}{\partial z} \right] + \mathbf{a}_\varphi \left[ \frac{\partial f_\rho}{\partial z} - \frac{\partial f_z}{\partial \rho} \right] + \mathbf{a}_z \frac{1}{\rho} \left[ \frac{\partial f_\varphi}{\partial \rho} - \frac{\partial f_\rho}{\partial \varphi} \right] \quad (1.34)$$

In spherical coordinates it is given by

$$\text{Curl } \mathbf{F} = \nabla \times \mathbf{F} = \frac{1}{r^2 \sin \theta} \begin{vmatrix} \mathbf{a}_r & r \mathbf{a}_\theta & r \sin \theta \mathbf{a}_\varphi \\ \frac{\partial}{\partial r} & \frac{\partial}{\partial \theta} & \frac{\partial}{\partial \varphi} \\ f_r & r f_\theta & r \sin \theta f_\varphi \end{vmatrix} \quad (1.35)$$

Expanding the matrix, we obtain

$$\begin{aligned} \text{Curl } \mathbf{F} = \mathbf{a}_r & \frac{1}{r^2 \sin \theta} \left[ \frac{\partial(r f_\varphi r \sin \theta)}{\partial \theta} - \frac{\partial(r f_\theta)}{\partial \varphi} \right] + \mathbf{a}_\theta \frac{1}{r} \left[ \frac{1}{\sin \theta} \frac{\partial f_r}{\partial \varphi} - \frac{\partial(r f_\varphi)}{\partial r} \right] \\ & + \mathbf{a}_\varphi \frac{1}{r} \left[ \frac{\partial(r f_\theta)}{\partial r} - \frac{\partial f_r}{\partial \theta} \right] \end{aligned} \quad (1.36)$$

### 1.4.5 Important vector identities

In handling the equations of electromagnetic theory, the following three vector identities related will be used in several places in this chapter. They are

$$\nabla \times (\nabla \times \mathbf{F}) = \text{Grad}(\text{Div } \mathbf{F}) - \nabla^2 \mathbf{F} \quad (1.37)$$

$$\text{Div} (\mathbf{F} \times \mathbf{G}) = -\mathbf{F} \cdot (\text{Curl } \mathbf{G}) + \mathbf{G} \cdot (\text{Curl } \mathbf{F}) \quad (1.38)$$

$$\text{Grad} (S) \times \mathbf{F} = \text{Curl} (S\mathbf{F}) - S\text{Curl } \mathbf{F} \quad (1.39)$$

Note that in the above equation  $S$  is a scalar function.

### 1.4.6 Relationship between the curl of a vector field and the line integral of that vector field around a closed path

Consider an infinitesimally small area  $ds$  in a vector field. This area can be defined as a vector  $\mathbf{ds}$  with magnitude  $|ds|$ . The direction of the vector is defined as the direction of the normal to the area. Now, consider the line integral of vector field  $\mathbf{F}$  performed around the outer boundary of the area  $ds$ . This line integral is denoted by

$$\text{Line integral} = \oint_l \mathbf{F} \cdot d\mathbf{l} \quad (1.40)$$

The circle on the integral denotes that the path is closed and the symbol  $l$  stands for line integral. It can be shown that as  $ds$  goes to zero the ratio  $\oint \mathbf{F} \cdot d\mathbf{l} / |ds|$  approaches the component of  $\text{Curl } \mathbf{F}$  in the direction of  $\mathbf{ds}$ . That is

$$\frac{\oint \mathbf{F} \cdot d\mathbf{l}}{|ds|} \rightarrow \text{Curl } \mathbf{F} \cdot \mathbf{ds} \text{ as } |ds| \rightarrow 0 \quad (1.41)$$

The positive direction of  $\mathbf{ds}$  is given by the right-handed screw rule as follows. Rotate a right-handed screw in the circular direction in which the line integral is performed. The direction of motion of the screw defines the positive direction of  $\mathbf{ds}$ . The above relationship shows that  $\text{Curl } \mathbf{F} \cdot \mathbf{ds}$  gives the value of the line integral of  $\mathbf{F}$  performed along the periphery of the infinitesimal area  $\mathbf{ds}$ .

### 1.4.7 The flux of a vector field through a surface

Let us denote a surface by  $S$ . The flux of  $\mathbf{F}$  going through this area is given by the integration:

$$\text{Flux} = \int_S \mathbf{F} \cdot \mathbf{ds} \quad (1.42)$$

The subscript  $S$  on the integration sign indicates that it is a surface integral. What was done above is to divide the surface into infinitesimal areas  $\mathbf{ds}$  and summing up

the contribution of  $\mathbf{F} \cdot \mathbf{ds}$  (which is the flux of  $\mathbf{F}$  through the infinitesimal area) from all the infinitesimal areas on the surface  $S$ .

### 1.4.8 Relationship between the divergence of a vector field and the flux of that vector field through a closed surface

Consider a small volume  $dv$  located at  $\mathbf{P}$ . This volume is bounded by a closed surface  $S$ . The flux of  $\mathbf{F}$  coming out of the closed surface is

$$\text{Flux of } \mathbf{F} \text{ coming out from a closed surface } S = \oint_S \mathbf{F} \cdot \mathbf{ds} \quad (1.43)$$

where  $\mathbf{ds}$  is an infinitesimal area on the closed surface  $S$ . The circle on the integral sign indicates that the surface is closed. The positive direction of  $\mathbf{ds}$  is defined as the outward normal to the closed surface at the point of interest. One can show that as the volume  $dv$  approaches zero the quantity  $\oint_S \mathbf{F} \cdot \mathbf{ds}/dv$  approaches the divergence of the vector field at point  $\mathbf{P}$ . That is

$$\frac{\oint_S \mathbf{F} \cdot \mathbf{ds}}{\Delta v} \rightarrow \text{Div } \mathbf{F} \text{ as } \Delta v \rightarrow 0 \quad (1.44)$$

In other words, if one considers an infinitesimal volume  $dv$  in a vector field, the quantity  $\text{Div } \mathbf{F} dv$  gives the flux of  $\mathbf{F}$  out of the infinitesimal volume.

### 1.4.9 Divergence theorem

The divergence theorem connects a volume integral of a vector field to a surface integral over the surface that bounds the volume. According to the divergence theorem

$$\int_V \text{Div } \mathbf{F} dv = \oint_S \mathbf{F} \cdot \mathbf{ds} \quad (1.45)$$

The symbol  $v$  on the integration sign indicates that it is a volume integral. Let us divide the volume into a large number of infinitesimal volumes. Now, calculate the divergence of  $\mathbf{F}$  at the location of each of these infinitesimal volumes and multiply that with the value of the infinitesimal volume  $dv$ . According to the above theorem, the sum of these products is equal to the flux of the vector field coming out of the surface bounding the volume. This theorem can be interpreted physically as follows. Observe that according to (1.44) the quantity  $\text{Div } \mathbf{F} dv$  is the flux of  $\mathbf{F}$  coming out of the infinitesimal volume  $dv$ . Thus, the left-hand side of (1.45) sums up the total flux of  $\mathbf{F}$  generated inside the volume. This quantity must be equal to the total flux of  $\mathbf{F}$  leaving the volume through the closed surface bounding this volume. This is exactly what the right-hand side of the equation says.

Using the divergence theorem one can convert a volume integral to a surface integral. This is a useful theorem in many branches of physics including electromagnetic theory.

### 1.4.10 Stokes theorem

Stokes theorem provides a relationship between a line integral of a vector field around a closed path to a surface integral of the curl of that vector field over a surface bounded by the closed path. Note that there is infinite number of surfaces bounded by that path and the relationship given below is valid for any of those surfaces. According to Stokes theorem

$$\oint_s \text{Curl } \mathbf{F} \cdot d\mathbf{s} = \oint_l \mathbf{F} \cdot d\mathbf{l} \quad (1.46)$$

The positive direction of  $d\mathbf{s}$  in calculating the flux of  $\text{Curl } \mathbf{F}$  in the above equation is given by the right-handed screw rule with the circular direction of rotation of the screw is given by the direction in which the line integral is performed.

Note that according to 1.41,  $\text{Curl } \mathbf{F} \cdot d\mathbf{s}$  is nothing but the integral of  $\mathbf{F}$  performed around the outer boundary of the infinitesimal area  $ds$ . As you sum up the contribution from each of the infinitesimal surface areas, the contributions from adjacent areas cancel out (note that the integral is performed in the same circular direction in each of the areas) leaving behind the line integral of  $\mathbf{F}$  around the boundary of the surface under consideration. This is exactly what the right-hand side of the integral says.

## 1.5 Static electric fields

### 1.5.1 Coulomb's law

This law specifies the force between two charges. Consider two charges  $q_1$  and  $q_s$  located in vacuum as shown in Figure 1.2. The location of the charges  $q_1$  and  $q_s$  are defined by the vectors  $\mathbf{R}_1$  and  $\mathbf{R}_s$ . The vector  $\mathbf{R}_{1s}$  defines the vector joining the two charges as shown in the Figure 1.2. According to Coulomb's law, the force on the test charge  $q_s$  caused by the charge  $q_1$  is given by

$$\mathbf{F} = \frac{q_1 q_s}{4\pi\epsilon_0 |\mathbf{R}_{1s}|^2} \mathbf{a}_{1s} \quad (1.47)$$

$$\mathbf{a}_{1s} = \frac{\mathbf{R}_{1s}}{|\mathbf{R}_{1s}|} = \frac{\mathbf{R}_s - \mathbf{R}_1}{|\mathbf{R}_s - \mathbf{R}_1|} \quad (1.48)$$

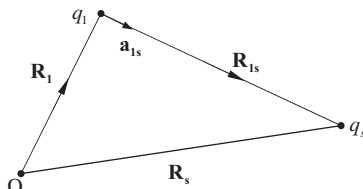


Figure 1.2 Definition of vectors used in defining Coulombs law (equation 5.1)

Note that the force is directed along the line joining the two charges. The E-field,  $\mathbf{E}$ , at point  $\mathbf{P}$  (shown in the Figure 1.2) due to charge  $q_1$  is defined as the force per unit charge at point  $\mathbf{P}$  as the magnitude of the test charge goes to zero. The last statement is necessary to guarantee that the test charge  $q_s$  will not disturb the electric field. Thus, the E-field at point  $\mathbf{P}$  (in vacuum) produced by the charge  $q_1$  is given by

$$\mathbf{E} = \frac{q_1 q_s}{4\pi\epsilon_0 q_s |R_{1s}|^2} \mathbf{a}_{1s} \text{ as } q_s \rightarrow 0 \quad (1.49)$$

In the case of several charges, the electric field produced by all the charges is the vector sum of the electric fields produced by individual charges. This is called the principle of superposition.

Consider a charge distribution in space defined by the volume charge density  $\rho$  that may vary from one point to another in space. Consider a small volume located at the point defined by the vector  $\mathbf{r}_0$  (see Figure 1.3). The charge density at this point is  $\rho(r_0)$ . The E-field produced by this element at point of observation  $\mathbf{P}$  is given by

$$d\mathbf{E}(r) = \frac{\rho_v(r_0) \cdot dv}{4\pi\epsilon_0 |\mathbf{r} - \mathbf{r}_0|^2} \cdot \frac{\mathbf{r} - \mathbf{r}_0}{|\mathbf{r} - \mathbf{r}_0|} \quad (1.50)$$

Then the total E-field at point  $\mathbf{P}$  is given by

$$\mathbf{E}(r) = \int \frac{\rho_v(r_0) \cdot dv}{4\pi\epsilon_0 |\mathbf{r} - \mathbf{r}_0|^2} \cdot \frac{\mathbf{r} - \mathbf{r}_0}{|\mathbf{r} - \mathbf{r}_0|} \quad (1.51)$$

In writing down the above equation, we have assumed that the charges and the point of observation were located in vacuum. If they are located in a homogeneous and isotropic dielectric medium with relative dielectric constant  $\epsilon_r$ , the  $\epsilon_0$  in the above equations has to be replaced by  $\epsilon_r \epsilon_0$ .

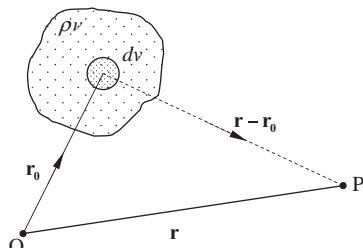


Figure 1.3 Vector notation used in defining the electric field at point  $P$  due to a volume charge distribution (equations 1.5.0 and 1.5.1)

### 1.5.2 Electric field produced by static charges is a conservative field

The nature of the electric field produced by static charges is such that the work done on a point charge moving it around a closed path located in such an electric field is equal to zero. Since the work done  $W$  in moving a charge  $q$  around a closed path is just the charge times the line integral of the electric field around the closed path, one can write

$$W = -q \oint_l \mathbf{E} \cdot d\mathbf{l} = 0 \quad (1.52)$$

Since  $W=0$  one can conclude that

$$\oint_l \mathbf{E} \cdot d\mathbf{l} = 0 \quad (1.53)$$

A field that satisfies the above condition is called a conservative field. One can also infer from the above condition that the work done in moving a charge from one point to another point in an electric field is independent of that path. Note that (1.53) provides us with information concerning static electric fields in an integral form. It gives you information concerning the spatial variation in the static electric field. But one can combine this equation together with Stokes theorem to obtain information concerning the electric field at a given point. Now, according to the Stokes theorem we can write

$$\oint_l \mathbf{E} \cdot d\mathbf{l} = \int_s (\text{Curl } \mathbf{E}) \cdot d\mathbf{s} \quad (1.54)$$

Since  $\oint_l \mathbf{E} \cdot d\mathbf{l} = 0$  this indicates that

$$\int_s (\text{Curl } \mathbf{E}) \cdot d\mathbf{s} = 0 \quad (1.55)$$

The above is true for any surface. Thus, it implies that

$$\text{Curl } \mathbf{E} = 0 \quad (1.56)$$

for the electric fields produced by static charges. Equation (1.56) provides us with information concerning the static electric field at a given point. However, both (1.53) and (1.56) convey the same information.

### 1.5.3 Gauss's law

Consider a closed volume in vacuum where there is an electric field. This volume is bounded by a closed surface  $S$ . The total flux of the E-field coming out of this closed surface is

$$\text{Flux out of the closed surface} = \oint_S \mathbf{E} \cdot d\mathbf{s} \quad (1.57)$$

In the above integration, the positive direction of  $d\mathbf{s}$  is defined as the outward normal to the surface at the point of interest. According to Gauss's law, the total flux of the E-field coming out of a closed surface is equal to the total charge located inside the closed surface divided by  $\epsilon_0$ . That is

$$\oint_S \mathbf{E} \cdot d\mathbf{s} = \frac{Q}{\epsilon_0} \quad (1.58)$$

The same equation can be written as

$$\oint_S \mathbf{D} \cdot d\mathbf{s} = Q \quad (1.59)$$

where  $\mathbf{D}$  is the electric flux density. In the case that the volume under consideration is inside a dielectric medium with relative dielectric constant  $\epsilon_r$ , (1.58) becomes

$$\oint_S \mathbf{E} \cdot d\mathbf{s} = \frac{Q}{\epsilon_r \epsilon_0} \quad (1.60)$$

However, (1.59) remains the same inside a dielectric medium. Now, the total charge inside a volume can be obtained by integrating the volume charge density  $\rho_v$  over the whole volume. That is

$$Q = \int_V \rho_v dv \quad (1.61)$$

With this expression for the total charge in the volume, (1.58) can be written as

$$\oint_S \mathbf{E} \cdot d\mathbf{s} = \frac{1}{\epsilon_0} \int_V \rho_v dv \quad (1.62)$$

Now, according to the divergence theorem

$$\oint_S \mathbf{E} \cdot d\mathbf{s} = \int_V \text{Div } \mathbf{E} dv \quad (1.63)$$

## 14 Lightning electromagnetics

substituting for the left-hand side from (1.62), we obtain

$$\int_v \operatorname{Div} \mathbf{E} dv = \frac{1}{\epsilon_0} \int_v \rho_v dv \quad (1.64)$$

Since this is true for any volume, we can conclude that in vacuum (or in air)

$$\operatorname{Div} \mathbf{E} = \frac{\rho_v}{\epsilon_0} \quad (1.65)$$

If the region is inside a dielectric medium, then  $\epsilon_0$  has to be replaced by  $\epsilon_0 \epsilon_r$ .

### 1.5.4 Electric scalar potential

The work done by an external agent against the electric forces to move a point positive charge from point  $P1$  to  $P2$  in an electric field is given by

$$W = - \int_{P1}^{P2} q \mathbf{E} \cdot d\mathbf{l} \quad (1.66)$$

We have seen earlier that for the E-field produced by static charges

$$\operatorname{Curl} \mathbf{E} = 0 \quad (1.67)$$

This indicates that we can express the electric field as the gradient of a scalar function. Let us denote this scalar function by  $\phi$ . Let us express the E-field as

$$\mathbf{E} = -\operatorname{Grad} \phi \quad (1.68)$$

This is in agreement with (1.67) because  $\operatorname{Curl}(\operatorname{Grad} \phi) = 0$ . The function  $\phi$ , which is a scalar function of location, is called the scalar potential. Substituting this expression for the E-field in (1.66), we obtain the work done by an external agent to move the charge  $q$  from  $P1$  to  $P2$  as

$$W = \int_{P1}^{P2} q \operatorname{Grad} \phi(r) \cdot d\mathbf{l} \quad (1.69)$$

Note that by denoting the scalar potential as  $\phi(r)$ , we are indicating that scalar potential depends on the location under consideration. The above equation can be written as

$$W = q \int_{P1}^{P2} d\phi(r) = q\{\phi(r_2) - \phi(r_1)\} \quad (1.70)$$

In the above equation,  $r_1$  and  $r_2$  represent the location of the points  $P1$  and  $P2$  respectively. The quantity  $W/q$  is called the potential difference between the two points  $P2$  and  $P1$ . If the point  $P1$  is at infinity where we define the scalar potential to be zero, then

$$\frac{W}{q} = - \int_{\infty}^{P2} \mathbf{E} \cdot d\mathbf{l} = \int_{\infty}^{P2} d\phi(r) = \phi(r_2) \quad (1.71)$$

In the above equation,  $W/q$  is the work done by an external agent against the electrical forces to move a unit point charge from infinity to the position  $P2$ . The function  $\phi(r_2)$  is called the potential at point  $P2$ .

Consider a point charge  $Q$  located at the origin O. The E-field produced by this point charge at any point  $P$  is given by

$$\mathbf{E} = \frac{Q}{4\pi\epsilon_0 r^2} \mathbf{a}_r \quad (1.72)$$

where  $\mathbf{a}_r$  is a unit vector in the direction of OP. The potential at point  $\mathbf{P}$  due to the point charge  $Q$  is given by

$$\phi = \frac{Q}{4\pi\epsilon_0 r} \quad (1.73)$$

where the two quantities (i.e.  $\mathbf{E}$  and  $\phi$ ) are connected by  $\mathbf{E} = -\text{Grad } \phi$ . Note also that the unit of potential is joules per coulomb. Using (1.73), the potential due to a charge distribution (see Figure 1.4) can be written as

$$\phi = \int_v \frac{\rho_v(r) dv}{4\pi\epsilon_0 r} \quad (1.74)$$

In the above equation  $\rho_v(r)$  is the volume charge density.

### 1.5.5 Poisson and Laplace equations

Let us write  $\mathbf{E} = -\text{Grad } \phi$  separated into three components in Cartesian coordinates. That is

$$\mathbf{E} = - \frac{\partial \phi}{\partial x} \mathbf{a}_x - \frac{\partial \phi}{\partial y} \mathbf{a}_y - \frac{\partial \phi}{\partial z} \mathbf{a}_z \quad (1.75)$$

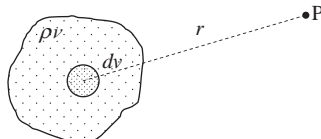


Figure 1.4 Geometry pertinent to the definition of potential at point  $P$  due to a volume charge distribution (equation 1.74)

Taking the divergence of the above, we obtain

$$\text{Div } \mathbf{E} = -\frac{\partial^2 \phi}{\partial x^2} - \frac{\partial^2 \phi}{\partial y^2} - \frac{\partial^2 \phi}{\partial z^2} \quad (1.76)$$

Since  $\text{Div } \mathbf{E} = -\rho_v/\epsilon_0$  in vacuum we find

$$\frac{\partial^2 \phi}{\partial x^2} + \frac{\partial^2 \phi}{\partial y^2} + \frac{\partial^2 \phi}{\partial z^2} = \frac{-\rho_v}{\epsilon_0} \quad (1.77)$$

This equation is called the Poisson's equation. The solution of electrostatic problems involves solving this equation with the given boundary conditions. Another important feature of this equation is that its solution is unique. That means, for a given set of boundary conditions only one solution exists to the Poisson's equation. Thus if one can find a solution of (1.77) that satisfies the specified boundary conditions by any means (even including guessing), then that solution is the correct one. In charge-free region this equation reduces to

$$\frac{\partial^2 \phi}{\partial x^2} + \frac{\partial^2 \phi}{\partial y^2} + \frac{\partial^2 \phi}{\partial z^2} = 0 \quad (1.78)$$

Equation (1.78) is called the Laplace equation.

### 1.5.6 Concept of images

A problem that occurs frequently in lightning research is to calculate the electric field produced by a charge located over a conducting ground plane. The concept of images can be used to calculate the electric field of charges located near conducting boundaries. In the theory, a conductor having a certain potential is replaced by one or several image charges in such a way that the conductor surface is replaced by an equipotential surface at the same potential. This concept is illustrated in Figure 1.5. In this transformation, the boundary conditions are conserved and the electric field obtained outside the conductor is the correct electric field. In order to illustrate the technique, consider the electric field produced by two-point charges: one positive and the other negative. The charges are located on the  $z$ -axis at the locations  $z$  and  $-z$ . In this charge distribution, the plane  $z=0$  is an equipotential plane with potential equal to zero. That means, this plane can be replaced by a conductor with zero potential without changing the field configuration in the upper half space (i.e.  $z > 0$ ). Thus, the electric field due to a point charge located over a conducting plane at zero potential (in dealing with electrostatic problems the ground is usually considered as a conducting plane at zero potential) can be obtained by replacing the ground plane by a negative (opposite) charge at the image position. In reality, the negative mirror image represents the effects of induced negative charges on the conducting plane due to

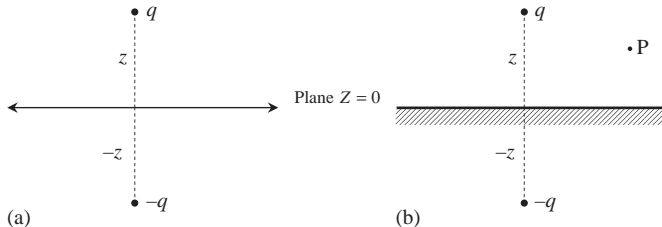


*Figure 1.5 In image theory a conductor having a certain potential (in this case zero potential) is replaced by one or several image charges in such a way that the conductor surface is replaced by an equipotential surface at the same potential*

the influence of the positive charge located above it. The distribution of the induced charge or the induced negative surface charge density on the surface can be obtained using the electrostatic boundary conditions at the conducting surface (see the next section).

### 1.5.7 Electrostatic boundary conditions

In order to satisfy the laws of electricity in different media, the electric field has to satisfy certain boundary conditions at a boundary separating two media. These conditions are known as boundary conditions. They can be derived by using the fact that the electrostatic field in both media should satisfy (1.53) and (1.60). Consider a boundary that separates two media, say 1 and 2, with relative dielectric constant  $\epsilon_{r1}$  and  $\epsilon_{r2}$  respectively (see Figure 1.6). Let us resolve the electric field in the two media into components parallel (tangential) and perpendicular (normal) to the surface. Let us denote the E-field parallel to the surface in the two media by  $E_{t1}$  and  $E_{t2}$ . The components perpendicular to the surface are denoted by  $E_{n1}$  and  $E_{n2}$ . The corresponding D-fields are  $D_{t1}$ ,  $D_{t2}$ ,  $D_{n1}$  and  $D_{n2}$ .

Consider a closed path as shown in Figure 1.6a. Applying (1.53) for this closed path and reducing the thickness of the path  $2\Delta l$  to zero one finds

$$E_{t1}\Delta W - E_{t2}\Delta W = 0 \quad (1.79)$$

Thus, the boundary condition satisfied by the tangential E-fields in the two media is

$$E_{t1} = E_{t2} \quad (1.80)$$

That is, the E-field component parallel to the surface is continuous across the boundary. In terms of D-fields (1.80) can be written as

$$\frac{D_{t1}}{D_{t2}} = \frac{\epsilon_{1r}}{\epsilon_{2r}} \quad (1.81)$$

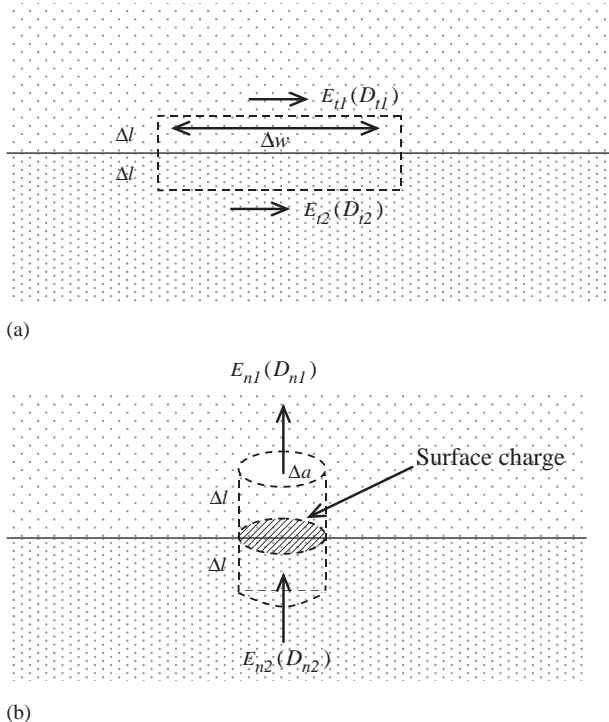


*Figure 1.6* (a) The contour along which the line integral of electric field is evaluated to obtain the electrostatic boundary conditions satisfied by the tangential electric field components. (b) The surface bounding the volume into which Gauss's law is applied to obtain the electrostatic boundary conditions satisfied by the normal electric field components

Now consider a closed volume in the shape of a pillbox as shown in Figure 1.6b. Applying (1.60) (Gauss's law) to this pillbox and reducing the height of the pillbox  $2\Delta l$  to zero, we obtain

$$D_{n1}\Delta a - D_{n2}\Delta a = \Delta Q = \rho_s \Delta a \quad (1.82)$$

where  $\rho_s$  is the surface charge density on the surface and  $\Delta a$  is the area of cross-section of the pillbox. Thus, the boundary condition satisfied by the normal component of D-field is

$$D_{n1} - D_{n2} = \rho_s \quad (1.83)$$

If the surface charge is zero (i.e.  $\rho_s = 0$ ), then the normal component of the D-field is continuous across the boundary. In terms of E-fields the boundary condition is

$$\varepsilon_0 \varepsilon_r 1 E_{n1} - \varepsilon_0 \varepsilon_r 2 E_{n2} = \rho_s \quad (1.84)$$

When the charge density is zero, the above equation reduces to

$$\epsilon_{r1}E_{n1} = \epsilon_{r2}E_{n2} \quad (1.85)$$

Now assume that one of the mediums under consideration is a vacuum (or air) and the other a conductor. A conductor contains free electrons, and the moment one attempts to apply an electric field inside the conductor the free electrons will displace inside the conductor and create an opposite electric field so as to make the electric field inside the conductor zero. This process of relaxation (or removal) of the electric field takes some time and this time, as we will see later in Section 1.6.3, depends on the conductivity and the dielectric constant of the conducting medium. In a perfect conductor the relaxation time is zero and therefore the electric field inside is zero at all times. If the conductivity is finite, then the relaxation time is not zero and it may take some time before the field is neutralized. However, it becomes zero under static conditions. Since the electric field is zero inside a perfect conductor, the boundary condition (1.80) shows that the tangential component of the E-field is zero on its surface. This is the case since the tangential component of the E-field is zero inside the conductor. Thus, the E-field at the surface of a perfect conductor is perpendicular to the surface. Since the component of the E-field normal to the surface inside the conductor is zero, the normal component of the E-field at the surface is given by

$$\epsilon_0 E_n = \rho_s \quad (1.86)$$

where  $\rho_s$  is the surface charge density on the conductor.

## 1.6 Static magnetic fields

Magnetic fields are generated by electric currents, and therefore before we proceed further let us consider how to represent the electric current in a given medium in terms of the properties of the charged particles that exist in the medium.

### 1.6.1 Electric current

Electric currents are created by the movement of charges. Consider a medium that contains mobile electric charges. The polarity of the charges can be either positive or negative. They can also be either ions or electrons. For our purpose at hand assume that the polarity of the mobile charge in the medium is positive. Let the density of the charged particles in the medium (i.e. number of charged particles per unit volume) be  $n_+$ . We also assume that the particles are singly charged. That is, the charge on them is equal to one electronic charge. If an electric field is applied to this medium, the charged particles will experience a force and they start accelerating in the direction of the electric field. However, due to the collisions with other particles in the medium they will reach a steady velocity that depends on the

background electric field and the size and the mass of the charged particles. This steady velocity is called drift velocity and it is a function of the electric field. The relationship between the drift velocity and the E-field is given by

$$\mathbf{V}_{d+} = \mu_+ \mathbf{E} \quad (1.87)$$

The parameter  $\mu_+$  is called the mobility of the positive charged particles under consideration. The movement of the charge gives rise to a flow of electric current in the medium. The current density  $\mathbf{J}$  in the direction of the electric field (i.e. the current flowing through a unit cross-section located perpendicular to the electric field) is given by

$$\mathbf{J} = e \mathbf{V}_{d+} n_+ \quad (1.88)$$

where  $e$  is the electronic charge. If the medium contained charge particles of both polarities all of which are singly charged, then

$$\mathbf{J} = e \mathbf{V}_{d+} n_+ + e \mathbf{V}_{d-} n_- \quad (1.89)$$

where the subscript with negative sign indicates quantities related to the negative charge particles. The above equation can be written as

$$\mathbf{J} = e \mu_+ \mathbf{E} n_+ + e \mu_- \mathbf{E} n_- \quad (1.90)$$

This can be written as

$$\mathbf{J} = \sigma \mathbf{E} \quad (1.91)$$

Where

$$\sigma = e \mu_+ n_+ + e \mu_- n_- \quad (1.92)$$

The parameter  $\sigma$  is called the conductivity of the medium. In general a medium may contain charge particles of both polarities and of different masses and charges. In evaluating the conductivity, one has to consider the contribution of each of these particles to the current flow and to the conductivity.

### 1.6.2 Conservation of electric charge

It is a law of nature that the electric charge cannot be created or destroyed. It can only move from one place to another in the form of electric currents. The conservation of charge provides restrictions on the electric current that can be present in a given region. Consider a closed volume in a region where there is a current flow. Let  $S$  be a closed surface enclosing this volume. Let the total current coming out of the volume be denoted by  $I$ . Let  $\mathbf{J}$  be the current density

at any given point on the surface. Then the total current coming out of the surface is

$$I = \oint_s \mathbf{J} \cdot d\mathbf{s} \quad (1.93)$$

Since the charge cannot be destroyed, the outward flow of current from the volume should reduce the charge inside the volume at a rate given by

$$I = \oint_s \mathbf{J} \cdot d\mathbf{s} = -\frac{dQ}{dt} \quad (1.94)$$

where  $Q$  is the charge in the volume at a given time. Now, the charge inside the volume at a given instant can be written as an integral of the volume charge density. Thus, we can write

$$\frac{dQ}{dt} = -\frac{d}{dt} \left( \int_v \rho_v dv \right) \quad (1.95)$$

Substituting this in (1.94), we obtain

$$\oint_s \mathbf{J} \cdot d\mathbf{s} = -\frac{d}{dt} \left( \int_v \rho_v dv \right) \quad (1.96)$$

Now according to the divergence theorem, we can write

$$\oint_s \mathbf{J} \cdot d\mathbf{s} = \int_v \text{Div } \mathbf{J} dv \quad (1.97)$$

Substituting this in (1.96), we obtain

$$\int_v \text{Div } \mathbf{J} dv = - \left( \int_v \frac{d\rho_v}{dt} dv \right) \quad (1.98)$$

Since the above relationship is true for any volume, we conclude that

$$\text{Div } \mathbf{J} = -\frac{\partial \rho_v}{\partial t} \quad (1.99)$$

This equation is an expression, in point form, of the conservation of electric charge.

### 1.6.3 Re-distribution of excess charge placed inside a conducting body

Consider an isotropic and homogeneous conductor with relative dielectric constant of  $\epsilon_r$  and conductivity  $\sigma$ . Assume that at time equal to zero, an excess charge is placed inside the conductor with charge density  $\rho_v(r, 0)$ . This charge will generate an electric field inside the conductor generating a current that will redistribute this charge and displace it to the surface of the conductor (recall that one can have electric charges on the surface of conductors) and making the electric field inside the conductor zero. Let us evaluate how fast this process will take place.

From the equation of charge conservation, we have

$$\text{Div } \mathbf{J}(r, t) = -\frac{\partial \rho_v(r, t)}{\partial t} \quad (1.100)$$

where  $\rho_v(r, t)$  is the charge density at any time inside the conductor. Substituting for  $\mathbf{J}$  in the above equation from  $\mathbf{J} = \sigma \mathbf{E}(r, t)$ , we obtain

$$\sigma \text{Div } \mathbf{E}(r, t) = -\frac{\partial \rho_v(r, t)}{\partial t} \quad (1.101)$$

We also know from Gauss's law that

$$\text{Div } \mathbf{E}(r, t) = \frac{\rho_v(r, t)}{\epsilon_0 \epsilon_r} \quad (1.102)$$

Substituting this in the previous equation, we obtain

$$\rho_v(r, t) = -\frac{\epsilon_0 \epsilon_r}{\sigma} \frac{\partial \rho_v(r, t)}{\partial t} \quad (1.103)$$

The solution of equation (1.103) is

$$\rho_v(r, t) = \rho_v(r, 0) e^{-\sigma t / \epsilon_0 \epsilon_r} \quad (1.104)$$

The above expression for the variation in charge density inside the conductor shows that the charge inside the conductor will decrease exponentially in time. The quantity  $\epsilon_0 \epsilon_r / \sigma$  is called the relaxation time of the conductor. In the same way if we create an electric field inside a conductor, it will decrease to zero exponentially with a time constant equal to the relaxation time. In a perfect conductor the conductivity is infinite and thus the relaxation time is zero. Thus, the electric field inside a perfect conductor is zero under all circumstances.

### 1.6.4 Magnetic field produced by a current element – Biot–Savart's law

Consider a current element  $dl$  through which a current  $I$  is flowing (see Figure 1.7). The current element can be represented by a vector  $\mathbf{dl}$  with magnitude  $dl$  and

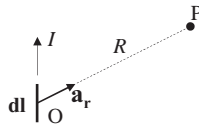


Figure 1.7 The geometry relevant to the evaluation of magnetic field at point  $P$  produced by a current element  $d\mathbf{l}$

direction specified by the direction of current flow. According to Biot–Savarts law, the B-field produced by this current element at point  $\mathbf{P}$  is given by

$$dB = \mu_0 I \cdot \frac{d\mathbf{l} \times \mathbf{a}_r}{4\pi |R|^2} \quad (1.105)$$

In the above equation,  $\mathbf{a}_r$  is a unit vector in the direction of  $OP$  (see Figure 1.7). Note that the direction of the magnetic field is perpendicular to both the current element  $d\mathbf{l}$  and the vector joining the current element and the point of observation (i.e.  $\mathbf{a}_r$ ). The magnitude of the magnetic field is proportional to the current in the current element and its strength decreases with  $1/R^2$ .

The magnetic field produced by a conductor of any shape can be calculated by dividing the conductor into elementary sections and summing up the contribution to the B-field from each element using the above equation.

### 1.6.5 Gauss's law for magnetic fields

One interesting fact of nature is the observation that magnetic poles, the sources of magnetic fields, always come in pairs. This means that the net flux of the magnetic field coming out from a surface has to be zero because there are no net magnetic charges inside any given volume. Thus, for any closed volume one can write

$$\oint_s \mathbf{B} \cdot d\mathbf{s} = 0 \quad (1.106)$$

The above says that the total flux of B-field coming out of a closed surface is equal to zero. Using divergence theorem one can write

$$\oint_s \mathbf{B} \cdot d\mathbf{s} = \int_v \text{Div } \mathbf{B} dv \quad (1.107)$$

Substituting this in (1.106), we obtain

$$\int_v \text{Div } \mathbf{B} dv = 0 \quad (1.108)$$

Since this is true for any closed volume, one can conclude that

$$\text{Div } \mathbf{B} = 0 \quad (1.109)$$

### 1.6.6 Ampere's law

Ampere's law relates the integral of the B-field or the H-field around a closed path to the electric current passing through it. Consider a closed path of any shape. Let  $S$  be any surface bounded by this closed path. As we have indicated previously, there are infinite number of surfaces satisfying this condition. The net current,  $I$ , passing through the closed path is given by

$$I = \int_S \mathbf{J} \cdot d\mathbf{s} \quad (1.110)$$

In the above equation, the net current is calculated by first considering a surface  $S$  bounded by the closed loop and taking the flux of current density through it. Note that in the above equation  $\mathbf{J} \cdot d\mathbf{s}$  gives the current passing through the element  $d\mathbf{s}$ . According to Ampere's law,

$$\oint_L \mathbf{H} \cdot d\mathbf{l} = \int_S \mathbf{J} \cdot d\mathbf{s} \quad (1.111)$$

In the above equation, the left-hand side defines the integral of the H-field around a closed path and the right-hand side defines the electric current passing thorough the same closed path. The parameter  $d\mathbf{s}$  defines a surface element on the surface and its positive direction is defined by the right-hand screw law. The positive direction of  $d\mathbf{s}$  is the direction of motion of a right-handed screw when rotated in the circular direction in which the line integral is performed. Now, using Stokes theorem one can write

$$\oint_L \mathbf{H} \cdot d\mathbf{l} = \int_S (\text{Curl } \mathbf{H}) \cdot d\mathbf{s} \quad (1.112)$$

Combining (1.111) and (1.112), we obtain

$$\int_S \mathbf{J} \cdot d\mathbf{s} = \int_S (\text{Curl } \mathbf{H}) \cdot d\mathbf{s} \quad (1.113)$$

Since this is true for any surface, we can conclude that

$$\text{Curl } \mathbf{H} = \mathbf{J} \quad (1.114)$$

In terms of B-field, this can be written as

$$\text{Curl } \mathbf{B} = \mu_0 \mathbf{J} \quad (1.115)$$

### 1.6.7 Boundary conditions for the static magnetic field

Similar to electric fields, the magnetic field should also satisfy boundary conditions at the boundary between two media. These boundary conditions can be obtained easily by applying Gauss's law for the magnetic fields and Ampere's law at the boundary. Consider a boundary that separates two media 1 and 2 with relative magnetic permeabilities  $\mu_{r1}$  and  $\mu_{r2}$  respectively (Figures 1.8a and 1.8b). Let us resolve the magnetic field in the two media into components parallel (tangential) and perpendicular (normal) to the surface. Let us denote the H-field parallel to the surface in the two media by  $H_{t1}$  and  $H_{t2}$ . The components perpendicular to the surface are denoted by  $H_{n1}$  and  $H_{n2}$ . The corresponding B-fields are  $B_{t1}$ ,  $B_{t2}$ ,  $B_{n1}$  and  $B_{n2}$ .

Consider a closed path as shown in Figure 1.8a. Applying Ampere's law for this closed path and reducing the thickness  $2\Delta l$  of the path to zero, one finds

$$H_{t1}\Delta W - H_{t2}\Delta W = J_s\Delta W \quad (1.116)$$

where  $J_s$  is the surface current density per unit length flowing perpendicular to the closed path. If the surface current on the surface is zero, the above reduces to

$$H_{t1} = H_{t2} \quad (1.117)$$

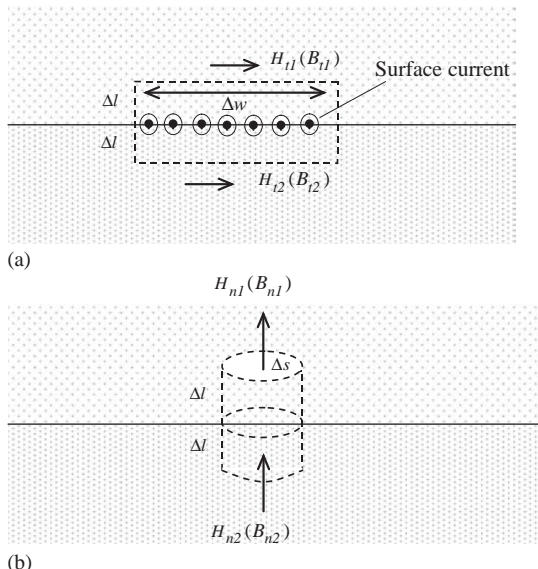


*Figure 1.8 (a) The contour along which the line integral of magnetic field is evaluated to obtain the magnetostatic boundary conditions satisfied by the tangential magnetic field components. (b) The surface bounding the volume into which Gauss's law is applied to obtain the magnetostatic boundary conditions satisfied by the normal magnetic field components*

This tells us that if there are no surface currents, the H-field parallel to the surface is continuous across the boundary. The boundary conditions to be satisfied by the parallel components of B-fields can be written as

$$\frac{B_{t1}}{\mu_o \mu_{1r}} - \frac{B_{t2}}{\mu_o \mu_{2r}} = J_s \quad (1.118)$$

$$\frac{B_{t1}}{B_{t2}} = \frac{\mu_{1r}}{\mu_{2r}} \text{ (when } J_s \text{ is equal to zero)} \quad (1.119)$$

Now consider a closed volume in the shape of a pillbox as shown in Figure 1.8b. Applying (1.106) (Gauss's law for magnetic fields) to this pillbox and reducing the height of the pillbox to zero, we obtain

$$B_{n1} \Delta s - B_{n2} \Delta s = 0 \quad (1.120)$$

Thus, the boundary condition satisfied by the normal component of the B-field is

$$B_{n1} = B_{n2} \quad (1.121)$$

The boundary condition to be satisfied by the normal component of the H-field is then given by

$$\mu_{1r} H_{n1} = \mu_{2r} H_{n2} \quad (1.122)$$

### 1.6.8 Vector potential

The fact that the magnetic field is divergence free (i.e.  $\text{Div } \mathbf{B} = 0$ ) makes it possible to define a vector function  $\mathbf{A}$  with the characteristics that

$$\mathbf{B} = \text{Curl } \mathbf{A} \quad (1.123)$$

This satisfies the condition that  $\text{Div } \mathbf{B} = 0$  because the divergence of a curl of a function is zero. The function  $\mathbf{A}$  defined above is called the vector potential. Let us now find the relationship between the vector potential and the current giving rise to the magnetic field. Let us start with the Ampere's law in point form.

$$\text{Curl } \mathbf{B} = \mu_0 \mathbf{J} \quad (1.124)$$

Substituting  $\mathbf{B} = \text{Curl } \mathbf{A}$  in the above equation, one obtains

$$\text{Curl}(\text{Curl } \mathbf{A}) = \mu_0 \mathbf{J} \quad (1.125)$$

Expanding  $\text{Curl}(\text{Curl } \mathbf{A})$  using the vector identity given in (1.37), we obtain

$$\text{Grad}(\text{Div } \mathbf{A}) - \nabla^2 \mathbf{A} = \mu_0 \mathbf{J} \quad (1.126)$$

Now, any vector function is not completely defined until both its curl and divergence are specified. We have already defined the curl of the function  $\mathbf{A}$ , but we are free to select the value of the function  $\text{Div } \mathbf{A}$ . Let us select  $\text{Div } \mathbf{A} = 0$ . This selection is called the Coulomb's Gauge. With this selection we find

$$\nabla^2 \mathbf{A} = -\mu_0 \mathbf{J} \quad (1.127)$$

The relationship given in (1.124) is a vector equation and it can be separated into its components as follows:

$$\begin{aligned}\nabla^2 A_x &= -\mu_0 J_x \\ \nabla^2 A_y &= -\mu_0 J_y \\ \nabla^2 A_z &= -\mu_0 J_z\end{aligned}\quad (1.128)$$

Note that  $A_x, A_y, A_z$  and  $J_x, J_y, J_z$  are scalar quantities. The above equation gives the relationship between the vector potential and the current generating the magnetic field. Let us now consider the solution of this equation.

### 1.6.8.1 Vector potential of a current distribution

Consider a current distribution in space (see Figure 1.9). Let us specify the current density at a given point by  $\mathbf{J}(r')$  where  $r'$  defines the coordinates of the current source. According to Biot-Savarts law, the magnetic field at point  $\mathbf{P}$  is given by

$$\mathbf{B} = \frac{\mu_0}{4\pi} \int_v \mathbf{J}(r') \times \left( \frac{\mathbf{a}_r}{r^2} \right) d\nu \quad (1.129)$$

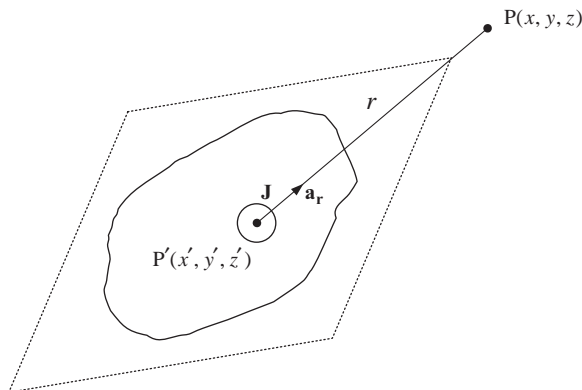


Figure 1.9 The geometry relevant to the derivation of vector potential at point  $P$  due to a current distribution

where in the above equation  $\mathbf{a}_r$  is a unit vector directed in the direction of  $r$  (see Figure 1.9). The above equation can be written as

$$\mathbf{B} = \frac{\mu_0}{4\pi} \int_v \nabla \left( \frac{1}{r} \right) \times \mathbf{J}(r') dv \quad (1.130)$$

Note that it is possible to write (1.129) as (1.130) because  $\nabla$  contains derivatives with respect to  $x$ ,  $y$  and  $z$  (coordinates of point of the field point), whereas  $\mathbf{J}$  is only a function of source coordinates,  $x'$ ,  $y'$  and  $z'$ . Now using the vector identity given by (1.39), we obtain

$$\nabla \left( \frac{1}{r} \right) \times \mathbf{J}(r') = \nabla \times \left( \frac{1}{r} \mathbf{J}(r') \right) - \left( \frac{1}{r} \right) \nabla \times \mathbf{J}(r') \quad (1.131)$$

The second term on the right-hand side is equal to zero because  $\nabla$  contains derivatives with respect to  $x$ ,  $y$  and  $z$  (coordinates of the point of observation), whereas  $\mathbf{J}$  is not a function of  $x$ ,  $y$  and  $z$ . Substituting this in the previous equation, we obtain

$$\mathbf{B} = \frac{\mu_0}{4\pi} \int_v \text{Curl} \left\{ \frac{\mathbf{J}(r)}{r} \right\} dv \quad (1.132)$$

Changing the order of differentiation and integration, we find

$$\mathbf{B} = \frac{\mu_0}{4\pi} \int_v \left\{ \frac{\mathbf{J}(r)}{r} \right\} dv \quad (1.133)$$

Comparing this with (1.123), we conclude that

$$\mathbf{A} = \frac{\mu_0}{4\pi} \int_v \frac{\mathbf{J}(r)}{r} dv \quad (1.134)$$

The  $x$ ,  $y$  and  $z$  components of this vector relationship are

$$\begin{aligned} A_x &= \int_v \frac{J_x \mu_0}{4\pi r} dv \\ A_y &= \int_v \frac{J_y \mu_0}{4\pi r} dv \\ A_z &= \int_v \frac{J_z \mu_0}{4\pi r} dv \end{aligned} \quad (1.135)$$

### 1.6.8.2 Vector potential due to a current element $d\mathbf{l}$

The problem under consideration is shown in Figure 1.10. Consider a current element  $d\mathbf{l}$ . The magnitude or the length of this element  $dl$ , i.e.  $dl = |\mathbf{dl}|$ . The direction of the vector  $d\mathbf{l}$  is in the direction of current flow. Assume that the current is

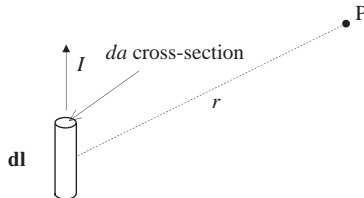


Figure 1.10 The geometry necessary to calculate the vector potential at point  $P$  due to a current element of length  $dl$  and of cross-section  $da$

flowing uniformly across the cross-section of the element. The current density in the element is given by  $\mathbf{J}$ . The vector potential due to the current element at a distance  $r$  when  $r \gg dl$  is

$$\mathbf{A} = \frac{\mu_0 \mathbf{J}}{4\pi r} (dl \cdot da) \quad (1.136)$$

where  $da$  is the cross-sectional area of the element. Note that the quantity  $dl \cdot da$  is the volume of the current element. Since the current density times when multiplied by the cross-sectional area gives the total current flowing through the element, we can write

$$\mathbf{A} = \frac{\mu_0 dl \mathbf{I}}{4\pi r} \text{ or } \mathbf{A} = \frac{\mu_0 \mathbf{dI} I}{4\pi r} \quad (1.137)$$

The above equation gives the vector potential at a given point due to a current element of length  $dl$ .

### 1.6.9 Force on a charged particle

Consider a region where there is both an E- and a B-fields. Assume that at any given instant a charged particle of charge  $q$  is at point  $(x, y, z)$  and it is moving with velocity  $\mathbf{v}$ . The particle will experience a force both due to E- and B-fields. This force is given by,

$$\mathbf{F} = q\mathbf{E}(x, y, z) + \mathbf{v} \times \mathbf{B}(x, y, z) \quad (1.138)$$

This force is called the Lorentz force. If the particle is stationary with respect to the B-field, it will experience a force only due to the E-field.

## 1.7 Energy density of an electric field

Let us evaluate the energy density of an electric field in vacuum. This we can do by creating an electric field in a given region in vacuum and evaluating the energy that was spent in creating that electric field. Consider a plane parallel capacitor in vacuum charged to potential  $V$ . The energy of the capacitor is stored in its

electric field. If one neglects the end effects of the capacitor, the electric field is uniform between the two plates. Now, the total energy spent in charging the capacitor is

$$W = \frac{1}{2}qV \quad (1.139)$$

where  $q$  is the charge on the capacitor. Now, neglecting the end effects, the E-field inside the capacitor is given by  $E = V/d$  where  $d$  is the separation between the plates. Applying Gauss's law and recalling that the E-field inside a conductor (in our case the plates of the capacitor) is zero, we find that

$$E = \frac{q}{A} \frac{1}{\epsilon_0} \quad (1.140)$$

where  $A$  is the area of the plates of the capacitor. Substituting for  $q$  and  $V$  in terms of  $E$ , we find that

$$W = \frac{1}{2}\epsilon_0 E^2 (Ad) \quad (1.141)$$

Since  $Ad$  is the volume of the capacitor, the energy per unit volume is given by

$$\frac{W}{Ad} = \frac{1}{2}\epsilon_0 E^2 \quad (1.142)$$

Since the energy of the capacitor is stored in the electric field, one can conclude that the energy density,  $EE_{den}$ , of an E-field in vacuum is given by

$$EE_{den} = \frac{1}{2}\epsilon_0 E^2 \quad (1.143)$$

## 1.8 Electrodynamics – Time-varying electric and magnetic fields

So far we have dealt with static electric and magnetic fields. Now, let us consider situations in which the electric and magnetic fields vary in time. Such situations occur when the charge densities (the sources of electric field) and current densities (sources of magnetic fields) vary in time. The variation in these quantities with time can take place in any arbitrary manner, but for many applications it is convenient to assume that the variations are sinusoidal. Indeed, any time variation can be represented as a sum of *sine* and *cosine* variations using Fourier analysis.

Consider an E-field that is varying as a cosine function. It is given by

$$E = E_{x0} \cos \omega t \quad (1.144)$$

The quantity  $\omega$  is called the angular frequency (measured in radians per second) and it is related to the frequency  $f$  (measured in cycles per second) by the relationship  $\omega = 2\pi f$ .

Using the identity

$$e^{j\omega t} = \cos \omega t + j \sin \omega t \quad (1.145)$$

one can write the E-field as the real part of  $E_{x0}e^{j\omega t}$ , that is

$$E = \operatorname{Re}[E_{x0}e^{j\omega t}] \quad (1.146)$$

An E-field varying as a sine function can be written as the imaginary part of  $E_{x0}e^{j\omega t}$ , i.e.  $\operatorname{Im}[E_{x0}e^{j\omega t}]$ . The advantage of this technique is that all the operations that need to be done on the E-field (or any other field of interest) can be done on  $E_{x0}e^{j\omega t}$  and the final solution can be obtained by taking the real part of the resulting expression if the electric field was changing as a cosine function. For example, consider the operation of taking the time derivative of the electric field. The result is

$$\frac{dE}{dt} = -E_x \omega \sin \omega t \quad (1.147)$$

On the other hand, one can perform the operation directly on  $E = E_{x0}e^{j\omega t}$  that results in

$$\frac{dE}{dt} = E_{x0}j\omega e^{j\omega t} = E_{x0}[j\omega \cos \omega t - \omega \sin \omega t] \quad (1.148)$$

The real part of this is  $-E_x \omega \sin \omega t$  that is the solution we need. So, instead of working with sine or cosine functions one can work with  $E = E_{x0}e^{j\omega t}$  and extract the final answer as either the real or the imaginary part of the final expression depending on whether the starting point was  $E = \operatorname{Re}[e^{j\omega t}]$  or  $E = \operatorname{Im}[e^{j\omega t}]$ . One advantage of this technique is that it simplifies all the equations by removing the time derivatives.

### 1.8.1 Faraday's law

The essence of Faraday's law is that it defines and quantifies the natural law that a changing magnetic field gives rise to an electric field. Consider a closed path in a region where there is a changing magnetic field. According to Faraday's law, the E-field  $\mathbf{E}$  generated by this changing magnetic field is such that

$$\oint_l \mathbf{E} \cdot d\mathbf{l} = -\frac{d\psi}{dt} \quad (1.149)$$

In the above equation, the left-hand side is the line integral of the electric field taken along the closed path and the right-hand side is equal to the negative rate of

change of magnetic flux  $\psi$  passing through the closed path. The magnetic flux passing through the closed path can be calculated as

$$\psi = \int_s \mathbf{B} \cdot d\mathbf{s} \quad (1.150)$$

where, as indicated previously, the surface integral is carried out over a surface that is bounded by the closed path. The positive direction of  $d\mathbf{s}$  is the direction of motion of a right-handed screw when rotated in the circular direction in which the line integral is performed. Since the electromotive force, *emf*, generated around the closed path under consideration is given by the line integral of the E-field along that path, one can write

$$emf = -\frac{d\psi}{dt} \quad (1.151)$$

If the closed path is replaced by a conducting wire, the *emf* given above will generate a current flow in the wire. The minus sign tells us that the direction of the induced current is such that it opposes the change in the magnetic field that gives rise to the *emf*. This phenomenon is described as Lenz's law.

Now, using Stokes theorem one can write

$$\int_s (\text{Curl } \mathbf{E}) \cdot d\mathbf{s} = \oint_l \mathbf{E} \cdot d\mathbf{l} \quad (1.152)$$

Combining (1.149), (1.150) and (1.152), one can write

$$\int_s (\text{Curl } \mathbf{E}) \cdot d\mathbf{s} = -\frac{d}{dt} \int_s \mathbf{B} \cdot d\mathbf{s} \quad (1.153)$$

Since the path is fixed in space in time, one can change the order of differentiation and integration. That gives rise to

$$\int_s (\text{Curl } \mathbf{E}) \cdot d\mathbf{s} = - \int_s \frac{\partial \mathbf{B}}{\partial t} \cdot d\mathbf{s} \quad (1.154)$$

Since the above equation is true for any surface, one can conclude that

$$\text{Curl } \mathbf{E} = -\frac{\partial \mathbf{B}}{\partial t} \quad (1.155)$$

The above equation is the point form description of Faraday's law.

### 1.8.2 Maxwell's modification of Ampere's law – the displacement current term

After scrutinizing the experimentally derived laws available to him, Maxwell realized that the Ampere's law as given in (1.111) or (1.115) cannot be complete. For example, take the divergence of both sides of the (1.115). We will get

$$\text{Div}(\text{Curl } \mathbf{H}) = \text{Div } \mathbf{J} \quad (1.156)$$

Since divergence of a curl of a function is always zero, the above equation implies that  $\text{Div } \mathbf{J} = 0$ . This cannot be true in general because

$$\text{Div } \mathbf{J} = -\frac{\partial \rho_v}{\partial t} \neq 0 \quad (1.157)$$

This shows that a term is missing in (1.111) and (1.115). Let us assume for the moment that the missing term is  $\mathbf{F}$ . The goal is to find an expression for this function in terms of known quantities. With this addition (1.115) can be written as

$$\text{Curl } \mathbf{H} = \mathbf{J} + \mathbf{F} \quad (1.158)$$

Taking the divergence of both sides, we obtain

$$\text{Div}(\text{Curl } \mathbf{H}) = \text{Div } \mathbf{J} + \text{Div } \mathbf{F} \quad (1.159)$$

From this, we obtain (since  $\text{Div}(\text{Curl } \mathbf{H}) = 0$ )

$$\text{Div } \mathbf{F} = -\text{Div } \mathbf{J} \quad (1.160)$$

However, from charge conservation we have already seen that

$$\text{Div } \mathbf{J} = -\frac{\partial \rho_v}{\partial t} \quad (1.161)$$

where  $\rho_v$  is the volume charge density. At the same time, from Gauss's law we know that

$$\rho_v = \text{Div } \mathbf{D} \quad (1.162)$$

Combining (1.160), (1.161) and (1.162), we obtain

$$\text{Div } \mathbf{F} = \text{Div} \left( \frac{\partial \mathbf{D}}{\partial t} \right) \quad (1.163)$$

From this, we conclude that the function  $\mathbf{F}$  is given by

$$\mathbf{F} = \frac{\partial \mathbf{D}}{\partial t} \quad (1.164)$$

Thus, the corrected form of the Ampere's law is

$$\text{Curl } \mathbf{H} = \mathbf{J} + \frac{\partial \mathbf{D}}{\partial t} \quad (1.165)$$

Maxwell coined the term ‘displacement current density’ for the new term that appears in the right-hand side of this equation. Note that the first term on the right-hand side is the conduction current density. The most important conclusion that one can reach from this equation is that a changing electric field will give rise to a magnetic field.

### 1.8.3 Energy density in a magnetic field

Consider a region in the form of a long tube in vacuum (see Figure 1.11). Let us set up a uniform B-field in this region. This can be done by creating circular current around this region as shown in Figure 1.11. The energy stored in the B-field can be obtained by the energy spent in creating it.

We start with zero current and increase it in some arbitrary manner until the final B-field in the volume is  $B$ . At any instant, the circular current per unit length flowing around the cylinder is  $i(t)$  and the corresponding B-field at that time is  $B_t(t)$ . Applying the Ampere’s law along the closed path shown in the figure, we obtain

$$B_t(t) \cdot l = \mu_0 \cdot i(t) \cdot l \quad (1.166)$$

Now, as the magnetic field is increasing it will generate an electric field, according to Faraday’s law, that opposes the increase in current. Consider a time interval  $t \rightarrow t + dt$ . The work done,  $dW$ , by the current per unit length opposing the effect of this electric field during this time interval is

$$dW = i(t) \cdot A \cdot \frac{dB_t(t)}{dt} dt \quad (1.167)$$

The total work done by the current per unit length in establishing the final B-field  $B$  is

$$W = \int_0^{t_0} i(t) \cdot A \cdot \frac{dB_t(t)}{dt} dt \quad (1.168)$$

where  $t_0$  is the time taken to establish the final B-field. Substituting for  $i(t)$  from (1.166), we obtain

$$W = \int_0^{t_0} \frac{B_t(t)}{\mu_0} \cdot A \cdot \frac{dB_t(t)}{dt} dt \quad (1.169)$$

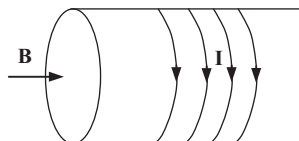


*Figure 1.11 The spatial arrangement of currents that can provide a uniform magnetic field in a volume in the form of a long tube*

This can be written as

$$W = \int_0^{t_0} \frac{A}{2\mu_0} \cdot \frac{dB_t^2(t)}{dt^2} dt \quad (1.170)$$

After performing the integration, we obtain

$$W = \frac{1}{2\mu_0} [B_t^2(t)]_0^{t_0} A \quad (1.171)$$

Since the B-field at  $t=0$  is zero and its value at  $t=t_0$  is  $B_0$ , we obtain

$$W = \frac{1}{2\mu_0} B_0^2 A \quad (1.172)$$

Recall that this is the energy spent in establishing the B-field per unit length of tube. This energy is now stored in the B-field. Since the volume per unit length of the tube is equal to  $A$  (the cross-sectional area times unity), the energy per unit volume of the B-field or the energy density of the B-field,  $EB_{den}$ , is

$$EB_{den} = \frac{W}{A} = \frac{1}{2\mu_0} B^2 \quad (1.173)$$

## 1.9 Summary of the laws of electricity

The laws of electricity that we have analysed so far can be summarized as

---

Integral form	Point form
$\oint \mathbf{E} \cdot d\mathbf{l} = - \int_s \frac{\partial \mathbf{B}}{\partial t} \cdot d\mathbf{s}$	$\text{Curl } \mathbf{E} = - \frac{\partial \mathbf{B}}{\partial t}$
$\oint \mathbf{H} \cdot d\mathbf{l} = \mathbf{I} + \int_s \frac{\partial \mathbf{D}}{\partial t} \cdot d\mathbf{s}$	$\text{Curl } \mathbf{H} = \mathbf{J} + \frac{\partial \mathbf{D}}{\partial t}$
$\oint \mathbf{D} \cdot d\mathbf{s} = \int_v \rho_v$	$\text{Div } \mathbf{D} = \rho_v$
$\oint \mathbf{B} \cdot d\mathbf{s} = 0$	$\text{Div } \mathbf{B} = 0$

---

These equations are known as Maxwell's equations. In the case of sinusoidally varying fields (i.e. fields varying as  $e^{j\omega t}$ ), (1.174b) and (1.175b) can be written as

$$\text{Curl } \mathbf{E} = -j\omega \mathbf{B} \quad (1.178)$$

$$\text{Curl } \mathbf{H} = \mathbf{J} + j\omega \mathbf{D} \quad (1.179)$$

In a medium of relative dielectric constant  $\epsilon_r$  and conductivity  $\sigma$ , (1.179) can be written as

$$\text{Curl } \mathbf{H} = \mathbf{J} + j\omega \epsilon_0 \epsilon_r \mathbf{E} \quad (1.180)$$

Substituting  $\sigma \mathbf{E}$  for  $\mathbf{J}$ , we obtain

$$\text{Curl } \mathbf{H} = \mathbf{E} \{ \sigma + j\omega \epsilon_0 \epsilon_r \} \quad (1.181)$$

Note that in a dielectric medium where  $\mathbf{J} = 0$  we have  $\text{Curl } \mathbf{H} = j \text{Curl } \mathbf{H} = j\omega \epsilon_0 \epsilon_r \mathbf{E}$ . Comparison of this with (1.181) shows us that a conducting medium can be considered as a medium with a complex dielectric constant given by  $\{(\sigma / j\omega) + \epsilon_0 \epsilon_r\}$ .

## 1.10 Wave equation

Any wave, either sound, electromagnetic or any other type satisfies the wave equation. The wave equation in three dimensions can be written as

$$\frac{\partial^2 W}{\partial t^2} = v^2 \left\{ \frac{\partial^2 W}{\partial x^2} + \frac{\partial^2 W}{\partial y^2} + \frac{\partial^2 W}{\partial z^2} \right\} \quad (1.182)$$

In this equation,  $W$  is the displacement associated with the wave (in the case of a transverse wave propagating along a string,  $W$  is the displacement of the string from its equilibrium position) and  $v$  is the speed of propagation of the wave. In one dimension, for example, a wave moving in  $z$ -direction, it reduces to

$$\frac{\partial^2 W}{\partial t^2} = v^2 \frac{\partial^2 W}{\partial z^2} \quad (1.183)$$

The solution of this equation takes the form,

$$W(t, z) = f \left( t - \frac{z}{v} \right) \quad (1.184)$$

or a linear combination of such solutions. For example, one-dimensional sinusoidal wave, which is a solution of (1.183), can be represented by

$$W(t, z) = W_0 \sin \omega \left\{ t - \frac{z}{v} \right\} \quad (1.185a)$$

or

$$W(t, z) = W_0 \sin\{\omega t - kz\} \quad (1.185b)$$

In the above representation of the solutions,  $\omega$  is the angular frequency that is related to the frequency  $f$  by  $\omega = 2\pi f$ . The wavelength of the wave  $\lambda$  is given by  $\lambda = v/f$ . The parameter  $k = \omega/v$  is called the wave number of the wave.

## 1.11 Maxwell's prediction of electromagnetic waves

Consider Maxwell's equations in vacuum. We assume that electric and magnetic fields vary as  $e^{j\omega t}$ . The space is free of charges and currents except at the sources of electromagnetic fields. We have

$$\text{Curl } \mathbf{E} = -j\omega\mu_0 \mathbf{H} \quad (1.186)$$

Taking the curl of both sides of this equation, we obtain

$$\text{Curl}(\text{Curl } \mathbf{E}) = -j\omega\mu_0 \text{Curl } \mathbf{H} \quad (1.187)$$

Using vector identity given in (1.37) and noting that in a region of space where there are no charges  $\text{Div } \mathbf{E} = 0$ , we obtain

$$\text{Curl}(\text{Curl } \mathbf{E}) = -\nabla^2 \mathbf{E} \quad (1.188)$$

Substituting for the left-hand side from (1.187), we obtain

$$\nabla^2 \mathbf{E} = j\omega\mu_0 \text{Curl } \mathbf{H} \quad (1.189)$$

However, we also know that in a region in vacuum where there are no current sources (because  $\mathbf{J} = 0$ )

$$\text{Curl } \mathbf{H} = j\omega\epsilon_0 \mathbf{E} \quad (1.190)$$

Substituting for  $\text{Curl } \mathbf{H}$  from (1.190) in (1.189), we obtain

$$\nabla^2 \mathbf{E} = -\mu_0\epsilon_0\omega^2 \mathbf{E} \quad (1.191)$$

Since  $\mathbf{E}$  has time dependence  $e^{j\omega t}$ , the above equation can be written as

$$\frac{\partial^2 \mathbf{E}}{\partial t^2} = \frac{1}{\mu_0\epsilon_0} \nabla^2 \mathbf{E} \quad (1.192)$$

If this is resolved into three components, we obtain

$$\frac{\partial^2 E_x}{\partial t^2} = \frac{1}{\mu_0 \epsilon_0} \left\{ \frac{\partial^2 E_x}{\partial x^2} + \frac{\partial^2 E_x}{\partial y^2} + \frac{\partial^2 E_x}{\partial z^2} \right\} \quad (1.193a)$$

$$\frac{\partial^2 E_y}{\partial t^2} = \frac{1}{\mu_0 \epsilon_0} \left\{ \frac{\partial^2 E_y}{\partial x^2} + \frac{\partial^2 E_y}{\partial y^2} + \frac{\partial^2 E_y}{\partial z^2} \right\} \quad (1.193b)$$

$$\frac{\partial^2 E_z}{\partial t^2} = \frac{1}{\mu_0 \epsilon_0} \left\{ \frac{\partial^2 E_z}{\partial x^2} + \frac{\partial^2 E_z}{\partial y^2} + \frac{\partial^2 E_z}{\partial z^2} \right\} \quad (1.193c)$$

This shows that each component of  $\mathbf{E}$  satisfies the wave equation. The speed of propagation of the wave  $v$  is given by  $(1/\sqrt{\mu_0 \epsilon_0})$ . Now let us consider the magnetic field. We start with the Maxwell's equation

$$\text{Curl } \mathbf{H} = j\omega \mu_0 \mathbf{E} \quad (1.194)$$

Taking the curl of both sides of this equation, we obtain

$$\text{Curl}(\text{Curl } \mathbf{H}) = j\omega \mu_0 \text{Curl } \mathbf{E} \quad (1.195)$$

Using the vector identity given in (1.37) and noting that  $\text{Div } \mathbf{H} = 0$ , we can show that

$$\text{Curl}(\text{Curl } \mathbf{H}) = -\nabla^2 \mathbf{H} \quad (1.196)$$

Substituting to the left-hand side from (1.195), we obtain

$$\nabla^2 \mathbf{H} = -j\omega \mu_0 \text{Curl } \mathbf{E} \quad (1.197)$$

But from Maxwell's equations, we have  $\text{Curl } \mathbf{E} = -j\omega \mu_0 \mathbf{H}$ . Substituting for  $\text{Curl } \mathbf{E}$  in (1.197) and recalling that  $\mathbf{H}$  has time dependence  $e^{j\omega t}$ , we get

$$\frac{\partial^2 \mathbf{H}}{\partial t^2} = \frac{1}{\mu_0 \epsilon_0} \nabla^2 \mathbf{H} \quad (1.198)$$

The above equation shows that each component of  $\mathbf{H}$  also satisfies the wave equation. The speed of propagation of the wave is again equal to  $(1/\sqrt{\mu_0 \epsilon_0})$ .

The above analysis shows that Maxwell's equations predict the existence of electromagnetic waves that move in vacuum with speed  $(1/\sqrt{\mu_0 \epsilon_0})$ . This speed is indeed equal to the speed of light in vacuum showing that light is an electromagnetic wave.

## 1.12 Plane wave solution

### 1.12.1 The electric field of the plane wave

Consider a wave moving in the  $z$ -direction. For a plane electromagnetic wave moving in the  $z$ -direction, the electric field is independent of  $x$  and  $y$ . Without losing the generality, we can assume that the electric field associated with this wave is in  $x$ -direction. We denote it by  $E_x$ . As mentioned previously in a plane wave,  $E_x$  does not vary in  $x$ - and  $y$ -directions. Thus, the wave equation for the electric field is

$$\frac{\partial^2 E_x}{\partial z^2} = \mu_0 \epsilon_0 \frac{\partial E_x}{\partial t^2} \quad (1.199)$$

We also assume, as before, that the time variation in  $E_x$  has the form  $e^{j\omega t}$ . Thus, the solution of the above wave equation takes the form

$$E_x = E_{x0} e^{j\omega(t-(z/v))} \quad (1.200)$$

or

$$E_x = E_{x0} e^{j\omega t} e^{-jkz} \quad (1.201)$$

The solution can also be written in terms of sine or cosine functions. For example, it can be written as

$$E_x = E_{x0} \cos(\omega t - kz) \quad (1.202)$$

or

$$E_x = E_{x0} \cos\left\{\omega\left(t - \frac{z}{v}\right)\right\} \quad (1.203)$$

since  $v = 1/\sqrt{\mu_0 \epsilon_0}$  we can write

$$E_x = E_{x0} \cos\left\{\omega\left(t - \sqrt{\mu_0 \epsilon_0}z\right)\right\} \quad (1.204)$$

### 1.12.2 The magnetic field of the plane wave

Recall that we are considering a plane wave moving in  $z$ -direction. The electric field is in the  $x$ -direction and it does not vary in  $x$ - or  $y$ -direction (because it is a plane wave).

Now consider the equation

$$\text{Curl } \mathbf{E} = -j\omega \mu_0 \mathbf{H} \quad (1.205)$$

Separating this into components, we obtain

$$\begin{aligned} (\text{Curl } \mathbf{E})_x &= -j\omega\mu_0 \mathbf{H}_x \\ (\text{Curl } \mathbf{E})_y &= -j\omega\mu_0 \mathbf{H}_y \\ (\text{Curl } \mathbf{E})_z &= -j\omega\mu_0 \mathbf{H}_z \end{aligned} \quad (1.206)$$

Now, expanding  $\text{Curl } \mathbf{E}$  into its components in the  $x$ -,  $y$ - and  $z$ -directions, we obtain

$$\text{Curl } \mathbf{E} = \left\{ \frac{\partial E_z}{\partial y} - \frac{\partial E_y}{\partial z} \right\} \mathbf{a}_x - \left\{ \frac{\partial E_z}{\partial x} - \frac{\partial E_x}{\partial z} \right\} \mathbf{a}_y + \left\{ \frac{\partial E_y}{\partial x} - \frac{\partial E_x}{\partial y} \right\} \mathbf{a}_z \quad (1.207)$$

Since  $E_z, E_y = 0$  ( $\mathbf{E}$ -field is in the  $x$ -direction) and all terms operated by  $(\partial/\partial x)$  and  $(\partial/\partial y)$  are zero (no variation in  $x$ - and  $y$ -directions), we obtain

$$(\text{Curl } \mathbf{E})_x = 0 \quad (1.208)$$

$$(\text{Curl } \mathbf{E})_z = 0 \quad (1.209)$$

$$(\text{Curl } \mathbf{E})_y = \frac{\partial E_x}{\partial z} \quad (1.210)$$

Substituting for  $(\text{Curl } \mathbf{E})_y$  from (1.206), we obtain

$$\frac{\partial E_x}{\partial z} = -j\omega\mu_0 H_y \quad (1.211)$$

Substituting for  $E_x$  from (1.211), we obtain an expression for  $\mathbf{H}$ -field as

$$H_y = \left( -\frac{1}{j\omega\mu_0} \right) (-jk) E_{x0} e^{-j kz} e^{j\omega t} \quad (1.212)$$

Substituting  $k = \omega/\sqrt{\mu_0\epsilon_0}$  in the above equation, we obtain

$$H_y = \sqrt{\frac{\epsilon_0}{\mu_0}} E_{x0} e^{-j kz} e^{j\omega t} \quad (1.213)$$

Thus, the  $\mathbf{E}$ - and  $\mathbf{H}$ - and  $\mathbf{B}$ -field components of the plane wave moving in the  $z$ -direction are given by

$$E_x = E_{x0} \cos(\omega t - kz) \quad (1.214)$$

$$H_y = \sqrt{\frac{\mu_0}{\epsilon_0}} E_{x0} \cos(\omega t - kz) \quad (1.215)$$

$$B_y = \sqrt{\mu_0\epsilon_0} E_{x0} \cos(\omega t - kz) \quad (1.216)$$

The above equation shows that, if the electric field component of a plane wave moving in the  $z$ -direction is directed in the  $x$ -direction, then the magnetic field is directed in the  $y$ -direction. That is, the magnetic field is perpendicular to the electric field. In fact the direction of propagation of the wave is given by the direction of  $\mathbf{E} \times \mathbf{H}$  (or  $\mathbf{E} \times \mathbf{B}$ ) where  $\mathbf{E}$  and  $\mathbf{H}$  (or  $\mathbf{B}$ ) are the electric and magnetic field components of the wave. In fact in a plane wave  $\mathbf{E}$ ,  $\mathbf{H}$  (or  $\mathbf{B}$ ) and the direction of propagation (in the above case  $x$ ,  $y$  and  $z$  respectively) form an orthogonal set. In a plane wave in vacuum (moving in the  $z$ -direction), the ratio of E-field and H-field components is given by

$$\frac{E_x}{H_y} = \sqrt{\frac{\mu_0}{\epsilon_0}} \quad (1.217)$$

The parameter  $\sqrt{\mu_0/\epsilon_0}$  is called the intrinsic impedance of vacuum (or free space) and is denoted usually by  $\eta_0$ . The ratio of the E- and B-field components of the plane wave is given by

$$\frac{E_x}{B_y} = \frac{1}{\sqrt{\mu_0\epsilon_0}} = \frac{1}{c} \quad (1.218)$$

where  $c$  is the speed of light in vacuum.

### 1.12.3 Energy transported by a plane wave – Poynting's theorem

Consider the divergence of quantity  $\mathbf{E} \times \mathbf{H}$  in a plane wave. We obtain (from 1.38)

$$\text{Div}(\mathbf{E} \times \mathbf{H}) = -\mathbf{E} \cdot (\text{Curl } \mathbf{H}) + \mathbf{H} \cdot (\text{Curl } \mathbf{E}) \quad (1.219)$$

Substituting for  $\text{Curl } \mathbf{H}$  and  $\text{Curl } \mathbf{E}$  from Maxwell's equations, we obtain

$$\text{Div}(\mathbf{E} \times \mathbf{H}) = -\mathbf{E} \cdot \epsilon_0 \frac{\partial \mathbf{E}}{\partial t} + \mathbf{H} \cdot \mu_0 \frac{\partial \mathbf{H}}{\partial t} \quad (1.220)$$

The above can be written as

$$\text{Div}(\mathbf{E} \times \mathbf{H}) = -\frac{\partial}{\partial t} \left\{ \frac{\epsilon_0 E^2}{2} + \frac{\mu_0 H^2}{2} \right\} \quad (1.221)$$

Consider a closed volume in a region in vacuum where a plane wave is propagating. This volume is bounded by a surface  $S$ . Now take the integral of the quantity  $\text{Div}(\mathbf{E} \times \mathbf{H})$  in this closed volume. We obtain

$$\int_v \text{Div}(\mathbf{E} \times \mathbf{H}) dv = -\frac{\partial}{\partial t} \int_v \left\{ \frac{\epsilon_0 E^2}{2} + \frac{\mu_0 H^2}{2} \right\} dv \quad (1.222)$$

Note that the quantity on the right-hand side of the above equation is the energy densities of the E- and B-fields ((1.143) and (1.173)). Thus, the right-hand side of this equation gives the rate of change of the energy or the energy lost from the closed volume. Now, converting the left-hand side using the divergence theorem, we obtain

$$\oint_s (\mathbf{E} \times \mathbf{H}) \cdot d\mathbf{s} = -\frac{\partial}{\partial t} \int_v \left\{ \frac{\epsilon_0 E^2}{2} + \frac{\mu_0 H^2}{2} \right\} dv \quad (1.223)$$

Since the right-hand side gives the rate of energy dissipation from the closed volume, the left-hand side tells us that the energy moving out from a unit area in a direction perpendicular to that unit area in a unit time is  $\mathbf{E} \times \mathbf{H}$ . Note that the direction of  $\mathbf{E} \times \mathbf{H}$  is the direction of propagation of the wave. Thus, the energy passing through a unit area per unit time perpendicular to the direction of propagation of the wave is  $\mathbf{E} \times \mathbf{H}$ . This is called the Poynting's theorem and  $\mathbf{E} \times \mathbf{H}$  is called the Poynting vector. In the example considered previously for a plane wave moving in the z-direction the E- and H-field components are given by (1.214) and (1.215). Using these in the Poynting vector we find the power flow  $P_z$  in the z-direction as

$$P_z = \frac{E_{x0}^2}{\eta_0} \cos^2(\omega t - kz) \quad (1.224)$$

The units of  $P_z$  is watts per metre<sup>2</sup> (W/m<sup>2</sup>).

## 1.13 Maxwell's equations and plane waves in different media (summary)

### 1.13.1 Vacuum

In vacuum we have  $\epsilon_r = 1$ ,  $\mu_r = 1$  and  $\mathbf{J} = 0$ . We also assume that the fields are varying as  $e^{j\omega t}$ . Thus, the corresponding Maxwell's equations are

$$\text{Div } \mathbf{E} = \frac{\rho}{\epsilon_0} \quad (1.225)$$

$$\text{Div } \mathbf{B} = 0 \quad (1.226)$$

$$\text{Curl } \mathbf{E} = -j\omega \mathbf{B} \quad (1.227)$$

$$\text{Curl } \mathbf{B} = j\omega \epsilon_0 \mu_0 \mathbf{E} \quad (1.228)$$

The E-field (assumed to be in the  $x$ -direction) associated with a plane moving in the  $z$ -direction is given by

$$E_x = E_{x0} e^{j\omega t} e^{-j\omega z \sqrt{\epsilon_0 \mu_0}} \quad (1.229a)$$

or

$$E_x = E_{x0} \sin\{\omega(t - z \sqrt{\epsilon_0 \mu_0})\} \quad (1.229b)$$

The H-field is given by (this is derived in Section 1.12.2)

$$H_y = \sqrt{\frac{\mu_0}{\epsilon_0}} E_{x0} e^{j\omega t} e^{-j\omega z \sqrt{\epsilon_0 \mu_0}} \quad (1.230a)$$

or

$$H_y = \sqrt{\frac{\mu_0}{\epsilon_0}} E_{x0} \sin\{\omega(t - z \sqrt{\epsilon_0 \mu_0})\} \quad (1.230b)$$

The speed of propagation of the wave,  $v$ , is given by  $v = 1/\sqrt{\epsilon_0 \mu_0}$ .

### 1.13.2 Isotropic and linear dielectric and magnetic media

Since the conductivity of the medium is zero, the conducting current  $\mathbf{J} = 0$ . Maxwell's equations take the form

$$\text{Div } \mathbf{E} = \frac{\rho}{\epsilon_r \epsilon_0} \quad (1.231)$$

$$\text{Div } \mathbf{B} = 0 \quad (1.232)$$

$$\text{Curl } \mathbf{E} = -j\omega \mathbf{B} \quad (1.233)$$

$$\text{Curl } \mathbf{B} = j\omega \mu_0 \epsilon_0 \mu_r \mu_0 \mathbf{E} \quad (1.234)$$

The E-field (assumed to be in the  $x$ -direction) associated with a plane moving in the  $z$ -direction is given by

$$E_x = E_{x0} e^{j\omega t} e^{-j\omega z \sqrt{\epsilon_0 \epsilon_r \mu_r \mu_0}} \quad (1.235a)$$

or

$$E_x = E_{x0} \sin\{\omega(t - z \sqrt{\epsilon_0 \epsilon_r \mu_r \mu_0})\} \quad (1.235b)$$

The H-field is given by (following the same procedure as in Section 1.12.2)

$$H_y = \sqrt{\frac{\mu_r \mu_0}{\epsilon_r \epsilon_0}} E_{x0} e^{j\omega t} e^{-j\omega z \sqrt{\epsilon_0 \mu_0}} \quad (1.236a)$$

or

$$H_y = \sqrt{\frac{\mu_r \mu_0}{\epsilon_r \epsilon_0}} E_{x0} \sin\{\omega(t - z \sqrt{\epsilon_0 \mu_0})\} \quad (1.236b)$$

The speed of propagation of the wave,  $v$ , is given by  $v = 1/\sqrt{\epsilon_0 \mu_r \mu_0 \epsilon_r}$

### 1.13.3 Conducting media

In a conducting media an electric field will give rise to a current. Thus, we have to assume that  $\mathbf{J} \neq 0$ . The Maxwell's equations take the form

$$\text{Div } \mathbf{E} = \frac{\rho}{\epsilon_r \epsilon_0} \quad (1.237)$$

$$\text{Div } \mathbf{B} = 0 \quad (1.238)$$

$$\text{Curl } \mathbf{E} = -j\omega \mathbf{B} \quad (1.239)$$

$$\text{Curl } \mathbf{B} = \mu_r \mu_0 \mathbf{J} + j\omega \mu_0 \mu_r \epsilon_0 \epsilon_r \mathbf{E} \quad (1.240)$$

The last equation can be written as (substituting  $\sigma \mathbf{E}$  for  $\mathbf{J}$ )

$$\text{Curl } \mathbf{B} = j\omega \mathbf{E} \left\{ \frac{\mu_r \mu_0 \sigma}{j\omega} + \mu_0 \mu_r \epsilon_0 \epsilon_r \right\} \quad (1.241)$$

In a highly conducting media the conductivity  $\sigma$  is very large with respect to  $\omega \epsilon_0 \epsilon_r$  (i.e. we assume that the conduction current is much larger than the displacement current) resulting in

$$\text{Curl } \mathbf{B} = j\omega \mathbf{E} \left\{ \frac{\mu_r \mu_0 \sigma}{j\omega} \right\} \quad (1.242)$$

In this case, the electric field associated with the plane wave moving in the  $a$  direction becomes

$$E_x = E_{x0} e^{j\omega t} e^{-j\omega z \sqrt{\mu_r \mu_0 \sigma / j\omega}} \quad (1.243)$$

This can be written as

$$E_x = E_{x0} e^{j\omega t} e^{-j\omega z(a+jb)} \quad (1.244)$$

with

$$a = \sqrt{\frac{\mu_0 \mu_r \sigma}{2\omega}} \quad (1.245)$$

$$b = -\sqrt{\frac{\mu_0 \mu_r \sigma}{2\omega}} \quad (1.246)$$

Substituting for  $a$  and  $b$  we obtain

$$E_x = E_{x0} e^{j\omega \{t - z\sqrt{\mu_r \mu_0 \sigma / 2\omega}\}} e^{-z\sqrt{\mu_r \mu_0 \sigma \omega / 2}} \quad (1.247)$$

The above equation can be written as

$$E_x = E_{x0} e^{j\omega \{t - z\sqrt{\mu_r \mu_0 \sigma / 2\omega}\}} e^{-z/\delta} \quad (1.248)$$

Starting with the Maxwell's equation  $\text{Curl } \mathbf{E} = -j\omega \mu_0 \mathbf{H}$  and following the same procedure used in Section 1.12.2, we obtain the H-field of the plane wave as

$$H_y = \left\{ (1-j) \sqrt{\frac{\sigma}{2\mu_r \mu_0 \omega}} \right\} E_{x0} e^{j\omega \{t - z\sqrt{\mu_r \mu_0 \sigma / 2\omega}\}} e^{-z/\delta} \quad (1.249)$$

Note first that there is a phase difference between the E-field and the H-field. Moreover, the above equations show that as the wave moves in the  $z$ -direction its amplitude will decrease exponentially. The parameter  $\delta$  is called the skin depth of the medium. Thus, the skin depth is given by

$$\delta = \sqrt{\frac{2}{\mu_r \mu_0 \sigma \omega}} \quad (1.250)$$

In terms of frequency of the wave,  $f$ , the skin depth is given by

$$\delta = \sqrt{\frac{1}{\mu_r \mu_0 \pi \sigma f}} \quad (1.251)$$

The speed of propagation of the wave,  $v$ , becomes

$$v = \sqrt{\frac{2\omega}{\epsilon_0 \mu_0 \mu_r \epsilon_r}} \quad (1.252)$$

This shows that the speed of propagation of the wave is a function of  $\omega$ . Thus, waves of different frequencies travel at different speeds in conducting media.

## 1.14 Retarded potentials

Recall that the scalar and vector potentials of static charge and current distributions are given by

$$V = \frac{1}{4\pi\epsilon_0} \int \frac{\rho_v dv}{r} \quad (1.253)$$

$$\mathbf{A} = \frac{\mu}{2\pi} \int \frac{\mathbf{J}(r) dv}{r} \quad (1.254)$$

Recall also that under static conditions  $V$  and  $\mathbf{A}$  satisfy the equations

$$\nabla^2 \phi = -\frac{\rho}{\epsilon_0} \quad (1.255)$$

$$\nabla^2 \mathbf{A} = -\mu_0 \mathbf{J} \quad (1.256)$$

Now, let us consider the case in which both  $\mathbf{J}$  and  $\rho_v$  depend on time. We start with the Maxwell's equation

$$\text{Curl } \mathbf{B} = \mu_0 \mathbf{J} + \mu_0 \frac{\partial \mathbf{D}}{\partial t} \quad (1.257)$$

This can be written as

$$\text{Curl}(\text{Curl } \mathbf{A}) = \mu_0 \mathbf{J} + \mu_0 \epsilon_0 \frac{\partial \mathbf{E}}{\partial t} \quad (1.258)$$

In the presence of time-varying fields the electric field has two components: One due to static charges and the other due to changing magnetic fields. The contribution due to static charges is given by  $-\text{Grad } \phi$ . The E-field component produced by the changing magnetic field, say  $\mathbf{E}_m$  is given by

$$\text{Curl } \mathbf{E}_m = -\frac{\partial \mathbf{B}}{\partial t} \quad (1.259)$$

substituting  $\mathbf{B} = \text{Curl } \mathbf{A}$ , we find that

$$\mathbf{E}_m = -\frac{\partial \mathbf{A}}{\partial t} \quad (1.260)$$

Thus, the total E-field is given by

$$\mathbf{E} = -\frac{\partial \mathbf{A}}{\partial t} - \text{Grad } \phi \quad (1.261)$$

Expanding the left-hand side of equation (1.258) and substituting for  $\mathbf{E}$  from (1.261) we obtain

$$\text{Grad}(\text{Div } \mathbf{A}) - \nabla^2 \mathbf{A} = \mu_0 \mathbf{J} - \mu_0 \epsilon_0 \frac{\partial^2 \mathbf{A}}{\partial t^2} - \mu_0 \epsilon_0 \frac{\partial}{\partial t} \text{Grad } \phi \quad (1.262)$$

Now we have already defined  $\text{Curl } \mathbf{A}$  but we have the freedom to select the function  $\text{Div } \mathbf{A}$ . Let us select it as

$$\text{Div } \mathbf{A} = -\mu_0 \epsilon_0 \frac{\partial \phi}{\partial t} \quad (1.263)$$

This is called the Lorentz Gauge. Substituting this in (1.262), we obtain

$$-\mu_0 \epsilon_0 \frac{\partial}{\partial t} \text{Grad } \phi - \nabla^2 \mathbf{A} = \mu_0 \mathbf{J} - \mu_0 \epsilon_0 \frac{\partial^2 \mathbf{A}}{\partial t^2} - \mu_0 \epsilon_0 \frac{\partial}{\partial t} \text{Grad } \phi \quad (1.264)$$

This reduces to

$$\nabla^2 \mathbf{A} - \mu_0 \epsilon_0 \frac{\partial^2 \mathbf{A}}{\partial t^2} = -\mu_0 \mathbf{J} \quad (1.265)$$

Now, let us consider the scalar potential. We start with (1.261). Taking the divergence of both sides of this equation, we obtain

$$\text{Div } \mathbf{E} = -\nabla^2 \phi - \frac{\partial}{\partial t} \text{Div } \mathbf{A} \quad (1.266)$$

However, in vacuum  $\text{Div } \mathbf{E} = \rho/\epsilon_0$  and substituting this in the above we obtain

$$\nabla^2 \phi + \frac{\partial}{\partial t} \text{Div } \mathbf{A} = -\frac{\rho}{\epsilon_0} \quad (1.267)$$

Now substituting for  $\text{Div } \mathbf{A}$  from the Lorentz condition (i.e. (1.263)), we obtain

$$\nabla^2 \phi - \mu_0 \epsilon_0 \frac{\partial^2 \phi}{\partial t^2} = -\frac{\rho}{\epsilon} \quad (1.268)$$

Note that both (1.267) and (1.269) reduce to (1.256) and (1.255), respectively, under static conditions.

In the case of time-varying charges and currents, the field at a given time is produced by charges and currents at some earlier time  $t_r$  where  $t_r = t - (r/c)$  and  $r$  is the distance to the location of the charge or the current that gives rise to the field. So the general solution for  $\phi$  and  $\mathbf{A}$  is

$$\phi = \frac{1}{4\pi\epsilon_0} \int \frac{\rho_v(r, t - (r/c))}{r} dv \quad (1.269)$$

$$\mathbf{A} = \frac{\mu_0}{4\pi} \int \frac{\mathbf{J}(r, t - (r/c))}{r} dv \quad (1.270)$$

In the above equation, the time  $t - r/c$  is called the retarded time  $\phi$  and  $\mathbf{A}$  as given by (1.269) and (1.270) are called retarded potentials.

### 1.14.1 Vector potential of a current element

Consider a current element with a time-varying current. Let us represent the current element by the vector  $d\mathbf{l}$ . The direction of this vector is given by the direction of current flow. Let us assume that the direction of current flow is in the  $z$ -direction. The geometry is shown in Figure 1.12. Using (1.270) we can write directly in the case of time-varying current

$$\mathbf{A}_z = \frac{\mu_0}{4\pi} d\mathbf{l} \frac{1}{r} I(t - (r/c)) \quad \text{or} \quad \mathbf{A}_z = \frac{\mu_0}{4\pi} dl \frac{1}{r} I(t - (r/c)) \mathbf{a}_z \quad (1.271)$$

In writing down this equation we have made two assumptions. The first one is that  $r \gg l$ . This assumption is necessary to make sure that the value of  $r$  inside the integral of (1.268) does not change from one point of the source to the other. The second one is that we have assumed that the current flowing through different parts of the element is the same at any given time. If we assume that the current in the element varies as  $e^{j\omega t}$ , i.e.

$$I = I_0 e^{j\omega t} \quad (1.272)$$

we obtain

$$\mathbf{A}_z = \frac{\mu_0 l}{4\pi r} e^{j\omega t} e^{jk_0 r} \quad (1.273)$$

In the above equation  $k_0 = \omega/c$  where  $c$  is the speed of propagation of the electromagnetic waves in vacuum (i.e. the speed of light).

## 1.15 Electromagnetic fields of a current element – electric dipole

Consider a current element of length  $dl$  located at the origin of the coordinate system. We use cylindrical coordinates and the current in the current element is directed in the  $z$ -direction. The current in the element is given by  $I = I_0 e^{j\omega t}$ . As before the vector potential at point  $\mathbf{P}$  (see Figure 1.12) is given by

$$\mathbf{A} = \frac{\mu_0}{4\pi} I_0 d\mathbf{l} \frac{e^{-jk_0 R_0}}{R_0} \quad (1.274)$$

Again in writing down this equation, we have made two assumptions. As mentioned in the previous section they are the following: (i)  $r \gg l$  (ii) At any given time the current does not change from one point of the element to another. This condition is satisfied when  $\lambda \gg l$  where  $\lambda$  is the wavelength. In the above equation, we

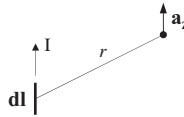


Figure 1.12 Geometry relevant to the derivation of the vector potential due to a short dipole

have suppressed the time variation  $e^{j\omega t}$  for simplicity. Moreover in that equation

$$R_0^2 = \rho^2 + z^2 \quad (1.275)$$

If the location of the current element is at height  $h$  above the origin, then  $R_0$  should be replaced by

$$R_0 = \rho^2 + (z - h)^2 \quad (1.276)$$

Now, the E-field at point  $\mathbf{P}$  is given by

$$\mathbf{E} = -j\omega \mathbf{A} - \text{Grad } \phi \quad (1.277)$$

where  $\mathbf{A}$  and  $\phi$  are the vector and scalar potentials at point  $\mathbf{P}$ , respectively. When all parameters are changing as  $e^{j\omega t}$  the Lorentz Gauge can be written as

$$\phi = -\frac{\text{Div } \mathbf{A}}{\epsilon_0 \mu_0 j\omega} \quad (1.278)$$

From this we obtain

$$\text{Grad } \phi = -\frac{1}{\epsilon_0 \mu_0 j\omega} \nabla(\nabla \cdot \mathbf{A}) \quad (1.279)$$

Substituting this in (1.277), we obtain

$$\mathbf{E} = \frac{1}{\epsilon_0 \mu_0 j\omega} \nabla(\nabla \cdot \mathbf{A}) - j\omega \mathbf{A} \quad (1.280)$$

The above can be written as

$$\mathbf{E} = \frac{1}{\epsilon_0 \mu_0 j\omega} [\nabla(\nabla \cdot \mathbf{A}) + \omega^2 \epsilon_0 \mu_0 \mathbf{A}] \quad (1.281)$$

Note that the above equation expresses the E-field completely in terms of the vector potential.

Using the expression for  $\nabla$  in cylindrical coordinates we find that the electric field components in cylindrical coordinates are given by

$$E_z = \frac{1}{j\omega\epsilon_0\mu_0} \left[ \frac{\partial^2 A_z}{\partial z^2} + k_0^2 A_z \right] \quad (1.282)$$

$$E_\rho = \frac{1}{j\omega\mu_0\epsilon_0} \frac{\partial^2 A_z}{\partial \rho \partial z} \quad (1.283)$$

Let us consider the B-field. It is given by

$$\mathbf{B} = \text{Curl } \mathbf{A} \quad (1.284)$$

Since  $\mathbf{A}$  has only a  $z$  component, B-field has a component only in the  $\varphi$  direction and it is given by

$$B_\varphi = -\frac{\partial^2 A_z}{\partial \rho} \quad (1.285)$$

Performing these derivatives in (1.282), (1.283) and (1.285), we find

$$E_z = -\frac{jk_0 I dl}{4\pi\epsilon_0 c R_0} \left\{ \sin^2 \theta - (2\cos^2 \theta - \sin^2 \theta) \left[ \frac{1}{jk_0 R_0} - \frac{1}{(jk_0 R_0)^2} \right] \right\} e^{-jk_0 R_0} \quad (1.286)$$

$$E_\rho = \frac{jk_0 I dl}{4\pi\epsilon_0 c R_0} \sin \theta \cos \theta \left[ 1 + \frac{3}{jk_0 R_0} + \frac{3}{(jk_0 R_0)^2} \right] e^{-jk_0 R_0} \quad (1.287)$$

$$B_\varphi = \frac{jk_0 \mu_0 I dl}{4\pi R_0} \sin \theta \left( 1 + \frac{1}{jk_0 R_0} \right) e^{-jk_0 R_0} \quad (1.288)$$

Note that the E-field has three components one varying as  $1/R_0$  (called the radiation field), the other varying as  $1/R_0^2$  (called the induction field) and the third component varying as  $1/R_0^3$  (called the static field). When the distance to the point of observation is such that  $k_0 R \gg 1$ , the contributions from the static and induction fields can be neglected leaving behind only the radiation fields. These are sometimes called far fields. The far fields are given by

$$E_z = -\frac{jk_0 I dl}{4\pi\epsilon_0 c R_0} \sin^2 \theta e^{-jk_0 R_0} \quad (1.289)$$

$$E_\rho = \frac{jk_0 I dl}{4\pi\epsilon_0 c R_0} \sin \theta \cos \theta e^{-jk_0 R_0} \quad (1.290)$$

$$B_\varphi = \frac{jk_0\mu_0 Idl}{4\pi R_0} \sin \theta e^{-jk_0 R_0} \quad (1.291)$$

The field components in spherical coordinates are given by

$$E_r = E_z \cos \theta + E_\rho \sin \theta \quad (1.292)$$

$$E_\theta = -E_z \sin \theta + E_\rho \cos \theta \quad (1.293)$$

$$B_\varphi = \frac{jk_0\mu_0 Idl}{4\pi R_0} \sin \theta e^{-jk_0 R_0} \quad (1.294)$$

After substituting for  $E_z$  and  $E_\rho$ , we obtain

$$E_r = \frac{I_0 le^{j\omega t} e^{-jk_0 r}}{2\pi\epsilon_0} \cos \theta \left[ \frac{1}{cr^2} + \frac{1}{j\omega r^3} \right] \quad (1.295)$$

$$E_\theta = \frac{I_0 le^{j\omega t} e^{-jk_0 r}}{4\pi\epsilon_0} \sin \theta \left[ \frac{j\omega}{c^2 r} + \frac{1}{cr^2} + \frac{1}{j\omega r^3} \right] \quad (1.296)$$

$$B_\varphi = \frac{\mu_0 I_0 le^{j\omega t} e^{-jk_0 r}}{4\pi} \sin \theta \left[ \frac{j\omega}{cr} + \frac{1}{r^2} \right] \quad (1.297)$$

These equations (or their counterpart in time domain) are frequently used in calculating the electromagnetic fields of lightning flashes. In these calculations, the lightning channel is divided in a series of infinitesimal current elements and the total field is obtained as a sum of the fields generated by these elements. The field due to each current element in frequency domain is given by the above equations.

## 1.16 Electromagnetic fields of a lightning return stroke

Consider a lightning return stroke located over ground that is assumed to be a perfect conductor. We assume that the lightning channel is straight and vertical. Let us divide this channel into a large number of elements. Consider a current element of length  $dz$  located at a height  $z$  above a perfectly conducting ground plane at zero potential (Figure 1.13). This plane represents the earth's surface. The goal is to write down an expression for the electric field at the surface of the conductor. The effect of the conductor can be taken into account by replacing it by an image current element located at a distance  $h$  below the ground plane (Figure 1.13). Note that when a positive current flows upwards along the current element, a negative

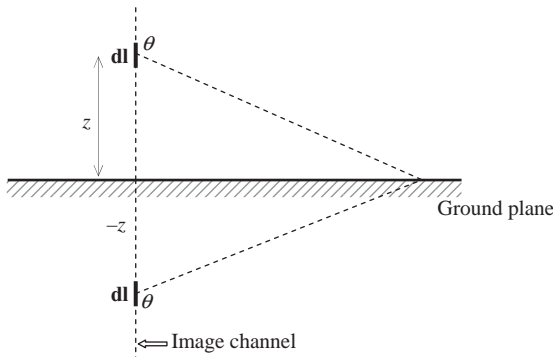


*Figure 1.13 Geometry relevant to the calculation of electromagnetic fields due to a lightning channel located above a perfectly conducting ground plane*

current flows downwards in the image. Writing down the E-field components due to the two current elements using (1.295) to (1.297) and summing up the contributions, we obtain the component of the E-field perpendicular to the ground as

$$dE_v = \frac{I_0 dz e^{j(\omega t - \beta r)}}{2\pi\epsilon_0} \left[ -\frac{\sin^2 \theta j\omega}{c^2 r} + (2 - 3\sin^2 \theta) \frac{1}{cr^2} + \frac{1}{j\omega r^3} (2 - 3\sin^2 \theta) \right] \quad (1.298)$$

The E-field component parallel to the surface or the horizontal E-field is zero. The B-field at the surface is given by

$$dB_\varphi = \frac{\mu_0 I_0 dz e^{j\omega t} e^{-jk_o r}}{2\pi} \sin \theta \left[ \frac{j\omega}{cr} + \frac{1}{r^2} \right] \quad (1.299)$$

Transforming these equations into time domain, one obtains (see also the chapter on dipole radiation)

$$dE_v(t) = \frac{dz}{2\pi\epsilon_0} \left[ -\frac{\sin^2 \theta dI(t - r/c)}{c^2 r} + (2 - 3\sin^2 \theta) \frac{1}{cr^2} + \frac{1}{r^3} (2 - 3\sin^2 \theta) \int_0^t I(z - r/c) dt \right] \quad (1.300)$$

$$dB_\varphi(t) = \frac{\mu_0 dz}{2\pi} \left[ \frac{\sin \theta dI(t - r/c)}{cr} + \frac{\sin \theta}{r^2} I(t - r/c) \right] \quad (1.301)$$

The electromagnetic field generated by a lightning return stroke can be obtained by summing the contribution from each element taking into account

the time delays properly. Thus, the total E- and B-fields due to a lightning flash are given by

$$E_v(t) = \int_0^H \frac{dz}{2\pi\epsilon_0} \left[ -\frac{\sin^2\theta}{c^2r} \frac{dI(t-r/c)}{dt} + \frac{(2-3\sin^2\theta)}{cr^2} I(t-r/c) \right. \\ \left. + \frac{1}{r^3} (2-3\sin^2\theta) \int_0^t I(z-r/c) dz \right] \quad (1.302)$$

$$B_\varphi(t) = \int_0^H \frac{\mu_0 dz}{2\pi} \left[ \frac{\sin\theta}{cr} \frac{dI(t-r/c)}{dt} + \frac{\sin\theta}{r^2} I(t-r/c) \right] \quad (1.303)$$

When the distance is very large compared to the dimension of the channel, only the terms which vary as  $1/r$  will contribute to the fields. These far or radiation fields are given by (note also that under these conditions  $\sin\theta=1$ )

$$E_{vr}(t) = - \int_0^H \frac{dz}{2\pi\epsilon_0} \left[ \frac{1}{c^2r} \frac{dI(t-r/c)}{dt} \right] \quad (1.304)$$

$$B_{qr}(t) = \int_0^H \frac{\mu_0 dz}{2\pi} \left[ \frac{1}{cr} \frac{dI(t-r/c)}{dt} \right] \quad (1.305)$$

Note that these fields satisfy the condition

$$E_{vr}(t) = cB_{qr}(t) \quad (1.306)$$

where  $c$  is the speed of light in vacuum.

## Further reading

1. Panofsky W. K. H., M. Phillips, *Classical Electricity and Magnetism*, Addison-Wesley, New York, 1962
2. Thidé B., *Classical Electrodynamics*, On-Line Textbook, <http://www.plasma.uu.se/CED/Book/>
3. Jackson J. D., *Classical Electrodynamics*, Wiley, New York, 1999



---

## *Chapter 2*

# **Application of electromagnetic fields of an accelerating charge to obtain the electromagnetic fields of a propagating current pulse**

*Gerald Cooray<sup>1</sup> and Vernon Cooray<sup>2</sup>*

---

## **2.1 Introduction**

Recently, Cooray and Cooray [1] have demonstrated that electromagnetic fields from accelerating charges can be utilized to evaluate the electromagnetic fields from lightning return strokes. In that publication, they have documented in detail how to utilize the equations to calculate electromagnetic fields of various engineering return stroke models, both current propagation and current generation types (see Chapter 7). They have also demonstrated how the equations can be utilized to calculate radiation fields generated by currents propagating along transmission lines in the presence of bends. The basics of this technique are summarized in this chapter by applying it to evaluate the electromagnetic fields of a propagating current pulse. First, let us consider the electromagnetic fields of a moving electric charge.

## **2.2 Electromagnetic fields of a moving charge**

The theory of electromagnetic fields generated by moving charges is described in any standard text book on electromagnetic theory, and it suffices to quote the results directly [2]. The geometry relevant to the problem under consideration is depicted in Figure 2.1. In this diagram,  $\mathbf{a}_r$  and  $\mathbf{a}_\theta$  are unit vectors one in the direction of increasing  $r$  and the other in the angular direction of increasing  $\theta$ . A charged particle is moving with velocity  $\mathbf{u}$  and acceleration  $\dot{\mathbf{u}}$ . We assume that the direction of  $\mathbf{u}$  does not change with time; that is, both  $\mathbf{u}$  and  $\dot{\mathbf{u}}$  are acting in the same direction. The electric field produced by this charge at point P (with  $\beta = (\mathbf{u}/c)$  and  $\mathbf{a}_r = (\mathbf{r}/r)$ ) is given by

---

<sup>1</sup>Department of Clinical Neuroscience, Karolinska Institute, Stockholm, Sweden

<sup>2</sup>Uppsala University, Uppsala, Sweden

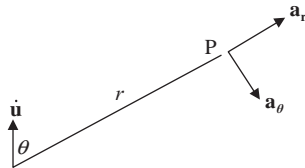


Figure 2.1 Definition of the parameters that appear in (2.1) and (2.2)

$$\begin{aligned}\mathbf{E} = & \frac{q}{4\pi\epsilon_0 r^2} \frac{1}{(1 - \beta \cdot \mathbf{a}_r)^3} (\mathbf{a}_r - \beta)(1 - \beta^2) \\ & + \frac{q}{4\pi\epsilon_0 c r (1 - \beta \cdot \mathbf{a}_r)^3} [\mathbf{a}_r \times (\mathbf{a}_r \times \dot{\beta})]\end{aligned}\quad (2.1)$$

$$\begin{aligned}\mathbf{B} = & \frac{q}{4\pi\epsilon_0 c r^2 (1 - \beta \cdot \mathbf{a}_r)^3} (\beta \times \mathbf{a}_r)(1 - \beta^2) \\ & + \frac{q}{4\pi\epsilon_0 c^2 (1 - \beta \cdot \mathbf{a}_r)^3 r} \{ \mathbf{a}_r \times [\mathbf{a}_r \times (\mathbf{a}_r \times \dot{\beta})] \}\end{aligned}\quad (2.2)$$

Note that the expressions for  $\mathbf{E}$  and  $\mathbf{B}$  both consist of two terms. The second term, which depends on the acceleration of the charge, is the radiation field, and the first term is called the velocity field. Note that the velocity field becomes zero when the velocity of propagation of the charge is equal to the speed of light.

### 2.3 Basic equations pertinent to the radiation and velocity field of a propagating current pulse

Consider the geometry shown in the top diagram of Figure 2.2. A pulse of current originates at point S1 and travels along the  $z$ -axis with constant velocity  $u$  and without any attenuation or dispersion. At the initiation of the current, charges will

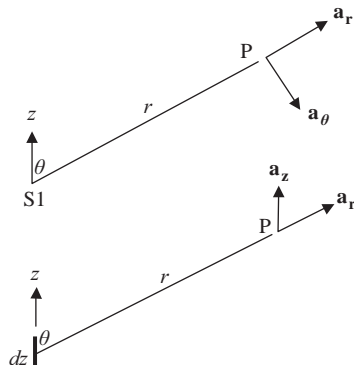


Figure 2.2 Geometry relevant to the parameters in (2.3) and (2.4) (top diagram) and (2.5) and (2.6) (bottom diagram)

be accelerated from rest to a velocity  $u$ . Once they attain this velocity, they travel with constant velocity along the  $z$ -axis. The acceleration of charge at S1 generates a radiation field, and the uniform propagation of charge along the  $z$ -axis generates a velocity field. Recently, using (2.1) and (2.2), Cooray and Cooray [1] derived expressions for the radiation field produced by the acceleration of charge at S1 and for the velocity field produced by the uniform motion. According to their results, the expressions for the electric and magnetic radiation fields generated by the charge acceleration are given respectively by

$$\mathbf{e}_{rad}(t) = \frac{i_b(t - r/c)u\sin\theta}{4\pi\epsilon_0 c^2 r} \frac{1}{[1 - (ucos\theta/c)]} \mathbf{a}_\theta \quad (2.3)$$

$$\mathbf{b}_{rad}(t) = \frac{i_b(t - r/c)u\sin\theta}{4\pi\epsilon_0 c^3 r} \frac{1}{[1 - (ucos\theta/c)]} \mathbf{a}_\phi \quad (2.4)$$

In these equations,  $i_b(t)$  is the temporal variation of the current emanating from S1. Now, consider a spatial element of length  $dz$  through which a current pulse  $i_b(t)$  is moving with velocity  $u$  (see the diagram at the bottom of Figure 2.2). The velocity fields generated by this element at point P are given by [1]

$$d\mathbf{e}_{vel} = \frac{i_b(t - r/c)dz}{4\pi\epsilon_0 r^2 [1 - (u/c)\cos\theta]^2} \left[ 1 - \frac{u^2}{c^2} \right] \left[ \frac{\mathbf{a}_r}{u} - \frac{\mathbf{a}_z}{c} \right] \quad (2.5)$$

$$d\mathbf{b}_{vel} = \frac{i_b(t - r/c)dz}{4\pi\epsilon_0 r^2 c^2 [1 - (u/c)\cos\theta]^2} \left[ 1 - \frac{u^2}{c^2} \right] \mathbf{a}_\phi \quad (2.6)$$

In the next section, these equations are used to derive the electric and magnetic fields of a current pulse that propagates with constant velocity without attenuation.

## 2.4 Electromagnetic fields generated by a current pulse propagating with uniform velocity and without attenuation

The geometry under consideration is shown in Figure 2.3. A current pulse originates at point S1 and travels without attenuation or dispersion towards S2. At S2, the current is terminated. The total electric field at point P, generated by this process, has five components. They are as follows: (i) the radiation field generated from S1 as the charge accelerates when the current is initiated, (ii) the radiation field generated from S2 during the charge deceleration as the current is terminated, (iii) the electrostatic field generated by the negative charge accumulated at S1 when the positive charge travels towards S2, (iv) the electrostatic field generated by the accumulation of positive charge at S2 and (v) the velocity field generated as the current pulse moves along the  $z$  direction. The magnetic field generated by the current pulse consists of three terms, namely two radiation fields generated at S1 and S2, and the velocity field generated as the current propagates along the path. Let us now write down the expressions for these field components.

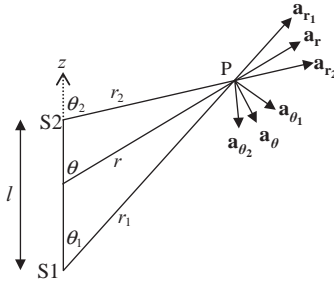


Figure 2.3 Geometry used in deriving the electromagnetic fields of a current channel

#### 2.4.1 The electric radiation field generated by the initiation of the current

Let us assume that the current pulse leaving S1 can be represented by  $i_b(t)$ . The radiation field at point P is given by (2.3), and with the geometry under consideration here, one can rewrite this as

$$\mathbf{e}_{rad,S_1} = \frac{i_b(t - r_1/c) u \sin\theta_1}{4\pi\epsilon_0 c^2 r_1} \frac{1}{[1 - (u \cos\theta_1/c)]} \mathbf{a}_{\theta_1} \quad (2.7)$$

#### 2.4.2 The electric radiation field generated by the termination of the current

The radiation field generated from S2 as the charges decelerate is given by

$$\mathbf{e}_{rad,S_2} = -\frac{i_b(t - r_2/c) u \sin\theta_2}{4\pi\epsilon_0 c^2 r_2} \frac{1}{[1 - (u \cos\theta_2/c)]} \mathbf{a}_{\theta_2} \quad (2.8)$$

#### 2.4.3 The static field generated by the accumulation of charge at the point of current initiation

As the current pulse leaves S1, an electric charge of opposite polarity but equal in magnitude to the integral of the current is accumulated at S1. The electrostatic field generated by the accumulated charge at any time  $t$  is given by

$$\mathbf{e}_{stat,S_1} = -\frac{\int_0^{t-r_1/c} i_b(\tau) d\tau}{4\pi\epsilon_0 r_1^2} \mathbf{a}_{r_1} \quad (2.9)$$

#### 2.4.4 The static field generated by the accumulation of charge at the point of current termination

The component of the static field generated by the accumulation of positive charge at S2 as the current is terminated is given by

$$\mathbf{e}_{stat,S_2} = \frac{\int_0^{t-l/u-r_2/c} i_b(\tau) d\tau}{4\pi\epsilon_0 r_2^2} \mathbf{a}_{r_2} \quad (2.10)$$

### 2.4.5 The velocity field generated by the propagating current pulse

The component attributable to the velocity field generated as the current pulse propagates along the channel element can be written directly using (2.5). The result is

$$\mathbf{e}_{vel} = \int_0^l \frac{i_b(t - z/u - r/c) \{1 - (u^2/c^2)\}}{4\pi\epsilon_0 r^2 [1 - (u/c)\cos\theta]^2} \left[ \frac{\mathbf{a}_r}{u} - \frac{\mathbf{a}_z}{c} \right] dz \quad (2.11a)$$

Since the vector  $\mathbf{a}_r$  varies along the channel, the above equation can be decomposed into components along vertical ( $z$ ) and horizontal ( $\rho$ ) directions as follows:

$$\mathbf{e}_{vel} = \int_0^l \frac{i_b(t - z/u - r/c) \{1 - (u^2/c^2)\}}{4\pi\epsilon_0 r^2 [1 - (u/c)\cos\theta]^2} \left[ \frac{\cos\theta \mathbf{a}_z}{u} + \frac{\sin\theta \mathbf{a}_\rho}{u} - \frac{\mathbf{a}_z}{c} \right] dz \quad (2.11b)$$

Note that  $\mathbf{a}_\rho$  is a unit vector in the horizontal (perpendicular to  $z$ -axis) or  $\rho$ -direction.

### 2.4.6 The magnetic radiation field generated by the initiation of the current

The magnetic radiation field generated from S1 is given by

$$\mathbf{b}_{rad,S1} = \frac{i_b(t - r_1/c) u \sin\theta_1}{4\pi\epsilon_0 c^3 r_1} \frac{1}{[1 - (u \cos\theta_1/c)]} \mathbf{a}_\phi \quad (2.12)$$

Note that the magnetic field is in the azimuthal direction and  $\mathbf{a}_\phi$  is a unit vector in that direction.

### 2.4.7 The magnetic radiation field generated by the termination of the current

The magnetic radiation field generated from S2 is given by

$$\mathbf{b}_{rad,S2} = - \frac{i_b(t - l/u - r_2/c) u \sin\theta_2}{4\pi\epsilon_0 c^3 r_2} \frac{1}{[1 - (u \cos\theta_2/c)]} \mathbf{a}_\phi \quad (2.13)$$

### 2.4.8 Magnetic velocity field generated by the current pulse

The velocity field generated as the current pulse propagates along the channel element is given by

$$\mathbf{b}_{vel} = \int_0^l \frac{i_b(t - z/u - r/c) \{1 - (u^2/c^2)\} \sin\theta}{4\pi\epsilon_0 r^2 c^2 [1 - (u/c)\cos\theta]^2} \mathbf{a}_\phi dz \quad (2.14)$$

The field components given by (2.7)–(2.14) provide a complete description of the electric and magnetic fields generated by a current pulse propagating

with uniform velocity without attenuation. Note also that the velocity field term becomes zero when the velocity of propagation of the pulse is equal to the speed of light. Now, let us introduce current attenuation and non-uniform velocity.

## 2.5 Electromagnetic fields generated by a current pulse propagating with non-uniform velocity and with attenuation

When both the velocity and the current amplitude vary along the path of propagation, the electric field at point P will have eight components. They are as follows: (i) the radiation field generated from S1 as the charge accelerates when the current is initiated, (ii) the radiation field generated from S2 during the charge deceleration as the current is terminated, (iii) the electrostatic field generated by the negative charge accumulated at S1 when the positive charge travels towards S2, (iv) the electrostatic field generated by the accumulation of positive charge at S2, (v) the velocity field generated as the current pulse moves along the path, (vi) the radiation field generated by the deceleration of electrical charges due to the attenuation of current amplitude along the path, (vii) the radiation field generated by the deceleration (or acceleration) of electrical charges caused by the change in velocity of the current along the path and (viii) the electrostatic field generated by the charge deposited on the channel. The magnetic field generated by the element consists of five terms, namely two radiation fields generated at S1 and S2, two radiation fields generated by the change in current and change in velocity along the path and the velocity field generated as the current propagates along the path. Let us now write down the expressions for these field components.

The geometry relevant to the analysis is still given by Figure 2.3. Let us represent the velocity of the current pulse by  $u(z)$  which is a function of  $z$ . Let us also denote the average velocity from the point of origin of the current pulse to any point  $z$  by  $u_{av}(z)$ . Thus

$$u_{av}(z) = \frac{z}{\int_0^z (d\xi/u(\xi))} \quad (2.15)$$

Since the current pulse attenuates as it propagates, the current at any level  $z$  along the path of propagation is given by

$$I(z, t) = A(z) i_b(t - z/u_{av}(z)) \quad (2.16)$$

In the above equation,  $A(z)$  is a function that represents the attenuation of the current pulse as it propagates along the  $z$ -axis. Now let us write down the different components of the electric and magnetic fields generated by this propagating current pulse.

### 2.5.1 The electric radiation field generated by the initiation of the current

As before,  $i_b(t)$  is the current pulse leaving S1. It leaves the source with a velocity equal to  $u(0)$ . The radiation field at point P generated by the initiation of this current pulse is

$$\mathbf{e}_{rad,S_1} = \frac{i_b(t - r_1/c)u(0)\sin\theta_1}{4\pi\epsilon_0 c^2 r_1} \frac{1}{[1 - (u(0)\cos\theta_1/c)]} \mathbf{a}_{\theta_1} \quad (2.17)$$

### 2.5.2 The electric radiation field generated by the termination of the current

The amplitude of the current reaching S2 is different from that left S1, and the current arrives at S2 with velocity  $u(l)$ . Therefore, the radiation field generated from S2 as the charges decelerate is given by

$$\mathbf{e}_{rad,S_2} = -\frac{A(l)i_b(t - l/u_{av}(l) - r_2/c)u(l)\sin\theta_2}{4\pi\epsilon_0 c^2 r_2} \frac{1}{[1 - (u(l)\cos\theta_2/c)]} \mathbf{a}_{\theta_2} \quad (2.18)$$

In the above equation,  $A(l)$  is the amount by which the current was attenuated in travelling from S1 to S2.

### 2.5.3 The static field generated by the accumulation of charge at the point of current initiation

The charge accumulation at S1 is equal to the integral of the current, and the field component generated by the charges is given by

$$\mathbf{e}_{stat,S_1} = -\frac{\int_0^{t-r_1/c} i_b(\tau)d\tau}{4\pi\epsilon_0 r_1^2} \mathbf{a}_{r_1} \quad (2.19)$$

### 2.5.4 The static field generated by the accumulation of charge at the point of current termination

The component of the static field generated by the accumulation of positive charge at S2 is given by

$$\mathbf{e}_{stat,S_2} = \frac{A(l) \int_0^{t-l/u_{av}(l)-r_2/c} I_b(\tau)d\tau}{4\pi\epsilon_0 r_2^2} \mathbf{a}_{r_2} \quad (2.20)$$

### 2.5.5 The velocity field generated as the current pulse propagates along the channel element

The component attributable to the velocity field generated as the current pulse propagates along the channel element can be written directly as before. The result is

$$\mathbf{e}_{vel} = \int_0^l \frac{A(z)i_b(t - z/u_{av}(z) - r/c) \left\{ 1 - (u(z)^2/c^2) \right\}}{4\pi\epsilon_0 r^2 [1 - (u(z)/c)\cos\theta]^2} \left[ \frac{\mathbf{a}_r}{u(z)} - \frac{\mathbf{a}_z}{c} \right] dz \quad (2.21a)$$

The above equation can be written as

$$\begin{aligned} \mathbf{e}_{vel} = & \int_0^l \frac{A(z)i_b(t - z/u_{av}(z) - r/c) \left\{ 1 - (u(z)^2/c^2) \right\}}{4\pi\epsilon_0 r^2 [1 - (u(z)/c)\cos\theta]^2} \\ & \left[ \frac{\cos\theta \mathbf{a}_z}{u(z)} + \frac{\sin\theta \mathbf{a}_p}{u(z)} - \frac{\mathbf{a}_z}{c} \right] dz \end{aligned} \quad (2.21b)$$

Note that the amplitude and the velocity of the current pulse are different at different positions along the channel.

### 2.5.6 *The magnetic radiation field generated by the initiation of the current*

The magnetic radiation field generated from S1 is given by

$$\mathbf{b}_{rad,S1} = \frac{i_b(t - r_1/c)u(0)\sin\theta_1}{4\pi\epsilon_0 c^3 r_1} \frac{1}{[1 - (u(0)\cos\theta_1/c)]} \mathbf{a}_\varphi \quad (2.22)$$

### 2.5.7 *The magnetic radiation field generated by the termination of the current*

The magnetic radiation field generated from S2 is given by

$$\mathbf{b}_{rad,S2} = -\frac{A(l)i_b(t - l/u_{av}(l) - r_2/c)u(l)\sin\theta_2}{4\pi\epsilon_0 c^3 r_2} \frac{1}{[1 - (u(l)\cos\theta_2/c)]} \mathbf{a}_\varphi \quad (2.23)$$

### 2.5.8 *Magnetic velocity field generated as the current pulse propagates along the channel element*

The velocity field generated as the current pulse propagates along the channel element is given by

$$\mathbf{b}_{vel} = \int_0^l \frac{A(z)i_b(t - z/u_{av}(z) - r/c) \left\{ 1 - (u(z)^2/c^2) \right\} \sin\theta}{4\pi\epsilon_0 r^2 c^2 [1 - (u(z)/c)\cos\theta]^2} dz \mathbf{a}_\varphi \quad (2.24)$$

### 2.5.9 *Electric radiation field generated due to the attenuation of the current along the channel*

Let us consider an element  $dz$  located at a distance  $z$  from S1. The amount of current that will be removed in passing through this element is

$$dI(z, t) = \frac{\partial A(z)}{\partial z} i_b(t - z/u_{av}(z)) dz \quad (2.25)$$

Thus, the radiation field generated due to the deceleration of charges as the current is attenuated is given by

$$d\mathbf{e}_{rad,ate} = \frac{\frac{\partial A(z)}{\partial z} i_b(t - z/u_{av}(z) - r/c) u(z) \sin\theta dz}{4\pi\epsilon_0 c^2 r} \frac{1}{[1 - (u(z)\cos\theta/c)]} \mathbf{a}_\theta \quad (2.26)$$

Thus, the total electric radiation field caused by the attenuation of the current is

$$\mathbf{e}_{rad,ate} = \int_0^l \frac{\frac{\partial A(z)}{\partial z} i_b(t - z/u_{av}(z) - r/c) u(z) \sin\theta dz}{4\pi\epsilon_0 c^2 r} \frac{1}{[1 - (u(z)\cos\theta/c)]} \mathbf{a}_\theta \quad (2.27a)$$

The above equation can be resolved into  $z$  and  $\rho$  directions as follows:

$$\begin{aligned} \mathbf{e}_{rad,ate} = & \int_0^l \frac{\frac{\partial A(z)}{\partial z} i_b(t - z/u_{av}(z) - r/c) u(z) \sin\theta dz}{4\pi\epsilon_0 c^2 r_1} \\ & \frac{1}{[1 - (u(z)\cos\theta/c)]} [\cos\theta \mathbf{a}_\rho - \sin\theta \mathbf{a}_z] \end{aligned} \quad (2.27b)$$

### 2.5.10 Magnetic radiation field generated due to the attenuation of the current along the channel

Analyzing the problem as before, the total magnetic radiation field generated due to the attenuation of the current along the channel is

$$b_{rad,ate} = \int_0^l \frac{\frac{\partial A(z)}{\partial z} i_b(t - z/u_{av}(z) - r/c) u(z) \sin\theta dz}{4\pi\epsilon_0 c^3 r} \frac{1}{[1 - (u(z)\cos\theta/c)]} \mathbf{a}_\varphi \quad (2.28)$$

### 2.5.11 Static field generated by the charge deposited along the channel by the current pulse

Since the current attenuates along the channel, in order to satisfy continuity equation it is necessary for the charge to be deposited along the channel. The charge deposited in element  $dz$ , located at  $z$ , by the current is given by

$$dQ(z, t) = \frac{\partial A(z)}{\partial z} dz \int_0^{t-z/u} i_b(\tau) d\tau \quad (2.29)$$

Thus, the electrostatic field produced at P by the charge deposited along the channel is given by

$$\mathbf{e}_{stat,ate} = \frac{1}{4\pi\epsilon_0} \int_0^l \frac{\partial A(z)}{\partial z} dz \frac{1}{r^2} \int_0^{t-z/u-r/c} i_b(\tau) d\tau \mathbf{a}_r \quad (2.30a)$$

This can be resolved into vertical and horizontal directions as follows:

$$\mathbf{e}_{stat,cha} = \frac{1}{4\pi\epsilon_0} \int_0^l \frac{\partial A(z)}{\partial z} \frac{dz}{r^2} \left\{ \int_{z/u}^t i_b(\tau) d\tau \right\} [\cos\theta \mathbf{a}_z + \sin\theta \mathbf{a}_p] \quad (2.30b)$$

### 2.5.12 Electric radiation field generated due to the variation of current velocity along the channel

Let us consider an element  $dz$  located at a distance  $z$  from S1. The change in velocity,  $du(z)$ , of the current propagating along the channel element is

$$du(z) = \frac{\partial u(z)}{\partial z} dz \quad (2.31)$$

Thus, the radiation field generated because of the deceleration (or acceleration) of charges due to the change in velocity is

$$d\mathbf{e}_{rad,vel} = \frac{i_b(t - z/u_{av}(z) - r/c) \sin\theta \, du(z)}{4\pi\epsilon_0 c^2 r} \frac{1}{[1 - (u(z)\cos\theta/c)]} \mathbf{a}_\theta \quad (2.32)$$

Thus, the total electric radiation field caused by the attenuation of the current is

$$\mathbf{e}_{rad,vel} = \int_0^l \frac{i_b(t - z/u_{av}(z) - r/c) \sin\theta \, \frac{\partial u(z)}{\partial z} dz}{4\pi\epsilon_0 c^2 r} \frac{1}{[1 - (u(z)\cos\theta/c)]} \mathbf{a}_\theta \quad (2.33a)$$

This can also be written as

$$\mathbf{e}_{rad,vel} = \int_0^l \frac{i_b(t - z/u_{av}(z) - r/c) \sin\theta \, \frac{\partial u(z)}{\partial z} dz}{4\pi\epsilon_0 c^2 r} \frac{1}{[1 - (u(z)\cos\theta/c)]} [\cos\theta \mathbf{a}_p - \sin\theta \mathbf{a}_z] \quad (2.33b)$$

### 2.5.13 Magnetic radiation field generated due to the variation of current velocity along the channel

Analyzing the problem as before, the total magnetic radiation field generated due to the change in velocity of the current along the channel is

$$b_{rad,vel} = \int_0^l \frac{i_b(t - z/u_{av}(z) - r/c) \sin\theta \, \frac{\partial u(z)}{\partial z} dz}{4\pi\epsilon_0 c^3 r} \frac{1}{[1 - (u(z)\cos\theta/c)]} \mathbf{a}_\varphi \quad (2.34)$$

These equations describe completely the electromagnetic field environment produced by a current pulse that moves with non-uniform velocity and with attenuation.

These equations reduce to the equations derived in Section 2.4 when there is no attenuation and the velocity of propagation is uniform.

## 2.6 Concluding remarks

In this chapter, we have described how to calculate the electromagnetic fields generated by a propagating current pulse using field equations of accelerating charges. The results show how the radiation is generated whenever the amplitude or the velocity of propagation of the current pulse is changed. The results can be easily extended to the case of a current channel over perfectly conducting ground by taking into account its image in the ground and calculating the electromagnetic fields from the image current in a manner similar to the way they were derived here for the real channel. The derived equations can also be used to calculate the electromagnetic fields generated by lightning return strokes when the spatial and temporal variation of the current is specified.

## References

- [1] Cooray, V. and G. Cooray, The electromagnetic fields of an accelerating charge: Applications in lightning return stroke models, *Trans. IEEE (EMC)*, **52**(4), 2010
- [2] Pannofsky, W. K. H. and M. Phillips, *Classical Electricity and Magnetism*, Addison-Wesley, Reading, MA, 1962



---

## *Chapter 3*

# **Basic discharge processes in the atmosphere**

*Vernon Cooray*<sup>1</sup>

---

### **3.1 Introduction**

The main constituents of air in the Earth's atmosphere are nitrogen (78%), oxygen (20%), noble gases (1%), water vapour (0.03%), carbon dioxide (0.97%) and other trace gas species. In general, air is a good insulator and it can maintain its insulating properties until the applied electric field exceeds about  $2.8 \times 10^4$  V/cm at standard atmospheric conditions (i.e.  $T = 293$  K and  $P = 1$  atm). When the background electric field exceeds this critical value, the free electrons in air generated mainly by the high energetic radiation of cosmic rays and radio active gases generated from the Earth start accelerating in this electric field and gain enough energy between collisions with atoms and molecules to ionize other atoms. This cumulative ionization leads to an increase in the number of electrons initiating the electrical breakdown of air. The threshold electric field necessary for electrical breakdown of air is a function of atmospheric density. For example, the critical electric field,  $E$ , necessary for electrical breakdown of air of density  $\delta$  is given by

$$E = E_0 \frac{\delta}{\delta_0} \quad (3.1)$$

where  $\delta_0$  is the density of air at sea level at standard atmospheric conditions and  $E_0$  is the corresponding critical electric field necessary for electrical breakdown under the same conditions. Since the density of air in the Earth's atmosphere decreases with height  $z$  (in m) as  $\delta = \delta_0 e^{-z/\lambda_p}$  with  $\lambda_p \approx 7.64 \times 10^3$  m, the critical electric field necessary to cause electrical breakdown in the atmosphere decreases with height as

$$E = E_0 e^{-z/\lambda_p} \quad (3.2)$$

When the electric field in the atmosphere increases beyond this critical value, the appearance of the resulting electrical discharge depends on the pressure and the spatial variation in the electric field. Irrespective of its apparent features the basic constituents of an electrical discharge in air can be separated into four parts. These

<sup>1</sup>Uppsala University, Uppsala, Sweden

are electron avalanches, streamer discharges, corona discharges and leaders. When the leaders reach an electrode of opposite polarity or a region of opposite charge density, a rapid neutralization of the charge on the leader takes place. This neutralization process is called a return stroke. The exact mechanism of the return stroke is not yet known, but different types of models have been developed to describe them. These models are described in several chapters of this book. Here, we will concentrate on the four discharge processes mentioned above. Some parts of this chapter are adopted and summarized from Reference 1 where an extensive description of basic physics of discharges is given.

### 3.2 Electron avalanche

Consider a free electron originated at  $x = 0$  in space and moving under the influence of a background electric field directed in the negative  $x$  direction. If the background electric field is larger than the critical value necessary for cumulative ionization, the electron may produce another electron through ionization collisions and these two electrons in turn will give rise to two more electrons. In this way the number of electrons increases with increasing  $x$ . Assume that the number of electrons at a distance  $x$  from the origin is  $n_x$ . Let  $\alpha$  be the number of ionizing collisions per unit length made by an electron travelling in the direction of the electric field. As the ionization processes increase the number of electrons in air, some of the electrons will get attached to electronegative gases such as oxygen in air. Let  $\eta$  be the number of electron attachments per unit length. The parameter  $\alpha$  is called the Townsend's first ionization coefficient and the parameter  $\eta$  is called the attachment coefficient. Consider an elementary length of width  $dx$  located at a distance  $x$  from the origin. In travelling across the length  $dx$ ,  $n_x$  number of electrons will give rise to  $dn$  additional electrons

$$dn = n_x(\alpha - \eta)dx \quad (3.3)$$

The solution of this equation is

$$n_x = e^{(\alpha-\eta)x} \quad (3.4)$$

This equation shows that the number of electrons increases exponentially with distance. This exponential growth of electrons with distance is called an electron avalanche. The equation also shows that cumulative ionization is possible only if  $(\alpha - \eta) > 0$ . The magnitude of both  $\alpha$  and  $\eta$  depends on the background electric field and the air density. The quantity  $(\alpha - \eta)$  is known as the effective ionization coefficient and denoted by  $\bar{\alpha}$ . For electric field values less than the critical value necessary for electrical breakdown,  $(\alpha - \eta) < 0$  and for higher electric fields  $(\alpha - \eta) > 0$ . This explains the reason for the existence of a critical electric field beyond which the air breaks down electrically.

As one can see from the above equation whether the avalanche will continue to grow (i.e.  $n_x$  continue to increase with distance) or whether it will start to decay after an initial growth (i.e.  $n_x$  will decrease with distance) depends on the spatial distribution of the electric field. As long as the background electric field is such that

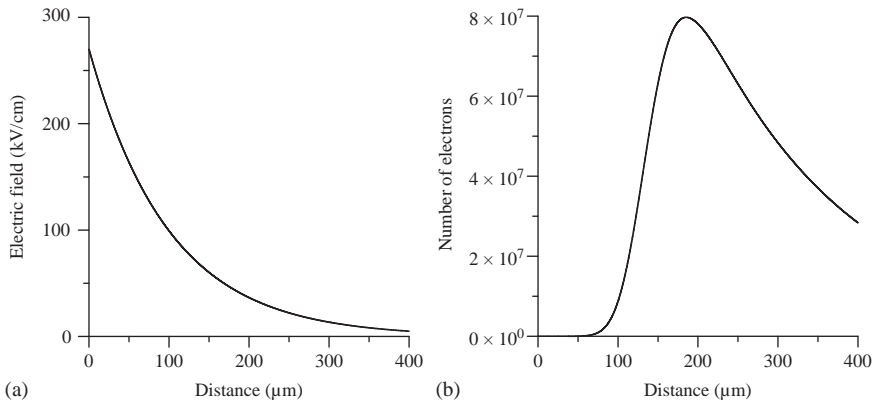


*Figure 3.1 (a) The electric field used in demonstrating the spatial variation in the number of electrons in the avalanche head as the avalanche advances in an electric field. (b) The variation in the number of electrons in the avalanche head as a function of distance as the avalanche propagates in the electric field shown in (a). Note that the origin of the avalanche is at the point corresponding to zero distance*

$(\alpha - \eta) > 0$ , the avalanche continues to grow while it starts to decay when  $(\alpha - \eta) < 0$ . In order to illustrate this, consider an electric field that originates from a pointed source and decreases exponentially with distance. The electric field at the source is larger than the critical value necessary for electrical breakdown in standard atmosphere (i.e.  $2.8 \times 10^4$  V/cm). An example is shown in Figure 3.1(a). Consider an electron avalanche that originates at the source and moves into the low field region. Figure 3.1(b) shows how the number of electrons at the avalanche head varies as the avalanche extends into the low field region. Observe that the number density of electrons increases initially, but it will start to decrease when the electric field goes below the critical value necessary for electrical breakdown. In calculating the electron number density in the avalanche, it is necessary to evaluate  $\alpha$  and  $\eta$  as a function of the background electric field. Denoting the gas density by  $N$  (in cm<sup>-3</sup>) and the background electric field by  $E$  (in V/cm), these dependencies can be described by the following equations [2, 3].

$$\frac{\alpha}{N} = 2.0 \times 10^{-16} \exp \left[ \frac{(-7.248 \times 10^{-15})}{\left( \frac{E}{N} \right)} \right] \text{cm}^2 \quad \text{for } \frac{E}{N} > 1.5 \times 10^{-15} \text{ V/cm}^2 \quad (3.5)$$

$$\frac{\alpha}{N} = 6.619 \times 10^{-17} \exp \left[ \frac{(-5.593 \times 10^{-15})}{\left( \frac{E}{N} \right)} \right] \text{cm}^2 \quad \text{for } \frac{E}{N} \leq 1.5 \times 10^{-15} \text{ V/cm}^2 \quad (3.6)$$

$$\frac{\eta}{N} = 8.889 \times 10^{-5} \left( \frac{E}{N} \right) + 2.567 \times 10^{-19} \text{ cm}^2 \quad \text{for } \frac{E}{N} > 1.05 \times 10^{-15} \text{ V/cm}^2 \quad (3.7)$$

$$\frac{\eta}{N} = 6.089 \times 10^{-4} \left( \frac{E}{N} \right) - 2.893 \times 10^{-19} \text{ cm}^2 \quad \text{for } \frac{E}{N} \leq 1.05 \times 10^{-15} \text{ V/cm}^2 \quad (3.8)$$

As the avalanche grows the number of electrons at the head increases. These electrons will spread out due to random diffusion causing the avalanche head to expand. The average radius of the avalanche head can be calculated from the equation  $r = \sqrt{4Dt}$  where  $t = x/v_d$  is the time of advance of the avalanche,  $D$  is the coefficient of diffusion and  $v_d$  is the drift velocity of the electrons in the electric field. The drift velocity of the electrons can be obtained from the equation:

$$v = 2.157 \times 10^{16} \left( \frac{E}{N} \right)^{0.6064} \text{ cm/s} \quad (3.9)$$

and the coefficient of diffusion  $D$  can be obtained from the following expressions [2]:

$$\frac{D}{\mu_e} = 5.645 \times 10^4 \left( \frac{E}{N} \right)^{0.3441} V \quad \text{for } \frac{E}{N} < 2.0 \times 10^{-17} \text{ V/cm}^2 \quad (3.10)$$

and

$$\frac{D}{\mu_e} = 2.173 \times 10^7 \left( \frac{E}{N} \right)^{0.46113} V \quad 2.0 \times 10^{-17} < \frac{E}{N} < 1.23 \times 10^{-16} \text{ V/cm}^2 \quad (3.11)$$

In the above equations  $\mu_e$  is the electron mobility that can be extracted from (3.9).

### 3.3 Streamer discharges

The analysis given in the previous section shows that as the avalanche increases in length, the charge accumulated at the head of the avalanche increases. As a result, the electric field produced by this charge located at the head of the avalanche also increases as the avalanche moves forward. If the background electric field supports the growth of the avalanche, a situation will be reached that the electric field produced by the charge located at the avalanche head will overwhelm the critical electric field necessary for electrical breakdown in the medium. At this stage the electric field produced by the charges located at the avalanche head, i.e. the space charge electric field, starts influencing the ionization processes taking place in the vicinity of the avalanche head. When this stage is reached, the avalanche will convert itself to a streamer discharge. The exact mechanism of the formation of a streamer discharge from an avalanche depends on the polarity of the source that

generates the background electric field. First consider a source at positive polarity. The source could be a charged graupel particle (in a thundercloud) in a background electric field, a Franklin rod exposed to the background electric field of a thundercloud or a high-voltage electrode. For clarity we will refer to it as the anode.

If the electric field in front of the anode is high enough, a photoelectron generated at a point located in front of the anode will initiate an avalanche that propagates towards the anode. The process is depicted in Figure 3.2. As the electron avalanche propagates towards the anode, mobile positive space charge accumulates at the avalanche head. When the avalanche reaches the anode, the electrons will be

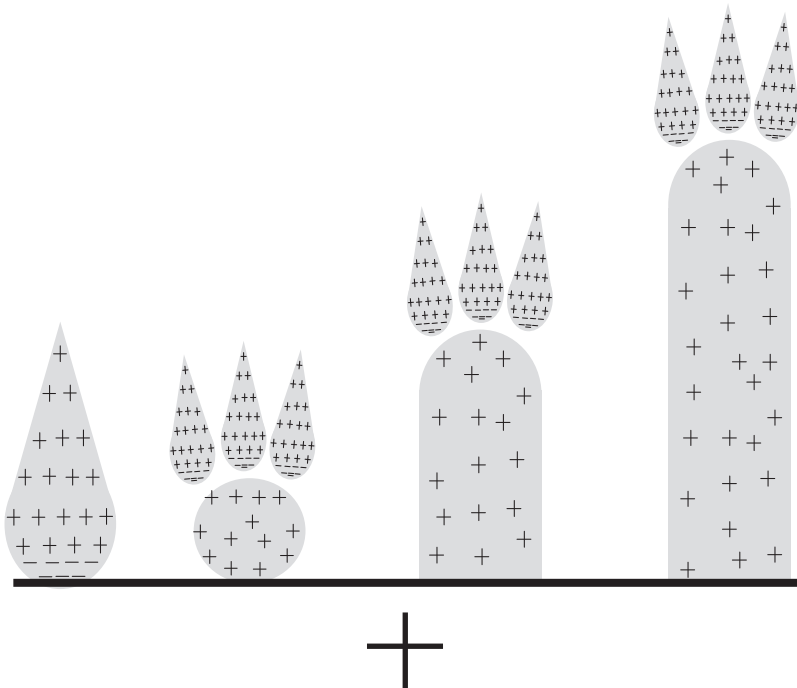


*Figure 3.2 Mechanism of positive streamers. A photoelectron generated at a point located in front of the anode will initiate an avalanche that propagates towards the anode. When the avalanche reaches the anode, the electrons will be absorbed into it leaving behind the net positive space charge. If the number of positive ions in the avalanche head is larger than a critical value, secondary avalanches created by the photons will be attracted towards the positive space charge. The positive space charge will be neutralized by the electrons in the secondary avalanches creating a weakly conducting channel. Consequently, a part of the anode potential will be transferred to the channel making it positively charged and increasing the electric field at the tip. The high electric field at the tip attracts more electron avalanches towards it and the channel grows as a consequence*

absorbed into it leaving behind the net positive space charge. Because of the recombination of positive ions and electrons, avalanche head is a strong source of high energetic photons. These photons will create other avalanches in the vicinity of the positive space charge. If the number of positive ions in the avalanche head is larger than a critical value, the electric field created by the space charge becomes comparable or overwhelms the critical electric field. As a result the secondary avalanches created by the photons will be attracted towards the positive space charge. The electrons in the secondary avalanches will be neutralized by the positive space charge of the primary avalanche leaving behind a new positive space charge, little bit away from the anode. Furthermore, the neutralization process leads to the creation of a weakly conducting channel and a part of the anode potential will be transferred to this channel making it positively charged and increasing the electric field at the tip. The high electric field at the tip of this weakly conducting channel attracts more electron avalanches towards it and the resulting neutralization process causes the weakly conducting channel to extend in a direction away from the anode. This discharge that travels away from the anode is called a positive streamer.

Now let us consider a source of negative polarity, i.e. a cathode. A photo-electron generated close to the cathode will generate an avalanche (primary avalanche) that moves away from the cathode leaving behind positive charge close to it. The process is depicted in Figure 3.3. When the avalanche reaches a critical size, the positive charge of the avalanche starts attracting secondary avalanches towards it. Like in the case of a positive streamer the electrons in the secondary avalanches neutralize this positive charge effectively moving it towards the cathode. When the positive charge reaches the cathode, the field enhancement associated with the proximity of positive space charge to the cathode leads to the emission of electrons from the latter. These electrons will neutralize the positive space charge creating a weakly conducting channel that connects the negative head of the electron avalanche to the cathode. As a consequence, a part of the cathode potential will be transferred to the head of this weakly ionized channel (i.e. negative streamer) increasing the electric field at its head. This streamer head will now act as a virtual cathode and the process is repeated. Repetition of this process leads to the propagation of the negative streamer away from the cathode.

If the background electric field is very high, the positive space charge of the primary avalanche may reach the critical size necessary for streamer formation before reaching the anode. This may lead to the formation of a bi-directional discharge, the two ends of which travel towards the anode and the cathode, former as a negative streamer and the latter as a positive streamer. Such a discharge is called a mid gap streamer.

So far we have not discussed the exact condition under which an avalanche will be converted to a streamer. As mentioned earlier, the avalanche to streamer transition takes place when the number of charged particles at the avalanche head exceeds a critical value,  $N_c$ . From cloud chamber photographs of the avalanches and streamers, Raether [4] estimated that an avalanche will convert to a streamer when the number of positive ions in the avalanche head reaches a critical value of about  $10^8$ . A similar conclusion is also reached independently by Meek [5]. On the other hand Bazelyan

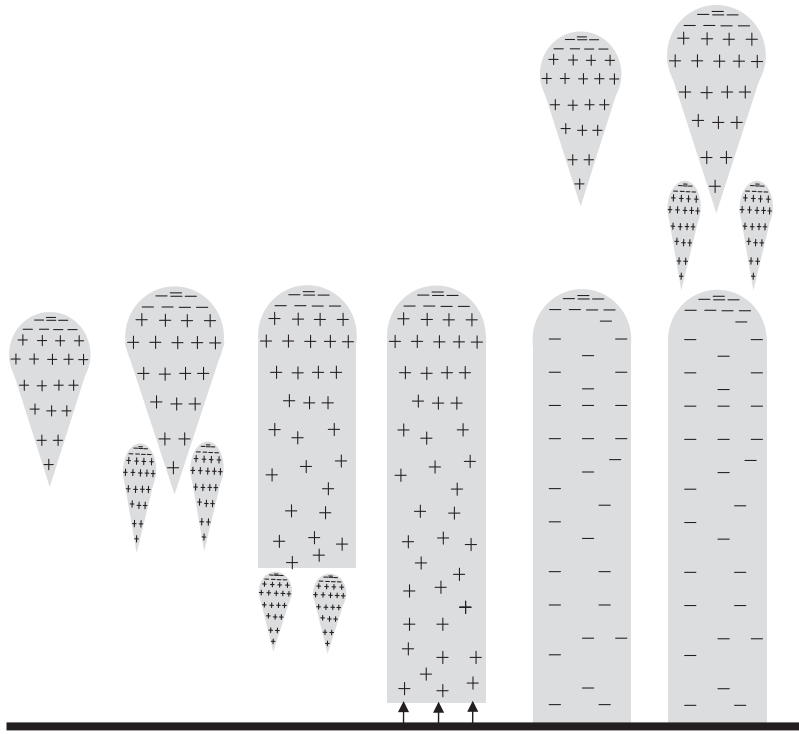


**Figure 3.3 Mechanism of negative streamers.** An photoelectron generated close to the cathode will generate an avalanche that moves away from the cathode leaving behind positive charge close to it. When the avalanche reaches a critical size, the positive charge of the avalanche starts attracting secondary avalanches towards it. Like in the case of a positive streamer, the electrons in the secondary avalanches neutralize this positive charge effectively moving it towards the cathode. When the positive charge reaches the cathode, the field enhancement associated with the proximity of positive space charge to the cathode leads to the emission of electrons from the latter. These electrons will neutralize the positive space charge creating a weakly conducting channel that connects the negative head of the electron avalanche to the cathode. A part of the cathode potential will be transferred to the head of this weakly ionized channel (i.e. negative streamer) increasing the electric field at its head. This streamer head will now act as a virtual cathode and the process is repeated. Repetition of this process leads to the propagation of the negative streamer away from the cathode

and Raizer [6] suggest  $10^9$  as a reasonable value for this transformation. Thus, the condition for the transformation of an avalanche to a streamer can be written as

$$e^0 \int_{x_0}^{x_c} [\alpha(x) - \eta(x)] dx = 10^8 - 10^9 \quad (3.12)$$

Note that in writing down the above equation, it is assumed that the electric field is not uniform and therefore both  $\alpha$  and  $\eta$  are a function of distance. Moreover, in the above equation the distance  $x$  is measured from the origin of the avalanche and  $x_c$  is the distance from the origin of the avalanche where the background electric field goes below the critical value necessary for electrical breakdown.

The advancement of the streamer in a given background electric field is facilitated by the large increase in the local electric field in the vicinity of the streamer head and by the enhanced production of the photons from the streamer head. The photons create secondary electrons in front of the streamer head and these secondary electrons give rise to secondary avalanches that will move, in the case of positive streamers, towards the streamer head. Once initiated, the streamers have been observed to travel in background electric fields that itself cannot support avalanche formation. Thus, the secondary avalanche formation in the streamer is confined to a very small region around the streamer head where the electric field exceeds  $2.8 \times 10^4$  V/cm, the minimum electric field required for the cumulative ionization in air at atmospheric pressure. This region is called the active region. The dimension of the active region is about 200  $\mu\text{m}$  and the streamer radius was found to be on the order of 10–50  $\mu\text{m}$  [7, 8]. This value, however, may correspond to short streamers. Since the electron multiplication in the active region is supported by the space charge electric field of the streamer head, the streamer can propagate in electric fields that are much smaller than the critical electric field necessary for cumulative electron ionization. In air, the background electric field necessary for positive streamer propagation lies in the range of  $4.5 - 5 \times 10^3$  V/cm [9–11]. For negative streamers it lies in the range of  $1 - 2 \times 10^4$  V/cm. Any variation in the electron loss processes can change this electric field. For example, when air is saturated with water vapour, the critical electric field for positive streamer propagation grows from  $4.7 \times 10^3$  V/cm at humidity of 3 g/m<sup>3</sup> to  $5.6 \times 10^3$  V/cm at 18 g/cm<sup>3</sup> [12, 13]. The critical electric field necessary for streamer propagation decreases approximately linearly with decreasing air density [6].

In background electric fields close to the critical value necessary for streamer propagation, the speed of streamers is about  $10^7$  cm/s. However, the streamer speed increases with increasing background electric field. No direct measurements are available today on the potential gradient of the streamer channels. Experiments conducted with long sparks show that the average potential gradient of the electrode gap when the positive streamers bridges the gap between the two electrodes is about  $5 \times 10^3$  V/cm [14]. This indicates that the potential gradient of the positive streamer channels in air at atmospheric pressure is close to this value. Note that this value is approximately the same as the critical electric field necessary for the propagation of positive streamers.

### 3.4 Corona discharges

In many situations, the electric field in air in the vicinity of objects exposed to high external electric fields may overwhelm the critical electric field necessary for the formation of electron avalanches in air. Moreover, the extent of the volume in which this high electric field exist may confine to a very small region around the object (i.e. the electric field is strongly non-uniform) so that it would not lead to any electrical breakdown between the object under consideration and another one in its vicinity. In this case the electrical activity will be concentrated and confined to a small volume around the object. These types of discharge activity are called corona discharges. Corona discharge consists of either electron avalanches, streamers or both.

During corona discharges ionic space charge of both polarities accumulate near the highly stressed electrode, thus modifying the electric field distribution. The equilibrium between accumulation and removal of space charge causes several modes of corona discharges. Moreover, the physical nature of these corona discharges is affected by the electronegativity of the gas under consideration.

Consider first the application of a positive voltage to a point, i.e. an anode. Initially, electron avalanches start from a certain distance from the anode and start moving towards it. If the electric field is high enough, some of these avalanches may reach a critical size necessary for avalanche to streamer conversion at the anode. As a consequence, the positive space charge left behind by the avalanches (note that the electrons will be absorbed into the anode) may give rise to positive streamers. These streamers may propagate a short distance into the gap (i.e. away from the anode) and stop. The streamers will leave behind positive space charge close to the anode and this positive charge reduces the electric field at the anode leading to the cessation of streamer formation until the space charge is removed. As the space charge moves away from the anode, the electric field recovers and a new set of streamers may start from the anode. Moreover, as the space charge screens one region of the anode, streamers may develop from another region. Thus, the discharge activity spreads across the anode. This discharge activity is called onset streamers.

As the electric field increases further the activity increases. However, as the electrons are not absorbed readily at the anode, they will form a negative ion sheath close to the anode and between the anode and the positive space charge. This ion sheath is called Hermitian sheath. The sheath increases the anode field but reduces the field outside so that streamer formation is quenched. The length of the high field region, i.e. the one between the anode and the negative sheath, is not long enough to give rise to streamers, but formation of electron avalanches takes place in there. Moreover, the electric field inside this zone is high enough to detach negative ions. This discharge is called glow corona or Hermitian glow. As the field increases further, the electric field outside the sheath becomes large enough and the streamer formation starts again. They are called breakdown streamers and they extend into the gap a distance depending on the applied voltage.

Now let us consider the case in which the source is of negative polarity, i.e. a cathode. As the electric field increases, electron avalanches start from the cathode. The resulting positive ions will travel towards the cathode. The collision of these

positive ions with the cathode gives out electrons that supports the formation of avalanches. The electron avalanches will move out a certain distance from the cathode, but as they move away from the cathode the electric field decreases and the electrons will be attached to oxygen molecules in air. This gives rise to a negative space charge region. This negative space charge will reduce the electric field and choke off the discharge activity. However, as the negative space charge moves away due to the action of the electric field, the electric field at the cathode recovers and a new discharge activity starts from the cathode. This mode of discharge, relaxation and continuation, continues for a considerable potential range. This oscillating corona discharge is called Trichel pulses because the current consists of pulses separated in time. The repetition frequency of the pulses depends on the applied voltage but can reach values about  $10^6 \text{ s}^{-1}$ .

As the electric field continues to increase, the negative ions are created too far from the cathode to choke off the discharge activity and a pulseless discharge activity, i.e. a glow discharge, starts from the cathode. This will continue for some range of potentials and with increasing electric fields negative streamers start to form from the cathode. Initially, they do not propagate far into the gap but with increasing voltage they move further and further into the gap.

### 3.5 Thermalization or heating of air by a discharge

In the streamer phase of the discharge, many free electrons are lost due to attachment to electronegative oxygen in air. Furthermore, a considerable amount of energy gained by electrons from the electric field is used in exciting molecular vibrations. Since the electrons can transfer only a small fraction of their energy to neutral atoms during elastic collisions, the electrons have a higher temperature than the neutrals. That is, the gas and the electrons are not in thermal equilibrium. As the gas temperature rises to about 1600–2000 K, rapid detachment of the electrons from oxygen negative ions supply the discharge with a copious amount of electrons thus enhancing the ionization [15]. As the temperature rises, the time necessary to convert the energy stored in the molecules as vibrational energy to thermal or translational energy decreases and the vibrational energy converts back to translational energy thus accelerating the heating process. As the ionization process continues, the electron density in the channel continues to increase. When the electron density increases to about  $10^{17} \text{ cm}^{-3}$ , a new process starts in the discharge channel. This is the strong interaction of electrons with each other and with positive ions through long-range Coulomb forces [15]. This leads to a rapid transfer of the energy of electrons to positive ions causing the electron temperature to decrease, while the ion temperature increases. The positive ions, having the same mass as the neutrals, transfer their energy very quickly, in a time on the order of  $10^{-8} \text{ s}$ , to neutrals. This results in a rapid heating of the gas. At this stage, the thermal ionization (ionization caused by the impact of ions and neutrals) sets in causing a rapid increase in the ionization and the conductivity of the channel. This process is called thermalization. During thermalization as the electron temperature decreases, the

gas temperature increases and very quickly all the components of the discharge namely, electrons, ions and neutrals, will achieve the same temperature and the discharge will reach local thermodynamic equilibrium.

### 3.6 Low-pressure electrical discharges

As described previously, avalanche to streamer transition requires that the avalanche grows to about  $10^8$ – $10^9$  electrons and the space charge in the avalanche tip creates an electric field that is capable of attracting electron avalanches towards it. As the pressure decreases, the avalanche has to grow to a longer and longer lengths before it can accumulate enough space charge at its head to modify the background electric field. This could be the case in the case of low-pressure discharges taking place in the upper atmosphere (i.e. sprites and elves) during thunderstorms. In these, the length of streamer like discharges may exceed hundreds of metres to kilometres. Another interesting feature of these low-pressure discharges is the lack of thermalization process. As mentioned earlier, the thermalization requires increasing the electron density beyond a certain limit. In low-pressure discharges, the density of molecules and atoms is such that the electron densities never reach the critical values necessary for thermalization. In these discharges, the electron temperature remains very high while the gas temperature remains close to ambient. The electron impacts are the dominant mechanism of ionization in these discharges.

### 3.7 Leader discharges

In Section 3.3, we have considered the conditions necessary for the initiation of streamer discharges in a given electric field configuration. The streamer is a cold discharge (i.e. the gas temperature in the channel is close to ambient) and the conductivity of the streamer channel is rather small. However, a leader discharge is a hot discharge and the conductivity of the discharge channel is high. Let us now consider how the streamers will be transformed into a leader and how the leader propagates in a background electric field. Let us first consider a positive leader discharge.

Consider an anode whose potential rises rapidly in time. When the electric field at the surface and in the vicinity of the anode increases to a value large enough to convert avalanches to streamers (i.e. (3.12) is satisfied), a bust of streamers is generated from the anode. Many of these streamers have their origin in a common channel called the streamer stem. The streamers stop when the electric field decreases below the critical value necessary for their propagation. Each individual streamer is a cold discharge and the current associated with this cannot heat the air sufficiently to make it highly conducting. However, the combined current of all streamers flowing through the stem causes this common region to heat up increasing the conductivity of the stem. The increase in the temperature causes the gas to expand making the  $E/N$  ( $E$  is the electric field and  $N$  is the gas density) ratio to increase leading to an increase in ionization and electron production. Thus, the current will be concentrated into a thin channel (i.e. the streamer stem) and this in

turn produce more heating and accelerate the ionization process. With increasing ionization, the process of thermalization sets in transforming the stem into a hot and conducting channel called the leader.

Owing to its high conductivity, most of the voltage of the anode will be transferred to the head of the leader channel resulting in a high electric field there. This high electric field leads to the production of streamer discharges now from a common stem located at the head of the leader channel. With the aid of cumulative streamer currents, the new stem gradually transforms itself to a newly created leader section with the streamer process now repeating at the new leader head. The streamer system located in front of the leader is the source of current that heats the air and makes possible the elongation of the leader. The main sequences of the propagation of a positive leader are shown Figure 3.4.

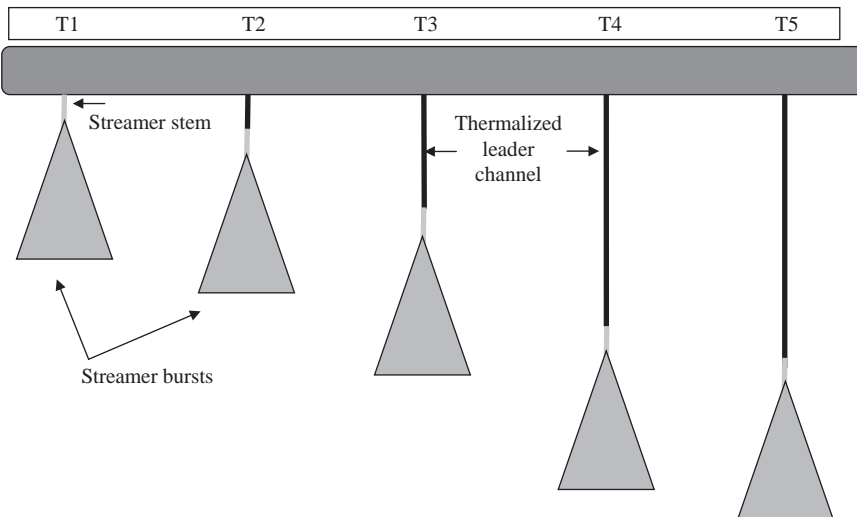


*Figure 3.4 Mechanism of positive leaders. When the electric field at the surface and in the vicinity of the anode increases to a value large enough to convert avalanches to streamers, a bust of streamers is generated from the anode (T1). Many of these streamers have their origin in a common channel called the streamer stem. The combined current of all streamers flowing through the stem causes this common region to heat up and, as a result, the stem will be transformed into a hot and conducting channel called the leader (T2). Owing to its high conductivity, most of the voltage of the anode will be transferred to the head of the leader channel resulting in a high electric field there. This high electric field leads to the production of streamer discharges now from a common stem located at the head of the leader channel (T2). With the aid of cumulative streamer currents, the new stem gradually transforms itself to a newly created leader section with the streamer process now repeating at the new leader head (T3, T4, T5)*

The leader usually supports a current of about 1 A at a relatively low longitudinal electric field of about  $10^3$  V/cm. The speed of propagation of the leader is about a few centimetres per second. The spectroscopic measurements show that the air in the leader channel is heated to about 5000 K [9, 10].

The development of the negative leader discharge is more complicated. As in the case of positive leaders, a negative leader also originates with a streamer burst issued from the high voltage electrode i.e. the cathode in this case. It also maintains its propagation with the aid of negative streamers generated from its head. However, the detailed mechanism of its propagation is different to that of positive leaders. A simplified schematic diagram giving the main features of propagation of a negative leader is shown in Figure 3.5. Once a negative streamer burst is generated from the leader head, a unique feature, called, a pilot system, that does not exist in the positive leaders manifests in the system. The pilot system consists of a bright spot called space stem, from which streamers of both polarity develops in opposite directions. The location of the space stem is usually at the edge of the negative streamer system. The action of these streamers heats the space stem and converts it to a hot channel. This is called a space leader. The positive streamers from the space leader propagate towards the head of the negative leader and the negative streamers generated from the other end of the space leader propagate in the opposite direction. Indeed, the positive streamers of the space stem propagate in the region previously covered by negative streamers. The space leader lengthens with a higher velocity towards the cathode ( $3 \text{ cm}/\mu\text{s}$ ) than towards the anode ( $1 \text{ cm}/\mu\text{s}$ ). As the space leader approaches the main leader, the velocity of both increases exponentially. The connection of the two leaders is accompanied by a simultaneous illumination of the whole channel starting from the meeting point. During this process, the space leader acquires the potential of the negative leader, and the negative end of the space leader becomes the new tip of the negative leader. In photographs it appears as if the negative leader extends itself abruptly in a leader step. The change in the potential of the previous space leader generates an intense burst of negative corona streamers from its negative end that has now become the new head of the negative leader. Now a new space stem appears at the edge of the new streamer system and the process repeats itself. Recent evidence shows that repeated interaction of the negative leader with the space leader is the reason for the stepwise elongation of the negative leaders as observed in negative stepped leaders in lightning flashes [16]. Models that describe the propagation of negative leaders taking into account the space leaders were published by Mazur *et al.* [17] and Arevalo and Cooray [18].

### 3.8 Some features of mathematical modelling of positive leader discharges

Consider an grounded object that is exposed to electric field. An example being a Franklin rod exposed to the electric field generated by a downward moving negative stepped leader. The goal is to simulate the initiation and propagation of the

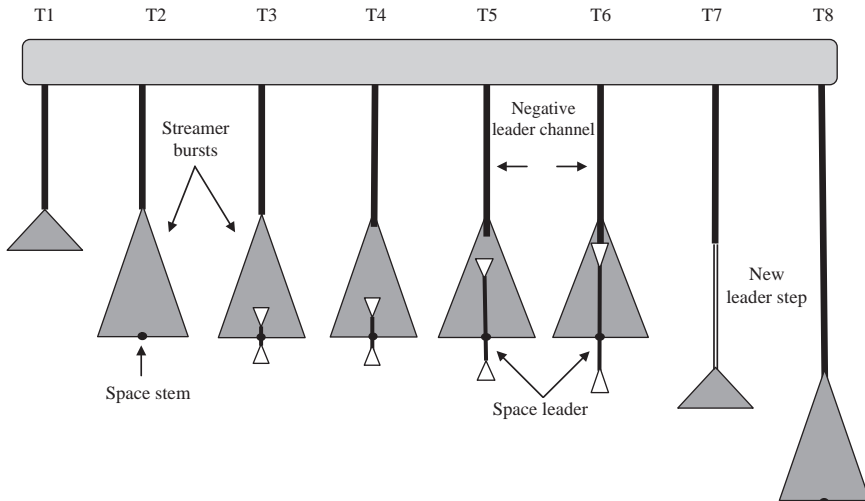


*Figure 3.5 Propagation of negative leaders. Once a negative streamer burst is generated from the leader head, a unique feature, called, a pilot system, that does not exist in the positive leaders manifest in the system. The pilot system consists of a bright spot called space stem, from which streamer of both polarity develop in opposite directions (T2–T3). The location of the space stem is usually at the edge of the negative streamer system. The action of these streamers heats the space stem and converts it to a hot channel. This is called a space leader. The space leader advances in both direction (the speed of extension of the positive end is generally higher than that of the negative end) through the cumulative action of positive streamers (generated from the side facing the negative leader) and negative streamers (generated from the opposite side) (T4–T5). The connection of the two leaders is accompanied by a simultaneous illumination of the whole channel starting from the meeting point (T6–T7). During this process the space leader acquires the potential of the negative leader. In fact, during this process (i.e. stepping process) the space leader becomes the new step or the new section of the negative leader channel and the negative end of the space leader becomes the new tip of the negative leader. During the formation of the step, a new streamer burst is generated from the new leader head and the process is repeated (T8). Note that while the space leader travels towards the negative leader, the latter itself may continue to grow in length as shown in the diagram. (The processes associated with the origin of the negative leader, which are almost identical to that of positive leaders, are not shown in the diagram.)*

connecting leader (a positive leader discharge) from the Franklin rod. A brief description of how this could be achieved is given below. The description is based on the work published previously by Becerra and Cooray [19–21].

Assume that the electric field at ground level as a function of time generated by the down coming stepped leader is known. This can be calculated, e.g. by using the leader charge distribution as extracted by Cooray *et al.* [22]. The simulation consists of several main steps and let us take them one by one.

- a) The first step is to extract the time or the height of the stepped leader when streamers are inception from the grounded rod. Since the background electric field is known, the electric field at the tip of the grounded rod can be calculated, e.g. by using charge simulation method. This field is used together with the avalanche to streamer conversion criterion given in (3.12) to investigate whether the electric field at the conductor tip is large enough to convert avalanches to streamers. The simulation continues using the time-varying electric field of the stepped leader until the streamer inception criterion is satisfied.
- b) The moment the streamer inception criterion is satisfied a burst of streamers will be generated by the tip of the rod. The next task is to calculate the charge in this streamer burst. The charge associated with the streamer burst is calculated using a distance-voltage diagram with the origin at the tip of the grounded conductor as follows (see Figure 3.6). The streamer zone is assumed to maintain a constant potential gradient  $E_{str}$ . In the distance-voltage diagram, this is represented by a straight line (note that the point of zero distance corresponds to the tip of the conductor). On the same diagram the background potential produced by the thundercloud and the down-coming stepped leader (taking also into account the presence of the lightning conductor) at the current time is depicted. If the area between the two curves up to the point where they cross is  $A$ , the charge in the streamer zone is given by

$$Q_0 \approx K_Q A \quad (3.13)$$

where  $K_Q$  is a geometrical factor. Becerra and Cooray [20] estimated its value to be about  $3.5 \times 10^{-11} \text{ C/V m}$ .

- c) The next task is to investigate whether this streamer burst is capable of generating a leader. This decision is based on the fact that in order to generate a leader a minimum of  $1 \mu\text{C}$  is required in the charge generated by the streamers. If the charge in the streamer zone is less than this value, then the procedure is repeated after a small time interval. Note that with increasing time the electric field generated by the stepped leader increases and, consequently, the charge in the streamer bursts increases. Thus at a certain time the condition necessary for the leader inception will be fulfilled.
- d) Assume that at time  $t$ , the condition necessary for leader inception is satisfied. The next task is to estimate the length and the radius of this initial leader section. In doing this it is assumed that the amount of charge you need to create a unit length of positive leader is  $q_l$ . The value of  $q_l$  is about  $40\text{--}65 \mu\text{C/m}$ . With this the initial length of the leader section  $L_1$  is given by  $Q_0/q_l$ . It is important to

point out here that Becerra and Cooray [21] utilized a more rigorous condition in which the charge necessary to thermalize a unit leader section depends on the speed of the leader. The initial radius of the leader,  $a_{L_1}(t)$ , is assumed to be  $10^{-3}$  m and the initial potential gradient of the leader section,  $E_{L_1}(t)$ , is assumed to be equal to the potential gradient of the streamer region, i.e.  $5.0 \times 10^3$  V/cm. Now we proceed to the next time step, i.e.  $t = t + \Delta t$ .

- e) During the time interval  $\Delta t$  the background potential is changed and we also have a small leader section of length  $L_1$ . Now the new charge in the streamer zone generated from the head of the new leader section is calculated as before but now including both the leader and its streamer zone in the distance-voltage diagram. The leader is represented by a line with a potential gradient  $E_{L_1}(t)$  (see Figure 3.6). The total charge is calculated from the area between this new curve and the background potential. The charge generated in the current time step is obtained by subtracting from this the charge obtained in the previous time step. Let the charge obtained thus be  $Q_1$ . This charge is used to evaluate the length of the new leader section  $L_2$ . Moreover, the flow of this charge through the leader

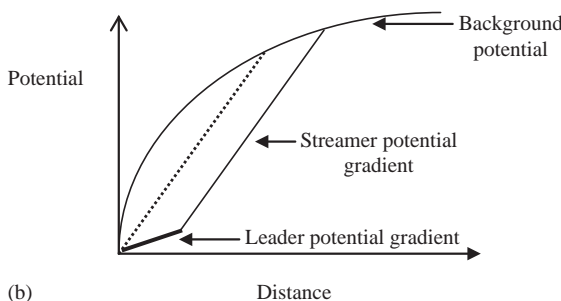
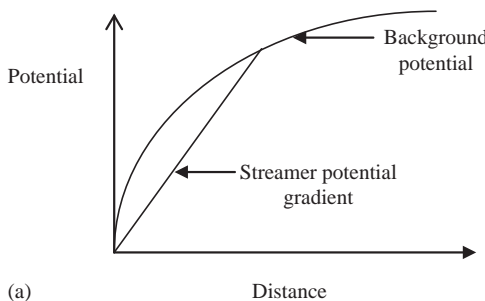


*Figure 3.6 The use of distance-voltage diagrams to calculate the streamer charge. (a) The charge in the first streamer burst is given by the area between the two curves representing the background potential and the streamer potential gradient. (b) To calculate the charge in subsequent streamer burst one has to include both the leader and the streamer region in a distance-voltage diagram*

channel changes the potential gradient and the radius of the older leader section  $L_1$ . The new potential gradient and the radius of  $L_1$  are given by  $E_{L_1}(t + \Delta t)$  and  $a_{L_1}(t + \Delta t)$ .

- f) Now let us consider the  $n$ th time step. There are  $n$  leader sections and they have there respective potential gradients and radii. The radius and the potential gradient of  $i$ th leader section are obtained from

$$\pi \cdot a_{L_i}^2(t + \Delta t) = \pi \cdot a_{L_i}^2(t) + \frac{\gamma - 1}{\gamma \cdot p_0} E_{L_i}(t) \cdot I_{L_i}(t) \cdot \Delta t \quad (3.14)$$

$$E_{L_i}(t + \Delta t) = \frac{a_{L_i}^2(t)}{a_{L_i}^2(t + \Delta t)} E_{L_i}(t) \quad (3.15)$$

In the above equation  $E_{L_i}(t)$  is the internal electric field and  $I_{L_i}(t)$  is the current of the leader section  $L_i$  at time  $t$ . With these, it is possible to calculate the time

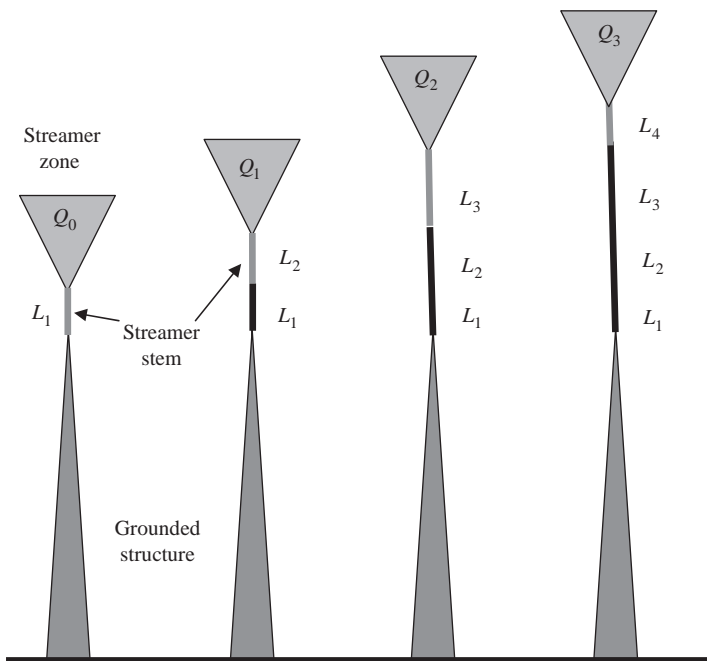


Figure 3.7 Pictorial definition of the parameters used in the mathematical modelling of positive leader discharges as described in Section 3.8. Note that  $Q_0, Q_1, Q_2$  etc. are the charges in the streamer zones. The flow of charge across the streamer stem makes it conducting and converts it to a leader section

evolution of the internal electric field for each segment and the potential drop along the leader channel (at a given time) as follows:

$$\Delta U_L = \sum_{i=1}^k E_{L_i}(t) \cdot L_i \quad (3.16)$$

The steps described above can be used to simulate the inception and propagation of positive leaders. Figure 3.7 describes the basics of the process schematically. The calculation can be simplified if, instead of calculating the time evolution of leader potential gradient in each segment as above, one uses the expression derived by Rizk [23] for the potential of the tip of the leader channel that is given by

$$U_{tip}^{(i)} = l_L^{(i)} E_\infty + x_0 E_\infty \ln \left[ \frac{E_{str}}{E_\infty} - \frac{E_{str} - E_\infty}{E_\infty} e^{-\{l_L^{(i)}/x_0\}} \right] \quad (3.17)$$

In the above equation  $l_L^{(i)}$  is the total leader length at the current simulation step,  $E_\infty$  is the final quasi-stationary leader gradient and  $x_0$  is a constant parameter given by the product  $v\theta$ , where  $v$  is the ascending positive leader speed and  $\theta$  is the leader time constant.

## References

1. Cooray, V., 2003. Mechanism of electrical discharges, in Cooray, V., (Ed.), *The Lightning Flash*, The Institution of Electrical Engineers, London, UK
2. Morrow, R., 1985. Theory of negative corona in oxygen, *Phys. Rev. A*, **32**, 1799–1809
3. Morrow, R. and Lowke, J. J., 1997. Streamer propagation in air, *J. Phys. D: Appl. Phys.*, **30**, 614–627
4. Raether, H., 1940. Zur Entwicklung von Kanaalentladungen, *Arch. Elektrotech.*, **34**, 49–56
5. Meek, J.M., 1940. A theory of spark discharge, *Phys. Rev.*, **57**, 722–728
6. Bazelyan, E.M. and Raizer, Yu.P., 1998. *Spark Discharge*, CRC Press, New York
7. Marode, E., 1983. The glow to arc transition, in Kunhardt, E. and Larssen, L., (Eds.), *Electrical Breakdown and Discharges in Gases*, Plenum Press, New York
8. Marode, E., 1975. The mechanism of spark breakdown in air at atmospheric pressure between a positive point and a plane, I. Experimental: Nature of the streamer track, II. Theoretical: Computer simulation of the streamer track, *J. Appl. Phys.*, **46**, 2005–2020
9. Les Renardières Group, 1977. Positive discharges in long air gaps – 1975 results and conclusions, *Electra*, **53**, 31–152
10. Les Renardières Group, 1981. Negative discharges in long air gaps, *Electra*, **74**, 67–216

11. Gao, L., Larsson, A., Cooray, V. and Scuka, V., 1999. Simulation of streamer discharges as finitely conducting channels, *IEEE Trans. Dielectr. Electr. Insul.*, **6**, 1, 35–42
12. Griffiths, R.F., and Phelps, C.T., 1976. The effects of air pressure and water vapour content on the propagation of positive corona streamers, *Quart. J.R. Mat. Soc.*, **102**, 419–426
13. Griffiths, R.F., and Phelps, C.T., 1976. Dependence of positive corona streamer propagation on air pressure and water vapour content, *J. Appl. Phys.*, **47**, 2929–2934
14. Paris, L. and Cortina, R., 1968. Switching and lightning impulse discharge characteristics of large air gaps and long insulator strings, *IEEE Trans.*, **PAS-98**, pp. 947–957
15. Gallimberti, I., 1979. The mechanism of long spark formation, *J. de Physique.*, **40**, 7, C7–193–250
16. Biagi, C.J., Uman, M.A., Hill, J.D., Jordan, D.M., Rakov, V.A. and Dwyer, J., 2010. Observations of stepping mechanisms in a rocket-and-wire triggered lightning flash, *J. Geophys. Res.*, **115**, D23215, doi:10.1029/2010JD014616
17. Mazur, V., Ruhnke, L., Bondiou-Clergerie, A. and Lalande, P., 2000. Computer simulation of a downward negative stepped leader and its interaction with a grounded structure, *J. Geophys. Res.*, **105**, D17, 22361–22369
18. Arevalo, L. and Cooray, V., 2011. Preliminary study on the modeling of negative leader discharges, *J. Phys. D: Appl. Phys.*, **44**, 31, doi: 10.1088/0022-3727/44/31/315204
19. Becerra, M. and Cooray, V., 2006a. A self-consistent upward leader propagation model, *J. Phys. D: Appl. Phys.*, **39**, 3708–3715
20. Becerra, M. and Cooray, V., 2006b. A simplified physical model to determine the lightning upward connecting leader inception, *IEEE Trans. Power Delivery*, **21**, 2, 897–908
21. Becerra, M. and Cooray, V., 2006c. Time dependent evaluation of the lightning upward connecting leader inception, *J. Phys. D: Appl. Phys.*, **39**, 4695–4702
22. Cooray, V., Rakov, V. and Theethayi, N., 2007. The lightning striking distance—Revisited, *J. Electrostat.*, **65**, 296–306
23. Rizk, F., 1989. A model for switching impulse leader inception and breakdown of long air-gaps, *IEEE Trans. Power Delivery*, **4**, 1, 596–603



---

# *Chapter 4*

## **Numerical simulations of non-thermal electrical discharges in air**

*Y. V. Serdyuk<sup>1</sup>*

---

### **4.1 Introduction**

Electrical gas discharges belong to the class of low-temperature plasmas. Depending on particular conditions, they can be equilibrium (thermal) or non-equilibrium (non-thermal) meaning that temperatures/energies of constituting particles (electrons, ions, neutral atoms/molecules) are either nearly equal or different. Examples of the former are electric arcs, sparks and microwave discharges, where such effects as Joule heating of the gas and its thermal ionization are significant. In contrast, non-thermal discharge plasmas are characterized by presence of highly energetic electrons in ‘cold’ neutral gas and ionic component with temperature close (or slightly higher) to that of gas. Typical examples of these are electron avalanches, glow discharges, streamers and electrical coronas, where the degree of ionization of the gas is much less than unity, the electron density rarely exceeds  $\sim 10^{14} \text{ cm}^{-3}$  and electron’s mean energy is normally below  $\sim 10 \text{ eV}$ .

This chapter deals with basic principles of numerical simulations of non-thermal electrical discharges in air, which are predecessors and indispensable attributes of a leader discharge (see, e.g. Reference 1). First, processes in such discharges and a theoretical background of so-called fluid model are considered. Further, numerical approaches utilized for computer implementation of the model are presented. Finally, examples are given including computer simulations of coronas as well as positive and negative streamers.

### **4.2 Outline of electrophysical processes in gaseous medium under electric fields**

Most of the gases under normal pressure and temperature can be considered as an ideal gas which obeys classical thermodynamic laws. Molecules of such a gas can be seen as randomly moving non-interacting particles with energy distributions

<sup>1</sup>Chalmers University of Technology, Gothenburg, Sweden

described by Maxwell–Boltzmann statistics. Gases at normal conditions, including air, are good electrical insulators. As it was found in early years of studying of gas discharges, if one applies a low voltage (weak electric field) to an air gap formed by a pair of parallel-plate metallic electrodes, a current with the density  $j_0 \sim 10^{-16}\text{--}10^{-17} \text{ A/cm}^2$  could be registered in the external circuit [2]. This current is observed as a consequence of natural background ionization processes (discussions on particular mechanisms can be found elsewhere [3, 4]) with a characteristic rate of  $R_0 \sim 1\text{--}10 \text{ ion pairs}/(\text{cm}^3 \text{ s})$  that leads to a permanent presence of  $n_0 \sim 10^3 \text{ ion pairs in } 1 \text{ cm}^3$ , each carrying charge  $q$  (typically, singly ionized atoms/molecules are present, and, hence,  $q$  is the electronic charge  $1.6 \cdot 10^{-19} \text{ C}$ ). The ions experience the electrostatic force  $q\mathbf{E}$  in the applied electric field  $\mathbf{E}$ ,  $\text{V/cm}$ , and drift in gas with the velocity  $\mathbf{w} = \mu\mathbf{E}$  ( $\mu$  is the mobility,  $\text{cm}^2/(\text{V s})$ ). The motion of charge carriers in a weak electric field is associated with predominantly elastic scattering collisions with neutral atoms/molecules and the energy  $\varepsilon = qE\lambda$  they gain on their free path  $\lambda = (N_0 \sigma)^{-1}$  is small (here,  $N_0$  is the density of gas molecules,  $\text{cm}^{-3}$ ;  $\sigma$  is the cross-section of the process,  $\text{cm}^2$ ). Simple estimations for electrons in air under normal conditions yield the free path of  $\lambda \sim 4 \times 10^{-4} \text{ cm}$  and the energy gained between collisions in the field of  $1 \text{ kV/cm}$   $\Delta\varepsilon \sim 0.4 \text{ eV}$  (calculated with  $N_0 \sim 2.5 \times 10^{19} \text{ cm}^{-3}$  and  $\sigma \sim 10^{-16} \text{ cm}^2$  that is typical scattering cross-section). Despite very small amount of charge carriers ( $n_0 \ll N_0$  at normal conditions), their directional flow gives rise to the measurable current  $\mathbf{j}_0 = qn_0\mathbf{w}$  between the electrodes and provides apparent electric conductivity of air on the level  $\sim 10^{-13} \text{ S/cm}$  [5].

#### 4.2.1 Generation of charged species in gas

If the external field becomes stronger (e.g. due to an increase of the applied voltage), electrons may gain energy which eventually can be high enough for non-elastic collisions associated with energy transfer between colliding partners. In this way, excited neutral atoms/molecules can be generated in the volume, and further, if the electron energy exceeds the so-called ionization potential of the gas  $\Delta\varepsilon > \varepsilon_{ion}$ , new electrons and positive ions can be produced in ionizing collisions according to the scheme  $e + A \rightarrow A^+ + e + e$  (here  $e$ ,  $A$  and  $A^+$  stand for the electron, atom/molecule and positive ion, respectively). The rate of the impact ionization then can be expressed as  $R_{imp} = (dn_e/dt)_{imp} = (dn_p/dt)_{imp} = k_i n_e N_A$ , where  $n_e$ ,  $n_p$  and  $N_A$  are the densities of electrons, positive ions and neutral atoms/molecules,  $\text{cm}^{-3}$ , respectively;  $t$  stands for time,  $\text{s}$ ; and  $k_i$  is the rate constant of the process,  $\text{cm}^3/\text{s}$ . The product  $\nu_i = k_i N_A$  defines the ionization frequency, i.e. the number of ionizing collisions per second, which being divided by the drift velocity yields well-known Townsend's ionization coefficient  $\alpha = \nu_i/w_e = \nu_i/(\mu_e E)$ ,  $\text{cm}^{-1}$ , that is the number of ionization events per  $1 \text{ cm}$  of length which electron passes in the field. Using this parameter, the ionization intensity can be rewritten as  $R_{imp} = (dn_e/dt)_{imp} = (dn_p/dt)_{imp} = \alpha n_e w_e = \alpha n_e \mu_e E$ , where  $n_e w_e$  is the magnitude of the electron flux. In practice, both formulations can be utilized. However, the former is preferable when dealing with individual components of plasma or when specific reactions between electrons and neutral species are of interest. In the latter approach, the

coefficient  $\alpha$  is utilized as a unique generic property of a gas or gas mixture. Dependencies of the ionization coefficient on electric field, which are normally given in the form of  $\alpha/p = f(E/p)$  ( $p$  is gas pressure), have been extensively studied over the years and experimental data are widely presented in the literature, see, e.g. References 6–9.

Note that under certain conditions, additional mechanisms of generation of charged particles in air volume may be activated and become intensive [6], e.g. step-wise ionization of excited particles  $A^*$  by electron impact  $e + A \rightarrow A^* + e$ ,  $e + A^* \rightarrow A^+ + e + e$ ; photoionization  $A + h\nu \rightarrow A^+ + e$  ( $h\nu$  represents a photon); associative ionization  $A + B \rightarrow AB^+ + e$ ; detachment of electrons from negative ions, which may take place according to  $A^- + B \rightarrow A + B + e$  ( $A^-$  stands for a negative ion); etc. Each of these processes is characterized by its own rate constant [10–11].

#### 4.2.2 Losses of charged species in gas

Production of charged particles in discharge plasma is accompanied by their losses, and depending on the rates of these, a discharge can transform into different forms or can be even terminated. An example of the former is an avalanche-to-streamer transition, and the latter situation occurs when losses dominate, e.g. when the applied voltage is switched off and plasma decay takes place.

There are several mechanisms of electronic losses in air plasmas and the most important for typical discharge conditions are recombination and attachment. These take place due to interactions of charged particles in two-body collisions and often in three-body collisions with participation of neutral species (see Reference [10] for a detailed list of possible reactions). For example, the most important reactions of electron attachment in air [6] are  $e + O_2 + O_2 \rightarrow O_2^- + O_2$  (zero and weak fields) and  $e + O_2 \rightarrow O^- + O$  (strong fields). In practice, other processes, including those with carbon dioxide and water molecules, can also contribute to the total loss of electrons and to an increase of concentration of negative ions in air discharges. Therefore, it is convenient to treat the intensity of electron attachment similarly to that of the impact ionization described above by introducing a generic attachment coefficient  $\eta$ ,  $\text{cm}^{-1}$ , which is the number of attachment events on 1 cm length passed by an electron in the field. Hence, the corresponding rate is  $R_{att} = (dn_n/dt)_{att} = -(dn_e/dt)_{att} = \eta n_e w_e = \eta n_e \mu_e E$  (here,  $n_n$  stands for the density of negative ions). Note that this approach is not applicable if kinetics of particular kinds of species is of interest. In this case, individual reactions with corresponding rate constants should be considered.

The rate of loss of electrons and positive ions in discharge plasma due to recombination can be found as  $R_{epr} = (dn_e/dt)_{epr} = (dn_p/dt)_{epr} = -\beta_{ep} n_e n_p$ , where  $\beta_{ep}$  is the recombination coefficient,  $\text{cm}^3/\text{s}$ . In case of three-body electron-ion recombination, its rate coefficient is proportional to the density of the third particles which can be neutrals, photons or additional electrons. However, this process is not typical for discharge conditions in air in contrast to three-body ion–ion recombination, for which the mechanism  $A + B^+ + C^- \rightarrow A + B + C$  dominates at moderate and high pressures [6]. The rate of this reaction can be written as  $R_{pnr} = (dn_p/dt)_{pnr} = (dn_n/dt)_{pnr} = -\beta_{pnr} n_p n_n$ , where  $\beta_{pnr} = k_{pnr} N_A$  is the corresponding recombination

coefficient and  $k_{pnr}$  is the rate constant. Note that  $\beta_{pnr}$  is proportional to  $N_A$ , i.e. to gas pressure  $p = N_A k_B T$  (here,  $k_B$  is Boltzmann's constant,  $T$  is absolute temperature).

Another mechanism, common for all kinds of particles in discharge plasma, is loss due to diffusion which occurs in presence of strong gradients of charged species. It is characterized by the coefficient  $D$ , cm<sup>2</sup>/s, which has different values depending on the type of diffusion (e.g. free or ambipolar) [6]. Diffusion may be especially important in air plasmas embedded in a discharge vessel, where electrons from plasma volume may diffuse to metallic or dielectric walls and can be further absorbed or neutralized by ions. The rates of the latter are determined not only by the interaction between reacting particles but also by the properties of the air–solid interface where the reactions take place.

#### *4.2.3 Dynamics of densities of charge carriers in discharge plasma*

Summarizing previous consideration, electrons and ions in an electrical discharge in air experience a drift in the electric field, diffuse due to gradients of their concentrations and interact with neutral particles and with each other (except of electronic collisions which are not important at low degrees of ionization) producing new charges or disappearing depending upon particular conditions. The generation and loss are described by rate equations with corresponding constants or generic coefficients. The total rates of particle interactions in a non-thermal air discharge plasma can be formally represented as corresponding sums of rates of individual processes:  $R_e = R_{imp} - R_{att} - R_{epr} + R_{ead}$  for electrons;  $R_p = R_{imp} - R_{epr} - R_{pnr} + R_{pad}$  for generic positive ions;  $R_n = R_{att} - R_{pnr} + R_{nad}$  for generic negative ions. Here, the terms  $R_{ead}$ ,  $R_{pad}$  and  $R_{nad}$  include rates of possible additional mechanisms of generation and loss which should enter the equations with positive and negative signs, respectively. Note that the equations are coupled via coefficients representing different processes and practically all of them are dependent on the electric field strength [12]. In its turn, the actual electric field in the volume occupied by discharge plasma is a superposition of an electrostatic field defined by the geometry of the system and a field produced by a space charge with the density  $\rho = q \cdot (n_p - n_e - n_n)$ , C/cm<sup>3</sup>, that makes the field being coupled to local concentrations of charge carriers. Under certain conditions, the effect of the space charge may become so strong that it may even lead to a change in the appearance of electrical discharge. An example of this is the electron avalanche-to-streamer transformation considered in Section 4.2.4.

#### *4.2.4 Concepts of electron avalanche and streamer*

Free electrons play especially important role in gas discharge development due to their low mass and the ability to be efficiently accelerated in the electric field (high mobility). If a voltage is applied between parallel-plate metallic electrodes immersed in gas and the corresponding applied field is sufficiently strong to provide the rate of ionization higher than the rate of losses, each free electron in discharge volume can produce an electron-positive ion pair in collisions with

neutral particles. This process provides conditions for multiplication of charge carriers and exponential growth of their densities  $n_{e,p} = n_0 \exp(\alpha x)$ , which is called an electron avalanche (in the expression,  $x$  is the length which electrons pass in the field). Primary and newly generated electrons that drift further in the field towards the anode are concentrated in the avalanche head while its tail is formed by the produced positive ions, which are much slower and move in the opposite direction to the cathode. Strong gradients of the electron density at the head lead to a diffusion that provides a typical conical shape of an electron avalanche, which was registered in early years of studying of gas discharges [13]. When the avalanche reaches the surface of a metallic anode, the electronic cloud at the avalanche head is absorbed/neutralized, and only the positively charged tail is left in the gap. There are two scenarios for further development depending upon the produced space charge density.

In case when the number of electrons in the avalanche head (and, correspondingly, ions in the tail) is relatively small (less than  $\sim 10^8$ ), the density of the accumulated space charge is not high enough to modify the field distribution and so-called Townsend's or dark discharge can occur. In such a discharge, secondary electrons can be emitted from the cathode surface due to impacts of positive ions, metastable excited molecules and photons left in the gap, and they give rise to the next generation of avalanches. If the generation rate becomes sufficiently high to compensate losses of electrons, i.e. each lost electron can be replaced by a new one emitted from the cathode, the discharge becomes self-sustained and an electrical breakdown occurs due to unlimited multiplication of avalanches. A conductive channel is created after breakdown, which can be further transformed into a spark or an electric arc depending upon the properties of the external circuit. The breakdown criterion for this so-called multi-avalanche mechanism is given by the well-known Townsend's condition  $ad = \log(1 + 1/\gamma)$ , where  $\gamma$  is the secondary ionization coefficient specifying electronic yield due to secondary processes on the cathode surface and a seed electron is assumed to appear in its vicinity and travel the whole distance  $d$  between the electrodes.

If the primary avalanche is strong and the density of the space charge produced is high enough to generate the field comparable with the electrostatic (external) field, conditions for a streamer discharge formation and propagation can be eventually created. The streamer theory is based on the concept of growth of a thin ionized channel between the electrodes, which follows the positively charged trail left by the primary intensive avalanche and is supported by secondary avalanches created due to photoionization in the gas volume at the streamer head. Streamer discharges in air are known to propagate with extremely high velocity up to  $\sim 10^8$  cm/s and once created, they are able to develop even in regions with low background fields. Streamers also exhibit different properties depending on the direction of propagation (so-called cathode- and anode-directed streamers). Depending on the arrangement of the discharge gap and ambient conditions, streamers developing between electrodes can either lead to a complete breakdown forming spark or arc discharges or serve as an initial stage for a leader process taking place in long gaps with non-uniform electrostatic fields.

The concepts of both electron avalanches and streamers are widely presented in the literature, e.g. References 2 and 6, and are not intended to be considered in details here. Instead, physical processes taking place in these kinds of discharges are analysed in Section 4.3 in conjunction with the examples of computer simulations.

### 4.3 Hydrodynamic description of gas discharge plasma

The processes in gas discharges outlined in the previous section involve effects related to collective motion of charged species such as drift in an electric field, their diffusion and collisions. Therefore, a self-consistent model of discharge plasma can be developed utilizing averaged swarm parameters of the processes characterizing particles kinetics and interactions.

In general, there are two approaches to describe dynamic behaviour of electron and ions ensembles at microscopic level. The first one is based on individual description while another one is based on some kind of statistical treatment, where particles distribution function  $f(\mathbf{v}, \mathbf{r}, t)$  is considered, which obeys Boltzmann's equation:

$$\frac{\partial f}{\partial t} + \mathbf{v} \cdot \nabla_r f + \frac{q\mathbf{E}}{m} \cdot \nabla_v f = \left( \frac{\partial f}{\partial t} \right)_c \quad (4.1)$$

Here,  $\mathbf{r}$  is the position vector in space,  $\mathbf{v}$  is the velocity vector,  $m$  is the particle mass, and the right-hand side represents so-called collision integral, i.e. the rate of change of the distribution function due to collisions, e.g. between electrons and neutrals/ions. The gradient operators in (4.1) are defined in configuration space (symbol  $r$ ) and in velocity space (symbol  $v$ ).

The individual description investigates not only the most probable distribution but also the probability of deviations from this distribution. Within this approach the movement of each particle is traced in configuration space at all stages of discharge development and, thus, it provides deep insight into evolution of a particle assemble. At the same time, this is the major practical drawback from the point of view of discharge modelling because such simulations require considerable amount of computational time and memory even when very few particles are used. Consequently, the later stages of discharges, such as avalanche-streamer transition and streamer propagation, cannot be modelled without introducing significant simplifications.

The kinetic approach deals with the averaged quantities and ignores individual deviations of parameters of motion of charge carriers. Even though such deviations are usually very small, (4.1) is still too difficult to be solved directly for most problems due to strong changes of the electric field in space and time. In practice, it is usually preferable to describe behaviour of charged particles in plasma on a macroscopic level by averaged quantities like particle fluxes, densities, velocities, etc., which are defined hierarchically by the corresponding moments of Boltzmann's equation (4.1). This approach leads to an infinite set of moment equations equivalent to the distribution function in the interested time scale of moments, and which are easier to solve.

Following this way, a fluid description of the particle assemblies is obtained, which treats the macroscopic properties in terms of the moments of particles distribution functions [14]. Thus, the evolution of electron density, electron average momentum and electron mean energy are defined by the zero-, first- and second-order moments. Higher order moments may be used in some expansions, but they usually have no physical significance for gas discharge simulation problems. The lowest moment is obtained by integrating (4.1) over  $d\mathbf{v}$ , the conservation of the momentum equation (first order) is obtained by multiplying (4.1) by  $m\mathbf{v}$  and integrating over  $d\mathbf{v}$ ; and the conservation of the energy equation (second order) is obtained by multiplying (4.1) by  $m\mathbf{v}^2/2$  and integrating over  $d\mathbf{v}$ . In this way, the non-equilibrium fluid model for electrons in the interelectrode air volume can be written as

$$\begin{aligned}\frac{\partial n_e}{\partial t} &= -\nabla_r \cdot (n_e \mathbf{v}_e) + R_e \\ \frac{\partial(mn_e \mathbf{v}_e)}{\partial t} &= -\nabla_r \cdot (mn_e \mathbf{v}_e^2) - q\mathbf{E}n_e - \nabla_r P_e - mn_e \mathbf{v}_e / \tau_m \\ \frac{\partial(n_e \psi)}{\partial t} &= -\nabla_r \cdot (n_e \epsilon \mathbf{v}_e) - q\mathbf{E}n_e \mathbf{v}_e - \nabla_r \cdot (P_e \mathbf{v}_e) - n_e(\psi - \psi_0) / \tau_\psi\end{aligned}\quad (4.2)$$

Here,  $R_e$  represents the total rate of generation and loss;  $\psi$  stands for electron mean energy;  $\psi_0$  is the background gas thermal energy. The electron pressure is defined by the ideal gas equation of state  $P_e = n_e k_B T_e$ , where  $k_B$  is the Boltzmann constant and  $T_e$  the electron temperature. Note that since the relationship between the electron mean energy and temperature is given by  $3k_B T_e/2 = \psi - mv_e^2/2$ , the electron pressure in (4.2) can be represented as  $P_e = 2n_e(\psi - mv_e^2/2)/3$ . In addition, the average velocity of electrons can be replaced with their drift velocity in the field.

In general, the electron average momentum and mean energy are in non-equilibrium states in the time scales corresponding to the characteristic times of the moment equations. The reason is that electrons gain momentum and energy from the local electric field and ionize the neutral gas in electron-neutral ionization collisions. Therefore, they lose a certain amount of momentum and energy through collisions. These losses are accounted for in the last terms of the right-hand sides in the corresponding equations (4.2) which express the fact that the average momentum and mean energy will reach quasi-equilibrium states in the time scales of their relaxation times  $\tau_m$  and  $\tau_\psi$ , respectively. For typical air discharge plasma conditions, the relaxation times are of order  $\sim 10^{-13}$  to  $10^{-12}$  s [2]. Thus if the time scale of interest is larger than that, one may assume that the electron average momentum and mean energy always reach a quasi-equilibrium state and use only zero-moment of the distribution function, namely the first equation in (4.2), to describe the kinetics of the electron ensemble. This greatly simplifies the formulation of the problem, but imposes some limitations, e.g. on the rate of change of the applied field or on its frequency. Note that this assumption is true for other kinds of particles in the discharge plasma since the characteristic time scales for processes, where ions or atoms/molecules are involved, are much larger than those for electrons due to differences in their mass and velocities.

The terms forming the collision integral in (4.1) may include as many reactions as are of physical significance and are of interest in a particular situation, and each particle type should be described by its own equation and each reaction by the corresponding rate. Very often such a detailed approach is not required and averaged properties are used. For example, behaviour of positive ions of a certain kind can be expressed by a single continuity equation similar to the first one in (4.2) with the kinetic parameter characteristic for this particular type of ions. Further simplifications can be made by considering generic kinds of particles, e.g. positive and negative ions in case of a discharge in air. This allows reducing the set of equation describing dynamics of charge carriers in discharge plasma to the three partial differential equations (PDEs) expressing conservation of their densities:

$$\begin{aligned}\frac{\partial n_e}{\partial t} + \nabla \cdot (-n_e \mathbf{w}_e - D_e \nabla n_e) &= R_e \\ \frac{\partial n_p}{\partial t} + \nabla \cdot (n_p \mathbf{w}_p - D_p \nabla n_p) &= R_p \\ \frac{\partial n_n}{\partial t} + \nabla \cdot (-n_n \mathbf{w}_n - D_n \nabla n_n) &= R_n\end{aligned}\quad (4.3)$$

In some cases the set (4.3) can be made even simpler by omitting some terms based on physical considerations and assumptions, e.g. the ionic diffusion can be neglected when analysing fast processes like streamer propagation, which typically lasts some hundreds of nanoseconds if the gap length is of order of units of centimetres while the diffusion of ions is much slower. The PDEs are to be complemented with boundary conditions describing interactions of discharge plasma with surrounding objects (metallic electrodes, dielectric walls, etc.) that is usually implemented by setting up fluxes of charge carriers or their concentrations on the interfaces. One should stress here that a correct choice of boundary conditions is crucial especially when surface reactions leading to generation/loss of charged species are to be considered. In addition, initial conditions should be provided for the equations (4.3) defining distributions of the densities of electrons and ions in space at the instant of discharge initiation.

The so-called source terms on the right-hand side of (4.3) include rates of processes taking place in the discharge volume discussed above. Thus, background ionization, electron impact ionization, electron attachment, electron-ion recombination and ion–ion recombination are the main phenomena to be accounted for when (4.3) is used to describe development of electron avalanches in air. In case of streamers, additional production of secondary electrons in the gas volume is defined by the rate of photoionization  $R_{ph}$  and the source terms can be written as

$$\begin{aligned}R_e &= \alpha n_e |\mathbf{w}_e| - \eta n_e |\mathbf{w}_e| - \beta_{ep} n_e n_p + R_0 + R_{ph} \\ R_p &= \alpha n_e |\mathbf{w}_e| - \beta_{ep} n_e n_p - \beta_{pn} n_p n_n + R_0 + R_{ph} \\ R_n &= \eta n_e |\mathbf{w}_e| - \beta_{pn} n_p n_n\end{aligned}\quad (4.4)$$

The list of the mechanisms represented in (4.4) may be extended depending upon particular conditions and may include, e.g. detachment of electrons from negative ions and ionization from excited states (so-called step-wise ionization). The former leads to generation of electrons and loss of negative ions and, therefore, the corresponding rates should be added with the correct signs. As for the description of interactions of electrons with excited gas molecules, this requires information on space and time variations of the densities of excited species and, hence, an additional PDE should be considered in (4.3).

One may notice that all the kinetic coefficients in (4.3) and (4.4) are functions of the local electric field strength and, hence, the set of equations (4.3) should be complemented by Poisson's equation:

$$\nabla \cdot (\varepsilon_0 \varepsilon \nabla \phi) = -\rho = -q(n_p - n_e - n_n) \quad (4.5)$$

Here,  $\phi$  stands for the distribution of the electric potential;  $\varepsilon_0 = 8.854 \cdot 10^{-12}$  F/m is the permittivity of vacuum;  $\varepsilon$  is the dielectric constant equal to unity for air. The term on the right-hand side represents the space charge density  $\rho_v$ , which is a function of space coordinates and implicitly time (via time variations of the densities of charge carriers). Solution of (4.5) with appropriate boundary conditions allows for obtaining a distribution of the electric field  $\mathbf{E} = -\nabla \phi$  in the discharge volume to be used for calculating kinetic coefficients in (4.3) and (4.4).

The coupled set of equations (4.3)–(4.5) accompanied with boundary and initial conditions and kinetic coefficients forms a self-consistent model describing evolution of gas discharge plasma. It provides information about spatial and temporal behaviour of densities of charged species and local electric fields. Based on the microscopic quantities, integral (measurable) characteristics can be obtained, such as electric current and its time dependencies, generated net charge in the gas volume and power dissipation. The discharge current through the gas between electrodes is usually one of the main parameters of interest which can be measured in experiments and used for verification and tuning of models. For discharges in air, it can be calculated by means of Sato's equation [15]:

$$I = \frac{q}{U_a} \int_V (n_p \mathbf{w}_p - n_e \mathbf{w}_e - n_n \mathbf{w}_n - D_p \nabla n_p + D_e \nabla n_e + D_n \nabla n_n) \cdot \mathbf{E}_L dV \\ + \frac{\varepsilon_0}{V_a} \int_V \frac{\partial \mathbf{E}_L}{\partial t} \cdot \mathbf{E}_L dV \quad (4.6)$$

Here,  $U_a$  is the applied voltage and  $\mathbf{E}_L$  is the vector of Laplacian field obtained by solving (4.5) with  $\rho_v = 0$ . Integration in (4.6) is to be performed over the whole discharge volume  $V$ . The first term in the equation yields a conductive component of the current due the drift and diffusion of charge carriers, and the second term represents a capacitive current.

The presented hydrodynamic approach (also called fluid or drift-diffusion model) has become popular among researchers dealing with numerical simulations of different kinds of non-thermal gas discharges. It has been extensively used to study avalanches and streamers [16–20], coronas [21–23], high frequency discharges [24, 25], barrier discharges [26, 27], etc. and also has been employed for analysis in many practical applications [28–31]. Discussions on limitations of the model imposed by neglecting higher order moments of Boltzmann’s equation (4.1) can be found elsewhere [32].

## 4.4 Solving gas discharge problems

Computer modelling of gas discharges with the approach described in Section 4.3 requires simultaneous solution of two different kinds of PDEs, namely hyperbolic equations (4.3) and elliptic equation (4.5). Main computational challenges in discharge simulations are related to the strong coupling, non-linearity and stiffness of the model equations as well as to a necessity to resolve properly space charges in the gas volume. The latter requires a very fine computational mesh especially in the vicinity of electrodes and in the regions where sharp gradients in charge carriers’ concentrations exist. Because of these complications, there is no ‘universal’ software which may be used for modelling all kinds of gas discharge plasmas that are of interest for practice and, therefore, most of the numerical simulations reported in the literature have been performed with homemade computer codes. However, recently developed tools for scientific computations offer a number of features which can be utilized for solving gas discharge problems. One of the most appropriate software available today is a finite-element package Comsol Multiphysics, which provides an extended flexibility on all stages of the modelling process and allows for solving coupled PDEs of different nature.

In this section, examples of numerical modelling of electrical discharges in air are presented. First, coronas in concentric cylinders and rod–plane electrode systems are considered focusing on computer implementation of the set of equations (4.3)–(4.5) in Comsol Multiphysics 3.5a and on an analysis of generic properties of corona discharges. Further, specific features of the model for positive and negative streamers and numerical techniques for solving corresponding set of PDEs are introduced followed by a discussion on typical parameters of streamers in air based on results of computer simulations.

### 4.4.1 Simulations of corona in air

Corona discharges appear in systems with strongly non-uniform electric fields provided that at some location the field strength exceeds ionization threshold of gas. The reasons for local field enhancements can be different. Corona can be initiated on electrodes with small radii of curvature or from sharp edges of elements of electrode systems. In a leader discharge, the leader stem can be considered as a highly conductive rod producing strong electric field at its tip. In any case, the nature and processes taking place in corona discharge are essentially similar.

Depending on the field (structure, time variations, polarity, etc.) and ambient conditions, discharges in strongly non-uniform fields in air are observed as glow, burst or streamer coronas [33]. In general, the corona regimes are defined by dynamics and configuration of space charges generated in the gas volume. Thus, the glow mode appears due to permanent presence of space charges in the close vicinity of the corona electrode, whereas the other two modes are determined by the motion of space charge cloud in the gas between electrodes. The simulations described in Section 4.4.2 focus on glow corona mode, although problem formulation and set-up for modelling of burst discharge are similar.

#### 4.4.2 Computer implementation of corona model

Simulation procedure in Comsol Multiphysics starts with a preparation stage where the dimensionality of the model and equations to be solved are to be defined. This is done in the Model Navigator window that appears after running the software. It is extremely important to choose a proper number of dimensions for the problem in hand to avoid unnecessary increase in the size of the model and to reduce its computational cost and time. For this, the considered geometry should be analysed first in order to find ways for its simplifications, e.g. by utilizing existing symmetry (if any), avoiding unimportant detail, etc. As an example, corona between concentric cylindrical electrodes can be modelled in 2D or even in 1D due to symmetry of the system, whereas for a rod–plane electrode arrangement a 2D model can be developed accounting for axial symmetry and providing that the symmetry axis coincides with the axis of the rod. Further, equations (4.3) are to be added to the model that is done using ‘Multiphysics’ window by clicking Application Modes → COMSOL Multiphysics → Convection and Diffusion → Transient analysis → Add. For each equation, one can specify a name for the dependent variable, e.g., in the examples considered here “e” stands for concentration of electrons, “pos” and “neg” for densities of positive and negative ions, respectively. Further, it is important to choose correct ‘Equation form’ for the convection–diffusion equations – it should be set to ‘Conservative’ to ensure that drift fluxes will appear under  $\nabla$ -sign in (4.3). Next step is to add Poisson’s equation (4.5) for the electric potential needed for computing local fields accounting for space charge effects that is done by choosing Application Modes → COMSOL Multiphysics → Electromagnetics → Electrostatics → Add. If the discharge current (4.6) is to be calculated, an additional electrostatic equation should be added to the list that is to be used with the space charge density  $\rho = 0$  (i.e. as Laplace equation) for obtaining electrostatic field distribution  $\mathbf{E}_L$ . Finally, one should make sure that ‘Quadratic’ finite elements are selected (the general rule is that the order of elements should not be smaller than the highest order of the equations in the model). The described settings are illustrated in Figure 4.1 for the case of axially symmetric electrode arrangement, e.g. rod–plane system. Note that the multiphysics problem can be also built on the basis of specialized modules if they are available, e.g. ‘Chemical Engineering’ and ‘AC/DC’ modules for convection–diffusion and electrostatics equations, respectively. The modules provide some useful predefined quantities as well as extended lists of available boundary conditions.

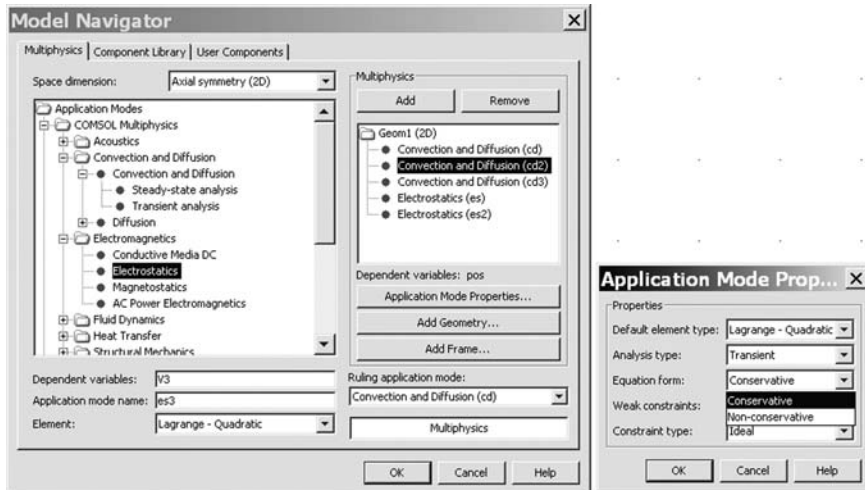


Figure 4.1 Defining dimensionality and choosing application modes in Model Navigator for solving set of equations (4.3)–(4.6)

After accepting the model settings, a CAD-tool window will appear where one may define a computational domain and draw geometry for the problem. A computational domain represents a part of space for which the problem is to be defined in terms of coefficients of (4.3)–(4.5), boundary and initial conditions. The coefficients in (4.3)–(4.5) are essentially material characteristics, which can be implemented using constants, expressions and functions available via ‘Options’ in the main menu. The geometry can be drawn using provided geometry primitives and utilizing Boolean operations (union, difference, intersection, etc.) or, alternatively, it can be imported from external CAD software or even from an image or sketch (see User Guide for corresponding procedures).

Constant quantities used in the model can be split into several groups: global (Boltzmann constant, elementary charge), conditional (pressure, temperature, initial charge density  $n_0$ , rate of background ionization  $R_0$ , etc.), those related to the applied stress (e.g. voltage magnitude and its rise/decay rates in case of step-wise DC or voltage amplitude and time constants for double-exponential representation of a voltage impulse), microscopic parameters of air (mobilities of ions, masses of particles, etc.) and auxiliary (e.g. artificial diffusion factors, see below). The constants can be implemented using corresponding ‘Options’ as illustrated in Figure 4.2, where typical values of air parameters are borrowed from References 9, 34 and 35.

The constants are further used either directly in the problem settings or in the expressions for calculating field/time/pressure/etc.-dependent characteristics. In the latter case, the expressions to be computed are specified as shown in Figure 4.3. Here, the reduced field  $E/N$ ,  $T_d$ , is defined in the first line using the in-built name for the field variable *normE\_es* in the Electrostatics equation. This quantity is

further utilized as an argument for functions describing field dependencies of electron drift velocities  $w_e(E/N)$  and their characteristic energies  $D_e/\mu_e = f(E/N)$  as well as ionization  $\alpha/N(E/N)$  and attachment  $\eta/N(E/N)$  coefficients. In contrast to electrons, most of the parameters of ions in non-thermal air discharge plasmas are dependent not only on electric field strength but also on gas temperature [34]. Therefore, kinetic temperatures of ions  $T_p$  and  $T_n$  (positive and negative, respectively) are calculated using masses of corresponding ions from ‘Constants’ and they are further employed for obtaining diffusion coefficients  $D_{p,n}$ , ion-ion recombination coefficient  $\beta_{ii}$  and detachment frequency  $\nu_{det}$  in (4.3) and (4.4). Knowing all the parameters, rates of ionization, attachment, recombination and detachment are computed and corresponding source terms (4.4) are formed, see Figure 4.3. The space charge density (variable  $\rho$ ) is calculated as it is given on the right-hand side of (4.5). Variables  $cur\_den\_cond$  and  $cur\_den\_cap$  represent conductive and capacitive current densities, respectively, which are under integral signs in (4.6). These quantities are used for computing integration coupling variables  $cur\_cond$

The screenshot shows a software window titled 'Constants'. It contains a table with four columns: 'Name', 'Expression', 'Value', and 'Description'. The table lists various constants used in the corona model, such as Boltzmann constant, elementary charge, reference pressure, and initial density of ions. The 'Value' column includes scientific notation for many entries. At the bottom of the window are standard Windows-style buttons for 'OK', 'Cancel', 'Apply', and 'Help'.

Name	Expression	Value	Description
kb	1.38e-23	1.38e-23	Boltzmann constant
q	1.6e-19	1.6e-19	elementary charge
p0	101325	1.01325e5	reference pressure, Pa
T0	293	293	reference temperature, K
pg	760	760	current pressure, Torr
tg	293	293	current temperature, K
N	pg*133.3/(kb*tg)	2.505515e25	gas density, m-3
delta	T0*pg*133.3/(tg*p0)	0.999832	air relative density
n0	1e9	10e8	initial density of ions, m-3
R0	1e6	10e5	rate of background ionization, 1/(m3s)
u_amp	250000	2.5e5	voltage amplitude, V
tau1	2700e-6	0.0027	time constant 1 for impulse
tau2	162e-6	1.62e-4	time constant 2 for impulse
gamma	1e-3	0.001	coefficient of secondary emission
mu_p	2.0e-4/delta	2.000336e-4	mobility of positive ions, m2/Vs
mu_n	2.7e-4/delta	2.700453e-4	mobility of negative ions m2/Vs
beta_ei	5e-14	5e-14	electron-ion recombination coefficient, m3/s
m_n	5.3e-26	5.3e-26	mass of O2- ion
m_e	9.109e-31	9.109e-31	mass of electron
m_g	m_n*m_e	5.299909e-26	mass of O2 molecule
m_p	m_g*m_e	5.299818e-26	mass of O2+ ion
ad_p	0.25	0.25	ad factor for pos ions
ad_n	0.25	0.25	ad factor for neg ions
ad_e	0.25	0.25	ad Factor for electrons

Figure 4.2 Definitions of constants in the corona model

and *cur\_cap* (conductive and capacitive current, respectively) by means of corresponding option available via Options → Integration coupling variables → Subdomain

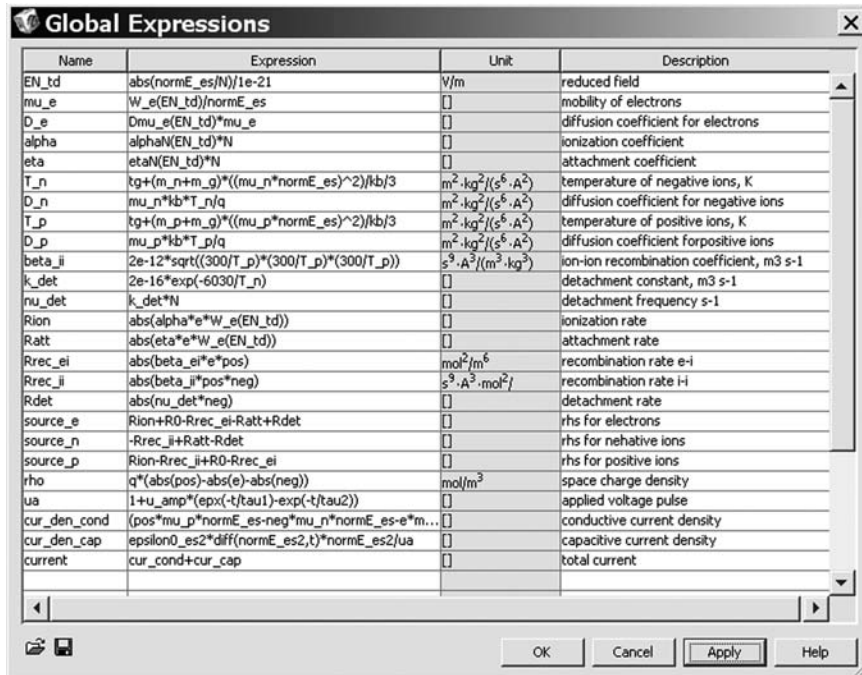


Figure 4.3 Expressions for calculating coefficients in (4.3)–(4.6)

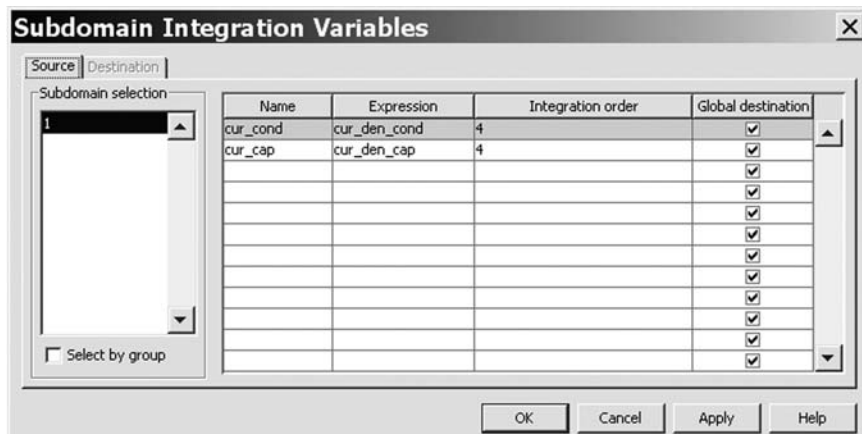


Figure 4.4 Implementation of integration coupling variables for computing discharge current

variables (see Figure 4.4). Finally, the total current (variable *current* in the expressions) is obtained as a sum of the two components.

Field-dependent characteristics of electrons in air (drift velocities, mean energies, ionization and attachment coefficients) have been studied extensively and have been presented in numerous scientific publications. However, detailed analysis of data available in the literature showed that there are large discrepancies in the experimental as well as calculated results obtained by different authors, which can be attributed to specific conditions of experiments and equipment used, methods of solving Boltzmann's equation, which yielded all the microscopic properties of interest, etc. The dependencies presented in Reference 36 (reproduced in Figure 4.5) seems to be most reliable and are adopted in the present analysis. In the software, the dependencies shown in Figure 4.5 are implemented as functions of the reduced field  $E/N$  using their tabular representations as demonstrated in Figure 4.6 (functions can be accessed via 'Options' in the main window of the software). The values between points given in the table may be required in the solution process and, therefore, interpolation of the data is needed. This can be

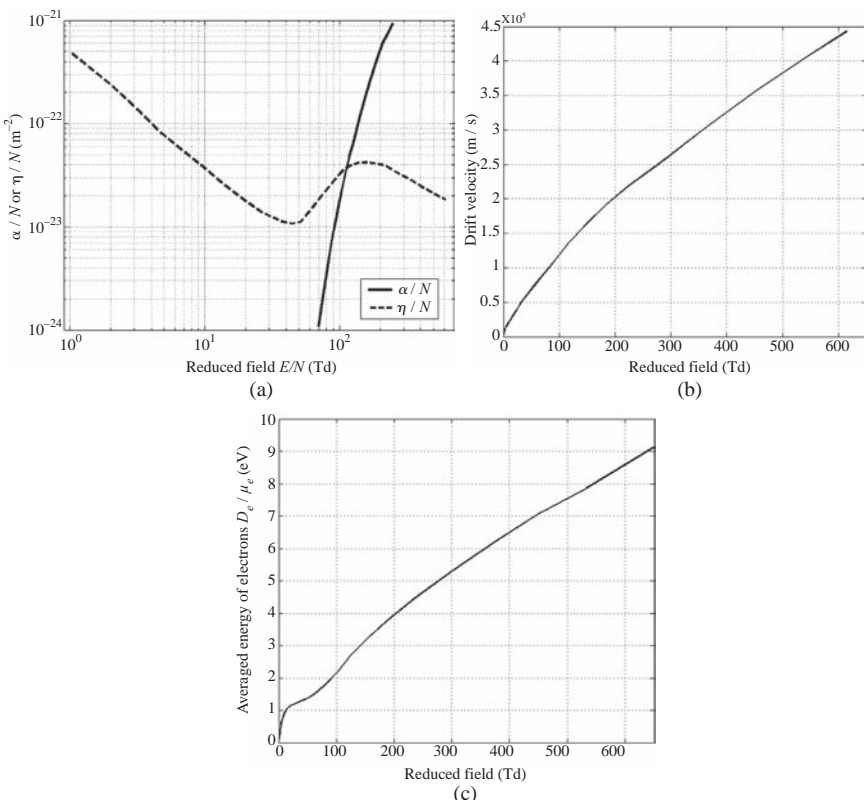


Figure 4.5 Field dependencies of the ionization and attachment coefficients (a), electron drift velocity (b) and mean electron energy (c) in air [36]

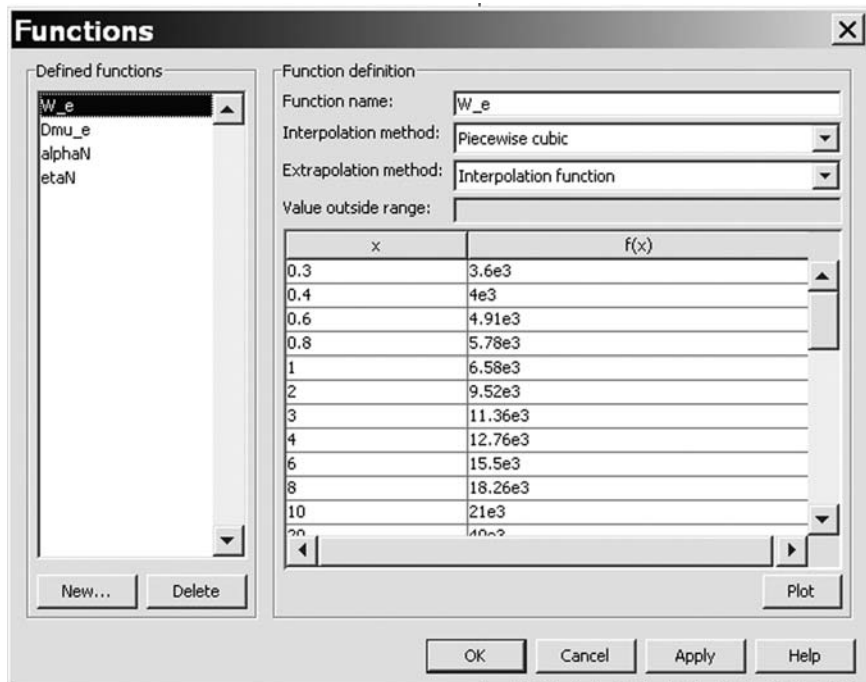


Figure 4.6 Implementation of field-dependent characteristics of electrons in air

implemented using, e.g. ‘Piecewise cubic’ interpolation method, which preserves the shapes of curves in Figure 4.5. To compute the functions outside the provided ranges, extrapolation is used (in Figure 4.6, the method is set to ‘Interpolation function’). Note that the specified functions can be used at any stage of the simulations (equation settings, post-processing, etc.) by providing a name and argument as it is shown, e.g. in lines 2–4 in Figure 4.3. Alternatively, functional dependencies can also be read from external data files. For this, one should prepare files according to the format used in Matlab and specify a path to the file for each function. The files are read during model initialization stage and data are kept in computer memory while solving the model.

Next step in building the model is to assign material characteristics for the computational domain. For the convection–diffusion equations, these include diffusion coefficients, components of the drift velocities of the charge carriers and the source terms (4.4). An example of the settings for electrons is shown in Figure 4.7(a) (note ‘–’ sign for the velocities of negatively charged particles which should be changed to ‘+’ for positively charged ones). Settings for Poisson’s equation (Figure 4.7(b)) include dielectric constant of the medium  $\epsilon_r = 1$  and space charge density  $\rho$  as defined in the expressions (Figure 4.3). Initial conditions are given via ‘Subdomain settings’ (tab ‘Init’ in Figure 4.7). It is usually assumed that initially (at zero field) the gas is electrically neutral and the concentrations of electrons and

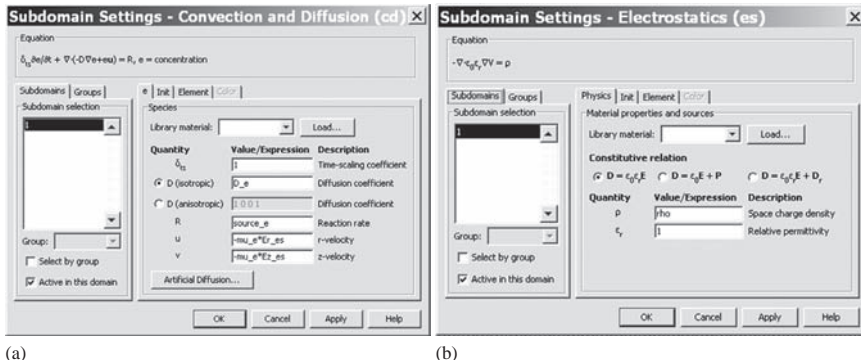
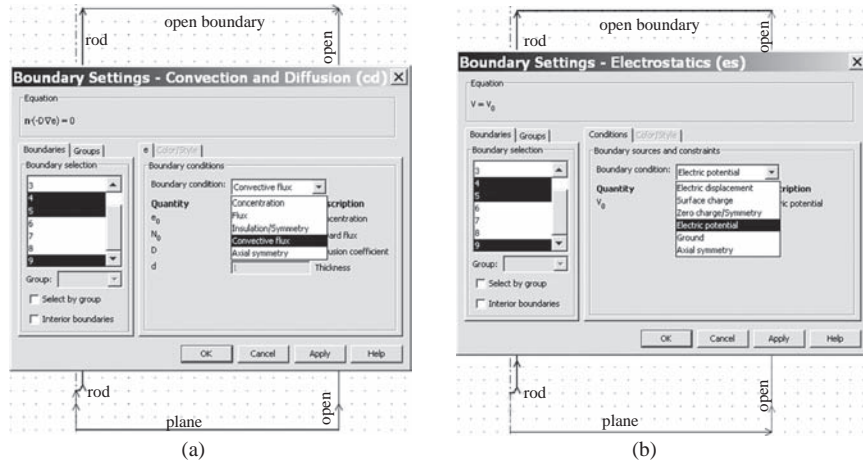


Figure 4.7 Settings for the convection–diffusion (a) and Poisson’s (b) equations

positive ions are set to  $n_0$  (see Figure 4.3 for the magnitude). This is not exactly true (see Reference 34 for discussion), but such assumption introduces errors in the solution only at very short instants after voltage application provided that equilibrium concentrations are set to the values corresponding to low space charge densities, which are not able to distort electrostatic field in the system. The concentrations of electrons and positive ions change to non-equilibrium distributions during several initial time steps and, also, negative ions density rises due to strong attachment in low field regions (Figure 4.5(a)). Actually, the provided initial values are used in the model just for initializing the simulation process and to compute quantities for the first time step. Further, the solution obtained on a current time step is utilized as initial value when calculating densities and potential distributions for the next step and, therefore, the specified initial state of the system is ‘forgotten’ after several successive steps.

Boundary conditions are essential for correct representation of a real physical picture in the model. When the computational domain is limited by physical boundaries (like in case of coaxial cylinders), one should focus on and implement actual processes taking place on gas–metal interfaces that may include injection of charges, their absorption/neutralization, etc. In most of the cases, a computational domain is limited also by artificially introduced boundaries and choice of conditions there becomes non-trivial. An example is shown in Figure 4.8 for rod–plane geometry represented in axially symmetric domain. When setting boundary conditions for this case, one should keep in mind that (4.3)–(4.5) are coupled. Hence, if a positive potential is applied to the rod (Figure 4.8(b)), a simplest set of boundary conditions includes ‘Convective flux’ for electrons (Figure 4.8(a)) and negative ions and ‘Concentration’ equal to zero for positive ions on the boundaries representing surface of the rod. By specifying convective fluxes, one ensures continuity of the current flow between electrodes. Opposite is valid for the grounded plane (horizontal boundary on the bottom): zero concentrations of electrons and negative ions and convective flux of positive ions are specified here. Note that injection of negative charges from the plane and positive ions from the needle is prevented when using such conditions. The left vertical boundary between the plane and the



*Figure 4.8 Implementation of boundary conditions for convection–diffusion (a) and electrostatics (b) equations*

needle represents physical symmetry of the system and ‘Axial symmetry’ is specified here for all equations. Finally, the choice of conditions for the open boundary (e.g. the rightmost vertical one) should be made taking into account field behaviour which controls incoming and outgoing fluxes of charged particles. Thus, if one sets ‘Zero charge/Symmetry’ for the potential here (which is natural), the field component normal to the boundaries will be set to zero and there will be no fluxes of charge carriers crossing the boundary that doesn’t reflect the real situation. In reality, charges existing in the gas are attracted/repelled to/from high field region and continuously move across the boundary. This motion is a result of the action of forces associated with the fields which are not tangential (parallel) to the boundary and can be modelled by, e.g. specifying a grounded surface there. However, this may alter field distribution in the region of interest located around the rod tip. Thus, a compromise between the two approaches is to be found. One way is to increase the size of the domain allowing artificial boundaries to be located far from the region of interest (surface of the rod) and to assign ‘Zero charge/Symmetry’ for the potential and ‘Normal fluxes’ for charge carriers. The effect of the external boundaries on the field distribution and fluxes of charges is minimized in this case, but the size of the model can rise significantly. Another option is to apply ‘Distributed capacitance’ conditions (available in AC/DC module) for the electrostatic equation (4.5) and ‘Convective flux’ for (4.3).

After introducing materials characteristics, initial and boundary conditions for all the equations in the model, a computational mesh is to be generated that is a crucial part of a finite-element problem affecting accuracy of a solution. In order to reduce the number of unknowns to solve for, it should be generated in an adaptive way to provide high resolution in regions where strong variations in the geometry

exist (curved surfaces and ages, thin layers, etc.) being not too dense in other regions. The software makes it possible to control mesh generation process by specifying a number of mesh parameters available via Mesh → Free mesh parameters in the main menu (there are also other options to control meshing, see User's guide for details).

All the procedures described above are the pre-processing steps of the problem. When completed, the actual solution process can be initiated. The problem in hands requires time-dependent solver which can be chosen via Solve → Solver Parameters (Figure 4.9). In this window, several important parameters should be specified. In the 'General' tab (Figure 4.9(a)), one should provide 'Times' for output, i.e. instants for which the solution will be available. One should also choose a solver for the linear system arising after discretization of the PDEs. Several types of direct and iterative solvers are available in 'Linear system solver'. In general, the most appropriate one can be chosen after analysing the nature of the problem, available computing power, memory, etc. For the problem under consideration, one may select direct solvers which are different in their requirements and efficiency: UMFPACK can be chosen if RAM size is high enough; alternatively, SPOOLES

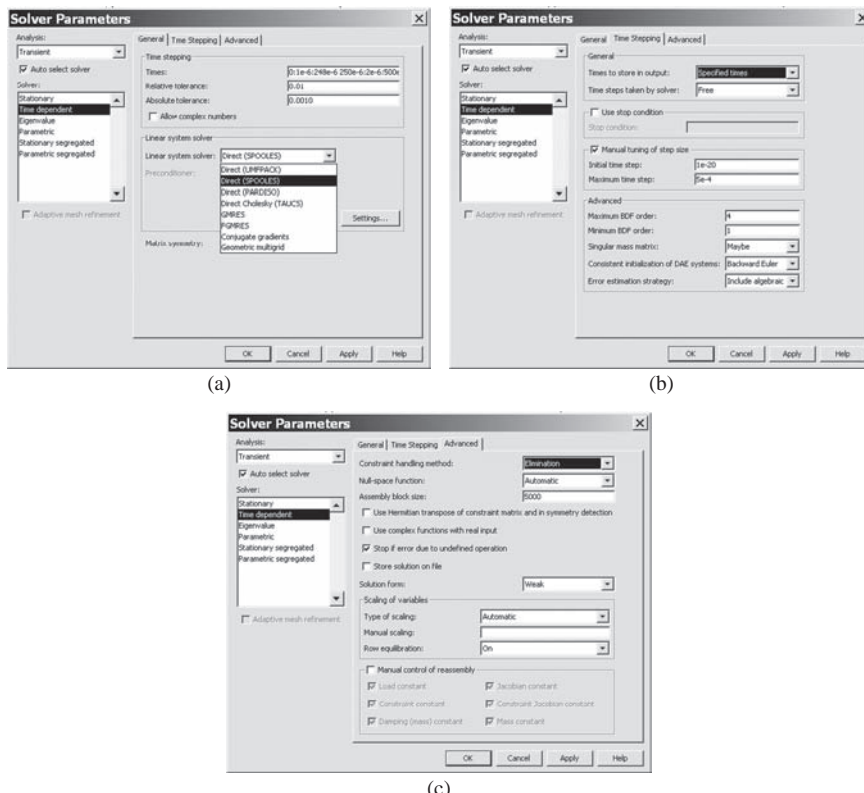


Figure 4.9 Choosing solver parameters

provides almost the same computational time but requires less memory; PARDISO is a parallel solver and can be an option if a computer is equipped with several processors. In the tab ‘Time stepping’ (Figure 4.9(b)), one can mark ‘Manual tuning of step size’ and provide initial time step and maximum time step. The first option helps the solver at the initialization stage and the second one is useful to avoid too large time steps using which some rapid variations of the quantities can be missed during solution process. Sometimes it is also useful to select ‘Strict’ option instead of ‘Free’ in General → Time steps taken by solver. Doing so, the solver is pushed to take intermediate steps between the output times that is helpful when, e.g. oscillations or other variations in the solution are expected. In some cases, one may reduce the ‘Maximum BDF order’ in Advanced field to switch to a more stable numerical scheme for the time-stepping algorithm (the default order is 5). However, this should be done with a care because small values here result in stronger numerical damping. In the ‘Advanced’ tab (Figure 4.9(c)), the option Weak may be chosen for the ‘Solution form’ to automatically convert the problem into an integral form that may help to prevent singularities in the solution. Also, ‘Assembly block size’ (number of mesh elements that the solver processes at once during the assembly process) can be increased if available RAM size is high enough. The described approach to specify solver settings is just a simplest option and it may be implemented in a more advanced way to increase the efficiency of the solution process, e.g. by utilizing time-dependent segregated solvers (see User’s guide for details).

In general, one can run the model at this stage. However, most likely such an attempt won’t be successful due to specific features of the system (4.3) and (4.5) already mentioned above. From mathematical point of view, it is very stiff (in a sense that it is characterized by different time scales and source terms for different kinds of charge carriers) and strongly non-linear (most of the terms are field-dependent). In addition, the velocities of the carriers in strong fields become extremely high that leads to their strongly drift-dominated flows with very high local Peclet numbers, which is a dimensionless number describing the relationship between the convective and diffusive terms in the convection–diffusion equations. These peculiarities make the discretized problem to be inherently very unstable that results in non-physical oscillations in the solution and even in negative concentrations magnitudes, primarily in regions where steep gradients of the charge densities are present. The oscillations can even be large enough to affect convergence of the solution. To resolve these problems, special algorithms or stabilization methods should be used. The software provides several stabilization techniques which can be selected for each equation (4.3) via Physics → Subdomain settings → Artificial diffusion (Figure 4.10). The experience showed that ‘Isotropic diffusion’ with the Tuning parameters  $ad$  defined in Constants (Figure 4.2) is one of the most appropriate choices for the considered problem. Note that tuning parameters should not be too high to avoid introducing large amount of artificial diffusion which may distort the solution. This is especially important in presence of interfaces between different materials where transport coefficients change abruptly.

After completing all the steps above, one may run solver and obtain solutions for output times specified in Solver Parameters (Figure 4.9(a)). The solution

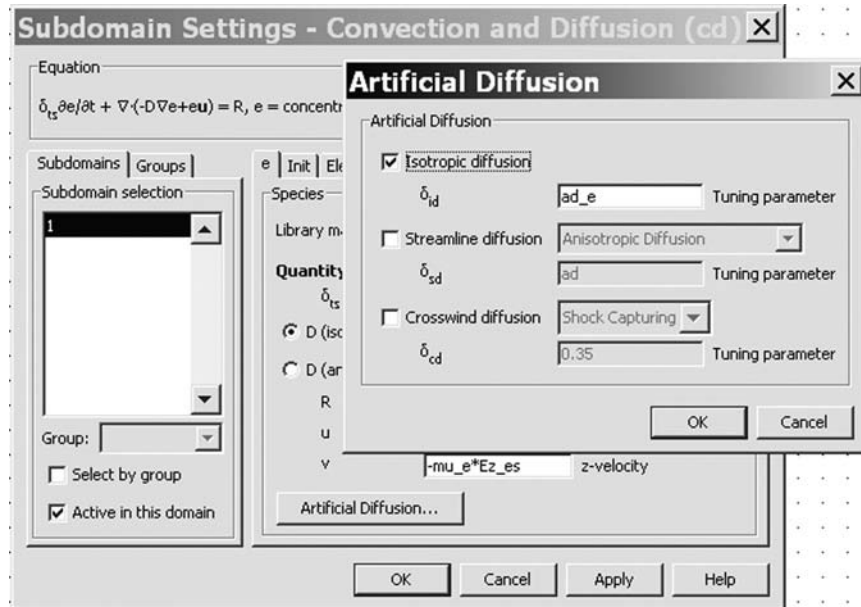


Figure 4.10 Choosing stabilization method for the convection–diffusion equation for electrons

progress is indicated in log-window showing current time and some auxiliary information from the solver. In addition, the convergence of the solution can be traced when using iterative solvers. After successfully completing the whole specified time interval, the software automatically switches to a post-processing mode where a wide range of graphical tools for visualization and analysis of the results is available to create 1D, 2D and 3D plots and time dependencies, perform integration and differentiation of different quantities, etc. These facilities are available via Post Processing → Plot parameters in the main menu. The post-processing tools allow also combining different kinds of plots to facilitate the analysis of the data.

#### 4.4.3 Study case: positive corona between coaxial cylinders

DC corona between coaxial cylinders has been a subject of numerous investigations. Most of them were performed quite long time ago starting from famous research [37]. An extensive description of corona phenomena can be found in [33]. The subject is also covered in many recent books and scientific articles. For the reference purposes, one of the most cited experimental data set presented in [38] is chosen in the present analysis. This research has been performed with a special concern to discharge stability preventing formation of streamers. The electrode system used in [38] consisted of a large cylinder diameter of  $D = 58.1$  cm and the internal one (corona electrode) whose diameter was varied in the range of  $d_0 = 0.3185\text{--}3.175$  cm. The voltage was applied between the cylinders, and voltage-current corona characteristics were recorded.

In the model, the experimental geometry is implemented in Cartesian coordinate system. To obtain corona voltage-current characteristic from a single run of the model, the applied voltage is implemented as a linearly increasing function of time rising from 0 to 200 kV within 1000 s with the ramping rate of 200 V/s that is low as compared with time constants of the processes in the discharge and, therefore, does not introduce any transient effects or significant capacitive currents. The conditions, the kinetic coefficients and other material parameters presented above are used. The choice of boundary conditions for the charge carriers is obvious in this case: since corona electrode surface is set to the positive potential, convective fluxes for electrons and negative ions and zero concentration for positive ions are specified here; the negative charges are repelled from the surface of the grounded outer cylinder (hence,  $n_e = n_n = 0$ ) and the current flow is due to positive ions only (convective flux condition). An example of the results of the simulations is presented below for the case of corona electrode diameter of  $d_0 = 1$  cm.

A two-dimensional surface plot showing the distribution of the density of positive ions for the applied voltage of 200 kV ( $t = 1000$  s) is presented in Figure 4.11. As one can observe, the ions are localized in the vicinity of the corona electrode where their concentration reaches  $\sim 10^{15} \text{ m}^{-3}$ , whereas it is significantly lower in the main part of the interelectrode gap. The volume around the corona wire within which the impact ionization and production of positive ions take place is called corona (or ionization) region. Its size and concentrations of charge carriers are dependent on field configuration and the applied voltage. As it is seen in Figure 4.12(a), the increasing voltage leads to growing electron density in the vicinity of the corona electrode due to rising field strength and, consequently, ionization intensity. However, the levels of the electronic concentrations are much lower than the densities of the positive ions (Figure 4.12(b)) at the corresponding voltages (time instants in the legend). The reason is that the electrons are lost on the surface of the corona electrode where convective flux boundary condition is specified and due to their attachment to electronegative components of air. The latter gives rise to increased densities of negative ions (Figure 4.23(c)) which, however, remain even lower than those for electrons. As a result, the positive space charge is dominating in the entire discharge space (Figure 4.12(d)) except a very thin layer around the internal cylinder on the surface where the concentration of positive ions is set to zero. This picture is natural for DC coronas where the external drift region is always filled with ions whose charge sign is similar to the sign of the potential applied to the corona electrode.

The space charge density in the interelectrode space becomes significant at certain voltage level (which slightly exceeds corona inception voltage) and the electrostatic field is distorted by the field generated by the space charge. This can be seen in Figure 4.13(a) where distributions for several time instants (applied voltage magnitudes) are shown. Thus, the curves for  $t = 100, 200, 300$  and  $400$  s (corresponding voltages are 20, 40, 60 and 80 kV) are simply shifted upwards towards higher field levels due to the increasing voltages while their shape defined by the geometry of the system is preserved. However, at longer times (= higher voltages), the main changes in the distributions appear in the external corona region

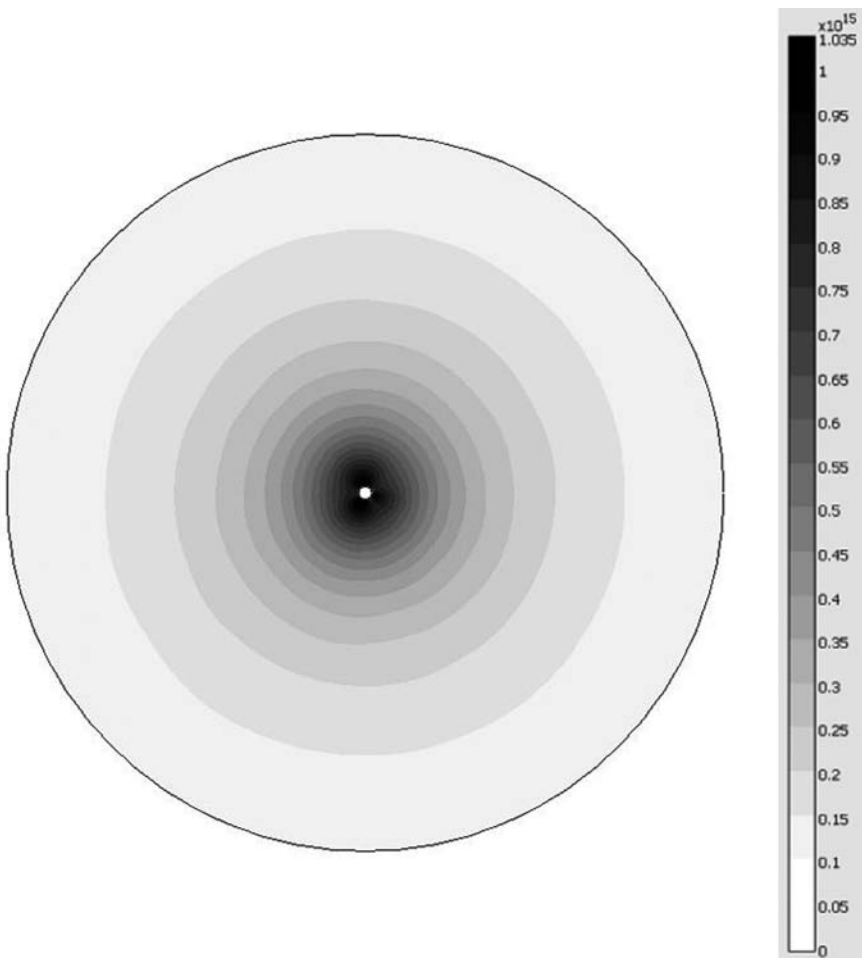


*Figure 4.11 Concentration of positive ions between cylinders at 200 kV*

(drift region) due to the accumulated space charge. The field strength increases here in accordance with the growth of the space charge density (Figure 4.12(d)). At the same time, the field remains constant on the surface of the corona electrode (Figure 4.13(b)). This fact is in agreement with numerous experimental findings (see, e.g. Reference 33 and the books mentioned at the beginning of the section). From Figure 4.13(b), one can identify the voltage level at which space charge dominated corona mode appears and which is normally identified as corona inception voltage. For the considered case of  $d_0 = 1$  cm, it is  $\sim 83$  kV that is in agreement with the experimental data given in Reference 38. The constant field on the surface of the corona electrode reflects the fact that the discharge is self-controlled. The surface field in Figure 4.13(b) is  $\sim 42$  kV/cm and it only slightly exceeds the ionization threshold of air ( $\sim 31$  kV/cm). This relatively low field (as compared with the

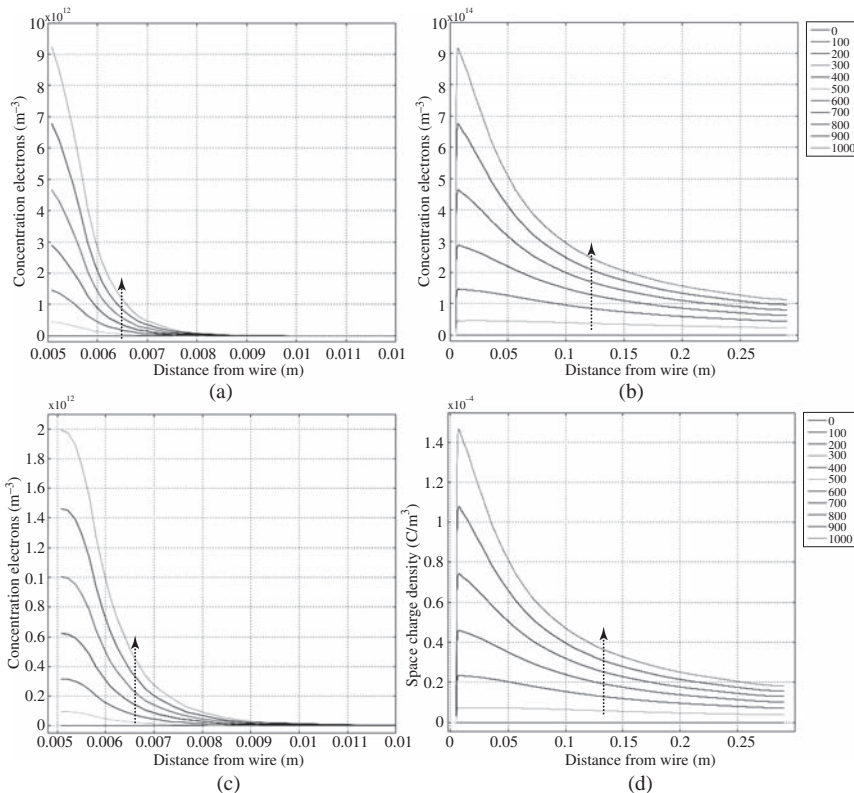


*Figure 4.12 Time variations of the distributions of the densities of electrons (a), positive ions (b), negative ions (c) and resulting space charge (d). Arrows indicate increase in the concentrations with time (voltage). Note that variations of the quantities at instants 0–400 s are not visible with the linear scale used*

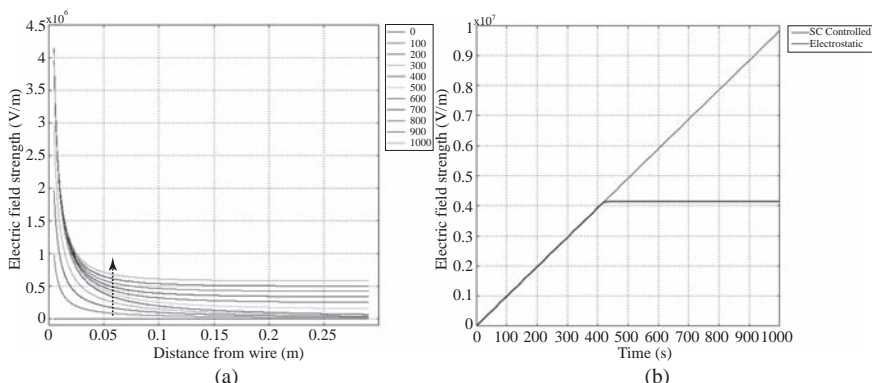


*Figure 4.13 Time variations of electric field distributions (a) and the field strength on the corona electrode surface (b)*

electrostatic one) provides rate of generation of ions needed just for compensation of ionic losses and results in a steady-state corona at the given voltage.

Any computational model should be validated against experimental data. For the considered case, voltage-current characteristics of the corona discharge dependencies in Reference 38 are used here as reference data for verification of the developed model. Additionally, known analytical expression is employed as a supplementary mean of the validation. The analytical formula representing functional dependence of the positive corona current on the applied voltage for coaxial cylindrical system is attributed to Townsend and it is written as (see, e.g. Reference 39)

$$I = \frac{8\pi\epsilon_0\mu_p}{R^2\log(R/r_0)} V(V - V_i), \text{ A/m} \quad (4.7)$$

Here,  $R = D/2$  and  $r_0 = d_0/2$  are the radii of the external and internal cylinders, respectively;  $V$  and  $V_i$  are the applied and corona inception voltages, respectively. The inception voltage is found from the known expression for the field between coaxial cylinders as  $V_i = E_{cr}r_0 \log(R/r_0)$ , where the critical field is obtained using Peek's formula:

$$E_{cr} = 3 \cdot 10^6 \delta \left( 1 + 0.03/\sqrt{\delta r_0} \right), \text{ V/m} \quad (4.8)$$

Here,  $\delta$  is the relative air density as defined in the expressions (Figure 4.2). Formulas (4.7) and (4.8) are empirical and have been validated in numerous studies. As one may see from (4.7), the corona current is proportional to  $V^2$  and it is meaningful only at voltages exceeding  $V_i$ . In addition, the magnitude of the current is affected by the value assigned to the mobility of positive ions  $\mu_p$ . Actually, the mobility is the only parameter to be chosen in (4.7) for given dimensions of the electrodes. The results of the calculations with (4.6) and (4.7) are shown in Figure 4.14 together with the experimental data. One can notice an agreement between the calculated and measured corona characteristics. However, the best fit between the measured results and calculations with (4.6) and (4.7) is found with slightly higher value of  $\mu_p = 2.8 \text{ cm}^2/\text{Vs}$  than that corresponding to typical mobility of positive ions in air. This difference can be attributed to the special conditions of experiments [38] where the interelectrode gap was irradiated with a radioactive  $\beta$ -source containing  $^{90}\text{Sr}$  of strength 0.4 mCi to achieve glow (streamer-less) mode of the corona discharge. The simulations performed with the developed model also agree well with the experiments, as it is seen in Figure 4.14, and the best fit in this case is obtained with a more realistic value for the mobility of positive ions  $\mu_p = 2.3 \text{ cm}^2/\text{Vs}$ . The fact that both analytical calculations and numerical simulations provide results that are slightly different from experimental ones demonstrates the importance of selecting reliable material characteristics for discharge modelling from available data.

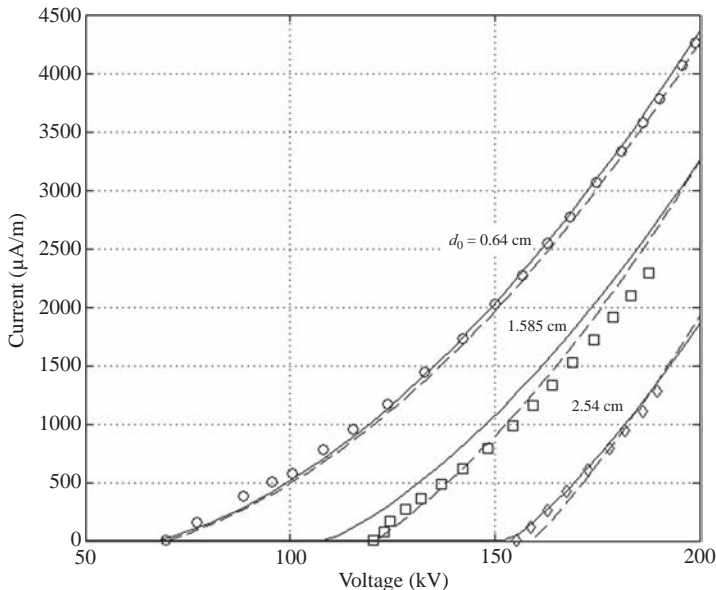


*Figure 4.14* Voltage-current characteristics of positive corona between coaxial cylinders: symbols – experimental data [38], broken lines – analytical calculations (4.6) and (4.7), solid lines – present simulations

#### 4.4.4 Study case: positive corona in rod-plane electrode system

Another ‘classical’ electrode configuration often used for corona research is a rod–plane arrangement. For this study case, the simulations are performed for the conditions of Reference 40, where positive DC corona in air gap of 1 m length was investigated for the diameter of the rod varying in the range  $d_r = 12.7\text{--}50.8\text{ mm}$ . The computational domain representing the geometry [40] is implemented in 2D ( $r$ - $z$  coordinates) utilizing axial symmetry of the system (Figure 4.15). The domain is limited by the symmetry axis and surface of the rod on the left, horizontal line on the bottom representing surface of the plane, and by two artificially introduced boundaries on the top and on the right-hand side. A positive potential is applied to the rod and the bottom plane is grounded. It is assumed that the potential changes linearly with time from 0 to 300 kV during 1000 s (similar to the previous case, but with increased ramping rate 300 V/s).

The boundary conditions for the charge carriers on the electrodes are similar to the ones used for the coaxial system above: if the signs of the charged particles correspond to the sign of the potential on the surface, zero concentrations are specified; otherwise, ‘Convective flux’ conditions are used. On the open boundaries, ‘Zero charge/Symmetry’ is set for the potential and inward fluxes of charge carriers are defined as normal convective fluxes. The latter condition is not strict because the fluxes are controlled here by the direction and magnitude of the electric field as it has been discussed above. The model settings for the internal part of the domain are similar to the ones used in the

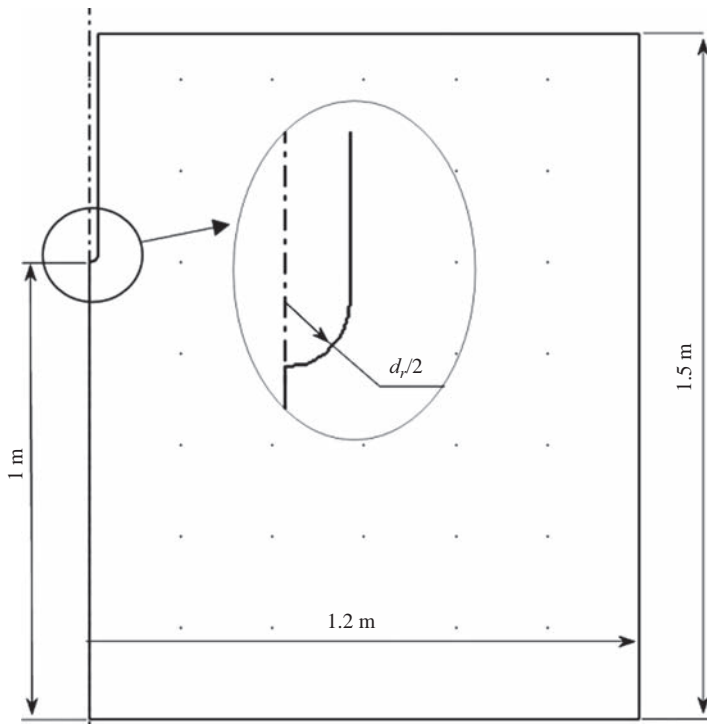
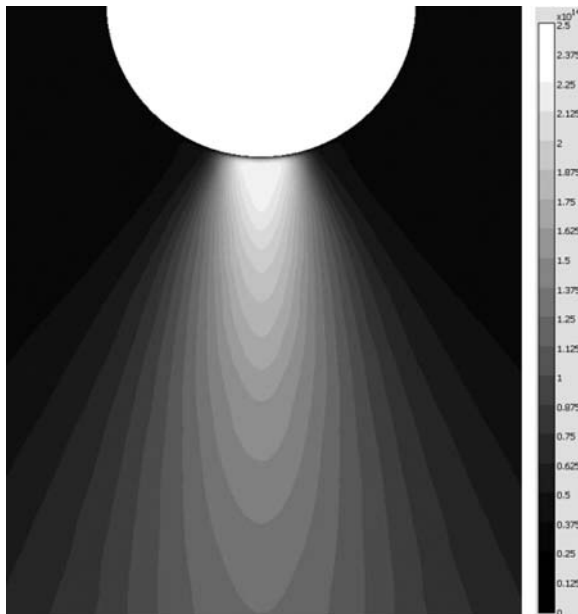


Figure 4.15 Computational domain and dimensions of the electrode system

simulations of the concentric electrodes. The computational mesh for the system in Figure 4.15 should be refined at the tip of the rod and along the symmetry axis, where most intensive discharge activity is expected. This is done using meshing facilities provided in the software. An example of the results obtained from the simulations is presented below for the case of  $d_r = 38.1$  mm.

The distribution of the concentration of positive ions in the corona discharge at the applied voltage of 300 kV is shown in Figure 4.16. One can observe that the ionic cloud is narrow and extends into the bulk of the gap in contrast to the case of corona around cylindrical conductor in Figure 4.11. Such shape has been observed in many experiments and it is the consequence of the distribution of the electric field which is strongest along the symmetry axis. The maximum of the density of the ions is located close to the rod tip and under the conditions of [40] reaches  $\sim 2.5 \times 10^{14} \text{ m}^{-3}$ .

The time variations of the concentration profiles of charge carriers along the symmetry axis are shown in Figure 4.17. One may see that the densities of negative carriers are much lower than the positive ones and they are localized in a thin ( $< 2$  mm) layer at the rod surface forming the corona region (Figure 4.17(a) and (c)). The drift region of the discharge covers practically the entire gap (Figure 4.17(b)). As a result, the whole space in front of the rod is positively charged except of a small volume around the tip of the rod where negative charges are dominating



*Figure 4.16 Profile of the concentration of positive ions at 300 kV (the region  $\sim 5 \times 5 \text{ cm}^2$  at the rod tip is shown)*

(Figure 4.17(d)). The space charge density increases with time (i.e. applied voltage); however, the shape of the profiles remains identical in the main part of the drift region at the distance from the rod larger than  $\sim 1 \text{ cm}$  (the curves are just shifted upwards and are parallel). Such behaviour of the space charges leads to the situations when the external field is almost completely screened out and the resulting distributions (Figure 4.18(a)) are characterized by extremely low field strength in the middle of the gap (at distances from the rod tip 0.2–0.3 m) and its enhancement at the surface of the plane. The field level at the tip of the corona electrode is the highest and it remains constant after corona inception (Figure 4.18(b)). This is similar to the case considered above for cylindrical system; however, the field magnitude is slightly lower (compare Figures 4.13(b) and 4.18(b)). Summarizing, one may state that corona discharge is a phenomenon completely controlled by space charges produced in the corona region which define its internal as well as external properties.

The corona current calculated using expression (4.6) is presented in Figure 4.19 as a function of the applied voltage for three sizes of the diameter of the corona rod together with the experimental results [40]. One may note that the best agreement between the computed and measured data is achieved for  $d_r = 50.8 \text{ mm}$  that is the largest size of the rod for which the simulations were performed. For the intermediate rod diameter  $d_r = 38.1 \text{ mm}$ , the observed discrepancies can be attributed, first of all, to the inconsistencies in the conditions of the experiments [40] and those under which the material parameters used in the model were measured.

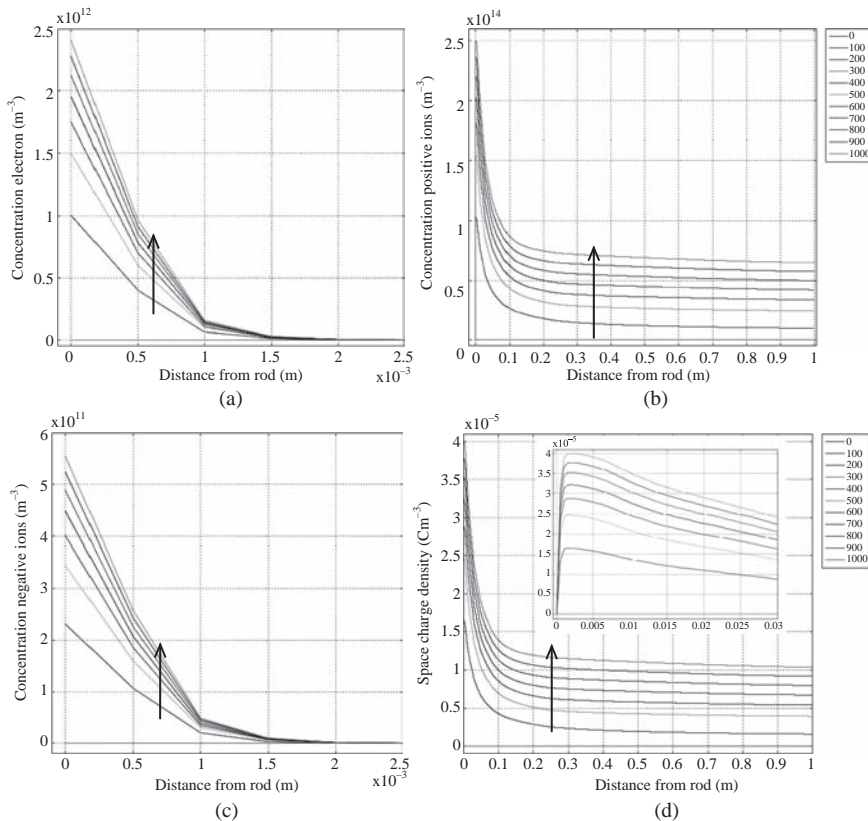


*Figure 4.17 Time variations of densities of charge carriers along symmetry axis: (a) electrons, (b) negative ions, (c) positive ions and (d) resulting space charge. The arrows indicate changes at longer instants (higher voltages). The inset in (d) shows the distributions of the space charge density in close vicinity of the rod tip*

Thus, the simulations are performed with the constant value of the mobility of positive ions. However, by analysing the behaviour of the characteristics in Figure 4.19, one may suggest that if the mobility is field dependent and increases with the increasing field strength (which is the result of either rising applied voltage or smaller rod diameter), it would lead to an increase in the slope of the characteristics, as it has been shown in Reference 38, and better agreement with experimental results could be achieved. Another explanation may be that the field magnitude in the arrangement with the largest rod diameter is not high enough to initiate transition to streamer corona mode, whereas this may happen for smaller rod sizes. There is no information in Reference 40 concerning corona modes observed in the experiments and if streamer corona took place, it would provide higher currents than those obtained from the simulation that is observed in Figure 4.19.

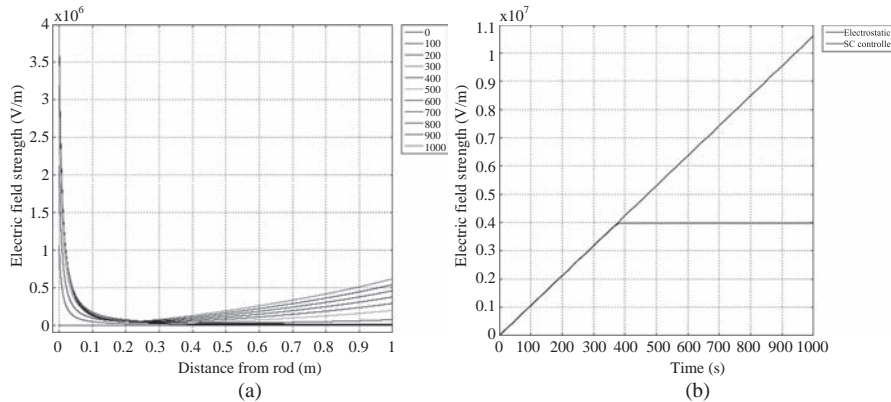


*Figure 4.18 Time variations of electric field distributions (a) and the field strength on the corona electrode surface (b)*

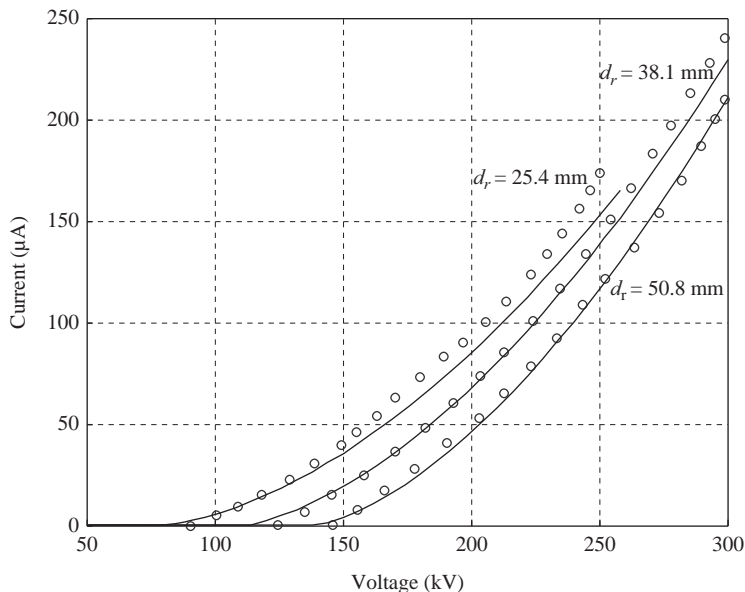


*Figure 4.19 Voltage-current characteristics of positive corona in rod-plane system: circles are experimental data [40]; lines are the results of the simulations*

## 4.5 Simulations of streamer discharges in air

Electrical discharges in high-pressure gases are usually associated with formation and development of filamentary plasma channels (streamers), which propagate in an ambient neutral gas. A streamer is a self-adjusting object. Since it has been formed, it

produces charged particles in a high field region at the front, needed to maintain high plasma conductivity in the channel. In its turn, the electric field at streamer tip is controlled by the produced space charge. This property allows streamers to develop in weak fields, much lower than the ionization threshold of the gas. Numerical solution of the set of PDEs (4.3)–(4.5) in case of streamer discharges is challenging. There is no commercial software available today, which can be used for modelling of streamers in a way similar to that introduced above for corona discharges. Main computational difficulties arising in modelling of streamers are outlined below and a simplified approach for solving (4.3)–(4.5) based on finite-difference method is introduced. Further, typical results that can be obtained from the numerical model are presented and discussed using achieved solutions for propagation of positive and negative streamers in weak homogeneous background electric fields as examples.

According to the basic theory, a streamer can be formed if a space charge produced in an electron avalanche is sufficiently strong to generate own field which is comparable with the external applied field. The condition of the avalanche-to-streamer transition is represented by well-known criterion  $\int_0^{x_c} \alpha(x)dx = \log(N_{cr})$ , where  $x_c$  is the critical length of the avalanche and  $N_{cr}$  stands for the critical number of electrons in the avalanche head, which is usually assumed to be equal to  $10^8$  (see also Section 4.2.4). Further development of a streamer in the interelectrode space requires additional mechanisms for production of secondary electrons in gas volume which, being accelerated in the strong field at the streamer head, produce secondary avalanches contributing to the total charge in the discharge channel and providing conditions for its growth and propagation. It is commonly accepted today that the secondary seeding electrons in air discharges can appear due to ionization of oxygen by photons emitted at quenching of highly excited non-resonant states of nitrogen molecules [41]. At direct photoionization, the energies of the photons exceed ionization potential of  $O_2$  (12.2 eV) and the wavelengths of the ionizing radiation are in the range 98–102.5 nm. The upper limit corresponds to the wavelength at which intensive absorption of photon by nitrogen takes place. According to Reference 41, the rate of production of secondary electrons at point  $x$  due to radiation source located at  $x'$  in the discharge volume can be expressed as

$$R_{ph} = \frac{p_q}{p + p_q} \frac{\xi\omega}{\alpha} \int \frac{R_{imp}(x')f(r)}{4\pi r^2} d^3x' \quad (4.9)$$

Here,  $p_q = 30$  Torr is the quenching pressure;  $R_{imp}(x')$  is the intensity of the electron impact ionization at the position of the source;  $r = |x - x'|$  and the ration  $(\xi\omega/\alpha) = 0.08$  at  $E/p = 100$  V/(cm·Torr). The absorption function of the radiation is given as

$$f(r) = \frac{\exp(-\chi_{min}p_{O_2}r) - \exp(-\chi_{max}p_{O_2}r)}{r\log(\chi_{max}/\chi_{min})} \quad (4.10)$$

where  $\chi_{max} = 2$  (cm · Torr) $^{-1}$  and  $\chi_{min} = 3.5 \cdot 10^{-2}$  (cm · Torr) $^{-1}$  are the maximum and minimum absorption cross-sections of  $O_2$  molecule in the interval of wavelengths mentioned above, and  $p_{O_2}$  is the partial pressure of oxygen in air.

The rate of the process (4.9) is to be incorporated in the expressions (4.4) for the total rates of generation and losses of charged species. However, direct use of (4.9) in numerical simulations is extremely costly. By its nature, photoionization is a non-local source of charge carriers in discharge plasma, meaning that production of ionizing agents (photons) and ionic pairs take place at different locations in space. Thus, the intensity of photoionization in each node of the computational mesh is to be calculated by summing up contributions from all other nodes. This leads to a necessity to create a full matrix containing  $R_{ph}$  values, which should be stored in computer memory (RAM) during solution process and should be updated on each time step. This situation can be avoided by considering the fact that the rate of photoionization in (4.9) is dependent on the intensity of electron impact ionization (physically, it is related to a large number of excited molecules in the regions with strong fields). Hence, the integration (4.9) can be performed only within regions where the ionization rate  $R_{imp}$  is high, e.g. at the streamer head. Moreover, the core of the integral can be approximated in some way and efficient techniques for numerical calculations can be successfully applied as it is proposed in, e.g. Reference 42. Recently, significant progress in computing photoionization in gas discharge-related problems was achieved by applying radiation transfer theory [43–46].

Simulations of propagating streamer requires an extremely fine computational mesh to accurately resolve charged layers in the vicinity of electrodes and in regions with steep gradients of the densities of charge carriers. This can be achieved by implementing static or dynamic meshes. The former may lead to unnecessary increase in the size of the problem and even make it unsolvable if large interelectrode distances and higher spatial dimensions (2D or 3D) are to be considered. A dynamic mesh is the most suitable option and it should be implemented in a way allowing for an adaptive mesh refinement (AMR) in the regions of strong variations of the carrier's densities. However, implementation of AMR for the streamer problem is not trivial and requires special consideration, particularly in case of positive (cathode-directed) discharges where the velocity of the ionization wave (streamer front) and the drift velocity of secondary electrons have opposite directions. Examples of 3D simulations performed with finite-differences (FD) and finite-elements (FE) methods using AMR can be found in References 47 and 48.

Another computational challenge is related to the numerical algorithm for solving drift-diffusion equations (4.3), which should be very accurate and provide monotonic positive solutions for concentration profiles free of unphysical features like oscillations, ripples and numerical diffusion. Conventional high-order algorithms (second order and above) being applied to (4.3) introduce dispersive ripples in the solution, particularly at locations of steep gradients. At the same time, low-order schemes, such as donor cell, Lax-Friedrichs, etc. or high-order schemes with zero-order diffusion added, produce no ripples, but suffer from excessive numerical diffusion. Since a discharge plasma channel propagating in a neutral gas can be considered as a kind of shock wave (ionization wave is the term commonly used in the literature), it is natural that the best alternative would be to use one of the high-order methods especially designed for shock capturing, such as Godunov's method, explicit two-step MacCormack's method and Van Leer's approach. Discussions on

numerical schemes and techniques used in gas discharge problems can be found in References 49–52. Among these methods, a finite-difference version of the so-called flux-corrected transport (FCT) [53–54] has been extensively studied, tested and applied for simulations of streamers; see, e.g. References 55 and 56. A finite-element implementation of FCT was developed as well [12, 57, 58], but has not become popular and it is still a subject of research.

The FCT belongs to the class of non-linear flux limiter methods. It is essential to note that FCT is not a numerical scheme, but it is rather a technique consisting of several stages. FCT constructs the net transportive flux  $\Gamma$  (the product of particle concentrations and their drift velocity  $\Gamma = nw$ ) point by point on a computational mesh as a weighted average of a flux computed by a low-order scheme and a flux computed by a high-order scheme. The weighting is dependent upon the local density profile (non-linearity) and it is done in a manner that ensures that the high-order flux is used to the greatest extent possible without introducing overshoots and undershoots in the solution. This weighting procedure is referred to as a ‘flux-correction’ or ‘flux-limiting’. The result is a family of transport algorithms capable of resolving moving contact discontinuities over 3–4 grid points, and shock fronts over 2 grid points, without overshoots or undershoots [54]. Formally, application of the FD-FCT procedure to a 1D continuity equation of type (4.3) includes the following actions [53] (fully multi-dimensional FCT approach has been developed in Reference 59):

1. Compute low-order fluxes  $\Gamma_{i-1/2}^L$  and  $\Gamma_{i+1/2}^L$  given by some low-order scheme to guarantee monotonic (ripple-free) results.
2. Compute high-order fluxes  $\Gamma_{i-1/2}^H$  and  $\Gamma_{i+1/2}^H$  with some high-order scheme.
3. Define the ‘antidiffusive’ fluxes as  $A_{i+1/2} \equiv \Gamma_{i+1/2}^H - \Gamma_{i+1/2}^L, A_{i-1/2} \equiv \Gamma_{i-1/2}^H - \Gamma_{i-1/2}^L$ .
4. Compute updated low-order (‘transported and diffused’) solution  $n_i^{td} = n_i^m - (\Gamma_{i+1/2}^L - \Gamma_{i-1/2}^L)/(\Delta t/\Delta x_i)$ .
5. Limit  $A_{i+1/2}$  in a manner such that  $n^{m+1}$  as computed in step 6 is free of extrema other than those found in  $n^{td}$  or  $n^m$ :  $A_{i+1/2}^C = C_{i+1/2} A_{i+1/2}, 0 \leq C_{i+1/2} \leq 1$ .
6. Apply the limited antidiffusive fluxes to obtain the convected density  $n_i^{m+1} = n_i^{td} - (A_{i+1/2}^C - A_{i-1/2}^C)(\Delta t/\Delta x_i)$ .

Here, index  $i$  stands for the current position on the computational grid, and  $i \pm 1/2$  indicates the positions of the interfaces of the neighbouring grid cells; indexes  $m$  and  $m + 1$  are used for the current and the following time instants, respectively;  $\Delta x_i$  is the current spatial step on the grid;  $\Delta t$  is the time step;  $C$  is the weighting function. One can observe that if  $A_{i+1/2}^C = A_{i+1/2}$ , i.e. in the absence of the flux limiter, the solution  $n^{m+1}$  will simply be the time-advanced high-order solution. Flux correction (step 5) is the critical stage in the FCT procedure. In the original algorithm [53], it is proposed to be implemented as

$$A_{i+1/2}^C = S \cdot \max \{0, \min [|A_{i+1/2}|, S(n_{i+2}^{td} - n_{i+1}^{td})\Delta x_{i+1}, S(n_i^{td} - n_{i-1}^{td})\Delta x_i]\} \quad (4.11)$$

Here,  $S = \text{sign}(A_{i+1/2})$ . To see what this flux-correction formula does, observe that if  $(n_{i+1}^{td} - n_i^{td}) > 0$ , then

$$A_{i+1/2}^C = \min[|A_{i+1/2}|, (n_{i+2}^{td} - n_{i+1}^{td})\Delta x_{i+1}, (n_i^{td} - n_{i-1}^{td})\Delta x_i], \text{ or } A_{i+1/2}^C = 0 \quad (4.12)$$

whichever is larger. The ‘raw’ antidiiffusive flux  $A_{i+1/2}$  always tends to decrease  $n_i^m$  and to increase  $n_{i+1}^m$ . Thus, the flux-limiting formula ensures that the corrected flux cannot push  $n_i^m$  below  $n_{i-1}^m$ , which would produce a new minimum, or push  $n_{i+1}^m$  above  $n_{i+2}^m$ , which would produce a new maximum. The equation above is constructed to take care of all cases for signs and slopes.

The FD-FCT technique for integrating continuity equations outlined above has been implemented in a library of FORTRAN routines [60], which can treat 1D Cartesian, cylindrical, spherical, or generalized coordinates on uniform or non-uniform Eulerian or Lagrangian grids. The procedure can be extended to higher spatial dimensions using time step splitting method.

As it has been demonstrated in the examples of simulations of corona discharges, the continuity equations (4.3) are to be solved in conjunction with Poisson’s equation (4.5) to obtain electric field distribution in the domain. In case of streamers, the concentrations of charge carriers are high, especially at the streamer head, and the field in the interelectrode space is fully controlled by the generated space charge. The distribution of the field reflects structure and dynamic variations of the space charge density and, therefore, it should be updated for each time step consequently with the system (4.3). The experience of simulations shows that solving Poisson’s equation takes approximately 70–80% of the total computational time [16] and, thus, high efficiency is one of the criteria when choosing a method for solving (4.5). Another requirement follows from the fact that even for the simplest so-called ‘1.5D model’ [61], when the radius of a cylindrical discharge channel is assumed to be constant and the transport equations are solved in 1D, the equation for potential distribution should be solved in two or, preferably, in three dimensions because the actual object has a 3D structure. Hence, taking into account fine computational mesh needed to resolve gradients at the plasma front, the problem becomes extremely computationally expensive and it is highly desired to decrease the amount of the consumed computer memory. To reduce the computational cost, some further simplifications can be considered, e.g. utilizing symmetry whenever possible. By doing so, one may reduce, e.g. symmetric physical 3D domain to a rotationally symmetric 2D rectangular computational domain formed by the surfaces of the electrodes, the symmetry axis of the gap and an open external boundary. Such problem is to be solved in cylindrical coordinates and the initial conditions are normally chosen in a way that the plasma channel develops along the symmetry axis, i.e. seed electrons are placed on the axis; the boundary conditions for Poisson’s equation (4.5) are defined as Dirichlet type on the electrodes’ surfaces and as Neumann type on other boundaries. Such approach is commonly used in practice and drastically reduces demands for computational resources. However, it

is applicable for modelling a single streamer only and such phenomenon like streamer branching cannot be treated accurately.

Methods for solving Poisson's equation have been elaborated for decades, which resulted in a large number of software packages available today [62,63] in which different numerical methods and schemes have been implemented. Several of them have been adapted, tested and used for discharge simulations. For example, the package ITPACK 2C [64] offers codes for solving linear systems of equations arising from discretization of partial differential equations utilizing seven different iterative methods (details can be found in Reference 65). Among those, the RSSI solver has been found to have the best performance for the problem in hands (Figure 4.20). Note that benchmarking similar to that in the figure is highly desirable when choosing a code which is best suited for particular purposes.

In majority of cases, formation and propagation of streamers are required to be analysed in systems where at least one of the electrodes forms a region with a strong electrostatic field, e.g. rod-plane, wire-plane, needle-plane, etc. and a proper computational mesh in a representative domain is to be generated. For numerical simulations utilizing the finite-difference approach, structured rectangular grids are normally used. The necessary refinements discussed above can be easily implemented for arbitrary rectangular domains; however, special approaches

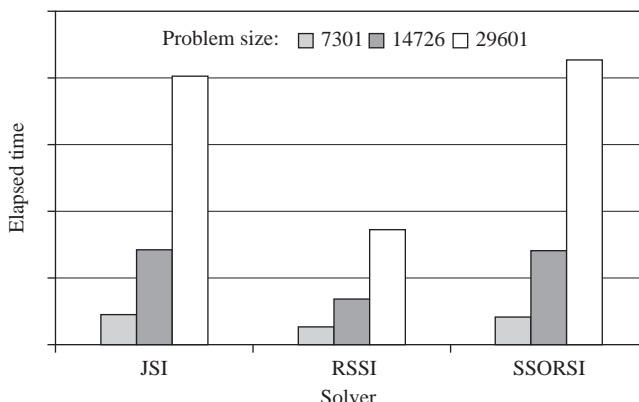


*Figure 4.20 Performance of three most efficient ITPACK 2C solvers: JS (Jacobi semi-iteration), RSSI (reduced system semi-iteration), SSORSI (symmetric successive over-relaxation semi-iteration). For benchmarking, (4.5) was discretized on a 2D uniform structured FD mesh that yielded a sparse block diagonal matrix, which was stored in Compressed Sparse Row format. The problem sizes: 150 × 50 nodes (7301 unknowns), 200 × 75 (14,726 unknowns), 300 × 100 (29,601 unknowns). The codes were compiled with Intel Fortran compiler and run on a desktop computer*

are required for meshing geometrically non-uniform computational regions. One of the methods is to introduce a set of so-called equivalent charges (maybe, e.g. point or line charges) in a uniform domain, which disturb the electric potential in a way reflecting its actual distribution [2, 66]. However, specifying magnitudes and locations of the equivalent charges may become very tricky in some situations, especially when the shape of the physical electrode is to be introduced very precisely. To resolve this, a method for solving Poisson's equation using domain transformation technique can be utilized. The idea of the method is (i) to transform the physical domain to a rectangular computational domain, (ii) to find the potential distribution in the rectangular region and (iii) to obtain the solution in the physical domain by back transformation. This approach is widely used in fluid mechanics for computing parameters of boundary layers, flows through nozzles, etc. [67]. As an example, consider the original equation (4.5) in 2D cylindrical coordinates  $(r, z)$

$$\frac{\partial^2 \varphi}{\partial z^2} + \frac{\partial^2 \varphi}{\partial r^2} + \frac{1}{r} \frac{\partial \varphi}{\partial r} = -R(r, z) \quad (4.13)$$

Here, for simplicity  $\epsilon = 1$ , and  $R$  stands for the space charge density divided with  $\epsilon_0$ . Following the steps described above, the physical domain containing a curved boundary (Figure 4.21) can be mapped into a rectangle  $0 \leq \theta \leq 1$ ,  $0 \leq \xi \leq 1$  using relations  $\theta = r/S_r$  and  $\xi = z/f(r)$ , where  $\theta$  and  $\xi$  are the axial and radial coordinates in the computational domain, and  $f(r) = z_{max} = S_z + F(r)$  is the geometry factor. The function  $F(r)$  determines the shape of the boundary and it is given in Table 4.1 for a variety of cases. After transformation, (4.13) in the new rectangular domain  $(\theta, \xi)$  becomes:

$$C_{zz} \frac{\partial^2 \varphi}{\partial \xi^2} + C_{zr} \frac{\partial^2 \varphi}{\partial \xi \cdot \partial \theta} + C_{rr} \frac{\partial^2 \varphi}{\partial \theta^2} + C_z \frac{\partial \varphi}{\partial \xi} + C_r \frac{\partial \varphi}{\partial \theta} = -R(\theta, \xi) \quad (4.14)$$

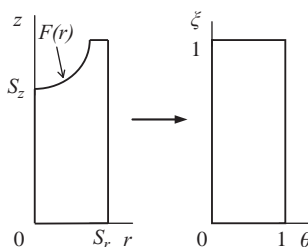


*Figure 4.21 Transformation of physical non-uniform  $(r,z)$  region to uniform computational  $(\theta,\xi)$  domain. Symbols  $S_z$  and  $S_r$  stand for the axial and radial dimensions of the physical domain, respectively*

Table 4.1 Definitions of the geometry function  $F(r)$ 

Electrode system	$F(r)$	Comments
Sphere-plane	$a - \sqrt{a^2 - r^2}$	$a$ is the radius of the sphere
Ellipse-plane	$a \cdot (1 - \sqrt{1 - r^2/b^2})$	$a, b$ are semi-axes of the ellipse
Paraboloid-plane	$a \cdot r^2/b^2$	$a$ is a height of the parabola $a = z(S_r) - S_z; b = S_r$
Hyperboloid-plane	$S_z \cdot (\sqrt{1 + r^2/b^2} - 1)$	$b$ is the imaginary semi-axis of the hyperbola
Protrusion of elliptic shape on plate-plane	$a \cdot (1 - \sqrt{1 - r^2/b^2}), r \leq b,$ $a, r > b$	$a, b$ are the semi-axes of the ellipse (height and radius of base of the protrusion, respectively)
Protrusion of parabolic shape on plate-plane	$a \cdot r^2/b^2, z < a + S_z,$ $a, z \geq a + S_z$	$a$ is the height of the protrusion; $b$ is the radius of base of the protrusion
Protrusion of hyperbolic shape on plate-plane	$S_z \cdot (\sqrt{1 + r^2/b^2} - 1),$ $z < a + S_z,$ $a, z \geq a + S_z,$	$a$ is the height of the protrusion; $b$ is the imaginary semi-axis of the hyperbola

The coefficients in (4.14) are

$$\begin{aligned} C_{zz} &= \xi \cdot G^2 + 1/f(r)^2; & C_{zr} &= -2\xi \cdot G/S_r; \\ C_{rr} &= 1/S_r; & C_z &= \xi \cdot (G^2 - Q - G/\theta); & C_r &= 1/\theta S_r \end{aligned} \quad (4.15)$$

The parameters  $G = d(\log(f(r)))/dr$  and  $Q = d^2(\log(f(r)))/dr^2$  are determined by the geometrical factor  $f(r)$ . After solving (4.14) in the rectangular domain, the components of electric field in the physical domain can be found as

$$E_z = -\frac{\partial \varphi}{\partial z} = -\frac{1}{f} \frac{\partial \varphi}{\partial \xi} \quad \text{and} \quad E_r = -\frac{\partial \varphi}{\partial r} = \xi G \frac{\partial \varphi}{\partial \xi} - \frac{1}{S_r} \frac{\partial \varphi}{\partial \theta} \quad (4.16)$$

In general, obtaining the potential distribution from (4.14) seems to be more complicated than by solving the original equation (4.13), mostly due to the second term containing cross-derivatives. However, the problems are, in general, of similar complexity and (4.14) can be solved effectively with an appropriate software package, e.g. MUDPACK [68]. This software is a collection of FORTRAN codes for automatic discretization and computing second- and fourth-order finite-difference approximations to the elliptic PDEs using multi-grid method (MG), which is a fast iterative method based on the multi-level or multi-scale paradigm [69]. It can be applied in combination with any of the common discretization techniques and it does not depend on the separability or other special properties of the equation. Extensive information about MG and available software can be found in Reference 70.

Typical flow chart for solving the coupled system of equations (4.3)–(4.5) with the presented FD techniques is shown in Figure 4.22. The input parameters for

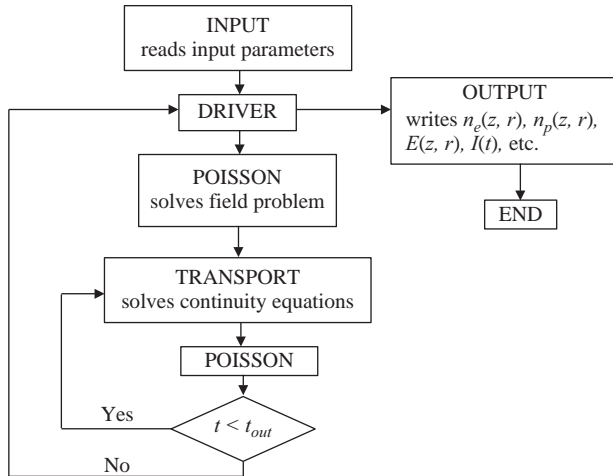


Figure 4.22 Flow chart of the algorithm for solving the coupled equations (4.3)–(4.5)

initializing calculations are the dimensions of the physical domain, gas pressure, potentials of the electrodes, number of nodes in the computational grid, desired output times and the initial distribution of space charges (if any). The routine **DRIVER** calculates data needed for the main solvers and calls subroutine **POISSON**, which solves the Poisson's equation (4.5). The output from it is the distribution of the electric field in the discharge gap (after the first call it gives the electrostatic field distribution if no space charge was set initially). Then the routine **TRANSPORT** is called for solving system 4.3–4.4. This routine calculates the time step limited by Courant–Friedrichs–Lewy condition, advances the profiles of the densities of charged particles taking into account the source terms and computes the space charge density profiles using the electric field distribution obtained earlier. Then, the current time is updated and the routine **POISSON** is called again to calculate the electric field corresponding to the new space charge distribution. If the current time is not greater than the desired output time, the loop **TRANSPORT**–**POISSON** is repeated until the condition is fulfilled. The output includes microscopic (the particle densities, electric field and potential distributions, etc.) and macroscopic (the electric current, electrostatic energy, Joule dissipation, etc.) discharge characteristics. Note that the algorithm is different from the one used for the simulations of corona discharges earlier in this chapter, where the discretized PDEs are solved simultaneously. In general, both approaches are valid as far as the correct sequence of calculations is utilized in the latter one.

#### 4.5.1 Study case: positive streamer in a weak homogeneous background field

Development of positive (cathode directed) streamers in air is a subject of great practical interest and has been studied extensively. In majority of real cases, electric fields distributed non-uniformly are being enhanced at surfaces of electrodes

with small radii of curvature and diminishing to very low magnitudes at some distances from them. Under such field conditions, two main stages in the discharge development can be recognized. The first one – streamer inception – is localized in a region of enhanced field in the vicinity of an electrode stressed with a positive electric potential and it is essentially the avalanche-to-streamer transition discussed above. After the formation stage is completed, a streamer is able to propagate in a region where the field may be considerably lower than the critical one  $\sim 30$  kV/cm. It has been determined experimentally [71, 72] that the so-called stability field, i.e. the background field needed to sustain a steady propagation of the discharge with constant velocity, is  $E_b = 4.3\text{--}5$  kV/cm for positive streamers under normal conditions in air. To understand mechanisms and internal discharge processes during its propagation in a weak field, numerical simulations have been utilized extensively owing to the well-known difficulties of experimental investigations of streamers (required high temporal and spatial resolution, low light emission from discharge plasma, etc.) [61]. Results of a numerical study of cathode-directed streamers in air under conditions of the experiments [72, 73] are presented below.

The propagation of streamers was considered between two parallel-plate metallic electrodes forming a gap  $S_z = 3.3$  cm with a uniform electric field  $E_b$ . One of the electrodes (anode) contained a needle protrusion of a hyperbolic shape providing local field enhancement. A streamer was formed at the needle tip, where according to electrostatic calculations the field strength reached  $\sim 200$  kV/cm, and it propagated further into the gap in a constant field  $E_b$  that was attained on the distance of  $\sim 0.4$  cm from the anode. Thus, the streamer passed  $\sim 3$  cm in the uniform weak field  $E_b$  the magnitude of which was varied in the simulations in order to observe its effect on streamer dynamics. The problem domain was similar to that shown in Figure 4.21 (left) which was transformed into a rectangular domain (Figure 4.21, right) utilizing the technique discussed above. The model used was a quasi two-dimensional one (1.5D) with the fixed radius of the discharge channel  $R_c = 200$   $\mu\text{m}$  and, hence, uniform distributions of charge carriers' densities within its cross-section were assumed. The value of  $R_c$  used can be found as an average magnitude obtained by fully two-dimensional simulations for weak fields, e.g. Reference 74, and it is in agreement with experimental observations (a discussion regarding streamer radius can be found in Reference 61). The field dependencies of the rate coefficients in (4.3) and (4.4) were taken from Reference 16 and the rate of photoionization was computed by applying (4.9) and (4.10) on the symmetry axis of the gap along which the discharge propagation takes place. The ionic diffusion was neglected due to its insignificance in the time scale of streamer development. The boundary conditions for the set of PDEs (4.3) included zero densities of positive ions on the anode and negative ions on the cathode  $n_p(S_z,t) = n_n(0,t) = 0$ ; the densities of electrons were set to zero on surfaces of both electrodes  $n_e(0,t) = n_e(S_z,t) = 0$ . Symmetry (Neumann) conditions were applied for all charge carriers on the other boundaries. For (4.5), the potentials  $\phi_c$  and  $\phi_a$  were specified on the cathode and anode, respectively, and symmetry condition was used on the boundary representing physical symmetry axis. On the outer boundary of the computational domain, the linear potential distribution was set. The magnitudes of  $\phi_c$  and  $\phi_a$  and the distribution on

the outer boundary were adjusted in a way to provide the distribution of the electrostatic field in the domain close to that appeared in the experiments [73]. The latter was justified by comparing the fields obtained by the presented method with the results of calculations performed using commercial finite-element software.

Solution of the set of equations (4.3) requires initial conditions for the densities of charge carriers. One of the approaches utilized in streamer simulations is based on the assumption that a quasi-neutral layer or ‘plasma spot’ with relatively high charge density exists in the high field region. This method allows avoiding modelling the avalanche stage, and streamer inception can be achieved during several time steps at the beginning of the simulations. However, it appears to be artificial because the location of initial charges and their densities are set arbitrarily. A more physical approach is presented in Reference 75 and it employs the fact that collisional detachment of electrons from negative ions is effective in air at atmospheric conditions. The rate of the process is  $R_0 = \nu_{det} n_{n0}$ , where  $\nu_{det}$  is the detachment frequency and  $n_{n0} \sim 10^3 \text{ cm}^{-3}$  is the equilibrium background concentration of negative ions. The magnitude of  $\nu_{det}$  is determined as  $\nu_{det} = k \nu_{el} \exp(-W_a/W_{ch})$ , where  $\nu_{el}$  is the frequency of elastic collisions,  $W_a$  electron affinity,  $W_{ch}$  the chaotic energy of negative ions, and  $k = 0.1$  is the similarity coefficient. Assuming negative ions of type  $O_3^-$  [75], the following magnitudes of the parameters can be used for evaluations:  $W_{ch} = M \cdot (\mu_{n0} \cdot E)^2 / 2$ , where the mobility  $\mu_{n0} = 2.55 \text{ cm}^2 \cdot \text{V}^{-1} \cdot \text{s}^{-1}$  and the mass of the ion  $M = 5.3 \times 10^{-23}$ ;  $W_a = 2.05 \text{ eV}$ ;  $\nu_{el} = 0.79 \times 10^{10} \text{ s}^{-1}$ . The rate  $R_0$  appeared to be field dependent and, e.g. for the field strength at the tip of the needle  $E = 200 \text{ kV/cm}$ , it is  $R_0 \sim 5 \text{ } 10^{11} \text{ cm}^{-3} \text{ s}^{-1}$  that is considerably lower than the magnitudes of other terms in  $R_e$  (4.4) and its influence during streamer development is negligible. However, the term  $R_0$  is important during streamer initiation stage for providing increased concentrations of seed electrons in the regions with enhanced fields and facilitating streamer inception.

The problem was solved on a uniform structured computational mesh  $16 \mu\text{m} \times 20 \mu\text{m}$  using the FCT technique for equations (4.3) – (4.4) implemented in Reference 60 and multi-grid solver [68] for (4.14). The time step  $\Delta t$  was limited by the Courant criterion  $c = \Delta t |w_e| / \Delta z = 0.3$  (here,  $\Delta z = 16 \mu\text{m}$  is the space resolution).

The results of the simulations can be seen in Figure 4.23, where time variations of the electron density profiles along the axis of the discharge at different magnitudes of the background field are presented. As one can observe, streamer inception takes less than one nanosecond after voltage application. The density of electrons increases during the formation stage up to  $\sim 10^{14} \text{ cm}^{-3}$  (see curves for  $t = 1 \text{ ns}$ ) due to strong field at the needle tip. During propagation stage, the streamer enters the region with the weak uniform field in the bulk of the gap, where conditions for its development are dependent upon the magnitude of  $E_b$ . Thus, if the background field is low, the losses of electrons exceed their production and the discharge can be terminated as it is seen in the plots for 3 and  $3.7 \text{ kV/cm}$ . The electron densities at the discharge front remain practically constant if propagation takes place in stronger background fields of  $4.3 \text{ kV/cm}$  and  $5 \text{ kV/cm}$ , indicating that the losses are compensated by the production of electrons at the streamer head. In the streamer

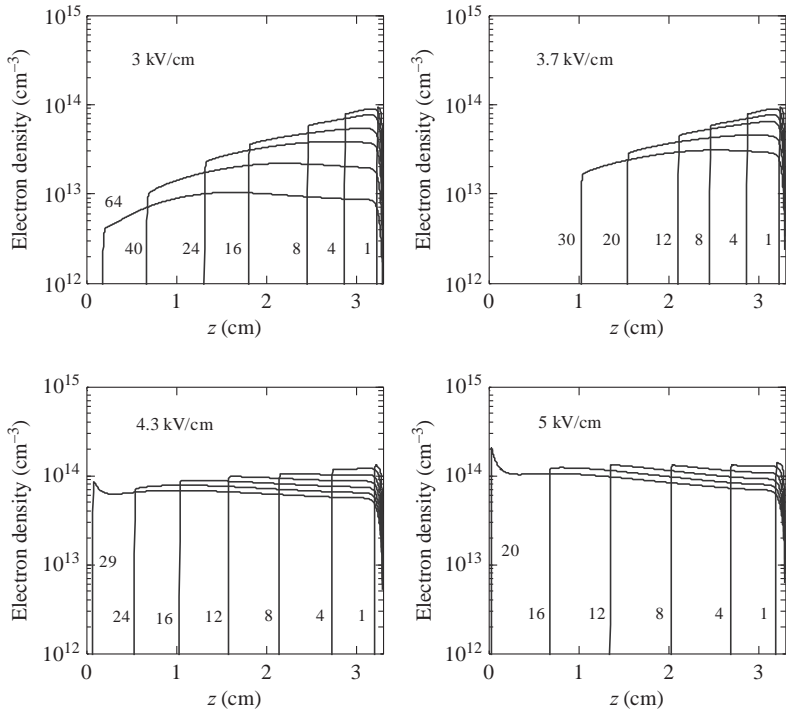
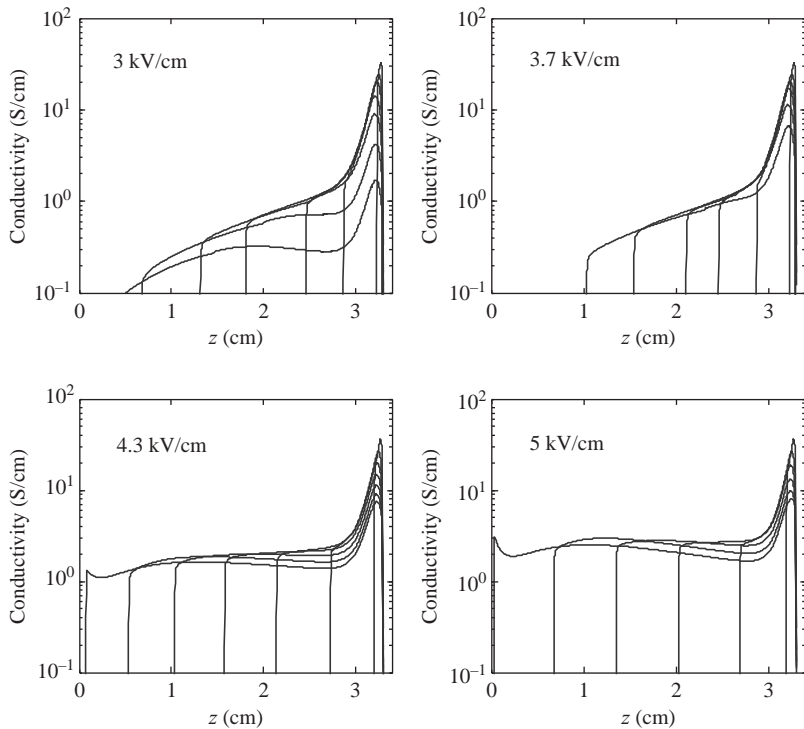


Figure 4.23 Time variations of the electron density at different magnitudes of  $E_b$  indicated on the plots. Time in ns is shown at the curves. The cathode is located on the left at  $z = 0$ , and the tip of the needle is found to the right at  $z = 3.3 \text{ cm}$

channel (especially in the anode region), the concentrations of electrons decrease with time continuously due to attachment and recombination. This, however, leads to just minor variations of the conductivity  $\sigma$  of the discharge plasma (Figure 4.24), which is defined as a sum of contributions of all kinds of charge carriers  $\sigma = q(n_e\mu_e + n_n\mu_n + n_p\mu_p)$ . One may notice that the conductivity of the channel remains on the level of  $\sim 0.2 \text{ S/cm}$  and  $\sim 0.3 \text{ S/cm}$  during propagation in the fields  $E_b = 4.3$  and  $5 \text{ kV/cm}$ , respectively, whereas it decreases rapidly in weaker background fields. The values of the discharge plasma conductivity obtained from the simulations agree well with known data [6, 61].

As it was mentioned above, streamers are essentially ionization waves propagating in an insulating medium. Conversion of a neutral gas into conductive plasma takes place at the streamer head, where extremely strong electric fields appear due to produced space charges as it is seen in Figure 4.25. One may observe that the field strength is low behind the discharge front due to high conductivity of plasma in the channel and also between the front and the cathode (located at  $z = 0$ ) where it is equal to  $E_b$ . Depending on the magnitude of the background field, the peaks associated with the streamer head may decrease



*Figure 4.24 Evolution of the conductivity of discharge plasma at different  $E_b$  (the magnitudes are indicated on the graphs). The instants and positions of the electrodes are similar to those in Figure 4.23*

during its propagation, as it happens at  $E_b = 3, 3.7$  and  $4.3$  kV/cm, or remain constant if the field is strong enough to support discharge development; see graph for  $E_b = 5$  kV/cm. The latter indicates a stable mode of the discharge. One should note, however, that under considered circumstances, the streamer is also able to cross the gap between electrodes even at lower magnitude of  $E_b$ , often referred as crossing field (see plot for  $4.3$  kV/cm), although this depends upon conditions on early stages of its formation in the vicinity of the needle (field strength, accumulated charge, acceleration, etc.). When the streamer front approaches the cathode region, a cathode-streamer head interaction can be observed, which is associated with an increase of the maximum of the electric field strength seen in the plots for  $E_b = 4.3$  and  $5$  kV/cm. This field enhancement leads to intensive ionization and to corresponding rise of the electron density and conductivity shown in Figures 4.23 and 4.24, respectively. It has been argued in Reference 76 that this phenomenon is conditioned by a release of electrostatic energy accumulated in a streamer channel – cathode system.

Based on the results of the simulations, the background field of  $5$  kV/cm can be considered as the streamer stability field. The length  $L_{st}$  of the streamer channel

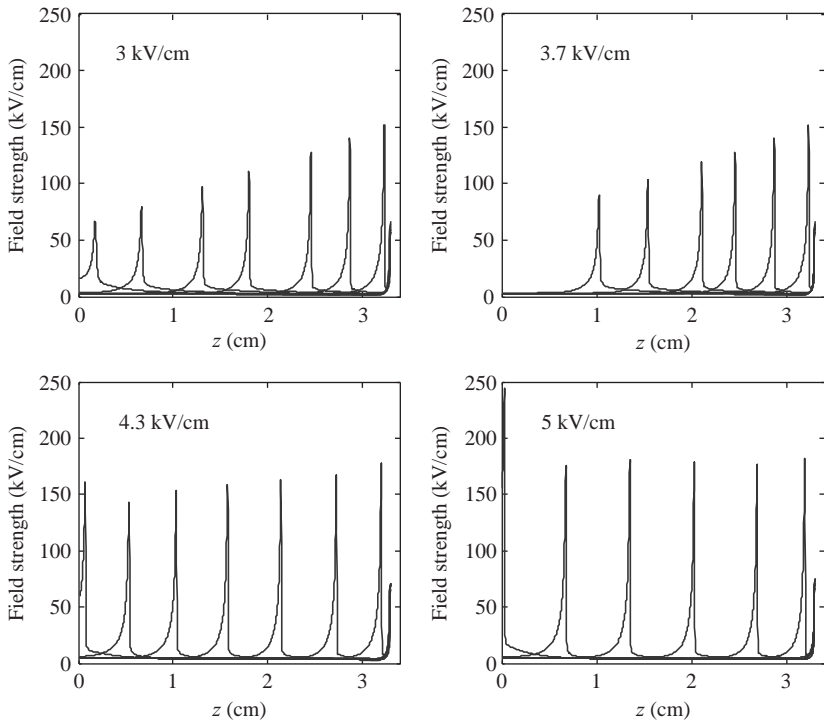


*Figure 4.25 Distributions of electric field at different magnitudes of  $E_b$  indicated on the graphs. The instants and positions of the electrodes are similar to those in Figures 4.23 and 4.24*

increases linearly with time during its stable propagation, as shown in Figure 4.26(a). The growth of the channel is slowed down in weaker background fields and the discharge becomes incapable of crossing the gap at  $E_b < 3 \text{ kV/cm}$ . The latter is defined as the minimal crossing field. This value obtained from the simulations agrees well with the magnitude of 2.9 kV/cm achieved from experimental observations [72].

As has been mentioned above, stable streamer propagation is associated with constant electric field strength at its head. Therefore, it is natural to expect that streamer velocity follows this behaviour since the intensity of photoionization and production of secondary electron avalanches needed for advancing the discharge front are governed by the electric field. Thus, constant field strength at the head  $\sim 180 \text{ kV/cm}$  (Figure 4.25) provides constant streamer velocity  $\sim 1.6 \times 10^8 \text{ cm/s}$  at  $E_b = 5 \text{ kV/cm}$ , as can be seen in Figure 4.26(b). In the background field of 4.3 kV/cm, the maximum field decreases with increased streamer length from  $\sim 170$  to  $\sim 140 \text{ kV/cm}$  that leads to the decrease in velocity from  $\sim 1.6 \times 10^8$  to  $\sim 1.1 \times 10^8 \text{ cm/s}$ . In weaker background fields, the velocity decreases with streamer length in the same linear manner as the field at its tip (see Figure 4.25). The discharge front acceleration in the cathode region (streamer length  $> 3 \text{ cm}$ ) also corresponds to

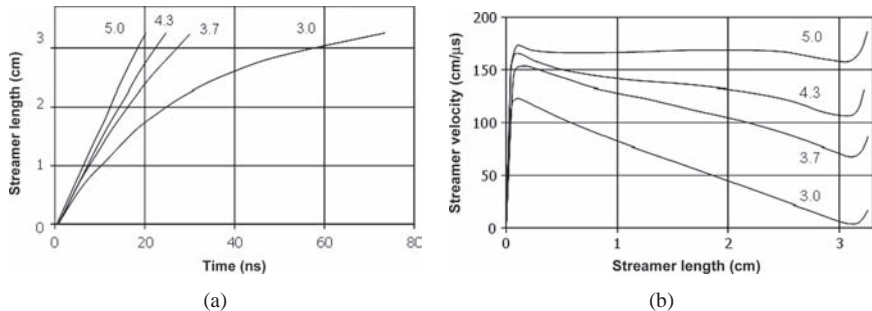


*Figure 4.26 Positive streamer length as function of propagation time (a) and streamer velocity as a function of its length (b). The magnitudes of the background field strength in kV/cm are indicated at the curves (b)*

the enhancement of the maximum field. It is necessary to note here that the magnitudes of the streamer velocities obtained in present simulations are slightly overestimated compared with the results of fully 2D simulations [74] due to neglected radial expansion of the discharge channel.

Finally, one should mention that propagation of positive streamers in weak fields is governed by the electrostatic energy  $Q$  accumulated in the system ( $Q$  is the volume integral of the energy density  $\epsilon_0 E^2/2$ ). An analysis of the computed distributions of the energy along the discharge channel showed that the stable streamer propagation is associated with a slight increase in the accumulated energy. In contrast to this, the magnitudes of  $Q$  decrease if the propagation taking place in the background fields is weaker than the stability threshold.

#### 4.5.2 Study case: negative streamer in weak homogeneous background fields

A negative (anode-directed) streamer can be initiated by stressing an electrode with a small radius of curvature with a negative potential provided that strong enough electric field exists in its vicinity. Similar to positive streamers, the negative ones may propagate for long distances in weak background fields. Data regarding stability field for negative streamers under normal conditions in air are ambiguous. One may refer to Reference 61, where the range of 8–16 kV/cm is mentioned based on available experimental data, and to the results of modelling [77], where the values of 10–15 kV/cm could be found for short streamers. However, it is obvious that the magnitude of the background field required for stable propagation of negative streamers is higher than that for the positive discharges. The reason is that secondary electrons produced by photoionization at negative streamer head experience an electrostatic force pushing them away from the plasma front towards the region with lower field strength. This process can be considered as an additional mechanism of electronic losses and it leads to a reduction of the intensity of secondary avalanches that should be compensated by an increase in the background field to maintain conditions (in particular, conductivity of the discharge channel) required for stable propagation.

The results of the simulations presented below were obtained for conditions similar to those used for the modelling of positive discharges described in Section 4.4. The flat electrode containing the protrusion was energized with a negative potential that resulted in an inception of a negative streamer at the needle tip. A parametric study was performed in order to determine the minimal field strength in the gap between the plate electrodes needed for stable streamer development.

The computed temporal variations of the electron density distributions along the streamer channel progressing in different background fields are shown in Figure 4.27. As it can be seen, streamer inception takes place in the high field region at the cathode ( $z > 3$  cm), where the electron densities rise quickly and reach  $\sim 10^{14} \text{ cm}^{-3}$  within 1 ns, similar to the case of positive discharges (Figure 4.23). Different behaviour can be observed when plasma front enters the bulk of the gap where the background field is weak. In case of negative streamers, the minimal crossing field is found to be  $\sim 7 \text{ kV/cm}$  and discharge propagation in this field is associated with the decrease of the electron density. If the magnitudes of  $E_b$  are lower than that, a streamer is terminated rapidly in the middle of the gap as

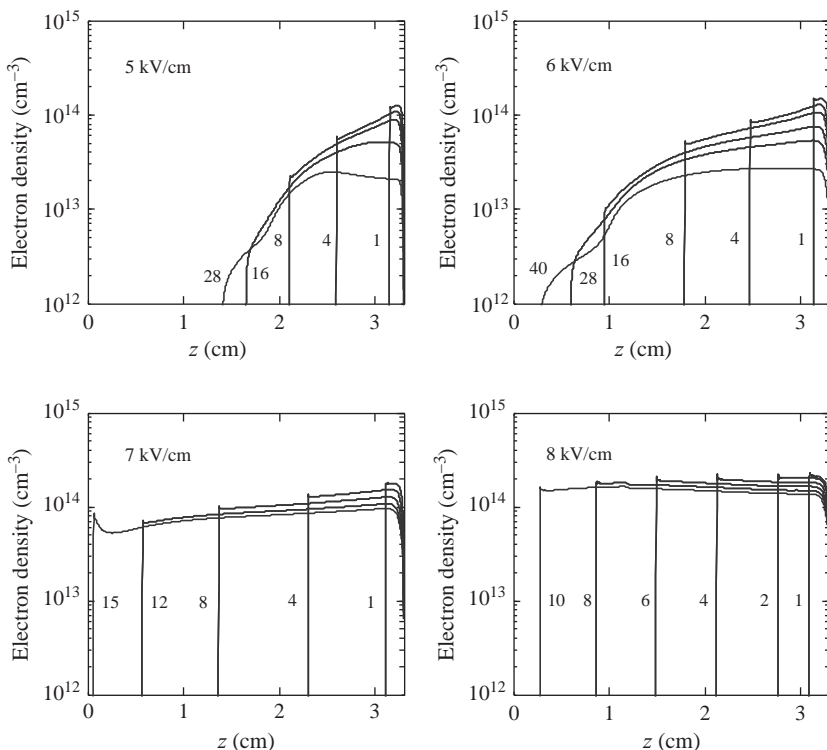
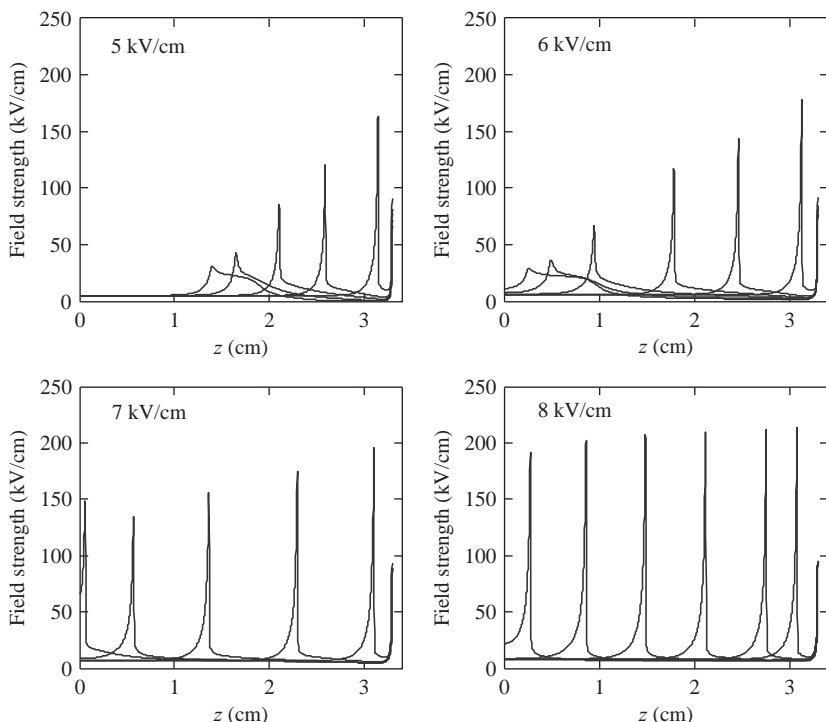


Figure 4.27 Time variations of the electron density at different magnitudes of  $E_b$  indicated on the plots. Time in ns is shown at the curves. The anode is located on the left at  $z = 0$ , and the tip of the needle is found to the right at  $z = 3.3 \text{ cm}$

observed for the strength of 5 and 6 kV/cm in which the discharge propagates for ~1.9 and 2.9 cm, respectively. The concentration of electrons is kept constant if the background field strength is raised to 8 kV/cm. In this case, losses of electrons in discharge plasma are compensated by the higher rate of their production, which is dependent on the local electric field strength at the streamer front. One can see in Figure 4.28 that the field strength at the head decreases rapidly when streamer termination takes place (graphs for 5 and 6 kV/cm) because the space charge produced is not strong enough. The situation is different when the discharge propagates in the background field  $E_b = 8$  kV/cm. In this case, the electric field associated with the streamer head reaches ~200 kV/cm and remains almost constant during propagation. Similar behaviour was obtained for positive streamers, where the peak field strength was found to be ~170 kV/cm (see Figure 4.25). The difference between these values is related to the different conditions needed to maintain intensive production of secondary avalanches at the head of the negative streamer as mentioned above. Note that the ionization coefficient  $\alpha$  depends exponentially on the field strength and, thus, even small increase of  $E$  results in a significant amount of generated secondary electrons.



*Figure 4.28 Distributions of the electric field at different magnitudes of  $E_b$  indicated on the graphs. The instants and positions of the electrodes are similar to those in Figure 4.27*

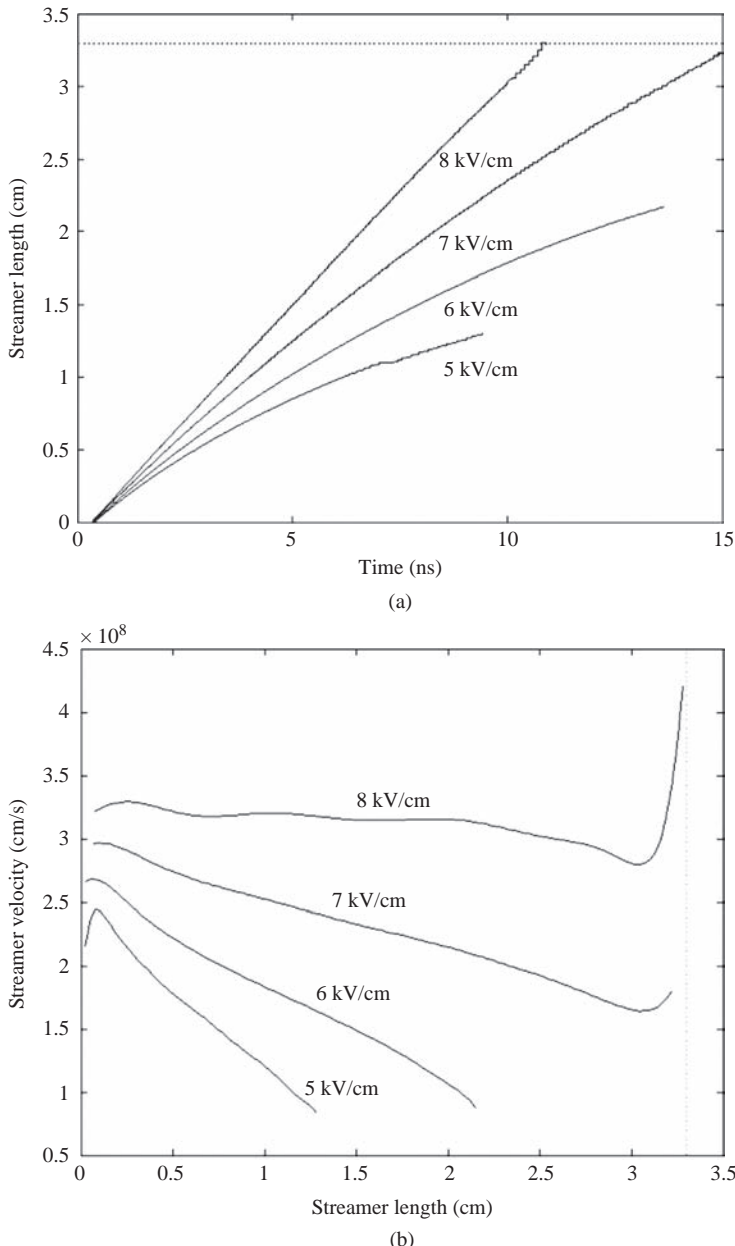


Figure 4.29 Negative streamer length as function of propagation time (a) and streamer velocity as a function of its length (b). The magnitudes of the background field strength in kV/cm are indicated at the curves (b)

The length of the channel of the negative discharge increases linearly with time during its stable propagation (Figure 4.29(a), curve for 8 kV/cm), similar to the case of the positive streamer (Figure 4.26(a), curve for 5 kV/cm). However, in contrast to the latter, the gap between the stability field and the minimal crossing field for negative streamers is smaller and negative discharges seem to be more sensitive to changes in the magnitudes of the background field strength than the positive ones. The data presented in Figures 4.27–4.29 indicate that just a minor reduction of  $E_b$  below 7 kV/cm may lead to rapid streamer termination. Another distinction of negative streamers obtained from the simulations is that the velocity corresponding to stable propagation  $\sim 3.2 \times 10^8$  cm/s (Figure 4.29(b), 8 kV/cm) is two times higher than that for the positive ones (compare with Figure 4.26(b), 5 kV/cm) due to the stronger field at the streamer front. Other features observed in Figure 4.29(b), like acceleration at the very late stage when the streamer head approaches the anode surface, and the linear decrease of the velocity with increasing length of the channel in the background fields lower than the stability level, are similar to those discussed earlier in this chapter for positive discharges.

## References

1. I. Gallimberti, G. Bacchigia, A. Bondiou-Clergerie and P. Lalande, Fundamental processes in long air gap discharges, *C. R. Physique*, vol. 3, pp. 1335–1359, 2002
2. E. Kuffel, W. S. Zaengl and J. Kuffel, *High Voltage Engineering: Fundamentals*, 2nd ed., Newnes, Oxford, UK, 2000
3. S. Panchesnyi, Role of electronegative gas admixtures in streamer start, propagation and branching phenomena, *Plasma Sources Sci. Technol.*, vol. 14, pp. 645–653, 2005
4. E. Nasser, *Fundamentals of Gaseous Ionization and Plasma Electronics*, John Wiley & Sons Inc., New York, USA, 1971
5. K. L. Aplin, Instrumentation for atmospheric ion measurements, PhD thesis, University of Reading, Berkshire, UK, 2000
6. Yu. P. Raizer, *Gas Discharge Physics*, Springer Verlag, Berlin Heidelberg, Germany, 1997
7. J. Dutton, A survey of electron swarm data, *J. Phys. Chem. Ref. Data*, vol. 4, no. 3, pp. 577–856, 1975
8. J. W. Gallagher *et al.*, An annotated compilation and appraisal of electron swarm data in electronegative gases, *J. Phys. Chem. Ref. Data*, vol. 12, no. 1, pp. 109–152, 1983
9. G. G. Raju, *Gaseous Electronics: Theory and Practice*, CRC Press, Boca Raton, Florida, USA, 2006
10. I. A. Kossyi *et al.*, Kinetic scheme of the non-equilibrium discharge in nitrogen-oxygen mixtures, *Plasma Sources Sci. Technol.*, vol. 1, pp. 207–220, 1992

11. K. Becker *et al.*, Air plasma chemistry, in *Non-equilibrium Air Plasmas at Atmospheric Pressure*, K. H. Becker, U. Kogelschatz, K. H. Schoenbach and R. J. Barker (eds.), IOP Publishing, Bristol, UK, 2005
12. G. E. Georgiou, A. P. Papadakis, R. Morrow and A. C. Metaxas, Numerical modelling of atmospheric pressure gas discharges leading to plasma production, *J. Phys. D: Appl. Phys.*, vol. 38, pp. R303–R328, 2005
13. H. Raether, The electron avalanche and its development, *Appl. Sci. Res., Sec. B*, vol. 5, no. 1, pp. 23–33, 1956
14. E. E. Kunhardt, Electron macrokinetics in partially ionized gases: The hydrodynamic regime, *Phys. Rev. A*, vol. 42, no. 2, pp. 803–814, 1990
15. R. Morrow and N. Sato, The discharge current induced by the motion of charged particles in time-dependent electric fields; Sato's equation extended, *J. Phys. D: Appl. Phys.*, vol. 32, pp. L20–L22, 1999
16. R. Morrow and J. J. Lowke, Streamer propagation in air, *J. Phys. D: Appl. Phys.*, vol. 30, pp. 614–627, 1997
17. M. C. Wang and E. E. Kunhardt, Streamer dynamics, *Phys. Rev. A*, vol. 42, no. 4, pp. 2366–2373, 1990
18. N. Y. Babaeva and G. V. Naidis, On streamer dynamics in dense media, *J. Electrostatics*, vol. 53, no. 2, pp. 123–133, 2001
19. N. L. Aleksandrov, E. M. Bazelyan and V. A. Vasil'ev, The effect of low direct voltage on streamer breakdown in long non-uniform air gaps, *J. Phys. D: Appl. Phys.*, vol. 36, pp. 2089–2095, 2003
20. A. A. Kulikovsky, The mechanism of positive streamer acceleration and expansion in air in a strong external field, *J. Phys. D: Appl. Phys.*, vol. 30, pp. 1515–1522, 1997
21. R. Morrow, Theory of electrical corona in SF<sub>6</sub>, *Nucl. Instr. Meth. Phys. Res.*, vol. A382, pp. 57–65, 1996
22. R. Morrow, The theory of positive glow corona, *J. Phys. D: Appl. Phys.*, vol. 30, pp. 3099–3114, 1997
23. C. Soria, F. Pontiga and A. Castellanos, Plasma chemical and electrical modelling of a negative DC corona in pure oxygen, *Plasma Sources Sci. Technol.*, vol. 13, pp. 95–107, 2004
24. G. E. Georgiou and A. C. Metaxas, Simulation of RF coronas using the FE-FCT method, *J. Microw. Power Electromagn. Energy*, vol. 35, pp. 151–164, 2000
25. A. Salabas, G. Gousset and L. L. Alves, Two-dimensional fluid modelling of charged particle transport in radio-frequency capacitively coupled discharges, *Plasma Sources Sci. Technol.*, vol. 11, pp. 448–465, 2002
26. Yu. B. Golubovskii, V. A. Maiorov, J. Behnke and J. F. Behnke, Modeling of the homogeneous barrier discharge in helium at atmospheric pressure, *J. Phys. D: Appl. Phys.*, vol. 36, pp. 39–49, 2003
27. Y. V. Yurgelenas and M. A. Leeva, Development of a barrier discharge in air in highly non-homogeneous electric field caused by the residual dielectric surface charges, *IEEE Trans. Plasma Sci.*, vol. 37, no. 6, pp. 809–815, 2009
28. J. P. Boeuf, Plasma display panels: physics, recent developments and key issues, *J. Phys. D: Appl. Phys.*, vol. 36, pp. R53–R79, 2003

29. A. Oda, Y. Sakai, H. Akashi and H. Sugawara, One-dimensional modeling of low-frequency and high-pressure Xe barrier discharges for the design of excimer lamps, *J. Phys. D: Appl. Phys.*, vol. 32, pp. 2726–2736, 1999
30. O. Eichwald, N. A. Guntoro, M. Yousfi and M. Benhenni, Chemical kinetics with electrical and gas dynamics modelization for NO<sub>x</sub> removal in an air corona discharge, *J. Phys. D: Appl. Phys.*, vol. 35, pp. 439–450, 2002
31. U. Kogelschatz, Dielectric-barrier discharges: Their history, discharge physics, and industrial applications, *Plasma Chem. Plasma Process.*, vol. 23, pp. 1–46, 2003
32. H. C. Kim, F. Iza, S. S. Yang, M. Radmilovic-Radjenovic and J. K. Lee, Particle and fluid simulations of low-temperature plasma discharges: benchmarks and kinetic effects, *J. Phys. D: Appl. Phys.*, vol. 38, pp. R283–R301, 2005
33. L. B. Loeb, *Electrical Coronas: Their Basic Physical Mechanisms*, University of California Press, Berkeley, 1965
34. N. Yu. Babaeva and J. K. Lee, Dust-grain charging in developing air plasma, *IEEE Trans. Plasma Sci.*, vol. 32, no. 2, pp. 823–828, 2004
35. J. Chen and J. H. Davidson, Model of the negative dc corona plasma: comparison to the positive dc corona plasma, *Plasma Chem. Plasma Process.*, vol. 23, no. 1, pp. 83–102, 2003
36. J. J. Lowke, Theory of electrical breakdown in air – the role of metastable oxygen molecules, *J. Phys. D: Appl. Phys.*, vol. 25, pp. 202–210, 1992
37. F. W. Peek, *Dielectric Phenomena in High-Voltage Engineering*, 3rd ed., McGraw-Hill, New York, 1929
38. R. T. Waters and W. B. Stark, Characteristics of the stabilized glow discharge in air, *J. Phys. D: Appl. Phys.*, vol. 8, pp. 416–427, 1975
39. J. Q. Feng, An analysis of corona currents between two concentric cylindrical electrodes, *J. Electrostatics*, vol. 46, pp. 37–48, 1999
40. T. E. Allibone, J. E. Jones, J. C. Saunderson, M. C. Taplamacioglu and R. T. Waters, Spatial characteristics of electric current and field in large direct-current coronas, *Proc. Royal Soc. London A*, vol. 441, pp. 125–146, 1993
41. M. B. Zheleznyak, A. K. Mnatsakanyan and S. V. Sizikh, Photo-ionization of nitrogen and oxygen mixtures by radiation from a gas discharge, *High Temp.*, vol. 20, no. 3, pp. 357–362, 1982
42. A. Luque, U. Ebert, C. Montijn and W. Hundsorfer, Photoionization in negative streamers: Fast computations and two propagation modes, *Appl. Phys. Lett.*, vol. 90, pp. 081501-1–081501-3, 2007
43. P. Segur, A. Bourdon, E. Marode, D. Bessieres and J. H. Paillol, The use of an improved Eddington approximation to facilitate the calculation of photoionization in streamer discharges, *Plasma Sources Sci. Technol.*, vol. 15, pp. 648–660, 2006
44. A. Bourdon, V. P. Pasko, N. Y. Liu, S. Celestin, P. Segur and E. Marode, Efficient models for photoionization produced by non-thermal gas discharges in air based on radiative transfer and the Helmholtz equations, *Plasma Sources Sci. Technol.*, vol. 16, pp. 656–678, 2007

45. N. Liu, S. Celestin, A. Bourdon, V. P. Pasko, P. Segur and E. Marode, Application of photoionization models based on radiative transfer and the Helmholtz equations to studies of streamers in weak electric fields, *Appl. Phys. Lett.*, vol. 91, pp. 211501-1–211501-3
46. J. Capeillere, P. Segur, A. Bourdon, S. Celestin and S. Pancheshnui, The finite volume method solution of the radiative equation for photon transport in non-thermal gas discharges: Application to the calculation of photoionization in streamer discharges, *J. Phys. D: Appl. Phys.*, vol. 41, pp. 234018–234031, 2008
47. S. Pancheshnyi, P. Segur, J. Capeillere and A. Bourdon, Numerical simulation of filamentary discharges with parallel adaptive mesh refinement, *J. Comput. Phys.*, vol. 227, pp. 6574–6590, 2008
48. L. Papageorgiou, A. C. Metaxas and G. E. Georghiou, Three-dimensional numerical modeling of gas discharges at atmospheric pressure incorporating photoionization phenomena, *J. Phys. D: Appl. Phys.*, vol. 44, pp. 045203–045213, 2011
49. P. J. Roache, *Fundamentals of Computational Fluid Dynamics*, Hermosa Publishers, Albuquerque, NM, 1998
50. K. Alhumaizi, Comparison of finite difference methods for the numerical simulation of reacting flow, *Comp. Chem. Eng.*, vol. 28, pp. 1759–1769, 2004
51. A. Bourdon, D. Bessieres, J. Paillol, A. Michau, K. Hassouni, E. Marode and P. Segur, Influence of numerical schemes on positive streamer propagation, *Proceedings of the XXVIIth International Conference on Phenomena in Ionized Gases (ICPIG)*, Eindhoven, the Netherlands, 18–22 July, 2005
52. A. Luque and U. Ebert, Density models for streamer discharges: Beyond cylindrical symmetry and homogeneous media, *J. Comput. Phys.*, 2011, doi:10.1016/j.jcp.2011.04.019
53. J. P. Boris and D. L. Book, Flux-corrected transport: I. SHASTA, a fluid transport algorithm that works, *J. Comput. Phys.*, vol. 11, pp. 38–69, 1973
54. D. Kuzmin, R. Löhner and S. Turek (eds.), *Flux-Corrected Transport: Principles, Algorithms and Applications*, Springer-Verlag, Berlin, Heidelberg, 2005
55. R. Morrow, Numerical solution of hyperbolic equations for electron drift in strongly non-uniform electric field, *J. Comput. Phys.*, vol. 43, pp. 1–15, 1981
56. P. Steinle, R. Morrow and A. J. Roberts, Use of implicit and explicit flux-corrected transport algorithms in gas discharge problems involving non-uniform velocity fields, *J. Comput. Phys.*, vol. 85, no. 2, pp. 493–499, 1989
57. G. E. Georghiou, R. Morrow and A. C. Metaxas, A two-dimensional, finite-element, flux-corrected transport algorithm for the solution of gas discharge problems, *J. Phys. D: Appl. Phys.*, vol. 33, pp. 2453–2466, 2000
58. O. Ducasse, L. Papageorgiou, O. Eichwald, N. Spyrou and M. Yousfi, Critical analysis on two-dimensional point-to-plane streamer simulations using the finite element and finite volume methods, *IEEE Trans. Plasma Sci.*, vol. 35, no. 5, pp. 1287–1300, 2007
59. S. T. Zalesak, Fully multidimensional flux-corrected transport algorithms for fluids, *J. Comput. Phys.*, vol. 31, pp. 335–362, 1979

60. J. Boris, A. Landsberg, E. Oran and J. Gardner, LCPFCT – *A Flux-corrected Transport Algorithm for Solving Generalized Continuity Equations*, Naval Research Laboratory, Report No. NRL/MR/6410-93-7192, Washington, 1993
61. E. M. Bazelyan and Yu. P. Raizer, *Spark Discharge*, CRC Press, Boca Raton, Florida, USA, 1998
62. NIST, GAMS: Guide to Available Mathematical Software, available from: <http://gams.nist.gov> [Accessed 8 Dec 2011]
63. Netlib Repository at UTK and ORNL, available from: <http://www.netlib.org> [Accessed 8 Dec 2011]
64. D. R. Kincaid, J. R. Respess, D. M. Young and R. G. Grimes, *ITPACK 2C: A FORTRAN Package for Solving Large Sparse Linear Systems by Adaptive Accelerated Iterative Methods*, Center for Numerical Analysis, University of Texas at Austin, TX, 1999
65. J. W. Demmel, *Applied Numerical Linear Algebra*, SIAM, Philadelphia, USA, 1997
66. H. Singe, H. Steinbigler and P. Weiss, A charge simulation method for the calculation of high voltage fields, *IEEE Trans. Power App. Syst.*, vol. PAS-93, no. 5, pp. 1660–1968, 1974
67. J. C. Tannehill, D. A. Anderson and R. H. Pletcher, *Computational Fluid Mechanics and Heat Transfer*, 2nd ed., Taylor & Francis, Philadelphia, USA, 1997
68. J. C. Adams, MUDPACK: Multigrid software for elliptic partial differential equations, National Center for Atmospheric Research, USA, 1998, available from: home-page: <http://www.scd.ucar.edu/css/software/mudpack> [Accessed 8 Dec 2011]
69. P. Wesseling, *An Introduction to Multigrid Methods*, John Wiley & Sons, Chichester, UK, 1992
70. MGnet Repository, available from: <http://www.mgnet.org> [Accessed 8 Dec 2011]
71. N. L. Allen and A. Ghaffar, The conditions required for the propagation of a cathode-directed positive streamer in air, *J. Phys. D: Appl. Phys.*, vol. 28, pp. 331–337, 1995
72. L. Gao, A. Larsson, V. Cooray and V. Scuka, Simulation of streamer discharges as finitely conducting channels, *IEEE Trans. Diel. Elec. Insul.*, vol. 6, no. 1, pp. 35–42, 1999
73. M. Akyuz, L. Gao, A. Larsson and V. Cooray, Streamer current in a three-electrode system, *IEEE Trans. Diel. Elec. Insul.*, vol. 8, no. 4, pp. 665–672, 2001
74. N. Yu. Babaeva and G. V. Naidis, Simulation of positive streamers in air in weak uniform electric field, *Phys. Lett. A*, vol. 215, pp. 187–190, 1996
75. A. F. Djakov, Y. K. Bobrov and Y. V. Yurgelenas, Modeling of positive streamer in air in non-uniform electric field, in *Physics and Technology of Electric Power Transmission*, A. F. Djakov (ed.), MPEI Publishers, Moscow, pp. 161–200, 1998 (in Russian)
76. I. Odrobina and M. Cernak, Numerical simulation of streamer-cathode interaction, *J. Appl. Phys.*, vol. 78, pp. 3635–3642, 1995
77. N. Y. Babaeva and G. V. Naidis, Dynamics of positive and negative streamers in air in weak uniform electric fields, *IEEE Trans. Plasma Sci.*, vol. 25, no. 2, 1997

---

## *Chapter 5*

# **Modelling of charging processes in clouds**

*Edward R. Mansell<sup>1</sup> and Donald R. MacGorman<sup>1</sup>*

---

### **5.1 Introduction**

Our goal in this chapter is to introduce the treatments of electrical processes used by numerical cloud models that integrate dynamic, microphysical, thermodynamic and electric processes to track what happens to several classes of water particles as they move through the cloud and interact with each other and with the environment as the cloud evolves. We consider primarily models that treat ice particles, as well as liquid water, because ice is now commonly recognized as a necessary ingredient for strong electrification. We ignore models whose winds or particle spectra are unchanging and models that treat electrification as interactions of electric circuit elements driven by a current, charge or voltage source unrelated to microphysics and dynamics.

When using cloud models, it is prudent to keep their limitations in mind, as no numerical model can reasonably be expected to replicate a storm exactly. Our computer resources and our knowledge of many relevant processes and of the environmental state are almost certainly never adequate to do that. What is done, therefore, is to use simplified mathematical descriptions called *parameterizations* to deal with the spectrum of particle types, to estimate the effects of poorly understood physics and to incorporate the effects of processes that occur on temporal or spatial scales too small to be included directly. The goal is for the parameterizations to incorporate enough physics, to treat a broad enough range of time and distance scales and to retain enough detail in the microphysical, electric, dynamic and thermodynamic fields that the model can simulate accurately the aspect of the phenomenon we are studying. To some extent, success is judged by examining how well the model simulates observations of related storm properties, such as the distribution and evolution of precipitation, cloud particles and electric field magnitudes. However, it often is difficult to assess how well a particular model has succeeded in simulating a given phenomenon. Relevant properties often are not observed well enough to judge simulations, and even if they have been observed well, it is often difficult to determine how good a match with observations is needed to establish that the model is adequately simulating the targeted behaviour.

<sup>1</sup>National Severe Storms Laboratory, Norman, Oklahoma, USA

Although any model involves uncertainties, models also have strengths that help circumvent the serious difficulties one faces trying to improve understanding of storm electrification by analysing measurements alone. A sensor may itself distort what is being measured, and ambiguities can arise when interpreting measurements by a particular sensor in terms of desired storm parameters. Furthermore, no combination of technologies is likely ever to be able to observe simultaneously all of the thermodynamic, kinematic, electric and hydrometeor fields in evolving clouds with enough temporal and spatial resolution to describe all their significant behaviours and interactions. Modelling addresses these shortcomings by attempting to calculate all of the relevant fields in a physically consistent way from as close to first principles as is feasible. By providing a complete set of simulated observations of the very complex system that is a thunderstorm, modelling provides a useful means for testing the plausibility and implications of ideas gained from theory and observations.

Thus, observations and models often complement each other in our efforts to advance understanding: (1) Laboratory, theory and field observations provide the knowledge needed to build a model. (2) Modelling experiments provide insight into storm processes and lead to predictions and model sensitivities that can be tested with observations. (3) New laboratory and field observations are acquired under model guidance to examine the predictions and sensitivities and refine the model. (4) The refined model is then used either to probe previously defined issues more deeply or to begin investigating new issues not possible to address with the previous version of the model. Note that progress in model capabilities is also often a result of increased computer memory and processing speed.

In this chapter, we limit ourselves to explaining the basics of the techniques involved in modelling electrification, as well as giving an overview of some of the electrification research pursued through modelling studies. We attempt to cover most electrical processes but present only selected examples of the treatments of each one. Beyond defining some terms, we do not review the microphysical and dynamical frameworks of cloud models, because doing so would make this chapter far too lengthy. An overview of microphysical and dynamical treatments is given by MacGorman and Rust (1998). More in-depth information about cloud models is available in several books, including Pruppacher and Klett (1997), Cotton and Anthes (1989), Houze (1993), Stensrud (2007), Straka (2009) and in many of the publications referenced in this chapter.

## 5.2 Definitions of some model descriptors

### 5.2.1 Basic terminology

Several basic terms are used to describe models. A *full simulation model*, the only kind we consider in this chapter, produces clouds through appropriate initial conditions in an ambient environment defined by one or more atmospheric soundings and has equations that govern the subsequent evolution of thermodynamic fields, wind fields and microphysics. A *kinematic model* (e.g. Ziegler, 1985, 1988) still

must have an ambient environment defined by soundings but has no equation for dynamics to govern the development of the wind field. Instead, the model ingests a cloud wind field obtained from Doppler radars. (The wind field either can be a single wind field, assumed to be steady state, or can vary in time from an early stage of the storm.) It then uses the thermodynamic equation of state and continuity equations for water substance to retrieve temperature, water vapour mixing ratio and hydrometeor mixing ratios throughout the model domain.

Models also are classified by the number of spatial dimensions of the model grid. To study storms in which three-dimensional structure and circulations are important, it obviously is necessary to use a *three-dimensional* model. However, for simpler situations or more limited investigations, modellers can reduce the number of spatial dimensions that they use. Because adding a spatial dimension to a model typically increases computer memory and storage requirements by more than an order of magnitude, reducing the number of dimensions greatly reduces the computer resources required to run a model.

Some electrification models are essentially *zero-dimensional* cloud models because most parameters do not vary with either height or horizontal distance. These models normally assume that the upper and lower boundaries are infinite horizontal planes, so that the ambient electric field is constant with the distance between them. Microphysics and vertical winds also are kept uniform between the horizontal planes: On each boundary there is a source of hydrometeors, usually a source of small particles at the bottom and a source of large particles at the top. Particles and charge can vary with time, and charges are collected at the boundaries as particles reach them, thereby changing the ambient electric field. The model domain normally is considered to represent only part of a cloud, with the upper plate corresponding to the centre of the upper positive charge, and the lower plate the centre of the lower negative charge in a thunderstorm charge distribution. Illingworth and Latham (1977) pointed out that a model with infinite planes will overestimate thunderstorm electric field magnitudes in most situations.

In a *one-dimensional* model, height is the only spatial coordinate that is retained. Cloud properties can vary with height but not with horizontal position. The model domain normally is defined as a cylinder whose radius  $R(z)$  is specified. The use of a finite horizontal extent makes it possible to incorporate parameterizations of entrainment and turbulent eddy fluxes and makes electric field magnitudes more realistic.

In a *two-dimensional* model, height and one horizontal coordinate are retained, and cloud properties over the remaining horizontal coordinate are constant. Two-dimensional models can be either slab-symmetric or axisymmetric. A *slab-symmetric* model uses Cartesian coordinates and keeps cloud properties constant along  $x$  or  $y$ . This symmetry is applied sometimes to squall lines. An *axisymmetric* model uses cylindrical coordinates and sets azimuthal variations to zero. This symmetry is useful for small thunderstorms and some aspects of hurricanes. Two-dimensional models have a particular limitation, however, in that turbulence incorrectly feeds upscale growth. Proper treatment of turbulence requires a three-dimensional model.

Unlike a one-dimensional model, two- and three-dimensional models do not need to specify cloud boundaries or entrainment. Instead, the model is provided the specified environmental thermodynamic and water vapour fields, and clouds form in the model wherever these fields interact to create them. (Slab-symmetric models also can use one horizontal component of environmental winds, but axisymmetric models can treat only radially converging or diverging horizontal wind.) Modelled air motions may be adequate to resolve entrainment, but eddy fluxes must be treated by parameterization of subgrid-scale turbulence.

### 5.2.2 Terms related to microphysics

Temporal and spatial variations in water vapour and water substance are defined by continuity equations for water vapour and water substance expressed in terms of mixing ratios. The mixing ratio  $q$  for the  $N$ th category of water substance is defined as the mass of the  $N$ th category per unit mass of dry air (often expressed as kilograms or grams of water per kilogram of dry air). The mixing ratio for total water substance then is the sum of the mixing ratios for water vapour and for all types of hydrometeors. For each category of water substance, there is a continuity equation of the form

$$\frac{dq_N}{dt} = \text{Transport}(q_N) + \text{Source}(q_N) + \text{Sink}(q_N) \quad (5.1)$$

where transport is the net transport of  $q_N$  into the volume by advection, turbulence and diffusion; source is the sum of all sources of  $q_N$  in the volume and sink is the sum of all loss mechanisms for  $q_N$ . Much of the challenge in parameterization is to develop physically realistic expressions for sources and sinks, once a partition of water into various categories is chosen.

The water substance in a cloud normally is partitioned into several categories. For example, the following categories are described by Houze (1993):

1. Water vapour ( $q_v$ ) is water in the gaseous phase.
2. Cloud liquid water ( $q_c$ ) consists of liquid droplets that are too small to have appreciable terminal fall speed (droplet radius less than roughly 100  $\mu\text{m}$ ).
3. Precipitation liquid water consists of liquid drops that are large enough to have an appreciable terminal fall speed. This category sometimes is divided by terminal fall speed into drizzle ( $q_{Dr}$ ) (radius roughly 0.1–0.25 mm) and rain ( $q_r$ ) (radius  $> 0.25$  mm).
4. Cloud ice ( $q_i$ ) indicates ice particles that are too small to have an appreciable terminal fall speed.
5. Precipitation ice consists of ice particles that have a terminal fall speed of  $\geq 0.3$  m/s. This category often is subdivided by density and fall speed. For example, snow ( $q_s$ ) has lower density and fall speeds of 0.3–1.5 m/s, graupel ( $q_g$ ) is denser and falls at  $\approx 1$ –10 m/s and hail ( $q_h$ ) is larger and still denser, with fall speeds up to 50 m/s.

Models that omit all forms of ice are referred to as *warm cloud models*. Models that include equations for the ice phase are referred to as *cold cloud models* or *mixed-phase models*.

Each category of water substance interacts with the other categories to create sources and sinks. For example, cloud water droplets coalesce to form drizzle, a process that is a source for drizzle and a sink for cloud liquid water. There are several types of basic interactions:

1. Condensation or deposition of water vapour onto cloud nuclei (called *nucleation*) to form cloud liquid water droplets and cloud ice particles, respectively, having size spectra characteristic of the model cloud's environmental conditions
2. Hydrometeor growth through vapour condensation or deposition
3. Collection of particles to form larger particles (Collection of the various types of particles consists of collisions followed by sticking together. The ways in which two particles stick together are labelled by specific terms depending on the types of particles involved: *coalescence* involves two or more liquid water particles; *aggregation* involves two or more ice particles; and *riming* is the process of cloud water droplets freezing into ice particles on contact. *Accretion* is used broadly to indicate collection of liquid particles by ice particles but often has a connotation of larger liquid particles sticking to larger ice particles.)
4. Breakup of drops or splintering of ice (These processes can increase the number of particles beyond what would be expected from nucleation. The increase from splintering is referred to as *ice multiplication*.)
5. Freezing of liquid water (Liquid water exists as supercooled water at heights above the 0°C isotherm, but all liquid water usually is assumed to have frozen by the time a parcel reaches the -40°C isotherm.)
6. Evaporation or sublimation of water vapour from hydrometeors
7. Melting of ice
8. Precipitation reaching the ground

It is possible to expand the number of categories and subcategories of hydrometeors considerably. Typical categories are cloud droplets ( $D < 50 \mu\text{m}$ ), rain ( $D > 50 \mu\text{m}$ ), small ice crystals, snow (or aggregated crystals), graupel and hail. To expand categories, e.g. a modeller might want to track different shapes (called habits) of ice particles separately (such as columns, plates and dendrites). However, as more categories of water are used, the number of interactions that must be considered increases rapidly. For that reason, modellers usually use only the categories and subcategories that are essential to simulating the particular phenomenon being studied.

To parameterize microphysics, models handle the size distributions of the various categories in one of two ways, referred to as *bulk microphysics* and *bin* (or *spectral*) microphysics. In bulk microphysics, the size distribution of particles is described by some simple function. The amount in a given category can be tracked at each grid point by a single parameter, such as the mixing ratio of water substance in that category, or by two or more parameters, such as the mixing ratio and number

density of particles in a category. Distributions using two or more parameters provide a more versatile description than distributions using one parameter.

In bulk microphysics, the size distribution of precipitating liquid often is described as a simplified gamma function of the form

$$n(D) = n_0 D^\alpha \exp(-\lambda D) \quad (5.2)$$

where  $n(D)$  is the number of particles per unit volume between  $D$  and  $D + \delta D$  and  $\alpha$  is the shape parameter, which controls the width of the spectrum. The intercept parameter  $n_0$  is a function of the total number concentration  $n_T$  and the slope parameter  $\lambda$ :

$$n_0 = \frac{n_T}{\Gamma(\alpha + 1)} \lambda^{\alpha+1} \quad (5.3)$$

where  $\lambda$  is defined as

$$\lambda = \left[ \frac{\Gamma(\alpha + 1 + d) c n_T}{\Gamma(\alpha + 1) \rho_{air} q} \right]^{1/d} \quad (5.4)$$

where the constants  $c$  and  $d$  come from the mass–diameter relationship  $m(D) = cD^d$ .

The moments  $M(j)$  of the distribution are given by

$$M(j) = A(j) \int_0^\infty D^j n(D) dD \quad (5.5)$$

where  $A(j)$  is some constant factor. For the simplified gamma distribution, the moments are

$$M(j) = \frac{A(j) n_T \Gamma(\alpha + 1 + j)}{\lambda^j \Gamma(\alpha + 1)} \quad (5.6)$$

For  $j = 0$  and  $A(0) = 1$ ,  $M(0) = n_T$ , so the zeroth moment is the number concentration. If the mass of a particle is  $m(D) = cD^3$ , then the third moment gives the total mass of the distribution.

Single-moment schemes predict  $q$  and usually diagnose  $n_T$  by setting assuming value for  $n_0$  (the intercept parameter). Models with two-moment bulk microphysics generally predict the mixing ratio  $q$  (third moment) and number concentration  $n_T$  (zeroth moment). Three-moment schemes can also diagnose the shape parameter  $\alpha$ .

Setting the shape parameter  $\alpha$  equal to zero results in the inverse exponential (IE) distribution. This form of the size distribution is often referred to as a *Marshall–Palmer* distribution (Marshall & Palmer, 1948).

In bulk microphysics, each property of the category has a single representative value at a given grid point in the model domain that somehow averages the values for all of the category's particles within the corresponding volume. For example, consider the sedimentation of liquid precipitation particles that have a terminal fall

speed relationship  $v(D) = aD^b$ . The moment-weighted fall speed is used for sedimentation of each bulk moment. For example, the mass-weighted fall speed  $V_{T,m}$  is given by

$$V_{T,m} = \frac{\int_0^\infty v(D)m(D)n(D)dD}{\int_0^\infty m(D)n(D)dD} \quad (5.7)$$

which is used for sedimentation of the total particle mass in a grid volume. Note that the denominator in (5.7) is the mass content (mass of condensate per volume). Then  $C$ , the net rate of change in a grid point's mass mixing ratio  $q$  due to sedimentation, is given by

$$C = \frac{d}{dz}(V_{T,m}q) \quad (5.8)$$

Moments of the distribution in a spectral bin model are calculated by an explicit summation over the range of sizes for the water substance category being considered. For example, the mixing ratio  $q_x$  of particle type  $x$ , modelled by  $J$  size bins and having mass increments of  $m_x(j)$ , is given by

$$q_x = \frac{1}{\rho_{air}} \sum_{j=1}^J m_x(j)n_x(j) \quad (5.9)$$

where  $n_x(j)$  is the number density of particles in mass bin  $j$ . To represent the size distribution of particles accurately, at least ten size bins must be included for each hydrometeor category being parameterized.

With bin microphysics, it is unnecessary to assume that the size distribution has a particular form. The overall size distribution is allowed to evolve naturally as particles of different sizes gain and lose mass through their interactions. This is a more direct approach than bulk microphysics, but even with many size bins, a bin parameterization is not an exact treatment. There are gaps in our knowledge of particle interactions, particularly for some size ranges and particle types, and these gaps introduce uncertainties in bin parameterizations. Furthermore, although particles within a given size bin are more uniform than in a category that spans all sizes in a bulk treatment, variations in properties, such as size, shape or density may occur within an individual bin being treated explicitly and can affect interactions involving this bin. When such variations are significant, spectral parameterizations need to avoid treating all particles in a size bin identically, because it would incorrectly cause all particles to transfer into a new size bin at the same time. To avoid this, a spectral parameterization can treat particles in a given size bin as having a distribution of sizes across the range of the bin and can use statistical techniques to govern gradual changes in the population.

The main disadvantage of bin microphysical treatments compared with bulk microphysics is that bin treatments require considerably more computational resources: Each bin must satisfy its own continuity equation, and interactions must be included between size bins, as well as between water substance categories.

Thus, bin microphysics usually is reserved for addressing questions that cannot be addressed by bulk microphysics. When specific microphysical treatments are used in the rest of this chapter, bulk microphysics is used instead of bin microphysics.

### 5.2.3 Categories of electrification mechanisms

Electrification processes are broadly categorized as either *inductive* or *non-inductive*. An *inductive* process is driven by an ambient electric field. Hydrometeors have naturally occurring free ions that can move enough in response to an electric field to polarize the particle. Figure 5.1 depicts a possible inductive (or polarization) charge separation process in which a small liquid water droplet collides with and rebounds from a graupel pellet. Other examples of possible inductive charge transfer include the shedding of liquid water from hail (melting or undergoing wet growth) and break-off of ice branches as snow melts (assuming the electric field forces free ions towards the material that breaks away from the larger ice particle). Research has suggested that inductive processes alone are not capable of providing strong electrification. However, they may provide secondary effects important in some regions, such as in melting layers and in regions having preferred attachment of one polarity of ion driven by the electric field (e.g. screening layer charge).

*Non-inductive* charging processes are defined as charge transfer that is independent of an external electric field. The collisional ice–ice mechanism is generally regarded as the primary electrification mechanism, although much about the mechanism is still not well understood. The non-inductive ice–ice mechanism has been best described by the relative growth rate theory of Baker *et al.* (1987), which states simply that when two ice surfaces collide and rebound, the surface that is growing faster by vapour deposition will gain positive charge (by losing negative charge). Supersaturation with respect to ice is required for deposition growth and significant charge transfer. One explanation for the mechanism is that partial melting occurs around the impact site, which mixes the (negative) charges from the two surfaces (Emersic, 2006). As the two particles separate, some of the melted mass is carried off by the smaller particle, resulting in a net charge transfer (Figure 5.2). Other proposed non-inductive mechanisms involve thermoelectric

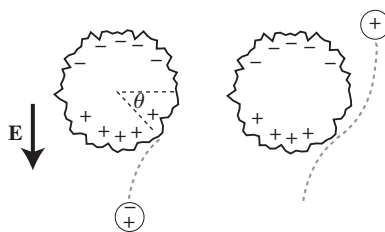
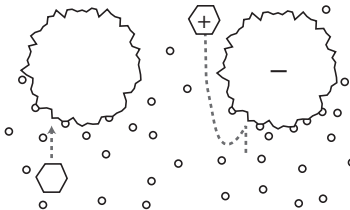


Figure 5.1 Example of an electric field-dependent inductive process. Here, a graupel particle and water droplet are polarized by an electric field (left). A rebounding collision transfers some negative charge from the droplet to the graupel particle (right)



*Figure 5.2 Example of an electric field-independent non-inductive process. Here, a graupel particle and ice crystal are initially uncharged in a cloud of small droplets (left). A rebounding collision transfers some charge between the ice and graupel particles (right). The sign of charge transfer could be positive or negative, depending on the vapour deposition growth of the interactive surfaces*

effects, contrasting surface potentials and electrical double layers arising from physical properties of ice surfaces.

#### 5.2.4 Other categorizations of cloud models

Besides the dynamic, thermodynamic and microphysical considerations discussed in the previous section, other choices also influence the complexity and computational requirements of models. Most cloud models are *time dependent*, meaning that cloud properties are allowed to evolve, but some simpler models use *steady-state* dynamics.

Many one-dimensional models and some two- and three-dimensional models use the *anelastic* form of the continuity equation. The more sophisticated two- and three-dimensional cloud models usually are *fully compressible*. The anelastic approximation eliminates sound waves, which often are considered undesirable because their magnitude can be large and other processes are of more interest in modelling studies, but doing so requires solution of an elliptic equation for the pressure field. Elliptic equations require iterative or implicit solvers, which can be inefficient. The fully compressible form retains sound waves and allows use of explicit (forward-in-time) numerical solvers. Efficiency is maintained by integrating sound waves separately ('*split explicit*' method).

A *full simulation model* produces clouds through appropriate initial conditions and simulates the subsequent evolution of all model fields. To simulate a cloud with a given one-dimensional, time-dependent model, a vertical profile of each relevant parameter of the ambient environment is specified, vertical forcing (e.g. a thermal perturbation or vertical velocity source) is applied at a low height and the model then computes how deviations from environmental values evolve. Similarly, a two-dimensional, axisymmetric model generally applies forcing centred on  $r = 0$ . Usually, two-dimensional, slab-symmetric models and three-dimensional models are initiated by introducing some type of forcing with a more complicated geometry into the specified environmental conditions. This forcing may be, e.g., in the form of convergence in some region at low levels on which are superimposed

thermal bubbles, whose size, location and temperature excess above ambient conditions must be chosen (either given specific values or chosen randomly from some range). Storms that result from a given model experiment can be influenced by the form and magnitude of forcing that is applied, as well as by assumed environmental conditions; this is especially true of small thunderstorms driven primarily by local heating.

Besides full simulation models, which simulate the dynamics, thermodynamics and microphysics of storms simultaneously beginning with initial forcing in a pre-storm atmospheric environment, another type of model, called a *kinematic model*, uses observed wind fields of storms to estimate the accompanying temperature and water vapour perturbations and microphysics in a particular atmospheric environment. In a kinematic model (e.g. Ziegler, 1985, 1988), the thermodynamic equation of state and continuity equations for water substance are the same as in a full simulation model, but there is no equation for dynamics to govern the development of the wind field. Instead, the model ingests an observed cloud wind field from Doppler radars and ambient environmental conditions from an atmospheric sounding. Then, the equation of state and continuity equations for water substance are solved to retrieve temperature, water vapour mixing ratio and hydrometeor mixing ratios throughout the model domain. In a time-dependent, kinematic model, the various fields are allowed to evolve from their state at an early stage of the cloud. Changes in the wind field are calculated by interpolating between observed wind fields at each time step. Changes in the retrieved fields then are calculated from changes in the wind fields.

Kinematic models have the disadvantage that, because the modelled cloud does not begin with initial cloud formation, there may be significant errors in fields that are sensitive to the cloud's history of evolution. Furthermore, the wind field of the model is not influenced by microphysics and thermodynamics, and kinematic models can be used only for periods when Doppler wind fields are available. However, a kinematic model has the advantage that it produces a model storm consistent with both the observed storm wind field and the complete set of thermodynamic and continuity equations. It can be difficult to use full simulation models to investigate some storms, especially small storms, because of model sensitivities to the form of initial forcing, to boundary conditions or to minor changes in the storm environment.

Most cloud models that have been used in electrification studies have tracked the properties of water substance categories at grid points fixed with respect to the Earth (these are sometimes called *Eulerian models*). *Particle tracing* or *Lagrangian models* (e.g. Kuettner *et al.*, 1981), however, compute changes to the properties of individual particles or groups of identical particles along trajectories that follow the particles through the storm, instead of at fixed grid points. Model fields related to the particles are derived after each model time step by interpolating particle parameters from particle locations to the model grid. This type of treatment typically is used with simplifications to other aspects of the model to keep computations tractable. Sometimes an Eulerian model uses statistical techniques to mimic a Lagrangian treatment for a particular type of particle.

### 5.3 Brief history of electrification modelling

In the 1950s and 1960s, there were several calculations of electrification rates from particle interactions that considered neither cloud dynamics nor the microphysics of the particles. The first attempt to include electrification in a numerical cloud model that considered these factors was by Pringle *et al.* (1973), who used a crude parameterization of charge separation that did not attempt to mimic any particular microphysical charging mechanism. Takahashi (1974) allowed hydrometeors to capture space charge in his one-dimensional, time-dependent cloud model but did not include charge exchange between particles. Ziv and Levin (1974), Scott and Levin (1975) and Levin (1976) studied inductive charging by considering hydrometeors that moved vertically and interacted between the two plates of an infinite horizontal capacitor but did not include any cloud dynamics. Illingworth and Latham (1977) included explicit parameterizations of several microphysical charging mechanisms in a one-dimensional model with steady-state dynamics. Kuettner *et al.* (1981) incorporated parameterizations of inductive and non-inductive charging in a two-dimensional Lagrangian model with steady-state dynamics. Although these last two studies were able to estimate the relative contributions to cloud electrification from the various mechanisms they modelled, the use of specific steady-state dynamics did not allow them to consider how electrification varied with evolving cloud dynamics. Relatively simple models continue to be used for tests of specific hypotheses (e.g. Mathpal & Varshneya, 1982; Singh *et al.*, 1986; Canosa *et al.*, 1993).

The next step in the evolution of electrification modelling was to add electrification processes to cloud simulation models that coupled electrification with both microphysics and dynamics. Early attempts at this coupling included only warm rain processes (i.e. there was no freezing or ice). Takahashi (1979) used a two-dimensional, time-dependent axisymmetric model with bin microphysics to study electrification of shallow, warm clouds. Chiu (1978) also developed a two-dimensional, time-dependent axisymmetric model, although with bulk microphysics, and was the first to include a parameterization of small ions and their interactions with particles in a cloud simulation model. By including ion-hydrometeor interactions, simulated clouds were able to form screening layers at cloud boundaries, and mechanisms such as the Wilson's selective ion capture mechanism could affect the charge on particles in appropriate regions. Helsdon (1980) used a similar model that was slab-symmetric instead of axisymmetric to study whether cloud electrification could be modified by injecting metal-coated chaff fibres into a warm cloud.

Since several scientists already had suggested that ice-particle interactions were important for thunderstorm electrification by the non-inductive mechanism, applications of warm cloud models were considered extremely limited, and there was considerable interest in developing electrification models that included ice processes. Rawlins (1982) included electrification in a cloud simulation model that parameterized ice processes in a three-dimensional model. The model used bulk

microphysics, a simple parameterization of the non-inductive mechanism and a traditional parameterization of the inductive mechanism. Electrification occurred only when graupel or hail interacted with snow or cloud ice, so no charge was generated by interactions involving liquid hydrometeors. Takahashi (1983, 1984) included ice processes in a two-dimensional, time-dependent axisymmetric model with bin microphysics. Parameterized charging mechanisms included inductive charging, ion-hydrometeor interactions and non-inductive charging based on the laboratory data of Takahashi (1978). Takahashi's model had much better grid resolution than Rawlins's but had a domain height of only 8 km, and so was limited to small storms.

Helsdon and Farley (1987b) added a simple non-inductive charging parameterization to the Chiu (1978) ion capture and inductive charging parameterizations in a two-dimensional, time-dependent, slab-symmetric model with bulk ice microphysics. They used the model to simulate a storm that was observed to produce a single lightning flash during the Cooperative Convective Precipitation Experiment in Montana. Modelled space charge and electric field distributions were similar to those observed by two aircrafts that penetrated the storm only in simulations in which both the non-inductive and inductive mechanisms operated together. In that case, the time required for model electrification to increase to the point that lightning occurred was comparable to that required by the observed storm. After publication of Helsdon and Farley, an error was found in the formulation of the non-inductive parameterization for experiments in which it was used alone. Wojcik (1994) repeated the investigation with the corrected formulation of the non-inductive mechanism acting alone and found that it produced an electric field consistent with the aircraft observations. Randell *et al.* (1994) used a non-inductive parameterization similar to Takahashi (1984) in a configuration of the Helsdon and Farley (1987b) model that omitted the inductive mechanism (and used the corrected non-inductive formulation). They simulated storms in three different environments to examine conditions under which the non-inductive mechanism could produce a thunderstorm.

Electrification processes have been incorporated into another cloud simulation model based on a simpler geometry. Mitzeva and Saunders (1990) developed a one-dimensional model that included no inductive mechanism or ion capture but used a sophisticated parameterization of non-inductive charging based on laboratory studies of Jayaratne *et al.* (1983) and Keith and Saunders (1989), instead of Takahashi (1978). Their model employed bulk microphysics and was used primarily to examine the evolution of non-inductive charging rates as a function of the intensity of precipitation produced by three storms.

The cloud models summarized above were simulation models, but some models have been kinematic models. Ziegler *et al.* (1986) used bulk microphysics in a one-dimensional, kinematic model whose domain consisted of a cylindrical cloud with a fixed radius. The only electrification mechanism was a parameterization of the non-inductive mechanism suggested by Gardiner *et al.* (1985). Ziegler *et al.* (1991) expanded the kinematic model to be three dimensional and modified the kinematic retrieval process to enable the model to assimilate

radar-derived wind fields that were available every three minutes, from early in the storm's lifetime throughout much of its life. They also added parameterizations of the inductive charging mechanism and of screening layer charge on the cloud boundary. Ziegler and MacGorman (1994) used the three-dimensional model to study a supercell storm (features that are not slab- or axisymmetric are critical to an adequate treatment of supercell storms).

Norville *et al.* (1991) developed a kinematic model that used bin microphysics. The only electrification mechanism that they included was a non-inductive charging mechanism based on the laboratory work of Jayaratne *et al.* (1983), Baker *et al.* (1987) and Keith and Saunders (1989). The geometry of their model cloud consisted of two concentric cylinders, in order to be able to model coexisting updrafts and downdrafts. Conditions were horizontally uniform inside the inner cylinder and different, but again uniform, between the inner and outer cylinders. This configuration has been called a one-and-one-half dimensional model. Norville *et al.* simulated the same storm studied by Helsdon and Farley (1987b). Their model was able to produce electric field magnitudes comparable to observed values by using only the non-inductive mechanism.

Most modelling studies prior to the 1990s, whether they used simulation or kinematic models, have examined electrification only in the absence of lightning. Without a lightning parameterization, models could simulate only the initial electrification of thunderstorms, because lightning modifies the charge distribution and limits the maximum magnitude of the electric field. Rawlins (1982) used a threshold electric field of  $500 \text{ kV m}^{-1}$  to initiate a lightning flash and a simple charge neutralization scheme. He found that the electric field regenerated quickly after a lightning flash. Helsdon *et al.* (1992) developed a detailed two-dimensional unbranched lightning flash parameterization that calculated the neutralized charge from the ambient electric field. It was used successfully to simulate a storm that produced a single lightning flash, and later was expanded to a three-dimensional unbranched channel (Helsdon *et al.*, 2002). Takahashi (1987) incorporated a simple parameterization of a lightning flash in his model to examine factors influencing the height and location of lightning. Ziegler and MacGorman (1994) developed a simple three-dimensional parameterization of the net effect of several flashes per time step to simulate a supercell storm. Baker *et al.* (1995) added a simple parameterization of lightning to their one-and-one-half dimensional, kinematic model with bin microphysics and Solomon and Baker (1996) developed an analytical treatment of a vertical, one-dimensional lightning channel for the same model. MacGorman *et al.* (2001) developed a three-dimensional treatment to simulate discrete flashes using the crude parameterization of neutralized charge by Ziegler and MacGorman (1994). Mansell *et al.* (2002) developed a detailed three-dimensional fractal lightning scheme that used Gauss's law to estimate the charge neutralized by branched equipotential lightning channels. These last two lightning parameterizations are described in detail in Section 5.5.

The two-dimensional simulation study of Helsdon *et al.* (2001) broke ground in comparing results from multiple non-inductive graupel–ice schemes. Helsdon *et al.* (2001) did not include lightning, however, so results were obtained only up to

the time of the first lightning flash. Helsdon *et al.* (2002), using a three-dimensional version of their model and a lightning parameterization, tested the so-called ‘convective’ charging hypothesis, which relies on screening layers formed by ion attachment to be advected into the storm updraft to generate electrification via inductive charging. Helsdon *et al.* (2002) found only weak, disorganized electrification that could not generate electric fields sufficient for lightning without inclusion of a non-inductive graupel–ice mechanism. A study by Mansell *et al.* (2005) investigated differences in electrification from multiple graupel–ice parameterizations as well as inductive graupel–droplet charge separation in a three-dimensional model with lightning.

Sun *et al.* (2002) employed a three-dimensional model with two-moment microphysics (mass and number concentration) to examine the effects of electrification on the microphysics and dynamics of a small storm. Feedback to dynamics was achieved through an electrical drag term in the momentum equations using the net charge density and electric field and by electric force adjustments to hydrometeor terminal speeds. The results with electrification and feedback differed appreciably from the non-electrical simulation. An increase in latent heating was found when electrical forces were enabled. The increased latent heating was attributed to reductions in graupel fall speeds at mid-levels of the storm, which increased its residence time and total riming growth. The model almost certainly overestimated electric force effects, however, in the assumption that hydrometeors of a given class are uniformly charged, which disagrees with in situ particle charge measurements. The maximum electric field also was allowed to increase to  $250 \text{ kV m}^{-1}$  before activating the lightning scheme (a three-dimensional adaptation of the Helsdon *et al.*, 1992, scheme). Sun *et al.* (2002) incorporated somewhat out-of-date parameterizations of electrification, including drop–droplet inductive charge separation (Chi, 1978), which is widely considered to be ineffectual due to enhanced drop coalescence even in relatively weak electric fields.

Mansell *et al.* (2002) simulated lightning behaviour in two different storms using the same charge separation schemes. A low-shear thunderstorm had a normal tripole charge structure (main negative charge with main positive charge above and lower positive charge below). A high-shear supercell simulation, however, exhibited an inverted tripole structure. The low-shear storm produced negative cloud-to-ground (CG) lightning that was initiated between the main negative and lower positive charge regions. The supercell storm simulation had positive CG lightning that was initiated between a main positive region and lower negative charge.

A new electrified model was described by Barthe *et al.* (2005), who presented initial results from a version of the Meso-NH model that included electrification and lightning parameterizations. They also included a sensitivity study of two graupel–ice schemes. Barthe and Pinty (2007) presented more details of the parameterizations used in Barthe *et al.* (2005), especially details concerning the lightning scheme.

The model used in Mansell *et al.* (2002) has been used in a number of later studies. Kuhlman *et al.* (2006) presented simulations of a severe supercell storm and compared results to observations of that storm. Fierro *et al.* (2006) investigated

the effects of an inhomogeneous environment on the simulated kinematics, electrification and lightning of a supercell storm. Fierro *et al.* (2007) investigated electrification of an idealized tropical cyclone. Mansell *et al.* (2010) used a two-moment microphysics scheme to compare simulated electrification and lightning of a small thunderstorm with observed lightning evolution.

A few recent cloud model studies have started examining lightning production of nitrogen oxides ( $\text{NO}_x$ ). Zhang *et al.* (2003) combined a chemistry model with an electrification and lightning model (Helsdon *et al.*, 2002) to study production, transport and subsequent chemical reactions of  $\text{NO}_x$ . Barthe *et al.* (2007) simulated the electrification and  $\text{NO}_x$  production in a strong storm but did not include a chemistry module. Results from both of these models were included in an inter-comparison study (Barth *et al.*, 2007).

The rest of this chapter describes some of the parameterizations of electrical processes used by the above cloud models.

## 5.4 Parameterization of electrical processes

To include electrification in numerical models, the various electrical processes of clouds must be parameterized and integrated with parameterizations of dynamical, thermodynamic and microphysical processes. In this section, we discuss how numerical models produce and transport charge on hydrometeors, how the electric field is calculated and how lightning is parameterized. We present only processes that laboratory studies suggest will have appreciable effect in storm electrification. In most cases, we give only one or two examples of how a particular process has been parameterized.

### 5.4.1 Calculating the electric field

Once a modelled storm has produced charged hydrometeors, it is necessary to calculate the resulting electric field, both for analysis of model results and for use in the next time step to calculate the results of processes dependent on the electric field. Electric field calculations in one-dimensional models are much simpler than in two- and three-dimensional models. For one-dimensional, infinite layer models, the only non-zero component of the electric field is the vertical component,  $E_z$ , which can be calculated from Gauss's law. If the contribution of the image charge below the conducting Earth is included,  $E_z$  at height  $z_0$  (above ground level) due to charge at the  $k$ th grid level at height  $z_k$  is

$$E_{z_0} = \begin{cases} -\frac{\rho_k \Delta z}{\epsilon} & \text{for } z_0 < z_k \\ -\frac{\rho_k \Delta z}{2\epsilon} & \text{for } z_0 = z_k \\ 0 & \text{for } z_0 > z_k \end{cases} \quad (5.10)$$

where  $\Delta z$  is the height increment between grid levels,  $\rho_k$  is the charge density at the  $k$ th grid level and  $\epsilon$  is the electrical permittivity of air ( $8.859 \times 10^{-12} \text{ Fm}^{-1}$ ).

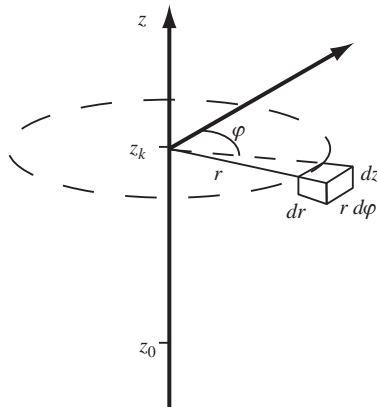


Figure 5.3 Geometry for calculating  $E$  at height  $z_0$  on the  $z$  axis from an infinitesimal element of a disk of charge at height  $z_k$

Because the electric field from an infinite layer is constant with height above and below the layer, this geometry is likely to give electric field profiles considerably different from profiles appropriate to most physically realistic thunderstorm geometries (although it might be suitable for extensive stratiform clouds).

More realistic electric field profiles usually can be obtained in a one-dimensional model in which the size of the cloud is limited to some radius. On the axis of a cloud with cylindrical symmetry, the only non-zero component of the electric field is again the vertical component. The contribution of an infinitesimal charge (including its image charge) to the vertical electric field on the axis at height  $z_0$  (Figure 5.3) is given by

$$dE_z(z_0) = \frac{\rho_k}{4\pi\epsilon} \left[ \frac{z_k - z_0}{[r^2 + (z_k - z_0)^2]^{3/2}} + \frac{z_k + z_0}{[r^2 + (z_k + z_0)^2]^{3/2}} \right] \cdot r dr d\varphi dz \quad (5.11)$$

The electric field on the axis due to a thin disk of charge of radius  $R(z)$  (i.e.  $R$  can vary with height) at the  $k$ th grid level then is obtained by integrating over  $r$  and  $\varphi$ . Some care is needed in determining the constants of integration to get

$$E_z(z_0) = \frac{\rho_k \Delta z}{2\epsilon} \left[ \frac{z_k - z_0}{[R^2 + (z_k - z_0)^2]^{1/2}} + \frac{z_k + z_0}{[R^2 + (z_k + z_0)^2]^{1/2}} - C \right] \quad (5.12)$$

where  $C = 0$  for  $z_k < z_0$ ,  $C = 1$  for  $z_k = z_0$  and  $C = 2$  for  $z_k > z_0$ .

For an arbitrary charge distribution in two or three dimensions, there are no simple expressions for the electric field. It would be possible to compute the electric potential or field at an arbitrary point by adding the contributions from the charge at every grid point (from the superposition principle), but computing the potential or field this way at every grid point would be too computationally intensive in many cases. Instead, what is done usually is to use standard numerical algorithms to solve for  $\phi$  at all grid points by inverting the Poisson equation

$$\nabla^2 \phi = -\frac{\rho}{\epsilon} \quad (5.13)$$

where  $\rho$  is the total space charge density at the point being evaluated. Then, the electric field is computed from the potential by using the relationship  $\mathbf{E} = -\nabla\phi$ . Note that, in a two-dimensional model, the symmetry of the model requires the component of the electric field perpendicular to the plane of the model to be zero. Each point in a two-dimensional (slab-symmetric) model physically represents an infinite line charge, which distorts the electric field relative to a three-dimensional model.

To use numerical Poisson solvers (e.g. multi-grid iteration) to determine  $\phi$ , it is necessary to specify boundary conditions for  $\phi$  on all sides of the grid. As an elliptic equation, boundary conditions specify the value of  $\phi$ , the normal derivative  $\partial\phi/\partial n$  or a linear combination of the two. Since the ground is a good conductor, hence an equipotential, it is obvious that the potential of the bottom layer of the grid at the ground should be set to a constant. The constant usually is chosen to be zero, although any constant could be chosen without affecting the resulting electric fields. It is generally inappropriate to set the potential to a constant at the lateral grid boundaries. The upper boundary can be set to a fair-weather value if it is high enough to approximate the electrosphere, as a constant potential at the top seems to result in more stable solutions than setting the normal derivative. Choosing boundary conditions for the other sides is not as straightforward as for the ground, and choices can depend on the cloud size and geometry being modelled. At  $r=0$  in an axisymmetric, two-dimensional model, for example,  $E_z$  is the only non-zero component of  $\mathbf{E}$ , so the boundary condition there would be  $\partial\phi/\partial r=0$ . In three-dimensional or slab-symmetric, two-dimensional models, however,  $E_x$  might well be large if the storm is near the boundary at  $x=0$  (or  $x=X$ ), so  $\partial\phi/\partial x=0$  would not be an accurate boundary condition on that side. It often is impossible to find simple boundary conditions that are exactly correct. However, if the cloud is completely contained by the grid, suitable a priori boundary conditions can be used to produce reasonably accurate calculations of  $\phi$ .

At least two strategies have been used to improve the solution of  $\phi$  when charges get close to the domain boundaries. One method is to use brute force to calculate  $\phi$  at the boundaries (e.g. Riousset *et al.*, 2007); this increases solution accuracy in the interior but is computationally expensive. An alternative method is to solve for  $\phi$  in an enlarged domain that has fair-weather charge densities between the model boundaries and the enlarged domain (e.g. Mansell *et al.*, 2005). Pushing

out the lateral and upper potential boundaries has the effect of pushing the mirror charges farther away, thereby reducing the error they cause in the solution.

### 5.4.2 Charge continuity

Continuity equations for charge are similar to the continuity equations for air and for water substance categories discussed earlier in this chapter. As for the hydrometeor mixing ratios, there must be a continuity equation for the charge on each water substance category. These equations govern how each water category gains and loses charge at a given grid point of a model. They express what in physics texts is called conservation of charge. The total charge at a grid point is then the sum of the charges on all the water substance categories that exist there, i.e., if  $\rho_t$  is the total charge density at a grid point, and  $\rho_n$ , the charge density on the  $n$ th water substance category at that location, then

$$\rho_t = \sum \rho_n \quad (5.14)$$

The charge density from ions is included as a category if a model treats ion processes.

To derive expressions for the continuity equations, first consider charged particles in a parcel of air. Here, a parcel is a fixed mass of air but with a volume that can change (e.g. can expand when rising and compress when sinking). If no charge enters or leaves the parcel, then the total charge  $Q_t$  in the parcel is invariant to parcel motion and volume changes, but the total charge density  $\rho_t = Q_t/V$  is not invariant (where  $V$  is the parcel volume at a given time). Thus, we can temporarily define a ‘charge mixing ratio’  $\tilde{\rho} = \rho/\rho_{air}$  as the charge per mass of air. Then the parcel-following (Lagrangian) advection equation for charge on hydrometeor type  $n$  is

$$\frac{d\tilde{\rho}_n}{dt} = S_{\tilde{\rho}_n} \quad (5.15)$$

where  $S_{\tilde{\rho}_n}$  represents processes that can change the charge on the  $n$ th hydrometeor type, such as collisional charge separation and ion attachment.  $S_{\tilde{\rho}_n}$  also includes transfer of charge in and out of the parcel by sedimentation (for precipitation particles) and turbulent mixing. The Lagrangian reference is then transformed to the fixed Eulerian grid volume reference frame by the coordinate transformation  $d/dt \equiv \partial/\partial t + \mathbf{V} \cdot \nabla$  as

$$\frac{\partial \tilde{\rho}_n}{\partial t} = -\mathbf{V} \cdot \nabla \tilde{\rho}_n + S_{\tilde{\rho}_n} \quad (5.16)$$

For consistency with typical cloud model equations, we multiply (5.16) by air density  $\rho_{air}$ .

$$\rho_{air} \frac{\partial \tilde{\rho}_n}{\partial t} = -\rho_{air} \mathbf{V} \cdot \nabla \tilde{\rho}_n + \rho_{air} S_{\tilde{\rho}_n} \quad (5.17)$$

Expanding the divergence term using a vector identity and dividing again by  $\rho_{air}$  gives

$$\frac{\partial \tilde{\rho}_n}{\partial t} = -\frac{1}{\rho_{air}} [\nabla \cdot (\tilde{\rho}_n \rho_{air} \mathbf{V}) - \tilde{\rho}_n \nabla \cdot (\rho_{air} \mathbf{V})] + S_{\tilde{\rho}_n} \quad (5.18)$$

Note that in the incompressible case we have  $\rho_{air} = \text{constant}$  and  $\nabla \cdot (\rho_{air} \mathbf{V}) = 0$ . Substituting  $\tilde{\rho}_n = \rho_n / \rho_{air}$  and cancelling the factors of  $\rho_{air}$ , one recovers the more familiar expression of local charge continuity,  $\partial \rho_n / \partial t = -\nabla \cdot \mathbf{J}_n$ , with the current density  $\mathbf{J}_n$  replacing the charge motion  $\rho_n \mathbf{V}$ .

Equations (5.17) and (5.18) are mathematically equivalent and known as the advective and flux forms, respectively. The flux form is generally preferred in finite difference models because it has immediate conservation properties that are not guaranteed in an advective form.

To (5.18), we now add the turbulent mixing and sedimentation terms (second and third terms, respectively, on the right-hand side of the following):

$$\begin{aligned} \frac{\partial \tilde{\rho}_n}{\partial t} &= -\frac{1}{\rho_a} [\nabla \cdot (\tilde{\rho}_n \rho_a \mathbf{V}) - \tilde{\rho}_n \nabla \cdot (\rho_a \mathbf{V})] + \frac{1}{\rho_a} \nabla \cdot (\rho_a K_h \nabla \tilde{\rho}_n) \\ &\quad + \frac{1}{\rho_a} \frac{\partial (\tilde{\rho}_n \rho_a \bar{V}_{\tilde{\rho}_n})}{\partial z} + S_{\tilde{\rho}_n} \end{aligned} \quad (5.19)$$

where  $K_h$  is a mixing coefficient determined by the closure scheme employed by a given cloud model. The fall speed,  $\bar{V}_{\tilde{\rho}_n}$ , is usually the mass-weighted fall speed. For single-moment bulk microphysics, it is best to use the mass-weighted fall speed to prevent the particle mass from getting out of phase with the charge. This prevents unrealistically large particle charges from occurring during sedimentation.

The term  $S_{\tilde{\rho}_n}$  in (5.19) now represents charge sources and sinks through particle interactions. Examples of sources and sinks for the  $n$ th category include ion capture, charge exchange during collisions with particles in another category, and mass loss or gain as particles are transferred from one category to another. When mass is lost from one category to another, the charge carried by the mass also must be transferred to the new category, thereby decreasing the magnitude of charge in the category losing mass. However, the magnitude of charge in the category gaining mass can either decrease or increase, because the polarity of the charge gained with the new mass can be either the same as or opposite to the polarity of charge already on particles in the category. Since most processes can be either a source or a sink of charge for a given category of particle, it is not worthwhile to try to distinguish sources from sinks. Thus, we group all such processes together.

Note that the storm as a whole does not lose or gain charge unless charge is transferred to or from a region outside the storm. When the charge on particles in one category is altered by interactions with particles in other categories, a compensating change (equal in magnitude, opposite in sign) must occur in the charge of the other categories, so that the net charge summed over all categories remains the same. There are no compensating changes in the charge within the storm when the

charge on particles is altered by a process involving charge from outside regions, such as ground flashes, cloud-to-air flashes, capture of ions emitted by point discharge from the ground and screening layer formation at cloud boundaries.

Equation (5.19) can be rewritten in terms of the charge density by substituting  $\tilde{\rho}_n = \rho_n/\rho_{air}$  and expanding the left-hand side:

$$\frac{\partial \rho_n}{\partial t} = -\nabla \cdot (\rho_n \mathbf{V}) + \nabla \cdot [\rho_a K_h \nabla(\rho_n/\rho_a)] + \frac{\partial(\rho_n \bar{V}_n)}{\partial z} + S_n \quad (5.20)$$

Note that the advection part has been reduced to one term and that the second term effectively retains  $\tilde{\rho}_n$ . In many models, however, the scalar advection formulation is designed for parcel invariants (such as mass mixing ratio), so the formulation of (5.19) can use the same model code without modification. The state variable  $\rho_n$  has more physical meaning, however, than  $\tilde{\rho}_n$ , so a compromise is to transform  $\rho_n$  to  $\tilde{\rho}_n$  for advection and turbulent mixing, and then back to  $\rho_n$  for electrification processes.

As discussed by Pruppacher and Klett (1997),  $\bar{V}_n$  can be generalized to include the effect of electrostatic force in addition to gravity. If this is done, the third term on the right of (5.19) should be replaced by  $(1/\rho_{air}) \nabla \cdot (\rho_{air} \tilde{\rho}_n \mathbf{V}_n)$ , where  $\mathbf{V}_n$  is now a vector, not a scalar.

Many microphysical processes are capable of placing charge on particles. The main processes that have been included in cloud models are the non-inductive graupel–ice mechanism, the inductive mechanism and ion capture. The rest of this section considers treatments of each of these. Electrification mechanisms that have not yet been used in models are not considered here, although other mechanisms may be significant in some situations (e.g. melting processes may play a role in electrifying the stratiform precipitation region of storm systems).

### 5.4.3 *The non-inductive graupel–ice collision mechanism*

#### 5.4.3.1 **Parameterized laboratory results**

Parameterizing the non-inductive collision charge separation mechanism requires that the charge per hydrometeor collision be determined and then included in a bin or a bulk parameterization of all collisions involving a particular water substance category at a grid point during a time step of the model. Laboratory studies have found (1) that the non-inductive mechanism appears to be most effective when rimed graupel collides with cloud-ice particles or snow in a region that also has liquid water (i.e. the mixed-phase region) and (2) that the sign and magnitude of the charge that is transferred depend on ambient temperature, liquid water content and impact speed. The simplest parameterization of the non-inductive mechanism assumes that a constant value of charge is transferred per collision between particular hydrometeor types, as was done by Rawlins (1982) and Helsdon and Farley (1987b), both of whom assumed that the sign of charge transfer reversed polarity at  $-10^{\circ}\text{C}$  (see Table 5.1).

Table 5.1 Non-inductive parameterization of Helsdon and Farley (1987b)

Growth mode	Interacting types	$\delta q^*$ ( $fC = 10^{-15} C$ )	Temperature range
Dry	Graupel/cloud ice	-2	$T < -10^\circ C$
		-2	$T > -10^\circ C$
Wet	Graupel/snow	200	$T < -10^\circ C$
		200	$T > -10^\circ C$
Wet	Graupel/rain <sup>†</sup>	100	All $T$
	Graupel/cloud water <sup>‡</sup>	0	All $T$
	Graupel/rain <sup>‡</sup>	0	All $T$
Other	Rain/cloud water	0	All $T$

\*Polarity is for charge transferred to graupel (to rain in growth mode 'Other'); charge transferred to the particle colliding with graupel is of equal magnitude, but opposite polarity; <sup>†</sup>Splashing interactions;

<sup>‡</sup>Shedding or limited accretion.

Takahashi (1983, 1984) used the laboratory non-inductive charging data directly from Takahashi (1978). A lookup table of Takahashi's results (shown contoured in Figure 5.4) was developed by Randell *et al.* (1994) and was used in that and later studies (e.g. Helsdon *et al.*, 2001; Mansell *et al.*, 2005). The base charge per collision  $\delta q'$  was interpolated (or extrapolated) from the lookup table. Note that Takahashi (1978) did not factor in a collection efficiency, so the actual charge per rebounding ice collision would be higher than the charge per collision (which includes sticking collisions). The table covers a temperature range of

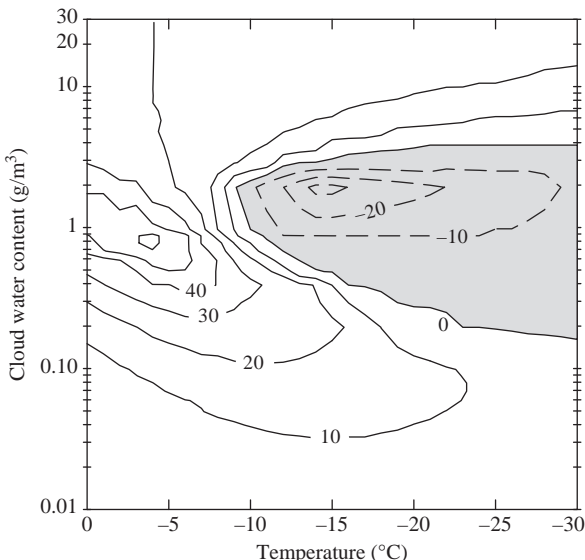


Figure 5.4 Takahashi (TAK) charging diagram (Takahashi, 1978), contoured from the tabulated data in Wojcik (1994), with charge separation in units of  $fC$

$0^{\circ}\text{C}$  to  $-30^{\circ}\text{C}$  and cloud water content from 0.01 to  $30 \text{ g/m}^3$ . For temperatures lower than  $-30^{\circ}\text{C}$ , the charge separation values at  $-30^{\circ}\text{C}$  were used. Takahashi (1984) accounted for charging dependence on crystal size and fall speed by multiplying the value obtained from the table by a factor  $\alpha$ :

$$\alpha = 5.0 \left( \frac{D_I}{D_0} \right)^2 \frac{\bar{V}_g}{V_0} \quad (5.21)$$

where  $D_I$  is the diameter of the ice crystal or snow particle,  $\bar{V}_g$  is the mass-weighted mean terminal fall speed of graupel and  $D_0 = 100 \mu\text{m}$  and  $V_0 = 8 \text{ m/s}$ . This factor was based on the work of Marshall *et al.* (1978). In Takahashi (1984), the value of  $\alpha$  was not allowed to be greater than 10.0 (i.e.  $\alpha \leq 10.0$ ). Thus, the final charge per collision is  $\delta q = \alpha \delta q'$ . Tsenova and Mitzeva (2009) tested the Takahashi scheme but used the results of Keith and Saunders (1990) regarding dependence on crystal size and impact speed, which significantly affected charge separation rates. Tsenova and Mitzeva (2009) also developed an equation set to parameterize the lookup table of the data from Takahashi (1978).

Based on the work of Jayaratne *et al.* (1983), Gardiner *et al.* (1985) suggested that the charge transferred to a rimed graupel/hail particle when it collides with a cloud-ice/snow particle could be parameterized by

$$\delta q = k_q D_i^m (\Delta v_{gi})^n (\text{LWC} - \text{LWC}_{crit}) \cdot f(\Delta T) \quad (5.22)$$

where  $k_q$  is a constant of proportionality approximately equal to 73,  $D_i$  is the diameter of the cloud-ice particle in centimeters,  $\Delta v_{gi}$  is the relative impact speed (in cm/s) between the graupel particle and ice crystal given by the difference in their terminal velocities,  $m \approx 4$ ,  $n \approx 3$ , LWC is the liquid (cloud) water content (in  $\text{g/m}^3$ ),  $\text{LWC}_{crit}$  is the value of the liquid water content below which the sign of  $\delta q$  reverses (a plot of  $\text{LWC}_{crit}$  as a function of  $T$  is given by Jayaratne *et al.*, 1983) and  $\Delta T$  is the degree of supercooling ( $\Delta T = 273.15 - T$  for  $T < 273.15 \text{ K}$  and is 0 otherwise). The function  $f(\Delta T)$  was a polynomial fit to the laboratory data of Jayaratne *et al.*:

$$f(\Delta T) = a\Delta T^3 + b\Delta T^2 + c\Delta T + d \quad (5.23)$$

where  $a = -17 \times 10^{-5}$ ,  $b = -0.003$ ,  $c = -0.05$ , and  $d = 0.13$  and  $\delta q$  is in fC ( $10^{-15}\text{C}$ ). Subsequent laboratory experiments showed that the increase in charge with ice-crystal diameter levelled off at large values of diameter, so the  $D_i^4$  dependence in (5.22) overestimated the charge transferred for large  $D_i$ .

Saunders *et al.* (1991) suggested a new, more complicated parameterization for  $\delta q$  that was based on laboratory experiments over a broader range of cloud-ice size, liquid water content and temperature. Their expression for charge (in fC), similar in functional form to that used by Gardiner *et al.* (1985), was

$$\delta q = BD_i^a (\Delta v_{gi})^b q(EW, T) \quad (5.24)$$

where  $EW$  is effective liquid water content, a parameter defined by Saunders *et al.* Unlike  $f(\Delta T)$  in (5.22) and (5.23), however,  $f(T, EW)$  had different functional forms in different regimes of temperature and effective liquid water content. Furthermore,  $k_q$ ,  $m$  and  $n$  depended on the size of the ice crystal and the polarity of charge transferred. These dependencies are shown in Table 5.2. Because data did not extend to temperatures greater than  $-7.4^\circ\text{C}$ , Helsdon *et al.* (2001) linearly extrapolated  $q(EW, T)$  at a particular  $EW$  from the value given by the expression in Table 5.2 for  $T = -7.4^\circ\text{C}$  to zero at  $T = -0^\circ\text{C}$ .

Saunders *et al.* (1991) used effective liquid water  $EW$  content instead of LWC, the liquid water content measured by in situ instruments and determined by most numerical cloud models, because their observations suggested that  $EW$  was more relevant to riming-based non-inductive charging.  $EW$  is a modification of LWC that includes only the accreted fraction of liquid water content in the path of graupel. Therefore, it is given by the product of the ambient liquid water content and the collection efficiency ( $EW = \text{LWC} \cdot E_{\text{collect}}$ ). The collection efficiency  $E_{\text{collect}}$  for graupel and water particles is equal to the product  $E_{\text{collect}} E_{\text{stick}}$ , where  $E_{\text{coll}}$  is the collision efficiency, a factor  $\leq 1$  that reduces the geometric cross section of graupel

Table 5.2 Non-inductive parameterization of Saunders *et al.* (1991)

Valid for				And for				
$T (\text{ }^\circ\text{C})$	$EW \text{ g/m}^3$	$\delta q$	Sign*	$q(EW, T)^*$ (fC)	$D_i (\mu\text{m})$	$B$	$a$	$b$
$<-20$ (PLEZ <sup>†</sup> )	$<0.16$	+		$2042EW - 129$ (for $0.06 < EW < 0.12$ )	$<155$	$4.92 \times 10^{13}$	3.76	2.5
				$-2900EW + 463$ (for $0.12 < EW < 0.16$ )	$155-452$	$4.04 \times 10^6$	1.9	
				$-314EW + 7.9$ (for $0.026 < EW < 0.14$ )	$>452$	52.8		0.44
$-7.4$ to $-16$ (NLEZ <sup>†</sup> )	$<0.22$	-		$419EW - 92.6$ (for $0.14 < EW < 0.22$ )	$<253$	$5.24 \times 10^8$	2.54	2.8
					$>253$	24		0.5
$-7.4$ to $T_r^{\ddagger}$	$>0.22$	+			$<155$	$4.92 \times 10^{13}$	3.76	2.5
				$20.2EW - 1.36T + 10.1$	$155-452$	$4.04 \times 10^6$	1.9	
					$>452$	52.8		0.44
$\leq 7.4^{\$}$	$>1.1^{\$}$	-			$<253$	$5.24 \times 10^8$	2.54	2.8
				$3.02 - 31.8EW + 26.5(EW)^2$	$\geq 253$	24		0.5

\*Sign (polarity) is for charge transferred to graupel. Charge on cloud-ice has opposite polarity. <sup>†</sup>PLEZ and NLEZ refer to positive/negative low  $EW$  zones (see Figure 5.5). <sup>‡</sup> $T_r$  is the temperature at which the polarity of charge gained by graupel reverses for a given value of liquid water content:  $T_r = -15.06EW - 7.38$ , for  $EW$  in  $\text{g/m}^3$  and  $T_r$  in  $^\circ\text{C}$ . <sup>§</sup>For regions where  $q(EW, T)$  is negative (at  $EW$  near 1.1 for  $T \leq -24^\circ\text{C}$ ), use  $q(EW, T) = 0$ . <sup>||</sup>Must also be outside previous ranges in  $T-EW$  space. For regions where  $q(EW, T)$  is positive (at  $-16^\circ\text{C} < T < -20^\circ\text{C}$  and  $EW \leq 0.1 \text{ g/m}^3$ ), use  $q(EW, T) = 0$ .

to account for aerodynamic effects that sweep small particles around graupel, and  $E_{\text{stick}}$  is the fraction of colliding particles that stick to the graupel surface (i.e. do not rebound). Saunders *et al.* (1991) noted that in their experiments,  $EW$  typically was roughly equal to  $\text{LWC}/2$ .

The polarity of charge that graupel gains for each combination of temperature and effective liquid water content under the parameterization described in Table 5.2 is shown graphically in Figure 5.5. The line dividing positive and negative charging for  $0.22 \text{ g/m}^3 < EW < 1.1 \text{ g/m}^3$  can be given in terms of critical values of either  $EW$  or  $T$ . Saunders *et al.* (1991) gave the following expression for  $EW_{\text{crit}}$  (in  $\text{g/m}^3$ ), valid for  $-10.7^\circ\text{C} > T > -23.9^\circ\text{C}$ :

$$EW_{\text{crit}} = -0.49 - 6.64 \times 10^{-2}T \quad (5.25)$$

An equation for the reversal temperature  $T_r$  can be obtained by inverting this equation (see footnote in Table 5.2).

Helsdon *et al.* (2001) noted that the expressions given in Table 5.2 resulted in much more charge per collision than observed for some particle sizes and collision speeds at small values of  $EW$  ( $<0.22 \text{ g/m}^3$  for positive charge and  $<0.16 \text{ g/m}^3$  for negative charge). Furthermore, model simulations using these expressions tended to produce thunderstorm charge distributions in which the majority of negative charge was located above positive charge during most of the period being simulated. When Helsdon *et al.* (2001) drastically reduced the amount of charge per collision to 10–20% of the value given by the expressions in Table 5.2 in the zones of low effective liquid water, model simulations produced a charge distribution similar to the charge distribution inferred from in situ measurements of the storm being analysed. Mansell *et al.* (2005) found that limiting the maximum charge transfer had an effect similar to that of reducing the influence of the low effective liquid water zones.

We note here that the charge per separation event reported by Saunders *et al.* (1991) was derived from the charging current, the ice crystal concentration

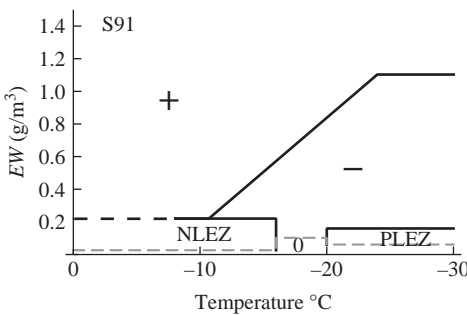


*Figure 5.5 Plot of the charging zones of the S91 (Saunders *et al.*, 1991) non-inductive ice–ice parameterization. The positive and negative low- $EW$  zones are indicated by PLEZ and NLEZ, respectively. Heavy dashed line indicates extrapolation to higher temperature (No charge separation occurs for conditions below the dashed grey line)*

(determined from Formvar slides) and an assumed ice crystal collection efficiency of approximately 0.5 (i.e. only about half of the colliding crystals will rebound). Models typically assume much lower collection efficiencies, with correspondingly higher rebound efficiencies. However, simulations generally have not accounted for this difference, which could cause overestimation of charging rates by up to a factor of 2.

Brooks *et al.* (1997) suggested that the rime accretion rate (RAR) may affect the sign and magnitude of charge per collision. They hoped to reconcile the results of Takahashi (1978) and Saunders *et al.* (1991), which had riming rod speeds of 9 m/s and 3 m/s, respectively. They converted the Saunders *et al.* (1991) results using  $RAR = EW\Delta V_{gi}/3$  (units of  $\text{gm}^{-2}\text{s}^{-1}$ ) in place of  $EW$  in the Saunders *et al.* (1991) parameterization, so that (5.25) became

$$RAR_{crit} = -1.47 - 0.02T \quad (5.26)$$

for the range  $-23.8^\circ\text{C} < T < -7.4^\circ\text{C}$ . (For  $T > -7.4^\circ\text{C}$  or  $T < -23.8^\circ\text{C}$ , one can use  $RAR_{crit}$  ( $T = -7.4^\circ\text{C}$ ) or  $RAR_{crit}$  ( $T = -23.8^\circ\text{C}$ ), respectively.) Brooks *et al.* (1997) also reported limited laboratory tests at  $-15^\circ\text{C}$  that showed that charging was similar for different combinations of  $V$  and  $EW$  that had the same  $RAR$ . Their reformulation left out the low effective liquid water zones, citing difficulty in reproducing results at low  $EW$ .

A follow-on study by Saunders and Peck (1998) examined charge reversal as function of  $RAR$ . They fit a sixth-order polynomial function  $RAR_{crit}$  to represent the critical  $RAR$  (Figure 5.6), above which graupel gained positive charge:

$$\begin{aligned} RAR_{crit}(T) = & 1.0 + 7.9262 \times 10^{-2}T + 4.4847 \times 10^{-2}T^2 \\ & + 7.4754 \times 10^{-3}T^3 + 5.4686 \times 10^{-4}T^4 \\ & + 1.6737 \times 10^{-5}T^5 + 1.7613 \times 10^{-7}T^6 \end{aligned} \quad (5.27)$$

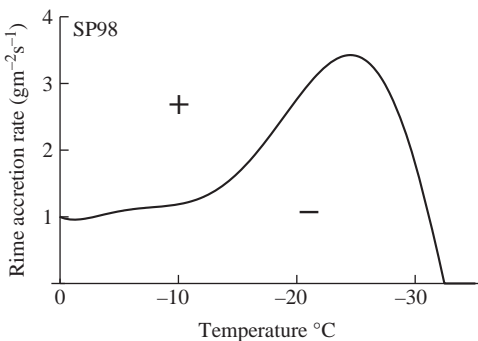


Figure 5.6 Plot of the critical rime accretion rate  $RAR_{crit}$  curve of Saunders and Peck (1998). Graupel charges positively at rime accretion rates above the curve and negatively below. Charge separation is assumed to cut off at about  $-33^\circ\text{C}$

which could then be used with the revised Brooks *et al.* (1997) charging parameterization. The fit is only valid to about  $-33^{\circ}\text{C}$ , below which Saunders and Peck (1998) expected charge separation to become negligible. Mansell *et al.* (2005) used a piece-wise continuous function to extend charge separation smoothly to zero over the low-temperature end of the curve from  $-33^{\circ}\text{C}$  to  $-40^{\circ}\text{C}$ .

For Brooks *et al.* (1997) and Saunders and Peck (1998), the mean separated charge per rebounding collision can be adapted for bulk distributions as

$$\delta q = k_q \overline{D}_{n,I}^m (\overline{V}_g - \overline{V}_I)^n q_{\pm}(\text{RAR}) \quad (5.28)$$

where  $\overline{V}_g$  and  $\overline{V}_I$  are the mass-weighted mean terminal speeds for graupel and cloud ice (or snow), respectively, and  $k_q$ ,  $m$  and  $n$  are constants that depend on crystal size as shown in Table 5.2. Mansell *et al.* (2005) altered the charge separation equations,  $q(\text{RAR}, T)$  from Brooks *et al.* (1997) so that they smoothly approach zero at  $\text{RAR} = \text{RAR}_{\text{crit}}$ . For positive charging of graupel ( $\text{RAR} > \text{RAR}_{\text{crit}}$ ),

$$q_+(\text{RAR}) = 6.74(\text{RAR} - \text{RAR}_{\text{crit}}) \quad (5.29)$$

For negative charging ( $0.1 \text{ gm}^{-2} \text{ s}^{-1} < \text{RAR} < \text{RAR}_{\text{crit}}$ ),

$$q_-(\text{RAR}) = 3.9(\text{RAR}_{\text{crit}} - 0.1) \times \left( 4 \left[ \frac{\text{RAR} - (\text{RAR}_{\text{crit}} + 0.1)/2}{(\text{RAR}_{\text{crit}} - 0.1)} \right]^2 - 1 \right) \quad (5.30)$$

Note that there is an implicit temperature dependence since  $\text{RAR}_{\text{crit}}$  varies with temperature. The negative charging equation (5.30) shifts the parabolic function given in Brooks *et al.* (1997) to fit between the limits of  $0.1 \text{ gm}^{-2} \text{ s}^{-1}$  and  $\text{RAR}_{\text{crit}}$ , removing the discontinuity at  $\text{RAR}_{\text{crit}}$  in the original formulation. Charging is assumed to be zero for  $\text{RAR} < 0.1 \text{ gm}^{-2} \text{ s}^{-1}$ .

Few quantitative results are available on charge separation at temperatures less than  $-30^{\circ}\text{C}$ . (One example is Saunders and Peck, 1998, which examined the sign of charging, but not the quantity, at lower temperature.) Therefore, lacking experimental guidance, Mansell *et al.* (2005) suggested limiting charging at low temperature by an arbitrary factor  $\beta$ , such as

$$\beta = \begin{cases} 1 & : T > -30^{\circ}\text{C} \\ 1 - [(T + 30)/13]^2 & : T_{\text{hom}} > T < -30^{\circ}\text{C} \\ 0 & : T < T_{\text{hom}} \end{cases} \quad (5.31)$$

The low-temperature cut-off is made at  $T_{\text{hom}} \approx -38^{\circ}\text{C}$  because all cloud droplets are homogeneously frozen by that temperature, so no further riming occurs. Deep convective updrafts, however, may maintain ice supersaturation for  $T < T_{\text{hom}}$ , which might support appreciable charge separation but no laboratory data exist. Mitzeva *et al.* (2006) used a one-dimensional cloud model to explore possible consequences of allowing collisional non-inductive charge separation in

regions with supersaturation with respect to ice but without any liquid hydrometeors.

### 5.4.3.2 General formulation

In models with bin microphysics for graupel and cloud ice, the derivation of an expression for the rate at which graupel and cloud-ice charge densities ( $\rho_g$  and  $\rho_i$ , respectively) build due to the non-inductive mechanism is fairly simple. Per unit time, the volume in which a graupel particle of diameter  $D_g$  collides with cloud-ice particles of diameter  $D_i$  is just the product of the cross-sectional area  $\pi(D_g + D_i)^2/4$  (the area of a circle in which graupel and ice particles just touch) times the vertical fall speed of graupel relative to cloud-ice particles,  $\Delta V_{gi} = |V_{gT} - V_{iT}|$ . To compute a charging rate, the volume swept out by a graupel particle per unit time must be multiplied by the collision separation efficiency for graupel and ice ( $E_{gi}$ ), which is the fraction of ice particles in this volume that collide with the graupel and separate from it.  $E_{gi}$  is equal to the product  $E_{colli} E_{sep}$ , where  $E_{colli}$  is a factor that accounts for aerodynamic effects, as discussed previously, and  $E_{sep}$  is the fraction of colliding particles that separate ( $E_{sep} = 1 - E_{stick}$ , where  $E_{stick}$  is the fraction accreted by graupel). The modified volume per unit time is called the collision kernel  $K_{gi}$  and can be expressed as

$$K_{gi} = \frac{\pi}{4} (D_g + D_i)^2 \Delta V_{gi} E_{gi} \quad (5.32)$$

If  $n_g$  is the number density of graupel particles of diameter  $D_g$ , then the rate at which  $n_g$  graupel particles collide and separate from  $n_i$  cloud-ice particles is given by  $K_{gi} n_g n_i$ , and the rate at which this process charges graupel of diameter  $D_g$  and cloud ice of diameter  $D_i$  is

$$\begin{aligned} \frac{\partial \rho_g}{\partial t} &= K_{gi} n_g n_i \delta q \\ &= - \frac{\partial \rho_i}{\partial t} \end{aligned} \quad (5.33)$$

The expression for non-inductive charging between graupel and snow is the same as (5.32) and (5.33), except that the parameters for cloud ice are replaced by those for snow ( $n_s$ ,  $D_s$ ,  $E_{gs}$  and  $\Delta V_{gs}$ ). Similarly for hail and snow, graupel parameters are changed to the values for hail ( $n_h$ ,  $D_h$ ,  $E_{hs}$  and  $\Delta V_{hs}$ ), although  $\delta q$  has not yet been determined by laboratory experiments specifically for hail.

To determine the rate of change in charge density for graupel in a particular size category of a model with bin microphysics, it is necessary to add together the contributions given by (5.33) for every size category of snow and cloud ice that interacts with the graupel. Likewise, the rate of change in charge density on a particular size category of cloud ice or snow must include the contribution from all size categories of graupel and hail.

To determine the rate of change in charge density on a particular type of hydrometeor in a model with bulk microphysics, two approaches have been used.

The first is to evaluate (5.33) at a grid point by determining mean values of  $\delta q$  and  $K_{gi}$  and the total concentrations across all sizes for  $N_g$  and  $N_i$  at that grid point. The second approach is to integrate the right-hand side of (5.33) across all sizes both of that hydrometeor category and of every other category with which that category interacts. For example, the change in charge density of graupel due to collisions with snow or cloud ice is

$$\frac{\partial \rho_g}{\partial t} = \frac{\pi}{4} \int \int (D_g + D_i)^2 \Delta V_{gi} E_{gi} n_g(D_g) n_i(D_i) \delta q \, dD_i \, dD_g \quad (5.34)$$

where the subscript  $i$  refers to either snow or cloud ice. The size distributions  $n(D)$  often are assumed to have the form of the inverse exponential distribution (5.2 with  $\alpha = 0$ ) with parameters  $n_0$  and  $\Lambda$ . For cloud ice, because  $D_i \ll D_g$  and  $V_{iT} \ll V_{gT}$ , the magnitude of sums and differences of these quantities can be approximated as  $D_g$  and  $V_{gT}$  in (5.34). To evaluate this integral for cloud ice, Ziegler *et al.* (1986) assumed further that, since cloud ice typically has a narrow size distribution, it can be approximated as a population with a single average diameter  $\bar{D}_i$ . If  $N_i$  is the total concentration of cloud-ice particles, this implies that

$$\frac{\partial \rho_g}{\partial t} = \frac{\pi}{4} N_i E_{gi} \int (D_g + \bar{D}_i)^2 \Delta V_{gi} n_g(D_g) \delta q \, dD_g \quad (5.35)$$

The general formulation of (5.34) for the non-inductive charge (density) separation rate  $\partial \rho_{xy}/\partial t$  between ice hydrometeor classes  $x$  and  $y$  is

$$\frac{\partial \rho_{xy}}{\partial t} = \int_0^\infty \int_0^\infty \frac{\pi}{4} \delta q'_{xy} (1 - E_{xy}) |\Delta V_{xy}| \times (D_x + D_y)^2 n_x(D_x) n_y(D_y) \, dD_x \, dD_y \quad (5.36)$$

where  $D_x$  and  $D_y$  are the diameters of the colliding particles,  $E_{xy}$  is collection efficiency,  $\Delta E_{xy}$  is the relative fall speed,  $n_x$  and  $n_y$  are number concentrations and  $\delta q'_{xy}$  is the charge separated per rebounding collision. In general,  $\delta q'_{xy}$  may be a function of ice-crystal diameter, impact speed, cloud water content and temperature. The collection efficiency  $E_{xy}$  is the product of the collision efficiency ( $E_{colli}$ , assumed to be unity) and the probability of sticking given a collision ( $E_{stick}$ ). In wet-growth mode, one may assume  $E_{x,y} = 1$ , and no charge separation occurs.

As it stands, (5.36) is not a tractable integrand. The equation can be approximated and simplified by assuming a form for  $\delta q'_{xy}$  that can be pulled out of the integral. Also, the fall speed difference is approximated by the difference of mass-weighted mean fall speeds. The collection efficiency is assumed to be constant. Multiplying and dividing by  $E_{xy}$  then isolates the number concentration collection rate integral ( $n_{xacy}$ ):

$$\frac{\partial \rho_{xy}}{\partial t} = \beta \delta q_{xy} (1 - E_{xy}) E_{xy}^{-1} (n_{xacy}) \quad (5.37)$$

where

$$n_{xacy} = E_{xy} \overline{\Delta V}_{xy} \times \int_0^\infty \int_0^\infty \frac{\pi}{4} (D_x + D_y)^2 n_x n_y dD_x dD_y \quad (5.38)$$

and  $\delta q_{xy}$  is now a representative (weighted average) separated charge per rebounding collision and  $(1 - E_{xy})$  represents the rebound probability. Each of the non-inductive charging schemes uses the monodisperse diameter  $D$  for pristine ice crystals (plates and solid columns) but the characteristic diameter  $D_n = 1/\lambda_n$  to represent the average size of an inverse exponential (IE) distribution (e.g. rimed cloud ice and ice aggregates). The number concentration collection rate  $n_{xacy}$  is calculated by an analytical approximation. For an inverse exponential distribution category ( $x_e$ ) interacting with a monodisperse distribution ( $y_m y_m$ ) the number concentration collection rate is

$$n_{x_e acy_m} = \frac{\pi}{4} E_{xy} n_y n_x \overline{\Delta V}_{xy} \times [\Gamma(3) D_{n,x}^2 + 2\Gamma(2) D_{n,x} D_y + \Gamma(1) D_y^2] \quad (5.39)$$

Similarly, for an inverse exponential distribution ( $x_e$ ) interacting with another inverse exponential distribution ( $y_e$ ), the number concentration collection rate is

$$n_{x_e acy_e} = \frac{\pi}{4} E_{xy} n_y n_x \overline{\Delta V}_{xy} [\Gamma(3) \Gamma(1) D_{n,x}^2 + 2\Gamma(2) \Gamma(2) D_{n,x} D_{n,y} + \Gamma(1) \Gamma(3) D_{n,y}^2] \quad (5.40)$$

Collision rates for other size distribution functions (e.g. a general Gamma function) are beyond the scope of this chapter. For other collision rates, readers are referred to studies of microphysics parameterizations such as Milbrandt and Yau (2005) and Seifert and Beheng (2006).

#### 5.4.4 The inductive charging mechanism

As defined above, the inductive mechanism occurs in the presence of an electric field. Laboratory studies (e.g. Aufdermaur and Johnson, 1972; Gaskell, 1981; Brooks and Saunders, 1994) and theory (e.g. Mason, 1988) suggest (1) the magnitude of charge transferred is a function of both the magnitude of the electric field and the angular distance of the impact point from the electric field vector through the centre of the particle, (2) inductive charging during collisions of ice particles appears to be negligible because charge transfer is too slow in ice (Latham and Mason, 1962), (3) collisions of rain drops and cloud droplets do not contribute significant charge because essentially no cloud droplets separate after they collide with rain drops in an electric field and (4) only a small fraction of colliding rain drops or colliding graupel and cloud droplets subsequently separate, but enough charge is separated to be significant (Aufdermaur and Johnson, 1972). The expression for the

induced charge gained by a spherical graupel or hail particle in a rebounding collision with a cloud droplet in an electric field is

$$\Delta Q_g = -4\pi\epsilon_0\gamma_1|E|\cos\theta_{E,r}r_{cld}^2 - A Q_g + B Q_{cld} \quad (5.41)$$

where  $r_{cld}$  is the radius of the cloud droplet;  $\theta_{E,r}$  is the angle between the impact point and the electric field vector through the centre of the graupel/hail particle (shown in Figure 5.1);  $Q_g$  and  $Q_{cld}$  are the charge already on the graupel/hail particle and cloud droplet, respectively;  $\gamma_1$ ,  $A$  and  $B$  are dimensionless functions of  $r_{cld}/r_g$  the ratio of the radii of the two particles:

$$A = \frac{\gamma_2(r_{cld}/r_g)^2}{1 + \gamma_2(r_{cld}/r_g)^2} \quad (5.42)$$

$$B = \frac{1}{1 + \gamma_2(r_{cld}/r_g)^2} \quad (5.43)$$

Parameterizing the inductive mechanism requires procedures similar to those used in parameterizing the non-inductive mechanism, except it is necessary to take into account that the mechanism's effectiveness is a function of where on their surfaces two particles collide. The charge produced by the inductive mechanism is strongly dependent on the angle between the impact point and the electric field vector. As shown in Figure 5.1 for a spherical graupel particle, the magnitude of the induced surface charge density is largest at the two ends of the diameter that parallels the electric field vector: As the angle from the electric field increases to  $90^\circ$ , the surface charge density decreases to zero. Besides this effect, the probability that colliding graupel and cloud droplets will separate can vary with the angle of the impact point from the vertical axis. Moore (1975) suggested that the separation probability is much larger for glancing collisions than for head-on collisions. Since colliding particles must separate for the inductive mechanism to work, the angular dependence of charge transfer and separation probability can interact in complicated ways. The mechanism will be most effective at the location on the graupel surface where the product of the induced surface charge density and the collision separation probability is largest.

Regardless of whether a model uses bulk or bin microphysics, the inductive parameterization must handle the complication of these interacting factors. Chiu (1978) treated them by defining a mean separation probability  $\langle S \rangle$  and a mean impact cosine  $\langle \cos \varphi \rangle$

$$\langle S \rangle = \frac{1}{\pi r_g^2} \int_0^{\pi/2} S(\varphi) 2\pi r_g^2 \sin \varphi \cos \varphi d\varphi \quad (5.44)$$

$$\langle \cos \varphi \rangle = \frac{1}{\langle S \rangle} \int_0^{\pi/2} 2S(\varphi) \sin \varphi \cos^2 \varphi d\varphi \quad (5.45)$$

where the weighting factor under the first integral is an infinitesimal area in the horizontal cross section of the graupel particle. Then the mean charge transferred to a graupel particle by colliding with and separating from cloud droplets is

$$\delta Q_g = \langle S \rangle [4\pi\epsilon_0\gamma_1 |\mathbf{E}| \cos \theta_{E,z} r_{cld}^2 \langle \cos \varphi \rangle - A \langle Q_g \rangle + B \langle Q_{cld} \rangle] \quad (5.46)$$

where  $\theta_{E,z}$  is the angle between the electric field vector and the lower vertical axis and  $\langle Q_g \rangle$  and  $\langle Q_{cld} \rangle$  are the mean charge per particle on graupel and cloud droplets, respectively. The rate at which this process charges a group of graupel particles of radius  $r_g$  due to collisions with cloud droplets of radius  $r_{cld}$  is found by multiplying the charge transferred per collision by the sweep-out volume of the graupel particle and the number concentrations of graupel and cloud particles:

$$\frac{\partial \rho_g(r_g, r_{cld})}{\partial t} = \pi r_g^2 \Delta v_{g,cld} E_{colli} n_g(r_g) n_{cld}(r_{cld}) \delta Q_g \quad (5.47)$$

where  $n_g(r_g)$  and  $n_{cld}(r_{cld})$  are the number density of graupel and cloud liquid water particles of radius  $r_g$  and  $r_{cld}$ , respectively, and  $E_{colli}$  in this case is the collision efficiency for graupel and cloud particles (i.e. the fraction of cloud particles in the volume swept out by the graupel particle that actually collide with it). This expression neglects  $r_{cld}$  in the sum  $r_{cld} + r_g$  for the cross-sectional area ( $\pi r_g^2$ ).

The rate at which charge is generated by a parameterization of the inductive mechanism depends strongly on the values selected for  $\langle S \rangle$  and  $\langle \cos \varphi \rangle$ . If the mean separation probability is 1 (i.e. all colliding particles separate) and  $\langle \cos \varphi \rangle = 0.67$ , then the mechanism's effectiveness is maximized. This is almost certainly an overestimate. Some studies, such as Moore (1975) and Aufdermaur and Johnson (1972), suggested that it is orders-of-magnitude too large. Helsdon and Farley (1987b) used a mean separation probability of 0.015 in their model experiment and a mean cosine of 0.5. Mansell *et al.* (2005) tested a range of values and found that higher efficiencies could have a significant effect on simulated charge structure.

As is the case for the graupel–ice non-inductive mechanism, models with bulk microphysics must integrate the charge produced by the inductive mechanism across all sizes of interacting hydrometeors, so the total rate of change in the charge density of graupel would be given by integrating (5.47) over all values for cloud radius and graupel radius. Helsdon and Farley (1987b) approximated the integration by replacing  $r_{cld}$ ,  $r_g$ ,  $\Delta v_{g,cld}$  and  $E_{colli}$  with their mean values at a grid point, thereby treating them as constants in the integral. The remaining integration of  $n_g(r_g) n_{cld}(r_{cld})$  over all radii gave simply the total number density of graupel times the total number density of cloud droplets at the grid point being considered.

Ziegler *et al.* (1991) developed a bulk parameterization based on several simplifying assumptions. Consistent with their parameterization of the non-inductive mechanism discussed above, they considered only  $D_{cld} \ll D_g$  and  $v_{cldT} \ll v_{gt}$  and so ignored the cloud droplet term in sums and differences of these quantities. Furthermore, they assumed that the narrow droplet size spectrum could be approximated as a population having a single diameter  $D_{cld}$ , and they used values of

$\gamma_1 \approx \pi^2/2$ ,  $\gamma_2 \approx \pi^2/6$  and  $A \approx \gamma_2(D_{cld}/D_g)^2$ , which were appropriate for  $D_{cld}/D_g \ll 1$ . In considering the collision process for inductive charging, it was assumed that only a small fraction of graupel and cloud particles separates after they collide, as found by Aufdermaur and Johnson (1972), and that rebounding occurs only during glancing collisions, as suggested by Moore (1975). Since the probability that any one cloud droplet will experience two rebounding collisions with graupel is much lower than the probability that it will experience one, the ‘B’ term involving pre-existing droplet charge (5.47) was omitted. (Droplets could not gain charge by any other mechanism in their model, which is not the case for models that treat small ion attachment or screening layers.) Furthermore, they considered only a vertical electric field, since it was the vertical electric field that had been hypothesized to contribute to thunderstorm electrification by the inductive mechanism. The equation for the rate at which charge was gained by a graupel particle of diameter  $D_g$  from the inductive mechanism then became

$$\frac{\partial Q_g}{\partial t} = \left(\frac{\pi}{4}\right) E_{gc} E_r D_g^2 v_g n_{cld} \alpha \left[ \left(\frac{\pi^3}{2}\right) D_{cld}^2 \varepsilon_0 E_z \langle \cos \varphi \rangle - \left(\frac{\pi^2}{6}\right) \langle Q_g \rangle \frac{D_{cld}^2}{D_g^2} \right] \quad (5.48)$$

where  $\alpha$  is the fraction of collisions that have glancing trajectories,  $n_{cld}$  is the total number concentration of cloud particles,  $E_{gc}$  and  $E_r$  are the collision and rebound probabilities and  $E_z$  is the vertical electric field component. Ziegler *et al.* (1991) integrated this equation for single-moment graupel (inverse exponential distribution with intercept  $n_{0g}$ ) to get

$$\frac{\partial \rho_g}{\partial t} = (\pi^3/8) \varepsilon_{gc} \varepsilon_r n_{cld} n_{0g} \alpha D_{cld}^2 (4g\rho_I/3C_D \rho_{air})^{1/2} \times \left[ \pi \Gamma(3.5) \varepsilon E_z \langle \cos \varphi \rangle \lambda_g^{-7/2} - \Gamma(1.5) \rho_g \lambda_g^{-3/2} / (3n_g) \right] \quad (5.49)$$

where  $\Gamma(1.5) = 0.886$  and  $\Gamma(3.5) = 3.323$ . They chose  $E_{gc} = 0.84$ ,  $E_r = 0.1$ ,  $\alpha = 0.022$  and  $\langle \cos \varphi \rangle = 0.1$ , which gave a probability of rebounding collisions  $p_{rbnd} = E_{gc} E_r \alpha$  near the lower end of the range found by Aufdermaur and Johnson (1972).

#### 5.4.5 Small ion processes

Some models (e.g. Chiu, 1978; Takahashi, 1979; Helsdon and Farley, 1987a; Mansell *et al.*, 2005) explicitly treat space charge on free ions (as opposed to charge carried by hydrometeors) and incorporate ion capture by hydrometeors in order to examine how ion capture affects cloud electrification. Although an explicit treatment of ions creates difficulties, it also enables a model to deal with important phenomena, including the early stages of electrification (when charging by other electrification processes is small or non-existent), precipitation capture of ions emitted as corona beneath a storm, screening layer charge at cloud boundaries, and the dispersal and capture of ions from a lightning channel.

Cosmic rays are the source of most ions in the fair-weather troposphere, except near the ground; radioactive decay from the surface contributes up to half of the ions found near ground. In fair weather, the number of positive ions is roughly equal to the number of negative ions, so the net charge density results from small differences of large numbers of ions. Ions move under the influence of the electric field  $\mathbf{E}$  and their average drift velocity in a given  $\mathbf{E}$  is the mobility times the electric field  $\mu_{\pm}\mathbf{E}$ , where subscript gives the polarity of the ions. The mobility  $\mu_{\pm}$  increases with decreasing pressure and so increases with height (i.e. the mean free path increases).

Each polarity of ion must obey its own continuity equation, which is similar to (5.20) for charge attached to hydrometeors. For ions, however, a term must be added to account for average charge motion under the influence of the electric field, since the resulting ion drift velocity can easily be much different than wind velocities. Also, the source/sink term often is split into sources and sinks occurring in fair weather and those requiring clouds or thunderstorms (e.g. Chiu, 1978; Helsdon and Farley, 1987b). The continuity equation for free ions can be written as

$$\frac{\partial n_{\pm}}{\partial t} = -\nabla \cdot [n_{\pm} \mathbf{V} \pm n_{\pm} \mu_{\pm} \mathbf{E}] + \frac{1}{\rho_{air}} \nabla \cdot K_m \nabla \left( \frac{n_{\pm}}{\rho_{air}} \right) + G - \alpha n_+ n_- - S_{att} + S_{pd} + S_{evap} \quad (5.50)$$

where  $n_+$  is the number density of positive ions and  $n_-$ , the number density of negative ions. Advection (the first term in the brackets) and turbulent mixing (the second full term) are treated the same as for the other scalar variables. The second term in the brackets is the ion drift motion, which can be treated similarly to the advection term.  $G$  is the background cosmic ray ion generation rate;  $\alpha n_+ n_-$  is the ion recombination rate and the last three terms, respectively, are ion attachment to hydrometeors (sink), point discharge current from the surface (source) and release of any charge as ions from hydrometeors that evaporate completely (source). If the ion drift speeds exceed the maximum for stable transport at the time step of the model, then the ion processes (except advection and turbulent mixing) can be performed on a subdivided time step, leaving the dynamical time step unchanged.

The fair-weather state can be defined as in Gish (1944), using the modified coefficients of Helsdon and Farley (1987b):

$$E_{z,FW} = E_0 (b_1 e^{-a_1 z} + b_2 e^{-a_2 z} + b_3 e^{-a_3 z}) \quad (5.51)$$

where  $E_0 = -80.0$  V/m,  $b_1 = 0.5$ ,  $a_1 = 4.5 \times 10^{-3}$ ,  $b_2 = 0.65$ ,  $a_2 = 3.8 \times 10^{-4}$ ,  $b_3 = 0.1$  and  $a_3 = 1.0 \times 10^{-4}$ .

At steady state in a fair-weather condition, the vertical positive and negative ion fluxes are

$$\frac{d}{dz} (n_+ \mu_+ E_{z,FW}) = G(z) - \alpha n_+ n_- \quad (5.52)$$

$$-\frac{d}{dz} (n_- \mu_- E_{z,FW}) = G(z) - \alpha n_+ n_- \quad (5.53)$$

where  $G(z)$  is the ion generation rate by cosmic rays (held constant as a function of altitude) and  $\alpha = 1.6 \times 10^{-12} \text{ m}^{-3} \text{ s}$  is the ionic recombination coefficient (Chiu, 1978).

The ion mobilities  $\mu$  from Shreve (1970) are given by

$$\mu_{\pm} = \beta_{\pm} e^{1.4 \times 10^{-4} z} \quad (5.54)$$

where  $\beta_+ = 1.4 \times 10^{-4} \text{ m}^2 \text{ V}^{-1} \text{ s}^{-1}$  and  $\beta_- = 1.9 \times 10^{-4} \text{ m}^2 \text{ V}^{-1} \text{ s}^{-1}$  and  $z$  is in metres. Diffusivity is derived from mobility by the Einstein relation

$$D_{\pm} = \frac{kT}{e} \mu_{\pm} \quad (5.55)$$

where  $k$  is Boltzmann's constant,  $T$  is the temperature (in Kelvin) and  $e$  is the electron charge magnitude (ions are assumed to be singly charged).

Under steady-state (i.e. fair-weather) conditions, one may assume that the ion currents and charge densities vary negligibly from constant values, so that  $\nabla \cdot \mathbf{j}_{\pm} = 0$ . Therefore, from (5.52) we get

$$G(z) = \alpha n_{+,FW}(z) n_{-,FW}(z) \quad (\text{steady state}) \quad (5.56)$$

(as in Takahashi, 1979) and the cosmic ray generation rate can be held constant in time throughout a simulation.

Ion attachment to hydrometeors is a combination of diffusion,  $S_{diff}$ , and conduction,  $S_{cond}$ . As in Chiu (1978), the two terms are calculated separately and added ( $S_{att} = S_{diff} + S_{cond}$ ). The equations from Chiu (1978) (based on Whipple and Chalmers, 1944) for attachment by conduction can be found in Table 5.3. In Chiu (1978), the vertical component of the electric field was used to calculate

*Table 5.3 Expressions for ion capture via conduction*

$Q_j$	$\mathbf{E} \parallel \mathbf{V}_T$ or $\mathbf{E} \parallel -\mathbf{V}_T$	$\mu_{\pm} E $	$\partial n_+/ \partial t^*$	$\partial n_- / \partial t^*$
$Q_j > Q_M^{\dagger}$	Either	Any value	0	$n_- n_j \mu_- Q_j \varepsilon^{-1}$
$Q_j < -Q_M^{\ddagger}$	Either	Any value	$-n_+ n_j \mu_+ Q_j \varepsilon^{-1}$	0
$0 < Q_j < Q_M$		$\mu_+  E  <  V_T $	0	
$-Q_M < Q_j < 0$	Parallel		$-n_+ n_j \mu_+ Q_j \varepsilon^{-1}$	$n_- n_j \mu_-  E  (3\pi r_j^2) \cdot [1 + Q_j/Q_M]$
$-Q_M < Q_j < Q_M$		$\mu_+  E  <  V_T $	$n_+ n_j \mu_+  E  (3\pi r_j^2) \cdot [1 - Q_j/Q_M]$	
$0 < Q_j < Q_M$		$\mu_-  E  <  V_T $		$n_- n_j \mu_- Q_j \varepsilon^{-1}$
$-Q_M < Q_j < 0$	Anti-parallel		$n_+ n_j \mu_+  E  (3\pi r_j^2) \cdot [1 - Q_j/Q_M]$	0
$-Q_M < Q_j < Q_M$		$\mu_-  E  <  V_T $		$n_- n_j \mu_-  E  (3\pi r_j^2) \cdot [1 + Q_j/Q_M]$

\*  $n_j = n_j(r_j)$ . † Hydrometeor completely positive. ‡ Hydrometeor completely negative; from Chiu (1978) based on Whipple and Chalmers (1944). The minimum charge on a particle needed to prevent polarization is  $Q_M \equiv 12\pi\varepsilon|E|r_j^2$ .

$S_{cond}$  (i.e.  $|E|$  is replaced by  $|E_z|$ ). The equation for diffusion attachment used by Mansell *et al.* (2005) is similar to Chiu (1978) and Helsdon (1980):

$$S_{diff\pm} = \left( \frac{\partial n_\pm}{\partial t} \right)_{diff} = \sum_j 4\pi r_j D_\pm n_\pm n_j f(X_j) \left[ 1 - \frac{r_j V_{Tj}}{2\pi D_\pm} \right] \quad (5.57)$$

where  $r_j$ ,  $V_{Tj}$  and  $n_j$  are the mean radius, mean terminal fall speed and number concentration of the  $j$ th hydrometeor category, respectively. The factor  $f(X_j)$  is from Helsdon (1980):

$$f(X_j) = \frac{X_j}{e^{X_j} - 1} \quad (5.58)$$

where  $X_j = Q_j/Q_D$ ;  $Q_j$  is the charge per particle in hydrometeor category  $j$  and  $Q_D = 4\pi r_j k_B T/e$  is the hydrometeor charge at which the electric potential and thermal energies are balanced at the surface. In Helsdon (1980),  $X_j$  was allowed to become negative, which enhances diffusion for ions of opposite charge [i.e.  $f(X_j) > 1$ ]. Alternatively, one can allow only non-negative values of  $X_j$  [i.e.  $f(X_j) \leq 1$ ] to avoid the possibility of double-counting the ion attachment by conduction (Chiu, 1978).

A point ion discharge current  $j_{pd}$  (corona current) from features at the surface can be allowed when the vertical electric field component at the ground exceeds a given threshold ( $|E_z| > E_0$ ). The formulation used here (as in Takahashi, 1984) follows Jhawar and Chalmers (1967) with values of Standler and Winn (1979):

$$j_{pd} = CE_z(|E_z| - E_0)^2 \quad (5.59)$$

where  $C = 2 \times 10^{-20}$  A m V $^{-3}$ , and  $E_0 = 5 \times 10^3$  V m $^{-1}$  and  $E_z$  is the vertical electric field component at the ground. The discharge current  $j_{pd}$  is converted to an ion concentration rate  $S_{pd\pm}$  as

$$S_{pd\pm} = \frac{j_{pd}}{q_e \Delta z} \quad (5.60)$$

where  $q_e$  is the electron charge magnitude and  $\Delta z$  is the vertical grid spacing at the first scalar grid point above ground. Note that  $S_{pd+} = 0$  for  $E_z < E_0$  and  $S_{pd-} = 0$  for  $E_z > -E_0$ .

When  $E_z$  exceeds 15–20 kV m $^{-1}$ , the cubic formulation begins to overpredict the average point discharge for a typical model time step of 3–5 s and thus can cause an overshoot in the ion density. A much smaller time step (e.g. Standler and Winn, 1979) would allow the initial large discharge rates to feed back quickly to limit further corona, as would occur in nature. Limiting the magnitude of  $E_z$  to 15 kV m $^{-1}$  in (5.59) still allows the modelled surface electric field to recover from large electric field impulses (over 30 kV m $^{-1}$ ) within a reasonable time (6–10 s) and avoids excessive responses in corona current (e.g. to impulses from CG flashes).

## 5.5 Lightning parameterizations

Simulations of electrical evolution need some form of lightning discharge parameterization to prevent electric field magnitudes from growing to unrealistic values. Lightning parameterizations also allow the study of relationships between storm properties (e.g. updraft mass flux and total graupel mass) and lightning discharge rates (e.g. flash rate and charge discharge rate). A number of discharge parameterizations were noted in Section 5.3. This section describes some recent parameterizations designed for three-dimensional models.

The lightning parameterization of MacGorman *et al.* (2001) attempted to overcome shortcomings of previous schemes, which either reduced high-charge regions in bulk (e.g. Rawlins, 1982; Takahashi, 1987; Ziegler and MacGorman, 1994) or did not treat horizontal branching (Heldson *et al.*, 1992) in one or more layers inferred from observations (e.g. Lhermitte and Krehbiel, 1979; MacGorman *et al.*, 1981; Shao and Krehbiel, 1996). MacGorman *et al.* (2001) applied the MacGorman *et al.* (1981) hypothesis that each layer of lightning channels corresponds to a major region of thunderstorm charge to develop a parameterization of lightning that could mimic observed lightning structure. The parameterization explicitly delineates lightning discharge regions according to ambient electric potential surfaces and charge density. The MacGorman *et al.* (2001) lightning parameterization has three basic steps: (1) A lightning channel is initiated in a region of high electric field as a bidirectional unbranched single channel. (2) Branching volumes are determined within the potential surfaces defined by the channel tip values when the channel propagation stops at a preselected threshold of the storm's electric field. (3) Charge is deposited at connected points of sufficient net charge density within the branching volumes.

In the MacGorman *et al.* (2001) scheme (Table 5.4), a flash occurs when the electric field magnitude exceeds the initiation threshold  $E_{init}$  anywhere in the model domain. In MacGorman *et al.* (2001), a uniform threshold of  $150 \text{ kV m}^{-1}$  was used

*Table 5.4 Variables and suggested values of the MacGorman *et al.* (2001) lightning parameterization affecting lightning structure or charge*

Variable	Value	Description
$E_{init}$	$150 \text{ kV m}^{-1}$	Threshold value of $E$ for determining when a flash will occur
$\delta E_{init}$	$10 \text{ kV m}^{-1}$	Offset from $E_{init}$ to determine grid points available for lightning initiation
$E_{stop}$	$15 \text{ kV m}^{-1}$	Minimum $ E $ above which initial channel propagation is allowed
$\rho_{chan}$	$0.5 \text{ nC m}^{-3}$	Minimum $ \rho(i, j, k) $ for grid points to be involved in lightning beyond initial propagation
$\rho_{neut}$	$0.5 \text{ nC m}^{-3}$	Magnitude of $ \rho(i, j, k) $ not available to a flash (threshold for neutralizing charge)
$f_p$	0.3	Fraction of the available charge density neutralized at a grid point by a flash
$Z_{cg}$	0.5 km	Height below which a flash is categorized as a CG flash

for the examples, but an alternate choice is the height-varying ‘breakeven’ or ‘runaway electron’ electric field  $E_{be}$  given in Marshall *et al.* (1995) (see also Gurevich *et al.*, 1992):

$$E_{be}(z) = \pm 167\rho_a(z) \quad (5.61)$$

$$\rho_a(z) = 1.208 \exp\left(\frac{-z}{8.4}\right) \quad (5.62)$$

where  $E_{be}$  has units of kV/m and  $\rho_a$  is the air density ( $\text{kg}/\text{m}^3$ ) as a function of altitude,  $z$  (km). Marshall *et al.* (1995) found that the runaway electron threshold was a better fit than the conventional breakdown threshold to the maximum electric field magnitudes seen in many thunderstorm soundings. The actual processes of natural lightning initiation are not understood well. Whether or not the runaway electron hypothesis correctly describes lightning initiation, it at least provides a good match to the maximum electric field magnitudes that have been observed as a function of height. More recently, Dwyer (2003) determined a higher threshold for runaway air breakdown:  $E_{init} = 2.84 \times 10^5 (\rho_{air}/\rho_o)$  V/m, where  $\rho_{air}$  is air density and  $\rho_o = 1.225 \text{ kg}/\text{m}^3$ .

In the first stage of a parameterized flash, the lightning initiation point is chosen randomly from among all the points where the electric field magnitude is greater than a lower threshold  $0.9E_{init}$ . The lower threshold and randomized choice are an attempt to allow lightning to occur over a larger range of locations, to account for some of the natural variability of lightning initiation due to unresolved subgrid-scale fluctuations in a cloud model. The development of the initial channel is similar to Helsdon *et al.* (1992) but traces the electric field line in subgrid steps (roughly one-tenth of the vertical grid spacing) rather than extending to the nearest model grid point. Beginning at the grid point chosen for initiation, a flash traces the electric field line outward in both directions (parallel and anti-parallel) until the magnitude of the ambient electric field at each end falls below some threshold value ( $E_{stop}$ ). The quantity  $E_{stop}$  can be set either to a fixed value or to a fixed percentage of  $E_{init}$  when  $E_{init}$  varies with height. MacGorman *et al.* (2001) used a value of  $E_{stop} = 15 \text{ kVm}^{-1}$ , but subsequent testing found that higher values were needed to control electric field growth. A lower value of  $E_{stop}$  tends to result in overshooting the charge layers closest to the initiation point.

The second stage of the MacGorman *et al.* (2001) lightning parameterization finds the branching regions. At each end of the flash inside storm charge, the parameterization uses a ‘wildfire’ technique to expand the flash from the end of the channel to all contiguous grid points satisfying two conditions:  $|\rho(i, j, k)| \geq \rho_{chan}$  and  $|\phi(i, j, k)| \geq |\phi_{end}|$ , where  $\rho(i, j, k)$  and  $\phi(i, j, k)$  are, respectively, the net charge density and the ambient electric potential at a grid point, and  $\phi_{end}$  the ambient electric potential at the end of the channel before extension. During the wildfire expansion, each new point that is added must adjoin a point that satisfied these conditions previously as the flash developed. The condition on  $|\phi(i, j, k)|$  keeps further flash development within the volume bounded by the equipotential surface that passes through the channel at the point where the initial stage of parameterized channel propagation stops.

Charge estimation and neutralization were parameterized by using the technique developed by Ziegler and MacGorman (1994), except that Ziegler and MacGorman neutralized charge at all grid points having  $|\rho(i, j, k)| \geq \rho_{chan}$  throughout the storm, but the new parameterization neutralizes charge only at such grid points within a single localized flash, defined by the volumes bounded by the equipotential surface  $|\phi_{end}|$  at each end. For cloud flashes, the MacGorman *et al.* (2001) parameterization added a condition not used by Ziegler and MacGorman (1994) to make sure that the volume of grid points for each polarity is sufficient to hold the neutralized charge without causing an electric field magnitude larger than  $E_{init}$  at the outer boundary of an equivalent sphere. When one end encompassed much more charge than the other before the correction for charge was computed, the correction occasionally added enough charge at the smaller end to create a new flash at the outer boundary of the original flash volume. In this situation, a real lightning flash would be expected to keep propagating. Therefore, the MacGorman *et al.* (2001) parameterization expands the volume of the flash at the end at which the uncorrected total charge magnitude is smaller, if the volume is too small to hold the corrected charge without causing breakdown. The condition on the flash volume means that the number of points in each branching volume must be greater than  $N_{crit}$ , which is given by

$$N_{crit} = \frac{4\pi}{3\delta v} \left( \frac{Q_{dis}}{4\pi\epsilon E_{init}} \right)^{3/2} \quad (5.63)$$

where  $\delta v$  is the volume represented by each grid point,  $\epsilon$  is the permittivity of air and  $Q_{dis}$  is the magnitude of the adjusted charge deposited in each branching volume. If one of the branching regions has fewer than  $N_{crit}$  points, then extra contiguous grid points with sufficient charge density are added to the region until it contains  $N_{crit} = 1$  points.

In a model that does not explicitly predict ion concentrations, lightning charge is deposited directly on hydrometeors according to their fractional surface area as in Ziegler and MacGorman (1994). If it does predict ion concentrations, the lightning charge at each grid point should be converted to an ion concentration and added to the ion concentration at that grid point.

### 5.5.1 Stochastic lightning model

Mansell *et al.* (2002) presented a stochastic branched lightning parameterization adapted from the dielectric breakdown model developed by Niemeyer *et al.* (1984) (NPW) and Wiesmann and Zeller (1986). The NPW model was developed to examine the branched structures of dielectric breakdown. Wiesmann and Zeller (1986) made the NPW model more physical by adding a critical electric field threshold ( $E_{crit}$ ) for propagation and allowing for an internal electric field ( $E_{init}$ ) in the discharge channel. The internal field simply specifies the voltage drop along the channel segment and accounts for the resistance of the channel. Previous studies Petrov and Petrova (e.g. 1993, 1999) and Pasko *et al.* (e.g. 2000) had also used the Wiesmann–Zeller version of the dielectric breakdown model to study electrical

discharges in the atmosphere but had been limited to two-dimensional slab-symmetric or axisymmetric model domains and did not include cloud models.

The lightning model simulates the step-by-step propagation of a bidirectional discharge from an initiation point by successively creating new breakdown extensions, or bonds, from the discharge structure. Figure 5.7 shows a sample two-dimensional grid with part of a discharge. Each new extension is chosen randomly from all possible new extensions. An extension from a grid point on the channel to an adjacent grid point is possible (i.e. has a non-zero probability) if the electric field vector favours propagation towards the adjacent grid point and the electric field magnitude between the two points exceeds a critical value,  $E_{crit}$ . Once all possible extensions have been identified, the probability  $p$  of choosing a particular extension is given by

$$p_i(E) = \begin{cases} \frac{1}{F} (E_i - E_{crit})^\eta & \text{for } E_i > E_{crit} \\ 0 & \text{for } E_i \leq E_{crit} \end{cases} \quad (5.64)$$

where  $\eta$  is a weighting exponent and  $E_i$  is the magnitude of the electric field component between the  $i$ th pair of candidate extensions from a grid point on the existing channel to an adjacent point not yet on the channel. The divisor  $F$  is the sum of the unnormalized probabilities,  $F = \sum_k (E_k - E_{crit})^\eta$ , so  $\sum p_i = 1$ . Each probability is transformed in a range of width  $p_i$  within the range (0,1):

$$p_i \rightarrow \left( \sum_{k=1, i-1} p_k, \sum_{k=1, i} p_k \right)$$

and a random number selects one new extension.

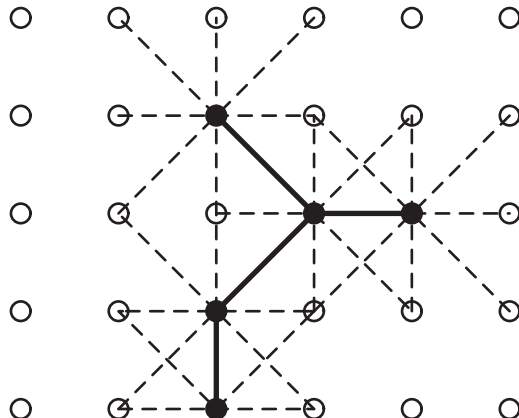


Figure 5.7 Sample grid showing a portion of a stochastic lightning model discharge in two dimensions. Open circles represent grid points not connected to the discharge. Filled circles and heavy lines indicate the discharge path. Dashed lines indicate possible new bonds. In three dimensions, connections are allowed along all of the unit cube directions

NPW had a critical field of zero ( $E_{crit}=0$ ) in their model and found that the density of branching decreases with increasing values of  $\eta$ . NPW found that ‘bush’ type (densely packed) discharges result for  $\eta \leq 1$ , but ‘branched’ structures result for  $\eta \geq 3$ . Wiesmann (1988) found that introducing  $E_{crit} > 0$  (with  $\eta=1$ ) has a similar effect as setting  $\eta > 1$ , since both tend to limit side branching. Dissado and Sweeney (1993) pointed out the difficulty in physically justifying any exponent other than  $\eta=1$ , however, so Mansell *et al.* (2002) assumed a linear relationship between  $p_i$  and  $E_i$  (i.e.  $\eta=1$ ), as well as  $E_{crit} > 0$ .

In the WZ model, electrical resistance of the channels is represented by an internal electric field  $E_{int}$ . A perfect conductor would have  $E_{int}=0$ , and its surface would have a constant potential, whereas a conductor with resistance has  $E_{int} > 0$ , and the potential varies along its length. A non-zero internal field acts to reduce the electric field between the channel and non-channel points and thus reduces the overall extent of the discharge structure (all other values being held equal). When a new grid point is added to the discharge, the electric potential  $\phi_{new}$  at the new channel point is calculated from the potential  $\phi_b$  of the point from which the channel segment extends:

$$\phi_{new} = \phi_b - sE_{int}d \quad (5.65)$$

where  $d$  is the length of the new segment and  $s$  is the sign of charge carried by the channel. Thus, the potential at a point that is  $n$  segments away from the initiation point can be written in terms of the reference potential  $\phi_{ref}$  of the starting point, so that (5.65) becomes

$$\phi(n) = \phi_{ref} - s \sum_{j=1}^n E_{int}(j)d_j \quad (5.66)$$

where the sum is along the path from the initiation point to segment  $n$ . Each channel point has a unique path from the initiation point because no branch is allowed to rejoin to another branch. For bidirectional discharges, the initial reference potential is taken as the average of the ambient potentials of the two initial grid points.

The electric potential  $\phi$  at grid points not on the channel must be updated after each extension of the conducting channel by solving Poisson’s equation (5.13). The electric potential is already defined by (5.66) along the discharge structure, which is treated as a boundary with Dirichlet conditions when solving (5.13). Because of the complex geometry of the discharge boundary, Poisson’s equation is most easily solved with an iterative technique such as successive over-relaxation, as described in Appendix A of Mansell *et al.* (2002). The charge density induced on the channel at a grid point can be found simply from Poisson’s equation ( $\rho = -e\nabla^2\phi$ ). The charge on the channel is not needed for solving (5.67) because the effect of this charge on  $\phi$  is included by satisfying the boundary condition imposed by the channel potential (5.66). The channel charge must be calculated periodically during development of bidirectional discharges to check for overall flash neutrality.

### 5.5.2 Pseudo-fractal lightning

Molinié *et al.* (2002) and Barthe *et al.* (2005) introduced a hybrid lightning parameterization designed for the computational efficiency of MacGorman *et al.* (2001) but also explicitly creating channels as in Mansell *et al.* (2002). Refinements to the scheme were presented in Barthe and Pinty (2007). An initial channel follows the electric field bidirectionally (grid point to grid point, as in Helsdon *et al.*, 1992) from an initiation point until the ambient electric field magnitude falls below  $20 \text{ kV m}^{-1}$ . The initial channel (1) determines whether the discharge will be intracloud or CG (i.e. determined whether one end descends to the CG flash altitude threshold or not) and (2) provides the starting points for the branching algorithm.

The second stage of the Barthe–Molinié scheme returns to the initiation point and begins adding branch points starting from the main channel. Any point that meets the electric potential and charge criteria of MacGorman *et al.* (2001) is considered a possible extension point. Here, however, the potential criterion was set by the initiation point rather than the value at the tip of the initial channel. The number of channel points allowed within a given distance of the initiation point is given by the fractal formula

$$N(d) \sim \frac{L_\chi}{L_{moy}} d^{\chi-1} \quad (5.68)$$

where  $d$  is the linear distance from the starting point and  $\chi$  is the assumed fractal dimension.  $L_\chi$  is a tunable length-scale parameter, and  $L_{moy}$  was described as the ‘average length of a grid mesh’ and could be interpreted as the cube root of the volume defined by the average horizontal and vertical grid spacings:  $L_{moy} = (\Delta x \Delta y \Delta z)^{1/3}$ . The  $L_\chi/L_{moy}$  factor was designed to help maintain consistency between simulations with different grid resolution. Barthe and Pinty (2007) found acceptable results for  $2.5 \leq \chi \leq 2.8$  and of  $500 \leq L_\chi \leq 1000$  in tests with a grid that had constant  $\Delta x = \Delta y = 1000 \text{ m}$  and constant  $\Delta z = 500 \text{ m}$ .

In practice, the number of allowed points are found within concentric shells with inner radius  $d$  and thickness  $\Delta l = (\Delta x \Delta y \Delta z)^{1/3}$  of the smallest grid volume in the domain (generally at the lowest level if the vertical spacing varies with altitude). The scheme iterates from the smallest to largest shells, randomly adding new channel points if another site is allowed by  $N(d)$  and a point adjacent to a current channel point meets the criteria of potential and charge density. All candidate points are given equal probability of being chosen. Once a shell is filled or has no more candidate points, the next larger shell is considered. Since the electric field at the channel tips is neither calculated nor taken into account, the growth of the structure is more akin to diffusion-limited aggregation models (e.g. Witten and Sander, 1981; Garik *et al.*, 1987) than dielectric breakdown models (e.g. Niemeyer *et al.*, 1984; Wiesmann and Zeller, 1986; Petrov and Petrova, 1993; Pasko *et al.*, 2000; Mansell *et al.*, 2002).

## 5.6 Some applications of models

By far the most frequent theme of modelling studies has been to examine the viability and relative contributions of various electrification mechanisms. This final section briefly covers model evaluations of ion attachment, inductive warm rain charging, non-inductive ice–ice charge separation and applications of modelled lightning.

### 5.6.1 Ion and inductive mechanisms

Some studies have included ion capture by hydrometeors. To the extent that they parameterize cloud boundary microphysics, mixing, transport and charge capture with enough fidelity and resolution, these could be used to evaluate at least some aspects of the Vonnegut (1953) hypothesis, which is frequently called the convective mechanism and which we call the Grenet–Vonnegut mechanism to give credit to Grenet (1947) (translated to English as Grenet, 1993). Briefly, the hypothesis states that storms can become electrified initially by lifting fair-weather charge (small ions), which then drive ion currents that result in attachment of small atmospheric ions to small hydrometeors at cloud boundaries (screening layer charge). Screening layer charge at the top of the cloud could then circulate down and be entrained back into the cloud, leading to stronger electric fields. The Grenet–Vonnegut mechanism does not involve precipitation processes and so would operate in both warm and cold clouds.

Chiu (1978) and Takahashi (1979) both tested inductive charging and ion capture in a cloud model with warm cloud microphysics (i.e. without the ice phase) in two-dimensional models. Chiu (1978) simulated a deeper cloud (approximately 7 km) with single-moment bulk microphysics and found only weak electrification from the Grenet–Vonnegut mechanism prior to precipitation formation. The simulations achieved maximum electric field magnitudes of 1–700 kV m<sup>-1</sup>, via inductive (polarization) charge exchange between rain drops and cloud droplets, depending heavily on the drop–droplet separation probability. The model used by Chiu (1978) did not predict the droplet number concentration, which was assumed to be a constant value, which would have resulted in overestimation of the concentration and therefore of the charge separation. Takahashi (1979), on the other hand, employed a spectral bin microphysics that could account for depletion of small droplet concentration via collection by larger drops. Takahashi (1979) simulated a shallower cloud than Chiu (1978) (approximately 3 km), and the model reproduced observations of weakly electrified warm maritime clouds reasonably well (maximum  $E$  of 100–200V/m), which suggests that ion capture can be important for weak electrification in these small storms. Takahashi (1979) found that the most important electrification process was ion capture by hydrometeors, which was significantly enhanced during evaporation and condensation, and that inductive polarization charging made little contribution.

Helsdon *et al.* (2002) used a full three-dimensional model to test the Grenet–Vonnegut mechanism in both weak and strong storm simulations. They also found

that the convective mechanism alone could produce only very weak electrification and that the charge structure tended to be opposite of what was expected by the hypothesis. Simulations that included ice–ice non-inductive charge separation, however, did produce substantial electric field magnitudes. A general result of these and other simulations (e.g. Mansell *et al.*, 2005) is that the process of ion attachment plays an important role in the formation of electrical screening layers, but by itself cannot result in strong electrification.

### 5.6.2 Non-inductive graupel–ice sensitivity

The disparate results of laboratory studies of non-inductive graupel–ice charge separation (e.g. Takahashi, 1978; Jayaratne *et al.*, 1983; Saunders *et al.*, 1991; Pereyra *et al.*, 2000) have naturally motivated numerical modelling studies to compare predictions of storm charge and lightning structure using parameterizations of the different sets of laboratory data. The laboratory data have sampled a relatively small range of conditions, so cloud models are useful for testing extrapolations of those results to a wide range of storm conditions, including conditions in turbulent dynamic clouds to which the various laboratory methods may be more or less applicable.

Helsdon *et al.* (2001) compared results based on two of the parameterizations described in Section 5.4.3.1: Takahashi (1978) and Saunders *et al.* (1991) (S91) in a two-dimensional model. Their model did not include a lightning discharge parameterization, so only the early electrification of the storm was examined. Helsdon *et al.* (2001) found that the low effective liquid water zones of the S91 parameterization would dominate the charge separation and result in unrealistic charge structures unless their charging rates were drastically reduced (by factors of 5–10). The two laboratory parameterizations produced starkly different initial charge structures, with Takahashi tending to produce a dominant positive dipole (positive over negative charge) and Saunders resulting in a negative dipole. However, the charge structure produced by the S91 parameterization switched towards a positive dipole later in the storm, so the two parameterizations had more similar results at later times.

Mansell *et al.* (2005) tested multiple parameterizations in a three-dimensional model that incorporated a lightning parameterization so the full life cycle of a multi-cell storm could be simulated. In their results, the two parameterizations tested by Helsdon *et al.* (2001) produced relatively similar charge and lightning polarities, in part because of parameter choices that reduced the early inverted charging in the S91 scheme. Mansell *et al.* (2005) also tested parameterizations based on Saunders and Peck (1998) (SP98), using the RAR and found that they tended to maintain an inverted polarity structure. Barthe *et al.* (2005) made a limited comparison of results produced by a parameterization of Takahashi (1978) and by a simple scheme with an adjustable charge reversal temperature (Helsdon and Farley, 1987b). They found comparable charge structures in their two simulations when the reversal temperature was set at  $-20^{\circ}\text{C}$ .

### 5.6.3 Charge structure and lightning type

Mansell *et al.* (2002) presented simulation results supporting the importance of lower positive charge (in the normal tripole structure) for instigating ordinary –CG flashes. Similarly, they showed that a lower negative charge was important for instigating +CG flashes, which were initiated between a mid-level positive charge region and a lower region of negative charge, as had been recently inferred from lightning mapping observations. The same particle charging parameterization was used for a multi-cell storm and a supercell storm. The multi-cell had a normal tripole structure and produced –CG flashes, but the supercell developed an inverted-polarity charge structure and produced +CG flashes.

Mansell *et al.* (2005) later showed that the same storm with different non-inductive graupel–ice parameterizations not only produced different charge structures, but also produced different lightning structure, particularly affecting the polarity of CG flashes. All or most of the CG flashes produced by the Takahashi and S91 parameterizations were –CG flashes, whereas CG flashes produced by the RAR-based parameterizations tended to be +CG flashes. Kuhlman *et al.* (2006) and Fierro *et al.* (2006) found similar variations in CG polarity for the different graupel–ice parameterizations in supercell storms. Mansell *et al.* (2005) and Helsdon *et al.* (2001) both noted important sensitivities to the assumptions about ice crystal concentrations, particularly in the warmer part of the mixed-phase region (0°C–10°C). Both studies used single-moment microphysics and had to diagnose the concentrations.

Differences in results produced by the Takahashi, S91 and the Saunders and Peck (1998) parameterization (SP98) when used in the multi-cell storm simulated by Mansell *et al.* (2005) are shown in Figures 5.8, 5.9 and 5.10. However, these simulations used two-moment microphysics (Mansell *et al.*, 2010) that predicts the number of particles per volume (zeroth moment) in addition to the total particle mass (third moment) for all hydrometeor types (cloud droplets, rain drops, ice crystals, snow and graupel). The electrification was not allowed to affect the dynamics, so the kinematic and microphysical structures (Figure 5.8) are identical in the three cases shown. The mixed-phase region is illustrated in Figure 5.8(b) as the intersection of the graupel and cloud droplet contents at temperatures between 0°C and about –38°C. This region is also characterized by updrafts, as cloud droplets tend to quickly evaporate in downdrafts.

Instantaneous graupel–ice charge separation rates are quite different for the three non-inductive parameterizations (Figure 5.9). Takahashi and S91 are more similar to each other, with the positive charging of graupel at lower altitude (higher temperature) and the negative charging of graupel at higher altitude. The positive charging from the Takahashi scheme extends higher and farther into the forward flank compared with results from S91, which has slightly weaker positive charging rates than the Takahashi scheme, but stronger negative charging rates aloft. Graupel charging in the SP98 simulation is almost completely positive, except for a pocket of weaker negative charging in the forward flank at about the same altitudes as in the Takahashi and S91 simulations.

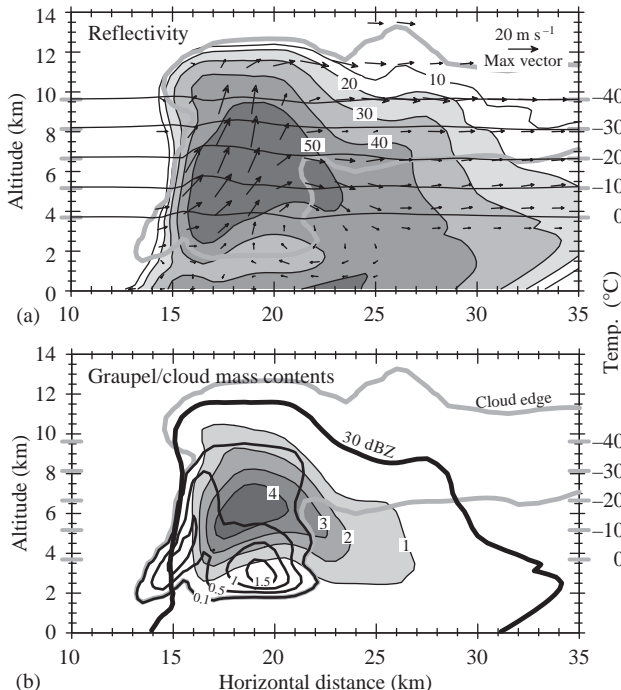


**Figure 5.8** Kinematic and microphysical structure of a simulated multi-cell thunderstorm at 52 min (used for Figures 5.9 and 5.10). (a) Simulated reflectivity (dBZ) and two-dimensional winds with cloud boundary (thick grey line) and isotherms (thin horizontal lines at 0–40°C). (b) Graupel mass content (grey-filled contours, g/m<sup>3</sup>) and cloud droplet mass content (black line contours, g/m<sup>3</sup>). Cloud edge contour follows the boundary of small cloud droplets and ice crystals

Differing charge structures (Figure 5.10(a)–(c)) and electric potential (Figure 5.10(d)–(f)) result from the cumulative effects of the respective charge separation schemes. Takahashi and S91 generally exhibit a ‘normal tripole’ structure in the updraft region, with a mid-level negative charge and upper and lower positive charge regions. The structure is more clearly seen in the positive and negative potential regions, because details in the charge structure are complicated by local reversals due to lightning charge. The lower and upper positive charges are mainly carried by graupel and ice crystals, respectively, while the main negative charge is carried in part by graupel and in part by ice crystals. The SP98 case, by contrast, has roughly an inverted dipole structure, with negative charge on ice crystals above positive charge on graupel.

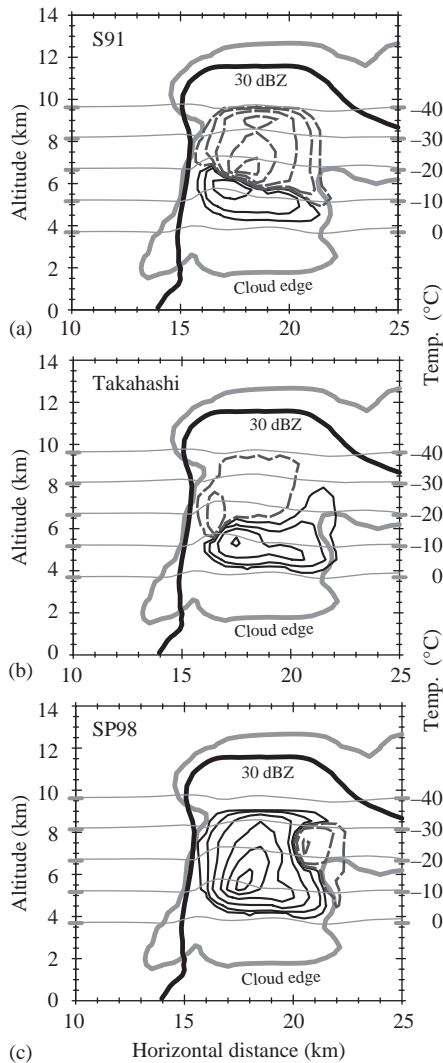


*Figure 5.9* Simulated non-inductive graupel–ice charge separation rates using the (a) S91, (b) Takahashi and (c) SP98 schemes.

Non-inductive charge separation rates have contour intervals of  $\pm 10, \pm 60$  and  $\pm 200 \text{ pC m}^{-3} \text{ s}^{-1}$  increasing thereafter by intervals of  $300 \text{ pC m}^{-3} \text{ s}^{-1}$  (negative (dashed) and positive (solid) charge to graupel)

The CG lightning produced in the simulations with two-moment microphysics is similar to the CG lightning in the original simulations with single-moment microphysics by Mansell *et al.* (2005). Approximate CG flash origins are cartooned in Figure 5.10(d)–(f). The Takahashi and SP98 simulations produce CG flashes that

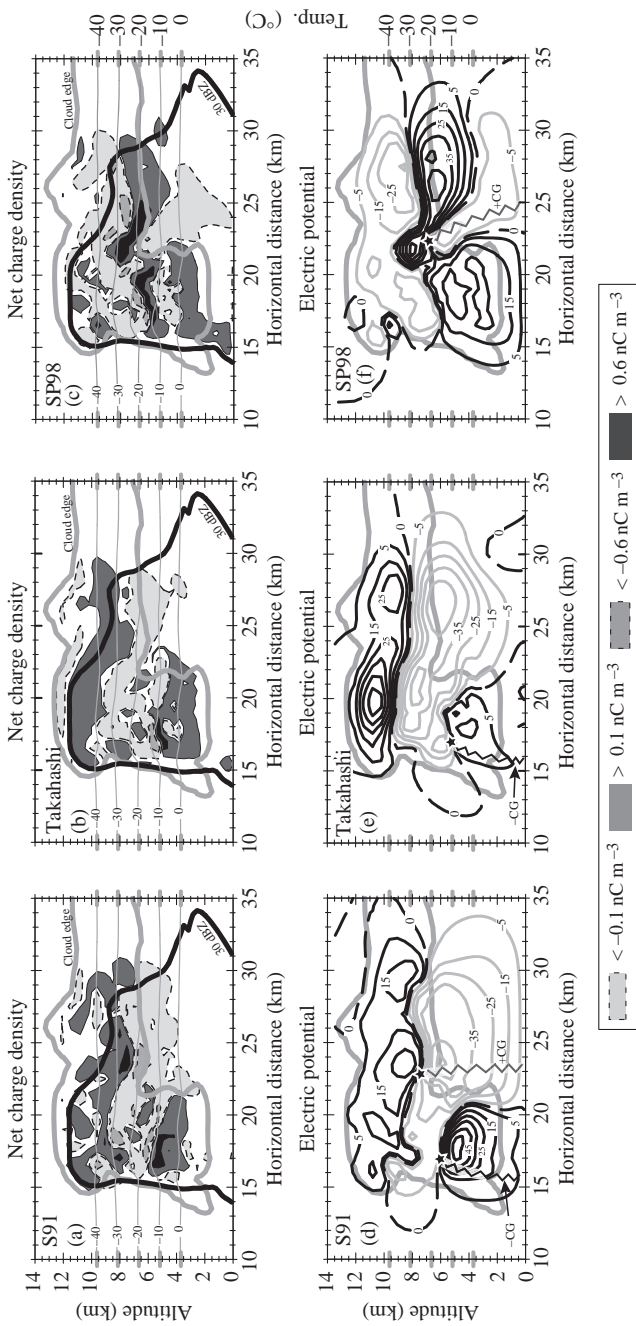


**Figure 5.10** Simulated charge structure (top) and electric potential (bottom) using the (a,d) S91, (b,e) Takahashi and (c,f) SP98 schemes. Contours of positive (black) and negative (grey) potential have intervals of  $\pm 1.5 \text{ MV}$ ,  $\pm 15 \text{ MV}$  and increasing thereafter by intervals of  $10 \text{ MV}$ . Local reversals of charge sign are caused by simulated lightning charge deposition. The stars (d,e,f) indicate approximate initiation points of cloud-to-ground (CG) near the time of the plots (52 min). The jagged lines connect the initiation points (stars) to approximate relative ground strike locations

were exclusively negative or positive, respectively. The S91 simulation, however, produces both polarities of CG lightning. Negative CG flashes (both Takahashi and S91) originated between the main negative and lower positive charge regions in the storm core, whereas +CG flashes (S91 and SP98) usually initiate downshear of the updraft core. The distribution of +CG and -CG flashes in the S91 results is much like the ‘lightning bipole’ pattern that has been observed in mesoscale convective systems (MCSs), with -CG lightning occurring in the convective line and +CG lightning offset downshear towards the transition zone.

#### 5.6.4 Concluding remarks

Numerical modelling has been a valuable tool in storm electrification research. Studies have strongly supported the primary role of graupel–ice collisions in generating electrification strong enough for lightning to occur. Many general features such as electrical screening layers and CG lightning have been produced by model simulations, but models have the additional benefit of providing complete, internally consistent storm data sets for analyses. The lightning behaviours that have been observed in storms have been simulated well enough (e.g. Kuhlmann *et al.*, 2006; Mansell *et al.*, 2010) to provide support for relationships inferred from observations as well as to help develop new hypotheses about relationships between lightning and other storm properties. Model sensitivity tests of laboratory data for graupel–ice charge separation have shown that the differences in the laboratory data can translate into stark differences in simulated charge structure, although the specific simulated differences may well be affected by the considerable uncertainties in the treatments of the mixed-phase region of storms (e.g. cloud water content, graupel and ice concentrations and graupel riming rates). Models can also help point out areas in which more laboratory research may be needed. For example, the lack of charge in some regions of simulated storms in which charge has been measured in real storms suggests a need to investigate particle charging during non-inductive ice–ice interactions in regions of ice supersaturation, but little or no liquid water.

Many challenges remain for numerical models. A primary challenge is the difficulty of simulating a particular storm case with sufficient similitude, something that requires a great deal of trial and error with deterministic simulations and may or may not succeed. Assimilation of radar and other data with variational and ensemble methods provides a means to force a modelled storm to look more like an observed storm, but at the costs of computational expense and perhaps unphysical adjustments to the non-electrical model fields. A number of regularly observed electrical features have not been well simulated (or not attempted), such as charge separation and lightning in storm anvils and in MCS stratiform precipitation regions, as well as charge structures associated with radar bright bands. A combination of further laboratory and storm observations and improvements to numerical models is needed to make progress in understanding storm electrification processes.

## References

- Aufdermaur, A. N. and D. A. Johnson, 1972: Charge separation due to riming in an electric field. *Quart. J. Roy. Meteor. Soc.*, **98**, 369–382
- Baker, B., M. B. Baker, E. R. Jayaratne, J. Latham and C. P. R. Saunders, 1987: The influence of diffusional growth rates on the charge transfer accompanying rebounding collisions between ice crystals and soft hailstones. *Quart. J. Roy. Meteor. Soc.*, **113**, 1193–1215
- Baker, M. B., H. J. Christian and J. Latham, 1995: A computational study of the relationships linking lightning frequency and other thundercloud parameters. *Quart. J. Roy. Meteor. Soc.*, **121**, 1525–1548
- Barth, M. C., S.-W. Kim, C. Wang, K. E. Pickering, L. E. Ott, G. Stenchikov, *et al.*, 2007: Cloud-scale model intercomparison of chemical constituent transport in deep convection. *Atmos. Chem. Phys.*, **7**, 4709–4731
- Barthe, C., G. Molinié and J.-P. Pinty, 2005: Description and first results of an explicit electrical scheme in a 3D cloud resolving model. *Atmos. Res.*, **76**, 95–113
- Barthe, C. and J.-P. Pinty, 2007: Simulation of a supercellular storm using a three-dimensional mesoscale model with an explicit lightning flash scheme. *J. Geophys. Res.*, **112**, doi:10.1029/2006JD007484
- Barthe, C., J.-P. Pinty and C. Mari, 2007: Lightning-produced NO<sub>x</sub> in an explicit electrical scheme tested in a Stratosphere-Troposphere Experiment: Radiation, Aerosols and Ozone case study. *J. Geophys. Res.*, **112**, doi:10.1029/2006JD007402
- Brooks, I. M. and C. P. R. Saunders, 1994: An experimental investigation of the inductive mechanism of thunderstorm electrification. *J. Geophys. Res.*, **99**, 10627–10632
- Brooks, I. M., C. P. R. Saunders, R. P. Mitzeva and S. L. Peck, 1997: The effect on thunderstorm charging of the rate of rime accretion by graupel. *Atmos. Res.*, **43**, 277–295
- Canosa, E. F., R. List and R. E. Stewart, 1993: Modeling of inductive charge separation in rainshafts with variable vertical electric fields. *J. Geophys. Res.*, **98**, 2627–2633
- Chiu, C.-S., 1978: Numerical study of cloud electrification in an axisymmetric, time-dependent cloud model. *J. Geophys. Res.*, **83**, 5025–5049
- Cotton, W. R. and R. A. Anthes, 1989: *Storm and Cloud Dynamics*. Academic Press, San Diego, 883 pp
- Dissado, L. A. and P. J. J. Sweeney, 1993: Physical model for breakdown structures in solid dielectrics. *Phys. Rev. B*, **48**, 16261–16268
- Dwyer, J. R., 2003: A fundamental limit on electric fields in air. *Geophys. Res. Lett.*, **30**, doi:10.1029/2003GL017781
- Emersic, C., 2006: *Investigations into Thunderstorm Electrification Processes*. Ph.D. thesis, University of Manchester, Manchester, England, UK, 327 pp
- Fierro, A. O., M. S. Gilmore, E. R. Mansell, L. J. Wicker and J. M. Straka, 2006: Electrification and lightning in an idealized boundary-crossing supercell simulation of 2 June 1995. *Mon. Wea. Rev.*, **134**, 3149–3172

- Fierro, A. O., L. Leslie, E. R. Mansell, J. M. Straka, D. R. MacGorman and C. L. Ziegler, 2007: A high-resolution simulation of microphysics and electrification in an idealized hurricane-like vortex. *Met. Atmos. Phys.*, **98**(1–2), 13–33
- Gardiner, B., D. Lamb, R. L. Pitter, J. Hallett and C. P. R. Saunders, 1985: Measurements of initial potential gradient and particle charges in a Montana summer thunderstorm. *J. Geophys. Res.*, **90**, 6079–6086
- Garik, P., K. Mullen and R. Richter, 1987: Models of controlled aggregation. *Phys. Rev. A.*, **35**, 3046–3055
- Gaskell, W., 1981: A laboratory study of the inductive theory of thunderstorm electrification. *Quart. J. Roy. Meteor. Soc.*, **107**, 955–966
- Gish, O. H., 1944: Evaluation and interpretation of the columnar resistance of the atmosphere. *Terr. Magn. Atmos. Electr.*, **49**, 159–168
- Grenet, G., 1947: Essai d'explication de la charge électrique des nuages d'orages. *Ann. Géophys.*, **3**, 306–307
- Grenet, G., 1993: Possible explanation for the electric charge in thunderclouds (Reprint of 1947 paper in English). *Atmos. Res.*, **30**, 175–179
- Gurevich, A. V., G. M. Milikh and R. Roussel-Dupre, 1992: Runaway electron mechanism of air breakdown and preconditioning during a thunderstorm. *Phys. Lett. A*, **165**, 463–468
- Helsdon, J. H., Jr., 1980: Chaff seeding effects in a dynamical-electrical cloud model. *J. Appl. Met.*, **19**, 1101–1125
- Helsdon, J. H., Jr. and R. D. Farley, 1987a: A numerical modeling study of a Montanathunderstorm: 1. Model results versus observations involving nonelectrical aspects. *J. Geophys. Res.*, **92**, 5645–5659
- Helsdon, J. H., Jr. and R. D. Farley, 1987b: A numerical modeling study of a Montana thunderstorm: 2. Model results versus observations involving electrical aspects. *J. Geophys. Res.*, **92**, 5661–5675
- Helsdon, J. H., Jr., S. Gattaleeradapan, R. D. Farley and C. C. Waits, 2002: An examination of the convective charging hypothesis: Charge structure, electric fields and Maxwell currents. *J. Geophys. Res.*, **107**, doi:10.1029/2001JD001495
- Helsdon, J. H., Jr., W. A. Wojcik and R. D. Farley, 2001: An examination of thunderstorm-charging mechanisms using a two-dimensional storm electrification model. *J. Geophys. Res.*, **106**, 1165–1192
- Helsdon, J. H., Jr., G. Wu and R. D. Farley, 1992: An intracloud lightning parameterization scheme for a storm electrification model. *J. Geophys. Res.*, **97**, 5865–5884
- Houze, R. A., Jr., 1993: *Cloud Dynamics*. Academic Press, San Diego, 573 pp
- Illingworth, A. J. and J. Latham, 1977: Calculations of electric field growth, field structure and charge distributions in thunderstorms. *Quart. J. Roy. Meteor. Soc.*, **103**, 277–298
- Jayaratne, E. R., C. P. R. Saunders and J. Hallett, 1983: Laboratory studies of the charging of soft hail during ice crystal interactions. *Quart. J. Roy. Meteor. Soc.*, **109**, 609–630
- Jhawar, D. S. and J. A. Chalmers, 1967: Point-discharge currents through small trees in artificial fields. *J. Atmos. Terr. Physics*, **29**, 1459–1463

- Keith, W. D. and C. P. R. Saunders, 1989: Charge transfer during multiple large ice crystal interactions with a riming target. *J. Geophys. Res.*, **94**, 13103–13106
- Keith, W. D. and C. P. R. Saunders, 1990: Further laboratory studies of the charging of groupel during ice crystal interactions. *Atmos. Res.*, **25**, 445–464
- Kuettner, J. P., Z. Levin and J. D. Sartor, 1981: Thunderstorm electrification—inductive or non-inductive? *J. Atmos. Sci.*, **38**, 2470–2484
- Kuhlman, K. M., C. L. Ziegler, E. R. Mansell, D. R. MacGorman and J. M. Straka, 2006: Numerically simulated electrification and lightning of the 29 June 2000 STEPS supercell storm. *Mon. Wea. Rev.*, **134**, 2734–2757
- Latham, J. and B. J. Mason, 1962: Electrical charging of hail pellets in a polarizing electric field. *Proc. R. Soc. London, Ser. A*, **266**, 387–401
- Levin, Z., 1976: A refined charge distribution in a stochastic electrical model of an infinite cloud. *J. Atmos. Sci.*, **33**, 1756–1762
- Lhermitte, R. and P. R. Krehbiel, 1979: Doppler radar and radio observations of thunderstorms. *IEEE Trans. Geosci. Electron.*, **GE-17**, 162–171
- MacGorman, D. R., A. A. Few and T. L. Teer, 1981: Layered lightning activity. *J. Geophys. Res.*, **86**, 9900–9910
- MacGorman, D. R. and W. D. Rust, 1998: *The Electrical Nature of Storms*. Oxford University Press, New York, 422 pp
- MacGorman, D. R., J. M. Straka and C. L. Ziegler, 2001: A lightning parameterization for numerical cloud models. *J. Appl. Meteor.*, **40**, 459–478
- Mansell, E. R., D. R. MacGorman, C. L. Ziegler and J. M. Straka, 2002: Simulated three-dimensional branched lightning in a numerical thunderstorm model. *J. Geophys. Res.*, **107**, doi:10.1029/2000JD000244
- Mansell, E. R., D. R. MacGorman, C. L. Ziegler and J. M. Straka, 2005: Charge structure and lightning sensitivity in a simulated multicell thunderstorm. *J. Geophys. Res.*, **110**, doi:10.1029/2004JD005287
- Mansell, E. R., C. L. Ziegler and E. C. Bruning, 2010: Simulated electrification of a small thunderstorm with two-moment bulk microphysics. *J. Atmos. Sci.*, **67**, 171–194, doi:10.1175/2009JAS2965.1
- Marshall, B. J. P., J. Latham and C. P. R. Saunders, 1978: A laboratory study of charge transfer accompanying collision of ice crystals with a simulated hailstone. *Quart. J. Roy. Meteor. Soc.*, **104**, 163–178
- Marshall, J. S. and W. M. Palmer, 1948: The distribution of raindrops with size. *J. Meteor.*, **5**, 165–166
- Marshall, T. C., M. P. McCarthy and W. D. Rust, 1995: Electric field magnitudes and lightning initiation in thunderstorms. *J. Geophys. Res.*, **100**, 7097–7103
- Mason, B. J., 1988: The generation of electric charges and fields in thunderstorms. *Proc. R. Soc. London, Ser. A*, **415**, 303–315
- Mathpal, K. C. and N. C. Varshneya, 1982: Riming electrification mechanism for charge generation within a thundercloud of finite dimensions. *Ann. de Géophys.*, **38**, 167–175
- Milbrandt, J. A. and M. K. Yau, 2005: A multimoment bulk microphysics parameterization. Part II: A proposed three-moment closure and scheme description. *J. Atmos. Sci.*, **62**, 3065–3081

- Mitzeva, R. P. and C. P. R. Saunders, 1990: Thunderstorm charging: Calculations of the effect of ice crystal size and graupel velocity. *J. Atmos. Terr. Phys.*, **52**, 241–245
- Mitzeva, R. P., C. P. R. Saunders and B. Tsenova, 2006: Parameterisation of non-inductive charging in thunderstorm regions free of cloud droplets. *Atmos. Res.*, **82**, 102–111, doi:10.1016/j.atmosres.2005.12.006
- Molinié, G., J.-P. Pinty and F. Roux, 2002: Some microphysical and electrical aspects of a cloud resolving model: Description and thunderstorm case study. *C. R. Phys.*, **3**, 1305–1324
- Moore, C. B., 1975: Rebound limits on charge separation by falling precipitation. *J. Geophys. Res.*, **80**, 2658–2662
- Niemeyer, L., L. Pietronero and H. J. Wiesmann, 1984: Fractal dimension of dielectric breakdown. *Phys. Rev. Lett.*, **52**, 1033–1036
- Norville, K., M. Baker and J. Latham, 1991: A numerical study of thunderstorm electrification: Model development and case study. *J. Geophys. Res.*, **96**, 7463–7481
- Pasko, V. P., U. S. Inan and T. F. Bell, 2000: Fractal structure of sprites. *Geophys. Res. Lett.*, **27**, 497–500
- Pereyra, R. G., E. E. Avila, N. E. Castellano and C. Saunders, 2000: A laboratory study of graupel charging. *J. Geophys. Res.*, **105**, 20803–20812
- Petrov, N. I. and G. N. Petrova, 1993: Physical mechanisms for intracloud lightning discharges. *Tech. Phys.*, **38**, 287–290
- Petrov, N. I. and G. N. Petrova, 1999: Physical mechanisms for the development of lightning discharges between a thundercloud and the ionosphere. *Tech. Phys.*, **44**, 472–475
- Pringle, J. E., H. D. Orville and T. D. Stechmann, 1973: Numerical simulation of atmospheric electricity effects in a cloud model. *J. Geophys. Res.*, **78**, 4508–4514
- Pruppacher, H. R. and J. D. Klett, 1997: *Microphysics of Clouds and Precipitation*. Kluwer Academic, Dordrecht, The Netherlands, 954 pp
- Randell, S. C., S. A. Rutledge, R. D. Farley and J. H. Helsdon, Jr., 1994: A modeling study of the early electrical development of tropical convection: Continental and oceanic (monsoon) storms. *Mon. Wea. Rev.*, **122**, 1852–1877
- Rawlins, F., 1982: A numerical study of thunderstorm electrification using a three dimensional model incorporating the ice phase. *Quart. J. Roy. Meteor. Soc.*, **108**, 779–800
- Riousset, J. A., V. P. Pasko, P. R. Krehbiel, R. J. Thomas and W. Rison, 2007: Three-dimensional fractal modeling of intracloud lightning discharge in a New Mexico thunderstorm and comparison with lightning mapping observations. *J. Geophys. Res.*, **112**, doi:10.1029/2006JD007621
- Saunders, C. P. R., W. D. Keith and R. P. Mitzeva, 1991: The effect of liquid water on thunderstorm charging. *J. Geophys. Res.*, **96**, 11007–11017
- Saunders, C. P. R. and S. L. Peck, 1998: Laboratory studies of the influence of the rime accretion rate on charge transfer during crystal/graupel collisions. *J. Geophys. Res.*, **103**, 13949–13956

- Scott, W. D. and Z. Levin, 1975: A stochastic electrical model of an infinite cloud: Charge generation and precipitation development. *J. Atmos. Sci.*, **32**, 1814–1828
- Seifert, A. and K. D. Beheng, 2006: A two-moment cloud microphysics parameterization for mixed-phase clouds. Part 1: Model description. *Met. Atmos. Phys.*, **92**, 45–66, doi:10.1007/s00703-005-0112-4
- Shao, X. M. and P. R. Krehbiel, 1996: The spatial and temporal development of intracloud lightning. *J. Geophys. Res.*, **101**, 26641–26668
- Shreve, E. L., 1970: Theoretical derivation of atmospheric ion concentrations, conductivity, space charge density, electric field and generation rate from 0 to 60 km. *J. Atmos. Sci.*, **27**, 1186–1194
- Singh, P., T. S. Verma and N. C. Varshneya, 1986: Some theoretical aspects of electric field and precipitation growth in a finite thundercloud. *Proc. Indian Acad. Sci.*, **95**, 293–298
- Solomon, R. and M. B. Baker, 1996: A one-dimensional lightning parameterization. *J. Geophys. Res.*, **101**, 14983–14990
- Standler, R. B. and W. P. Winn, 1979: Effects of coronae on electric fields beneath thunderstorms. *Quart. J. Roy. Meteor. Soc.*, **105**, 285–302
- Stensrud, D. J., 2007: *Parameterization Schemes: Keys to Understanding Numerical Weather Prediction*. Cambridge University Press, UK, 459 pp
- Straka, J. M., 2009: *Cloud and Precipitation Microphysics: Principles and Parameterizations*. Cambridge University Press, UK, 392 pp
- Sun, A., H.-Y. Chun, J.-J. Baik and M. Yan, 2002: Influence of electrification on microphysical and dynamical processes in a numerically simulated thunderstorm. *J. Appl. Meteor.*, **41**, 1112–1127
- Takahashi, T., 1974: Numerical simulation of warm cloud electricity. *J. Atmos. Sci.*, **31**, 2160–2181
- Takahashi, T., 1978: Riming electrification as a charge generation mechanism in thunderstorms. *J. Atmos. Sci.*, **35**, 1536–1548
- Takahashi, T., 1979: Warm cloud electricity in a shallow axisymmetric cloud model. *J. Atmos. Sci.*, **36**, 2236–2258
- Takahashi, T., 1983: Numerical simulation of winter cumulus electrification. Part I: Shallow cloud. *J. Atmos. Sci.*, **40**, 1257–1280
- Takahashi, T., 1984: Thunderstorm electrification – a numerical study. *J. Atmos. Sci.*, **41**, 2541–2558
- Takahashi, T., 1987: Determination of lightning origins in a thunderstorm model. *J. Meteor. Soc. Japan*, **65**, 777–794
- Tsenova, B. D. and R. P. Mitzeva, 2009: New parameterization of non-inductive charge transfer based on previous laboratory experiments. *Atmos. Res.*, **91**, 79–86
- Vonnegut, B., 1953: Possible mechanism for the formation of thunderstorm electricity. *Bull. Amer. Meteor. Soc.*, **34**, 378
- Whipple, F. J. W. and J. A. Chalmers, 1944: On Wilson's theory of the collection of charge by falling drops. *Quart. J. Roy. Meteor. Soc.*, **70**, 103–118
- Wiesmann, H. J., 1988: Realistic models of dielectric breakdown. *Fractals' Physical Origin and Properties*, L. Pietronero, ed., Plenum Press, New York, 243–257

- Wiesmann, H. J. and H. R. Zeller, 1986: A fractal model of dielectric breakdown and prebreakdown in solid dielectrics. *J. Appl. Phys.*, **60**, 1770–1773
- Witten, T. A., Jr. and L. M. Sander, 1981: Diffusion-limited aggregation, a kinetic critical phenomenon. *Phys. Rev. Lett.*, **47**, 1400–1403
- Wojcik, W. A., 1994: *An Examination of Thunderstorm Charging Mechanisms Using the IAS 2D Storm Electrification Model*. Master's thesis, South Dakota School of Mines and Technology, Rapid City, SD, 113 pp
- Zhang, X., J. H. Helsdon, Jr. and R. D. Farley, 2003: Numerical modeling of lightning-produced NO<sub>x</sub> using an explicit lightning scheme: 2. Three-dimensional simulation and expanded chemistry. *J. Geophys. Res.*, **108**, doi:10.1029/2002JD003225
- Ziegler, C. L., 1985: Retrieval of thermal and microphysical variables in observed convective storms. Part I: Model development and preliminary testing. *J. Atmos. Sci.*, **42**, 1487–1509
- Ziegler, C. L., 1988: Retrieval of thermal and microphysical variables in observed convective storms. Part II: Sensitivity of cloud processes to variation of the microphysical parameterization. *J. Atmos. Sci.*, **45**, 1072–1090
- Ziegler, C. L. and D. R. MacGorman, 1994: Observed lightning morphology relative to modeled space charge and electric field distributions in a tornadic storm. *J. Atmos. Sci.*, **51**, 833–851
- Ziegler, C. L., D. R. MacGorman, J. E. Dye and P. S. Ray, 1991: A model evaluation of non-inductive graupel-ice charging in the early electrification of a mountain thunderstorm. *J. Geophys. Res.*, **96**, 12833–12855
- Ziegler, C. L., P. S. Ray and D. R. MacGorman, 1986: Relations of kinematics, microphysics and electrification in an isolated mountain thunderstorm. *J. Atmos. Sci.*, **43**, 2098–2114
- Ziv, A. and Z. Levin, 1974: Thundercloud electrification: Cloud growth and electrical development. *J. Atmos. Sci.*, **31**, 1652–1661

---

## *Chapter 6*

# The physics of lightning flash development

*Vladislav Mazur<sup>1</sup> and Lothar H. Ruhnke<sup>2</sup>*

---

### **6.1 Introduction**

Lightning is a powerful and fascinating natural phenomenon that has a significant presence in, and effects on, human lives. Historically, lightning research has evolved as an observational science, and is still predominantly in the observational or analysis stage, with many studies devoted to describing, labelling and comparing the various lightning processes. Thus, not unexpectedly, descriptions of observed and measured lightning effects, features and characteristics preceded the understanding of their physics. The study of atmospheric electricity and, therefore, lightning research, had their beginnings in the 18th century, with the work of Benjamin Franklin, and is the only branch of physics with its own sign convention that is different (actually opposite) from that in general physics. The contradiction of having two opposite sign conventions in two branches of physics awaits its resolution.

A model of a lightning discharge as a unidirectional, uniformly charged leader originating from a space charge source (the ‘source charge model’) has been proposed by Schonland in Reference 1, subsequent to significant achievements in lightning studies in South Africa that began in the 1930s. Since its introduction, this model has become deeply embedded in the lightning literature.

The source charge model suggests that, during the negative leader stage in cloud-to-ground (CG) flashes, ‘negative charge is progressively removed from the cloud, and becomes distributed along the whole leader channel’ [2]. This implies that a physical process exists by which cloud charges can be forced into a leader channel.

The very fact that the electric field changes calculated using this model are similar to those of natural lightning leaders was a comforting realization for supporters of the source charge model. It should be pointed out, however, that by assuming a uniform charge-per-unit length, the source charge model contradicts the basic physical principle for a conductor placed in an ambient E-field, which is to have induced charges distributed according to the potential function of the E-field.

<sup>1</sup>NOAA/National Severe Storms Laboratory, Norman, Oklahoma, USA

<sup>2</sup>NOAA Cooperative Institute for Mesoscale Meteorological Studies, The University of Oklahoma, Norman, Oklahoma, USA

In other words, there is no potential function in nature that will produce uniformly distributed induced charges on a conductor in an ambient E-field.

The source charge model is still being used to calculate the locations of lightning origins for the interpretation of lightning processes from remote measurements, and in relation to storm structures. Producing waveforms similar to those measured in lightning is a necessary requirement for a model; however, the source charge model does not satisfy the laws of physics, which is another, equally necessary requirement for any valid model.

In the 1950s, Heinz Kasemir [3] applied the fundamental principles of electrostatics to lightning, viewing it as a conductor in an ambient electric field. However, the concept of the bidirectional, uncharged leader proposed and developed by Kasemir [3–5] was overlooked or ignored by most researchers involved in field observations of lightning. Widespread recognition of this concept by the lightning research community has been a lengthy process which has taken, by various estimates, nearly 50 years.

The concept introduced by Kasemir in the 1950s was verified in the 1980s with measurements of aircraft-triggered lightning [6]. The essence of this concept is: development of a lightning flash, after initiation in a thunderstorm, occurs as a bidirectional, bipolar, zero-net-charge leader and electrodeless discharge. This process takes place in intracloud (IC), CG, aircraft-triggered and so-called ‘tipsy’ rocket-triggered flashes (with a conductive wire isolated from the ground). The long-delayed acceptance of this concept has led to significant changes in our understanding of the essential physical processes in lightning flashes, and of the analytical relationship between the electrical structure of a cloud and lightning parameters. These changes are described in this chapter, with an emphasis on the unifying nature of the bidirectional leader concept in interpreting the various lightning processes.

## 6.2 Definitions and attributes of lightning processes

A key component of any lightning process is the leader, which is a self-propagating discharge in an ambient electric field that produces a hot plasma channel with a continuing current. Leader formation occurs during the transition from, or transformation of, millions of cold corona streamers focused like sun rays through a magnifying glass, on the tip of an electrode, or on the tip of an existing conductive leader. This process produces the element of a ‘thermalized’ plasma channel ahead of the tip and, thus, extends the leader channel. Thermalization occurs at temperatures above 5000–6000 K, and is characterized by ionization dominated by thermal collisions [7].

With regard to leader polarity, we define a negative leader as one carrying a negative charge at its tip; and we define a positive leader as one carrying a positive charge at its tip. This definition does not apply to the polarity of the net charge of an entire leader, which could even be zero, as in the case of some bipolar and bidirectional leaders.

The streamer-leader transition process that leads to elongation and, thus, to the propagation of leaders is different for positive and negative leaders. For positive

leaders, the positive corona streamers are in the shape of a cone at the tip of the leader (Figure 6.1(a)), and their development occurs continuously. For negative leaders, the streamer-leader transition includes the formation, at some distance ahead of the leader, of a piece of plasma, called a space leader, with bidirectional coronas emanating from it: a negative corona pointed outward, and a positive corona pointed towards the tip of the main leader channel (Figure 6.1(b)). The bidirectional development of coronas from the space leader leads to an arc discharge between the main and space leaders (not shown in Figure 6.1(b)). This arc discharge produces a step-type leader extension, and is the main source of strong radiation in the VHF-UHF band. The difference in the streamer-leader transition processes for positive and negative leaders is the main reason why negative leaders may be easily mapped with lightning mapping systems, while positive leaders are nearly undetectable by these systems.

Leader initiation and progression depend on corona streamer formation. The length of the corona streamers is determined by the ambient potential profile ahead of the leader, and by the constant E-field maintained along the corona streamers, which is  $750 \text{ kV m}^{-1}$ , for negative streamers, and is  $450 \text{ kV m}^{-1}$ , for positive streamers. Thus, the potential gradient at the tip of the leader drives leader development after leader initiation. The propagation of the leader channel ceases when the potential gradient at its tip is below the threshold levels required to continue an electrical breakdown ahead of the tip. When this condition occurs, leader propagation stops and, with it, the continuing current in the leader dies; in this way the entire lightning process comes to an end. The longitudinal electric field in a leader is usually much smaller than the ambient electric field, and, therefore, any leader channel may be assumed to be equipotential. When started inside a thunderstorm (by a mechanism that is still poorly understood), or started on a floating conductor

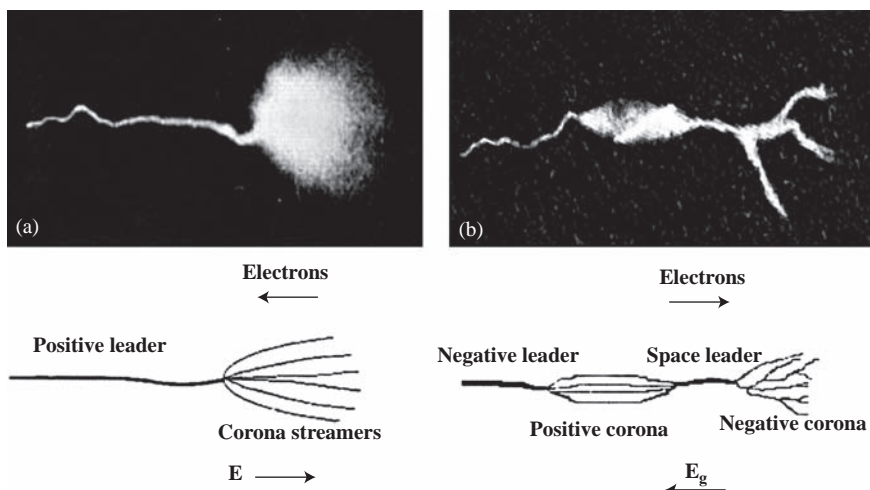


Figure 6.1 The streamer-leader transition zone structure for positive and negative leaders [adapted from Reference 8]

(an aircraft or a rocket), a lightning flash develops as a bidirectional, bipolar and zero-charge leader. (The initiation and development of lightning started from a grounded structure is discussed in Section 6.9.)

The electrostatic energy accumulated in a thundercloud is the result of cloud electrification processes that produce an ambient electric field, by separating the cloud charges residing on different types of hydrometeors. This energy is converted by electrostatic induction into charges on propagating leaders, like conductors placed in an ambient electric field. The presence of induced charges diminishes the electrostatic energy of the cloud and changes the ambient electric field. The magnitude and distribution of induced charges on the leader are determined by the ambient potential distribution. These changes can be measured by electric field sensors on the ground, or on the aircraft. During the lifetime of a lightning flash, cloud charges do not move and do not change, and the lightning flash does not ‘discharge’ the cloud. To paraphrase from Kasemir [5]: ‘Lightning flashes do, in fact, transport the opposite charge into the cloud volume. During the lifetime of the lightning flash, this charge is still confined close to the lightning channel. The actual neutralization between cloud and lightning charge occurs after the lightning process is over. This neutralization may take a minute or more, rather than a second or less’.

An essential part in the development of lightning flashes is the phenomenon of current or channel cut-off, observed as the visual disappearance of a channel (branch) that was previously attached to the ground or to an existing conducting leader channel. The current in the disconnected channel or branch drops to zero. Current cut-off is a common feature in multiple CG flashes; it separates the subsequent dart leader/return stroke cycles. It will be shown in Section 6.3.1 that the current cut-off also precedes the occurrence of recoil leaders in branched positive leaders.

## 6.3 The composition of a lightning flash

Prior to a discussion of the composition of different types of lightning flashes, we must introduce leaders that are not involved in the initial stages of flash development, but that occur during the following stages of most flashes.

### 6.3.1 *The nature of ‘recoil streamers’ and dart leaders*

In the past, recoil streamers were identified as being equivalents to ‘mini-return strokes’ (this may be a reason for the word ‘recoil’), carrying negative charges in IC flashes or during the IC development of CG flashes, when some undefined positive leaders reached pockets of negative space charge inside the cloud [9]. Here, as in Schonland’s ‘source charge’ leader model, the charge transfer from a space charge to a conducting leader was assumed to be by a mechanism that does not exist in nature. The characterization of recoil streamers as mini-return strokes (also called K-changes) came from E-field measurements [e.g. 9, 10], and was largely due to the similarity of their step-like E-field changes to those of return strokes in CG flashes. However, the nature of recoil streamers and their role in the sequence of lightning processes remained confusing.

The current interpretation of recoil streamers is that they are actually negative leaders. The term, ‘recoil leaders’, replacing the term ‘recoil streamers’, reflects their true physical nature, because streamers are cold corona filaments of the length of a few meters, while leaders are propagating hot plasma channels. Recoil leaders originate somewhere along the previously developed trails of positive leaders, and move towards the origins of these leaders. This hypothesis was explicitly proposed in Reference 6, after a comparison of airborne measurements of aircraft-triggered lightning against a radiation map of IC flashes obtained with an interferometer. The hypothesis was positively confirmed only quite recently, with high-speed video observations [11], an example of which is in Figure 6.2. Obtained with a high-speed video system, the sequence of video images of a branched upward positive leader from a tall tower in Figure 6.2 illustrates the nature of recoil leaders.

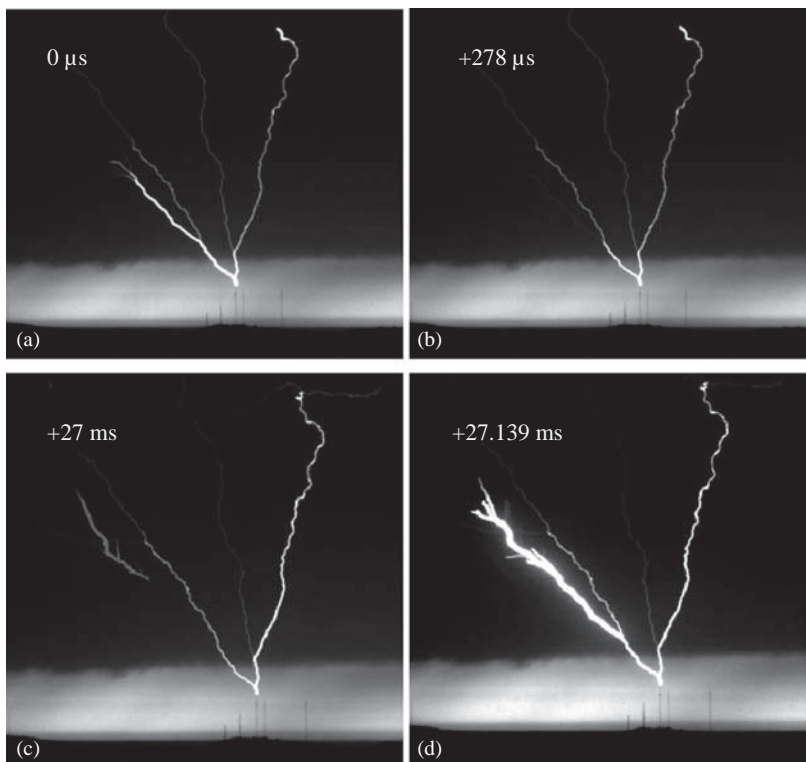


*Figure 6.2 Video images of the stages of an upward leader from a tall tower, recorded with a speed of  $7200 \text{ fr s}^{-1}$  [courtesy of T. A. Warner]. A branch of an upward positive leader visible in (a) that has a current cut-off and is, therefore, disappearing in (b). A recoil leader seen as a floating conductor 27 ms later in (c) is traversing the old path of the decayed branch towards the branching-point (the origin). The recoil leader makes a new branch (actually renews an old branch) after the attachment (d)*

The propagation of recoil leaders towards the origin of the preceding positive leaders is also illustrated in Figure 6.3, which shows a composite image of all recoil leader channels in an IC flash to be coming from the periphery towards the flash origin above.



*Figure 6.3 Composite image of all recoil leaders in an intracloud flash from a video sequence obtained with a high-speed video system ( $7200 \text{ fr s}^{-1}$ ) [courtesy of T.A. Warner]*

The view that recoil and dart leaders are the same events because of their identical polarity and similar origins was expressed in References 12 and 13, and is based on analysis of the time-resolved VHF images of lightning processes obtained with an interferometer. The only difference between recoil and dart leaders lies in the points of their attachment. Dart leaders end by touching the ground, while recoil leaders may end by connecting to a branching-point of a conductive channel to ground (of either a positive leader or a return stroke channel of a negative CG flash), or by dying out without reaching it. Thus, dart leaders in CG flashes are recoil leaders that actually reach the ground. Both leaders are electrodeless (floating) discharges, whose conducting channel propagates in an ambient electric field. As such, both leaders are bidirectional, with their potentials comparable to those of the negative-stepped leaders of CG flashes. The conditions under which initiation of recoil leaders occur will be discussed in Section 6.6.

### 6.3.2 *Intracloud flashes*

The mapping of lightning radiation sources with either the Difference of Time-of-Arrival (DTOA) or Interferometric technique [e.g. 14, 15] allows us to ‘see’ lightning processes inside the cloud, which are not visible through use of other

techniques. By applying the bidirectional leader concept to the interpretation of maps of lightning radiation sources, we are able to uncover the composition of lightning flashes, as well as the dynamics of lightning development in a cloud.

It is important to emphasize that both lightning radiation mapping techniques (i.e. DTOA and interferometer) operate in the VHF-UHF band, and are able to locate radiation sources produced primarily by negative breakdown processes in lightning flashes. Radiation associated with positive breakdown during the development of positive leaders is different in its nature from the radiation in a negative breakdown; and is much weaker than that of negative leaders in the VHF-UHF band [16]. This is why neither of the mapping systems is able to detect positive leaders in positive CG flashes [17], during IC development of negative CG flashes, or in rocket-triggered flashes. Occasional powerful positive breakdowns at the upper tips of the return stroke channels in negative CG flashes have been reported in the literature [13]. These events take place when a return stroke, carrying with it a near-zero ground potential, reaches the upper tip of a preceding leader that is in a region of high ambient cloud potential. A positive breakdown of this type may precede the formation of a new positive leader. We are able to recognize the path of positive leaders in maps of radiation sources because, as mentioned earlier, negative recoil leaders mark the paths of previously existing positive leaders.

A radiation map of a typical IC flash obtained with the DTOA technique [15] shown in Figure 6.4 exhibits in time, range and altitude a two-layer structure of radiation sources. The lightning flash started with the vertical development of

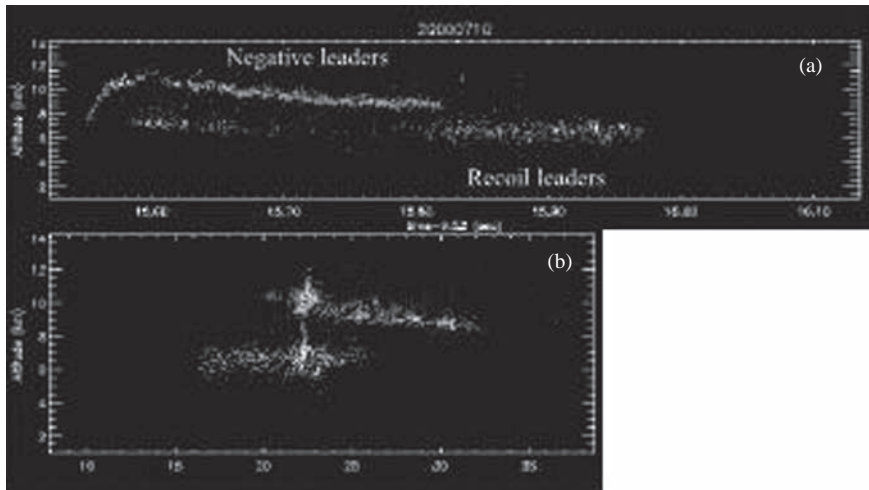


*Figure 6.4 Lightning radiation map of an IC flash [courtesy Ron Thomas, New Mexico Institute of Mining and Technology]. The (a) and (b) panels depict the altitude (km)-time (s) and altitude (km)-range (km) progression of radiation sources. The recoil leaders (lower layer) have a much greater dispersion and lesser density of sources than the initial negative leaders (upper layer)*

negative leaders, due to the primarily vertical potential gradient at the lightning origin (here at 7.0 km altitude). Then, negative leaders propagated mostly horizontally within the 9–11 km altitude region. Recoil leaders were first noticed at 30 ms after flash initiation, at approximately the same altitude as the initial negative leaders, and then developed horizontally, in the 6–7 km altitude region. The negative leader radiation appears on the map as a dense pattern of sources and is different from that of the recoil leader radiation, which is much more dispersed and less well organized.

During the first 30 ms of the initial stage of the flash, we have no evidence of the development of negative recoil leaders and positive leaders. It is reasonable, however, to assume that positive leaders did occur at this time, but that the current cut-off in their branches, which precedes the appearance of the recoil leaders, took place later. Negative leaders in the IC flash cease propagating, and their radiation also ceases, beginning at 270 ms after initiation (after 15.82 s in Figure 6.4(a)). Recoil leaders, on the other hand, become more numerous and dominant after this time. Their continuing presence indicates the continuing development of positive leaders.

The conceptual sketch in Figure 6.5 provides the interpretation of the lightning radiation map in Figure 6.4, and depicts the general features of bidirectional leader development. The initial stage of IC flashes corresponds to the occurrence of a bipolar leader, with a negative leader on one end and a positive leader on the other end of the bipolar lightning ‘tree’. The leaders’ progress in opposite directions is seen in the radiation map in Figure 6.4(b) and in the conceptual sketch in Figure 6.5, during the periods from  $t_1$  to  $t_3$ . The later stage of the flash (period  $t_4$  in Figure 6.5) corresponds only to the horizontal development in the positive part of the bipolar lightning tree (from the point of lightning origin outwards). This development

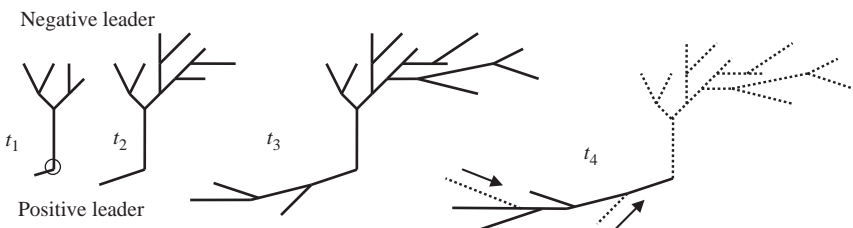


*Figure 6.5 Development of a bipolar lightning ‘tree’ in an IC flash consisting of positive and negative leaders. The depicted structures correspond to radiation sources at different periods of the IC flash in Figure 6.4: initiation of a bipolar and bidirectional leader from the origin (circle) at  $t_1$ ; branching and progression of the bidirectional leader during the initial stage of the flash at  $t_2-t_3$ ; current cut-off in the trunk connecting positive and negative parts of lightning tree; intermittent occurrence of negative recoil leaders (arrows) at  $t_4$ . There are no radiation sources or current flow at the negative end of the tree during period  $t_4$ . The branches in which current cut-off took place are shown as dashed lines*

consists of both positive leaders and intermittently occurring negative recoil leaders. No new negative leaders appear at the negative end of the tree during the later stage.

Recent observations with the DTOA system detected IC flashes with the same bilevel radiation structure as in typical IC flashes (e.g. Figure 6.4), but with the radiation sources of the recoil leaders residing in the layer *above* the layer containing the negative leaders. These were called ‘inverted’ IC flashes. The dynamics of inverted IC flashes are the same as those depicted in the conceptual sketch (Figure 6.5).

### 6.3.3 Cloud-to-ground flashes

A typical multi-stroke negative CG flash (Figure 6.6) exhibits cyclical development, with each cycle consisting of a downward stepped or dart leader, followed by a return stroke and, usually, by IC development of positive leaders. The latter is recognized in the record of the electric field change, by the presence of continuing current in the current record, or by the presence of recoil leaders in radiation-source maps or video observations. Stepped leaders propagate in virgin air, and produce a wide radiation path. Only a few radiation sources are detected in dart leaders prior to subsequent return strokes, because their propagation paths are along the still-ionized remnants of preceding return strokes. The stages of negative CG flash development, before a stepped leader touches the ground, are the same as in IC flashes, namely, both include bidirectional, bipolar and zero-net-charge leaders. The propagation of the negative leaders towards the ground and the occurrence of return strokes upon leaders touching the ground (see the conceptual sketch in Figure 6.7) make CG flashes different from IC flashes. The return stroke that propagates along the preceding bidirectional leader brings its upper tip to near ground potential. This may initiate the development of the unidirectional positive

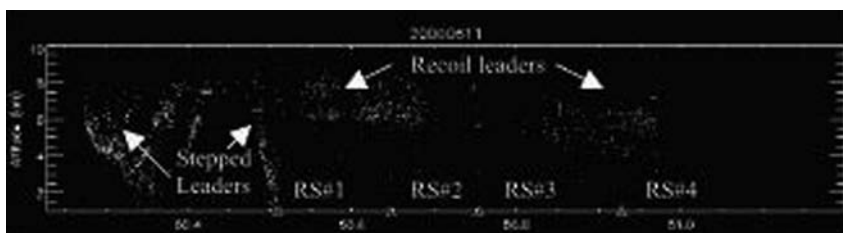
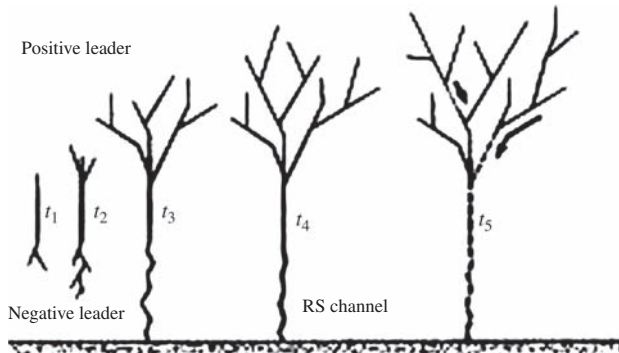


Figure 6.6 A lightning radiation map, showing altitude (km)-time (s), of a multi-stroke negative cloud-to-ground flash [courtesy Ron Thomas, New Mexico Institute of Mining and Technology]. Stepped leaders started at an altitude of 6 km, first terminating in the air and then reaching the ground at time 50.5 s. Four return strokes (RS) are marked with symbol  $\Delta$  on the time axis. Negative dart leaders are virtually invisible on the radiation map because of their propagation along the weakly ionized channels of previous return strokes, rather than through virgin air, as in the case of stepped leaders



*Figure 6.7 Development of a bidirectional, bipolar lightning ‘tree’ in a negative CG flash made of positive leaders, above, and negative leaders, below.  $t_1$  shows initiation of a bipolar and bidirectional leader;  $t_2$  shows progression of the bidirectional leader;  $t_3$  shows the ground contact of the negative leader;  $t_4$  shows the return stroke;  $t_5$  shows the current cut-off and progression of the positive leader, with the intermittent occurrence of negative recoil and dart leaders (arrows) travelling towards the flash origin*

leader, which may continue as a branched leader, even after current cut-off occurs in the channel to ground (period  $t_5$  in Figure 6.7). Current cut-off may also occur in the first return stroke channel before it reaches the upper tip, due to the preceding branched stepped leaders in the CG flash (see Section 6.7). Recoil leader radiation in CG flashes is observed following the return strokes, and it indicates the development of positive leaders during interstroke intervals (see Figure 6.6).

In cases of positive CG flashes, an initial negative leader progression occurs within a region identified as ‘a bright band’ in a vertical cross-section of radar images of decaying thunderstorms. Radiation from positive leaders to the ground is not detected by lightning mapping systems, although the points where they touch the ground are determined (after careful examination) from the slightly more pronounced radiation path of the return strokes. The same concept, of the bidirectional, zero-net-charge leader, also describes the initial stages of positive CG flashes until the attachment of the positive leader to ground (see Figure 6.7). The final stage of this flash is an upward negative leader progression energized by the return stroke, after it reaches the upper tip of the preceding bidirectional leader. The negative leader progression ends when all branches of the leader meet their potentials, which means that the potential gradient at the tip is below the threshold needed for leader formation. The absence of recoil leaders in positive CG flashes represents their primary difference from negative CG flashes.

This brings us to the issue of the multiplicity of return strokes, or rather, the absence of such multiplicity in positive CG flashes. Numerous successful triggering of upward negative leaders, by rockets with a trailing grounded wire in winter

storms in Japan, have shown that there are no downward positive recoil leaders that travel back along the remnants of the previous channel to ground after the leader channel cut-off. This means that there were no observed analogs to the dart or dart-stepped negative leaders in positive CG flashes [18], which commonly occur in multi-stroke negative CG flashes. In fact, during the entire multi-year duration of the rocket-triggered lightning program in winter storms in Japan, there were no cases of the triggering of a positive CG flash; only upward negative leaders were triggered by this technique [19]. This evidence strongly supports the hypothesis [20] that positive CG flashes cannot have multiple return strokes as a result of recoil leaders. This hypothesis is consistent with the observation that positive CG flashes most often have only one return stroke [21].

Positive CG flashes, with several channels to ground separated by distances of tens of kilometers from each other have been observed and mapped with the DTOA system in summer thunderstorms in the United States [22]; however, these were not multi-stroke flashes. In defining multiplicity in CG flashes, we assume at least a partially common path for downward leaders inside a cloud, with the possibility of different attachment points on the ground. It would be a mistake to pronounce closely occurring signatures of positive CG flashes in electric field change records in the time domain as evidence of a multiple CG flash.

In discussing the various types of lightning flashes, we cannot avoid the topic of branching, which occurs in any leader development in virgin air. It is reasonable to assume that in general, branching is governed by the potential gradient in the direction of the leader's propagation. The exact conditions for branching initiation are still unknown. The propagation of branches ends when the potential of a branch reaches approximately the same potential as the environment.

## **6.4 Continuing current as an indicator of a developing leader**

The existence of continuing current has been consistently acknowledged in the past, and its presence has been detected in the records of current and slow electric field changes after return strokes in CG flashes, in the current records of rocket-triggered lightning (see Figure 6.8) and upward leaders, and as the continuing luminosity of visible channels. However, until recently, this was considered to be a separate process in lightning development; events with continuing current were called 'continuing current discharges' [24]. Another definition was suggested in Reference 25: 'The continuing current... can be viewed as a quasi-stationary arc between the cloud charge source and ground along the path created by the preceding leader-return stroke sequence'. This definition of continuing current implies an assumption that a physical process exists by which cloud charges can be squeezed into the conducting channel. As in the Schonland's 'source charge' model of the leader, such a physical process does not exist in nature.

We arrive at a clear explanation and clear definition of continuing current through the acceptance of the bidirectional leader concept. Our present understanding is that continuing current is the result of the changing distribution of

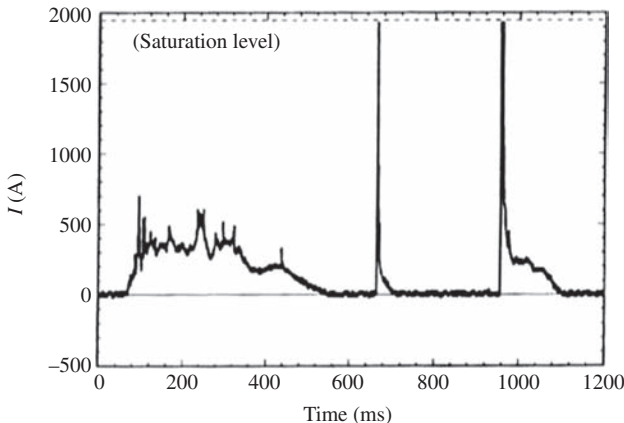


*Figure 6.8 Current record of a rocket-triggered cloud-to-ground flash showing continuing current during the positive leader phase and after each of two return strokes [adapted from Reference 23]*

induced charges on a conducting leader channel during its development (elongation) in the ambient electric field [26] (see also Section 6.6). This continuing current is an inseparable part of any leader process, regardless of polarity. In close proximity to the leader tip, especially that of the negative leader, continuing current is superimposed on the pulse current, which originates at the tip as a result of the breakdown process in the corona streamer zone ahead of the leader [27]. The presence of continuing current is an indication of a developing leader in the flash. The duration of continuing current varies from a few to hundreds of milliseconds. A continuing current of some duration is present after most return strokes, since, normally, leader development immediately follows each return stroke in a CG flash.

## 6.5 Spider lightning

‘Spider lightning’ (see Figure 6.9) has long been a well-known phenomenon frequently observed during the decaying stage of a thunderstorm, and recognized by its numerous, stratified ‘fingers’ (luminous channels) which stretch for tens of kilometres under the cloud base. Spider lightning was originally perceived as a type of lightning discharge in its own class. Its true nature has been unveiled only recently, after comprehensive measurements in time- and space-domains using the Interferometric technique for mapping radiation sources, combined with observations of the electric, magnetic fields, as well as optical and high-speed video recordings [28]. It has been determined that spider lightning is a negative leader propagating in virgin air and, thus, is similar to a negative stepped leader in CG flashes, although with a somewhat different branching structure. Spider lightning is



Figure 6.9 ‘Spider’ lightning: visible, stratified lightning channels propagating over large distances near the cloud base during the decaying stage of a storm [courtesy National Severe Storms Laboratory archives]

the negative part of a bidirectional lightning tree, with the positive part represented by positive leaders, and then recoil leaders, which are usually hidden inside the cloud. Spider lightning can be a part of either IC or positive CG flashes during the decaying stage of the storm [28]. The stratification of spider lightning channels is related to the stratification of potential distribution during the *decaying* stage of a storm; this is different from the potential distribution structure during the *mature* stage of a storm, when most negative-stepped leaders occur.

## 6.6 The analytical relationship between the electrical structure of a cloud and lightning parameters

A consistent physical model which describes the relationship between cloud charges and lightning enhances our understanding of the lightning processes in a thunderstorm. Kasemir [3, 4] was the first to analyse the relationships between cloud charges and lightning discharges, by applying the potential theory of electrostatics to the Wilson-Simpson thunderstorm model. The two-dimensional physical model developed in Reference 26 simulates the dynamics of the bidirectional leader process of a vertical, non-branching, equipotential leader in a mature storm. Both tips of the bidirectional leader are assumed to develop equally. This model allows us to determine the quantitative relationships that exist among cloud charges, potentials, electric fields, induced charges and currents in the lightning channel from the numerical solution of Poisson’s equation for an assumed cloud charge model. All lightning parameters are functions of the ambient potential distribution. This model [26] considers only vertical development, which might be valid for the early development of lightning channels, but is not so for lightning channels with branches.

### 6.6.1 Physical model of the development of intracloud and cloud-to-ground leaders

In the two-dimensional physical model presented in Reference 26, the development of an IC discharge starts in the region between upper positive and lower negative cloud charges where the highest electric field exists, which is at a 9.0 km altitude for the hypothetical case (see the cloud vertical potential distribution in Figure 6.10 (a)). The development of a CG discharge starts in the region of the maximum electric field between the lower negative and lower positive cloud charges, at a 5.0 km

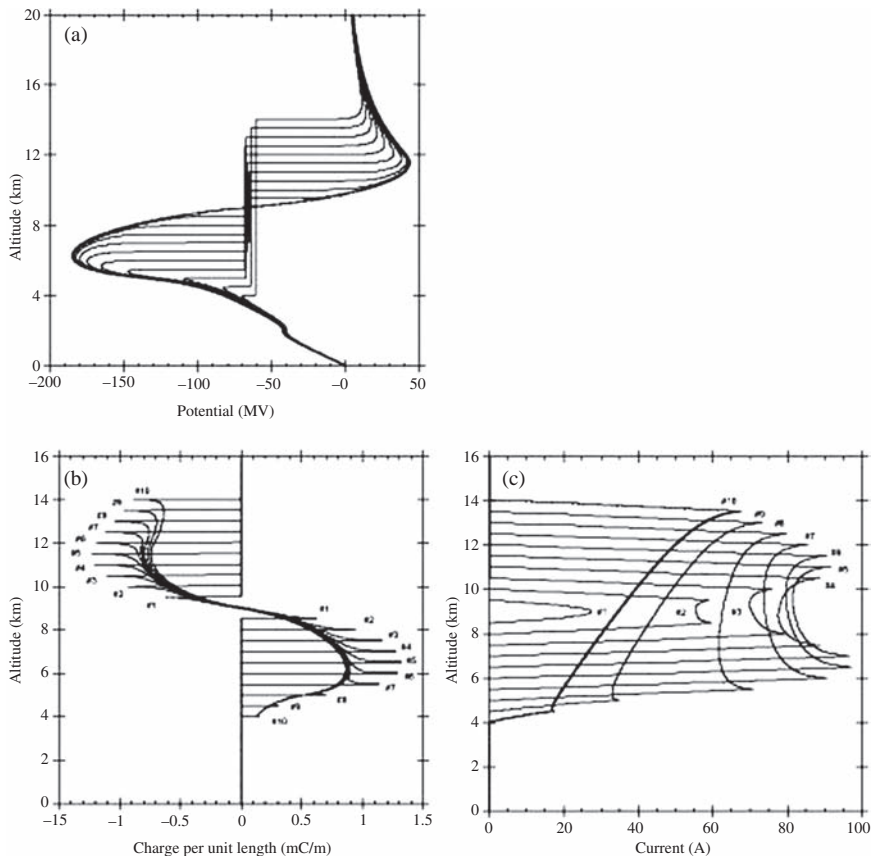


*Figure 6.10 Evolution of potential profiles (a), induced charges (b) and continuing current (c) of the developing intracloud leader, from computer simulation in Reference 26. Stages of bidirectional leader extension are marked with numbers 1–10. The bidirectional leader starts at altitude of 9 km. The lower, positive leader reaches an altitude of ~4 km and stops, while the upper, negative leader continues propagating upward [adapted from Reference 26]*

altitude, in the example used in the model (see the vertical potential distribution in Figure 6.11(a)). The maximum potential gradient at the tip is aligned with the leader's direction.

For both the IC and CG leaders, the model shows that vertical development of the upper, positive tip of the CG leader, and the lower, negative tip of the IC leader, stops when the potential difference there reaches a level below the threshold value. Meanwhile, the development at the opposite tip of the bidirectional leader continues: downward in the CG leader and upward in the IC leader, respectively (Figures 6.10(a) and 6.11(a)). During the leader's progression, a continuous

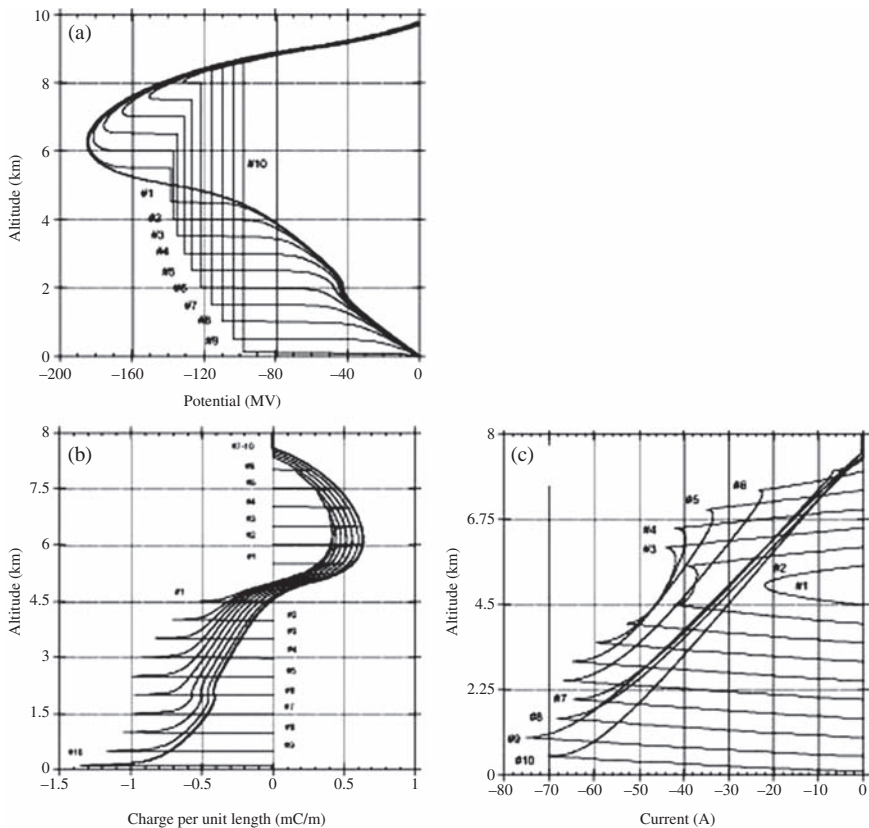


**Figure 6.11** Evolution of potential profiles (a), induced charges (b) and continuing current (c) of the developing cloud-to-ground leader, from computer simulation in Reference 26. Stages of bidirectional leader extension are marked with numbers 1–10. The bidirectional leader starts at an altitude of 5 km. The lower, negative leader reaches the ground, while the upper, positive leader stops at an altitude of 8.5 km when the potential gradient at the tip reaches a value below the threshold [adapted from Reference 26]

redistribution of induced charges occurs along the leader's length, in order to maintain a zero net charge (Figures 6.10(b) and 6.11(b)). The attributes of lightning development observed in the model do exist in nature. One example of this is the limitation of vertical development of leaders seen in the lightning radiation map of the IC flash in Figure 6.3. The model also indicates that an IC flash can propagate outside the upper cloud boundary where the ambient electric field is lower than inside the thunderstorm. Events like these have been observed from space [29].

## 6.7 Current cut-off in developing lightning flashes

Malan and Schonland [30] suggested that lightning has multiple return strokes because the channel to ground becomes resistive and is cut off, while the upper part of the channel continues to extend. Krehbiel *et al.* [24] concluded that ‘observational evidence of channel cut-off comes from electric field measurements of close ground (negative CG) discharges, which often exhibit a fast recovery …’ Similar evidence is found in electric field records produced by negative leaders triggered using the classic rocket-triggering technique (Figure 6.12), and in positive CG flashes observed in winter storms in Japan [18].

What produces current cut-off? First, let us consider the case of a single, non-branching channel. For this type of lightning channel, Krehbiel *et al.* [24] suggested that two factors: ‘negative resistance of the arc, and available source current work interactively to result in increasing resistance along the channel to ground, thus causing the current cutoff’. This concept resembles the one suggested by Malan and Schonland [30].

The conditions for leader progression for a non-branching leader connected to ground are similar to that of a non-branching return stroke channel; therefore, by reaching its potential at the tip, the propagation of either the leader or return stroke will stop, and with it, the current, also. This will be the defined end of a flash.

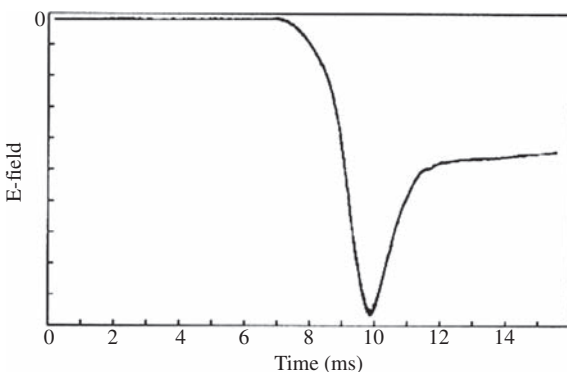


Figure 6.12 An example of the fast decay of E-field on the ground near a negative leader triggered by the classic rocket-triggering technique [adapted from Reference 18]

Heckman [31] proposed a concept of channel instability for a straight, or bending, or tortuous lightning channel of several kilometres in length. This concept implies that the channel is extinguished between strokes, if it carries less than about 100 A. Heckman equated lightning to a circuit consisting of an arc connected to a current source at the leader tip, with the circuit becoming unstable if its RC ( $R$  = resister,  $C$  = capacitor) time constant exceeds the characteristic cooling time. The unsupported assumption in Heckman's concept is the existence of a current source at the leader tip. The actual current source for a return stroke or an upward leader is in the ground. What Heckman's concept describes is what we perceive to be the end of leader propagation due to the reaching of its potential, which is also the end of the flash. Neither Krehbiel's nor Heckman's concepts leave room for the recoil or dart leader processes after their 'current cut-off'. Our definition of the end of a flash explains the current 'cut-off' in a non-branching lightning channel that these researchers have attempted less successfully to address.

A different approach to the current cut-off process was suggested by Mazur and Ruhnke [20] for branching leader channels. In this approach, the authors applied the relationship between the induced charges on a leader channel and the ambient potential discovered by Kasemir [32], who calculated the induced charges on a vertical leader, and found that the charges are proportional to the ambient potential, with only a slight effect of self-screening. Self-screening is the decrease, by the charges on the upper part of the channel, of the ambient electric field near the lower part of the channel. The consequence of self-screening is the reduction in induced charges on the lower part of channel. For example, after advancing several kilometres upward, the charge density on the lower part of the leader changes less than 10 per cent. We ignore this decrease in charge density in our conceptual model.

In our conceptual model, the progression of a non-branching leader in a constant electric field is depicted as stage A, in Figure 6.13. In the middle and upper panels of stage A, there is an increasing charge-per-unit length and a constant current along the channel.

The situation, however, changes drastically if we consider branching at any level (see stage B of Figure 6.13). Branching of the developing leader would screen off (like an umbrella) the electric field below. This mechanism is similar to that of the 'field choking' effect on secondary streamers by a space charge deposited by primary streamers in laboratory discharges [33]. The screening lowers the ambient electric field and potential distribution near the lower part of the main channel, and with it, the distribution of induced charges on the vertical channel. This effect can be seen conceptually as removing the excess of positive charges from the channel to ground. This removal of the excessive positive charge along the vertical stem occurs linearly, and the amount of the charge removed increases as the screening increases. The resulting negative current in the stem varies: it is highest at the ground, and zero at the branch point. The effect of field screening is shown in stage B of Figure 6.13 as a decrease in charge distribution along the vertical channel, and as a decrease in the leader's current flow from the ground. The screening effect of branching on the current in the stem occurs simultaneously with upward development of the branched leader, which causes a steady growth of the

constant current in the vertical channel. Both contributions to the total current (from the screening effect and from the effect of steady growth) work in opposite directions, and affect it at different rates. Because the screening by this effect is never perfect, a current cut-off by this screening process alone is unlikely.

The situations will change, however, if multiple layers are present, as depicted in stage C of Figure 6.13. Any new branches that develop above the existing branches will also screen the lower branches, and will thus decrease, or end, their propagation. This will lead to a flow of positive charges from the lower branches to the upper branches, reducing the total current from the ground. This process, together with the decrease in current by the screening effect shown in stage B, will overwhelm the ever-increasing current in the stem of the branch (vertical channel in Figure 6.13), and will eventually lead to current cut-off at the ground. In general, any branch point can become a current cut-off point. The ‘fast recovery’ of the electric field in branched upward leaders (e.g. Figure 6.12), and also in branched return strokes, is easily explained by the effect of branch screening described in our concept.

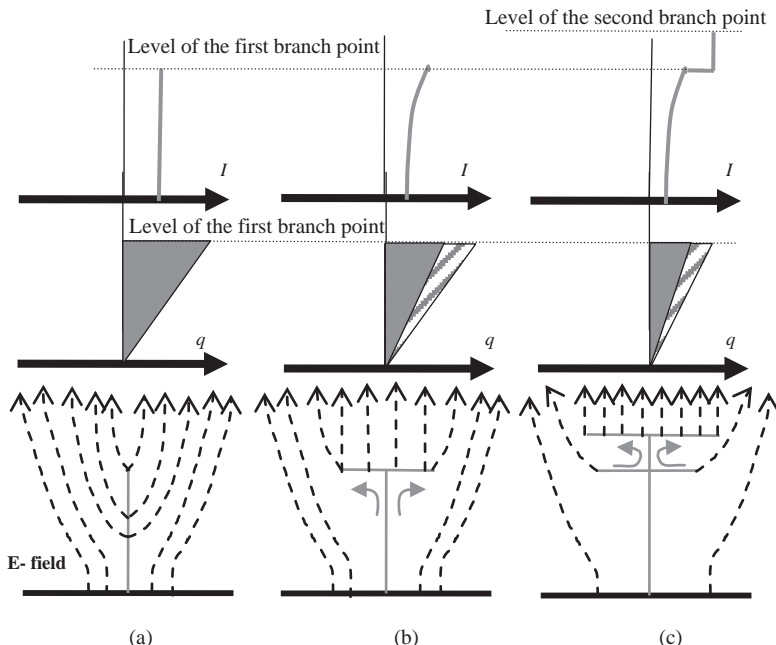


*Figure 6.13* Screening of the ambient electric field below the branched portion of an advancing leader reduces the charge distribution and current in the main channel prior to the current cut-off [adapted from Reference 20]. Panels (a), (b) and (c) represent the stages of (1) induced currents,  $I$ , and their vertical distribution up to the first branch point during the growth process, (2) charge distribution,  $q$ , on the main (vertical) channel and (3) electric field lines (dashed arrows) around the leader channel. Solid arrows show the direction of current flow

Most current records of upward positive leaders show the continuing current increasing linearly for about 10 ms, and then hovering at intermediate levels, or gradually decreasing for up to 500 ms, until a current cut-off occurs that may be followed by several dart leader-return stroke cycles, with a current cut-off between each cycle, as seen in Figures 6.8 and 6.16.

The cut-off process described in the model [20] is not limited to cut-off at the lowest branching-point, but may occur at any branching-point and in any branching structure, regardless of its connection to ground. However, even after many of its branches are cut off, the conditions for leader propagation may still exist at a tip (or tips) of the branched structure. Leader propagation would stop when each tip reaches an ambient potential insufficient for a streamer-leader transition, in other words, the leader reaches its own potential. Reaching its own potential in all of the leader's branches constitutes the end of the life of the flash, and may take place after several hundreds of ms of development. This phenomenon is also observed in upward positive leaders or return stroke channels without branches, but it is not a current cut-off, by the definition applied in Reference 20.

### *6.7.1 Current cut-off and recoil leaders*

Recoil leaders in IC flashes and in positive leaders during the IC development of CG flashes appear following channel cut-offs in the branched, positive end of a bidirectional and bipolar lightning tree (see Section 6.2.1 and Figure 6.2). Some recoil leaders produce M-components in conducting channels to ground (more about M-components in Section 6.10). When a recoil leader traverses the remnants of the channel to ground of a previously existing (after current cut-off) branched positive leader or a branched return stroke of a CG flash, it becomes the dart leader of a subsequent dart leader-return stroke cycle. This situation takes place in upward positive leaders followed by a CG flash, and also in multi-stroke CG flashes.

Mazur and Ruhnke [20] proposed a mechanism for recoil leader formation, following current cut-off, in the established positive leader's channel that includes (1) the conservation of a unipolar charge trapped in the channel after it is cut off, and (2) the induction of dipole-type charges on the floating conducting channel of the leader in the ambient electric field.

After current cut-off, and during its continuous, upward propagation, the floating leader will have a dipole charge in addition to a residual charge, with the net charge remaining constant. The potential of the extending floating channel shifts towards the cloud potential, while the remnants of the channel below the cut-off point remain at near-zero potential. This difference of potentials near the cut-off point may be sufficient to initiate an electrical breakdown and the formation of a downward-propagating leader. This is a recoil leader. A somewhat similar process occurs in 'altitude-triggered lightning' (with a trailing wire insulated from the ground), where a positive leader develops at the upper tip of the rocket, and a negative leader starts much later, at the low end of the trailing wire, and propagates towards ground.

Logic would suggest that this mechanism should work independently of the polarity of the floating leaders. However, while negative recoil leaders do occur after

cut-off in positive leaders and in return stroke channels of negative CG flashes, there is no observational evidence of positive recoil leaders occurring either in negative leaders triggered by the rocket-triggering technique, or in return stroke channels of positive CG flashes after the channel cut-off, or at the negative end of the lightning tree during the initial stage of the IC flash. To date, we still lack a physical explanation for these phenomena.

## 6.8 The remaining puzzle of positive cloud-to-ground flashes

The lightning processes in positive CG flashes continue to be less well investigated than those in negative CG flashes. We have only a relatively small amount of comprehensive data on rocket-triggered upward negative leaders, which resemble return strokes of positive CG flashes. There is also very little known about the characteristics of downward positive leaders in positive CG flashes. The inability of the two lightning mapping techniques (DTOA and Interferometric) to map positive leaders (see Section 6.2), and the absence of other methods to trace downward positive leaders, make it difficult to discover the origins of positive CG flashes of a complex structure during the decaying stage of summer thunderstorms [e.g. 28]. It is encouraging that in positive CG flashes of a less-complex structure, in Japanese winter storms, the origin of a positive leader is found at the origin of the negative leader's radiation, identifiable in lightning radiation maps [34]. Not surprisingly, this observation fits the bidirectional leader concept very well.

Among the parameters of positive CG flashes, the values of return stroke currents and charge transfers have been obtained from direct current measurements on tall structures, or estimated from electric field records, by using various models. The difference between the charge transferred by the return stroke in negative and positive CG flashes is especially significant. Brook *et al.* [35] and Uman [36] attributed the huge charge transfers in positive CG flashes (up to 1000 C in positive CG flashes, vs. up to only 10 C in negative CG flashes) to the much-longer period and much-greater values of continuing current in a single-stroke positive CG flash than those in a single-stroke negative CG flash. One may go further in the interpretation of these differences: The long duration of continuing current typical for positive CG flashes equates with the long duration of and, thus, the significant length of the upward negative leader's development. For comparison, the long continuing current periods in negative CG flashes are typically observed only after some subsequent return strokes in multi-stroke CG flashes. The greater amplitude of the continuing current in positive CG flashes indicates the considerable spatial dimension of the rapid branching in the negative leaders following return strokes. (Each new branch represents an additional current source feeding the return stroke channel.) These attributes in positive CG flashes are especially noticeable when comparing video images, obtained with a high-speed and high-resolution video system (Figures 6.14 and 6.15), of return strokes in positive versus negative CG flashes. The video images confirm the profound difference that exists between the

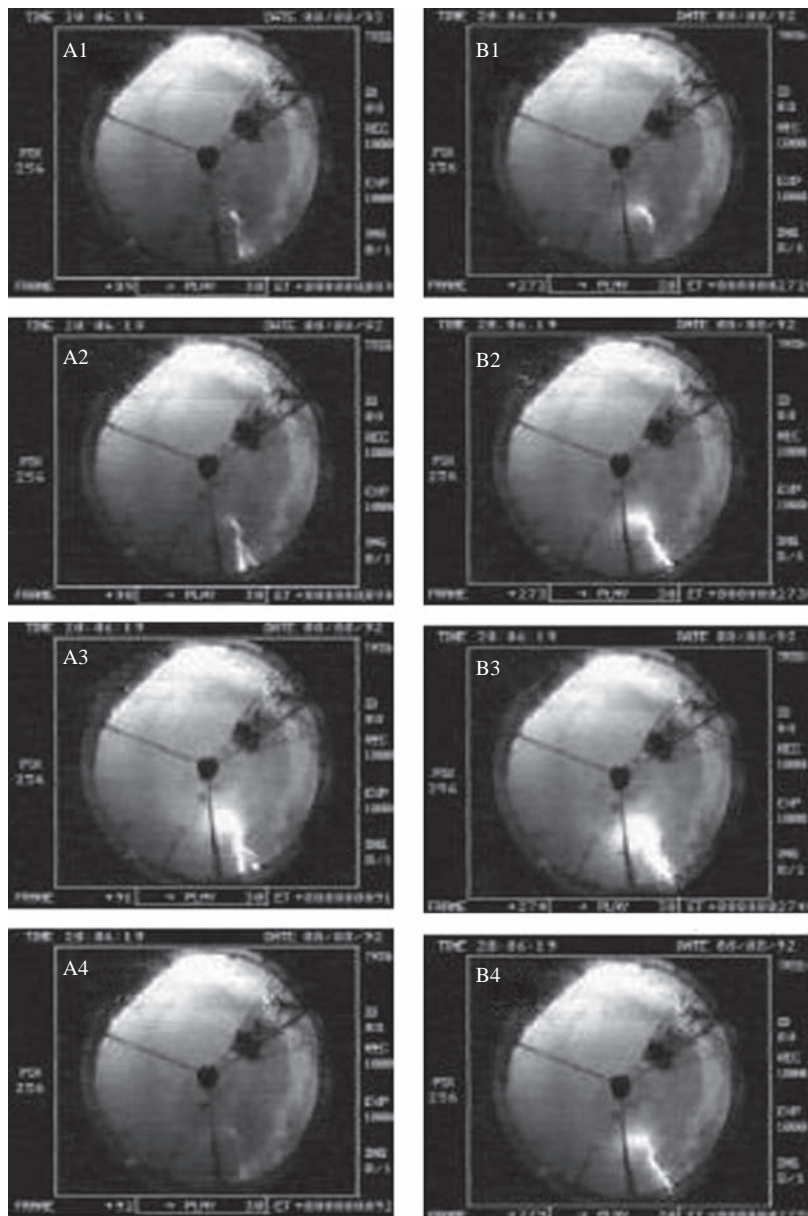
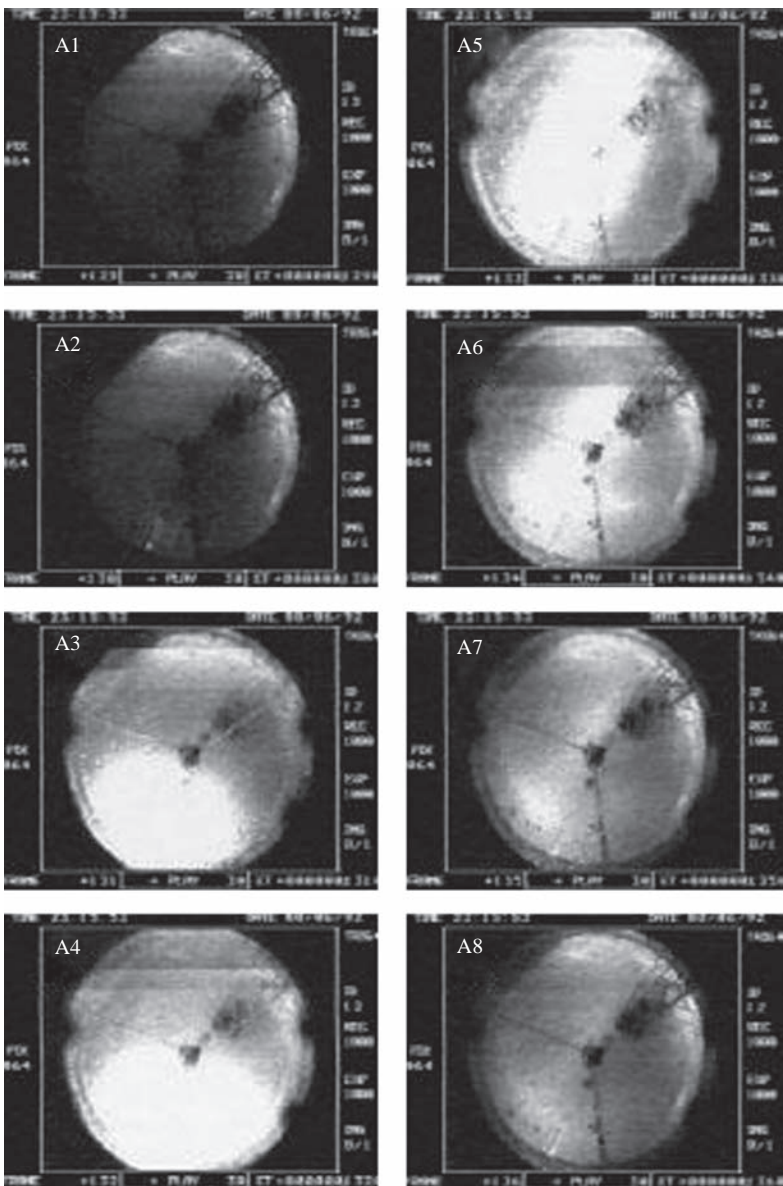


Figure 6.14 Series of video frames of a multi-stroke negative CG flash seen in a parabolic mirror, obtained with a high-speed (time resolution of 1 ms) video system [12]. In series A: the stepped leader (A1, A2), the first return stroke (A3) and the continuing current (A4). In series B: a dart leader (B1, B2), the fourth return stroke (B3) and the continuing current (B4)



**Figure 6.15** Series of video frames of reflections of a positive CG flash seen in a parabolic mirror, obtained with a high-speed (time resolution of 1 ms) video system [28]. Prior to flash (A1), the positive leader (A2); the return stroke (A3); development of the negative leader energized by the return stroke connected with the luminous channel to ground, visible in A3–A6; visible continuing current (A7–A8). The video system setting was the same for images in Figures 6.14 and 6.15

durations and spatial extents of leader development energized by the return stroke in positive and negative CG flashes. The difference in the spatial extents is explained by the highly dendritic branching in a negative leader versus the much - lesser branching in positive leaders. The difference in the durations of leader development may be due to differences in the ambient potential distributions in the storm stages (mature stage vs. decaying stage) during which CG flashes of each polarity may occur.

## 6.9 Upward lightning

Upward lightning represents the majority of lightning strikes to tall structures of more than 100 m in height. Every upward lightning flash starts as an upward leader characterized by a sustained propagation, and may or may not be followed by a CG flash, i.e. by a dart leader-return stroke cycle. Of all types of lightning, upward *positive* leaders are the most closely studied, because they are very frequent in summer-type thunderstorms. Much less studied are upward *negative* leaders; they are rare in summer thunderstorms, but are frequently triggered with a classic rocket-triggering technique, especially in winter storms in Japan. Our understanding of the physical processes that take place during propagation of upward leaders from tall structures is limited, and consists primarily of characterizations of the different current waveforms derived from measurements of upward leader current on instrumented tall towers [e.g. 37, 38] and rocket-triggered lightning studies [e.g. 39] (see, e.g. Figure 6.16).

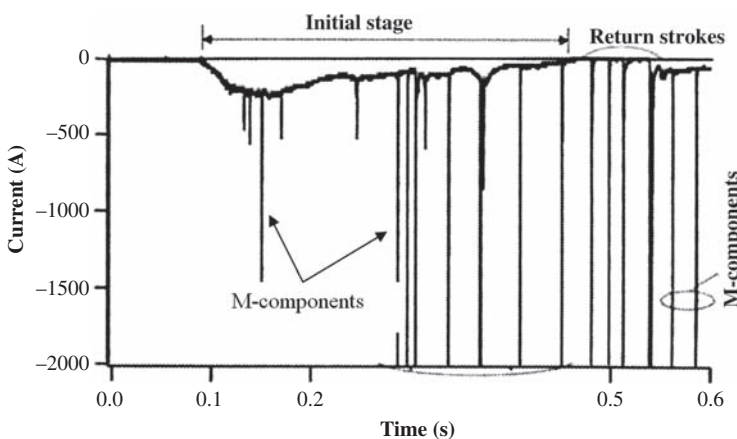


*Figure 6.16 Current record of a positive upward leader followed by a multiple cloud-to-ground flash (in Atmospheric Electricity sign convention) [adapted from Reference 39]. The phase of the upward positive leader is identified in the figure as the initial stage. It consists of continuing current with superimposed current pulses of M-components. M-components also occur following the fourth return stroke*

Continuing current in an upward positive leader is evidence of its continuing propagation, and has an average duration of 300 ms, with a maximum value of ~700 ms. Its amplitude ranges from 15 A to 2.1 kA [39]. The impulsive current during the upward leader phase is superimposed on the continuing current, and is in the range of weak return stroke currents (averaging 4.5 kA) [39]. Negative upward leaders do not have a distinct impulsive current similar to that in an upward positive leader, as seen in Figure 6.16 as M-components. Continuing current usually has a shorter duration, but a much greater amplitude in kA range, about 10 times higher than that of positive upward leaders (Figure 6.17).

Upward positive leaders from tall structures are triggered by passing in-cloud leaders, as suggested first by Berger and Vogelsander [40], or by return strokes carrying charges of the opposite polarity. This triggering mechanism is analogous to the application of a high-voltage pulse to an electrode in a high-voltage chamber, in order to start a leader. In the case of an upward positive leader, a similar effect, of breaking the corona shield surrounding the tip of the structure, is produced by

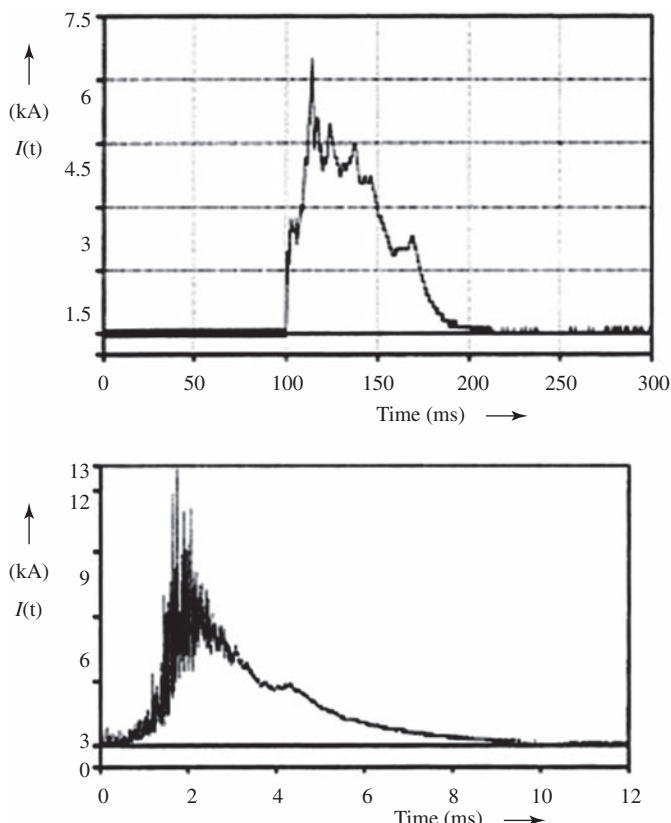


*Figure 6.17 Current records of two negative upward leaders from a tall tower [adapted from Reference 37]*

the fast-changing electric field of an approaching negative leader (see Figure 6.18), or a return stroke of a positive CG flash (also of negative polarity).

Upward leaders from tall structures may be considered to be examples of associated, or ‘sympathetic’, discharges [29, 41], so named because one lightning process produces the conditions for starting another in the space of a few milliseconds, some distance away, and without evidence of any physical connection between the two discharges.

Still poorly understood are the initiation conditions for upward leaders without the presence of triggering factors, such as in-cloud leaders or return strokes. Wang *et al.* [42] identified such cases from the analysis of upward lightning strikes to a wind turbine and a protective mast (both about 100 m tall) during winter storms in Japan. There is a suggestion, in the data presented in Reference 42, that a strong wind near the top of the mast at the time of upward leader initiation was conducive to removing the corona shield, thus exposing the mast to a very high electric field typical for winter storms in Japan.

Visually, upward positive leaders exhibit two types of developing patterns: non-branching, with slow variation in channel luminosity (e.g. Figure 6.19); and

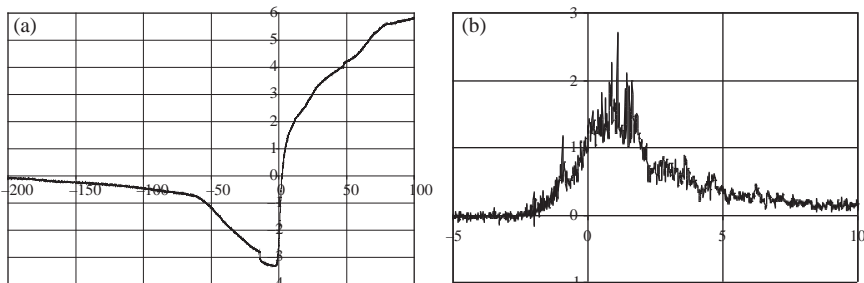
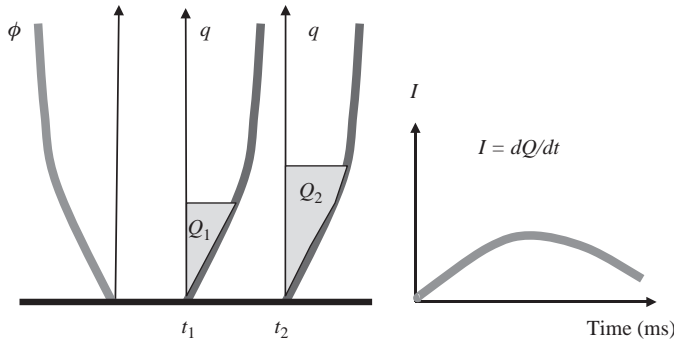


Figure 6.18 (a) The  $dE$  record (in  $kV\ m^{-1}$  and ms) and (b) the raw  $dE/dt$  record (in V and ms) of an upward positive leader from a tall tower triggered by a bypassing negative intracloud leader. The zero-time in both records corresponds to the instant of triggering of the video system [adapted from Reference 11]



Figure 6.19 A non-branching upward positive leader from a tall tower in Rapid City, South Dakota [courtesy of T. A. Warner]. The channel lasted for 83 ms, and exhibited slowly changing luminosity



*Figure 6.20 Conceptual sketch explaining the varying luminosity of the ascending upward leader channel. Depicted are the vertical potential profile ( $\phi$ ), induced charges ( $q$ ) on the vertical conducting channel at two times,  $t_1$  and  $t_2$ , and also the current ( $I$ ) in the ascending channel, as a function of time*

branching, with both initial, slowly changing luminosity of the channel to ground, and later, with pulse-type luminosity in the region of branching also affecting the channel to ground (e.g. Figure 6.21).

We interpret the slow variation in the upward leader's luminosity during its ascent to be a result of propagation of the conducting channel through a region of varying ambient potential. Following is an explanation of our concept, illustrated in Figure 6.20.

If the vertical profile of ambient potential distribution is the curve  $\phi$ , then the induced charges,  $q$ , on the ascending conducting channel will be distributed along a profile which is a mirror image of curve  $\phi$  [32]. The current in the leader channel,  $I$ , is the result of changing induced charges during the ascent of the leader (e.g. between times  $t_1$  and  $t_2$  in the sketch). Thus, although the current remains constant along the channel at any given moment, its amplitude changes with time, and so does the channel's luminosity.

## 6.10 M-component

In addition to slowly changing luminosity, branched upward positive leaders exhibit a pulse-type brightening, which, with its electric signatures (a ‘hook’-shaped electric field change), fits the definition of an M-component [25, 43]. An example of a visual and electrical record of an M-component is shown in Figure 6.21.

The ‘hook type’  $dE$  record of an M-event in Figure 6.21 shows a negative change indicative of an approaching negative leader, followed by its attachment to the continuing current channel, and the addition of a new positive charge (notice the upward jump in the record). The upward leader progression continues after the attachment, as indicated by the same angle in the upward slope before and after the event.

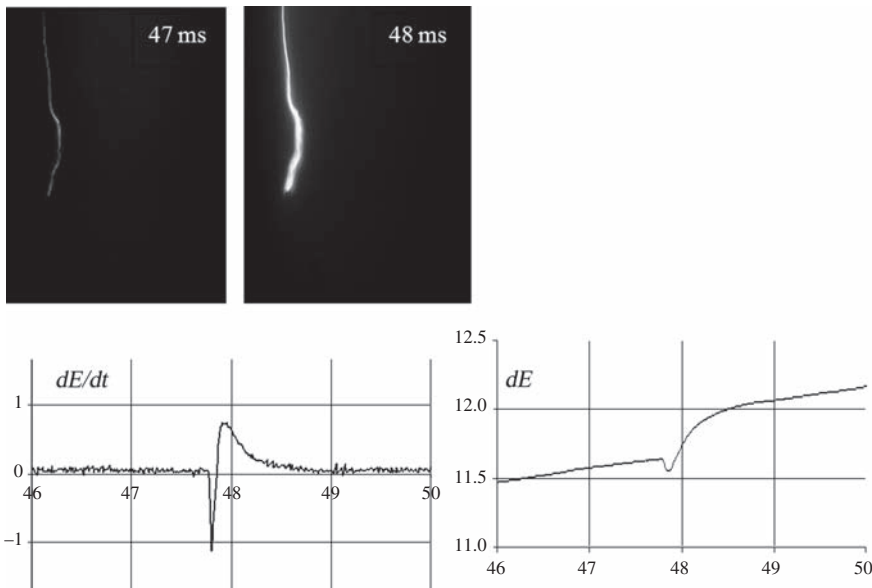


Figure 6.21 Pulse-type luminosity in a positive upward leader from a tower, and the electric field changes associated with it [adapted from Reference 11]

Studies of CG flashes using interferometers and high-speed video [12,13] identify, as an ‘M-event’, the result of collision between recoil leaders and the conducting (luminous) channels connected to ground following the return stroke. The newly introduced term ‘M-event’ implies that this is a process, the outcome of which is an ‘M-component.’ In our view, the term M-event is more appropriate, as well as less confusing, than the term M-component.

Development of a recoil leader along the path of a previous positive leader branch was illustrated in Figure 6.2. Upon attachment to the positive leader channel connected to ground, there is pulse-type re-illumination of the attached new branch and the channel below it (see Figure 6.2(d)).

Following interception with the leader channel, the newly established branch obtains ground potential as a result of current flow from the conducting upward leader channel connected to ground (see the concept in Figure 6.23). This often leads to new positive breakdowns at the upper part of the new branches (Figure 6.22).

The series of events leading to M-components in upward positive leaders are:

1. branching of a positive leader;
2. current cut-off of a branch;
3. occurrence of a recoil leader along the path of an old branch, and
4. attachment of the recoil leader to a branching-point of an old branch on the conducting channel of the positive leader.



**Figure 6.22** A composite image of recoil leaders during the entire lifetime of an upward positive leader from a tall tower taken with a high-speed video system at  $7,200 \text{ fr s}^{-1}$  [courtesy of T.A. Warner]. Recoil leaders propagate towards the branching-points of previously existing branches of upward leaders. Some recoil leaders are seen to terminate before reaching a branching-point. However, some branching-points where recoil leaders attach are not on a leader channel connected to ground. A current pulse and a 'hook'-type electric field change of M-component records are produced upon the attachment of a recoil leader to the positive leader channel connected to ground

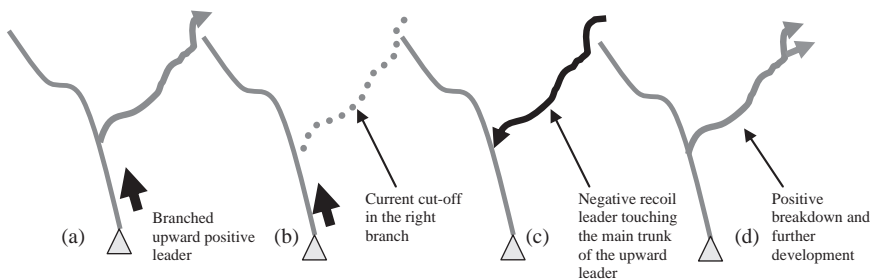


**Figure 6.23** A conceptual sketch for a pulse-type brightening of the upward leader channel. Shown from left to right are four stages in upward leader development: (a) leader with a branch, (b) visual disappearance of the branch after the current cut-off at the branching-point, (c) a recoil leader retracing the path of a previously existing branch, and colliding with the stem of the upward leader at the branching-point and (d) a new positive breakdown at the tip of the newly re-established branch

## 6.11 The electrostatic model of M-events

The simplified electrostatic model of an M-event utilizes a bidirectional, zero-net-charge leader concept, and is based on the following assumptions and known facts:

- A linearly increasing ambient potential, and thus, a constant ambient E-field. The charge distribution along the vertical conducting channel mirrors the ambient potential distribution [32];
- the net charge of the recoil leader is assumed to be zero, although, in reality, some net charge may be present;
- the charges associated with any leader channel are produced by corona streamers at the tip of the developing leader during the streamer-leader transition phase [8];
- the corona streamers produce a corona envelope with a much smaller-diameter leader channel inside;
- the corona envelope contains static charges that decay with a relaxation time constant that is much longer than the lifetime of the lightning;
- the charges of the old channel remain distributed in accordance with the ambient potential distribution;
- the old channel is on ground potential even after the current has disappeared;
- the longitudinal electric field in the channel is ignored because it is much smaller than the ambient electric field;
- the capacitance-per-unit-length of the channel is assumed to be constant, and the capacitance end-effect is ignored.

The assumed ambient potential distribution and, therefore, the linear vertical distribution of induced charges-per-unit-length on an upward positive leader channel, or on a return stroke channel of a negative CG flash, are depicted in Figure 6.24.

Two basic principles are applied in developing the electrostatic model of an M-event: They are

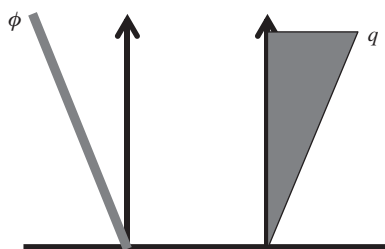


*Figure 6.24 Vertical distribution of the ambient potential and of the induced charges-per-unit-length for the conducting channel of an upward positive leader or a return stroke of a negative CG flash [adapted from Reference 32]*

1. recoil and dart leaders are the same physical processes, both traversing previously existing leader channels; and
2. return strokes of negative CG flashes resulting from dart leaders that touch the ground are the same, physically, as those resulting from stepped leaders.

For a better understanding of the proposed new models, it would be helpful to review first the electrostatic model of the stepped leader-return stroke sequence before, and following, ground attachment [26]. Prior to touching the ground, the bidirectional- and bipolar stepped leader has a negative potential of tens to hundreds of MV, and induced dipole charges that reside in a corona envelope (Figure 6.21(a)). Upon touching the ground, uniformly-distributed positive charges flow from the ground into the leader channel, bringing it to zero ground potential. Through this process, the bipolar distribution of induced charges on the stepped leader (before it touches the ground) turns into a unipolar distribution of the positive charge of the return stroke channel (Figure 6.21(b)). The added positive charge at the upper tip of the channel may produce new positive breakdowns and, thus, a renewal of positive leader development that manifests itself as a continuing current. The upward leader development following the return stroke eventually ends with a current cut-off from the ground. Although the continuing current flow in the channel ceases, the charges in the corona envelope remain, maintaining for some time the same vertical distribution that existed before the current cut-off (Figure 6.25(c)).

In view of the similarity between dart and recoil leaders, the next logical step is to examine the process of the attachment of a dart leader to ground. A physical model describing this process electrostatically does not exist in the literature, so a model of a dart leader-return stroke sequence that produces end results similar to those at the end of the stepped leader attachment to ground is proposed here (see Figure 6.25).

As a floating conductor in an ambient electric field, a dart leader is bidirectional and may have a residual charge, with a bipolar distribution of induced charges that mirrors the ambient potential distribution along the channel length (Figure 6.26(a)). For simplicity, we neglect the residual charge on a dart leader.

A dart leader propagates towards ground along the path of a previous return stroke channel, after a period of tens of milliseconds, following the channel's current cut-off. A considerable amount of indirect evidence points to the conclusion that the path a dart leader follows to the ground is sufficiently conductive to guide it. This evidence includes (a) the fact that continuous propagation occurs, rather than stepping (which is typical for the breakdown of negative leaders in virgin air), and (b) the speed of dart leader propagation, an order of magnitude higher than that of stepped leaders, but an order of magnitude lower than that of return strokes. This weakly-conductive channel to ground is surrounded by space charges of the previous corona envelope. Neither charge relaxation, nor Coulomb forces, nor turbulence, will change the corona envelope significantly over the lifetime of a lightning event. These space charges are seen in Figure 6.26(a) as a positively charged region between the dart leader and the ground. Because the old weakly-conductive channel is at ground potential, the dart leader that penetrates it will produce, by

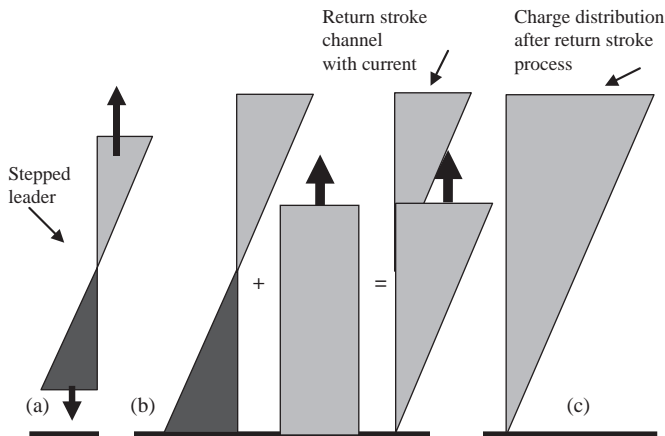


**Figure 6.25** A simplified electrostatic charge representation of a stepped leader-return stroke sequence in a negative cloud-to-ground flash [11]. Here and also in Figures 6.25 and 6.26, the abscissa is the charge density on the channels, and the ordinate is the height of the channels above ground. The ambient electric field is assumed to be constant, so the ambient potential distribution and the induced charge distribution are linear. (a) Induced charges on a bidirectional and bipolar-stepped leader with a strong negative potential. (b) Transition of charge distribution during the leader's attachment to ground (at zero potential), with a uniform positive charge deposited to the leader channel by a return stroke current, which is constant along the channel. (c) Remaining charges in the return stroke channel at the end of the return stroke process. Solid arrows indicate upward movement of the uniform charge (return stroke current) along the channel. In this figure, and also in Figures 6.26 and 6.27, the solid colour represents established charges (dark grey = negative, and light grey = positive charges)

induction, uniformly-distributed influence charges on its channel. The upper part of the dart leader remains influenced by the ambient potential, so its influence charges remain linearly distributed (see Figure 6.26(b)). Up to the instant of touching the ground, the bipolar charge distribution on the dart leader has a zero-net-charge, and only its distribution changes shape (compare Figures 6.26(a) and (b)). Like a stepped leader upon touching the ground, the entire dart leader channel assumes a zero ground potential after the return stroke deposits upon it a uniform positive charge (see Figure 6.26(b)). This positive charge changes the charge distribution along the return stroke channel, with a zero charge at the ground point and the maximum positive charge at the top. This distribution of charge is similar to that which occurs in the stepped leader attachment process (Figure 6.26(c)). Thus, by the end of the

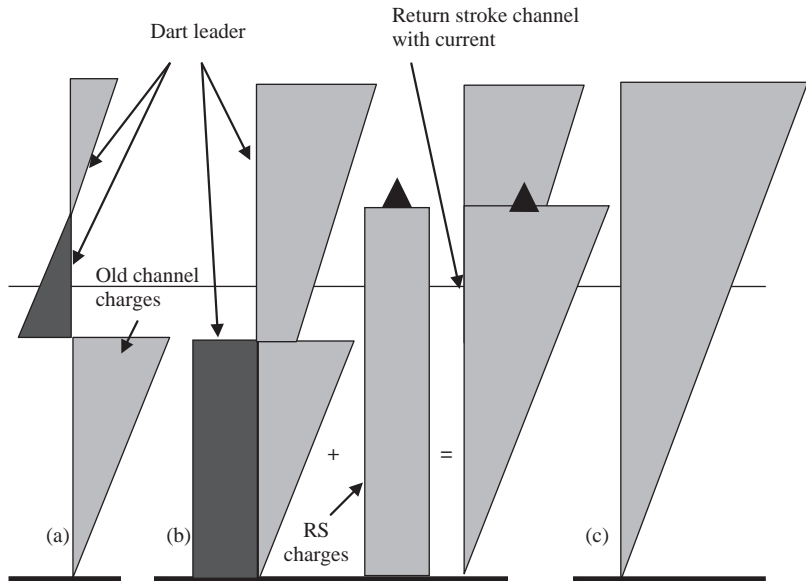


*Figure 6.26 A simplified electrostatic charge representation of a dart leader-return stroke sequence in a negative cloud-to-ground flash. (a) A bidirectional and bipolar dart leader develops above the cut-off point and propagates towards the ground. (b) The transition of charge distribution during leader attachment to the ground (at zero potential), with a uniform positive charge deposited on the leader channel by the return stroke current. (c) The final charge distribution of the subsequent return stroke channel [adapted from Reference 11]*

transformation, the charges on the subsequent return stroke channel are in agreement with the ambient potential distribution, similar to that in Figure 6.25(c).

The physical concept depicted in Figure 6.26, for dart leaders touching ground, is applicable also to recoil leaders (in view of the similarity between them) that attach to the current-carrying main trunk of an upward-growing positive leader (see Figure 6.27). As in the case of a dart leader, after current cut-off in a branch of an upward leader, the former corona envelope of the branch remains charged (Figure 6.27(b)). As soon as the recoil leader makes contact with the upward leader, current flows into the branch and, by adding a uniform net charge to the recoil leader channel, brings the attached recoil leader to the near-zero potential of the current-carrying trunk of the upward leader (Figures 6.27(c) and (d)). This transforms the bipolar charge distribution on a recoil leader channel into a unipolar charge distributed along the new branch born from the recoil leader (Figure 6.26 (c)). The additional positive charge at the upper tip of the new branch may lead to positive breakdowns there, as well as to further growth of the branch. Now, the new branch and the upward leader are both in agreement with the ambient potential

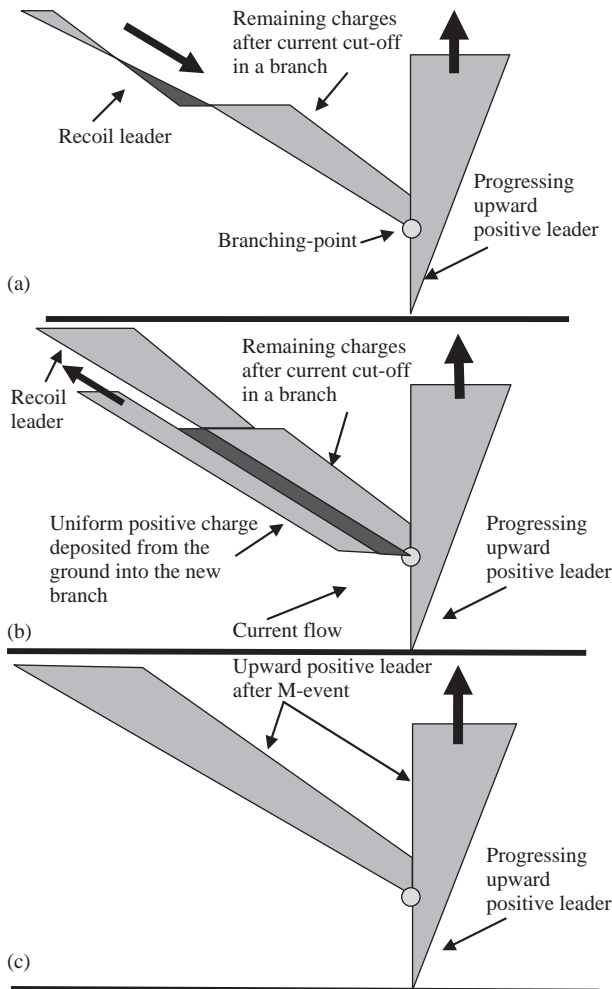


**Figure 6.27** A simplified electrostatic charge representation of the attachment of a recoil leader to an upward leader channel. (a) A bidirectional and bipolar recoil leader that develops above the cut-off point, and the remaining charges along the previous upward leader branch (no current, no light emission). (b) The transition of charge distribution during the recoil leader's attachment to the main channel, which is at zero potential. The uniform positive charge is deposited to the new branch by the current flowing through part of the upward leader channel (between the ground and the branching-point) from the ground. The arrows indicate the direction of charge movement (current flow) into the added branch, formerly the recoil leader. (c) The final charge distribution of the upward leader with the new branch [adapted from Reference 11]

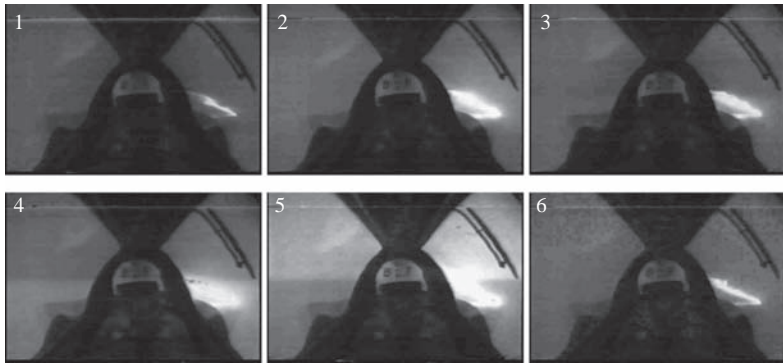


*Figure 6.28 Sequence of video fields (17.5 ms apart) showing pulsing luminosity of the lightning channel attached to the NASA F-106B aircraft (aft-view) [adapted from Reference 6]*

distribution. Also, the charge density of the new branch at the junction level becomes equal to the charge density of the upward leader at the same level.

The current flow to the new branch from the ground upward is actually seen in video images as a brightening of the branch and the section of the main leader channel below the branching-point (see Figure 6.1(d)). It is important to notice that, during the interception of the upward leader channel by the recoil leader, the charge distribution on the trunk of the upward leader below the branching-point does not change. This implies that a  $dE$  sensor on the ground near the leader channel will record a field change which results only from charge changes on the new branch situated above the branching-point.

Attributes of M-events were also observed during the development of lightning flashes triggered by aircraft penetrating thunderstorms (see examples of video records in Figure 6.28). The hypothesis proposed in Reference 44, that brightening of the established channel attached to aircraft was a result of interception by K-changes (correctly identified now as recoil leaders), was confirmed subsequently by studies of CG flashes that used the Interferometric system for the mapping of lightning radiation sources [12, 13], and also by recent studies of upward positive leaders from tall towers, using a high-speed video system. This brings us to the conclusion that M-events are universal in their nature, representing interactions between recoil leaders and their origins, which are branching positive leaders in all types of lightning flashes.

## 6.12 Summary

The bidirectional, zero-net-charge leader concept first proposed by Heinz Kasemir [3] provided a strong physical basis to the interpretation of many elements of the lightning puzzle which had previously been described only from observations, and

also fundamentally changed our understanding of the lightning processes in thunderstorms. Now, instead of merely disjointed fragments of the ‘big picture’, the fully, elegant structure of a lightning flash built of two basic processes (i.e. positive and negative leaders) emerges. This basic structure remains valid for all types of lightning flashes in a wide variety of electrical conditions inside thunderstorms.

## References

1. Schonland, B.F.J., Progressive lightning, IV, *Proc. R. Soc. London, Ser. A*, **164**, 132–150, 1938
2. Malan, D.J. *Physics of Lightning*, English University Press, London, **46056**, 1963
3. Kasemir, H. W., Qualitative Ubersicht über Potential-, Feld- und Ladungsverhältnisse bei einer Blitzentladung in der Gewitterwolke (Qualitative Survey of the Potential, Field and Charge Conditions during a Lightning discharge in the Thunderstorm Cloud), in *Das Gewitter* (H. Israel, ed.), Akadem. Verlagsgesellschaft, Leipzig, 1950
4. Kasemir, H. W., A contribution to the electrostatic theory of a lightning discharge, *J. Geophys. Res.*, **65**, 1873–1878, 1960
5. Kasemir, H.W., Static discharge and triggered lightning, in Proceedings of 8th International Aerospace and Ground Conference on Lightning and Static Electricity, Fort Worth, Tex., DOT/FAA/CT-83/25, 24.1–24.11, June 21–23, 1983
6. Mazur, V., Triggered lightning strikes to aircraft and natural intracloud discharges, *J. Geophys. Res.*, **94**, 331–332, 1989
7. Lalande, P., A. Bondiou-Clergerie, G. Bacchigia and I. Gallimberti, Observations and modeling of lightning leaders, *C.R. Physique*, **3**, 10, 1375–1392, 2002
8. Gallimberti, I., G. Bacchigia, A. Bondiou-Clergerie and P. Lallande, Fundamental processes in long air gap discharges, *C.R. Physique*, **3**, 10, 1335–1360, 2002
9. Ogawa, T. and M. Brook, The mechanism of the intracloud lightning discharge, *J. Geophys. Res.*, **69**, 5141–5150, 1964
10. Brook, M. and T. Ogawa, The cloud discharge, in *Lightning, Vol.1, Physics of Lightning* (R. H. Golde, ed.), Academic Press, New York, pp. 191–230, 1977
11. Mazur, V. and L. H. Ruhnke, Physical processes during development of upward leaders from tall structures, *J. Electrostatics*, doi:10.1016/j.elstat.2011.01.003, 2011
12. Mazur, V., P. R. Krehbiel and X. M. Shao, Correlated high-speed video and radio interferometric observations of a cloud-to-ground lightning flash, *J. Geophys. Res.*, **100**, 25, 731–753, 1995
13. Shao, X.M., P.R. Krehbiel, R. J. Thomas and W. Rison, Radio interferometric observations of cloud-to-ground lightning phenomena in Florida, *J. Geophys. Res.* **100**, 2749–2783, 1995

14. Richard, P. and G. Auffray, VHF-UHF interferometric measurements, applications to lightning discharge mapping, *Radio Sci.*, **20**, 171–192, 1985
15. Rison, W., R. J. Thomas, P. R. Krehbiel, T. Hamlin and J. Harlin, A GPS-based three-dimensional lightning mapping system: initial observations geophys, *Res. Lett.*, **26**, 3573–3576, 1999
16. Bondiou, A., I. Taudiere, P. Richard and F. Helloco, Analyse spatio-temporelle du rayonnement VHF-UHF associe a l'éclair, (in French), *Revue Phys. Appl.*, **25**, 147–157, 1990
17. Shao, X. M., C. T. Rhodes and D. N. Holden, RF radiation observations of positive cloud-to-ground flashes, *J. Geophys. Res.*, **104**, 9801–9808, 1999
18. Kawasaki, Z. I. and V. Mazur, Common physical processes in natural and triggered lightning in winter storms in Japan, *J. Geophys. Res.*, **97**, **12**, 935–945, 1992
19. Zen-Ichiro Kawasaki, personal communication, 2002
20. Mazur, V. and L. H. Ruhnke, Common physical processes in natural and artificially triggered lightning, *J. Geophys. Res.*, **98**, **12**, 913–930, 1993
21. Beasley, W., Positive cloud-to-ground lightning observations, *J. Geophys. Res.*, **90**, 6131–6138, 1985
22. Ron Thomas, personal communication, 2001
23. Fisher, R. J. and G. H. Schnetzer, 1993 Triggered Lightning Test Program, Sandia Report, SAND94-0311 UC-706, 1994
24. Krehbiel, P. R., M. Brook and R. A. McCrory, An analysis of the charge structure of lightning discharges to ground, *J. Geophys. Res.*, **84**, 2432–2456, 1979
25. Rakov, V.A. and M. Uman, *Lightning, Physics and Effects*, Cambridge University Press, Cambridge, UK, 2003
26. Mazur, V. and L. H. Ruhnke, Model of electric charges in thunderstorms and associated lightning, *J. Geophys. Res.*, **103**, **23**, 573–584, 1998
27. Chen, M., N. Takagi, T. Watanabe, D. Wang, Z. I. Kawasaki and X. Liu, Spatial and temporal properties of optical radiation produced by stepped leaders, *J. Geophys. Res.*, **104**, **27**, 573–584, 1999
28. Mazur, V., X. M. Shao and P. R. Krehbiel, “Spider” lightning in intracloud and positive cloud-to-ground flashes, *J. Geophys. Res.*, **103**, **19**, 811–819, 822, 1998
29. Vaughan, O.H. and B. Vonnegut, Recent observations of lightning discharges from the top of a thundercloud into the clear air above, *J. Geophys. Res.* **94**, **13**, 179–182, 1989
30. Malan, D. J. and B. F. J. Schonland, The electrical processes in the intervals between the strokes of a lightning discharge, Proceedings of the Royal Society of London, Serial A, **206**, 145–163, 1951
31. Heckman, S., Ph.D thesis, *Why Does a Lightning Flash Has Multiple Strokes?* Massachusetts Institute of Technology, **134** pp., 1992
32. Kasemir, H. W., Model of lightning flashes triggered from the ground, International Aerospace and Ground Conference on Lightning and Static Electricity, Dayton, Ohio, p. 39-I, 1986

33. Gallimberti, I., The mechanism of long spark formation, *J. Phys., C*, **40**, 193–250, 1979
34. Kawasaki, Z. I., K. Matsuura, T. Matsui and M. Adachi, Is the bi-leader progression concept true?, Proceeding of 10th International Conference Atmospheric Electricity, Osaka, Japan, pp. 596–598, 1996
35. Brook, M., M. Nakano, P. Krehbiel and T. Takeuti, The electrical structure of the Hokuriku winter thunderstorms, *J. Geophys. Res.*, **87**, 1207–1215, 1982
36. Uman, M., *The Lightning Discharge*, Academic Press, New York, 1987
37. Heidler, F., Lightning current measurements at the Peissenberg telecommunication tower, Proceeding of International Conference on Grounding and Earthing, GROUND'2002, 117–122, November 4–7, Rio de Janeiro, Brazil, 2002
38. Diendorfer, G., H. Pichler and M. Mair, Characteristics of positive upward lightning measured on an instrumented tower, *Geophys. Res. Abstracts*, **7**, 10175, 2005
39. Miki, M., V.A. Rakov, T. Shindo, G. Diendorfer, M. Mair, F. Heidler, W. Zischank, M.A. Uman, R. Thottappillil and D. Wang, Initial stage in lightning initiated from tall objects and in rocket-triggered lightning, *J. Geophys. Res.*, **110**, D02109, 2005
40. Berger, K. and Vogelsander, E., New results of lightning observations, in *Planetary Electrodynamics* (S.C. Coronti and J. Highes, eds.), Gordon and Breach, New York, pp. 489–510, 1969
41. Mazur, V., Associated lightning discharges, *Geophys. Res. Ltrs*, **9**, 1227–1230, 1982
42. Wang, D., N. Takagi, T. Watanabe, H. Sakurano and M. Hashimoto, Observed characteristics of upward leaders that are initiated from a windmill and its lightning protection tower, Proceeding of 29th International Conference on Lightning Protection, paper 9c, Uppsala, Sweden, 2008
43. Malan, D.J. and B.F.J. Schonland, Progressive lightning, Part 7, Directly correlated photographic and electrical studies of lightning from near thunderstorms, *Proc. Roy. Soc., A* **191**, 485–503, 1947
44. Mazur, V. and J. P. Moreau, Aircraft-triggered lightning: processes following strike initiation that affect aircraft, *J. Aircraft*, **29**, 4, 575–580, 1992



---

## *Chapter 7*

# **Return stroke models for engineering applications\***

*Vernon Cooray<sup>1</sup>*

---

### **7.1 Introduction**

From the point of view of an electrical engineer, the return stroke is the most important event in a lightning flash; it is the return stroke that causes most of the destruction and disturbance in electrical and telecommunication networks. In their attempts to provide protection, engineers seek the aid of return stroke models for three reasons: firstly, they would like to characterize and quantify the electromagnetic fields produced by return strokes at various distances to provide them with the input for mathematical routines that analyse the transient voltages and currents induced in electrical networks by these fields. This calls for return stroke models that are capable of generating electromagnetic fields similar to those created by natural return strokes. Secondly, their profession demands detailed knowledge of the effects of direct injection of lightning current. In a real situation, this direct injection will be superimposed on currents and voltages induced by electromagnetic fields in the system under consideration. This necessitates the use of return stroke models that are capable of generating channel base currents similar to those in nature. Finally, in order to evaluate the level of threat posed by lightning, engineers require statistical distributions of peak currents and peak current derivatives in lightning flashes. Even though the characteristics of return stroke currents can be obtained through measurements at towers equipped with current measuring devices or by utilizing rocket triggering techniques, gathering statistically significant data samples in different regions and under different weather conditions is an exceptionally difficult enterprise. Accurate return stroke models can simplify this task to a large extent by providing the connection between the electromagnetic fields and the currents so that the latter can be extracted from the measured electromagnetic fields.

In the case of return strokes, a model is a mathematical representation that is capable of predicting the temporal and spatial variation of the return stroke current,

\*This chapter also appeared in *Lightning Protection*, edited by V. Cooray, The IET, London, 2010.

<sup>1</sup>Uppsala University, Uppsala, Sweden

the variation of return stroke speed, the temporal and spatial characteristics of optical radiation, the features of electromagnetic fields at different distances and the signature of thunder. From the point of view of an engineer, the lightning parameters of particular interest are the return stroke current and its electromagnetic fields, whence most of the return stroke models available today, especially the engineering models, are constructed to predict either one or both of these features. On the basis of the concepts and aims of return stroke models, they can be separated into four main groups: (1) the electrothermodynamic models, (2) the transmission line or LCR models, (3) antenna models and (4) engineering models [1, 2]. Here we concentrate on the engineering models [The reader is referred to Chapters 8, 9 and 10 for a description of other models].

Even though the name ‘engineering models’ may give the impression that these models have downplayed the physics completely, all these models are built using a valid physical concept as a foundation. However, the physics is somewhat neglected when selecting the input parameters necessary to build up the model. In many of these models, input parameters are not evaluated using fundamental principles. Some of these parameters are obtained from available experimental data and the other parameters are selected, sometimes without any physical foundation, in such a way that the model predictions agree with experimental data. One problem with this procedure is the lack of uniqueness in the way in which the input parameters could be combined to generate the required result. The basic concept on which all the engineering models are built on, whether it is stated as such or not, can be traced back to the physics of transmission lines. Using the basic physics of transmission line theory, three types of engineering models can be constructed. These are the current generation models, the current propagation models and the current dissipation models. Figure 7.1 shows a summary of the development of engineering return stroke models. At a later stage in this chapter, we will show how these different types of return stroke models are related to each other.

In this chapter, we will describe and discuss several engineering models that can be utilized either to evaluate electromagnetic fields from lightning flashes or to study the direct effects of lightning attachment to various structures including tall towers. We will start by describing the basic concepts of engineering return stroke models. This discussion will be followed by a description of various return stroke models and the equations necessary for the evaluation of electromagnetic fields using these return stroke models.

## 7.2 Current propagation models (CP models)

### 7.2.1 Basic concept

Consider a uniform and lossless transmission line. A current pulse injected into this line will propagate along the line with uniform speed without any change in the amplitude of the wave shape. The transmission line does not interfere with the current (of course this is not true in the case of a transmission line going into corona). It will only provide a path for the propagation of the current pulse from

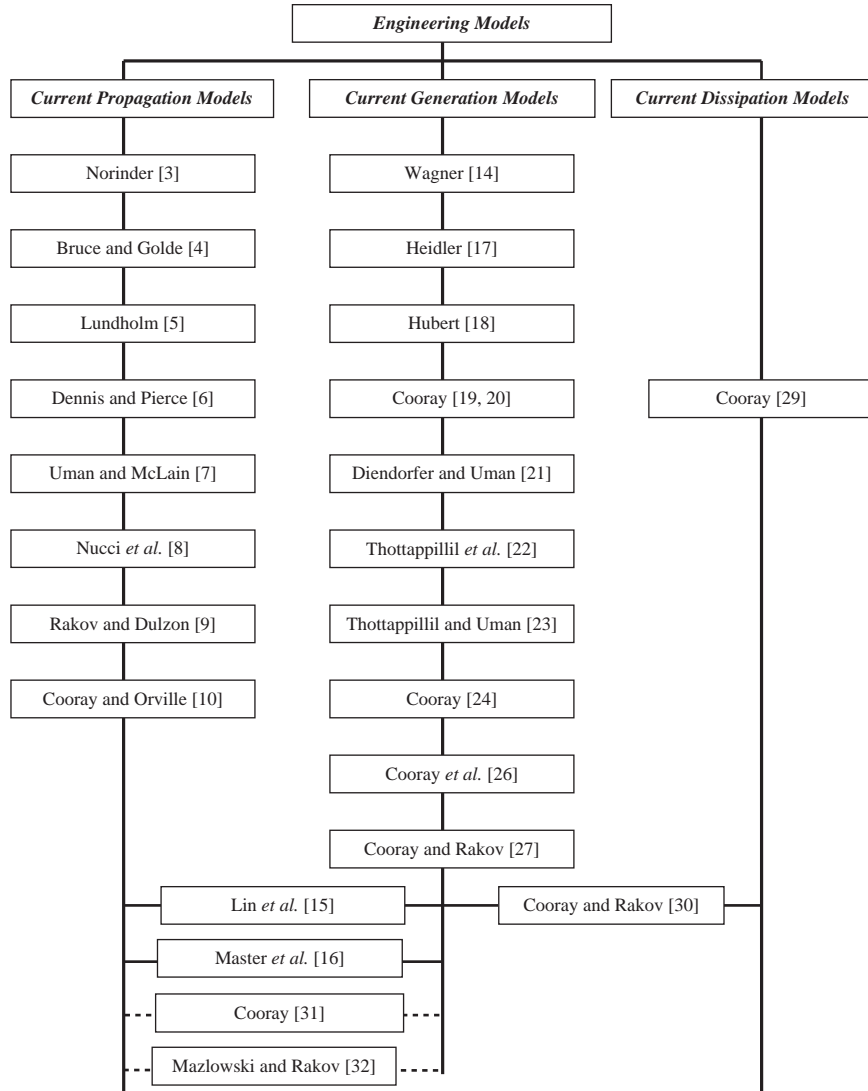


Figure 7.1 Historical development of engineering return stroke models. Note that Cooray [31] and Mazlowski and Rakov [32] are papers that discuss the relationship between current generation and current propagation models

one location to another. This is the basis of the current propagation models. In these models, it is assumed that the return stroke is a current pulse originating at ground level and propagating from ground to cloud along the transmission line created by the leader. The engineering models using this postulate as a base were constructed by Norinder [3], Bruce and Golde [4], Lundholm [5], Dennis and Pierce [6], Uman

and McLain [7], Nucci *et al.* [8], Rakov and Dulzon [9] and Cooray and Orville [10]. The models differ from each other by the way they prescribe how the return stroke current varies as it propagates along the leader channel. For example, in the model introduced by Uman and McLain [7], popularly known as the transmission line model, the current is assumed to propagate along the channel without attenuation and constant speed. In the model introduced by Nucci *et al.* [8] (MTLE – modified transmission line model with exponential current decay), the current amplitude decreases exponentially and in the one introduced by Rakov and Dulzon [9] (MTLL – modified transmission line model with linear current decay), the current amplitude decreases linearly. Cooray and Orville [10] introduced both current attenuation and dispersion while allowing the return stroke speed to vary along the channel.

### 7.2.2 Most general description

To generalize the description of the model, let us assume that the return stroke process consists of two waves. The first one travels with speed  $u$  (which very well could be a function of height) preparing the channel for the transport of charge and current. The second one is the current wave and the associated charge travelling upwards with average speed  $v$ , depending again on the height. The current cannot be finite ahead of the plasma front which prepares the channel for conduction. Thus, the current at level  $z$  is given by

$$I(z, t) = A(z)F(z, t - z/v), \quad t > z/u \quad (7.1)$$

In the above equation  $A(z)$  is a function that represents the attenuation of the peak current and  $F(z, t)$  describes the wave shape of the current at height  $z$ . Note also that  $F(z, t) = 0$  for  $t < 0$ . One can define the function  $F(z, t)$  as follows:

$$F(z, t) = \int_0^t I_b(\tau)R(z, t - \tau)d\tau \quad (7.2)$$

where  $I_b(t)$  is the channel base current and  $R(z, t)$  is a function that describes how the shape of the current waveform is being modified with height. However, this operation itself leads to the attenuation of the current and if we would like to represent the attenuation only by the factor  $A(z)$ , then we have to normalize this function to unity. Let  $t_p$  be the time at which the peak of the function defined in (7.2) is reached. Then the normalization can be done as follows:

$$F(z, t) = I_p \frac{\int_0^t I_b(\tau)R(z, t - \tau)d\tau}{\int_0^{t_p} I_b(\tau)R(z, t - \tau)d\tau} \quad (7.3)$$

Table 7.1 Basic features of current propagation models

The model	v	u	A(z)	R(z, t)
Norinder [3]	$\infty$	$\infty$	1.0	$\delta(t)$
Lundholm [5]	v varies as a function of peak current. The value of is evaluated as a function of peak current using Wagner's equation [12]	$u = v$ or $u = \infty$	1.0	$\delta(t)$
Bruce and Golde [4] Dennis and Pierce [6]	$v = v_b e^{-\gamma_b t}$ $v = v_d e^{-\gamma_d t}$	$\infty$ Case 1: $u = v$ Case 2: $u = c$	1.0 1.0	$\delta(t)$ $\delta(t)$
Uman and McLain [7]	For first: $v = v_d e^{-\gamma_d t}$	$u = v$	For first: $A(z) = I_p \frac{v}{v_d}$	$\delta(t)$
	For subsequent: $v = v_u$		For subsequent: $A(z) = 1.0$	
Rakov and Dulzon [9]	$v = v_r$ Authors have also considered exponentially decaying speeds	$u = v$	$A(z) = (1 - \frac{z}{H})^2$	$\delta(t)$
Nucci <i>et al.</i> [8] Coray and Orville [10]	$v = v_n$ $v = v_1 \left\{ \begin{array}{l} ae^{-z/\lambda_1} \\ +be^{-z/\lambda_2} \end{array} \right\}$	$u = v$ $u = v$	$A(z) = e^{-z/\lambda}$ $A(z) = \left\{ \begin{array}{l} ge^{-z/\lambda_3} \\ +de^{-z/\lambda_4} \end{array} \right\}$	$\delta(t)$ $R(z, t) = \frac{e^{-t/\tau(z)}}{\tau(z)}$ $\tau(z) = \eta z$ $\tau(z) = 1 - e^{-z/\lambda_5}$ $\tau(z) = 1 - e^{-(z/\lambda_6)^2}$

Parameters:  $v_d = 8.0 \times 10^7 \text{ m/s}$ ,  $\gamma = 2 \times 10^4 \text{ s}^{-1}$ ,  $v_u = 8.0 \times 10^7 \text{ m/s}$ ,  $I_p$  is the peak current selected in the model,  $v_r = 1.5 \times 10^8 \text{ m/s}$ ,  $H = 7.5 \text{ km}$ ,  $v_n = 1.1 \times 10^8 \text{ m/s}$ ,  $\lambda = 2000 \text{ m}$ ,  $v_1 = 2.2 \times 10^8$ ,  $a = 0.5$ ,  $b = 0.5$ ,  $\lambda_1 = 100.0 \text{ m}$ ,  $\lambda_2 = 5000 \text{ m}$ ,  $g = 0.3$ ,  $d = 0.7$ ,  $\lambda_3 = 100 \text{ m}$ ,  $\lambda_4 = 3000 \text{ m}$ ,  $\lambda_5 = 500 \text{ m}$ ,  $\lambda_6 = 500-250 \text{ m}$ ,  $c$  is the speed of light.

where  $I_p$  is the peak current at channel base. If the speeds of propagation of the pulses depend on  $z$ , then  $u$  and  $v$  in (7.1) have to be replaced by the average speeds. In Table 7.1, the expressions for the parameters of (7.1)–(7.3) pertinent to different return stroke models are presented. In analysing these models, the following points should be kept in mind:

- (a) The numerical values of the parameters given in the table are only of historical value. The important point is the way in which different scientists attempted to incorporate the observed facts into the models.
- (b) In all the models, the channel base current is given as an input parameter. It varies from one return stroke model to another, but these variations are mainly due to the lack of information available in the literature concerning the return stroke current at the time of the creation of the model. Thus, one can replace it with analytical forms created recently by scientists to represent the return stroke current. One exception to this is the Lundholm model [5] in which, for the reasons of mathematical simplicity, the channel base current is assumed to be a step.
- (c) The return stroke speed is another input parameter of these models. In some models the return stroke speed is assumed to be uniform, whereas in others it is assumed to decrease exponentially. Cooray and Orville [10] assumed a more complicated function containing two exponentials to represent the variation of return stroke speed with height. However, recent information shows that the speed can actually increase initially, reach a peak and then continue to decay [11].
- (d) Note that Cooray and Orville [10] changed the rise time of the current directly with height without first defining the function  $R(z, t)$ . The functions given in Table 7.1 are the ones which approximate this variation in the standard form written above. However, the use of this function in the model will not only change the rise time but also change the shape of the current waveform with height. On the other hand, any physically reasonable dispersion process will affect not only the rise time but also the fast variations in any other part of the current.
- (e) In the case of Lundholm model, one can either use  $u = c$  or  $u = \infty$ . This is the case because in this model the current waveform is replaced by a step function.

## 7.3 Current generation models (CG models)

### 7.3.1 Basic concept

If a transmission line goes into corona, the corona currents released at each line element will give rise to currents propagating along the line and an observer will be able to measure a current appearing at the base of the line [13]. A similar scenario is used in the current generation models to describe the creation of the return stroke current. In these models, the leader channel is treated as a charged transmission line and the return stroke current is generated by a wave of ground potential that travels

along it from ground to cloud. The arrival of the wave front (i.e. return stroke front) at a given point on the leader channel changes its potential from cloud potential to ground potential causing the release of bound charge on the central core and the corona sheath giving rise to the current in the channel (this is called the corona current in the literature). These models postulate that as the return stroke front propagates upwards, the charge stored on the leader channel collapses into the highly conducting core of the return stroke channel. Accordingly, each point on the leader channel can be treated as a current source that is turned on by the arrival of the return stroke front at that point. The corona current injected by these sources into the highly conducting return stroke channel core travels to ground with a speed denoted by  $v_c$ . As we will see later, in most of the return stroke models it is assumed that  $v_c = c$  where  $c$  is the speed of light.

The basic concept of CG models was first introduced by Wagner [14]. He assumed that the neutralization of the corona sheath takes a finite time and therefore the corona current can be represented by a decaying exponential function. The decay time constant associated with this function is called the *corona decay time constant*. Wagner assumed, however, that the speed of propagation of the corona current down the return stroke channel is infinite. Lin *et al.* [15] introduced a model in which both CG and CP concepts are incorporated in the same model. In the portion of the current described by CG concept, the corona current is represented by a double exponential function. The speed of propagation of corona current down the channel is assumed to be the same as the speed of light. A modified form of this model is introduced by Master *et al.* [16], but in this modification the CG description remained intact. Heidler [17] constructed a model based on this principle in which the channel base current and the return stroke speed are assumed as input parameters. Furthermore, it was assumed that the neutralization of the corona sheath is instantaneous and hence the corona current generated by a given channel section can be represented by a Dirac Delta function. The speed of propagation of the corona current down the return stroke channel is assumed to be equal to the speed of light. This model gives rise to a current discontinuity at the return stroke front which, according to the author's understanding, is not physically reasonable. Hubert [18] constructed a current generation model rather similar to that of the Wagner's model with the exception that the downward speed of propagation of the corona current is equal to the speed of light. He utilized this model to reproduce experimental data (both current and electromagnetic fields) obtained from triggered lightning. Cooray [19, 20] introduced a model in which the distribution of the charge deposited by the return stroke (i.e. sum of the positive charge necessary to neutralize the negative charge on the leader and the positive charge induced on the channel due to the action of the background electric field) and the decay time constant of the corona current are taken as input parameters with the model predicting the channel base current and return stroke speed. Moreover, he took into consideration that the process of neutralization of the corona sheath takes a finite time in reality and, as a consequence, the corona current was represented by an exponential function with a finite duration. This is the first model in which the decay time constant of the corona current (and hence the duration of the corona

current) is assumed to increase with height. Since the leader channel contains a hot core surrounded by a corona sheath, he also divided the corona current into two parts, one fast and the other slow. The fast one was associated with the neutralization of the core and the slow one with the neutralization of the corona sheath. Furthermore, by treating the dart leader as an arc and assuming that the electric field at the return stroke front is equal to the electric field that exists in this arc channel, he managed to derive the speed of the return stroke. Diendorfer and Uman [21] introduced a model in which the channel base current, return stroke speed and the corona decay time constant were assumed as input parameters. They also divided the corona current into two parts, one fast and the other slow. Thottappillil *et al.* [22] and Thottappillil and Uman [23] modified this model to include variable return stroke speed and a corona decay time constant that varies with height. Cooray [24] developed the ideas introduced in References 19 and 20 to create a CG model with channel base current as an input. Cooray [25] and Cooray *et al.* [26] extended the concept to include first return strokes with connecting leaders.

In CG models one has the choice of selecting the channel base current,  $I_b(t)$ , the distribution of the charge deposited by the return stroke along the channel,  $\rho(z)$ , the return stroke speed,  $v(z)$ , and the magnitude and variation of the corona discharge time constant with height,  $\tau(z)$  as input parameters. Any set of three of these four input parameters will provide a complete description of the temporal and spatial variation of the return stroke current. Most of the CG models use  $v(z)$  and either the  $\rho(z)$  or  $\tau(z)$  in combination with  $I_b(t)$  as input parameters. Recently, Cooray and Rakov [27] developed a model in which  $\rho(z)$ ,  $\tau(z)$  and  $I_b(t)$  are selected as input parameters. The model could generate  $v(z)$  as a model output.

### 7.3.2 Mathematical background

As mentioned above, a current generation model needs three input parameters that can be selected from a set of four parameters, i.e.  $\rho(z)$ ,  $\tau(z)$ ,  $I_b(t)$  and  $v(z)$ . Once three of these parameters are specified, the fourth can be evaluated either analytically or numerically. Let us now consider the mathematics necessary to do this.

#### 7.3.2.1 Evaluate $I_b(t)$ , given $\rho(z)$ , $\tau(z)$ and $v(z)$

Since the current at any given level on the channel is the cumulative effect of corona currents associated with channel elements located above that level, the return stroke current at any height in the return stroke channel  $I(z, t)$  can be written as

$$I(z, t) = \int_z^{h_e} I_{cor}(t - \xi/v_{av}(\xi) - (\xi - z)/v_c) d\xi, \quad t > z/v_{av}(z) \quad (7.4)$$

$$I_{cor}(z) = \frac{\rho(z)}{\tau(z)} \exp\{-(t - z/v_{av}(z))\}, \quad t > z/v_{av}(z) \quad (7.5)$$

Note that  $I_{cor}(z)$  is the corona current per unit length associated with a channel element at height  $z$  and  $v_{av}(z)$  is the average return stroke speed over the channel section of length  $z$  with one end at ground level. The latter is given by

$$v_{av}(z) = \frac{z}{\int_0^z \frac{1}{v(\xi)} dz} \quad (7.6)$$

The value of  $h_e$  can be obtained from the solution of the following equation:

$$t = \frac{h_e}{v_{av}(h_e)} + \frac{h_e - z}{v_c} \quad (7.7)$$

The current at the channel base is given by

$$I_b(0, t) = \int_0^{h_0} I_{cor}(t - \xi/v_{av}(\xi) - \xi/v_c) d\xi \quad (7.8)$$

$$t = \frac{h_0}{v_{av}(h_0)} + \frac{h_0}{v_c} \quad (7.9)$$

### 7.3.2.2 Evaluate $\tau(z)$ , given $I_b(t)$ , $\rho(z)$ and $v(z)$

In most of the return stroke models, corona current is represented by a single exponential function. An exponential function gives an instantaneous rise time to the corona current which is not physically reasonable. For this reason in a few models it is represented by a double exponential function. For this reason in the analysis to be given below we assume that the corona current is represented by a double exponential function. The corona current in this case is given by

$$I_{cor}(z) = \frac{\rho(z)}{\tau(z) - \tau_r} [\exp\{-(t - z/v_{av}(z))/\tau(z)\} - \exp\{-(t - z/v_{av}(z))/\tau_r\}], \quad t > z/v_{av}(z) \quad (7.10)$$

where both  $\rho(z)$ ,  $\tau_r$  are known but  $\tau(z)$  is unknown. Results pertinent to a corona current with a single exponential function can be obtained by letting  $\tau_r = 0$ . With this corona current, the return stroke current at ground level is given by

$$I_b(0, t) = \int_0^{h_0} \frac{\rho(z) dz}{\tau(z) - \tau_r} [\exp\{-(t - z/v_{av}(z) - z/v_c)/\tau(z)\} - \exp\{-(t - z/v_{av}(z) - z/v_c)/\tau_r\}] \quad (7.11)$$

where  $h_o$  can be extracted by the solution of (7.9). If we divide the channel into a large number of segments of equal length  $dz$ , the above integral can be written as a summation as follows:

$$I_b(t_m) = \sum_{n=1}^m \frac{\rho_n}{\tau_n - \tau_r} \exp \left\{ - \left( t_m - \frac{(n-1)dz}{v_{av,n}} - \frac{(n-1)dz}{v_c} \right) / \tau_n \right\} \\ - \sum_{n=1}^m \frac{\rho_n}{\tau_n - \tau_r} \exp \left\{ - \left( t_m - \frac{(n-1)dz}{v_{av,n}} - \frac{(n-1)dz}{v_c} \right) / \tau_r \right\} \quad (7.12)$$

where  $\rho_n$  is the charge deposited per unit length on the  $n$ th section,  $\tau_n$  is the decay time constant of the corona current of the  $n$ th section and  $v_{av,n}$  is the average return stroke speed over the channel section connecting the ground and the  $n$ th element. In this equation,  $t_m$  is the time for the corona current released from the  $m$ th segment to reach the ground. This is given by the equation

$$t_m = \left[ \left( m - \frac{1}{2} \right) / v_{av,m} + \left( m - \frac{1}{2} \right) / v_c \right] dz \quad (7.13)$$

If the return stroke speed and the current at the channel base are known, then the value of the discharge time constant at different heights can be estimated progressively by moving from  $m = 1$ . For example when  $m = 1$  the only unknown is the  $\tau_1$ . Once this is found, one can consider the case  $m = 2$ . In the resulting equation, the only unknown is the value of  $\tau_2$ , and it can be obtained by solving that equation. In this way, the values of discharge time constants up to the  $m$ th element can be obtained sequentially [22, 24].

### 7.3.2.3 Evaluate $\rho(z)$ , given $I_b(t)$ , $\tau(z)$ and $v(z)$

Equations (7.12) and (7.13) can also be used to evaluate the discharge time constant when the other parameters are given as inputs. For example, in this case when  $m = 1$  the only unknown is the value of  $\rho_1$ . Once this is found, one can consider the case  $m = 2$ . In the resulting equation the only unknown is the value of  $\rho_2$ , and it can be obtained by solving that equation. In this way, the values of discharge time constants up to any  $m$ th element can be obtained sequentially.

### 7.3.2.4 Evaluate $v(z)$ , given $I_b(t)$ , $\rho(z)$ and $\tau(z)$

As before, we start with (7.12). Since  $I_b(t)$ ,  $\rho(z)$  and  $\tau(z)$  are given, the only unknown parameter in these equations is  $v_{av,n}$ , the average speed along the  $n$ th channel segment. Solving the equations as before, one can observe that when  $m = 1$  the only unknown is  $v_{av,1}$ , the average speed over the first channel segment. Once this is found, the value of  $v_{av,2}$  can be obtained by considering the situation of  $m = 2$ . In this way, the average return stroke speed as a function of height can be obtained. It is important to point out that in this evaluation the value of  $dz$  in (7.12) should be selected in such a manner that it is reasonable to assume constant return stroke speed along the channel element. Once the average return stroke speed as a function of height is known, the return stroke speed as a function of height can be obtained directly from it.

### 7.3.3 CG models in practice

As mentioned in the introduction, several current generation models are available in the literature and they differ from each other by the way in which input parameters are selected. In the sections to follow, information necessary to use CG models to calculate the spatial and temporal variation of the return stroke current is given.

#### 7.3.3.1 Model of Wagner [14]

This is the first CG model to be introduced in the literature and therefore the credit for the creation of current generation models goes to Wagner. He is the first scientist to come up with the concept of corona current and to treat the return stroke current as a sum of corona currents generated by channel elements located along the channel. The input parameters of the Wagner's model are the distribution of the charge deposited by the return stroke, corona decay time constant and the return stroke speed. In the model, Wagner assumed that the speed of propagation of the corona current down the return stroke channel is infinite. The parameters of Wagner's model are the following:

- *Channel base current:*

The channel base current can be calculated using the parameters given below in (7.4).

- *Corona current per unit length:*

$$I_c(t, z) = \frac{\rho(z)}{\tau} e^{-t/\tau} \text{ with } \tau = 6.66 \times 10^{-6} \text{ s.}$$

- *Speed of the corona current:*

$$v_c = \infty$$

- *Linear density of the charge deposited by the return stroke:*

$\rho(z) = \rho_0 e^{-z/\lambda}$ . The peak current at ground level varies with  $\rho_0$  and the latter can be selected to get the desired current peak at ground level,  $\lambda = 10^3$  m.

- *Return stroke speed:*

$v(z) = v_0 e^{-\gamma z}$  where  $\gamma = 3 \times 10^4 \text{ s}^{-1}$  and  $v_0$ , which is a constant, is assumed to vary between  $0.1c$  and  $0.5c$  where  $c$  is the speed of light.

*Comment:* Note that the predicted current at ground level has a double exponential shape. The rise time of the current is determined by  $\tau$  and the decay time by  $\lambda$  and  $\gamma$ .

#### 7.3.3.2 Model of Heidler [17]

Heidler is the first scientist to introduce the channel base current as an input parameter in CG models and to connect the other parameters of the model to the channel base current. The input parameters of the model in addition to the channel base current are the return stroke speed and the corona discharge time constant. In the model, Heidler assumed that the discharge time constant of the corona current is 0, i.e. the discharge process takes place instantaneously. With these parameters, the model can predict the distribution of the charge deposited by the return stroke along the channel. The parameters of the model are given below. Observe that the linear density of the charge deposited by the return stroke can be derived analytically.

- *Channel base current:*

$I_b(0, t) = \frac{I_p}{\eta} \frac{k^n}{1+k^n} e^{-t/\tau_2}$  with  $k = t/\tau_1$ ,  $n = 10$ ,  $\tau_1 = 1.68 \mu\text{s}$ ,  $\tau_2 = 20-150 \mu\text{s}$  and  $\eta$  is the factor that has to be adjusted to get the exact current peak value.

- *Corona current per unit length:*

$$I_c(t, z) = \rho(z) \delta(t)$$

- *Speed of the corona current:*

$$v_c = c$$

- *Linear density of the charge deposited by the return stroke:*

$$\rho(z) = \frac{I_b(0, z/v + z/v_c)}{v^*} \quad \text{with} \quad \frac{1}{v^*} = \frac{1}{v} + \frac{1}{v_c}$$

- *Return stroke speed:*

In the model,  $v$  is assumed to be a constant.

### 7.3.3.3 Model of Hubert [18]

Hubert utilized a model based on CG concept to generate a fit to the measured currents and electromagnetic fields of triggered lightning flashes. The values of various model parameters were selected so that the predictions agree with experiment. The input parameters of the model are the distribution of the charge deposited by the return stroke, return stroke speed and the corona decay time constant. The parameters of the model are the following.

- *Channel base current:*

The channel base current can be calculated using the parameters given below in (7.4).

- *Corona current per unit length:*

$$I_c(t, z) = \frac{\rho(z)}{\tau} e^{-t/\tau}, \tau = 10^{-7} \text{s}$$

- *Speed of the corona current:*

$$v_c = c$$

- *Linear density of the charge deposited by the return stroke:*

$\rho(z) = \rho_0 e^{-z/\lambda}$  where  $\lambda = 15 \times 10^3 \text{ m}$  and the value of  $\rho_0$  is selected to provide the required peak current at ground level.

- *Return stroke speed:*

In the model,  $v$  is assumed to be a constant equal to  $1.0 \times 10^8 \text{ m/s}$ .

### 7.3.3.4 Model of Cooray [19, 20]

Cooray introduced a CG model where for the first time the discharge time constant is assumed to increase with height. He also assumed that the neutralization process

can be divided into two parts, one fast and the other slow. The fast one is assumed to be generated by the neutralization of the charge on the central core of the leader channel and the slow one by the neutralization of the cold corona sheath. The input parameters of the model are the corona discharge time constant and the distribution of the charge deposited by the return stroke on the channel. Cooray also attempted to evaluate the return stroke speed by connecting the electric field at the return stroke front to the potential gradient of the leader channel. The results showed that the return stroke speed increases initially, reaches a peak and then continues to decrease with increasing height. However, in using this model in engineering studies, one can skip this iterative calculation and use it as a normal CG model by plugging in a speed profile similar to that predicted by the full model as an input parameter. An approximate for this speed profile is given by

$$v(z) = v_1 + (v_2/2)[2 - e^{-(z-1)/a} - e^{-(z-1)/b}], \quad 1.0 \leq z \leq 50 \text{ m} \quad (7.14)$$

$$v(z) = v_3 e^{-z/a_1} + v_4 e^{-z/b_1}, \quad z \geq 50 \text{ m} \quad (7.15)$$

with  $v_1 = 1.02 \times 10^8 \text{ m/s}$ ,  $v_2 = 1.35 \times 10^8 \text{ m/s}$ ,  $v_3 = 7.11 \times 10^7 \text{ m/s}$ ,  $v_4 = 1.66 \times 10^8 \text{ m/s}$ ,  $a = 1.4 \text{ m}$ ,  $b = 7.4 \text{ m}$ ,  $a_1 = 400 \text{ m}$ ,  $b_1 = 2100 \text{ m}$ . The other model parameters are summarized below.

- *Channel base current:*

Inserting the parameters given below in (7.4), one can calculate the return stroke current at any level along the channel.

- *Corona current per unit length of the hot corona sheath:*

$$I_{hc}(t, z) = \frac{\rho_h(z)}{\tau_h - \tau_b} [e^{-t/\tau_h} - e^{-t/\tau_b}] \text{ with } \tau_h \approx 50-100 \text{ ns}, \tau_b = 5 \text{ ns.}$$

- *Corona current per unit length of the cold corona sheath:*

$$I_{cc}(t, z) = \frac{\rho_c(z)}{\tau_s - \tau_h} [e^{-t/\tau_s} - e^{-t/\tau_h}] \text{ where } \tau_s = \tau_{so}[1 - e^{-z/\lambda_s}] \text{ and } \tau_{so} = 1 \mu\text{s}, \lambda_s = 200 \text{ m.}$$

- *Corona current per unit length:*

$$I_c(t, z) = I_{hc}(t, z) + I_{cc}(t, z)$$

- *Speed of corona current:*

$$v_c = c$$

- *Total linear density of the charge deposited by the return stroke on the leader channel:*

$$\rho(z) = \rho_0[0.3e^{-z/\lambda_1} + 0.7e^{-z/\lambda_2}] \text{ with } \rho_0 = 0.0001 \text{ C/m (for a typical subsequent stroke)}, \lambda_1 = 600 \text{ m}, \lambda_2 = 5000 \text{ m.}$$

- *Linear density of charge deposited by the return stroke on the hot core:*

$$\rho_h(z) = \rho_0 e^{-z/\lambda_c} \text{ with } \lambda_c = 50 \text{ m.}$$

- *Linear density of charge deposited by the return stroke on the corona sheath:*

$$\rho_c(z) = \rho(z) - \rho_h(z)$$

- *Return stroke speed:*

Predicted by the model; speed profile given by (7.14) and (7.15) can be used as an input parameter.

*Comment:* Observe that the peak value of the current at ground level varies linearly with  $\rho_0$ .

### 7.3.3.5 Model of Diendorfer and Uman [21]

Diendorfer and Uman introduced a return stroke model where, similar to the model of Cooray [19, 20] described above, the corona current is separated into two parts, one fast and the other slow. The fast corona current is assumed to be generated by the neutralization of the leader core and the slow one by the corona sheath. However, in contrast to Cooray model they utilized the channel base current as one of the input parameters. In the model, this current was separated into two parts. One part was assumed to be generated by the cumulative effects of the fast corona current and the other part by the cumulative effects of the slow corona currents. In addition to the channel base current, the input parameters of the model are the return stroke speed and the discharge time constants. The input parameters of this model are the following:

- *Channel base current:*

$$I_b(0, t) = i_h(t) + i_c(t)$$

- *Channel base current component associated with the leader core:*

$$i_h(t) = \frac{I_{01}}{\eta_1} \frac{(t/\tau_{11})^2}{(t/\tau_{11})^2 + 1} e^{-t/\tau_{21}} \quad \text{with } I_{01} = 13 \text{ kA}, \eta_1 = 0.73, \tau_{11} = 0.15 \mu\text{s} \text{ and} \\ \tau_{21} = 3.0 \mu\text{s} \text{ for typical subsequent strokes and } I_{01} = 28 \text{ kA}, \eta_1 = 0.73, \tau_{11} = 0.3 \mu\text{s} \\ \text{and } \tau_{21} = 6.0 \mu\text{s} \text{ for typical first strokes.}$$

- *Channel base current component associated with the corona sheath:*

$$i_c(t) = \frac{I_{02}}{\eta_2} \frac{(t/\tau_{12})^2}{(t/\tau_{12})^2 + 1} e^{-t/\tau_{22}} \quad \text{with } I_{02} = 7 \text{ kA}, \eta_2 = 0.64, \tau_{12} = 5 \mu\text{s} \text{ and } \tau_{22} = 50 \mu\text{s}$$

for typical subsequent strokes and  $I_{02} = 16 \text{ kA}, \eta_2 = 0.53, \tau_{12} = 10 \mu\text{s}$  and  $\tau_{22} = 50 \mu\text{s}$  for typical first strokes.

- *Corona current per unit length from the leader core:*

$$I_h(t, z) = \frac{\rho_h(z)}{\tau_h} e^{-t/\tau_h} \quad \text{with } \tau_h = 0.6 \mu\text{s.}$$

- *Corona current per unit length from the corona sheath:*

$$I_c(t, z) = \frac{\rho_c(z)}{\tau_c} e^{-t/\tau_c} \quad \text{with } \tau_c = 5 \mu\text{s.}$$

- Total corona current:

$$I_c(t, z) = I_h(t, z) + I_c(t, z)$$

- Linear density of charge deposited by the return stroke on the leader core:

$$\rho_h(z) = \frac{i_h(0, z/v^*) + \tau_h \frac{di_h(0, z/v^*)}{dt}}{v^*} \text{ with } \frac{1}{v^*} = \frac{1}{v} + \frac{1}{v_c}.$$

- Linear density of charge deposited by the return stroke on the corona sheath:

$$\rho_c(z) = \frac{i_c(0, z/v^*) + \tau_c \frac{di_c(0, z/v^*)}{dt}}{v^*} \text{ with } \frac{1}{v^*} = \frac{1}{v} + \frac{1}{v_c}.$$

- Total linear charge density deposited by the return stroke:

$$\rho(z) = \rho_h(z) + \rho_c(z)$$

- Speed of corona current:

$$v_c = c$$

- Return stroke speed:

In the model,  $v$  is assumed to be a constant equal to  $1.3 \times 10^8$  m/s.

*Comment:* Note that the charge densities are not input parameters but could be derived once the channel base current, return stroke speed and the corona decay time constants are given.

### 7.3.3.6 First modification of the Diendorfer and Uman model by Thottappillil *et al.* [22]

Thottappillil *et al.* modified the Diendorfer and Uman model to introduce a return stroke speed that varies with height. The parameters are tabulated below.

- Channel base current:

$$I_b(0, t) = i_h(t) + i_c(t)$$

- Channel base current component associated with the leader core:

$$i_h(t) = \frac{I_{01}}{\eta_1} \frac{(t/\tau_{11})^2}{(t/\tau_{11})^2 + 1} e^{-t/\tau_{21}} \text{ with } I_{01} = 13 \text{ kA}, \eta_1 = 0.73, \tau_{11} = 0.15 \mu\text{s} \text{ and } \tau_{21} = 3.0 \mu\text{s}$$

for typical subsequent strokes and  $I_{01} = 28 \text{ kA}, \eta_1 = 0.73, \tau_{11} = 0.3 \mu\text{s}$  and  $\tau_{21} = 6.0 \mu\text{s}$  for typical first strokes.

- Channel base current component associated with the corona sheath:

$$i_c(t) = \frac{I_{02}}{\eta_2} \frac{(t/\tau_{12})^2}{(t/\tau_{12})^2 + 1} e^{-t/\tau_{22}} \text{ with } I_{02} = 7 \text{ kA}, \eta_2 = 0.64, \tau_{12} = 5 \mu\text{s} \text{ and } \tau_{22} = 50 \mu\text{s}$$

for typical subsequent strokes and  $I_{02} = 16 \text{ kA}, \eta_2 = 0.53, \tau_{12} = 10 \mu\text{s}$  and  $\tau_{22} = 50 \mu\text{s}$  for typical first strokes.

- Corona current per unit length from the leader core:

$$I_h(t, z) = \frac{\rho_h(z)}{\tau_h} e^{-t/\tau_h} \text{ with } \tau_h = 0.6 \mu\text{s}.$$

- *Corona current per unit length from the corona sheath:*

$$I_c(t, z) = \frac{\rho_c(z)}{\tau_c} e^{-t/\tau_c} \text{ with } \tau_c = 5 \text{ } \mu\text{s}.$$

*Total corona current:*

$$I_c(t, z) = I_h(t, z) + I_c(t, z)$$

- *Linear density of charge deposited by the return stroke on the leader core:*

$$\rho_h(z) = \frac{i_h(0, z/v_{av}(z) + z/v_c) + \tau_h \frac{di_h(0, z/v_{av}(z) + z/v_c)}{dt}}{\Gamma} \text{ with } \frac{1}{\Gamma} = \frac{v_{av}(z) - z \frac{dv_{av}(z)}{dz}}{(v_{av}(z))^2} + \frac{1}{v_c}.$$

- *Linear density of charge deposited by the return stroke on the corona sheath:*

$$\rho_c(z) = \frac{i_c(0, z/v_{av}(z) + z/v_c) + \tau_c \frac{di_c(0, z/v_{av}(z) + z/v_c)}{dt}}{\Gamma}$$

- *Total linear charge density deposited by the return stroke:*

$$\rho(z) = \rho_h(z) + \rho_c(z)$$

- *Speed of corona current:*

$$v_c = c$$

- *Return stroke speed:*

$$v = v_0 e^{-z/\lambda} \text{ with } v_0 = 1.3 \times 10^8 \text{ m/s and } \lambda \text{ varying between 1000 and 3000 m.}$$

### 7.3.3.7 Second modification of the Diendorfer and Uman model by Thottappillil and Uman [23]

In a subsequent publication, Thottappillil and Uman modified the Diendorfer and Uman model to include a discharge time constant that increases with height. The input parameters of the model are the charge density, return stroke speed and the channel base current. These input parameters are tabulated below.

- *Channel base current:*

$$I_b(0, t) = i_h(t) + i_c(t)$$

$$i_h(t) = \frac{I_{01}}{\eta_1} \frac{(t/\tau_{11})^2}{(t/\tau_{11})^2 + 1} e^{-t/\tau_{21}} \text{ with } I_{01} = 13 \text{ kA}, \eta_1 = 0.73, \tau_{11} = 0.15 \text{ } \mu\text{s} \text{ and } \tau_{21} = 3.0 \text{ } \mu\text{s} \\ \text{for typical subsequent strokes and } I_{01} = 28 \text{ kA}, \eta_1 = 0.73, \tau_{11} = 0.3 \text{ } \mu\text{s} \text{ and } \tau_{21} = 6.0 \text{ ms for typical first strokes.}$$

$$i_c(t) = \frac{I_{02}}{\eta_2} \frac{(t/\tau_{12})^2}{(t/\tau_{12})^2 + 1} e^{-t/\tau_{22}} \text{ with } I_{02} = 7 \text{ kA}, \eta_2 = 0.64, \tau_{12} = 5 \text{ } \mu\text{s} \text{ and } \tau_{22} = 50 \text{ } \mu\text{s} \\ \text{for typical subsequent strokes and } I_{02} = 16 \text{ kA}, \eta_2 = 0.53, \tau_{12} = 10 \text{ } \mu\text{s} \text{ and } \tau_{22} = 50 \text{ } \mu\text{s} \\ \text{for typical first strokes.}$$

- *Corona current per unit length:*

$$I_{cor}(t, z) = \frac{\rho(z)}{\tau(z)} e^{-t/\tau(z)}; \tau(z) \text{ has to be evaluated from (7.12).}$$

- Linear density of charge deposited by the return stroke on the leader channel:

$$\rho(z) = \frac{i_h(0, z/v^*) + \tau_h \frac{di_h(0, z/v^*)}{dt}}{v^*} + \frac{i_c(0, z/v^*) + \tau_c \frac{di_c(0, z/v^*)}{dt}}{v^*}$$

where  $\frac{1}{v^*} = \frac{1}{v} + \frac{1}{v_c}$ . The values of  $\tau_h$  and  $\tau_c$  are given in the Section 7.3.3.5.

- Speed of corona current:

$$v_c = c$$

- Return stroke speed:

In the model,  $v$  is assumed to be a constant equal to  $1.3 \times 10^8$  m/s.

- Comment: Note that the charge distribution used as an input to the model is identical to that obtained in the original Diendorfer and Uman model.

### 7.3.3.8 Model of Cooray [24]

In constructing the model, Cooray utilized the same principles as the ones used in his original model but utilized the channel base current as one of the input parameters. The other input parameter is the distribution of the charge deposited by the return stroke. Both the variation of the corona discharge time constant with height and the return stroke speed were extracted from the model. To obtain the return stroke speed, he assumed that the electric field at the front of the return stroke is equal to the potential gradient of the leader channel. Again it is observed that the return stroke speed increases initially, reaches a peak and then continues to decrease. However, one can skip the additional numerical procedures by treating the return stroke speed as an input parameter. Then the model can be used as a normal CG model. The parameters of the model are given below.

- Channel base current:

$$I_b(0, t) = \frac{I_{01}}{\eta} \frac{(t/\tau_1)^2}{(t/\tau_1)^2 + 1} e^{-t/\tau_2} + I_{02}(e^{-t/\tau_3} + e^{-t/\tau_4}); \text{ for a typical subsequent return stroke: } I_{01} = 9.9 \text{ kA}, \eta = 0.845, \tau_1 = 0.072 \mu\text{s}, \tau_2 = 5 \mu\text{s}, I_{02} = 7.5 \text{ kA}, \tau_3 = 100 \mu\text{s} \text{ and } \tau_4 = 6 \mu\text{s}.$$

- Corona current per unit length:

$$I_{cor}(t, z) = \frac{\rho(z)}{\tau(z) - \tau_b} [e^{-t/\tau(z)} - e^{-t/\tau_b}], \tau_b = 5 \text{ ns}, \tau(z) \text{ has to be evaluated from (7.12).}$$

Linear charge density deposited by the return stroke:

$\rho(z) = \rho_0[1 - \frac{z}{H}]$ ; the value of  $\rho_0$  scales linearly with peak current with  $100 \mu\text{C/m}$  for a  $10 \text{ kA}$  current.  $H$  is the height of the return stroke channel (assumed to be  $9 \text{ km}$  in the model).

- Speed of corona current:

$$v_c = c$$

- Return stroke speed:

Predicted by the model. But one can use the model as a normal CG model by using the return stroke speed as an input parameter. Equations (7.14) and (7.15), which agree with model prediction, provide a good approximation that can be used as an input.

### 7.3.3.9 Model of Cooray and Rakov [27]

Since the return stroke speed is one of the possible input parameters of CG models, Cooray and Rakov realized that if the charge deposited by the return stroke, corona decay time constant and channel base current are given as input parameters, one can utilize the return stroke model itself to predict the return stroke speed profile without any additional mathematics. A model that can do that is introduced by Cooray and Rakov. The model showed again that the return stroke speed increases initially, reaches a peak and then continues to decay. The input parameters of the model are tabulated below.

- *Channel base current:*

$$I_b(0, t) = \frac{I_{01}}{\eta} \frac{(t/\tau_1)^2}{(t/\tau_1)^2 + 1} e^{-t/\tau_2} + I_{02}(e^{-t/\tau_3} + e^{-t/\tau_4}); \text{ for a typical subsequent return stroke: } I_{01} = 9.9 \text{ kA}, \eta = 0.845, \tau_1 = 0.072 \mu\text{s}, \tau_2 = 5 \mu\text{s}, I_{02} = 7.5 \text{ kA}, \tau_3 = 100 \mu\text{s} \text{ and } \tau_4 = 6 \mu\text{s}.$$

- *Corona current per unit length:*

$$I_{cor}(t, z) = \frac{\rho(z)}{\tau(z)} e^{-t/\tau(z)}; \tau(z) = \tau_i + \mu z \text{ with } \tau_i = 10^{-8} \text{ s and } \mu = 10^{-9} \text{ s/m.}$$

- *Linear charge density along the channel:*

$$\rho(z) = a_o I_p \frac{(a+bz)}{1+cz+dz^2}; I_p \text{ is the peak return stroke current, } a_o = 5.09 \times 10^{-6} \text{ (s/m), } a = 1.325 \times 10^{-5} \text{ (s/m), } b = 7.06 \times 10^{-6} \text{ (s/m}^2\text{), } c = 2.089 \text{ (m}^{-1}\text{), } d = 1.492 \times 10^2 \text{ (m}^{-2}\text{).}$$

- *Speed of corona current:*

$$v_c = c$$

- *Return stroke speed:*

Evaluated from the model using (7.12).

### 7.3.3.10 Model of Cooray, Rakov and Montano [26]

All the CG models described so far have been introduced to describe subsequent return strokes. Recently, Cooray, Rakov and Montano introduced a CG model to describe first return strokes with the channel base current as an input parameter. In the model, they assumed that the return stroke is initiated when the connecting leader reaches the streamer region of the stepped leader and the slow front, usually observed in the first return stroke current waveforms, is generated during the time of passage of the return stroke front through the streamer region of the stepped leader. The rapid rise in the current occurs when the upward moving return stroke front reaches the hot core of the leader. It is important to point out that the model assumes that the return stroke is initiated at the moment when the connecting leader enters into the streamer region of the stepped leader. In the case of tall towers, the tower may initiate a connecting leader before the arrival of leader streamers at the top of the tower. In this case, the point of initiation of the return stroke is located not at the tip of the tower but at some height above the tower, i.e. at the extremity of the streamer region of the stepped leader. In the case of short structures, the

initiation of the connecting leader takes place when the streamers of the stepped leader reach the structure and in such cases the point of initiation of the return stroke is located on the structure. The model parameters are given below.

- *Channel base current:*

$I_b(0, t) = I_{01} \frac{(t/\tau_1)^n}{(t/\tau_1)^n + 1} + I_{02}[1 - e^{-(t/\tau_1)^3}](ae^{-t/\tau_2} + be^{-t/\tau_3})$ ; for a typical first return stroke current, these authors suggested the following parameters.  $I_{01} = 7.8$  kA,  $\tau_1 = 5$   $\mu$ s,  $n = 100$ ,  $I_{02} = 32.5$  kA,  $\tau_2 = 4$   $\mu$ s,  $\tau_3 = 100$   $\mu$ s,  $a = 0.2$  and  $b = 0.8$ .

- *Corona charge per unit length:*

$$I_{cor}(t, z) = \frac{\rho(z)}{\tau(z)} e^{-t/\tau(z)}, \tau(z) \text{ has to be evaluated from (7.12).}$$

- *Speed of corona current:*

$$v_c = c$$

- *Speed of return stroke:*

$v(z) = v_0 e^{z/\lambda_c}$  for  $z < l_c$ ;  $v(z) = v_0 e^{l_c/\lambda_c} e^{-(z-l_c)/\lambda_r}$  for  $z > l_c$  where  $l_c$  is the length of the streamer region of the stepped leader. In the model, it is assumed that  $v_0 e^{l_c/\lambda_c} = 2.0 \times 10^8$  m/s and for a typical first stroke  $l_c \approx 70$  m. Note that  $v_0 e^{l_c/\lambda_c}$  is the speed of the return stroke front at the moment of its contact with the hot core of the leader channel. Utilizing the concepts of CG, one can show that the duration of the slow front time  $t_f$  is given by  $t_f = [\lambda_c(1 - e^{-l_c/\lambda_c})/v_0] + l_c/c$  where  $t_f$  is the duration of the slow front in the current waveform. From this information,  $l_c$  and  $v_0$  are estimated.

- *Linear density of charge deposited by the return stroke:*

The charge density is assumed to be uniform along the channel (i.e.  $\rho(z) = \rho_0$ ) and for a typical first stroke  $\rho_0 = 0.001$  C/m.

*Comment:* Observe that the model assumes that the return stroke speed increases exponentially as it moves along the streamer region of the leader channel, reaches a peak when it encounters the hot core and then continues to decay as it proceeds further up.

## 7.4 Current dissipation models (CD models)

### 7.4.1 General description

As mentioned previously, if a current pulse is propagating without corona along a transmission line, it will travel along the line without any attenuation and modification of the current wave shape. This concept is used as a base in creating current propagation models. When the current amplitude is larger than the threshold current necessary for corona generation, each element of the transmission line acts as a corona current source. Half of the corona current generated by the sources travels downwards and the other half travels upwards. The upward moving corona currents interact with the front of the injected current pulse in such a way that the speed of the upward moving current pulse is reduced, and for a transmission line in air, to a value less than the speed of light [28]. In a recent publication, Cooray [29] showed that the upward moving corona current concept can also be used to create return stroke models. He

coined the term ‘Current Dissipation Models’ for the same. The basic features of the current dissipation models are depicted in Figure 7.2. The main assumptions of the current dissipation models are the following: The return stroke is initiated by a current pulse injected into the leader channel from the grounded end. The arrival of the return stroke front at a given channel element will turn on a current source that will inject a corona current into the central core. It is important to stress here that by the statement *the arrival of the return stroke front at a given channel element* it is meant the onset of the return stroke current in that channel element (i.e. point B in Figure 7.2). Once in the core, this corona current will travel upwards along the channel. In the case of negative return strokes, the polarity of the corona current is such that it will deposit positive charge on the corona sheath and transport negative charge along the central core. Let us now incorporate mathematics into this physical scenario.

Assume that the return stroke is initiated by a current pulse injected into the leader channel at ground level. This current pulse propagates upwards along the

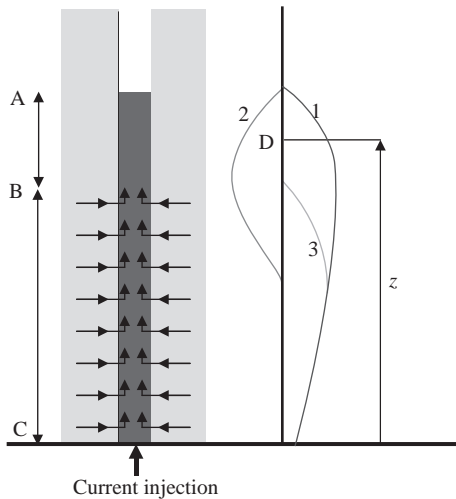


*Figure 7.2 Pictorial description of the processes associated with a current dissipation model at a given time  $t$ . The injected current (waveform 1 to the right) and the sum of corona currents (waveform 2 to the right) travel upwards with speed  $v_c$ . Point A is the front of these current waveforms. In the region A–B, these two currents cancel each other making the current above point B equal to 0. The cancellation is not complete below point B and therefore the net current below this point is finite (waveform 3 to the right). Thus, point B is the front of the net current (i.e. return stroke front) moving upwards. Distance AC is equal to  $v_c t$  and the distance BC is  $vt$  where  $v$  is the average speed of propagation of the net current front (i.e. return stroke front). Note that the current waveforms are not drawn to scale [adapted from Reference 29]*

channel with speed  $v_c$ . When the return stroke front (i.e. the net current front) reaches a given channel element, a corona source is turned on. This source will generate a corona current that will travel upwards along the central core with the same speed as the current pulse injected at the channel base (i.e.  $v_c$ ). Note that the polarity of the upward moving corona current is opposite to that of the upward moving current injected at the channel base. For example, in the case of negative return stroke, the current injected at the channel base carries positive charge upwards, whereas the corona current transports negative charge upwards. According to this model, the total current at a given point of the channel consists of two parts – upward moving current pulse injected at the channel base and the total contribution of the upward moving corona currents. The upward moving corona current being of opposite polarity leads to the dissipation of the current pulse injected at the channel base.

#### 7.4.2 Mathematical background

Consider the diagram to the right in Figure 7.2. This depicts a situation at any given time  $t$ . At this time, the tip of the injected current is located at point A and the return stroke front is located at point B. The net current at any point above the return stroke front is zero. This is the case since the injected current and the cumulative effects of the corona current cancel each other above the return stroke front. Now, let us consider a point D located above the return stroke front. The height of this point from ground level is  $z$ . The net corona current at that point is given by (note that since the corona current is defined as positive here it has to be subtracted from the injected current)

$$I_{cor,total}(z, t) = - \int_0^{h_d} I_c(\xi, t - \xi/v_{av}(z) - (z - \xi)/v_c) d\xi \quad (7.16)$$

the value of  $h_d$ , the highest point on the channel whose corona current can reach point  $z$  at time  $t$  can be obtained by solving the equation

$$t - \frac{h_d}{v_{av}(h_d)} + \frac{z - h_d}{v_c} = 0 \quad (7.17)$$

The injected current at point  $z$  at time  $t$  is given by

$$I_{in}(z, t) = I_b(0, t - z/v_c) \quad (7.18)$$

Since the corona current annihilates the injected current at all points above the return stroke front we have

$$I_b(0, t - z/v_c) = \int_0^{h_d} I_c(\xi, t - \xi/v_{av}(\xi) - (z - \xi)/v_c) d\xi \quad (7.19)$$

Changing the variable, we can write

$$I_b(0, t') = \int_0^{h_s} I_c(\xi, t' - \xi/v_{av}(\xi) + \xi/v_c) d\xi \quad (7.20)$$

with  $h_s$  given by

$$t' - \frac{h_s}{v_{av}(h_d)} + \frac{h_s}{v_c} = 0 \quad (7.21)$$

Now, a comparison of (7.20) and (7.21) with (7.8) and (7.9) shows that the only difference in the equations when moving from current generation concept to current dissipation concept is that  $v_c$  is replaced by  $-v_c$ . Moreover, as in the case of current generation models, the input parameters of current dissipation models are the charge deposited on the channel by the return stroke, corona decay time constant, return stroke speed and the channel base current. When three of these parameters are given, the fourth one can be obtained in the same manner as it was done in the case of current generation models. But in equations (7.4)–(7.12),  $v_c$  has to be replaced by  $-v_c$  when using the equations in connection with current dissipation models (see Reference 29).

#### 7.4.3 Cooray and Rakov model – a combination of current dissipation and current propagation models [30]

In current generation models, the corona current generated by current sources located along the return stroke channel travels downwards with a speed equal to the speed of light (i.e.  $v_c = c$ ). In general, it is assumed that this current waveform travelling down the channel will be completely absorbed by the ground. However, it is more correct to assume that the incident current would be reflected completely at ground level. If the current is reflected at ground level, it will propagate up with the speed of light similar to the injected current in the current dissipation models. In the model, the incident current at ground level is represented by current generation model principles and the propagation of the reflected current along the channel is represented by current dissipation principles. Since the incident current is assumed to be completely reflected at ground level, the incident current component contributes to half of the channel base current, and the other half is caused by the reflected current component.

In treating the incident current at ground level, Cooray and Rakov [30] used the channel base current (i.e. half of the total channel base current), corona current and the return stroke speed as the input parameters. Since the return stroke speed and the discharge time constant are common for both current components (i.e. there is only one return stroke front), these together with the channel base current (i.e. half of the total channel base current) are used as the input parameters of the current dissipation model that simulated the reflected wave. The main features of the model are given below.

- *Channel base current:*

$$I_b(0, t) = i_i(t) + i_r(t)$$

- Incident component of the channel base current:

$i_i(t) = \frac{1}{2} \left\{ \frac{I_{01}}{\eta} \frac{(t/\tau_1)^2}{(t/\tau_1)^2 + 1} e^{-t/\tau_2} + I_{02} (e^{-t/\tau_3} + e^{-t/\tau_4}) \right\}$ ; for a typical subsequent return stroke:  $I_{01} = 9.9$  kA,  $\eta = 0.845$ ,  $\tau_1 = 0.072$   $\mu$ s,  $\tau_2 = 5$   $\mu$ s,  $I_{02} = 7.5$  kA,  $\tau_3 = 100$   $\mu$ s and  $\tau_4 = 6$   $\mu$ s.

- Corona current per unit length associated with the incident current:

$$I_i(t, z) = \frac{\rho_i(z)}{\tau} e^{-t/\tau}, \tau = 0.1 \text{ } \mu\text{s}$$

- Linear density of charge deposited by the incident current [29]:

$$\rho_i(z) = \frac{i_i(0, z/v^*) + \tau \frac{di_i(0, z/v^*)}{dt}}{v^*} \text{ where } \frac{1}{v^*} = \frac{1}{v} + \frac{1}{v_c}$$

- Reflected component of the channel base current:

$i_r(t) = \frac{1}{2} \left\{ \frac{I_{01}}{\eta} \frac{(t/\tau_1)^2}{(t/\tau_1)^2 + 1} e^{-t/\tau_2} + I_{02} (e^{-t/\tau_3} + e^{-t/\tau_4}) \right\}$ ; for a typical subsequent return stroke:  $I_{01} = 9.9$  kA,  $\eta = 0.845$ ,  $\tau_1 = 0.072$   $\mu$ s,  $\tau_2 = 5$   $\mu$ s,  $I_{02} = 7.5$  kA,  $\tau_3 = 100$   $\mu$ s and  $\tau_4 = 6$   $\mu$ s.

- Corona current per unit length associated with the reflected current:

$$I_r(t, z) = \frac{\rho_r(z)}{\tau} e^{-t/\tau}, \tau = 0.1 \text{ } \mu\text{s}$$

- Linear density of charge deposited by the reflected current:

$$\rho_r(z) = \frac{i_r(0, z/v^{**}) + \tau \frac{di_r(0, z/v^{**})}{dt}}{v^{**}} \text{ where } \frac{1}{v^{**}} = \frac{1}{v} - \frac{1}{v_c}$$

- Speed of corona current:

$$v_c = c$$

- Speed of the return stroke:

In the model,  $v$  is assumed to be a constant equal to  $1.3 \times 10^8$  m/s.

## 7.5 Generalization of any model to current generation type

Cooray [31] showed that any return stroke model can be converted to a current generation model by introducing an effective corona current. Here we will illustrate the mathematical analysis that led to that conclusion.

Consider a channel element of length  $dz$  at height  $z$  and let  $I(z, t)$  represent the temporal variation of the total return stroke current at that height. In the case of CG models, this current is generated by the action of corona current sources located above this height. Assume for the moment that the channel element does not generate any corona current. In this case, the channel element will behave as a passive element that will just transport the current that is being fed from the top. In this case, one can write

$$I(z + dz, t) = I(z, t + dz/v_c) \quad (7.22)$$

That is, the current injected at the top of the element will appear without any change at the bottom of the channel element after a time  $dz/v_c$  which is the time taken by the current to travel from the top of the channel element to the bottom.

Now let us consider the real situation in which the channel element  $dz$  will also generate a corona current. As the current injected at the top passes through the channel element, the corona sources will add their contribution resulting in a larger current appearing at the bottom than the amount injected at the top. The difference in these two quantities will give the corona current injected by the channel element. Thus, the average corona current generated by the element  $dz$  is given by

$$I_{cg}(z, t)dz = I(z, t + dz/v_c) - I(z + dz, t) \quad (7.23)$$

Using the Taylor's expansion, the above equation can be rewritten as

$$I_{cg}(z, t)dz = I(z, t) - I(z + dz, t) + \frac{dz}{v_c} \frac{\partial I(z, t)}{\partial t} \quad (7.24)$$

Dividing both sides by  $dz$  and taking the limit  $dz \rightarrow 0$ , the corona current per unit length,  $I_{cg}(z, t)$ , injected into the return stroke channel at height  $z$  is given by

$$I_{cg}(z, t) = -\frac{\partial I(z, t)}{\partial z} + \frac{1}{v_c} \frac{\partial I(z, t)}{\partial t} \quad (7.25)$$

This equation can be utilized to transfer any return stroke model to a current generation model with an equivalent corona current. It is important to stress here that even though the distribution of the return stroke current as a function of height remains the same during this conversion, there is a radical change in the corona current. If one attempts to extract the physics of the leader charge neutralization process using the temporal variation of the corona current as predicted by a return stroke model, the information one gathers will depend strongly on the way in which the return stroke model is formulated. This can be easily illustrated using the transmission line model [7]. In the current propagation scenario of the TL model, the upward propagating current will not give rise to any corona and therefore the corona current is 0. On the other hand, if the same model is converted to a current generation model then the equivalent corona current associated with the converted model (obtained from (7.25)) becomes bipolar [31]. The physics of the neutralization process pertinent to this equivalent corona current is the following: As the rising part of the upward moving current passes through a given channel element, the corona sheath located around that channel element will be neutralized by injection of positive charge into it. During the decaying part of the upward moving current, all the deposited positive charge will be removed bringing the corona sheath back to its original state. Thus, the physics of corona dynamics in the two

scenarios is completely different even though the longitudinal distribution of current and the charge along the channel at any given time is the same in the two formulations. This shows that conversion of a model from one type to another will change the underlying physics even though both descriptions are identical from a point of view of the total current as a function of height. Thus, one has to apply caution in deriving the physics of corona neutralization process using these models because the information extracted concerning it will be model dependent.

## 7.6 Generalization of any model to a current dissipation type model

An analysis similar to the one presented in Section 7.5 was conducted by Cooray [29] for current dissipation type models. That analysis is presented below.

Consider a channel element of length  $dz$  at height  $z$  and let  $I(z, t)$  represent the temporal variation of the total return stroke current at that height. Assume for the moment that the channel element does not generate any corona current. In this case, the channel element will behave as a passive element that will just transport the current that is being fed from the top. In this case, one can write

$$I(z + dz, t) = I(z, t - dz/v_c) \quad (7.26)$$

That is, the current injected at the bottom of the channel element will appear without any change at the top of the channel element after a time  $dz/v_c$  which is the time taken by the current to travel from the bottom of the channel element to the top.

Now let us consider the real situation in which the channel element  $dz$  will also generate a corona current. As the current injected at the bottom passes through the channel element the corona sources will add their contribution, and since the polarity of the corona current is opposite to that of the injected current, it will result in a smaller current appearing at the top than the amount of current injected at the bottom. The difference in these two quantities will give the corona current injected by the channel element. Thus, the average corona current generated by the element  $dz$  is given by

$$I_{cd}(z, t)dz = I(z, t - dz/v_c) - I(z + dz, t) \quad (7.27)$$

Using the Taylor's expansion, the above equation can be rewritten as

$$I_{cd}(z, t)dz = I(z, t) - I(z + dz, t) - \frac{dz}{v_c} \frac{\partial I(z, t)}{\partial t} \quad (7.28)$$

Dividing both sides by  $dz$  and taking the limit  $dz \rightarrow 0$ , the corona current per unit length,  $I_{cd}(z, t)$ , injected into the return stroke channel at height  $z$  is given by

$$I_{cd}(z, t) = -\frac{\partial I(z, t)}{\partial z} - \frac{1}{v_c} \frac{\partial I(z, t)}{\partial t} \quad (7.29)$$

Note that this equation is completely symmetrical to the one derived for the current generation model (i.e. (7.25)) except that the second term has a negative sign. This equation can be utilized to transfer any return stroke model to a current dissipation model with an equivalent corona current. The discussion given at the end of Section 7.5 is also applicable here.

## 7.7 Current dissipation models and the modified transmission line models

If the return stroke current associated with a current propagation model is assumed to decrease with height (as in the case of modified transmission line models [8, 9]), the conservation of charge requires deposition of charge along the channel as the return stroke front propagates upwards. This leakage of charge from the central core to the corona sheath can be represented by a radially flowing corona current. Recently, Maslowski and Rakov [32] showed that this corona current is given by

$$I_{cp}(z, t) = -\frac{\partial I(z, t)}{\partial t} - \frac{1}{v} \frac{\partial I(z, t)}{\partial z} \quad (7.30)$$

where  $I_{cp}(z, t)$  is the corona current per unit length at height  $z$ ,  $I(z, t)$  is the longitudinal return stroke current at the same height as predicted by the return stroke model and  $v$  is the *speed of the return stroke front*. Note that the direction of flow of the corona current is radial and, in contrast to the current generation or current dissipation models, it does not have a component flowing along the return stroke channel, i.e. it is a stationary corona current. Maslowski and Rakov [32] showed that any return stroke model could be reformulated as a current propagation model with an equivalent stationary corona current given by (7.30).

Let us now go back to the current dissipation models. Cooray [29] showed that in general the speed of propagation of the return stroke front in current dissipation models is less than that of the injected current (i.e.  $v_c$ ). However, he also showed that one can select the parameters of the corona current in such a way that the speed of the return stroke front remains the same as that of the injected current pulse and the corona current. When such a choice is made, current dissipation models reduce to MTL models. This can be illustrated mathematically as follows. Let us represent the injected current at the channel base as  $I_b(0, t)$ . The injected current at height  $z$  is given by

$$I_b(z, t) = I_b(0, t - z/v_c) \quad (7.31)$$

Assume that the corona current per unit length at level  $z$  is given by

$$I_{cd}(z, t) = I_b(0, t - z/v_c)A(z) \quad (7.32)$$

where  $A(z)$  is some function of  $z$ . According to this equation, the corona current at a given height is proportional to the injected current at that height. Substituting this expression in (7.29), one finds that

$$I_b(0, t - z/v_c)A(z) = -\frac{\partial I(z, t)}{\partial z} - \frac{1}{v_c}\frac{\partial I(z, t)}{\partial t} \quad (7.33)$$

One can easily show by substitution that the solution of this equation is given by

$$I(z, t) = A'(z)I_b(0, t - z/v_c) \quad (7.34)$$

with

$$A'(z) = - \int A(z)dz \quad (7.35)$$

Note that  $I(z, t)$  in the above equation is the total current, i.e. sum of the corona current and the injected current. According to (7.34), the total current propagates upwards with the same speed as that of the injected current and corona current. Moreover, it propagates upwards without any distortion, whereas its amplitude varies with height according to the function  $A'(z)$ . Indeed, (7.34) describes an MTL model. In this special case, (7.29) reduces to (7.30) derived by Mazlowski and Rakov [32] because the return stroke speed  $v$  becomes equal to  $v_c$ . Thus, (7.30) is a special case of (7.29) and the latter reduces to the former in the case of MTL models. The above also demonstrates that all the current propagation models available in the literature are special cases of current dissipation models.

## 7.8 Effect of ground conductivity

The way in which the ground conductivity can be incorporated into CG-type return stroke models and the effect of ground conductivity on the return stroke current have been described by Cooray and Rakov [30]. The procedure they have used to incorporate ground conductivity into return stroke models is the following.

Consider the physical process that leads to the formation of the corona current through the neutralization process. The neutralization process takes place when the channel core changes its potential from cloud to ground value. If this change is instantaneous, then in principle, the corona decay time constant could be very small and the shape of the corona current can be replaced by a Dirac Delta Function. However, when the ground is finitely conducting, the ground potential cannot be transferred to the channel faster than the relaxation time of the finitely conducting ground. Thus, the relaxation time limits the rapidity at which the channel potential could be changed. In other words, the neutralization time and hence the corona decay time constant depends on the ground conductivity. Assume that the ground is perfectly conducting. Then the ground potential cannot be transferred at a time less than approximately 10 ns, which is the time necessary for the heating and transfer

of electron energy to the ions and neutrals in the central core. This sets a lower limit to the value of corona decay time constant. When the ground is finitely conducting and the relaxation time is larger than the thermalization time, then the minimum

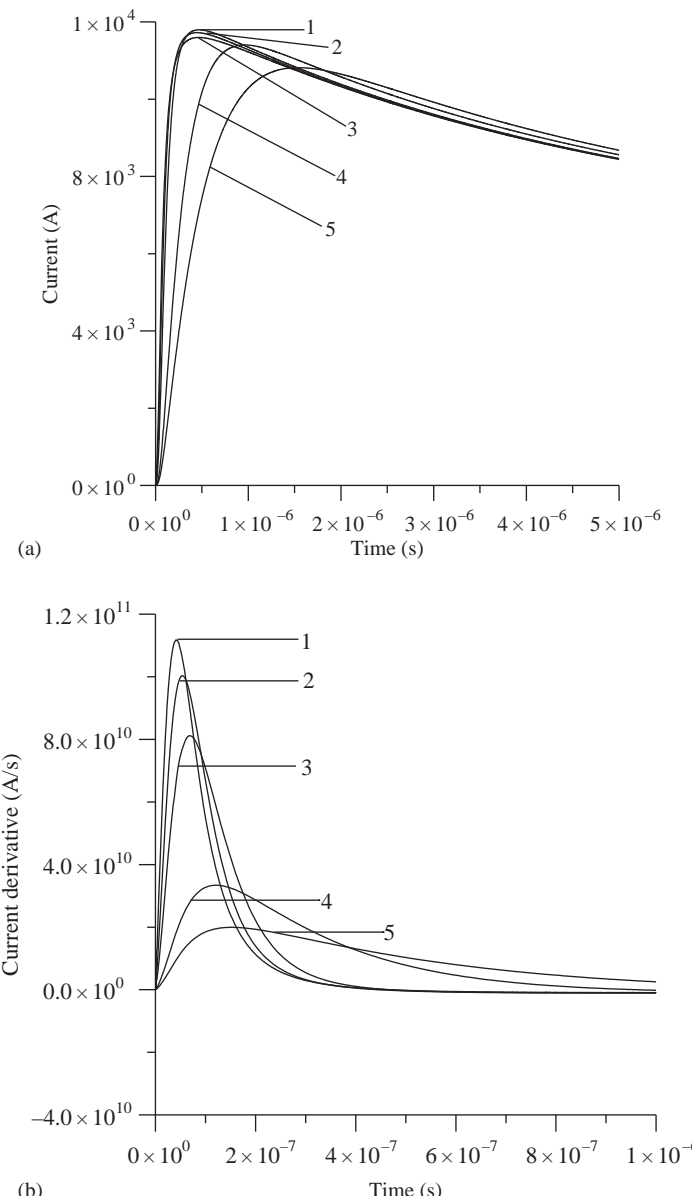


Figure 7.3 (a) and (b) The effect of ground conductivity on the channel base current as predicted by the model of Cooray and Rakov [30]: (1)  $0.01 \text{ S/m}$ , (2)  $0.002 \text{ S/m}$ , (3)  $0.001 \text{ S/m}$ , (4)  $0.0002 \text{ S/m}$  and (5)  $0.0001 \text{ S/m}$

value of the corona decay time constant is determined by the relaxation time. Thus, one can write

$$\tau_o = \tau_t \quad \tau_r \leq \tau_t \quad (7.36)$$

$$\tau_o = \tau_r \quad \tau_r \geq \tau_t \quad (7.37)$$

$$\tau_r = \epsilon \epsilon_0 / \sigma \quad (7.38)$$

In the above equations,  $\epsilon$  is the relative permittivity of the ground,  $\epsilon_0$  is the permittivity of air,  $\sigma$  is the conductivity of soil and  $\tau_r$  is the relaxation time of soil. The value of  $\tau_t$  (thermalization time) is 10 ns. The effects of ground conductivity on the return stroke current and return stroke current derivative as derived by Cooray and Rakov [30] are shown in Figure 7.3. Note that for typical ground conductivities (0.01–0.001 S/m) the change in the peak current is insignificant, whereas it influences the return stroke peak current derivative significantly.

## 7.9 Concluding remarks

In this chapter we have presented the basic principles underlying engineering return stroke models together with the information necessary to use available return stroke models to evaluate the spatial and temporal variation of the return stroke current and to use that information to calculate the electromagnetic fields generated by return strokes.

It is important to note here that any new return stroke model that is introduced into the scientific literature should be able to present a new way of studying the return stroke process. On the other hand, the model parameters should be considered as information that should or could be changed when more experimental data becomes available concerning the return stroke process. Unfortunately, some scientists give more emphasis to the model parameters and by doing so lose the important message that a model builder is trying to convey to the scientific establishment. This wrong way of looking at the models also leads to the creation of ‘new models’ by changing one or two parameters of an existing model.

## References

1. Gomes, C. and V. Cooray, Concepts of lightning return stroke models, *IEEE Trans. Electromagn. Compat.*, vol. 42, no. 1, 2000
2. Rakov, V. A. and M. A. Uman, Review and evaluation of lightning return stroke models including some aspects of their application, *IEEE Trans. Electromagn. Compat.*, vol. 40, pp. 403–426, 1998
3. Norinder, H., *Quelques essais récents relatifs à la détermination des surtensions indirectes*, CIGRE Session 1939, . Paris, p. 303, 1939, 29 June – 8 July
4. Bruce, C. E. R. and R. H. Golde, The lightning discharge, *J. Inst. Elect. Eng.*, vol. 88, pp. 487–520, 1941
5. Lundholm, R., Ph.D. dissertation, KTH, Stockholm, Sweden, 1957

6. Dennis, A. S. and E. T. Pierce, The return stroke of lightning flash to earth as a source of atmospherics, *Radio Sci.*, pp. 777–794, 1964
7. Uman, M. A. and D. K. McLain, Magnetic field of lightning return stroke, *J. Geophys. Res.*, vol. 74, pp. 6899–6910, 1969
8. Nucci, C. A., C. Mazzetti, F. Rachidi, and M. Ianoz, On lightning return stroke models for LEMP calculations, paper presented at 19th International Conference on Lightning Protection, Graz, Austria, 1988
9. Rakov, V. A. and A. A. Dulzon, A modified transmission line model for lightning return stroke field calculation, in *Proceedings of the 9th International Symposium on EMC*, Zurich, Switzerland, 44H1, pp. 229–235, 1991
10. Cooray, V. and R. E. Orville, The effects of variation of current amplitude, current risetime and return stroke velocity along the return stroke channel on the electromagnetic fields generated by return strokes, *J. Geophys. Res.*, vol. 95, no. D11, pp. 18,617–18,630, 1990
11. Olsen, R. C., D. M. Jordan, V. A. Rakov, M. A. Uman and N. Grimes, Observed one-dimensional return stroke propagation speeds in the bottom 170 m of a rocket-triggered lightning channel, *Geophys. Res. Lett.*, vol. 31, p. L16107, doi: 10.1029/2004GL020187, 2004
12. Wagner, C. F., Relation between stroke current and velocity of return stroke, *Trans. Inst. Electr. Electron. Eng. Power Appl. Syst.*, pp. 609–617, 1963
13. Cooray, V. and N. Theethayi, Effects of corona on pulse propagation along transmission lines with special attention to lightning return stroke models and return stroke velocity, in *Proceedings of the VIII International Symposium on Lightning Protection*, Invited Paper, Brazil, 2005
14. Wagner, C. F., A new approach to the calculation of the lightning performance of transmission lines, *AIEE Trans.*, vol. 75, pp. 1233–1256, 1956
15. Lin, Y. T., M. A. Uman and R. B. Standler, Lightning return stroke models, *J. Geophys. Res.*, vol. 85, pp. 1571–1583, 1980
16. Master, M., Y. T. Lin, M. A. Uman and R. B. Standler, Calculations of lightning return stroke electric and magnetic fields above ground, *J. Geophys. Res.*, vol. 86, pp. 12,127–12,132, 1981
17. Heidler, F., Traveling current source model for LEMP calculation, in *Proceedings of the 6th International Symposium on EMC*, Zurich, Switzerland, 29F2, pp. 157–162, 1985
18. Hubert, P., New model of lightning return stroke – confrontation with triggered lightning observations, in *Proceedings of the 10th International Aerospace and Ground Conference on Lightning and Static Electricity*, pp. 211–215, Paris, 1985
19. Cooray, V., A return stroke model, in *Proceedings of the International Conference on Lightning and Static Electricity*, University of Bath, September 1989
20. Cooray, V., A model for the subsequent return strokes, *J. Electrostat.*, vol. 30, pp. 343–354, 1993
21. Diendorfer, G. and M. A. Uman, An improved return stroke model with specified channel base current, *J. Geophys. Res.*, vol. 95, pp. 13,621–13,644, 1990

22. Thottappillil, R., D. K. McLain, M. A. Uman and G. Diendorfer, Extension of Diendorfer-Uman lightning return stroke model to the case of a variable upward return stroke speed and a variable downward discharge current speed, *J. Geophys. Res.*, vol. 96, pp. 17,143–17,150, 1991
23. Thottappillil, R. and M. A. Uman, Lightning return stroke model with height-variable discharge time constant, *J. Geophys. Res.*, vol. 99, pp. 22,773–22,780, 1994
24. Cooray, V., Predicting the spatial and temporal variation of the current, the speed and electromagnetic fields of subsequent return strokes, *IEEE Trans. Electromagn. Compat.*, vol. 40, pp. 427–435, 1998
25. Cooray, V., A model for negative first return strokes in negative lightning flashes, *Phys. Scr.*, vol. 55, pp. 119–128, 1997
26. Cooray, V., R. Montano and V. Rakov, A model to represent first return strokes with connecting leaders, *J. Electrostat.*, vol. 40, pp. 97–109, 2004
27. Cooray, V. and V. Rakov, A current generation type return stroke model that predicts the return stroke velocity, *J. Lightning Res.*, vol. 1, pp. 32–39, 2007
28. Cooray, V. and N. Theethayi, Pulse propagation along transmission lines in the presence of corona and their implication to lightning return strokes, antennas and propagation, *IEEE Trans.*, vol. 56, no. 7, pp. 1948–1959, doi: 10.1109/TAP.2008.924678, 2008
29. Cooray, V., A novel procedure to represent lightning strokes – current dissipation return stroke models, *Trans. IEEE(EMC)*, vol. 51, pp. 748–755, 2009
30. Cooray, V. and V. Rakov, Engineering lightning return stroke models incorporating current reflection from ground and finitely conducting ground effects, *Proc. IEEE (EMC)*, vol. 53, pp. 773–781, 2011
31. Cooray, V. On the concepts used in return stroke models applied in engineering practice, *Trans. IEEE (EMC)*, vol. 45, pp. 101–108, 2003
32. Maslowski, G. and V. A. Rakov, Equivalency of lightning return stroke models employing lumped and distributed current sources, *Trans. IEEE (EMC)*, vol. 49, pp. 123–132, 2007



---

## *Chapter 8*

# **Electromagnetic models of lightning return strokes**

*Yoshihiro Baba<sup>1</sup> and Vladimir A. Rakov<sup>2</sup>*

---

## **8.1 Introduction**

Lightning return-stroke models are needed in studying lightning effects on various objects and systems, and in characterizing the lightning electromagnetic environment. Clearly, conclusions drawn from these studies are influenced by the choice and validity of lightning return-stroke model employed. Rakov and Uman (1998), based on governing equations, have categorized return-stroke models into four classes: gas dynamic models, electromagnetic models, distributed-circuit models and ‘engineering’ models.

Engineering return-stroke models are equations relating the longitudinal current along the lightning channel at any height and any time to the current at the channel origin (the origin is usually situated at ground level but can be at the top of a tall grounded strike object (e.g. Rachidi *et al.* 2002)). The return-stroke wavefront speed in these models can be set arbitrarily, since it is one of the input parameters. Engineering return-stroke models have been reviewed by Nucci *et al.* (1990), Thottappillil and Uman (1993), Thottappillil *et al.* (1997), Rakov and Uman (1998) and Gomes and Cooray (2000).

Distributed-circuit models of the lightning return stroke usually consider the lightning channel as an  $R$ - $L$ - $C$  transmission line (e.g. da F. Mattos and Christopoulos 1988; Baum and Baker 1990), where  $R$ ,  $L$  and  $C$  are series resistance, series inductance and shunt capacitance, all per unit length, respectively. In an  $R$ - $L$ - $C$  transmission line model, voltage and current are the solutions of the telegrapher’s equations. Note that the telegrapher’s equations can be derived from Maxwell’s equations assuming that the electromagnetic waves guided by the transmission line have a transverse electromagnetic (TEM) field structure. Strictly speaking, the latter assumption is not valid for a vertical conductor above ground. Indeed, any current wave suffers attenuation as it propagates upwards along a vertical conductor, except for the special (unrealistic) case

<sup>1</sup>Department of Electrical Engineering, Doshisha University, 1-3 Miyakodani, Tatara, Kyotanabe, Kyoto 610-0321, Japan. Email: ybaba@mail.doshisha.ac.jp.

<sup>2</sup>Department of Electrical and Computer Engineering, University of Florida, 553 Engineering Building #33, Gainesville, FL 32611-6130, USA. Email: rakov@ece.ufl.edu.

of a zero-radius conductor (Thottappillil *et al.* 2001) and the resultant electromagnetic field structure is non-TEM (e.g. Kordi *et al.* 2002, 2003a; Baba and Rakov 2003, 2005a). Clearly, an incorrect assumption on the electromagnetic field structure (e.g. TEM when it is actually non-TEM) in the vicinity of lightning channel will result in an incorrect current distribution along the channel (e.g. Baba and Rakov 2003). Distributed-circuit models have been reviewed by Rakov and Uman (1998). There has lately been a renewed interest in developing distributed-circuit models (e.g. Theethayi and Cooray 2005; Visacro and De Conti 2005).

Electromagnetic return-stroke models are based on Maxwell's equations (Rakov and Uman 1998). These are relatively new and most rigorous (no TEM assumption) models suitable for specifying the source in studying lightning interaction with various systems and with the environment. In this class of models, Maxwell's equations are solved to yield the distribution of current along the lightning channel using numerical techniques, such as the method of moments (MoM) (Harrington 1968; Van Baricum and Miller 1972; Miller *et al.* 1973) and the finite-difference method (Yee 1966). The resultant distribution of channel current can be used to compute electric and magnetic fields radiated by the lightning channel. To reduce the speed of the current wave propagating along the channel-representing vertical wire to a value lower than the speed of light in air,  $c$ , a wire is loaded by additional distributed series inductance (e.g. Kato *et al.* 1999), surrounded by a dielectric medium (other than air) that occupies the entire half space above ground (e.g. Moini *et al.* 1997), coated by a dielectric material (e.g. Kato *et al.* 2001) or coated by a fictitious material having high relative permittivity and high relative permeability (e.g. Miyazaki and Ishii 2004a). Two parallel wires having additional distributed shunt capacitance have been also suggested (Bonyadram *et al.* 2005). In contrast with distributed-circuit and engineering models, electromagnetic return-stroke models allow a self-consistent full-wave solution for both lightning-current distribution and resultant electromagnetic fields. One of the advantages of the use of electromagnetic models, although it may be computationally expensive, is that one does not need to employ any model of field-to-conductor coupling in analysing lightning-induced effects on electrical circuits (e.g. Pokharel *et al.* 2003; Tatematsu *et al.* 2004). Electromagnetic models are generally capable of reproducing most salient features of observed electric and magnetic fields at distances ranging from tens of metres to hundreds of kilometres (e.g. Shoory *et al.* 2005; Baba and Rakov 2009).

Note that the so-called hybrid electromagnetic/circuit (HEM) model (e.g. Visacro and Silveira 2004) has been also applied to representing lightning return strokes. It employs electric scalar and magnetic vector potentials for taking account of electromagnetic coupling but is formulated in terms of circuit quantities, voltages and currents. Since the HEM model, on the one hand, yields a non-TEM close electromagnetic field structure (as do electromagnetic models) and, on the other hand, apparently considers electric and magnetic fields as decoupled (as in distributed-circuit models), it occupies an intermediate place between electromagnetic and distributed-circuit models. Applications of HEM model to lightning return-stroke studies and to analysing the interaction of lightning with grounded

objects are described by Visacro and Silveira (2004) and by Visacro and Silveira (2005), respectively. Baba and Rakov (2007) have shown that the current distribution along a vertical resistive wire, representing a lightning channel, predicted by the HEM model, is consistent with that obtained using electromagnetic models.

In this chapter, electromagnetic models of the lightning return stroke, proposed as of today, are reviewed. This chapter is organized as follows. In Section 8.2, it is shown that a current wave necessarily suffers attenuation (dispersion to be exact) as it propagates upwards along a vertical non-zero-thickness wire above perfectly conducting ground excited at its bottom by a lumped source, even if the wire has no ohmic losses. This is a distinctive feature of electromagnetic return-stroke models. In Section 8.3, lightning return-stroke electromagnetic models are classified into six types depending on lightning channel representation used to find the distribution of current along the channel. In Section 8.4, distributions of current along a vertical channel and electromagnetic fields calculated for different channel representations are presented. In Section 8.5, methods of excitation used in electromagnetic return-stroke models are described. In Section 8.6, representative numerical procedures for solving Maxwell's equations used in electromagnetic models of the lightning return stroke are compared. In Section 8.7, applications of lightning return-stroke electromagnetic models are reviewed.

## 8.2 General approach to finding the current distribution along a vertical perfectly conducting wire above ground

All electromagnetic return-stroke models involve a representation of the lightning channel as a non-zero-thickness vertical wire. In this section, using Chen's analytical equation (1983), we show that a current wave necessarily suffers attenuation as it propagates along a vertical wire of uniform non-zero thickness that is located above perfectly conducting ground and excited at its bottom by a lumped source, even if the wire has no ohmic losses. This effect, well known in the radio science community, but not in the lightning research community (e.g. Bermudez *et al.* 2003), is usually attributed to radiation losses. Here, it is shown that current attenuation (dispersion) is necessary to satisfy the boundary condition on the tangential electric field on the surface of vertical wire.

### 8.2.1 Current distribution along a vertical perfectly conducting wire above ground

Chen (1983) has derived an approximate analytical equation for the transient current  $I(z', t)$  along an infinitely long perfectly conducting cylinder in air excited in the middle by a zero-length voltage source generating step voltage  $V$ . This equation is reproduced below:

$$I(z', t) = \frac{2V}{\eta} \tan^{-1} \left( \frac{\pi}{2 \ln(\sqrt{c^2 t^2 - z'^2}/a)} \right) \quad (8.1)$$

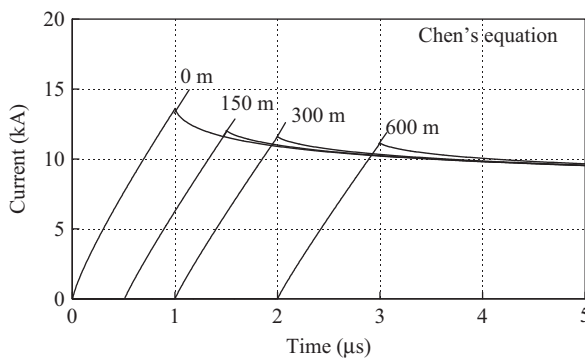
where  $\eta$  is free space impedance ( $120 \pi \omega$ ),  $\ln$  is the natural logarithm and  $a$  is the radius of the cylinder. If one applies (8.1) to a vertical cylinder on flat perfectly conducting ground excited at its bottom by a zero-length step-voltage source, one has only to multiply the magnitude of resultant current by 2 in order to account for the image source. Chen's analytical equation (8.1) can be used in testing the accuracy of numerical techniques employed in electromagnetic models of the lightning return stroke.

Figure 8.1 shows current waveforms at different heights along a vertical perfectly conducting wire of radius 0.23 m in air above ground excited at its bottom by a zero-length source that produces a ramp-front wave having a magnitude of 5 MV and a risetime of 1  $\mu$ s. Note that the response to this ramp-front voltage wave was obtained using numerical convolution since (8.1) yields the solution for a step voltage excitation.

It is clear from Figure 8.1 that a current wave suffers attenuation as it propagates along the vertical perfectly conducting wire above ground. It will be shown in Section 8.6.3 that current waveforms calculated using the MoM in the time and frequency domains and the FDTD method agree well with those calculated using Chen's equation.

### 8.2.2 Mechanism of attenuation of current wave in the absence of ohmic losses

According to analytical equation (8.1), any current wave suffers attenuation as it propagates upwards along a vertical perfectly conducting wire above flat perfectly conducting ground excited at its bottom by a lumped source (the same result follows from numerical solution of Maxwell's equations; e.g. Kordi *et al.* 2002, 2003a; Baba



*Figure 8.1 Current waveforms at different heights calculated using Chen's analytical equation (see (8.1)) for a vertical perfectly conducting cylinder of radius 0.23 m in air above perfectly conducting ground excited at its bottom by a zero-length voltage source. The source produces a ramp wave having a magnitude of 5 MV and a risetime of 1  $\mu$ s [adapted from Baba and Rakov (2007)]*

and Rakov 2003, 2005a), except for the ideal (unrealistic) case of a zero-thickness wire excited by a zero-length source (Thottappillil *et al.* 2001; Baba and Rakov 2008b). In this section, we discuss the mechanism of current attenuation in the absence of ohmic losses.

Baba and Rakov (2005a) have visualized the mechanism of attenuation of the current wave propagating along a vertical non-zero-thickness perfectly conducting wire as illustrated in Figure 8.2. A reference (no interaction with the wire, no attenuation) positive current pulse  $I_{inc}$  propagating upwards generates an incident spherical TEM wave (Thottappillil *et al.* 2001), with vertical electric field component on the surface of the wire being directed downwards. Cancellation of this field, as required by the boundary condition on the tangential electric field on the surface of a perfectly conducting wire, gives rise to an induced or ‘scattered’ current  $I_{scat}$ . This scattered current  $I_{scat}$  modifies  $I_{inc}$ , so that the resultant total current pulse  $I_{tot}$  appears attenuated as it propagates along the vertical wire. The attenuation of the total current pulse is accompanied by the lengthening of its tail, such that the total charge transfer is independent of height. The electromagnetic field structure associated with an attenuated current distribution along a vertical wire is non-TEM. Baba and Rakov (2005a) have shown that the current attenuation becomes more pronounced as (1) the thickness

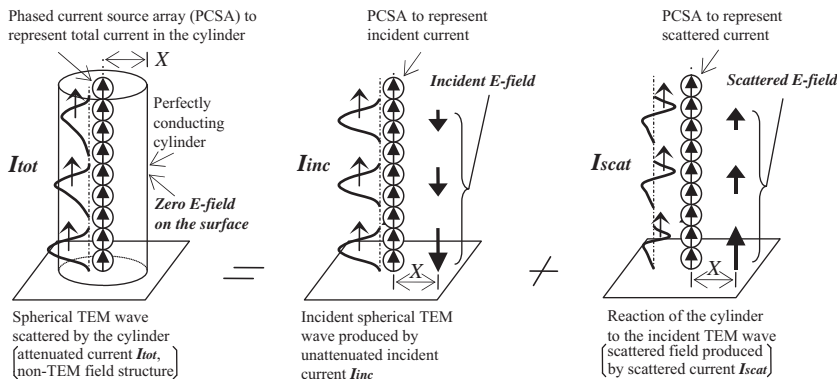


**Figure 8.2** Conceptual picture to explain the mechanism of current attenuation along a vertical non-zero-thickness perfectly conducting wire above perfectly conducting ground. All currents are assumed to flow on the axis. An attenuated ‘total’ current pulse  $I_{tot}$  is separated into an ‘incident’ unattenuated current pulse  $I_{inc}$  and an induced or ‘scattered’ current pulse  $I_{scat}$ .  $I_{inc}$  generates an incident downward vertical electric field at a horizontal distance  $x$  from the axis (on the lateral surface of the cylinder).  $I_{scat}$  produces a scattered upward vertical electric field that cancels the incident downward vertical electric field on the surface of the cylinder, and modifies the incident current  $I_{inc}$ . The resultant current pulse,  $I_{tot} = I_{inc} + I_{scat}$ , appears attenuated and its tail is lengthened as this pulse propagates along the wire [adapted from Baba and Rakov (2005a)]

of vertical wire increases, (2) the source height decreases, (3) the frequency increases and (4) the height above the excitation point decreases.

In summary, current attenuation (or more generally, dispersion) is necessary to satisfy the boundary condition on the tangential electric field on the surface of vertical wire. The resultant field structure is non-TEM, particularly in the vicinity of the excitation point.

### 8.3 Representation of the lightning return-stroke channel

In this section, electromagnetic return-stroke models are classified into six types depending on channel representation:

1. a perfectly conducting/resistive wire in air above ground;
2. a wire loaded by additional distributed series inductance in air above ground;
3. a wire surrounded by a dielectric medium (other than air) that occupies the entire half space above ground (the artificial dielectric medium is used only for finding current distribution along the lightning channel, which is then removed for calculating electromagnetic fields in air);
4. a wire coated by a dielectric material in air above ground;
5. a wire coated by a fictitious material having high relative permittivity and high relative permeability in air above ground; and
6. two parallel wires having additional distributed shunt capacitance in air (this fictitious configuration is used only for finding current distribution, which is then applied to a vertical wire in air above ground for calculating electromagnetic fields).

All the representations, except for type 1, are used to reduce the speed of the current wave propagating along the channel-representing wire to a value lower than the speed of light in air. Table 8.1 gives a list of papers on electromagnetic models of the lightning return stroke that are grouped into six categories depending on the channel representation.

In the following, we will review the return-stroke speed and channel characteristic impedance corresponding to each of the six types of channel representation. The return-stroke speed, along with the current peak, largely determines the radiation field initial peak (e.g. Rakov and Dulzon 1987), while the characteristic impedance of lightning channel influences the magnitude of lightning current and/or the current reflection coefficient at the top of strike object when a lumped voltage source is employed. It is desirable that the following two features are reproduced by models:

- (i) Typical values of return-stroke wavefront speed are in the range from  $c/3$  to  $c/2$  (Rakov 2007), as observed using optical techniques, where  $c$  is the speed of light.
- (ii) The equivalent impedance of the lightning return-stroke channel is expected to be in the range from 0.6 to 2.5 k $\Omega$  (Gorin and Shkilev 1984), as estimated

from measurements of lightning current at different points along the 530-m-high Ostankino Tower in Moscow.

Values of the radius of the lightning channel in Table 8.1 are larger than expected, approximately 30 mm (e.g. Rakov 1998), but this geometry was necessary to achieve agreement of the characteristic impedance of the simulated channel with expected equivalent channel impedance values (0.6–2.5 k $\Omega$ ).

Note that the resistance per unit length of a lightning return-stroke channel (behind the return-stroke front) is estimated to be approximately 0.035  $\Omega$ /m and approximately 3.5  $\Omega$ /m ahead of the return-stroke front (Rakov 1998). Values of distributed resistance (for the case of resistive channel) in Table 8.1 are between these two expected values.

### *8.3.1 Type 1: a perfectly conducting/resistive wire in air above ground*

Podgorski and Landt (1987) and Podgorski (1991), using the modified Thin-Wire Time-Domain (TWTD) code (Van Baricum and Miller 1972), have represented a lightning strike to the 553-m-high CN Tower in Toronto by a resistive (0.7  $\Omega$ /m) vertical wire with a non-linear resistor (10 k $\Omega$  prior to the attachment and 3  $\Omega$  after the attachment) connected between the bottom of the resistive wire and the top of the CN Tower (or the top of uncharged wire simulating the upward connecting leader from the tower).

The speed of the current wave propagating along such a wire is nearly equal to the speed of light, which is two to three times larger than typical measured values of return-stroke wavefront speed:  $c/3$  to  $c/2$  (e.g. Rakov 2007). This discrepancy is the main deficiency of the type-1 model. This should result in overestimation of remote electric and magnetic fields, since their magnitudes are expected to be proportional to the current wave propagation speed (e.g. Uman *et al.* 1975; Rakov and Dulzon 1987).

The characteristic impedance of the channel-representing vertical wire of radius 3 cm is estimated to be approximately 0.6 k $\Omega$  at a height of 500 m above ground (it varies with height above ground). This is right at the lower bound of its expected range of variation (0.6–2.5 k $\Omega$ ).

### *8.3.2 Type 2: a wire loaded by additional distributed series inductance in air above ground*

In this section, the TEM-wave-based  $R$ - $L$ - $C$  uniform transmission line theory is reviewed. Then, based on this theory, representation of the lightning return-stroke channel using a vertical wire loaded by additional distributed series inductance is discussed. Note that applying the  $R$ - $L$ - $C$  transmission-line theory to describing a vertical wire above ground is an approximation, since inductance  $L$  and capacitance  $C$ , both per unit length, vary with height along the vertical wire, and the resultant electromagnetic field structure is non-TEM.

Table 8.1 List of papers on electromagnetic models of the lightning return stroke grouped into six categories depending on the lightning channel representation

Representation	Papers	Channel radius (mm)	$\epsilon_r$	R ( $\Omega/m$ )	L ( $\mu\text{H}/\text{m}$ )	C ( $\text{pF}/\text{m}$ )	Phase velocity
Perfectly conducting or resistive wire in air above ground	<i>Reviewed journal papers</i> Podgorski and Landt (1987) Kordi <i>et al.</i> (2002) Mozumi <i>et al.</i> (2003) Baba and Ishii (2003) Kordi <i>et al.</i> (2003b) Baba and Rakov (2003, 2005a) Pokharel <i>et al.</i> (2004) Baba and Rakov (2008b) Baba and Rakov (2009) <i>Other publications</i> Podgorski (1991) Chai <i>et al.</i> (1994) Kato <i>et al.</i> (2001) Kordi <i>et al.</i> (2003a) Greev <i>et al.</i> (2003) Maslowski (2004)	Unknown 50 100 50 100 230 2000* 100 68 680	1 1 1 1 1 1 1 1 1 1 1 1 1	0.7 0 0 0, 0.1 0.07 0 0 0.1 0 0 0 0.7 Unknown 0 0 0 0 0 1	0 0 0 0 0 0 0 0 0 0 0 0 0	— — — — — — — — — — — — —	c c c c c c c c c c c c c
Wire loaded by additional distributed series inductance in air above ground	<i>Reviewed journal papers</i> Baba and Ishii (2001, 2003) Pokharel <i>et al.</i> (2003, 2004) 100	300 50 100	1 1 1	1 0.5 1	3 6 9	— — —	0.56c 0.43c 0.43c 0.37c

Noda <i>et al.</i> (2007)	230	1	0	10	—	0.33c
Pokharel and Ishii (2007)	Unknown	1	0.6	6	—	0.5c
Bonyadi-ram <i>et al.</i> (2008)	20	1	0.45	Non-uniform	—	0.53c to 0.3c
Miyazaki and Ishii (2008a, 2008b)	100	1	Unknown	Unknown	—	Unknown
Baba and Rakov (2009)	50	1	1	6	—	0.5c
<i>Other publications</i>	680	1	0.5	2.5	—	0.5c
Kato <i>et al.</i> (1999, 2001)	10	1	0	0.1	—	0.33c
Aniserowicz (2004, 2008)	10	1	0	2.5	—	0.7c
Bonyadi-ram <i>et al.</i> (2004)	50	1	1	4.5–7.5	—	0.43c
Miyazaki and Ishii (2004b, 2005)	50	1	1	4.5	—	0.5c
Tatematsu <i>et al.</i> (2004)	20	1	0.3	8	—	0.43c
Petrache <i>et al.</i> (2005)	Unknown	1	1	3	—	0.5c
Mosaddeghi <i>et al.</i> (2008)	Unknown	1	1	3	—	0.5c
Silveira and Visaciro (2008)	460	1	0	1.5, 10	—	0.6c, 0.3c
	100	1	1	3	—	0.5c
	10	1	1	8.9	—	0.4c
	10	1	0.5	Unknown	—	0.7c
<i>Reviewed journal papers</i>						
Moini <i>et al.</i> (1998, 2000)	Unknown	4	0	0	—	0.5c
Shoory <i>et al.</i> (2005)	Unknown	5.3	0.07	0	—	0.43c
Gerannayeh <i>et al.</i> (2006)	50	5.3	0.1	0	—	0.43c
Baba and Rakov (2009)	5	5.3	0	0	—	0.43c
	680	4	0	0	—	0.5c
<i>Other publications</i>						
Moini <i>et al.</i> (1997)	Unknown	5.3	0.1	0	—	0.43c
Griev <i>et al.</i> (2003)	50	5.3	0	0	—	0.43c
Alaee <i>et al.</i> (2007)	20	5.3	Non-linear	0	—	0.43c

(Continues)

Table 8.1 *Continued*

Representation	Papers	Channel radius (mm)	$\epsilon_r$	$R$ ( $\Omega/m$ )	$L$ ( $\mu\text{H}/\text{m}$ )	$C$ ( $\text{pF}/\text{m}$ )	Phase velocity
Wire coated by a dielectric material of $\epsilon_r > 1$ in air above ground	<i>Reviewed journal papers</i> Baba and Rakov (2009) 10-m-radius coating	680 ( $\epsilon_r = 400$ )	1 0	0	—	—	$0.7c$
	<i>Other publications</i> Kato <i>et al.</i> (2001) 4-m-radius coating	10 ( $\epsilon_r = 200$ )	1 0	0	—	—	$0.7c$
Wire coated by a fictitious material of $\epsilon_r > 1$ and $\mu_r > 1$ in air above ground	<i>Reviewed journal papers</i> Baba and Rakov (2009) 10-m-radius coating	680 ( $\epsilon_r = 5, \mu_r = 5$ )	1 0.25	0	—	—	$0.5c$
	<i>Other publications</i> Miyazaki and Ishii (2004a) ( $\epsilon_r, \mu_r$ : unknown)	10 ( $\epsilon_r, \mu_r$ : unknown)	1 0	0	—	—	Unknown
Two parallel wires having additional distributed shunt capacitance in air	<i>Reviewed journal papers</i> None	—	—	—	—	—	—
	<i>Other publications</i> Bonyadi-ram <i>et al.</i> (2005)	20	1 0.2	0	50	0.43c	—

$R$ ,  $L$  and  $C$  are the additional resistance, inductance and capacitance (each per unit length), respectively, of the equivalent lightning channel. \*2 m  $\times$  2 m rectangular cross section.

The propagation constant  $\gamma_0$  of the  $R-L-C$  uniform transmission line, the phase velocity  $v_{p0}$  of a wave propagating along this line and the characteristic impedance  $Z_{c0}$  of the line are given by (e.g. Sadiku 1994; Rakov 1998),

$$\gamma_0 = \sqrt{j\omega C_0(R_0 + j\omega L_0)} \quad (8.2)$$

$$v_{p0} = \frac{\omega}{\text{Im}(\gamma_0)} = \frac{1}{\sqrt{L_0 C_0}} \left[ \frac{2}{\sqrt{1 + (R_0/\omega L_0)^2} + 1} \right]^{1/2} \quad (8.3)$$

$$Z_{c0} = \sqrt{\frac{R_0 + j\omega L_0}{j\omega C_0}} \quad (8.4)$$

where  $\text{Im}(\gamma_0)$  stands for the imaginary part of  $\gamma_0$ ,  $\omega$  is the angular frequency ( $2\pi f$ ),  $R_0$  is the series resistance per unit length,  $L_0$  is the natural series inductance per unit length and  $C_0$  is the natural shunt capacitance per unit length. If  $\omega L_0$  is much larger than  $R_0$  at a frequency of interest, (8.3) and (8.4) reduce to

$$v_{p0} \simeq \frac{1}{\sqrt{L_0 C_0}} \quad (8.5)$$

$$Z_{c0} \simeq \sqrt{\frac{L_0}{C_0}} \quad (8.6)$$

The assumption that (8.5) and (8.6) are based on is satisfied at frequencies  $f = 1$  MHz or higher for  $L_0 = 2.1 \mu\text{H/m}$  (evaluated for a 3-cm-radius horizontal wire at a height of 500 m above ground (Rakov 1998)) and  $R_0 = 1 \Omega/\text{m}$ , where  $\omega L_0 (= 13 \Omega/\text{m}) \gg R_0 (= 1 \Omega/\text{m})$ . If the transmission line is surrounded by air,  $v_{p0}$  given by (8.5) is equal to  $c$ .

If the transmission line has additional distributed series inductance  $L$ , the phase velocity  $v_{pi}$  and the characteristic impedance  $Z_{ci}$  for such a line are

$$v_{pi} \simeq \frac{1}{\sqrt{(L_0 + L)C_0}} = \sqrt{\frac{L_0}{L_0 + L}} v_{p0} = \sqrt{\frac{L_0}{L_0 + L}} c \quad (8.7)$$

$$Z_{ci} \simeq \sqrt{\frac{L_0 + L}{C_0}} = \sqrt{\frac{L_0 + L}{L_0}} Z_{c0} = \frac{c}{v_{pi}} Z_{c0} \quad (8.8)$$

Equations (8.7) and (8.8) show that if  $L = 3L_0$ ,  $v_{pi}$  becomes  $0.5c$  and  $Z_{ci}$  becomes  $2Z_{c0}$ . In this representation,  $Z_{ci}$  increases linearly with decreasing  $v_{pi}$ . Note that additional inductance has no physical meaning and is invoked only to reduce the speed of the current wave propagating along the wire to a value lower than the speed of light. Electromagnetic waves radiated from the vertical inductance-loaded wire into air propagate at the speed of light. The use of this representation allows one to calculate both the distribution of current along the channel-representing wire and the radiated electromagnetic waves in a single, self-consistent procedure.

If the natural inductance of a vertical wire is assumed to be  $L_0 = 2.1 \mu\text{H/m}$  (evaluated for a 3-cm-radius horizontal wire at a height of 500 m above ground by Rakov 1998), the additional inductance needed to obtain typical values of  $v_{pi} = 0.5c$  and  $0.33c$  is estimated from (8.7) to be  $L = 6$  and  $17 \mu\text{H/m}$ , respectively. These inductance values ( $6$  and  $17 \mu\text{H/m}$ ) are not much different from those employed to date, which range from  $1.5$  (Tatematsu *et al.* 2004) to  $10 \mu\text{H/m}$  (Noda *et al.* 2007; Tatematsu *et al.* 2004), except for that employed by Kato *et al.* (1999), who used  $0.1 \mu\text{H/m}$  additional inductance. The speeds of the current wave propagating along the wire are approximately  $0.6c$  and  $0.3c$  for the wire loaded by  $L = 1.5$  and  $10 \mu\text{H/m}$ , respectively, and  $0.33c$  for  $0.1 \mu\text{H/m}$ . In summary, in order to simulate a typical speed of return-stroke waveform, values of additional distributed inductance should be in the range roughly from  $1$  to  $20 \mu\text{H/m}$ .

From (8.8),  $Z_{ci}$  is  $1.2 \text{ k}\Omega$  for  $v_{pi} = 0.5c$ , and  $1.8 \text{ k}\Omega$  for  $v_{pi} = 0.33c$ , respectively, if the characteristic impedance of a vertical wire of radius 3 cm is  $0.6 \text{ k}\Omega$  (estimated at a height of 500 m above ground). The characteristic impedance of the inductance-loaded wire ( $Z_{ci} = 1.2\text{--}1.8 \text{ k}\Omega$ ) is within the range of expected values (from  $0.6$  to  $2.5 \text{ k}\Omega$  (Gorin and Shikilev 1984)).

Baba and Ishii (2001, 2003) added distributed series resistance of  $1 \Omega/\text{m}$  to the inductance-loaded wire in order to stabilize non-physical oscillations caused by the employed numerical procedure. This same approach was also used by Aniserowicz (2004, 2008), Miyazaki and Ishii (2004b, 2005, 2008a, 2008b), Petrache *et al.* (2005), Pokharel *et al.* (2004) and Mosaddeghi *et al.* (2008).

### 8.3.3 Type 3: a wire embedded in a dielectric (other than air) above ground

In this section, (8.5) and (8.6), which are based on the  $R\text{-}L\text{-}C$  uniform transmission line approximation, are used to examine phase velocity and characteristic impedance of a vertical wire above ground surrounded by a dielectric (other than air) that has relative permittivity  $\epsilon_r$  and occupies the entire half space above ground. From (8.5) and (8.6), the phase velocity  $v_{pd}$  and the characteristic impedance  $Z_{cd}$  for this representation are

$$v_{pd} \simeq \frac{1}{\sqrt{L_0 \epsilon_r C_0}} = \frac{v_{p0}}{\sqrt{\epsilon_r}} = \frac{c}{\sqrt{\epsilon_r}} \quad (8.9)$$

$$Z_{cd} \simeq \sqrt{\frac{L_0}{\epsilon_r C_0}} = \frac{Z_{c0}}{\sqrt{\epsilon_r}} = \frac{v_{pd}}{c} Z_{c0} \quad (8.10)$$

Equations (8.9) and (8.10) show that  $Z_{cd}$  decreases linearly with decreasing  $v_{pd}$ . When  $\epsilon_r$  ranges from  $4$  to  $9$ ,  $v_{pd}$  ranges from  $0.5c$  to  $0.33c$ , which corresponds to typical measured speeds of the lightning return-stroke waveform (e.g. Rakov 2007). The corresponding characteristic impedance  $Z_{cd}$  is  $0.3 \text{ k}\Omega$  for  $v_{pd} = 0.5c$ , and  $0.2 \text{ k}\Omega$  for  $v_{pd} = 0.33c$ , if  $Z_{c0} = 0.6 \text{ k}\Omega$ . This characteristic impedance ( $Z_{cd} = 0.2\text{--}0.3 \text{ k}\Omega$ ) is smaller than values of the expected equivalent impedance of the lightning return-stroke channel ( $0.6\text{--}2.5 \text{ k}\Omega$ ) (Gorin and Shikilev 1984). This

does not cause significant differences in resultant current distributions in analysing a branchless subsequent lightning stroke terminating on flat ground, in which upward connecting leaders are usually neglected and the return-stroke current wave propagates upwards from the ground surface. However, in analysing lightning strikes to a grounded metallic object (Rakov 2001), one needs to insert several-hundred-ohm lumped resistance between the lightning channel and the strike object in order to obtain a realistic impedance of the lightning return-stroke channel seen by waves entering the channel from the strike object. Note that the artificial dielectric medium is used only for finding current distribution along the lightning channel, which is then removed for calculating electromagnetic fields in air.

Aniserowicz (2004) has found a useful relation between a resistive wire loaded by additional distributed series inductance and a resistive wire (characterized by  $R_0$ ,  $L_0$  and  $C_0$ ) embedded in a dielectric. From (8.2), the propagation constant for a resistive transmission line embedded in a dielectric of relative permittivity  $\epsilon_r$  is given by

$$\gamma_d = \sqrt{j\omega\epsilon_r C_0(R_0 + j\omega L_0)} \quad (8.11)$$

which can be written as

$$\gamma_i = \sqrt{j\omega C_0(\epsilon_r R_0 + j\omega \epsilon_r L_0)} \quad (8.12)$$

Equations (8.11) and (8.12) show that the effect of distributed resistance  $\epsilon_r R_0$  ( $= 5.3 R_0$ ) of a wire in air loaded by additional distributed series inductance of  $L = (\epsilon_r - 1)L_0$  ( $= 4.3L_0$ ) on the propagation constant is the same as that of  $R_0$  of a wire embedded in a dielectric of relative permittivity  $\epsilon_r$  ( $= 5.3$ ). For example, the effect of  $R_0 = 0.07 \Omega/m$  of a wire embedded in a dielectric of  $\epsilon_r = 5.3$  (e.g. Moini *et al.* 2000) on the propagation constant is the same as that of  $\epsilon_r R_0 = 0.37 \Omega/m$  of a wire in air loaded by  $L = 4.3L_0$ .

It follows from (8.3) that the phase velocity  $v_{pi}$  for a wire above ground surrounded by air having a distributed series resistance of  $\epsilon_r R_0$  and an additional distributed series inductance of  $L = (\epsilon_r - 1)L_0$  is the same as the phase velocity  $v_{pd}$  for a wire having a distributed series resistance of  $R_0$  and being embedded in a dielectric of  $\epsilon_r$ . The characteristic impedances of these two representations are given respectively by

$$Z_{ci} = \sqrt{\frac{\epsilon_r R_0 + j\omega \epsilon_r L_0}{j\omega C_0}} = \sqrt{\epsilon_r} Z_{c0} \quad (8.13)$$

$$Z_{cd} = \sqrt{\frac{R_0 + j\omega L_0}{j\omega \epsilon_r C_0}} = \frac{Z_{c0}}{\sqrt{\epsilon_r}} = \frac{Z_{ci}}{\epsilon_r} \quad (8.14)$$

Equations (8.13) and (8.14) show that the effect of distributed resistance  $\epsilon_r R_0$  of a wire in air loaded by an additional distributed series inductance of  $L = (\epsilon_r - 1)L_0$  on the characteristic impedance, relative to that of total inductance  $\epsilon_r L_0$ , is the same as that of  $R_0$  of a wire embedded in a dielectric of relative permittivity  $\epsilon_r$ , relative to that of natural inductance  $L_0$ .

### 8.3.4 Type 4: a wire coated by a dielectric material in air above ground

Kato *et al.* (2001) have represented the lightning channel by a vertical perfectly conducting wire, which is placed along the axis of a 4-m-radius dielectric cylinder of relative permittivity 200. This dielectric cylinder was surrounded by air. The speed of the current wave propagating along the wire is approximately  $0.7c$ . Such a representation allows one to calculate both the distribution of current along the wire and the remote electromagnetic fields in a single, self-consistent procedure, while that of a vertical wire surrounded by an artificial dielectric medium occupying the entire half space (type 3 described above) requires two steps to achieve the same objective. However, electromagnetic fields produced by this configuration (dielectric-coated wire in air) are influenced by the presence of coating, which will be shown in Section 8.4.2. Note that a conductor with dielectric coating is also known as the Goubau waveguide (Goubau 1950).

### 8.3.5 Type 5: a wire coated by a fictitious material having high relative permittivity and high relative permeability in air above ground

Miyazaki and Ishii (2004a) have represented the lightning channel by a vertical wire, which is placed along the axis of a cylinder or parallelepiped-shaped block having high relative permittivity and high relative permeability (transverse dimensions of the block, and the values of relative permittivity and permeability are not given). This structure is surrounded by air. The speed of the current wave propagating along the wire was approximately  $0.5c$ . Similarly to the type-4 model, this representation allows one to calculate both the distribution of current along the wire and the remote electromagnetic fields in a single, self-consistent procedure. For the same speed of current wave, the characteristic impedance value for this channel representation is higher than that for the type-4 model, since both relative permittivity and permeability are set at higher values in the type-5 model.

### 8.3.6 Type 6: two wires having additional distributed shunt capacitance in air

In this section, we use (8.5) and (8.6) to examine phase velocity and characteristic impedance of a transmission line having additional distributed shunt capacitance. From (8.5) and (8.6), the phase velocity  $v_{pc}$  and the characteristic impedance  $Z_{cc}$  for this case are given by

$$v_{pc} \simeq \frac{1}{\sqrt{L_0(C_0 + C)}} = \sqrt{\frac{C_0}{C_0 + C}} v_{p0} = \sqrt{\frac{C_0}{C_0 + C}} c \quad (8.15)$$

$$Z_{cc} \simeq \sqrt{\frac{L_0}{C_0 + C}} = \sqrt{\frac{C_0}{C_0 + C}} Z_{c0} = \frac{v_{pc}}{c} Z_{c0} \quad (8.16)$$

Bonyadi-ram *et al.* (2005) have evaluated the distribution of current along a lightning channel approximating this channel and its image by two 7-km-long parallel wires with additional shunt capacitance between them and excited at their one end by a lumped voltage source. Each wire has a radius of 2 cm, and the separation between the wires is 30 m. The resultant parallel-wire transmission line also has a distributed series resistance of  $0.2 \Omega/\text{m}$ . The additional shunt capacitance is  $C = 50 \text{ pF/m}$ , which allows them to reduce the speed of the current wave propagating along the parallel wires to  $v = 0.43c$ . The current distribution, obtained for the two capacitively loaded parallel wires, is used to calculate electric and magnetic fields 0.5, 5 and 100 km from a vertical lightning channel above ground.

Similar to the type-3 model described above, the type-6 model employs a fictitious configuration for finding a reasonable distribution of current along the lightning channel, and then this current distribution is applied to the actual configuration (vertical wire in air above ground). The type-6 model is not further considered in this paper.

## 8.4 Comparison of model-predicted current distributions and electromagnetic fields for different channel representations

In this section, current distributions along a vertical channel above perfectly conducting ground excited at its bottom by a lumped current source, which are predicted by electromagnetic models of types 1–5 described above, are presented. Then, vertical electric and azimuthal magnetic field waveforms, calculated for these models, are presented and compared with typical measured electric and magnetic field waveforms due to natural and triggered lightning return strokes at different distances.

### 8.4.1 Comparison of distributions of current for different channel representations

The five representations of lightning channel excited at its bottom above flat perfectly conducting ground, to be analysed using the finite-difference time-domain (FDTD) method (Yee 1966) in the 2D-cylindrical coordinate system, are illustrated in Figure 8.3. Figure 8.3(a) shows a vertical perfectly conducting wire in air (type 1). Figure 8.3(b) shows a vertical wire in air loaded by additional distributed series inductance  $L = 2.5 \mu\text{H/m}$  and distributed series resistance  $R = 0.5 \Omega/\text{m}$  (type 2). Note that the  $0.5-\Omega/\text{m}$  resistance is employed in order to stabilize high-frequency oscillations that appear when additional series distributed inductance is included. Figure 8.3(c) shows a vertical perfectly conducting wire embedded in dielectric of  $\epsilon_r = 4$ , which occupies the entire half space (type 3). Figure 8.3(d) shows a vertical perfectly conducting wire embedded in a 10-m-radius dielectric cylinder of  $\epsilon_r = 400$  surrounded by air (type 4). Figure 8.3(e) shows a vertical wire loaded by  $R = 0.25 \Omega/\text{m}$  and embedded in a 10-m-radius cylinder of  $\epsilon_r = 5$  and  $\mu_r = 5$  surrounded by air (type 5). The length of the channel-representing wire is set to 30 km.

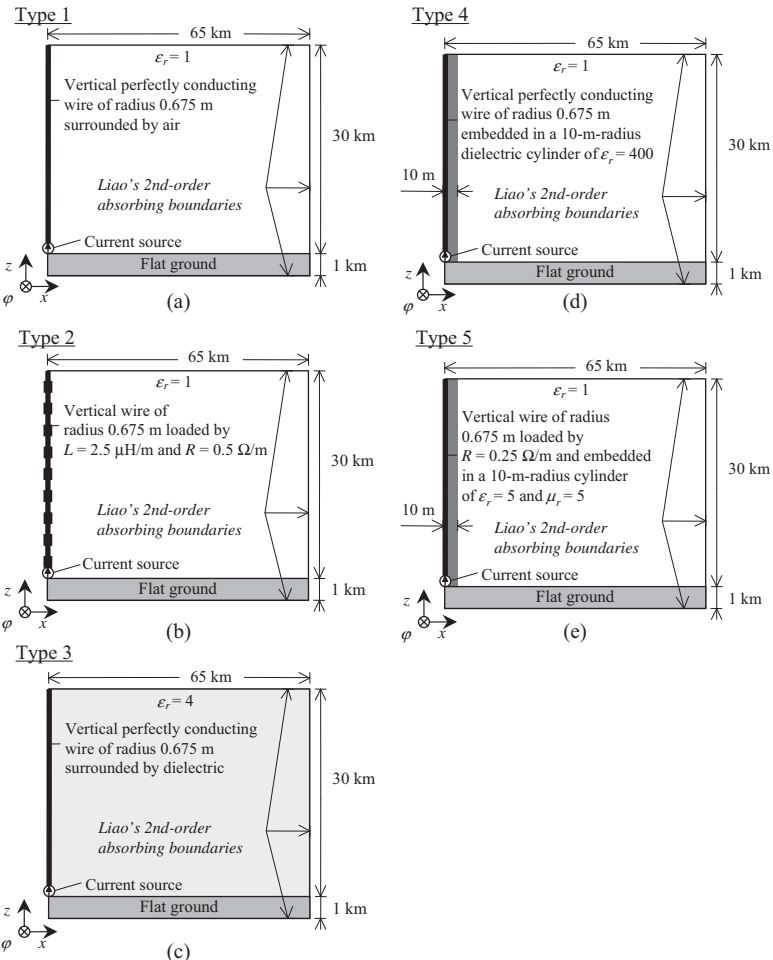


*Figure 8.3* Five representations of lightning return-stroke channel excited at its bottom by a 10-m current source above flat perfectly conducting ground, to be analysed using the 2D-cylindrical FDTD method:  
 (a) a vertical perfectly conducting wire surrounded by air (type 1),  
 (b) a vertical wire loaded by additional distributed series inductance  $L = 2.5 \mu\text{H/m}$  and distributed series resistance  $R = 0.5 \Omega/\text{m}$  in air (type 2), (c) a vertical perfectly conducting wire embedded in dielectric of  $\epsilon_r = 4$ , which occupies the entire half space (type 3), (d) a vertical perfectly conducting wire embedded in a 10-m-radius dielectric cylinder of  $\epsilon_r = 400$  surrounded by air (type 4) and (e) a vertical wire loaded by  $R = 0.25 \Omega/\text{m}$  and embedded in a 10-m-radius cylinder of  $\epsilon_r = 5$  and  $\mu_r = 5$  surrounded by air (type 5). For representation (a)  $v = c$ , for representations (b), (c) and (e)  $v = 0.5c$  and for representation (d)  $v = 0.7c$  [adapted from Baba and Rakov (2009)]

This unrealistically long wire is employed in order to avoid effects of any reflections from the upper end of the channel in field waveforms during at least the first 100  $\mu\text{s}$  ( $= 30 \text{ km}/v$  for  $v = c$ ). The length of vertical channel section is expected to be 5–8 km, with contributions from higher sections being relatively small (particularly at close distances). At 50 km, however, the computed fields after 50  $\mu\text{s}$  or so may be influenced by the unrealistic vertical channel section above 8 km and, hence, should be viewed with caution. The assumed higher resistance at larger heights (see Figures 8.7 and 8.8(c)) serves to alleviate this problem.

The lumped current source located at the bottom of simulated channel has a length of 10 m and produces a current waveform having a peak of 11 kA, a 10–90% risetime ( $RT$ ) of 1  $\mu\text{s}$  and a time to half-peak value of 30  $\mu\text{s}$  (see the waveform labelled ‘ $z' = 0$ ’ in Figure 8.4). This channel-base current waveform is the same as the waveform, proposed by Nucci *et al.* (1990) and thought to be typical for subsequent lightning return strokes, except for its rising portion ( $RT = 1 \mu\text{s}$  here vs. 0.15  $\mu\text{s}$  in Nucci *et al.* (1990)). For the FDTD calculations, the vertical conducting wire is represented by a zero-radius wire placed at the left-side boundary ( $r = 0$ ) in the working space of  $65 \text{ km} \times 31 \text{ km}$ , which is divided into  $5 \text{ m} \times 10 \text{ m}$  rectangular cells. When cells having a lateral side length of 5 m are used, the vertical ( $z$ -directed) zero-radius perfectly conducting wire placed at  $x = 0$  has an equivalent radius of  $0.675 \text{ m} = 0.135 \times 5 \text{ m}$  (Taniguchi *et al.* 2008). Liao’s second-order absorbing boundaries (Liao *et al.* 1984) are set at the bottom, top and right-side boundaries in order to avoid reflections there. The time increment is set to 10 ns.

Figure 8.4 shows FDTD-calculated distributions of current along the lightning return-stroke channel for its different representations shown in Figure 8.3. For representation (a)  $v = c$ , for representations (b), (c) and (e)  $v = 0.5c$  and for representation (d)  $v = 0.7c$ . Note that these speeds were calculated based on times needed for current waves to propagate from  $z' = 0$  to 2 km along a vertical wire, which were determined by tracking an intersection point between a straight line passing through 10 and 90% points on the rising part of the current waveform and the time axis. In Figure 8.4(b), (c) and (e), parameters of channel representation were adjusted to achieve the same value of  $v = 0.5c$ .

It appears from Figure 8.4(d) that in order to reduce the speed of current wave propagating along a vertical wire having a dielectric coating (type 4), which is surrounded by air, to a value similar to the typical measured return-stroke speed (Rakov 2007), the relative permittivity of the dielectric coating would need to be set to a very high value (much higher than that in the case of dielectric half space). The current-wave propagation speed decreases with increasing the thickness of the dielectric coating and its relative permittivity, but the dependency is weak (Baba and Rakov 2007). The initial peak of the longitudinal current decays significantly owing to the presence of dielectric coating having very high relative permittivity. It follows from comparison of Figure 8.4(d) and (e) that increasing both relative permittivity and relative permeability of the coating (the effect of  $R = 0.25 \Omega/\text{m}$  is minor) is more efficient in reducing the current-wave propagation speed (also yields more realistic current profile) than increasing the relative permittivity only.

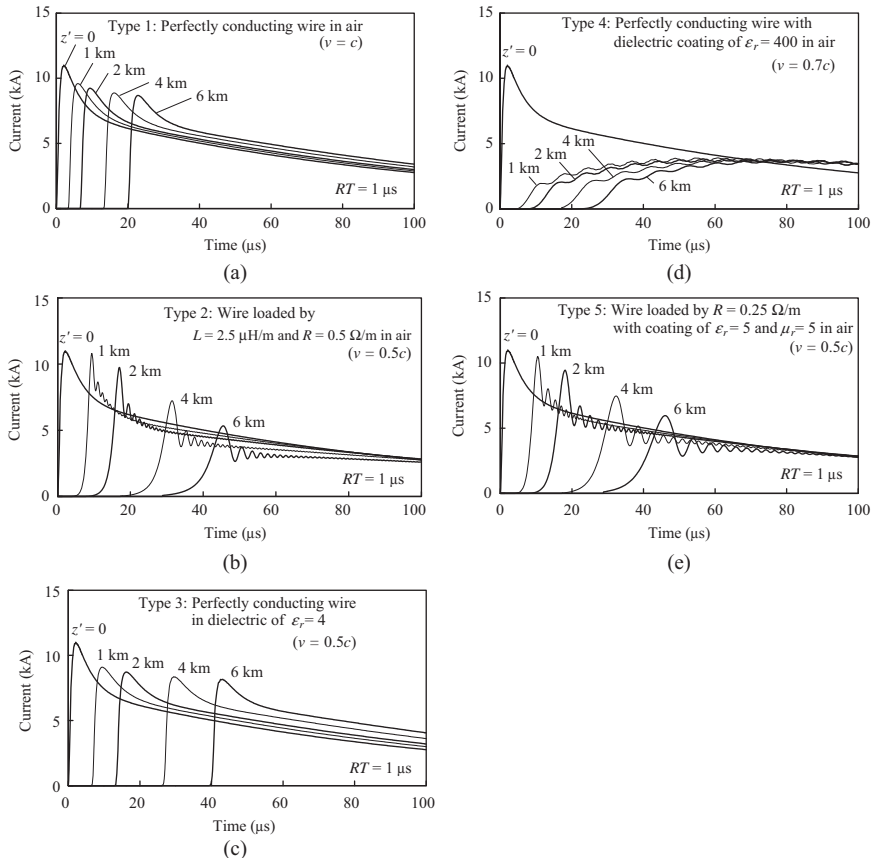


*Figure 8.4 Current waveforms at different heights calculated using the FDTD method for five representations of the lightning return-stroke channel shown in Figure 8.3: (a) type 1, (b) type 2, (c) type 3, (d) type 4 and (e) type 5 [adapted from Baba and Rakov (2009)]*

#### 8.4.2 Comparison of model-predicted electric and magnetic fields with measurements

In this section, vertical electric and azimuthal magnetic field waveforms, calculated using the FDTD method for different channel representations, are compared with typical measured electric and magnetic field waveforms due to first and subsequent natural lightning return strokes at distances  $d = 5$  and 50 km, and triggered lightning strokes at  $d = 50$  m.

The following five features, shown in Figure 8.5, have been identified in electric and magnetic field waveforms measured at distances ranging from 1 to 200 km from first and subsequent natural lightning return strokes (Lin *et al.* 1979), and at tens to hundreds of metres from triggered lightning strokes (Crawford *et al.* 2001).

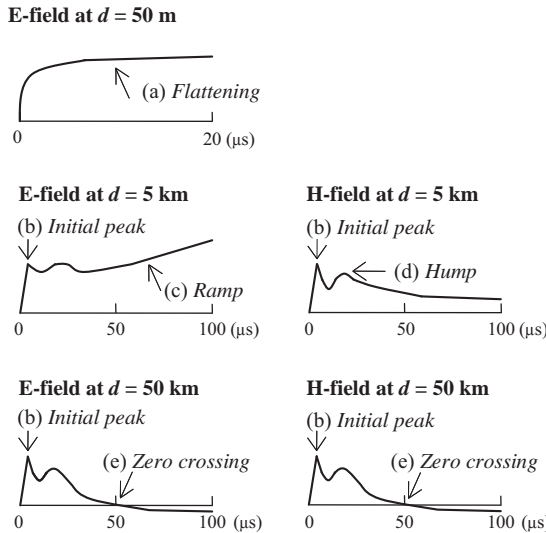


Figure 8.5 Typical features of vertical electric and azimuthal magnetic field waveforms measured at different distances from lightning return strokes (Rakov and Uman 1998)

These features have been used as a benchmark in testing the validity of various lightning return-stroke models (e.g. Rakov and Uman 1998):

- (a) characteristic flattening of vertical electric field at tens to hundreds of metres within 15  $\mu$ s or so of the beginning of return stroke;
- (b) sharp initial peak in both electric and magnetic field waveforms at a few kilometres and beyond;
- (c) slow ramp following the initial peak in electric field waveforms measured within few tens of kilometres;
- (d) hump following the initial peak in magnetic field waveforms measured within several tens of kilometres; and
- (e) zero-crossing within tens of microseconds in both electric and magnetic field waveforms measured at 50 km and beyond.

Figure 8.6(a), (b) and (c) shows vertical electric field waveforms at  $d = 50$  m, 5 km and 50 km, calculated using the FDTD method for different representations of the lightning return-stroke channel shown in Figure 8.3 (types 1, 2, 3, 4 and 5). Figure 8.6(d) shows FDTD-calculated waveforms of azimuthal magnetic field at  $d = 5$  km.

Feature (a) is reproduced by type-2 and type-5 models. Feature (b) is reproduced by all model types considered, except for type 4. Feature (c) is reproduced by type-2 and type-5 models. Features (d) and (e) are not reproduced by any model considered. Overall, it follows that fields predicted by type-2 and type-5 models better match experimental data than those predicted by any other model considered here.

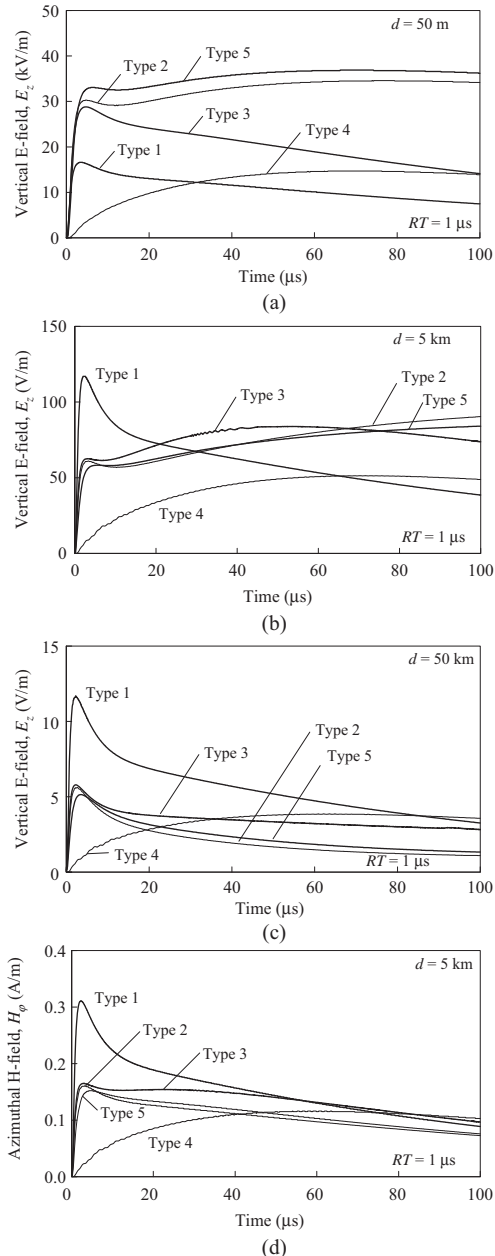


*Figure 8.6* Vertical electric field waveforms at (a)  $d = 50$  m, (b)  $d = 5$  km and (c)  $d = 50$  km, and (d) azimuthal magnetic field waveforms at  $d = 5$  km, calculated using the FDTD method for different representations of the lightning return-stroke channel shown in Figure 8.3 (types 1–5) [adapted from Baba and Rakov (2009)]

It follows from the electromagnetic field calculations that no electromagnetic model with the input parameters considered can reproduce either feature (d), hump of the magnetic field, or feature (e), zero-crossing of the remote fields. Baba *et al.* (2004) have shown, using their engineering return-stroke model, that significant current attenuation within a few tens of metres of the return-stroke channel base is needed to reproduce feature (d) and appreciable attenuation along the upper part of the channel is needed to reproduce feature (e). Note that Thottappillil *et al.* (1991) have shown that the TCS and DU models with a somewhat different channel-base current waveform whose time to half-peak value is 20  $\mu\text{s}$  reproduce features (b) to (e). Further, Cooray *et al.* (2008) have found that a horizontal section of the channel inside the cloud may be responsible for the observed zero-crossing in distant fields.

Vertical electric and azimuthal magnetic field waveforms at  $d = 50$  m, 5 km and 50 km from the lightning channel, calculated using the most promising type-2 and type-5 models that are modified here to include non-uniformly distributed series resistance, are considered next. The modified type-2 model has non-uniformly distributed series resistance:  $R = 2 \Omega/\text{m}$  for  $z' = 0\text{--}0.5 \text{ km}$ ,  $0.65 \Omega/\text{m}$  for  $z' = 0.5\text{--}4 \text{ km}$ ,  $1 \Omega/\text{m}$  for  $z' = 4\text{--}7.5 \text{ km}$  and  $10 \Omega/\text{m}$  for  $z' > 7.5 \text{ km}$ . The modified type-5 model has non-uniformly distributed series resistance:  $R = 1 \Omega/\text{m}$  for  $z' = 0\text{--}0.5 \text{ km}$ ,  $0.3 \Omega/\text{m}$  for  $z' = 0.5\text{--}4 \text{ km}$ ,  $0.5 \Omega/\text{m}$  for  $z' = 4\text{--}7.5 \text{ km}$  and  $5 \Omega/\text{m}$  for  $z' > 7.5 \text{ km}$ . The specified resistance profiles with relatively high resistance within the bottom 0.5 km appear to be consistent with observed light profiles along both natural subsequent return-stroke channels (Jordan *et al.* 1997) and rocket-triggered lightning channels (Olsen *et al.* 2004), showing that the light intensity decays significantly with height near ground. The reason for assuming the quite high channel resistance above 7.5 km is to diminish the current above 7.5 km. Note that it is not expected for the vertical lightning channel to extend above 7.5 km.

Figure 8.7(a) and (b) shows FDTD-calculated distributions of current along the lightning channel for type-2 and type-5 models. Comparisons of Figures 8.7(a) and 8.4(b), and of Figures 8.7(b) and 8.4(e) show that, when distributed resistance is not uniform, a current wave attenuates more significantly below  $z' = 1 \text{ km}$  and above  $z' = 4 \text{ km}$ . The current propagation speed is little influenced by the higher distributed resistance or the non-uniformly distributed resistance, and remains at about  $v = 0.5c$ .

Figure 8.8(a), (b) and (c) shows FDTD-calculated vertical electric field waveforms at  $d = 50$  m, 5 km and 50 km for type-2 and type-5 models for the case of non-uniform  $R$ . Figure 8.8(d) shows FDTD-calculated waveforms of azimuthal magnetic field at  $d = 5 \text{ km}$ . It is clear from Figure 8.8 that all five features are well reproduced by both type-2 and type-5 models with non-uniformly distributed series resistance.

## 8.5 Excitations used in electromagnetic models of the lightning return stroke

In this section, methods of excitation used to date in electromagnetic return-stroke models are described, and distributions of current along a vertical perfectly

conducting wire above perfectly conducting ground corresponding to different excitation methods are compared. Methods of excitation used in electromagnetic models are listed below:

1. closing a charged vertical wire at its bottom end with a specified impedance (or circuit);

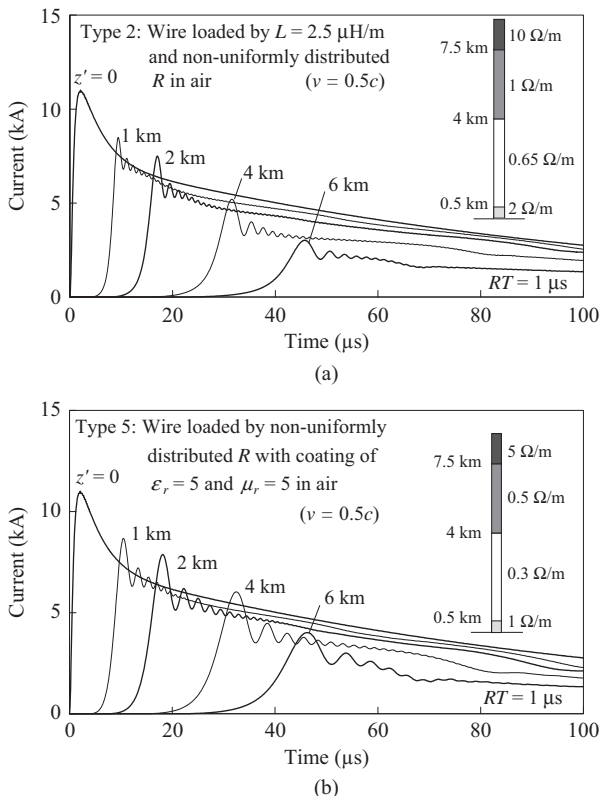


*Figure 8.7* Current waveforms at different heights calculated using the FDTD method for (a) type-2 model and (b) type-5 model shown in Figure 8.3(b) and (e) but with non-uniformly distributed series resistance. For type-2 model, uniformly distributed additional series inductance is  $L = 2.5 \mu\text{H/m}$ , and non-uniformly distributed series resistance is  $R = 2 \Omega/\text{m}$  for  $z' = 0\text{--}0.5 \text{ km}$ ,  $0.65 \Omega/\text{m}$  for  $z' = 0.5\text{--}4 \text{ km}$ ,  $1 \Omega/\text{m}$  for  $z' = 4\text{--}7.5 \text{ km}$  and  $10 \Omega/\text{m}$  for  $z' > 7.5 \text{ km}$ . For type-5 model, the relative permittivity and permeability of 10-m-radius cylinder containing the vertical wire are  $\epsilon_r = 5$  and  $\mu_r = 5$ , and non-uniformly distributed series resistance is  $R = 1 \Omega/\text{m}$  for  $z' = 0\text{--}0.5 \text{ km}$ ,  $0.3 \Omega/\text{m}$  for  $z' = 0.5\text{--}4 \text{ km}$ ,  $0.5 \Omega/\text{m}$  for  $z' = 4\text{--}7.5 \text{ km}$  and  $5 \Omega/\text{m}$  for  $z' > 7.5 \text{ km}$  [adapted from Baba and Rakov (2009)]

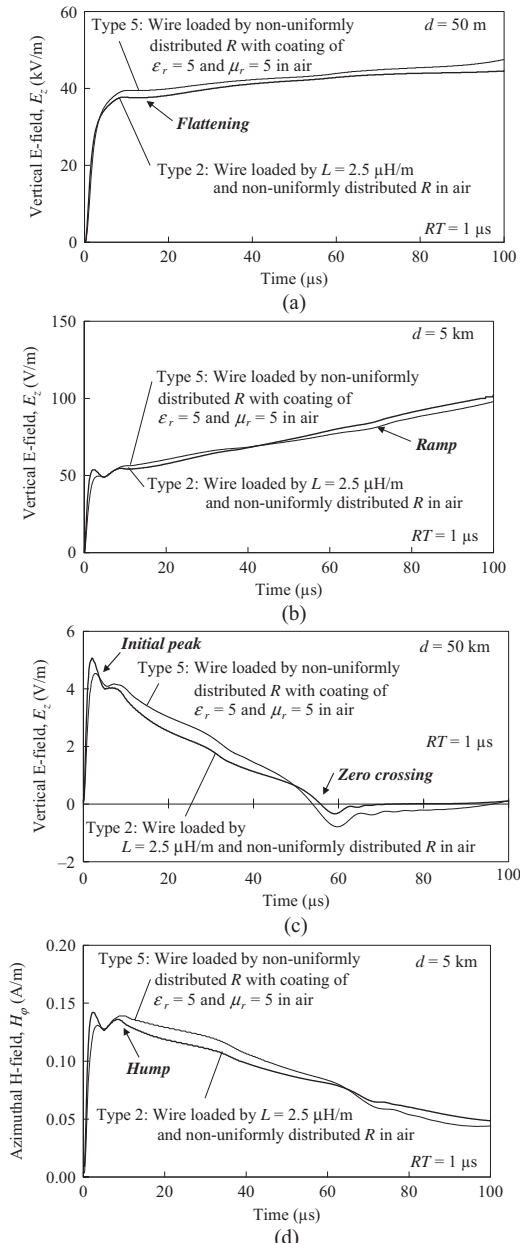


Figure 8.8 Vertical electric field waveforms at (a)  $d = 50$  m, (b)  $d = 5$  km, and (c)  $d = 50$  km, and (d) azimuthal magnetic field waveforms at  $d = 5$  km, calculated using the FDTD method for type-2 and type-5 models shown in Figure 8.3(b) and (e) but with non-uniformly distributed series resistance [adapted from Baba and Rakov (2009)]

2. a lumped voltage source (delta-gap electric-field source); and
3. a lumped current source.

Table 8.2 gives a list of papers on electromagnetic models of the lightning return stroke that are grouped into three categories depending on the method of excitation.

### *8.5.1 Closing a charged vertical conducting wire at its bottom end with a specified circuit*

Podgorski and Landt (1987) and Podgorski (1991) have represented a leader/return-stroke sequence by a pre-charged vertical resistive wire representing the lightning channel connected, via a non-linear resistor, to the top of a vertical perfectly conducting wire representing the 553-m-high CN Tower or to the tip of the upward connecting leader emanated from the top of the tower. In their model, closing a charged vertical wire in a grounded circuit constitutes return-stroke excitation of the lightning channel.

*Table 8.2 List of papers on electromagnetic models of the lightning return stroke grouped into three categories depending on the method of excitation employed*

<b>Excitation</b>	<b>Reviewed journal papers</b>	<b>Other publications</b>
Closing charged channel with a specified impedance	Podgorski and Landt (1987)	Podgorski (1991)
Lumped voltage source (delta-gap electric-field source)	Moini <i>et al.</i> (1998, 2000) Baba and Ishii (2001, 2003) Kordi <i>et al.</i> (2002, 2003b) Mozumi <i>et al.</i> (2003) Pokharel <i>et al.</i> (2003, 2004) Pokharel and Ishii (2007) Miyazaki and Ishii (2008a, b) Baba and Rakov (2008)	Chai <i>et al.</i> (1994) Moini <i>et al.</i> (1997) Kato <i>et al.</i> (1999, 2001) Kordi <i>et al.</i> (2003a) Aniserowicz (2004, 2008) Miyazaki and Ishii (2004a, b, 2005) Petrache <i>et al.</i> (2005) Bonyadi-ram <i>et al.</i> (2005) Alaee <i>et al.</i> (2007) Mosaddeghi <i>et al.</i> (2008) Silveira and Visacro (2008)
Lumped current source	Baba and Rakov (2003, 2005a, 2009) Shoory <i>et al.</i> (2005) Geranmayeh <i>et al.</i> (2006) Noda <i>et al.</i> (2007) Bonyadi-ram <i>et al.</i> (2008)	Maslowski (2004) Bonyadi-ram <i>et al.</i> (2004) Tatematsu <i>et al.</i> (2004) Grcev <i>et al.</i> (2003)

### 8.5.2 Lumped voltage source

A lumped voltage source (delta-gap electric-field source) is located at ground surface (e.g. Moini *et al.* 1998) or at the top of a grounded strike object (e.g. Chai *et al.* 1994). This type of source generates a specified electric field, which is independent of magnetic field surrounding the source or current flowing through it. Since such a lumped voltage source has zero internal impedance, its presence in series with the lightning channel and a strike object does not disturb any transient processes in them. If necessary, one could insert a lumped resistor in series with the lumped voltage source to adjust the impedance seen by waves entering the channel from the strike object to a value consistent with the expected equivalent impedance of the lightning channel.

### 8.5.3 Lumped current source

A lumped current source is located at ground surface (e.g. Grcev *et al.* 2003) or at the top of a grounded strike object (e.g. Noda *et al.* 2007). If reflected waves returning to the current source are negligible, the use of a lumped current source inserted at the attachment point does not cause any problem. This is the case for a branchless subsequent lightning stroke terminating on flat ground, in which upward connecting leaders are usually neglected and the return-stroke current wave propagates upwards from the ground surface. The primary reason for the use of a lumped current source at the channel base is a desire to use directly the channel-base current, known from measurements for both natural and triggered lightning, as an input parameter of the model. When one employs a lumped ideal current source at the attachment point in analysing lightning strikes to a tall grounded object, the lightning channel, owing to the infinitely large impedance of the ideal current source, is electrically isolated from the strike object, so that current waves reflected from ground cannot be directly transmitted to the lightning channel. Since this is physically unreasonable, a series ideal current source is not suitable for modelling of lightning strikes to tall grounded objects.

### 8.5.4 Comparison of current distributions along a vertical perfectly conducting wire excited by different sources

In this section, distributions of current along a vertical perfectly conducting wire in air energized by different methods of excitation described above are compared. Figure 8.9 shows three representations of lightning return stroke attached to flat perfectly conducting ground by (a) closing a pre-charged vertical perfectly conducting wire of radius 0.23 m in air with a non-linear resistor (left panel may be viewed as representing leader process and right panel the return-stroke process), (b) a vertical perfectly conducting wire of radius 0.23 m in air excited at its bottom by a 10-m-long lumped voltage source and (c) a vertical perfectly conducting wire of radius 0.23 m in air excited at its bottom by a 10-m-long lumped current source. The lumped voltage source of the model shown in Figure 8.9(a) generates a ramp-front wave having a magnitude of 10 MV/m (100 MV along the 10-m-long source) and a risetime of 1  $\mu$ s, while that of the model shown in Figure 8.9(b) generates a

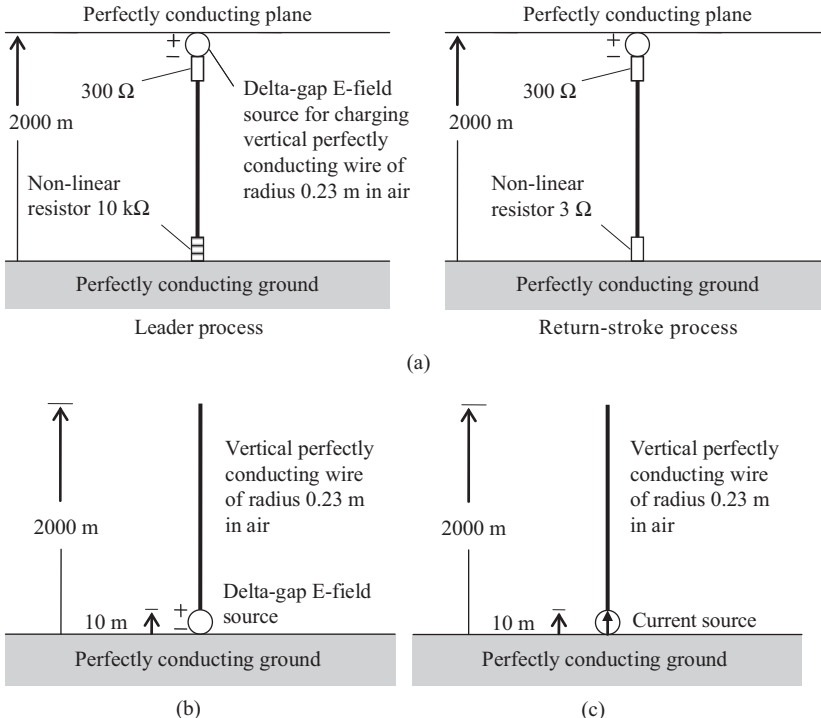


*Figure 8.9* Three representations of the lightning return-stroke channel above flat perfectly conducting ground by (a) a vertical perfectly conducting wire of radius 0.23 m in air that is essentially open-circuited at its bottom end when being charged by a lumped voltage source at its top (left panel) and then connected to flat ground via a  $3\Omega$  resistor during its discharging (right panel), (b) a vertical perfectly conducting wire of radius 0.23 m in air excited at its bottom by a 10-m-long lumped voltage source and (c) a vertical perfectly conducting wire of radius 0.23 m in air excited at its bottom by a 10-m-long lumped current source [adapted from Baba and Rakov (2007)]

ramp-front wave having a magnitude of 500 kV/m (5 MV along the 10-m-long source) and a risetime of 1  $\mu$ s. The current waveform injected by the lumped current source in Figure 8.9(c) is set to be the same as the resultant current waveform injected by the lumped voltage source in Figure 8.9(b).

Figure 8.10 shows distributions of current along the 0.23-m-radius vertical perfectly conducting wire in air excited by different sources (see Figure 8.9) that are calculated using the FDTD method. It is clear from Figure 8.10(b) and (c) that the distributions of current along the vertical wire excited at its bottom by the lumped voltage source and by the lumped current source are identical. Therefore, resultant electric and magnetic fields generated around the vertical wire are also

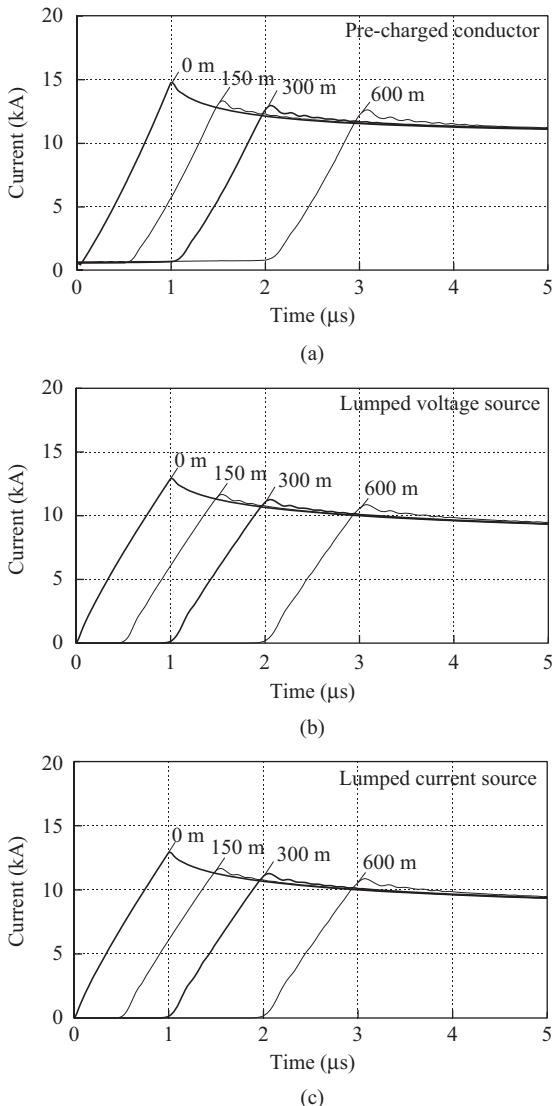


Figure 8.10 Current waveforms at different heights calculated using the FDTD method for three methods of excitation of the lightning return-stroke channel shown in Figure 8.9(a), (b) and (c) [adapted from Baba and Rakov (2007)]

identical (the use of either voltage or current source makes no difference in electric and magnetic fields in the case of lightning strike to flat ground, if there are no downward reflections in the channel). It is clear from Figure 8.10(a) and (b) that the distribution of current along the charged vertical wire closed with the non-linear

resistor is similar to that along the same vertical wire excited at its bottom by the lumped voltage source.

## 8.6 Numerical procedures used in electromagnetic models of the lightning return stroke

In this section, numerical procedures used in electromagnetic models of the lightning return stroke are briefly explained. They include (in chronological order of their usage in electromagnetic models):

1. the MoM in the time domain,
2. the MoM in the frequency domain, and
3. the FDTD method.

Table 8.3 includes a list of papers on electromagnetic models of the lightning return stroke grouped depending on the numerical procedure used.

### 8.6.1 *Methods of moments (MoMs) in the time and frequency domains*

#### 8.6.1.1 MoM in the time domain

The MoM in the time domain (Van Baricum and Miller 1972; Miller *et al.* 1973) is widely used in analysing responses of thin-wire metallic structures to external time-varying electromagnetic fields. The entire conducting structure representing the lightning channel is modelled by a combination of cylindrical wire segments whose radii are much smaller than the wavelengths of interest. It is assumed that current  $I$  and charge  $q$  are confined to the wire axis (thin-wire approximation). Then the so-called electric-field integral equation for a perfectly conducting thin wire in air (see Figure 8.11), which is based on Maxwell's equations and expresses the boundary condition on the tangential electric field on the surface of the wire (this field component must be equal to 0), is given by

$$\hat{\mathbf{s}} \cdot \mathbf{E}_{inc}(\mathbf{r}, t) = \frac{\mu_0}{4\pi} \int_C \left[ \frac{\hat{\mathbf{s}} \cdot \hat{\mathbf{s}}' \frac{\partial I(\mathbf{s}', t')}{\partial r'}}{R} + C \frac{\hat{\mathbf{s}} \cdot \mathbf{R} \frac{\partial I(\mathbf{s}', t')}{\partial s'}}{R^2} - c^2 \frac{\hat{\mathbf{s}} \cdot \mathbf{R}}{R^3} q(\mathbf{s}', t') \right] ds \quad (8.17)$$

where

$$q(\mathbf{s}', t') = - \int_{-\infty}^{t'} \frac{\partial I(\mathbf{s}', \tau)}{\partial s'} d\tau$$

$C$  is an integration path along the wire axis,  $\mathbf{E}_{inc}$  denotes the incident electric field that induces current  $I$ ,  $\mathbf{R} = \mathbf{r} - \mathbf{r}'$ ,  $\mathbf{r}$  and  $t$  denote the observation point location (a point on the wire surface) and time, respectively,  $\mathbf{r}'$  and  $t'$  denote the source point location (a point on the wire axis) and time, respectively,  $s$  and  $s'$  denote the distance along the wire surface at  $\mathbf{r}$  and that along the wire axis at  $\mathbf{r}'$ ,  $\hat{\mathbf{s}}$  and  $\hat{\mathbf{s}}'$  denote unit vectors tangent to path  $C$  in (8.17) at  $\mathbf{r}$  and  $\mathbf{r}'$ ,  $\mu_0$  is the permeability of vacuum and  $c$  is the speed of light. The time-dependent current distribution along the wire

*Table 8.3 List of papers on electromagnetic models of the lightning return stroke grouped into three categories depending on the numerical procedure used*

Numerical technique	Reviewed journal papers	Other publications
MoM in the time domain	Podgorski and Landt (1987) Moini <i>et al.</i> (1998, 2000) Kordi <i>et al.</i> (2002, 2003b) Mozumi <i>et al.</i> (2003) Pokharel and Ishii (2007)  Bonyadi-ram <i>et al.</i> (2008)	Podgorski (1991) Moini <i>et al.</i> (1997) Kato <i>et al.</i> (1999) Kordi <i>et al.</i> (2003a) Bonyadi-ram <i>et al.</i> (2004, 2005)  Alaee <i>et al.</i> (2007)
MoM in the frequency domain	Baba and Ishii (2001, 2003)  Pokharel <i>et al.</i> (2003, 2004) Shoory <i>et al.</i> (2005) Geranmayeh <i>et al.</i> (2006) Pokharel and Ishii (2007) Miyazaki and Ishii (2008a, 2008b)	Kato <i>et al.</i> (2001) Grcev <i>et al.</i> (2003) Aniserowicz (2004, 2008) Maslowski (2004) Miyazaki and Ishii (2004b, 2005) Petrache <i>et al.</i> (2005) Mosaddeghi <i>et al.</i> (2008) Silveira and Visacro (2008)
FDTD method	Baba and Rakov (2003, 2005a, 2008b, 2009) Noda <i>et al.</i> (2007)	Tatematsu <i>et al.</i> (2004)  Miyazaki and Ishii (2004a)

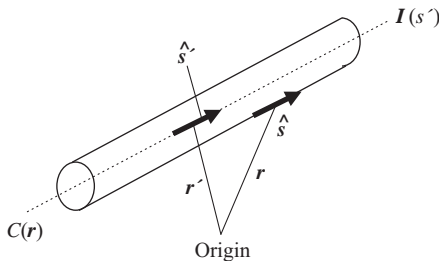


*Figure 8.11 Thin-wire segment for MoM-based calculations. Current is confined to the wire axis, and the tangential electric field on the surface of the wire is set to zero*

structure (lightning channel), excited by a lumped source, can be obtained by numerically solving (8.17).

The TWTD code (Van Baricum and Miller 1972) (available from the Lawrence Livermore National Laboratory) is based on the MoM in the time domain. One of the advantages of the use of the time-domain MoM is that it can incorporate non-linear effects such as the lightning attachment process (e.g.

Podgorski and Landt 1987), although it does not allow lossy ground and wires buried in lossy ground to be incorporated.

### 8.6.1.2 MoM in the frequency domain

The MoM in the frequency domain (Harrington 1968) is widely used in analysing the electromagnetic scattering by antennas and other metallic structures. To obtain the time-varying responses, Fourier and inverse Fourier transforms are employed. The electric-field integral equation derived for a perfectly conducting thin wire in air (see Figure 8.11) in the frequency domain is given by

$$-\hat{\mathbf{s}} \cdot \mathbf{E}_{inc}(\mathbf{r}) = \frac{j\eta}{4\pi k} \int_C I(\mathbf{s}') \left( k^2 \hat{\mathbf{s}} \cdot \hat{\mathbf{s}}' - \frac{\partial^2}{\partial s \partial s'} \right) g(\mathbf{r}, \mathbf{r}') ds \quad (8.18)$$

where

$$g(\mathbf{r}, \mathbf{r}') = \exp\left(\frac{-jk|\mathbf{r} - \mathbf{r}'|}{|\mathbf{r} - \mathbf{r}'|}\right), \quad k = \omega\sqrt{\mu_0\epsilon_0}, \quad \eta = \sqrt{\frac{\mu_0}{\epsilon_0}}$$

$\omega$  is the angular frequency,  $\mu_0$  is the permeability of vacuum and  $\epsilon_0$  is the permittivity of vacuum. Other quantities in (8.18) are the same as those in (8.17). Current distribution along the lightning channel can be obtained by numerically solving (8.18).

This method allows lossy ground and wires in lossy ground (e.g. grounding of a tall strike object) to be incorporated into the model (Burke and Miller 1984). The commercially available numerical electromagnetic codes (e.g. NEC-2 (Burke and Poggio 1980), and NEC-4 (Burke 1992)) are based on the MoM in the frequency domain.

### 8.6.2 Finite-difference time-domain (FDTD) method

The FDTD method (Yee 1966) employs a simple way to discretize Maxwell's equations in differential form. In the Cartesian coordinate system, it requires discretization of the entire space of interest into small cubic or rectangular-parallelepiped cells. Cells for specifying or computing electric field (electric field cells) and magnetic field cells are placed relative to each other as shown in Figure 8.12. Electric and magnetic fields of the cells are calculated using the discretized Maxwell's equations given below.

$$\begin{aligned} E_z^n\left(i, j, k + \frac{1}{2}\right) &= \frac{1 - \sigma(i, j, k + 1/2)\Delta t/[2\epsilon(i, j, k + 1/2)]}{1 + \sigma(i, j, k + 1/2)\Delta t/[2\epsilon(i, j, k + 1/2)]} \times E_z^{n-1}\left(i, j, k + \frac{1}{2}\right) \\ &\quad + \frac{\Delta t/\epsilon(i, j, k + 1/2)}{1 + \sigma(i, j, k + 1/2)\Delta t/[2\epsilon(i, j, k + 1/2)]} \frac{1}{\Delta x \Delta y} \\ &\quad \times \left[ H_y^{n-\frac{1}{2}}\left(i + \frac{1}{2}, j, k + \frac{1}{2}\right) \Delta y - H_y^{n-\frac{1}{2}}\left(i - \frac{1}{2}, j, k + \frac{1}{2}\right) \Delta y \right. \\ &\quad \left. - H_x^{n-\frac{1}{2}}\left(i, j + \frac{1}{2}, k + \frac{1}{2}\right) \Delta x + H_x^{n-\frac{1}{2}}\left(i, j - \frac{1}{2}, k + \frac{1}{2}\right) \Delta x \right] \end{aligned} \quad (8.19)$$

$$\begin{aligned}
 H_x^{n+\frac{1}{2}}(i, j - \frac{1}{2}, k + \frac{1}{2}) = & H_x^{n-\frac{1}{2}}(i, j - \frac{1}{2}, k + \frac{1}{2}) + \frac{\Delta t}{\mu(i, j - 1/2, k + 1/2)} \frac{1}{\Delta y \Delta z} \\
 & \times \left[ \begin{array}{l} -E_z^n(i, j, k + \frac{1}{2}) \Delta z + E_z^n(i, j - 1, k + \frac{1}{2}) \Delta z \\ + E_y^n(i, j - \frac{1}{2}, k + 1) \Delta y - E_y^n(i, j - \frac{1}{2}, k) \Delta y \end{array} \right] \tag{8.20}
 \end{aligned}$$

Equation (8.19), which is based on Ampere's law, is an equation updating  $z$  component of electric field,  $E_z(i, j, k + 1/2)$ , at point  $x = i \Delta x$ ,  $y = j \Delta y$  and  $z = (k + 1/2) \Delta z$ , and at time  $t = n \Delta t$ . Equation (8.20), which is based on Faraday's law, is an equation updating  $x$  component of magnetic field,  $H_x(i, j - 1/2, k + 1/2)$ , at point  $x = i \Delta x$ ,  $y = (j - 1/2) \Delta y$  and  $z = (k + 1/2) \Delta z$ , and at time  $t = (n + 1/2) \Delta t$ . Equations updating  $x$  and  $y$  components of electric field, and  $y$  and  $z$  components of magnetic field can be written in a similar manner. Note that  $\sigma(i, j, k + 1/2)$  and  $\epsilon(i, j, k + 1/2)$  are the conductivity and permittivity at point  $x = i \Delta x$ ,  $y = j \Delta y$  and  $z = (k + 1/2) \Delta z$ , respectively,  $\mu(i, j - 1/2, k + 1/2)$  is the permeability at point  $x = i \Delta x$ ,  $y = (j - 1/2) \Delta y$  and  $z = (k + 1/2) \Delta z$ . By updating electric and magnetic fields at every point using (8.19) and (8.20), transient fields throughout the computational domain are obtained. Since the material constants of each cell can be specified individually, a complex inhomogeneous medium can be analysed easily.

To analyse fields in unbounded space, an absorbing boundary condition (e.g. Liao *et al.* 1984; Berenger 1984) has to be set on each plane which limits the space to be analysed, so as to avoid reflections there. The FDTD method allows one to incorporate wires buried in lossy ground, such as strike-object grounding electrodes (Noda *et al.* 2007), and non-linear effects (Tatematsu *et al.* 2007).

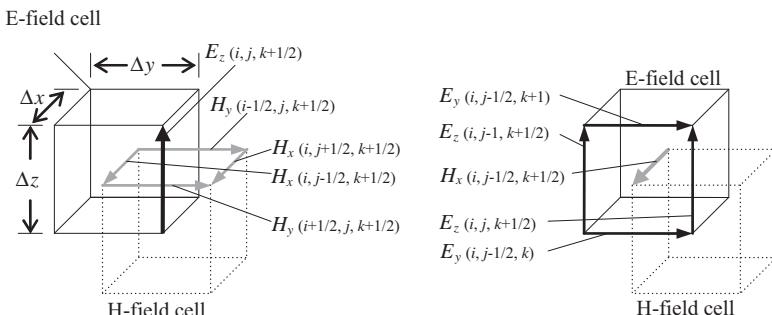


Figure 8.12 Placement of electric-field and magnetic-field cells for solving discretized Maxwell's equations using the FDTD method

### 8.6.3 Comparison of current distributions along a vertical perfectly conducting wire calculated using different numerical procedures with those predicted by Chen's analytical equation

In this section, distributions of current along a channel-representing vertical wire, calculated using MoMs in the time and frequency domains and the FDTD method, are compared with that based on Chen's analytical equation (8.1) that is shown in Figure 8.1. Figure 8.13 shows configuration to be used for comparison of different numerical procedures: a vertical perfectly conducting wire of radius 0.23 m in air located above perfectly conducting ground and excited at its bottom by a 10-m-long lumped voltage source. The lumped voltage source produces a ramp-front wave having a magnitude of 500 kV/m (5 MV along the 10-m-long source) and a risetime of 1  $\mu$ s. Figure 8.14 (a), (b) and (c) shows current waveforms at different heights calculated using the TWTD code (MoM in the time domain), the NEC-2 code (MoM in the frequency domain) and the FDTD method, respectively. As expected, waveforms calculated using the three different approaches agree well. Further, they all agree reasonably well with those calculated using Chen's analytical equation (see Figure 8.1).

For the TWTD calculations, the 2000-m-long vertical conducting wire was divided into 10-m-long segments and the response was calculated up to 5  $\mu$ s with a 33.3-ns increment. For the NEC-2 calculations, the vertical conducting wire was divided into 10-m-long segments, and the responses were calculated from 9.77 kHz to 10 MHz with a 9.77-kHz increment (corresponded to a time range from 0 to 102  $\mu$ s with a 50-ns increment). To suppress non-physical oscillations caused by the NEC-2 numerical procedure, the vertical wire above 1500 m from the bottom was loaded by distributed series resistance. This resistive loading did not influence the current at the bottom ( $z' = 0$ ) for the first 10  $\mu$ s and that at a height of 600 m for the first 8  $\mu$ s. For the FDTD calculations, the vertical wire of 0.23 m radius was replaced by a zero-radius perfectly conducting wire placed in the working volume of 60 m  $\times$  60 m  $\times$  2300 m, which was divided into 1 m  $\times$  1 m  $\times$  10 m cells. When cells having a cross-sectional area of 1 m  $\times$  1 m are used, the vertical ( $z$ -directed) zero-radius perfectly conducting wire in air has an equivalent radius of 0.23 m (Noda and Yokoyama 2002). Perfectly matched layers (PMLs) (Berenger 1994) (absorbing boundaries) were set at the top and sides of the working volume in order to avoid reflections there. The time increment was set to 2 ns.

## 8.7 Applications of electromagnetic models of the lightning return stroke

In this section, applications of electromagnetic models of the lightning return stroke to studying lightning effects are reviewed (Burke and Miller 1984). These include the following:

1. strikes to flat ground;
2. strikes to free-standing tall objects;

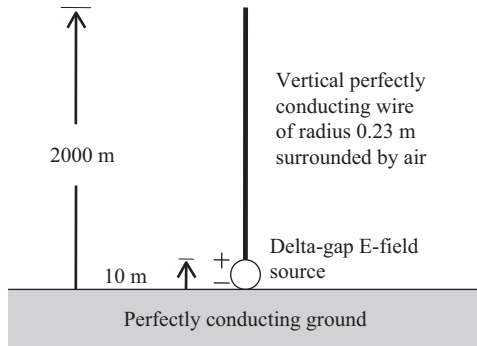


*Figure 8.13 A vertical perfectly conducting wire of radius 0.23 m in air above perfectly conducting ground excited at its bottom by a 10-m-long lumped voltage source. The source produces a ramp-front wave having a magnitude of 500 kV/m (5 MV along the 10-m-long source) and a risetime of 1  $\mu$ s. This configuration was used for comparison of different numerical procedures employed in electromagnetic models [adapted from Baba and Rakov (2007)]*

3. strikes to overhead power transmission lines; and
4. strikes to wire-mesh-like structures.

Table 8.4 gives a list of papers for each of these four configurations.

### 8.7.1 Strikes to flat ground

Moini *et al.* (1997, 2000), Kordi *et al.* (2002, 2003a), Baba and Ishii (2003), Grcev *et al.* (2003), Aniserowicz (2004), Bonyadi-ram *et al.* (2004, 2005), Maslowski (2004), Shoory *et al.* (2005), Geranmayeh *et al.* (2006), Alaee *et al.* (2007), Bonyadi-ram *et al.* (2008) and Baba and Rakov (2009) have calculated waveforms of vertical electric and azimuthal magnetic fields due to lightning return strokes at different distances from the lightning channel attached to flat ground, and compared them with typical measured waveforms of electric and magnetic fields (Lin *et al.* 1979; Crawford *et al.* 2001). In these calculations, a typical subsequent-stroke waveform of channel-base current (Nucci *et al.* 1990) and a typical propagation speed of return-stroke wavefront ( $0.43c$  in most cases) were used. Note that Alaee *et al.* (2007) incorporated (non-linear) distributed series resistance, which decreased with increasing the magnitude of lightning return-stroke current, and Bonyadi-ram *et al.* (2008) incorporated (non-uniform) additional distributed series inductance, which increased with increasing height along the channel. Typical features of vertical electric and azimuthal magnetic field waveforms measured at different distances from lightning return strokes are described in Section 8.4.2 and illustrated in Figure 8.5.

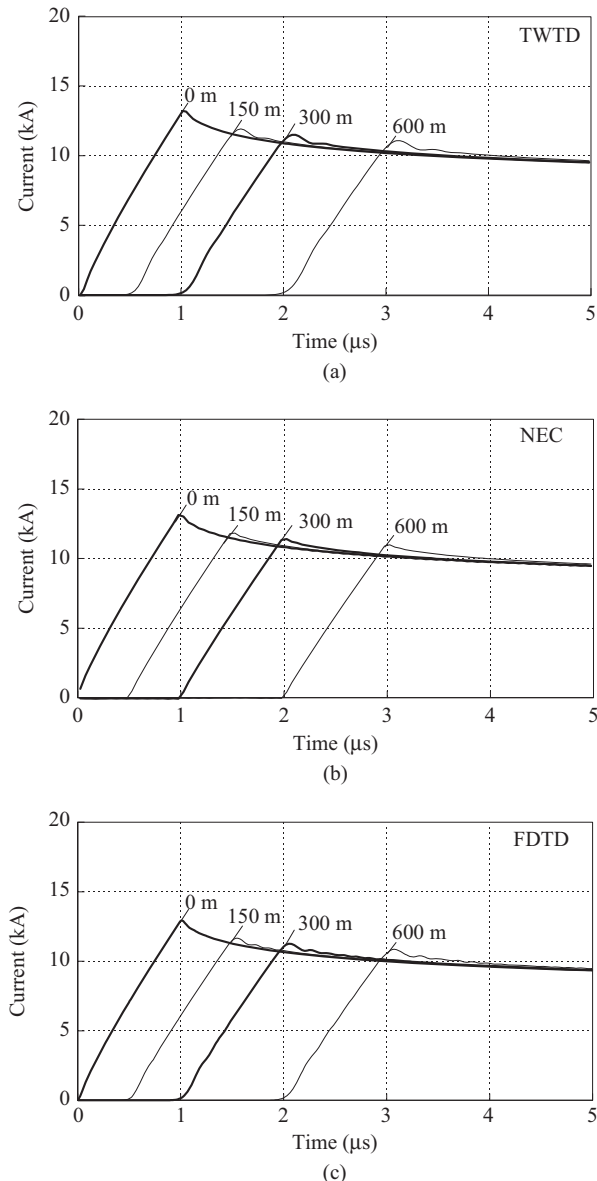


*Figure 8.14* Current waveforms at different heights calculated using (a) the TWTD code (based on the MoM in the time domain), (b) the NEC-2 code (based on the MoM in the frequency domain) and (c) the FDTD method for the configuration shown in Figure 8.13 [adapted from Baba and Rakov (2007)]

Table 8.4 List of papers on applications of electromagnetic models of the lightning return stroke

Configuration	Reviewed journal papers	Other publications
Strike to flat ground	Moini <i>et al.</i> (1998, 2000) Kordi <i>et al.</i> (2002) Baba and Ishii (2003) Pokharel <i>et al.</i> (2003)* Baba and Rakov (2003, 2005a) Shoory <i>et al.</i> (2005)* Geranmayeh <i>et al.</i> (2006) Pokharel and Ishii (2007) Bonyadi-ram <i>et al.</i> (2008) Baba and Rakov (2009)*	Moini <i>et al.</i> (1997) Kato <i>et al.</i> (2001) Kordi <i>et al.</i> (2003a) Grcev <i>et al.</i> (2003) Aniserowicz (2004) Bonyadi-ram <i>et al.</i> (2004, 2005) Maslowski (2004)* Tatematsu <i>et al.</i> (2004)* Alaee <i>et al.</i> (2007) Silveira and Visacro (2008)*
Strike to a free-standing tall object	Podgorski and Landt (1987) Baba and Ishii (2001) Kordi <i>et al.</i> (2003b) Pokharel <i>et al.</i> (2004)* Baba and Rakov (2008b)*	Kato <i>et al.</i> (1999) Miyazaki and Ishii (2004a, 2004b)* Petrache <i>et al.</i> (2005)* Aniserowicz (2008)* Mosaddeghi (2008)*
Strike to a power transmission line	Mozumi <i>et al.</i> (2003) Noda <i>et al.</i> (2007)* Pokharel and Ishii (2007) Miyazaki and Ishii (2008b)*	
Strike to a wire-mesh-like structure	Miyazaki and Ishii (2008a)	Chai <i>et al.</i> (1994)* Miyazaki and Ishii (2005)

Papers with '\*' consider lossy ground in finding current distribution along the lightning channel.

Moini *et al.* (1998), Pokharel *et al.* (2003), Tatematsu *et al.* (2004), Pokharel and Ishii (2007) and Silveira and Visacro (2008) have calculated transient induced voltages on overhead wires due to lightning strikes to flat ground. These studies are reviewed below.

Moini *et al.* (1998) have calculated transient voltages on overhead perfectly conducting wires of different geometries such as parallel and non-parallel wires above flat perfectly conducting ground using the MoM in the time domain. To find the distribution of current along the lightning channel, they represented it by a vertical perfectly conducting wire, which was excited at its bottom by a lumped voltage source. The wire was surrounded by a dielectric medium with a relative permittivity of 4 that occupied the entire space above ground. The speed of the current wave propagating along the wire was approximately  $0.5c$ . Using the resultant distribution of

current along this channel-representing vertical wire and replacing the artificial dielectric medium by air, they calculated transient voltages induced on the overhead wires. The authors conclude that scattering-theory approach is more appropriate in calculating induced effects on non-uniform wires or complex-shape wires than that based on field-to-conductor electromagnetic coupling models (e.g. Agrawal *et al.* 1980) based on transmission line theory (telegrapher's equations with source terms).

Pokharel *et al.* (2003) have calculated transient voltages on a 25-m-long horizontal overhead perfectly conducting wire above flat ground having conductivity 0.06 S/m shown in Figure 8.15, using the Numerical Electromagnetic Code (NEC-2) (Burke and Poggio 1980) that is based on the MoM in the frequency domain. They represented the lightning channel by a 28-m-long vertical 0.5- $\Omega$ /m resistive wire having additional distributed series inductance of 6  $\mu$ H/m. The wire was excited at its bottom by a lumped voltage source in series with 750- $\Omega$  lumped resistance. The speed of the current wave propagating along the wire was approximately 0.43c. Induced voltages were computed within the first 300 ns, so that they are not influenced by reflections from the open end of the 28-m-long vertical wire. Figure 8.16(a) and (b) shows calculated induced-voltage waveforms at the close and remote ends of the horizontal wire, respectively, and those measured by Ishii *et al.* (1999). Calculated waveforms agree well with corresponding measured waveforms. This work showed for the first time that voltages induced on an overhead wire above lossy ground could be calculated reasonably accurately using the NEC-2 code.

Tatematsu *et al.* (2004) have calculated transient voltages on an overhead perfectly conducting wire above flat perfectly conducting and lossy ground using the FDTD method and shown that FDTD-calculated voltages agree well with the voltages calculated using field-to-conductor electromagnetic coupling models of Rusck (1958) and Agrawal *et al.* (1980). They represented the lightning channel by a vertical perfectly conducting wire having additional distributed series inductance of 10  $\mu$ H/m above flat ground having conductivity of 1 mS/m. The wire was excited at its bottom by a lumped current source. The speed of the current wave propagating along the wire was approximately 0.3c. This work showed for the first time that voltages induced on an overhead wire above lossy ground could be calculated with reasonable accuracy using the FDTD method.

Pokharel and Ishii (2007) have calculated transient voltages on a 500-m-long horizontal overhead perfectly conducting wire above flat perfectly conducting ground, using the TWTD code (Van Baricum and Miller 1972) based on the MoM in the time domain. A non-linear element simulating a surge arrestor was connected between the wire at its centre point and ground. The lightning return-stroke channel was represented by a vertical 0.6- $\Omega$ /m resistive wire having additional distributed series inductance of 6  $\mu$ H/m that was excited at its bottom by a lumped voltage source. The speed of the current wave propagating along the wire was approximately 0.48c. The use of TWTD code allows one to incorporate non-linear elements but makes it impossible to consider the frequency-dependent effects of lossy ground.

Silveira and Visacro (2008) have calculated transient voltages on a 1-km-long horizontal overhead perfectly conducting wire above flat ground having conductivity 1 mS/m, using the NEC-4 code (Burke 1992) and using the hybrid

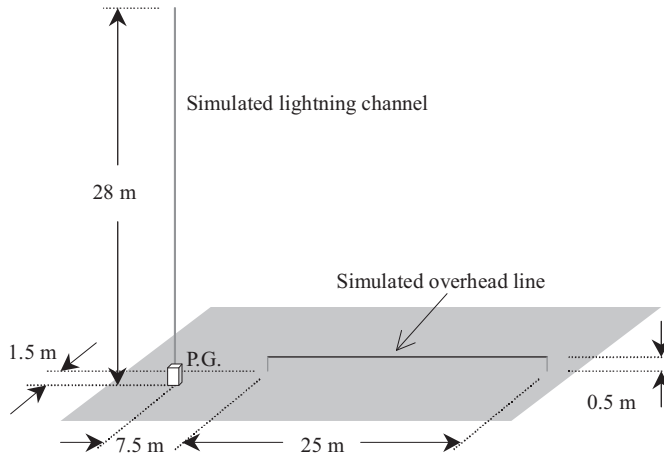


**Figure 8.15** Lightning interaction with a 25-m-long horizontal perfectly conducting wire above flat ground having conductivity  $0.06 \text{ S/m}$  represented using the NEC-2 code. Lightning channel is represented by a vertical wire loaded by distributed series resistance of  $0.5 \Omega/\text{m}$  and additional distributed series inductance of  $6 \mu\text{H}/\text{m}$ , with the current-wave propagation speed being approximately  $0.43c$ . One end of the horizontal wire is located at distances  $x = 7.5 \text{ m}$  and  $y = 1.5 \text{ m}$  from the lightning channel, as in Ishii et al.'s (1999) small-scale experiment. Both ends of the horizontal wire are terminated in  $430\text{-}\Omega$  resistance in parallel with  $20\text{-pF}$  capacitance [adapted from Pokharel et al. (2003)]

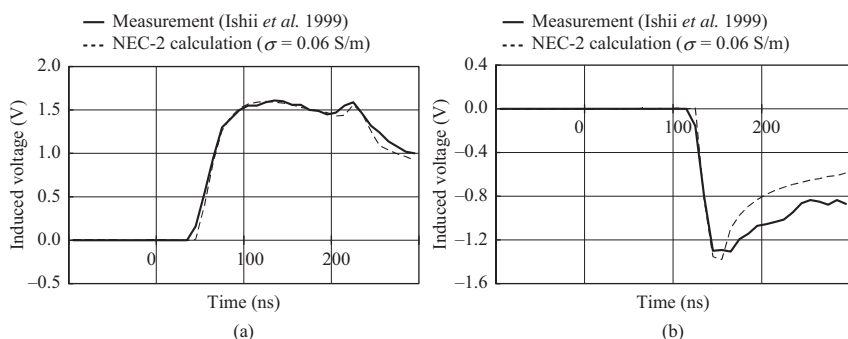


**Figure 8.16** Waveforms of voltage induced at (a) close and (b) remote ends of the 25-m-long horizontal wire above flat ground measured by Ishii et al. (1999) and those calculated, using the NEC-2 code, for ground conductivity  $0.06 \text{ S/m}$  by Pokharel et al. (2003) [adapted from Pokharel et al. (2003)]

electromagnetic/circuit theory (HEM) model (Visacro and Silveira 2004). They represented the lightning return-stroke channel by a vertical resistive wire having additional distributed series inductance. The wire was excited at its bottom by a lumped voltage source. The speed of the current wave propagating along the wire was approximately  $0.77c$ . NEC-4- and HEM-calculated waveforms agree well with each other.

### 8.7.2 *Strikes to free-standing tall object*

Podgorski and Landt (1987) and Podgorski (1991), using the modified TWTD code (Van Baricum and Miller 1972) that is based on the MoM in the time domain, have represented a lightning strike to the 553-m-high CN Tower by a resistive ( $0.7 \Omega/m$ ) vertical wire with a non-linear resistance ( $10 \text{ k}\Omega$  prior to the attachment and  $3 \Omega$  after the attachment) connected between the bottom of the wire and the top of the CN Tower (or the top of uncharged wire simulating the upward connecting leader from the tower). The CN Tower was represented by a perfectly conducting wire. The calculated waveform of current near the top of the tower was found to be similar to the corresponding measured waveform.

Kato *et al.* (1999) have calculated waveforms of lightning current and associated electric and magnetic fields 200 m from the strike point, assuming perfectly conducting ground, due to lightning strikes to the 553-m-high CN Tower and to the 168-m-high Peissenberg tower using the MoM in the time domain, and compared them with corresponding measured waveforms. Baba and Ishii (2001) have calculated electric and magnetic fields 2 km and 630 m from the strike point, assuming perfectly conducting ground, due to lightning strikes to the CN Tower and the 200-m-high Fukui chimney using the NEC-2 code, and compared those with corresponding measured waveforms. Figure 8.17 shows NEC-2-calculated waveforms for the Fukui chimney case with corresponding waveforms measured by Goshima *et al.* (2000). NEC-2-calculated waveforms agree well with corresponding measured waveforms. Miyazaki and Ishii (2004a) have carried out similar calculations using the FDTD method and shown that FDTD-calculated waveforms agree well with corresponding measured waveforms. Kordi *et al.* (2003b) have calculated waveforms of lightning current and associated electric and magnetic fields 2 km away from the strike point, assuming perfectly conducting ground, due to a lightning strike to the CN Tower using the MoM in the time domain, and compared them with corresponding measured waveforms. Miyazaki and Ishii (2004b) have calculated, using the NEC-2 code, lightning current and associated electric and magnetic fields on the surface of ground having conductivity of  $1 \text{ mS/m}$  at distances ranging from 100 m to 500 km from the lightning channel due to lightning strikes to tall towers whose heights ranged from 60 to 240 m. Petrache *et al.* (2005) have studied, using the NEC-4 (Burke 1992), influence of ground conductivity ( $1$ ,  $10 \text{ mS/m}$ , and  $\infty$ ) on the lightning current in the CN Tower and associated electric and magnetic fields 2 km away from the tower. In these five works, except for Kordi *et al.*'s one, the lightning channel was represented by a vertical wire having additional distributed series inductance, and the lightning

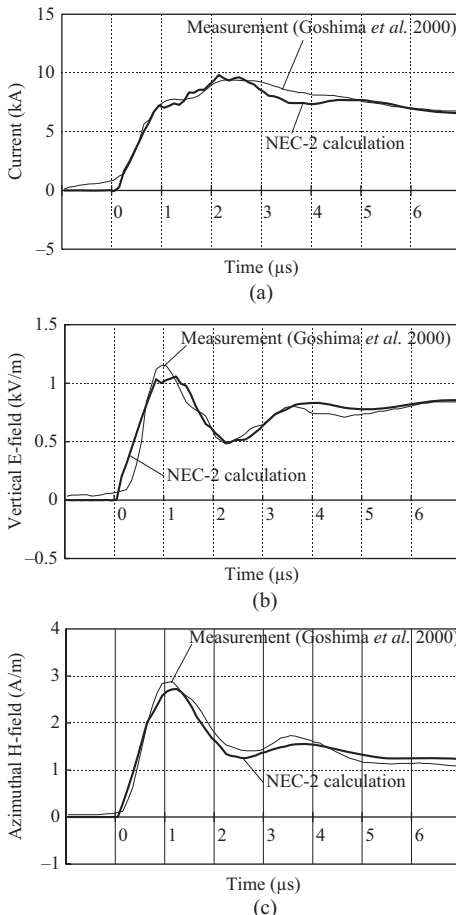


Figure 8.17 Waveforms of (a) current at the top of the 200-m-high Fukui chimney, (b) vertical electric field and (c) azimuthal magnetic field 630 m from the chimney, calculated by Baba and Ishii (2001) using the NEC-2 code and assuming perfectly conducting ground, and those measured by Goshima et al. (2000). The lightning channel is represented by a vertical conductor having distributed series resistance of  $1 \Omega/\text{m}$  and additional distributed series inductance of  $3 \mu\text{H}/\text{m}$ , with the current-wave propagation speed being approximately  $0.5c$ . The 200-m-high chimney is represented by a vertical perfectly conducting wire. The lightning channel and the chimney are excited by a delta-gap electric-field source in series with a  $400-\Omega$  lumped resistor [adapted from Baba and Ishii (2001)]

channel and the tall strike object were excited by a delta-gap electric-field source inserted between them. In Kordi *et al.*'s work (2003b), the lightning channel was represented by a resistive wire in air and excited by a delta-gap electric-field source.

Pokharel *et al.* (2004) have calculated, using the NEC-2 code, induced voltages on an overhead wire due to a lightning strike to the 200-m-high Fukui chimney and compared those with corresponding measured voltage waveforms (Michishita *et al.* 2003). They represented the lightning channel by a vertical wire having distributed series resistance of  $1 \Omega/m$  and additional distributed series inductance of  $9 \mu H/m$ . The lightning channel and the chimney were excited by a delta-gap electric-field source in series with a lumped  $100\Omega$  resistor inserted between them. The propagation speed of current wave along the channel was approximately  $0.37c$ . Figure 8.18 shows the plan view of the overhead wire and the chimney. Figure 8.19 shows waveforms of current at the top of the chimney and voltages induced on the overhead wire near the terminations, measured by Michishita *et al.* (2003). Figure 8.20 shows those calculated by Pokharel *et al.* (2004) assuming ground conductivity to be  $0.02 S/m$ , for which best agreement with measured waveforms was found. Induced voltages corresponding to perfectly conducting ground are also shown for comparison.

Podgorski (1991) calculated lightning current waveform in the CN Tower simulating lightning channel by a  $0.7\Omega/m$  resistive wire having many  $0.7-$  or  $7\Omega/m$  resistive twigs (representing radial corona discharge). Kato *et al.* (1999) studied the influence of inclined lightning channel attached to the Peissenberg tower on lightning electromagnetic field. Pokharel *et al.* (2004) investigated the influence of inclined lightning channel attached to the Fukui chimney on lightning-induced voltages.

Aniserowicz (2008) have calculated, using the MoM in the frequency domain, electromagnetic fields inside a wire-mesh lightning protection system located on perfectly conducting ground due to a nearby lightning strike to a 70-m-high object. He represented the lightning channel by a vertical wire of radius 50 mm having distributed series resistance of  $1 \Omega/m$  and additional distributed series inductance  $4.5 \mu H/m$ . The lightning channel and the 70-m-high object were excited by a lumped voltage source inserted between them. The speed of the current wave propagating along the channel was approximately  $0.5c$ .

Baba and Rakov (2008b) have calculated, using the FDTD method, vertical and horizontal electric fields, and azimuthal magnetic fields generated on the lossy ground surface by lightning strikes to 160- and 553-m-high towers that represent the Peissenberg tower in Germany and the CN Tower in Canada, respectively. The lightning channel was represented by a vertical perfectly conducting wire of radius 68 mm in air. The fields were calculated at distances from the bottom of the tower ranging from 5 to 100 m for the 160-m-high tower and from 10 to 300 m for the 553-m-high tower. In all cases considered, waveforms of horizontal electric field and azimuthal magnetic field are not much influenced by the presence of strike object, while waveforms of vertical electric field are. Waveforms of vertical electric field are essentially unipolar (as they are in the absence of strike object) when the ground conductivity is  $10 mS/m$  (the equivalent transient grounding impedance is several ohms) or greater. For the 160-m-high tower and for the ground

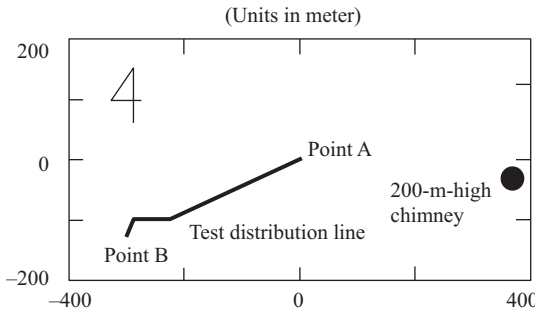


*Figure 8.18 Plan view of a single overhead wire and a nearby 200-m-high chimney. Voltages on the overhead wire induced by a lightning strike to the chimney were calculated using the NEC-2 code by Pokharel et al. (2004). The lightning channel is represented by a vertical conductor having distributed series resistance of  $1 \Omega/m$  and additional distributed series inductance of  $9 \mu H/m$ , with the current-wave propagation speed being approximately  $0.37c$ . The 200-m-high chimney is represented by a vertical perfectly conducting wire. The lightning channel and the chimney are excited by a delta-gap electric-field source in series with a lumped  $100\Omega$  resistor inserted between them [adapted from Pokharel et al. (2004)]*

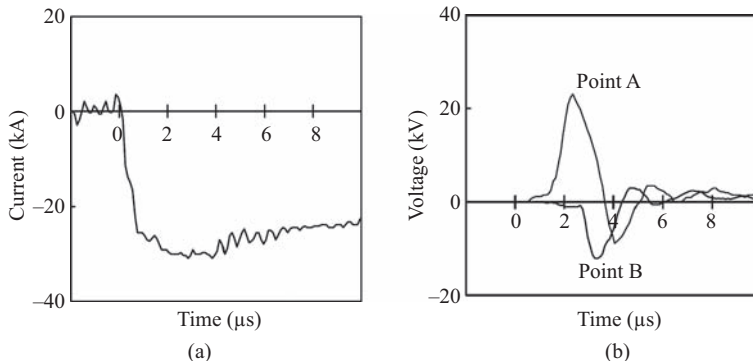


*Figure 8.19 Waveforms of (a) current at the top of the 200-m-high chimney and (b) voltages induced on the overhead wire near its terminations, measured by Michishista et al. (2003) [adapted from Pokharel et al. (2004)]*

conductivity being equal to 1 and  $0.1 \text{ mS/m}$ , waveforms of vertical electric field become bipolar (exhibit polarity change) at distances within  $10 \text{ m}$  and within  $50 \text{ m}$ , respectively. The source of opposite polarity vertical electric field is the potential rise at the object base. Using the NEC-4 code, Mosaddeghi et al. (2008) have carried out a similar calculation for a  $100\text{-m-high}$  tower that represents the

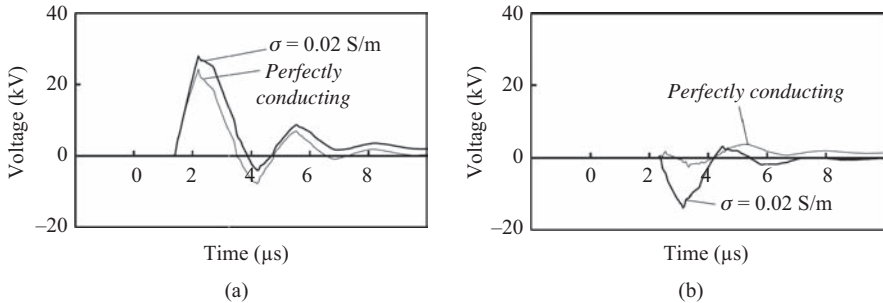


*Figure 8.20* Waveforms of voltage induced on the overhead wire near the terminations (a) closer to the chimney (point A in Figure 8.18), and (b) farther from it (point B in Figure 8.18), calculated by Pokharel et al. (2004) assuming perfectly conducting ground and ground conductivity 0.02 S/m [adapted from Pokharel et al. (2004)]

Gaisberg tower in Austria. The lightning channel was represented by a vertical wire of radius 10 mm having additional distributed series inductance of  $8.9 \mu\text{H}/\text{m}$  and distributed series resistance of  $1 \Omega/\text{m}$ . The speed of the current wave propagating along the wire was  $0.4c$

### 8.7.3 Strikes to overhead power transmission lines

Mozumi et al. (2003) have calculated, using the TWTD code, voltages across insulators of a 500-kV double-circuit power transmission line tower with two overhead ground wires, in the case that the tower top is struck by lightning and thereby back-flashover occurs across the insulator of one phase. Ground was assumed to be perfectly conducting. To analyse back-flashover using the TWTD code, they modified it to incorporate a flashover model (Motoyama 1996). For the TWTD calculations, the lightning channel was represented by a vertical perfectly conducting wire of radius 0.1 m in air. The lightning channel and the tower were excited by a lumped voltage source in series with a  $5\text{-k}\Omega$  lumped resistor inserted between them.

Noda et al. (2007) have calculated, using the FDTD method, voltages across insulators of a 500-kV double-circuit power transmission line tower, in the case that the tower top is struck by lightning. In their calculations, lightning channel was represented by a 0.23-m-radius (Noda et al. 2002) vertical perfectly conducting wire having additional distributed series inductance of  $10 \mu\text{H}/\text{m}$ , and the speed of the current wave propagating along the wire was  $0.33c$ . The lightning channel and the tower were excited by a lumped current source inserted between them. Ground was assumed to have conductivity of  $10 \text{ mS}/\text{m}$ .

Pokharel and Ishii (2007) have calculated, using the TWTD and the NEC-2 codes, the transient voltage across an insulator of a simplified 60-m-high transmission-line tower, assuming perfectly conducting ground. The lightning channel was represented by a vertical perfectly conducting wire. The speed of the current wave propagating along the wire was essentially equal to the speed of light. The lightning channel and the tower were excited by a lumped voltage source in series with a  $5\text{-k}\Omega$  resistor inserted

between the lightning channel and the tower. The TWTD-calculated voltage waveform agrees well with the NEC-2-calculated waveform.

Miyazaki and Ishii (2008b) have calculated, using the NEC-4 code, vertical electric and azimuthal magnetic fields on the ground surface due to lightning strikes to free-standing towers of height 50, 100, 120, 150 or 200 m and to the midpoint of a 3-km-long transmission line with seven 120-m-high towers. The ground conductivity was set to 3 mS/m, 10 mS/m and infinity. Fields were calculated at distances ranging from 100 m to 500 km from the lightning channel. The lightning channel was represented by a vertical 0.1-m-radius wire having additional distributed series inductance of 6  $\mu\text{H}/\text{m}$  and distributed series resistance of 1  $\Omega/\text{m}$ . The speed of the current wave propagating along the wire was  $0.5c$ . The lightning channel and the tower or the transmission line were excited by a lumped voltage source inserted between them. They showed that the magnitude of vertical electric field in the vicinity of the isolated tower or the transmission line was reduced, compared to the case of strike to flat ground, while at far distances it was enhanced.

#### 8.7.4 Strikes to wire-mesh-like structures

Chai *et al.* (1994) have studied, using the NEC-2 code, the electromagnetic environment inside of a wire-array lightning protection system for a launch vehicle when the protection system was subjected to a direct lightning strike. In their analysis, lightning channel was represented by a resistive wire, and the excitation was accomplished using a lumped voltage source. Ground conductivity was assumed to be 10 mS/m.

Miyazaki and Ishii (2005) have calculated, using the NEC-4 code, distributions of lightning current inside buildings of height ranging from 10 to 40 m struck by lightning, assuming perfectly conducting ground. They represented the lightning channel attached to the building top by a vertical wire having distributed series resistance and additional distributed series inductance and the buildings, including internal electric power wires, by a perfectly conducting wire grid. The internal wires were directly connected to the building in their calculations in order to simulate the condition when surge protective devices connected between the building and the power wires were operating. They inserted a lumped voltage source between the lightning channel and the building. Magnitudes of current flowing in electric power wires on the top and bottom floors were largest regardless of the building height. Miyazaki and Ishii (2008a) have also calculated, using the NEC-4 code, time derivatives of magnetic field inside a 30-m-high building struck by lightning, assuming perfectly conducting ground. They represented the vertical lightning channel attached to the building in the same manner as Miyazaki and Ishii (2005) (see above). Miyazaki and Ishii (2008a) showed that time derivatives of magnetic field in upper parts of building were largest but could be reduced by installing a finer conducting mesh on the building roof.

## 8.8 Summary

In this chapter, electromagnetic models of the lightning return stroke have been reviewed and evaluated. This relatively new class of models can be used for

specifying the source in studying lightning interaction with various systems and with the environment.

It has been shown that a current wave necessarily suffers attenuation as it propagates upwards along a vertical non-zero-thickness wire above perfectly conducting ground excited at its bottom by a lumped source, even if the wire has no ohmic losses, which is a distinctive feature of this class of models. Mechanism of this attenuation is related to the boundary condition for the tangential electric field on the surface of the wire.

Electromagnetic models proposed as of today have been classified into six types depending on lightning channel representation: (1) a perfectly conducting/resistive wire in air above ground; (2) a wire loaded by additional distributed series inductance in air above ground; (3) a wire surrounded by a dielectric medium (other than air) that occupies the entire half space above ground (the artificial dielectric medium is used only for finding current distribution along the lightning channel, which is then removed for calculating electromagnetic fields in air); (4) a wire coated by a dielectric material in air above ground; (5) a wire coated by a fictitious material having high relative permittivity and high relative permeability in air above ground and (6) two parallel wires having additional distributed shunt capacitance in air (this fictitious configuration is used only for finding current distribution, which is then applied to a vertical wire in air above ground for calculating electromagnetic fields). Type-2 and type-5 models reproduce the maximum number (three out of five) of characteristic features of electric and magnetic field waveforms observed at distances ranging from 1 to 200 km from natural lightning, and at distances ranging from tens to hundreds of metres from rocket-triggered lightning. Modifications of type-2 and type-5 models in which distributed channel resistance is not uniform (relatively high within the bottom 0.5 km and above 4 km) can reproduce all of the five features. It is also desirable that models are capable of reproducing the following two features of the lightning return stroke: typical values of optically measured return-stroke wavefront speed in the range from  $0.33c$  to  $0.5c$ , and the expected equivalent impedance of the lightning return-stroke channel in the range from 0.6 to 2.5 k $\Omega$ .

Different methods of excitation used to date in lightning return-stroke electromagnetic models have been compared: (1) closing a charged vertical wire at its bottom with a specified impedance, (2) a lumped voltage source (or a delta-gap electric-field source) and (3) a lumped current source. Distributions of current along the vertical perfectly conducting wire in air excited at its bottom by the lumped voltage source and by the lumped current source are identical, as expected. Also, the distribution of current along the charged vertical perfectly conducting wire closed with the non-linear resistor is similar to that along the same wire excited at its bottom by the lumped voltage source.

Distributions of current along the vertical perfectly conducting wire in air excited at its bottom by the lumped voltage source, calculated using different numerical procedures, MoMs in the time and frequency domains, and the FDTD method, have been compared. As expected, current distributions calculated using these three procedures agree well. They also agree reasonably well with those calculated using Chen's analytical equation.

Applications of lightning return-stroke electromagnetic models to analyse (1) lightning strikes to flat ground, (2) strikes to free-standing tall objects, (3) strikes to overhead power transmission lines and (4) strikes to wire-mesh-like structures, have been reviewed.

## References

- Agrawal, A. K., H. J. Price and S. H. Gurbaxani (1980), Transient response of multiconductor transmission lines excited by a non-uniform electromagnetic field, *IEEE Trans. Electromagn. Compat.*, EMC-22 (2), 119–129
- Alaee, R., R. Moini, S. Bonyadi and S. H. H. Sadeghi (2007), A non-linear antenna theory model of lightning return stroke channel, paper presented at 18th International Zurich Symposium on Electromagnetic Compatibility, Munich, pp. 321–324
- Aniserowicz, K. (2004), A new algorithm for antenna theory modeling of a lightning return stroke, paper presented at 27th International Conference on Lightning Protection, Soc. de l'Electr., de l'Electron., et des Technol. de l'Inf. et de la Commun., Avignon, France
- Aniserowicz, K. (2008), Computer analysis of electromagnetic field inside LPS in the case of lightning strike to a nearby tall object, paper presented at 29th International Conference on Lightning Protection, 3a-04, Uppsala, Sweden, 9pp.
- Baba, Y. and M. Ishii (2001), Numerical electromagnetic field analysis of lightning current in tall structures, *IEEE Trans. Power Deliv.*, PWRD-16 (2), 324–328
- Baba, Y. and M. Ishii (2003), Characteristics of electromagnetic return-stroke models, *IEEE Trans. Electromagn. Compat.*, EMC-45 (1), 129–135
- Baba, Y. and V. A. Rakov (2003), On the transmission line model for lightning return stroke representation, *Geophys. Res. Lett.*, 30 (24), doi:10.1029/2003GL018407
- Baba, Y. and V. A. Rakov (2005a), On the mechanism of attenuation of current waves propagating along a vertical perfectly conducting wire above ground: application to lightning, *IEEE Trans. Electromagn. Compat.*, EMC-47 (3), 521–532
- Baba, Y. and V. A. Rakov (2005b), On the interpretation of ground reflections observed in small-scale experiments simulating lightning strikes to towers, *IEEE Trans. Electromagn. Compat.*, EMC-47 (3), 533–542
- Baba, Y. and V. A. Rakov (2007), Electromagnetic models of the lightning return stroke, *J. Geophys. Res.*, 112 (D04102), doi:10.1029/2006JD007222, 18pp.
- Baba, Y. and V. A. Rakov (2008a), Applications of electromagnetic models of the lightning return stroke, *IEEE Trans. Power Deliv.*, PWRD-23 (2), 800–811
- Baba, Y. and V. A. Rakov (2008b), Influence of strike object grounding on close lightning electric fields, *J. Geophys. Res.*, 113 (D12109), doi:10.1029/2008JD009811, 17pp.

- Baba, Y. and V. A. Rakov (2009), Electric and magnetic fields predicted by different electromagnetic models of the lightning return stroke versus measured fields, *IEEE Trans. Electromagn. Compat.*, EMC-51 (3), 479–487
- Baba, Y., S. Miyazaki and M. Ishii (2004), Reproduction of lightning electromagnetic field waveforms by engineering model of return stroke, *IEEE Trans. Electromagn. Compat.*, EMC-46 (1), 130–133
- Baum, C. E. and L. Baker (1990), Analytic return-stroke transmission-line model, *Lightning Electromagnetics*, Hemisphere, New York, pp. 17–40
- Berenger, J. P. (1994), A perfectly matched layer for the absorption of electromagnetic waves, *J. Comput. Phys.*, 114, 185–200
- Bermudez, J. D., M. Rubinstein, F. Rachidi, F. Heidler and M. Paolone (2003), Determination of reflection coefficients at the top and bottom of elevated strike objects struck by lightning, *J. Geophys. Res.*, 108 (D14), doi:10.1029/2002JD002973
- Bonyadi-ram, S., R. Moini and S. H. H. Sadeghi (2004), Incorporation of distributed inductive loads in the antenna theory model of lightning return stroke channel, paper presented at 27th International Conference on Lightning Protection, Soc. de l'Electr., de l'Electron., et des Technol. de l'Inf. et de la Commun., Avignon, France
- Bonyadi-ram, S., R. Moini, S. H. H. Sadeghi and V. A. Rakov (2005), Incorporation of distributed capacitive loads in the antenna theory model of lightning return stroke, paper presented at 16th International Zurich Symposium and Technical Exhibition on Electromagnetic Compatibility, Swiss Federal Institute of Technology, Zurich, Switzerland, pp. 213–218
- Bonyadi-ram, S., R. Moini, S. H. H. Sadeghi and V. A. Rakov (2008), On representation of lightning return stroke as a lossy monopole antenna with inductive loading, *IEEE Trans. Electromagn. Compat.*, EMC-50 (1), 118–127
- Burke, G. J. (1992), *Numerical Electromagnetic Code (NEC-4) – Method of Moments*, UCRL-MA-109338, Lawrence Livermore National Laboratory, California
- Burke, G. J. and E. K. Miller (1984), Modeling antennas near to and penetrating a lossy interface, *IEEE Trans. Antennas Propagat.*, AP-32 (10), 1040–1049
- Burke, G. J. and A. J. Poggio (1980), *Numerical Electromagnetic Code (NEC) – Method of Moments*, Technical Document 116, Naval Ocean Systems Center, San Diego
- Chai, J. C., H. A. Heritage and R. Briet (1994), Electromagnetic effects of the four-tower supported catenary wires array lightning protection system, paper presented at 16th International Aerospace and Ground Conference on Lightning and Static Electricity, Mannheim, Germany, pp. 377–386
- Chen, K. C. (1983), Transient response of an infinite cylindrical antenna, *IEEE Trans. Antennas Propagat.*, AP-31 (1), 170–172
- Cooray, V., V. A. Rakov, F. Rachidi, R. Montano and C. A. Nucci (2008), On the relationship between the signature of close electric field and the equivalent corona current in lightning return stroke models, *IEEE Trans. Electromagn. Compat.*, IEEE Trans. Electromagn. Compat., 50 (4), 921–927

- Crawford, D. E., V. A. Rakov, M. A. Uman, G. H. Schnetzer, K. J. Rambo, M. V. Stapleton, *et al.* (2001), The close lightning electromagnetic environment: dart-leader electric field change versus distance, *J. Geophys. Res.*, 106 (D14), 14909–14917
- da F. Mattos, M. A. and C. Christopoulos (1988), A nonlinear transmission line model of the lightning return stroke, *IEEE Trans. Electromagn. Compat.*, EMC-30 (3), 401–406
- Geranmayeh, A., R. Moini and S. H. H. Sadeghi (2006), Numerical simulation of electromagnetic fields radiated by lightning return stroke channels: a wavelet-based approach, *IEEE Trans., Electromagn. Compat.*, EMC-48 (1), 225–233
- Gomes, C. and V. Cooray (2000), Concepts of lightning return stroke models, *IEEE Trans. Electromagn. Compat.*, EMC-42 (1), 82–96
- Gorin, B. N. and A. V. Shkilev (1984), Measurements of lightning currents at the Ostankino tower, *Electrichestrovo*, 8, 64–65 (in Russian)
- Goshima, H., H. Motoyama, A. Asakawa, A. Wada, T. Shindo and S. Yokoyama (2000), Characteristics of electromagnetic fields due to lightning stroke current to a high stack in winter lightning, *IEEJ Trans. PE*, 120 (1), 44–49
- Goubau, G. (1950), Surface waves and their application to transmission lines, *J. Appl. Phys.*, 21, 1119–1128
- Grcev, L., F. Rachidi and V. A. Rakov (2003), Comparison of electromagnetic models of lightning return strokes using current and voltage sources, paper presented at 12th International Conference on Atmospheric Electricity, Versailles, France, pp. 593–596
- Harrington, R. F. (1968), *Field Computation by Moment Methods*, Macmillan Company, New York
- Ishii, M., K. Michishita and Y. Hongo (1999), Experimental study of lightning-induced voltage on an overhead wire over lossy ground, *IEEE Trans. Electromagn. Compat.*, EMC-41 (1), 39–45
- Jordan, D. M., V. A. Rakov, W. H. Beasley and M. A. Uman (1997), Luminosity characteristics of dart leaders and return strokes in natural lightning, *J. Geophys. Res.*, 102 (D18), 22,025–22,032
- Kato, S., T. Narita, T. Yamada and E. Zaima (1999), Simulation of electromagnetic field in lightning to tall tower, paper presented at 11th International Symposium on High Voltage Engineering, 467, London, UK
- Kato, S., T. Takinami, T. Hirai and S. Okabe (2001), A study of lightning channel model in numerical electromagnetic field computation, paper presented at 2001 IEEJ National Convention, Nagoya, Japan, pp. 7–140 (in Japanese)
- Kordi, B., R. Moini and V. A. Rakov (2002), Comment on ‘Return stroke transmission line model for stroke speed near and equal that of light’ by R. Thottappillil, J. Schoene and M. A. Uman, *Geophys. Res. Lett.*, 29 (10), doi:10.1029/2001GL014602
- Kordi, B., R. Moini and V. A. Rakov (2003a), Comparison of lightning return stroke electric fields predicted by the transmission line and antenna theory models, paper presented at 15th International Zurich Symposium and

- Technical Exhibition on Electromagnetic Compatibility, Swiss Federal Institute of Technology, Zurich, Switzerland, pp. 551–556
- Kordi, B., R. Moini, W. Janischewskyj, A. M. Hussein, V. O. Shostak and V. A. Rakov (2003b), Application of the antenna theory model to a tall tower struck by lightning, *J. Geophys. Res.*, 108 (D17), doi:10.1029/2003JD003398
- Liao, Z. P., H. L. Wong, B.-P. Yang and Y.-F. Yuan (1984), A transmitting boundary for transient wave analysis, *Sci. Sin.*, A27 (10), 1063–1076
- Lin, Y. T., M. A. Uman, J. A. Tiller, R. D. Brantley, W. H. Beasley, E. P. Krider, et al. (1979), Characterization of lightning return stroke electric and magnetic fields from simultaneous two-station measurements, *J. Geophys. Res.*, 84 (C10), 6307–6314
- Maslowski, G. (2004), Some aspects of numerical modeling of lightning return stroke current based on antenna theory, paper presented at 27th International Conference on Lightning Protection, Soc. de l'Electr., de l'Electron., et des Technol. de l'Inf. et de la Commun., Avignon, France
- Michishita, K., M. Ishii, A. Asakawa, S. Yokoyama and K. Kami (2003), Voltage induced on a test distribution line by negative winter lightning strokes to a tall structure, *IEEE Trans. Electromagn. Compat.*, EMC-45 (1), 135–140
- Miller, E. K., A. J. Poggio and G. J. Burke (1973), An integro-differential equation technique for the time-domain analysis of thin wire structures, *J. Comput. Phys.*, 12, 24–48
- Miyazaki, S. and M. Ishii (2004a), Reproduction of electromagnetic fields associated with lightning return stroke to a high structure using FDTD method, paper presented at 2004 IEEJ National Convention, no. 7-065, Kanagawa, Japan, p. 98 (in Japanese)
- Miyazaki, S. and M. Ishii (2004b), Influence of elevated stricken object on lightning return-stroke current and associated fields, paper presented at 27th International Conference on Lightning Protection, Soc. de l'Electr., de l'Electron., et des Technol. de l'Inf. et de la Commun., Avignon, France, pp. 122–127
- Miyazaki, S. and M. Ishii (2005), Lightning current distribution inside of directly hit building, paper presented at 14th International Symposium on High Voltage Engineering, A-26, Beijing, China
- Miyazaki, S. and M. Ishii (2008a), Role of steel frames of buildings for mitigation of lightning-induced magnetic fields, *IEEE Trans. Electromagn. Compat.*, EMC-50 (2), 333–339
- Miyazaki, S. and M. Ishii (2008b), Influence of independent towers and transmission lines on lightning return stroke current and associated fields, *IEEE Trans. Electromagn. Compat.*, EMC-50 (2), 358–368
- Moini, R., V. A. Rakov, M. A. Uman and B. Kordi (1997), An antenna theory model for the lightning return stroke, paper presented at 12th International Zurich Symposium and Technical Exhibition on Electromagnetic Compatibility, Swiss Federal Institute of Technology, Zurich, Switzerland, pp. 149–152
- Moini, R., B. Kordi and M. Abedi (1998), Evaluation of LEMP effects on complex wire structures located above a perfectly conducting ground using electric field

- integral equation in time domain, *IEEE Trans. Electromagn. Compat.*, EMC-40 (2), 154–162
- Moini, R., B. Kordi, G. Z. Rafi and V. A. Rakov (2000), A new lightning return stroke model based on antenna theory, *J. Geophys. Res.*, 105 (D24), 29693–29702
- Mosaddeghi, A., D. Pavanello, F. Rachidi and M. Rubinstein (2008), On the bipolar waveform of electric field at very close range from a tower struck by lightning, paper presented at International Conference on Lightning Protection, Uppsala, Sweden, 3-b-8, 4pp.
- Motoyama, H. (1996), Development of a new flashover model for lightning surge analysis, *IEEE Trans. Power Deliv.*, PWRD-11 (2), 972–979
- Mozumi, T., Y. Baba, M. Ishii, N. Nagaoka and A. Ametani (2003), Numerical electromagnetic field analysis of archorn voltages during a back-flashover on a 500 kV twin-circuit line, *IEEE Trans. Power Deliv.*, PWRD-18 (1), 207–213
- Noda, T. and S. Yokoyama (2002), Thin wire representation in finite difference time domain surge simulation, *IEEE Trans. Power Deliv.*, PWRD-17 (3), 840–847
- Noda, T., A. Tetematsu and S. Yokoyama (2007), Improvements of an FDTD-based surge simulation code and its application to the lightning overvoltage calculation of a transmission tower, *Electr. Power Syst. Res.*, 77, 1495–1500
- Nucci, C. A., G. Diendorfer, M. A. Uman, F. Rachidi, M. Ianoz and C. Mazzetti (1990), Lightning return stroke current models with specified channel-base current: a review and comparison, *J. Geophys. Res.*, 95 (D12), 20395–20408
- Olsen III, R. C., D. M. Jordan, V. A. Rakov, M. A. Uman and N. Grimes (2004), Observed one-dimensional return stroke propagation speeds in the bottom 170 m of a rocket-triggered lightning channel, *Geophys. Res. Lett.*, 31 (L16107), doi:10.1029/2004GL02187
- Petrache, E., F. Rachidi, D. Pavanello, W. Janischewskyj, A. M. Hussein, M. Rubinstein, *et al.* (2005), Lightning strikes to elevated structures: influence of grounding conditions on currents and electromagnetic fields, paper presented at 2005 IEEE International Symposium on Electromagnetic Compatibility, Chicago, Illinois
- Podgorski, A. S. (1991), Three-dimensional time domain model of lightning including corona effects, paper presented at 1991 International Aerospace and Ground Conference on Lightning and Static Electricity, Cocoa Beach, Florida, USA
- Podgorski, A. S. and J. A. Landt (1987), Three dimensional time domain modelling of lightning, *IEEE Trans. Power Deliv.*, PWRD-2 (3), 931–938
- Pokharel, R. K. and M. Ishii (2007), Applications of time-domain numerical electromagnetic code to lightning surge analysis, Pokharel, *IEEE Trans. Electromagn. Compat.*, EMC-49 (3), 623–631
- Pokharel, R. K., M. Ishii and Y. Baba (2003), Numerical electromagnetic analysis of lightning-induced voltage over ground of finite conductivity, *IEEE Trans. Electromagn. Compat.*, EMC-45 (4), 651–666
- Pokharel, R. K., Y. Baba and M. Ishii (2004), Numerical electromagnetic field analysis of transient induced voltages associated with lightning to a tall structure, *J. Electrostat.*, 60 (2), 141–147

- Rachidi, F., V. A. Rakov, C. A. Nucci and J. L. Bermudez (2002), Effect of vertically extended strike object on the distribution of current along the lightning channel, *J. Geophys. Res.*, 107 (D23), doi:10.1029/2002JD002119
- Rakov, V. A. (1998), Some inferences on the propagation mechanisms of dart leaders and return strokes, *J. Geophys. Res.*, 103 (D2), 1879–1887
- Rakov, V. A. (2001), Transient response of a tall object to lightning, *IEEE Trans. Electromagn. Compat.*, EMC-43 (4), 654–661
- Rakov, V. A. (2007), Lightning return stroke speed, *J. Lightning Res.*, 1, 80–89
- Rakov, V. A. and A. A. Dulzon (1987), Calculated electromagnetic fields of lightning return stroke, *Tekh. Electrodinam.*, 1, 87–89 (in Russian)
- Rakov, V. A. and M. A. Uman (1998), Review and evaluation of lightning return stroke models including some aspects of their application, *IEEE Trans. Electromagn. Compat.*, EMC-40 (4), 403–426
- Rusck, S. (1958), Induced lightning over-voltages on power-transmission lines with special reference to the over-voltage protection of low-voltage networks, *Transactions of the Royal Institute of Technology*, Stockholm, Sweden
- Sadiku, M. N. O. (1994), *Elements of Electromagnetics*, Oxford University Press, Orlando, Florida
- Shoory, A., R. Moini, S. H. H. Sadeghi and V. A. Rakov (2005), Analysis of lightning-radiated electromagnetic fields in the vicinity of lossy ground, *IEEE Trans. Electromagn. Compat.*, EMC-47 (1), 131–145
- Silveira, F. and S. Visacro (2008), Influence of a lossy ground on lightning-induced voltages using the hybrid electromagnetic model, paper presented at International Conference on Lightning Protection, Uppsala, Sweden, 3-b-11, 9pp.
- Taniguchi, Y., Y. Baba, N. Nagaoka and A. Ametani (2008), Representation of an arbitrary-radius wire for FDTD calculations in the 2D cylindrical coordinate system, *IEEE Trans. Electromagn. Compat.*, EMC-50 (4), 1114–1118
- Tatematsu, A., T. Noda and S. Yokoyama (2004), Simulation of lightning-induced voltages on a distribution line using the FDTD method, paper presented at International Workshop on High Voltage Engineering, HV-04-48, Sapporo, Japan
- Tatematsu, A., T. Noda and H. Motoyama (2007), *Development of simulation techniques for super-thin wires and nonlinear elements in the FDTD method*, CRIEPI Report, H06006 (in Japanese)
- Theethayi, N. and V. Cooray (2005), On the representation of the lightning return stroke as a current pulse propagating along a transmission line, *IEEE Trans. Power Deliv.*, PWRD-20 (2), 823–837
- Thottappillil, R. and M. A. Uman (1993), Comparison of lightning return-stroke models, *J. Geophys. Res.*, 98, 22903–22914
- Thottappillil, R., M. A. Uman and G. Diendorfer (1991), Influence of channel base current and varying return stroke speed on the calculated fields of three important return stroke models, paper presented at International Conference on Lightning and Static Electricity, Cocoa Beach, FL, USA

- Thottappillil, R., V. A. Rakov and M. A. Uman (1997), Distribution of charge along the lightning channel: relation to remote electric and magnetic fields and to return-stroke models, *J. Geophys. Res.*, 102, 6987–7006
- Thottappillil, R., J. Schoene and M. A. Uman (2001), Return stroke transmission line model for stroke speed near and equal that of light, *Geophys. Res. Lett.*, 28 (18), 3593–3596
- Uman, M. A., D. K. McLain and E. P. Krider (1975), The electromagnetic radiation from a finite antenna, *Am. J. Phys.*, 43, 33–38
- Van Baricum, M. and E. K. Miller (1972), *TWTD – A Computer Program for Time-Domain Analysis of Thin-Wire Structures*, UCRL-51-277, California
- Visacro, S. and A. De Conti (2005), A distributed-circuit return-stroke model allowing time and height parameter variation to match lightning electromagnetic field waveform signatures, *Geophys. Res. Lett.*, 32 (L23805), doi:10.1029/2005GL024336
- Visacro, S. and F. H. Silveira (2004), Evaluation of current distribution along the lightning discharge channel by a hybrid electromagnetic model, *J. Electrostat.*, 60 (2), 111–120
- Visacro, S. and F. H. Silveira (2005), Lightning current waves at short instrumented towers: the influence of sensor position, *Geophys. Res. Lett.*, 32 (L18804), doi:10.1029/2005GL023255
- Yee, K. S. (1966), Numerical solution of initial boundary value problems involving Maxwell's equations in isotropic media, *IEEE Trans. Antennas Propagat.*, AP-14 (3), 302–307



---

## *Chapter 9*

# **Antenna models of lightning return-stroke: an integral approach based on the method of moments**

*Rouzbeh Moini<sup>1</sup> and Seyed Hossein Hesamedin Sadeghi<sup>1</sup>*

---

## **9.1 Introduction**

Lightning is a transient, high-current electric discharge with the height in kilometre range. Cloud-to-ground lightning is less common than the other kinds of lightning (i.e. cloud-to-cloud and interclub lightning), but they are more important for protection studies of electric and electronic apparatus used in power systems, information technology systems, etc. The complete discharge, known as flash, has a time duration of about 0.5 s and is made up of various components, including stepped leader, return-strokes and dart leaders. The part of a flash, which has been of great interest for protection purposes, is the return-stroke phase.

The expression ‘lightning return-stroke model’ is generally used to describe a specification of the time and height-dependent current in the return-stroke channel (RSC) so as to make possible the calculation of resultant remote electromagnetic fields [1]. A suitable model should be characterized by a minimum number of adjustable parameters and be consistent with the measured characteristics of the return-stroke namely:

- Current at the base of the channel.
- Variation of light intensity with height.
- Upward propagation speed of the luminosity front.
- Electromagnetic fields at various distances from the channel.

It is worth mentioning that other physical parameters (such as existing space charge in the vicinity of the lightning channel) could also be included in a realistic model for describing lightning phenomena. However, considering each of these parameters will add to the complexity of the model, making it impractical for most applications.

---

<sup>1</sup>Center of Excellence on Radio Communication Systems, Department of Electrical Engineering, Amirkabir University of Technology, Tehran, Iran

Many models have been proposed to describe the behaviour of lightning and predict its effects. All these models can be placed in four categories [1], namely: physical models, distributed-circuit models, engineering models and electromagnetic models.

Physical models or gas dynamic models solve the gas dynamic equations [2, 3]. They do not consider the longitudinal evolution of the lightning channel. They also usually ignore the electromagnetic skin effect (found to be negligible) [4], the corona sheath which presumably contains the bulk of the leader charge and any heating of the air surrounding the current carrying channel by preceding lightning processes [5]. An attempt to include the previous heating in a gas dynamic model is also made in Reference 6.

Distributed-circuit models assume a transmission line representation of the lightning RSC considering only the TEM wave propagation along the channel. They solve the so-called telegrapher's expressions to obtain a current distribution along the channel [7]. It is known that the representation of a vertical conductor as a non-uniform transmission line enables leading a spatial and temporal current distribution essentially close to those obtained by the full-wave solutions [8]. Recently, proposed distributed-circuit models [9, 10] have shown to predict electromagnetic fields in good agreement with experimental data. In Reference 10, a lightning return-stroke model based on a dynamic non-uniform transmission line contemplating the corona sheath and core losses is formulated. Also, recently proposed transmission line equations in air in presence of corona (considered as a series of corona current sources distributed along the line) are derived to model how the measured return-stroke speed is less than the speed of light [11].

Engineering models [1] specify a closed-form relation between the current distribution along the channel and current at the channel base. The most used engineering models can themselves be classified in two categories. The first category includes travelling current source type models. The Diendorfer-Uman (DU) model and the travelling current source (TCS) model are placed in this category. The second category contains transmission line type models, namely the transmission line (TL) model, the modified transmission line model with linear current decay with height (MTLL) and the modified transmission line model with exponential current decay with height (MTLE).

A great deal of attention has been recently devoted to the electromagnetic models [12–14]. In these models, the lightning RSC is usually considered as a monopole wire antenna above a perfectly conducting ground. In these models, Maxwell's equations are solved numerically to obtain a current distribution along the channel, using which remote electromagnetic fields are readily computed. Electromagnetic models provide several degrees of freedom to simulate all known behaviours of the lightning RSC [15]. These models are relatively new and considered to be the most rigorous. They solve Maxwell's equations for current distributions along the lightning channel. Because of the lack of analytical solution, these are usually done with the aid of numerical techniques. The first category of electromagnetic models solve the time-domain Maxwell's equations using the finite-difference time-domain technique [16] assuming a distributed array of

current sources representing the lightning RSC [17]. The model is used to describe some wave propagation effects prescribed by the transmission line theory.

The second category of electromagnetic models, known as antenna theory (AT) models, use the method of moments (MOM) solution of the electric field integral equation (EFIE) form of the electromagnetic problem in either the time domain [18] or the frequency domain [19]. In these models, the lightning RSC is modelled by a thin wire antenna [13, 20]. The antenna can be excited through a voltage source [13] or a current source [21]. The idea behind the AT models was at first proposed by Podgorski and Landt in 1985 [22]. They worked on a frequency domain code for modelling of lightning strike to the CN tower. Later on in 1987 they used a thin-wire time-domain code [23] to analyse lightning strike to tall structures [24]. In 1997, Moini *et al.* [13] considered a monopole antenna above a perfect conducting ground to represent lightning RSC. They adjusted the propagation speed and the value of distributed resistance along the channel to make EM fields similar to measured fields [25], especially at close ranges. In 2001, Baba and Ishii [20] applied a set of distributed inductive and resistive loads on the wire representing the lightning channel. This distributed inductive loads reduced the propagation speed of current wave along the channel consistent with optical observation. The channel was analysed in frequency domain and with the help of Numerical Electromagnetics Code (NEC-2); therefore, a huge amount of calculations in a wide range of frequency sampling points needed to be done.

Time-domain AT models have also been developed in recent years. Bonyadi-Ram *et al.* [26, 27] considered a monopole antenna above a perfect conducting ground to model the lightning RSC. They applied distributed inductances along the monopole antenna to control the propagation speed of current wave along it [27]. Therefore, with this way, speed of current wave along the channel can be controlled consistent with optical observation ( $v < 3 \times 10^8$  m/s) [28, 29]. In fact, in this model, values of L and R were applied along the channel chosen by trial and error, which resulted  $v = 1.3 \times 10^8$  m/s for current wave propagation along the channel, and dispersion of this current is consistent with optical observations of Wang *et al.* [29] and Jordan and Uman [28].

Using a similar approach, another treatment based on capacitive loading has also been proposed in Reference 30, where the distributed capacitance is applied to a two-wire parallel transmission line to obtain the desired characteristics of the current distribution along the channel. The resultant current waveform is then applied to a dipole antenna to calculate the radiated electromagnetic fields. Introducing inductive or capacitive energy storing elements further provides current wave dispersion while propagating upward along the channel. Moosavi *et al.* [31] have modified the time-domain AT model with fixed inductive loading (ATIL-F) electromagnetic model to include non-linear resistive loading in the presence of fixed inductive loading of the channel. Resistive elements are considered as a non-linear distributed load the resistance of which is a function of both current and time. This is done in a consistent manner from an available physical model with respect to the varying value of the channel radius from its base to the cloud [31]. Considering the channel load resistance as a non-linear element, they aim to better

model losses along the channel. They use the Braginskii model [2, 32] to provide a non-linear resistive load along the channel by the ATIL-F model.

The chapter focuses on the problem of integral approach for the AT modelling of lightning return-stroke, using the MOM. First, we give a general formulation of the problem where the governing frequency and time-domain electromagnetic field equations are derived. The MOM used for numerical solutions of these equations is then described. Special treatments required for channel excitation, channel path and lossy ground are addressed next. Finally, we evaluate the performance of the modelling technique by presenting results in a number of case studies.

## 9.2 General formulation

The schematic of a lightning RSC located above a ground is shown in Figure 9.1. In this figure, the RSC is modelled by a long conductive thin wire excited by a voltage or current source at its lower end at the ground surface. Using the zero-tangential electric field boundary condition along the surface of a straight thin wire leads to the EFIE which is solved for the distribution of current along the channel.

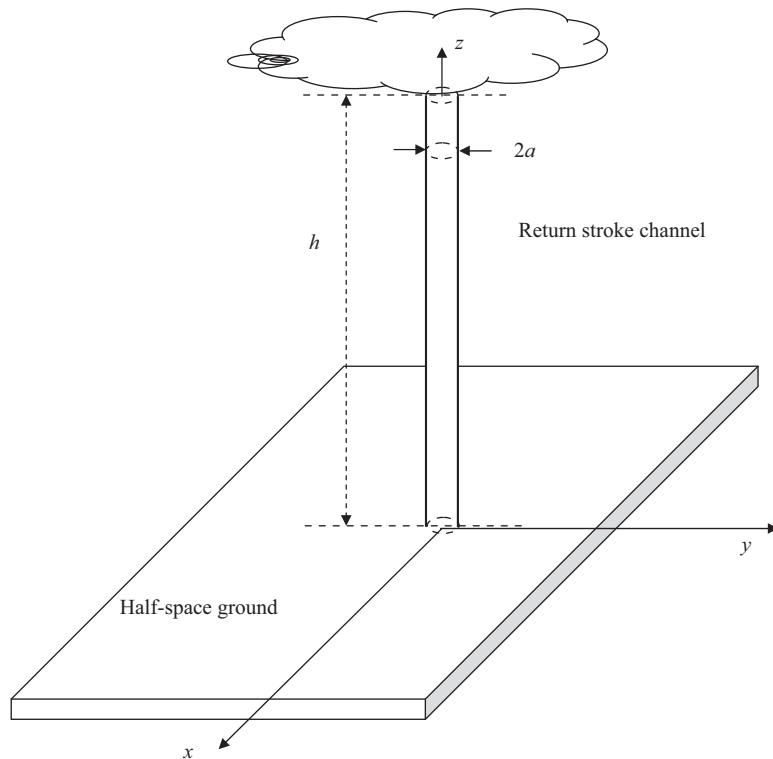


*Figure 9.1 Schematic of the problem*

The methods used for the analysis of the above-mentioned problems can be classified as time domain and frequency domain. Time-domain techniques generate accurate results and are well suited to the analysis of transients and non-linear problems [33]. However, they cannot be easily used to deal with problems involving a lossy ground. Since the lightning phenomenon provides a narrow pulse, the frequency-domain analysis of the problem should be performed for many frequencies, which is a time-consuming process [34]. Additionally, the treatment of non-linearity in frequency domain is not straightforward. As with the other frequency-domain analysis methods of transient phenomena, it is also necessary to appropriately adjust sampling rate and total analysis time to avoid undesirable aliasing or circular convolution. Alternately, frequency-domain counterparts can use a lossy ground assumption [21].

### 9.2.1 Time-domain formulation

The starting point of the analysis is the time-domain Maxwell's equations for a linear, homogeneous and time-invariant medium:

$$\begin{aligned}\nabla \times \mathbf{e}(\mathbf{r}, t) &= -\mu \frac{\partial \mathbf{h}(\mathbf{r}, t)}{\partial t} \\ \nabla \times \mathbf{h}(\mathbf{r}, t) &= \mathbf{j}(\mathbf{r}, t) + \epsilon \frac{\partial \mathbf{e}(\mathbf{r}, t)}{\partial t} \\ \nabla \cdot \mathbf{e}(\mathbf{r}, t) &= \frac{\rho(\mathbf{r}, t)}{\epsilon} \\ \nabla \cdot \mathbf{h}(\mathbf{r}, t) &= 0\end{aligned}\tag{9.1}$$

where  $\epsilon$  and  $\mu$  are the electric permittivity and magnetic permeability of medium,  $\mathbf{e}$  and  $\mathbf{h}$  are the electric and magnetic field intensities, and  $\mathbf{j}$  and  $\rho$  are the volume current and charge densities, respectively.  $\mathbf{r}$  is the position vector of a point in space and  $t$  denotes time of observation. The relation between  $\mathbf{j}$  and  $\rho$  is specified by the current continuity equation:

$$\nabla \cdot \mathbf{j}(\mathbf{r}, t) = -\frac{\partial \rho(\mathbf{r}, t)}{\partial t}\tag{9.2}$$

Combining Maxwell's equations yields the following expressions (wave equations):

$$\begin{aligned}\nabla^2 \mathbf{e}(\mathbf{r}, t) - \frac{1}{\nu^2} \frac{\partial^2 \mathbf{e}(\mathbf{r}, t)}{\partial t^2} &= \mu \frac{\partial \mathbf{j}(\mathbf{r}, t)}{\partial t} + \frac{1}{\epsilon} \nabla \rho(\mathbf{r}, t) \\ \nabla^2 \mathbf{h}(\mathbf{r}, t) - \frac{1}{\nu^2} \frac{\partial^2 \mathbf{h}(\mathbf{r}, t)}{\partial t^2} &= -\nabla \times \mathbf{j}(\mathbf{r}, t)\end{aligned}\tag{9.3}$$

where  $\nu = 1/\sqrt{\epsilon\mu}$

If we consider a perfectly conducting antenna in a homogeneous medium, the volume current and charge densities,  $\mathbf{j}$  and  $\rho$ , can be replaced by the surface current

and charge densities,  $\mathbf{j}_s$  and  $\rho_s$ :

$$\begin{aligned}\mathbf{j}(\mathbf{r}, t) &= \mathbf{j}_s(\mathbf{r}_0, t)\delta_s(\mathbf{r} - \mathbf{r}_0) \\ \rho(\mathbf{r}, t) &= \rho_s(\mathbf{r}_0, t)\delta_s(\mathbf{r} - \mathbf{r}_0) \\ \delta_s(\mathbf{r} - \mathbf{r}_0) &= \begin{cases} \infty & \text{if } r = r_0 \\ 0 & \text{otherwise} \end{cases}\end{aligned}\quad (9.4)$$

where  $\mathbf{r}_0$  is the position vector of a point on the surface of the antenna and  $\delta_s$  is the two-dimensional impulse function.

The Green's solution (g) of a non-homogeneous wave equation:

$$\begin{aligned}\nabla^2 g - \frac{1}{v^2} \frac{\partial^2 g}{\partial t^2} &= -\delta(\mathbf{r} - \mathbf{r}_0)\delta(t - t_0) \\ \delta(\mathbf{r} - \mathbf{r}_0) &= \delta(x - x_0)\delta(y - y_0)\delta(z - z_0)\end{aligned}\quad (9.5)$$

is given by Stratton [35]:

$$g(\mathbf{r}, \mathbf{r}_0, t - t_0) = \frac{1}{4\pi} \frac{\delta(t - t_0 - (R/v))}{R} \quad (9.6)$$

In this equation,  $R = |\mathbf{r} - \mathbf{r}_0|$ ;  $\mathbf{r}_0$  the spatial location and  $t_0$  the initial temporal point of the source (current or charge density on the surface of the conductor).

Applying the above solution to (9.3), we obtain the radiated fields produced by surface current density  $\mathbf{j}_s$  [36]:

$$\begin{aligned}\mathbf{e}(\mathbf{r}, t) &= - \iint_{S_0} \left[ \mu \frac{\partial \mathbf{j}_s(\mathbf{r}_0, t)}{\partial t} \hat{*}_{(t)} g(\mathbf{r}, \mathbf{r}_0, t) + \frac{1}{\epsilon} \int_0^t \nabla \cdot \mathbf{j}_s(\mathbf{r}_0, \tau) d\tau \hat{*}_{(t)} \nabla_0 g(\mathbf{r}, \mathbf{r}_0, t) \right] ds_0 \\ \mathbf{h}(\mathbf{r}, t) &= \iint_{S_0} \mathbf{j}_s(\mathbf{r}_0, t) \hat{*}_{(t)} \nabla_0 g(\mathbf{r}, \mathbf{r}_0, t) ds_0\end{aligned}\quad (9.7)$$

where the subscript  $(t)$  refers to convolution operator variable (time), and the subscript zero is related to the differentiation variable ( $\mathbf{r}_0$ ). The symbol  $\hat{*}_{(t)}$  denotes the cross-product with respect to space and convolution in time, and integration is performed over the outer surface of the antenna ( $s_0$ ).

The response of a monopole antenna (see Figure 9.2) above a perfectly conducting ground to an electromagnetic wave produced by an external source can be found considering the scattering of electromagnetic fields by a metallic object. The boundary condition on the surface of a perfect conductor can be expressed as

$$\mathbf{n} \times (\mathbf{e}^a + \mathbf{e}) = 0 \quad (9.8)$$

where  $\mathbf{e}^a$  is the applied field and  $\mathbf{n}$  is the normal vector to the surface of conducting object. For a non-ideal conductor, the right-hand side of (9.8) is not

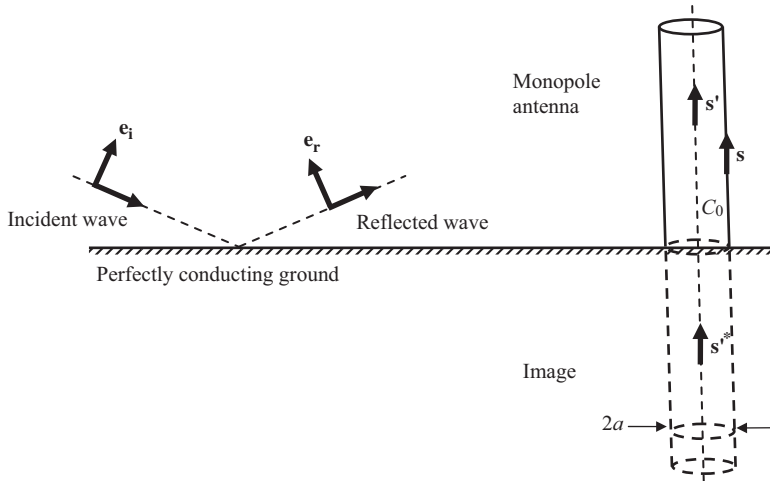


Figure 9.2 Geometry of vertical monopole antenna in receiving mode located above a perfectly conducting ground

equal to zero and depends on resistance per unit length. Combining (9.7) and (9.8), we have

$$\begin{aligned} \mathbf{n} \times \mathbf{e}^a(\mathbf{r}, t) = & \mathbf{n} \times V_p \iint_{S_0} \left[ \mu \frac{\partial \mathbf{j}_s(\mathbf{r}_0, t)}{\partial t} * g(\mathbf{r}, \mathbf{r}_0, t) \right. \\ & \left. + \frac{1}{\varepsilon} \int_0^t \nabla \cdot \mathbf{j}_s(\mathbf{r}_0, \tau) d\tau * \nabla_0 g(\mathbf{r}, \mathbf{r}_0, t) \right] ds_0 \end{aligned} \quad (9.9)$$

where  $V_p$  is the principal value of the integral operator [13].

In the case of homogeneous, linear and time-invariant media, inserting (9.6) into (9.9) will yield the following equation:

$$\begin{aligned} \mathbf{n} \times \mathbf{e}^a(\mathbf{r}, t) = & \frac{\mathbf{n}}{4\pi} \times V_p \iint_{S_0} \left[ \frac{\mu}{R} \frac{\partial \mathbf{j}_s(\mathbf{r}_0, t)}{\partial t} + \frac{\mathbf{R}}{\varepsilon \nu R^2} \nabla \cdot \mathbf{j}_s(\mathbf{r}_0, t - R/\nu) \right. \\ & \left. + \frac{\mathbf{R}}{\varepsilon R^3} \int_0^t \nabla \cdot \mathbf{j}_s(\mathbf{r}_0, \tau) d\tau \right] ds_0 \end{aligned} \quad (9.10)$$

where  $\mathbf{R} = \mathbf{r} - \mathbf{r}_0$ .

We will use the thin-wire approximation [13] according to which the current  $i(s, t)$  on a wire structure of radius  $a$  satisfies the equations:

$$\begin{aligned} i(s, t) &= 2\pi a j(s, t) \\ \mathbf{j}(s, t) &= \frac{i(s, t)}{2\pi a} \mathbf{s} \end{aligned} \quad (9.11)$$

where  $s$  is the location of a point on the wire structure and  $\mathbf{s}$  is the corresponding tangential unit vector (see Figure 9.2).

Because of the presence of ground, the total excitation (or applied) field produced by the source above ground is

$$\mathbf{e}^a = \mathbf{e}^i + \mathbf{e}^r \quad (9.12)$$

where  $\mathbf{e}^i$  is the incident field and  $\mathbf{e}^r$  is the reflected field from the ground. The excitation field  $\mathbf{e}^a$  induces current  $i(\mathbf{s}, t)$  at each point of the antenna. According to (9.10) and thin-wire approximation (9.11), one can determine the scattered field  $\mathbf{e}$ , which can be described in the following form:

$$\mathbf{e}(\mathbf{s}, t) = \mathbf{L}[i(\mathbf{s}, t)] \quad (9.13)$$

where  $\mathbf{L}$  is an integro-differential operator [37]. Note that  $\mathbf{e}^a$  is independent of the presence of the antenna, and  $\mathbf{e}$  can be viewed as a reaction of the antenna to  $\mathbf{e}^a$ . For the receiving antenna mode, illustrated in Figure 9.2,  $\mathbf{e}^a$  is produced by an external source and exists everywhere in space. For the transmitting antenna mode,  $\mathbf{e}^a$  is produced by a lumped source connected between the lower end of the antenna and the ground and is zero everywhere except for the position of the source. Similar to the receiving mode,  $\mathbf{e}^a$  is totally independent of the presence of antenna. The source, whose voltage is related to  $\mathbf{e}^a$  as described later in this section, launches a current wave along the antenna. Electric field produced by this current wave is scattered field  $\mathbf{e}$  which, similar to the receiving mode, can be viewed as a reaction of the antenna to  $\mathbf{e}^a$ .

The continuity of tangential component of the total electric field at any point on the antenna surface requires that

$$\mathbf{s} \cdot (\mathbf{e}^a(\mathbf{s}, t) + \mathbf{L}[i(\mathbf{s}, t)]) = 0 \quad (9.14)$$

which is the same as (9.8). As stated above for (9.8), for a non-ideal conductor the right-hand side of (9.14) is not equal to zero. Using the definition of the  $\mathbf{L}$  operator and the thin-wire approximation [37, 38], we can write:

$$\begin{aligned} \mathbf{s} \cdot \mathbf{e}^a(\mathbf{s}, t) &= \frac{\mu_0}{4\pi} \int_{C_0} \left[ \frac{\mathbf{s} \cdot \mathbf{s}' \partial i(\mathbf{s}', t')}{R} \frac{\partial}{\partial t'} + \nu \frac{\mathbf{s} \cdot \mathbf{R}}{R^2} \frac{\partial i(\mathbf{s}', t')}{\partial s'} \right. \\ &\quad \left. + \nu^2 \frac{\mathbf{s} \cdot \mathbf{R}}{R^3} \int_0^{t'} \left( \frac{\partial i(\mathbf{s}', \tau)}{\partial s'} d\tau \right) \right. \\ &\quad \left. - \frac{\mathbf{s} \cdot \mathbf{s}''^*}{R^*} \frac{\partial i(\mathbf{s}', t'^*)}{\partial t'^*} - \nu \frac{\mathbf{s} \cdot \mathbf{R}^*}{R^{*2}} \frac{\partial i(\mathbf{s}', t'^*)}{\partial s'} \right. \\ &\quad \left. - \nu^2 \frac{\mathbf{s} \cdot \mathbf{R}^*}{R^{*3}} \int_0^{t'^*} \frac{\partial i(\mathbf{s}', \tau)}{\partial s'} d\tau \right] ds' \end{aligned} \quad (9.15)$$

where

$$\begin{aligned} R &= (|\mathbf{s} - \mathbf{s}'|^2 + a^2)^{1/2} \\ R^* &= (|\mathbf{s} - \mathbf{s}'^*|^2 + a^2)^{1/2} \\ t' &= t - \frac{R}{\nu}, \quad t'^* = t - \frac{R^*}{\nu} \end{aligned}$$

where  $C_0$  is the path along which the current is flowing,  $a$  is the radius of the antenna (Figure 9.1) and  $\nu$  is the wave propagation speed for the case of non-resistive channel. Further,  $s$  and  $s'$  are the observation and source points on the antenna, respectively,  $s'^*$  is the image of the source point  $s'$ , and  $\mathbf{s}$ ,  $\mathbf{s}'$  and  $\mathbf{s}'^*$  are the corresponding unit tangential vectors. The last three terms in the right-hand side of (9.15) represent the effect of perfect ground. The left-hand side of (9.15) represents the applied (excitation) electric field tangential to the surface of the antenna. For the case of transmitting antenna, the applied field  $\mathbf{e}^a(\mathbf{s}, t)$  is produced by a voltage source (not shown in Figure 9.1, which illustrates the receiving antenna mode). The relation between  $e^a(\mathbf{s}, t)$  and source voltage  $v(\mathbf{s}, t)$  according to Herault *et al.* [37] is

$$\mathbf{e}^a(\mathbf{s}, t) = \begin{cases} -\nabla v(\mathbf{s}', t) & \text{if } \mathbf{s} = \mathbf{s}' = 0 \\ 0 & \text{elsewhere} \end{cases} \quad (9.16)$$

The numerical solution of (9.15), the EFIE in time domain, by the MOM [18] yields the time-space distribution of current along the antenna.

### 9.2.2 Frequency-domain formulation

In Section 9.2.1, we have presented Maxwell's equations for general time-varying electromagnetic fields. To derive frequency-domain formulation, the time variations of electromagnetic waves can be represented by  $e^{j\omega t}$ , where  $j = \sqrt{-1}$  and  $\omega$  is the angular frequency. The starting point is the frequency-domain Maxwell's equations for a linear, homogeneous and time-invariant medium, i.e.:

$$\begin{aligned} \nabla \times \mathbf{E}(\mathbf{r}) &= -j\omega\mu\mathbf{H}(\mathbf{r}) \\ \nabla \times \mathbf{H}(\mathbf{r}) &= \mathbf{J}(\mathbf{r}) + j\omega\epsilon\mathbf{E}(\mathbf{r}) \\ \nabla \cdot \mathbf{E}(\mathbf{r}) &= \frac{\mathbf{P}(r)}{\epsilon} \\ \nabla \cdot \mathbf{H}(\mathbf{r}) &= 0 \end{aligned} \quad (9.17)$$

where  $\mathbf{E}$  and  $\mathbf{H}$  are the complex electric and magnetic field intensities, and  $\mathbf{J}$  and  $\mathbf{P}$  are the complex volume current and charge densities, respectively.  $\mathbf{r}$  is the position vector of a point in space. The relation between  $\mathbf{J}$  and  $\mathbf{P}$  is specified by the current continuity equation:

$$\nabla \cdot \mathbf{J}(\mathbf{r}) = -j\omega\mathbf{P} \quad (9.18)$$

Electric field induced by a volume current density is as follows:

$$\mathbf{E}(\mathbf{r}) = \nabla(\nabla \cdot \Pi) - \gamma^2 \Pi \quad (9.19)$$

where the Hertz vector potential is defined as

$$\Pi(\mathbf{r}) = \frac{\gamma^2}{4\pi j\omega\mu} \int_V \mathbf{J}(\mathbf{r}') \mathbf{g}(\mathbf{r}, \mathbf{r}') dV' \quad (9.20)$$

where  $\mathbf{r}'$  is a position vector on the source. Thus

$$\mathbf{E}(\mathbf{r}) = \frac{\gamma^2}{4\pi j\omega\mu} \int_V \mathbf{J} \cdot \bar{\mathbf{G}}(\mathbf{r}, \mathbf{r}') dV' \quad (9.21)$$

where the Dyadic Green's function  $\bar{\mathbf{G}}$  is defined as follows [39]:

$$\begin{aligned} \bar{\mathbf{G}}(\mathbf{r}, \mathbf{r}') &= (\nabla\nabla \cdot -\gamma^2 \bar{\mathbf{I}}) \mathbf{g}(\mathbf{r}, \mathbf{r}') \\ g(\mathbf{r}, \mathbf{r}') &= \frac{e^{-\gamma|\mathbf{r}-\mathbf{r}'|}}{|\mathbf{r}-\mathbf{r}'|} \\ \gamma &= \sqrt{j\omega\mu(\sigma + j\omega\varepsilon)} \end{aligned} \quad (9.22)$$

and  $\gamma$  is the medium complex wave number. In (9.22), the identity dyadic tensor  $\bar{\mathbf{I}}$  in three dimensions is defined as

$$\bar{\mathbf{I}} = \hat{x}\hat{x} + \hat{y}\hat{y} + \hat{z}\hat{z} \quad (9.23)$$

If we consider a perfectly conducting antenna in a homogeneous medium, the volume current  $\mathbf{J}$  can be replaced by the surface current  $\mathbf{J}_s$ , simplifying (9.21) as

$$\mathbf{E}(\mathbf{r}) = \frac{\gamma^2}{4\pi j\omega\mu} \iint_{S_0} \mathbf{J}_s(\mathbf{r}') \cdot \bar{\mathbf{G}}(\mathbf{r}, \mathbf{r}') ds_0 \quad (9.24)$$

The boundary condition on the surface of a perfect conductor can be expressed as

$$\mathbf{n} \times [\mathbf{E}^a(\mathbf{r}) + \mathbf{E}(\mathbf{r})] = 0 \quad (9.25)$$

where  $\mathbf{E}^a$  is the applied field and  $\mathbf{n}$  is the normal vector to the surface of conducting object. Combining (9.24) and (9.25), we have the EFIE in frequency domain:

$$\frac{\gamma^2}{4\pi j\omega\mu} \mathbf{n} \times \iint_{S_0} \mathbf{J}_s(\mathbf{r}') \cdot (\nabla\nabla \cdot -\gamma^2 \bar{\mathbf{I}}) \mathbf{g}(\mathbf{r}, \mathbf{r}') ds_0 = -\mathbf{n} \times \mathbf{E}^i(\mathbf{r}) \quad (9.26)$$

The vector equation (9.26) is an electric field equation for surfaces and is converted to scalar equation by thin-wire approximation. The wire antenna

representing a lightning channel satisfies the thin-wire approximation [40] since its radius is much smaller than the wavelength and its length is much greater than the radius. This implies that (1) current on the wire flows only in the longitudinal direction and (2) circumferential or radial variations in the axial current are negligible. According to the thin-wire approximation, the current  $I(s)$  on a wire structure of radius  $a$  satisfies the following equations [40]:

$$\begin{aligned} I(s) &= 2\pi a J_s(s) \\ \mathbf{J}_s(s) &= \frac{I(s)}{2\pi a} \mathbf{s} \end{aligned} \quad (9.27)$$

where  $s$  is the location of a point on the wire structure and  $\mathbf{s}$  is the corresponding tangential unit vector (see Figure 9.3).

Now, consider a perfectly conducting wire placed in a medium with conductivity  $\sigma$ , permittivity  $\epsilon$  and permeability  $\mu$ , shown in Figure 9.3. As mentioned in Section 9.2.1, EFIE expresses the fact that the total tangential electric field on the wire surface vanishes:

$$\mathbf{s} \cdot (\mathbf{E}^a + \mathbf{E}) = 0 \quad (9.28)$$

where the two terms in the parentheses are the applied  $\mathbf{E}^a$  and scattered  $\mathbf{E}$  fields.

The electric field  $\mathbf{E}$  is related to the vector potential  $\mathbf{A}$  and scalar potential  $\Phi$  by

$$\mathbf{E} = -\nabla\Phi - j\omega\mathbf{A} \quad (9.29)$$

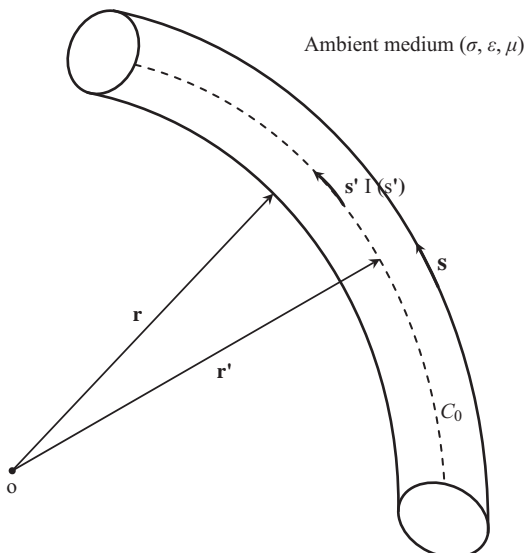


Figure 9.3 Thin-wire approximation

where

$$\begin{aligned}\mathbf{A}(\mathbf{r}) &= \frac{\mu}{4\pi} \int_{C_0} \mathbf{s}' I(s') g(\mathbf{r}, \mathbf{r}') ds' \\ \Phi(\mathbf{r}) &= \frac{j\omega}{4\pi(\sigma + j\omega\epsilon)} \int_{C_0} \rho_l(s') g(\mathbf{r}, \mathbf{r}') ds'\end{aligned}\quad (9.30)$$

and  $\rho_l$  is the linear charge density and  $C_0$  is the path along which the current is flowing.  $s'$  is the source point on the antenna and  $\mathbf{s}'$  is the corresponding unit tangential vector. The relation between  $I(s')$  and  $\rho_l(s')$  is specified by the current continuity equation:

$$\nabla \cdot \mathbf{s}' I(s') + j\omega \rho_l(s') = 0 \quad (9.31)$$

Combining (9.28) and (9.31) yields the expression for the electric field due to the current of a thin wire in a homogeneous medium:

$$\mathbf{E}(\mathbf{r}) = \frac{\gamma^2}{4\pi j\omega\mu} (\nabla\nabla - \gamma^2) \int_{C_0} \mathbf{s}' I(s') g(\mathbf{r}, \mathbf{r}') ds' \quad (9.32)$$

The term under integral in (9.32) is always continuous because the minimum distance between the source and observation points cannot be less than the radius of the thin wire. In addition, integration is done for source while differentiation is done for observation point. Therefore, it is permitted to change the order of integration and differentiation in (9.32):

$$\mathbf{E}(\mathbf{r}) = \frac{\gamma^2}{4\pi j\omega\mu} \int_{C_0} (\nabla\nabla \cdot -\gamma^2) \mathbf{s}' I(s') g(\mathbf{r}, \mathbf{r}') ds' \quad (9.33)$$

By applying the vector identity:

$$\begin{aligned}\nabla\nabla \cdot (\beta\mathbf{C}) &= (\nabla\beta)\nabla \cdot \mathbf{C} \\ &\quad + \beta\nabla\nabla \cdot \mathbf{C} + \nabla\beta \times \nabla \times \mathbf{C} \\ &\quad + (\mathbf{C} \cdot \nabla)\nabla\beta + (\nabla\beta \cdot \nabla)\mathbf{C}\end{aligned}\quad (9.34)$$

and the use of some mathematical operations, (9.33) is reduced to

$$\mathbf{E}(\mathbf{r}) = \frac{\gamma^2}{4\pi j\omega\mu} \int_{C_0} \left\{ \begin{array}{l} [\mathbf{s}' I(s') \cdot \nabla] \nabla g(\mathbf{r}, \mathbf{r}') \\ -\gamma^2 \mathbf{s}' I(s') g(\mathbf{r}, \mathbf{r}') \end{array} \right\} ds' \quad (9.35)$$

Combining (9.28) and (9.35), we have

$$-\mathbf{s} \cdot \mathbf{E}^a = \frac{\gamma^2}{4\pi j\omega\mu} \int_{C_0} I(s') G(\mathbf{r}, \mathbf{r}') ds' \quad (9.36)$$

where  $G(\mathbf{r}, \mathbf{r}')$  is the kernel of integral equation and is related to the Green's function by

$$G(\mathbf{r}, \mathbf{r}') = [(\mathbf{s}' \cdot \nabla)(\nabla \cdot \mathbf{s}) - \gamma^2 \mathbf{s} \cdot \mathbf{s}'] g(\mathbf{r}, \mathbf{r}') \quad (9.37)$$

The numerical solution of (9.37), the EFIE in frequency domain, by the MOM [18] yields the space distribution of current along the antenna at a given frequency.

### 9.3 Numerical treatment

It is more than a century that the analysis of wire antennas has been investigated by researchers [41, 42]. Despite being an old issue, wire antennas are widely used to model a variety of electromagnetic problems, including antenna design, scattering and electromagnetic compatibility. In problems involving antennas, parameters such as current distribution, input impedance, radiation efficiency, gain and radiated field are of great interest, whereas in the modelling of scattering problems, a different set of parameters such as radar cross-section, scattering matrix and scattered field are to be determined. Because of the limitations in the available memory size and processing speed in the case of large structures, high-frequency approximation techniques have been recommended. Examples are geometrical optics, physical optics and geometrical theory of diffraction [43].

Electromagnetic compatibility problems involving lightning RSC, lightning protection systems and grounding systems can be analysed by wire antenna modelling. The main objective in wire antenna modelling is to obtain the current distribution on each wire. In the preceding sections, we have shown that the current on the wire is the kernel of the EFIEs obtained from Maxwell's equations in time or frequency domain. Since there is no closed-form solution for such integral equations, a numerical method is to be employed. Because of the nature of the wire antennas, a numerical method based on the MOM is found to be appropriate. For transient studies, the time-domain MOM is preferred [44, 45], whereas the frequency-domain technique is more appropriate for narrow-band frequency analyses [46].

In the following sections, we first outline the steps required to implement the MOM for solving integral equations. We then present necessary formulations for treating time-domain and frequency-domain problems. Finally, we describe how a lossy ground is treated.

#### 9.3.1 Method of moments

The use of MOM for solving electromagnetic problems was first introduced by Richmond in 1965 [47] and later extended by Harrington in 1967 [48]. This method, also called method of weighted residuals, is a general solution for a linear-operator equation, i.e.:

$$L(f) = g \quad (9.38)$$

where  $L$  is an integro-differential operator,  $f$  is an unknown function (response) and  $g$  is a known function (excitation).

Solving (9.38) by the MOM generally involves the following steps:

- Extracting an appropriate integral equation.
- Transforming the integro-differential equation into a matrix equation using proper basis and test functions.

- Acquiring the so-called impedance matrix elements.
- Solving the impedance matrix equation and obtaining the unknown quantities.

To this end, the unknown function  $f$  is initially expanded by a set of basis functions  $f_n$ ,  $n = 1, \dots, N$ :

$$f = \sum_{n=1}^N \alpha_n f_n \quad (9.39)$$

Given that the operator  $L$  is linear, the replacement in this series into (9.37) leads to

$$\sum_{n=1}^N \alpha_n L(f_n) = g \quad (9.40)$$

The aim is to obtain the unknown coefficients  $\alpha_n$ , which lead to determine  $f$  in linear-operator equation. Equation (9.40) is an equation with  $N$  unknowns. To ensure a unique solution, one needs to establish  $N$  equations. A set of equations for the coefficients  $\alpha_n$  are then obtained by taking the inner product of (9.38) with a set of test functions  $w_m$ ,  $m = 1, \dots, N$ :

$$\sum_{n=1}^N \alpha_n \langle w_m, L(f_n) \rangle = \langle w_m, g \rangle \quad (9.41)$$

or

$$\begin{pmatrix} \langle w_1, L(f_1) \rangle & \langle w_1, L(f_2) \rangle & \dots & \langle w_1, L(f_N) \rangle \\ \langle w_2, L(f_1) \rangle & \langle w_2, L(f_2) \rangle & \dots & \langle w_2, L(f_N) \rangle \\ \vdots & \vdots & \ddots & \vdots \\ \langle w_N, L(f_1) \rangle & \dots & \dots & \langle w_N, L(f_N) \rangle \end{pmatrix} \begin{pmatrix} \alpha_1 \\ \alpha_2 \\ \vdots \\ \alpha_N \end{pmatrix} = \begin{pmatrix} \langle w_1, g \rangle \\ \langle w_2, g \rangle \\ \vdots \\ \langle w_N, g \rangle \end{pmatrix} \quad (9.42)$$

which can be summarized as follows:

$$[z_{mn}][\alpha_n] = [v_m] \quad (9.43)$$

Here,  $[Z_{mn}]$ ,  $[\alpha_n]$  and  $[v_m]$  are called impedance matrix, coefficient matrix and excitation matrix, respectively. Note that the choice of basis and test functions is very important for an accurate and efficient solution.

### 9.3.2 Time-domain formulation

In this section, we describe how the MOM [34, 45] is used to treat time-domain lightning problems by solving (9.15). In this regard, we first divide the thin wire into  $N$  elementary segments of length  $\Delta_i$ , whereas the time span is divided into  $N_T$

equal steps of length  $\Delta_t$ . Then, a set of rectangular basis functions is defined for expressing the known current in each segment, i.e.:

$$i(s_0, t_0) = \sum_{i=1}^N \sum_{j=1}^{N_T} I_{ij}(s_i'', t_j'') U(s_i'') V(t_j''), \quad (9.44)$$

where  $s_i'' = s_0 - s_i$ ,  $t_i'' = t_0 - t_i$  and

$$U(s_i'') = \begin{cases} 1 & |s_i''| \leq \Delta_i/2 \\ 0 & \text{otherwise} \end{cases} \quad V(t_i'') = \begin{cases} 1 & |t_i''| \leq \Delta_i/2 \\ 0 & \text{otherwise} \end{cases} \quad (9.45)$$

A second-order polynomial representation is used to evaluate  $I_{ij}(s_i'', t_j'')$  and the interpolation is chosen to be Lagrangian:

$$I_{ij}(s_i'', t_j'') = \sum_{l=-1}^{+1} \sum_{m=v}^{v+2} B_{ij}^{(l,m)} I_{i+1,j+1} \quad (9.46)$$

with

$$B_{ij}^{(l,m)} = \prod_{p=-1}^{+1} \prod_{q=v}^{v+2} \frac{(s_\circ - s_{i+p})(t_\circ - t_{j+q})}{(s_{i+1} - s_{i+p})(t_{j+m} - t_{j+q})}$$

$$\begin{cases} v = -1; & \Delta R = \frac{R}{c(t_j - t_{j-1})} > 0.5 \\ v = -2; & \Delta R < 0.5 \end{cases} \quad (9.47)$$

Note that  $I_{i+1,j+m}$  is the current value at the centre of the  $(i + 1)$ th space segment and the  $(j + m)$ th time step.

The next step consists of choosing the test functions in order to obtain a system of linear equations [45]. Here, we use the point matching method, based on Dirac distributions, i.e.:

$$\begin{aligned} \delta(t - t_u) &\quad \text{in the space} \\ \delta(t - t_v) &\quad \text{in the time} \end{aligned} \quad (9.48)$$

Applying the test functions to (9.15), we obtain the following system of linear equations:

$$\begin{bmatrix} z_{11} & \dots & z_{1N} \\ \vdots & \ddots & \vdots \\ z_{N1} & \dots & z_{NN} \end{bmatrix} \begin{bmatrix} I_{1,j} \\ \vdots \\ I_{N,j} \end{bmatrix} = \begin{bmatrix} V_{1,j} \\ \vdots \\ V_{N,j} \end{bmatrix} \times \frac{1}{\Delta_i} \quad (9.49)$$

or equivalently

$$\mathbf{ZI}_j = \mathbf{V}_j \times \frac{1}{\Delta_i} \quad (9.50)$$

where  $\mathbf{Z}$  is called per-unit-length impedance matrix,  $\Delta_i$  is the wire structure segment length,  $\mathbf{I}_j$  is the vector of current distribution at each wire segment  $i(=1, 2, \dots, N)$  at time step  $j (=1, 2, \dots, N_T)$  and  $\mathbf{V}_j$  is the vector of segment voltages at the corresponding time step.

For convenience, we use the electric fields of each segment instead of voltage:

$$\mathbf{E}_j^{\text{total}} = \mathbf{E}_j^a + \mathbf{E}_j = \mathbf{Z}\mathbf{I}_j, \quad (9.51)$$

As stated earlier,  $\mathbf{Z}$  is a spatial-temporal matrix related to the structure that is generated considering the electromagnetic interaction between segments. Matrix  $\mathbf{Z}$  also expresses the relation between the current and the total fields for the structure, which is time invariant only if the shape of the structure remains unchanged during computations.

In the case where the segments are loaded with additional elements, (9.50) should be updated as follows:

$$\mathbf{E}_j^{\text{total}} = \mathbf{Z}\mathbf{I}_j + \mathbf{E}_j^{\text{Load}} = (\mathbf{Z}\mathbf{I}_j + \mathbf{Z}_j^{\text{Load}}\mathbf{I}_j) = (\mathbf{Z} + \mathbf{Z}_j^{\text{Load}})\mathbf{I}_j \quad (9.52)$$

where  $\mathbf{Z}_j^{\text{Load}}$  describes the effect of the segment loads in time step  $j$ . For resistive loading, the values of segment resistive loads are added to diagonal elements of the  $\mathbf{Z}$  matrix. Regarding the voltage-current relation of an inductor in series with a resistor, additional tangential electric field due to inductive load at segment  $i$  at time step  $j$  can be discretized using the classical backward finite difference approximation as follows [27]:

$$E_{i,j}^R = \frac{V_{i,j}^R}{\Delta i} = \frac{1}{\Delta i} R_i I_{i,j} = \frac{1}{\Delta i} (R_i^F + R_{i,j-1}^N) I_{i,j} \quad (9.53)$$

$$E_{i,j}^L = \frac{V_{i,j}^L}{\Delta i} = \frac{1}{\Delta i} L_i \frac{dI_{i,j}}{dt} = \frac{L_i}{\Delta i} \frac{3}{2\Delta t} I_{i,j} + \frac{L_i}{\Delta i} \left\{ \frac{1}{2\Delta t} I_{i,j-2} - \frac{2}{\Delta t} I_{i,j-1} \right\} \quad (9.54)$$

where  $R_i^F$  is a fixed resistance,  $R_{i,j-1}^N$  is a non-linear resistance being a function of current,  $I_{i,j-1}$ , and time,  $(j-1)\Delta t$ , and  $L_i$  is a fixed inductance all calculated in segment  $i$ , respectively;  $\Delta t$  is the duration of time interval  $j$ ,  $\Delta i$  is the segment length and  $I_{i,j}$  denotes the current in segment  $i$  at time step  $j$ .

We can now separate  $\mathbf{E}_j^{\text{Load}}$  into two parts, namely  $E_{i,j}^{\text{Load}_1}$  for unknown part as [27]

$$E_{i,j}^{\text{Load}_1} = \frac{V_{i,j}^{L_1}}{\Delta i} = \left\{ \frac{R_i^F}{\Delta i} + \frac{R_{i,j-1}^N}{\Delta i} + \frac{L_i}{\Delta i} \frac{3}{2\Delta t} \right\} I_{i,j} = Z_{ii}^{\text{Load}_1} I_{i,j} \quad (9.53a)$$

and  $E_{i,j}^{\text{Load}_2}$  for known part (available at time step  $j$ ) as

$$E_{i,j}^{\text{Load}_2} = \frac{V_{i,j}^{L_2}}{\Delta i} = \frac{1}{\Delta i} \left\{ \frac{L_i}{2\Delta t} I_{i,j-2} - \frac{2L_i}{\Delta t} I_{i,j-1} \right\} = E_{i,j}^{\text{addLoad}} \quad (9.54a)$$

Substituting (9.53a) and (9.54a) in (9.52) leads to the matrix form of the discretized EFIE, i.e.:

$$\mathbf{E}_j^{\text{scattered}} + \mathbf{E}_j^{\text{incident}} - \mathbf{E}_j^{\text{addLoad}} = (\mathbf{Z} + \mathbf{Z}_j^{\text{Load}_1})\mathbf{I}_j \quad (9.55)$$

When the thin-wire is not loaded or when it is loaded with static elements such as resistors, inductors or capacitors rather than with dynamic elements, the impedance matrix is not a time-dependent matrix and, hence, one needs to invert it once in a whole time-domain solution and then use the inverted matrix at each time step to obtain the corresponding solution. As stated earlier, the effect of these types of loads only results in modification of the diagonal or semi-diagonal elements of the impedance matrix. However, for the case of dynamic non-linear load, the impedance matrix is a time-dependent matrix and thus must be inverted at each time step, introducing an inevitable computational cost [49].

### 9.3.3 Frequency-domain formulation

To solve the governing EFIE (9.36) for longitudinal current distribution on the wire,  $I(s)$ , it is expanded in a finite series of  $N$  overlapped sinusoidal and additional sinusoidal monopole at the injection point, as depicted in Figure 9.4:

$$I(s) = \sum_{k=0}^N I_k F_k(s) \quad (9.56)$$

where  $I_k$  are the unknowns to be determined,  $s$  is the distance along the wire and  $F_k(s)$  are the normalized sinusoidal currents over the length of one dipole or injection monopole, expressed as follows [21]:

$$F_k(s) = \frac{P_{k1}(s) \sinh \gamma(s - s_{k1})}{\sinh \gamma d_{k1}} + \frac{P_{k2}(s) \sinh \gamma(s_{k3} - s)}{\sinh \gamma d_{k2}} \quad (9.57)$$

$$P_{k1}(s) = \begin{cases} 1, & s_{k1} \leq s \leq s_{k2} \\ 0, & \text{elsewhere} \end{cases}, \quad P_{k2}(s) = \begin{cases} 1, & s_{k2} \leq s \leq s_{k3} \\ 0, & \text{elsewhere} \end{cases}$$

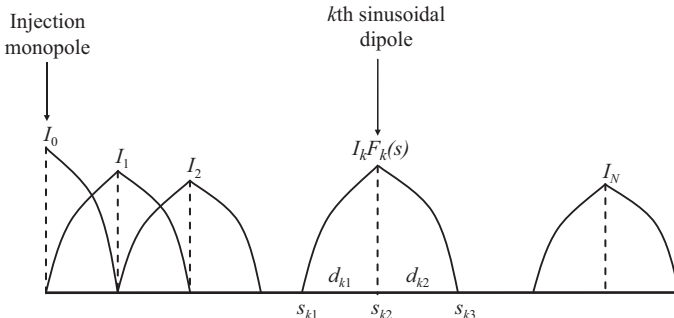


Figure 9.4 Sinusoidal current expansion

where for the  $k$ th dipole,  $s_{k2}$  is the mid (terminal) point;  $s_{k1}, s_{k3}$  are the end points ( $k = 1, 2, \dots, N$ ), and  $d_{k1}, d_{k2}$  are the dipole-arm lengths. For the injection monopole ( $k = 0$ ), only the second term of (9.54) is used.

Applying (9.56) and (9.57) to (9.36) and using the Galerkin method [21], one can obtain a system of  $N$  linear algebraic equations of the form  $\mathbf{ZI} = \mathbf{V}$ , where  $\mathbf{I}$  is the current vector to be solved for,  $\mathbf{V}$  is the excitation vector and  $\mathbf{Z}$  is the impedance matrix. Evaluating the elements of  $\mathbf{Z}$  and  $\mathbf{V}$  requires numerical double integrations. To increase computation efficiency and accuracy, it is desirable, when possible, to replace numerical integrations with appropriate analytic expressions. Such an alternative exists only for the sinusoidal current expansion [21] whose near-field expressions are available in rigorous form. Rigorous field expressions of a sinusoidal monopole in cylindrical coordinate system (see Figure 9.5) are given below [21]:

$$E_\rho = \frac{\gamma}{\rho(\sigma + j\omega\epsilon)} \frac{1}{4\pi \sinh \gamma d} \begin{bmatrix} (I_1 e^{-\gamma R_1} - I_2 e^{-\gamma R_2}) \sinh \gamma d \\ +(I_1 \cosh \gamma d - I_2) e^{-\gamma R_1} \cos \theta_1 \\ +(I_2 \cosh \gamma d - I_1) e^{-\gamma R_2} \cos \theta_2 \end{bmatrix} \quad (9.58)$$

$$E_\varphi = \frac{\gamma}{(\sigma + j\omega\epsilon)} \frac{1}{4\pi \sinh \gamma d} \begin{bmatrix} (I_1 - I_2 \cosh \gamma d) \frac{e^{-\gamma R_2}}{R_2} \\ +(I_2 - I_1 \cosh \gamma d) \frac{e^{-\gamma R_1}}{R_1} \end{bmatrix} \quad (9.59)$$

$$H_\varphi = \frac{1}{4\pi \rho \sinh \gamma d} \begin{bmatrix} (I_1 \sinh \gamma d \cos \theta_1 + I_1 \cosh \gamma d - I_2) e^{-\gamma R_1} \\ -(I_2 \sinh \gamma d \cos \theta_2 - I_2 \cosh \gamma d + I_1) e^{-\gamma R_2} \end{bmatrix} \quad (9.60)$$

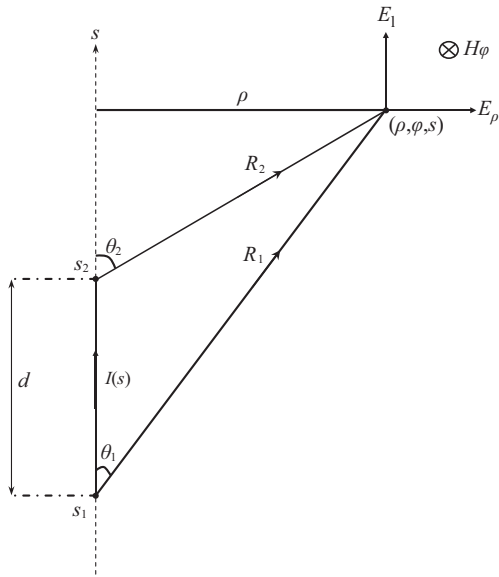


Figure 9.5 The geometry of sinusoidal monopole and its electromagnetic fields

where  $I_1$  and  $I_2$  are the values of monopole current,  $I(s)$ , at  $s_1$  and  $s_2$ , respectively:

$$I(s) = \frac{I_1 \sinh \gamma(s_2 - s) + I_2 \sinh \gamma(s - s_1)}{\sinh \gamma d} \quad (9.60)$$

Other quantities are depicted in Figure 9.5. Using these field components, one can replace the inner integrals for  $\mathbf{Z}$  and  $\mathbf{V}$  by their analytic expressions.

To show the advantages of the current-source excitation, we first consider the voltage source case. In this latter case [13, 21, 27], the source voltage,  $V(f)$ , is obtained as follows:

$$V(f) = Z_{in}(f) \cdot I(f) \quad (9.61)$$

where  $Z_{in}(f)$  is the input impedance of the wire antenna and  $I(f)$  is the Fourier transform of the specified channel-base current. Once the exciting voltage is obtained, it can be used in the following  $(N + 1) \times (N + 1)$  linear matrix equation to obtain the current distribution:

$$\begin{pmatrix} z_{00} & z_{01} & \dots & z_{0N} \\ z_{10} & z_{11} & \dots & z_{1N} \\ \vdots & \vdots & \ddots & \vdots \\ z_{N0} & z_{N1} & \dots & z_{NN} \end{pmatrix} \begin{pmatrix} I_0 \\ I_1 \\ \vdots \\ I_N \end{pmatrix} = \begin{pmatrix} V(f) \\ 0 \\ \vdots \\ 0 \end{pmatrix} \quad (9.62)$$

The input impedance calculation increases the computation time and may introduce an additional error in the solution. In this study, we use a current source to excite the wire antenna, so that (9.62) reduces to

$$\begin{pmatrix} z_{00} & z_{01} & \dots & z_{0N} \\ z_{10} & z_{11} & \dots & z_{1N} \\ \vdots & \vdots & \ddots & \vdots \\ z_{N0} & z_{N1} & \dots & z_{NN} \end{pmatrix} \begin{pmatrix} I_0 \\ I_1 \\ \vdots \\ I_N \end{pmatrix} = \begin{pmatrix} 0 \\ 0 \\ \vdots \\ 0 \end{pmatrix} \quad (9.63)$$

where  $I_0$  is determined by the current source. In this case, there are  $(N + 1)$  equations with  $N$  unknowns. Consequently, (9.63) can be transformed to the following  $N \times N$  linear matrix equation:

$$\begin{pmatrix} z_{11} & z_{12} & \dots & z_{1N} \\ z_{21} & z_{22} & \dots & z_{2N} \\ \vdots & \vdots & \ddots & \vdots \\ z_{N1} & z_{N2} & \dots & z_{NN} \end{pmatrix} \begin{pmatrix} I_1 \\ I_2 \\ \vdots \\ I_N \end{pmatrix} = \begin{pmatrix} -z_{10}I_0 \\ -z_{20}I_0 \\ \vdots \\ -z_{N0}I_0 \end{pmatrix} \quad \text{or} \quad \mathbf{ZI} = \mathbf{V} \quad (9.64)$$

where  $z_{mn}$  ( $m, n = 1, 2, \dots, N$ ) are the mutual impedances between the sinusoidal dipoles defined as follows:

$$z_{mn} = \int_m F_m(s) E_n^t(s) ds \quad (9.65)$$

and  $z_{m0}$  ( $m = 1, 2, \dots, N$ ) are the mutual impedances between the injection monopole and sinusoidal dipoles given below:

$$z_{m0} = \int_m F_m(s) E_0^t(s) ds \quad (9.66)$$

where  $E_n^t(s)$  ( $n = 1, 2, \dots, N$ ) and  $E_0^t(s)$  are, respectively, the electric fields tangential to the wire surface due to the  $n$ th dipole (basis function) and the injection monopole. Also,  $F_m(s)$  is the  $m$ th test dipole and integrations are carried out over its length.

In the case that it is necessary to include distributed resistance,  $R_D$ , along the wire antenna, leading to the new impedance matrix given below [21]:

$$Z_{mn} = z_{mn} - R_D \underbrace{\int_m F_m(s) H_n^q(s) ds}_{z'_{mn}} \quad (9.67)$$

where  $H_n^q(s)$  is the azimuthal magnetic field due to the  $n$ th dipole, and  $z'_{mn}$  is the contribution from the distributed resistance. The introduction of distributed resistance requires modification of only diagonal and semi-diagonal elements in the impedance matrix [50]. Also, the limits of integral in the expression for  $z'_{mn}$  extend over two-wire segments in the domain of test dipole  $F_m(s)$ .

Utilizing simplifying approximations, one can obtain [35]:

$$H_n^q = \frac{F_n(s)}{2\pi a} \quad (9.68)$$

Hence:

$$z'_{mn} = \frac{R_D}{2\pi a} \int_{m,n} F_n(s) F_m(s) ds \quad (9.69)$$

where  $a$  is the radius of wire antenna and region  $(m, n)$  is the wire surface shared by dipoles  $m$  and  $n$ . The expression for  $z'_{mn}$  reduces to [21]

$$z'_{mn} = \begin{cases} \frac{R_D}{4\pi\gamma a} \frac{\sinh(2\gamma d) - 2\gamma d}{\sinh^2(\gamma d)} & \text{if } (m = n) \\ \frac{R_D}{4\pi\gamma a} \frac{\gamma d \cosh(\gamma d) - \sinh(\gamma d)}{\sinh^2(\gamma d)} & \text{if } (m = n \pm 1) \\ 0 & \text{elsewhere} \end{cases} \quad (9.70)$$

### 9.3.4 Lossy half-space problem

So far, we have assumed that the ground is a perfect conductor. In this section, we describe how a lossy ground is treated in wire-antenna modelling. Figure 9.6 schematically shows a lightning channel above a lossy half-space. The thin-wire model of lightning channel can be considered as the superposition of infinitesimal dipoles. Electromagnetic radiation of a dipole above a lossy half-space has been first investigated by Sommerfeld [51]. The approach involves semi-infinite integrals of Bessel functions that are characterized by highly oscillatory and weakly damping behaviour. For very close observation points, various approximations have been proposed. In this chapter, when evaluating elements of  $\mathbf{Z}$  and  $\mathbf{V}$  matrices in (9.64) for each sinusoidal dipole, its modified image is also included. Modified image theory was first introduced in Reference 52. As an illustration of this simple theory, consider a point current source placed in a dielectric medium above the interface of a lossy half-space (see Figure 9.6). The field in the upper half-space, medium one, is the superposition of contributions from the original source and its mirror image multiplied by a correction factor  $\alpha_{11}$ , and the field in the lower half-space, medium two, is due to the original source multiplied by a correction factor  $\alpha_{12}$ . Applying the boundary conditions at the interface (i.e. the

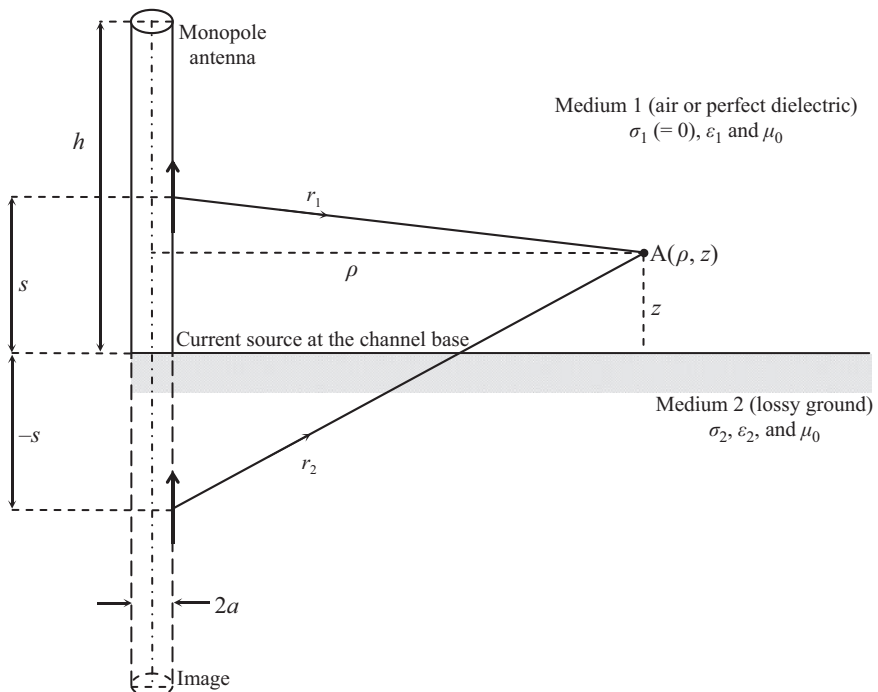


Figure 9.6 Lightning channel above a lossy half-space

continuity of tangential electric field vector and scalar potential), one can obtain correction factors given below [52]:

$$\alpha_{11} = \frac{j\omega\epsilon_1 - (\sigma_2 + j\omega\epsilon_2)}{j\omega\epsilon_1 + (\sigma_2 + j\omega\epsilon_2)}; \quad \alpha_{12} = \frac{2(\sigma_2 + j\omega\epsilon_2)}{j\omega\epsilon_1 + (\sigma_2 + j\omega\epsilon_2)} \quad (9.71)$$

Once  $\mathbf{Z}$  and  $\mathbf{V}$  are known,  $\mathbf{I}$  can be determined from (9.64) utilizing a suitable solution of linear algebraic equations. The resultant current distribution can be used to calculate various field components in air. Since surface waves become significant as the observation point is moved farther from the source, the modified image theory is not applicable to distant field calculations. Thus, a different treatment is necessary. An accurate solution of this problem requires the time-consuming evaluation of Sommerfeld integrals. For the situation examined here (the magnitude of ground's complex wave number is much greater than that of free space), these integrals can be represented by closed-form expressions. In this regard, King [53] derived the complete expressions for electromagnetic fields of a vertical electric dipole over an imperfectly conducting (lossy) half-space. Also, King and Sandler [54] verified the suitability of these expressions for a dipole above certain types of lower half-space. The complete electromagnetic field expressions for a vertical straight wire antenna of length  $L$  above a lossy half-space in air (i.e.  $\epsilon_1 = \epsilon_0$  in Figure 9.6) are reproduced below:

$$H_{ap}(\rho, z, j\omega) = \int_{C_0} \frac{I(s)}{2\pi} \left[ \frac{e^{-\gamma_1 r_1}}{2} \left( \frac{\rho}{r_1} \right) \left( \frac{1 + \gamma_1 r_1}{r_1^2} \right) + \frac{e^{-\gamma_1 r_2}}{2} \left( \frac{\rho}{r_2} \right) \left( \frac{1 + \gamma_1 r_2}{r_2^2} \right) - e^{-\gamma_1 r_2} \left( \frac{\gamma_1^3}{\gamma_2} \right) \left( \frac{\pi}{j\gamma_1 \gamma_2} \right)^{1/2} e^{-jP} F(P) \right] ds \quad (9.72)$$

$$E_{ap}(\rho, z, j\omega) = \frac{j\omega\mu_0}{2\pi\gamma_1} \int_{C_0} I(s) \left\{ \frac{e^{-\gamma_1 r_1}}{2} \left( \frac{\rho}{r_1} \right) \left( \frac{z-s}{r_1} \right) \left( \frac{3 + 3\gamma_1 r_1 + \gamma_1^2 r_1^2}{\gamma_1 r_1^3} \right) + \frac{e^{-\gamma_1 r_2}}{2} \left( \frac{\rho}{r_2} \right) \left( \frac{z+s}{r_2} \right) \left( \frac{3 + 3\gamma_1 r_2 + \gamma_1^2 r_2^2}{\gamma_1 r_2^3} \right) + \frac{\gamma_1}{\gamma_2} e^{-\gamma_1 r_2} \left[ - \left( \frac{\rho}{r_2} \right) \left( \frac{1 + \gamma_1 r_2}{r_2^2} \right) + \frac{\gamma_1^3}{\gamma_2} \left( \frac{\pi}{j\gamma_1 \gamma_2} \right)^{1/2} e^{-jP} F(P) \right] \right\} ds \quad (9.73)$$

$$\begin{aligned}
E_{az}(\rho, z, j\omega) = & \frac{j\omega\mu_0}{2\pi\gamma_1} \int_{C_0} I(s) \left\{ \frac{e^{-\gamma_1 r_1}}{2\gamma_1 r_1^3} \left[ (1 + \gamma_1 r_1 + \gamma_1^2 r_1^2) - \left( \frac{z-s}{r_1} \right)^2 (3 + 3\gamma_1 r_1 + \gamma_1^2 r_1^2) \right] \right. \\
& + \frac{e^{-\gamma_1 r_2}}{2\gamma_1 r_2^3} \left[ (1 + \gamma_1 r_2 + \gamma_1^2 r_2^2) - \left( \frac{z+s}{r_2} \right)^2 (3 + 3\gamma_1 r_2 + \gamma_1^2 r_2^2) \right] \\
& \left. - e^{-\gamma_1 r_2} \left( \frac{\gamma_1^3}{\gamma_2} \right) \left( \frac{\pi}{j\gamma_1 \gamma_2} \right)^{1/2} \left( \frac{\rho}{r_2} \right) e^{-jP} F(P) \right\} ds
\end{aligned} \tag{9.74}$$

where subscript *a* denotes observation points in air,  $\omega$  is the angular frequency,  $(\rho, \varphi, z)$  is the cylindrical coordinate system. Also:

$$\gamma_1 = j\omega\sqrt{\mu_0\varepsilon_0}; \quad \gamma_2 = \sqrt{j\omega\mu_0(\sigma_2 + j\omega\varepsilon_2)} \tag{9.75}$$

where  $\varepsilon_0$  and  $\mu_0$  are free space permittivity and permeability, respectively.

$$r_1 = \sqrt{\rho^2 + (z-s)^2}; \quad r_2 = \sqrt{\rho^2 + (z+s)^2} \tag{9.76}$$

$$P = j \frac{\gamma_1^3 r_2}{2\gamma_2^2} \left[ \frac{\gamma_1 r_2 + \gamma_2(z+s)}{\gamma_1 \rho} \right]^2 \tag{9.77}$$

$$F(P) = \frac{1}{\sqrt{2\pi}} \int_p^\infty \frac{e^{jz}}{\sqrt{z}} dz = \frac{1}{2} (1+j) - C_2(P) - jS_2(P) \tag{9.78}$$

where  $C_2(P)$  and  $S_2(P)$  are, respectively, the Fresnel cosine and sine integrals of complex argument expressed as [55]:

$$C_2(P) = \frac{1}{\sqrt{2\pi}} \int_0^P \frac{\cos z}{\sqrt{z}} dz; \quad S_2(P) = \frac{1}{\sqrt{2\pi}} \int_0^P \frac{\sin z}{\sqrt{z}} dz \tag{9.79}$$

Equations (9.72)–(9.74) are accurate everywhere in air or on the air–ground interface provided that the following single condition is satisfied [21]:

$$|\gamma_2|^2 \gg |\gamma_1|^2 \quad \text{or} \quad |\gamma_2| \geq 3|\gamma_1| \tag{9.80}$$

Each of the field expressions (9.72)–(9.74) contains three terms: a term in  $r_1$ , which is the direct wave from the source dipole, a similar term in  $r_2$ , which is the reflected wave from the image dipole, and a term containing Fresnel integrals, which is the surface or lateral wave. This surface wave is defined as the total field

minus the perfect-ground approximation (geometrical optics field), as opposed to the Zenneck surface wave (ZSW), which never exists as the sole contribution for the ground wave from a localized source [56]. Our surface wave might be considered as the Norton surface wave (NSW) [57, 58]. One can readily observe that these field expressions reduce to those assuming the perfect-ground approximation when only the first two terms of each expression are considered.

Under the condition of  $|P| \geq 4$  (e.g. at far observation points [21]), the Fresnel integrals have asymptotic expansions that allow one to simplify the field expressions. Specifically:

$$\frac{\gamma_1^3}{\gamma_2} \left( \frac{\pi}{j\gamma_1 r_2} \right)^{1/2} e^{-jP} F(P) \xrightarrow{|P| \geq 4} \frac{\gamma_1^3}{\gamma_2} \left( \frac{\pi}{j\gamma_1 r_2} \right)^{1/2} \frac{1}{(2\pi P)^{1/2}} \left( \frac{1}{2P} + j \right) \quad (9.81)$$

$$\frac{\gamma_1^3}{\gamma_2} \left( \frac{\pi}{j\gamma_1 r_2} \right)^{1/2} e^{-jP} F(P) \xrightarrow{|P| \geq 4} \frac{\gamma_1^3}{\gamma_2} \left( \frac{\pi}{j\gamma_1 r_2} \right)^{1/2} \frac{1}{(2\pi P)^{1/2}} \left( \frac{1}{2P} + j \right) \quad (9.82)$$

While most of the conventional methods [59, 60] use different treatments for the two components of electric field, the simple closed-form electric field expressions (9.73) and (9.74) employed here are parts of the same solution. It can be shown that the Cooray–Rubinstein formula for the horizontal electric field component is a special case of equation (9.73) when the Fresnel term is neglected. Also, the magnetic field component given by (9.72) is obtained using the same methodology [21].

## 9.4 Various AT models

The expression ‘lightning return-stroke model’ is generally used to describe a specification of the time- and height-dependent current in the RSC to make possible the calculation of resultant remote electromagnetic fields [1]. Most of the return-stroke models specify an analytical relation between the current at each point of the channel and the channel-base (ground level) current. Such an analytical relation also describes the propagation of the current wave along the channel.

In the AT model, the lightning RSC is represented by a vertical, monopole antenna above a conducting ground. The antenna is fed at its lower end by a source whose voltage is determined using the assumed antenna input current waveform. The distribution of current along the antenna is determined by applying the boundary condition for the tangential component of electric field on the surface of the antenna. The solution is found numerically, using the MOM. The resultant distribution of current along the antenna is allowed to radiate into free space.

In this section, various time- and frequency-domain models of RSC, based on antenna theory, i.e. on a complete solution of Maxwell’s equations, are presented and used to obtain the channel current and charge density profiles.

### 9.4.1 Time-domain AT model

As mentioned earlier, in the AT model, the antenna representing the RSC is fed at its lower end by a source that launches a current wave along the antenna. In fact, the source radiates electromagnetic fields into a non-conducting medium whose electrical permittivity is selected such that the wave propagates at a specified speed (lower than the speed of light). The artificial change of permittivity is used to account for the effect of corona on the wave propagation speed.

The distribution of current along the antenna is determined by applying the boundary condition for the tangential component of electric field on the surface of the antenna. The solution is found numerically, using the MOM, with ohmic losses in the antenna being taken into account by introducing the resistive loading  $R$  (series resistance per unit length). The evolution of the current and charge along the channel is described by Maxwell's equations. In order to compare 'engineering' models with the AT model quantitatively, we need to use the same input current in all the models. This means that the voltage source for the monopole antenna should produce the same current as the channel-base current assumed in the 'engineering' models. The voltage of the source is given by the following equation:

$$v(t) = \mathbf{F}^{-1}[Z(f) \cdot I(0,f)] \quad (9.83)$$

where  $I(0,f)$  is the Fourier transform of the specified channel-base current,  $Z(f)$  is the input impedance of the lossy monopole antenna and  $\mathbf{F}^{-1}$  denotes the inverse Fourier transform. The input impedance of the monopole antenna, which is a function of its length and distributed resistance, is calculated applying the MOM to the EFIE. To find the input impedance of the monopole antenna, a modulated Gaussian waveform, shown in Figure 9.7, was used. Figure 9.8 depicts this waveform in frequency domain. Using (9.16) and solving the EFIE (9.15) by the MOM,

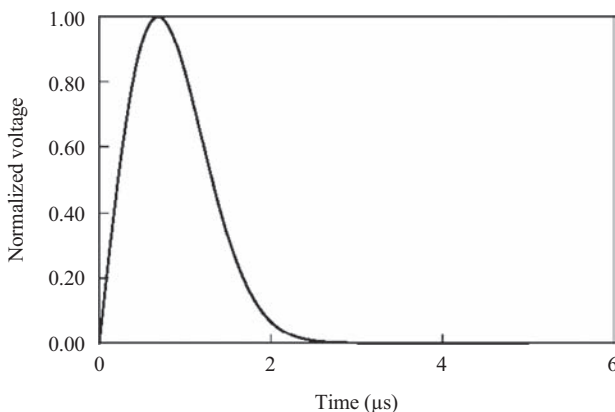
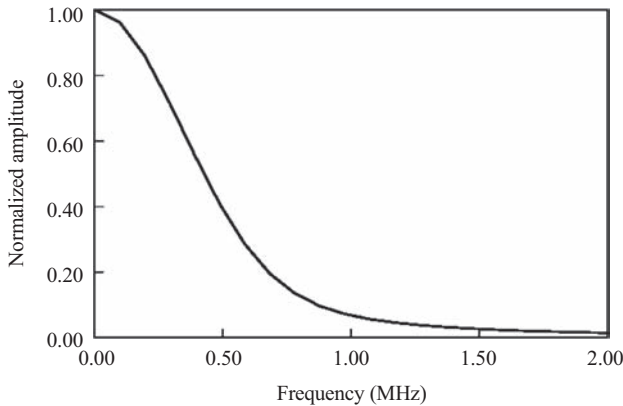
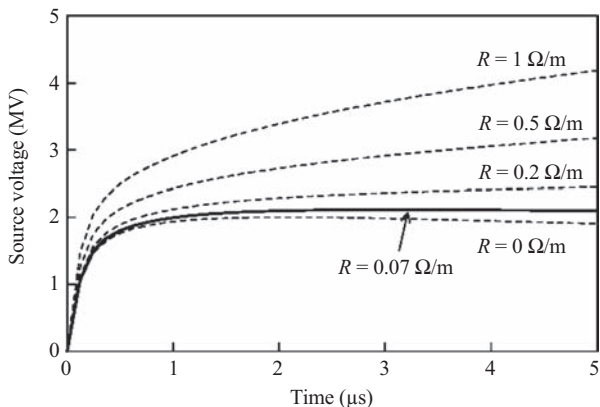


Figure 9.7 Normalized modulated Gaussian waveform in the time domain which has been used as a source voltage to calculate the input impedance of the monopole antenna [adapted from Moini et al. [13]]



*Figure 9.8 Normalized amplitude of the modulated Gaussian waveform in the frequency domain corresponding to the time domain waveform shown in Figure 9.7 [adapted from Moini et al. [13]]*



*Figure 9.9 Calculated source voltage waveform corresponding to the channel-base current for different values of the resistance per unit channel length [adapted from Moini et al. [13]]*

which allowed to include resistive loading, we obtained the input current of the monopole antenna corresponding to the modulated Gaussian voltage waveform. The input impedance of the antenna is then found by dividing the input voltage by the input current in the frequency domain. Figure 9.9 shows the source voltage, found using the computed input impedance and specified current at the channel base, for different values of resistance  $R$  per unit length. The waveform of the source voltage is almost independent of  $R$  during the first tenths of microseconds. The value of  $R = 0.07 \Omega/m$  has been selected for the calculations presented in this chapter, since this value provides the best agreement between model-predicted and

observed electric field waveforms at close (tens of metres) ranges. Interestingly, Rakov [61] estimated the resistance per unit channel length to be  $0.035 \Omega/\text{m}$  behind the return-stroke front.

Once the voltage  $v(t)$  of the source is determined, the corresponding applied electric field  $e^a$ , to be substituted in (9.15), is estimated as the ratio of this voltage and the length  $\Delta z$  of the excitation (source) segment of the antenna.

To reduce the propagation speed of the current wave in the AT model to a value consistent with observations,  $\nu < 3 \times 10^8 \text{ m/s}$ , we use  $\varepsilon > \varepsilon_0$  in calculating the current variation along the channel, and then use that current distribution to calculate the electromagnetic fields radiated by the antenna in free space ( $\varepsilon = \varepsilon_0$ ). The arbitrary increase in  $\varepsilon$  in determining the channel current distribution serves to account for the fact that channel charge is predominantly stored in the radial corona sheath whose radius is much larger than that of the channel core that carries the longitudinal channel current, resulting in  $\nu < 3 \times 10^8 \text{ m/s}$ . This simulates an increase of shunt capacitance per unit antenna length due to corona. The use of  $\varepsilon > \varepsilon_0$  additionally introduces the effect of radiation into the fictitious medium, but the resultant current distribution along the channel is unlikely to differ significantly from the case of no such effect (the transmission line current is expected to dwarf the antenna current). An alternative approach to modelling corona effect on propagation speed would be to introduce capacitive antenna loading. Ohmic losses in the antenna further reduce  $\nu$ , but for the selected value of resistance per unit length, this additional reduction in  $\nu$  is expected to be relatively small. In the AT model, there are only two parameters to be adjusted, the propagation speed  $\nu$  for the case of non-resistive antenna and the value of distributed resistance  $R$ . The value of resistance per unit length was selected (by trial and error) to provide an agreement between model-predicted and measured electric fields at close distances. It was assumed for the AT model that  $R = 0.07 \Omega/\text{m}$  and that  $\nu = 1.3 \times 10^8 \text{ m/s}$ , which corresponds to  $\varepsilon_r = 5.3$ . As stated above, the spatial and temporal distribution of current along the antenna was determined solving the EFIE (9.15) using MOM.

In Section 9.5, we compare the AT model with other models in terms of (a) spatial and temporal current distribution, (b) line charge density distribution and (c) remote electromagnetic fields. In doing so, we assume the same lightning channel-base current waveform as that used by Nucci *et al.* [62], Rakov and Dulzon [63] and Thottappillil *et al.* [64]. This waveform is depicted in Figure 9.10.

#### 9.4.2 Time-domain AT model with inductive loading

In the AT model, the assumption of  $\varepsilon_r > 1$  was only used to find the current distribution along the channel, which was then allowed to radiate into free space with  $\varepsilon_r = 1$  [27]. However, even the current distribution along the channel can be potentially influenced to some (presumably small) extent by the unrealistic assumption  $\varepsilon_r > 1$ .

In the ATIL model, a modification is made in the original AT model [13] to include inductive loading of the channel in order to avoid the unrealistic assumption of higher permittivity of the surrounding medium. In this model, in order to

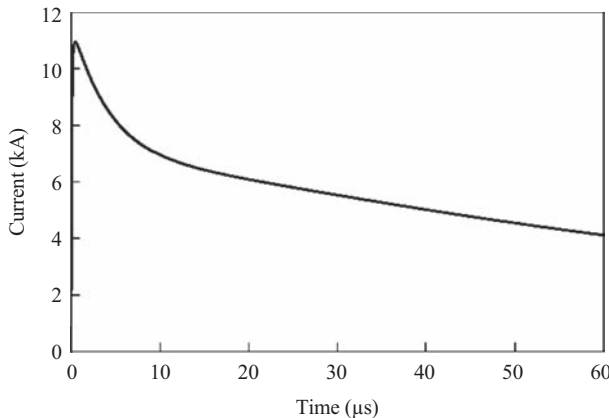


Figure 9.10 Channel-base current waveform used for the comparison of different models. The peak current is about 11 kA, and peak current rate of rise is about 105 kA/μs [adapted from Nucci *et al.* [62]]

control the return-stroke speed, inductive energy-storing elements are included in the antenna representation of the lightning channel, which is a monopole antenna with distributed resistance above a perfectly conducting ground [27]. In fact, the ATIL is a step forward to finding a method to reduce the speed of current waves propagating on a vertical conductor in air, such that the evolution of wave shape is consistent with optical observations of lightning.

The use of energy-storing elements in the antenna and transmission line studies has been previously described in a number of works. Induction phenomenon in solving electrical circuits using the time-domain EFIE was studied by Bost *et al.* [65]. Guedira [66] applied local inductive and capacitive loads to the feeding point of a dipole antenna and determined resultant antenna currents. The additional distributed capacitance has been used to describe the effect of corona on transmission lines [67]. Applying shunt distributed capacitive loads, representing the radial corona sheath, to an antenna introduces some difficulties, as discussed by Bonyadi-Ram *et al.* [30]. One difficulty is related to the fact that distributed shunt capacitors require a return conductor parallel to the antenna, which turns the monopole antenna to a transmission line. Since the phase velocity is a function of the product of the inductance and capacitance (each per unit length), appropriately selected series distributed inductance can be used, instead of distributed shunt capacitance, to simulate the corona effect on the propagation speed [26].

An unloaded horizontal, perfectly conducting wire above perfectly conducting ground behaves as a lossless uniform transmission line, and propagation speed along the wire is constant and equal to the speed of light,  $c = 1/\sqrt{L_0 C_0}$ , where  $L_0$  and  $C_0$  are per unit length inductance and capacitance, respectively. Strictly speaking, this speed is not applicable to a vertical monopole antenna and its image because the per unit length capacitance and inductance of such an antenna vary with height. As a result, the equivalent transmission line is non-uniform and the

propagation speed is slightly lower than the speed of light. Further, in the case of lightning, the speed is reduced (typically by a factor of two or three) relative to the speed of light due to the presence of corona sheath and transformation of the leader channel to the RSC. Also, as noted above, the optically observed speed decreases with increasing height (we do not consider here the non-monotonic variation of speed with height reported by Olsen *et al.* [68]). The bottom line here is that considering the lightning channel as a vertical wire above ground with its intrinsic capacitance and inductance per unit length does not allow one to reproduce observed lightning return-stroke speed profiles.

If we introduce an additional, height-variable distributed inductance along the antenna without any resistive loading, the resultant height variable propagation speed along the simulated lightning channel will be given by

$$\nu(z) = \frac{1}{\sqrt{L'(z) \cdot C_0(z)}} = \frac{1}{\sqrt{(L_0(z) + L^{\text{add}}(z)) \cdot C_0(z)}} \quad (9.84)$$

where  $L^{\text{add}}(z)$  is the additional height-dependent distributed inductance per unit length. As a result, for a specified height-variable speed,  $\nu(z)$ ,  $L^{\text{add}}(z)$  is given by

$$L^{\text{add}}(z) = \frac{1}{v^2(z) \cdot C_0(z)} - L_0(z) \quad (9.85)$$

The capacitance,  $C_0$ , and inductance,  $L_0$ , per unit length for a cylindrical metallic wire of radius  $a$  can be estimated using the following equations given by Kodali *et al.* [69]:

$$C_0(z) = \frac{2\pi\epsilon_0}{\ln(2z/a)} \text{ (F/m)} \quad (9.86)$$

$$L_0(z) = \frac{\mu_0}{2\pi} \ln(2z/a) \text{ (H/m)} \quad (9.87)$$

where  $z$  is the height above ground. Applicability of these equations, derived for a horizontal wire above ground, to a vertical conductor is discussed by Kodali *et al.* [69]. Considering typical speed profiles for lightning shows that the values of intrinsic capacitance and inductance of an ideal cylindrical antenna above a perfectly conducting ground given by (9.86) and (9.87) cannot yield the variation of speed as specified by (9.84), and hence an additional height variable reactive element is needed to simulate such a speed profile. Note that additional distributed inductance along the channel has no physical meaning and is invoked only to reduce the speed of current wave to a value lower than the speed of light.

In the following, we will consider two types of inductive loading, namely fixed (uniform) and height-varying (non-uniform). In the ATIL-F model, additional inductance per unit length was selected (by trial and error) to obtain a specified average speed. It turned out that fixed loading results in an almost uniform speed profile (see the numerical results in Section 9.5). For example,  $L^{\text{add}} = 8.0 \times 10^{-6} \text{ H/m}$

results in  $v = 1.3 \times 10^8$  m/s. Interestingly, this value of  $L^{\text{add}}$  is approximately equal to  $L^{\text{add}}$  that is computed from (9.85) using constant values  $C_0$  and  $L_0$  evaluated at  $a = 0.02$  m and  $z = 3500$  m from (9.86) and (9.87), respectively. Note that the values of  $C_0$  and  $L_0$  at  $z = 3500$  m are applied to the entire channel. This is a commonly used simplification (e.g. Reference 69) based on the fact that the dependencies of  $C_0$  and  $L_0$  on  $z$  are weak (logarithmic).

In the ATIL model with variable inductive loading (ATIL-V), a speed profile was chosen to achieve acceptable consistency with the published optical measurements. Optical observations are mainly limited to the visible part of the channel, usually extending from ground to a height of 1–3 km. The return-stroke speed typically decreases by 25% or more over the visible part of the channel with respect to the speed at the bottom of the channel [70]. Here, we use an exponentially decaying speed profile  $v(z)$  that is described by the following equation:

$$v(z) = v_h - (v_h - v_0)e^{-z/\lambda} \quad (9.88)$$

where  $\lambda$  is the decay height constant,  $v_0$  is the propagation speed at the channel base (at ground level) and the final speed at the upper end of the channel (at  $z=h$ ) asymptotically approaches  $v_h$ . Thottappillil and Uman [71] have used a similar relation in the modified Diendorfer–Uman model model in which  $v_h=0$ , i.e. the speed tends to zero at larger altitudes. The use of a non-zero value of  $v_h$  gives us more control of the propagation speed profile, especially in the upper part of the channel. Optical observations have shown that the propagation speed near the bottom of the channel varies between  $c/2$  to  $c/3$  [72] and decreases with height. Here, we computed a speed profile along a 3.5-km lightning RSC using (9.88) with  $\lambda = 450$  m,  $v_0 = 1.6 \times 10^8$  m/s and  $v_h = 0.9 \times 10^8$  m/s. This profile is shown in Figure 9.11.

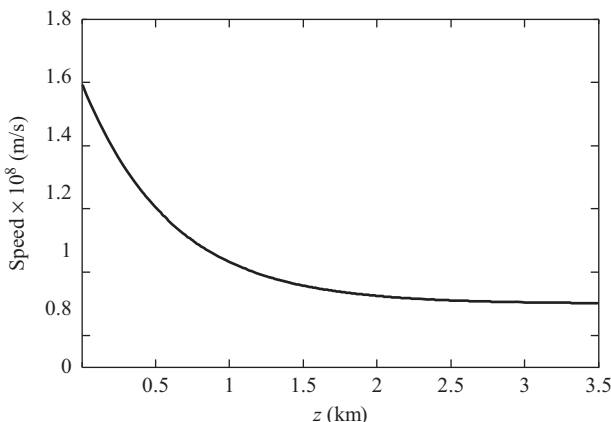


Figure 9.11 Propagation speed as a function of height for the ATIL-V model obtained using (9.88) with  $\lambda = 450$  m,  $v_0 = 1.6 \times 10^8$  m/s and  $v_h = 0.9 \times 10^8$  m/s [adapted from Bonyadi-Ram et al. [30]]

Note that at  $z = 3.5$  km,  $v = 0.9 \times 10^8$  m/s, which is essentially equal to the assumed value of  $v_h$ . It should be noted that there is essentially no limitation on the length of analysed channel. Longer lightning channels could be analysed if the information on speed profile were available. In time-domain methods, the length of analysed channel is limited by duration of analysis. We selected the analysis duration such that the travelling wave will never hit the top of the channel. This is a widely used approach in lightning research [1].

The corresponding additional distributed inductance as a function of height, calculated using (9.85), is depicted in Figure 9.12. The  $L_0(z)$  and  $L^{\text{add}}(z)$  profiles for the ATIL-F model with  $v = 1.3 \times 10^8$  m/s are also shown in Figure 9.12 for comparison.

Let us consider a lightning channel with a height of 3.5 km and radius of 0.02 m above a perfectly conducting ground. The current at the channel base is the same as that used in Section 9.4.1. The inductance per unit length for the ATIL-F model is set to  $L^{\text{add}} = 8.0 \times 10^{-6}$  H/m. Distributed resistance of the channel for the ATIL-F model is  $0.5 \Omega/\text{m}$ , considerably larger than  $0.07 \Omega/\text{m}$  in the AT model. For the AT model,  $\varepsilon_r$  is set to 5.3, while for both versions of the ATIL model,  $\varepsilon_r = 1$ .

For the ATIL-V model, one can use the profile of the distributed inductance shown in Figure 9.12 while setting the distributed resistance to  $0.45 \Omega/\text{m}$ . The reason for using different values of distributed resistance in the AT ( $0.07 \Omega/\text{m}$ ), ATIL-F ( $0.5 \Omega/\text{m}$ ) and ATIL-V ( $0.45 \Omega/\text{m}$ ) models is discussed in Section 9.5. A typical length of each channel segment for all three models is 10 m.

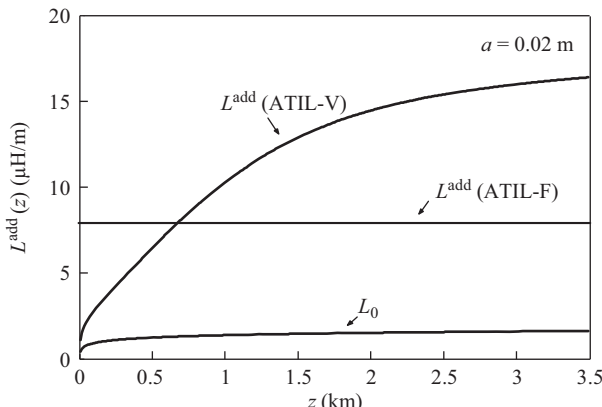


Figure 9.12 Additional distributed inductance per unit length,  $L^{\text{add}}$ , as a function of height for the ATIL-V (computed using (9.85)) and ATIL-F (determined by trial and error) models. The speed profile for the ATIL-V model is shown in Figure 9.11, and the speed for the ATIL-F is  $1.3 \times 10^8$  m/s. Also shown is the intrinsic inductance of the monopole antenna computed using (9.87),  $L_0$ , as a function of height [adapted from Bonyadi-Ram et al. [30]]

### 9.4.3 Time-domain AT model with non-linear loading

The physical models, which are based on gas dynamic models of RSC, predict nonlinearities in the channel parameters, including per unit length inductance, capacitance and resistance [2, 3]. To attain a more realistic model of RSC, attempts were made to include such nonlinearities in the AT modelling. This section describes the modifications made in the ATIL-F model to include non-linear resistive loading in the presence of fixed inductive loading of the channel. Resistive elements are considered as a non-linear distributed load whose resistance is a function of both current and time.

The non-linear ATIL-F model adopts the method proposed by Braginskii, which uses a distribution of non-linear load for representing the non-linear phenomenon occurring during lightning strike to flat grounds [2]. In this method, a strong-shock approximation is used to develop a spark channel model for describing the time variation of such parameters as radius, temperature, pressure and resistance as a function of the input channel current. Initial conditions, that are meant to characterize the channel created by a lightning leader, include temperature (of the order of 10,000 K), channel radius (of the order of 1 mm) and either pressure equal to ambient (1 atm) or mass density equal to ambient (of the order of  $10^{-3}$  g cm $^{-3}$ ), the latter two conditions representing, respectively, the older and the newly created channel sections.

The initial condition assuming ambient pressure probably best represents the upper part of the leader channel since that part has had sufficient time to expand and attain equilibrium with the surrounding atmosphere, whereas the initial condition assuming ambient density is more suitable for the recently created, bottom part of the leader channel. In the latter case, variations in the initial channel radius and initial temperature are claimed to have little influence on model predictions [2, 73]. It is noted that the Braginskii's method assumes, as initial conditions, ambient density and pressure much higher than the surrounding ambient [74].

For a current  $i(t)$  linearly increasing with time  $t$ , the channel radius,  $a(i(t), t)$  can be obtained as follows [2]:

$$a(i(t), t) = 9.35[i(t)]^{1/3}t^{1/2} \quad (9.89)$$

where  $a(i(t), t)$  is in centimetres,  $i(t)$  in amperes and  $t$  in seconds.

In the derivation of (9.89), presumably applicable to the early stages of the discharge, the general expression of the arc channel radius is simplified [75], i.e.:

$$a \approx \sqrt{\left(\frac{4}{\rho_0 \pi^2}\right)^{1/3} \int_0^t (\sigma \xi)^{-1/3} i^{2/3} dt + a_i^2} \quad (9.90)$$

where  $a_i$  is the initial radius in metre,  $\sigma$  is the channel conductivity in S/m,  $\rho_0$  is the ambient atmospheric density in g cm $^{-3}$  and  $\xi$  is a factor describing the rate of radial expansion of the arc channel. This is done by assuming a linearly increasing current, which results in the expansion of the channel radius according to  $a \sim t^{\text{constant}}$ ,  $a_i = 0$ ,  $\xi = 4.5$ ,  $\rho_0 = 1.29 \times 10^{-3}$  g cm $^{-3}$  and  $\sigma = 2.22 \times 10^4$  ( $\Omega \text{ m}$ ) $^{-1}$ .

For a known value of  $a(i(t), t)$ , the resistance per unit channel length can be found as [2]:

$$R(i(t), t) = \frac{1}{\pi \sigma a^2(i(t), t)} \quad (9.91)$$

Equation (9.91) without any other constraints gives very large as well as very small values of resistance; thus, we introduce upper  $R_{max}$  and lower  $R_{min}$  limits. These limits (corresponding to  $a_{min}$  and  $a_{max}$ , respectively) are physical limits and they bring the theoretical estimation closer to the experimental ones. Theoretical estimations give initial and final values of channel radius as 1 and 20 mm, respectively [2, 73]. Experimental estimates give a final channel radius from 10 to 35 mm [76, 77]. To reach a model with realistic results consistent with the experimental data, we assume  $\xi \approx 20$  and  $\sigma = 5 \times 10^3$  S/m. Using these values in (9.89) and (9.91) determine the values of  $a_{min}$  and  $a_{max}$ , and hence, the values of  $R_{max}$  and  $R_{min}$ , as 0.01 and 0.18 m, and 0.6764 and 0.040  $\Omega/m$ , respectively.

Here we need to apply larger distributed resistance than that used in the original AT model. An additional distributed resistance is required for fixing the attenuation constant  $\alpha$  in the same level with that of the AT model. Note that inductive loading forces  $\alpha$  to decrease [27].

The effect of resistive loading on the phase velocity of the propagation can be described using the transmission lines theory. The phase velocity,  $v_\varphi$ , for a transmission line is given by

$$v_\varphi = \frac{\omega}{\beta} \quad (9.92)$$

where  $\omega$  is the angular frequency and  $\beta$  is the phase constant derived from the expression for propagation constant:

$$\gamma = \alpha + j\beta = \sqrt{(R + j\omega L)(G + j\omega C)} \quad (9.93)$$

where  $j = \sqrt{-1}$ , and  $R$ ,  $L$ ,  $G$  and  $C$  are, respectively, the per unit length resistance, inductance, conductance and capacitance of the transmission line. By a proper definition of  $p = \tan^{-1}(R/\omega L)$  and  $q = \tan^{-1}(G/\omega C)$ , (9.93) can be rewritten as

$$\gamma = \sqrt{\omega L \left( \frac{R}{\omega L} + j \right) \cdot \omega C \left( \frac{G}{\omega C} + j \right)} = \omega \sqrt{LC} \sqrt{(\tan p + j) \cdot (\tan q + j)} \quad (9.94)$$

which can be further simplified to

$$\gamma = \alpha + j\beta = \frac{\omega \sqrt{LC}}{\sqrt{\cos p \cos q}} \cdot \sin \frac{p+q}{2} + j \frac{\omega \sqrt{LC}}{\cos p \cos q} \cdot \cos \frac{p+q}{2} \quad (9.95)$$

Extracting  $\beta$  from (9.95) and inserting it in (9.92), one can determine  $v_\varphi$  as follows:

$$v_\varphi = \frac{\omega}{\beta} = \frac{1}{\sqrt{LC}} \cdot \frac{\cos p \cos q}{\cos(p+q/2)} \quad (9.96)$$

Using the expressions discussed in Reference 69 applied to a vertical conductor above the ground, for a RSC as a 9-km-long conductor with a radius of 2 cm, the values of  $L$  and  $C$  are calculated as  $2.74 \mu\text{H/m}$  and  $4.056 \text{ pF/m}$ , respectively. A typical value for the highest angular frequency of interest is  $62800 \text{ rad/s}$ . Note that this frequency coincides with the  $-3 \text{ dB}$  frequency of a waveform spectrum defined by the sum of a Heidler function and a double exponential function, which is assumed to be the excitation current source at the channel base.

Substituting the selected values of  $L$ ,  $C$  and  $\omega$  in (9.96), and assuming  $G=0$ , it is deduced that,  $v_\varphi$ , becomes only a function of  $R$  for that frequency. To adjust the value of  $v_\varphi$  to a value lower than the speed of light, one can use a similar approach to that adopted in the ATIL-F model [27, 69]. This is done by adding an additional distributed inductance,  $L_{\text{add}}$ , along the channel. The value of  $L_{\text{add}}$  is calculated by a classical theory of transmission lines model. Using the new value of  $L$  together with other parameters, one can use (9.96) to plot the current wave propagation speed vs.  $R$  for various locations along the RSC.

Figure 9.13 shows variations of  $v_\varphi$  vs.  $R$  for both the channel base and tip. In the case of the channel base,  $L_{\text{add}} = 4.024 \mu\text{H/m}$ ,  $L = 5.6 \mu\text{H/m}$  and  $C = 6.94 \text{ pF/m}$ , whereas for the channel tip  $L_{\text{add}} = 27.7 \mu\text{H/m}$ ,  $L = 30.4 \mu\text{H/m}$  and  $C = 4.05 \text{ pF/m}$ . Knowing that the propagation speed of the current wave varies between  $c/2$  and

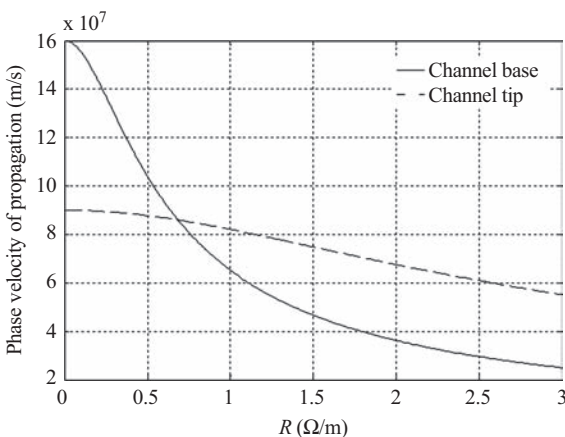


Figure 9.13 *Phase velocity of wave propagation vs. resistive loss at  $f = 10 \text{ kHz}$  for an RSC modelled by a transmission line with length of 9 km and radius of 2 cm, both at the channel base (loaded by additional inductance  $4.024 \mu\text{H/m}$ ) and channel tip (loaded by an additional inductance  $27.7 \mu\text{H/m}$ ) [adapted from Seyed-Moosavi et al. [31]]*

Table 9.1 Calculated values of inductance and capacitance at the bottom and tip of the RSC

RSC parameter value	RSC parameter unit	Formulation used	RSC bottom (channel base touching the ground)	RSC tip (channel top touching the clouds)
$z$	m	$z$	25.7	8974.3
$C_0(z)$	pF/m	$C_0(z) = \frac{2\pi\epsilon_0}{\ln(2z/a)} (\text{F/m})$	7.0816	4.0567
$L_0(z)$	$\mu\text{H}/\text{m}$	$L_0(z) = \frac{\mu_0}{2\pi} \ln(2z/a) (\text{H/m})$	1.569	2.739
$L^{\text{add}}(z)$	$\mu\text{H}/\text{m}$	$L^{\text{add}}(z) = \frac{1}{v^2(z) \cdot C_0(z)} - L_0(z)$	4.2252	27.694
$L(z)$	$\mu\text{H}/\text{m}$	$L(z) = L_0(z) + L^{\text{add}}(z)$	5.6	30.4
$v(z)$	m/s	[29]	$1.6 \times 10^8$	$0.9 \times 10^8$

$c/3$  [31], one can use the results shown in Figure 9.13 to determine the approximate range of  $R$ . Table 9.1 summarizes calculated values of inductance and capacitance at the bottom and tip of the RSC incorporated with related formulations used.

Using Figure 9.13, a variation range in the resistive load value,  $R = 0.540\text{--}1.1764 \Omega/\text{m}$ , is selected to ensure that the propagation speed of current wave varies between  $c/2$  and  $c/3$ . One can adopt a similar approach to that used in Reference 27 for the ATIL-F model: the value of  $R$  can be split into a fixed distributed resistive load of  $R^F = 0.5 \Omega/\text{m}$  and a non-linearly varying resistive load in the range of  $R^N = 0.040\text{--}0.6764 \Omega/\text{m}$ , obtained from (9.91).

With reference to Figure 9.1, in all simulations presented in Section 9.5, we assume the value of  $a$  is changing with time and space, having an average value of  $a_0 = 0.02 \text{ m}$ . We also assume that the electrical conductivity of the channel is  $\sigma = 5 \times 10^3 \text{ S/m}$  and is unchanged everywhere along the channel. In addition,  $L_{\text{add}} = 11.8 \mu\text{H}/\text{m}$ , which is obtained by averaging out the values of  $L_{\text{add}}$  at the channel base and at 1 km above the ground.

A comparison of this model with the ATIL-F model with fixed distributed resistance  $R = 0.5 \Omega/\text{m}$  and distributed inductance  $L = 11.8 \mu\text{H}/\text{m}$  [27] will be presented.

In Section 9.5, current distribution along the channel and the associated radiated electromagnetic fields, as well as the speed of propagation profile for the non-linear model, are discussed and compared with that predicted by the ATIL-F model.

#### 9.4.4 Frequency-domain AT model

As mentioned earlier in this chapter, the frequency-domain model of RSC is often preferred when dealing with problems involving a lossy ground. To give an account of the model, consider the thin-wire antenna model of RSC above a lossy ground as illustrated in Figure 9.6. The antenna has length  $h = 2600 \text{ m}$ , radius  $a = 0.05 \text{ m}$  and distributed resistance  $R_D = 0.1 \Omega/\text{m}$ . It is driven at its bottom end by a current

source whose waveform is the same as that used in Reference 62. This waveform (Figure 9.10) is characterized by a peak value of about 11 kA and a peak current rate rise of about 105 kA/ $\mu$ s. In finding the distribution of current along the antenna,  $\epsilon_1 = 5.3 \epsilon_0$  is set for the ambient medium in order to obtain a current wave propagation velocity of  $1.3 \times 10^8$  m/s [13]. Accordingly, lossy ground effect is incorporated using this value of permittivity for the upper medium (medium 1) in (9.71).

Having determined the current distributions along the RSC, the respective current waveforms are used in field expressions (9.72)–(9.74) to calculate remote field components above a lossy ground assuming  $\epsilon_1 = \epsilon_0$  (i.e. assuming that medium 1 is air or free space).

Frequency-domain calculations are usually carried out at 8192 frequencies up to 10 MHz with frequency intervals of 2.44 kHz. This corresponds to a sampling interval of 0.05  $\mu$ s over a time window of 409.6  $\mu$ s. To ensure the convergence of the MOM, the smallest segment length should not exceed one-fourth of the minimum wavelength. That means, the 2600 m wire representing the lightning channel is to be divided into 800 segments, each 3.25 m in length.

In Section 9.5, current distributions and associated remote field components for the case of a perfect ground are computed using the proposed approach and compared with those obtained using the AT model described in Reference 13. Also, a comparison is made between the Cooray–Rubinstein formula (and the Cooray modified formula) for the horizontal electric field and the generalized expression for the horizontal electric field employed in this chapter. Finally, various field components over different lossy media are computed and discussed.

## 9.5 Numerical results

In this section, we discuss the merits of various AT models in modelling a lightning return-stroke. In particular, we analyse the predicted current characteristics along the RSC as well as radiated electromagnetic fields at various distances from the channel.

### 9.5.1 AT Model

#### 9.5.1.1 Current profiles

Current waveforms as a function of time at different heights along the channel for five models, the TL, MTLL, MTLE, DU and AT models, are compared in Figure 9.14(a)–(e). For the TL model, the current waveforms at different heights are the same, and for the MTLL and MTLE models, the current amplitude decreases with height, whereas the waveshape remains the same. For the DU model, both attenuation and dispersion of current waveform are observed. The current peak and current rise time each as a function of height for the five models are shown in Figure 9.15 (a) and (b). For the TL model, neither current peak nor current rise time changes with height. The MTLL and MTLE models are characterized by linear and exponential decrease of the current peak with height,

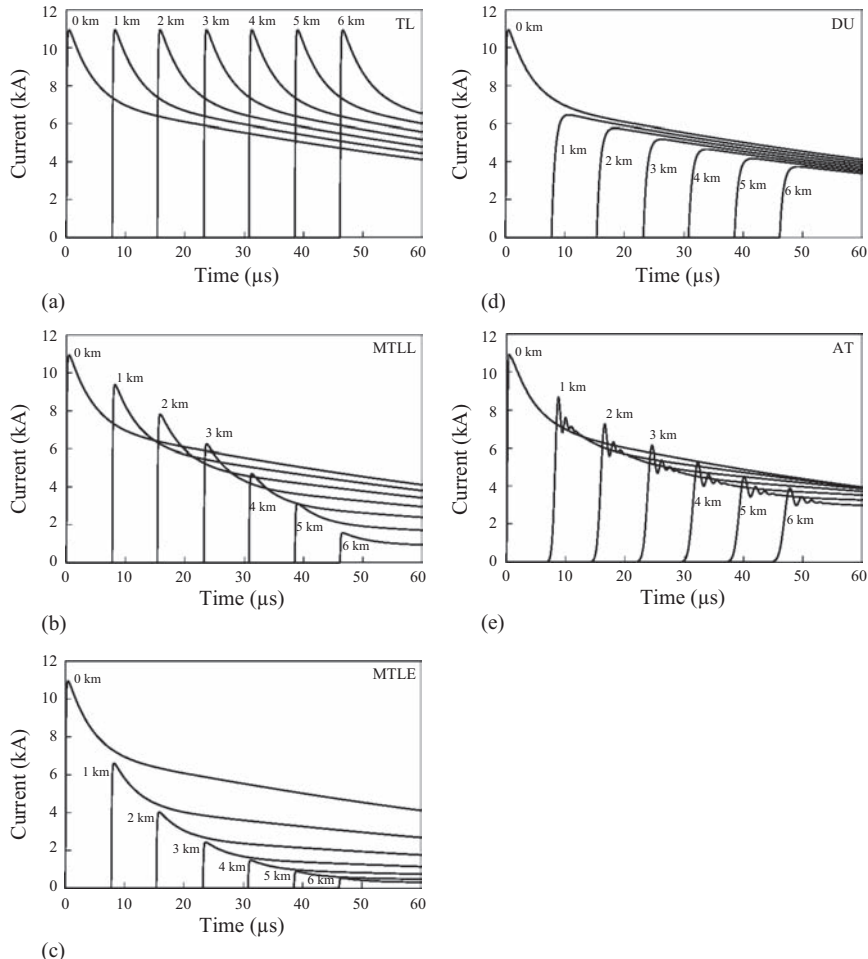


*Figure 9.14* Channel current as a function of time at different heights above ground as predicted by (a) the TL model, (b) the MTL model, (c) the MTLE model, (d) the DU model and (e) the AT model. For the AT model, it is assumed that  $\epsilon_r = 5.3$  and  $R = 0.07 \Omega/m$  [adapted from Moini et al. [13]]

respectively, whereas the current rise time remains the same at all heights. For the AT model, the variation of current peak with height within the lowest 4 km or so of the channel is similar to that for the MTL model. Both the DU and the AT models are characterized by the increase of current rise time with height, but for the DU model, the pronounced increase occurs only within the lowest 1 km or so of the channel. Note that for the AT model the current peak decreases with height due to both ohmic losses in the antenna and radiation losses; i.e. a decrease of current peak with increasing height would be observed even if the ohmic losses were neglected.

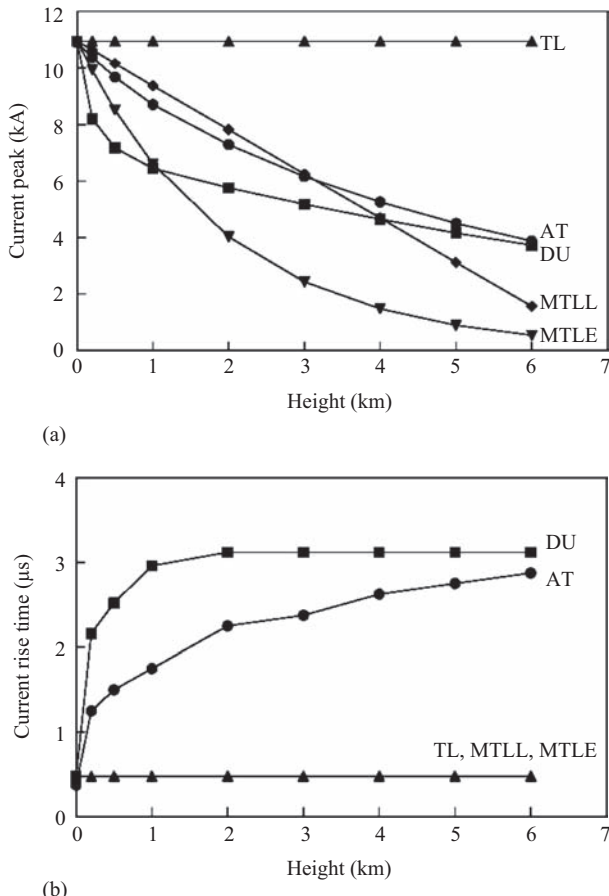


Figure 9.15 (a) Current peak as a function of height predicted by the TL, MLLL, MTLE, DU and AT models. (b) Current rise time to peak as a function of height predicted by the TL, MLLL, MTLE, DU and AT models [adapted from Moini *et al.* [13]]

### 9.5.1.2 Line charge density profiles

The line charge density at any height  $z'$  on a straight vertical lightning channel at any time  $t$  is given by Thottappillil *et al.* [64]:

$$\rho_L(z', t) = \frac{i(z', z'/\nu)}{\nu} - \int_{z'/\nu}^t \frac{\partial i(z', \tau)}{\partial z'} d\tau \quad (9.97)$$

The first term of (9.97) represents only the deposited charge density component, whereas the second term can contribute to both transferred and deposited charge

density components, the two components being defined by Thottappillil *et al.* [64]. Applying the Leibnitz formula to (9.97), we obtain:

$$\rho_L(z', t) = -\frac{d}{dz'} \int_{z'/v}^t i(z', \tau) d\tau \quad (9.98)$$

Equation (9.98) has been applied to five return-stroke models, and the resultant charge density profiles at  $t = 60 \mu\text{s}$  are shown in Figure 9.16. For the TL model, there is no deposited charge, and the total charge density is equal to transferred charge density which becomes equal to zero when the current ceases to flow in all channel sections of interest [64]. For the other four models, the total charge density at  $60 \mu\text{s}$  is a combination of transferred and deposited charge density components. When the current ceases to flow everywhere in the channel, the transferred charge density component becomes zero and the total charge density becomes equal to the deposited charge density component. As seen in Figure 9.16, the MTLE model has a total charge density near ground two to three times higher than that predicted by the AT, MTL and DU models. This disparity translates into an appreciable difference in the model-predicted return-stroke electric fields at close ranges, as shown in the simulation of remote electromagnetic field.

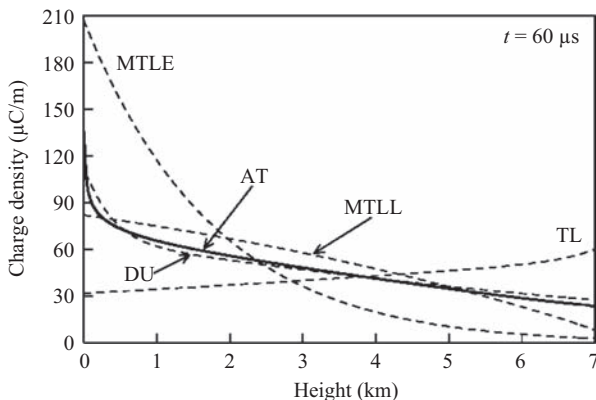
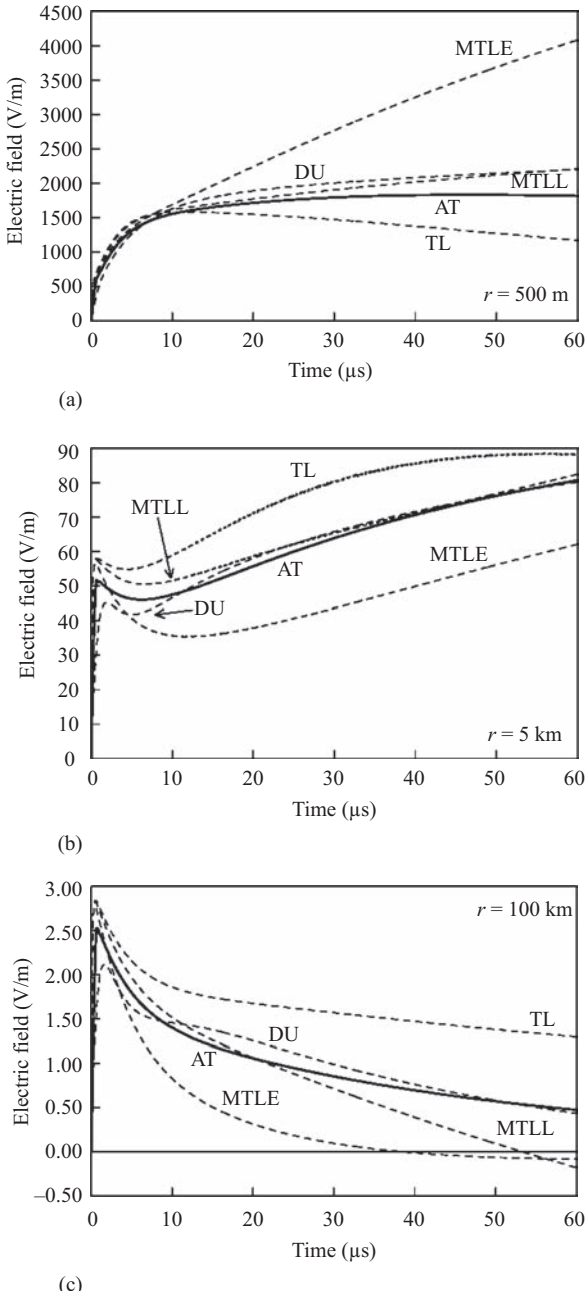


Figure 9.16 Line charge density distribution along the channel calculated for different models at  $t = 60 \mu\text{s}$  [adapted from Moini *et al.* [13]]

### 9.5.1.3 Electromagnetic fields

Figure 9.17(a)–(c) and Figure 9.18(a)–(c) illustrate the calculated electric and magnetic fields at various distances from the channel, displayed on two different timescales. The fields were computed using traditional equations found, e.g. in the work of Rakov and Uman [1]. The calculations were performed up to  $60 \mu\text{s}$ , and for the AT model the channel segment length  $\Delta z$  was 15 m. The calculated fields can be compared with typical measurement presented in Reference 25. Except for the TL and MTLE models, the 500 m electric field waveforms predicted by all the



*Figure 9.17* Vertical component of electric field calculated at different distances ( $r$ ) from the channel: (a)  $r = 500 \text{ m}$ , (b)  $r = 5 \text{ km}$  and (c)  $r = 100 \text{ km}$  [adapted from Moini et al. [13]]

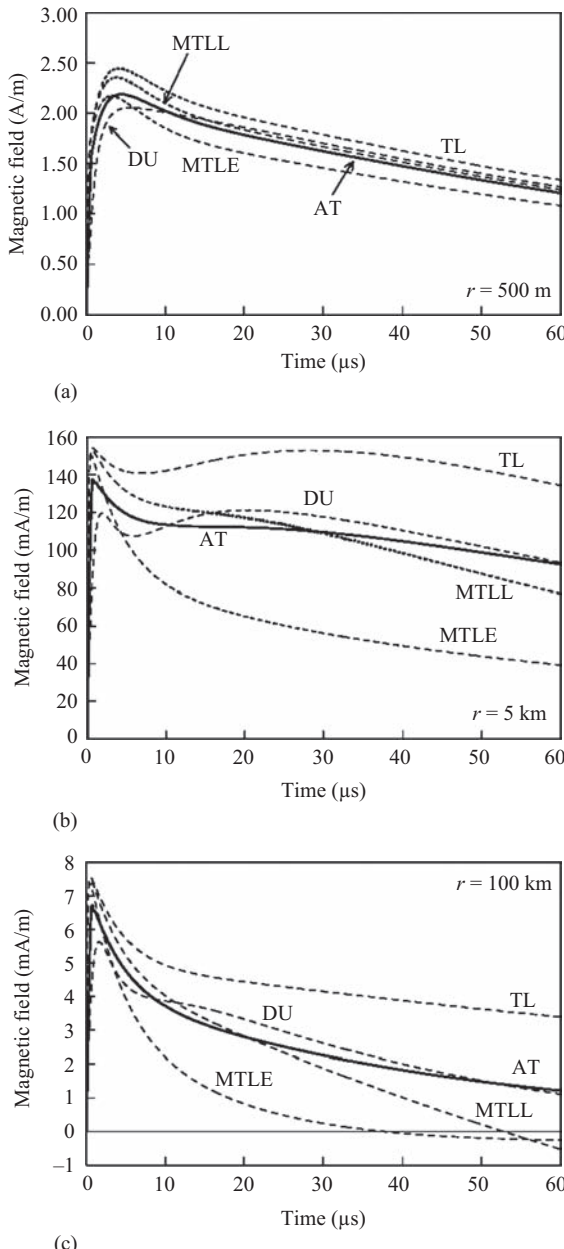


Figure 9.18 Horizontal component of magnetic field calculated at different distances ( $r$ ) from the channel: (a)  $r = 500 \text{ m}$ , (b)  $r = 5 \text{ km}$  and (c)  $r = 100 \text{ km}$  [adapted from Moini et al. [13]]

models are more or less consistent with experimental data. In particular, the electric fields predicted by the MTLL, DU and AT models show little variation after 10  $\mu\text{s}$  or so, following the initial relatively rapid change, in keeping with observations. At 5 km, the electric field exhibits a ramp after the initial peak for all the models, except for the TL model (see also Reference 62). In fact, at distances of the order of some kilometres, the TL model allows the reproduction of only the first few tens of microseconds of the characteristic electric field ramp observed in the experimental data to last for more than a hundred of microseconds. Note that at distances greater than a few kilometres the initial rapid transition in electric field is reasonably reproduced by all the models because (a) this feature is formed when the current wave is very close to the ground and (b) the same current waveform at ground level is assumed for all models. In contrast with the other models, the DU model predicts a non-monotonic rise to the initial peak (a spike within the first some hundreds of nanoseconds), as seen in Figures 9.17 and 9.18. At far distances from the channel base, e.g.  $r = 100$  km, all the models predict more or less similar field peak values. On the other hand, the MTLL and MTLE models predict a zero crossing after a few tens of microseconds, a feature generally considered to be characteristic of distant fields [25], whereas the TL, DU and AT models do not do so.

In summary, it appears that the TL model is not a realistic model for calculating lightning electric fields at times greater than some tens of microseconds at distances of the order of some kilometres (see also Reference 62) and after only a few microseconds at distances of the order of tens of metres from the channel [64]. The MTLL-model-predicted fields are consistent with observed fields at all ranges. The MTLE model is incapable of reproducing adequately the observed electric field waveforms at very close (tens to hundreds of metres) ranges [64]. The DU and AT models do not reproduce the zero crossing at far ranges. However, this latter feature depends on the assumed channel-base current waveform, in particular, on the rate of decrease of current after the peak and on channel geometry. Indeed, the field zero crossing occurs when the contribution from the leading positive and trailing negative portions of the spatial current derivative wave becomes equal in magnitude, the time of this event being a function of channel inclination with respect to the observer. As an example, we present in Figure 9.19(a) and (b) electric field waveforms measured at distances of about 250 km in Florida, one of which shows zero crossing within 100  $\mu\text{s}$  of the initial peak, but the other does not. Note that the two waveforms were apparently produced in the same thunderstorm within less than 3 min of each other.

## 9.5.2 ATIL Model

### 9.5.2.1 Current profiles

Figure 9.20(a)–(c) illustrates the current distribution along the RSC for the AT, ATIL-F and ATIL-V models. There are appreciable differences between the AT and ATIL-F models in terms of the general shape of current waveforms. The effect of height-variable speed can also be observed in the current distribution for the ATIL-V model. Both versions of the ATIL model predict more pronounced current dispersion than the AT model. To facilitate comparison with AT-model results, we assumed the

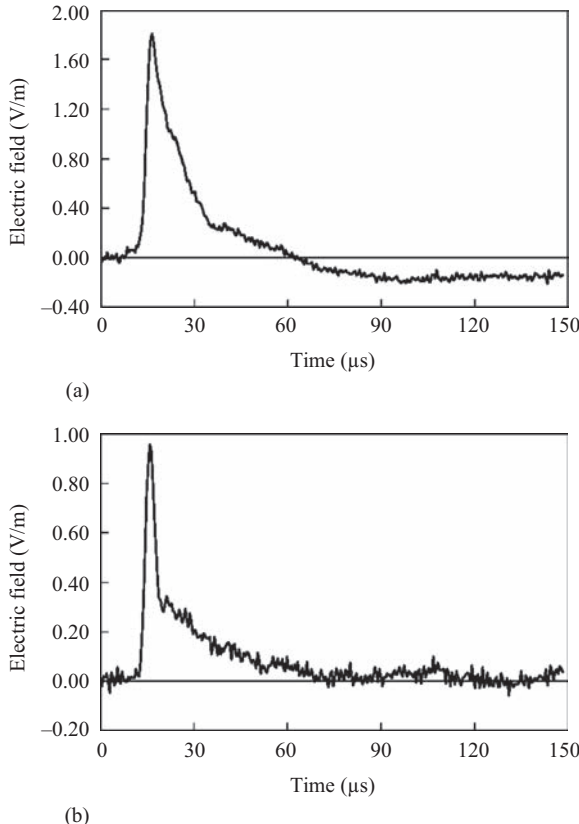


*Figure 9.19* Measured electric field waveforms due to lightning discharges at distances of about 250 km in Florida. Note that one of the waveforms shows a zero crossing, while the other one does not [adapted from Moini et al. [13]]

same attenuation rate for all models, which required larger distributed resistances in the ATIL models, compared to the AT model. This additional distributed resistance in the ATIL models can be described using the transmission line theory. The square of attenuation factor for a transmission line is given by the following formula:

$$\alpha^2 = \text{Re}[(R + j\omega L)(G + j\omega C)] \quad (9.99)$$

where  $R$ ,  $L$ ,  $G$  and  $C$  are, respectively, the per unit length resistance, inductance, conductance and capacitance of the transmission line,  $\omega$  is the angular frequency,  $j = \sqrt{-1}$ , and ‘Re’ stands for the real part of a complex quantity. This equation can be rewritten in the following form:

$$\alpha^2 = \text{Re}[(RG + jRC\omega + jLG\omega - LC\omega^2)] = RG - LC\omega^2 \quad (9.100)$$

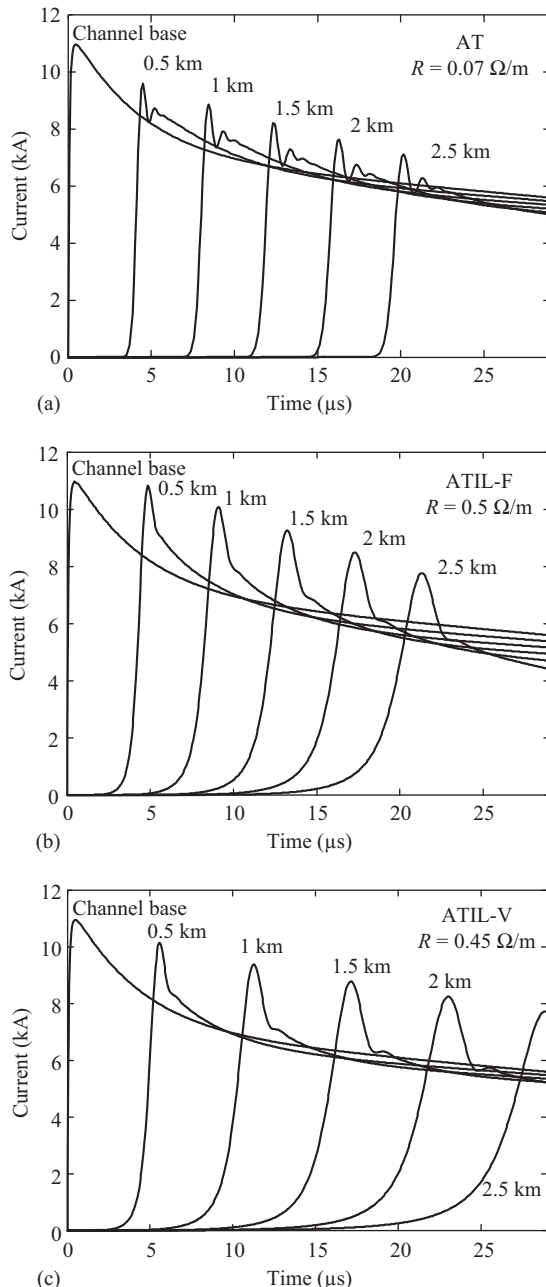


*Figure 9.20* Current distributions along the channel for (a) AT, (b) ATIL-F and (c) ATIL-V models. Shown are current vs. time waveforms at the channel base and at heights of 500 m, 1 km, 1.5 km, 2 km and 2.5 km above ground [adapted from Bonyadi-Ram et al. [30]]

or

$$\alpha = \sqrt{RG - LC\omega^2} \quad (9.101)$$

Equation (9.101) shows that the attenuation factor decreases with increasing  $L$  and hence in order to have a constant  $\alpha$ ,  $R$  should be increased.

In the AT model, the current attenuation in the lower sections of the channel is more pronounced than for both versions of the ATIL model. In other words, the attenuation is reduced in the presence of inductive loads, although the distributed resistance for both versions of the ATIL model is greater than that for the AT model. As can be seen in Figure 9.12, the ATIL-V model employs smaller values of inductance in the lower sections of the channel than the ATIL-F model does and, hence, more attenuation is observed for the ATIL-V model. Both versions of the ATIL model predict more or less similar attenuation in the higher sections of the channel due to similar amounts of inductive and resistive loading.

### 9.5.2.2 Current dispersion

It is clear that the ATIL-F and ATIL-V models (see Figure 9.20(b) and (c)) predict considerably larger current dispersion than the AT model does (see Figure 9.20(a)). This larger dispersion is in agreement with optical observations of Jordan and Uman [28] and Wang *et al.* [29]. The observed current dispersion in the inductively loaded channel can be explained using the transmission line theory. The upward travelling current wave in the channel can be decomposed into two components [78].

- Antenna-mode current, which is governed by the scattering theory. The propagation speed of this component is equal to the electromagnetic wave propagation speed,  $v$ , in the surrounding medium, which is the speed of light when  $\epsilon_r = 1$ .
- Transmission line-mode current, which is governed by the transmission line theory and propagates at an adjusted speed  $v(z)$ .

The propagation speed of each of the two current components is a function of  $\epsilon_r$ . The AT model yields a full wave solution for the current distribution along the metallic structure including both the TL-mode and antenna-mode currents [78]. The resultant current wave propagation speed is a function of relative permittivity of the medium. Adding distributed inductive loads as the circuit elements to the discretized EFIE dramatically affects the propagation speed of the TL-mode current because the current passes through loaded segments. On the other hand, the antenna-mode component of the current is independent of the circuit elements because loaded segments do not play dominant role in the electromagnetic coupling between the segments. Different propagation speeds for the two-current components result in noticeable current dispersion along the channel, which increases with height.

### 9.5.2.3 Current wave propagation speed

The choice of tracking point will affect the model-predicted speed, since the shape of current (or luminosity) waveform changes with height. Here, we analyse variations of return-stroke speed along the channel predicted by the AT, ATIL-F and ATIL-V models. Olsen *et al.* [68] obtained different speed values tracking different

reference points, including 10%, 20%, 90% and 100% of peak, as well as the maximum rate of rise of the return-stroke luminosity pulse. The point of initial deflection from zero level is usually masked by noise and, hence, difficult to identify in optical measurements. We have chosen 10%, 20% and 100% of peak, and the maximum time derivative of current waveform (the latter corresponds to the time at which the current waveform reaches its maximum rate of rise,  $di/dt$ ) as reference points. Speed  $v_k$  in segment  $k$  is calculated at the centre of the segment by dividing the vertical distance between adjacent viewed heights,  $h_k - h_{k-1}$ , by the tracked time interval,  $t_k - t_{k-1}$ . The resultant speed profiles for the AT, ATIL-F and ATIL-V models are shown in Figures 9.21(a)–(c). In order to facilitate direct comparison, the ‘theoretical’ speed profiles (given by (9.88) for the ATIL-V model or constant value equal to  $1.3 \times 10^8$  m/s for the AT and ATIL-F models) are also shown in this figure. The current-peak and  $di/dt$ -peak speed profiles at heights greater than some hundreds of metres above ground are fairly similar to the theoretical profiles for the AT and the ATIL-V models. The estimated speed at lower sections of the channel is noticeably greater than the theoretical speed. This may be due to significant changes in current wave shape in the lower sections of the channel (e.g. compare current wave shapes at the channel base and at a height of 500 m above ground in Figure 9.20(a)). Propagation speeds for the AT and ATIL-F, as expected, are almost constant over the entire channel length considered. The difference between speeds obtained from the four estimated profiles (current peak, peak of  $di/dt$ , 10% of the peak and 20% of the peak) for the AT model is less than those predicted by the ATIL-F and the ATIL-V models. This is because of lower current dispersion predicted by the AT model. It can also be observed that tracking a lower percentage of peak results in a higher propagation speed, which is in agreement with optical data reported in Reference 68. It is also observed that both versions of the ATIL model predict propagation speeds that appear to be nearly equal to the speed of light if the point of initial deflection from zero level is tracked, whereas in the AT model the propagation speed remains near  $1.3 \times 10^8$  m/s. This difference is expected, since in both versions of the ATIL model, the antenna-mode current propagates at the speed of light, whereas in the AT model, it propagates at  $v = 1.3 \times 10^8$  m/s.

#### 9.5.2.4 Electromagnetic fields

Figure 9.22(a)–(c) and Figure 9.23(a)–(c) illustrate the electric and magnetic fields, respectively, at three different distances, 500 m, 5 km and 100 km from the lightning channel base calculated using the AT, ATIL-F and ATIL-V models. At  $r = 500$  m, after 10  $\mu$ s, all three examined models predict similar magnetic field waveforms. The ATIL-F model predicts a higher initial peak of the magnetic field than the other two models, since the current in the lower parts of the channel for the ATIL-F is greater than for the other two models (see Figure 9.20). On the other hand, the time of the magnetic field peak for the AT model is greater than those for the ATIL-F and ATIL-V models. At  $r = 500$  m, predicted electric fields prior to 1  $\mu$ s for both ATIL-F and ATIL-V models are nearly identical, which suggests that the variation of propagation speed cannot alter the electric field waveform at close

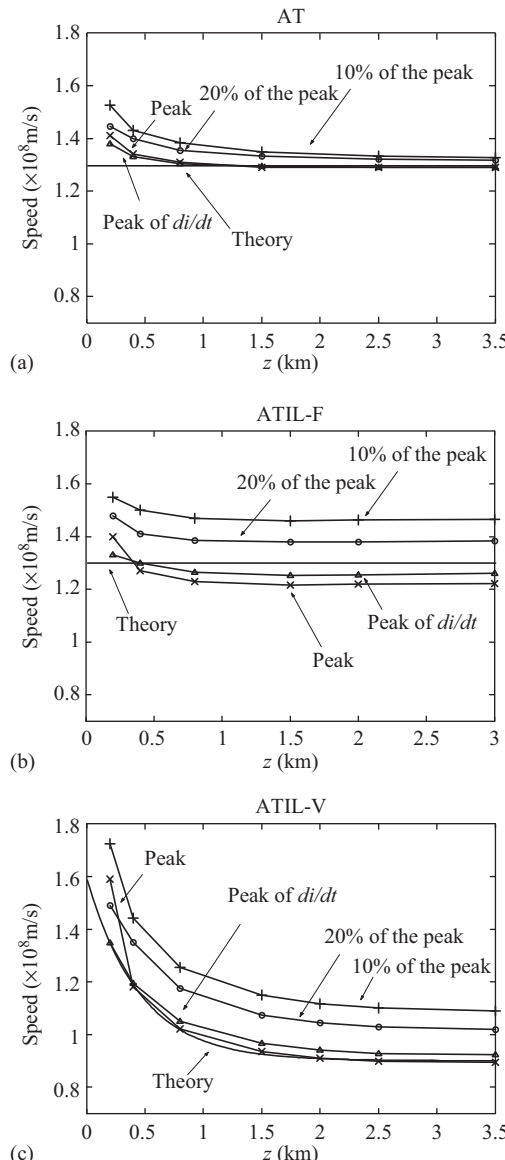


Figure 9.21 Return-stroke speed profiles for the (a) AT, (b) ATIL-F and (c) ATIL-V models obtained using different reference points on the current waveform, peak, 10% of peak on the wave front, 20% of peak on the wave front and peak of  $di/dt$ . 'Theoretical' speed profiles,  $v = 1.3 \times 10^8 \text{ m/s} = \text{constant}$ , for the AT and ATIL-F models and the curve shown in Figure 9.11 for the ATIL-V are also shown [adapted from Bonyadi-Ram et al. [30]]

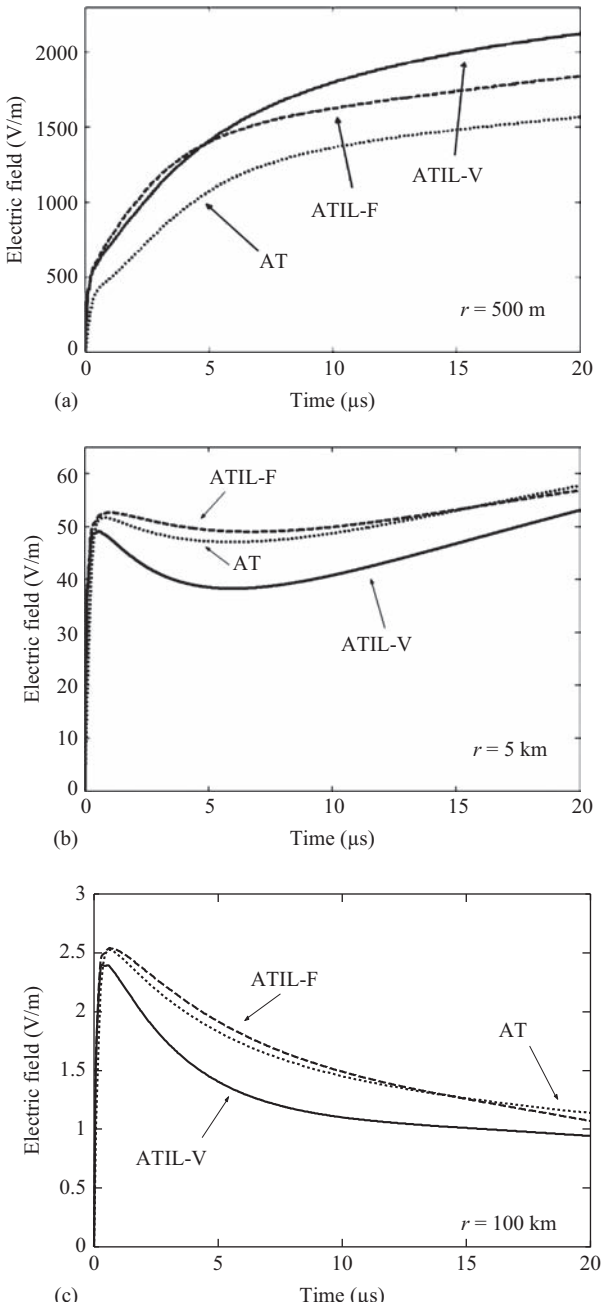


Figure 9.22 Vertical component of electric field for the AT, ATIL-F and ATIL-V models calculated at (a)  $r = 500 \text{ m}$ , (b)  $r = 5 \text{ km}$  and (c)  $r = 100 \text{ km}$  from the lightning channel [adapted from Bonyadi-Ram et al. [30]]

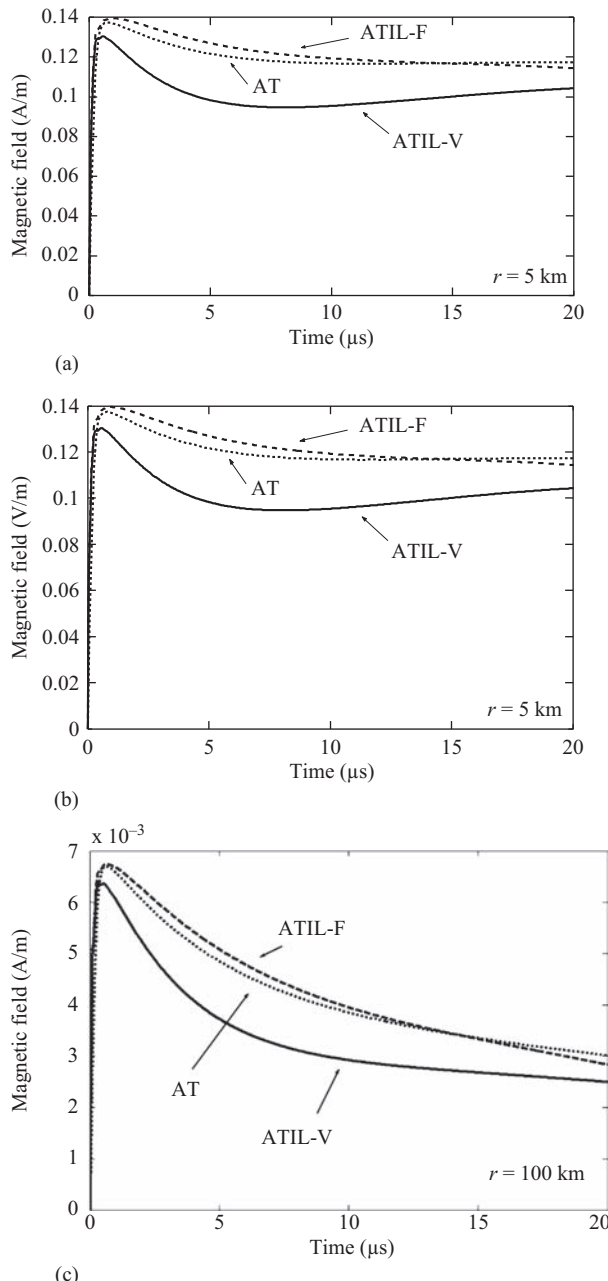


Figure 9.23 Horizontal component of magnetic field for the AT, ATIL-F and ATIL-V models calculated at (a)  $r = 500 \text{ m}$ , (b)  $r = 5 \text{ km}$  and (c)  $r = 100 \text{ km}$  from the lightning channel [adapted from Bonyadi-Ram et al. [30]]

distances during the first microsecond or so. The AT model predicts the lowest electric field, while its rising slope after 5  $\mu\text{s}$  is similar to that for the ATIL-F model. Due to higher propagation speed in the lower part of the channel for the ATIL-F model, after 1  $\mu\text{s}$ , this model predicts the steepest electric field slope as well as a greater final field value. The AT model and both versions of the ATIL model do not show the magnetic field hump at 50  $\mu\text{s}$ , which can be seen in typical measured waveforms of Reference 25.

The electric and magnetic fields at 5 km are more or less similar for all the models considered. The ATIL-V model predicts a smaller overall electric or magnetic field value, a steeper falling slope after the initial peak, and a higher rising slope than the other two models, which is more consistent with the typical waveforms measured at 5 km [25]. This is because of a higher propagation speed in the lower sections of the lightning channel (causes a steeper falling slope) and a lower speed in higher parts of the channel (results in a higher rising slope) in the ATIL-V model.

At 100 km, the electric and magnetic field wave shapes are similar. At this distance, the ATIL-V predicts lower fields than the other two models. This is due to a lower propagation speed in the upper part of the lightning channel, which causes a greater delay in illuminating higher parts of the channel (compare the current at 2500 m at 20  $\mu\text{s}$  in Figure 9.20(a)–(c)). During the initial 13  $\mu\text{s}$  or so, the ATIL-F and the AT models exhibit fairly similar behaviour in predicting far electromagnetic fields, whereas the ATIL-V model predicts a lower peak and a steeper falling slope after the peak. Due to a lower propagation speed in the upper part of the channel, the final falling slope for the ATIL-V is less than that for the other two models considered. None of the three models considered here can predict zero crossing within about 50–60  $\mu\text{s}$ , as typically seen in most waveforms measured at this distance.

### 9.5.3 AT model with non-linear loading

#### 9.5.3.1 Current profiles

First, through the computational process for the time-domain current distribution along the channel, temporal-spatial curves for the RSC radius as well as the non-linear per unit length resistance utilized in the proposed model are shown in Figure 9.24(a) and (b), respectively. As seen in these figures, for a selected range of  $R = 0.040\text{--}0.6764 \Omega/\text{m}$ , the value of RSC radius,  $a$ , varies between 0.18 and 0.01 m, respectively. Also, from these figures one can deduce that for a given time the lower section of the channel generally holds a large cross-sectional area with small resistance, whereas the higher section of the channel tends to be narrower with large values of resistance.

Next, the current at 2250, 4500 and 6750 m distant from the channel base is obtained using the proposed model and the ATIL-F model. The temporal variation of the excitation current source at the channel base is assumed to be the sum of a Heidler function and a double exponential [62], i.e.:

$$i(t) = \frac{I_{o1}}{\eta} \cdot \frac{(t/\tau_1)^n}{1 + (t/\tau_1)^n} \cdot e^{-t/\tau_2} + I_{o2} \cdot (e^{-t/\tau_3} - e^{-t/\tau_4}) \quad (9.102)$$

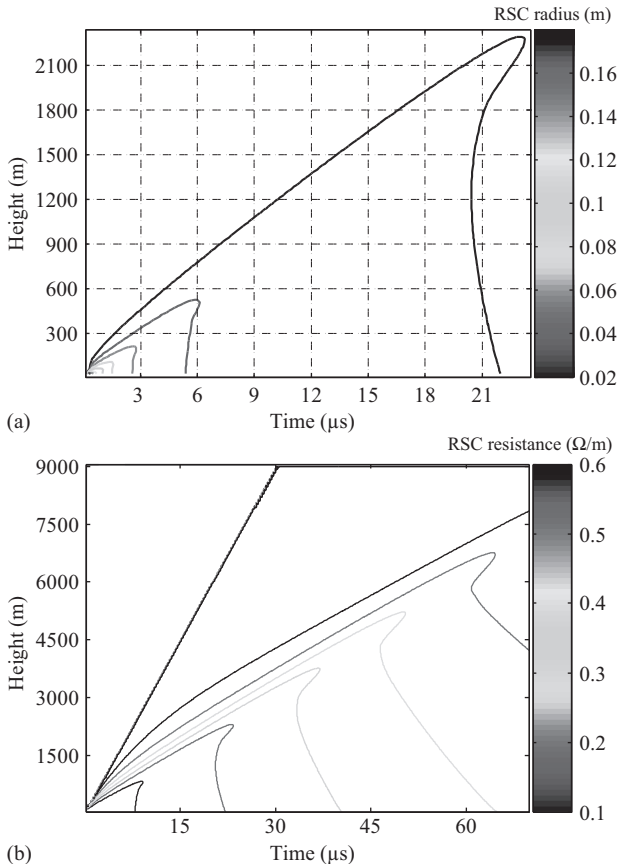


Figure 9.24 Temporal-spatial plot of return-stroke channel (a) radius and (b) resistance per unit length [adapted from Seyed-Moosavi et al. [31]]

where the related parameters are considered as  $I_{o1} = 9900$  A,  $I_{o2} = 7500$  A,  $\eta = 0.845$ ,  $n = 4$ ,  $\tau_1 = 0.072 \times 10^{-6}$  s,  $\tau_2 = 5 \times 10^{-6}$  s,  $\tau_3 = 100 \times 10^{-6}$  s and  $\tau_4 = 6 \times 10^{-6}$  s.

A comparison of the results shown in Figure 9.25 shows that both the current attenuation and dispersion rates in the proposed model are higher than that predicted by the ATIL-F model.

### 9.5.3.2 Current peak and current rise time

Current peak values at different heights along the lightning channel and the corresponding rise time values are shown in Figures 9.26 and 9.27, respectively. The value of rise time is assumed to be 10–90% of the current peak time. These two parameters can be considered as major contributors to the zero crossing at far

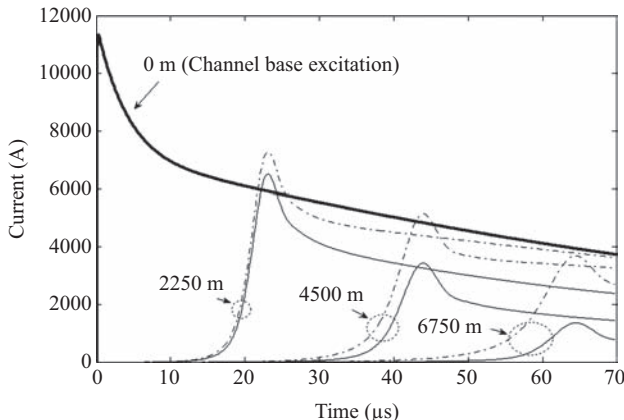


*Figure 9.25 Current distribution along the channel for the ATIL model and the non-linear AT model, non-linear AT model (solid) and the ATIL-F model (dashed) [adapted from Seyed-Moosavi et al. [31]]*

radiated electromagnetic fields and the hump in the intermediate magnetic field [13]. As is clearly observed in Figure 9.26, the current peak for the proposed method is often smaller than that predicted by the ATIL-F model, showing more attenuation. Also, the rise time of the upward travelling current wave for the proposed method is often smaller than that of the ATIL-F model. In addition, both quantities exhibit non-linear behaviours in the case of the proposed method, whereas they are essentially linear in the case of the ATIL-F model.

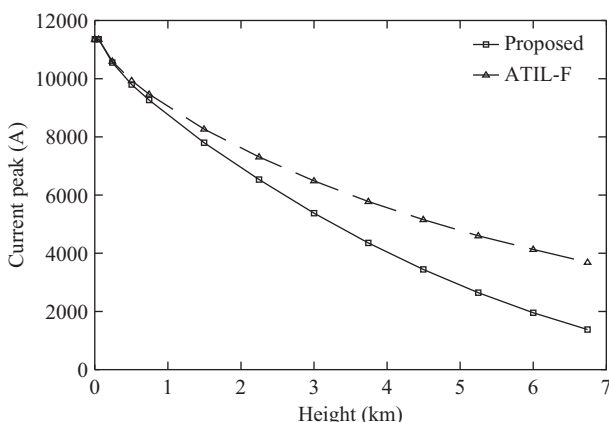


*Figure 9.26 Peak for different heights along the lightning channel for the proposed method and the ATIL-F method [adapted from Seyed-Moosavi et al. [31]]*

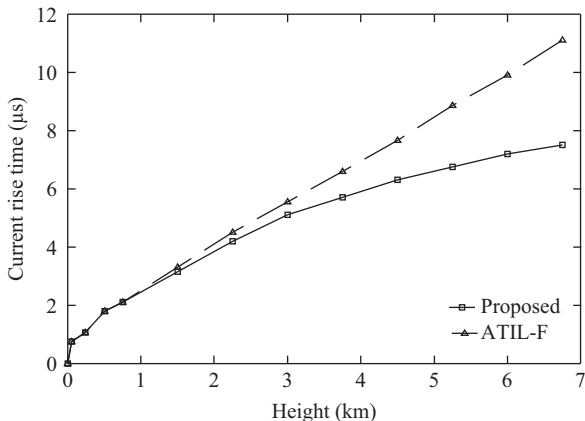


Figure 9.27 Current rise time for different heights along the lightning channel for the proposed method and the ATIL-F method [adapted from Seyed-Moosavi et al. [31]]

### 9.5.3.3 Electromagnetic fields

Field waveforms are calculated for three different ranges of distances from the channel, namely near distance (500 m), intermediate distance (5 km) and far distance (100 km). The electric field waveforms are shown in Figure 9.28(a)–(c). As can be seen in Figure 9.28(a), the electric field waveforms predicted by both models are initially (i.e. 15  $\mu$ s) consistent while departing from each other later on. At the intermediate distance (Figure 9.28(b)), the results are following each other and essentially the same. The main feature of the proposed model is demonstrated in the case of far distance (Figure 9.28(c)) where, as opposed to the ATIL-F model, a zero crossing at  $t = 50 \mu$ s takes place in the predicted electric field waveform. Note that the zero crossing is an important feature observed in all measurement results [25].

The magnetic field waveforms at near distance (500 m), intermediate distance (5 km) and far distance (100 km) for the two models are shown in Figure 9.29(a)–(c), respectively. Generally speaking, similar observations to those described above for the case of electric field waveforms can be deduced from the results shown in Figure 9.29.

To study the effect of the electrical conductivity  $\sigma$  in resistive loads along the channel on the predicted field waveform, the magnitudes of electric and magnetic fields at far distance (i.e. 100 km) vs. time for various values of  $\sigma$  are calculated. The results are shown in Figure 9.30(a) and (b), where  $\sigma = 5 \times 10^3$ ,  $6 \times 10^3$  and  $7 \times 10^3$  S/m. Also, a similar study is done for the predicted current peak and current rise time vs. height and the results are shown in Figure 9.31(a) and (b). A comparison of the results shown in these figures shows that as the value of  $\sigma$  increases, both electric and magnetic field waveforms, as well as current peak and current rise time, tend to approach their ATIL-F counterparts. In particular, the zero crossings

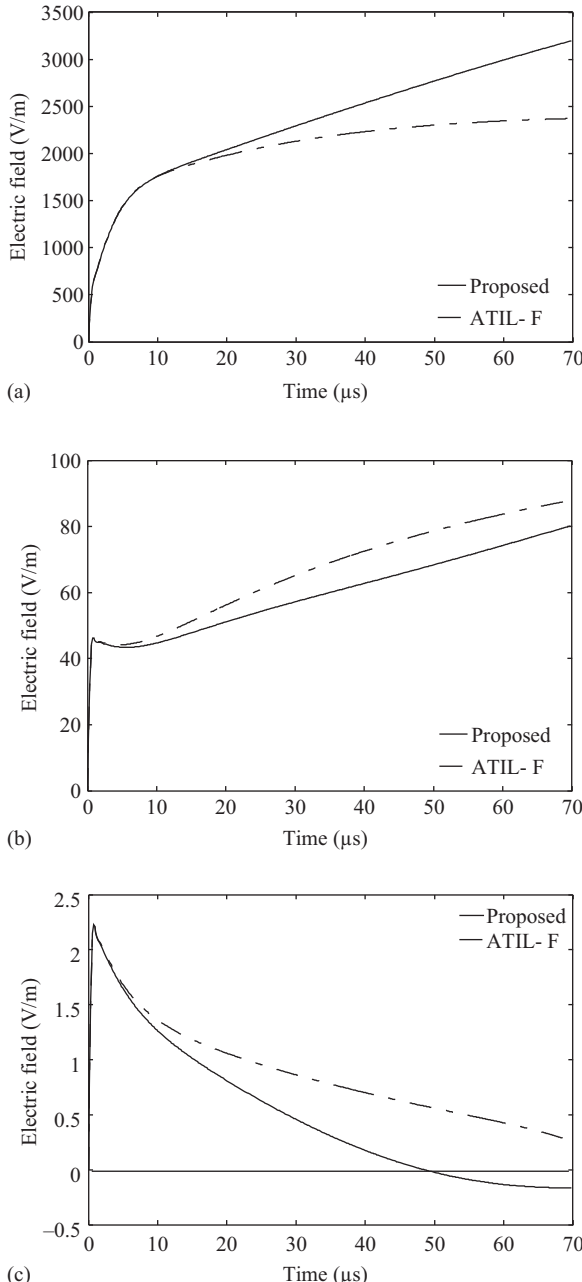


Figure 9.28 Electric field waveform at different distances from the channel base: (a) 500 m, (b) 5 km and (c) 100 km [adapted from Seyed-Moosavi et al. [30]]

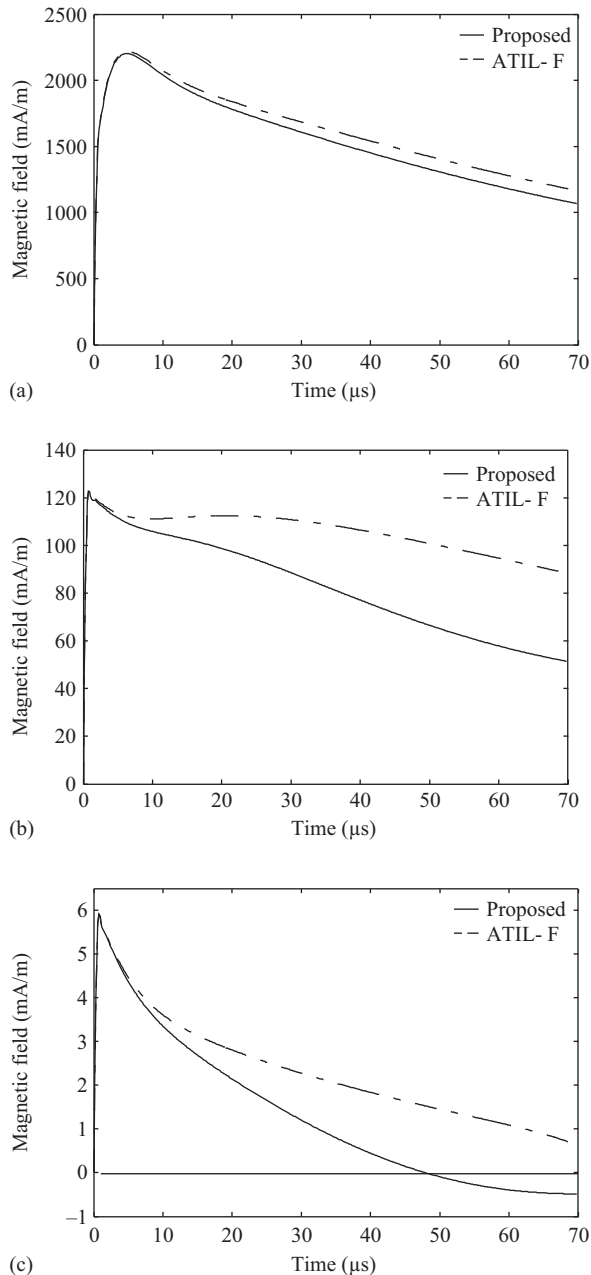
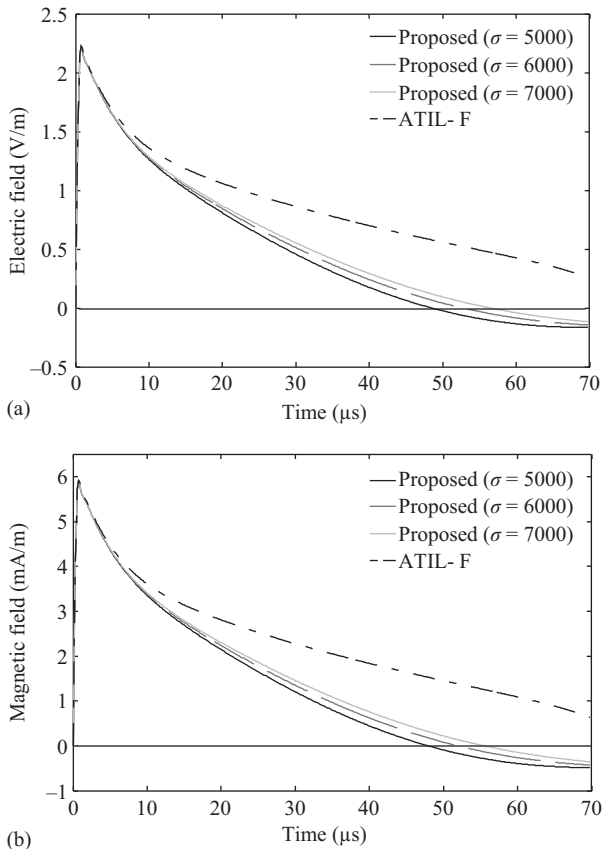


Figure 9.29 Magnetic field waveform at different distances from the channel base: (a) 500 m, (b) 5 km and (c) 100 km [adapted from Seyed-Moosavi et al. [31]]



*Figure 9.30 Electric field (a) and magnetic field (b) waveforms at 100 km from the channel base for different conductivities of the channel ( $\sigma$  in S/m) [adapted from Seyed-Moosavi et al. [31]]*

in both electric and magnetic field waveforms tend to disappear. This is thought to be due to the fact that a large value of  $\sigma$  results in a small value of non-linear part of channel resistance  $R^N$ , leading to a less-shared resistive non-linearity out of the total resistive loading, i.e.  $R = R^F + R^N$ . With upper bound for the non-linear resistance part of the channel loading, a behavioural study of increase in conductivity is presented in Figure 9.32 for the time instant 30.45  $\mu$ s, while the upward propagated initiated first return-stroke touches the clouds. The results shown in this figure demonstrates that by increasing the value of conductivity from  $\sigma = 5 \times 10^3$  S/m to  $6 \times 10^3$  S/m and then  $7 \times 10^3$  S/m, non-linear channel resistance part tends to decrease as  $R^N = 0.6764 \Omega/\text{m}$  to  $0.5703 \Omega/\text{m}$  and then to  $0.4946 \Omega/\text{m}$ , respectively.

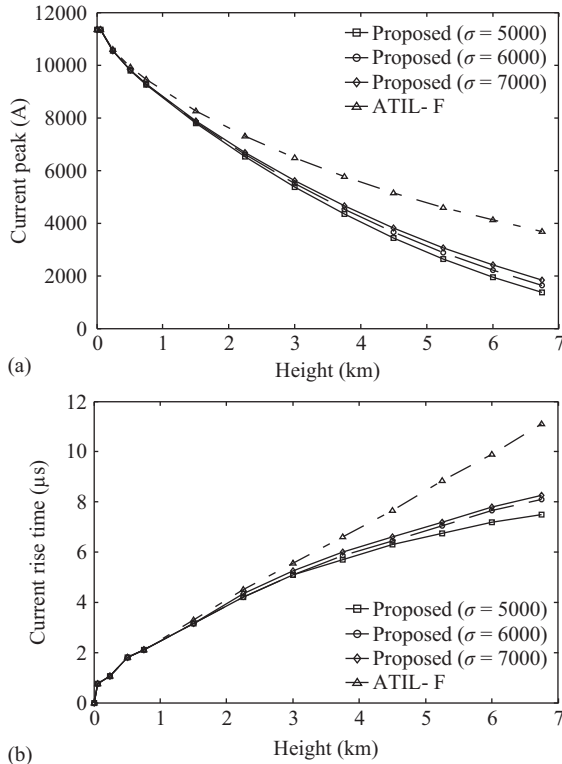


Figure 9.31 Current peak (a) and current rise time (b) for different conductivities of the channel ( $\sigma$  in S/m) [adapted from Seyed-Moosavi et al. [30]]

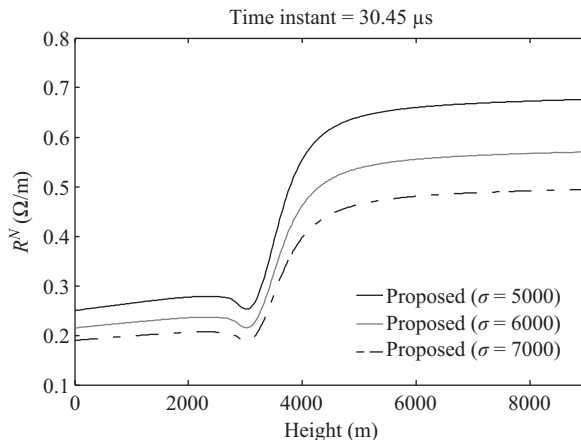


Figure 9.32 Non-linear part of resistance along the channel for different conductivities of the channel ( $\sigma$  in S/m) [adapted from Seyed-Moosavi et al. [30]]

### 9.5.3.4 Current wave propagation speed

Current wave propagation speed variations along the RSC predicted by the proposed model are shown in Figure 9.33. Different speed values tracking different reference points, including 10%, 20%, 90% and 100% of the peak value, and the maximum time derivative of current waveform  $di/dt$  at which the current reaches to its maximum rate of rise are selected as reference points. Knowing that the value of the distributed inductive load in the proposed model is unchanged along the channel, one may expect a constant speed profile in the proposed model [27]. This is not, however, the case as demonstrated in Figure 9.13 where the dependency of phase velocity and resistance are clearly shown.

### 9.5.4 Frequency-domain AT model

#### 9.5.4.1 Current profiles

The current source excitation of the antenna in the frequency-domain AT model is implemented by using a Dirac delta source [79] connected across a 3.25 m gap, whereas in the AT model a voltage source (delta-gap generator) is connected across the gap. There are other differences between the two excitation methods. For example, the channel-base current remains unchanged upon the arrival of a wave reflected from the wire top end in the case of current excitation, although we consider the times before the arrival of the first reflection from the top. This is not the case when voltage excitation is used. Also, the AT model proposed here solves a modified version of the EFIE for space-time-dependent currents with the excitation being the current source. Direct use of channel-base current in the MOM eliminates preliminary steps, including calculation of antenna's input impedance, and increases method's reliability.

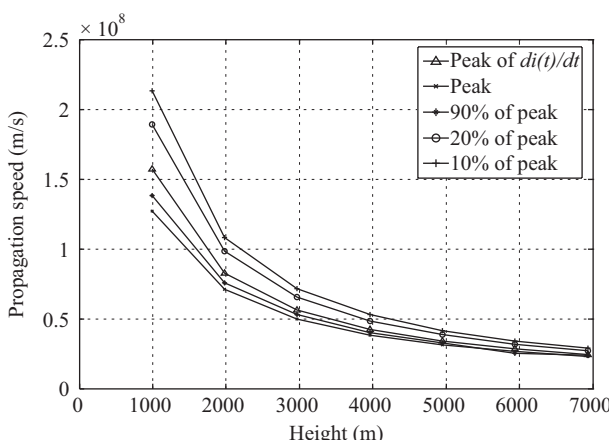


Figure 9.33 Return-stroke speed profile along the channel for the proposed model [adapted from Seyed-Moosavi et al. [30]]

To demonstrate the capabilities of the proposed model, it is compared with the AT model for the case of a perfectly conducting ground. Current distributions obtained using the two models are presented in Figure 9.34 as a function of time at heights of 650, 1300 and 1950 m from the channel-base. It is worth mentioning that the plots for the AT model show oscillations around the current peak. These are due to the numerical instabilities and could be eliminated by increasing the computation accuracy. Like the AT model in time domain, the AT model in frequency domain predicts attenuation and dispersion of the current pulse as it propagates along the lightning channel. Note that the observed variation of current with height follows from the solution of Maxwell's equations, in contrast with the commonly used engineering models in which imposed current distributions are used. A detailed comparison between the AT model and commonly used engineering models is made in Section 9.5.1.

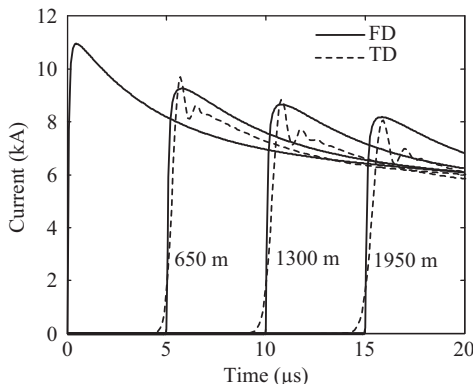


Figure 9.34 Current waveforms at three heights, 650 m, 1300 m and 1950 m [adapted from Shoory et al. [21]]

#### 9.5.4.2 Electromagnetic fields

Figure 9.35 depicts the distributions of electric and magnetic fields predicted by the frequency-domain and the original AT models at different distances from the channel base on a perfectly conducting ground. As seen in this figure, except small differences in the values of the field amplitude and rise time, the results predicted by the two models are similar. The differences between field amplitudes predicted by the two models may be related to the differences between current waveforms of the two models that are mainly due to the different techniques implemented for the solution of the EFIE in time and frequency domains. Also, differences between the rise times of field waveforms are thought to be due to numerical instabilities in the time-domain AT.

When the electromagnetic field features tabulated in Reference 1 are considered as a benchmark, both models reproduce all known attributes except for the hump following the initial peak in far magnetic fields and zero crossing in both electric and magnetic fields at far ranges.

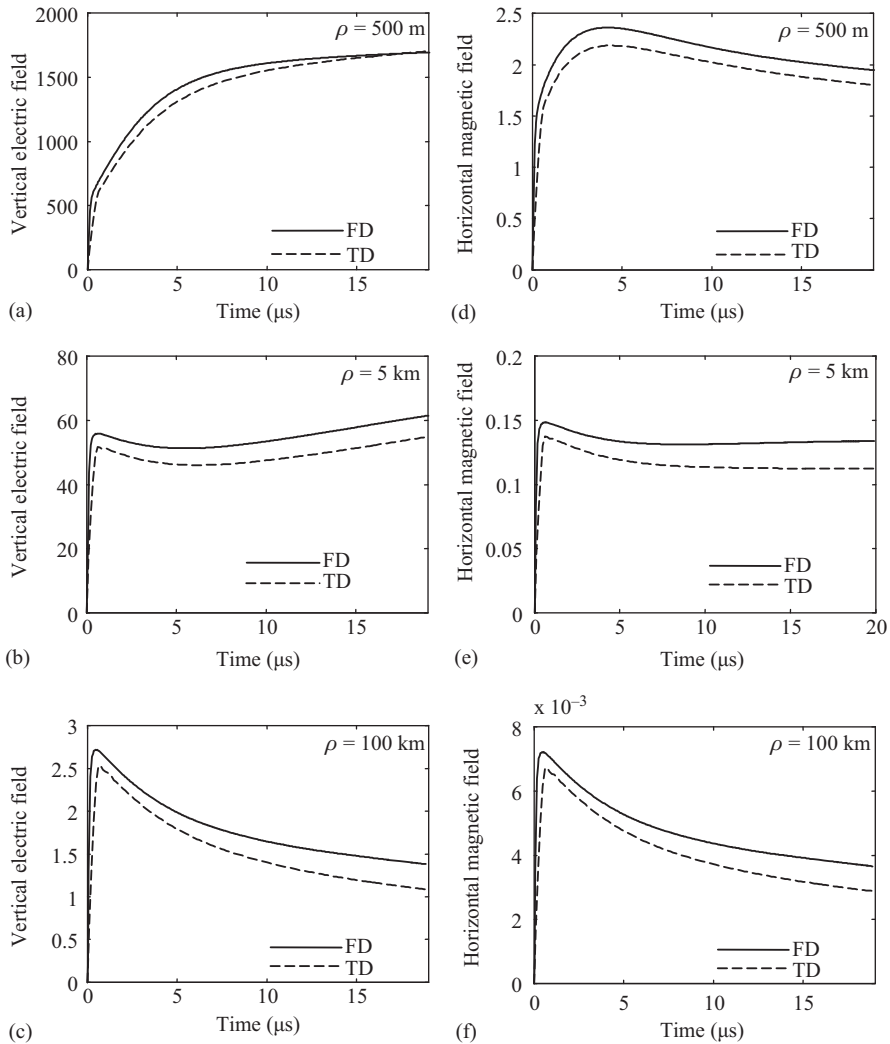


Figure 9.35 Vertical electric (a–c) and horizontal magnetic (d–f) fields at the air-ground interface 500 m, 5 km and 100 km from the lightning channel base for a perfect ground computed using the frequency-domain AT and the time-domain AT models [adapted from Shoory et al. [21]]

### 9.5.4.3 Electromagnetic fields above lossy half-space

#### Horizontal electric field

In studies related to the coupling of lightning radiated electromagnetic fields and overhead power lines, it is more convenient to use the horizontal component of electric field [80, 81]. Up to now, the Cooray–Rubinstein formula [81] or Cooray modified formula [59] has been probably the best simple approximations presented

for the calculation of horizontal electric field. For convenience, we rewrite the Cooray–Rubinstein formula as follows:

$$\begin{aligned} E_{ap}(\rho, z, j\omega) &= E_{app}(\rho, z, j\omega) - \sqrt{\frac{j\omega\mu_0}{\sigma_2 + j\omega\varepsilon_2}} H_{app}(\rho, 0, j\omega) \\ &= E_{app}(\rho, z, j\omega) + E_{ap}(\rho, 0, j\omega), \end{aligned} \quad (9.103)$$

where  $\rho$  is the azimuthal distance from the channel base,  $z$  is the height above ground and the subscript  $p$  denotes the perfect-ground assumption (see Figure 9.6). Cooray [59] proposed a modification to the first term in (9.103), weakening the contribution of its radiation component:

$$\begin{aligned} E_{ap}(\rho, z, j\omega) &= 0.4E_{app,r}(\rho, z, j\omega) + E_{app,i}(\rho, z, j\omega) + E_{app,s}(\rho, z, j\omega) \\ &\quad + E_{ap}(\rho, 0, j\omega), \end{aligned} \quad (9.104)$$

where  $E_{app,r}$ ,  $E_{app,i}$ ,  $E_{app,s}$  are, respectively, the radiation, induction and static terms of  $E_{app}(\rho, z, j\omega)$  in (9.103). In fact, in the expression for horizontal electric field above a perfect ground,  $E_{app,r}$  is the term with  $1/r^3$  dependence,  $E_{app,i}$  is the term with  $1/r^4$  dependence and  $E_{app,s}$  is the term with  $1/r^5$  dependence. Although this approach predicts a more accurate initial peak of the horizontal electric field at near ranges, it is not applicable to the case of a perfect ground [59].

Horizontal electric field waveforms at 20 m height above ground with conductivity  $\sigma_2 = 0.04$  S/m and permittivity  $\varepsilon_2 = 8\varepsilon_0$  for various distances from the channel base are shown (on a 5  $\mu$ s timescale) in Figure 9.36. Fields are obtained using the method presented in previous sections, the Cooray–Rubinstein formula [82] and the Cooray modified formula [59]. It is clearly seen from Figure 9.36 that at near ranges (e.g. 200 m), most important in studying lightning-induced overvoltages on power distribution lines, the fields predicted by these three methods are in close agreement. When the observation point is moved to intermediate and far ranges (e.g. 100 km), differences between the approach of this chapter and Cooray–Rubinstein or Cooray modified formulas become considerable. It is worth mentioning that at far ranges the Cooray–Rubinstein and the Cooray modified formulas yield results that are very close to those predicted by the wavetilt formula. It can be analytically shown that for a far observation point a few tens of metres above ground, the Cooray–Rubinstein (or Cooray modified) formula approximately reduces to the wavetilt expression [56, 82]. At these ranges, the limiting case of the Cooray–Rubinstein and wavetilt formulas is indeed exact if one deals with a pure ZSW. However, such never exists as the only contribution from a localized source [56]. It follows from Figure 9.36 that the surface wave component, which in our approach is not necessarily the ZSW, is not adequately accounted for in the Cooray–Rubinstein, Cooray modified and wavetilt formulas. While the Fresnel term is negligible at near ranges, it becomes significant at intermediate and far ranges. For convenience, we re-write the surface wave

component of the horizontal electric field, the terms in the brackets in (9.73), as follows:

$$\begin{aligned} E_{aps}(\rho, z, j\omega) = & -\frac{j\omega\mu_0}{2\pi\gamma_1} \int_0^h I(s) \left[ \frac{\gamma_1}{\gamma_2} e^{-\gamma_1 r_2} \left( \frac{\rho}{r_2} \right) \left( \frac{1 + \gamma_1 r_2}{r_2^2} \right) \right] ds \\ & + \frac{j\omega\mu_0}{2\pi\gamma_1} \int_0^h I(s) \left[ e^{-\gamma_1 r_2} \frac{\gamma_1^4}{\gamma_2^2} \left( \frac{\pi}{j\gamma_1 \gamma_2} \right)^{1/2} e^{-jP} F(P) \right] ds \end{aligned} \quad (9.105)$$

where subscript  $s$  denotes the surface wave. Only the first term of (9.105) is included in the Cooray–Rubinstein formula. As Figure 9.36 indicates, the difference between the results of this paper and those predicted by Cooray–Rubinstein and Cooray modified formulas at distant points is more pronounced at early times and gradually diminishes at later times. Further, for high values of ground's

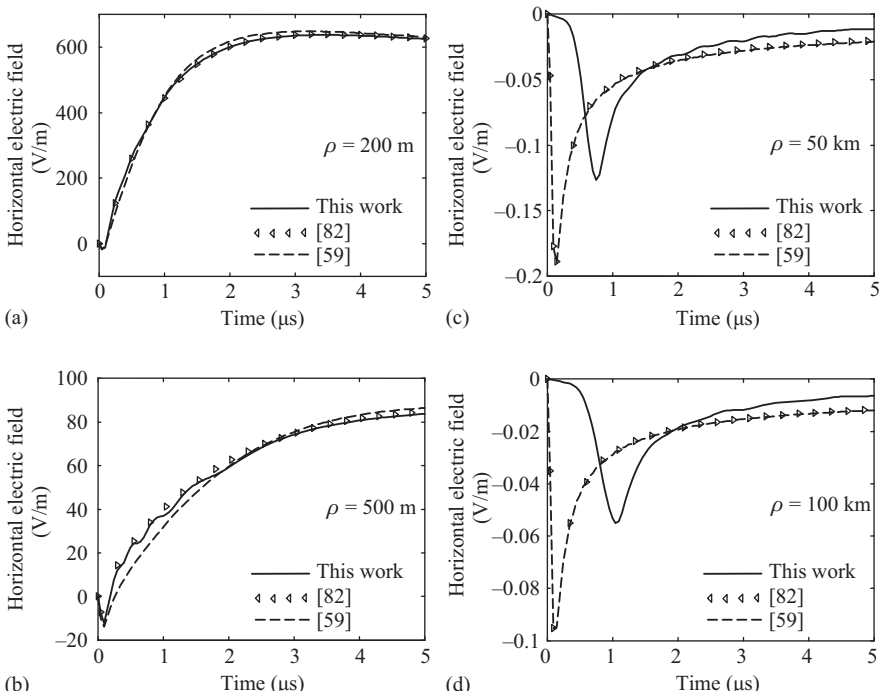


*Figure 9.36* Horizontal electric field at 20 m height above ground with conductivity  $\sigma_2 = 0.04$  S/m and permittivity  $\epsilon_2 = 8\epsilon_0$  computed using the approach of this chapter, the Cooray–Rubinstein formula and the Cooray modified formula (a) 200 m, (b) 500 m, (c) 50 km and (d) 100 km from the lightning channel base displayed on a 5 μs timescale [adapted from Shoory et al. [21]]

conductivity and permittivity, our approach, the Cooray–Rubinstein formula and the Cooray modified formula (and even the wavetilt formula for remote observation points a few tens of metres above ground), all predict similar fields, since the Fresnel term in this case is very small.

### *Surface waves*

We now consider three practical cases of the lower half-space: seawater, relatively high conductivity earth and relatively low conductivity earth. The electrical parameters of these cases are given in Table 9.2 and are similar to those given in Reference 54. Figure 9.37 illustrates contributions of the surface waves to the vertical electric and horizontal magnetic fields. In order to better resolve all significant features of the waveforms occurring at early times, only the first 2  $\mu\text{s}$  are shown. Calculations were carried out at the air–ground interface at two distances, 50 and 100 km from the channel base. This figure reveals four interesting features of surface waves, which are listed below:

- Surface waves exhibit flattening after the rapid variation (sharp initial peak) during the first some hundreds of nanoseconds.
- The amplitude of surface waves tends to decrease as the observation point is moved farther away from the source. This is best seen from the curves of both electric and magnetic fields for relatively low conductivity earth.
- For a given observation point, surface waves become more pronounced as the conductivity of the lower half-space decreases.
- For a given observation point, surface waves exhibit smoother rise as the conductivity of the lower half-space decreases.

Figure 9.37 also shows that the initial rise time of each field component increases as the observation point is moved farther away from the channel base. It follows that neglecting of surface waves, as commonly done in the calculation of lightning radiated electromagnetic fields, is only justified when the lower half-space has relatively high conductivity.

### *Total electric and magnetic fields*

The conductivity of the lower half-space could strongly influence the characteristics of lightning radiated fields. Field components suffer from propagation effects as they travel along the interface. The lossy interface preferentially attenuates high frequency components of radiated electric and magnetic fields, which results in an increase in the rise time and a decrease in the magnitude. These are shown in Figure 9.38. Calculations are performed for three types of the lower half-space: sea

*Table 9.2 Electrical parameters of three realistic cases of the lower half-space*

Medium	$\sigma_2, \text{S/m}$	$\epsilon_2/\epsilon_0$
Seawater	4.0	80
Relatively high conductivity earth	0.4	12
Relatively low conductivity earth	0.04	8

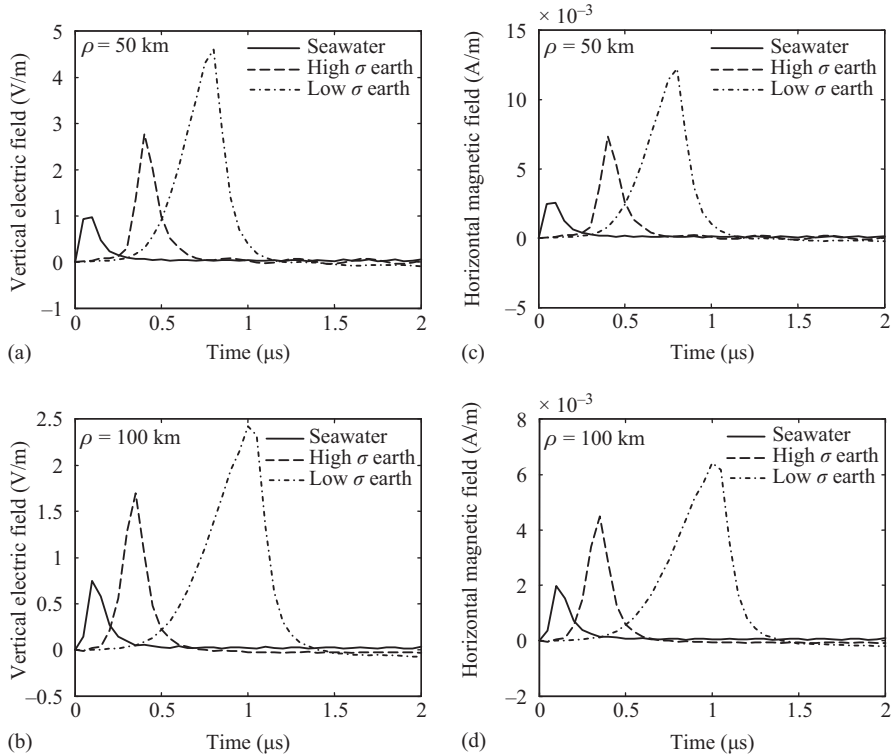


*Figure 9.37* Surface wave components of the vertical electric (*a* and *b*) and horizontal magnetic (*c* and *d*) fields computed at the air-ground interface for three types of the lower half-space 50 km and 100 km from the lightning channel base displayed on a 2  $\mu$ s timescale [adapted from Shoory et al. [21]]

water, relatively high conductivity earth and relatively low conductivity earth at distances of 200 m, 50 km and 100 km from the lightning channel base (displayed on a 5  $\mu$ s timescale). Figure 9.39 depicts horizontal electric fields for the same situation as in Figure 9.38. As seen from these figures, as the lower half-space becomes less conductive, distortions in the radiated vertical electric, horizontal electric and horizontal magnetic fields become more significant, and horizontal electric fields become larger. The results of this study indicate that in the analysis of lightning radiated electromagnetic fields over practical lower half-spaces, the perfect-ground assumption yields results that may be considerably different from those predicted by the more realistic approach described here, particularly at larger distances from the lightning channel.

We now discuss the polarity of the horizontal electric field as a function of distance. The results of Figure 9.39 reveal that for the three types of the lower half-space, the horizontal electric field at the air-ground interface exhibits the same

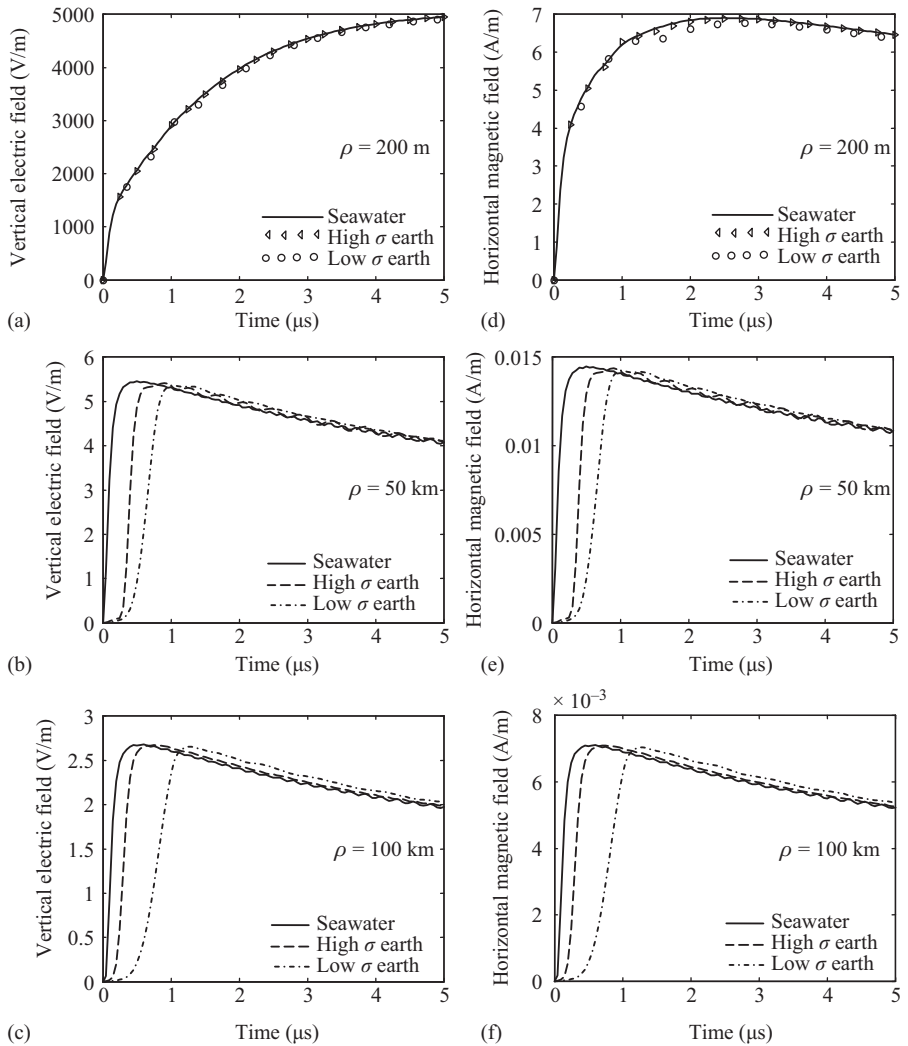
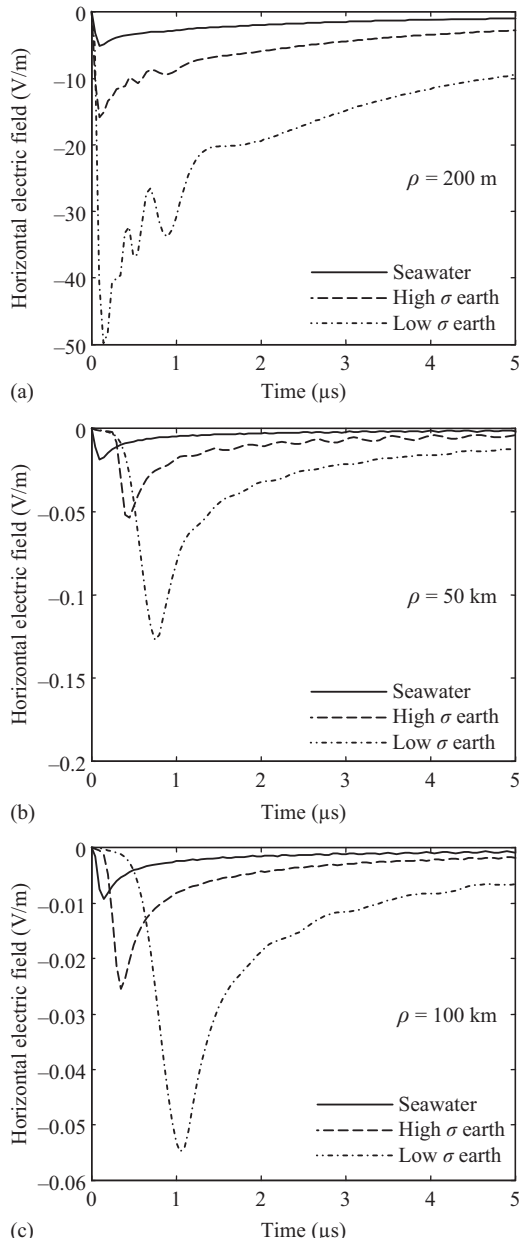


Figure 9.38 Vertical electric (a–c) and horizontal magnetic (d–f) fields at the air–ground interface for three types of the lower half-space 200 m, 50 km and 100 km from the lightning channel base displayed on a 5  $\mu\text{s}$  timescale [adapted from Shoory et al. [21]]

(negative) polarity for the entire range of distances (200 m to 100 km) considered. This is in contrast with the results of Figure 9.36 where the horizontal electric field waveforms are shown for observation points at a height of 20 m above ground. In this latter case, the horizontal electric field exhibits positive polarity for close distances and negative polarity for far distances. Such dissimilarity is due to the difference in height of the observation point above ground. In the



*Figure 9.39* Horizontal electric fields at the air-ground interface for three types of the lower half-space (a) 200 m, (b) 50 km and (c) 100 km from the lightning channel base displayed on a 5  $\mu\text{s}$  timescale [adapted from Shoory et al. [21]]

Cooray–Rubinstein expression for the horizontal electric field (9.103), or in the expression proposed in this chapter, the contribution from the first term (i.e. the horizontal electric field corresponding to the perfect-ground assumption) exhibits positive polarity [82], while the remainder of the expression shows negative polarity. The former dominates at near observation points few tens of metres above ground, resulting in the positive polarity of the total horizontal electric field. As the observation point moves toward the air–ground interface or farther away from the channel base, the contribution from the latter becomes dominant. Consequently, when the observation point is at the air–ground interface or at a large distance, the total horizontal electric field has negative polarity.

It is worth noting that the oscillations seen in Figure 9.38(d) and Figure 9.39(a) during the initial 2  $\mu\text{s}$  of field waveforms for relatively low conductivity earth 200 m from the channel base are related to the oscillatory behaviour of Fresnel integrals of complex argument.

## 9.6 Summary

In this chapter, we have presented the AT-based electromagnetic models of lightning return-stroke where the lightning RSC is considered as a monopole wire antenna above a conducting ground. We have also described the time- and frequency-domain solutions of the governing EFIE, utilizing the MOM. The solution of the EFIE is aimed to determine the current distribution along the channel from which remote electromagnetic fields are readily computed.

In the original AT model in time domain, the lightning RSC is represented by a lossy vertical monopole antenna, which is fed at its lower end by a voltage source. The voltage waveform is specified on the basis of the assumed input current of the antenna and antenna resistance per unit length. There are only two adjustable parameters in this model, namely the wave propagation speed for a non-resistive channel and the value of the distributed channel resistance. Once these two parameters are specified, the spatial and temporal distributions of the current along the channel are found by solving the governing EFIE, using the MOM. The time-domain AT model has been compared with other lightning return-stroke models in terms of current and line charge density distributions along the channel, and the predicted remote electromagnetic fields. The primary features of the time-domain AT model are as follows: (a) the current amplitude decreases and current rise time increases as the current wave propagates along the channel, in agreement with optical observations, (2) the current wave propagates along the channel at a speed lower than the speed of light due to both the effect of corona and ohmic losses in the channel and (3) the model-predicted electric and magnetic fields are reasonably consistent with typical measured fields.

In the ATIL model, the lightning RSC is represented by a lossy vertical monopole antenna above a perfectly conducting ground loaded by a set of constant (ATIL-F) or height-variable (ATIL-V) distributed inductances, fed at its lower end by a voltage source. The ATIL-V model allows one to have more control of the

variation of propagation speed along the channel and also of the current distribution and resultant electromagnetic field waveforms, without artificially changing the relative permittivity of the surrounding medium, as done in the original AT model. The ATIL-F and ATIL-V models are compared to the original AT in terms of the current distribution along the channel and remote electromagnetic fields. The current dispersion predicted by both the ATIL-F and ATIL-V models is more consistent (relative to the original AT model) with optical observations of lightning. It has been shown that the adjusting relative permittivity of the surrounding medium, as done in the AT model, does not affect the current dispersion along the RSC, whereas in both versions of the ATIL model, the current dispersion increases with increasing propagation speed.

We have also described a non-linear AT model. In this model, the lightning RSC is modelled with fixed inductive loading while resistive elements are considered as non-linear distributed loads whose resistance is a function of both current and time. Characteristics of the resistive loads are drawn from physical models and observations of the channel. The main feature of the proposed model is its ability to predict the zero crossing in both electric and magnetic field waveforms at far distances, as observed in all measurement data. It has been shown that the model can successfully predict the most well-known features of lightning RSC, including EM fields at intermediate and far distances, current distribution along the channel, current wave propagation speed profile and line charge density distribution, although it fails to predict the electric field flattening in the near distance.

In the frequency-domain AT model, the RSC is represented by a lossy vertical straight wire antenna above ground. A current source is used for the excitation of the wire in order to eliminate antenna's input impedance calculations required in the time-domain AT model. The model can reproduce all electromagnetic field benchmark features used for model evaluation, except for the hump following the initial peak in far magnetic fields and zero crossing in both electric and magnetic fields at far ranges. The finite conductivity of lower half-space is accounted for in computing lightning radiated electromagnetic fields by including a surface wave component. Complete electromagnetic fields over lossy ground are analysed, and it has been shown that the rise time and peak value of both electric and magnetic fields are significantly influenced by propagation over a poorly conducting ground. Decreasing ground's conductivity results in the increase in rise time and decrease in peak value. The related results also suggest that neglecting the influence of ground's finite conductivity is not acceptable in most practical situations.

Overall, various AT models provide an appropriate representation of the lightning RSC in terms of predicted currents and electromagnetic fields. AT models provide several degrees of freedom to simulate all known behaviours of the lightning RSC consistent with measured characteristics. The main feature of the approach described here is its ability to include nearby metallic structures in the modelling stage of the RSC. This feature enables one to study more effectively various lightning-related problems such as the coupling effect of the RSC on overhead and buried lines with complex geometry, the current distribution along a tall structure when struck by lightning, etc.

## References

1. V. A. Rakov, M. A. Uman, ‘Review and evaluation of lightning return-stroke models including some aspects of their application’, *IEEE Trans. Electromagn. Compat.*, vol. 40, no 4, pp. 403–426, 1998
2. S. I. Braginskii, ‘Theory of developing of a spark channel’, *Sov. Phys. JETP*, vol. 34, pp. 1068–1074, 1958
3. E. I. Dubovoy, M. S. Mikhailov, A. L. Ogonkov and V. I. Pryazhinsky, ‘Measurement and numerical modeling of radio sounding reflection from a lightning channel’, *J. Geophys. Res.*, vol. 100, pp. 1497–1502, 1995
4. M. N. Plooster, ‘Numerical model of the return-stroke of the lightning discharge’, *Phys. Floyds*, vol. 14, pp. 2124–2133, 1971
5. V. A. Rakov, ‘Characterization of lightning electromagnetic fields and their modeling’, in *Proc. 14th Int. Zurich Symp. EMC*, Supplement, Zurich, Switzerland, pp. 3–16, February 20–22, 2001
6. A. S. Bizjaev, V. P. Larionov and E. H. Prokhorov, ‘Energetic characteristics of lightning channel’, in *Proc. 20th Int. Conf. on Lightning Protection*, Interlaken, Switzerland, pp. 1.1/1-3, 1990
7. P. F. Little, ‘Transmission line representation of lightning return-stroke’, *J. Physics*, vol. 11, pp. 1893–1910, 1978
8. Y. Baba and V. Rakov, ‘On the mechanism of attenuation of current waves propagating along a vertical perfectly conducting wire above ground: Application to lightning’, *IEEE Trans. Electromagn. Compat.*, vol. 47, no. 3, pp. 521–532, 2005
9. N. Theethayi and V. Cooray, ‘On the representation of the lightning return-stroke as a current pulse propagating along a transmission line’, *IEEE Trans. Power Del.*, vol. 20, no. 2, pp. 823–837, 2005
10. S. Visacro and A. De Conti, ‘A distributed-circuit return-stroke model allowing time and height parameter variation to match lightning electromagnetic field waveform signatures’, *Geophys. Res. Lett.*, vol. 32, L23805, doi: 10.1029/2005GLO24336, 2005
11. V. Cooray and N. Theethayi, ‘Pulse propagation along transmission lines in the presence of corona and their implication to lightning return-strokes’, *IEEE Trans. Antennas Propag.*, vol. 56, no. 7, pp. 1948–1959, Digital Object Identifier doi: 10.1109/TAP.2008.924678, 2008
12. V. A. Rakov, ‘Lightning return-stroke modeling: Recent developments’, in *Proc. 3rd Brazilian Workshop Atmospheric Electricity/Int. Conf. Grounding and Earthing*, Rio de Janeiro, Brazil, pp. 85–96, Nov. 4–7, 2002
13. R. Moini, B. Kordi, G. Z. Rafi and V. A. Rakov, ‘A new lightning return-stroke model based on antenna theory model’, *J. Geophys. Res.*, vol. 105, no. D24, pp. 29, 693–629, 702, 2000
14. B. Kordi, R. Moini, W. Janischewskyj, A. M. Hussein, V. Shostak and V. A. Rakov, ‘Application of the antenna theory model to a tall tower struck by lightning’, *J. Geophys. Res.*, vol. 108, no. D17, pp. 4542, doi: 10.1029/2003JD003398, 2003

15. Y. Baba and V. A. Rakov, ‘Electromagnetic models of the lightning return-stroke’, *J. Geophys. Res.*, vol. 112, D04102, doi:10.1029/2006JD007222, 2007
16. A. Taflove, *Advances in Computational Electrodynamics: The Finite-Difference Time-Domain Method*, Norwood, MA: Artech House, 1998
17. Y. Baba and V. A. Rakov, ‘On the transmission line model for lightning return-stroke representation’, *Geophys. Res. Lett.*, vol. 30, no. 24, 2294, doi: 10.1029/2003GL018407, 2003
18. E. K. Miller, A. J. Poggio and G. J. Burke, ‘An integrodifferential equation for time-domain analysis of thin wire structure, part I’, *J. Comput. Phys.*, vol. 12, pp. 24–48, 1973
19. G. J. Burke and A. J. Poggio, *Numerical Electromagnetic Code (NEC)—Method of Moments*, Naval Ocean System Center, San Diego, CA, Tech. Document 116, Jan. 1980
20. Y. Baba and M. Ishii, ‘Numerical electromagnetic field analysis of lightning current in tall structure’, *IEEE Trans. Power Del.*, vol. 16, no. 2, pp. 324–328, 2001
21. A. Shoory, R. Moini, S. H. H. Sadeghi and V. A. Rakov, ‘Analysis of lightning radiated electromagnetic fields in the vicinity of lossy ground’, *IEEE Trans. Electromagn. Compat.*, vol. 47, no. 1, pp. 131–145, 2005
22. A. S. Podgorski and J. A Landt, ‘Numerical analysis of the lightning CN-tower interaction’, paper presented at the Int. Zurich Symp. Electromagn. Compat., Zurich, Switzerland, 1985
23. M. Van Blaricum and E. K. Miller, ‘TWTD—A computer program for time-domain analysis of thin-wire structures’, Lawrence Livermore Laboratory, California, Rept. UCRL-51 277, 1972
24. A. S. Podgorski and J. A Landt, ‘Three dimensional time domain modeling of lightning’, *IEEE Trans. Power Del.*, vol. PWRD-2, no. 3, pp. 931–938, 1987
25. Y. M. Lin, M. A. Uman, J. A. Tiller, R. D. Brantley, W. H. Beasley, E. P. Krider, *et al.*, ‘Characterization of lightning return-stroke electric and magnetic fields from simulation two-station measurements’, *J. Geophys. Res.*, vol. 84, pp. 6307–6314, 1979
26. S. Bonyadi-Ram, R. Moini and S. H. H. Sadeghi, ‘Incorporation of distributed inductive loads in the antenna theory model of lightning return-stroke channel’, paper presented at the Int. Conf. Lightning Protection (ICLP), Avignon, France, 2004
27. S. Bonyadi-Ram, R. Moini, S. H. H. Sadeghi and V. A. Rakov, ‘On representation of lightning return-stroke as a lossy monopole antenna with inductive loading’, *IEEE Trans. Electromagn. Compat.*, vol. 50, no. 1, pp. 118–127, 2008
28. D. M. Jordan and M. A. Uman, ‘Variation in light intensity with height and time from subsequent lightning return-stroke’, *J. Geophys. Res.*, vol. 88, pp. 6555–6562, 1983
29. D. Wang, N. Takagi, T. Watanabe, V. A. Rakove and M. A. Uman, ‘Observed leader and return-stroke propagation characteristic in the bottom 400 m of a rocket triggered lightning channel’, *J. Geophys. Res.*, vol. 104, no. D12, pp. 14369–14376, 1999

30. S. Bonyadi-Ram, R. Moini, S. H. H. Sadeghi and V. A. Rakov, ‘Incorporation of capacitive loads in the antenna theory model of lightning return-stroke channel’, in *Proc. Int. Symp. Electromagn. Compat. (EMC)*, Zurich, Switzerland, 2005
31. S. H. Seyed-Moosavi, R. Moini and S. H. H. Sadeghi, ‘Representation of lightning return-stroke channel as a nonlinearly loaded thin-wire antenna’, *IEEE Trans. Electromagn. Compat.*, vol. 51, no. 3, pp. 488–498, 2009
32. S. I. Drabkina, ‘The theory of the development of the spark channel’, *Sov. Phys. JETP*, vol. 21, pp. 473–483, 1951
33. K. Sheshyekani, S. H. H. Sadeghi and R. Moini, ‘A combined MoM-AOM approach for frequency domain analysis of nonlinearly loaded antennas in the presence of a lossy ground’, *IEEE Trans. Antennas Propag.*, vol. 56, no. 6, pp. 1717–1724, 2008
34. R. Moini, S. H. H. Sadeghi and B. Kordi, ‘An electromagnetic model of lightning return-stroke channel using electric field integral equation in time Domain’, *J. Eng. Analysis with Boundary Elements*, vol. 27, pp. 305–314, 2003
35. J. A. Stratton, *Electromagnetic Theory*, USA: McGraw-Hill, 1941
36. A. Reineix, ‘Analyse theorique de la diffraction d’ondes electromagnetiques impulsionnelles’, *Doctorat*, Univ. de Limoges, France, 1986
37. J. Herault, R. Moini, A. Reineix and B. Jecko, ‘A new approach to microstrip antenna using a mixed analysis: Transient-frequency’, *IEEE Trans. Antennas Propag.*, vol. 38, pp. 1166–1175, 1990
38. R. Moini, B. Kordi and M. Abedi, ‘Evaluation of LEMP effects on complex wire structures located above a perfectly conducting ground using electric field integral equation in time domain’, *IEEE Trans. Electromagn. Compat.*, vol. 40, no. 2, pp. 154–162, 1998
39. C. T. Tai, *Dyadic Green Functions in Electromagnetic Theory*, USA: IEEE Press, 1993
40. J. H. Richmond, ‘Radiation and scattering by thin-wire structures in the complex frequency domain’, in *Computational Electromagnetics*, E. K. Miller, Ed., New York: IEEE Press, 1992
41. H. C. Pocklington, ‘Electrical Oscillations in Wire’, *Proc. Cambridge Philos. Soc.*, vol. 9, pp. 324–332, 1897
42. Tapan K. Sarkar, ‘A study of various methods for computing electromagnetic field utilizing thin wire integral equation’, *Radio Sci.*, vol. 18, pp. 29–38, 1983
43. A. Ishimaru, *Electromagnetic Wave Propagation, Radiation, and Scattering*, USA: Prentice-Hall, 1991
44. J. A. Landt, E. K. Miller and F. J. Deadrick, *Time-Domain Computer Models of Thin-Wire Antennas and Scatterers*, Interaction Notes, Note 206, Lawrence Livermore Laboratory, California University, California, Nov. 1973
45. E. K. Miller and J. A. Landt, *Direct Time-Domain Techniques for Transient Radiation and Scattering*, USA: Interaction Notes, Note 334, Lawrence Livermore Laboratory, and Los Alamos Scientific Laboratory, Jul. 1976

46. G. J. Burke and A. J. Poggio, *Numerical Electromagnetic Code (NEC)—Method of Moments*, USA: Lawrence Livermore Laboratory, 1981
47. J. H. Richmond, ‘Digital computer solutions of the rigorous equations for scattering problems’, *Proc. IRE*, vol. 53, pp.796–804, 1965
48. R. F. Harrington, ‘Matrix methods for field problems’, *Proc. IEEE*, vol. 55, no. 2, pp. 136–149, 1967
49. S. H. Seyed-Moosavi, R. Moini, S. H. H. Sadeghi and B. Kordi, ‘Application of the nonlinear antenna theory model to a tall tower struck by lightning for the evaluation of return stroke channel current and radiated electromagnetic fields’, *J. Geophys. Res.*, vol. 116, D11118, doi:10.1029/2010JD014684, 2011
50. L. Grcev, ‘Computer analysis of transient voltages in large grounding systems’, *IEEE Trans. Power Del.*, vol. 11, no. 2, pp. 815–823, 1996
51. A. Sommerfeld, ‘Über die ausbreitung der Wellen in der drahtlosen Telegraphie’, *Ann. Phys.*, vol. 28, p. 665, 1909
52. T. Takashima, T. Nakae and R. Ishibashi, ‘Calculation of complex fields in conducting media’, *IEEE Trans. Elect. Ins.*, vol. EI-15, pp. 1–7, 1980
53. R. W. P. King, ‘Electromagnetic field of a vertical electric dipole over an imperfectly conducting half-space’, *Radio Sci.*, vol. 25, pp. 149–160, 1990
54. R. W. P. King and S. S. Sandler, ‘The electromagnetic field of a vertical electric dipole over the earth or sea’, *IEEE Trans. Antennas Propag.*, vol. 42, no. 3, pp. 382–389, 1994
55. M. Abramowitz and I. Stegun, *Handbook of Mathematical Functions*, New York: Dover, 1970
56. J. R. Wait, ‘On the wavetilt at high frequencies—a personal view’, *IEEE Trans. Electromagn. Compat.*, vol. 39, no. 1, p. 65, 1997
57. J. R. Wait, ‘The ancient and modern history of EM ground-wave propagation’, *IEEE Antennas Propagat. Mag.*, vol. 40, no. 5, pp. 7–24, 1998
58. J. R. Wait, *Electromagnetic Waves in Stratified Media*, New York: IEEE Press, 1996
59. V. Cooray, ‘Some considerations on the Cooray–Rubinstein formulation used in deriving the horizontal electric field of lightning return-strokes over finitely conducting ground’, *IEEE Trans. Electromagn. Compat.*, vol. 44, no. 4, pp. 560–566, 2002
60. V. Cooray and S. Lundquist, ‘Effects of propagation on the rise times and the initial peaks of radiation fields from return-strokes’, *Radio Sci.*, vol. 22, pp. 409–415, 1983
61. V. A. Rakov, ‘Some inferences on the propagation mechanisms of dart leaders and return-strokes’, *J. Geophys. Res.*, vol. 103, pp. 1879–1887, 1998
62. C. A. Nucci, G. Diendorfer, M. A. Uman, F. Rachidi, M. Ianoz and C. Mazzetti, ‘Lightning return-stroke current models with specified channel base current: A review and comparison’, *J. Geophys. Res.*, vol. 95, pp. 20395–20408, 1990
63. V. A. Rakov and A. Dulzon, ‘A modified transmission line model for lightning return-stroke field calculations’, *Proc. Int. Zurich Symp. Electromagn. Compat.*, vol. 9, pp. 229–235, 1991

64. R. Thottappillil, V. A. Rakov and M. A. Uman, ‘Distribution of charge along the lightning channel: Relation to remote electric and magnetic fields and to return-stroke models’, *J. Geophys. Res.*, vol. 102, pp. 6987–7006, 1997
65. F. Bost, L. Nikolas and G. Rojat, ‘Study of conduction and induction phenomena in electric circuits using a time-domain integral formulation’, *IEEE Trans. Magnetics*, vol. 36, no. 4, pp. 960–963, 2000
66. M. R. Guedira, ‘Etude en régime transitoire du comportement de structures filaires présentant de charges linéaires ou non linéaires’, *These pour l’obtention du doctorat*, Université de Limoges, France, 1983
67. C. A. Nucci, S. Guerrieri, M. T. Correia de Barros and F. Rachidi, ‘Influence of corona on the voltages induced by nearby lightning on overhead distribution lines’, *IEEE Trans. Power Del.*, vol. 15, no. 4, pp. 1265–1273, 2000
68. R. C. Olsen III, D. M. Jordan, V. A. Rakov, M. A. Uman and N. Grimes, ‘Observed one-dimensional return-stroke propagation speeds in the bottom 170 m of a rocket triggered lightning channel’, *Geophys. Res. Lett.*, vol. 31, L16107, doi: 10.1029/2004GL020187, 2004
69. V. Kodali, V. A. Rakov, M. A. Uman, K. J. Rambo, G. H. Schentzer, J. Schoene, *et al.*, ‘Triggered-lightning properties inferred from measured currents and very close electric fields’, *Atmos. Res.*, vol. 76, pp. 355–376, 2005
70. V. P. Idone and R. E. Orville, ‘Lightning return-stroke velocities in the thunderstorm research international program (TRIP)’, *J. Geophys. Res.*, vol. 87, pp. 4903–4915, 1982
71. R. Thottappillil and M. Uman, ‘Comparison of lightning return-stroke models’, *J. Geophys. Res.*, vol. 98, no. D12, pp. 22903–22914, 1993
72. C. E. Baum, ‘Return-stroke initiation’, in *Proc. EMC Symposium*, Zurich, pp. 383–388, 1989
73. M. N. Plooster, ‘Numerical simulation of spark discharges in air’, *Phys. Fluids*, vol. 14, pp. 2111–2123, 1971
74. M. N. Plooster, ‘Numerical model of the return-stroke of the lightning discharge’, *Phys. Fluids*, vol. 14, pp. 2124–2133, 1971
75. A. De Conti, S. Visacro, N. Theethayi and V. Cooray, ‘A comparison of different approaches to simulate a nonlinear channel resistance in lightning return-stroke models’, *J. Geophys. Res.*, 113, D14129, doi:10.1029/2007JD009395, 2008
76. R. H. Golde, *Lightning*, Vol.1—*Physics of Lightning*, New York: Academic Press, 1977
77. R. C. Jones, ‘Return-stroke core diameter’, *J. Geophys. Res.*, vol. 73, no. 2, pp. 809–814, 1968
78. C. R. Paul, *Analysis of Multi-Conductor Transmission Lines*, New York: Wiley, 1994
79. L. Grcev, F. Rachidi and V. A. Rakov, ‘Comparison of electromagnetic models of lightning return-strokes using current and voltage sources’, in *Proc. 12th Int. Conf. Atmospheric Electricity*, Versailles, France, pp. 593–596, 2003

80. F. Rachidi, ‘Formulation of the field-to-transmission line coupling equations in terms of magnetic excitation fields’, *IEEE Trans. Electromagn. Compat.*, vol. 35, no. 3, pp. 404–407, 1993
81. M. Rubinstein, ‘An approximate formula for the calculation of the horizontal electric field from lightning at close, intermediate, and long ranges’, *IEEE Trans. Electromagn. Compat.*, vol. 38, no. 3, pp. 531–535, 1996

---

## *Chapter 10*

# **Transmission line models of lightning return stroke**

*Alberto De Conti<sup>1</sup>, Fernando H. Silveira<sup>1</sup> and  
Silverio Visacro<sup>1</sup>*

---

### **10.1 Introduction**

A typical return stroke in downward negative lightning is initiated when the bottom of a negatively charged leader propagating downward from the cloud is brought to ground potential. In first strokes, this happens when the stepped-leader encounters, at some tens of metres above the ground, one of the upward-propagating, positively charged leaders induced by the downward leader. The negative charges deposited by the stepped-leader are then gradually neutralized by voltage and current waves that propagate along the leader path, while the positive charges deposited by the upward-connecting leader are neutralized by downward-propagating voltage and current waves. This is somehow analogous to a negatively charged transmission line that is switched to ground potential through a short transmission line grounded at its bottom, or, alternatively, to the excitation of an initially uncharged transmission line by a series lumped voltage source located somewhere down the line, this transmission line being also grounded at its bottom. A similar description can be applied to subsequent strokes, except that now the return stroke is initiated when the dart leader reaches the ground. The resulting transient process is, in this case, analogous to either a negatively charged, lossy transmission line that is suddenly switched to ground potential through a lumped grounding impedance or the injection of a positive current pulse at one end of an initially neutral transmission line by a lumped current or voltage source.

Transmission line models of the return stroke use the analogy above to represent the propagation of the return stroke as being equivalent to the propagation of

---

<sup>1</sup>LRC – Lightning Research Center, Federal University of Minas Gerais, Av. Antonio Carlos 6.627 Pampulha, 31270.901, Belo Horizonte, Brazil. Emails: conti@cpdee.ufmg.br; silveira@cpdee.ufmg.br; Lrc@cpdee.ufmg.br.

current and voltage pulses along a transmission line.\* In these models, the propagating pulse is initiated either with the discharge to ground of a previously charged transmission line or with the use of a lumped source to excite the channel. Currents and voltages along the lightning channel are then found from the solution of the well-known telegrapher's equations, which for constant, linear and uniform per-unit-length parameters can be written in time domain as

$$-\frac{\partial V(z, t)}{\partial z} = L \frac{\partial I(z, t)}{\partial t} + RI(z, t) \quad (10.1)$$

$$-\frac{\partial I(z, t)}{\partial z} = C \frac{\partial V(z, t)}{\partial t} + GV(z, t) \quad (10.2)$$

where  $L$ ,  $C$ ,  $R$  and  $G$  are, respectively, the per-unit-length inductance, capacitance, resistance and conductance of the transmission line assumed to represent the lightning channel,  $z$  is the axial coordinate specifying position on the line and  $t$  is time. Equations (10.1) and (10.2) are derived from Maxwell's equations under the assumption of a quasi-transverse electromagnetic (TEM) field structure, which means, for a two-conductor transmission line with both conductors parallel to the axial coordinate  $z$ , that the  $z$ -directed electric field component associated with the propagating current and voltage pulses is negligible compared to the electric field components laying on planes transverse to the  $z$  coordinate (Paul, 1994). By using Kirchhoff's laws, (10.1) and (10.2) can also be derived from the equivalent circuit illustrated in Figure 10.1, which uses a combination of lumped circuit elements to

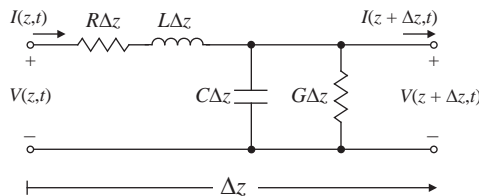


*Figure 10.1 Lumped-circuit model of a short transmission line segment with length  $\Delta z$*

\*The engineering and electromagnetic return stroke models also consider the return stroke as being somehow analogous to a current (voltage) pulse propagating along a conducting path (Rakov and Uman, 2003). However, instead of solving (10.1) and (10.2) for a given set of  $R$ ,  $L$ ,  $C$  and  $G$  parameters, engineering return stroke models make use of mathematical expressions to relate the spatial and temporal distribution of the channel current to a current waveform assumed at the channel base (Rakov and Uman, 2003), while electromagnetic return stroke models use some kind of numerical technique to solve Maxwell's equations applied to the problem of a lossy vertical antenna (Baba and Rakov, 2007). Although usually not classified as an electromagnetic return stroke model in a strict sense, the hybrid electromagnetic model (HEM) of Visacro and Soares (2005) also solves Maxwell's equations numerically to determine currents along a lightning channel represented as a long vertical wire (Visacro and Silveira, 2004).

represent a short line section of length  $\Delta z$  (Paul, 1994). For this reason, the transmission line models of the return stroke are also called distributed-circuit return stroke models (Rakov and Uman, 1998).

All information regarding the electric and magnetic fields associated with current and voltage pulses propagating in a transmission line is implicitly described by the per-unit-length parameters  $R$ ,  $L$ ,  $C$  and  $G$ . If these parameters are known, telegrapher's equations (10.1) and (10.2) can be solved for any given boundary conditions and any type of excitation by using either a numerical or an analytical approach depending on the complexity of the problem. If the cross section and the properties of the dielectric between the line conductors are independent of  $z$ , as well as the cross section and the properties of the line conductors themselves, the per-unit-length parameters do not vary with the position on the line and the transmission line is said to be uniform (Paul, 1994). If, however, any of these conditions is violated, the transmission line is said to be non-uniform. This is exactly the case if the lightning channel is assumed to be represented as a long vertical wire positioned over a perfectly conducting plane, which leads to a variation of  $L$  and  $C$  with height (*Theethayi and Cooray*, 2005). The channel capacitance is also affected by the presence of the cloud at the top of the leader channel (Little, 1978), by the existence of a corona sheath surrounding the channel core whose radius is believed to vary with height (Gorin, 1985), and also, to a lesser extent, by possible variations in the leader core radius with height, the latter also affecting the channel inductance.

In addition to  $L$  and  $C$ , the channel resistance and conductance per unit length are also expected to be dependent of  $z$ , the former mostly due to variations in leader temperature, radius and conductivity (Borovski, 1995; Rakov, 1998), the latter due to variations in the radius and conductivity of the ionized region existing in the vicinity of the channel core (Maslowski and Rakov, 2006). Other factors, such as the channel tortuosity and the existence of branches, can also be approximately taken into account by attributing to specific channel sections different per-unit-length parameters, or different charge distributions. It is thus apparent that if the lightning channel is to be represented as a transmission line, this transmission line should be non-uniform.

The complexity of the problem increases if the time-varying and non-linear nature of the channel parameters is also considered. It is known that the leader channel is composed of a thin, negatively charged core of few millimetres surrounded by a radially formed corona sheath that presumably contains the bulk of the charges deposited by the leader and whose external radius is believed to range from some centimetres to tens of metres (Rakov, 1998). When the return stroke is initiated, the gradual neutralization of the charges deposited by the leader is accompanied by the heating and expansion of the channel core and by the collapse of the corona sheath that surrounds it. If the lightning channel is represented as a transmission line, one can therefore expect such a transmission line to have different per-unit-length parameters ahead and behind the return stroke front. Indeed, in a subsequent stroke, the resistance of the leader channel is believed to decay about two orders of magnitude with the passage of the return stroke current

(Rakov, 1998), and to vary non-linearly with this current (Braginskii, 1958). In addition, the gradual neutralization of the corona sheath that surrounds the channel core results in a non-linear variation of the channel capacitance and conductance (Gorin, 1985; Baum and Baker, 1990; Theethayi and Cooray, 2005; Visacro and De Conti, 2005). Finally, the channel inductance and capacitance are also affected by the expansion of the channel core, although this variation is believed to be not much significant (Strawe, 1979). It is thus apparent that, in addition to being non-uniform, the transmission line representing the lightning channel is also non-linear.

Several transmission line models have been proposed by different authors to represent the lightning return stroke. In general, different assumptions are made in the derivation of the channel parameters per unit length and in the way these parameters are assumed to vary with position and time. Differences are also found in the form of excitation of the transmission line representing the channel, and in the method applied to solve telegrapher's equations (10.1) and (10.2). Section 10.2 presents a brief overview of these models, dividing them into discharge type models and lumped-excitation models. Section 10.3 is dedicated to the derivation of the per-unit-length parameters to be used in a simplified transmission line model of a subsequent stroke. Section 10.4 presents computed results in which the effect of various channel parameters on predicted lightning currents and remote electromagnetic fields is discussed on the basis of the simplified return stroke model proposed in Section 10.3. The obtained results suggest that the consideration of non-uniform and non-linear channel parameters changes the model predictions in such a way that they come closer to characteristics typically observed in actual lightning. Section 10.5 presents summary and conclusions.

## 10.2 Overview of transmission line models of lightning return stroke

The existing transmission line models of the return stroke can be roughly classified into two categories, namely discharge-type models or lumped-excitation models. Discharge-type models represent the leader channel as a transmission line charged to some potential  $U$ , the return stroke being the result of the line discharge to ground (e.g. Price and Pierce, 1977; Little, 1978; Gorin, 1985; Mattos and Christopoulos, 1988). Lumped-excitation models represent the leader channel as an initially neutral transmission line that is excited at its bottom by a lumped source (e.g. Amoruso and Lattarulo, 1993; Theethayi and Cooray, 2005; Visacro and De Conti, 2005). One could possibly include a third category of transmission line models that uses the analogy between lightning and transmission lines to derive, on the basis of expected lightning properties, relevant quantities such as the per-unit-length channel resistance and the channel radius (e.g. Rakov, 1998). In some cases, one model can fall into more than one category, such as the model of Oetzel (1968), which is intended essentially to estimate lightning parameters but can also be viewed as a discharge-type model.

A brief overview of transmission line models of the return stroke pertaining to the discharge-type and lumped-excitation categories is presented throughout this section. This overview is focused on the main assumptions adopted in the representation of the lightning channel and on the overall agreement between model (mostly current and remote electromagnetic field) predictions with experimental data. Models dedicated to the estimation of lightning parameters are not discussed here in detail because they usually present neither channel currents nor remote electromagnetic field predictions. Their estimates for the channel diameter and for the per-unit-length resistance will be, however, useful in verifying the validity of assumptions adopted in other models.

### 10.2.1 Discharge-type models

Most of the existing transmission line models of the return stroke are of discharge type. The main idea behind these models is illustrated in Figure 10.2. It consists of representing the leader channel as a charged transmission line that is suddenly brought to ground potential through the closing of a switch. The return stroke is assumed to be equivalent to the transient process resulting from the line discharge. Examples of models pertaining to this category are the models of Oetzel (1968), Price and Pierce (1977), Little (1978), Strawé (1979), Takagi and Takeuti (1983), Gorin (1985, 1992), Mattos and Christopoulos (1988, 1990), Baker (1990), Baum and Baker (1990) and Bazelyan and Raizer (2000).

In general, return stroke models of discharge type assume the channel to be straight and vertical. A voltage difference in the range of  $10^7$  to  $10^8$  V based on the estimates of Uman (1984) is usually assumed to exist between the tip of the leader and the ground plane in the simulation of first strokes. Channel lengths varying from 1.5 (Baker, 1990) to 9.6 km (Strawé, 1979) are found in the literature, values between 3 and 6 km being typical (e.g. Oetzel, 1968; Little, 1978; Takagi and Takeuti, 1983; Mattos and Christopoulos, 1988; Bazelyan and Raizer, 2000). In some cases, infinite channels are also assumed for allowing an analytical solution

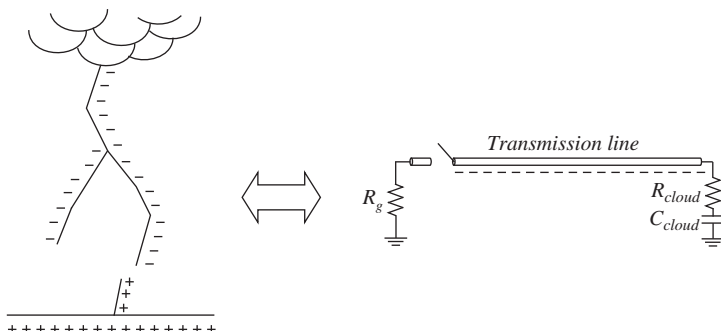


Figure 10.2 Typical representation adopted in discharge-type, transmission line models of the return stroke

to the transients in the line (e.g. Price and Pierce, 1977; Baum and Baker, 1990). In general, the cloud termination of the leader channel is assumed to be open-circuited (Strawe, 1979; Baker, 1990; Bazelyan and Raizer, 2000), purely capacitive (Oetzel, 1968; Little, 1978; Takagi and Takeuti, 1983) or resistive–capacitive (Mattos and Christopoulos, 1988, 1990), with capacitance values ranging from 0.01 to 1  $\mu\text{F}$  and resistance values of the order of 1  $\text{k}\Omega$ . The selection of these parameters is based on assumptions that are often not completely justified and need further experimental validation. The bottom of the channel is usually short-circuited (Oetzel, 1968) or terminated in a lumped ground resistance with values ranging from 50 to 200  $\Omega$  (e.g. Strawe, 1979; Little, 1978; Takagi and Takeuti, 1983; Mattos and Christopoulos, 1988; Baker, 1990). The use of a matching resistance at the channel bottom, although unrealistic, was assumed by Price and Pierce (1977) in order to let the solution of the line transients analytically tractable. In some cases, as in the model of Baum and Baker (1990), the boundary conditions at the bottom of the channel were not clearly specified. Most of the aforementioned models consider attachment points ranging from 0 to 100 m above ground. They are therefore able to represent both first and subsequent strokes.

Although the channel inductance  $L$  and capacitance  $C$  per unit length are expected to vary with position and time, as discussed in Section 10.1, the models of Oetzel (1968), Price and Pierce (1977), Strawe (1979), Takagi and Takeuti (1983) and Bazelyan and Raizer (2000) assumed these parameters to be constant and uniform. Little (1978) and later Mattos and Christopoulos (1988) assumed the channel capacitance to vary with height due to the influence of both ground plane and cloud, but the obtained values were assumed to remain constant during the return stroke. The influence of a corona sheath surrounding the channel core was considered by Strawe (1979), Gorin (1985), Mattos and Christopoulos (1990), Bazelyan and Raizer (2000), Baker (1990) and Baum and Baker (1990) in the form of an increase in the capacitance associated with the channel core. The models of Gorin (1985), Baker (1990) and Baum and Baker (1990) also considered this parameter to vary non-linearly due to the neutralization of the corona sheath.

In spite of the non-linear nature of channel losses, the assumption of linear, constant and uniformly distributed series channel resistance is frequent in discharge-type models. This is the case, for instance, of the models of Little (1978) ( $R = 1 \Omega/\text{m}$ ), Price and Pierce (1977) ( $R \approx 0.06 \Omega/\text{m}$  if  $L = 2 \mu\text{H}/\text{m}$  is assumed in their paper) and Takagi and Takeuti (1983) ( $R = 0.08 \Omega/\text{m}$ ). Although sometimes selected without a clear physical justification, the values of  $R$  indicated above are in the range of channel resistances estimated by Rakov (1998) for the leader ( $R = 3.5 \Omega/\text{m}$ ) and return stroke ( $R = 0.035 \Omega/\text{m}$ ) channels. A more complex representation of channel losses was considered by Strawe (1979), Baker (1990), Mattos and Christopoulos (1988, 1990), Gorin (1985, 1992) and Bazelyan and Raizer (2000), who applied either hydrodynamic models or arc resistance models with different simplifying assumptions to simulate the non-linear variation of the channel resistance.

Currents predicted by models of discharge type usually present decay in magnitude and increase in rise time with increasing channel height, which is

consistent with return stroke luminosity profiles (Jordan and Uman, 1983). However, the agreement between predicted channel-base currents and measured current waveforms is often poor (see, e.g. Mattos and Christopoulos, 1990, Fig. 3) or not clearly specified (e.g. Baker, 1990, discussion of Figs. 4 and 5). Disagreements have also been found between estimated current parameters at the channel base and measured data (e.g. Price and Pierce, 1977; Little, 1978).

Strawe (1979), by defining the speed of current waves propagating along the channel in terms of the arrival of 63% of the peak current at a given channel height, obtained a resultant current speed ranging from 0.2 to  $0.3c$  in his model predictions, where  $c$  is the speed of light. These values are in the range of return stroke speeds inferred from optical measurements of lightning luminosity profiles, which are seen to vary from approximately 0.1 to  $2c/3$  (Uman, 1984). Other authors have also obtained average propagation speeds in the first kilometre or so of the lightning channel that fall into the limits above, namely Bazelyan and Raizer (2000) ( $0.4c$ ), Gorin (1985) ( $0.1\text{--}0.6c$ ), Little (1978) ( $0.5c$ ), Takagi and Takeuti (1983) ( $2c/3$ ) and Mattos and Christopoulos (1990) ( $\approx 0.5c$ ), but it is not clear which criteria they considered to estimate this parameter. In general, the models above predict a decay of the propagation speed with increasing height that is consistent with measured lightning luminosity profiles (Jordan and Uman, 1983).

Remote electromagnetic fields predicted by discharge-type models are usually inconsistent with measured data. This is the case of the models of Price and Pierce (1977, Fig. 4), Takagi and Takeuti (1983, Figs. 12 and 13), Baker (1990, Fig. 3 and 6) and Mattos and Christopoulos (1990, Figs. 7–9). Other investigators such as Little (1978), Strawe (1979), Baum and Baker (1990), Gorin (1985, 1992) and Bazelyan and Raizer (2000) did not calculate remote electromagnetic fields with their models. Since the agreement between measured and predicted field waveforms is probably the single the most important factor in assessing the validity of return stroke models, the overall validity of discharge-type models can be considered limited.

### 10.2.2 Lumped-excitation models

In the transmission line models of the return stroke that consider lumped excitation, the leader channel is represented as an initially uncharged transmission line that has one of its terminals excited by a lumped current or voltage source (see Figure 10.3). Examples of models pertaining to this category are the models of Uman and McLain (1969), Amoruso and Lattarulo (1993), Rondón et al. (2002), Theethayi and Cooray (2004, 2005), Visacro and De Conti (2005) and De Conti et al. (2008a).

The simplest transmission line model of the return stroke considering lumped excitation is the well-known TL model (Uman and McLain, 1969). This model assumes that the current  $i(z,t)$  at any point  $z$  of the channel at any time  $t$  is a delayed replica of the current  $I(0,t)$  injected at the channel base by a lumped current source, the delay being dependent on the assumed wave speed  $v$ . Since the propagating current pulse is neither attenuated nor distorted in the TL model, the return stroke channel is analogous to a lossless uniform two-conductor transmission line surrounded by a medium with permittivity  $\epsilon$  and permeability  $\mu$ , where  $v = (\mu\epsilon)^{-0.5}$ .

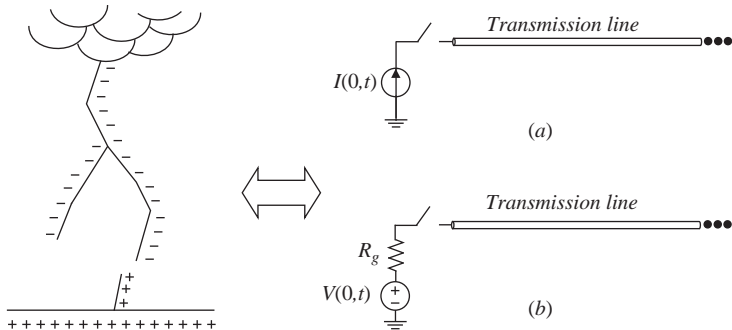


*Figure 10.3 Typical representation of a return stroke in a transmission line return stroke model considering lumped excitation: (a) use of an ideal current source at the bottom of the channel; (b) use of a voltage source with internal resistance  $R_g$  at the bottom of the channel*

The solution of telegrapher's equations leads in this case to a simple closed-form expression relating the current at any position of the channel to the current injected at the channel base. For this reason, the TL model is usually classified as an 'engineering' return stroke model. Since a whole chapter is dedicated in this book to the engineering return stroke models, a detailed discussion of the TL model will be omitted here in favour of other transmission line models of the return stroke. Some of its characteristics and predictions will be, however, used for comparison purposes whenever necessary.

In the models of Amoruso and Lattarulo (1993), Rondón et al. (2002), Theethayi and Cooray (2005), Visacro and De Conti (2005) and De Conti et al. (2008a), many of the simplifications adopted in the TL model are removed in an attempt to let the modelling of the lightning channel more realistic, mostly with the consideration of non-uniform and/or non-linear per-unit-length parameters. However, several simplifying assumptions are still adopted in the formulation of these models. For instance, the presence of channel branches and tortuosities is neglected, and as a consequence the channel is modelled as a straight vertical transmission line. Also, an ideal lumped current source is assumed to inject the lightning current at the bottom of the channel, even though a lumped voltage source with internal impedance representing the equivalent grounding impedance seen by the leader would be more adequate for assuring the appropriate boundary conditions at the lightning attachment point. This, however, does not pose a problem since identical model predictions can be obtained with either approach even if non-linear and non-uniform channel parameters are considered in the simulation of lightning strikes to flat ground (De Conti and Visacro, 2009).

As opposed to the TL model, in which the channel inductance  $L$  and capacitance  $C$  per unit length are assumed to be independent of the  $z$  coordinate along the channel, the approximations adopted in the models of Rondón et al. (2002), Theethayi and Cooray (2005), Visacro and De Conti (2005) and De Conti et al. (2008a) result in a logarithmic variation of these parameters with height.

Amoruso and Lattarulo (1993) represented the lightning channel as a lossless transmission line in which an exponential variation was attributed to  $L$  and  $C$  with respect to  $z$ . Such an exponential variation was justified by the authors as being the result of a channel core radius exponentially expanding with decreasing channel height. In their model and also in the model of Theethayi and Cooray (2005),  $L$  and  $C$  were assumed to be constant and linear and the effect of the corona sheath surrounding the channel core was neglected. Visacro and De Conti (2005) considered a time-varying capacitance to represent the corona sheath surrounding the channel core, with  $L$  assumed to be constant and linear. De Conti et al. (2008a) included the variation of  $L$  and  $C$  with time due to the radial expansion of the channel core, the presence of a radially formed corona sheath surrounding the channel core being neglected. Neither of the models above considered the effect of the charges accumulated in the cloud in the calculation of the channel capacitance, although it is not clear to what extent such inclusion would be relevant in terms of predicted channel currents and remote electromagnetic fields.

Except for the models of Amoruso and Lattarulo (1993) and Rondón et al. (2002), and for the simple TL model, which assume a lossless channel, the effect of non-linear channel losses is usually included in the transmission line models of the return stroke that consider lumped excitation. Theethayi and Cooray (2005) and also Visacro and De Conti (2005) assumed the series resistance of the leader channel to decay exponentially with time after the arrival of the lightning current at a given point along the channel. Initial resistance values of the order of a few ohms to tens of ohms were assumed by both authors, with decay time constants varying from a fraction of microseconds to tens of microseconds. De Conti et al. (2008a) evaluated different approaches to simulate the non-linear channel resistance in a transmission line model of the return stroke, namely an exponential decay of this parameter with time, the use of a simplified hydrodynamic model for describing the radial expansion of the channel core with time and several arc resistance models. The latter two approaches were shown to be more consistent than the simple exponential approach for incorporating, according to different simplifications, the dependence that exists between the shape of the propagating current and the rate of change of the channel resistance. In addition to representing ohmic losses in the channel core, Theethayi and Cooray (2004, 2005) introduced in their model a shunt conductance representing corona losses.

The lossy behaviour of the lightning channel and the non-uniform variation of  $L$  and  $C$  lead to the attenuation and distortion of the return stroke currents predicted by the models of Theethayi and Cooray (2004, 2005), Visacro and De Conti (2005) and De Conti et al. (2008a), which is in agreement with luminosity profiles for the return stroke (Jordan and Uman, 1983). The models above also predict a decay of the propagation speed with height that is consistent with available experimental data (Mach and Rust, 1989). De Conti and Visacro (2006) obtained speed profiles presenting in some cases an increase with increasing height at the bottom of the channel followed by a decrease with increasing height, which is consistent with speed profiles observed in some rocket-triggered lightning experiments (Rakov, 2004). In the model of Amoruso and Lattarulo (1993), the propagation speed was

set as  $c/3$ . The time to peak current predicted by their model at various channel heights seems to be independent of the channel height, which is unrealistic. This is also the case of the simple TL model, which assumes the lightning current to propagate undistorted and unattenuated.

As opposed to the discharge-type models discussed in Section 10.2.1, most of the lumped-excitation models discussed in this section predict remote electromagnetic fields in overall good agreement with experimental data. This is the case of the models of Visacro and De Conti (2005), Theethayi and Cooray (2005) and De Conti et al. (2008a), although some of the characteristics observed in the electromagnetic field predictions of Visacro and De Conti (2005, Fig. 2) and Theethayi and Cooray (2005, Figs. 9(c), 10, 20 and 21) were later shown by De Conti et al. (2008a) to be artefacts of assuming the channel resistance to decay exponentially with time without any interaction with the shape of the lightning current. Remote field predictions of Amoruso and Lattarulo (1993) were shown to present features that are in some instances consistent with measured data (see, e.g. Fig. 3 in their paper), but the impedance mismatch at the upper end of the channel is seemingly responsible for unrealistic discontinuities at the tail of predicted field waveforms depending on selected model parameters (see Figs. 4 and 5 in their paper).

### 10.3 Calculation of channel parameters per unit length

As discussed in Section 10.1, all information regarding the electric and magnetic fields associated with a current (voltage) pulse propagating along a transmission line is contained in the per-unit-length parameters  $R$ ,  $L$ ,  $C$  and  $G$ . If these parameters are known, the spatial and temporal distribution of the channel current can be found from the solution of telegrapher's equations (10.1) and (10.2). From Section 10.1 it is also known that a more realistic representation of the lightning channel should include time-varying (non-linear) and non-uniform channel parameters per unit length. However, it is clear from the overview presented in Section 10.2 the great diversity of assumptions found in the conception of the transmission line models of the return stroke, which makes it difficult not only a direct comparison between model predictions but also a comparison between the techniques used by each author for deriving the channel parameters. For this reason, a simplified model is formulated in this chapter for representing a subsequent stroke, based on which a few possibilities are discussed for determining the channel parameters per unit length. This model assumes a lumped current source to inject the desired channel-base current at the bottom of a straight vertical transmission line positioned over a perfectly conducting ground and considers the existence of two different regions in the lightning channel, which are described as follows:

1. *Leader channel:* The leader channel is the region ahead of the return stroke front, which is formed by the dart leader while propagating downward from the cloud. It consists of a lossy core of a few millimetres surrounded by a corona sheath whose radius can reach several metres containing the bulk of negative charges deposited by the leader.

2. *Return stroke channel:* The return stroke channel is the region behind the return stroke front, where the negative charges deposited by the leader are gradually neutralized by the return stroke and the channel core radius expands due to an increase in channel temperature and pressure. As a consequence of the gradual neutralization of the corona sheath, part of the charge injected at the channel base is subtracted from the upward-propagating current at each channel section. In addition, the expansion of the channel core and the variation of its physical properties lead to a progressive decay of the channel series resistance with time.

The description above is used in the next subsections as a reference for calculating the per-unit-length parameters to be used in the modelling of a typical subsequent stroke.

### 10.3.1 Channel inductance and capacitance

If corona, channel tortuosity, losses and the influence of the cloud termination are neglected, the return stroke channel can be represented as an infinitely long vertical wire positioned over a ground plane. This is equivalent to a two-conductor transmission line in which one of the conductors is the vertical wire and the return conductor is the ground. Assuming the line excitation to consist of a lumped source inserted between the ground plane and the bottom of the vertical conductor, the cross section of the dielectric between the two transmission line conductors increases as the observer moves along the  $z$  coordinate from the ground to the cloud. This leads to a decrease in the channel per-unit-length capacitance  $C$  and an increase in the channel per-unit-length inductance  $L$  with increasing height, so both quantities are a function of  $z$ ,  $L(z)$  and  $C(z)$ .

The derivation of  $L(z)$  and  $C(z)$  is relatively simple if the cylindrical conductor representing the vertical transmission line is treated as a conical antenna of infinite length whose cone angle is very small (Jordan and Balmain, 1968). If losses are neglected, the characteristic impedance of such a vertical transmission line is given by

$$Z(z) = 60 \ln \frac{2z}{r_a} \quad (10.3)$$

where  $z$  is the distance from the observation point on the line to the ground plane (or, strictly, to the lumped source inserted between the ground plane and the bottom of the vertical conductor) and  $r_a$  is the conductor radius. The characteristic impedance given by (10.3) relates voltage and current at any point of the vertical transmission line, yielding larger values as  $z$  increases. The variation of  $Z(z)$  with position supports the idea that if the propagation of voltage and current waves along a vertical conductor is to be modelled using transmission line theory, a non-uniform transmission line model is required.

If the characteristic impedance of the line is known, it can be related to the line inductance and capacitance per unit length by

$$Z(z) = \sqrt{\frac{L(z)}{C(z)}} \quad (10.4)$$

Also, if the medium surrounding the vertical transmission line is air and losses are neglected,  $L(z)$  and  $C(z)$  are simply related by

$$v(z) = \frac{1}{\sqrt{L(z)C(z)}} = \frac{1}{\sqrt{\epsilon_0\mu_0}} = c \quad (10.5)$$

where  $v(z)$  is the propagation speed of the current and voltage waves along the line,  $\epsilon_0 = 8.85 \times 10^{-12}$  F/m,  $\mu_0 = 4\pi \times 10^{-7}$  H/m and  $c$  is the speed of light. The relation expressed by (10.5) is independent of the position  $z$  on the vertical line even though the inductance and capacitance of the line vary with height.

From (10.3)–(10.5), one can straightforwardly obtain the following equations expressing the per-unit-length inductance and capacitance of a vertical transmission line

$$L(z) = \frac{\mu_0}{2\pi} \ln \frac{2z}{r_a} \quad (10.6)$$

$$C(z) = \frac{2\pi\epsilon_0}{\ln 2z/r_a} \quad (10.7)$$

Equations (10.6) and (10.7) were used by Gorin (1985) and Rakov (1998) in their return stroke models. A logarithmic variation of  $L(z)$  and  $C(z)$  with height was also considered, under different approximations, in the models of Rondón et al. (2002), Theethayi and Cooray (2005), Visacro and De Conti (2005) and De Conti et al. (2008a). Differences in the values of  $L(z)$  and  $C(z)$  obtained with their models are not likely to significantly affect the currents that propagate along the vertical conductor provided a lumped current source is used to excite the channel base and corona is neglected. In this particular case, it can be shown that if  $L(z)$  and  $C(z)$  vary logarithmically with increasing height, their logarithmic variation (and implicitly the logarithmic variation of  $Z(z)$ ) is more important for the characterization of the return stroke current than the absolute values these parameters may assume (De Conti and Visacro, 2006).

The variation of the channel inductance and capacitance with height as predicted by (10.6) and (10.7) is illustrated in Figure 10.4 for channel radii of 1 mm and 1 cm. Both values are within the limits suggested by Oetzel (1968) and Rakov (1998) for the leader and return stroke channels. If a channel radius of 1 mm is assumed, an increase of 44% is observed in the per-unit-length inductance if an observer moves vertically from a point on the channel located 25 m above the ground plane to a point 3000 m high. As expected, the per-unit-length capacitance is reduced by the same amount. In the case of a channel radius of 1 cm, the variation of the channel parameters in the considered range is larger, reaching 56%. Finally, due to the logarithmic nature of the channel parameters, a tenfold increase in the channel radius from 1 mm to 1 cm leads to a variation in  $L(z)$  and  $C(z)$  of less than 30%. This suggests that the radial expansion of the channel core during the leader–return stroke transition is not likely to affect the channel inductance and capacitance per unit length significantly.

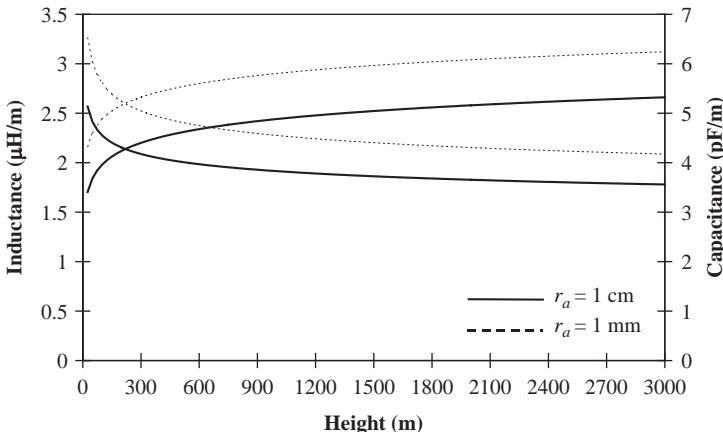
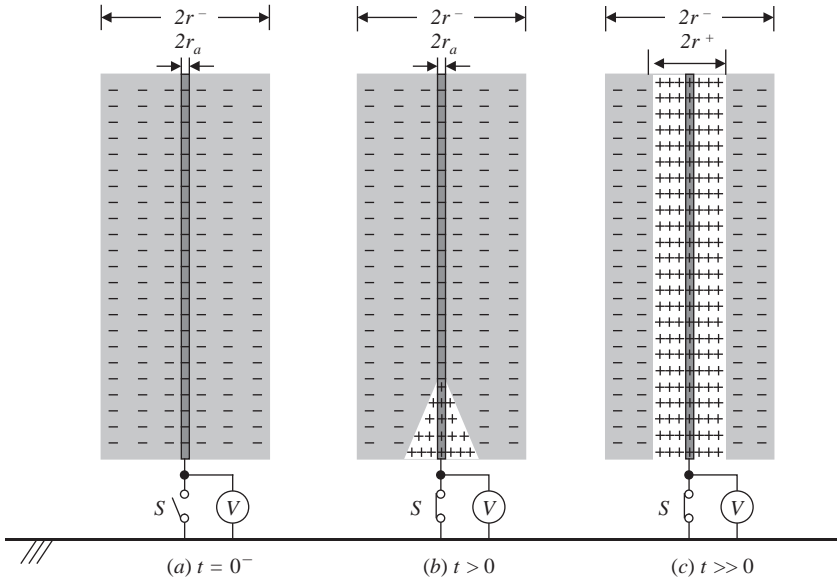


Figure 10.4 Per-unit-length inductance (monotonically increasing curves) and capacitance (monotonically decreasing curves) obtained from (10.6) and (10.7) for two different radii

### 10.3.2 Effect of corona on the calculation of channel parameters

The equations presented in Section 10.3.1 for calculating the per-unit-length inductance and capacitance of a vertical conductor representing the lightning channel are derived neglecting the effect of corona. If, however, the magnitude of the current propagating along the vertical conductor is such that the associated voltage exceeds a certain critical level, streamers will radiate from it. As a consequence, the air in the vicinity of the conductor will be filled with either positive or negative charges depending on the polarity of the propagating pulse. The accumulation of corona charges at a given channel section can be interpreted as a dynamic increase of the capacitance of that section, while the associated corona losses can be interpreted as the effect of a dynamic conductance (Cooray and Theethayi, 2008). The equations presented in Section 10.3.1 for calculating the channel capacitance must therefore be modified to include the corona effect. In addition, suitable equations must be proposed for representing the shunt conductance of the vertical conductor representing the lightning channel. The accumulation of corona charges is not expected to affect the channel inductance because the current propagating in the  $z$  direction is essentially confined to the channel core. For this reason, the calculation of the channel inductance as outlined in Section 10.3.1 remains unaltered if the corona effect is taken into account.

Different theories have been proposed to explain the mechanisms of formation and neutralization of corona in lightning discharges. It is not the objective of this section to present a thorough account of existing corona theories, but instead to concentrate on the effect of corona on the calculation of the channel parameters, namely the capacitance and conductance per unit length. The discussion presented here is based essentially on the corona models of Gorin (1985), Cooray (2000), Cooray and Theethayi (2008) and Maslowski and Rakov (2006). More details on



**Figure 10.5** Idealization of the reverse corona mechanism in lightning assuming a coaxial structure to describe both the channel and corona geometry. The central conductor with radius  $r_a$  represents the leader/return stroke core,  $r^-$  represents the outer radius of the negative corona sheath created by the leader and  $r^+$  represents the outer radius of the positive corona sheath created by the return stroke. The return conductor with radius  $r_b > r^-$  is not shown in the figure for clarity

corona mechanisms and corona modelling in lightning discharges, as well as corona interpretations that differ from the one presented here, can be found in Heckman and Williams (1989), Rao and Bhattacharya (1966) and Baum and Baker (1990).

### 10.3.2.1 Leader and return stroke channels in the presence of corona

Let one assume for the sake of simplicity that the leader channel can be represented as a coaxial line whose lateral view is shown in Figure 10.5(a). The central conductor with radius  $r_a$  represents the leader core, which is isolated from ground by the switch  $S$ ,  $r^-$  represents the external radius of the corona sheath created by the leader, which is assumed to have cylindrical symmetry, and finally an external conductor with radius  $r_b > r^-$  not shown in the figure represents an effectively grounded return conductor. The distribution of negative charges in the region  $r_a \leq r \leq r^-$  is assumed to decay inversely with the radial distance from the central core, which leads to a uniform voltage gradient  $E^-$  in the corona sheath (Gorin, 1985; Cooray, 2000). The voltage gradient  $E^-$  is assumed as equal to the critical electric field necessary for the

stable propagation of negative streamers, which is of the order of 1–1.5 MV/m (Cooray, 2000).

The amount of negative charge deposited by the leader in a subsequent stroke must be such that the voltmeter placed across the switch  $S$  in Figure 10.5(a) will measure a negative voltage  $V_0 = V(z=0, t=0^-)$  of the order of several MV. When the switch is closed at  $t=0$ , the voltage difference between the central conductor and the return conductor will drop to zero. Let this transition be such that the voltage  $V(z=0, t)$  across the switch decays exponentially from its initial value  $V_0$  to a final value  $V_\infty = V(z=0, t \rightarrow \infty) = 0$ . Since the negative space charge deposited by the leader within  $r^-$  will not flow back instantaneously to the central conductor at the moment of switching, a certain amount of positive charge will be induced in the central conductor in order to assure the expected voltage decay across the switch (Cooray, 2000). The positive charge at first cancels out the negative charge deposited by the leader in the central conductor and then starts to accumulate thus forming an excess of bounded positive charge within  $r_a$ . As a consequence, an inversion of polarity will be observed in the electric field at the surface of the central conductor. As soon as the positive electric field at  $r=r_a$  attains a certain critical level  $E^+$ , positive streamers will radiate from it. As a consequence, positive charges will be deposited in the region formerly occupied by the negative leader charges. The positive streamers will propagate until they reach a radius  $r^+$  beyond which the electric field due to the net positive charge within that region is less than  $E^+$  (Gorin, 1985). The value of  $E^+$  is generally greater than the critical field necessary for the stable propagation of positive streamers in virgin air, reaching values of the order of 1.0–1.5 MV/m (Cooray, 2000). With the continuous deposition of positive charges in the region formerly filled with negative charges, the voltage read by the voltmeter gradually approaches zero. The net charge per unit length also decays progressively due to the superposition of positive and negative charges until complete (or nearly complete) neutralization is attained (Hermosillo and Cooray, 1996). A pictorial description of the progressive deposition of positive charges within the radius  $r^+$  after the return stroke is initiated is illustrated in Figure 10.5(b) for times just after the closing of the switch, and in Figure 10.5(c) for longer times.

The reverse corona mechanism described above is supported by the experiments performed by Cabrera and Cooray (1992) and Hermosillo and Cooray (1996), which showed that during the application of a negative voltage pulse on a cylindrical structure streamers were initiated from the central conductor and the region between the coaxial conductors was filled with negative space charge. Then, if the central conductor was suddenly grounded, the space charge was neutralized by streamers of opposite polarity initiated from the central conductor. The obtained results formed the basis of the corona model proposed by Cooray (2000). Similar considerations were made in the development of the theoretical model of Gorin (1985), whose argument was later used by Maslowski and Rakov (2006) to infer corona properties using engineering return stroke models.

If the theories developed to explain the accumulation and neutralization of space charges in coaxial structures can be extended to lightning, the neutralization

of the negative corona charges deposited by the leader can be thought of as the result of the propagation through the leader channel of the voltage change  $\Delta V(0,t)$  created at the channel base after the attachment process is completed. For example, in order to model an exponential decay of the leader voltage  $V_0$  at the base of a channel surrounded by negative corona charges, one can simply assume the application of an exponentially increasing voltage change  $\Delta V(0,t)$  with final value  $|V_0|$  at the bottom of an electrically neutral channel. When the electric field due to the voltage change  $\Delta V(0,t)$  exceeds  $E^\Delta = E^+ + E^-$ , reverse corona will be initiated and positive corona charges will be deposited around the channel (Gorin, 1985). The total voltage at the channel base will then be the superposition of the effects due to  $\Delta V(0,t)$  and  $V_0$ . This idea is depicted in Figure 10.6.

With the propagation of the voltage change  $\Delta V(0,t)$  along the channel, the occurrence of reverse corona at each channel section will determine the deposition of a certain amount of positive charge to neutralize the negative charge previously deposited by the leader. As a consequence, there will be positive corona currents leaving the channel transversally along the whole channel extension, the superposition of which will constitute both the current that propagates longitudinally along the channel and the resulting current at the channel base provided the appropriate time delays are taken into account. Alternately, if one thinks of a lumped current source injecting the desired current waveform at the bottom of an initially neutral conductor intended to represent the channel core, the resulting voltage waveform at the channel base will correspond to the voltage change  $\Delta V(0,t)$ . The deposition of positive corona charges at each channel section will determine the attenuation and delay of the return stroke current as it propagates along the channel (Cooray and Theethayi, 2008).

Although strictly valid for coaxial structures, an approximate account of the reverse corona currents leaving the lightning channel can be made with the model proposed by Cooray (2000). The input parameters of his model are the instantaneous voltage at a given channel section, the critical breakdown electric field

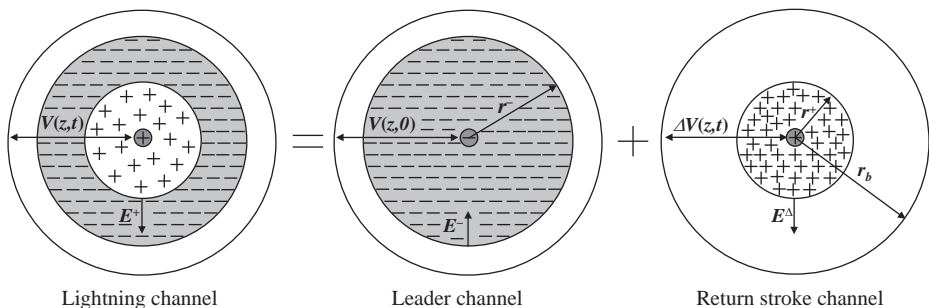


*Figure 10.6* *Idealization of the charge distribution in the vicinity of a channel section located at vertical coordinate  $z$  as the superposition of the negative charge deposited by the leader (initial condition at  $t=0$ ) with the positive charge deposited by the return stroke due to the voltage change  $\Delta V(z,t)$  (Gorin, 1985)*

obtained from Peek's formula, the inner ( $r_a$ ) and outer ( $r_b$ ) radius of the coaxial structure assumed to represent the lightning channel, the critical field  $E^+$  necessary for stable propagation of streamers during the reverse corona mechanism and the critical field  $E^-$  necessary for the stable propagation of negative streamers. Once the total return stroke voltage (leader voltage plus voltage change) at a given channel section is calculated, both the amount of positive charges deposited by the reverse corona and the radius  $r^+$  can be calculated iteratively at that channel section. The corona current can then be obtained as the time derivative of the positive corona charge. Details of such formulation can be found in Cooray (2000). However, if (1)  $\Delta V(0,t)$  is much larger than the voltage necessary for the initiation and stabilization of the reverse corona mechanism, (2)  $\Delta V(0,t)$  is sufficiently large so that the voltage due to the charges deposited in the channel core can be neglected and finally (3) it is assumed that  $r^+ \gg r_a$ , one can resort to a simpler corona model proposed by Gorin (1985). His equations, which are given below as (10.8) and (10.9), allow the calculation of the positive charge  $q^+(z,t)$  deposited at each channel section as a function of the voltage change  $\Delta V(z,t)$ , the critical electric field  $E^\Delta$  and the outer radius of the coaxial structure.

$$r^+ \left[ 1 + \ln \frac{r_b}{r^+} \right] E^\Delta \approx \Delta V(z,t) \quad (10.8)$$

$$q^+(z,t) \approx 2\pi\epsilon_0 r^+ E^\Delta \quad (10.9)$$

where the dependence of  $r^+$  with time and vertical coordinate  $z$  were omitted for convenience. From (10.9), the corona current per unit length  $i_c(z,t)$  can be calculated as

$$i_c(z,t) = \frac{dq^+(z,t)}{dt} \quad (10.10)$$

Equations (10.8) and (10.9) are valid for  $\Delta V(z,t) \geq V^\Delta = r_a \ln(r_b/r_a) E^\Delta$ , where  $V^\Delta$  is the corona voltage threshold associated with  $E^\Delta$ . If such condition is not met, no reverse corona will develop and  $r^+$  should be assumed as equal to  $r_a$ . In (10.8) and (10.9), it is further assumed that  $r^+$  does not contract after reaching its maximal distance from the channel core.

Examples of reverse corona currents calculated with (10.8), (10.9) and (10.10) are illustrated in Figure 10.7 for  $r_a = 1$  cm,  $r_b = 10$  m,  $E^\Delta = 2.5$  MV/m ( $E^+ = 1$  MV and  $E^- = 1.5$  MV) and  $\Delta V(z,t) = |V_0| [1 - \exp(-5 \times 10^6 t)]$ . As explained before,  $V_0$  can be thought of as the voltage associated with the negative charges deposited by the leader at a given channel section, while  $\Delta V(z,t)$  is the voltage change necessary for bringing that channel section to ground potential. Of course, an increase in the absolute value of the leader potential is associated with a larger amount of negative charges deposited by the leader. Consequently, larger leader potentials will require a larger amount of positive charges to be deposited by the return stroke. Thus, as expected, the reverse corona currents increase with increasing  $|V_0|$ , which is shown in Figure 10.7 for values of  $|V_0|$  ranging from 5 to 10.0 MV. An increase in the outer

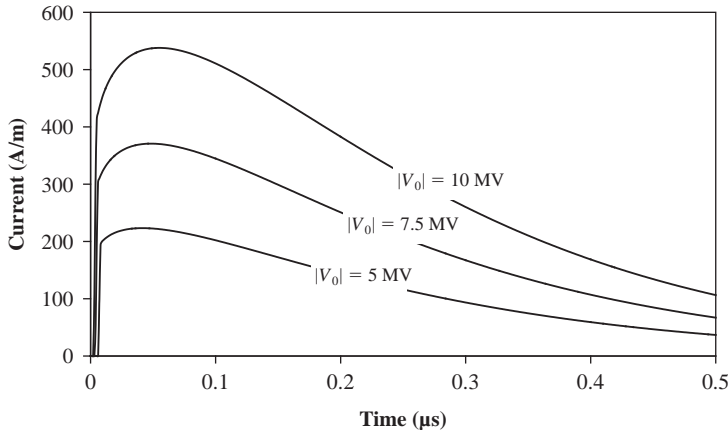


Figure 10.7 Reverse corona currents calculated with (10.8), (10.9) and (10.10) for a coaxial structure with  $r_a = 1 \text{ cm}$ ,  $r_b = 10 \text{ m}$ ,  $E^\Delta = 2.5 \text{ MV/m}$  and an applied voltage change  $\Delta V(z,t) = |V_0|/[1 - \exp(-5 \times 10^6 t)]$ , considering different values of  $V_0$

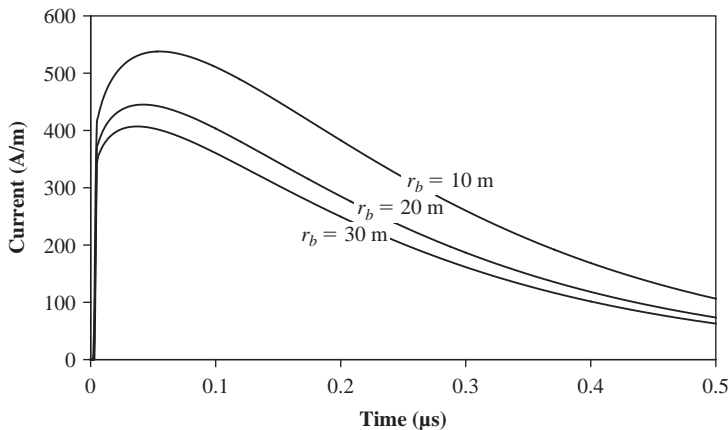


Figure 10.8 Same as Figure 10.7 but considering  $|V_0| = 10 \text{ MV}$  and assuming different values of  $r_b$

radius  $r_b$ , on the other hand, will lead to a decrease in the corona currents. This is illustrated in Figure 10.8 for  $|V_0| = 10 \text{ MV}$  and three different values of  $r_b$ .

Since (10.8) and (10.9) are in principle valid only for coaxial structures, its extension for calculating corona currents in a vertical conductor requires further approximations and therefore must be viewed with caution. One of the possibilities is to assume that the radius  $r_b$  of the return conductor pertaining to the coaxial structure representing the channel increases with increasing height according to some law, as suggested by Gorin (1985) and Cooray and Theethayi (2008).

### 10.3.2.2 Transmission line equations in the presence of corona

In order to analyse the effect of corona on the calculation of the capacitance and conductance of the return stroke channel, it is useful to rewrite telegrapher's equations (10.1) and (10.2) as

$$\frac{\partial V(z, t)}{\partial z} + RI(z, t) + L(z) \frac{\partial I(z, t)}{\partial t} = 0 \quad (10.11)$$

$$\frac{\partial I(z, t)}{\partial z} + C(z, t) \frac{\partial V(z, t)}{\partial t} + G(z, t) V(z, t) = 0 \quad (10.12)$$

Equation (10.11) is identical to (10.1), except that now the dependence of the inductance on position is explicitly shown. This is necessary because the inductance of the vertical conductor intended to represent the lightning channel increases with increasing height. Equation (10.12), on the other hand, differs from (10.2) by the consideration of per-unit-length parameters that present variation with both time and position. This modification is necessary for including the effect of corona charges on voltage and current pulses that propagate along the vertical conductor (Cooray and Theethayi, 2008). If the voltage at point  $z$  is below the corona voltage threshold, only the variation of the channel capacitance with height is needed in (10.12). In this case,  $C(z, t)$  reduces to  $C(z)$ , with  $G(z, t)$  becoming negligible. If the voltage pulse exceeds the corona inception voltage  $V^\Delta$ , corona charges will be deposited around the vertical conductor and determine a non-linear increase in its total capacitance, which will now be given by

$$C(z, t) = C(z) + C_{dyn}(z, t) \quad (10.13)$$

where  $C_{dyn}(z, t)$  is the dynamic capacitance introduced by the deposited corona charges. For positive reverse corona, which is the case for return strokes in negative lightning,  $C_{dyn}(z, t)$  is given by

$$C_{dyn}(z, t) = \begin{cases} 0 & V(z, t) < V^\Delta \\ \frac{q^+(z, t)}{V(z, t)} & V(z, t) \geq V^\Delta, \quad \frac{\partial V(z, t)}{\partial t} > 0 \\ 0 & V(z, t) \geq V^\Delta, \quad \frac{\partial V(z, t)}{\partial t} < 0 \end{cases} \quad (10.14)$$

Also, it can be shown that

$$G(z, t) = \frac{\partial C_{dyn}(z, t)}{\partial t} \quad (10.15)$$

The derivation of (10.11)–(10.15) is presented in detail in Cooray and Theethayi (2008). In the same reference it is shown that (10.12) can be equivalently written as

$$\frac{\partial I(z, t)}{\partial z} + C(z) \frac{\partial V(z, t)}{\partial t} = -i_c(z, t) \quad (10.16)$$

where  $i_c(z,t)$  is the corona current given by (10.10) and  $C(z)$  is the capacitance of the vertical conductor in the absence of corona, considering  $C_{dyn}(z,t)=0$ . The pair of equations (10.11) and (10.16) describes a non-uniform transmission line embedded in air in which distributed current sources account for the corona effect. If the series resistance is neglected in (10.11), the speed of the propagating voltage and current pulses will still be given by (10.5). In other words, current pulses generated by the corona sources will travel along the line with the speed of light. The superposition of the voltage and current pulses due to the distributed corona sources, however, will lead to resultant waveforms that give the idea of a propagation speed that is slower than the speed of light (Cooray and Theethayi, 2008).

The modification of the channel capacitance  $C(z,t)=C(z)+C_{dyn}(z,t)$  given by (10.13) and (10.14) due to the corona currents shown in Figure 10.7 can be seen in Figure 10.9. For the assumed values of  $r_a=1$  cm and  $r_b=10$  m, the geometric capacitance  $C(z)$  can be easily calculated as  $2\pi\epsilon_0/\ln(r_b/r_a)=8.0$  pF. As shown in the figure, after corona inception the total capacitance rises monotonically until reaching a final value that depends on the amplitude of the applied voltage change. In the illustrated cases, the final values of  $C(z,t)$  are 2.5–3.3 times larger than  $C(z)$ .

The variation of the per-unit-length conductance due to the corona currents shown in Figure 10.7 is illustrated in Figure 10.10. As expected from (10.15), the conductance presents an initial rise that is related to the initial expansion of the corona sheath and the associated increase in channel capacitance. After reaching a peak, it decays monotonically to zero as the corona sheath reduces its expansion rate. Both the amplitude and inception time of the conductance curves are dependent on the value of  $V_0$ .

If all uncertainties involved in the modelling of the return stroke as a transmission line are taken into consideration, a simplified account of corona could possibly consider only the dynamic capacitance. One should keep in mind,

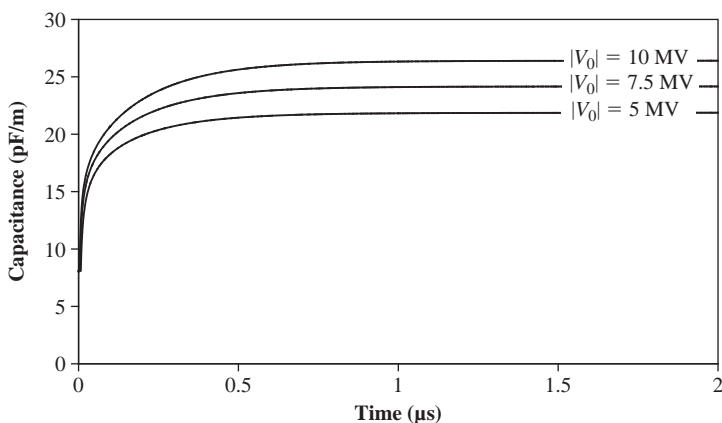


Figure 10.9 Variation of the total capacitance  $C(z,t)=C(z)+C_{dyn}(z,t)$  of a coaxial structure with  $r_a=0.01$  m and  $r_b=10$  m associated with the corona currents shown in Figure 10.7

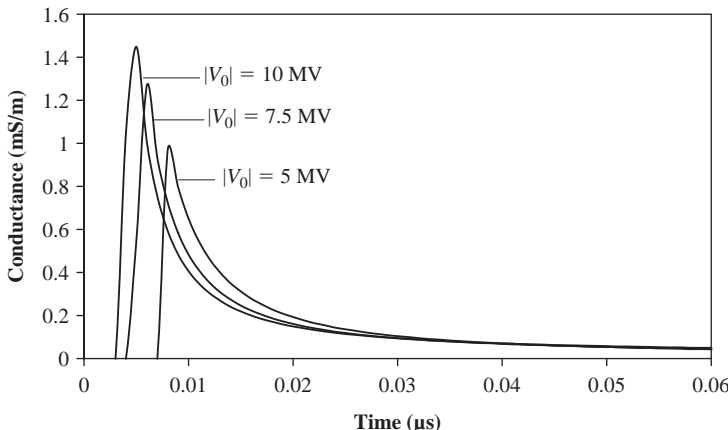


Figure 10.10 Variation of the per-unit-length conductance with time in a coaxial structure with  $r_a = 0.01\text{ m}$  and  $r_b = 10\text{ m}$  associated with the corona currents shown in Figure 10.7. Note that, as per (10.15), the curves shown in this figure are the time derivatives of the curves shown in Figure 10.9

however, that if one neglects the contribution of the dynamic conductance in (10.12) the associated corona currents will lose the fast rise observed in the waveforms shown in Figure 10.7 and reach different peak values. Also, there will be no losses due to charge leak. This procedure results in minimizing the role of corona in the calculation of voltage and current pulses propagating along the line, and therefore should be viewed with caution.

### 10.3.3 Calculation of channel resistance

The calculation of channel resistance requires that account be made of several physical phenomena underlying the transition from the leader to the return stroke stage of lightning. In the case of a subsequent stroke, the channel temperature rises rapidly from approximately 20 000–30 000 K or more as the leader channel is gradually brought to ground potential, with the channel pressure rising to values of several atmospheres. As the channel pressure exceeds the pressure of the surrounding ambient, a shock wave is created and the channel core expands until its pressure equals the atmospheric pressure. The channel expansion takes place initially at a faster rate due to the significant channel overpressure. Then, as a state of pressure equilibrium is gradually reached in tens of microseconds after the return stroke initiation and the channel temperature cools down to approximately 20 000 K or below, the channel expansion becomes gradually slower. The variation of channel temperature and pressure also leads to variations of electron and heavy particle densities in the channel core. As a consequence, the channel conductivity is expected to change in the various stages of the return stroke. This variation ranges from approximately  $1 \times 10^4$  to  $5 \times 10^4\text{ S/m}$  in the initial phase of channel expansion

(the strong-shock region) to values below  $10^4$  S/m in the final stage of channel expansion (the weak-shock region), when the channel is cooled down to temperatures below 15 000 K (Plooster, 1971a, 1971b; Paxton et al., 1986; Rakov, 1998).

If the lightning channel is represented as a vertical transmission line, the gradual expansion of the channel core and the continuous change of its physical properties result in the time variation of the resistance per unit length of the channel. The inductance and capacitance per unit length are also affected by the radial expansion of the core to some extent, so (10.11) and (10.12) should be rewritten as

$$\frac{\partial V(z, t)}{\partial z} + R(z, t)I(z, t) + L(z, t)\frac{\partial I(z, t)}{\partial t} = 0 \quad (10.17)$$

$$\frac{\partial I(z, t)}{\partial z} + C(z, t)\frac{\partial V(z, t)}{\partial t} + G(z, t)V(z, t) = 0 \quad (10.18)$$

where the time dependence of  $R(z, t)$  and  $L(z, t)$  is now explicitly shown (neglecting skin effect), and  $C(z, t)$  is supposed to include not only the dynamic nature of corona but also the channel core expansion. The channel resistance is also allowed to vary with position in (10.17) in order to accommodate not only the local variation of this parameter during the return stroke but also a presumed increase of its initial value at the upper part of the leader channel due to channel cooling.

In practice, the channel inductance and capacitance are much less affected by the expansion of the central core than the channel resistance due to their logarithmic dependence on the core radius. It is therefore reasonable to assume that the channel core expansion and the continuous change of its physical properties will be significant only for the resistance calculation. This is confirmed by numerical results presented in Section 10.4.1.2.

A rigorous proceeding for determining  $R(z, t)$  requires the solution of three hydrodynamic equations representing the conservation of mass, momentum and energy applied to a short cylindrical channel segment, with the assumed lightning current as input parameter (Rakov and Uman 1998). Examples of such hydrodynamic (or gas dynamic) models are the models of Braginskii (1958), Plooster (1971a, 1971b) and Paxton et al. (1986), which usually have as output parameters the channel temperature, pressure and electrical conductivity as a function of radial coordinate and time. Gas dynamic models present different degrees of complexity depending on the assumptions made. Although the models of Paxton et al. (1986) and Plooster (1971a, 1971b) are perhaps the most complete, their extension for use in transmission line models of the return stroke is not straightforward because the simultaneous solution of hydrodynamic and voltage-current propagation equations is needed. Given the difficulties imposed by a rigorous solution to this problem, approximations are usually required for representing the non-linear channel resistance. A detailed analysis of different approximations suitable for representing the non-linear (time-varying) nature of the channel resistance is presented in De Conti et al. (2008a). A brief account of two of such approximations is presented in

Sections 10.3.3.1 and 10.3.3.2, which deal, respectively, with the strong-shock approximation proposed by Braginskii (1958) for representing the radial expansion of spark channels and the arc resistance equation of Toepler (1906).

### 10.3.3.1 Strong-shock approximation

The strong-shock approximation consists of solving the hydrodynamic equations describing the radial expansion of a spark channel by considering the pressure in the channel to be much higher than the pressure in the surrounding ambient. According to the strong-shock approximation, three radial regions can be defined (Strawe, 1979): (1) a central core containing the hot, low-density plasma, (2) an outward-expanding shell with negligible thickness containing the mass excluded from the channel and (3) an undisturbed region located beyond the shell radius. By assuming uniform temperature, pressure, electrical conductivity and mass density in the central core, Braginskii (1958) used the strong-shock approximation to obtain a self-similar solution describing the dependence of the channel radius on the current traversing a short channel segment. His solution in integral form can be written as (Barannik et al., 1975).

$$r_a(z, t) \approx \sqrt{\left(\frac{4}{\rho_0 \pi^2}\right)^{1/3} \int_0^t [\sigma(z) \xi]^{-1/3} i(z, t)^{2/3} dt + r_i(z)^2} \quad (10.19)$$

where  $r_a(z, t)$  is the arc channel radius in metres,  $i(z, t)$  is the current in amperes,  $r_i(z)$  is the initial radius,  $\sigma(z)$  is the channel conductivity,  $\rho_0 = 1.29 \text{ kg/m}^3$  is the ambient atmospheric density and  $\xi$  is a factor describing the rate of radial expansion of the arc channel. Although the strong-shock approximation is strictly valid during the initial phase of channel expansion, De Conti et al. (2008a) have shown that channel radii predicted by (10.19) compares well with predictions of the more accurate hydrodynamic model of Plooster (1971b) even in the weak-shock region. Assuming that (10.19) is also valid for representing the radial expansion of the lightning channel and neglecting skin effect, the per-unit-length channel resistance can be approximately obtained from

$$R(z, t) = \frac{1}{\sigma(z) \pi r_a(z, t)^2} \quad (10.20)$$

It is to be noted that a constant channel conductivity is assumed in (10.19) and (10.20), which is reasonable in the initial stage of the return stroke since this parameter is not expected to vary significantly for plasma temperatures above 15 000 K and channel pressures ranging from 1 to 100 atm (Plooster, 1971a). However, this assumption introduces an error in (10.20) by specifying a monotonic resistance decay that is not valid at later times. This is explained as follows. If the channel conductivity is allowed to vary with time in (10.19) and (10.20), the overall variation of  $R(z, t)$  with time can be roughly separated in three different stages: (1) in the strong-shock regime, the fast expansion of the channel core and the

relative increase of the channel conductivity lead to a sharp resistance decay from an initial value ranging from 1 to 50  $\Omega/\text{m}$  associated with the characteristics of the leader channel (core radius of a few millimetres and a conductivity of approximately  $10^4 \text{ S/m}$ ) to a value about two orders of magnitude lower (Oetzel, 1968; Rakov, 1998); (2) as the channel core continues to expand and the core conductivity presents a relative decay due to gradual channel cooling, the resistance tends to reduce its decay rate, eventually reaching some stability because conductivity and radius will have opposite effects in (10.20); (3) in the final stage of the return stroke, as the channel expands at reduced rate and the channel conductivity decays more significantly due to channel cooling, the counteracting effect of both parameters in (10.20) will eventually lead to a relative increase of the channel resistance (De Conti et al., 2008a). This is exactly the behaviour observed in experiments with spark channels (Engel et al., 1989). Since the relative increase of the channel resistance cannot be predicted if a constant channel conductivity is assumed, (10.20) will inevitably underestimate the channel resistance in the weak-shock regime at the current tail.

### 10.3.3.2 Toepler's arc resistance equation

Toepler's (1906) empirical formula is an arc resistance equation that assumes the per-unit-length resistance of the spark to be inversely proportional to the time integral of the input current according to

$$R(t) = \frac{\alpha}{q(0) + \int_{0^+}^t i(t) dt} \quad (10.21)$$

where  $\alpha$  is an empirical constant and  $q(0)$  is the initial charge in the spark channel, which is equal to zero prior to arc initiation. To what extent (10.21) is valid for simulating the non-linear resistance of the lightning channel is not known. However, it seems reasonable, at least in an engineering perspective, to assume that the leader channel behaves similarly as a long stationary arc that is subjected to a sudden expansion during the transition to the return stroke. Since the leader channel is believed to conduct currents of the order of  $10^2 \text{ A}$  (Rakov, 1998),  $q(0)$  can be reasonably assumed as different from zero at the time when the return stroke is initiated. In such perspective, if  $q(0)$  is known  $\alpha$  can be suitably selected for adjusting the initial channel resistance. However, similarly as with the strong-shock approximation, (10.21) leads to a monotonic resistance decay. For this reason, the resistance values predicted by (10.21) in the final stage of the return stroke are probably underestimated.

### 10.3.3.3 Computation of the channel resistance

For illustrating the use of the strong-shock approximation and Toepler's equation in the modelling of the non-linear channel resistance, the channel-base current proposed by Nucci et al. (1990) was assumed as the input current in (10.19) and (10.21). It has a peak value of 11 kA, a front time of approximately 0.5  $\mu\text{s}$  and a maximum steepness of 105 kA/ $\mu\text{s}$ . The obtained results are shown in Figure 10.11,

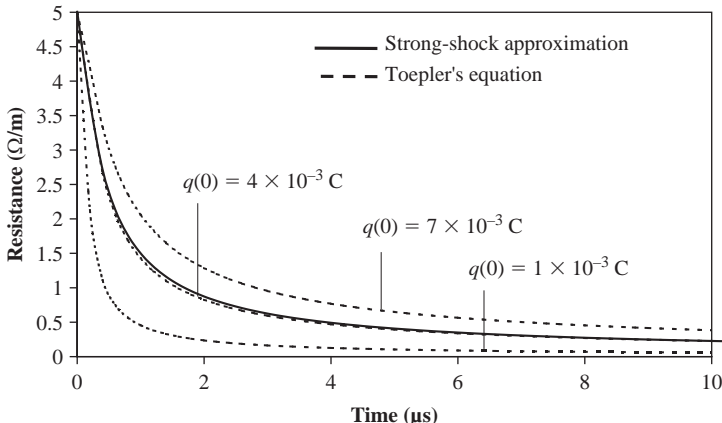


Figure 10.11 Channel resistance predicted by (10.19) and (10.20) with  $\xi = 4.5$ ,  $\sigma(z) = 2.2 \times 10^4$  S/m and  $r_i(z) = 1.7$  mm (strong-shock approximation), and by (10.21) with  $q(0) = 1, 4$  or  $7$  mC, and  $\alpha = q(0)R_i$  (Toepler's law). The current waveform of Nucci et al. (1990] was assumed as input current.  $R_i$  is the initial resistance (De Conti et al., 2008b)

with the solid line corresponding to the resistance curve obtained with the strong-shock approximation and the dashed lines corresponding to resistance curves obtained with Toepler's equation for three different sets of parameters. In the simulation with the strong-shock approximation,  $\sigma(z) = 2.2 \times 10^4$  S/m,  $\xi = 4.5$  and  $r_i(z) = 1.7$  mm were considered in (10.19) and (10.20). The values assumed for  $\sigma(z)$  and  $\xi$  are the same used by Braginskii (1958). The value assumed for  $r_i(z)$  is within the limits suggested by Rakov (1998) for the leader channel. The combination of  $\sigma(z) = 2.2 \times 10^4$  S/m and  $r_i(z) = 1.7$  mm in (10.20) leads to an initial channel resistance of  $5\ \Omega/\text{m}$ . The parameters  $\alpha$  and  $q(0)$  used in Toepler's equation were selected in order to match this initial resistance value and to produce different decay rates for this parameter (De Conti et al., 2008b).

It is seen in Figure 10.11 that the channel resistance initially presents a faster decay, which is associated with the rise of the input current, and then starts to decay more slowly. As expected, an increase in  $q(0)$  determines a slower decay rate for the channel resistance predicted by Toepler's equation. This happens because in this case the integral term plays a role that is comparatively less important in the denominator of (10.21). After 40  $\mu\text{s}$  (time not shown in Figure 10.11), the channel resistance reaches either  $0.07\ \Omega/\text{m}$  (strong-shock approximation and Toepler's law with  $q(0) = 4 \times 10^{-3}\ \text{C}$ ),  $0.02\ \Omega/\text{m}$  (case  $q(0) = 1 \times 10^{-3}\ \text{C}$ ) or  $0.13\ \Omega/\text{m}$  (case  $q(0) = 7 \times 10^{-3}\ \text{C}$ ). The value of  $0.07\ \Omega/\text{m}$  obtained with the strong-shock approximation after 40  $\mu\text{s}$  corresponds to a channel core radius of 1.44 cm. Such values of channel radius and channel resistance are consistent with the predictions of Rakov (1998) for the return stroke channel.

It is apparent from Figure 10.11 that the resistance decay predicted by Toepler's equation agrees very well with that obtained with the strong-shock approximation if  $q(0) = 4 \times 10^{-3}$  C. Indeed,  $q(0)$  and  $\alpha$  can always be adjusted to provide a good match with resistance curves obtained with the strong-shock approximation (De Conti et al., 2008a). This suggests that either of the theories presented in Sections 10.3.3.1 and 10.3.3.2 can in principle be equivalently used in the modelling of the channel resistance. In particular, consistent results can be obtained with the strong-shock approximation provided initial channel radii of the order of a few millimetres, channel conductivities of the order of  $10^4$  S/m and  $\xi$  ranging from 1 to 10 are assumed (De Conti et al., 2008a, 2008b, 2008c). The selection of the constants to be used in Toepler's equation can be made after preliminary analysis with (10.19) and (10.20), or simply by selecting a desired initial channel resistance and a certain decay rate. In any case, regardless of the adopted calculation procedure, one should bear in mind that (10.19)–(10.21) have limitations especially in the weak-shock regime, and that a more accurate description of the non-linear behaviour of the channel resistance requires the simultaneous solution of hydrodynamic and voltage–current equations.

## 10.4 Computed results

In this section, the return stroke model outlined in Section 10.3 is used to simulate a subsequent stroke to flat ground. First, the influence of various channel parameters on the return stroke current is investigated in Section 10.4.1. The analysis is presented in such way as to indicate how channel non-uniformity, losses and corona let the characteristics of the calculated currents closer to observed lightning properties. A suitable combination of channel parameters is then selected for the calculation of lightning electromagnetic fields. The results are presented in Section 10.4.2 together with a comparison with measured data.

### 10.4.1 Channel currents

The calculation of channel currents with the return stroke model described in Section 10.3 requires the numerical solution of telegrapher's equations (10.17) and (10.18) in time domain. Different solution methods are applicable to this problem, most notably the finite-difference time-domain (FDTD) technique and the method of characteristics (Paul, 1994). The numerical results presented in this section were obtained with a first-order FDTD scheme assuming an ideal lumped current source to inject the current waveform of Nucci et al. (1990) at the bottom of the channel.

#### 10.4.1.1 Lossless non-uniform channel

To evaluate the modelling of the return stroke as a transmission line according to the discussion presented in Section 10.3, it is initially assumed that the channel is lossless and corona free. The obtained results are illustrated in Figure 10.12 in terms of channel currents calculated at heights of 0, 100, 300, 600 and 900 m above the ground surface. A radius  $r_a = 1$  mm was considered for the calculation of

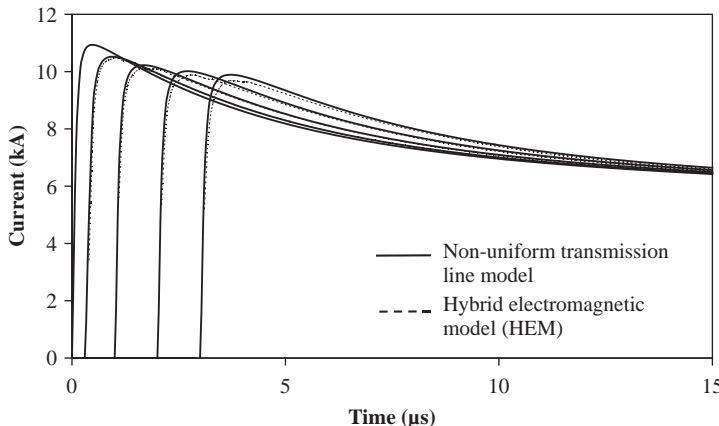


*Figure 10.12 Currents calculated at heights of 0, 100, 300, 600 and 900 m (waveforms from left to right in the figure) with two different models considering an ideal current source to excite the bottom of a lossless channel with core radius of 1 mm in the absence of corona*

the channel inductance and capacitance with (10.6) and (10.7). As discussed in Section 10.3.1, this leads to the representation of the lightning channel as a non-uniform transmission line with inductance and capacitance varying with the vertical coordinate  $z$ . For comparison purposes, channel currents were also calculated with the hybrid electromagnetic model (HEM) (Visacro and Soares, 2005; Visacro and Silveira, 2004) assuming the channel to be represented as an infinitely long vertical monopole excited by an ideal current source at its lower end. The HEM model solves Maxwell's equations numerically in frequency domain by formulating the problem in terms of the vector magnetic and scalar electric potentials, with time domain solutions being obtained through the inverse Fourier transform.

The waveforms illustrated in Figure 10.12 clearly indicate that the injected current propagates with the speed of light along the channel. This is expected because the medium surrounding the lossless vertical wire representing the channel is air. It is also seen in Figure 10.12 that the propagating current is attenuated and distorted even in the absence of losses and corona. This is explained by the non-TEM field structure associated with the propagation of current waves along a vertical wire (Baba and Rakov, 2005). In the HEM model, the non-TEM field structure is implicitly considered in the numerical solution of Maxwell's equations. In the transmission line model of the channel, however, the attenuation and distortion of the propagating current are a result of non-uniform channel parameters, which determine the occurrence of multiple current reflections at each channel section (Baba and Rakov, 2005; Theethayi and Cooray, 2005). The very good agreement seen in Figure 10.12 between currents calculated with the transmission line model of the vertical wire and currents calculated with the numerical solution of Maxwell's equations suggests that the representation of the lightning channel as a non-uniform transmission line is able to emulate satisfactorily the non-TEM field

structure associated with this problem. This result is in line with the analysis of Baba and Rakov (2005), who studied this problem in detail.

Interestingly, a lossless vertical monopole with infinitesimally small radius excited by a point current source can be shown to support a spherical TEM field structure, which means that the injected current will in this particular case propagate unattenuated and undistorted with the speed of light (Thottappillil et al., 2004). This somehow provides a physical justification for the popular TL model (Uman and McLain, 1969), which assumes the lightning current to propagate unattenuated and undistorted along a uniform transmission line. The hypothesis of an undisturbed lightning current is, however, not supported by measured lightning luminosity profiles, which indicates that the return stroke current should reduce its amplitude and increase its rise time while propagating up to the cloud (Jordan and Uman, 1983). This suggests that the representation of the lightning channel as a non-uniform transmission line and its effect on the channel currents as seen in Figure 10.12 change the model predictions in such way that they will come closer to the experimental observations, at least to some extent.

#### **10.4.1.2 Lossy non-uniform channel**

The variation of the channel inductance and capacitance with the vertical coordinate  $z$  is an important step in the modelling of the lightning channel as a transmission line, but the results presented in Figure 10.12 assumed a lossless channel, which is unrealistic. In this section, this simplifying assumption is removed and the return stroke current is calculated for a lossy non-uniform channel. The channel resistance is assumed to be governed by the strong-shock approximation described in Section 10.3.3.1, with  $\sigma(z) = 2.2 \times 10^4$  S/m,  $r_i(z) = 1$  mm and  $\xi = 4.5$ . This set of parameters leads to an initial channel resistance of  $10.5 \Omega/\text{m}$  that is representative of the pre-return-stroke channel (De Conti et al., 2008). At the channel base, the resistance decays from its initial value to 1.88, 0.43 and  $0.13 \Omega/\text{m}$  after 1.0, 5.0 and 20  $\mu\text{s}$  of the return stroke initiation, while the core radius expands from 1 mm to 1.4 cm in 40  $\mu\text{s}$ . Resulting channel currents calculated at heights of 0, 100, 300, 600 and 900 m above the ground surface are shown in Figure 10.13. The dashed lines were obtained considering the radial core expansion predicted by (10.19) to affect the inductance and capacitance, while the solid lines were obtained neglecting this effect and considering  $r_a = 1$  mm in (10.6) and (10.7).

It is apparent from Figure 10.13 that, compared to the lossless case illustrated in Figure 10.12, the consideration of a non-linear channel resistance increases the attenuation and distortion of the propagating current. This feature, which is consistent with measured lightning luminosity profiles (Jordan and Uman, 1983; Mach and Rust, 1989), is seen in Figure 10.13 to remain nearly unaffected if inductance and capacitance are allowed to vary with time due to channel core expansion. This confirms the discussion of Section 10.3.3 that the core expansion is likely to be significant only for the resistance calculation, with the assumption of a constant core radius being acceptable for the calculation of the channel inductance and capacitance.

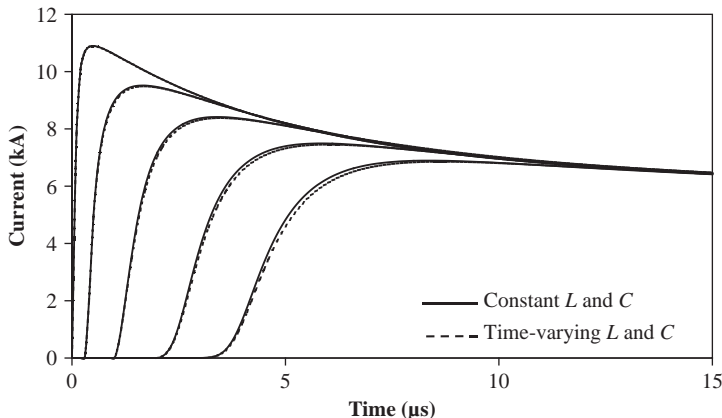


**Figure 10.13** Currents calculated at heights of 0, 100, 300, 600 and 900 m (waveforms from left to right in the figure) considering an ideal current source to excite the bottom of a lossy channel with  $r_i = 1 \text{ mm}$ ,  $\sigma(z) = 2.2 \times 10^4 \text{ S/m}$  and  $\xi = 4.5$  in the absence of corona. The channel inductance and capacitance were assumed to either change their values following the radial expansion of the channel core or keep a constant value calculated with  $r_a = 1 \text{ mm}$  in (10.6) and (10.7)

It can also be inferred from the current waveforms shown in Figure 10.13 that the consideration of a non-linear channel resistance leads to a reduction of the return stroke speed to values below the speed of light and also to a monotonic decay of the propagating speed with increasing height, both features supported by experimental data (Idone and Orville, 1982; Mach and Rust, 1989). One possible approach to evaluate the return stroke speed is the use of the apparent speed  $v(z)$ , defined as the ratio between the distance  $z$  propagated by the return stroke current and the time required for this current to reach a certain threshold level that can be related to the minimum energy necessary to excite any optical instrument used in measuring lightning luminosity profiles (Theethayi and Cooray, 2005). If the threshold level is assumed to be 2.5% of the current peak at the channel base, a monotonic decay of  $v(z)$  from approximately  $2.9 \times 10^8 \text{ m/s}$  near the channel base to  $2.0 \times 10^8 \text{ m/s}$  at a height of 3000 m is obtained for the set of parameters considered in Figure 10.13. If the channel conductivity is reduced from  $2.2 \times 10^4 \text{ S/m}$  to  $1.0 \times 10^4 \text{ S/m}$ ,  $v(z)$  will vary from  $2.6 \times 10^8 \text{ m/s}$  near the channel base to  $1.5 \times 10^8 \text{ m/s}$  at a height of 3000 m (De Conti et al., 2008). These values approach the estimates of Mach and Rust (1989) for the return stroke speed, in which upper limits of the order of  $2.8 \times 10^8 \text{ m/s}$  and  $2.0 \times 10^8 \text{ m/s}$  were, respectively, obtained for natural and triggered negative lightning.

Overall, the results presented in this section show that channel currents calculated with the lightning channel represented as a lossy non-uniform transmission line (considering the non-linear variation of the channel resistance) behave closer to measured data than if channel losses are neglected.

### 10.4.1.3 Lossy non-uniform channel with corona

In this section, in order to include more of lightning physics into the lossy non-uniform transmission line model used so far, the corona model of Section 10.3.2 is assumed to govern the radial diffusion of electric charges from the central core. The outward expansion of the corona radius and the deposited corona charge are calculated with (10.8) and (10.9) assuming  $r_b = 2z$  and  $E^\Delta = 2 \text{ MV/m}$  as in (Gorin, 1985). The dynamic capacitance and conductance associated with the corona currents are obtained from (10.14) and (10.15), respectively. A core radius of 1 cm is used for calculating  $V^\Delta$ , the corona voltage threshold associated with  $E^\Delta$ . The same radius is used for calculating the channel inductance and geometrical capacitance. The obtained results are shown in Figure 10.14 in terms of currents calculated at heights of 0, 100, 300, 600 and 900 m above ground level. The solid lines shown in the figure were calculated assuming a lossless channel. The dashed lines were obtained assuming the channel resistance to be governed by the strong-shock approximation with the same parameters of Section 10.4.1.2. To avoid a premature resistance decay, a current threshold level  $I^\Delta = V^\Delta/Z(z)$  was defined at each channel section below which a constant resistance is assumed, where  $Z(z)$  is given by (10.3).

It is seen in Figure 10.14 that currents below the corona threshold level propagate unaffected by corona. This is clearer in the lossless case, in which the leading tip of the current waveforms is well defined and propagates with the speed of light. In the lossy case, the leading tip is severely attenuated by the channel

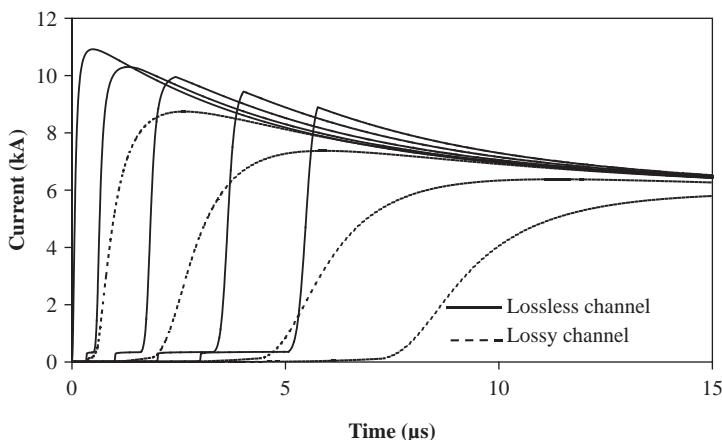


*Figure 10.14 Currents calculated at heights of 0, 100, 300, 600 and 900 m (waveforms from left to right in the figure) considering an ideal current source to excite the bottom of the channel in the presence of corona. The solid lines were obtained for a lossless channel. The dashed lines were calculated assuming the channel resistance to decay according to the strong-shock approximation, with  $r_i = 1 \text{ mm}$ ,  $\sigma(z) = 2.2 \times 10^4 \text{ S/m}$  and  $\xi = 4.5$*

resistance, resulting both in slower propagation speed and a concave profile in the rising part of the return stroke current.

Above the corona threshold level, the apparent speed of the upward moving front is significantly reduced as a result of the superimposition of the injected current with the forward and backward moving corona currents, all of which propagating with the speed of light (Cooray and Theethayi, 2008). In the lossless case, for example, an average value of  $1.9 \times 10^8$  m/s can be inferred for  $v(z)$  in the first kilometre or so of the channel if the lower edge of the slowly moving part of the current is taken as reference. In the lossy case, as a result of attenuation and distortion, the apparent propagation speed is seen to decay monotonically from  $1.8 \times 10^8$  m/s near the channel base to  $1.5 \times 10^8$ ,  $1.3 \times 10^8$  and  $1.2 \times 10^8$  m/s at heights of 300, 600 and 900 m above the ground plane if a threshold level of 2.5% of the peak current at the channel base is considered. These values are in the range of the average propagation speed of negative return strokes in natural and triggered lightning, which is typically between one-third and one-half of the speed of light (Rakov, 2004). The monotonic decrease of the return stroke speed with increasing height inferred from the calculated current waveforms is also supported by measured data (e.g. Idone and Orville, 1982), although there is experimental evidence that the return stroke speed may vary non-monotonically along the lightning channel, initially increasing in the first several tens of metres of the channel and then decreasing with increasing height (Rakov, 2004). Overall, it is seen that the inclusion of corona let the model predictions very close to experimental observations.

#### *10.4.2 Predicted electromagnetic fields*

The results presented in Section 10.4.1.3 show that the modelling of the lightning channel as a lossy non-uniform transmission line in the presence of corona is able to reproduce the most important characteristics of subsequent return stroke currents in negative lightning. However, a more complete assessment of the validity of a return stroke model requires the computation of remote electromagnetic fields and the comparison of predicted field waveforms with signatures observed in measured lightning electromagnetic fields. This task is performed here by assuming the lightning channel to consist of an array of short vertical dipoles excited by the currents calculated at each channel section with the considered transmission line model. The remote electromagnetic fields are then calculated in time domain using the formulation of Uman et al. (1975). The results are illustrated in Figure 10.15, which shows electromagnetic fields calculated at distances of 50 m, 5 km and 100 km from the channel base. In the simulations, the lightning channel was modelled as a lossy non-uniform transmission line in the presence of corona. The same parameters of Section 10.4.1.3 were considered, except that a lower limit of  $0.145 \Omega/m$  was assumed for the channel resistance. This value is exactly two orders of magnitude lower than the initial resistance of  $14.5 \Omega/m$  associated with the leader channel in the simulated case, which is in line with the discussion presented in (Rakov, 1998). The use of such a limiting value was necessary for avoiding a monotonic decay of the channel resistance, which is unrealistic as discussed in

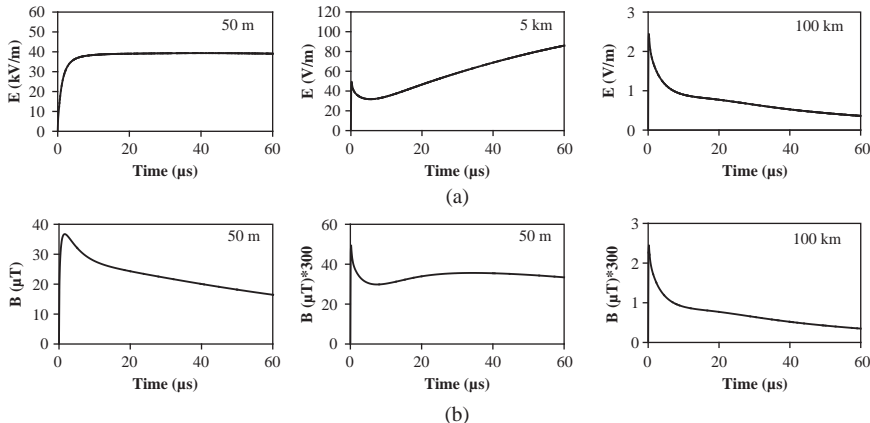


*Figure 10.15* Remote (a) electric and (b) magnetic fields associated with the currents shown as dashed lines in Figure 10.14. The channel resistance is assumed to decay according to the strong-shock approximation, with  $r_i = 1 \text{ mm}$ ,  $\sigma(z) = 2.2 \times 10^4 \text{ S/m}$  and  $\xi = 4.5$ , with a final resistance value of  $0.0145 \Omega/\text{m}$ . The channel is assumed to be in corona, with  $r_a = 1 \text{ cm}$ ,  $r_b = 2z$  and  $E^\Delta = 2 \text{ MV/m}$

Section 10.3.3, and also for leading to more realistic electric field waveforms in the very close range at later times. Despite the use of a lower limit for the channel resistance, the resulting channel currents are essentially the same as those illustrated as dashed lines in Figure 10.14.

For analysing the field waveforms illustrated in Figure 10.15, it is useful to resort to Table 10.1, which summarizes the signatures typically observed in measured lightning electromagnetic fields (Lin et al., 1979; Rakov and Uman, 1998). The ability of the evaluated model to reproduce each of the listed signatures is also shown in the table. It is seen that most of the field signatures are reproduced by the model, namely a sharp initial peak in electric and magnetic fields at 5 km and 100 km, a slow ramp after the initial peak in electric fields at 5 km, a hump after the initial peak in magnetic fields at 5 km and the flattening of electric fields measured

*Table 10.1* Main signatures observed in measured lightning electromagnetic fields

Field signature	Model prediction
(i) Sharp initial peak at 5 km and 100 km	Yes
(ii) Slow ramp after the initial peak in electric fields at 5 km	Yes
(iii) Hump after the initial peak in magnetic fields at 5 km	Yes
(iv) Zero crossing in the tail of field waveforms at 100 km	No
(v) Flattening of electric fields measured at 50 m	Yes

at 50 m. The only feature that is not predicted by the evaluated model is the zero crossing usually observed at the tail of remote field measurements. In Visacro and De Conti (2005), it is argued that an increase of the initial channel resistance with increasing height due to the cooling of the upper part of the leader channel could be one of the factors determining the zero crossing. This could be easily included in the evaluated model by assuming non-uniformly distributed values for both channel conductivity and radius. Another possible reason for the lack of zero crossing in the far-field waveforms is that the strong-shock approximation used in the evaluated model is not able to accurately predict the dynamics of the channel resistance in the weak-shock regime, for which a more complete hydrodynamic model would be necessary.

In any case, the lack of zero crossing in the far-field region is not a problem if one is primarily interested in using the return stroke model discussed in this chapter for evaluating the interaction of lightning with nearby electrical systems (e.g. calculating lightning-induced voltages on transmission lines). This conclusion is supported by the fact that the considered model satisfactorily reproduces all signatures observed in lightning electromagnetic fields measured at distances below 5 km. This conclusion remains essentially unaffected if a more accurate resistance model is used, since modifications in the final value of channel resistance are unlikely to affect the peak values and shape of predicted field waveforms in the first tens of microseconds, which are of more importance in this type of analysis.

## 10.5 Summary and conclusion

This chapter discusses the modelling of the return stroke channel as a transmission line. A brief review of the pertinent literature indicates that the transmission line models of the return stroke can be roughly classified as either discharge-type models, which assume the return stroke to correspond to the discharge of a previously charged transmission line to ground through a closing switch, lumped-excitation models, which assume the return stroke to correspond to an initially neutral transmission line that is fed by a lumped voltage or current source at one of its terminations, or finally as models that use transmission line or distributed-circuit theory to infer relevant lightning properties.

A discussion is presented on the calculation of the per-unit-length parameters necessary for simulating the return stroke channel as a transmission line. It is shown that if a transmission line is intended to represent the lightning channel, it must be non-uniform (in order to accommodate the variation of the channel parameters with position) and non-linear (in order to accommodate the temporal variation of the channel resistance as a function of the channel current and also the gradual neutralization of the corona sheath surrounding the channel core). Engineering equations are presented for estimating the per-unit-length parameters associated with a vertical transmission line in the presence of non-linear losses and corona. The proposed equations are suitable to computer simulation and can be easily implemented using a first-order FDTD scheme.

Computed results show that the modelling of the lightning channel as a lossy non-uniform transmission line in the presence of corona is able to reproduce the most important characteristics of subsequent return strokes of negative lightning, including the reduction in amplitude and increase in front time of the lightning current with increasing height, realistic return stroke speeds, realistic speed profiles and, if a suitable set of parameters is selected, essentially all signatures typically observed in measured electromagnetic fields. Besides confirming the consistency of modelling the return stroke channel using transmission line theory, the obtained results suggest that the consideration of relevant lightning properties let model predictions closer to measured data. It can be expected, therefore, that model predictions are likely to consistently improve if better models become available for representing the various complex mechanisms involved in the lightning discharge. A transmission line model of the return stroke is flexible enough to accommodate virtually any model improvement provided it can be written, analytically or numerically, in the form of per-unit-length parameters.

## References

- Amoruso, V. and F. Lattarulo (1993), The electromagnetic field of an improved lightning return-stroke representation, *IEEE Trans. Electromagn. Compat.*, 35(3), 317–328
- Baker, L. (1990), Return-stroke transmission line model, In *Lightning Electromagnetics*, edited by R. L. Gardner, pp. 63–74, Hemisphere, New York
- Barannik, S. I., S. B. Vasserman and A. N. Lukin (1975), Resistance and inductance of a gas arc, *Sov. Phys. Tech. Phys.*, 19(11), 1449–1453
- Baum, C. E. and L. Baker (1990), Analytic return-stroke transmission-line model, In *Lightning Electromagnetics*, edited by R. L. Gardner, pp. 17–40, Hemisphere, New York
- Baba, Y. and V. A. Rakov (2005), On the mechanism of attenuation of current waves propagating along a vertical perfectly conducting wire above ground: Application to lightning, *IEEE Trans. Electromagn. Compat.*, 47(3), 521–532
- Baba, Y. and V. A. Rakov (2007), Electromagnetic models of the lightning return stroke, *J. Geophys. Res.*, 112(D04102), doi: 10.1029/2006JD007222
- Bazelyan, E. M. and Y. P. Raizer (2000), *Lightning Physics and Lightning Protection*, 325 pp., IOP Publishing, Bristol
- Borovskii, J. E. (1995), An electromagnetic description of lightning return-strokes and dart leaders: guided wave propagation along conducting cylindrical channels, *J. Geophys. Res.*, 100(D2), 2697–2726
- Braginskii, S. I. (1958), Theory of the development of a spark channel, *Sov. Phys. JETP*, 34, 1068–1074
- Cabrera, V. M and V. Cooray (1992), On the mechanism of space charge generation and neutralization in a coaxial cylindrical configuration in air, *J. Electrostat.*, 28, 187–196

- Cooray, V. (2000), Charge and voltage characteristics of corona discharge in a coaxial geometry, *IEEE Trans. Dielectr. Electr. Insul.*, 7(6), 734–743
- Cooray, V. and N. Theethayi (2008), Pulse propagation along transmission lines in the presence of corona and their implication to lightning return strokes, *IEEE Trans. Antennas Propag.*, 56(7), 1948–1959
- De Conti, A. and S. Visacro (2006), Reproducing lightning electromagnetic field signatures with a new current return-stroke model based on a distributed-circuit approach, In *Proceedings of 28th International Conference on Lightning Protection*, Kanazawa, Japan
- De Conti, A. and S. Visacro (2009), On the use of lumped sources in a nonlinear lightning return stroke model and extension for evaluating strikes to tall objects, *J. Geophys. Res.*, 114(D11115), doi: 10.1029/2008JD011120
- De Conti, A., S. Visacro, N. Theethayi and V. Cooray (2008a), A comparison of different approaches to simulate a nonlinear channel resistance in lightning return stroke models, *J. Geophys. Res.*, 113(D14129), doi: 10.1029/2007JD009395
- De Conti, A., S. Visacro, N. Theethayi and V. Cooray (2008b), Modeling of the nonlinear channel resistance using some simplified theories, In *Proceedings of GROUND 2008 - International Conference on Grounding and Earthing & 3rd LPE – International Conference on Lightning Physics and Effects*, Florianopolis, Brazil
- De Conti, A., S. Visacro, N. Theethayi and V. Cooray (2008c), Simulation of the time varying channel resistance: Exponential decay versus strong-shock approximation, In *Proceedings of the 29th International Conference on Lightning Protection*, Uppsala, Sweden
- Engel, T.G., A. L. Donaldson, M. Kristiansen (1989), The pulsed discharge arc resistance and its functional behavior, *IEEE Trans. Plasma Sci.*, 17(2), 323–329
- Gorin, B. N. (1985), Mathematical modeling of the lightning return stroke (in Russian), *Elektrichestvo*, 4, 10–16, (in Russian)
- Gorin, B. N. (1992), The closing-switch model of lightning return-stroke, In *Proceedings of 9th International Conference on Atmospheric Electricity*, The St. Petersburg Scientific Centre of the Russia Academy of Sciences, St. Petersburg, Russia
- Heckman, S. J. and E. R. Williams (1989), Corona envelopes and lightning currents, *J. Geophys. Res.*, 94(D11), 13287–13294
- Hermosillo, V. F. and V. Cooray (1996), Space-charge generation and neutralisation in a coaxial cylindrical configuration in air under a negative voltage impulse, *J. Electrostat.*, 37, 139–149
- Idone, V. and R. Orville (1982), Lightning return stroke velocities in the thunderstorm research international program (TRIP), *J. Geophys. Res.*, 87(C7), 4903–4915
- Jordan, E. C. and K. G. Balmain (1968), *Electromagnetic Waves and Radiating Systems*, pp. 384–388, Prentice-Hall, Inc., Englewood Cliffs, New Jersey

- Jordan, D. M. and M. A. Uman (1983), Variation in light intensity with height and time from subsequent lightning return strokes, *J. Geophys. Res.*, 88(C11), 6555–6562
- Lin, Y. T., M. A. Uman, J. A. Tiller, R. D. Brantley, W. H. Beasley, E. P. Krider, *et al.* (1979), Characterization of lightning return stroke electric and magnetic fields from simultaneous two-station measurements, *J. Geophys. Res.*, 84, 6307–6314
- Little, P. F. (1978), Transmission line representation of a lightning return stroke, *J. Phys. D: Appl. Phys.*, 11, 1893–1910
- Mach, D. M. and W. D. Rust (1989), Photoelectric return stroke velocity and peak current estimates in natural and triggered lightning, *J. Geophys. Res.*, 94, 13237–13247
- Maslowski, G. and V. A. Rakov (2006), A study of the lightning channel corona sheath, *J. Geophys. Res.*, 111(D14110), 1–16
- Mattos, M. A. F. and C. Christopoulos (1988), A nonlinear transmission line model of the lightning return stroke, *IEEE Trans. Electromagn. Compat.*, 30(3), 401–406
- Mattos, M. A. da F. and C. Christopoulos (1990), A model of the lightning channel, including corona, and prediction of generated electromagnetic fields, *J. Phys. D: Appl. Phys.*, 23, 40–46
- Nucci, C. A., G. Diendorfer, M. A. Uman, F. Rachidi, M. Ianoz and C. Mazzetti (1990), Lightning return stroke current models with specified channel-base current: A review and comparison, *J. Geophys. Res.*, 95(D12), 395–408
- Oetzel, G. N. (1968), Computation of the diameter of a lightning return stroke, *J. Geophys. Res.*, 73(6), 1889–1896
- Paul, C. R. (1994), *Analysis of Multiconductor Transmission Lines*, 559 pp., Wiley, New York
- Paxton, A. D., R. L. Gardner and L. Baker (1986), Lightning return stroke: A numerical calculation of the optical radiation, *Phys. Fluids*, 29, 2736–2741
- Plooster, M. N. (1971a), Numerical simulation of spark discharges in air, *Phys. Fluids*, 14(10), 2111–2123
- Plooster, M. N. (1971b), Numerical model of the return stroke of the lightning discharge, *Phys. Fluids*, 14(10), 2124–2133
- Price, G. H. and E. T. Pierce (1977), The modeling of channel current in the lightning return stroke, *Radio Sci.*, 12(3), 381–388
- Rakov, V. A. (1998), Some inferences on the propagation mechanisms of dart leaders and return strokes, *J. Geophys. Res.*, 103(D2), 1879–1887
- Rakov, V. A. and M. A. Uman (1998), Review and evaluation of lightning return stroke models including some aspects of their application, *IEEE Trans. Electromagn. Compat.*, 40(4), 403–426
- Rakov, V. A. and M. A. Uman (2003), *Lightning Physics and Effects*, 687 pp., Cambridge University Press, New York
- Rakov, V. A. (2004), Lightning return stroke speed: A review of experimental data, In *Proceedings of the 27th International Conference on Lightning Protection*, Cent. de Génie Electr. de Lyon, Avignon, France, pp. 139–144

- Rao, M. and H. Bhattacharya (1966), Lateral corona currents from the return stroke channel and the slow field change after the return stroke in a lightning discharge, *J. Geophys. Res.*, 71(11), 2811–2814
- Rondón, D. A., F. H. Silveira and S. Visacro (2002), A varying surge impedance transmission line model for simulation of lightning return current in time domain, In *Proceedings of Int. Conf. on Grounding and Earthing*, Rio De Janeiro, Brazil
- Strawe, D. F. (1979), Non-linear modeling of lightning return strokes, In *Proceedings of the Federal Aviation Administration/Florida Institute of Technology Workshop on Grounding and Lightning Technology*, Report FAA-RD-79-6, Melbourne, Florida, USA
- Takagi and Takeuti (1983), Oscillating bipolar electric field changes due to close lightning strokes, *Radio Sci.* 18(3), 391–398
- Theethayi, N. and V. Cooray (2004), Representation of the return stroke as a transmission line—The apparent return stroke velocity, In *Proceedings of the 27th International Conference on Lightning Protection*, Cent. de Génie Electr. de Lyon, Avignon, France
- Theethayi, N. and V. Cooray (2005), On the representation of the lightning return stroke as a current pulse propagating along a transmission line, *IEEE Trans. Power Del.*, 20(2), 823–837
- Thottappillil, R., M. A. Uman and N. Theethayi (2004), Electric and magnetic fields from a semi-infinite antenna above a conducting plane, *J. Electrostat.*, 61, 209–221
- Toepler, M. (1906), Zur kenntnis der gesetz der gleitfunkenbildung, *Ann. Phys. D.*, 4(21), 193–222
- Uman, M. A. and D. K. McLain, (1969), Magnetic field of the lightning return stroke, *J. Geophys. Res.*, 74, 6899–6910
- Uman, M. A., D. K. McLain and E. P. Krider (1975), The electromagnetic radiation from a finite antenna, *American J. Phys.*, 43, 33–38
- Uman, M. A. (1984), Lightning, 298 pp., Dover Publications, Inc., New York
- Visacro, S. and F. H. Silveira (2004), Evaluation of current distribution along the lightning discharge channel by a hybrid electromagnetic model, *J. Electrostat.*, 60(2), 111–120
- Visacro, S. and A. Soares Jr. (2005), HEM: A model for simulation of lightning-related engineering problems, *IEEE Trans. Power Del.*, 20(2), 1206–1208
- Visacro, S. and A. De Conti (2005), A distributed-circuit return-stroke model allowing time and height parameter variation to match lightning electromagnetic field waveform signatures, *Geophys. Res. Lett.*, 32(L23805), doi: 10.1029/2005GL024336



---

## *Chapter 11*

# **On the various approximations to calculate lightning return stroke-generated electric and magnetic fields over finitely conducting ground**

*Vernon Cooray<sup>1</sup>*

---

### **11.1 Introduction**

The knowledge concerning the characteristics of electromagnetic fields generated by lightning flashes is of importance in evaluating the interaction of these electromagnetic fields with electrical networks and in the remote sensing of lightning current parameters from the measured fields. However, electromagnetic fields generated by lightning flashes change their character as they propagate over the ground surface due to selective attenuation of the high-frequency signals by finitely conducting ground (i.e. propagation effects). Thus, depending on the distance of propagation and the conductivity of ground, the peak and the rise time of the lightning-generated electromagnetic fields and their time derivatives measured at a given distance from the lightning channel may deviate more or less from the values that would be present over perfectly conducting ground.

Propagation effects on lightning return stroke-generated electromagnetic fields have been studied experimentally by Uman *et al.* [1] and Cooray *et al.* [2]. Theoretical evaluation of propagation effects on lightning flashes have been conducted by Cooray *et al.* [2], Gardner [3], Cooray and Lundquist [4], Le Vine *et al.* [5], Cooray [6], Ming and Cooray [7], Cooray and Ming [8], Cooray [9, 10], Cooray and Cummins [11, 12], Shoori *et al.* [13, 14] and Delfino *et al.* [15, 16].

Theoretical quantification of propagation effects on lightning return stroke-generated electromagnetic fields requires knowledge concerning the electromagnetic fields of electrical dipoles located over finitely conducting ground. Once the electromagnetic fields due to a dipole are known, the corresponding fields due to lightning return strokes can be calculated by representing the lightning channel as a series of infinitesimal dipoles.

The exact solution to the electromagnetic fields generated by electric dipoles located above a finitely conducting ground plane was obtained by Sommerfeld [17].

---

<sup>1</sup>Uppsala University, Uppsala, Sweden

He presented his results in the form of a set of integrals. Since the numerical solutions of these integrals are time-consuming, attempts have been made to find approximate solutions to these integrals [10, 18, 19]. In this chapter, various approximate solutions and procedures that have been used to calculate electromagnetic fields of return strokes over finitely conducting ground will be presented together with their limits of validity. (Reader is also referred to chapters 12 and 13 of this book.)

## 11.2 Exact expressions for the electromagnetic fields of a dipole located over finitely conducting ground and their extension to return stroke fields

### 11.2.1 Exact expressions for the vector potential of a dipole over finitely conducting ground

The geometry under consideration is shown in Figure 11.1. The finitely conducting ground plane is represented by the surface  $\zeta = 0$  and the lightning channel is located at the origin of the coordinate system. The lightning channel is assumed to be straight, vertical and without any branches. Medium  $\zeta > 0$  is free space with dielectric constant  $\epsilon_0$  and magnetic permeability  $\mu_0$ . The region  $\zeta < 0$  consists of finitely conducting ground of conductivity  $\sigma$  and dielectric constant  $\epsilon = \epsilon_0\epsilon_r$ , where  $\epsilon_r$  is the relative dielectric constant. The point of observation is located at a horizontal distance  $\rho$  from the lightning channel. Note that, for points of observations located above ground  $\zeta > 0$  and for points located below the ground  $\zeta < 0$ . Consider a vertical electrical dipole (a channel element) of length  $dz$  located at a height  $z$  from ground level, i.e. at the point  $(0, 0, z)$ . The vertical component of the magnetic vector potential at a point  $(\rho, 0, \zeta)$  (i.e. W in Figure 11.1) located above ground due to the dipole is given by [20]

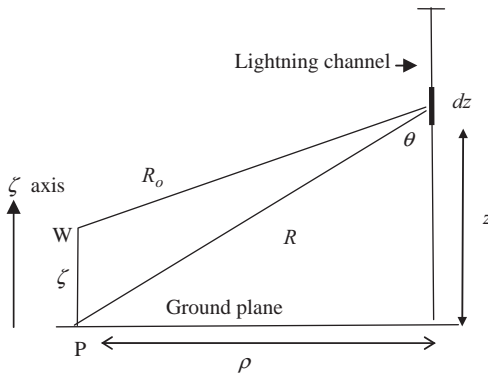


*Figure 11.1 The geometry relevant to the problem under consideration. The dipole (or a channel element of the return stroke channel) is located at height  $z$  above ground. The region  $\zeta > 0$  is air and the region  $\zeta < 0$  is finitely conducting homogeneous ground of conductivity  $\sigma$  and relative dielectric constant  $\epsilon_r$ . Point P is located at the finitely conducting surface at a horizontal distance  $\rho$  from the dipole*

$$A_z = \frac{\mu_o I(j\omega) dz}{4\pi} \left[ \frac{\exp(-jk_o R_o)}{R_o} - \frac{\exp(-jk_o R_1)}{R_1} \right] + \frac{\mu_o I(j\omega) dz}{4\pi} \left\{ 2k_1^2 \int_0^\infty \frac{J_0(\lambda\rho) \exp\left[-(z+\xi)\sqrt{(\lambda^2 - k_o^2)}\right]}{k_1^2 \sqrt{(\lambda^2 - k_o^2)} + k_o^2 \sqrt{(\lambda^2 - k_1^2)}} \lambda d\lambda \right\} \quad (11.1a)$$

The above expression can also be written as [20]

$$A_z = \frac{\mu_o I(j\omega) dz}{4\pi} \left[ \frac{\exp(-jk_o R_o)}{R_o} + \frac{\exp(-jk_o R_1)}{R_1} \right] - \frac{\mu_o I(j\omega) dz}{4\pi} \left\{ 2k_0^2 \int_0^\infty \frac{J_0(\lambda\rho)(\lambda^2 - k_1^2) \exp\left[-(z+\xi)\sqrt{(\lambda^2 - k_o^2)}\right]}{k_1^2 \sqrt{(\lambda^2 - k_o^2)} + k_o^2 \sqrt{(\lambda^2 - k_1^2)}} \frac{\lambda}{\sqrt{\lambda^2 - k_o^2}} d\lambda \right\} \quad (11.1b)$$

The corresponding vertical component of the magnetic vector potential inside the ground is given by

$$A_{z1} = \frac{\mu_o I(j\omega) dz}{4\pi} \int_0^\infty \left\{ \frac{2k_1^2}{k_1^2 \sqrt{(\lambda^2 - k_o^2)} + k_o^2 \sqrt{(\lambda^2 - k_1^2)}} J_0(\lambda\rho) \exp\left[-z\sqrt{(\lambda^2 - k_o^2)} + \xi\sqrt{(\lambda^2 - k_1^2)}\right] \lambda d\lambda \right\} \quad (11.2)$$

$$k_o^2 = \omega^2 \mu_o \epsilon_o \quad (11.3)$$

$$k_1^2 = -j\omega \mu_o (\sigma + j\omega \epsilon_o \epsilon_r) \quad (11.4)$$

$$R_o = \sqrt{\rho^2 + (\xi - z)^2}, \quad R_1 = \sqrt{\rho^2 + (\xi + z)^2} \quad (11.5)$$

In the above equations,  $I(j\omega)$  is the current in the dipole in the frequency domain,  $\omega$  is the angular frequency,  $J_0$  represents the Bessel function of the first kind of order zero and  $j = \sqrt{-1}$ .

### 11.2.2 The exact expressions for the electromagnetic fields of a dipole over finitely conducting ground

#### 11.2.2.1 Vertical electric field in air and underground

The vertical component of the electric field in the frequency domain in air due to the dipole can be obtained from the magnetic vector potential by

$$de_z(j\omega) = \frac{-j\omega}{k_o^2} \left( \frac{\partial^2 A_z}{\partial \xi^2} + k_o^2 A_z \right) \quad (11.6)$$

Performing this operation on (11.1a), one obtains the vertical electric field in frequency domain at point  $P$  at ground level, i.e. at the point  $(\rho, 0, 0)$ , as

$$de_z(z, j\omega, \rho) = \frac{I(j\omega)dz}{4\pi j\omega \epsilon_o} \left\{ 2k_1^2 \int_0^\infty \frac{J_0(\lambda\rho) \exp \left[ -z\sqrt{(\lambda^2 - k_o^2)} \right]}{k_1^2 \sqrt{(\lambda^2 - k_o^2)} + k_o^2 \sqrt{(\lambda^2 - k_1^2)}} \lambda^3 d\lambda \right\} \quad (11.7)$$

The vertical electric field under ground can be obtained from

$$de_{z,under}(z, j\omega, \rho) = \frac{-j\omega}{k_1^2} \left( \frac{\partial^2 A_{z1}}{\partial \xi^2} + k_1^2 A_{z1} \right) \quad (11.8)$$

After performing this operation one obtains the vertical electric field under ground as

$$de_{z,under}(z, j\omega, \rho) = -\frac{\mu_o I(j\omega)j\omega dz}{4\pi k_1^2} \int_0^\infty \left\{ \frac{2k_1^2}{k_1^2 \sqrt{(\lambda^2 - k_o^2)} + k_o^2 \sqrt{(\lambda^2 - k_1^2)}} J_0(\lambda\rho) \right. \\ \left. \exp \left[ -z\sqrt{(\lambda^2 - k_o^2)} + \xi\sqrt{(\lambda^2 - k_1^2)} \right] \lambda^3 d\lambda \right\} \quad (11.9)$$

#### 11.2.2.2 The azimuthal magnetic field in air and underground

The azimuthal component of the magnetic field in the frequency domain due to the dipole can be obtained from the magnetic vector potential by

$$db_\varphi(z, j\omega, \rho) = -\frac{\partial A_z}{\partial \rho} \quad (11.10)$$

Performing this operation on (11.1a), one obtains the azimuthal magnetic field in frequency domain at point  $P$  at ground level, i.e. at the point  $(\rho, 0, 0)$ , as

$$db_\varphi(z, j\omega, \rho) = \frac{\mu_o I(j\omega) dz}{4\pi} \left\{ 2k_1^2 \int_0^\infty \frac{J_1(\lambda\rho) \exp\left[-z\sqrt{(\lambda^2 - k_o^2)}\right]}{k_1^2 \sqrt{(\lambda^2 - k_o^2)} + k_o^2 \sqrt{(\lambda^2 - k_1^2)}} \lambda^2 d\lambda \right\} \quad (11.11)$$

where  $J_1$  represents Bessel functions of first kind of order 1. The magnetic field under ground can be obtained by performing the operation given in (11.10) on  $A_{z1}$ . The resulting field is given by

$$\begin{aligned} db_{\varphi,under}(z, j\omega, \rho) &= \frac{\mu_o I(j\omega) dz}{4\pi} \int_0^\infty \left\{ \frac{2k_1^2}{k_1^2 \sqrt{(\lambda^2 - k_o^2)} + k_o^2 \sqrt{(\lambda^2 - k_1^2)}} J_1(\lambda\rho) \right. \\ &\quad \left. \exp\left[-z\sqrt{(\lambda^2 - k_o^2)} + \xi\sqrt{(\lambda^2 - k_1^2)}\right] \lambda^2 d\lambda \right\} \end{aligned} \quad (11.12)$$

### 11.2.2.3 Horizontal electric field in air and underground

The horizontal component of the electric field in air in the frequency domain due to the dipole can be obtained from the magnetic vector potential by

$$de_\rho(z, j\omega, \rho) = \frac{-j\omega}{k_0^2} \frac{\partial^2 A_z}{\partial \rho \partial \xi} \quad (11.13)$$

Performing this operation on (11.1b), one obtains the horizontal field in frequency domain for  $\xi > 0$  as

$$\begin{aligned} de_\rho(z, j\omega, \rho) &= -\frac{\mu_o I(j\omega) dz j\omega}{4\pi k_o^2} \frac{\partial^2}{\partial \rho \partial \xi} \left( \frac{e^{-jk_o R_o}}{R_o} + \frac{e^{-jk_o R_1}}{R_1} \right) \\ &\quad + \frac{\mu_o I(j\omega) dz j\omega}{4\pi} \int_0^\infty \left\{ \frac{2\sqrt{(\lambda^2 - k_1^2)}}{k_1^2 \sqrt{(\lambda^2 - k_o^2)} + k_o^2 \sqrt{(\lambda^2 - k_1^2)}} J_1(\lambda\rho) \right. \\ &\quad \left. \exp\left[-z\sqrt{(\lambda^2 - k_o^2)} - \xi\sqrt{(\lambda^2 - k_o^2)}\right] \lambda^2 d\lambda \right\} \end{aligned} \quad (11.14)$$

When the point of observation is at ground level (i.e.  $\xi = 0$ ), this equation reduces to

$$de_\rho(z, j\omega, \rho) = \frac{\mu_o I(j\omega) dz j\omega}{4\pi} \int_0^\infty \left\{ \frac{2\sqrt{(\lambda^2 - k_1^2)}}{k_1^2 \sqrt{(\lambda^2 - k_o^2)} + k_o^2 \sqrt{(\lambda^2 - k_1^2)}} J_1(\lambda\rho) \right. \\ \left. \exp \left[ -z\sqrt{(\lambda^2 - k_o^2)} \right] \lambda^2 d\lambda \right\} \quad (11.15)$$

The horizontal electric field at a given depth below the ground surface (i.e.  $\xi < 0$ ) can be obtained from the magnetic vector potential from

$$de_{\rho,under}(z, j\omega, \rho) = \frac{-j\omega}{k_1^2} \frac{\partial^2 A_{z1}}{\partial \rho \partial \xi} \quad (11.16)$$

Performing this operation one finds that

$$de_{\rho,under}(z, j\omega, \rho) = \frac{\mu_o I(j\omega) dz j\omega}{4\pi} \int_0^\infty \left\{ \frac{2\sqrt{(\lambda^2 - k_1^2)}}{k_1^2 \sqrt{(\lambda^2 - k_o^2)} + k_o^2 \sqrt{(\lambda^2 - k_1^2)}} J_1(\lambda\rho) \right. \\ \left. \exp \left[ -z\sqrt{(\lambda^2 - k_o^2)} + \xi\sqrt{(\lambda^2 - k_1^2)} \right] \lambda^2 d\lambda \right\} \quad (11.17)$$

where, as indicated earlier,  $J_1$  represents Bessel functions of first kind of order 1.

### 11.2.3 Electromagnetic fields of return strokes

The electromagnetic fields in time domain generated by a dipole over finitely conducting ground can be obtained by inverse Fourier transformation of the frequency domain results presented in the earlier sections and the corresponding electromagnetic fields due to the lightning flash can be obtained by dividing the lightning channel into a series of infinitesimal dipoles and integrating the dipole fields from  $z = 0$  to  $z = H$  where  $H$  is the height of the return stroke. For example, the time domain vertical electric field at the surface of the ground,  $E_z(t, \rho)$  is given by

$$E_z(t, \rho) = \int_0^H dE_z(z, t, \rho) \quad (11.18)$$

In the above equation,  $dE_z(z, t, \rho)$  is the inverse Fourier transformation of  $de_z(z, j\omega, \rho)$ .

### 11.3 Return stroke models utilized in testing the approximate expressions

To calculate the electric fields from return strokes, an expression for  $I(z, t)$ , the spatial and temporal variation of the return stroke current, is required. Since no direct experimental data are available today to quantify the way in which the return stroke current signature varies as a function of height, it is necessary to rely on return stroke models to obtain an expression for  $I(z, t)$ . There are a number of return stroke models that predict the spatial and temporal variation of the return stroke current (21, see also Chapters 7, 8, 9 and 10 of this book). Any one of these models could be utilized for the purpose at hand. However, the published studies whose results are presented in this chapter had utilized the modified transmission line model (MTLE) for this purpose. According to the MTLE model, the temporal and spatial variation of the return stroke current is given by [22]

$$I(z, t) = P(z)I(0, t - z/v) \quad (11.19)$$

with

$$P(z) = \exp(-z/\lambda_e) \quad (11.20)$$

In this equation  $\lambda_e$  is the current decay height constant,  $P(z)$  is the current attenuation factor,  $v$  is the return stroke speed assumed to be uniform and  $I(0, t)$  is the current at the base of the channel. The two analytical expressions for the channel base current that have been used frequently in the literature and specially in the literature related to propagation effects are the following: The first expression that represents the channel base current of a subsequent strokes is given by [23]

$$I(t, 0) \frac{I_1}{\eta} \left( \frac{t}{\tau_1} \right)^2 \frac{e^{-t/\tau_2}}{1 + (t/\tau_1)^2} + I_2 \left\{ \exp \left( \frac{-t}{\tau_3} \right) - \exp \left( \frac{-t}{\tau_4} \right) \right\} \quad (11.21)$$

where  $I_1 = 10.8$  kA,  $I_2 = 8.2$  kA,  $\eta = 0.845$ ,  $\tau_1 = 7.2 \times 10^{-8}$  s,  $\tau_2 = 5.0 \times 10^{-6}$  s,  $\tau_3 = 100.0 \times 10^{-6}$  s and  $\tau_4 = 6.0 \times 10^{-6}$  s. This current exhibits a peak value of 12 kA and a maximum time derivative of 115 kA/μs. The above expression is constructed by adding a Heidler function [24] to a double exponential function.

The other expression, consists of the sum of two Heidler functions, that is being used to describe both first and subsequent return strokes is given by [16]

$$I_b(0, t) = \frac{I_1}{\eta_1} \left( \frac{t}{\tau_{11}} \right)^{n_1} \frac{e^{-t/\tau_{12}}}{1 + (t/\tau_{11})^{n_1}} + \frac{I_2}{\eta_2} \left( \frac{t}{\tau_{21}} \right)^{n_2} \frac{e^{-t/\tau_{22}}}{1 + (t/\tau_{21})^{n_2}} \quad (11.22)$$

$$\eta_m = \exp \left[ - \left( \frac{\tau_{m1}}{\tau_{m2}} \right) \left( \frac{n_m \tau_{m2}}{\tau_{m1}} \right)^{1/n_m} \right] \quad (11.23)$$

The parameters used to represent first and subsequent stroke currents are given in Table 11.1.

*Table 11.1 Parameters of first (FS) and subsequent (SS) return stroke current*

	$I_1$ (kA)	$\tau_{11}$ (μs)	$\tau_{12}$ (μs)	$n_1$	$I_2$ (kA)	$\tau_{21}$ (μs)	$\tau_{22}$ (μs)	$n_2$
FS	28	1.8	95	2				
SS	10.7	0.25	2.5	2	6.5	2	280	2

## 11.4 Summary of exact propagation effects in the vicinity of the channel

Many of the approximate expressions that account for the effects of finitely conducting ground (to be described later) fail when the distance to the point of observation is close to the channel. Thus, it is important to describe the extent of propagation effects close to the channel, so that the reader can decide for himself whether the propagation effects could be neglected or whether it is necessary to appeal to full expressions given earlier to calculate the electromagnetic fields (See also chapter 13).

Let us first consider the return stroke vertical electric fields at ground level evaluated by numerical integration of the Sommerfeld's integrals. Several such examples corresponding to distances between 10 m and 1 km from the lightning channel for ground conductivities of 0.01 and 0.001 S/m are presented by Cooray [9, 10]. In the calculation the effective dielectric constant was kept constant at 5. The calculated electric fields and electric field derivatives at several distances from the lightning channel are shown in Figures 11.2 and 11.3, respectively. In each diagram, the vertical electric field that would be present at the same distance over perfectly conducting ground is also shown by a dotted line for comparison purposes.

The results presented in Figure 11.2 show that as far as the vertical electric field is concerned the propagation effects will not cause any significant changes, except for a slight change in the slope of the rising part, for distances within approximately 1000 m from the lightning channel and for conductivities greater than approximately 0.001 S/m. Similar conclusions concerning the non-significant propagation effects on the electric field in the vicinity of the channel have also been arrived at previously by Baba and Rakov [25] and Mimouni *et al.* [26]. In the study conducted by Mimouni *et al.* [26], the electromagnetic field was calculated at a height of 10 m. It is important to mention here that the propagation effects on the field at higher elevations are slightly less than those on the ones at ground level. The possibility to neglect the propagation effects on the magnetic field in the vicinity of the lightning channel can also be inferred from the research work of Caligaris *et al.* [27] and Rubinstein [28]. On the other hand, the calculations of Cooray [10] show that the derivative of the electric field is much more sensitive to the propagation effects and they could be significantly distorted by propagation effects even within approximately 1 km from the channel (see Figure 11.3). The

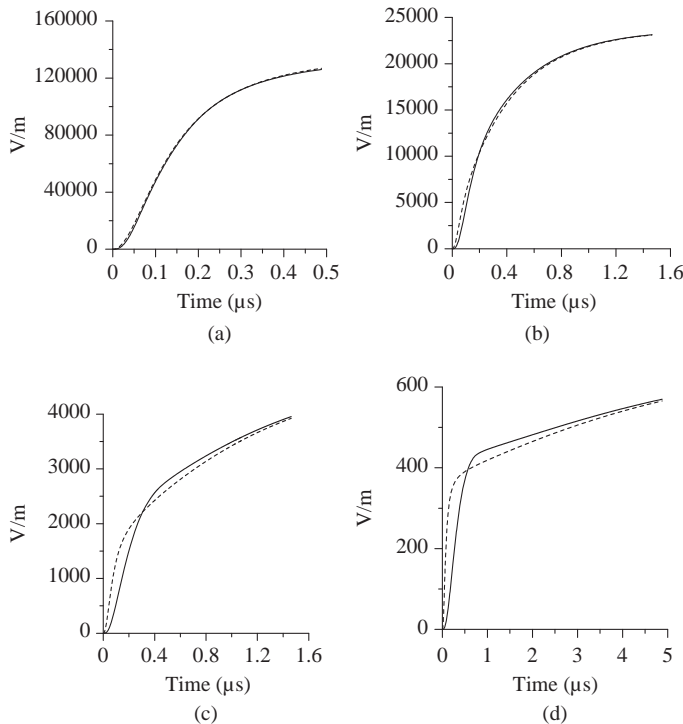


**Figure 11.2** Vertical electric field at ground level at (a) 10 m, (b) 50 m, (c) 200 m and (d) 1000 m from the lightning channel. The solid line shows the field over finitely conducting ground calculated using Sommerfeld's integrals and the dotted line shows the corresponding one over perfectly conducting ground. The conductivity of the ground is 0.001 S/m and the relative dielectric constant is 5. In the calculations, the return stroke is modelled by using the MTLE model with a current decay height constant  $\lambda_e = 2$  km. The return stroke speed is kept at  $1.5 \times 10^8$  m/s. The current waveform at ground level is simulated by the analytical expression given by (11.21) (adapted from Cooray [10])

peak amplitude of the time derivative of the vertical electric field will decrease by approximately 30%, 40% and 70% in propagating 100, 200 and 1000 m, respectively, over finitely conducting ground of 0.001 S/m of conductivity. The corresponding results for 0.01 S/m conductivity are 4%, 8% and 27%. The calculations of Cooray [10] show that very close to the channel, i.e. within approximately 20 m, the propagation effects will lead to a slight increase in the peak of the time derivative. The reason for this is the following. A significant fraction of the electric field time derivative very close to the lightning channel is coming from the induction and static terms. The peak of the time derivative of the induction and static terms occurs at a time slightly longer than the time at which the peak of the

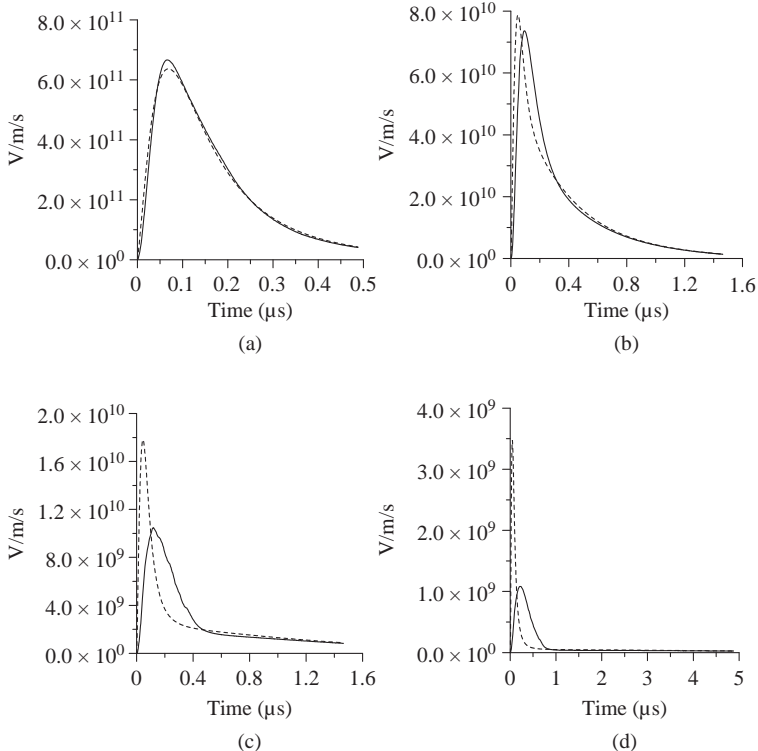


*Figure 11.3 Time derivative of the vertical electric field at ground level at (a) 10 m, (b) 50 m, (c) 200 m and (d) 1000 m from the lightning channel. The solid line shows the time derivative of the electric field over finitely conducting ground and the dotted line shows the corresponding one over perfectly conducting ground. The conductivity of the ground is 0.001 S/m and the relative dielectric constant is 5. In the calculations, the return stroke is modelled by using the MTLE model with a current decay height constant  $\lambda_e = 2$  km. The return stroke speed is kept at  $1.5 \times 10^8$  m/s. The current waveform at ground level is simulated by the analytical expression given by (11.21) (adapted from Cooray [10])*

time derivative of the radiation field takes place. The propagation effects will not only decrease the peak amplitude of the radiation field time derivative but also increase the time at which the peak occurs. This propagation delay will shift the peak of the radiation field time derivative closer to the peak of the time derivative of the static field component making their sum to contribute more efficiently to the peak of the time derivative of the total electric field. This effect will compensate for the decrease in the total field component due to the attenuation of the radiation

field. At distances larger than approximately 20 m, the latter effect will take over making the peak of the derivative of the electric field to decrease.

Now, let us consider the magnetic fields. The calculations by Cooray [9] show that, similar to the electric fields within approximately 1 km from the lightning channel, the propagation effects on the magnetic fields can be neglected as far as the rise time and the peak of these fields are concerned. For larger distances the approximate expressions to be described later can provide reasonable results. However, this is not the case for the magnetic field derivative. Similar to the electric field time derivative, the magnetic field time derivative also attenuates significantly even within 1 km from the lightning channel. Figure 11.4 depicts how the peak magnetic field time derivative varies with distance over finitely conducting ground for conductivities in the range 0.01 S/m to 0.0001 S/m. Since, the temporal behaviour of magnetic and electric field time derivatives are almost identical up to about a few tens of metres from the lightning channel, propagation effects on them are almost identical.

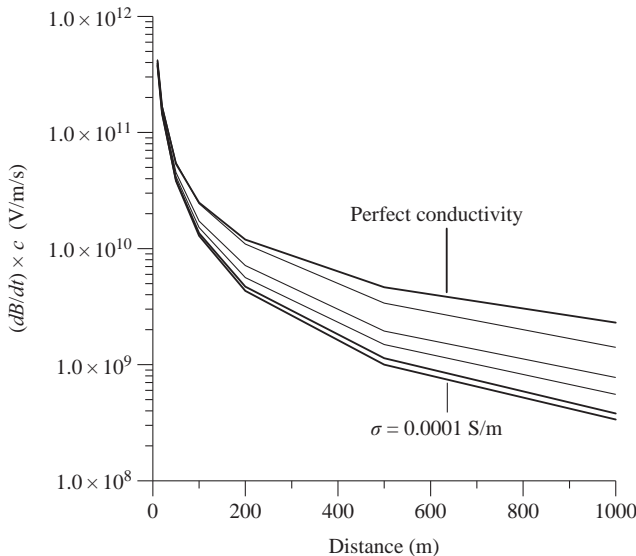


*Figure 11.4 The peak amplitude of the magnetic field time derivative multiplied by the speed of light in free space as a function of distance for several conductivities. The results are shown for perfectly conducting ground,  $\sigma = 0.01, 0.001, 0.0005, 0.0002$  and  $0.0001 \text{ S/m}$ . Note that the peak amplitude at a given distance decreases as the conductivity decreases from infinity (perfect conductivity) to  $0.0001 \text{ S/m}$ . In the calculations, the return stroke is modelled by using the MTLE model with a current decay height constant  $\lambda_e = 2 \text{ km}$ . The return stroke speed is kept at  $1.5 \times 10^8 \text{ m/s}$ . The current waveform at ground level is simulated by the analytical expression given by (11.21) (adapted from Cooray [9])*

## 11.5 Simplified procedures to calculate electric and magnetic fields over finitely conducting ground

### 11.5.1 Norton and Bannister's approximations

According to the analysis presented by Norton [18], the vertical electric field at ground level at point  $P$  due to a dipole located at height  $z$  is given by

$$de_z(z, j\omega, \rho) = \frac{I(j\omega)dz}{2\pi\epsilon_0} \left[ \frac{2 - 3\sin^2\theta}{j\omega R^3} + \frac{2 - 3\sin^2\theta}{cR^2} + \Delta_o \frac{\cos\theta}{cR^2} + j\omega \frac{\sin^2\theta}{c^2 R} a(z, j\omega, \rho) \right] e^{-j\omega R/c} \quad (11.24)$$

Bannister had presented expressions for the vertical electric field, horizontal electric field and the magnetic field both in air and in underground. According to Bannister [19] the vertical electric field at ground level is given by

$$de_z(z, j\omega, \rho) = \frac{I(j\omega)dz}{2\pi\epsilon_0} \left[ \frac{2 - 3\sin^2\theta}{j\omega R^3} + \frac{2 - 3\sin^2\theta}{cR^2} + j\omega \frac{\sin^2\theta}{c^2 R} a(z, j\omega, \rho) \right] e^{-j\omega R/c} \quad (11.25)$$

In the above equations

$$a(z, j\omega, \rho) = \frac{1}{2} [(1 + R_v) + (1 - R_v) w_{1-1}(\rho)] \quad (11.26)$$

$$R = \sqrt{\rho^2 + z^2}, \quad \cos\theta = z/R \quad (11.27)$$

$$R_v = \frac{\cos\theta - \Delta_1}{\cos\theta + \Delta_1} \quad (11.28)$$

$$\Delta_1 = \frac{k_o}{k_1} \left( 1 - \frac{k_o^2}{k_1^2} \sin^2\theta \right)^{1/2} \quad (11.29)$$

$$\eta = -\frac{j\omega R}{2c\sin^2\theta} (\cos\theta + \Delta_1)^2 \quad (11.30)$$

$$w_{1-1}(\rho) = 1 - j(\pi\eta)^{1/2} e^{-\eta} erfc(j\eta^{1/2}) \quad (11.31)$$

In these equations *erfc* stands for the complementary error function. The function  $a(z, \omega, \rho)$  is the attenuation function corresponding to a dipole at height  $z$  over homogeneous and finitely conducting ground of surface impedance  $\Delta_1$ . With  $\cos\theta = 0$  the function  $w_{1-1}(\rho)$  becomes the attenuation function corresponding to a dipole at ground level over homogeneous ground of surface impedance  $\Delta_1$ .

Note that the expression for the electric field at ground level derived by Norton [18] contains an additional term that is not present in Bannister's derivation. However, as shown by Cooray [10], this additional term will make only a very small contribution in the case of lightning electromagnetic fields making the results obtained by Norton [18] equation almost identical to that of Bannister [19].

### **11.5.1.1 Comparison of Norton's and Bannister's approximate expressions for the vertical electric field with exact calculations**

Cooray [10] compared the predictions of Norton's and Bannister's expressions for the vertical electric field against the ones calculated by numerical integration of Sommerfeld's integrals. Figure 11.5 depicts the exact vertical electric fields together with the electric fields obtained with the Norton and Bannister's approximations. Figure 11.6 shows the time derivative of the vertical electric fields. The solid line (black) in each diagram shows the exact vertical electric field. The short-dashed line shows the Bannister approximation and the long-dashed line shows the Norton approximation. First, note that the difference between Norton's and Bannister's approximations is very small and for distances larger than approximately 200 m both Norton and Bannister approximations generate identical results. This shows that the third term inside the bracket of Norton's equation (11.24) does not contribute significantly to the electric field at ground level. The results also show that except for a difference of not more than a few percent, both the Norton and the Bannister approximations provide a good fit to the results based on the exact theory. The results are shown only for the conductivity of 0.001 S/m because the agreement is even better when the conductivity is 0.01 S/m. One can conclude, therefore, that in calculating propagation effects on the lightning-generated vertical electric field at ground level one can use either the Norton's or the Bannister's equations without resorting to integration of the cumbersome Sommerfeld's equations.

To estimate the errors associated with the predictions of Norton's and Bannister's theories, the peak time derivatives of the magnetic field predicted by these theories were calculated by Cooray [9], and the errors associated with the predicted values were obtained by comparing them with the values obtained using Sommerfeld's integrals. The peak magnetic field derivative was used for this purpose because it is more sensitive to propagation effects than the peak magnetic field. The results obtained by Cooray [9] are tabulated in Table 11.2. Note that the mean error (estimated from seven data points corresponding to 10, 20, 50, 100, 200, 500 and 1000 m) associated with these formulations increases with decreasing conductivity and it can reach approximately 20% for conductivity of 0.0001 S/m. For conductivity less than approximately 0.001, the approximations generate results with errors less than approximately 5% and for all practical purposes these approximations can be used instead of the numerical solution of Sommerfeld's equations.

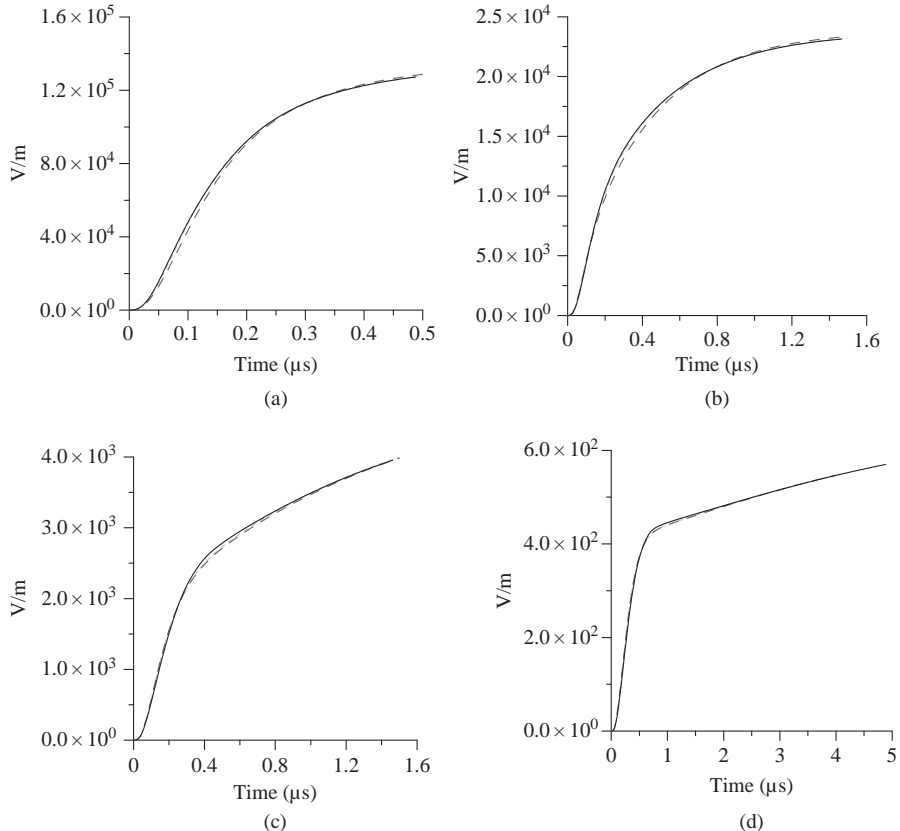


**Figure 11.5** Vertical electric field at ground level at (a) 10 m, (b) 50 m, (c) 200 m and (d) 1000 m from the lightning channel. The solid line shows the field obtained from Sommerfeld's equation, the short-dashed line the Bannister approximation and the long-dashed line the Norton approximation. The conductivity of the ground is 0.001 S/m and the relative dielectric constant is 5. In the calculations, the return stroke is modelled by using the MTLF model with a current decay height constant  $\lambda_e = 2$  km. The return stroke speed is kept at  $1.5 \times 10^8$  m/s. The current waveform at ground level is simulated by the analytical expression given by (11.21) (adapted from Cooray [10])

### 11.5.2 Simplified expressions derived by Cooray and Lundquist [4] and Cooray [6] to calculate vertical electric field and horizontal magnetic field over finitely conducting ground

Cooray and Lundquist [4] and Cooray [6] simplified the calculation of the vertical electric field and horizontal magnetic field from lightning return strokes over finitely conducting ground using two simplifying approximations. Let us consider these approximations one at a time.

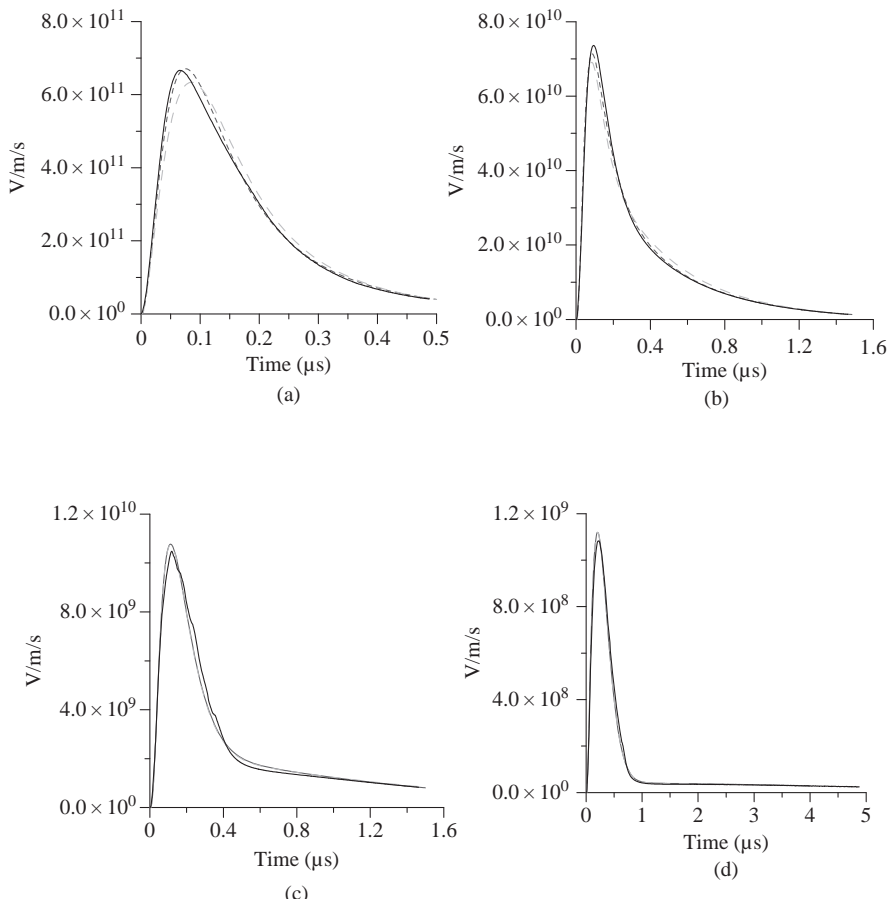


Figure 11.6 The time derivative of the vertical electric field at ground level at (a) 10 m, (b) 50 m, (c) 200 m and (d) 1000 m from the lightning channel. The solid line shows the field obtained from Sommerfeld's equation, the short-dashed line the Bannister approximation and the long-dashed line the Norton approximation. The conductivity of the ground is 0.001 S/m and the relative dielectric constant is 5. In the calculations, the return stroke is modelled by using the MTLE model with a current decay height constant  $\lambda_e = 2$  km. The return stroke speed is kept at  $1.5 \times 10^8$  m/s. The current waveform at ground level is simulated by the analytical expression given by (11.21) (adapted from Cooray [10])

*Table 11.2 The mean error and the standard deviation, based on the peak magnetic field derivative, associated with the predictions of Bannister's and Norton's approximation*

$\sigma(\text{S/m})$	Mean error	Standard deviation
0.01	4.1	4.0
0.001	5.8	4.0
0.0005	8.5	4.1
0.0002	14.8	3.7
0.0001	17.4	8.6

Adapted from Cooray [9].

### 11.5.2.1 Approximation 1

According to the Bannister's approximation, the total electric field due to a lightning flash over finitely conducting ground at a horizontal distance  $\rho$  is given by

$$e_z(j\omega, \rho) = \int_0^H \frac{I(j\omega) dz}{2\pi \epsilon_o} \left[ \frac{2 - 3\sin^2\theta}{j\omega R^3} + \frac{2 - 3\sin^2\theta}{cR^2} + j\omega \frac{\sin^2\theta}{c^2 R} a(z, j\omega, \rho) \right] e^{-j\omega R/c} dz \quad (11.32)$$

In the above equation  $R = \sqrt{z^2 + \rho^2}$ . The same result is obtained if one neglects the third term inside the bracket of Norton's equation (i.e. (11.24)). Note that the above equation is nothing but the integration (or summing up) of the dipole fields generated by elementary dipoles into which the channel is divided taking into account the proper time delays.

Cooray and Lundquist [4] and Cooray [6] simplified this equation by using the following arguments. As far as the propagation effects are concerned the section of the waveform which is of interest is that occurring within the first few microseconds. If the speed of propagation of the return stroke front is approximately  $10^8$  m/s, the length of the channel that contributes to the radiation field during this time would not be larger than a few hundred metres. Thus, in the above equation, the attenuation function  $a(z, j\omega, \rho)$  can be replaced by  $a(0, j\omega, \rho)$  (i.e.  $w_{1-1}(\rho)$ ), the attenuation function corresponding to a dipole located at ground level. With this approximation the above equation can be transformed into time domain to find an expression for the vertical electric field over finitely conducting ground. The result is

$$E_{z,app1}(t, \rho) = E_{z,s}(t, \rho) + E_{z,i}(t, \rho) + \int_0^t E_{z,r}(t - \tau, \rho) W_{1-1}(\rho) d\tau \quad (11.33)$$

where  $W_{1-1}(\rho)$  is the inverse Fourier transformation of  $w_{1-1}(\rho)$ . In this equation  $E_{z,s}(t, \rho)$ ,  $E_{z,i}(t, \rho)$  and  $E_{z,r}(t, \rho)$  are the static, induction and radiation field

components, respectively, of the electric fields generated by the return stroke over perfectly conducting ground. These field components are given by

$$E_{z,s}(t, \rho) = \int_0^H \frac{dz}{2\pi\epsilon_o} \left[ \frac{2 - 3\sin^2\theta}{R^3} \int_0^t i(z, \tau - R/c) d\tau \right] \quad (11.34)$$

$$E_{z,i}(t, \rho) = \int_0^H \frac{dz}{2\pi\epsilon_o} \frac{2 - 3\sin^2\theta}{cR^2} i(z, t - R/c) \quad (11.35)$$

$$E_{z,r}(t, \rho) = \int_0^H \frac{dz}{2\pi\epsilon_o} \frac{\sin^2\theta}{c^2 R} \frac{\partial i(z, t - R/c)}{\partial t} \quad (11.36)$$

According to the above equations, only the radiation field term is disturbed by propagation effects while the static and induction terms remain intact. One has to remember that (11.33) is an approximation, and it should not be used to justify the claim that electrostatic fields are not disturbed by propagation effects. However, as we will show in the next section, this equation provides a reasonable approximation to the exact fields obtained by Sommerfeld's equations demonstrating that the propagation effects on the static fields are not very significant.

*Comparison between exact theory and the predictions of approximation 1*  
 Calculations presented by Cooray [10] show that the difference in the electric field and the time derivative of the electric field as predicted by the exact theory and (11.33) is no more than a few percent in the distant range of 10 m to 1 km. For example Figure 11.7 depicts the electric field derivative at several distances as predicted by exact theory (solid line) and approximation1 (dashed line) for ground conductivity of 0.001 S/m. The agreement becomes even better with increasing distance and increasing conductivity. Thus, one can conclude that (11.33) provides an accurate description of the propagation effects on lightning generated electromagnetic fields.

### 11.5.2.2 Approximation 2

In (11.33)  $W_{1-1}(\rho)$  is the inverse Fourier transformation of  $w_{1-1}(\rho)$ . Use of this equation to calculate the vertical electric field requires performing the inverse Fourier transformation at every distance of interest. On the other hand, Wait [29] has derived an analytical approximation for  $W_{1-1}(\rho)$  that can be used in (11.33) to reduce the computational time. The analytical approximation to  $W_{1-1}(\rho)$  derived by Wait [29] is given by

$$W_{1-1}(\rho)_{Wait} = \frac{d}{dt} \left[ 1 - \exp \left( -\frac{t^2}{4\xi^2} \right) + 2\beta(\epsilon_r + 1) \frac{Q(t/2\xi)}{t} \right] \quad (11.37)$$

with

$$Q(x) = x^2(1 - x^2)\exp(-x^2) \quad (11.38)$$

$$\beta = \frac{1}{\mu_0 \sigma c^2} \quad (11.39)$$

$$\xi^2 = \frac{\rho}{2\mu_0 \sigma c^3} \quad (11.40)$$

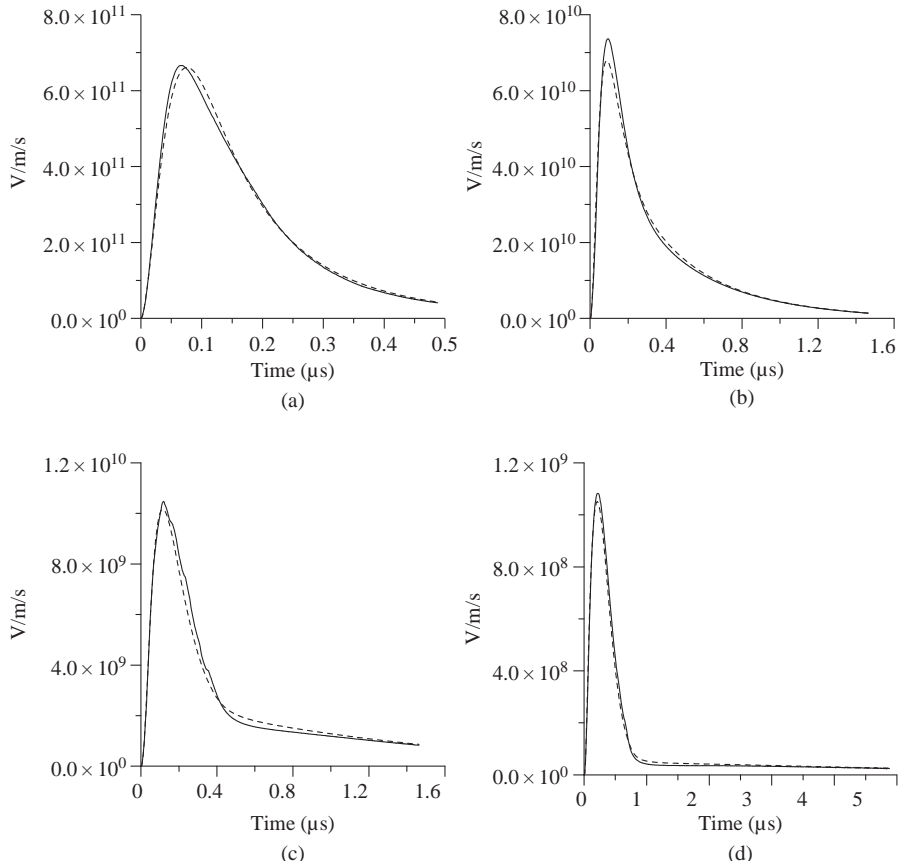


*Figure 11.7* The time derivative of the vertical electric field at ground level at (a) 10 m, (b) 50 m, (c) 200 m and (d) 1000 m from the lightning channel. The solid line shows the time derivative of the field obtained from Sommerfeld's equation and the dotted line shows the data obtained using approximation 1 outlined in Section 11.5.2.1. The conductivity of the ground is 0.001 S/m and the relative dielectric constant is 5. In the calculations, the return stroke is modelled by using the MTLE model with a current decay height constant  $\lambda_e = 2$  km. The return stroke speed is kept at  $1.5 \times 10^8$  m/s. The current waveform at ground level is simulated by the analytical expression given by (11.21) (adapted from Cooray [10])

The third term inside the bracket of (11.37) is a term that takes into account approximately the displacement current in the ground. If one neglects this term, the equation can be written as

$$W_{1-1}(\rho)_{Wait} = \frac{d}{dt} \left[ 1 - \exp\left(-\frac{t^2}{4\xi^2}\right) \right] \quad (11.41)$$

Using this analytical expression instead of the Fourier transform of  $w_{1-1}(\rho)$  in (11.33) one obtains

$$E_{z,app2}(t, \rho) = E_{z,s}(t, \rho) + E_{z,i}(t, \rho) + \int_0^t E_{z,r}(t - \tau, \rho) W_{1-1}(\rho)_{Wait} d\tau \quad (11.42)$$

Cooray and Lundquist [4] and Cooray [6] used the third term of the above equation to calculate the propagation effects on return stroke radiation fields. Note that if the expression given in (11.41) is substituted for  $W_{1-1}(\rho)_{Wait}$ , then the predicted propagation effects depend only on the parameter  $\rho/\sigma$ .

*Comparison between exact theory and the predictions of approximation 2*  
 Cooray [10] had compared the predictions of (11.42) with the exact results obtained using Sommerfeld's equations. Here we present these results. First, let us consider (11.42) with the attenuation function as given by (11.37). The results obtained from this equation are depicted in Figure 11.8 (dashed line) together with the results corresponding to the Sommerfeld's equations (solid line). Note that the shape of the electric field derivative calculated using the above approximation differ from that obtained from Sommerfeld's equations. Analysis done by Cooray [10] showed that this difference is caused by the first-order approximation for the displacement current (third term in the bracket of (11.37)). Now, let us consider (11.42) with the attenuation function given by (11.41). The results of Cooray's calculations are shown in Figure 11.9. Note that the predicted electric field time derivatives are in better agreement with the Sommerfeld's results. Cooray [10] also have studied the effect of the displacement current term carefully and realized that slight change in the displacement current term can make the predictions of this simple theory agree rather well with the Sommerfeld's over the whole range of distances spanning 10–1000 m and for ground conductivities equal to or less than 0.001 S/m. The agreement becomes even better with increasing distance. The slight modification to the attenuation function that Cooray [10] has come up with is given by the following formula:

$$W_{1-1}(\rho)_{Wait-mod} = \frac{d}{dt} \left[ 1 - \exp\left(-\frac{t^2}{4\xi^2}\right) + \beta \sqrt{\frac{\sigma}{\sigma_o}} \frac{(\epsilon_r + 1)}{\epsilon_r} \frac{Q(t/2\xi)}{t} \right] \quad (11.43)$$

where  $\sigma_o = 10^{-4}$  S/m. The results obtained by using attenuation function given by (11.43) in (11.42) are depicted in Figure 11.10 together with the Sommerfeld's

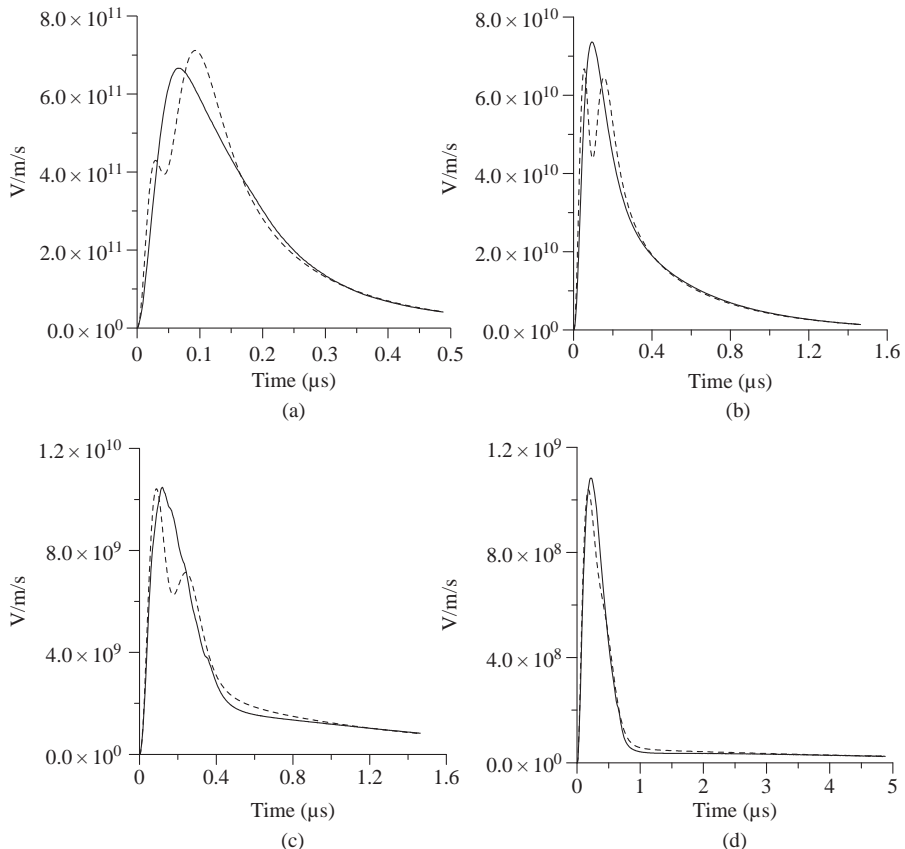


*Figure 11.8* The time derivative of the vertical electric field at ground level at (a) 10 m, (b) 50 m, (c) 200 m and (d) 1000 m from the lightning channel. The solid line shows the time derivative of the field obtained from Sommerfeld's equation and the dotted line shows the results obtained using approximation 2 outlined in Section 11.5.2.2 with attenuation function given by (11.37). The conductivity of the ground is 0.001 S/m and the relative dielectric constant is 5. In the calculations, the return stroke is modelled by using the MTLE model with a current decay height constant  $\lambda_e = 2$  km. The return stroke speed is kept at  $1.5 \times 10^8$  m/s. The current waveform at ground level is simulated by the analytical expression given by (11.21) (adapted from Cooray [10])

results. Note that this equation provides a good fit to the Sommerfeld's results in the distance range of 10 m to 1 km. The agreement between the two theories becomes better with increasing distance. The conclusion to be reached from this study is that (11.42) together with the attenuation function given in (11.43) can be

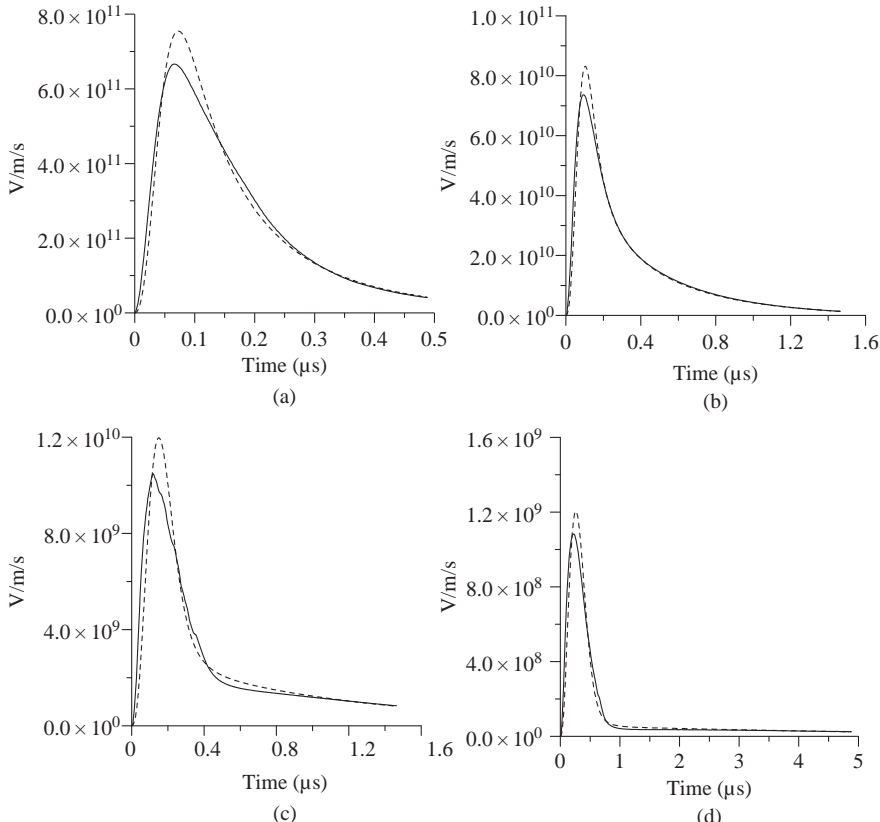


*Figure 11.9 Same as that in Figure 11.8 except that the dotted line shows the results obtained using approximation 2 outlined in Section 11.5.2.2 with attenuation function given by (11.41). The conductivity of the ground is 0.001 S/m and the relative dielectric constant is 5. In the calculations, the return stroke is modelled by using the MTLE model with a current decay height constant  $\lambda_e = 2$  km. The return stroke speed is kept at  $1.5 \times 10^8$  m/s. The current waveform at ground level is simulated by the analytical expression given by (11.21) (adapted from Cooray [10])*

used to calculate propagation effects within 1 km from the lightning channel to an accuracy better than 10%. For larger distances, the simple formula provides a better accuracy.

Cooray [10] had presented calculations also to illustrate the effect of dielectric constant on the calculated results. The results showed that for values of dielectric constants lying within the range of 3–15, which is typical of many soils, the dielectric constant does not influence the propagation effects significantly.

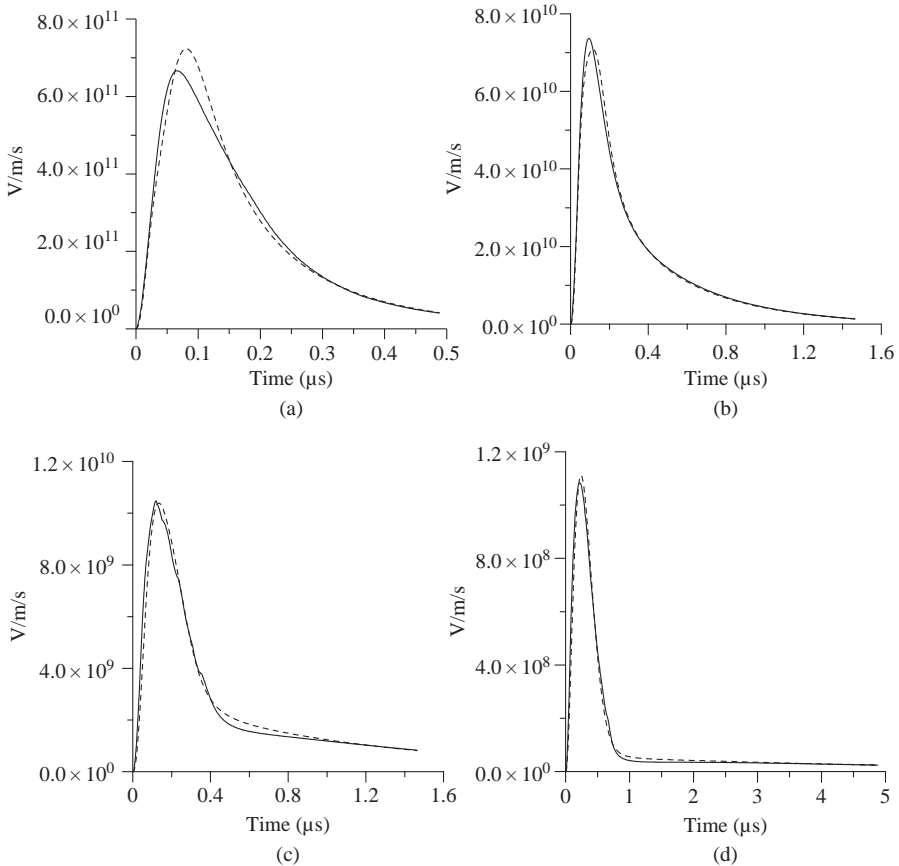


*Figure 11.10* Same as that in Figure 11.8 except that the dotted line shows the results obtained using approximation 2 outlined in Section 11.5.2.2 with attenuation function given by (11.43). The conductivity of the ground is 0.001 S/m and the relative dielectric constant is 5. In the calculations, the return stroke is modelled by using the MTLE model with a current decay height constant  $\lambda_e = 2$  km. The return stroke speed is kept at  $1.5 \times 10^8$  m/s. The current waveform at ground level is simulated by the analytical expression given by (11.21) (adapted from Cooray [10])

### 11.5.3 Simplified expressions to calculate the horizontal electric field

Horizontal electric field is of interest in many engineering studies. This field component plays a significant role in the source terms of the transmission line equations used to solve the problem of interaction of lightning-generated electromagnetic fields with power lines. Moreover, in lightning protection studies, this

field component is of interest in evaluating the surface spark over probability at the point of strike and also in evaluating the step potential experienced by a person standing in the vicinity of a lightning strike point. Here several expressions that are being used to evaluate the horizontal electric field are presented together with their limits of accuracy.

### 11.5.3.1 Quasi-static expression to calculate horizontal electric field close to the lightning channel

A popular approximation that is being used frequently to obtain the horizontal electric field at ground level in the vicinity of the return stroke channel is given by

$$E_\rho(t, \rho) = -\frac{I(t)}{2\pi\rho^2\sigma} \quad (11.44)$$

where  $E_\rho(t, \rho)$  is the horizontal electric field in time domain at ground level at a distance  $\rho$  from the strike point and  $I(t)$  is the current at the channel base. This quasi-static approximation is used frequently in lightning protection studies to estimate lightning hazards caused, for example, by step potentials.

### 11.5.3.2 Surface impedance expression

The surface impedance expression connects the horizontal electric field to the horizontal magnetic field present over finitely conducting ground. This is also a part of the Cooray–Rubinstein approximation used frequently in calculating induced over voltages in power lines due to lightning [28, 30]. According to the surface impedance approximation, the horizontal electric field at ground level is given by

$$e_\rho(j\omega, \rho) = -cb_{\varphi,\sigma}(j\omega, \rho)\frac{k_o}{k_1} \quad (11.45)$$

where  $\rho$  is the horizontal distance to the point of observation from the strike point,  $e_\rho(j\omega, \rho)$  is the horizontal electric field at the surface of the ground and  $b_{\varphi,\sigma}(j\omega, \rho)$  is the azimuthal magnetic field at the surface of the ground. If one neglects the effects of finitely conducting ground on the magnetic field, one can write the above equation as

$$e_\rho(j\omega, \rho) = -cb_\varphi(j\omega, \rho)\frac{k_o}{k_1} \quad (11.46)$$

where  $b_{\varphi,\sigma}(j\omega, \rho)$  is the magnetic field over perfectly conducting ground.

### 11.5.3.3 Comparison of the predictions of the quasi-static approximation and predictions of surface impedance expression with exact calculations

Cooray [31] evaluated the horizontal electric field generated by first and subsequent return strokes using the exact theory and the results were compared with those

predicted by (11.44)–(11.46). The results obtained by Cooray [31] are presented in Figures 11.11–11.18. The results of the comparison show the following on the quasi-static approximation: (a) The quasi-static approximation provides reasonable results at small distances and at long times. For a given distance and time, the agreement between the exact and the quasi-static approximation becomes better with decreasing conductivity. For a given conductivity and distance, the agreement becomes better at longer times. For example, for a given conductivity and distance, the error associated with the peak value of the subsequent stroke horizontal electric field is larger than that of the first strokes. The reason for this is that the peak value of the subsequent stroke occurs at times earlier than the first return stroke peak.

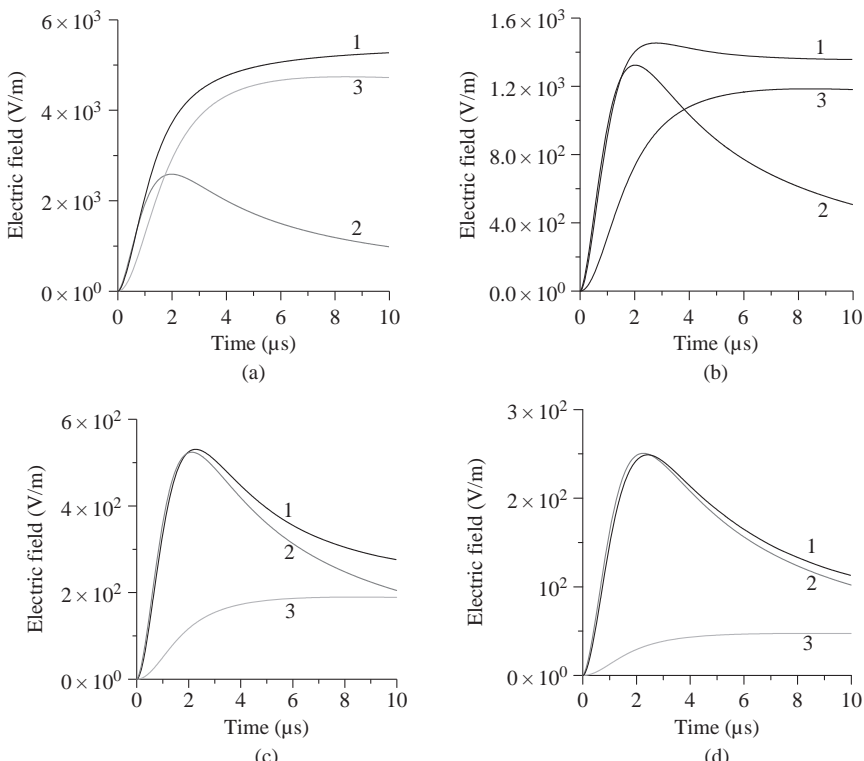


*Figure 11.11 First stroke horizontal electric field at ground level for (a)  $\rho = 10\text{ m}$ ,  $\sigma = 0.01\text{ S/m}$  (b)  $\rho = 20\text{ m}$ ,  $\sigma = 0.01\text{ S/m}$  (c)  $\rho = 50\text{ m}$ ,  $\sigma = 0.01\text{ S/m}$  and (d)  $\rho = 100\text{ m}$ ,  $\sigma = 0.01\text{ S/m}$ . Curve 1: Sommerfeld's integrals; curve 2: surface impedance expression (11.46); curve 3: quasi-static approximation. In the calculations, the return stroke is modelled by using the MTLE model with a current decay height constant  $\lambda_e = 2\text{ km}$ . The return stroke speed is kept at  $1.5 \times 10^8\text{ m/s}$ . The current waveform at ground level is simulated by the analytical expression given by (11.22) (adapted from Cooray [31])*

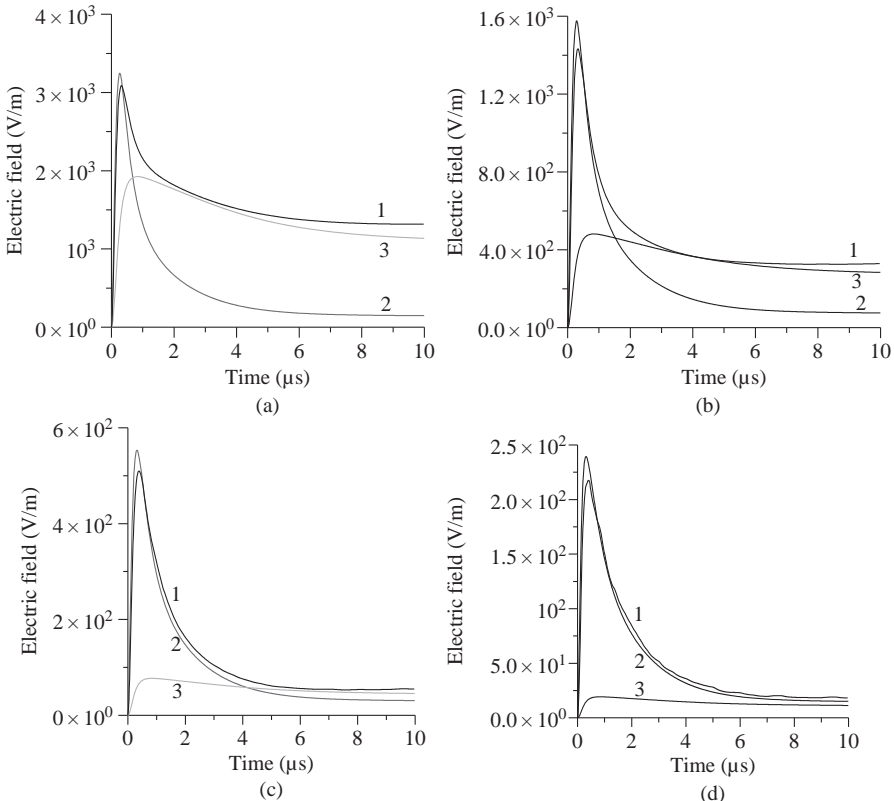


*Figure 11.12 Subsequent stroke horizontal electric field at ground level for (a)  $\rho = 10 \text{ m}$ ,  $\sigma = 0.01 \text{ S/m}$ ; (b)  $\rho = 20 \text{ m}$ ,  $\sigma = 0.01 \text{ S/m}$ ; (c)  $\rho = 50 \text{ m}$ ,  $\sigma = 0.01 \text{ S/m}$ ; (d)  $\rho = 100 \text{ m}$ ,  $\sigma = 0.01 \text{ S/m}$ . Curve 1: Sommerfeld's integrals; curve 2: surface impedance expression (11.46); curve 3: quasi-static approximation. In the calculations, the return stroke is modelled by using the MTLE model with a current decay height constant  $\lambda_e = 2 \text{ km}$ . The return stroke speed is kept at  $1.5 \times 10^8 \text{ m/s}$ . The current waveform at ground level is simulated by the analytical expression given by (11.22) (adapted from Cooray [31])*

According to these calculations of Cooray [31], the surface impedance expressions as given in (11.46) provide accurate results at distances larger than approximately 50 m for 0.01 S/m, 200 m for 0.001 S/m (100 m if only the peak field is concerned), 400 m for 0.0003 S/m and approximately 600 m for 0.0001 S/m. The error associated with this expression at smaller distances is significant. Furthermore, for a given distance the agreement is better at short times than at

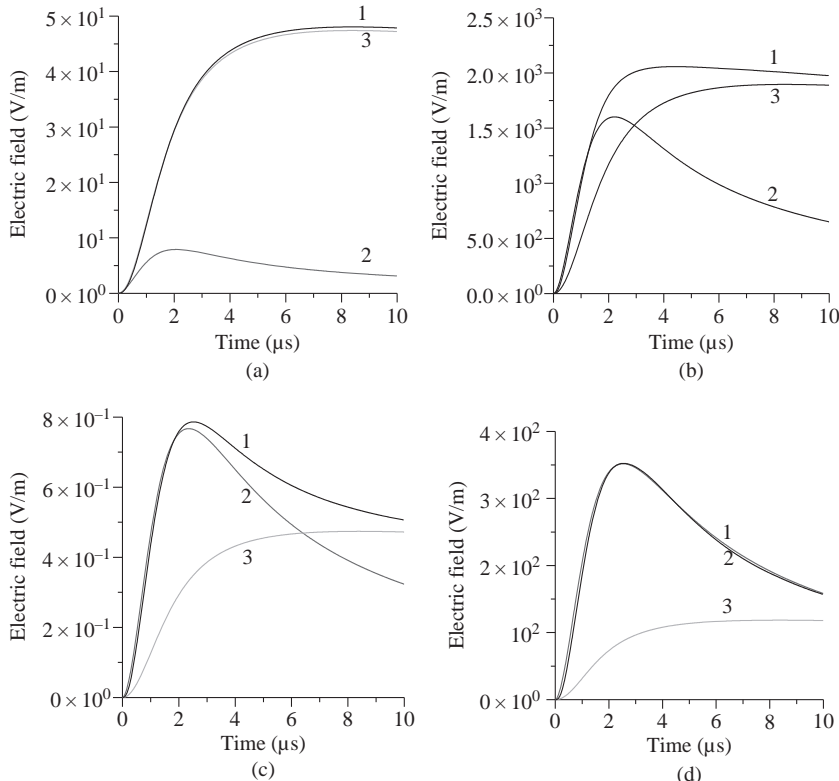


*Figure 11.13 First stroke horizontal electric field at ground level for (a)  $\rho = 10 \text{ m}$ ,  $\sigma = 0.001 \text{ S/m}$ ; (b)  $\rho = 50 \text{ m}$ ,  $\sigma = 0.001 \text{ S/m}$ ; (c)  $\rho = 100 \text{ m}$ ,  $\sigma = 0.001 \text{ S/m}$ ; (d)  $\rho = 200 \text{ m}$ ,  $\sigma = 0.001 \text{ S/m}$ . Curve 1: Sommerfeld's integrals; curve 2: surface impedance expression (11.46); curve 3: quasi-static approximation. In the calculations, the return stroke is modelled by using the MTLE model with a current decay height constant  $\lambda_e = 2 \text{ km}$ . The return stroke speed is kept at  $1.5 \times 10^8 \text{ m/s}$ . The current waveform at ground level is simulated by the analytical expression given by (11.22) (adapted from Cooray [31])*

long times. The results obtained for subsequent return strokes also show the same tendency as that of first return strokes. However, for a given distance the agreement between the peak field values generated by exact theory and the ones obtained from surface impedance expression is better in the case of subsequent return strokes than in the first. These results show clearly that the surface impedance expression can be used to evaluate the horizontal electric field at the surface of the ground provided that the distance of interest is kept beyond a certain critical value, which is a function of conductivity.

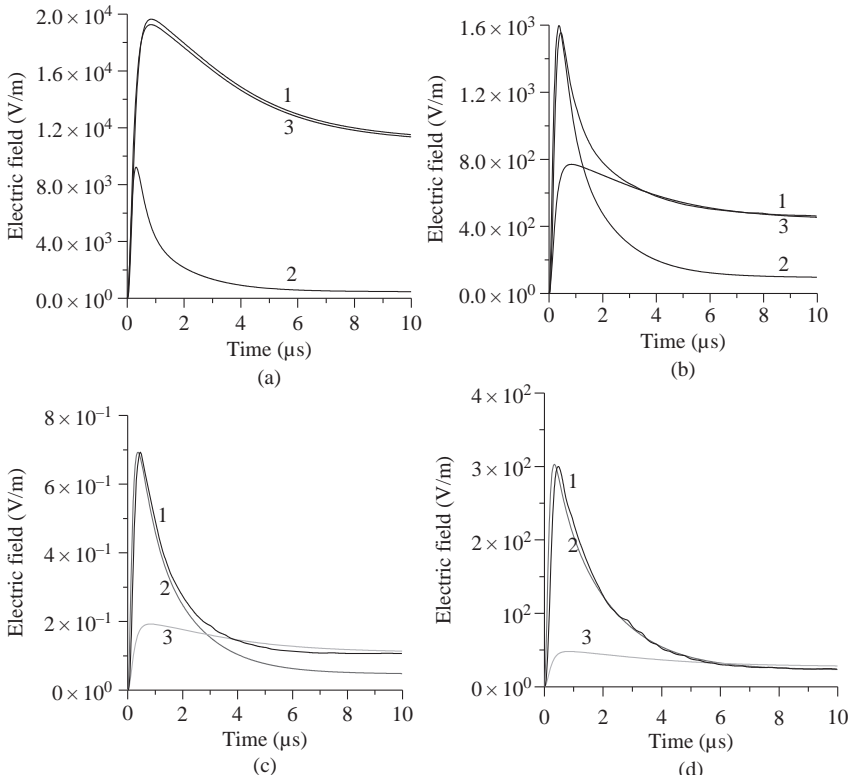


*Figure 11.14 Subsequent stroke horizontal electric field at ground level for  
 (a)  $\rho = 10 \text{ m}$ ,  $\sigma = 0.001 \text{ S/m}$ ; (b)  $\rho = 50 \text{ m}$ ,  $\sigma = 0.001 \text{ S/m}$ ;  
 (c)  $\rho = 100 \text{ m}$ ,  $\sigma = 0.001 \text{ S/m}$ ; (d)  $\rho = 200 \text{ m}$ ,  $\sigma = 0.001 \text{ S/m}$ . Curve 1: Sommerfeld's integrals; curve 2: surface impedance expression (11.46); curve 3: quasi-static approximation. In the calculations, the return stroke is modelled by using the MTLE model with a current decay height constant  $\lambda_e = 2 \text{ km}$ . The return stroke speed is kept at  $1.5 \times 10^8 \text{ m/s}$ . The current waveform at ground level is simulated by the analytical expression given by (11.22) (adapted from Cooray [31])*

Recall that in the above comparison was made between the predictions of (11.46) and the exact horizontal electric field. In this equation, the magnetic field corresponds to the one that exist over perfectly conducting ground. However, the exact expressions as given by (11.45) involve the magnetic field over finitely conducting ground. The propagation effects on the magnetic field can be included using the simple procedure outlined in Section 11.5.2. One can show that when this is done the agreement between the horizontal electric field calculated using the surface impedance expression and the exact one becomes better. When the distance

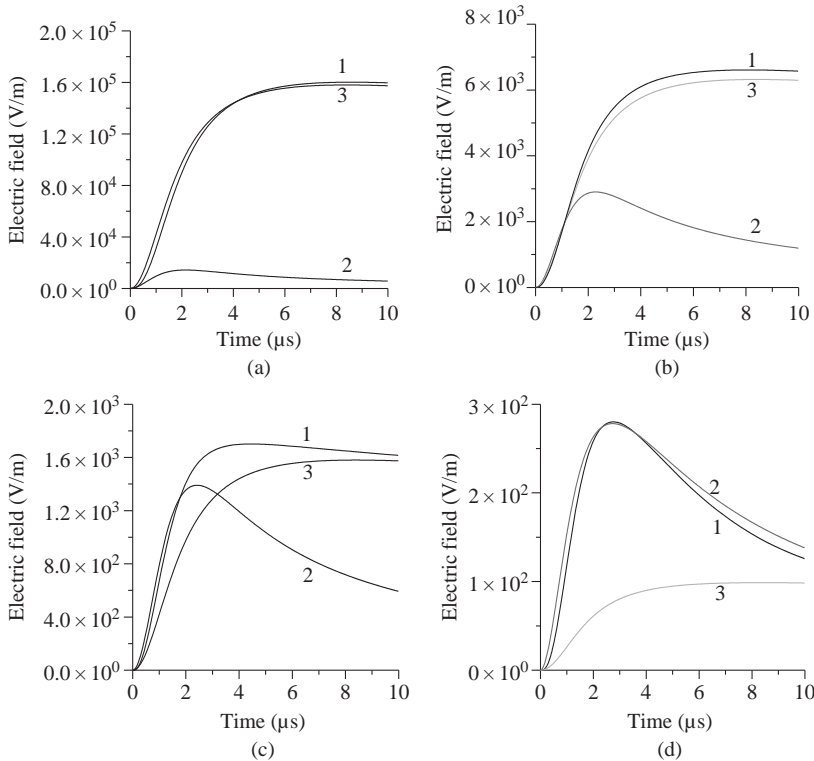


*Figure 11.15 First stroke horizontal electric field at ground level for (a)  $\rho = 10 \text{ m}$ ,  $\sigma = 0.0003 \text{ S/m}$ ; (b)  $\rho = 50 \text{ m}$ ,  $\sigma = 0.0003 \text{ S/m}$ ; (c)  $\rho = 100 \text{ m}$ ,  $\sigma = 0.0003 \text{ S/m}$ ; (d)  $\rho = 400 \text{ m}$ ,  $\sigma = 0.0003 \text{ S/m}$ . Curve 1: Sommerfeld's integrals; curve 2: surface impedance expression (11.46); curve 3: quasi-static approximation. In the calculations, the return stroke is modelled by using the MTLE model with a current decay height constant  $\lambda_e = 2 \text{ km}$ . The return stroke speed is kept at  $1.5 \times 10^8 \text{ m/s}$ . The current waveform at ground level is simulated by the analytical expression given by (11.22) (adapted from Cooray [31])*

to the lightning flash is large and the ground conductivity is poor, it is necessary to use (11.45) to obtain reasonable results. For example, Figure 11.19 shows the horizontal electric fields at a distance of 100 km obtained (1) using exact formulation, (2) using surface impedance expression with magnetic field over perfectly conducting ground as an input (i.e. (11.46)) and (3) using surface impedance expression with magnetic field over finitely conducting ground as an input (i.e. (11.45)). The conductivity of the ground in this example is 0.01 S/m. Note the significant error in the horizontal electric field calculated without taking

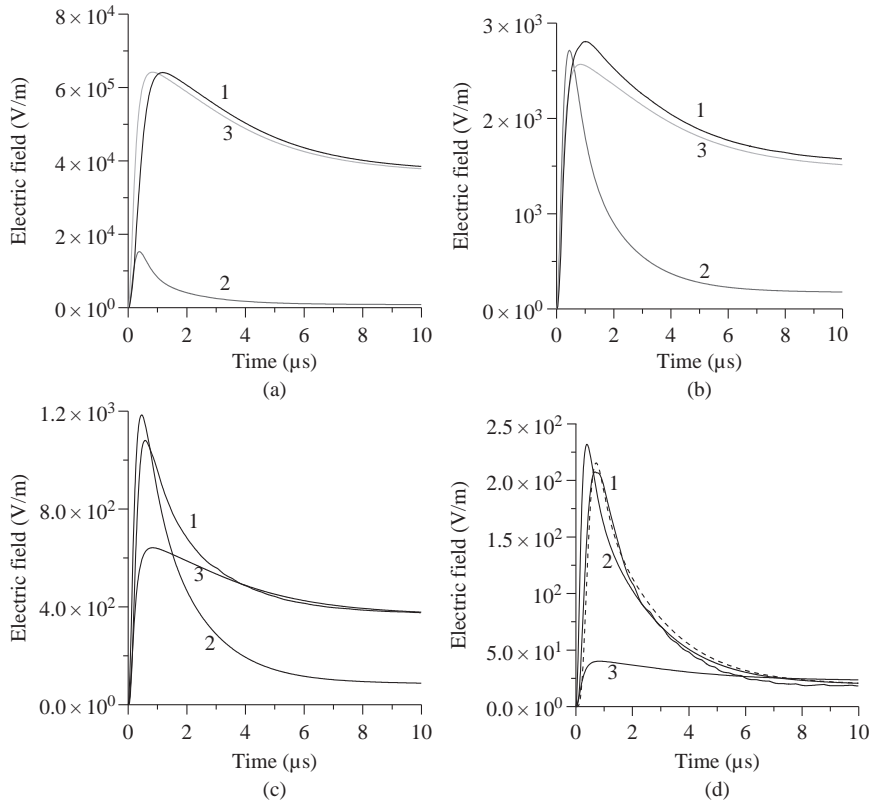


**Figure 11.16** Subsequent stroke horizontal electric field at ground level for (a)  $\rho = 10 \text{ m}$ ,  $\sigma = 0.0003 \text{ S/m}$ ; (b)  $\rho = 50 \text{ m}$ ,  $\sigma = 0.0003 \text{ S/m}$ ; (c)  $\rho = 100 \text{ m}$ ,  $\sigma = 0.0003 \text{ S/m}$ ; (d)  $\rho = 400 \text{ m}$ ,  $\sigma = 0.0003 \text{ S/m}$ . Curve 1: Sommerfeld's integrals; curve 2: surface impedance expression (11.46); curve 3: quasi-static approximation. The dotted line shows the prediction from (11.45). In the calculations, the return stroke is modelled by using the MTLE model with a current decay height constant  $\lambda_e = 2 \text{ km}$ . The return stroke speed is kept at  $1.5 \times 10^8 \text{ m/s}$ . The current waveform at ground level is simulated by the analytical expression given by (11.22) (adapted from Cooray [31])

propagation effects on the magnetic field into account. Calculations of Cooray [31] show that propagation effects have to be included in the magnetic field already at distances larger than approximately 300 m for conductivities around  $10^{-3} \text{ S/m}$  and at distances larger than approximately 200 m for  $10^{-4} \text{ S/m}$  to obtain accurate results, especially in the case of subsequent strokes. This can also be seen by the data given in Figures 11.16–11.18 (dotted lines).

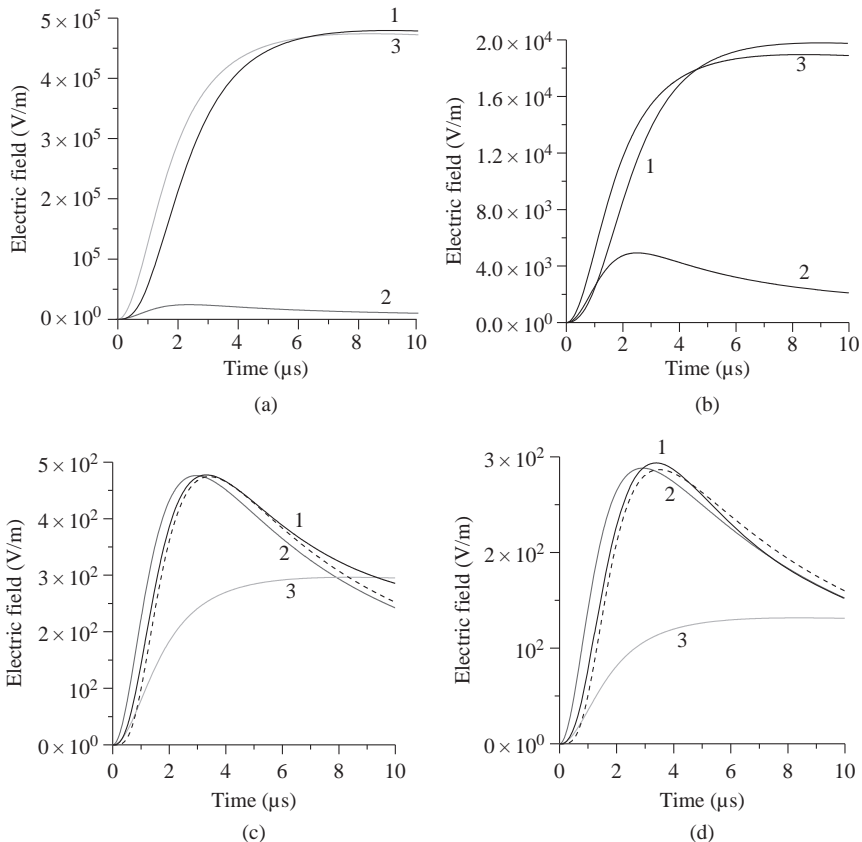


**Figure 11.17** First stroke horizontal electric field at ground level for (a)  $\rho = 10 \text{ m}$ ,  $\sigma = 0.0001 \text{ S/m}$ ; (b)  $\rho = 50 \text{ m}$ ,  $\sigma = 0.0001 \text{ S/m}$ ; (c)  $\rho = 400 \text{ m}$ ,  $\sigma = 0.0001 \text{ S/m}$ ; (d)  $\rho = 600 \text{ m}$ ,  $\sigma = 0.0001 \text{ S/m}$ . Curve 1: Sommerfeld's integrals; curve 2: surface impedance expression (11.46); curve 3: quasi-static approximation. The dotted lines show the prediction from (11.45). In the calculations, the return stroke is modelled by using the MTLE model with a current decay height constant  $\lambda_e = 2 \text{ km}$ . The return stroke speed is kept at  $1.5 \times 10^8 \text{ m/s}$ . The current waveform at ground level is simulated by the analytical expression given by (11.22) (adapted from Cooray [31])

#### 11.5.4 Barbosa and Paulino [32] expression to calculate the horizontal electric field

Recently, Barbosa and Paulino [32] derived an expression to calculate the horizontal electric field in the vicinity of the lightning channel. Assume that the magnetic field generated by a return stroke in the vicinity of its channel is a step of

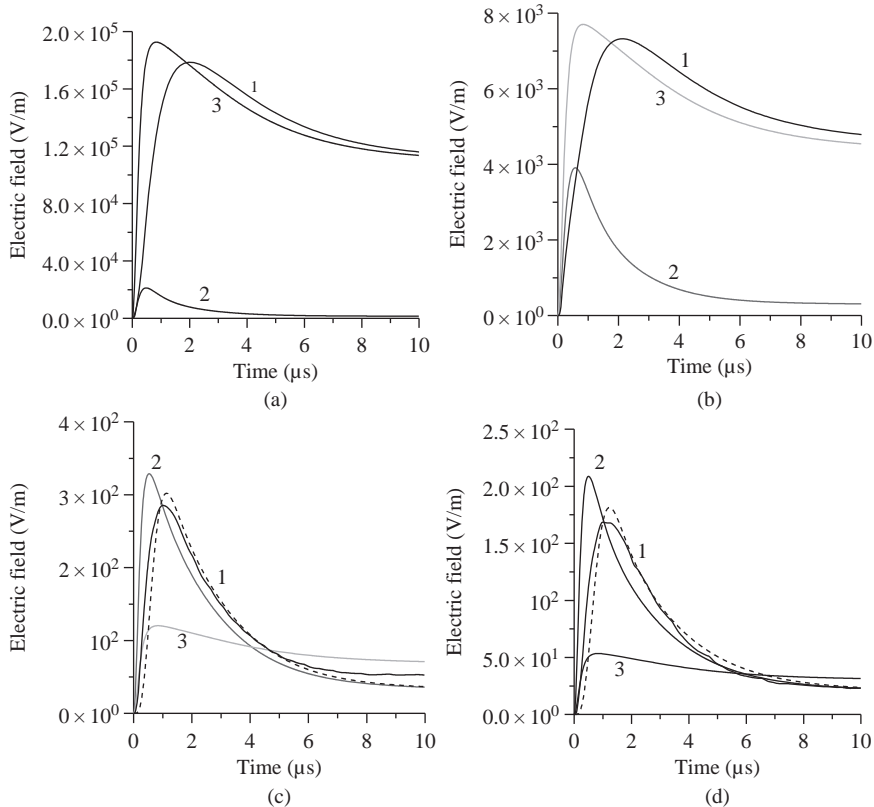
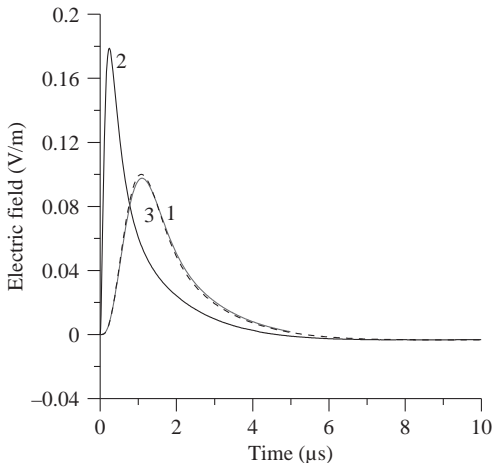


Figure 11.18 Subsequent stroke horizontal electric field at ground level for (a)  $\rho = 10 \text{ m}$ ,  $\sigma = 0.0001 \text{ S/m}$ ; (b)  $\rho = 50 \text{ m}$ ,  $\sigma = 0.0001 \text{ S/m}$ ; (c)  $\rho = 400 \text{ m}$ ,  $\sigma = 0.0001 \text{ S/m}$ ; (d)  $\rho = 600 \text{ m}$ ,  $\sigma = 0.0001 \text{ S/m}$ . Curve 1: Sommerfeld's integrals; curve 2: surface impedance expression (11.46); curve 3: quasi-static approximation. The dotted lines show the prediction from (11.45). In the calculations, the return stroke is modelled by using the MTLE model with a current decay height constant  $\lambda_e = 2 \text{ km}$ . The return stroke speed is kept at  $1.5 \times 10^8 \text{ m/s}$ . The current waveform at ground level is simulated by the analytical expression given by (11.22) (adapted from Cooray [31])

amplitude  $B_o$ . According to Barbosa and Paulino [32], the horizontal electric field induced in the vicinity of the lightning channel by such a return stroke is given by

$$E_\rho(\tau) = -\frac{Z_e B_o}{\mu_0} \left[ \frac{2\varepsilon_r + a\tau(1 + 3b\varepsilon_r + 2ab\tau)}{2(1 + ab\tau)^{1/2}(\varepsilon_r + a\tau)^{3/2}} \right] \quad (11.47)$$



*Figure 11.19* Horizontal electric field at ground level for  $\rho = 100 \text{ km}$ ,  $\sigma = 0.01 \text{ S/m}$ . Curve (1) obtained from Sommerfeld's integrals. Curve (2) obtained from surface impedance expression with magnetic field over perfectly conducting ground as input (11.46). Curve (3) obtained from surface impedance expression with magnetic field over finitely conducting ground as input (11.45). In the calculations, the return stroke is modelled by using the MTLE model with a current decay height constant  $\lambda_e = 2 \text{ km}$ . The return stroke speed is kept at  $1.5 \times 10^8 \text{ m/s}$ . The current waveform at ground level is simulated by the analytical expression given by (11.22) (adapted from Cooray [31])

with  $a = \pi\sigma/4\epsilon_0$  and  $b = (1/Z_e \sigma\rho)^2$  where  $Z_e$  is the impedance of free space,  $\sigma$  is the conductivity of soil,  $\epsilon_r$  is the relative dielectric constant of soil,  $\tau$  is the time from the arrival of the wave to the point of interest and  $\rho$  is the distance from the lightning channel to the point of observation. The horizontal electric field caused by a return stroke of any arbitrary magnetic field can be obtained from (11.47) using Duhammel's integral.

Barbosa and Paulino [32] had compared the predictions of this equations with the exact horizontal electric field calculated in the vicinity of the lightning channel by Cooray [31]. They showed that the expression can predict the horizontal electric field to a reasonable accuracy. Figure 11.20 shows the predictions of this equation plotted together with the horizontal electric field calculated at 10 m from the lightning channel.

### 11.5.5 Approximate time domain expressions to calculate underground electric fields

Cooray [33] had utilized the dipole fields as derived by Bannister [19] to extract time domain expressions for the vertical electric field, azimuthal magnetic field and

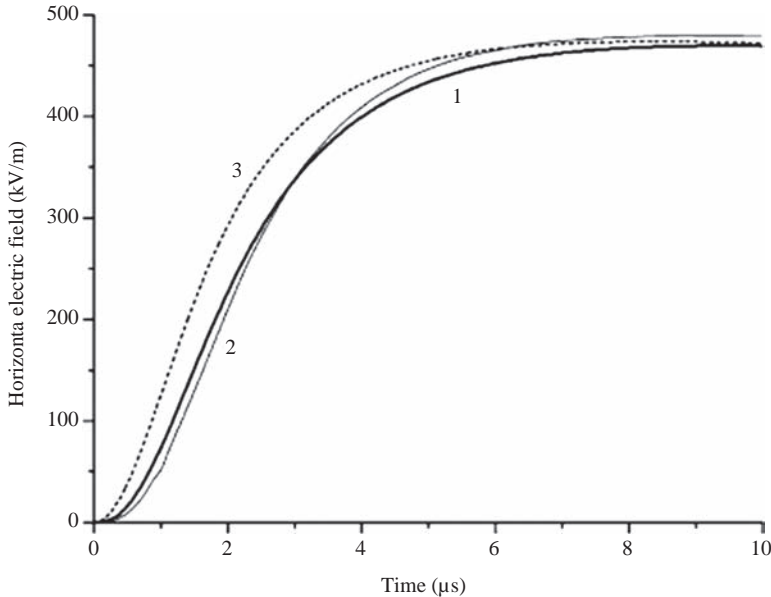


Figure 11.20 Horizontal electric field at the surface for the first stroke. Curve 1: equation (11.47); curve 2: Sommerfeld integrals from Reference 31; curve 3: quasi-static approximation (i.e. equation (11.44)). The distance to the point of observation is 10 m (adapted from Reference 32)

horizontal electric field at a given depth below a finitely conducting ground. The analysis conducted by Cooray [33] is presented below.

### 11.5.5.1 Vertical electric field at the surface and at different depths below the ground

According to Bannister [19] the vertical electric field at a depth  $\zeta$  below the surface of a finitely conducting ground produced by a dipole located at height  $z$  above ground level is given by

$$de_{z,b,under}(z, j\omega, \rho) = \frac{I(j\omega)}{2\pi \epsilon_o} \left[ \frac{j\omega e^{-jk_1 \zeta}}{(\sigma/\epsilon_o) + j\omega \epsilon_r} \right] \left[ \frac{2 - 3\sin^2\theta}{j\omega R^3} + \frac{2 - 3\sin^2\theta}{cR^2} + j\omega \frac{\sin^2\theta}{c^2 R} a(z, j\omega, \rho) \right] e^{-j\omega R/c} \quad (11.48)$$

All the parameters appearing in the above equation were defined earlier in Section 11.5.1.

A comparison of (11.48) and (11.25) shows that the vertical electric field at a depth  $\varsigma$  below the ground is related to the vertical electric field at the surface by the equation

$$de_{z,under}(z, j\omega, \rho) = de_z(z, j\omega, \rho) \left[ \frac{j\omega e^{-jk_1\varsigma}}{(\sigma/\epsilon_o) + j\omega\epsilon_r} \right] \quad (11.49)$$

Since the lightning return stroke channel can be represented by a series of dipoles distributed along the channel and that the principle of superposition is valid one can write

$$e_{z,under}(j\omega, \rho) = e_z(j\omega, \rho) \left\{ \frac{j\omega e^{-jk_1\varsigma}}{(\sigma/\epsilon_o) + j\omega\epsilon_r} \right\} \quad (11.50)$$

where  $e_{z,under}$  is the total vertical electric field at a depth  $\varsigma$  below the ground surface and  $e_z$  is the total electric field at the ground surface (note that in (17) of Cooray [33] a term  $j\omega$  is missing in the numerator). Transforming this into time domain, one can obtain the vertical component of electric field at depth  $\varsigma$  as a function of the vertical electric field at the surface. After some mathematical manipulation and by resorting to conventional Laplace transformations, one can write

$$E_{z,under}(t, \rho) = \int_0^t E_z(t - \tau, \rho) \Psi(\tau) d\tau \quad (11.51)$$

where

$$\Psi(t) = \int_0^t \Psi_1(t - \tau) \Psi_2(\tau) d\tau \quad (11.52)$$

$$\Psi_1(t) = \frac{1}{\epsilon} \left[ \delta(t) - \frac{\sigma}{\epsilon_o \epsilon} u(t) \right] e^{-at} \quad (11.53)$$

$$\Psi_2(t) = \frac{e^{-at/2} ak}{2\sqrt{t^2 - k^2}} I_1 \left( \frac{a\sqrt{t^2 - k^2}}{2} \right) u(t - k) + e^{-at/2} \delta(t - k) \quad (11.54)$$

$$a = \frac{\sigma}{\epsilon_o \epsilon} \quad k = \varsigma \sqrt{\mu_o \epsilon_o \epsilon} \quad (11.55)$$

In these equations  $\delta(t)$  is the delta function,  $u(t)$  is the Heaviside's unit step function and  $I_1(t)$  is the modified Bessel functions of order 1. Note that there is a typographical error in the expressions for  $\Psi_1$  and  $\Psi_2$  given by Cooray [33] and they should be replaced by the above expressions.

### 11.5.5.2 Azimuthal magnetic field at the surface and at different depths below the ground

According to Bannister [19] the azimuthal magnetic field at the surface of a finitely conducting ground produced by a dipole located at height  $z$  above ground level is given by

$$db_\varphi(z, j\omega, \rho) = \frac{I(j\omega)}{2\pi \epsilon_0 c} \frac{dz}{cR^2} \left[ \frac{\sin \theta}{cR^2} + \frac{j\omega \sin \theta}{c^2 R} a(z, j\omega, \rho) \right] e^{-j\omega R/c} \quad (11.56)$$

The azimuthal magnetic field at a depth  $\varsigma$  at the same distance is given by

$$db_{\varphi,under}(z, j\omega, \rho) = \frac{I(j\omega)}{2\pi \epsilon_0 c} \frac{dz}{cR^2} e^{-jk_1 \varsigma} \left[ \frac{\sin \theta}{cR^2} + \frac{j\omega \sin \theta}{c^2 R} a(z, j\omega, \rho) \right] e^{-j\omega R/c} \quad (11.57)$$

Combination of (11.56) and (11.57) shows that the underground return stroke field can be connected to the surface field by the equation

$$b_{\varphi,under}(j\omega, \rho) = b_\varphi(j\omega, \rho) e^{-\gamma \varsigma} \quad (11.58)$$

This can also be converted to the time domain after some mathematical manipulation with the result

$$B_{\varphi,under}(t, \rho) = \int_0^t B_\varphi(t - \tau, \rho) Y(\tau) d\tau \quad (11.59)$$

with

$$Y(t) = \frac{e^{-at/2} ak}{2\sqrt{t^2 - k^2}} I_1 \left( \frac{a\sqrt{t^2 - k^2}}{2} \right) u(t - k) + e^{-at/2} \delta(t - k) \quad (11.60)$$

where  $B_\varphi(t, \rho)$  is the azimuthal magnetic field in the time domain on the surface of the ground,  $B_{\varphi,under}(t, \rho)$  is the azimuthal magnetic field at depth  $\varsigma$ , and  $I_1(t)$  is the first-order modified Bessel function of the first kind. [Note that in Cooray [33] it was written  $I_o(t)$  due to a typographical mistake.]

### 11.5.5.3 Horizontal electric field at the surface and at different depths below the ground

According to the results of Bannister [19] the horizontal electric field penetrates into the ground exactly in the same way as the azimuthal magnetic field. Thus the horizontal electric field in frequency domain at a depth  $\varsigma$  below the surface of a finitely conducting ground,  $E_{\rho,under}(t, \rho)$ , is given by

$$E_{\rho,under}(t, \rho) = \int_0^t E_\rho(t - \tau, \rho) Y(\tau) d\tau \quad (11.61)$$

where  $E_\rho(t, \rho)$  is the horizontal electric field at the surface. The horizontal electric field at the surface can be calculated exactly using Sommerfeld's integrals or an

approximate to this field can be obtained using the surface impedance expression. For example, (11.45) can be transferred into time domain giving the horizontal electric field as

$$E_{\rho}(t, \rho) = \int_0^t B_{\varphi, \sigma}(t - \tau, \rho) S(\tau) d\tau \quad (11.62)$$

with

$$S(t) = \frac{c}{\sqrt{\epsilon}} \zeta e^{-\zeta t} [I_1(\zeta t) - I_o(\zeta t)] \quad (11.63)$$

where  $\zeta = \epsilon \epsilon_o / \sigma$ ,  $B_{\varphi, \sigma}(t, \rho)$  is the magnetic field at the surface of the ground and  $I_o(\zeta t)$  and  $I_1(\zeta t)$  are the modified Bessel functions of order 0 and 1, respectively. Cooray [31] had considered the prediction of (11.61) for both cases (i.e. calculating the horizontal electric field exactly at the surface or using (11.62) to obtain it) by comparing the results with the exact underground horizontal electric field calculated using the Sommerfeld's integrals. His results are presented in the next section.

### *Comparison with exact calculations*

Figures 11.21 and 11.22 show the examples presented by Cooray [31] of underground horizontal electric field calculated using three different procedures. The curve 1 gives the exact field calculated using Sommerfeld's integrals. The curve 2 shows the underground electric field calculated from (11.61) using the exact horizontal electric field at the surface of the ground. Curve 3 shows the underground electric field calculated using the same equation with but the horizontal electric field at ground level calculated using (11.62). The results presented above shows that (11.61) can be used to obtain the underground electric fields provided that the horizontal electric field at ground level is calculated (or measured) accurately. It is possible to show that the results obtained using the horizontal electric field calculated from (11.61) that connects the surface horizontal electric field to the underground horizontal electric field is valid for ground conductivities encountered in practices and for depths much less than the lateral distance to the lightning strikes. One can also use these equations with high accuracy to calculate the underground electric field if the horizontal electric field at the surface of the ground is measured. If the depth is comparable to the distance to the lightning strike, as can be observed from Figures 11.21 and 11.22, this equation can generate large errors. Since the depths that are of interest in practice are on the order of metres, (11.61) (together with the exact horizontal electric field at ground level) can be used to evaluate underground fields at distances larger than approximately 50 m from the lightning strike. Note the significant error in the underground electric field when the surface horizontal electric field is calculated using the surface impedance expression. As shown in Section 11.5.3.2, the surface impedance expression can introduce significant errors in the horizontal electric field when the point of observation is in the

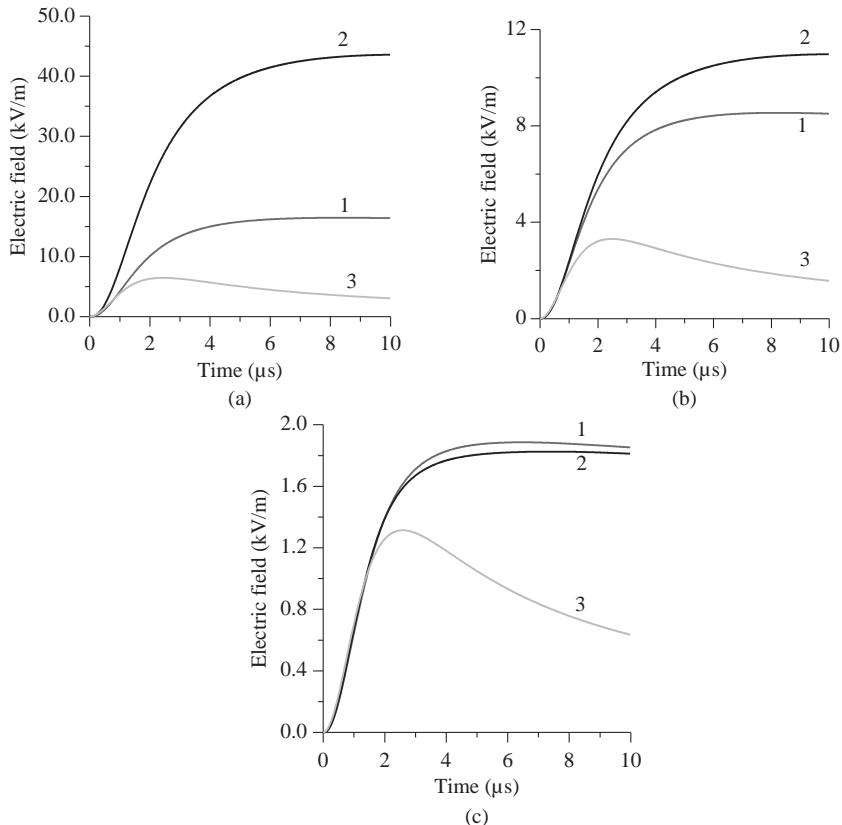


*Figure 11.21* Underground first stroke horizontal electric fields at a depth of 10 m for (a)  $\rho = 10 \text{ m}$ ,  $\sigma = 0.001 \text{ S/m}$ ; (b)  $\rho = 20 \text{ m}$ ,  $\sigma = 0.001 \text{ S/m}$ ; (c)  $\rho = 50 \text{ m}$ ,  $\sigma = 0.001 \text{ S/m}$ . Curve 1: Sommerfeld's integrals; curve 2: equation (11.61) with exact horizontal electric field at ground as input; curve 3: equation (11.61) with horizontal electric field calculated using surface impedance as input. In the calculations, the return stroke is modelled by using the MTLE model with a current decay height constant  $\lambda_e = 2 \text{ km}$ . The return stroke speed is kept at  $1.5 \times 10^8 \text{ m/s}$ . The current waveform at ground level is simulated by the analytical expression given by (11.22) (adapted from Cooray [31])

vicinity of the lightning channel and the same errors causes the underground electric field to deviate significantly from the exact one. However, when the distance to the point of observation is large or when the conductivity of the ground is high this procedure can give results to a reasonable accuracy. This was also illustrated in the work of Delfino *et al.* (34, see also Chapter 13).

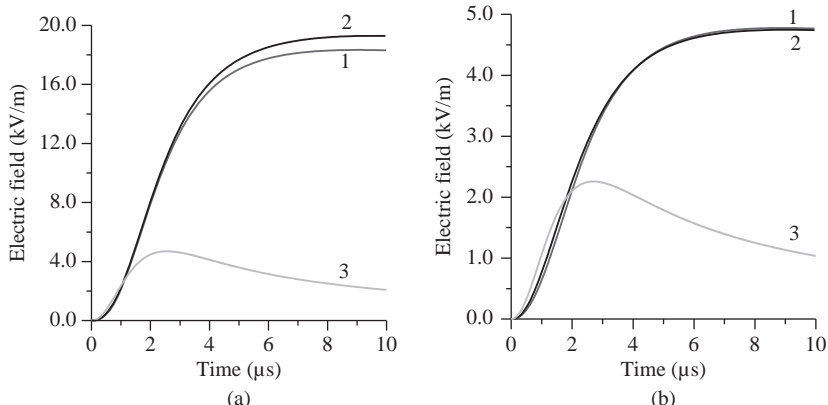


*Figure 11.22* Underground first stroke horizontal electric fields at a depth of 10 m for (a)  $\rho = 50 \text{ m}$ ,  $\sigma = 0.0001 \text{ S/m}$  and (b)  $\rho = 100 \text{ m}$ ,  $\sigma = 0.0001 \text{ S/m}$ . Curve 1: Sommerfeld's integrals; curve 2: equation (11.61) with exact horizontal electric field at ground as input; curve 3: equation (11.61) with horizontal electric field calculated using surface impedance as input. In the calculations, the return stroke is modelled by using the MTLE model with a current decay height constant  $\lambda_e = 2 \text{ km}$ . The return stroke speed is kept at  $1.5 \times 10^8 \text{ m/s}$ . The current waveform at ground level is simulated by the analytical expression given by (11.22) (adapted from Cooray [31])

## 11.6 Propagation over vertically stratified ground

### 11.6.1 Expressions for the attenuation function for a dipole at ground level

The geometry relevant to the question under consideration is shown in Figure 11.23. Let us represent the path of propagation of the electromagnetic field as consisting of several laterally stratified sections. In each section, the soil conductivity is assumed to be uniform. Each section is represented by a distance  $\rho_n$ , conductivity  $\sigma_n$  and relative dielectric constant  $\epsilon_m$ . The lightning channel is located at a distance  $\rho$  from the point of observation. In the calculation, the lightning channel is assumed to be straight and vertical. To write down the equations corresponding to paths with many land sections in compact form, let us define the parameters  $\rho_{1,0} = 0$ ,  $\rho_{1,1} = \rho_1$ ,  $\rho_{1,2} = \rho_1 + \rho_2$ ,  $\rho_{1,3} = \rho_1 + \rho_2 + \rho_3$ , etc. Then for a land path of  $M$  sections  $\rho_{1,M} = \rho$  where  $\rho$  as defined above is the total path length.

Let us represent the attenuation function in frequency domain for a dipole at *ground level* over finitely conducting uniform ground of surface impedance  $\Delta_1$  at a distance  $\rho$  from the dipole as  $w_{1-1}(\rho)$  (see (11.31)). With this notation, the attenuation function corresponding to a dipole over homogeneous ground of surface impedance  $\Delta_s$  is represented by  $w_{s-s}(\rho)$ .

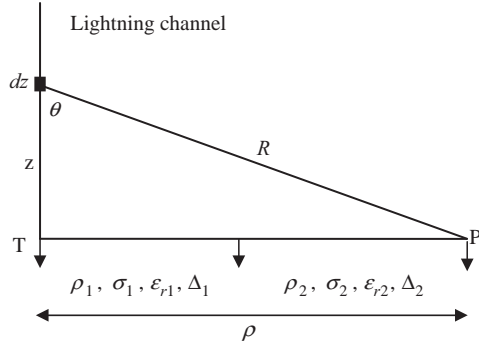


Figure 11.23 The geometry and the definition of various distances pertinent to the calculation of propagation effects caused by multi-section mixed path

The attenuation function corresponding to a dipole at ground level over a two-section land path is given by [20, 35]

$$w_{1-2}(\rho) = w_{2-2}(\rho) - \left( \frac{j\rho}{2\lambda_0} \right)^{1/2} \int_0^{\rho_1} (\Delta_1 - \Delta_2) w_{1-1}(y_1) w_{2-2}(\rho - y_1) \frac{dy_1}{\sqrt{y_1(\rho - y_1)}} \quad (11.64)$$

where  $w_{1-2}(\rho)$  is the attenuation function for the two-section path,  $w_{2-2}(x)$  is the attenuation function associated with a path length of  $x$  over a ground of surface impedance  $\Delta_2$  and  $w_{1-1}(x)$  is the corresponding path over a surface impedance of  $\Delta_1$ . In the case of three-section path

$$w_{1-3}(\rho) = w_{3-3}(\rho) - \left( \frac{j\rho}{2\lambda_0} \right)^{1/2} \int_0^{\rho_{1,1}} (\Delta_1 - \Delta_3) w_{1-1}(y_1) w_{3-3}(\rho - y_1) \frac{dy_1}{\sqrt{y_1(\rho - y_1)}} \\ - \left( \frac{j\rho}{2\lambda_0} \right)^{1/2} \int_{\rho_{1,1}}^{\rho_{1,2}} (\Delta_2 - \Delta_3) w_{1-2}(y_1) w_{3-3}(\rho - y_1) \frac{dy_1}{\sqrt{y_1(\rho - y_1)}} \quad (11.65)$$

Note in this equation  $w_{1-2}(x)$  corresponds to the attenuation function of a two-section path with path length,  $\rho_{1,1}$  over surface impedance of  $\Delta_1$  and a distance of  $x - \rho_{1,1}$  over surface impedance of  $\Delta_2$ . In the case of  $M$ -section land path

$$w_{1-M}(\rho) = w_{M-M}(\rho) - \left( \frac{j\rho}{2\lambda_0} \right)^{1/2} \sum_{m=1}^M (\Delta_m - \Delta_M) \int_{\rho_{1,m-1}}^{\rho_{1,m}} w_{1-m}(y_1) w_{M-M}(\rho - y_1) \frac{dy_1}{\sqrt{y_1(\rho - y_1)}} \quad (11.66)$$

Note that in the above equation  $\rho_{1,0} = 0$ . These equations define the attenuation function for multi-section land. For any given path, this can be first calculated in frequency domain and the result can be Fourier transformed to get the time domain response that is necessary to get the time domain electromagnetic fields. In the next section, we illustrate by example several interesting cases of propagation effects.

### 11.6.2 Simplified expression for the electromagnetic fields from lightning over vertically stratified ground

Recall that according to the approximations described in Section 11.5.2.1, the radiation field at a distance  $\rho$  over homogeneous ground is given by

$$E_{z,\sigma}(t, \rho) = \int_0^t E_z(t - \tau, \rho) W_{s-s}(\rho) d\tau \quad (11.67)$$

where  $W_{s-s}(\rho)$  is the inverse Fourier transformation of the attenuation function corresponding to a dipole at ground level over the homogeneous ground surface of surface impedance  $\Delta_s$ . In the above equation,  $E_z(t, \rho)$  is the radiation field over perfectly conducting ground. In the case of stratified ground of  $M$  sections, the radiation field at a distance  $\rho$  is given by

$$E_{z,v-stra}(t, \rho) = \int_0^t E_z(t - \tau, \rho) W_{1-M}(\rho) d\tau \quad (11.68)$$

In the above equation  $W_{1-M}(\rho)$  is the inverse Fourier transformation of  $W_{1-M}(\rho)$  given by (11.66).

### 11.6.3 Validation of the simplified expression

The accuracy of the above equation was tested by Shoory *et al.* [13] taking as reference full-wave simulations obtained using the finite difference time domain technique. It was shown that the above equation is capable to reproduce the distant peak field and the wave shape to a good accuracy. Several examples of the comparison as given by Shoory *et al.* are given in Figures 11.24 and 11.25 (see also Chapter 12).

### 11.6.4 Some interesting effects of vertically stratified ground on radiation fields as described by Cooray and Cummins [11]

#### 11.6.4.1 Sea gain effects

Let us consider how the electromagnetic field will vary in the case of two section land where one section is highly conducting and the other section relatively a poor conductor. This represent, for example, the case of an electromagnetic field generated by a lightning flash located over the sea and what happens to it as it propagates inland and vice-versa. First, let us consider how an electromagnetic field generated by a return stroke located over the sea is modified as it penetrates into land. In the calculation, the conductivity of the ground is 0.001 S/m. Figure 11.26 shows what happens to the peak and the width of the pulse as it penetrates into the land path. The removal of high frequencies leads to both the attenuation and the broadening of the

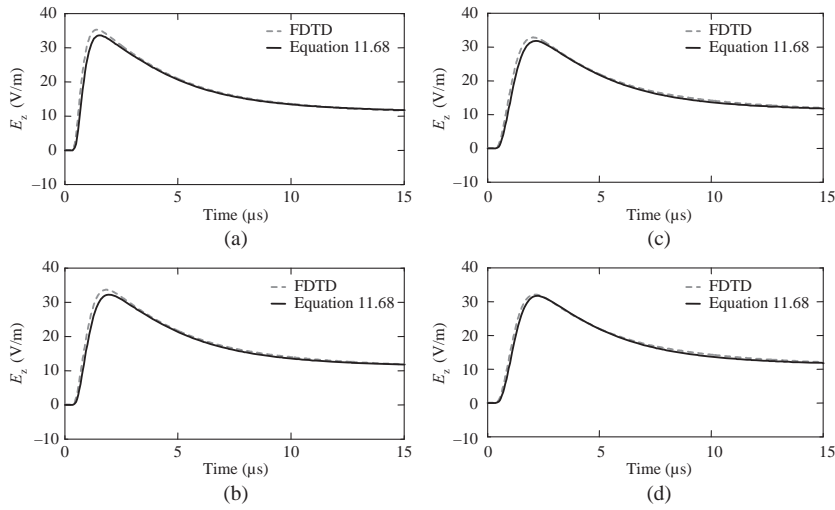


Figure 11.24 Vertical electric field at the surface of a mixed-path ground (two sections) at a distance of  $\rho = 10 \text{ km}$  for  $\sigma_1 = 0.001 \text{ S/m}$ ,  $\epsilon_{r1} = 10$ ,  $\sigma_2 = 4 \text{ S/m}$ ,  $\epsilon_{r2} = 30$ . (a)  $\rho_2 = 7.5 \text{ km}$ ; (b)  $\rho_2 = 2.5 \text{ km}$ ; (c)  $\rho_2 = 0.5 \text{ km}$ ; (d)  $\rho_2 = 0.1 \text{ km}$  (adapted from Reference 13)

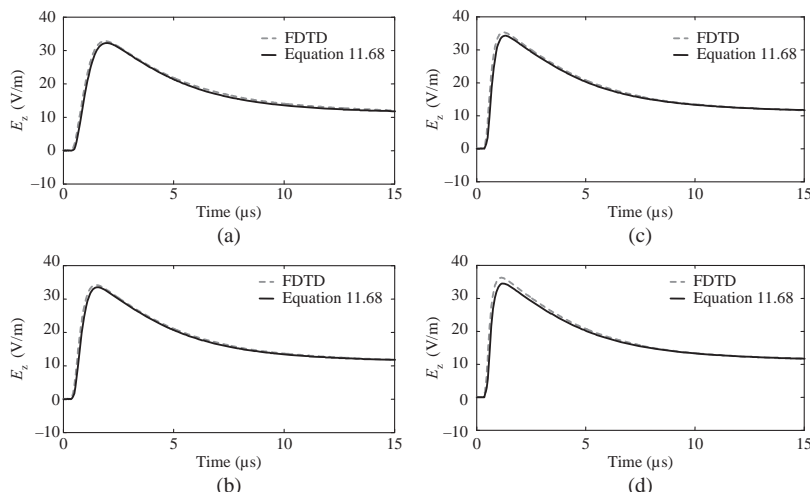
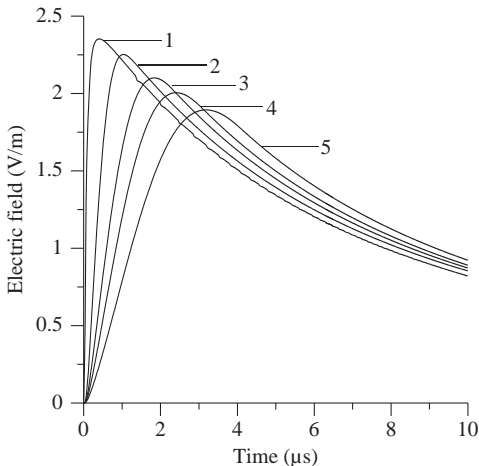


Figure 11.25 Vertical electric field at the surface of a mixed-path (two section) ground at a distance of  $\rho = 10 \text{ km}$  for  $\sigma_1 = 4 \text{ S/m}$ ,  $\epsilon_{r1} = 30$ ,  $\sigma_2 = 0.001 \text{ S/m}$ ,  $\epsilon_{r2} = 10$ . (a)  $\rho_2 = 7.5 \text{ km}$ ; (b)  $\rho_2 = 2.5 \text{ km}$ ; (c)  $\rho_2 = 0.5 \text{ km}$ ; (d)  $\rho_2 = 0.1 \text{ km}$  (adapted from Reference 13)



*Figure 11.26 Signature of the electric field of a lightning return stroke located over the sea at 100 km from the coast as it penetrates into land path. The conductivity of the land path is 0.002 S/m. The length of the land path is (2) 10 km, (3) 50 km, (4) 100 km and (5) 200 km. The curve 1 represents the electric field over perfectly conducting ground. Conductivity of sea water is 4 S/m and all waveforms are normalized to a common distance of 100 km. In the calculations, the return stroke is modelled by using the MTLE model with a current decay height constant  $\lambda_e = 2$  km. The return stroke speed is kept at  $1.5 \times 10^8$  m/s. The current waveform at ground level is simulated by the analytical expression given by (11.21) (adapted from Cooray and Cummins [11])*

initial peak and an increase in the rise time of the pulse. An interesting situation arises when the lightning flash is located over land but the electromagnetic field penetrates into the sea path. The length of the land path is now fixed at 100 km and the distance to the sea path is changed. The results are shown in Figure 11.27. Note that as the electromagnetic field propagates further into the sea it recovers some of the high frequencies. As a result the rise time starts decreasing and the peak amplitude starts increasing. The recovery can be seen clearly in the case of electric field time derivatives shown in Figure 11.27b. This recovery is actually caused by the gaining of some of the energy lost into the ground by the electromagnetic field propagating close to ground from the other parts of the field. It is actually not a reversal of the propagation effects.

#### 11.6.4.2 Reciprocity

According to the principle of reciprocity, the same propagation effects should be observed when the receiver and the transmitter are interchanged. Though this is not apparent in the equations, calculations can be used to demonstrate its validity.

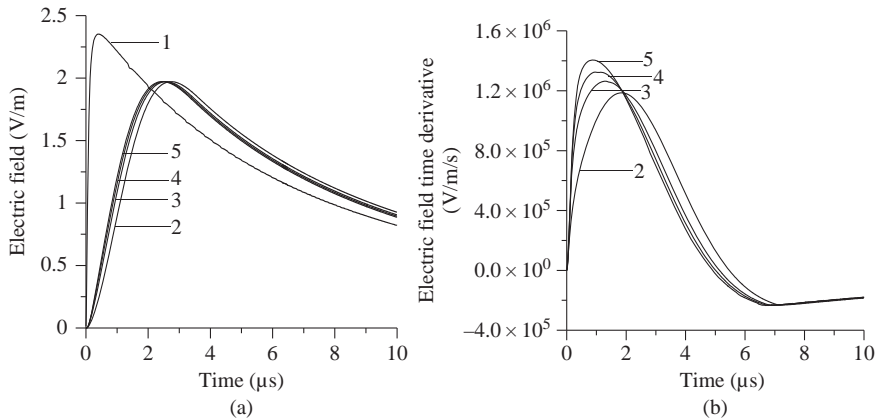


**Figure 11.27** Signature of the (a) electric field and (b) electric field time derivative of a lightning return stroke located over land at 100 km from a coast line as it penetrates into the sea path. The length of the sea path is (2) 10 km, (3) 50 km, (4) 100 km and (5) 200 km. The curve 1 represents the electric field over perfectly conducting ground (this is not shown in (b)). Conductivity of sea water is 4 S/m and the conductivity of the land path is 0.002 S/m. All waveforms are normalized to a common distance of 100 km. In the calculations, the return stroke is modelled by using the MTLE model with a current decay height constant  $\lambda_e = 2$  km. The return stroke speed is kept at  $1.5 \times 10^8$  m/s. The current waveform at ground level is simulated by the analytical expression given by (11.21) (adapted from Cooray and Cummins [11])

An example of the calculation corresponding to the interchange of the path for two-section layer is shown in Figure 11.28. As one can see the results are identical showing that the propagation effects are the same for the same path irrespective of the location of transmitter and receiver. This effect could actually be utilized to study whether there is any difference in the electromagnetic fields striking the ground and the sea. Measurements conducted at two stations, one inland and the other located over the ocean, can be used to check these effects. The measurements of electromagnetic fields of lightning striking at reciprocal locations in this case will provide information whether there is any difference in the electromagnetic fields. This is the case since the propagation effects have to be the same along the two paths. Such data can be obtained from the lightning location systems that provide the rise times and the amplitudes of lightning flashes striking at two locations. Of course the experiment can be done completely over land sites if one can isolate lightning flashes in two regions one highly conducting and the other low conducting and then studying statistics of rise time of lightning flashes striking in one region as measured from the lightning location systems in the other region.

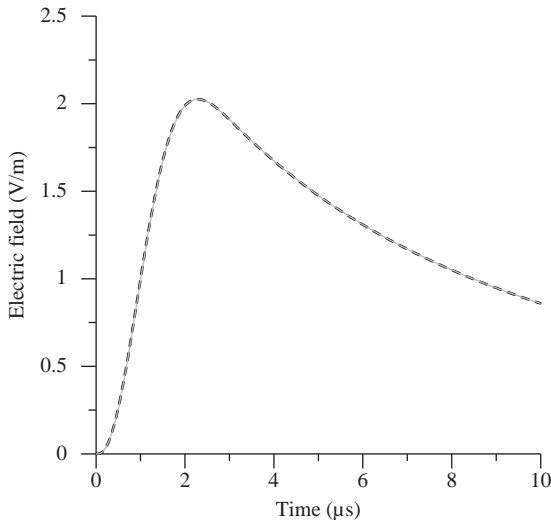


Figure 11.28 Effect of reversing the direction of the path of propagation. The solid line shows forward direction and the dashed line shows the reverse direction. Parameters of the calculation are  $\rho_1 = 200 \text{ km}$ ,  $\sigma_1 = 0.01 \text{ S/m}$ ,  $\rho_2 = 50 \text{ km}$  and  $\sigma_2 = 0.005 \text{ S/m}$ . In the calculations, the return stroke is modelled by using the MTLE model with a current decay height constant  $\lambda_e = 2 \text{ km}$ . The return stroke speed is kept at  $1.5 \times 10^8 \text{ m/s}$ . The current waveform at ground level is simulated by the analytical expression given by (11.21) (adapted from Cooray and Cummins [11])

#### 11.6.4.3 Equivalent conductivity

Cooray and Perez [36] and Cooray and Cummins [11] have investigated whether a multi-section ground can be replaced by a homogeneous ground with equivalent conductivity. They showed that the equivalent conductivity of  $M$ -section land can be written as

$$\sigma_e = \frac{\sum_{m=1}^M \rho_m}{\sum_{m=1}^M \rho_m / \sigma_m} \quad (11.69)$$

In the case of two-section land, it reduces to

$$\sigma_e = \frac{\rho_1 + \rho_2}{\rho_1/\sigma_1 + \rho_2/\sigma_2} \quad (11.70)$$

In the above equations  $\rho_1, \rho_2$ , etc. are the lengths of different land paths and  $\sigma_1, \sigma_2$ , etc. are the respective conductivities. Cooray and Cummins [11] have compared

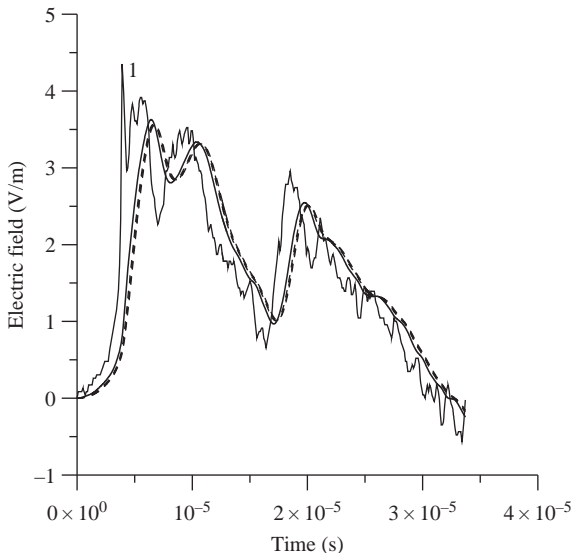


**Figure 11.29** The signature of the waveform marked 1 after it has propagated along a three-section path. The path parameters are  $\rho_1 = 40 \text{ km}$ ,  $\sigma_1 = 0.01 \text{ S/m}$ ,  $\rho_2 = 40 \text{ km}$ ,  $\sigma_2 = 0.001 \text{ S/m}$ ,  $\rho_3 = 40 \text{ km}$ ,  $\sigma_3 = 0.005 \text{ S/m}$ . The solid line shows the propagated waveform calculated using complete equations and the dashed line shows the one calculated using equivalent conductivity. The original waveform is obtained from a collection of range normalized first return stroke electric fields measured at a coastal station by Bailey and Willett [37] and Izumi and Willett [38]

the actual calculations with the calculations conducted with this equivalent conductivity, and a reasonable agreement was found confirming the possibility of using the above as the equivalent conductivity for vertically stratified ground. An example based on three-section land is shown in Figure 11.29.

## 11.7 Propagation effects over horizontally stratified ground

### 11.7.1 Wait's simplified expressions for the attenuation function for a dipole at ground level

The geometry relevant to the question under consideration is shown in Figure 11.30. Let us represent the ground as a stratum of thickness  $h_1$ , conductivity  $\sigma_1$  and relative dielectric constant  $\epsilon_{r1}$  below which the medium is semi-infinite with conductivity  $\sigma_2$  and dielectric constant  $\epsilon_{r2}$ . The surface impedance of the two layers are denoted by  $\Delta_1$  and  $\Delta_2$ . The dipole is located at a distance  $\rho$  from the point of observation.

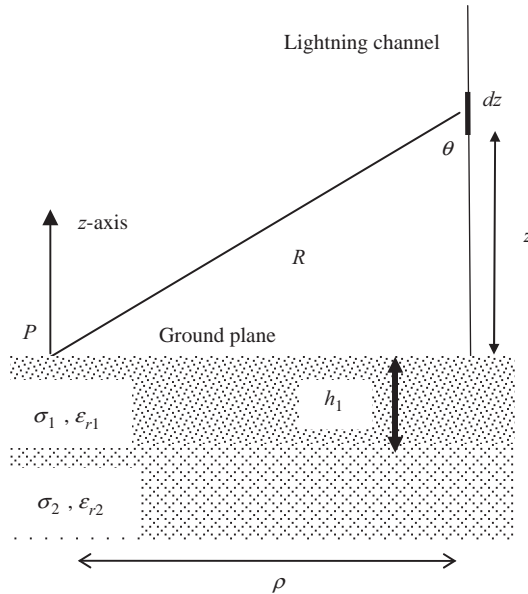


Figure 11.30 Geometry relevant to the analysis of propagation over horizontally stratified ground

According to Wait [39] the attenuation function corresponding to a dipole at ground level over horizontally stratified ground can be obtained by replacing the surface impedance in (11.26)–(11.31) by the effective surface impedance given by

$$\Delta_{eff} = \Delta_1 Q \quad (11.71)$$

where

$$Q = \frac{\Delta_2 + \Delta_1 \tanh(ju_1 h_1)}{\Delta_1 + \Delta_2 \tanh(ju_1 h_1)}, \quad u_1 = k_1 \left[ 1 - \left( \frac{k_o}{k_1} \right)^2 \right] \quad (11.72a)$$

The ratios  $(k_o/k_1)^2$  and  $(k_o/k_2)^2$  are much less than unity in many cases. In those cases, the above equation will be reduced to

$$Q = \frac{k_1 + k_2 \tanh(jk_1 h_1)}{k_2 + k_1 \tanh(jk_1 h_1)} \quad (11.72b)$$

In the above equations

$$\Delta_1 = \frac{k_o}{k_1} \left( 1 - \frac{k_o^2}{k_1^2} \right)^{1/2} \quad (11.73a)$$

$$\Delta_2 = \frac{k_o}{k_2} \left( 1 - \frac{k_o^2}{k_2^2} \right)^{1/2} \quad (11.73b)$$

$$k_1 = k_o [\varepsilon_{r1} - j60\sigma_1\lambda_o]^{1/2} \quad (11.74a)$$

$$k_2 = k_o [\varepsilon_{r2} - j60\sigma_2\lambda_o]^{1/2} \quad (11.74b)$$

The attenuation function corresponding to a dipole at ground level over horizontally stratified ground is then given by

$$w_{h-str}(\rho) = 1 - j(\pi\eta)^{1/2} e^{-\eta} erfc(j\eta^{1/2}) \quad (11.75)$$

with

$$\eta = -\frac{j k_o \rho}{2} (\Delta_{eff})^2 \quad (11.76)$$

### 11.7.2 Simplified expression for the electromagnetic fields from lightning over vertically stratified ground

Again using the same approximation as in the case of vertically stratified ground, the radiation field at a distance  $\rho$  over horizontally stratified ground is given by

$$E_{z,h-str}(t, \rho) = \int_0^t E_z(t - \tau, \rho) W_{h-str}(\rho) d\tau \quad (11.77)$$

where  $W_{h-str}(\rho)$  is the inverse Fourier transformation of the attenuation function  $w_{h-str}(\rho)$  corresponding to a dipole at ground level over horizontally stratified ground.

### 11.7.3 Validity of simplified expression

The accuracy of the above equation was tested by Shoory *et al.* [14] taking as reference the full-wave simulations obtained using the finite difference time domain technique. It was shown that the above equation is capable to reproduce the distant peak field and the wave shape to a good accuracy. Several examples of the comparison as given by Shoory *et al.* are given in Figures 11.31 and 11.32 (see also Chapter 12).

### 11.7.4 Some interesting effects of horizontally stratified ground on radiation fields as presented by Cooray and Cummins [12]

#### 11.7.4.1 Stratified ground with two layers – field enhancement caused by stratified ground

The attenuation function in frequency domain for several values of  $\sigma_2$  while keeping  $\sigma_1$  and  $h_1$  constant is shown in Figure 11.33. In the calculation the relative

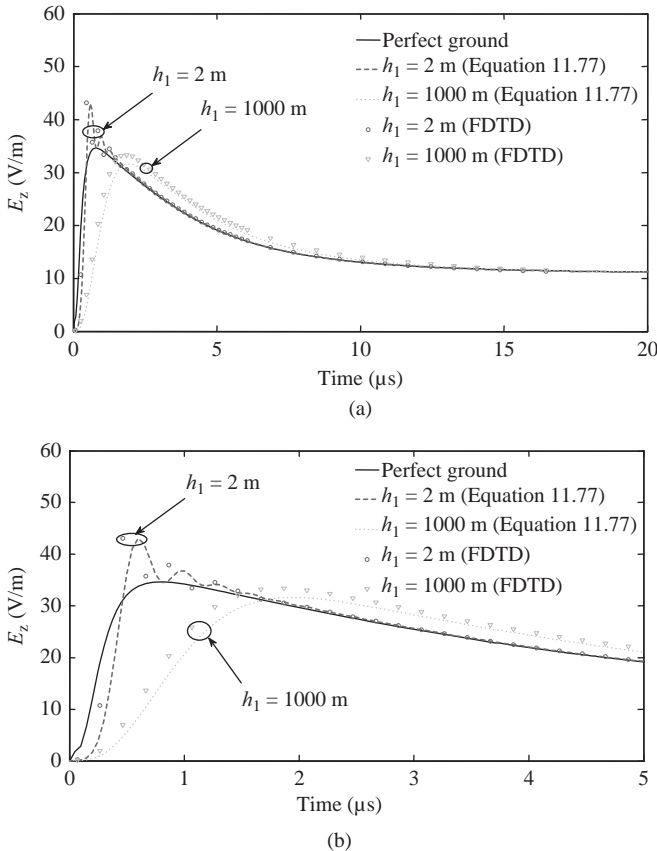


*Figure 11.31* Vertical electric field at ground level at a distance of  $\rho = 10$  km with  $h_1 = 2$  m and  $h_1 = 1000$  m obtained using (11.77) and FDTD technique. (a) 20- $\mu$ s time window and (b) 5- $\mu$ s time window. The electrical parameters used in the calculation are  $\sigma_1 = 0.001$  S/m,  $\epsilon_{r1} = 10$ ,  $\sigma_2 = 4$  and  $\epsilon_{r2} = 30$  (adapted from Reference 14)

dielectric constants  $\epsilon_{r1}$  and  $\epsilon_{r2}$  were kept constant at 5. Note that for  $\sigma_1 < \sigma_2$  the attenuation function is larger than unity for certain frequencies. The reason for this is that when  $\sigma_1 < \sigma_2$  the energy is being guided along the surface [39]. Of course this enhancement of the field depends on the thickness of the upper layer. If the thickness of the upper layer is much larger than the skin depth corresponding to a certain frequency then for that particular frequency the stratified ground behaves as homogeneous ground with conductivity  $\sigma_1$ . In the case of  $\sigma_1 > \sigma_2$  the amplitude of the attenuation function is always less than unity and it decreases monotonically with increasing frequency.

Figure 11.34 shows the electric field at 10 km generated by a lightning flash over stratified ground. For comparison purposes the electric fields that would be

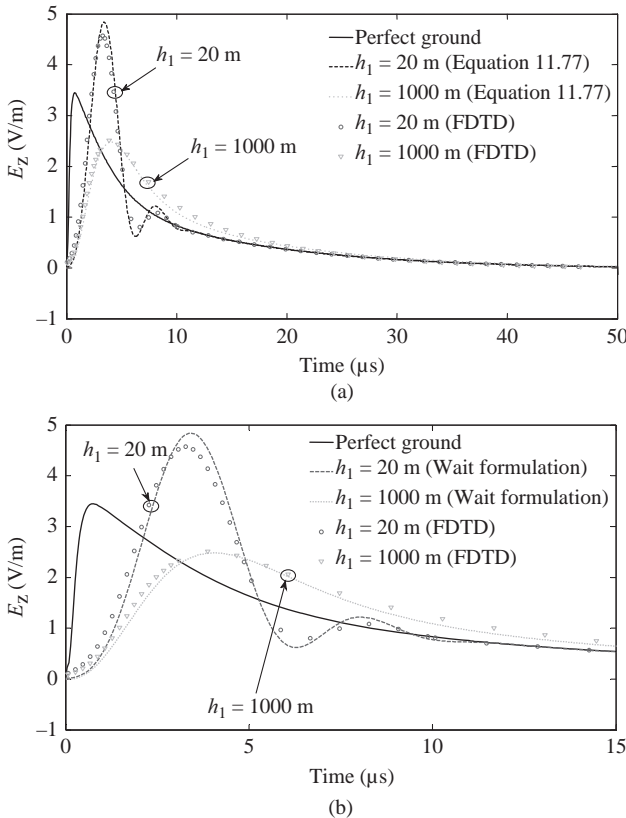
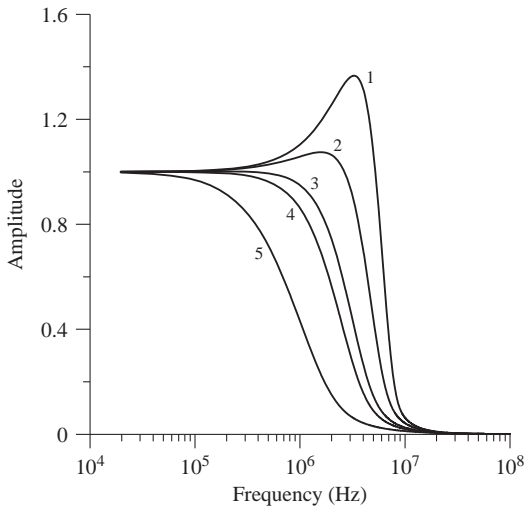


Figure 11.32 Vertical electric field at ground level at a distance of  $\rho = 100$  km with  $h_1 = 20$  m and  $h_1 = 1000$  m obtained using the Wait's formulation of Section II.A and FDTD technique. (a) 50- $\mu$ s time window and (b) 15- $\mu$ s time window. The electrical parameters used in the calculation are  $\sigma_1 = 0.001$  S/m,  $\epsilon_{r1} = 10$ ,  $\sigma_2 = 4$  and  $\epsilon_{r2} = 30$  (adapted from Reference 14)

present over perfectly conducting ground and over homogeneous ground with conductivity equal to that of the upper or lower layer are also shown in the diagram. Figure 11.35 depicts the corresponding waveforms at 50 km distances. Note that when  $\sigma_1 > \sigma_2$  the peak electric field is always lower than the one that is present over perfectly conducting ground. On the other hand, when  $\sigma_1 < \sigma_2$  the electric field may contain a peak larger than its counterpart over perfectly conducting ground.

#### 11.7.4.2 Continuously stratified ground

In reality, the conductivity of the soil depends on the moisture content. The moisture content in soil can change in a complicated manner depending on the



*Figure 11.33 Attenuation function at 10 km as a function of frequency for stratified ground with two layers. The thickness of the upper layer,  $h_1$ , is 2 m. (1)  $\sigma_1 = 0.001 \text{ S/m}$ ,  $\sigma_2 = 0.1 \text{ S/m}$ . (2)  $\sigma_1 = 0.001 \text{ S/m}$ ,  $\sigma_2 = 0.01 \text{ S/m}$ . (3)  $\sigma_1 = 0.001 \text{ S/m}$ ,  $\sigma_2 = 0.002 \text{ S/m}$ . (4)  $\sigma_1 = 0.001 \text{ S/m}$ ,  $\sigma_2 = 0.001 \text{ S/m}$ . (5)  $\sigma_1 = 0.001 \text{ S/m}$ ,  $\sigma_2 = 0.0001 \text{ S/m}$ . In the calculation  $\epsilon_{r1}$  and  $\epsilon_{r2}$  were kept constant at 5 (adapted from Reference 12)*

weather conditions such as rain and dry seasons. This makes the conductivity profile of soil as a function of depth more complicated. During rain the conductivity of upper soil increases and as the moisture penetrate into the ground the soil layers located at different depths will gradually become conducting. So immediately after the rain, the conductivity is high at the surface and it decreases with increasing depth. However, at the end of the rainy season the surface soil layers gradually dry up while the layer with high conductivity moves down. Thus, the conductivity profile varies with time, and this provides a possibility to utilize the attenuation on high frequencies and electromagnetic fields to remote sense the soil parameters. Cooray and Cummins [12] studied the effects of such a conductivity profile on electromagnetic fields. Figure 11.36 shows two conductivity profiles analysed by Cooray and Cummins [12] that is in line with this description. In one profile the conductivity is high at the surface while in the other it increases with depth initially and then decreases again.

Figure 11.37 shows how the amplitude of the electromagnetic field at different frequencies varies as a function of distance when the ground is stratified according to Figure 11.36. Note that the shifting of the high conducting layer downwards produces a significant change in the amplitude of the electromagnetic field at the two frequencies considered. They have also studied the effect of this conductivity

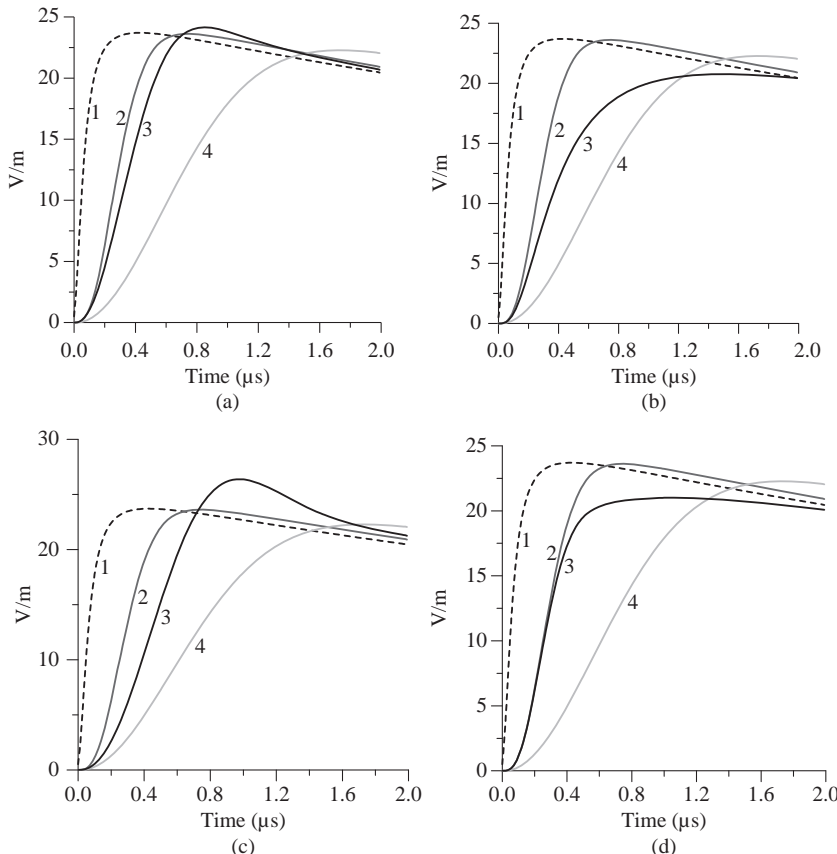


*Figure 11.34 Electric field at 10 km generated by a lightning flash over stratified ground. In each figure, curve 1 is the field over perfectly conducting ground, curve 2 is the field over finitely conducting homogeneous ground of conductivity  $0.01 \text{ S/m}$  and curve 4 is the field over finitely conducting homogeneous ground of conductivity  $0.001 \text{ S/m}$ . Curve 3 corresponds to the electric field over stratified ground. (a)  $\sigma_1 = 0.001 \text{ S/m}$ ,  $\sigma_2 = 0.01 \text{ S/m}$ ,  $h_1 = 2 \text{ m}$ ; (b)  $\sigma_1 = 0.01 \text{ S/m}$ ,  $\sigma_2 = 0.001 \text{ S/m}$ ,  $h_1 = 2 \text{ m}$ ; (c)  $\sigma_1 = 0.001 \text{ S/m}$ ,  $\sigma_2 = 0.01 \text{ S/m}$ ,  $h_1 = 5 \text{ m}$ ; (d)  $\sigma_1 = 0.01 \text{ S/m}$ ,  $\sigma_2 = 0.001 \text{ S/m}$ ,  $h_1 = 5 \text{ m}$ . In the calculations, the return stroke is modelled by using the MTLE model with a current decay height constant  $\lambda_e = 2 \text{ km}$ . The return stroke speed is kept at  $1.5 \times 10^8 \text{ m/s}$ . In the calculation,  $\epsilon_{r1}$  and  $\epsilon_{r2}$  were kept constant at 5. The current waveform at ground level is simulated by the analytical expression given by (11.21) (adapted from Reference [12])*

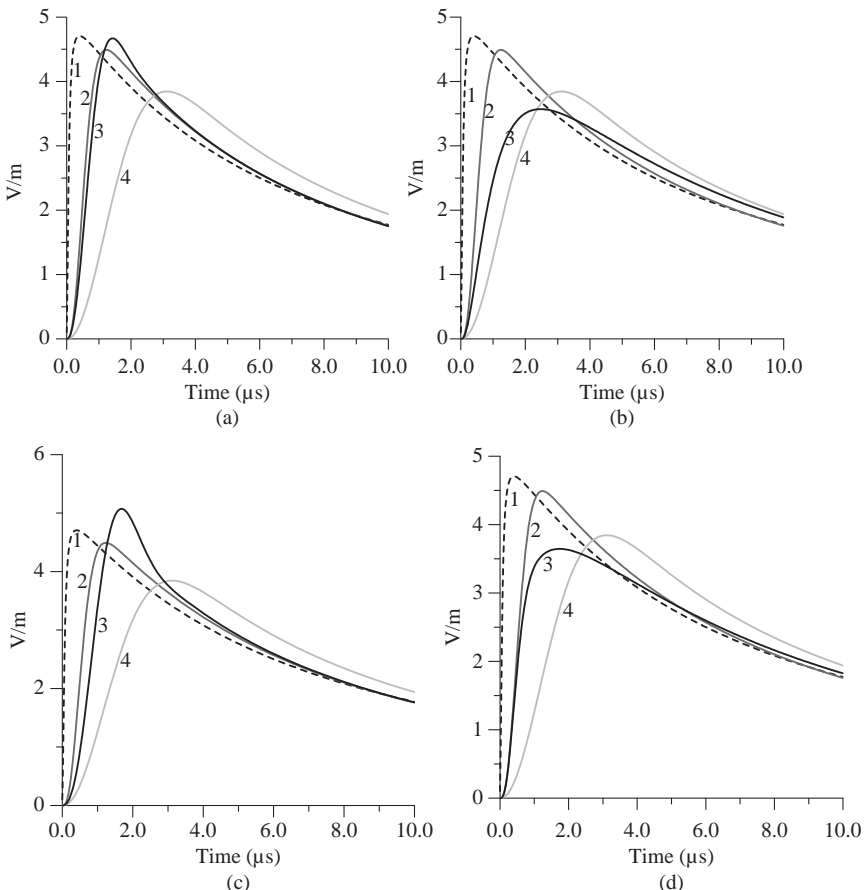


**Figure 11.35** Electric field at 50 km generated by a lightning flash over stratified ground. In each figure, curve 1 is the field over perfectly conducting ground, curve 2 is the field over finitely conducting homogeneous ground of conductivity 0.01 S/m and curve 4 is the field over finitely conducting homogeneous ground of conductivity 0.001 S/m. Curve 3 corresponds to the electric field over stratified ground. (a)  $\sigma_1 = 0.001 \text{ S/m}$ ,  $\sigma_2 = 0.01 \text{ S/m}$ ,  $h_1 = 2 \text{ m}$ ; (b)  $\sigma_1 = 0.01 \text{ S/m}$ ,  $\sigma_2 = 0.001 \text{ S/m}$ ,  $h_1 = 2 \text{ m}$ ; (c)  $\sigma_1 = 0.001 \text{ S/m}$ ,  $\sigma_2 = 0.01 \text{ S/m}$ ,  $h_1 = 5 \text{ m}$ ; (d)  $\sigma_1 = 0.01 \text{ S/m}$ ,  $\sigma_2 = 0.001 \text{ S/m}$ ,  $h_1 = 5 \text{ m}$ . In the calculations, the return stroke is modelled by using the MTLE model with a current decay height constant  $\lambda_c = 2 \text{ km}$ . The return stroke speed is kept at  $1.5 \times 10^8 \text{ m/s}$ . In the calculation,  $\epsilon_{r1}$  and  $\epsilon_{r2}$  were kept constant at 5. The current waveform at ground level is simulated by the analytical expression given by (11.21) (adapted from Reference [12])

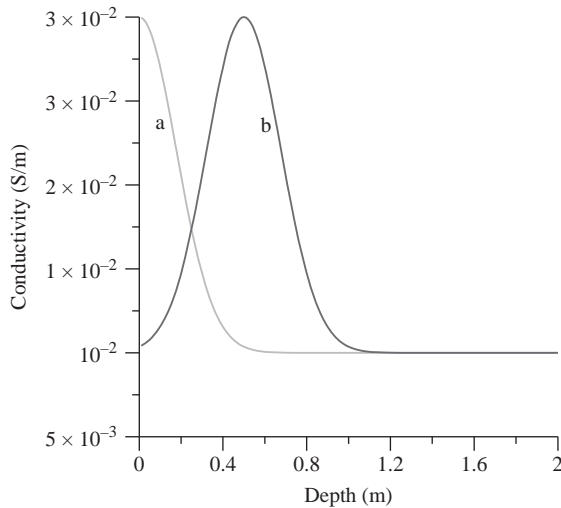


*Figure 11.36 Two conductivity profiles selected in the calculations. In profile (a) the conductivity is maximum at the surface, and in profile (b) it has moved to depth of about 0.6 m. The variation of conductivity with depth is assumed to be Gaussian (adapted from Reference 12)*

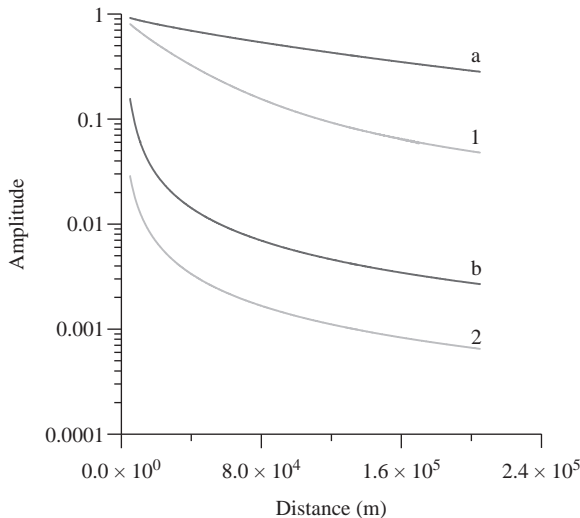


*Figure 11.37 The amplitude of the electromagnetic field at different distances corresponding to conductivity profile (a) in Figure 11.36 (curves marked 1 and 2) and conductivity profile (b) in Figure 11.36 (curves marked a, b). The frequencies corresponding to the curves are: 10<sup>6</sup> Hz (1 and a), and 10<sup>7</sup> Hz (2 and b). In the calculation, the relative dielectric constant of all layers were fixed at 5 (adapted from Reference 12)*

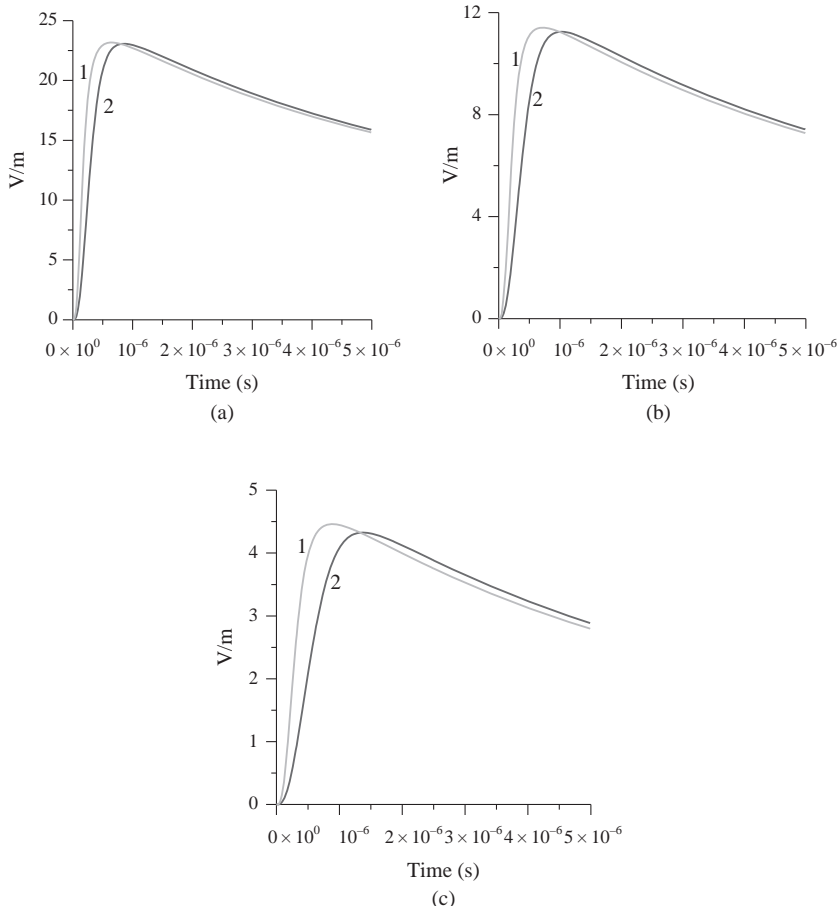


*Figure 11.38* Electric field corresponding to two conductivity profiles shown in Figure 11.36. (a) 10 km; (b) 20 km; (c) 50 km. The curves marked 1 correspond to profile (b) in Figure 11.36 and the curves marked 2 correspond to profile (a) in Figure 11.36. In the calculations, the return stroke is modelled by using the MTLE model with a current decay height constant  $\lambda_e = 2$  km. The return stroke speed is kept at  $1.5 \times 10^8$  m/s. The current waveform at ground level is simulated by the analytical expression given by (11.21). In the calculation, the relative dielectric constant of all layers were fixed at 5 (adapted from Reference [12])

profiles on the time domain electromagnetic fields radiated by lightning flashes. Figures 11.38 and 11.39 depict the electric field and the electric field derivative at 10 km, 20 km and 50 km for the two conductivity profiles shown in Figure 11.36. Note that there is a significant difference in the field derivatives in the two cases. However, the difference is not that significant in the case of the rise time.

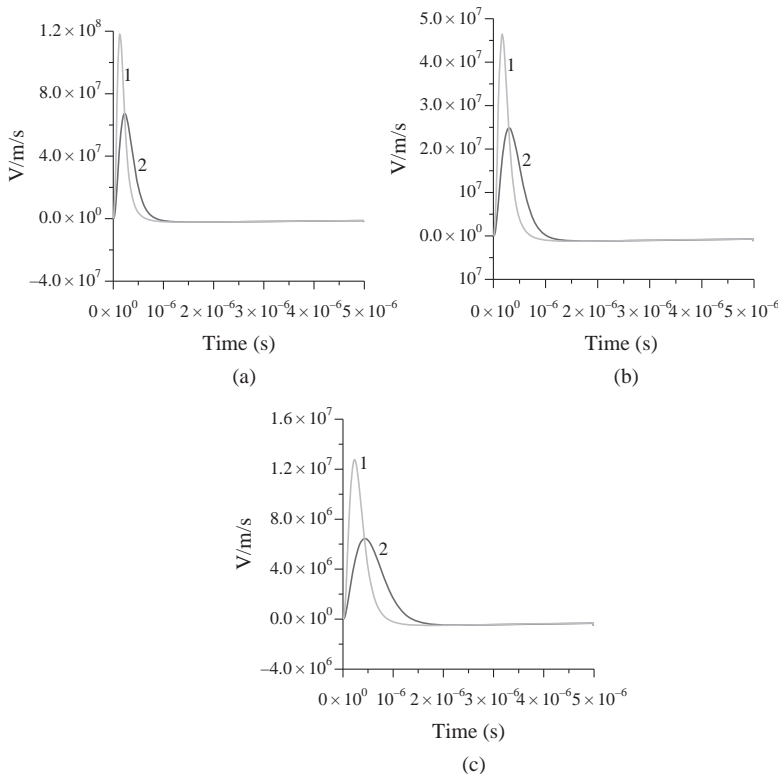


*Figure 11.39 Electric field time derivative corresponding to two conductivity profiles shown in Figure 11.36. (a) 10 km; (b) 20 km; (c) 50 km. The curves marked 1 correspond to profile (b) in Figure 11.36 and the curves marked 2 correspond to profile (a) in Figure 11.36. In the calculations, the return stroke is modelled by using the MTLE model with a current decay height constant  $\lambda_e = 2$  km. The return stroke speed is kept at  $1.5 \times 10^8$  m/s. The current waveform at ground level is simulated by the analytical expression given by (11.21). In the calculation, the relative dielectric constant of all layers were fixed at 5 (adapted from Reference [12])*

The results show that one can use either single frequencies over the range of  $10^6$ – $10^7$ , the rise time of the radiation field or the time derivative of the radiation field to remote sense the seasonal variations of electrical parameters of the soil.

## 11.8 Future studies

The large-scale deployment of lightning localization systems based on time of arrival and the demand on the accuracy of these systems, which to a large extend depends on the propagation effects, calls for more detailed experimental and

theoretical studies of propagation effects. In this respect, not much research work has been conducted on the effects of propagation along irregular terrain especially propagation across mountains. In addition to advancing our knowledge of the effects of propagation, such studies would lead to more accurate lightning localization systems.

## References

1. Uman, M. A., C. E. Swanberg, J. A. Tiller, Y. T. Lin and E. P. Krider, Effects of 200 km propagation on lightning return stroke electric fields, *Radio Sci.*, vol. 11, 985–990, 1976
2. Cooray, V., M. Fernando, T. Sørensen, T. Götschl and Aa. Pedersen, Propagation of lightning generated transient electromagnetic fields over finitely conducting ground, *J. Atm. Terr. Phys.*, vol. 62, 583–600, 2000
3. Gardner, R. L., Effects of propagation on lightning induced transient fields, *Radio Sci.*, vol. 16, 337–384, 1981
4. Cooray, V. and S. Lundquist, Effects of propagation on the risetime and the initial peaks of radiation fields from return strokes, *Radio Sci.*, vol. 18, 409–415, 1983
5. Le Vine, D. M., L. Gesell and M. Kao, Radiation from lightning return strokes over a finitely conducting earth, *J. Geophys. Res.*, vol. 91, 11897–11908, 1986
6. Cooray, V., Effects of propagation on the return stroke radiation fields, *Radio Sci.*, vol. 22, 757–768, 1987
7. Ming, Y. and V. Cooray, Propagation effects caused by a rough ocean surface on the electromagnetic fields generated by lightning return strokes, *Radio Sci.*, vol. 29, 73–85, 1994
8. Cooray, V. and Y. Ming, Propagation effects on the lightning generated electromagnetic fields for homogeneous and mixed sea land paths, *J. Geophys. Res.*, vol. 99, 10641–10652, 1994
9. Cooray, V., Propagation effects due to finitely conducting ground on lightning generated magnetic fields evaluated using Sommerfeld's equations, *IEEE Trans. EMC*, vol. 51, 526–531, 2009
10. Cooray, V., On the accuracy of several approximate theories used in quantifying the propagation effects on lightning generated electromagnetic fields, *Trans. IEEE: Ante. Prop.*, vol. 56, no. 7, 1960–1967, 2008
11. Cooray, V. and K. Cummins, Propagation effects caused by multi-section mixed paths on electric fields of lightning return strokes, International Symposium on Lightning Protection, Kirubita, Brazil, 2009
12. Cooray, V. and K. L. Cummins, Propagation effects caused by stratified ground on electromagnetic fields of return strokes, in *20th International Lightning Detection Conference & 2nd International Lightning Meteorology Conference*, Tucson, Arizona, USA, 2008

13. Shoory, A., A. Mimouni, F. Rachidi, V. Cooray, and M. Rubinstein, On the accuracy of approximate techniques for the evaluation of lightning electromagnetic fields along a mixed propagation path, *Radio Sci.*, vol. 46, 2011, doi:10.1029/2010RS004480
14. Shoory, A., A. Mimouni, F. Rachidi, V. Cooray, R. Moini, and S. H. Hesamedin, Validity of simplified approaches for the evaluation of lightning electromagnetic fields above a horizontally stratified ground, *IEEE Trans. EMC*, vol. 52, no. 3, 657–663, 2010
15. Delfino, F., R. Procopio and M. Rossi, Lightning return stroke current radiation in presence of a conducting ground: 1. Theory and numerical evaluation of electromagnetic fields, *J. Geophys. Res.*, vol. 115, 2008, doi:10.1029/2007JD008553
16. Delfino, F., R. Procopio, M. Rossi, F. Rachidi and C. A. Nucci, An algorithm for the exact evaluation of the underground lightning electromagnetic fields, *IEEE Trans. EMC*, vol. 49, 401–411, 2007
17. Sommerfeld, A., Über die Ausbreitung der Wellen in der drahtlosen Telegraphie, *Ann. Phys.*, vol. 28, 665, 1909
18. Norton, K. A., Propagation of radio waves over the surface of Earth and in the upper atmosphere, II, *Proc. IEEE*, vol. 25, 1203–1236, 1937
19. Bannister, P. R., *Extension of infinitely conducting Earth-image-theory results to any range*, Technical report, Naval Underwater systems center, January 1984
20. Maclean, T. S. M. and Z. Wu, *Radio Wave Propagation Over Ground*, Chapman & Hall, London, 1993
21. Gomes, C. and V. Cooray, Concepts of lightning return stroke models. *IEEE Trans. EMC*, vol. 42, no. 1, 82–96, 2000
22. Nucci, C. A., C. Mazzetti, F. Rachidi and M. Ianoz, On lightning return stroke models for LEMP calculations, Paper presented at 19th International Conference on Lightning Protection, Graz, Austria, 1988
23. Nucci, C. A., G. Diendorfer, M. A. Uman, F. Rachidi, M. Ianoz and C. Mazzetti, Lightning return stroke models with specified channel base current: A review and comparison, *J. Geophys. Res.*, vol. 95, 20395–20408, 1990
24. Heidler, F., Analytische blitzstromfunktion zur LEMP-berechnung, 18th International Conference on Lightning Protection, Munich, Germany, 1985
25. Baba, Y. and V. A. Rakov, Evaluation of lightning return stroke electromagnetic models, 29th International Conference on Lightning Protection, Uppsala, Sweden, 2008
26. Mimouni, A., F. Rachidi and A. Azzouz, Electromagnetic fields in the immediate vicinity of a tower struck by lightning, 29th International Conference on Lightning Protection, Uppsala, Sweden, 2008
27. Caligaris, C., F. Delfino and R. Procopio, Cooray-Rubinstein formula for the evaluation of lightning radial electric fields: Derivation and implementation in the time domain, *IEEE Trans. EMC*, vol. 50, 194–197, 2008
28. Rubinstein, M., An approximate formula for the calculation of the horizontal electric field from lightning at close, intermediate and long range, *IEEE Trans. EMC*, vol. 38, 531–535, 1996

29. Wait, J. R., Transient fields of a vertical dipole over homogeneous curved ground, *Can. J. Phys.*, vol. 36, 9–17, 1956
30. Cooray, V., Horizontal fields generated by return strokes, *Radio Sci.*, vol. 27, 529–537, 1992
31. Cooray, V., Horizontal electric field above and underground produced by lightning flashes, *IEEE Trans. EMC*, vol. 52, 936–943, 2010
32. Barbosa, C. F. and J. O. Paulino, A time domain formula for the horizontal electric field at the Earth surface in the vicinity of lightning, *IEEE Trans. EMC*, vol. 52, no. 3, 640–645, 2010
33. Cooray, V., Underground electromagnetic fields generated by the return strokes lightning flashes, *IEEE Trans. EMC*, vol. 43, 75–84, 2001
34. Delfino, F., R. Procopio, M. Rossi, F. Rachidi and C. A. Nucci, Lightning return stroke current radiation in presence of a conducting ground: 2. Validity assessment of simplified approaches, *J. Geophys. Res.*, vol. 113, D05111, 2008, doi:10.1029/2007JD008567
35. Wait, J. R., On the theory mixed-path ground-wave propagation on a spherical Earth, *J. Res. Natl. Inst. Stand. Technol.*, vol. 65D, no. 4, 401–410, 1961
36. Cooray, V. and H. Perez, Propagation effects on the first return stroke radiation fields: Homogeneous paths and mixed two section paths, Propagation effects on return stroke fields, 22nd ICLP, paper R1a-06, Budapest, 1994
37. Bailey, J. C. and J. C. Willett, Catalog of absolutely calibrated, range normalised, wideband, electric field waveforms from located lightning flashes in Florida, NRL memorandum Report 6497, Naval Research Laboratory, Washington, DC, USA, 1989
38. Izumi, Y. and J. C. Willett, Catalog of absolutely calibrated, range normalised, wideband, electric field waveforms from located lightning flashes in Florida, Environmental Research Papers, No. 1082, Phillips Laboratory, Directorate of Geophysics, Hanscom air force base, Massachusetts, USA, 1991
39. Wait, J. R., *Electromagnetic Waves in Stratified Media*, Pergamon Press, Oxford, England, 1962

---

## *Chapter 12*

# **Propagation effects on electromagnetic fields generated by lightning return strokes: Review of simplified formulas and their validity assessment**

*A. Shoory<sup>1</sup>, F. Rachidi<sup>2</sup> and V. Cooray<sup>3</sup>*

---

## **12.1 Introduction**

Several efforts have been made in the past years to model the effect of the ground on the propagation of lightning-radiated electromagnetic fields [1]. Assuming the lightning channel as a lossless vertical antenna above a finitely conducting ground, the associated electromagnetic fields can be evaluated using three different approaches [2]: (1) use of dedicated algorithms (e.g. [3–6]); (2) use of numerical methods such as the method of moments (e.g. [7]) or finite-difference time-domain (FDTD) technique (e.g. [8–10]) and (3) use of simplified approaches (e.g. [11–14]). The use of simplified approaches is particularly interesting when the electromagnetic fields need to be evaluated at a significant number of points in the space, i.e. in field-to-transmission line coupling calculations. In this case, the use of dedicated algorithms or numerical methods might be very costly in terms of computation time and memory requirement.

In this chapter, we present a review of simplified formulas developed for the evaluation of electromagnetic fields generated by lightning return strokes above the ground. Three types of soil will be considered: (1) a homogeneous lossy ground, (2) a horizontally stratified ground and (3) a vertically stratified ground. The range of validity of the simplified formulas will be discussed taking as reference rigorous results obtained using full-wave approaches and dedicated algorithms.

## **12.2 Basic assumptions**

When electromagnetic field components above an imperfect ground are sought in the time domain, it is always preferred to derive them from the corresponding field

<sup>1</sup>ABB Corporate Research, Baden-Dättwil, Switzerland

<sup>2</sup>Swiss Federal Institute of Technology (EPFL), Lausanne, Switzerland

<sup>3</sup>Uppsala University, Uppsala, Sweden

components above an ideal, perfectly conducting ground (perfect ground). The electromagnetic fields due to an elevated dipole above an imperfect ground at a given height above the ground are affected mainly by three effects: the height-gain functions associated with the elevated source and the observation point, and the propagation along an imperfect ground [15]. In the derivation of simplified formulas, generally the height-gain effects are neglected and only the propagation effects are considered for a dipole located at the channel base [12]. In fact, the propagation affects essentially the high-frequency components of the electromagnetic fields. In time-domain, this would correspond to the fast, early time (first few microseconds) response. The return-stroke speed being about  $1 \times 10^8$  m/s, the length of the channel that contributes to the radiation field during this time would not be larger than a few hundred metres. Therefore, it is reasonable to assume that the propagation affects predominantly the dipoles near the ground level.

### 12.2.1 Formulation of the electromagnetic fields above a perfect ground in the time domain

Let's consider the geometry shown in Figure 12.1. The lightning channel is assumed simply as a straight and vertical line above a perfect ground. It is assumed that the current at a given height  $z'$  along the channel and at a time  $t$  denoted in Figure 12.1 by  $i(z', t)$  can be obtained from the channel base current

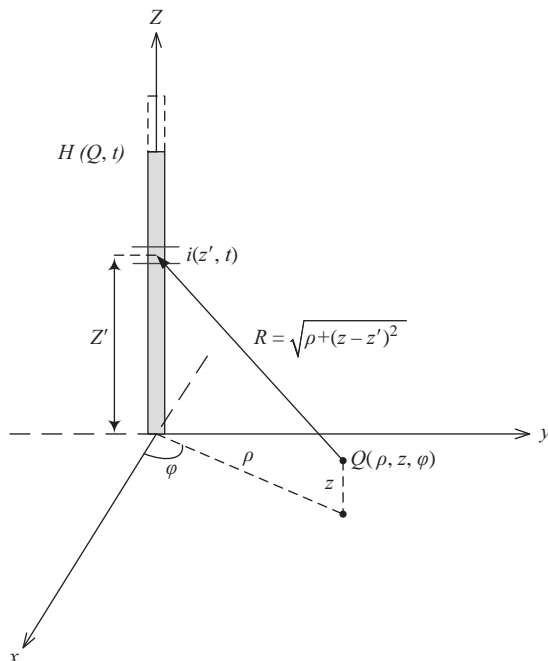


*Figure 12.1 Straight vertical lightning channel above perfect ground*

$i(0, t)$  assuming any of the engineering return-stroke models [16]. Because of the axial symmetry of the geometry, there are only three field components, namely, vertical electric field, horizontal electric field and azimuthal magnetic field that are given by [17, 18].

$$e_{zP}(\rho, z, t) = \frac{1}{2\pi\epsilon_0} \int_0^{H(\rho, z, \varphi, t)} \left[ \frac{2(z - z')^2 - \rho^2}{R^5(z')} \int_{\frac{z'}{v} + \frac{R(z')}{c}}^t i\left(z', \tau - \frac{R(z')}{c}\right) d\tau \right. \\ \left. + \frac{2(z - z')^2 - \rho^2}{cR^4(z')} i\left(z', t - \frac{R(z')}{c}\right) - \frac{\rho^2}{c^2 R^3(z')} \frac{\partial i\left(z', t - \frac{R(z')}{c}\right)}{\partial t} \right] dz' \\ - \frac{1}{2\pi\epsilon_0} \frac{\rho^2}{c^2 R^3(H(\rho, z, \varphi, t))} i\left(H(\rho, z, \varphi, t), \frac{H(\rho, z, \varphi, t)}{v}\right) \frac{dH(\rho, z, \varphi, t)}{dt} \quad (12.1)$$

$$e_{\rho P}(\rho, z, t) = \frac{1}{2\pi\epsilon_0} \int_0^{H(\rho, z, \varphi, t)} \left[ \frac{3\rho(z - z')}{R^5(z')} \int_{\frac{z'}{v} + \frac{R(z')}{c}}^t i\left(z', \tau - \frac{R(z')}{c}\right) d\tau \right. \\ \left. + \frac{3\rho(z - z')}{cR^4(z')} i\left(z', t - \frac{R(z')}{c}\right) - \frac{\rho(z - z')}{c^2 R^3(z')} \frac{\partial i\left(z', t - \frac{R(z')}{c}\right)}{\partial t} \right] dz' \\ - \frac{1}{2\pi\epsilon_0} \frac{\rho(z - z')}{c^2 R^3 H(\rho, z, \varphi, t)} i\left(H(\rho, z, \varphi, t), \frac{H(\rho, z, \varphi, t)}{v}\right) \frac{dH(\rho, z, \varphi, t)}{dt} \quad (12.2)$$

$$h_{qP}(\rho, z, t) = \frac{1}{2\pi} \int_0^{H(\rho, z, \varphi, t)} \left[ \frac{\rho}{R^3(z')} i\left(z', t - \frac{R(z')}{c}\right) + \frac{\rho}{cR^2(z')} \frac{\partial i\left(z', t - \frac{R(z')}{c}\right)}{\partial t} \right] dz' \\ + \frac{1}{2\pi} \frac{\rho}{cR^2(H(\rho, z, \varphi, t))} i\left(H(\rho, z, \varphi, t), \frac{H(\rho, z, \varphi, t)}{v}\right) \frac{dH(\rho, z, \varphi, t)}{dt} \quad (12.3)$$

in which  $\epsilon_0$  and  $\mu_0$  are the free-space permittivity and permeability and  $c$  is the speed of light in free space.  $H(\rho, z, \varphi, t)$  is the apparent height of the wavefront as seen by an observer at  $Q$  at time  $t$ . In (12.1)–(12.3), the terms proportional to the time integral of the current are usually referred to as static field components, the terms proportional to the current itself are called induction components and the terms proportional to the time derivative of the current are referred to as radiation components. The last term in any of these field expressions is the so-called turn-on term field component

accounting for possible discontinuity at the return-stroke wavefront, as introduced and discussed by Rubinstein and Uman [19, 20]. Note that, in (12.1)–(12.3) the first subscript in the field components accounts for the component of the field and the second subscript  $P$  holds for the field above a perfect ground.

### 12.2.2 Using the electromagnetic fields above a perfect ground as the input for calculating the fields above a lossy ground

In the most general representation, the simplified versions of electromagnetic fields above either a homogeneous lossy ground, a horizontally stratified ground or a vertically stratified ground can be written in the time domain as

$$e_z(\rho, z, t) = e_{zP}(\rho, z, t) * f(t) \quad (12.4)$$

$$e_\rho(\rho, z, t) = e_{\rho P}(\rho, z, t) - h_{\varphi P}(\rho, 0, t) * f(t) * z(t) \quad (12.5)$$

$$h_\varphi(\rho, z, t) = h_{\varphi P}(\rho, z, t) * f(t) \quad (12.6)$$

in which  $f(t)$  is the attenuation function accounting for the propagation effects and  $*$  holds for convolution of time-dependent functions.  $z(t)$  is the surface impedance of the ground that, in its most universal form, is defined as the inverse Fourier transform of the frequency domain ratio of the electric and magnetic fields on the ground surface. Expressions for the attenuation function and ground surface impedance can be obtained in the frequency domain and the corresponding time-domain expression can be derived using inverse Fourier transforms, i.e.

$$f(t) = F^{-1}[F(j\omega)] \quad (12.7)$$

$$z(t) = F^{-1}[Z(j\omega)] \quad (12.8)$$

where  $\omega (= 2\pi f)$  is the angular frequency. Equations (12.4)–(12.6) are therefore expressed in the frequency domain by using (12.7)–(12.8) as follows:

$$E_z(\rho, z, j\omega) = E_{zP}(\rho, z, j\omega)F(j\omega) \quad (12.9)$$

$$E_\rho(\rho, z, j\omega) = E_{\rho P}(\rho, z, j\omega) - H_{\varphi P}(\rho, 0, j\omega)F(j\omega)Z(j\omega) \quad (12.10)$$

$$H_\varphi(\rho, z, j\omega) = H_{\varphi P}(\rho, z, j\omega)F(j\omega) \quad (12.11)$$

Usually, for the calculation of the horizontal electric field in (12.5), the effects of propagation on the magnetic field component are neglected [21]. Such an approximation appears to be reasonable for the case of a homogeneous ground and for distances not exceeding 200 m for conductivities of the ground not lower than 0.001 S/m, and 100 m for conductivities of 0.0001 S/m or larger. However, this approximation becomes even less accurate for the determination of the horizontal field component for the case of a horizontally stratified ground.

It is worth noting that the attenuation function used in (12.4)–(12.11) does not consider the curvature of the ground as distances of observation point to be studied herewith do not exceed 300 km. Beyond this limit one can use the general form of the attenuation function given by Hill and Wait [22, 23]. In the following sections, these definitions will be used for each of the three ground types mentioned above and the necessary validations using full-wave techniques will be provided. Note that, for the case when the ground is homogeneous or horizontally stratified, such simplified formulations can be viewed in fact as approximations to the rigorous developments based on Sommerfeld integrals [24, 25]. The introduction of attenuation function to model propagation effects to account for the frequency-selective attenuation of high-frequency components can be found in early works of Norton [26, 27]. This concept was generalized by *Wait* [15] to consider the case of a horizontally stratified ground. It is to be noted here that the formula for the horizontal electric field at and above the surface of a horizontally stratified ground was first proposed by Shoory *et al.* [28, 29] that in the most general form can be represented by (12.10). This formula will be discussed in Section 12.4.1.

### 12.3 Propagation along a homogeneous lossy ground

One of the first simplified approximations for the electromagnetic fields due to a vertical dipole above a homogeneous lossy ground involving Sommerfeld integrals is due to *Norton* [26, 27]. In his formulation, electromagnetic fields are simply expressed using complementary error functions appearing in the definition of attenuation functions. The work was later elaborated by *Wait* (see [15] for a historical review) that in its latest forms are represented by (12.4) and (12.6). The expression for the attenuation function above a homogeneous ground (see Figure 12.2) with conductivity  $\sigma$  and relative permittivity  $\epsilon_r$  reads [26, 27]

$$F(j\omega) = 1 - j\sqrt{\pi p} e^{-p} \operatorname{erfc}(j\sqrt{p}) \quad (12.12)$$

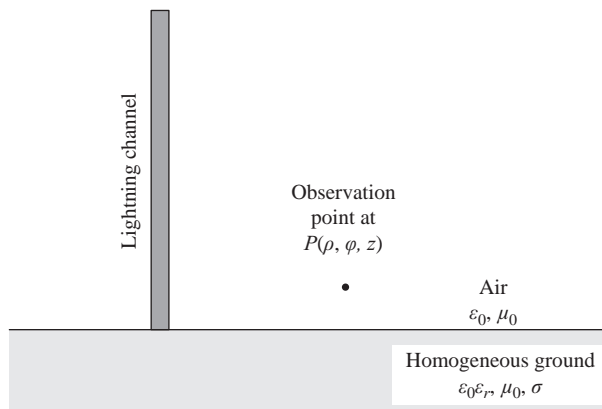


Figure 12.2 Propagation of lightning-radiated electromagnetic waves above a homogeneous lossy ground

where  $p$  is the so-called numerical distance defined as

$$p = -0.5\gamma_0\rho\Delta^2 \quad (12.13)$$

in which  $\gamma_0$  is the free-space wave number defined as

$$\gamma_0 = j\omega\sqrt{\mu_0\varepsilon_0} \quad (12.14)$$

and  $\Delta$  is the normalized surface impedance of the homogeneous ground given by

$$\Delta = \frac{Z(j\omega)}{\sqrt{(\mu_0/\varepsilon_0)}} \quad (12.15)$$

in which

$$Z(j\omega) = \sqrt{\frac{j\omega\mu_0}{\sigma + j\omega\varepsilon_0\varepsilon_r}} \quad (12.16)$$

is the expression for the surface impedance of the homogeneous ground.  $\text{erfc}$  is the complementary error function of complex value [30].

Several efforts have been made to apply these formulations in the time domain for studying the propagation effects on lightning-radiated electromagnetic fields along a homogeneous lossy ground (e.g. the works by Gardner [31], Cooray and Lundquist [11], LeVine *et al.* [32] and Cooray [12]). Experimental studies of the effect of ground losses on lightning electromagnetic fields have also been reported, e.g. by Johler and Lilley [33] where they have attempted to ascertain the ground conductivity from two-station measurements of lightning return-stroke electromagnetic fields. Other efforts were also reported on remote sensing of lightning from its measured electromagnetic fields, e.g. by Fisher and Uman [34], Lin and Uman [35], Krider and Radda [36], Tiller *et al.* [37] and Cooray and Lundquist [11] confirming the increase in the rise times and decrease in the peak values of the measured vertical electric fields due to the propagation along imperfect ground. Especially, Cooray and Lundquist [11] have shown that simplified formulas can be used to predict such effects on lightning electromagnetic fields. Besides such extensive experimental studies, efforts have also been carried out to test the validity of the simplified formulations using full-wave dedicated algorithms. In this section, we provide a review of such efforts and the main conclusions.

### 12.3.1 Vertical electric and azimuthal magnetic fields

Validation of the simplified approximations for the vertical electric and azimuthal magnetic fields above a homogeneous ground have been recently addressed by Cooray [38–40] and Delfino *et al.* [6]. In this regard, numerical evaluation of the corresponding Sommerfeld integrals was used as a reference. Regarding the

vertical electric field, it is shown by Cooray [39] that, for an observation point on the surface of the ground with a conductivity of 0.001 S/m, the vertical electric field is not significantly affected by the ground finite conductivity at distance ranges from 50 m to 1000 m. However, the peak value of the time derivative of the vertical electric field can be attenuated by about 70% in propagating 1000 m along the ground. Cooray also showed that, for ground conductivities not less than 0.001 S/m and observation points not farther than 1000 m, the approximations proposed by Norton [27] predict adequately the vertical electric field components. On the other hand, for observation points at about 10 m above the ground surface and as close as 100 m to the channel base, Delfino *et al.* [6], by using exact Sommerfeld solution, have shown that the perfectly conducting ground is a reasonable assumption for obtaining vertical electric and azimuthal magnetic fields above a homogeneous lossy ground. However, for larger distances and for ground conductivities smaller than 0.001 S/m, some disagreements can be found between fields above a perfect ground and those above a homogeneous lossy ground.

Further, Cooray [41, 40] studied the propagation effects on lightning-generated magnetic fields and has concluded that, although the magnetic fields are not significantly affected by propagation along a lossy ground, their time derivative peak decreases by about 30%, 40% and 70% in propagating 100 m, 200 m and 1000 m, respectively, over a finite ground of conductivity 0.001 S/m. The largest observed error of Norton [27] approximation in predicting time derivative magnetic field peak for ground conductivities as low as 0.0001 S/m and observation point distance in the 10–1000 m range was 20%.

### 12.3.2 Horizontal electric field

The Cooray-Rubinstein (CR) formula is essentially one of the most widely used simplified formulas for the calculation of the horizontal electric field above a homogeneous lossy ground. The formula was first proposed by Cooray [42] for an observation at ground level and then generalized by Rubinstein [43] for elevated observation points. Note that (12.10) using the expression in (12.16) for the surface impedance of the homogeneous ground and neglecting propagation effects on the azimuthal magnetic field reduces to the CR formula, as shown by Wait [44], given by

$$E_\rho(\rho, z, j\omega) = E_{\rho P}(\rho, z, j\omega) - H_{\varphi P}(\rho, 0, j\omega) \sqrt{\frac{j\omega\mu_0}{\sigma + j\omega\epsilon_0\epsilon_r}} \quad (12.17)$$

Using the expression given by Norton [27] as the reference, Cooray concluded that, for ground conductivities ranging from 0.001 to 0.01 S/m, the CR formula can produce accurate results for observation points at distances as close as 200 m from the channel base. On the other hand, for a 6-m elevated observation point and using the numerical evaluation of the Sommerfeld integrals carried out by Zeddam and Degauque [45], Rubinstein [43] showed that the CR formula is valid for observation points down to 100 m from the channel for a ground with conductivity of

0.01 S/m. The formulation was found to lose its accuracy for ground conductivities in the 0.0001 S/m range for an observation point at 500 m distance from the channel base. Note that time-domain implementations of the CR formula can also be found in the works of Cooray [42] and Caligaris [46].

The validity of simplified formulas for horizontal electric field at ground level and also at a given height above the ground was recently analysed by Delfino *et al.* [6] and Cooray [21] in a more comprehensive way. Delfino *et al.* [6] have shown that, for ground conductivities in the 0.01 S/m range and for observation points located a few metres above the ground level, the perfect ground approximation is a reasonable assumption for obtaining the horizontal electric field. For ground conductivities in the 0.001 S/m range and observation points at a few metres above ground and at horizontal distances down to 20 m, the CR formula is a good approximation to the exact solution. However, for very poor ground conductivities in the range of 0.0001 S/m, the predictions of the CR formula deviate significantly from the Sommerfeld solution for an observation point located at 10 m above the ground surface and at a horizontal distance of 250 and 500 m away from the channel base.

Cooray [21] showed that the surface impedance approximation (a more general concept for obtaining the horizontal electric field given in (12.10)) is mainly a high frequency and far field approximation that can generate correct horizontal electric field for observation points farther than 50 m, 200 m and 500 m for ground conductivities of 0.01, 0.001 and 0.0001 S/m, respectively. Cooray also emphasized that, to obtain a better accuracy of the horizontal electric field in the surface impedance approximation, propagation effects should be considered in the calculation of the magnetic field for distances beyond 200 m for conductivities of about 0.001 S/m and beyond 100 m for conductivities of about 0.0001 S/m. The omission of the propagation effects on the magnetic fields would result in inaccuracies that become more significant for subsequent return strokes, which are characterized by higher frequency components compared to first return strokes.

More recently, Barbosa and Paulino [47] proposed a time-domain formula for the horizontal electric field component originated by a lightning discharge. The proposed formula was compared with numerical solutions of Sommerfeld's integrals and with the CR formula and very good agreement was found. In Reference [48], they compared their simulations with measured horizontal electric field waveforms associated with triggered lightning. They obtained good agreement between measurements and calculations for the early times. However, some discrepancies were observed in the late-time response of the field. Barbosa *et al.* modified the formula [48, 49] to take into account the so-called conduction currents in the ground, which resulted in a much better agreement between calculation and measurements for both early-time and late-time responses. Note that back in 1992, Kravchenko and Link [50] had also emphasized the importance of taking into account the conduction current in the calculation of nearby horizontal electric fields from a cloud-to-ground lightning discharge (see Reference [51] for a thorough discussion on this topic).

## 12.4 Propagation along a horizontally stratified ground

Simplified formulations for electromagnetic wave propagation above a stratified ground can be considered essentially as generalizations of those above a homogeneous lossy ground proposed early on by Norton [26]. A historical and comprehensive review of the formulations, their domains of applicability and theoretical bottlenecks, e.g. resulting from the presence of surface waves on ‘wrong’ Riemann sheets were given in the review papers by Wait [52, 15].

Using the concept of mutual impedance between two vertically oriented dipoles on the surface of the ground, Wait [53, 54] and Hill and Wait [23] derived the attenuation function for the vertical electric field propagating over a horizontally stratified ground. The theory was later used by Ming and Cooray [55] and Cooray and Cummins [56] to evaluate such effects on lightning return-stroke electromagnetic fields.

The main idea behind the formulations for either a homogeneous or stratified ground is, as mentioned earlier in this chapter, the use of the surface impedance concept that is defined as the ratio of the frequency domain electric and magnetic fields tangential to the ground surface [57].

Despite a considerable number of studies related to the theoretical and experimental validation of the simplified formulation for transient wave propagation along a homogeneous ground, there was a lack of systematic analysis for the case of a stratified ground except until recently when Shoory *et al.* [58, 59, 28, 60, 29] provided a review of these formulations along with their validation using the FDTD technique [59, 28] and dedicated algorithm based on the numerical evaluation of the Sommerfeld integrals [60, 29]. In this section, we present the formulation for obtaining lightning-radiated electromagnetic fields above a two-layer horizontally stratified ground and its validation using the FDTD technique and the numerical evaluation of the corresponding Sommerfeld integrals.

### 12.4.1 Simplified formulations for the lightning electromagnetic fields above a two-layer horizontally stratified ground

In analogy with the homogenous ground case, the expression for the attenuation function of a two-layer horizontally stratified ground (schematized in Figure 12.3) needed in (12.9)–(12.11) was derived by Wait [12, 61, 15, 58, 59].

$$F_{str,h}(j\omega) = 1 - j\sqrt{\pi p_{str,h}} e^{-p_{str,h}} \operatorname{erfc}(j\sqrt{p_{str,h}}) \quad (12.18)$$

in which the numerical distance  $p_{str,h}$  is defined as

$$p_{str,h} = -0.5\gamma_0\rho\Delta_{str,h}^2 \quad (12.19)$$

where  $\Delta_{str,h}$  is the normalized surface impedance of the two-layer ground given by

$$\Delta_{str,h} = \frac{Z_{str,h}(j\omega)}{\sqrt{(\mu_0/\epsilon_0)}} \quad (12.20)$$

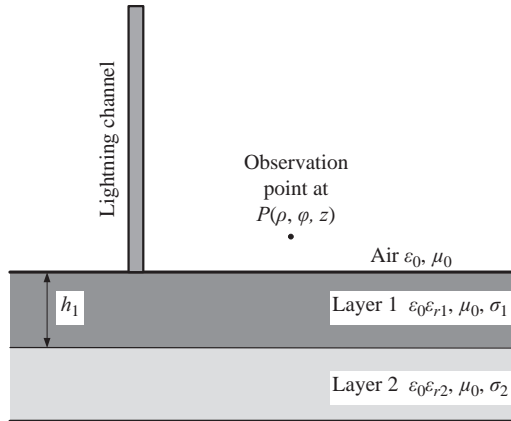


*Figure 12.3 Propagation of lightning-radiated electromagnetic field over a two-layer horizontally stratified ground*

where

$$Z_{str,h}(j\omega) = K_1 \frac{K_2 + K_1 \tanh(u_1 h_1)}{K_1 + K_2 \tanh(u_1 h_1)} \quad (12.21)$$

is the surface impedance of the two-layer horizontally stratified ground (this expression is used in (12.10) for obtaining the horizontal electric field) and

$$K_1 = \frac{u_1}{\sigma_1 + j\omega \epsilon_0 \epsilon_{r1}} \quad (12.22)$$

$$K_2 = \frac{u_2}{\sigma_2 + j\omega \epsilon_0 \epsilon_{r2}} \quad (12.23)$$

$$u_1 = \sqrt{\gamma_1^2 - \gamma_0^2} \quad (12.24)$$

$$u_2 = \sqrt{\gamma_2^2 - \gamma_0^2} \quad (12.25)$$

and

$$\gamma_1 = \sqrt{j\omega \mu_0 (\sigma_1 + j\omega \epsilon_0 \epsilon_{r1})} \quad (12.26)$$

$$\gamma_2 = \sqrt{j\omega \mu_0 (\sigma_2 + j\omega \epsilon_0 \epsilon_{r2})} \quad (12.27)$$

are wave numbers in each ground layer. Note that, in the above expressions where we encounter square roots of complex quantities, we will choose the roots on the upper Riemann sheet [62].

### 12.4.2 Test and validation of the simplified formulas

The case where the magnitude of the complex refractive index of the lower ground layer is larger than that of the upper layer is interesting because, as it was shown by Cooray [63], it gives rise to field amplitudes larger than that above a perfect ground. For the first set of simulations presented in this section (corresponding to this case), we consider an observation point at ground level and at distances of  $\rho = 10$  km and  $\rho = 100$  km from the channel base. The adopted values for the electrical parameters of the ground are  $\sigma_1 = 0.001$  S/m,  $\epsilon_{r1} = 10$  and  $\sigma_2 = 4$  S/m,  $\epsilon_{r2} = 30$ . For the return-stroke model, the modified transmission line model with exponential decay (MTLE) of Nucci *et al.* [64] and Rachidi and Nucci [65] is adopted with a current decay constant  $\lambda = 2$  km and a return-stroke speed of  $v = 1.5 \times 10^8$  m/s. The channel base current is that of Rachidi *et al.* [66], which corresponds to a typical subsequent return-strokes based on the observations of Berger *et al.* [67] and is defined as

$$i(0, t) = \frac{I_{01}}{\eta_1} \frac{(t/\tau_{11})^{n_1}}{1 + (t/\tau_{11})^{n_1}} e^{-t/\tau_{12}} + \frac{I_{02}}{\eta_2} \frac{(t/\tau_{21})^{n_2}}{1 + (t/\tau_{21})^{n_2}} e^{-t/\tau_{22}} \quad (12.28)$$

where

$$\eta_1 = e^{-(\tau_{11}/\tau_{12})(n_1 \tau_{12}/\tau_{11})^{\frac{1}{n_1}}} \quad (12.29)$$

$$\eta_2 = e^{-(\tau_{21}/\tau_{22})(n_2 \tau_{22}/\tau_{21})^{\frac{1}{n_2}}} \quad (12.30)$$

This current is characterized by a peak value of 12 kA and a maximum steepness of 40 kA/μs. The numerical values, corresponding to this current waveform drawn from Rachidi *et al.* [66], are  $I_{01} = 10.7$  kA,  $I_{02} = 6.5$  kA,  $\tau_{11} = 0.25$  μs,  $\tau_{12} = 2.5$  μs,  $\tau_{21} = 2.1$  μs,  $\tau_{22} = 230$  μs,  $n_1 = n_2 = 2$ .

For the observation points at the ground surface, the simplified equations for the horizontally stratified ground are validated against the FDTD simulation technique. The details of the technique and its implementation can be found in Reference [68]. The procedure is essentially the same as that used by Mimouni *et al.* in References [4, 8, 69, 10]. The simulation domain of the FDTD technique is shown in Figure 12.4. The technique solves the two Maxwell's curl equations by means of the so-called Yee discretization scheme [68]. As mentioned earlier in this chapter, in this regard, one needs to solve only for the vertical and horizontal electric fields and the azimuthal magnetic field due to the axial symmetry of the problem. The spatial and temporal derivatives are represented simply using the first-order finite differences. More details on the technique can be found, e.g. in Reference [8]. The depth of the upper soil layer for  $\rho = 10$  km was set to  $h_1 = 2$  m. For  $\rho = 100$  km, because of the limitations in the computational resources, the smallest possible

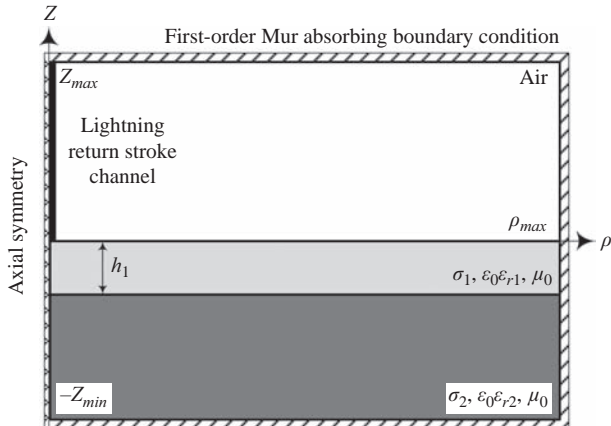


*Figure 12.4 Side view of the simulation domain of the FDTD technique used for the validation of the simplified approaches. For  $\rho = 10 \text{ km}$  we used  $\rho_{\max} = 11 \text{ km}$ ,  $z_{\max} = 7.5 \text{ km}$  and  $z_{\min} = 100 \text{ m}$ , and for  $\rho = 100 \text{ km}$  we used  $\rho_{\max} = 101 \text{ km}$ ,  $z_{\max} = 52.5 \text{ km}$  and  $z_{\min} = 100 \text{ m}$  [adapted from Shoory et al. [59]]*

value for  $h_1$  was 20 m.\* In the FDTD simulations, a value for the time step of 2 ns was considered for  $\rho = 10 \text{ km}$  and a value of 20 ns was considered for  $\rho = 100 \text{ km}$ . The overall time interval was set to  $T_{\max} = 50 \mu\text{s}$  for  $\rho = 10 \text{ km}$  and  $T_{\max} = 380 \mu\text{s}$  for  $\rho = 100 \text{ km}$ . This corresponds to 25,000 time steps for  $\rho = 10 \text{ km}$  and 19,000 time steps for  $\rho = 100 \text{ km}$ . The spatial discretization interval was chosen to be 2 m for  $\rho = 10 \text{ km}$  and 20 m for  $\rho = 100 \text{ km}$ .

According to Figure 12.4, the simulation domain was truncated using the first-order Mur absorbing boundary conditions at  $\rho_{\max} = 11 \text{ km}$ ,  $z_{\max} = 7.5 \text{ km}$  and  $z_{\min} = 100 \text{ m}$  for  $\rho = 10 \text{ km}$  and at  $\rho_{\max} = 101 \text{ km}$ ,  $z_{\max} = 52.5 \text{ km}$  and  $z_{\min} = 100 \text{ m}$  for  $\rho = 100 \text{ km}$ . Making use of the axial symmetry of the problem (left-most boundary coinciding  $z$ -axis), this corresponds to  $5500 \times 3800$  spatial cells for  $\rho = 10 \text{ km}$  and  $5050 \times 2630$  spatial cells for  $\rho = 100 \text{ km}$ .

The simulation results for vertical electric field are shown in Figure 12.5. For more clarity, the curves are also given in smaller timescales. It can be seen that the Wait's formulation appears to be quite accurate in reproducing the electric field waveform. Furthermore, both oscillatory and enhancement effects are confirmed in the full-wave FDTD simulations. Table 12.1 presents the values of the field peaks and zero-to-peak rise times predicted by the Wait's formulation and by the FDTD method. It can be observed that the Wait's formulation is able to reproduce these two parameters with an accuracy of 20% for  $\rho = 10 \text{ km}$  and 8.8% for  $\rho = 100 \text{ km}$ . Larger errors observed for  $\rho = 10 \text{ km}$  are reasonable because Wait's approximate

\*This is due to the fact that we are simply using square cells and not adaptive meshing scheme. This would result in a prohibitive number of cells if we decrease the depth of the upper ground layer.

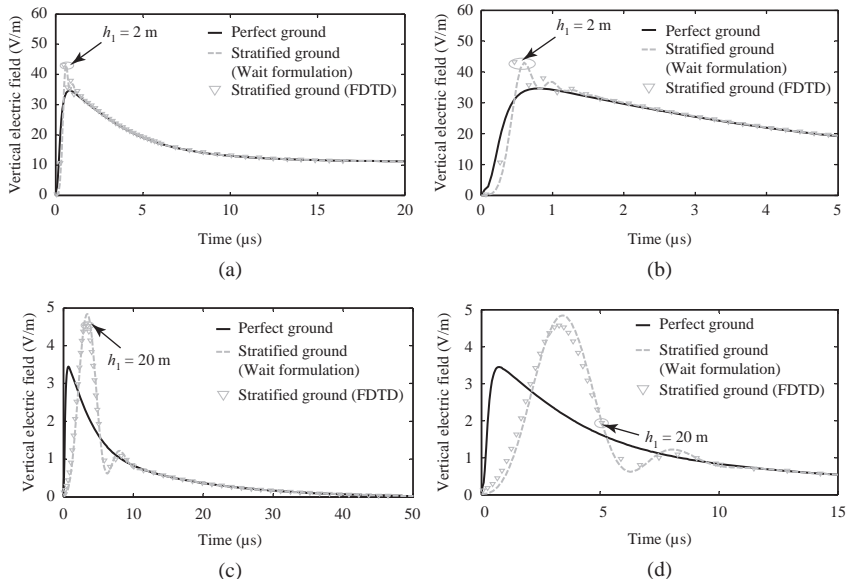


*Figure 12.5* Vertical electric field at ground level at a distance of  $\rho = 10$  km ((a) and (b)) with  $h_1 = 2$  m and  $\rho = 100$  km ((c) and (d)) with  $h_1 = 20$  m obtained using the Wait's formulation of Section 12.4.1 and FDTD technique. The results for a perfectly conducting ground are also shown for comparison. (a,c) longer time window, (b,d) shorter time window [adapted from Shoory et al. [59]]

*Table 12.1* Peak and rise times of the far vertical electric field predicted using Wait's formulation and FDTD simulations m [adapted from Shoory et al. [59]]

$\rho$ (km)	$h$ (m)	Peak (V/m)			Rise time (μs)		
		Wait	FDTD	Error (%)	Wait	FDTD	Error (%)
10	2	39.3	43.1	8.8	0.6	0.5	20
100	20	4.8	4.6	4.3	3.4	3.3	3.0

formula applies to distant fields where the radiation term is the dominant component.

It is worth mentioning that higher amplitudes in the predicted field waveforms above a horizontally stratified ground compared with those above a perfect ground does not mean any gain of energy for the propagating wave. In fact, instantaneous or frequency-selective enhancement are possible while the fields satisfy the radiation condition that enforces the conservation of energy.

The simulations results of the horizontal electric field are on the other hand shown in Figure 12.6. The results obtained using the simplified formula proposed by Shoory *et al.* [28] appear to be in very good agreement with the FDTD results. It is also interesting to observe that the stratified ground results in the same oscillatory behaviour for the horizontal electric field as observed in the vertical electric field component shown in Figure 12.5.

The second set of simulations here are dedicated to observation point at close distances of  $\rho = 50$  m and  $\rho = 1000$  m and at height of  $z = 0.5$  m. Two different depths are assumed for the upper ground layer according to Figure 12.3 namely  $h_1 = 2$  m and  $h_1 = 5$  m. The channel base current and current propagation model is the same as those used in Figures 12.5 and 12.6. However, different values are used for ground electrical parameters that are adapted from Shoory *et al.* [29].  $\sigma_1 = 0.002$  S/m,  $\epsilon_{r1} = 5$ ,  $\sigma_2 = 0.1$  S/m,  $\epsilon_{r2} = 80$  are assumed as the conductivities and relative permittivities of each ground layer. For test of validity of the simplified formulations for the vertical electric field and the azimuthal magnetic field proposed by Wait and the simplified formulation for the horizontal electric field at elevated observation points proposed by Shoory *et al.* [29], use is made of a dedicated algorithm for the solution of Sommerfeld integrals presented by Delfino *et al.* [60]. The simulations results of the vertical electric field, azimuthal magnetic field and horizontal electric field are shown in Figure 12.7 for  $\rho = 50$  m and in Figure 12.8 for  $\rho = 1000$  m. The figures also include curves of the electromagnetic fields above a perfect ground. As can be seen, the agreement between simplified approaches and the exact solutions is excellent for both depths of the upper ground layer and distances of observation points from the channel base. Some differences – even though minimal – can be observed for the late-time response of the vertical electric field. It can be further seen that, for the vertical electric (Figure 12.7(a) and (d) and Figure 12.8(a) and (d)) and the azimuthal magnetic (Figure 12.7(c) and (f) and Figure 12.8(c) and (f)) fields, the results considering the two-layer horizontally stratified ground obtained using both exact and simplified approximate techniques

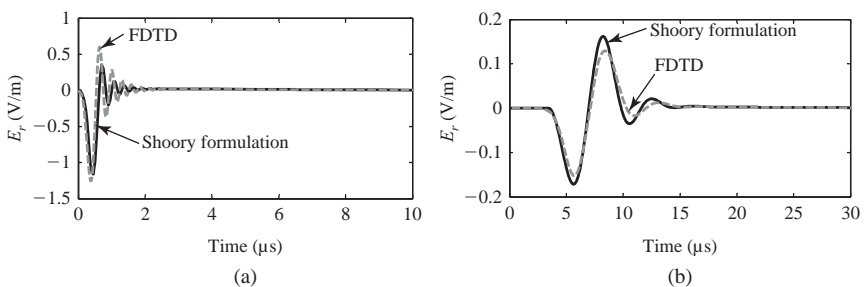


*Figure 12.6 Horizontal electric field at ground level at a distance of (a)  $\rho = 10$  km with  $h_1 = 2$  m and (b)  $\rho = 100$  km with  $h_1 = 20$  m obtained using the formula proposed by Shoory *et al.* [28] and FDTD technique [adapted from Shoory *et al.* [28]]*

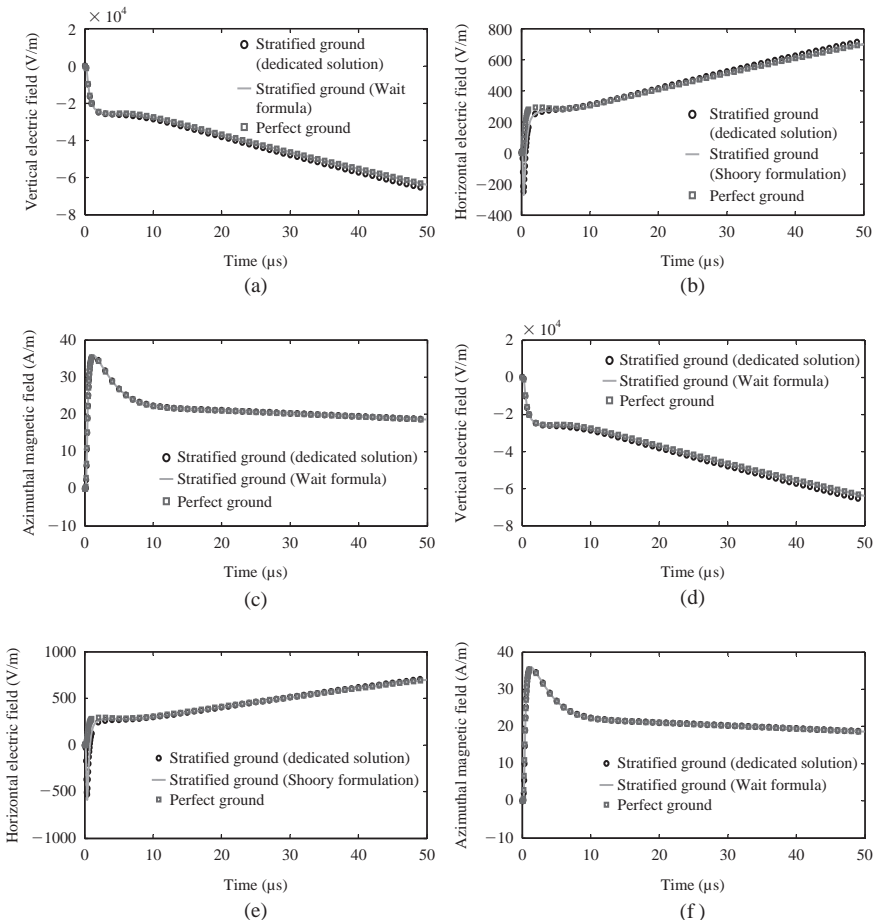
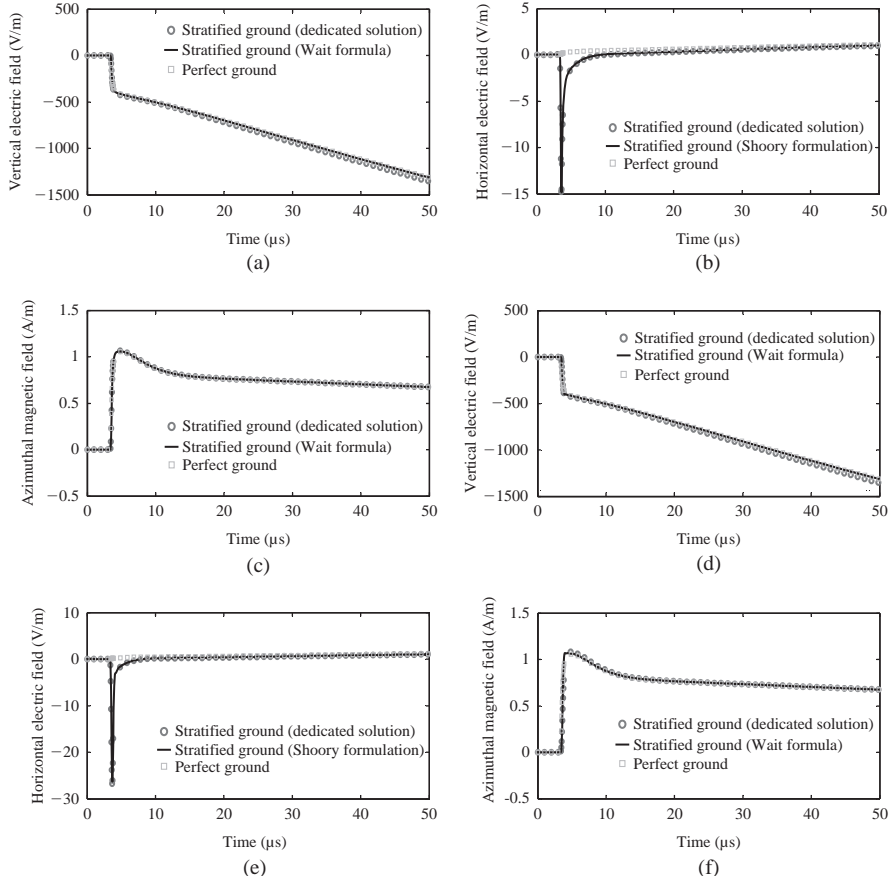


Figure 12.7 Vertical electric (a,d), horizontal electric (b,e), and azimuthal magnetic (c,f) field components for an observation point at the height of  $z = 0.5$  m above a two-layer horizontally stratified ground (see Figure 12.3) at a distance of  $\rho = 50$  m from the channel base. Height of upper ground layer is assumed to be  $h_1 = 2$  m for (a,b,c) and  $h_1 = 5$  m for (d,e,f) [adapted from Shoory et al. [29]]

are very similar to those obtained assuming a perfect ground. This is, however, not the case for the horizontal electric field waveforms shown in Figure 12.7(b) and (e) and Figure 12.8(b) and (e). While the horizontal electric field is essentially positively polarized at  $\rho = 50$  m, at  $\rho = 1000$  m, it is characterized by a bipolar waveshape with a dominant initial negative excursion followed by a positive excursion at the later times. Detailed discussion on this effect can be found in Reference 29.



*Figure 12.8* Vertical electric (a,d), horizontal electric (b,e) and azimuthal magnetic (c,f) field components for an observation point at the height of  $z = 0.5$  m above a two-layer horizontally stratified ground (see Figure 12.3) at a distance of  $\rho = 1000$  m from the channel base. Height of upper ground layer is assumed to be  $h_1 = 2$  m for (a,b,c) and  $h_1 = 5$  m for (d,e,f) [adapted from Shoory et al. [29]]

## 12.5 Propagation along a vertically stratified ground

The study of wave propagation along a vertically stratified ground goes back to the early works of Millington [70], Kirke [71], Suda [72] and Bremmer [73]. In particular, using an integral equation formulation, Bremmer [73] showed that the semi-empirical work of Millington [70] was valid for a wide range of frequencies and ground parameters. The recovery effect, namely the increase in the wave steepness when it passes from a poor conducting ground to a high conducting ground, can also be satisfactorily reproduced by Millington's approach. Wait [74] extended the

formulation of Bremmer [73] to low and medium frequencies by using the compensation theorem (e.g. [75]) and the mutual impedances between two vertical dipoles located above ground. A set of simulation results and related curves were presented and discussed by Wait and Householder [76] and Wait and Walters [77]. They showed that the simulation results are in acceptable agreement with measured data. Further confirmation of the technique was then given by King *et al.* [78], who reported excellent agreement between the Wait formulation [74] and experimental data obtained from reduced scale experiments carried out at the frequency of 4.765 GHz.

The main idea behind the Wait's formulation is the use of the surface impedance concept as discussed earlier in this chapter for the cases of homogeneous and horizontally stratified grounds [15, 79].

The application of these studies to the analysis of lightning electromagnetic field propagation was first carried out by Cooray and Ming [13] and Cooray and Perez [14]. It was specifically shown by Cooray and Ming [13] that, when the propagation is over a mixed (sea-land) path whose land portion is less than a few hundred metres long, the attenuation of the vertical electric field is not significant. However, the peak time derivative of the vertical electric field would suffer significant attenuation of about 40% in propagating more than a few tens of metres over the land portion. Such a theoretical development was also used by Cooray and Ming [13] for the interpretation of the experimental data by Willett *et al.* [80] and Cooray [81] where the measuring station was located a few tens of metres from the sea-land interface. Good agreement was found between measured waveforms and theoretical predictions for vertical electric fields and their time derivatives. The errors in predicting peak current and peak current derivative from peak vertical electric field and peak vertical electric field derivative were also discussed by Cooray and Ming [13]. Such a theoretical analysis was later used by Michishita *et al.* [82], to estimate the ground electrical parameters from measured horizontal and vertical electric fields radiated by distant lightning.

In fact, the accuracy of the simplified analytical expressions for the case of a mixed-path (vertically stratified) ground has been only studied using a limited number of reduced scale experiments and only in the frequency domain [78]. The first systematic analysis for a such problem is again due to Shoory *et al.* [58, 83]. In this section, we present the simplified formulations and their validation taking as reference full-wave simulations obtained using the FDTD technique.

### 12.5.1 Simplified approaches for the lightning far field above a vertically stratified ground

#### 12.5.1.1 Formulations

In the same way we have done for the case of a horizontally stratified ground, we use the subscript  $str,v$  to represent the attenuation function above a two-layer, vertically stratified ground. The expressions for the attenuation function of a two-layer, vertically stratified ground (schematized in Figure 12.9) needed in (12.9)–(12.11) is given in what follows in two different forms. Note once again that

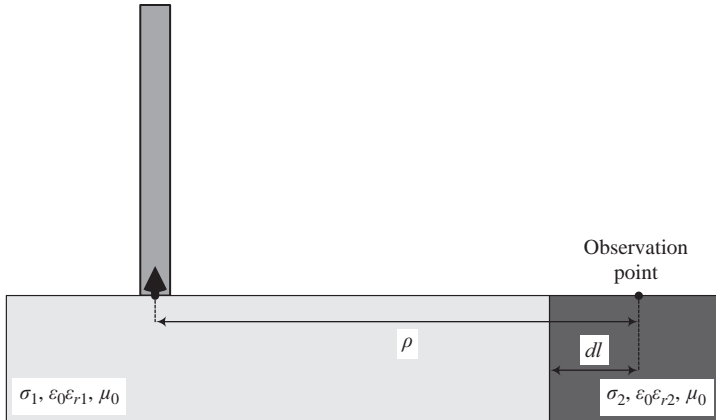


Figure 12.9 Propagation of lightning-radiated electromagnetic field over a two-layer vertically stratified ground

the attenuation function corresponds to a dipole located in the lower end of the channel. The two different expressions for the mixed-path ground attenuation function given by Wait and Householder [76], Wait [84, 85] and Wait and Walters [77, 86] read

$$F_{str,v}(\rho) = F_1(\rho) - \sqrt{\frac{\gamma_0 \rho}{2\pi}} [\Delta_2 - \Delta_1] \int_0^{\rho} \frac{F_1(\rho - x) F_2(x)}{\sqrt{x(\rho - x)}} dx \quad (12.31)$$

$$F_{str,v}(\rho) = F_2(\rho) - \sqrt{\frac{\gamma_0 \rho}{2\pi}} [\Delta_1 - \Delta_2] \int_0^{\rho-dl} \frac{F_2(\rho - x) F_1(x)}{\sqrt{x(\rho - x)}} dx \quad (12.32)$$

where  $F_1(x)$  and  $F_2(x)$  are the attenuation functions of each section of the ground represented as a function of the horizontal distance from the source to the observation point, defined as follows:

$$F_n(x) = 1 - j\sqrt{\pi p_n} e^{-p_n} erfc(j\sqrt{p_n}) \quad (12.33)$$

where

$$p_n(x) = -0.5\gamma_0 x \Delta_n^2 \quad (12.34)$$

in which  $\Delta_n$  ( $n = 1, 2$ ) is the normalized surface impedance of each ground section defined as (e.g. by Hill and Wait [79])

$$\Delta_n = \frac{\sqrt{j\omega \epsilon_0 [\sigma_n + j\omega \epsilon_0 (\epsilon_{rn} - 1)]}}{\sigma_n + j\omega \epsilon_0 \epsilon_{rn}} \quad (12.35)$$

Hill and Wait [22] have suggested to use (12.31) when  $|\Delta_2| < |\Delta_1|$ , and to use (12.32) when  $|\Delta_2| > |\Delta_1|$ . They have also shown that there are singularities in the integrands of (12.31) and (12.32), and they have provided the necessary steps to remove them. The final results are given below

$$F_{str,v}(\rho) = F_1(\rho) - \sqrt{\frac{\gamma_0 \rho}{2\pi}} [\Delta_2 - \Delta_1] \left\{ 2 \sqrt{\frac{\delta}{\rho}} F_1(\rho) + \int_{\delta}^{\rho} \frac{F_1(\rho-x) F_2(x)}{\sqrt{x(\rho-x)}} dx \right\} \quad (12.36)$$

$$F_{str,v}(\rho) = F_2(\rho) - \sqrt{\frac{\gamma_0 \rho}{2\pi}} [\Delta_1 - \Delta_2] \left\{ 2 \sqrt{\frac{\delta}{\rho}} F_2(\rho) + \int_{\delta}^{\rho} \frac{F_2(\rho-x) F_1(x)}{\sqrt{x(\rho-x)}} dx \right\} \quad (12.37)$$

where  $\delta$  is a small distance over which one can assume the attenuation functions to be constant.

It is to be emphasized that the above-simplified formulations are obtained assuming the stationary phase approximation or, equivalently, the line-of-sight assumption for wave propagation between the channel base and the observation point. In this regard, the formulations are valid for either straight or circular boundary line between the two media in Figure 12.9.

### 12.5.1.2 Numerical results

For the time-domain simulations, similar to the case of horizontally stratified ground, we adopted again the MTLE model of Nucci *et al.* [64] and Rachidi and Nucci [65] with a current decay constant  $\lambda = 2$  km and a return-stroke speed of  $v = 1.5 \times 10^8$  m/s. The channel base current is that of Rachidi *et al.* [66]. Two cases are considered for the parameters of each ground layer according to Figure 12.9:

- case 1:  $\sigma_1 = 0.001$  S/m,  $\epsilon_{r1} = 10$ , and  $\sigma_2 = 4$  S/m,  $\epsilon_{r2} = 30$ ;
- case 2:  $\sigma_1 = 4$  S/m,  $\epsilon_{r1} = 30$ , and  $\sigma_2 = 0.001$  S/m,  $\epsilon_{r2} = 10$ .

Time-domain simulation results of the vertical electric field at the ground level and at a distance of  $\rho = 100$  km from the channel base for a mixed-path ground with  $dl = 25$  km and with the electrical parameters for case 1 and case 2 are shown in Figures 12.10(a) and 12.10(b) respectively. The curves are obtained using the two previously introduced formulations (12.36) and (12.37). The figure also includes two curves of the limiting cases obtained when the ground is homogeneous with the parameters of medium 1 and medium 2, respectively. It is seen that the two formulations predict almost the same results for the vertical electric field. It can also be observed that the vertical electric field over a vertically stratified ground falls in between the two curves of limiting homogeneous ground cases confirming the conclusions given in Chapter 7 of Reference 63. Further, by virtue of the reciprocity theorem, the two formulations are transparent to the direction of wave propagation from one medium to the other. In other words, by interchanging the lightning channel and the observation point, the wave at the observation point does not change. As mentioned earlier in this paper, it is computationally more efficient in

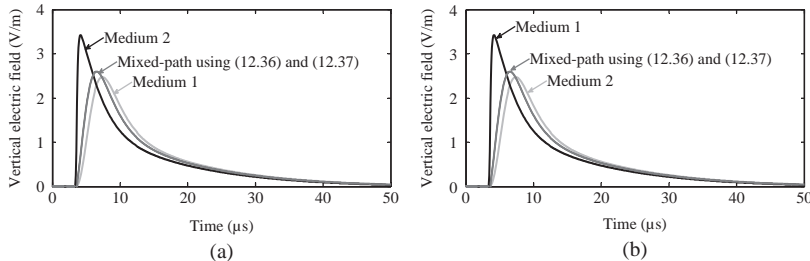


*Figure 12.10* Vertical electric field at ground level at a distance of  $\rho = 100$  km from the channel base over mixed-path ground with  $dl = 25$  km obtained using the two formulations of (12.36) and (12.37) (a) case 1 with  $\sigma_1 = 0.001$  S/m,  $\epsilon_{r1} = 10$ ,  $\sigma_2 = 4$  S/m, and  $\epsilon_{r2} = 30$  and (b) case 2 with  $\sigma_1 = 4$  S/m,  $\epsilon_{r1} = 30$ ,  $\sigma_2 = 0.001$  S/m, and  $\epsilon_{r2} = 10$  [adapted from Shoory et al. [83]]

this case for the curves of Figure 12.10(a) to use (12.36) instead of (12.37) and for the curves of Figure 12.10(b) to use (12.37) instead of (12.36).

### 12.5.2 Test and validation of the simplified formulae

In this section, the reviewed simplified formulations for a vertically stratified ground are validated against the same FDTD simulation technique described in the previous section for a horizontally stratified ground. Two sets of simulations have been performed for a distance of  $\rho = 10$  km according to the two different mixed-path arrangements of case 1 and case 2. The simulation domain for the FDTD technique is shown in Figure 12.11. In the FDTD simulations, a value for the time step of 2 ns was considered. The overall time interval was set to  $T_{max} = 50$  μs. This corresponds to 25000 time steps. The spatial discretization interval was chosen to be 2 m. According to Figure 12.11, the simulation domain was truncated using the first-order Mur absorbing boundary conditions at  $\rho_{max} = 11$  km,  $z_{max} = 7.5$  km and  $z_{min} = 100$  m. Making use of the axial symmetry of the problem (left-most boundary coinciding with the z-axis), this corresponds to  $5500 \times 3800$  spatial cells. Note that the axial symmetry of the problem in such a two-dimensional axially symmetric problem implies a circular boundary between the two media for which as mentioned earlier the simplified formulations are still valid.

Note that a shorter distance of  $\rho = 10$  km (instead of  $\rho = 100$  km in Figure 12.10) was used in this section due to the lack of computational resources necessary for simulations in the FDTD technique. In fact, with the available resources, the smallest spatial discretization interval for  $\rho = 100$  km satisfying the *Courant* stability criterion [87] is 20 m, which imposes significant numerical dispersion on the predicted benchmark waveforms. In fact, for the case of propagation along a lossy half space, numerical dispersion might occur because of the dependence of wave propagation speed on frequency. In general, the bigger the spatial discretization interval, the larger the numerical dispersion. While for an observation point at

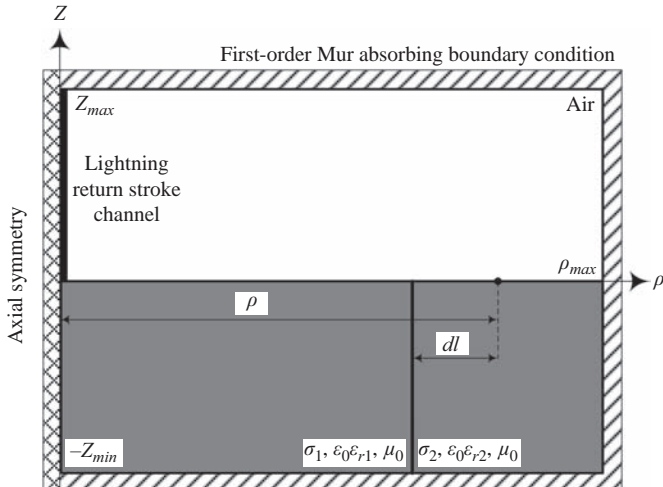


Figure 12.11 Side view of the simulation domain of the FDTD technique used for the validation of the simplified approaches. We used  $\rho_{max} = 11$  km,  $z_{max} = 7.5$  km and  $z_{min} = 100$  m

$\rho = 10$  km the results obtained using a spatial step of 2 m are free from numerical dispersion, this is not the case for an observation point at  $\rho = 100$  km with spatial step of 20 m. In order to minimize this effect, a finer mesh should be considered.

Simulation results of a vertical electric field at a distance of  $\rho = 10$  km from the channel base at ground level according to the case 1 are shown in Figure 12.12 for four different values of  $dl$ , namely 7.5 km, 2.5 km, 0.5 km and 0.1 km. The same results for the case 2 are shown in Figure 12.13. It can be seen that Wait's formulation appears to be quite accurate in reproducing the vertical electric field waveforms.

Table 12.2 presents the values of the field peaks and zero-to-peak rise times predicted by Wait's formulation and by the FDTD method. It can be seen that Wait's formulation can predict field peaks with an error of less than 4.8% and field rise times with an error of less than 18.0%.

## 12.6 Summary

In this chapter, we provided a review of simplified formulations for obtaining propagation effects on lightning-radiated electromagnetic fields for the case of (i) a homogeneous lossy ground, (ii) a two-layer horizontally stratified ground and (iii) a two-layer vertically stratified ground. The validity assessment of the simplified approaches was evaluated using as reference full-wave results obtained by either FDTD implementation or the numerical evaluation of Sommerfeld integrals using dedicated algorithms.

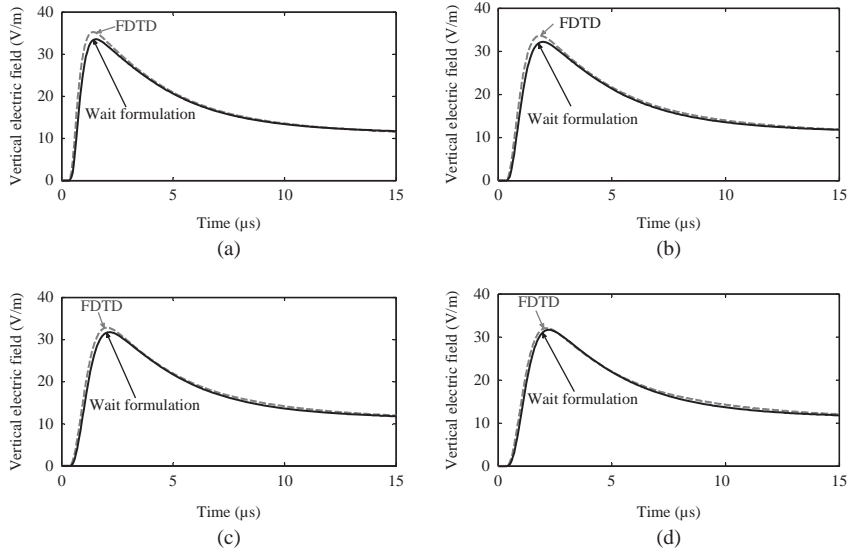


*Figure 12.12* Vertical electric field at the surface of a mixed-path ground at a distance of  $\rho = 10$  km for case 1 in Table 12.1, (a)  $dl = 7.5$  km, (b)  $dl = 2.5$  km, (c)  $dl = 0.5$  km and (d)  $dl = 0.1$  km [adapted from Shoory et al. [83]]

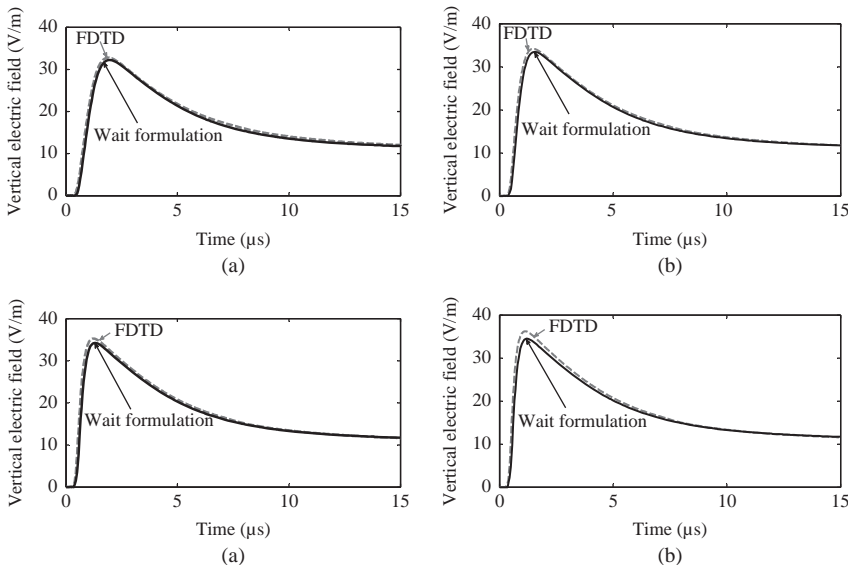


*Figure 12.13* Vertical electric field at the surface of a mixed-path ground at a distance of  $\rho = 10$  km for case 1 in Table 12.1, (a)  $dl = 7.5$  km, (b)  $dl = 2.5$  km, (c)  $dl = 0.5$  km and (d)  $dl = 0.1$  km [adapted from Shoory et al. [83]]

Table 12.2 Peak and rise times of the vertical electric field predicted using Wait's formulation and FDTD simulation [adapted from Shoory *et al.* [83]]

Case no	$dl$ (km)	Peak (V/m)			Rise time ( $\mu$ s)		
		Wait	FDTD	Error (%)	Wait	FDTD	Error (%)
1	7.5	33.5	35.2	4.8	1.3	1.1	18
	2.5	32.2	33.6	4.2	1.6	1.5	6.3
	0.5	31.8	32.8	3.0	1.8	1.7	5.9
	0.1	31.6	32.1	1.6	2	1.8	10
2	7.5	32.2	32.7	1.5	1.6	1.6	0.0
	2.5	33.6	34.1	1.5	1.3	1.2	8.3
	0.5	34.4	35.3	2.5	1.0	0.9	11.1
	0.1	34.7	36.2	4.1	0.9	0.8	12.5

The simplified approaches are based on the concept of the ground surface impedance and its corresponding attenuation function.

For the case of a homogeneous ground, the CR formula has shown to be, in general, accurate for typical values of ground conductivity. For close distances and for observation points on the ground surface, the formula of Barbosa *et al.* that includes the low-frequency conduction current in the ground should be used.

For the case of a two-layer horizontally stratified ground, it was shown that the results obtained using the simplified approaches are in excellent agreement with exact results in near (50 m), intermediate (1000 m) and far (100 km) distance ranges. It was seen that, at near and intermediate distance ranges and for elevated observation points, vertical electric and azimuthal magnetic field components appear not to be appreciably affected by the ground finite conductivity and can be evaluated assuming the ground as a perfectly conducting ground. On the other hand, the horizontal electric field above a horizontally stratified ground is very much affected by the ground electrical parameters. Further, the recent formula proposed by Shoory *et al.* was shown to reproduce in a satisfactory manner the horizontal electric field above a two-layer ground. For far observation points and for the cases where the upper ground layer has a lower conductivity than the lower layer, it was observed that the waveforms of the vertical electric field along a horizontally stratified ground feature an oscillatory behaviour in their early-time response. The peak value of the field was larger than that corresponding to the case of a perfect ground. It was shown that these features have been reproduced accurately in the simplified formulations in comparison with the reference waveforms based on the FDTD technique.

Finally, for the case of a two-layer vertically stratified ground, two different formulations proposed by Wait depending on the relative values of the ground surface impedances were discussed. Both formulations give nearly the same results for the time-domain electric field. However, depending on the values of the normalized surface impedance for each ground section, the use of one of the two formulations is computationally more efficient. The accuracy of the Wait

formulations was examined taking as reference full-wave simulations obtained using the FDTD technique. It was shown that Wait's simplified formulas are able to reproduce the distant field peak and waveshape with a good accuracy.

## References

1. F. Rachidi, C. A. Nucci, I. M. and C. Mazzetti, "Influence of a lossy ground on lightning-induced voltages on overhead lines", *IEEE Transactions on Electromagnetic Compatibility*, vol. 38, pp. 250–263, 1996
2. V. A. Rakov and F. Rachidi, "Overview of recent progress in lightning research and lightning protection", *IEEE Transactions on Electromagnetic Compatibility*, vol. 51, pp. 428–442, August 2009
3. F. Delfino, R. Procopio, M. Rossi, F. Rachidi and C. A. Nucci, "An algorithm for the exact evaluation of the underground lightning electromagnetic fields", *IEEE Transactions on Electromagnetic Compatibility*, vol. 49, pp. 401–411, May 2007
4. A. Mimouni, F. Delfino, R. Procopio and F. Rachidi, "On the computation of underground electromagnetic fields generated by lightning: A comparison between different approaches", in *IEEE PES PowerTech*, Lausanne, Switzerland, 2007
5. F. Delfino, R. Procopio and M. Rossi, "Lightning return stroke current radiation in presence of a conducting ground: 1. Theory and numerical evaluation of the electromagnetic fields", *Journal of Geophysical Research*, vol. 113, 2008
6. F. Delfino, R. Procopio, M. Rossi, F. Rachidi and C. A. Nucci, "Lightning return stroke current radiation in presence of a conducting ground: 2. Validity assessment of simplified approaches", *Journal of Geophysical Research*, vol. 113, 2008
7. A. Shoory, R. Moini, S. H. H. Sadeghi and V. A. Rakov, "Analysis of lightning-radiated electromagnetic fields in the vicinity of lossy ground", *IEEE Transactions on Electromagnetic Compatibility*, vol. 47, pp. 131–145, Feb 2005
8. A. Mimouni, F. Rachidi and Z. Azzouz, "Electromagnetic environment in the immediate vicinity of a lightning return stroke", *Journal of Lightning Research*, vol. 2, pp. 64–75, 2007
9. Y. Baba and V. A. Rakov, "Evaluation of lightning return stroke electromagnetic models", in *International Conference on Lightning Protection (ICLP)*, Uppsala, Sweden, 2008, pp. 1a11–1a18
10. A. Mimouni, F. Rachidi and Z. E. Azzouz, "A finite-difference time-domain approach for the evaluation of electromagnetic fields radiated by lightning strikes to tall structures", *Journal of Electrostatics*, vol. 66, pp. 504–513, September 2008
11. V. Cooray and S. Lundquist, "Effects of propagation on the rise times and the initial peaks of radiation fields from return strokes", *Radio Science*, vol. 18, pp. 409–15, 1983

12. V. Cooray, "Effects of propagation on the return stroke radiation fields", *Radio Science*, vol. 22, pp. 757–68, 1987
13. V. Cooray and Y. Ming, "Propagation effects on the lightning-generated electromagnetic fields for homogeneous and mixed sea-land paths", *Journal of Geophysical Research*, vol. 99, pp. 10641–10652, 1994
14. V. Cooray and H. Perez, "Propagation effects on the first return stroke radiation fields: homogenous paths and mixed two section paths", in *22nd International Conference Lightning Protection (ICLP)*, Budapest, 1994, pp. R1a-06
15. J. R. Wait, "The ancient and modern history of EM ground-wave propagation", *Antennas and Propagation Magazine, IEEE*, vol. 40, pp. 7–24, 1998
16. V. A. Rakov, "Engineering models of the lightning return stroke", in *International Symposium on Lightning Protection (VII SIPDA)*, Curitiba, Brazil, 2003
17. R. Thottappillil, V. Rakov and M. Uman, "Distribution of charge along the lightning channel: relation to remote electric and magnetic fields and to return-stroke models", *Journal of Geophysical Research*, vol. 102, pp. 6987–7006, 1997
18. V. A. Rakov and M. A. Uman, *Lightning: Physics and Effects*, United Kingdom: Cambridge University Press, 2003
19. M. Rubinstein and M. A. Uman, "On the radiation field turn-on term associated with traveling current discontinuities in lightning", *Journal of Geophysical Research*, vol. 95, pp. 3711–3713, 1990
20. M. Rubinstein and M. A. Uman, "Transient electric and magnetic fields associated with establishing a finite electrostatic dipole, revisited", *IEEE Transactions on Electromagnetic Compatibility*, vol. 33, pp. 312–20, 1991
21. V. Cooray, "Horizontal electric field above- and underground produced by lightning flashes", *Electromagnetic Compatibility, IEEE Transactions on*, vol. 52, pp. 936–943, 2010
22. D. A. Hill and J. R. Wait, "HF ground wave propagation over mixed land, sea, and sea-ice paths", *Geoscience and Remote Sensing, IEEE Transactions on*, vol. GE-19, pp. 210–216, 1981
23. D. A. Hill and J. R. Wait, "HF radio wave transmission over sea ice and remote sensing possibilities", *Geoscience and Remote Sensing, IEEE Transactions on*, vol. GE-19, pp. 204–209, 1981
24. A. Sommerfeld, "The propagation of electromagnetic waves in wireless telegraphy", *Annual Physics*, vol. 81, pp. 1135–1153, 1926
25. A. Baños, *Dipole Radiation in the Presence of a Conducting Half-Space*, New York, USA: Oxford, 1966
26. K. A. Norton, "The propagation of radio waves over the surface of the earth and in the upper atmosphere, PART I", *Proceedings of the IRE*, vol. 24, pp. 1367–1387, 1936
27. K. A. Norton, "The propagation of radio waves over the surface of the earth and in the upper atmosphere, PART II", *Proceedings of the IRE*, vol. 25, pp. 1203–1236, 1937

28. A. Shoory, A. Mimouni, F. Rachidi, V. Cooray and M. Rubinstein, “Lightning horizontal electric fields above a two-layer ground”, in *International Conference on Lightning Protection (ICLP)*, Cagliari, Italy, 2010, pp. 1285, 1–1285, 5
29. A. Shoory, F. Rachidi, F. Delfino, R. Procopio and M. Rossi, “Lightning electromagnetic radiation over a stratified conducting ground — 2. Validity of simplified approaches”, *Journal of Geophysical Research*, vol. 116, p. 10, 2011
30. M. Abramowitz and I. Stegun, *Handbook of Mathematical Functions*, New York: Dover, 1970
31. R. L. Gardner, “Effect of the propagation path on lightning-induced transient fields”, *Radio Science*, vol. 16, pp. 377–84, 1981
32. D. M. LeVine, L. Gesell and M. Kao, “Radiation from lightning return strokes over a finitely conducting Earth”, *Journal of Geophysical Research*, vol. 91, pp. 897–908, 1986
33. J. R. Johler and C. M. Lilley, “Ground-conductivity determinations at low radio frequencies by an analysis of the sferic signatures of thunderstorms”, *Journal of Geophysical Research*, vol. 66, pp. 3233–3244, 1961
34. R. J. Fisher and M. A. Uman, “Measured electric field risetimes for first and subsequent lightning return strokes”, *Journal of Geophysical Research*, vol. 77, pp. 399–406, 1972
35. Y. Tao Lin and M. A. Uman, “Electric radiation fields of lightning return strokes in three isolated Florida thunderstorms”, *Journal of Geophysical Research*, vol. 78, pp. 7911–7915, 1973
36. E. P. Krider and G. J. Radda, “Radiation field wave forms produced by lightning stepped leaders”, *Journal of Geophysical Research*, vol. 80, pp. 2653–2657, 1975
37. J. A. Tiller, M. A. Uman, Y. T. Lin, R. D. Brantley and E. P. Krider, “Electric field statistics for close lightning return strokes near Gainesville, Florida”, *Journal of Geophysical Research*, vol. 81, pp. 4430–4434, 1976
38. V. Cooray, “On the validity of several approximate theories used in quantifying the propagation effects on lightning generated electromagnetic fields”, in *VIII SIPDA*, Sao Paulo, Brazil, pp. 112–119, 2005
39. V. Cooray, “On the accuracy of several approximate theories used in quantifying the propagation effects on lightning generated electromagnetic fields”, *IEEE Transactions on Antennas and Propagation*, vol. 56, no. 7, pp. 1960–1967, 2008
40. V. Cooray, “Propagation effects due to finitely conducting ground on lightning generated magnetic fields using Sommerfeld’s integrals”, *IEEE Transactions on Electromagnetic Compatibility*, 2009
41. V. Cooray, “Propagation effects due to finitely conducting ground on lightning generated magnetic fields using Sommerfeld’s integrals”, presented at the IX SIPDA, Foz do Iguaçu, Brazil, 2007
42. V. Cooray, “Horizontal fields generated by return strokes”, *Radio Science*, vol. 27, pp. 529–537, July-August 1992

43. M. Rubinstein, "An approximate formula for the calculation of the horizontal electric field from lightning at close, intermediate, and long range", *IEEE Transactions on Electromagnetic Compatibility*, vol. 38, pp. 531–535, 1996
44. J. R. Wait, "On the wave tilt at high frequencies-a personal view", *Electromagnetic Compatibility, IEEE Transactions on*, vol. 39, p. 65, 1997
45. A. Zeddam and P. Degauque, "Current and voltage induced on telecommunications cable by a lightning return stroke", in *Lightning Electromagnetics*, R. L. Gardner, Ed., New York: Hemisphere, 1990, pp. 377–340
46. C. Caligaris, F. Delfino and R. Procopio, "Cooray-rubinstein formula for the evaluation of lightning radial electric fields: Derivation and implementation in the time domain", *IEEE Transactions on Electromagnetic Compatibility*, vol. 50, pp. 194–197, 2008
47. C. F. Barbosa and J. O. S. Paulino, "An approximate time-domain formula for the calculation of the horizontal electric field from lightning", *IEEE Transactions on Electromagnetic Compatibility*, vol. 49, pp. 593–601, 2007
48. C. F. Barbosa, J. O. S. Paulino, G. C. de Miranda, W. do Couto Boaventura, F. E. Nalin, S. Person and A. Zeddam, "Measured and modeled horizontal electric field from rocket-triggered lightning", *IEEE Transactions on Electromagnetic Compatibility*, vol. 50, pp. 913–920, 2008
49. C. F. Barbosa and J. O. S. Paulino, "A time-domain formula for the horizontal electric field at the earth surface in the vicinity of lightning", in *X-SIPDA*, Curitiba, Brazil, 2009, pp. 477–481
50. V. I. Kravchenko, "Investigation of electromagnetic environment produced by the lightning discharge ‘cloud-earth’". in *EMC 92 international wroclaw symposium on electromagnetic compatibility*, 1992
51. A. Shoory, F. Rachidi, M. Rubinstein and R. Thottappillil, "On the measurement and calculation of horizontal electric fields from lightning", *IEEE Transaction on Electromagnetic Compatibility*, 2010
52. J. R. Wait, "Propagation effects for electromagnetic pulse transmission", in *Proceedings of the IEEE*, vol. 74, pp. 1173–1181, 1986
53. J. R. Wait, "Radiation from a vertical electric dipole over a stratified ground", *I.R.E. Transactions on Antennas and Propagation*, vol. 1, pp. 9–11, 1953
54. J. R. Wait, "On the theory of transient electromagnetic sounding over a stratified earth", *Canadian Journal of Physics*, vol. 50, pp. 1055–1061, June 1972
55. Y. Ming and V. Cooray, "Electromagnetic radiation fields generated by lightning return strokes over a stratified ground", in *22nd International Conference on Lightning Protection (ICLP)*, Budapest, pp. R1c-05, 1994
56. V. Cooray and K. L. Cummins, "Propagation effects caused by stratified ground on electromagnetic fields of return strokes", presented at the 20th International Lightning Detection Conference & 2nd International Lightning Meteorology Conference, Tucson, Arizona, USA, 2008
57. J. R. Wait, "Electromagnetic surface impedance for a layered earth for general excitation", *Radio Science*, vol. 15, 1980

58. A. Shoory, F. Rachidi, V. Cooray, R. Moini and S. H. H. Sadeghi, “On simplified approaches for the evaluation of lightning electromagnetic fields above stratified ground”, in *X-SIPDA*, Curitiba, Brazil, 2009, pp. 483–488
59. A. Shoory, A. Mimouni, F. Rachidi, V. Cooray, R. Moini and S. H. H. Sadeghi, “Validity of simplified approaches for the evaluation of lightning electromagnetic fields above a horizontally stratified ground”, *IEEE Transactions on Electromagnetic Compatibility*, doi: 10.1109/TEMC.2010.2045229, vol. 52, pp. 657–663, 2010
60. F. Delfino, R. Procopio, M. Rossi, A. Shoory and F. Rachidi, “Lightning electromagnetic radiation over a stratified conducting ground: Theory and numerical evaluation of the electromagnetic fields”, *Journal of Geophysical Research*, vol. 116, p. 8, 2011
61. J. R. Wait, *Electromagnetic waves in stratified media*, Oxford: IEEE Press, 1996
62. W. C. Chew, *Waves and Fields in Inhomogeneous Media*, New York: IEEE Press, 1995
63. V. Cooray, *The Lightning Flash*, United Kingdom: IET, 2003
64. C. A. Nucci, C. Mazzetti, F. Rachidi and M. Ianoz, “On lightning return stroke models for LEMP calculations”, in *19th International Conference on Lightning Protection (ICLP)*, Graz, Austria, 1988
65. F. Rachidi and C. A. Nucci, “On the Master, Uman, Lin, Standler and the modified transmission line lightning return stroke current models”, *Journal of Geophysical Research*, vol. 95, pp. 20389–94, 1990
66. F. Rachidi, W. Janischewskyj, A. M. Hussein, C. A. Nucci, S. Guerrieri, B. Kordi and J. S. Chang, “Current and electromagnetic field associated with lightning return strokes to tall towers”, *IEEE Transactions on Electromagnetic Compatibility*, vol. 43, pp. 356–367, August 2001
67. K. Berger, R. B. Anderson and H. Kroninger, “Parameters of lightning flashes”, *Electra*, vol. 41, pp. 23–37, 1975
68. K. S. Yee, “Numerical solution of initial boundary value problems involving Maxwell’s equations in isotropic media”, *IEEE Transactions on Antennas and Propagation*, vol. 14, pp. 302–307, 1966
69. A. Mimouni, F. Rachidi and Z. Azzouz, “Electromagnetic fields in the immediate vicinity of a tower struck by lightning”, in *International Conference on Lightning Protection (ICLP)*, Uppsala, Sweden, 2008, pp. 3b21–3b28
70. G. Millington, “Ground wave propagation over an inhomogeneous smooth earth, part 1”, *Proceedings of the IEE*, 1949
71. H. L. Kirke, “Calculation of ground wave field strength over a composite land path”, *Proceedings of the IRE*, vol. 96, 1949
72. K. Suda, “Field strength calculations-new method for mixed paths”, *Wireless Engineer*, vol. 31, 1954
73. H. Bremmer, “The extension of the Sommerfeld’s formula for the propagation of radio waves over a flat earth to different conductivities of the soil”, *Physica*, vol. 20, 1954
74. J. R. Wait, “Mixed path ground wave propagation: 1. short distances”, *Journal of Research NBS*, vol. 57, pp. 1–15, July 1956

75. G. D. Monteath, *Application of the Electromagnetic Reciprocity Principle*, Oxford, England: Pergamon Press, 1973
76. J. R. Wait and J. Householder, “Mixed-path ground wave propagation: 2. Larger distances”, *Journal of Research NBS*, vol. 59, pp. 19–26, 1957
77. J. R. Wait and L. Walters, “Curves for ground wave propagation over mixed land and sea paths”, *Antennas and Propagation, IEEE Transactions on*, vol. 11, pp. 38–45, 1963
78. R. J. King, S. H. Cho and D. H. Jaggard, “Height-gain experimental data for ground wave propagation, 2, Heterogeneous paths”, *Radio Science*, vol. 8, pp. 17–22, 1973
79. D. A. Hill and J. R. Wait, “Ground wave attenuation function for a spherical earth with arbitrary surface impedance”, *Radio Science*, vol. 15, pp. 637–643, May-June 1980
80. J. C. Willett, V. P. Idone, R. E. Orville, C. Leteinturier, A. Eybert Berard, L. Barret and E. P. Krider, “An experimental test of the ‘transmission-line model’ of electromagnetic radiation from triggered lightning return strokes”, *Journal of Geophysical Research*, vol. 93, pp. 3867–3878, 1988
81. V. Cooray, “A novel method to identify the radiation fields produced by positive return strokes and their submicrosecond structure”, *Journal of Geophysical Research*, vol. 91, pp. 7907–7911, 1986
82. K. Michishita, M. Ishii and J.-I. Hojo, “Measurement of horizontal electric fields associated with distant cloud-to-ground strokes”, *Journal of geophysical Research*, vol. 101, pp. 3861–3867, 1996
83. A. Shoory, A. Mimouni, F. Rachidi, V. Cooray and M. Rubinstein, “On the accuracy of approximate techniques for the evaluation of lightning electromagnetic fields along a mixed propagation path”, *Radio Science*, vol. 46, p. 8, 2011
84. J. R. Wait, “On the theory of mixed-path ground-wave propagation on a spherical earth”, *Journal of Research NBS*, vol. 65D, pp. 401–410, July-August 1961
85. J. R. Wait, “Recent analytical investigations of electromagnetic ground wave propagation over inhomogeneous earth models”, *Proceedings of the IEEE*, vol. 62, pp. 1061–1072, 1974
86. J. R. Wait and L. Walters, “Correction to ‘Curves for ground wave propagation over mixed land and sea paths’,” *Antennas and Propagation, IEEE Transactions on*, vol. 11, pp. 329–329, 1963
87. R. Courant, K. Friedrichs and H. Lewy, “On the partial difference equations of mathematical physics”, *IBM Journal (English translation of the 1928 German original paper)*, pp. 215–234, 1967



---

## *Chapter 13*

# **Lightning electromagnetic field calculations in presence of a conducting ground: the numerical treatment of Sommerfeld's integrals**

*Federico Delfino<sup>1</sup>, Renato Procopio<sup>1</sup> and Mansueto Rossi<sup>1</sup>*

---

### **13.1 Introduction**

During the past decades, much attention has been paid to the problem of the interaction between lightning electromagnetic fields and overhead and buried conductors. This has led to the formulation of different reliable field-to-transmission line coupling models (Paul, 1994; Tesche *et al.*, 1997). All these models require an accurate evaluation of the lightning electromagnetic fields along the line, taking into account the effect of the ground finite conductivity, since the approximation of perfectly conducting ground becomes unacceptable especially in the evaluation of the horizontal electric field (Rachidi *et al.*, 1996).

Different models can be adopted to represent a lossy soil; the simplest one assumes that both the conductivity  $\sigma$  and the relative permittivity  $\varepsilon_r$  are constant. Enhanced representations could then consider the influence of the working frequency on  $\sigma$  and  $\varepsilon_r$  or their dependence on the depth, in the case of a horizontally stratified ground. In the following, such configurations will be examined with the final aim to derive lightning field expressions (radial and vertical electric field, azimuthal magnetic one) and to propose numerical procedures for their efficient and accurate calculation. It is important to highlight from the beginning that the presence of a ground with finite conductivity will be responsible of the appearance in field expressions of the so-called Sommerfeld's integrals. The numerical evaluation of such integrals represent a hard task due to the singular, oscillating and divergent behaviour of their integrands and, as a consequence, suitable strategies have to be identified to guarantee at the same time precision in execution and acceptable computational costs.

The chapter is organized as follows. In Section 13.2, the ground parameters will be considered constant; under such assumption both the derivation and the calculation of the lightning electromagnetic field components will be presented,

<sup>1</sup>Department of Naval & Electrical Engineering – Electrical Section, University of Genoa, Via Opera Pia 11a, I-16145 Genova, Italy. Email: federico.delfino@unige.it.

together with some guidelines to discover the cases in which the well-known approximate approaches provide accurate results.

Next, in Section 13.3, the influence of the frequency-dependent behaviour of the ground electrical parameters will be studied. Finally, in Section 13.4, the problem of the derivation of the lightning electromagnetic fields over a stratified conducting ground will be faced and the effect of the stratification on the field waveforms will be analysed.

## **13.2 Lightning electromagnetic field calculation in presence of a lossy ground with constant electrical parameters**

In order to determine the electromagnetic field produced by a lightning current distribution along a channel of height  $H$  over a conducting half-space, one has first to solve the elementary problem of the vertical electric dipole radiation. Such problem was solved by Arnold Sommerfeld in his works (Sommerfeld, 1909, 1949), where the complete theory that underlies the derivation of the Green functions for any kind of scattering problem in presence of an absorbing earth is presented. Although the work by Sommerfeld set up the theoretical bases, further research was developed since the publication of his first paper on the subject (Sommerfeld, 1909) in order to investigate the application of the theory to several propagation and radiation problems of practical interest (Norton, 1937; Longman, 1956; Novikov and Makarov, 1961; Wait, 1964; Baños, 1966). With the coming of numerical analysis techniques, an ever-growing attention was paid to the development of methods for the evaluation of both the Green functions and their integrals on the scattering geometries (Siegel and King, 1970; Bubenik, 1977; Mittra *et al.*, 1979; Parhami *et al.*, 1980; Parhami and Mittra, 1980; Rahmat-Samii *et al.*, 1981; Maclean and Wu, 1993; Cui and Chew, 2000a; Cui and Chew, 2000b). It should be noticed indeed that the Green functions expressions involve the Sommerfeld's integrals, which require a huge computational effort, due to their characteristics of slow convergence. From a mathematical standpoint, the Sommerfeld's integrals are improper integrals (i.e. over a semi-infinite domain) of complex functions characterized by the presence of two branch points. The presence in the integrand of the highly oscillating Bessel function and of an integrable singularity are the main causes of numerical troubles. Such troubles led some authors, involved in antenna modelling, to address their research to the investigation of some sort of approximate approaches in order to find simplified formulas and methods (Sarkar, 1975; Bannister, 1984; Michalski and Mosig, 1997; Michalski, 1998; Wait, 1999; Baumann and Sampaio, 1999).

During the development of lightning studies, when the problem of the lightning electromagnetic field evaluation in presence of a lossy ground was addressed, researchers resorted to methods and techniques already investigated by antenna specialists (e.g. Norton's approximation (Norton, 1937) and surface impedance (Maclean and Wu, 1993)) and often made use of codes already developed in this context (e.g. NEC (Burke and Poggio, 1981), NEC-2) (Gardner, 1981; Høidalen

*et al.*, 1997; Wait and Hill, 2000; Pokharel *et al.*, 2003). Recently, the application of more sophisticated numerical techniques widely employed in full-Maxwell electromagnetic field analysis (like FDTD and MoM) has been investigated (Yang and Zhou, 2004; Shoory *et al.*, 2005; Baba and Rakov, 2006).

On the other hand, several authors decided to work on approximate formulas specifically intended to the lightning horizontal electric field evaluation (namely the component that mostly affects line overvoltages). Among them, the most remarkable ones are those proposed by Cooray and Rubinstein (Cooray, 1992; Rubinstein, 1996; Cooray, 2002). Such formulas have been intensively employed for the evaluation of lightning-induced overvoltages on overhead power line (Rachidi *et al.*, 1996; Borghetti *et al.*, 2004). Approximated approaches were also developed for the numerical evaluation of Sommerfeld's integrals appearing in the expressions of the lightning fields (Zeddam and Degauque, 1990; Cooray, 2005) or for maximum overvoltage estimation (Darveniza, 2007).

In this section, our aim is to present in a systematic way the derivation of the electromagnetic fields generated by a lightning return stroke current respectively in the half-space 'air' and in the half-space 'lossy ground' and to propose an efficient method for the numerical computation of the field expressions.

### 13.2.1 Overground electromagnetic field

#### 13.2.1.1 Overview on Green's functions theory

The problem of determining the exact expression of the electromagnetic field radiated by a lightning discharge can be faced using the principles of Green's function theory (Balanis, 1989; Zauderer, 1998). Let

$$Lu = \nabla \cdot (\nabla u) + k^2 u = F \quad (13.1)$$

be a *partial* differential equation defined in the domain  $A \subset \Re^3$ , associated with the well-known Sommerfeld's radiation condition at the infinity (Sommerfeld, 1949):

$$\lim_{r \rightarrow \infty} \sqrt{r} \left( \frac{\partial u}{\partial r} - jku \right) = 0 \quad (13.2)$$

expressed in cylindrical coordinates.

$L$  is a differential operator,  $F$  is an assigned function over the domain  $\Re^3$ ,  $k$  is a given constant,  $u$  is the unknown of the problem and  $j^2 = -1$ .

Let  $w$  be the solution of

$$\begin{cases} Lw = \delta(P - P') \\ \lim_{r \rightarrow \infty} \sqrt{r}(\partial w / \partial r - jkw) = 0 \end{cases} \quad (13.3)$$

where  $\delta(\cdot)$  is the Dirac function and  $P$  and  $P'$  are respectively the observation and the source point.

It can be shown that (Zauderer, 1998)

$$u = \int_A w F dP' \quad (13.4)$$

Equation (13.4) states that the solution of problem (13.1) for a generic right-hand-side  $F$  can be easily obtained by solving only once problem (13.3) and calculating the particular solution  $w$ , which is called *Green's function* (Balanis, 1989; Zauderer, 1998).

According to such results, the lightning electromagnetic field calculation problem we have to deal with can be solved into two steps:

1. evaluation of the field due to an elementary current dipole, i.e. the physical counterpart of the Dirac  $\delta$  function of system (13.3), in order to obtain the Green's function;
2. evaluation of an integral of the kind (13.4) over the lightning channel, in order to obtain the real unknown, i.e. the radiated electromagnetic field.

### 13.2.1.2 Derivation of the Green's functions for the overground electromagnetic field

Here, the problem is to determine the field radiated by a vertical dipole lying at height  $z'$  over a lossy ground.

With reference to Figure 13.1, the vertical dipole is placed at source point  $P'(0,0,z')$ , while the observation point is  $P(r,\phi,z)$ . The upper half-space is air, which is assumed to be lossless and characterized by magnetic permeability  $\mu_0$  and electric permittivity  $\epsilon_0$ . The lossy ground (lower half-space) has conductivity  $\sigma$  and electric permittivity  $\epsilon$ .

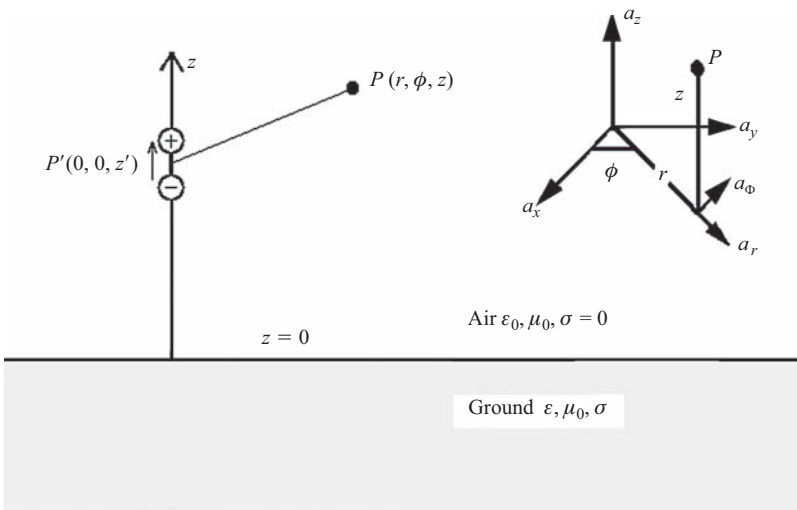


*Figure 13.1 Model geometry: the dipole radiation over a conducting ground*

As well known (Sommerfeld, 1949), the set of equations solving this problem is the following:

$$\begin{cases} \Delta \vec{A} + k^2 \vec{A} = -\mu_0 \delta(P - P') \vec{e}_3 & z > 0 \\ \Delta \vec{A} + k_E^2 \vec{A} = 0 & z < 0 \\ A = A_E & z = 0 \\ n^2 \frac{\partial \vec{A}}{\partial z} = \frac{\partial \vec{A}_E}{\partial z} & z = 0 \\ \lim_{r \rightarrow \infty} \sqrt{r} \left( \frac{\partial \vec{A}}{\partial r} - jkA \right) = 0 \end{cases} \quad (13.5)$$

where  $\vec{A}(\vec{A}_E)$  is the vector potential in the half-space air (earth),  $k^2 = \omega^2 \mu_0 \epsilon_0$  the wave number in the same half-space (being  $\omega$  the angular frequency),  $k_E^2 = \omega^2 \epsilon \mu_0 + j\omega \mu_0 \sigma$  the wave number in the half-space earth Ah,  $n^2 = k_E^2/k^2$  the complex refractive index and  $\delta$  the Dirac function. The first and second Helmholtz equations hold respectively in air and in earth, while the third and fourth ones are the interface conditions, which must be satisfied in order to ensure the continuity of the tangential magnetic and electric fields at ground level. Sommerfeld showed (Sommerfeld, 1949) that, with the addition of the fifth equation, the well-known radiation condition, the problem has a unique solution.

It should be observed that the set of equation (13.5) has been derived assuming for all variables a time-harmonic dependence of the kind  $e^{-j\omega t}$ .

Once (13.5) has been solved and the vector potential spatial distribution has been obtained, the expression of the three nonzero components of the field can be easily derived according to the following relationships:

$$\begin{cases} E_z = \frac{j\omega}{k^2} \left( \frac{\partial^2 A}{\partial z^2} + k^2 A \right) \\ E_r = \frac{j\omega}{k^2} \left( \frac{\partial^2 A}{\partial z \partial r} \right) \\ H_\varphi = -\frac{1}{\mu_0} \frac{\partial A}{\partial r} \end{cases} \quad (13.6)$$

being  $A$  the vertical component of the vector potential.

In order to solve problem (13.5), it is first necessary to face the simplified case of the vertical dipole radiation in free space (Figure 13.2). Such problem is described only by the first and the fifth equations of system (13.5) respectively the governing equation and the condition at the infinity. Of course, due to the different symmetry of the problem, a system of spherical coordinates is now used.

As well known (Sommerfeld, 1949), the solution in terms of the vector potential spatial distribution is the following:

$$A(R) = \frac{\mu_0}{4\pi} \frac{e^{jkR}}{R} \quad (13.7)$$

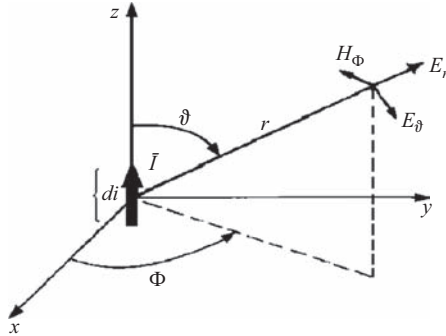


Figure 13.2 Model geometry: the dipole radiation in free space

being  $R = \sqrt{r^2 + (z - z')^2}$  the distance between the source point and the observation one. Developing (13.7) as a superposition of the Helmholtz equation eigenfunctions in a cylindrical domain (Sommerfeld, 1949), after some mathematical manipulations (Gradshteyn and Ryzhik, 1980), one gets

$$\frac{\mu_0 e^{jkr}}{4\pi R} = \frac{\mu_0}{4\pi} \int_0^{+\infty} \frac{\lambda}{\mu} e^{-\mu|z-z'|} J_0(\lambda r) d\lambda \quad (13.8)$$

being  $\mu^2 = \lambda^2 - k^2$  and  $J_0$  the Bessel function of first kind and zeroth order.

Coming back now to the primary problem of Figure 13.1, one has to modify (13.8) by adding a further integral term, in order to satisfy the interface conditions (at  $z = 0$ ) of system (13.5). Such term can have the following form:

$$\frac{\mu_0}{4\pi} \int_0^{+\infty} G(\lambda) \cdot J_0(\lambda r) \cdot e^{-\mu(z+z')} d\lambda \quad (13.9)$$

This is again a superposition of eigenfunctions and the function  $G$  appearing in it, which can be seen as the spectral distribution in the  $\lambda$ -continuum of the eigenfunctions (Sommerfeld, 1949), will be determined imposing the interface conditions.

Similarly, the expression for  $A_E$  can be searched in the following form:

$$A_E = \frac{\mu_0}{4\pi} \left[ \int_0^{+\infty} G_E(\lambda) \cdot J_0(\lambda r) \cdot e^{\mu_E z - \mu z'} d\lambda \right] \quad (13.10)$$

being  $\mu_E^2 = \lambda^2 - k_E^2$  and  $G_E$  an unknown function, whose meaning is the same as  $G$ .

Imposing now the interface conditions, one gets

$$\begin{cases} \frac{\lambda}{\mu} + G - G_E = 0 \\ \mu_E G_E - n^2(\lambda - \mu G) = 0 \end{cases} \quad (13.11)$$

and finally

$$\begin{aligned} G(\lambda) &= \frac{\lambda}{\mu} \left( 1 - \frac{2\mu_E}{n^2\mu + \mu_E} \right) \\ G_E(\lambda) &= \lambda \left( \frac{2n^2}{n^2\mu + \mu_E} \right) \end{aligned} \quad (13.12)$$

which can be put into (13.9) and (13.10), respectively, to obtain the expression for  $A$  and  $A_E$ .

As far as  $A$  is concerned, one therefore has that

$$A(r, z, z') = \frac{\mu_0}{4\pi} \left[ \frac{e^{jkR}}{R} + \int_0^{+\infty} \frac{\lambda}{\mu} \left( 1 - \frac{2\mu_E}{n^2\mu + \mu_E} \right) \cdot J_0(\lambda r) \cdot e^{-\mu(z+z')} d\lambda \right] \quad (13.13)$$

Now, recalling (13.8) and defining  $R' = \sqrt{r^2 + (z + z')^2}$ , it readily follows that

$$\frac{\mu_0}{4\pi} \frac{e^{jkR'}}{R'} = \frac{\mu_0}{4\pi} \int_0^{+\infty} \frac{\lambda}{\mu} e^{-\mu(z+z')} J_0(\lambda r) d\lambda \quad (13.14)$$

which means that the part of the vector potential  $A$  due to the first term of  $G$  can be interpreted as the image effect.

Equation (13.13) can be then rewritten as

$$A = \frac{\mu_0}{4\pi} \left[ \frac{e^{jkR}}{R} + \frac{e^{jkR'}}{R'} - 2 \int_0^{+\infty} \frac{\mu_E}{n^2\mu + \mu_E} \cdot J_0(\lambda r) \cdot e^{-\mu(z+z')} d\lambda \right] \quad (13.15)$$

Here, it should be noticed that only the first two terms would be present if the ground conductivity was zero and so they represent the expression for the ‘ideal’ vector potential (i.e. the one corresponding to perfectly conducting ground), while the last one takes into account the ground conductivity (i.e. the Sommerfeld integral). Inserting (13.15) into system (13.6), it is now possible to obtain the expression for the fields:

$$\left\{ \begin{array}{l} E_z = E_{zi} - \frac{j}{2\pi\omega\epsilon_0} \int_0^{+\infty} \frac{\mu_E}{n^2\mu + \mu_E} \cdot J_0(\lambda r) \cdot e^{-\mu(z+z')} \cdot \frac{\lambda^3}{\mu} d\lambda \\ E_r = E_{ri} - \frac{j}{2\pi\omega\epsilon_0} \int_0^{+\infty} \lambda^2 J_1(\lambda r) e^{-\mu(z+z')} \frac{\mu_E}{n^2\mu + \mu_E} d\lambda \\ H_\varphi = H_{\varphi i} - \frac{1}{2\pi} \int_0^{+\infty} \frac{\mu_E}{n^2\mu + \mu_E} \cdot J_1(\lambda r) \cdot e^{-\mu(z+z')} \cdot \frac{\lambda^2}{\mu} d\lambda \end{array} \right. \quad (13.16)$$

where the terms  $E_{ri}$ ,  $E_{zi}$  and  $H_{qi}$  are the ‘ideal’ fields, whose expressions can be found in (Delfino *et al.*, 2003).

### 13.2.1.3 Derivation of the lightning return stroke overground electromagnetic field

The Green functions (13.16) are now utilized to evaluate the electromagnetic field expression due to a lightning event. In order to reach this goal, it is necessary to multiply the Green functions for the current distribution and to integrate along the channel (see Figure 13.3) (Balanis, 1989; Zauderer, 1998). Let us assume for the current the following model (Rakov and Uman, 1998):

$$I(z', \omega) = P(z') I(0, \omega) e^{j\omega \frac{z'}{v}} \quad (13.17)$$

being  $I(0, \omega)$  the channel-base current,  $P(z')$  the height-dependent attenuation function and  $v$  the current wavefront speed.

In this case, setting  $P(z') = e^{-z'/a}$  (MTLE model (Rakov and Uman, 1998)), the expressions of the lightning fields are

$$\begin{cases} E_{zL} = E_{zil} - \frac{jI(0, \omega)}{2\pi\omega\epsilon_0} \int_0^{+\infty} \frac{\mu_E}{n^2\mu + \mu_E} \cdot J_0(\lambda r) \cdot e^{-\mu z'} \cdot \frac{\lambda^3}{\mu} Q(\lambda) d\lambda \\ E_{rL} = E_{ril} - \frac{jI(0, \omega)}{2\pi\omega\epsilon_0} \int_0^{+\infty} \lambda^2 J_1(\lambda r) e^{-\mu z} \frac{\mu_E}{n^2\mu + \mu_E} Q(\lambda) d\lambda \\ H_{qL} = H_{qil} - \frac{I(0, \omega)}{2\pi} \int_0^{+\infty} \frac{\mu_E}{n^2\mu + \mu_E} \cdot J_1(\lambda r) \cdot e^{-\mu z} \cdot \frac{\lambda^2}{\mu} Q(\lambda) d\lambda \end{cases} \quad (13.18)$$

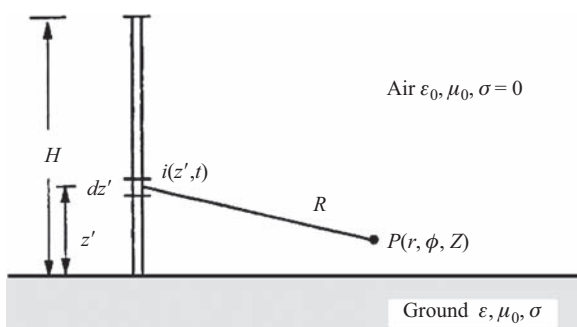


Figure 13.3 Model geometry: the lightning radiation over a conducting ground

The function  $Q$  appearing in (13.18) is the result of the integration along the channel, namely

$$Q(\lambda) = \int_0^H e^{(j\frac{\omega}{v} - \mu - \frac{1}{a})z'} dz' = \frac{e^{(j\frac{\omega}{v} - \mu - \frac{1}{a})H} - 1}{(j\frac{\omega}{v} - \mu - \frac{1}{a})} \quad (13.19)$$

The expressions for the ‘ideal field’ terms, namely  $E_{ziL}$ ,  $E_{riL}$  and  $H_{qiL}$ , are (Rachidi *et al.*, 1996):

$$E_{ziL} = \frac{I(0, \omega)}{4\pi\varepsilon_0} \int_{-H}^H \left[ \frac{2(z-z')^2 - r^2}{cR^4} + \frac{2(z-z')^2 - r^2}{-j\omega R^5} + j\omega \frac{r^2}{c^2 R^3} \right] \cdot e^{j\omega \left( \frac{R}{c} + \frac{|z'|}{v} \right)} P(z') dz' \quad (13.20)$$

$$E_{riL} = \frac{I(0, \omega)}{4\pi\varepsilon_0} \int_{-H}^H \left[ \frac{3r(z-z')}{cR^4} + \frac{3r(z-z')}{-j\omega R^5} + j\omega \frac{r(z-z')}{cR^3} \right] \cdot e^{j\omega \left( \frac{R}{c} + \frac{|z'|}{v} \right)} P(z') dz' \quad (13.21)$$

and

$$H_{qiL} = \frac{I(0, \omega)}{4\pi} \int_{-H}^H \left[ \frac{r}{R^3} - j\omega \frac{r}{cR^2} \right] e^{j\omega \left( \frac{R}{c} + \frac{|z'|}{v} \right)} P(z') dz' \quad (13.22)$$

### 13.2.1.4 Evaluation of the Sommerfeld’s integrals

The quantity,

$$I = \int_0^{+\infty} J_v(\lambda r) e^{-\mu z} \frac{\mu_E}{n^2 \mu + \mu_E} \frac{\lambda^n}{\mu^m} Q(\lambda) d\lambda \quad (13.23)$$

appearing in system (13.18) with different values of  $n$ ,  $m$  and  $v$  is known as *Sommerfeld’s integral*. In this section, the main mathematical features of this kind of integral are analysed in order to find out a fast and reliable procedure for its numerical treatment.

#### *The branch points*

The integrand of  $I$  is a function of a complex variable  $\lambda$  and is not uniquely determined because of the square roots  $\mu$  and  $\mu_E$  that appear in it.

Corresponding to the four combinations of signs of  $\mu$  and  $\mu_E$ , the integral (13.23) is four-valued, and its Riemann surface (Rudin, 1986) has four sheets. In order to ensure the convergence of the integral and its vanishing for  $z \rightarrow \pm\infty$ , one must take  $\mu = \sqrt{\lambda^2 - k^2}$  with positive real part. As shown in (Sommerfeld, 1949),

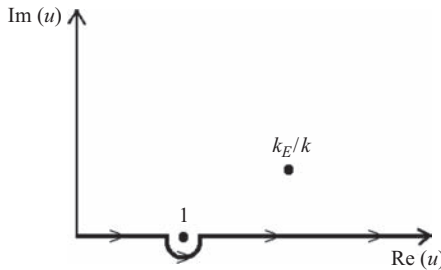


Figure 13.4 Integration path for the Sommerfeld's integrals

also  $\mu_E$  has to be taken with positive real part in order to make the integrals expressing the vector potential and the fields in the earth converge.

Stating this rule of signs, only one of the four sheets is singled out as a ‘permissible sheet’. This means that in performing the integration, it is necessary that the chosen path lie only on the permissible sheet. This is achieved by joining the two branch points  $\mu$  and  $\mu_E$  by two branch cuts, which may not be intersected by the path of integration. The chosen path is the one depicted in Figure 13.4, in which the integration variable is  $u = \lambda/k$ , so as the branch points occur at  $u = 1$  and  $u = k_E/k$ .

In order to get the expressions for  $\mu$  and  $\mu_E$ , one can make the following considerations.

Let us start with  $\mu_E$ . As stated before, one must choose:

$$\operatorname{Re}(\mu_E) > 0 \quad (13.24)$$

Recalling the definition of  $\mu_E^2$ , it readily follows that  $\operatorname{Im}(\mu_E^2) < 0$ . So, indicating with  $\phi$  the phase angle of  $\mu_E^2$ , one has that  $\pi < \phi < 2\pi$ . As a consequence, if  $\theta$  is the phase angle of  $\mu_E$ , one has that either  $\theta = \phi/2$  or  $\theta = \phi/2 + \pi$  can be chosen. In the second case  $3\pi/2 < \theta < 2\pi$ , while in the first one  $\pi/2 < \theta < \pi$ . So, to meet the requirement (13.24),  $\theta = \phi/2 + \pi$  must be chosen and, as a consequence, it results:

$$\cos \theta = \cos\left(\frac{\phi}{2} + \pi\right) = -\cos \frac{\phi}{2} = +\sqrt{\frac{1 + \cos \phi}{2}} \quad (13.25)$$

and

$$\sin \theta = \sin\left(\frac{\phi}{2} + \pi\right) = -\sin \frac{\phi}{2} = -\sqrt{\frac{1 - \cos \phi}{2}} \quad (13.26)$$

Now, expressing  $\mu_E$  in polar form, it follows:

$$\mu_E = |\mu_E| \left( \sqrt{\frac{1 + \cos \phi}{2}} - j \sqrt{\frac{1 - \cos \phi}{2}} \right) \quad (13.27)$$

being

$$\cos \phi = \frac{\lambda^2 - \frac{\epsilon}{\epsilon_0} k^2}{\sqrt{\left(\lambda^2 - \frac{\epsilon}{\epsilon_0} k^2\right)^2 + \sigma^2 k^2 \frac{\mu_0}{\epsilon_0}}} \quad (13.28)$$

and

$$|\mu_E| = \sqrt[4]{\left(\lambda^2 - \frac{\epsilon}{\epsilon_0} k^2\right)^2 + \sigma^2 k^2 \frac{\mu_0}{\epsilon_0}} \quad (13.29)$$

where the square roots are all real functions.

As far as  $\mu$  is concerned, one can observe that  $\mu = \lim_{\sigma \rightarrow 0^+} \mu_E$ , and thus it results:

$$\mu = \begin{cases} \sqrt{\lambda^2 - k^2} & \text{for } \lambda > k \\ -j\sqrt{k^2 - \lambda^2} & \text{for } \lambda < k \end{cases} \quad (13.30)$$

### The $\sigma$ -dependent term

The term  $g_s(\lambda) = \mu_E / (n^2 \mu + \mu_E)$  would be zero if the ground were a perfect conductor (PEC). As a matter of fact, for fixed  $k$ , it is a function of  $\lambda$ , and, as can be seen from Figures 13.5 and 13.6, its behaviour shows some sort of ‘resonance’ for  $\lambda = k$ .

As a consequence, the integrand of (13.23), in the neighbourhood of  $k$ , in spite of being continuous, is not, so to speak, ‘smooth’.

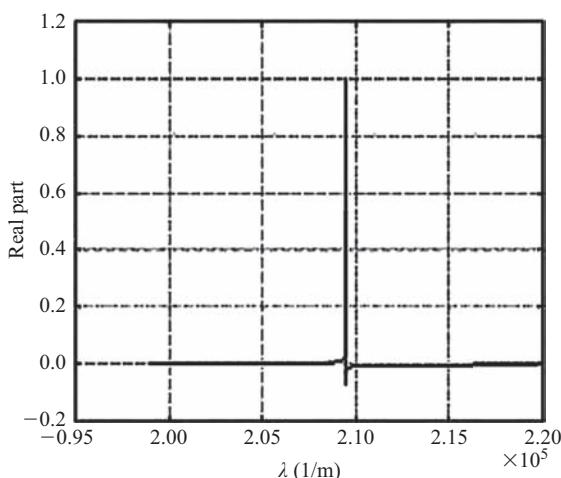


Figure 13.5 Real part of the  $\sigma$ -dependent term for  $k = 2.09 \times 10^{-5}$

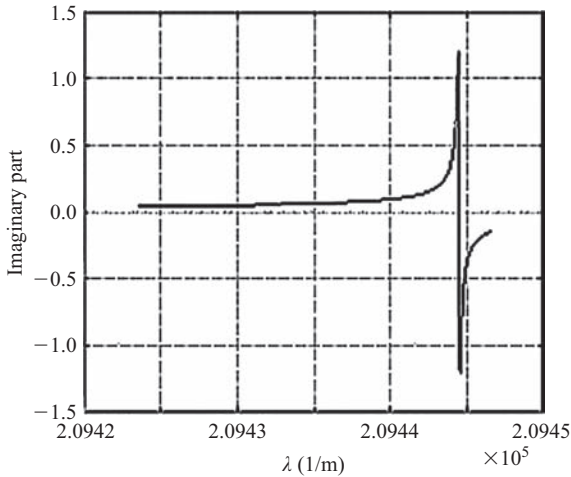


Figure 13.6 Imaginary part of the  $\sigma$ -dependent term for  $k = 2.09 \times 10^{-5}$

This fact has an important consequence: the integral (13.23) is a Hankel transform, but the above-mentioned property makes it impossible for the traditional Hankel transform algorithms (Anderson, 1979) (which basically are Gaussian quadrature methods) to correctly evaluate the integral in (13.23), as shown in

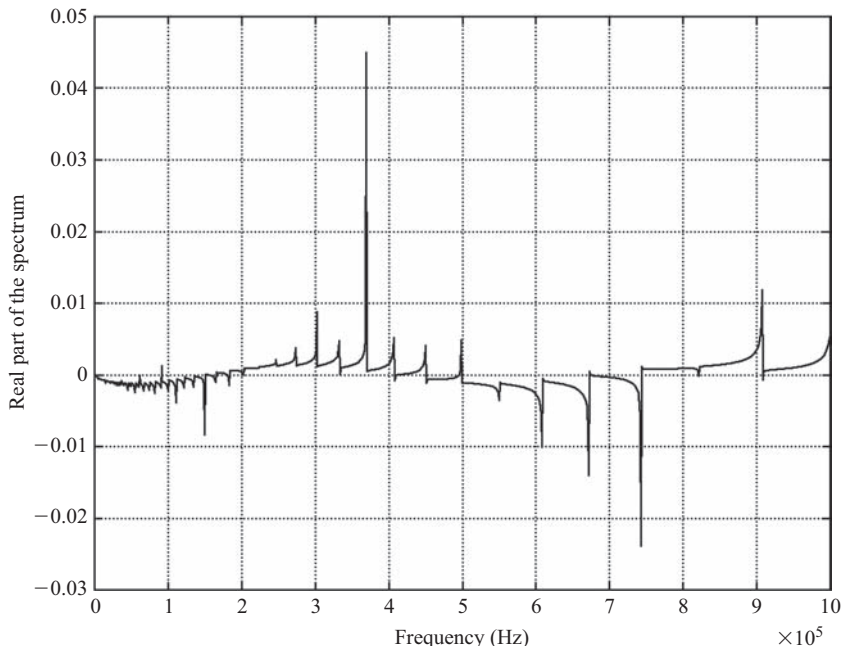


Figure 13.7 Failure of the classical routine for the Hankel transform

Figure 13.7, where the real part of the spectrum is depicted (the same holds for the imaginary one).

### 13.2.1.5 The vertical component of the electric field

The inverse Fourier transform of the ideal term (13.20) can be performed analytically, thus obtaining

$$\begin{aligned} e_{zIL}(t) = & \frac{1}{4\pi\varepsilon_0} \int_{-vt}^{vt} \left[ \frac{2(z-z')^2 - r^2}{cR^4} i\left(0, t - \frac{R}{c} - \frac{|z'|}{v}\right) \right. \\ & + \left. \frac{2(z-z')^2 - r^2}{R^5} \int_0^t i\left(0, s - \frac{R}{c} - \frac{|z'|}{v}\right) ds + -\frac{r^2}{c^2 R^3} \frac{\partial i\left(0, t - \frac{R}{c} - \frac{|z'|}{v}\right)}{\partial t} \right] P(z') dz' \end{aligned} \quad (13.31)$$

having indicated with lower-case letters the time-domain functions.

Here, the range of integration is  $(-vt, vt)$  instead of  $(-H, H)$ , since the current  $i(z', t)$  is identically zero for  $z' > vt$ . This is the reason why, if one performs the fields calculations in the time domain and is interested in the first microseconds of the transient, the channel height is of no use.

As far as the Sommerfeld term is concerned, the inverse Fourier transform must be carried out numerically. This requires to evaluate numerically the corresponding Sommerfeld integral appearing in the first of system (13.18) for many different values of frequency in an assigned range (i.e. [0 Hz,  $10^7$  Hz]). Moreover, if one observes that, for each frequency:

- the integrand contains both the Bessel function (which is highly oscillating) and the  $\sigma$ -dependent term (whose behaviour is shown in Figures 13.5 and 13.6);
- the integrand is singular for  $\lambda = k$ ;
- the integral must be carried out over a semi-infinite domain,

one is easily convinced that such calculation requires a huge computational effort.

To overcome the first problem, a Romberg method (Davis and Rabinowitz, 1984; Press *et al.*, 1992; Krommer and Ueberhuber, 1994) has been used, dividing the interval of integration into sub-intervals, with particular attention to the neighbourhood of  $k$ , namely

$$k \int_0^\infty f(ku) du = \left( k \int_0^{0.99} f(ku) du + k \int_{0.99}^1 f(ku) du + k \int_1^{1.01} f(ku) du + k \int_{1.01}^\infty f(ku) du \right) \quad (13.32)$$

having posed  $u = \lambda/k$  and having indicated with  $f$  the integrand function of the first integral of system (13.18).

As far as the singularity is concerned, let us consider the integral  $I_1$  between 0.99 and 1:

$$I_1 = \int_{0.99}^1 \frac{u}{\sqrt{1-u^2}} h_1(u) du \quad (13.33)$$

with

$$h_1(u) = J_0(kru)k^3 u^2 g_s(ku) e^{jk\sqrt{1-u^2}z} Q(ku) \quad (13.34)$$

Setting  $s = \sqrt{1-u^2}$ , one has that

$$I_1 = \int_0^{\sqrt{1-0.99^2}} h_1(\sqrt{1-s^2}) ds \quad (13.35)$$

being the integrand not singular in the range of integration.

Indicating with  $I_2$  the integral between 1 and 1.01, one has that

$$I_2 = \int_1^{1.01} \frac{u}{\sqrt{u^2-1}} h_2(u) du \quad (13.36)$$

being

$$h_2(u) = J_0(kru)k^3 u^2 g_s(ku) e^{-k\sqrt{u^2-1}z} Q(ku) \quad (13.37)$$

Setting now  $s = \sqrt{u^2-1}$ , one has that

$$I_2 = \int_0^{\sqrt{1.01^2-1}} h_2(\sqrt{1+s^2}) ds \quad (13.38)$$

being again the integrand not singular in the range of integration.

The integral between 1.01 and  $\infty$  requires to ‘approximate the infinity’, that is to say to find out a number  $M$  such that the difference between the original integral and the one between 1.01 and  $M$  is sufficiently small. Typically the number  $M$  is searched with iterative procedures; here it is possible to derive an upper bound for the error  $Err$  in the so-called integral tail for each frequency and so to estimate  $M$  in an analytical way, thus reducing the computational costs.

Let

$$Err(M) = \left| \int_M^\infty J_0(kru) \frac{k^3 u^3}{\sqrt{u^2-1}} g_s(ku) e^{-k\sqrt{u^2-1}z} Q(ku) du \right| \quad (13.39)$$

it readily follows that

$$Err(M) \leq \int_M^\infty \left| J_0(kru) \frac{k^3 u^3}{\sqrt{u^2 - 1}} g_s(ku) e^{-k\sqrt{u^2 - 1}z} Q(ku) \right| du \quad (13.40)$$

Observing that

- the absolute values of both  $Q$  and  $g_s$  are decreasing functions for  $u > 1$ ;
- if  $M > 4/3$ ,  $\sqrt{u^2 - 1} \geq u/2$ ;
- $|J_0(kru)| < \sqrt{2/\pi kru}$  (Gradshteyn and Ryzhik, 1980),

one has

$$Err(M) \leq |g_s(kM)Q(kM)| \frac{2\sqrt{2}k^3}{\sqrt{\pi kr}} \int_M^\infty e^{-k\frac{u}{2}z} u^{\frac{3}{2}} du \quad (13.41)$$

Finally, since the integral in relation (13.41) is known analytically (Gradshteyn and Ryzhik, 1980), it follows:

$$Err(M) \leq |g_s(kM)Q(kM)| \frac{2\sqrt{2}k^3}{\sqrt{\pi kr}} \left(\frac{kz}{2}\right)^{-\frac{5}{2}} \Gamma\left(\frac{5}{2}, \frac{kMz}{2}\right) \quad (13.42)$$

being  $\Gamma$  the incomplete Gamma function (Gradshteyn and Ryzhik, 1980).

In Figure 13.8, the ratio between the upper bound of the tail and the absolute value of the integral between 0 and  $M$  has been plotted as a function of the frequency, having set  $M = 4\pi/5k$ , showing that our goal has been achieved.

The position  $u = \lambda/k$  is not possible for  $f = 0$  Hz. This implies that another method must be used to perform the so-called *static term*.

Let us reconsider the Sommerfeld integral appearing in the first of (13.16); observing that, if  $k$  approaches 0:

$$\begin{cases} n^2 \rightarrow \frac{j\sigma}{\omega\epsilon_0} \\ \mu_E^2 \rightarrow \lambda^2 \\ \mu^2 \rightarrow \lambda^2 \\ \frac{\mu_E}{n^2\mu + \mu_E} \rightarrow \frac{\omega\epsilon_0}{j\sigma} \end{cases} \quad (13.43)$$

one has that (Gradshteyn and Ryzhik, 1980)

$$\begin{aligned} & \frac{-j}{2\pi\omega\epsilon_0} \int_0^{+\infty} \frac{\mu_E}{n^2\mu + \mu_E} \cdot J_0(\lambda r) \cdot e^{-\mu(z+z')} \cdot \frac{\lambda^3}{\mu} d\lambda \\ & \rightarrow \frac{-1}{2\pi\sigma} \int_0^{+\infty} J_0(\lambda r) \cdot e^{-\lambda(z+z')} \lambda^2 d\lambda = \frac{-1}{\pi\sigma R'3} F\left(\frac{3}{2}, -1, 1, \frac{r^2}{R'^2}\right) \end{aligned} \quad (13.44)$$

being  $F$  the hypergeometric function (Gradshteyn and Ryzhik, 1980).

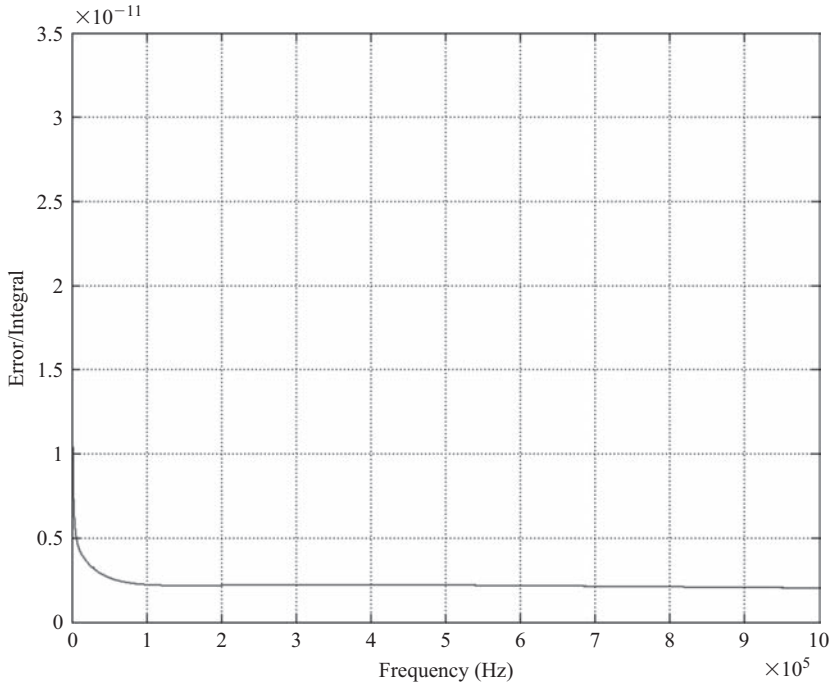


Figure 13.8 Ratio between the upper bound of the tail and the absolute value of the integral between 0 and  $M$  as a function of the frequency

As a consequence, the static term for the Sommerfeld integral appearing in the first of (13.18) is given by

$$\begin{aligned} \lim_{k \rightarrow 0} -\frac{jI(0, \omega)}{2\pi\omega\epsilon_0} \int_0^{+\infty} \frac{\mu_E}{n^2\mu + \mu_E} \cdot J_0(\lambda r) \cdot e^{-\mu z'} \cdot \frac{\lambda^3}{\mu} Q(\lambda) d\lambda \\ = \frac{-I(0, 0)}{\pi\sigma} \int_0^H \frac{1}{R'3} F\left(\frac{3}{2}, -1, 1, \frac{r^2}{R'^2}\right) P(z') dz' \end{aligned} \quad (13.44)$$

### 13.2.1.6 The radial component of the electric field

The inverse Fourier transform of the ideal term (13.21) can be performed analytically, thus obtaining

$$\begin{aligned} e_{riL}(t) = \frac{1}{4\pi\epsilon_0} \int_{-vt}^{vt} \left[ \frac{3r(z-z')}{cR^4} i\left(0, t - \frac{R}{c} - \frac{|z'|}{v}\right) + \frac{3r(z-z')}{R^5} \int_0^t i\left(0, s - \frac{R}{c} - \frac{|z'|}{v}\right) ds \right. \\ \left. + \frac{r(z-z')}{c^2 R^3} \frac{\partial i\left(0, t - \frac{R}{c} - \frac{|z'|}{v}\right)}{\partial t} \right] P(z') dz' \end{aligned} \quad (13.46)$$

having indicated with lower-case letters the time-domain functions.

As far as the Sommerfeld term is concerned, again the inverse Fourier transform must be carried out numerically. This requires to numerically evaluate the corresponding Sommerfeld integral appearing in the second of (13.18) for many different values of frequency in an assigned range (i.e. [0 Hz, 107 Hz]). From a numerical point of view, here things go better, since the integral function is not singular for  $\lambda = k$ .

Therefore, again a Romberg method is used, splitting the range of integration into many sub-intervals, as done for the  $z$ -component of the electric field, but the neighbourhood of  $k$  does not require a ‘special treatment’ as before.

The only problems to solve are the ones relevant to the integral tail and the static term.

Indicating again with  $Err$  the upper bound for the integral tail and with  $M$  the last point of the interval on which the integral is taken, one has

$$Err(M) = \left| \int_M^\infty J_1(kru) k^3 u^2 g_s(ku) e^{-k\sqrt{u^2-1}z} Q(ku) du \right| \quad (13.47)$$

With considerations similar to the ones done in the previous section, it follows that

$$Err(M) \leq |g_s(kM)Q(kM)| \frac{\sqrt{2}k^3}{\sqrt{\pi kr}} \int_M^\infty e^{-k\frac{uz}{2}} u^{\frac{3}{2}} du \quad (13.48)$$

and again (Gradshteyn and Ryzhik, 1980):

$$Err(M) \leq |g_s(kM)Q(kM)| \frac{\sqrt{2}k^3}{\sqrt{\pi kr}} \left(\frac{kz}{2}\right)^{-\frac{5}{2}} \Gamma\left(\frac{5}{2}, \frac{kMz}{2}\right) \quad (13.49)$$

As far as the static term is concerned, now one has that

$$\begin{aligned} & \frac{-j}{2\pi\omega\epsilon_0} \int_0^{+\infty} \frac{\mu_E}{n^2\mu + \mu_E} \cdot J_1(\lambda r) \cdot e^{-\mu(z+z')} \cdot \lambda^2 d\lambda \\ & \rightarrow \frac{-1}{2\pi\sigma} \int_0^{+\infty} J_1(\lambda r) \cdot e^{-\lambda(z+z')} \lambda^2 d\lambda = \frac{-3r}{2\pi\sigma R'^4} F\left(2, -\frac{1}{2}, 2, \frac{r^2}{R'^2}\right) \end{aligned} \quad (13.50)$$

As a consequence, the static term for the Sommerfeld integral appearing in the second of (13.18) is given by

$$\begin{aligned} \lim_{k \rightarrow 0} - \frac{jI(0, \omega)}{2\pi\omega\epsilon_0} \int_0^{+\infty} \frac{\mu_E}{n^2\mu + \mu_E} \cdot J_1(\lambda r) \cdot e^{-\mu z'} \cdot \lambda^2 Q(\lambda) d\lambda \\ = \frac{-3rI(0, 0)}{2\pi\sigma} \int_0^H \frac{1}{R'^4} F\left(2, -\frac{1}{2}, 2, \frac{r^2}{R'^2}\right) P(z') dz' \end{aligned} \quad (13.51)$$

### 13.2.1.7 The azimuthal component of the magnetic field

The inverse Fourier transform of the ideal term (13.22) can be performed analytically, thus obtaining:

$$h_{qil}(t) = \frac{1}{4\pi} \int_{-vt}^{vt} \left[ \frac{r}{cR^2} \frac{\partial i(0, t - \frac{R}{c} - \frac{|z'|}{v})}{\partial t} + \frac{r}{R^3} i(0, t - \frac{R}{c} - \frac{|z'|}{v}) \right] P(z') dz' \quad (13.52)$$

having indicated with lower-case letters the time-domain functions.

As far as the Sommerfeld term is concerned, in the numerical evaluation of the integral (carried out again with a Romberg method for a number of frequencies ranging between 0 and  $10^7$  Hz), one has to face:

- the singularity in the integrand function for  $\lambda = k$ ;
- the integral tail;
- the static term.

The first problem can be solved in the same way as for the vertical component of the electric field, with the only difference that now:

$$h_1(u) = J_1(kru)k^2 u g_s(ku) e^{jk\sqrt{1-u^2}z} Q(ku) \quad (13.53)$$

and

$$h_2(u) = J_1(kru)k^2 u g_s(ku) e^{-k\sqrt{u^2-1}z} Q(ku) \quad (13.54)$$

The quantity  $Err$  is now:

$$Err(M) = \left| \int_M^\infty J_1(kru) \frac{k^2 u^2}{\sqrt{u^2 - 1}} g_s(ku) e^{-k\sqrt{u^2-1}z} Q(ku) du \right| \quad (13.55)$$

In this case, the upper bound is given by

$$Err(M) \leq |g_s(kM)Q(kM)| \frac{2\sqrt{2}k^2}{\sqrt{\pi kr}} \int_M^\infty e^{-k\frac{uz}{2}} u^{\frac{1}{2}} du \quad (13.56)$$

and, finally (Gradshteyn and Ryzhik, 1980),

$$Err(M) \leq |g_s(kM)Q(kM)| \frac{2\sqrt{2}k^2}{\sqrt{\pi kr}} \left(\frac{kz}{2}\right)^{-\frac{3}{2}} \Gamma\left(\frac{3}{2}, \frac{kMz}{2}\right) \quad (13.57)$$

As far as the static term is concerned, recalling the third of (13.18), one can observe that such term must vanish, since

$$\frac{\mu_E}{n^2\mu + \mu_E} \rightarrow \frac{\omega\epsilon_0}{j\sigma} \quad (13.58)$$

and the coefficient before the Sommerfeld integral in the third of system (13.18) does not depend on the frequency.

### 13.2.2 Underground electromagnetic field

In this section, the derivation of the underground lightning electromagnetic fields expression is presented, starting from the expression for their Green's functions.

The situation is now the one depicted in Figure 13.9, in which the vertical dipole is placed at source point  $P'(0, 0, z')$ , while the observation point is  $P(r, \phi, z)$ , with  $z < 0$ .

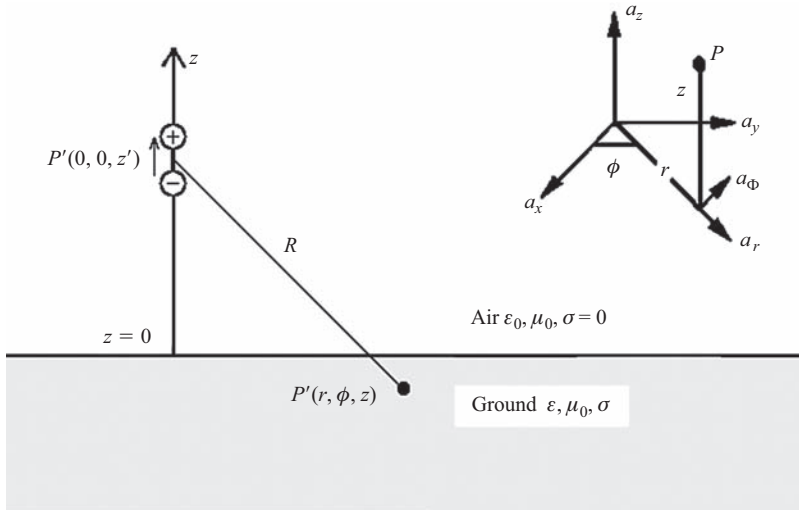


Figure 13.9 The electric dipole radiation in the subsoil

Combining (13.10) and (13.12), one can easily get

$$A_E = \frac{\mu_0}{4\pi} \left[ 2n^2 \int_0^{+\infty} \frac{\lambda}{n^2\mu + \mu_E} \cdot J_0(\lambda r) \cdot e^{-(\mu z' - \mu_E z)} d\lambda \right] \quad (13.59)$$

Furthermore, the three non-zero components of the fields are related to the vector potential in the earth by the following:

$$\begin{cases} E_z = \frac{j\omega}{k_E^2} \left( \frac{\partial^2 A_E}{\partial z^2} + k_E^2 A_E \right) \\ E_r = \frac{j\omega}{k_E^2} \left( \frac{\partial^2 A_E}{\partial z \partial r} \right) \\ H_\varphi = -\frac{1}{\mu_0} \frac{\partial A_E}{\partial r} \end{cases} \quad (13.60)$$

Now, inserting (13.59) into (13.60), it follows:

$$\left\{ \begin{array}{l} E_z = \frac{j}{2\pi\omega\epsilon_0} \int_0^{+\infty} \frac{\lambda^3}{n^2\mu + \mu_E} \cdot J_0(\lambda r) \cdot e^{-\mu z'} e^{\mu_E z} d\lambda \\ E_r = -\frac{j}{2\pi\omega\epsilon_0} \int_0^{+\infty} J_1(\lambda r) e^{-\mu z'} e^{\mu_E z} \frac{\lambda^2 \mu_E}{n^2\mu + \mu_E} d\lambda \\ H_\varphi = \frac{n^2}{2\pi} \int_0^{+\infty} \frac{\lambda^2}{n^2\mu + \mu_E} \cdot J_1(\lambda r) \cdot e^{-\mu z'} e^{\mu_E z} d\lambda \end{array} \right. \quad (13.61)$$

Assuming now the same expression for the current distribution in the lightning channel used in the previous case (see equation (13.17)), with the same attenuation function  $P(z')$ , the lightning fields are given by

$$\left\{ \begin{array}{l} E_{zL} = \frac{jI(0, \omega)}{2\pi\omega\epsilon_0} \int_0^{+\infty} \frac{\lambda^3}{n^2\mu + \mu_E} \cdot J_0(\lambda r) \cdot Q(\lambda) e^{\mu_E z} d\lambda \\ E_{rL} = -\frac{jI(0, \omega)}{2\pi\omega\epsilon_0} \int_0^{+\infty} J_1(\lambda r) Q(\lambda) e^{\mu_E z} \frac{\lambda^2 \mu_E}{n^2\mu + \mu_E} d\lambda \\ H_{\varphi L} = -\frac{n^2 I(0, \omega)}{2\pi} \int_0^{+\infty} \frac{\lambda^2}{n^2\mu + \mu_E} \cdot J_1(\lambda r) \cdot Q(\lambda) e^{\mu_E z} d\lambda \end{array} \right. \quad (13.62)$$

From a numerical point of view, the same considerations can be done as in the previous subsection, concerning the troubles in the evaluation of the integrals, due to the characteristics of the integrand functions.

Here, for the sake of brevity, we simply give the expressions for the upper bound of the error that is made truncating the integral tail and for the static term for the three nonzero components of the fields.

Vertical electric field:

- upper bound:  $E(M) \leq |g_{sz}(kM)Q(kM)| \frac{\sqrt{2}k^4}{\sqrt{\pi kr}} \left(-\frac{kz}{2}\right)^{-\frac{7}{2}} \Gamma(\frac{7}{2}, \frac{-kMz}{2})$ , being  $g_{sz}(\lambda) = \frac{1}{n^2\mu + \mu_E}$ ;
- static term:

$$\lim_{k \rightarrow 0} \frac{jI(0, \omega)}{2\pi\omega\epsilon_0} \int_0^{+\infty} \frac{\lambda^3}{n^2\mu + \mu_E} \cdot J_0(\lambda r) \cdot e^{\mu_E z} Q(\lambda) d\lambda = \frac{I(0, 0)}{\pi\sigma} \int_0^H \frac{1}{R^3} F(\frac{3}{2}, -1, 1, \frac{r^2}{R^2}) P(z') dz'.$$

Radial electric field:

- upper bound:  $E(M) \leq |g_{sr}(kM)Q(kM)| \frac{\sqrt{2}k^2}{\sqrt{\pi kr}} \left(-\frac{kz}{2}\right)^{-\frac{5}{2}} \Gamma(\frac{5}{2}, \frac{-kMz}{2})$ , being  $g_{sr}(\lambda) = \frac{\mu_E}{n^2\mu + \mu_E}$ ;
- static term:

$$\lim_{k \rightarrow 0} -\frac{jI(0, \omega)}{2\pi\omega\epsilon_0} \int_0^{+\infty} \frac{\mu_E}{n^2\mu + \mu_E} \cdot J_1(\lambda r) \cdot e^{\mu_E z} \cdot \lambda^2 Q(\lambda) d\lambda = -\frac{3rI(0, 0)}{2\pi\sigma} \int_0^H \frac{1}{R^3} F(2, -\frac{1}{2}, 2, \frac{r^2}{R^2}) P(z') dz'.$$

Azimuthal magnetic field:

- upper bound:  $E(M) \leq |g_{sz}(kM)Q(kM)| \frac{2\sqrt{2}k^3}{\sqrt{\pi kr}} \left(\frac{-kz}{2}\right)^{-\frac{3}{2}} \Gamma\left(\frac{5}{2}, \frac{-kMz}{2}\right);$
- static term:  

$$\lim_{k \rightarrow 0} \frac{n^2 I(0, \omega)}{2\pi} \int_0^{+\infty} \frac{\lambda^2}{n^2 \mu + \mu_E} \cdot J_1(\lambda r) \cdot e^{\mu_E z} Q(\lambda) d\lambda = \frac{rI(0, 0)}{2\pi} \int_0^H \frac{1}{R^3} F\left(\frac{3}{2}, 0, 2, \frac{r^2}{R^2}\right) P(z') dz'.$$

### 13.2.3 Validation of the simplified approaches

In this subsection, a comparative analysis between the presented approach for overground and underground lightning field calculations and some of the most employed simplified formulas is performed.

#### 13.2.3.1 Overground electromagnetic field

Since it is well known (Cooray, 1992; Rubinstein, 1996) that the horizontal electric field is the most influenced by the ground conductivity and since its correct evaluation is of great interest especially for the problem of coupling with overhead power lines (Paul, 1994; Tesche *et al.*, 1997) when using the Agrawal *et al.* coupling model (Agrawal *et al.*, 1980; Nucci and Rachidi, 1995), some approximate approaches have been developed in a recent past in order to circumvent the task of the Sommerfeld's integrals evaluation in the computation of such field component.

Here, we will refer to the so-called Cooray–Rubinstein (CR) formula (Rubinstein, 1996), which allows the estimation of  $E_r$  from the knowledge of the electromagnetic field for the case of a perfectly conducting ground:

$$E_r(z, r) = -H_{\phi i}(0, r) \frac{\sqrt{\mu_0}}{\sqrt{\epsilon - \frac{\sigma}{j\omega}}} + E_{ri}(z, r) \quad (13.63)$$

where

- $E_r(r, z)$  is the horizontal electric field
- $H_{\phi i}(0, z)$  is the ideal azimuthal magnetic field at ground level
- $E_{ri}(r, z)$  is the ideal horizontal electric field (i.e. calculated with perfectly conducting ground)
- $\mu$  is the magnetic permeability in empty space
- $\epsilon$  and  $\sigma$  are respectively the ground electric permittivity and the conductivity
- $\omega$  is the angular frequency.

In order to perform a comparative analysis between such approximate formula and the exact approach, we considered two channel-base current waveforms, corresponding respectively to typical first and subsequent return strokes, based on the observations of Berger *et al.* (1975) Rachidi *et al.* (2001).

The channel-base currents are reproduced by a sum of two Heidler's functions (Heidler, 1985). The first return stroke channel-base current is characterized by a peak value of 30 kA and a maximum steepness of 12 kA/ $\mu$ s, whereas the

subsequent return stroke current has a peak value of 12 kA and a maximum steepness of 40 kA/μs.

The Heidler current expression is the following one:

$$i(0, t) = i_1(0, t) + i_2(0, t) \quad (13.64)$$

being respectively

$$i_1(0, t) = \frac{I_{01}}{\eta_1} \frac{\left(\frac{t}{\tau_{11}}\right)^{n1}}{1 + \left(\frac{t}{\tau_{11}}\right)^{n1}} e^{-\frac{t}{\tau_{12}}}, \quad i_2(0, t) = \frac{I_{02}}{\eta_2} \frac{\left(\frac{t}{\tau_{21}}\right)^{n2}}{1 + \left(\frac{t}{\tau_{21}}\right)^{n2}} e^{-\frac{t}{\tau_{22}}}, \quad (13.65)$$

$$\eta_1 = e^{-\left(\frac{\tau_{11}}{\tau_{12}}\right)\left(n_1 \frac{\tau_{12}}{\tau_{11}}\right)^{1/n1}} \quad \text{and} \quad \eta_2 = e^{-\left(\frac{\tau_{21}}{\tau_{22}}\right)\left(n_2 \frac{\tau_{22}}{\tau_{21}}\right)^{1/n2}} \quad (13.66)$$

The numerical values, corresponding to the first and subsequent stroke, are given in Table 13.1.

*Table 13.1 Parameters of the two Heidler's functions used to reproduce the channel-base current waveshape*

	$I_{01}$ (kA)	$\tau_{11}$ (μs)	$\tau_{12}$ (μs)	$n_1$	$I_{02}$ (kA)	$\tau_{21}$ (μs)	$\tau_{22}$ (μs)	$n_2$
First stroke	28	1.8	95	2	—	—	—	—
Subsequent stroke	10.7	0.25	2.5	2	6.5	2	230	2

The decay constant  $\alpha$  in the MTLE model is assumed to be equal to 2 km, a value that has been determined using experimental data (Rachidi *et al.*, 2001; Nucci and Rachidi, 1989).

As far as the speed within the lightning channel is concerned, the value adopted is  $1.5 \times 10^8$  m/s, while the channel height is assumed to be equal to 8 km. Such number is useless whenever all the calculations are carried out in the time domain; but, since the Sommerfeld's integrals evaluation is in the frequency domain, the knowledge of the channel height becomes necessary. In addition, it is worth noting that the choice of another model for  $P(z')$  (e.g. the TL model) would lead to similar results for the first transient (about 1 μs), since in this time range the lightning channel current waveform reaches a height of about 150 m (at the speed  $v = 1.5 \times 10^8$  m/s). For such a short height, the differences between MTLE and TL models are small. Finally, we decided to limit our analysis to the first microsecond of transient because we verified that the main differences between the exact formulation and the simplified approaches occur in such time frame.

In (Delfino *et al.*, 2008b) a detailed discussion on the results obtained by the comparative simulation campaign can be found. Here, we simply report the main comments that can be made:

- for very low conductivities ( $\sigma$  about  $10^{-4}$  S/m), the use of the exact approach is recommended (see Figure 13.10);

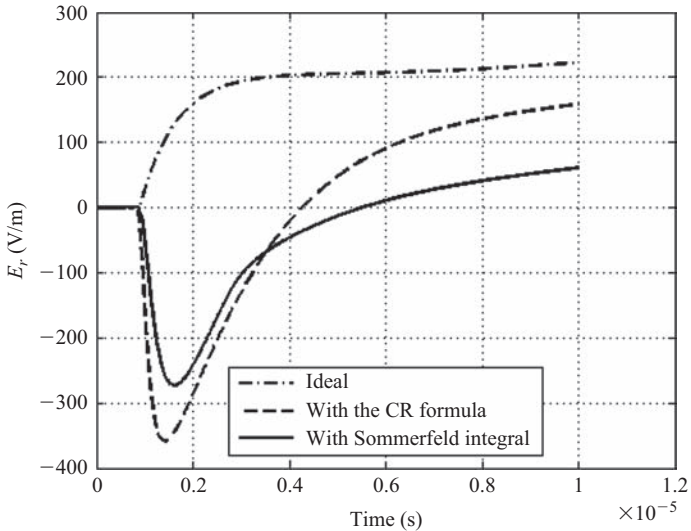


Figure 13.10 Radial electric field calculated with the CR formula, the Sommerfeld's integral and under the assumption of perfectly conducting ground ( $r = 250$  m,  $z = 10$  m and  $\sigma = 0.0001$  S/m). Channel-base current typical of subsequent strokes

- for very high conductivities ( $\sigma$  about  $10^{-2}$  S/m), the CR formula and the exact approach predict the same results (see Figure 13.11);
- for intermediate conductivities ( $\sigma$  about  $10^{-3}$  S/m) and close distances ( $r < 100$  m) to the lightning channel, the ‘ideal’ field is a quite good approximation (see Figure 13.12);
- for intermediate conductivities ( $\sigma$  about  $10^{-3}$  S/m) and observation points at a distance  $r$  from the lightning channel larger than 100 m, the CR formula is accurate and effective for the first stroke (Figure 13.13) and deviates from the exact approach of some per cent in the early time response and this only for typical subsequent strokes (see Figure 13.14).

As far as the other two components are concerned, neglecting the term involving the ground conductivity leads to satisfactory results for practically any value of the soil parameters and for horizontal distances up to 1 km (Delfino *et al.*, 2008b).

### 13.2.3.2 Underground electromagnetic field

As before, our attention will be mainly focused on the radial component of the electric field, since this is the predominant component of the lightning electric field that penetrates the ground and appears as the source term in the field-to-buried cables coupling equations (Paolone *et al.*, 2005; Petrache *et al.*, 2005).

The most popular approximate formula has been proposed by Cooray (Cooray, 2001) and provides the horizontal electric field produced by a vertical lightning

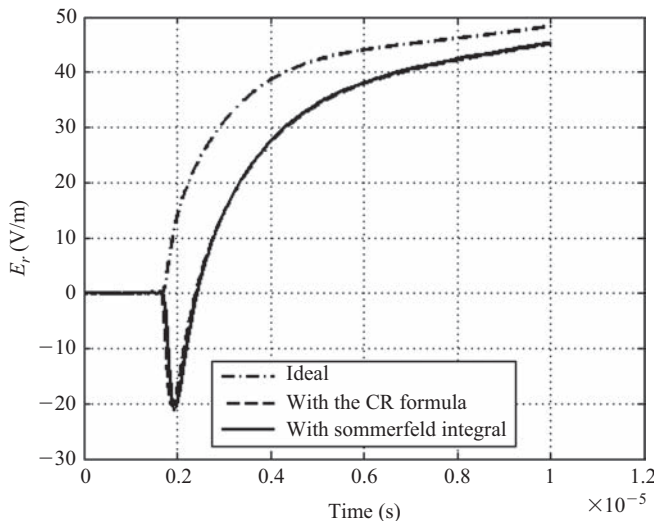


Figure 13.11 Radial electric field calculated with the CR formula, the Sommerfeld's integral and under the assumption of perfectly conducting ground ( $r = 500 \text{ m}$ ,  $z = 10 \text{ m}$  and  $\sigma = 0.01 \text{ S/m}$ ). Channel-base current typical of subsequent strokes

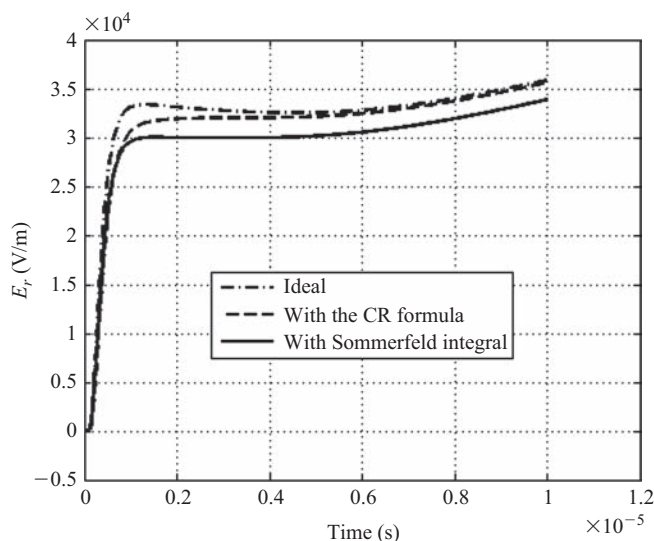


Figure 13.12 Radial electric field calculated with the CR formula, the Sommerfeld's integral and under the assumption of perfectly conducting ground ( $r = 20 \text{ m}$ ,  $z = 10 \text{ m}$  and  $\sigma = 0.001 \text{ S/m}$ ). Channel-base current typical of subsequent strokes

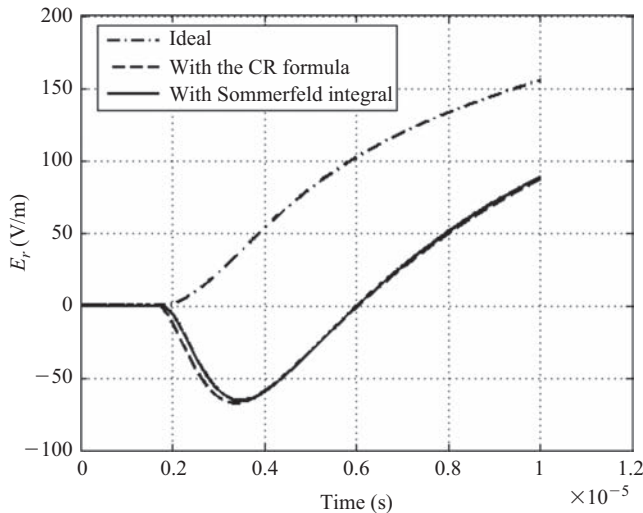


Figure 13.13 Radial electric field calculated with the CR formula, the Sommerfeld's integral and under the assumption of perfectly conducting ground ( $r = 500 \text{ m}$ ,  $z = 10 \text{ m}$  and  $\sigma = 0.001 \text{ S/m}$ ). Channel-base current typical of first strokes

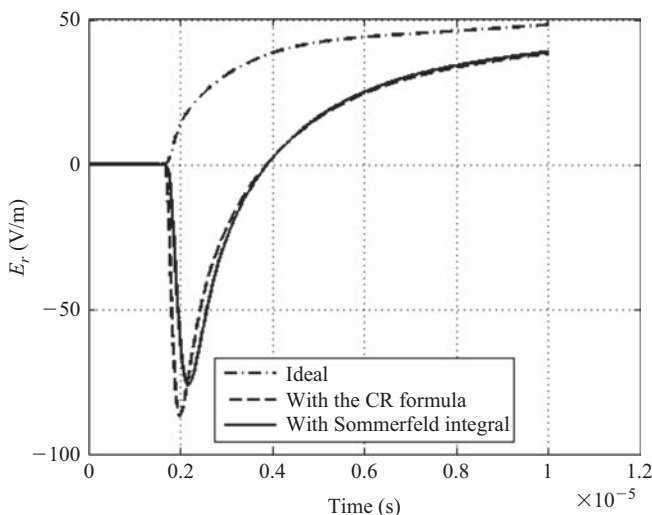


Figure 13.14 Radial electric field calculated with the CR formula, the Sommerfeld's integral and under the assumption of perfectly conducting ground ( $r = 500 \text{ m}$ ,  $z = 10 \text{ m}$  and  $\sigma = 0.001 \text{ S/m}$ ). Channel-base current typical of subsequent strokes

channel below the ground surface, as a function of the electric field at the air–soil interface.

In the time domain, one has that

$$e_{rL}(t, r, z) = \int_0^t e_{rL}(t-s, r, 0)y(s)ds \quad (13.67)$$

having indicated with low-case letters time-domain functions. The function  $y$  is defined as

$$y(t) = \frac{e^{-at/2}at_z}{2\sqrt{t^2 - t_z^2}} I_0\left(a\sqrt{t^2 - t_z^2}\right) u(t - t_z) + e^{-at_z/2}\delta(t - t_z) \quad (13.68)$$

being  $a = \sigma/\epsilon$ ,  $t_z = -z\sqrt{\mu_0\epsilon}$ ,  $\delta$  the Dirac function,  $u$  the step function and  $I_0$  the modified Bessel function of first type and zeroth order.

To compute the convolution integral (13.67) one must know the horizontal field at ground level, which can be calculated using the (CR) formula (Rubinstein, 1996).

The main conclusions of such comparative analysis are the following: at very close distances from the lightning channel, there are two main situations:

- for large values of the soil conductivity (say  $\sigma = 0.01$  S/m), the approximate formula produces accurate results both for the first and the subsequent strokes (see Figures 13.15 and 13.16).
- For smaller values of conductivities (say  $\sigma = 0.001$  S/m), the approximate formula yields to less satisfactory results, especially for the late time response

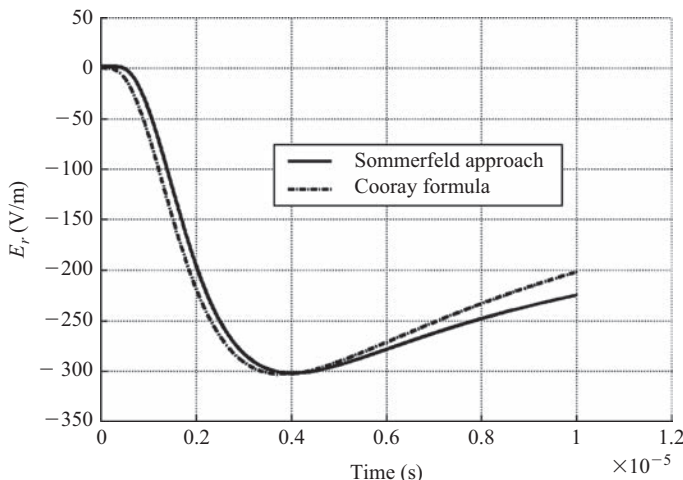


Figure 13.15 *Underground horizontal electric field generated by the first-stroke current ( $r = 50$  m,  $z = -10$  m and  $\sigma = 0.01$  S/m)*

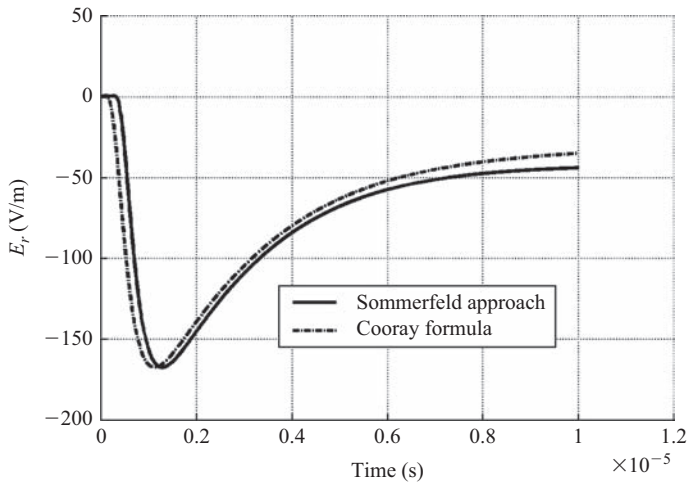


Figure 13.16 Underground horizontal electric field generated by a subsequent-stroke current ( $r = 50 \text{ m}$ ,  $z = -10 \text{ m}$  and  $\sigma = 0.01 \text{ S/m}$ )

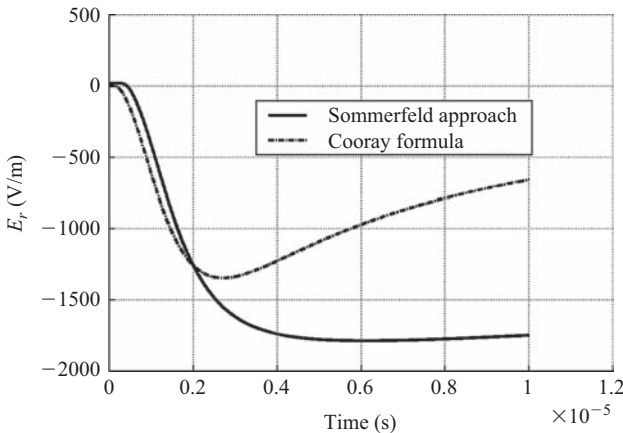


Figure 13.17 Underground horizontal electric field generated by the first-stroke current ( $r = 50 \text{ m}$ ,  $z = -10 \text{ m}$  and  $\sigma = 0.001 \text{ S/m}$ )

in the case of the first stroke (see Figure 13.17); while it seems to provide better results for the subsequent strokes (see Figure 13.18), even though at the late time some differences still persist. This is probably due to the fact that Cooray's expression is derived considering only the radiation component of the underground fields and that, for small distances, the radiation term is dominant only for the first microsecond or so.

If the horizontal distance grows up, the differences become less significant, since the radiation term plays a more dominant role (Delfino *et al.*, 2007).

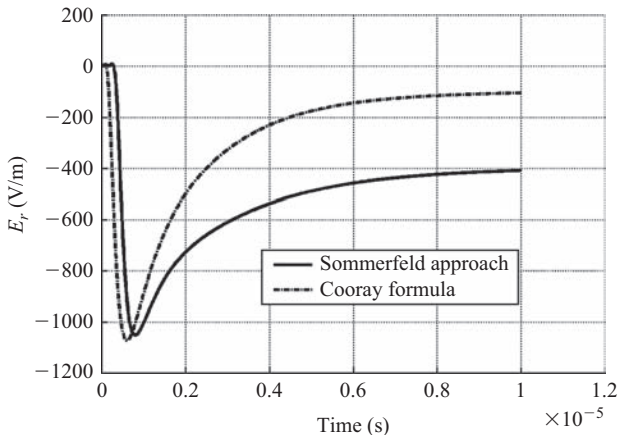


Figure 13.18 *Underground horizontal electric field generated by a subsequent-stroke current ( $r = 50$  m,  $z = -10$  m and  $\sigma = 0.001$  S/m)*

### 13.3 Lightning electromagnetic field calculation in presence of a lossy ground with frequency-dependent electrical parameters

In the previous paragraphs, even though no mathematical approximations were used in the theory underlying the outlined work, one major, yet commonly adopted, simplifying assumption was made on the considered model: the relevant soil electrical parameters, namely conductivity and permittivity, were assumed to be frequency independent. The validity of this hypothesis could be questionable, as extensive research on the subject, conducted since the early years of the last century (Smith-Rose, 1933, 1935), shows a non-negligible dependence of both permittivity and conductivity on the frequency (Fuller and Ward, 1970; Ramo *et al.*, 1994). As a matter of fact, ground electrical parameters are heavily affected by soil heterogeneous components and structure and, remarkably, by its water content (distinction between ‘wet ground’ and ‘dry ground’ is typically made (Fuller and Ward, 1970). Furthermore, a number of different phenomena take place over the frequency range of interest for lightning electromagnetic field evaluation (up to a few MHz), including dipolar molecules polarization, counter-ion diffusion polarization (due to separation of cations and anions), interfacial (Maxwell–Wagner) polarization, other polarization effects and various conduction and loss mechanisms, each acting on a specific frequency interval (De Loor, 1983; Rinaldi and Francisca, 1999), thus making conductivity and permittivity behave as frequency-dependent functions. As an example, according to (Fuller and Ward, 1984), for frequencies  $f$  up to 1 MHz, wet rocks conductivity slowly varies with  $f$  and typically lies in the range between  $10^{-1}$  and  $10^{-5}$  S/m, with the 1 MHz value seldom exceeding the low frequency one by more than one order of magnitude, while the relative dielectric permittivity asymptotically tends to a value less than that of the water for higher

frequencies and is usually inversely proportional to  $f$  in the lower portion of the range (where for some minerals and mixtures its value can be as high as  $10^4$  and even  $10^8$  below 1 Hz). In the same frequency range, the conductivity of dry rocks is proportional to  $f$ , with starting values (i.e. at low frequencies) lying in the range from  $10^{-6}$  to  $10^{-12}$  S/m, while their relative permittivity seldom exceeds 10, slowly varies with  $f$  and is characterized by a ratio between low frequencies and 1 MHz values seldom exceeding one order of magnitude.

In light of these considerations, our aim here is to investigate how the actual frequency-dependent characteristics of both permittivity and conductivity affect the electromagnetic fields radiated by a cloud-to-ground lightning return stroke. To do this, we make use of suitable relations, which have been proven effective to represent the frequency dependence of ground conductivity and permittivity for a number of soil types over the frequency range of interest (Scott, 1966; Longmire and Smith, 1975). Experimental measurements of the electrical parameters for various soils, mixtures and minerals, as well as theoretical explanations and proposed representations for their frequency behaviour can be found, e.g. in (De Loor, 1983; Fuller and Ward, 1984; Rinaldi and Francisca, 1999).

### 13.3.1 The dependence of soil conductivity and permittivity on the frequency

In 1966, Scott (1966) reported the results of measurements of the dielectric constant  $\epsilon$  and of the conductivity  $\sigma$  of many samples of soil, over the frequency range [ $10^2$ – $10^6$  Hz] and noted that the results for the many samples could be correlated quite well in terms of just one parameter, the water content  $p$ . By averaging these data, the author produced a set of curves  $\sigma(\omega)$  and  $\epsilon(\omega)$  as functions of the angular frequency  $\omega$  for different values of the water content. This means that, if one knows the water content of the soil, one can obtain a sufficiently accurate waveform expressing the functional dependence of the ground conductivity and permittivity on the angular frequency.

In 1975, Longmire and Smith (1975) proposed a model for the soil in order to provide an analytical expression for its conductivity and permittivity. Starting from the well-known relationship, which states that

$$J = (j\omega\epsilon + \sigma)E \quad (13.69)$$

$J$  being the (total) current density in the soil and  $E$  the electric field, it is possible to define an admittance  $Y = (j\omega\epsilon + \sigma)$  that allows to assimilate a cubic metre of soil to a network of resistor and capacitors (Figure 13.19).

Once the parameters of such a network are determined, it is possible to infer the conductivity and the permittivity of the ground from the real and the imaginary parts of the admittance respectively.

Specifically, with reference to the network of Figure 13.19, the admittance reads:

$$Y = \frac{1}{R_0} + j\omega C_\infty + \sum_{n=1}^N \frac{1}{R_n + \frac{1}{j\omega C_n}} \quad (13.70)$$

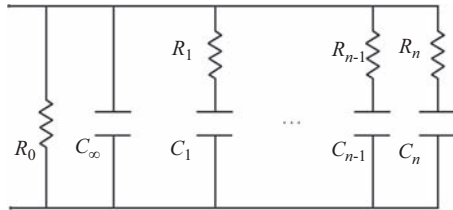


Figure 13.19 Soil equivalent network

Therefore, it follows that

$$\varepsilon = C_\infty + \sum_{n=1}^N \frac{C_n}{1 + (\omega/\beta_n)^2} \quad (13.71)$$

and

$$\sigma = \frac{1}{R_0} + \sum_{n=1}^N \frac{C_n \beta_n (\omega/\beta_n)^2}{1 + (\omega/\beta_n)^2} \quad (13.72)$$

with  $\beta_n = \frac{1}{R_n C_n}$ .

Now, defining

$$\left\{ \begin{array}{l} \varepsilon_\infty = \frac{C_\infty}{\varepsilon_0} \\ \sigma_0 = \frac{1}{R_0} \\ a_n = \frac{C_n}{\varepsilon_0} \\ f_n = \frac{\beta_n}{2\pi} \end{array} \right. \quad (13.73)$$

The relative permittivity  $\varepsilon_r$  and the conductivity can be written respectively in the following form:

$$\varepsilon_r(f) = \varepsilon_\infty + \sum_{n=1}^N \frac{a_n}{1 + (f/f_n)^2} \quad (13.74)$$

$$\sigma(f) = \sigma_0 + 2\pi\varepsilon_0 \sum_{n=1}^N \frac{a_n f_n (f/f_n)^2}{1 + (f/f_n)^2} \quad (13.75)$$

Finally, in order to have good fitting between (13.74–13.75) and the experimental curves obtained by Scott, Longmire and Smith (1975) have shown that it is sufficient to set

$$\varepsilon_{\infty} = 5 \quad (13.76)$$

$$\sigma_{\infty} = 8 \cdot 10^{-3} \left( \frac{p}{10} \right)^{1.54} \left[ \frac{S}{m} \right] \quad (13.77)$$

$$f_n = \left( \frac{p}{10} \right)^{1.28} 10^{n-1} [\text{Hz}] \quad (13.78)$$

where  $p$  is the per cent water volume, which typically ranges between 2 and 30. Lower values imply lots of ‘rock-like’ content. The values for the coefficients  $a_n$  are reported in Table 13.2. Our analysis assumes radially homogenous soil type and moisture content.

Table 13.2 Coefficients  $a_n$

$n$	1	2	3	4	5	6	7	8	9	10	11	12	13
$a_n$	$3.4 \cdot 10^6$	$2.74 \cdot 10^5$	$2.58 \cdot 10^4$	$3.38 \cdot 10^3$	$5.26 \cdot 10^2$	$1.33 \cdot 10^2$	$2.72 \cdot 10^1$	$1.25 \cdot 10^1$	4.8	2.17	0.98	0.392	0.173

Otherwise, it would be necessary to take into account the fact that, for any given location, the moisture content in the top metre varies seasonally by at least a factor of two, leading to a (roughly) factor-of-four gradient in electrical conductivity in the top two metres of soil. This creates an additional frequency-dependent behaviour at higher frequencies due to dependence of skin depth on frequency. The hypothesis of radially homogenous soil justifies (13.77) and (13.78) and allows us not to consider such an effect.

As an example, Figures 13.20 and 13.21 present the variation in conductivity and relative permittivity as a function of the frequency in the range ( $0$ – $5 \cdot 10^6$  Hz) and for water content  $p$  equal to 0.2%, 1% (to simulate rock-like ground), 2%, 10% and 30%, respectively.

### 13.3.2 Numerical simulation of overground and underground lightning electromagnetic field

Let us reconsider (13.18) and (13.62) that express respectively the overground and underground lightning electromagnetic fields: since they are carried out in the frequency domain, it is apparent that, if one is interested to consider the effect of the frequency-dependent ground parameters on the fields, it is sufficient to insert in

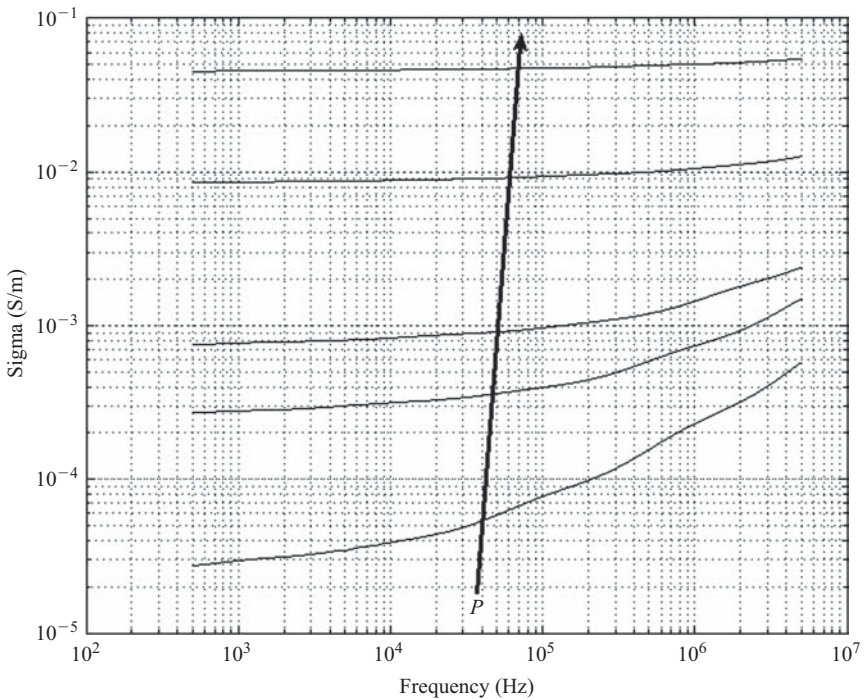


Figure 13.20 Ground conductivity as a function of the frequency for water content  $p$  equal to 0.2%, 1%, 2%, 10% and 30%, respectively

those expressions the functions  $\varepsilon_r(\omega/2\pi)$  and  $\sigma(\omega/2\pi)$  defined in (13.74) and (13.75) respectively, thus obtaining

$$\left\{ \begin{array}{l} E_{zL} = E_{zil} - \frac{jI(0, \omega)}{2\pi\omega\varepsilon_0} \int_0^{+\infty} \frac{\mu_E}{n^2\mu + \mu_E} \cdot J_0(\lambda r) \cdot e^{-\mu z'} \cdot \frac{\lambda^3}{\mu} Q(\lambda) d\lambda \\ E_{rL} = E_{ril} - \frac{jI(0, \omega)}{2\pi\omega\varepsilon_0} \int_0^{+\infty} \lambda^2 J_1(\lambda r) e^{-\mu z} \frac{\mu_E}{n^2\mu + \mu_E} Q(\lambda) d\lambda \\ H_{\varphi L} = H_{\varphi iL} - \frac{I(0, \omega)}{2\pi} \int_0^{+\infty} \frac{\mu_E}{n^2\mu + \mu_E} \cdot J_1(\lambda r) \cdot e^{-\mu z} \cdot \frac{\lambda^2}{\mu} Q(\lambda) d\lambda \end{array} \right. \quad (13.79)$$

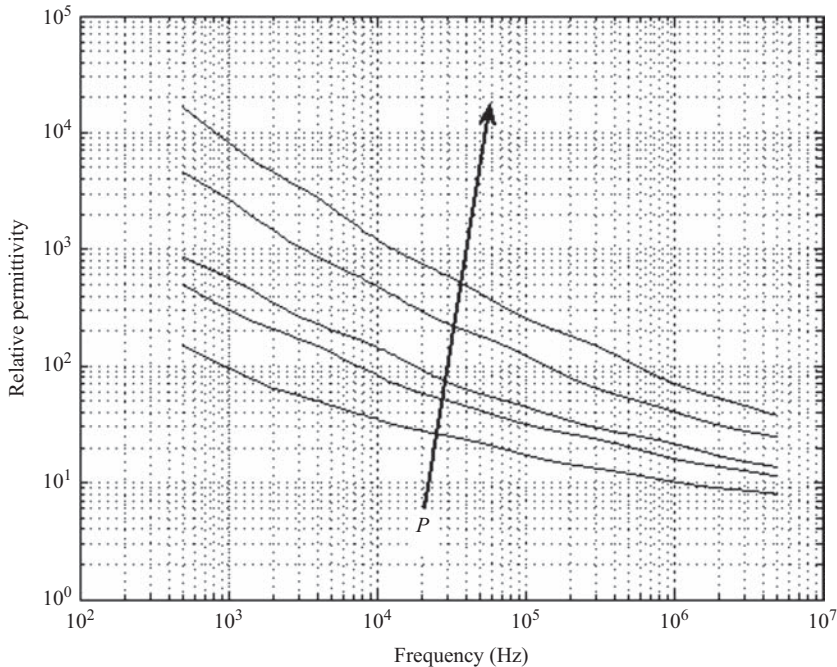


Figure 13.21 Ground relative permittivity as a function of the frequency for water content  $p$  equal to 0.2%, 1%, 2%, 10% and 30%, respectively

for the overground lightning electromagnetic field and

$$\left\{ \begin{array}{l} E_{zL} = \frac{jI(0, \omega)}{2\pi\omega\epsilon_0} \int_0^{+\infty} \frac{\lambda^3}{n^2\mu + \mu_E} \cdot J_0(\lambda r) \cdot Q(\lambda) e^{\mu_E z} d\lambda \\ E_{rL} = \frac{jI(0, \omega)}{2\pi\omega\epsilon_0} \int_0^{+\infty} J_1(\lambda r) Q(\lambda) e^{\mu_E z} \frac{\lambda^2\mu_E}{n^2\mu + \mu_E} d\lambda \\ H_{\varphi L} = -\frac{n^2 I(0, \omega)}{2\pi} \int_0^{+\infty} \frac{\lambda^2}{n^2\mu + \mu_E} \cdot J_1(\lambda r) \cdot Q(\lambda) e^{\mu_E z} d\lambda \end{array} \right. \quad (13.80)$$

for the underground one. Equations (13.79) and (13.80) are formally identical to (13.18) and (13.62), since the dependence of the soil parameters on the frequency is hidden in the definition of the quantities  $n^2$  and  $\mu_E$ .

In Delfino *et al.*, 2009 a detailed analysis on the effects of taking into account the frequency-dependent behaviour of the soil characteristics in the evaluation of

*Table 13.3 Summary of the results and recommended models for the calculation of electromagnetic fields generated by lightning return strokes*

<b>Field component</b>	<b>Aboveground</b>	<b>Underground</b>
$E_r$	For low per cent water volume ( $p \leq 1\%$ ), it is necessary to include the frequency dependence of ground electrical parameters	Significant differences between the model with constant soil parameters and the one with $\sigma$ and $\epsilon$ variable with $\omega$ only for very low ( $p \leq 1\%$ ) and very high per cent ( $p \geq 30\%$ ) water volume
$E_z$	The Sommerfeld term is negligible, no matter the model adopted for $\sigma$ and $\epsilon$	Significant differences between the model with constant soil parameters and the one with $\sigma$ and $\epsilon$ variable with $\omega$ for very low ( $p \leq 1\%$ ) and very high per cent ( $p \geq 30\%$ ) water volume
$H_\phi$	The Sommerfeld term is negligible, no matter the model adopted for $\sigma$ and $\epsilon$	Significant differences between the model with constant soil parameters and the one with $\sigma$ and $\epsilon$ variable with $\omega$ only for very high per cent ( $p \geq 30\%$ ) water volume

the electromagnetic fields is presented. Here, we simply limit our discussion to summarize in Table 13.3 the main results.

### 13.4 Lightning electromagnetic field calculation in presence of a lossy and horizontally stratified ground

In the previous sections, the ground parameters have been considered either constant or frequency dependent; in both cases, they have been treated as homogeneous.

The aim of the present section is to investigate the effect of the soil stratification on the evaluation of the lightning electromagnetic fields.

One of the first studies on the propagation of electromagnetic waves along a stratified medium is due to Wait, who showed that the concepts of ground surface impedance and attenuation function can be used to represent the effect of a multi-layered soil (Wait, 1996). For the case of the lightning radiation over a stratified conducting ground, a recent literature review can be found in (Shoory *et al.*, 2010). Here, the formulation proposed by Wait (1996) for a dipole is extended to account for the presence of the lightning channel and the derivation of the final formulas is presented in details starting from the field problem, consisting of one Helmholtz equation for each layer and the suitable boundary conditions (Sommerfeld, 1949; Delfino *et al.*, 2003).

### 13.4.1 Statement of the problem and derivation of the Green's functions for the electromagnetic field

Here, we are interested in determining the field radiated by a vertical dipole located at a height  $z'$  over a lossy stratified ground.

The geometry of the problem is shown in Figure 13.22. The upper half-space is air, which is assumed to be lossless and characterized by a magnetic permeability  $\mu_0$  and an electric permittivity  $\epsilon_0$ . The lossy ground (lower half-space) has two layers, with conductivities  $\sigma_1$  and  $\sigma_2$  and relative electric permittivities  $\epsilon_{r1}$  and  $\epsilon_{r2}$ . The depth of the first layer is  $h_1$ . The observation point is  $P(r, \phi, z)$ .

The following set of equations applies to this problem (Sommerfeld, 1949):

$$\Delta \vec{A} + k^2 \vec{A} = -\mu_0 \delta(P - P') \vec{e}_3 \quad z > 0 \quad (13.81)$$

$$\Delta \vec{A}_{E1} + k_{E1}^2 \vec{A}_{E1} = 0 \quad -h_1 < z < 0 \quad (13.82)$$

$$\Delta \vec{A}_{E2} + k_{E2}^2 \vec{A}_{E2} = 0 \quad z < -h_1 \quad (13.83)$$

$$\lim_{r \rightarrow \infty} \sqrt{r} \left( \frac{\partial A}{\partial r} - jkA \right) = 0 \quad (13.84)$$

$$A = A_{E1} \quad z = 0 \quad (13.85)$$

$$\frac{1}{k^2} \frac{\partial A}{\partial z} = \frac{1}{k_{E1}^2} \frac{\partial A_E}{\partial z} \quad z = 0 \quad (13.86)$$

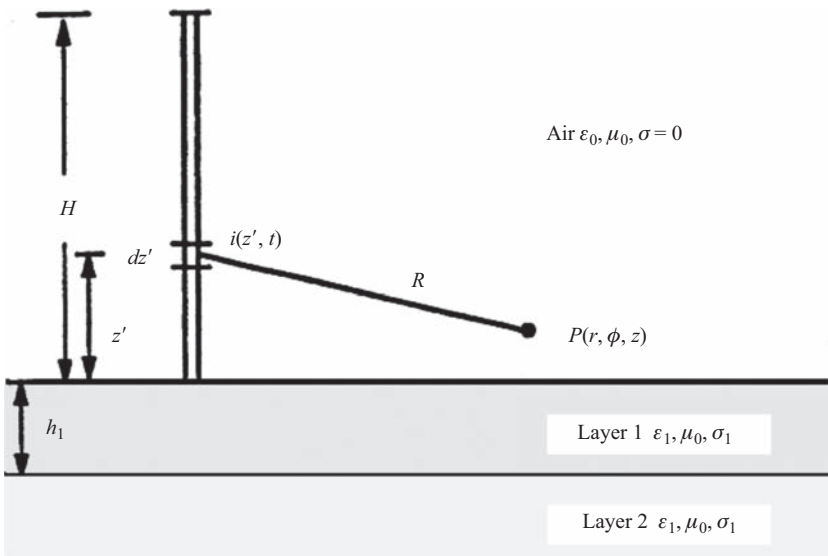


Figure 13.22 Model geometry: the lightning radiation over a multilayered ground

$$A_{E1} = A_{E2} \quad z = -h_1 \quad (13.87)$$

$$\frac{1}{k_{E1}^2} \frac{\partial A_{E1}}{\partial z} = \frac{1}{k_{E2}^2} \frac{\partial A_{E2}}{\partial z} \quad z = -h_1 \quad (13.88)$$

where  $\vec{A}$  is the vector potential in the upper half-space (air),  $\vec{A}_{E1}(\vec{A}_{E2})$  is the vector potential in the first (second) ground layer,  $k^2 = \omega^2 \mu_0 \epsilon_0$  is the wave number in air ( $\omega$  being the angular frequency),  $k_{E1(2)}^2 = \omega^2 \epsilon_0 \epsilon_{r1(2)} \mu_0 + j\omega \mu_0 \sigma_{1(2)}$  is the wave number in the first (second) ground layer and  $\delta$  is the Dirac distribution. Equations (13.81)–(13.83) are Helmholtz equations that hold respectively in air and in the two earth layers, while (13.85–13.88) are the interface conditions, which must be satisfied in order to ensure the continuity of the tangential magnetic and electric fields at ground level and at the transition between the first and the second layers. Finally, as shown by Sommerfeld (1949), with the addition of the well-known radiation condition (13.84), the problem has a unique solution.

It should be observed that the set of equations (13.81–13.88) has been derived assuming, as in the previous sections, for all variables a time-harmonic dependence of the kind  $e^{-j\omega t}$ .

In order to solve these equations (Sommerfeld, 1949), one can first solve (13.84) and then modify the obtained solution in order to meet the interface conditions. Sommerfeld himself showed that  $A_p = (\mu_0/4\pi)(e^{ikR}/R)$  with  $R = \sqrt{r^2 + (z-z')^2}$  is the solution of (13.81) and (13.84). Moreover, he proved that

$$A_p = \frac{\mu_0}{4\pi} \int_0^{+\infty} \frac{\lambda}{\mu} e^{-\mu|z-z'|} J_0(\lambda r) d\lambda \quad (13.89)$$

where  $\mu^2 = \lambda^2 - k^2$  and  $J_0$  is the Bessel function of first kind and zeroth order. Thus, it is sufficient to find a solution of the homogeneous Helmholtz equation, which, added to  $A_p$ , meets the interface conditions to find the final solution of the problem. It can be easily proven that the function  $u$  defined as

$$u(r, z) = e^{\pm\mu z} J_0(\lambda r) \quad (13.90)$$

is a solution of the problem  $\Delta u + h^2 u = 0$  in cylindrical coordinates for any  $\lambda$  and with  $\lambda^2 = \mu^2 + h^2$  (Sommerfeld, 1949). As a consequence, also the function  $\frac{\mu_0}{4\pi} \int_0^{+\infty} b_0(\lambda) J_0(\lambda r) e^{-\mu(z+z')} d\lambda$  is a solution of the homogeneous Helmholtz problem in air for any function  $b_0$ .

This means that, in order to meet the interface conditions, one can look for a solution of the kind:

$$A = A_p + \frac{\mu_0}{4\pi} \left[ \int_0^{+\infty} b_0(\lambda) J_0(\lambda r) e^{-\mu(z+z')} d\lambda \right] \quad (13.91)$$

$$A_{E1} = \frac{\mu_0}{4\pi} \left[ \int_0^{+\infty} e^{-\mu z'} J_0(\lambda r) (a_1(\lambda) e^{-\mu_{E1} z} + b_1(\lambda) e^{\mu_{E1} z}) d\lambda \right] \quad (13.92)$$

and

$$A_{E2} = \frac{\mu_0}{4\pi} \left[ \int_0^{+\infty} e^{-\mu z'} J_0(\lambda r) b_2(\lambda) e^{\mu_{E2} z} d\lambda \right] \quad (13.93)$$

where the functions  $b_0, a_1, b_1$  and  $b_2$  can be determined imposing the four interface conditions and  $\mu_{Ei}^2 = \lambda^2 - k_{Ei}^2, i = 1, 2$ . It should be noticed that the coefficient of the term  $e^{-\mu_{E2} z}$  is set to zero in order to ensure the convergence of the integral when  $z \rightarrow -\infty$ . Imposing the interface conditions, one obtains that

$$b_0(\lambda) = R(\lambda) \frac{\lambda}{\mu} \quad (13.94)$$

$R$  being the reflection coefficient (Wait, 1996), defined as

$$R(\lambda) = \frac{w_0(\lambda) - z_1(\lambda)}{w_0(\lambda) + z_1(\lambda)} \quad (13.95)$$

where

$$w_0(\lambda) = \frac{\mu_{E1}}{k_{E1}^2} \quad (13.96)$$

and  $z_1$  is the surface impedance given by

$$z_1(\lambda) = w_1(\lambda) \frac{w_2(\lambda)(e^{\mu_{E1} h_1} + e^{-\mu_{E1} h_1}) + w_1(\lambda)(e^{\mu_{E1} h_1} - e^{-\mu_{E1} h_1})}{w_1(\lambda)(e^{\mu_{E1} h_1} + e^{-\mu_{E1} h_1}) + w_2(\lambda)(e^{\mu_{E1} h_1} - e^{-\mu_{E1} h_1})} \quad (13.97)$$

where the quantities  $w_1$  and  $w_2$  appearing in (13.97) are defined as

$$w_1(\lambda) = \frac{\mu_{E1}}{k_{E1}^2} \quad (13.98)$$

and

$$w_2(\lambda) = \frac{\mu_{E2}}{k_{E2}^2} \quad (13.99)$$

A brief discussion on the physical interpretation of the reflection coefficient is in order: equation (13.89) states that, for each frequency, the vector potential  $A_p$  due to the vertical dipole in the free space is a superposition of waves (belonging to a continuous spectrum) of the kind defined in (13.90), each characterized by a different value of  $\lambda$  and whose amplitude is  $\lambda/\mu$ . The presence of the soil generates, for each value of  $\lambda$ , a reflected wave, whose amplitude is related to the corresponding incident wave by the coefficient  $R$ .

Once the vector potential spatial distribution has been obtained, the expression of the three nonzero components of the overground field can be easily derived according to the following relationships:

$$\begin{aligned} E_z &= \frac{j\omega}{k^2} \left( \frac{\partial^2 A}{\partial z^2} + k^2 A \right) \\ E_r &= \frac{j\omega}{k^2} \left( \frac{\partial^2 A}{\partial z \partial r} \right) \\ H_\varphi &= -\frac{1}{\mu_0} \frac{\partial A}{\partial r} \end{aligned} \quad (13.100)$$

Substituting (13.91) and (13.94) into (13.100), one obtains the expression of the fields that read:

$$\begin{aligned} E_z &= \frac{1}{4\pi\omega\epsilon_0} \left[ \begin{array}{l} \frac{2(z-z')^2 - r^2}{cR^4} \\ + \frac{2(z-z')^2 - r^2}{-j\omega R^5} \\ + j\omega \frac{r^2}{c^2 R^3} \end{array} \right] e^{j\omega(\frac{R}{c})} - \frac{j}{2\pi\omega\epsilon_0} \int_0^{+\infty} \frac{1-R(\lambda)}{2} J_0(\lambda r) e^{-\mu(z+z')} \frac{\lambda^3}{\mu} d\lambda \\ E_r &= \frac{1}{4\pi\epsilon_0} \left[ \begin{array}{l} \frac{3r(z-z')}{cR^4} \\ + \frac{3r(z-z')}{-j\omega R^5} \\ + j\omega \frac{r(z-z')}{cR^3} \end{array} \right] e^{j\omega(\frac{R}{c})} - \frac{j}{2\pi\omega\epsilon_0} \int_0^{+\infty} \lambda^2 J_1(\lambda r) e^{-\mu(z+z')} \frac{1-R(\lambda)}{2} d\lambda \\ H_\varphi &= \frac{1}{4\pi} \left[ \frac{r}{R^3} - j\omega \frac{r}{cR^2} \right] e^{j\omega(\frac{R}{c} + \frac{|z'|}{v})} - \frac{1}{2\pi} \int_0^{+\infty} \frac{1-R(\lambda)}{2} J_1(\lambda r) e^{-\mu(z+z')} \frac{\lambda^2}{\mu} d\lambda \end{aligned} \quad (13.101)$$

The first terms in the above expressions of the fields are as in the previous sections called ‘ideal fields’, since they would be the only nonzero terms if the ground was a PEC.

In a similar way, one can easily determine the underground fields first by obtaining the following expressions of the coefficients  $a_1$ ,  $b_1$  and  $b_2$  (which can be

done imposing again the interface conditions (13.85–13.88)),

$$\begin{cases} a_1(\lambda) = \frac{w_1 \left( \frac{\lambda}{\mu} + b_0(\lambda) \right) - w_0 \left( \frac{\lambda}{\mu} - b_0(\lambda) \right)}{2w_2} \\ b_1(\lambda) = \frac{w_1 \left( \frac{\lambda}{\mu} + b_0(\lambda) \right) + w_0 \left( \frac{\lambda}{\mu} - b_0(\lambda) \right)}{2w_2} \\ b_2(\lambda) = \frac{b_1(\lambda)w_1}{w_1 + w_2} e^{h_1(\mu_{E2} - \mu_{E1})} \end{cases} \quad (13.102)$$

then inserting them in (13.92) and (13.93) and finally recalling the relationships between the vector potential and the fields that state:

$$\begin{cases} E_{z1(2)} = \frac{j\omega}{k_{E1(2)}^2} \left( \frac{\partial^2 A_{E1(2)}}{\partial z^2} + k_{E1(2)}^2 A_{E1(2)} \right) \\ E_{r1(2)} = \frac{j\omega}{k_{E1(2)}^2} \left( \frac{\partial^2 A_{E1(2)}}{\partial z \partial r} \right) \\ H_{\varphi 1(2)} = -\frac{1}{\mu_0} \frac{\partial A_{E1(2)}}{\partial r} \end{cases} \quad (13.103)$$

### 13.4.2 Derivation of the lightning electromagnetic field

The Green's functions (13.101) are now utilized to obtain the expressions for the electromagnetic field due to a lightning return stroke. In order to reach this goal, it is sufficient to do as in section 13.2.1.3. Here, as an example, we report the expression for the overground field, that is to say

$$\begin{cases} E_{zL} = E_{ziL} - \frac{jI(0, \omega)}{2\pi\omega\epsilon_0} \int_0^{+\infty} \frac{1 - R(\lambda)}{2} J_0(\lambda r) e^{-\mu z'} \frac{\lambda^3}{\mu} Q(\lambda) d\lambda \\ E_{rL} = E_{riL} - \frac{jI(0, \omega)}{2\pi\omega\epsilon_0} \int_0^{+\infty} \lambda^2 J_1(\lambda r) e^{-\mu z} \frac{1 - R(\lambda)}{2} Q(\lambda) d\lambda \\ H_{\varphi L} = H_{\varphi iL} - \frac{I(0, \omega)}{2\pi} \int_0^{+\infty} \frac{1 - R(\lambda)}{2} J_1(\lambda r) e^{-\mu z} \frac{\lambda^2}{\mu} Q(\lambda) d\lambda \end{cases} \quad (13.104)$$

where the expressions of the ideal fields  $E_{ziL}$ ,  $E_{riL}$  and  $H_{\varphi iL}$  are those defined in (13.20–13.22).

### 13.4.3 The reflection coefficient $R$

We will discuss now the main mathematical properties of the reflection coefficient  $R$ , defined in (13.95). First of all, it can be shown that the absolute values of both  $R$  and  $(1 - R)/2$  are decreasing as  $\lambda$  increases for  $\lambda \gg k$ . This observation will be useful in the numerical treatment of the integrals in order to find an upper bound for the integral tail. Second, one can easily verify that

$$\lim_{h_1 \rightarrow \infty} \frac{1 - R(\lambda)}{2} = \frac{\mu_E}{n^2 \mu + \mu_E} \quad (13.105)$$

which confirms the fact that (13.104) reduces to the expression of the field in the case of a one-layer soil. Then, in order to evaluate the static limit of the Sommerfeld integrals (i.e. the DC fields), it is necessary to analyse the behaviour of the function  $(1 - R)/2$  when  $\omega$  approaches zero. Since it is apparent that, for small values of  $\omega$

$$\begin{aligned} n_i^2 &\rightarrow \frac{j\sigma_i}{\omega\epsilon_0}; \quad w_0 \rightarrow \frac{\lambda}{k^2} \\ \mu_{Ei}^2 &\rightarrow \lambda^2; \quad w_i \rightarrow \frac{\lambda}{k^2} \frac{\omega\epsilon_0}{j\sigma_i} \\ \mu^2 &\rightarrow \lambda^2 \end{aligned} \quad (13.106)$$

it readily follows that

$$\lim_{\omega \rightarrow 0} \frac{1 - R(\lambda)}{2} = \frac{\omega\epsilon_0}{j\sigma_1} \frac{\frac{e^{\lambda h_1} - e^{-\lambda h_1}}{\sigma_1} + \frac{e^{\lambda h_1} + e^{-\lambda h_1}}{\sigma_2}}{\frac{e^{\lambda h_1} + e^{-\lambda h_1}}{\sigma_1} + \frac{e^{\lambda h_1} - e^{-\lambda h_1}}{\sigma_2}} \quad (13.107)$$

which states that the limit is zero and the function  $(1 - R)/2$  is linear in the neighbourhood of  $\omega = 0$ .

After some algebraic manipulations, (13.107) can be rewritten as

$$\lim_{k \rightarrow 0} \left( \frac{1 - R(\lambda)}{2} \right) = \frac{\omega\epsilon_0}{j\sigma_1} f(\lambda) \quad (13.108)$$

in which

$$f(\lambda) = \frac{(\sigma_2 + \sigma_1)e^{\lambda h_1} + (\sigma_1 - \sigma_2)e^{-\lambda h_1}}{(\sigma_2 + \sigma_1)e^{\lambda h_1} - (\sigma_1 - \sigma_2)e^{-\lambda h_1}} \quad (13.109)$$

It can be observed that the function  $f$  is decreasing with  $\lambda$  if the conductivity of the first layer is greater than the conductivity of the second one; in the other case the function is increasing with  $\lambda$  but always remaining smaller than one. This means that in any case an upper bound for the function  $f$  is given by

$$|f(\lambda)| \leq \max\{1, f(M)\} \quad \lambda \geq M \quad (13.110)$$

Such bound will be useful when evaluating the upper bound for the static term.

Figures 13.23–13.27 illustrate some of the most important physical properties of the reflection coefficient  $R$ , obtained considering for the first layer  $\sigma_1 = 0.002 \text{ S/m}$  and  $\varepsilon_{r1} = 5$  and for the second  $\sigma_2 = 0.1 \text{ S/m}$  and  $\varepsilon_{r2} = 80$ . In Figures 13.23 and 13.24, the ratios between the function  $(1 - R)/2$  and the equivalent function for the case of homogenous ground  $g_s$  (Delfino *et al.*, 2008a) are plotted for two different values of

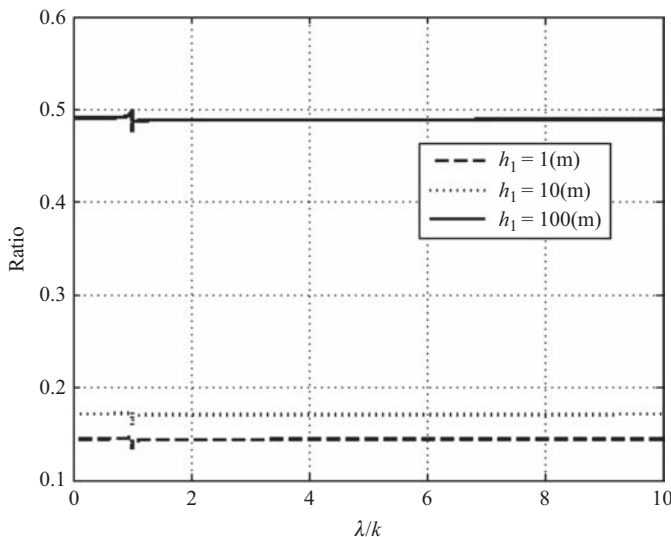


Figure 13.23 Ratio between the function  $(1 - R)/2$  and the function  $g_s$  for  $f = 1 \text{ kHz}$

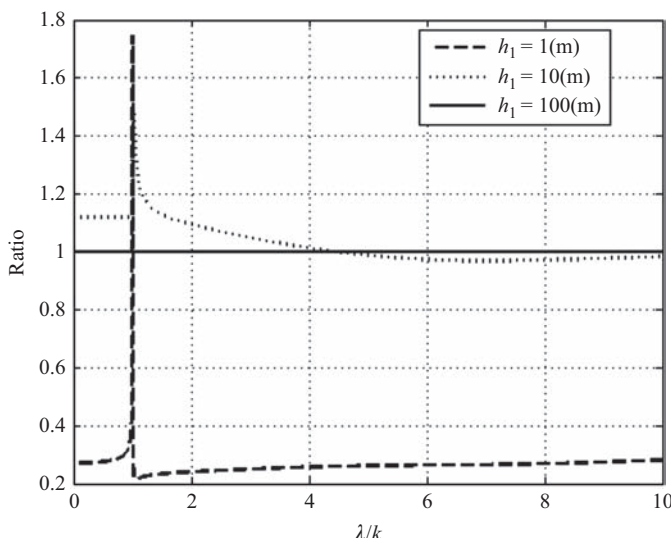


Figure 13.24 Ratio between the function  $(1 - R)/2$  and the function  $g_s$  for  $f = 1 \text{ MHz}$

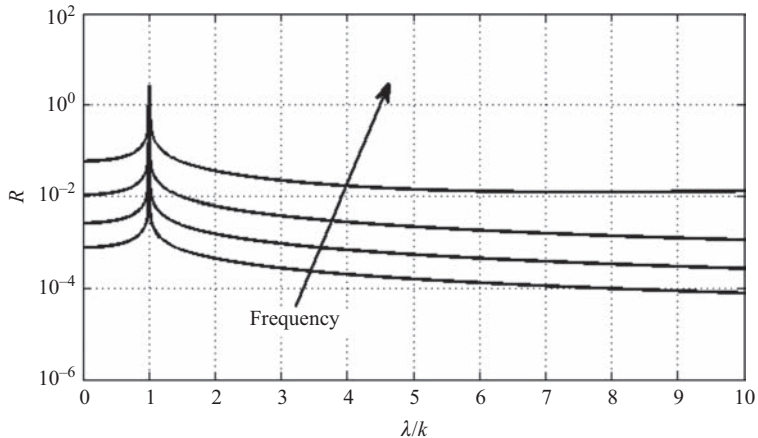


Figure 13.25 Reflection coefficient for first layer depth of 1 m

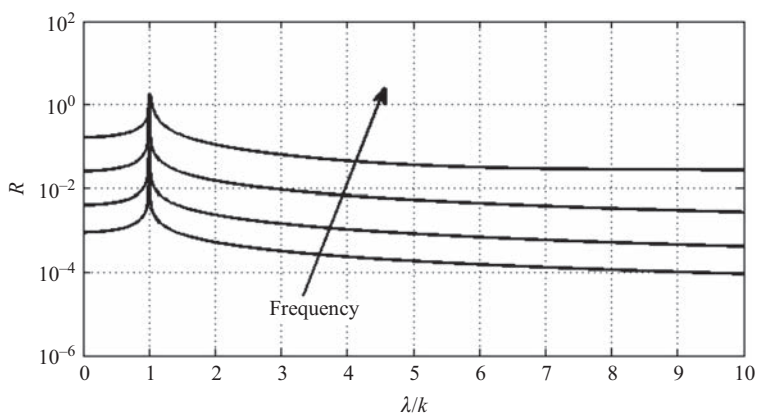


Figure 13.26 Reflection coefficient for first layer depth of 10 m

the frequency, namely 1 kHz and 1 MHz. As can be seen from the figures, if the frequency increases from 1 kHz to 1 MHz, it is sufficient to have a smaller depth of the first layer to make the ratio become closer to one and therefore to make the corresponding fields become closer one to each other.

In other words, the more high frequencies are ‘present’ in the spectrum of the lightning channel current, the closer are the corresponding fields to the ones that would be present in the case of a homogeneous ground.

Figure 13.25 shows the absolute value of the reflection coefficient for four different values of the frequency and in the case of a first layer depth of 1 m. As can be seen, at higher frequencies the reflected wave is larger. The same observation applies to the case of larger first layer depth, namely 10 m (Figure 13.26) and

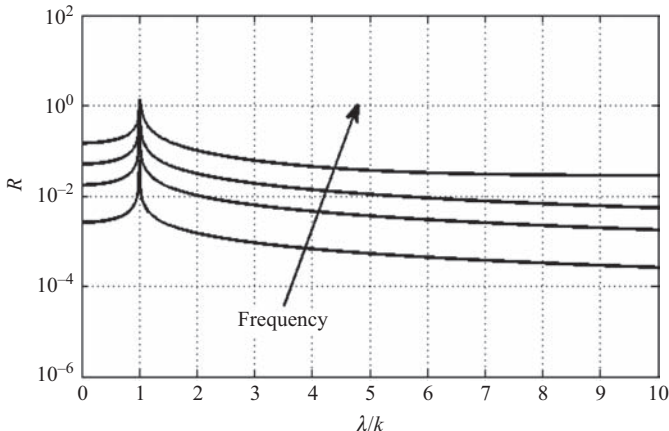


Figure 13.27 Reflection coefficient for first layer depth of 100 m

100 m (Figure 13.27), with the only difference that, for each frequency, the corresponding values are higher. Extrapolating this result, we can conclude that the maximum magnitude of the reflected wave is obtained for a homogeneous single-layer ground.

#### 13.4.4 The effect of the stratified soil on the overground electromagnetic field

The aim of this section is to investigate the effect of the soil stratification on the evaluation of the electromagnetic field in air. Let us assume the same model (and the same numerical values of the parameters) for the channel current as in the previous sections. Furthermore, let the height of the observation point be fixed to 10 m, and suppose to choose two horizontal distances, 50 m and 1000 m, to represent a very near observation point and a farer one.

As far as the soil properties are concerned, we have assumed that both layers have the same magnetic constant, i.e.  $\mu_0$ . The first layer conductivity has been fixed to 0.002 S/m and the relative permittivity is assumed to be 5. The second layer is characterized by  $\sigma = 0.1$  S/m and  $\varepsilon_r = 80$ . Two values for the depth of the first layer have been chosen: 2 m and 5 m.

As far as the vertical component of the electric field and the azimuthal component of the magnetic one are concerned, no matter the distance, the kind of the stroke and the depth of the first layer, the stratified soil has practically no effect on the field. This is not surprising, since, in Section 2.3.1, it has been shown that the vertical component of the electric field is not affected by the presence of the ground, which can be considered as a PEC.

The case of the radial field is analysed in Figures 13.28–13.33. The label ‘only first (second) layer’ appearing in the graphs means that we considered the case of

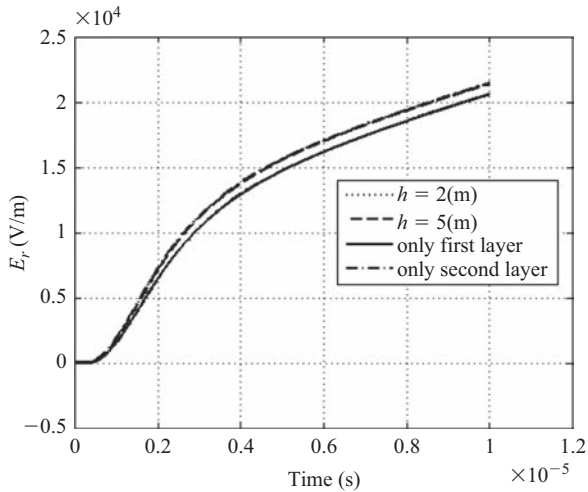


*Figure 13.28 Radial component of the electric field at a distance of 50 m generated by a first-stroke current*

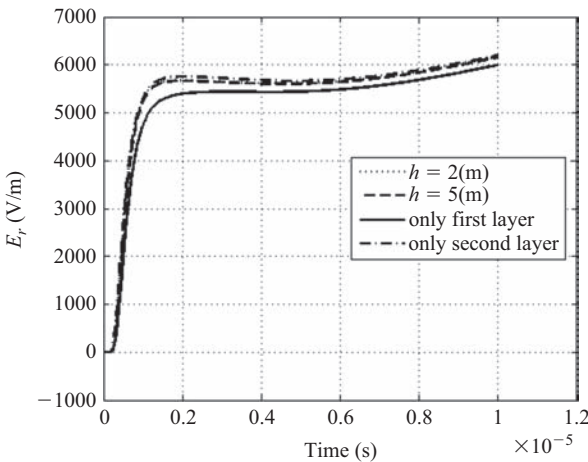


*Figure 13.29 Radial component of the electric field at a distance of 50 m generated by a subsequent-stroke current*

homogeneous lossy soil with the properties of the first (second) layer. Figures 13.28–13.29 plot the case of radial distance of 50 m.

The following considerations can be done:

- With the considered value of  $\sigma$ , the second layer is substantially a PEC; so the ‘only second layer’ graphs are practically the PEC case ones.

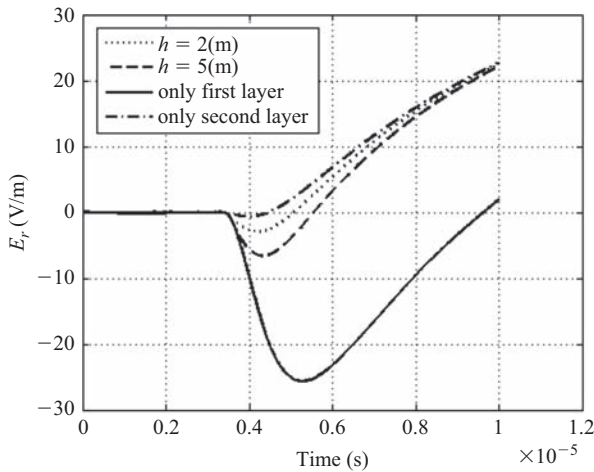


Figure 13.30 Radial component of the electric field at a distance of 1000 m generated by a first-stroke current

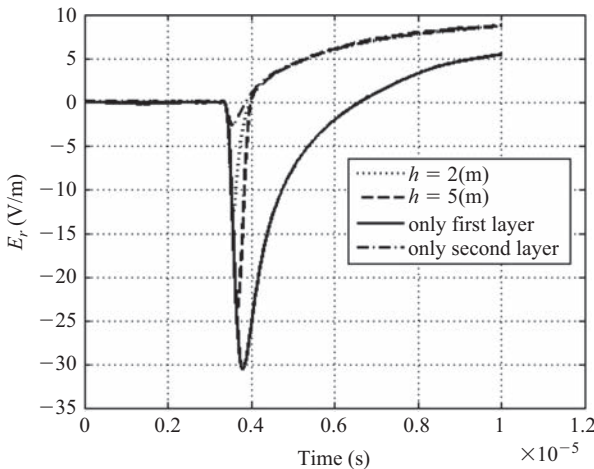
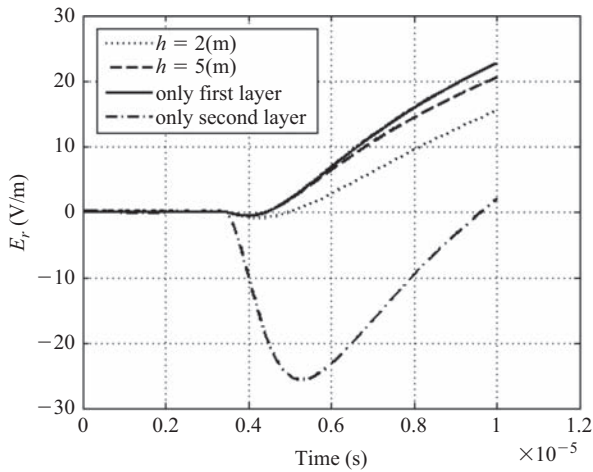
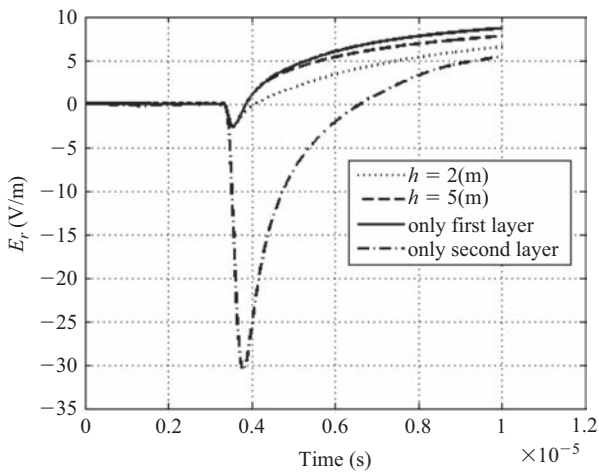


Figure 13.31 Radial component of the electric field at a distance of 1000 m generated by a subsequent-stroke current

- The ‘only second layer’ field is greater than the others, since the Sommerfeld term, which is negative, here is negligible with respect to the ideal one. This does not happen in the ‘first layer’ field, where the effect of the soil is stronger.
- No matter the first layer depth, the presence of the second one makes the field be substantially equal to the ‘only second layer’ case. If such depth becomes greater than 5 m, the resulting graph will always be ‘between’ the ones characterized by homogeneous soil. So, they represent a sort of upper and lower bound for the field.



*Figure 13.32 Radial component of the electric field at a distance of 1000 m generated by a first-stroke current*



*Figure 13.33 Radial component of the electric field at a distance of 1000 m generated by a subsequent-stroke current*

Figures 13.30–13.31 plot the case of radial distance of 1000 m.

The main difference with respect to the previous case is that, for such radial distance, the Sommerfeld (negative) term is always greater than the ideal one. So, now the greatest field is the one relevant to the ‘only first layer case’. The multi-layer fields are again ‘between’ the ‘one-layer’ ones, and, as expected, if the first layer depth grows up, the graph is nearer to the ‘first layer’ plot.

In order to verify if such observations are still valid if the second layer has lower conductivity than the first, we have inverted the properties of the layers,

obtaining the results depicted in Figures 13.32–13.33, relevant to a radial distance of 1000 m.

Comparing Figures 13.30 with 13.32 and 13.31 with 13.33, one observes that inverting the layers, the multilayer fields are now nearer to the first layer ones, at least in the very first transient. Since the first layer is now the one with greater conductivity, we can say that it acts as a sort of shield, which attenuates the effect of the remaining part of the lossy soil.

## 13.5 Conclusions

The electromagnetic field due to a lightning event in presence of a lossy ground has been studied considering three main situations:

1. homogeneous lossy ground with constant conductivity and permittivity;
2. homogeneous lossy ground with frequency-dependent soil electrical parameters;
3. stratified lossy ground.

In all the cases, the exact field expressions have been derived starting from the Maxwell equations both in air and in the ground. Particular attention has been devoted to the numerical treatment of the Sommerfeld integrals involved in all the field expressions and a suitable algorithm has been proposed in order to evaluate them fastly and efficiently. Finally, for the first situation, a comparative analysis with the well-known approximate approaches has been conducted; for the other cases, the results obtained considering the enhanced model have been compared with those coming from the basic case 1, and the situations in which significant differences arise have been pointed out.

## References

- Agrawal, A. K., Price, H. J., Gurbaxani, S. H. (1980), Transient response of multiconductor transmission lines excited by a nonuniform electromagnetic field, *IEEE Trans. Electromagn. Compat.*, 22 (3), 150–156
- Anderson, W. L. (1979), Computer program numerical integration of related Hankel transforms of orders 0 and 1 by adaptive digital filtering, *Geophysics*, 44 (7), 1287–1305
- Baba, Y., Rakov, V. A. (2006), Voltages induced on an overhead wire by lightning strikes to a nearby tall grounded object, *IEEE Trans. Electromagn. Compat.*, 48 (1), 212–224
- Balanis, C. A. (1989), *Advanced Engineering Electromagnetics*, John Wiley & Sons, New York
- Bannister, P. R. (1984), New formulas that extend Norton's far field elementary dipole equations to the quasinear field range, *Nav. Under Water Syst. Cent.*, Technical Report 59007

- Baños, A. (1966), *Dipole Radiation in the Presence of a Conducting Half-Space*, Pergamon Press, New York
- Baumann, C. E., Sampaio, E. E. S. (1999), Electric field of a horizontal antenna above a homogeneous half-space: implications for GPR, *J. Geoph.*, 65 (3), 823–835
- Berger, K., Anderson, R. B., Kroninger, H. (1975), Parameters of Lightning Flashes, *Electra*, 41, 23–37
- Borghetti, A., Gutierrez, J. A., Nucci, C. A., Paolone, M., Petrache, E., Rachidi, F. (2004), Lightning-induced voltages on complex distribution systems: models, advanced software tools and experimental validation, *J. Electrostat.*, 60 (2–4), 163–174
- Bubenik, D. M. (1977), A practical method for the numerical evaluation of Sommerfeld integrals, *IEEE Trans. Antennas Propagat.*, AP-25, 904–906
- Burke, G. J., Poggio, A. J. (1981), Numerical Electromagnetic Code (NEC) – Method of Moments, *Naval Ocean Systems Center*, Technical Document 116
- Cooray, V. (1992), Horizontal fields generated by return strokes, *Radio Sci.*, 27 (4), 529–537
- Cooray, V. (2001), Underground electromagnetic fields generated by the return stroke of lightning flashes, *IEEE Trans. Electromagn. Compat.*, 43 (1), 75–84
- Cooray, V. (2002), Some considerations on the “Cooray-Rubinstein” formulation used in deriving the horizontal electric field of lightning return strokes over finitely conducting ground, *IEEE Trans. Electromagn. Compat.*, 44 (4), 560–566
- Cooray, V. (2005), On the validity of several approximate theories used in quantifying the propagation effects on lightning generated electromagnetic fields, *Proc of the VIII International Symposium on Lightning Protection SIPDA*, São Paulo
- Cui, T. J., Chew, W. C. (2000a), Modeling of arbitrary wire antennas above ground, *IEEE Trans. Geosci. Remote Sens.*, 38 (1), 357–365
- Cui, T. J., Chew, W. C. (2000b), Accurate model of arbitrary wire antennas in free space, above or inside ground, *IEEE Trans. Antennas Propagat.*, 48 (4), 482–493
- Darveniza, M. (2007), A practical extension of rusck’s formula for maximum lightning-induced voltages that accounts for ground resistivity, *IEEE Trans. Power Deli.*, 22 (1), 605–612
- Davis, P. J., Rabinowitz, P. (1984), *Methods of Numerical Integration*, Academic Press, New York
- Delfino, F., Procopio, R., Rossi, M., Verolino, L. (2003), Lightning current identification over a conducting ground plane, *Radio Sci.*, 38 (3), 1049, doi:10.1029/2001RS002521
- Delfino, F., Procopio, R., Rossi, M., Rachidi, F., Nucci, C. (2007), An algorithm for the exact evaluation of the underground lightning electromagnetic fields, *IEEE Trans. Electromagn. Compat.*, 49 (2), 401–411
- Delfino, F., Procopio, R., Rossi, M. (2008a), Lightning return stroke current radiation in presence of a conducting ground: 1. Theory and numerical evaluation of the electromagnetic fields, *J. Geophys. Res.*, D05110, doi:10.1029/2007JD008553

- Delfino, F., Procopio, R., Rossi, M., Rachidi, F., Nucci, C. (2008b), Lightning return stroke current radiation in presence of a conducting ground: 2. Validity assessment of simplified approaches, *J. Geophys. Res.*, D05111, doi:10.1029/2007JD008567
- Delfino, F., Procopio, R., Rossi, M., Rachidi, F. (2009), The influence of frequency dependent soil electrical parameters on the evaluation of lightning electromagnetic fields in air and underground, *J. Geophys. Res.*, 114, D11113, doi: 10.1029/2008JD011127
- De Loor, G. P. (1983), The dielectric properties of wet materials, *IEEE Trans. Geosc. Remote Sens.*, GE-21 (3), 364–369
- Fuller, B. D., Ward, S. H. (1970), Linear system description of the electrical parameters of rocks, *IEEE Trans. Geosci. Electron.*, Ge-8 (1), 7–18
- Gardner, R. L. (1981), Effects of the propagation path on lightning-induced transient fields, *Radio Sci.*, 16 (3), 377–384
- Gradshteyn, I. S., Ryzhik, I. W. (1980) *Table of Integrals, Series and Products*, Academic Press, San Diego
- Heidler, F. (1985), Analytische Blitzstromfunktion zur LEMP-Berechnung, *Proc. 18th International Conference on Lightning Protection*, Munich, Germany, Sep. 1985, pp. 63–66
- Høidalen, H. K., Sletbak, J., Henriksen, T. (1997), Ground effects from nearby lightning, *IEEE Trans. Electromagn. Compat.*, 39 (4), 269–278
- Krommer, A. R., Ueberhuber, C. W. (1994), *Numerical Integration on Advanced Computer Systems*, Springer-Verlag, Berlin
- Longman, I. M. (1956), Note on a method for computing infinite integrals of oscillatory functions, *Proc. Cambridge Phil. Soc.*, 52, 764–768
- Longmire, C. L., Smith, K. S. (1975), Mission, a universal impedance for soils, *Topical Report for period July 1–September 30, prepared for Defense Nuclear Agency*
- Maclean, T. S. M., Wu, Z. (1993), *Radiowave Propagation Over Ground*, Kluwer Academic Publisher, New York
- Michalski, K. A., Mosig, J. R. (1997), Multilayered media Green's functions in integral equation formulations, *IEEE Trans. Antennas Propag.*, 45, 508–519
- Michalski, K. A. (1998), Extrapolation methods for Sommerfeld integral tails, *IEEE Trans. Antennas Propag.*, 46 (10), 1405–1418
- Mittra, R., Parhami, P., Rahmat-Samii, Y. (1979), Solving the current element problem over lossy half-space without Sommerfeld integrals, *IEEE Trans. Antennas Propag.*, AP-27 (6), 778–782
- Norton, K. A. (1937), The propagation of radio waves over the surface of the Earth and in the upper atmosphere, *Proc. IRE*, 25 (9), 1203–1236
- Novikov, V. V., Makarov, G. I. (1961), Propagation of pulsed signals over a homogeneous flat earth, *Radio Eng. Electron. Phys.*, 5, 644–652
- Nucci, C. A., Rachidi, F. (1989), Experimental validation of a modification to the transmission line model for LEMP calculations, *Proc. 8th Int. Symp. Electromagnetic Compatibility*, Zurich, Switzerland, March, 7–9, 389–394

- Nucci, C. A., Rachidi, F. (1995), On the contribution of the electromagnetic field components in field-to-transmission lines interaction, *IEEE Trans. Electromagn. Compat.*, 37 (4), 505–508
- Paul, C. R. (1994), *Analysis of Multiconductor Transmission Lines*, John Wiley & Sons, New York
- Parhami, P., Mittra, R. (1980), Wire antennas over a lossy half-space, *IEEE Trans. Antennas Propag.*, AP-28 (3), 397–403
- Parhami, P., Rahmat-Samii, Y., Mittra, R. (1980), An efficient approach for evaluating Sommerfeld integrals encountered in the problem of a current element radiating over lossy ground, *IEEE Trans. Antennas Propag.*, AP-28 (1), 100–104
- Paolone, M., Petrache, E., Rachidi, F., Nucci, C. A., Rakov, V., Uman, M., Jordan, D., Rambo, K., Jerauld, J., Nyffeler, M., Schoene, J. (2005), Lightning-induced disturbances in buried cables part II: experiment and model validation, *IEEE Trans. Electromagn. Compat.*, 47 (3), 509–520
- Petrache, E., Rachidi, F., Paolone, M., Nucci, C. A., Rakov, V., Uman, M. (2005), Lightning-induced disturbances in buried cables part I: theory, *IEEE Trans. Electromagn. Compat.*, 47 (3), 498–508
- Pokharel, R. K., Ishii, M., Baba, Y. (2003), Numerical electromagnetic analysis of lightning-induced voltage over ground of finite conductivity, *IEEE Trans. Electromagn. Compat.*, 45 (4), 651–656
- Press, W. H., Flannery, B. P., Teukolsky, S. A., Vetterling, W. T. (1992), *Numerical Recipes in FORTRAN: The Art of Scientific Computing*, 2nd ed., Cambridge University Press, Cambridge
- Rachidi, F., Nucci, C. A., Ianoz, M., Mazzetti, C. (1996), Influence of a lossy ground on lightning-induced voltages on overhead lines, *IEEE Trans. Electromagn. Compat.*, 38 (3), 250–264
- Rachidi, F., Janischewskyj, W., Hussein, A. M., Nucci, C. A., Guerrieri, S., Korddi, B., Jen-Shih, Chang (2001), Current and electromagnetic field associated with lightning-return strokes to tall towers, *IEEE Trans. Electromagn. Compat.*, 43 (3), 356–363
- Rahmat-Samii, Y., Mittra, R., Parhami, P. (1981), Evaluation of Sommerfeld integrals for lossy half-space problems, *Electromagnetics*, 1 (1), 1–28
- Rakov, V. A., Uman, M. A. (1998), Review and evaluation of lightning return stroke models including some aspects of their application, *IEEE Trans. Electromagn. Compat.*, 40 (4), 403–426
- Ramo, S., Whinnery, J. R., Van Duzer, T. (1994), *Fields and Waves in Communication Electronics*, 3rd ed., John Wiley, New York
- Rinaldi, V. A., Francisca, F. M. (1999), Impedance analysis of soil dielectric dispersion (1 MHz-1 GHz), *J. Geotech. Geoenviron. Eng.*, 125 (2), 111–121
- Rubinstein, M. (1996), An approximate formula for the calculation of the horizontal electric field from lightning at close, intermediate and long ranges, *IEEE Trans. Electromagn. Compat.*, 38 (3), 531–535
- Rudin, W. (1986), *Real and Complex Analysis*, McGraw-Hill, New York

- Sarkar, T. K. (1975), Analysis of radiation by arrays of vertical wire antennas over imperfect ground (reflection-coefficient method), *IEEE Trans. Antennas Propag.*, A-23, 749
- Scott, J. H. (1966), *Electrical and Magnetic Properties of Rock and Soil*, U.S. Geological Survey, Department of the Interior, Washington, DC
- Shoory, A., Moini, R., Hesam Sadeghi, S. H., Rakov, V. A. (2005), Analysis of lightning-radiated electromagnetic fields in the vicinity of lossy ground, *IEEE Trans. Electromagn. Compat.*, 47 (1), 131–145
- Shoory, A., Mimouni, A., Rachidi, F., Cooray, V., Moini, R., Sadeghi S. H. H. (2010), Validity of simplified approaches for the evaluation of lightning electromagnetic fields above a horizontally stratified ground, *IEEE Trans. Electromagn. Compat.*, 52 (3), 657–663
- Siegel, M., King, R. W. P. (1970), Electromagnetic fields in a dissipative half-space: a numerical approach, *J. Appl. Phys.*, 41, 2415–2423
- Smith-Rose, R. L. (1933), The electrical properties of soils for alternating currents at radiofrequencies, *Proc. Roy. Soc.*, 140 (841A), 359–377
- Smith-Rose, R. L. (1935), The electrical properties of soils at frequencies up to 100 megacycles per second; with a note on the resistivity of ground in the United Kingdom, *Proc. Phys. Soc.*, 47 (262), 923–931
- Sommerfeld, A. (1909), Über die ausbreitung der Wellen in der drahtlosen Telegraphie, *Ann. Phys.*, 28, 665
- Sommerfeld, A. (1949), *Partial Differential Equations in Physics*, Academic Press, New York
- Tesche, F., Ianoz, M., Karlsson, T. (1997), *EMC Analysis Methods and Computational Models*, John Wiley & Sons, New York
- Wait, J. R. (1964), Electromagnetic surface waves, *Advances in Radio Research*, 1, edited by J. A. Saxton, Academic Press, New York, 157–170
- Wait, J. R. (1996), *Electromagnetic Waves in Stratified Media*, IEEE Press, Oxford
- Wait, J. R. (1999), Influence of finite ground conductivity on the fields of a vertical traveling wave of current, *IEEE Trans. Electromagn. Compat.*, 41 (1), 78
- Wait J. R., Hill, D. A. (2000), Ground wave of an idealized lightning return stroke, *IEEE Trans. Electromagn. Compat.*, 48 (9), 1349–1353
- Yang, C., Zhou, B. (2004), Calculation methods of electromagnetic fields very close to lightning, *IEEE Trans. Electromagn. Compat.*, 46 (1), 133–141
- Zauderer, E. (1998), *Partial Differential Equations of Applied Mathematics*, 2nd ed., John Wiley & Sons, New York
- Zeddam, A., Degauque, P. (1990), Current and voltage induced on telecommunication cables by a lightning stroke, *Lightning Electromagnetics*, edited by R. L. Gardner, Hemisphere Public. Corp., Washington, DC 377–400



---

## *Chapter 14*

# **Measurements of lightning-generated electromagnetic fields**

*Mahendra Fernando<sup>1</sup> and Vernon Cooray<sup>2</sup>*

---

## **14.1 Introduction**

The vertical component of the electric field generated by lightning flashes can be measured either using a field mill [1] or using a flat plate (or a vertical whip) antenna [2, 3]; each method having its advantages and disadvantages. The three components of the electric field can be measured by using specially adapted spherical antennas [4].

The conventional method used to measure the magnetic field is the crossed loop antenna [5–7], but in some studies magnetometers have been used to measure this field component. The frequency spectrum of the electromagnetic fields generated by lightning flashes can be estimated by either Fourier transforming the broadband signal or using antenna systems tuned to the desired frequencies [8–13].

A brief description of the theory pertinent to these measuring techniques is given in this chapter. Some parts of this chapter are adapted from Reference 14.

## **14.2 Electric field mill or generating voltmeter**

The principle of operation of the field mill is illustrated in Figure 14.1. The plate marked  $S$  is the detector that is placed in a background electric field assumed for the moment to be uniform and steady. The plate marked  $M$  is a movable electrode that is at ground potential. This electrode can be moved back and forth in front of the sensing plate either exposing it to or screening it from the background electric field. Consider the situation shown in the Figure 14.1 in which the sensing plate is completely exposed to the electric field. The electric field lines end on the plate and the total charge induced on the sensing plate is  $A\epsilon_0 E$  where  $A$  is the area of the plate. Assume that the plate  $M$  is moved back and forth in front of the sensing plate. This will change the exposed area of the sensing plate as a function of time, and since the charge induced on the plate is a function of

---

<sup>1</sup>University of Colombo, Colombo, Sri Lanka

<sup>2</sup>Uppsala University, Uppsala, Sweden

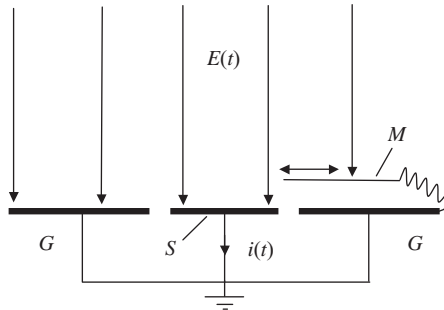


*Figure 14.1 Diagram to illustrate the basic principle of the electric field mill*

the exposed area of the sensing plate, a current will flow between the sensing plate and ground. If the background electric field is constant, this current is given by

$$i(t) = \frac{da(t)}{dt} \varepsilon_0 E \quad (14.1)$$

where  $a(t)$  is the instantaneous exposed area of the sensing plate. Thus, knowing the way in which the exposed area of the sensing plate varies in time, the background electric field can be obtained by measuring the current flowing between the sensing plate and ground.

Assume that  $M$  moves periodically back and forth over the sensing plate, thus alternatively shielding and un-shielding the sensing plate from the background electric field. If  $M$  moves back and forth  $n$  times per second, then the output current oscillates with a period,  $T_p$  equal to  $1/n$  and the peak amplitude of the output is proportional to the background electric field. If the background electric field varies with the time, then the envelope of the oscillating output voltage follows the background electric field. However, any rapid variation in the background electric field faster than the period  $T_p$  cannot be measured using the field mill. In other words, the time resolution of the field mill is on the order of  $T_p$ . Thus, the rate of the periodic motion of  $M$  gives an upper limit to the resolution of the field that can be measured by a field mill. In modern field mills, the time resolution is increased by utilizing a rotating vaned wheel that alternatively shield or un-shield the sensing electrode from the electric field as each vane rotates over it. If the rotational speed of the metal vane is  $n$  revolutions per second, and if it has  $m$  vanes, then the time resolution of the field mill will decrease to  $1/mn$ . Such field mills can measure faster variations in the background electric field than the one described above. In general, the upper frequency limit of the modern field mills may range from 1 to 10 kHz. The main advantage of the field mill is that it can be used to measure the absolute value of the background field.

### 14.3 Plate or whip antenna

#### 14.3.1 Measurement of electric field

The physical configuration of the plate (or whip) antenna is shown in Figure 14.2. In principle, the antenna is a metal object connected to ground through an electric

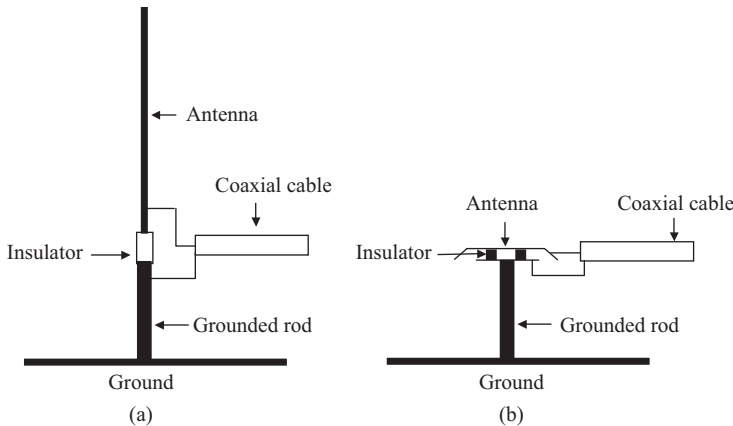


Figure 14.2 Antennas for the measurement of lightning-generated fields. (a) Whip antenna. (b) Plate antenna

circuitry. As the background electric field varies in time, the charge induced on the antenna also varies in time generating a current in the electrical circuitry.

If the dimension of the antenna is much smaller than the minimum wavelength of interest in the time-varying electric field, the antenna will act as a capacitive voltage source with the voltage proportional to the background electric field,  $e(t)$ . The constant of proportionality between the background electric field and the output voltage is called the effective height of the antenna.

The equivalent circuit of the antenna shown in Figure 14.2 is depicted in Figure 14.3, where  $C_a$  is the capacitance of the antenna to ground and  $C_c$  is the capacitance of the cable connected to the antenna. The effective height of the antenna can be either calculated from theory or measured by applying a known electric field to the antenna and measuring the output voltage.

The electronic circuitry that can be used to obtain the background electric field from a plate or whip antenna is given in Figure 14.4(a) [14]. The equivalent circuit of the electronic circuitry when connected to the antenna is given in Figure 14.4(b).

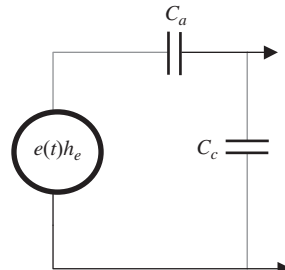


Figure 14.3 Equivalent circuit of the antenna and the attached cable.  $C_g$  is the capacitance of the antenna and the capacitance of the cable is given by  $C_{ca}$

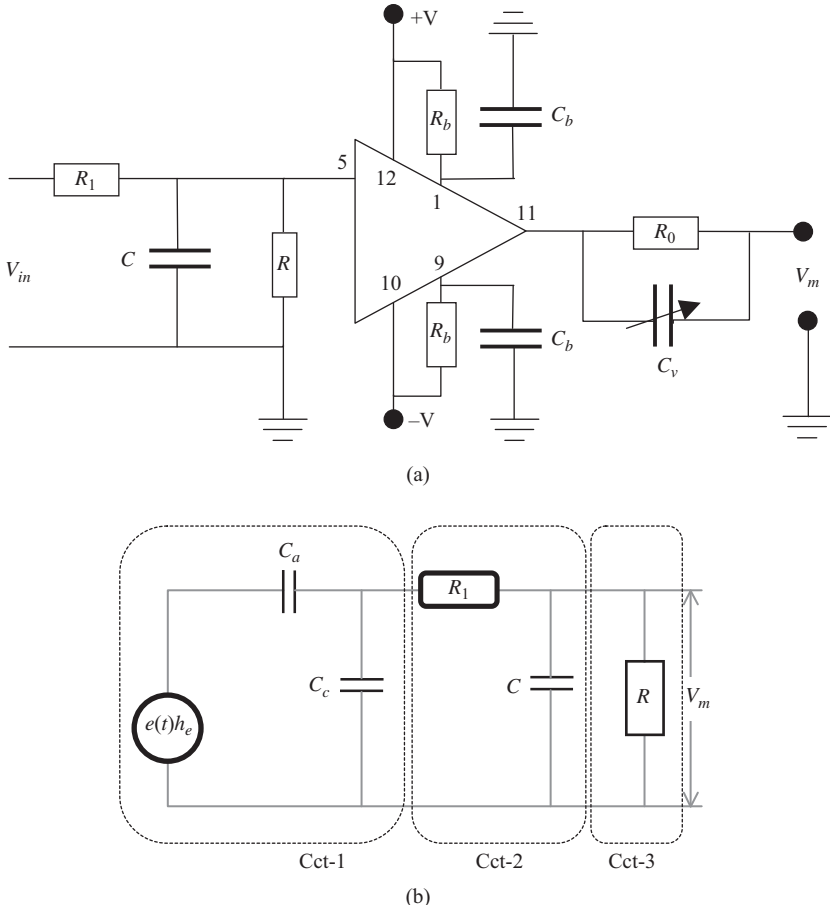


Figure 14.4(a) Electronic circuit of the buffer amplifier system (b) Equivalent circuit of the antenna system together with the attached electronics

The relationship between the output signal,  $V_m$  of the circuit and the electric field incident on the antenna is given in frequency domain by

$$V_m = E(s)h_e \frac{sC_aR}{1 + sRC + s^2RR_1C(C_a + C_c) + s(R_1 + R)(C_a + C_c)} \quad (14.2)$$

where  $s$  is the Laplace variable,  $h_e$  is the effective height of the antenna and  $E(s)$  is the Laplace transform of the background electric field,  $e(t)$ . In general the resistance  $R_1$  (equal to the cable impedance) can be neglected in comparison to  $R$  in the term  $(R_1 + R)$  in the denominator and with that the above equation reduces to

$$V_m = E(s)h_e \frac{sC_aR}{1 + sRC + s^2RR_1C(C_a + C_c) + sR(C_a + C_c)} \quad (14.3)$$

When  $4R_1C(C_a + C_c) \ll R(C_a + C_c + C)^2$ , which is true in practice, the time-domain solution of the above equation when the incident field is a Heaviside step function can be written as

$$v_m(t) = e(t)h_e \frac{C_a}{C_a + C_c + C} (e^{-t/\tau_d} - e^{-t/\tau_r}) \quad (14.4)$$

where

$$\tau_r = R_1C \frac{(C_a + C_c)}{(C + C_a + C_c)} \quad (14.5)$$

and

$$\tau_d = R(C_a + C_c + C) \quad (14.6)$$

Since  $\tau_r \ll \tau_d$ , at small times the above can be written as

$$v_m(t) = e(t)h_e \frac{C_a}{C + C_a + C_c} \left[ 1 - e^{-\{t/\tau_r\}} \right] \quad (14.7)$$

and at large times it reduces to

$$v_m(t) = e(t)h_e \frac{C_a}{C + C_a + C_c} e^{-\{t/\tau_d\}} \quad (14.8)$$

The above equations show that the output signal can be distorted both at the high and low frequencies depending on the circuit parameters. Since the applied field is a step the above results show that  $\tau_r$  and  $\tau_d$  controls the ability of the circuit to faithfully represent the high-frequency and low-frequency contents respectively of the background electric field to be measured. In other words,  $\tau_r$  determines the high-frequency limit of the bandwidth of the measuring system; The higher 3 dB frequency limit of the bandwidth is given by  $1/2\pi\tau_r$ . Similarly,  $\tau_d$  determines the low-frequency limit of the bandwidth of the measuring system; The lower 3 dB frequency limit of the bandwidth is given by  $1/2\pi\tau_d$ . To obtain an accurate measurement of the time-varying background electric field, the rise time constant of the antenna and the measuring system should be much shorter than the rising edge of background field and the decay time constant of the antenna system should be much longer than the total duration of the time-varying field. This point is illustrated further in the waveforms shown in Figures 14.5(a) and 14.5(b) where the effect of the time constants on the measurement of distant radiation field generated by a return stroke is illustrated. The data show that in order to obtain an accurate measurement of the distant radiation field of a return stroke, the rise time and the duration of which are about 0.1 and 100  $\mu$ s, the rise time and decay time constants of the measuring system should be about 0.01  $\mu$ s and 1 ms, respectively. They translate to 3 dB frequency limits of  $1.6 \times 10^2$  Hz and  $1.6 \times 10^7$  Hz. At close distances, due to the influence of

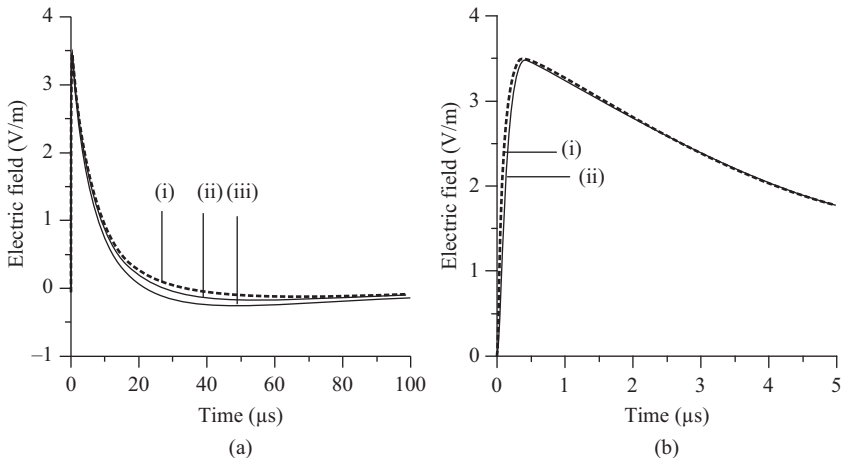


*Figure 14.5 The influence of the rise time constant and the decay time constant of the antenna system on the measurement of the electric radiation field of a return stroke. The dashed line shows the actual electric field at 100 km and the solid lines show the output from the antenna. (a) Effect of the decay time constant: (i)  $\tau_d = 5\text{ ns}$ , (ii)  $\tau_d = 1\text{ ms}$ , (iii)  $\tau_d = 250\text{ }\mu\text{s}$ . (b) Effect of the rise time constant: (i)  $\tau_r = 10\text{ ns}$ ,  $\tau_d = 1\text{ ms}$ , (ii)  $\tau_r = 50\text{ ns}$ ,  $\tau_d = 1\text{ ms}$ . The electric field is calculated using the modified transmission line model MTLE (see Chapter 7). Note that the curves corresponding to (i) coincide with the actual electric field*

the static electric field the duration of the electric field increases and therefore the decay time constant should also be increased to get a faithful representation of the close field. In general, a decay time constant of about 1 sec is needed to measure the close electric fields produced by lightning flashes faithfully.

It is important to mention here that the upper frequency limit of the bandwidth of the measuring system is also influenced by the physical dimension of the antenna, the electronic components used in the circuitry and the recording system used to record the output of the measuring system. If  $l$  is the length or the diameter of the antenna, it is necessary that  $l \ll \lambda_m/4$  where  $\lambda_m$  is the minimum wavelength of interest in the electric field measurements. If this condition is not satisfied, the current induced in different parts of the antenna will reach the electronic circuitry at different times, thus invalidating the theory presented above. However, in many practical applications  $l$  may not exceed a few metres in the case of whip antenna and a few tens of centimetres in the case of plate antenna. Thus, the upper frequency limit of the bandwidth is determined mainly by the electronics circuitry and the recording system.

This antenna system has an advantage over the field mill in providing a higher time resolution in the measurements. However, the disadvantage of this system is that, due both to the effect of leakage currents across insulators (limiting the highest value of  $R$ ) and to the drastic reduction in the output amplitude (limiting the highest

value of  $C$ ), there is a limit to which the decay time constant could be increased. Thus, it is difficult to use this antenna system and the associated electronics to measure the very low-frequency components of the electric fields including DC.

#### 14.3.2 Measurement of the derivative of the electric field

When both  $\tau_r$  and  $\tau_d$  are much smaller than the time variations in the signal under consideration, the output signal of the antenna system follows the temporal behaviour of the electric field derivative. For example, when these conditions are satisfied, the terms containing  $s$  (i.e. frequency) in the denominator of (14.3) can be neglected in comparison to unity leading to

$$V_m(s) = E(s) h_e s C_a R \quad (14.9)$$

If the incident background electric field is a Heaviside step function, the output of the circuit in time domain,  $v_m(t)$ , is given by

$$v_m(t) = h_e C_a R \delta(t) \quad (14.10)$$

where  $\delta(t)$  is the Dirac delta function which indeed is the derivative of the Heaviside step function (i.e. the input electric field). Figure 14.6 depicts the output of the antenna system for several values of rise and decay time constants. The output signal is normalized by removing the effect of changing circuit parameters as  $\tau_r$  and

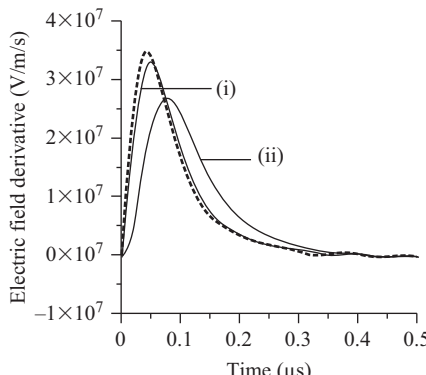


*Figure 14.6 Diagram to show that the output of the antenna system approaches that of the electric field derivative when the rise time constant and the decay time constant are much less than the rise time of the radiation field. The dashed line shows the derivative of the electric radiation field at 100 km. The solid lines show the output of the antenna system after taking into account the changes in the output when the circuit parameters are changed. (i)  $\tau_r = 2$  ns,  $\tau_d = 5$  ns, (ii)  $\tau_r = 5$  ns,  $\tau_d = 30$  ns. The electric field is calculated using the modified transmission line model MTLE (see Chapter 7)*

$\tau_d$  is varied. Note that in order to get the electric field derivative faithfully  $\tau_r$  and  $\tau_d$  has to be much less than about 0.01  $\mu\text{s}$  which approximately is the rise time of the electric radiation field under consideration.

#### 14.4 Measurements of the three electric field components in space

Almost all the studies reported in the literature deal with the vertical component of the electric field at ground level. If the ground is a perfect conductor, then the electric field at ground level has only a vertical component. However, at points above the ground the electric field has three components one vertical ( $z$ -direction) and two horizontal ( $x$ - and  $y$ -direction). If the ground is finitely conducting, the electric field at ground level too will have a horizontal component. The horizontal component (or  $x$ - and  $y$ -component) of the lightning-generated electric field is smaller than the vertical component for the ground conductivities of practical interest. But it plays a significant role in creating lightning-induced voltages on long horizontal conductors.

Thomson and co-workers measured the three components of the lightning electric fields using a spherical antenna system [4]. A schematic diagram of the antenna system used by these authors is shown in the Figure 14.7(a).

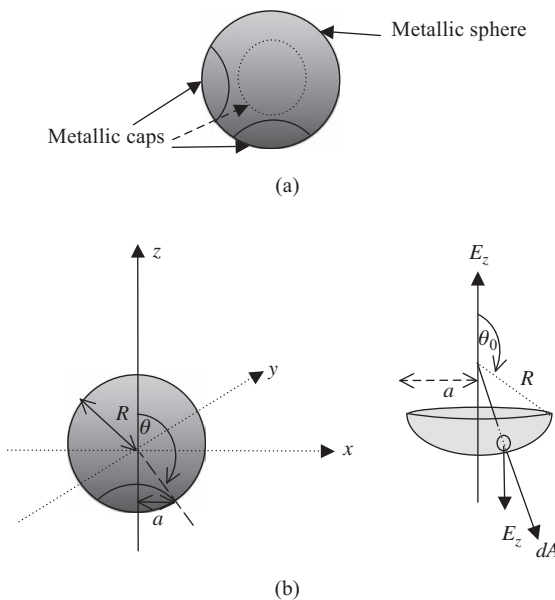


Figure 14.7(a) Block diagram of the three-dimensional electric field sensor. The sensor consists of a metallic sphere with three caps placed perpendicular to each other (b) A schematic diagram of the antenna system and a cap

The sensor is a metallic sphere with three caps placed perpendicular to each other. The diameter of the sphere was about 45 cm and the cap radius was set to 7.6 cm. All detecting and controlling electronics were placed at the centre of sphere. The sensor is supported by an insulating structure and is placed about 1.5 m (about three times the dimension of the sphere) above the ground level to minimize any perturbation on the ambient surface charge density. By measuring the charge induced on the three caps in the presence of a background electric field, the three components of the field in the  $x$ -,  $y$ - and  $z$ -directions can be calculated. Note that only the field component perpendicular to the cap will induce a net charge on the cap. In order to illustrate the theory assume that the electric field component is directed in the  $z$ -direction (see Figure 14.7(b)). This field component will induce a net charge only in the cap perpendicular to the  $z$ -direction, i.e. bottom cap in the figure. The total charge induced on this cap due to an electric field  $E_z$  (directed along the  $z$ -axis) is given by

$$Q = \int \sigma(\theta) dA \quad (14.11)$$

where  $\sigma(\theta)$  is the angular-dependent surface charge density on the cap. Now, the angular distribution of charge density induced on the sphere by  $E_z$  is given by

$$\sigma(\theta) = 3\epsilon_0 E_z \cos \theta \quad (14.12)$$

Moreover

$$dA = R^2 \sin \theta d\theta d\varphi \quad (14.13)$$

In the above equation  $\epsilon_0$  is the permittivity of air and  $\varphi$  is the azimuthally angle of the area element  $dA$ .

Then the total charge induced on the cap is

$$Q_T = 3\epsilon_0 E_z R^2 \int_{\theta_0}^{\pi} \int_0^{2\pi} \sin \theta \cos \theta d\theta d\varphi \quad (14.14)$$

After performing the integration we obtain

$$Q_T = -3\epsilon_0 \pi a^2 E_z \quad (14.15)$$

where

$$\theta_0 = \pi - \sin^{-1}(a/R) \quad (14.16)$$

From the measured charge on the cap and knowing the geometrical parameters, the electric field component perpendicular to the cap can be obtained from (14.15). By measuring the induced charge on all the three caps, the three-dimensional field configuration can be estimated.

## 14.5 Crossed loop antennas to measure the magnetic field

The voltage induced in a loop antenna due to an incoming magnetic field is proportional to the area of the loop multiplied by the derivative of the magnetic field component perpendicular to the loop. By measuring the voltage induced in two magnetic loops placed orthogonal to each other, the component of the magnetic field parallel to the plane containing the two axes of the loops can be obtained. The magnetic field generated by a vertical lightning channel is parallel to the ground plane and is directed perpendicular to the line joining the point of observation and the lightning channel. Therefore, the direction of the lightning flash from a given point can be obtained by measuring the ratio of the voltages induced in two orthogonal magnetic loops.

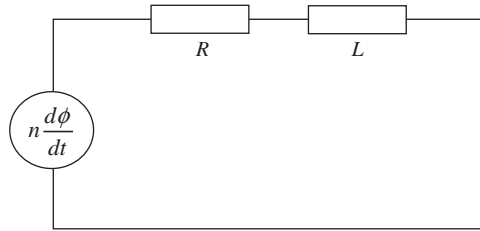


*Figure 14.8 Equivalent circuit of the magnetic loop*

The equivalent circuit of the loop antenna is shown in Figure 14.8. Here  $L$  is the inductance of the loop and  $R$  is its resistance. In practice the resistance of the loop can be neglected. The voltage,  $V$ , induced in the loop, assumed to be electrically small, is given by

$$V = -n \frac{d\varphi}{dt} \quad (14.17)$$

where  $n$  is the number of turns in the loop and  $\varphi$  is the magnetic flux threading the loop. The flux is given by

$$\varphi = B(t)A\cos\theta \quad (14.18)$$

where  $B(t)$  is the time-varying magnetic field,  $A$  is the area of the loop and  $\theta$  is the angle between the axis of the loop and the magnetic vector. Since the output of the antenna is proportional to the derivative of the magnetic field, it has to be integrated to obtain a signal that is proportional to the magnetic field. An antenna and the corresponding electronics suitable for this purpose, as developed by Krider and Noggle [6], are shown in Figure 14.9.

The lower limit of the bandwidth of the magnetic field measuring system is determined by the integration time constant of the integrator. Thus, the integration time constant of the system should be much longer than the duration of the waveforms of interest. In the circuit shown in Figure 14.9, with  $C_1 = 1000$  pF the time

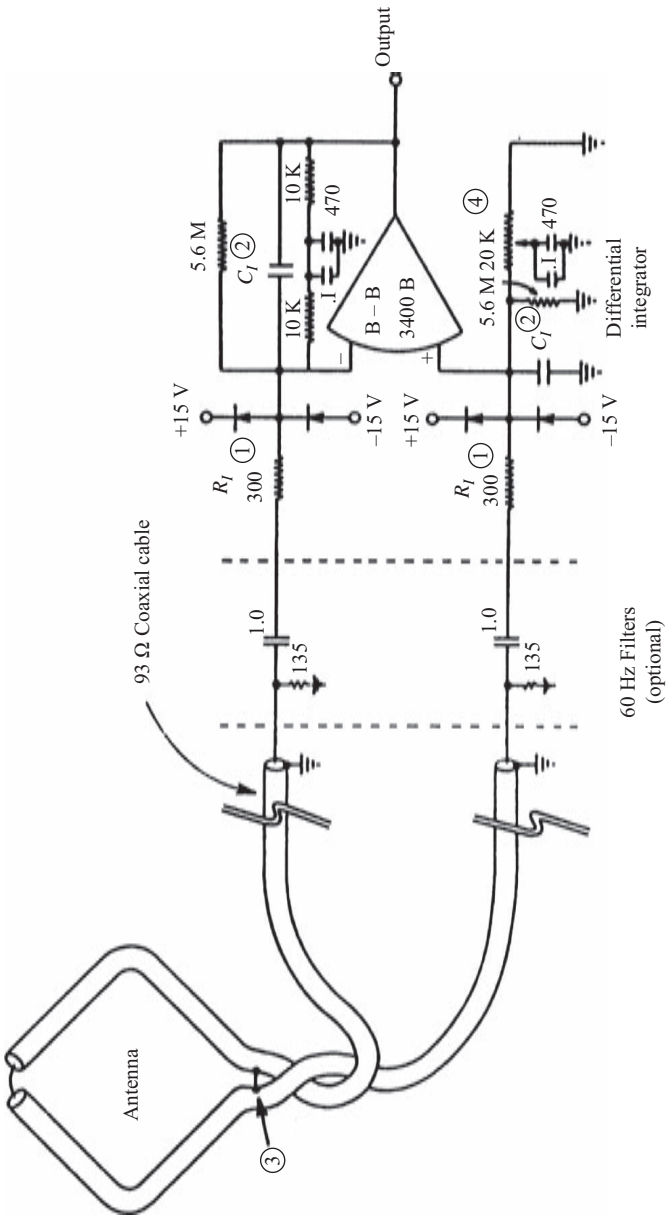


*Figure 14.9 An antenna and the corresponding electronics suitable for the measurement of the magnetic field generated by a lightning return stroke. From Krider and Noggle [5]*

constant of the integrator was 4 ms without the 60 Hz filters and 1.3 ms when they were included. As in the electric field measuring system the upper limit of the bandwidth is determined by the electronic circuitry and the recording system.

In measuring magnetic fields, it is also necessary to avoid any contamination of the measurements due to the electric fields. In the measuring system shown in the Figure 14.9, this is achieved (a) by shielding the magnetic field sensor with a outer screen that is broken at the top to avoid any circulating currents and (b) by measuring the difference in the voltages induced at the two ends of the antenna thus cancelling out any contribution from the electric field.

## 14.6 Magnetic field measurements using anisotropic magnetoresistive (AMR) sensors

Even though the loop antenna systems are widely used in magnetic field measurements as well as in direction finding systems, one problem in using loop antenna systems is the necessity of integrating the measured voltage signal. This can be avoided by using magnetometers [e.g. 15–18]. The fluxgate magnetometer used by Williams and Brook [15] was sensitive for the changes as low as 10  $\mu\text{G}$ . Apart from the sensors used in the above studies, Hall effect sensors and anisotropic magnetoresistive sensors (or AMR sensors) are also possible to use for magnetic field measurements. Fernando *et al.* [19] used the Honeywell's HMC1022, AMR sensor to measure the magnetic field generated by lightning. Their results suggest that AMR sensors can be used successfully for lightning magnetic field measurements. Honeywell's HMC1022 sensor has two sensors oriented perpendicularly to each other on a single chip. It has a resolution of as low as 85  $\mu\text{G}$  through  $\pm 6 \text{ G}$ , a typical sensitivity of 1 mV/V/G and bandwidth of 5 MHz with angular accuracy of  $\pm 1^\circ$ . Sensitivity of the measuring set-up was increased using the LMH6624 op-amp. The measuring set-up can measure magnetic fields as low as 300  $\mu\text{G}$  in the range of DC to 4 MHz. A block diagram of the sensor set-up used by Fernando *et al.* [19] is shown in Figure 14.10.

## 14.7 Narrowband measurements

Frequency content of lightning electric fields span from VLF to UHF range. Basically, two techniques were used in different studies to obtain the frequency spectrum. In one technique, the measured (as described in Section 14.2) broadband signal is Fourier transformed to obtain the frequency spectrum [see, e.g. 8–10]. In the other technique, narrowband oscillators were used to sample the electric field at the desired frequency [see, e.g. 11–13].

Narrowband oscillators in the VLF and HF range mostly consist of passive devices such as inductors and capacitors. Since the antenna (flat plate or whip) acts as a capacitor (say  $C_a$ ), one can design a narrowband oscillator in principle by connecting an inductor  $L$  and a resistor  $R$  in series with the antenna [13, 20]. The equivalent circuit of such a system is given in the Figure 14.11. Let the measured

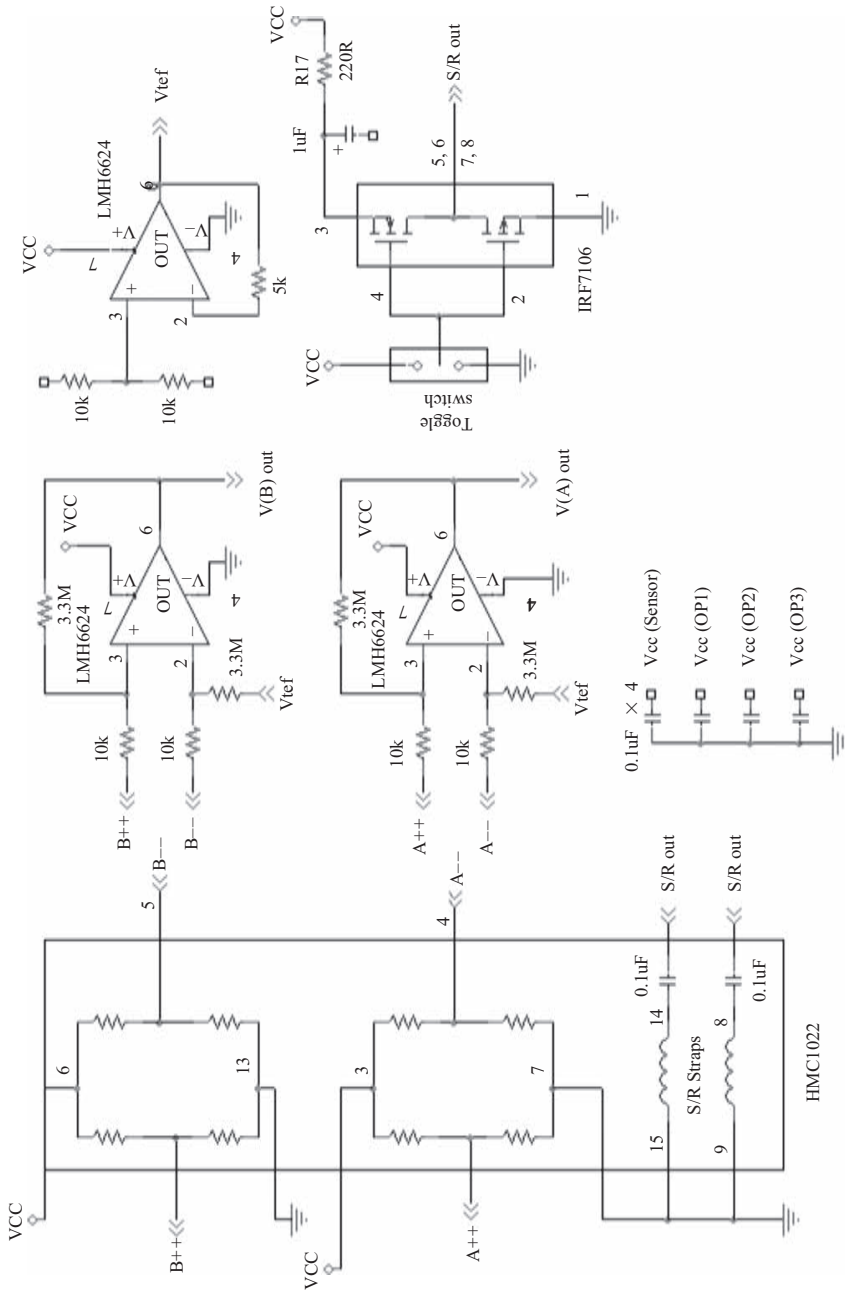
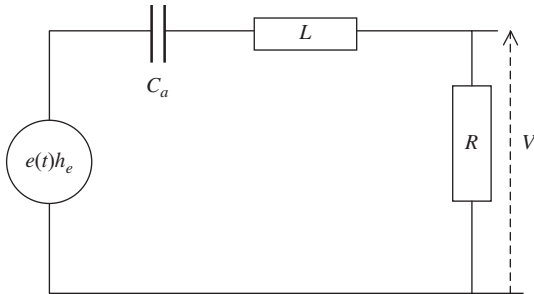


Figure 14.10 Block diagram of the electronic circuit for HMC 1022 sensor as given in Reference 19



*Figure 14.11 Block diagram of the narrowband oscillator circuit. Here,  $C_a$  is the antenna capacitance,  $L$  is the inductor and  $R$  is the resister connected between the antenna and ground*

voltage across the resister is  $V$ . Then it is a simple matter to show that

$$V(s) = E(s)h_e \frac{sR}{s^2L + sR + \frac{1}{C_a}} \quad (14.19)$$

where, as before,  $h_e$  is the effective height of the antenna,  $s$  is the Laplace variable and  $E(s)$  is the Laplace transform of the background electric field,  $e(t)$ . Assume that the incident electric field is a Heaviside step function. Then the antenna output in time domain is given by

$$v(t) = h_e \sqrt{LC_a} e^{-\frac{R}{2L}t} \sin \frac{t}{\sqrt{LC_a}} \quad (14.20)$$

The output oscillates with a frequency  $f_o$  given by  $1/2\pi\sqrt{LC_a}$  and it decays exponentially with a time constant of  $2L/R$ . The larger the  $R$  the smaller the time constant and the signal decays to zero rapidly. Thus, by selecting the values of  $R$  and  $L$  one can confine the oscillations of the circuit created by a given impulse in the electric field to a desired time duration.

## References

1. Malan, D. J. and B. F. J. Schonland, An electrostatic fluxmeter of short response time for use in studies of transient field changes, *Proc. Phys. Soc. London Ser. B*, 63, 402–408, 1950
2. Kitagawa, N. and M. Brook, A comparison of intracloud and cloud-to-ground lightning discharges, *J. Geophys. Res.*, 65, 1189–1201, 1960
3. Cooray, V. and S. Lundquist, On the characteristics of some radiation fields from lightning and their possible origin in positive ground flashes, *J. Geophys. Res.*, 87, 11203–11214, 1982

4. Tomson, E. M., E. J. Medelius and M. A. Uman, A remote sensor for the three components of transient electric field., August 1988, *IEEE Trans. Indus. Electro.*, 35, 426–433, 1988
5. Norinder, H. and O. Dahle, Measurements by frame areals of current variations in lightning discharges, *Ark. Mat. Astron. Fys.*, 32A, 1–70, 1945
6. Krider, E. P. and R. C. Noggle, Broadband antenna system for lightning magnetic fields, *J. Appl. Meterolog.*, 14, 252–256, 1975
7. Krider, E. P., R. C. Noggle, A. E. Pifer and D. L. Vance, Lightning direction-finding system for forest fire detection, *Bull. Am. Meteorol. Soc.*, 61(9), 980–986, 1980
8. Willet, J. C., J. C. Bailey, C. Leteinturier and E. P. Krider, Lightning electromagnetic radiation field spectra in the interval from 0.2 to 20 MHz, *J. Geophys. Res.*, 95(D12), 20367–20387, 1990
9. Weidman, C. D. and E. P. Krider, The amplitude spectra of lightning radiation fields in the interval from 1 to 20 MHz, *Radio Sci.*, 21(6), 964–970, 1986
10. Sonnadara, U., V. Cooray and M. Fernando, The lightning radiation field spectra of cloud flashes in the interval from 20 KHz to 20 MHz, *IEEE Trans. Electromagnetic Compatibility*, 48(1), 234–239, 2006
11. Malan, D. J., Radiation from lightning discharges and its relation to the discharge process, In Recent Advances in Atmospheric Electricity, *Proceedings of the 2nd Conference on Atmospheric Electricity*, pp. 557–563, 1958
12. LeVine, D. M. and E. P. Krider, The temporal structure of HF and VHF radiation during Florida lightning return strokes, *Geophys. Res. Lett.*, 4, 13–16, 1977
13. Cooray, V., Temporal behaviour of lightning HF radiation at 3 MHz near the time of return strokes, *J. Atmos. Terr. Phys.*, 48, 73–78, 1986
14. Cooray, V., Mechanism of the lightning flash, in: Cooray, V. (Ed.), *The Lightning Flash*, The Institution of Electrical Engineers, London, UK, 2003
15. Williams, D. P. and Brook, M., Magnetic measurement of thunderstorms currents, 1. Continuing currents in lightning, *J. Geophys. Res.*, 68, 3243–3247, 1963
16. Meese, A. D. and W. H. Evans, Charge transfer in the lightning stroke as determined by the magnetograph, *J. Franklin Inst.*, 273, 375–382, 1962
17. Nelson, L. D., Magnetographic measurements of charge transfer in the lightning flash, *J. Geophys. Res.*, 73, 5967–5972, 1968
18. Pierce, E. T., The charge transferred to earth by a lightning flash, *J. Franklin Inst.*, 268, 353–354, 1968
19. Fernando, M. et al., Use of AMR sensors for lightning magnetic field measurement, *Proceedings of the Technical Sessions, IPSL*. Vol. 22, pp. 37–45, 2006
20. Jayaratne, K. P. S. C. and V. Cooray, Lightning HF radiation at 3 MHz during leader and return stroke processes, *J. Atmos. Terr. Phys.*, 56, 493–501, 1994



---

*Chapter 15*  
**The Schumann resonances**  
*Colin Price<sup>1</sup>*

---

## 15.1 Introduction

The Schumann resonances (SR) are global electromagnetic resonances excited within the Earth–ionosphere waveguide, primarily by lightning discharges. These resonances occur in the extremely low frequency (ELF) range, with resonant frequencies around 8, 14, 20, 26, ... Hz. The history of the SR is an interesting story (Besser, 2007). While Schumann (1952a) got most of the credit for the first prediction of the existence of the SR, the idea of natural global electromagnetic resonances were first presented by George F. Fitzgerald in 1893, and then again by Nikola Tesla in 1905 (Tesla, 1905). However, while others formulated the idea before Schumann, it was Schumann, together with König, who attempted to measure the resonant frequencies for the first time, unsuccessfully (Schumann, 1952a, 1952b, 1952c; Schumann and König, 1954). It was not until measurements made by Balser and Wagner (1960a, 1960b, 1962a, 1962b and 1963) that adequate analysis techniques were available to extract the resonance information from the background noise. Today, we know that we need 5–10 minutes of data to detect the SR clearly in the spectrum. For further insight into the history of the SR, the reader is pointed to the excellent review by Besser (2007).

Following Schumann’s landmark paper in 1952, there was an increasing interest in SR in a wide variety of fields. Because of the low attenuation of ELF waves in the SR band ( $\sim 0.5$  dB/Mm), it was discovered that not only lightning can produce SR but any large explosion in the atmosphere will also induce SR transients (Balser and Wagner, 1963; Gendrin and Stefant, 1962a, b). Hence, until the ban of atmospheric nuclear explosions in the 1960s, there was great interest in using the SR to monitor the enemy’s nuclear explosions in remote parts of the globe. Another application of ELF waves related to the SR, due to the low attenuations of the ELF waves, was the man-made transmission of these waves for long-range communications with submarines (Wait, 1974a, 1977). However, due to the extremely long wavelengths at ELF, such transmitters need to be huge ( $>200$  km

<sup>1</sup>Department of Geophysical, Atmospheric and Planetary Sciences, Tel Aviv University, Ramat Aviv, Israel 69978

length), with huge power outputs due to very low efficiencies of these transmitters. Nevertheless, since the signals propagate globally, the superpowers were still using these ELF transmitters until recently. The United States transmitter broadcasts at 76 Hz (Fraser-Smith and Bannister, 1998), while the Russian transmitter broadcasts at 82 Hz (Yano *et al.*, 2010).

Besides the military uses of ELF resonances and propagation theory, from the very beginning of SR studies there was an interest to track global lightning activity using the SR (Holzer, 1958; Balser and Wagner, 1962a; Nickolaenko and Rabinowicz, 1995; Nickolaenko *et al.*, 1998; Heckman *et al.*, 1998; Yang *et al.*, 2009). It has also been suggested that extraterrestrial lightning may be detected and studied using SR (Nickolaenko and Rabinowicz, 1982, 1987; Pechony and Price, 2004). However, the recent focus on SR research since the 1990s was a result of the connection between lightning activity and the Earth's climate. It was first suggested in 1990 that global warming may result in significant increases in lightning activity (Price and Rind, 1990). Since the SR is one way to monitor global lightning activity, Williams (1992) suggested that the SR may be used to monitor global temperature variations, acting as a global thermometer. This started a new interest in SR research as related to global climate change that continues today.

Finally, with the discovery of transient luminous events (TLEs) such as sprites, elves, jets etc., it was shown that SR transient pulses are closely linked to the occurrence of TLEs – sprites and elves (Boccippio *et al.*, 1995; Huang *et al.*, 1999; Price *et al.*, 2002; Sato *et al.*, 2003; Sato and Fukunishi, 2003). Hence, SR research is now also a major part of a new field of research related to upper atmospheric discharges.

## 15.2 Theoretical background

Lightning discharges are considered as the primary natural source of SR. The vertical lightning channels behave like huge antennas that radiate electromagnetic energy at frequencies below about 100 kHz (Volland, 1984). While the maximum radiated energy occurs around 10 kHz, the attenuation at these frequencies is about 10 dB/Mm. Hence, these frequencies can only be detected at a range of thousands of kilometres from the lightning discharge. While lightning signals below 100 Hz are very weak, the attenuation is only 0.5 dB/Mm, and hence the electromagnetic waves from an individual discharge can propagate a number of times around the globe before decaying into the background noise. For this reason, the Earth–ionosphere waveguide behaves like a resonator at ELF frequencies, and amplifies the spectral signals from lightning at the resonance frequencies due to constructive interference if electromagnetic waves propagating around the globe in opposite directions (Volland, 1984).

If the terrestrial waveguide was an ideal one, the resonant frequencies  $f_n$  would have been determined by the Earth's radius  $a$  and the speed of light  $c$  – equation (15.1) (Schumann, 1952a). Even Schumann made these assumptions and arrived at the expected SR first mode of 10 Hz. However, the Earth–ionosphere waveguide is not a perfect electromagnetic cavity. Losses due to finite ionosphere conductivity

make the system resonate at lower frequencies than would be expected in an ideal case (7.8 Hz), and the observed peaks are wider than expected. In addition, there are a number of horizontal asymmetries – day–night transition, latitudinal changes in the Earth magnetic field, sudden ionospheric disturbances, polar cap absorption etc. – that complicate the SR power spectra.

$$f_n = \left( \frac{c}{2\pi a} \right) \sqrt{n(n+1)} \quad n = 1, 2, 3, \dots \quad (15.1)$$

The problem of wave propagation in the Earth–ionosphere cavity is most naturally formulated in spherical coordinates  $(r, \theta, \varphi)$ . The excitation source is represented by a vertical dipole with a current moment ( $Ids$ ) located between two concentric spherical shells at  $\theta = 0$ . The radius of the inner shell – the Earth – is denoted by  $r = a$ , and the radius of the outer shell – the ionosphere – by  $r = a + h$ , assuming a sharp and frequency independent upper boundary. Both the observer and the source are assumed to be located on the Earth surface. Maxwell's equations are then solved assuming time dependence of  $e^{i\omega t}$  and requiring continuity on the boundaries (ground–cavity transition at  $r = a$ , and cavity–ionosphere transition at  $r = a + h$ ). The electric and magnetic components are then (Wait, 1962):

$$E_r = i \frac{Ids}{8\pi a^2 \epsilon_0 f} \frac{\nu(\nu+1)}{h} \frac{P_v^0(-\cos\theta)}{\sin\nu\pi}; \quad H_\varphi = - \frac{Ids}{4a} \frac{1}{h} \frac{P_v^1(-\cos\theta)}{\sin\nu\pi} \quad (15.2)$$

In (15.2)  $\epsilon_0$  is a free space permittivity and  $P_v^l$  are the associated Legendre functions. The complex parameter  $\nu$  is calculated in terms of the complex sine of the wave incidence angle  $S$  via (Galejs, 1972):

$$S^2 = \frac{\nu(\nu+1)}{(\kappa_0 a)^2} \quad (15.3)$$

where  $\kappa_0$  is the free space wave number. The dimensionless quality factor  $Q$  of the resonant cavity may be determined as a ratio between the stored energy and the energy loss per cycle. Considering only the electrically stored energy (Galejs, 1972):

$$Q = \frac{\text{Re } S}{2 \text{ Im } S} \quad (15.4)$$

On Earth, the resonance is characterized by a quality factor  $Q$  ranging from 4 to 6 (Nickolaenko and Hayakawa, 2002).

The resulting fields are shown in Figure 15.1 for the first three SR modes. For a single lightning discharge, the E-field always has a maximum at the location of the flash and the antipode, while the magnetic field (orthogonal to electric) has a minimum at the same locations, regardless of the mode. For other locations, the relative intensity of the electric and magnetic fields depends uniquely on the source-observer distance (SOD). Figure 15.2 shows the theoretical spectra for the vertical electric field as a function of different SODs. At a distance of 10 Mm from

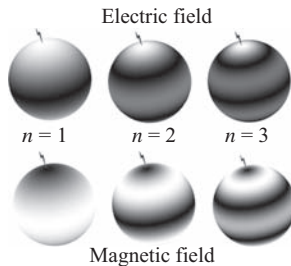


Figure 15.1 Electric and magnetic fields of the first three SR modes

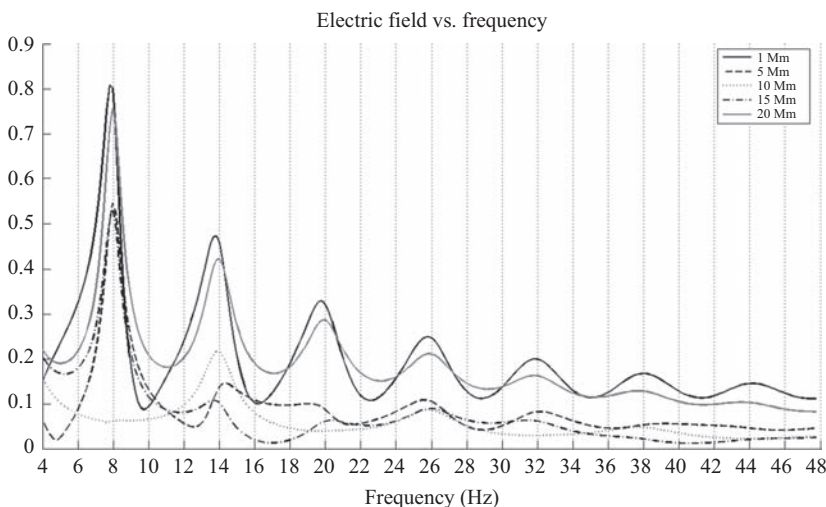


Figure 15.2 Electric field spectra as a function of SOD

the source lightning (dotted curve), the electric field shows a minimum intensity at 8 and 20 Hz ( $n = 1, 3$ ) while a maximum occurs at 14 and 26 Hz ( $n = 2, 4$ ). Every distance has a specific spectral pattern in both the electric and magnetic fields, a characteristic often used in SR geolocation of intense lightning flashes using a single station (Kemp and Jones, 1971; Burke and Jones, 1992; Nickolaenko, 1997; Boccippio *et al.*, 1998; Haung *et al.*, 1999; Price and Asfur, 2002; Greenberg and Price, 2004).

More realistic models are far more complex. Methods of introducing more complicated ionosphere structure include two-layer (Jones, 1974a) and multi-layer models (Jones, 1967; Yamashita, 1967, 1968; Hynninen and Galyuck, 1972), and the more realistic two-exponential (Greifinger and Greifinger, 1978), ‘knee’ (Mushtak and Williams, 2002), and ‘multi-knee’ (Pechony and Price, 2004) profiles.

### 15.3 SR measurements

The electromagnetic sensors used to measure SRs normally consist of two horizontal induction coils for detecting the horizontal magnetic field in the north-south ( $H_{NS}$ ) and the east-west ( $H_{EW}$ ) direction, and one vertical antenna for observing the vertical electric field,  $E_Z$  (Figure 15.3). The electric component is commonly measured with a ball antenna, suggested by Ogawa *et al.* (1966), connected to a high-impedance amplifier. The magnetic induction coils consist of tens of thousands of turns around material with very high magnetic permeability. The measured ELF AC fields are very small (mV/m for the electric field, and pT for the magnetic fields) compared with the DC static electric and magnetic fields in the atmosphere that ranges from 100 V/m in the fair weather to kV/m on a stormy day, and a magnetic field of 50,000 nT.

Man-made noise produces various interferences in the ELF band, from high voltage power supply lines to traffic and pedestrians (Nickolaenko and Hayakawa, 2002), forcing us to locate SR measuring stations in isolated rural areas, away from industrial activity. When choosing a site, the electromagnetic field sensors should be located as far away from power supply lines as possible. Complete battery power supply is preferable, but is expensive and limits long-term monitoring. Open spaces with uniform underlying geology and high soil conductivity should also be considered (Nickolaenko and Hayakawa, 2002). Since the sensors are exposed to external static electric and magnetic fields, even the slightest vibration of an antenna will result in huge signals induced at the input of the receiver. Hence, the horizontal magnetic antennas should be buried in the ground to avoid the signals induced by ground vibrations or wind. Ideally, electric and magnetic channels

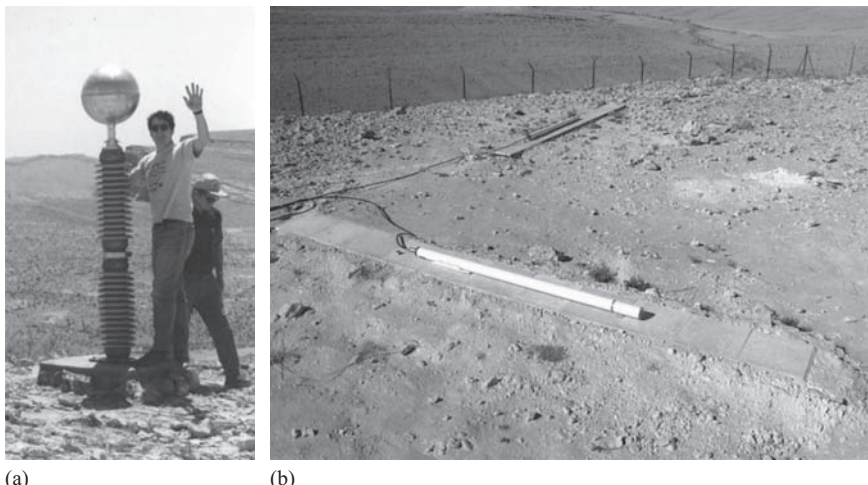


Figure 15.3 (a) Vertical electric field ball antenna with author; and (b) two horizontal induction coils at the Mitzpe Ramon, Israel SR site

should be identical, being calibrated periodically, sampled using a 16 bit A/D (analog-to-digital) converter, equipped by a GPS clock for time stamping the data, and if necessary, a notch filter for reducing the anthropogenic 50 Hz (or 60 Hz) interference. The sampling frequency can vary from several tens of hertz to a few hundreds of hertz in order to cover the SR band without aliasing. It is advisable to save all raw data for later post-processing, although some groups use real-time analysis and save only the spectral parameters of the SR (peak frequency, peak amplitude and *Q*-factor) (Price and Melnikov, 2004), together with short time segments of ELF transients.

In the time domain, the electric and magnetic signals produce a constant background signal, which is a superposition of individual pulses arriving from about 50 random lightning flashes per second occurring all over the world (Christian *et al.*, 2003). Superimposed upon the background noise are intense transient pulses from individual powerful lightning discharges, with amplitudes often 10 times higher than that of the background noise (Figure 15.4(a)) (Greenberg and Price, 2007). After processing the time series by using the Fast Fourier Transform (FFT) algorithm, SR modes can usually be observed in the frequency domain at 8, 14, 20, 26 ... Hz (Figure 15.4(b)). For studies of global lightning activity, the SR spectra are normally fitted to a set of Lorentzian curves (Sentman, 1987; Mushtak and Williams, 2009) where the curve for each mode is described by three parameters: peak amplitude, peak frequency and the quality factor.

As mentioned above, the duration of data collection of up to 10 minutes is needed to obtain stable estimates of the SR spectrum. Nickolaenko and Hayakawa (2002) suggest that this may explain the unsuccessful early experiments by Schumann and König (1954) to detect the global resonances: the natural signal is actually random ‘noise’ and the resonance peaks become visible only after relatively long integration time. A 10 minutes interval was used in the first successful experiment by Balser and Wagner (1960a, 1960b).

## 15.4 SR background observations of global lightning activity

At any given time, there are about 2000 thunderstorms around the globe (Ogawa *et al.*, 1966; Clayton and Polk, 1977; Sentman and Fraser, 1991; Williams, 1992; Nickolaenko and Rabinowicz, 1995; Heckman *et al.*, 1998). Producing ~50 lightning events per second (Christian *et al.*, 2003), these thunderstorms create the background SR signal.

Determining the spatial lightning distribution from the background SR records is a complex problem: in order to properly estimate the lightning intensity from SR records, it is necessary to account for the distance to sources. The common approach to this problem is based on the preliminary assumption of the spatial lightning distribution. The most widely used approaches are the models of the three thunderstorm centres – Southeast Asia, Africa and South America (Nickolaenko *et al.*, 1996, 1998; Satori *et al.*, 1996; Heckman *et al.*, 1998; Belyaev *et al.*, 1999; Shvets, 1999), and a single thunderstorm centre travelling around the globe

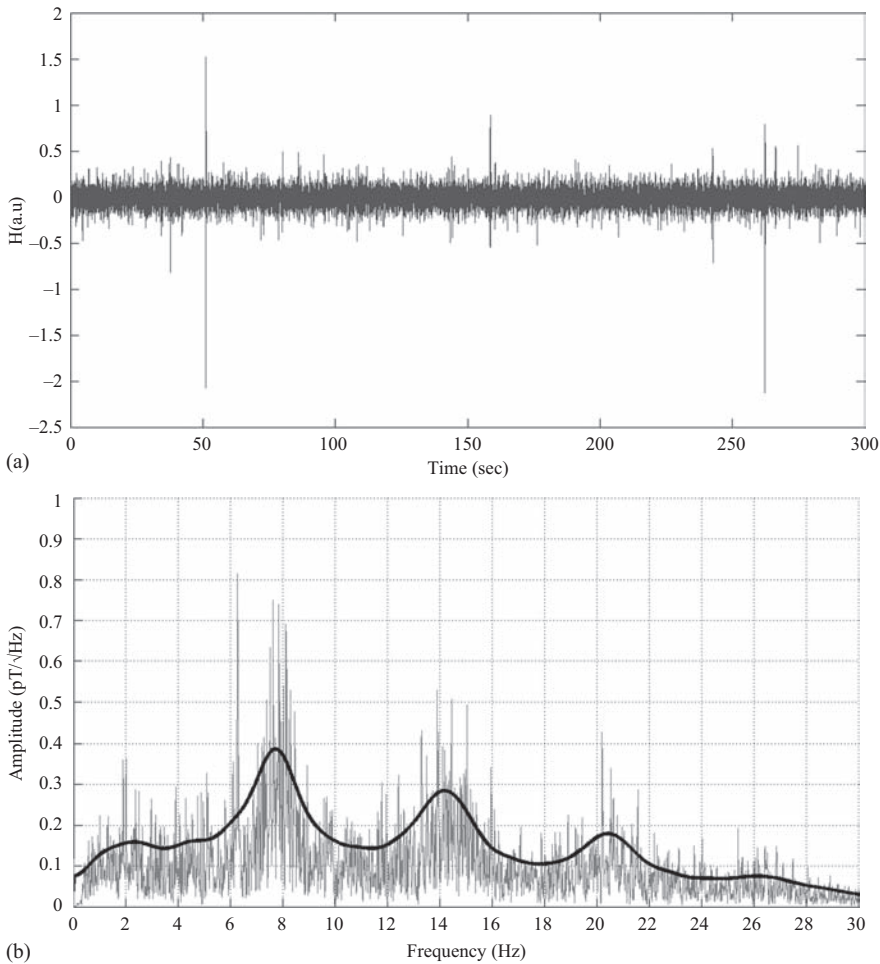


*Figure 15.4 (a)* Time series of 5 minutes of raw magnetic field data showing the background ELF field, together with transient ELF pulses; and *(b)* the spectrum of the time series showing the first four modes of the SR. The Lorentzian fits to the data are also shown

(Bliokh *et al.*, 1980; Nickolaenko and Hayakawa, 2002; Yatsevich *et al.*, 2005). An alternative approach is placing the receiver at the North or South Pole, which remains approximately equidistant from the main thunderstorm centres during the day (Nickolaenko, 1997). A new distinct method, not requiring preliminary assumptions on the lightning distribution (Shvets, 2001; Shvets *et al.*, 2009; Shvets and Hayakawa, 2011), is based on the decomposition of the average background SR spectra, utilizing ratios between the average electric and magnetic spectra and between their linear combinations.

The best documented and the most debated features of the SR phenomenon are the diurnal variations in the background SR power spectrum. Some of the earliest studies were made by Holzer (1958), Raemer (1961), Balser and Wagner (1962a), Polk and Fitchen (1962). The first investigators realized that SR field power variations were related to global thunderstorm activity (Holzer, 1958; Raemer, 1961; Balser and Wagner 1962a; Rycroft, 1963). Thus, SR measurements became a convenient tool for studying global lightning activity (Madden and Thompson, 1965; Polk, 1968; Jones, 1974b; Williams, 1992; Nickolaenko *et al.*, 1996; Fullekrug and Fraser-Smith, 1997; Sátori and Zieger, 1999; Price and Melnikov, 2004). Figure 15.5 shows the daily mean values of the first SR mode (8 Hz) measured simultaneously in Israel and California, over a 25-day period (Price, 2000). The agreement is quite remarkable given that the instruments, data acquisition and software algorithms were entirely independent of each other. This agreement is further evidence of the global nature of the SR, and its value of studying global lightning variability and trends.

Figure 15.6 shows the four-year (1999–2002) mean diurnal and seasonal power variations in the first SR mode from the Mitzpe Ramon (MR), Israel ELF station, after fitting the data with Lorentzian curves. The geographical location of the MR site (32N, 34E) results in the clear spatial and temporal separation of the three main thunderstorm source regions. Two maxima in the  $H_{NS}$  component are easily identified around 9:00 and 20:00 UT and are associated with increased thunderstorm activity from Southeast Asia and South America in the late afternoon, local time. In the  $H_{EW}$  component, there is a strong maximum around 14:00 UT associated with the peak in afternoon African lightning activity. The three dominant maxima are clearly seen during all seasons, associated with the three ‘hot spots’ of planetary lightning activity. The time and amplitude of the peaks vary throughout the year, reflecting the seasonal changes in lightning activity. The electric field sensor is sensitive to lightning activity from all directions, and hence shows a combination of all three peaks in the diurnal variations.

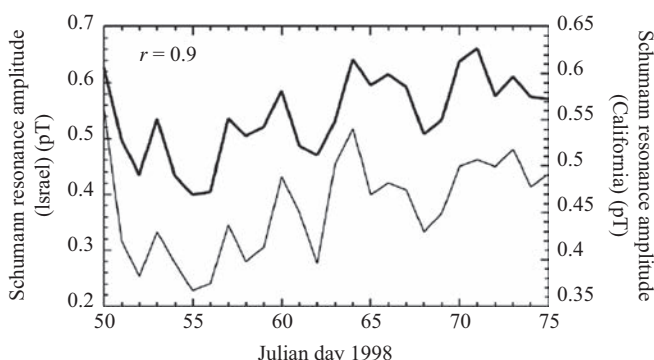


*Figure 15.5 Comparison of the SR amplitude of the first mode (8 Hz) measured simultaneously in Israel and California (from Price, 2000)*

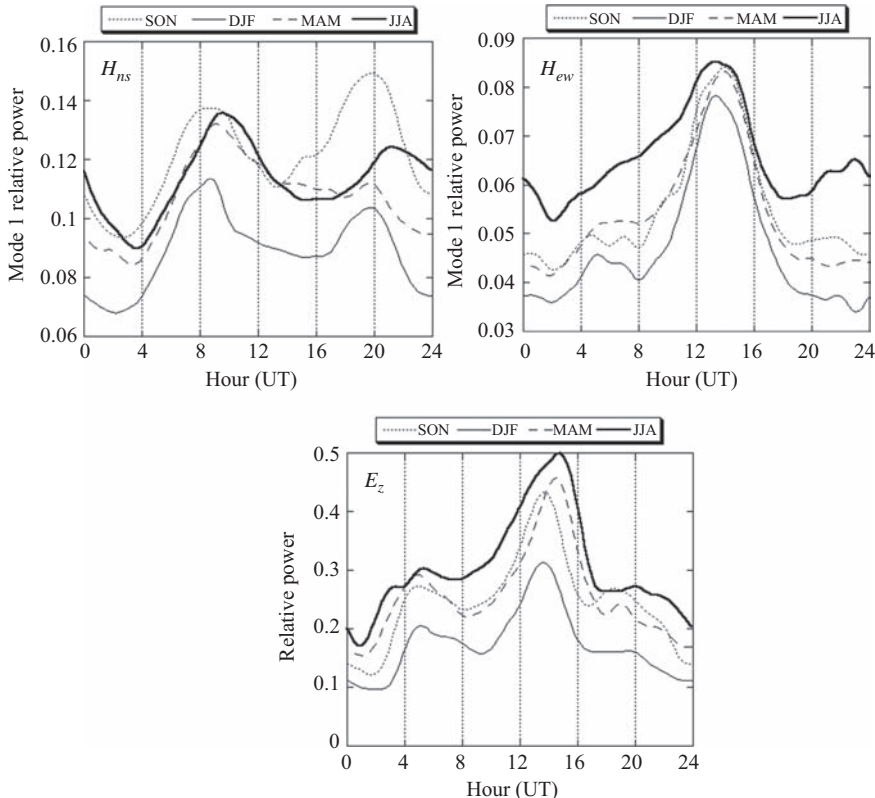
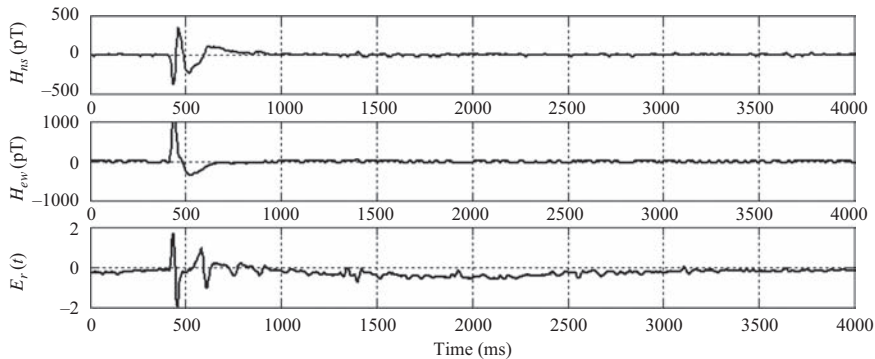


Figure 15.6 The 4-year mean diurnal and seasonal variations in the SR power for the first mode – individual electromagnetic components of the SR field (from Price and Melnikov, 2004)

## 15.5 SR transient measurements of global lightning activity

One of the most interesting problems in SR studies is determining the lightning source characteristics (the ‘inverse problem’). Temporally resolving each individual flash in the background SR signal is impossible due to the overlapping of many different lightning waveforms at ELF frequencies. However, there are intense ELF transient events, also named ‘Q-bursts’, which appear as prominent excursions above the SR background signal (Figure 15.7). Q-bursts are triggered by intense lightning strikes, associated with a large charge transfer and often high peak current (Ogawa *et al.*, 1966; Haung *et al.*, 1999; Nickolaenko *et al.*, 2010). Amplitudes of Q-bursts can exceed the SR background level by a factor of 10 and they appear with intervals from ~10 s to a few minutes (Shvets, 2001). This separation in time allows



*Figure 15.7 Example of ELF transient recorded at Mitzpe Ramon (32N, 34E) station, Israel*

us to consider the Q-bursts as isolated events and to determine their source lightning locations and charge moments (Kemp and Jones, 1971; Ishaq and Jones, 1977; Bliokh *et al.*, 1980; Jones and Burke, 1992; Nickolaenko, 1997; Burke and Jones, 1995; Greenberg and Price, 2004; Price *et al.*, 2004; Nakamura *et al.*, 2010).

The lightning location problem can be solved with either multi-station or single-station techniques. The multi-station techniques are the more accurate, but require more complicated and expensive facilities, involving a network of direction finders or time-of-arrival sensors (Rafalsky *et al.*, 1995). Single-station systems usually combine a direction finder technique with a SOD estimation technique (Figure 15.2). The transients can be geolocated with SOD and/or source-bearing techniques, based on the relationship between the electric and the magnetic field components (Kemp and Jones, 1971; Burke and Jones, 1992; Boccippio *et al.*, 1998; Haung *et al.*, 1999; Price *et al.*, 2002; Greenberg and Price, 2004). Source location techniques can be calibrated using the general location of flashes above continental regions (Kemp, 1971; Burke and Jones, 1995), the proximity of cold cloud tops in visible and infrared satellite images (Schmidt, 1993), global lightning measurements from space by the Optical Transient Detector (OTD) and the Lightning Imaging Sensor (LIS) (Boccippio *et al.*, 1998), and local measurements of lightning with ground networks, such as US National Lightning Detection Network in North America (Price *et al.*, 2002). Geolocation of the source lightning using the single-station SR methodology can be identified with an accuracy of  $\sim 1$  Mm anywhere on the globe.

## 15.6 Using SR as a climate research tool

The warming of the Earth has been the subject of intense debate and concern for many scientists for at least the past two decades. One of the important aspects in

understanding global climate change is the development of tools and techniques that would allow continuous and long-term monitoring of processes affecting, and being affected by, the global climate. SRs are one of the very few tools that can provide such *global* information continuously, reliably and cheaply.

Williams (1992) suggested that global temperature may be monitored via the SR. The link between SR and temperature is lightning flash rate, which increases nonlinearly with temperature (Price and Rind, 1990; Williams, 1992, 2005; Price, 1993; Price and Rind, 1994). The nonlinearity of the lightning-to-temperature relation provides a natural amplifier of the subtle (several tenths of  $1^{\circ}\text{C}$  (Angell, 1986; Jones *et al.*, 1986)) temperature changes and makes SR a sensitive ‘thermometer’. Additional analysis using other SR data sets also shows strong positive correlations between surface temperatures and SR power on seasonal and daily timescales (Price and Asfur, 2006). Figure 15.8 presents an example of daily observations of the 8 Hz magnetic field recorded in Israel, and surface temperatures integrated over South America. Although the correlation coefficient is only 0.57, it is clear that on warmer days there is more lightning activity than on cooler days.

Monitoring and predicting global climate change requires the understanding and modelling of factors that determine atmospheric concentrations of important greenhouse gases and feedbacks that determine the sensitivity of the climate system. Continental deep-convective thunderstorms produce most of the lightning discharges on Earth. In addition, they transport large amounts of water vapour into the upper troposphere, dominating the variability of global upper tropospheric water vapour (UTWV). UTWV is a key element of the Earth’s climate, which has

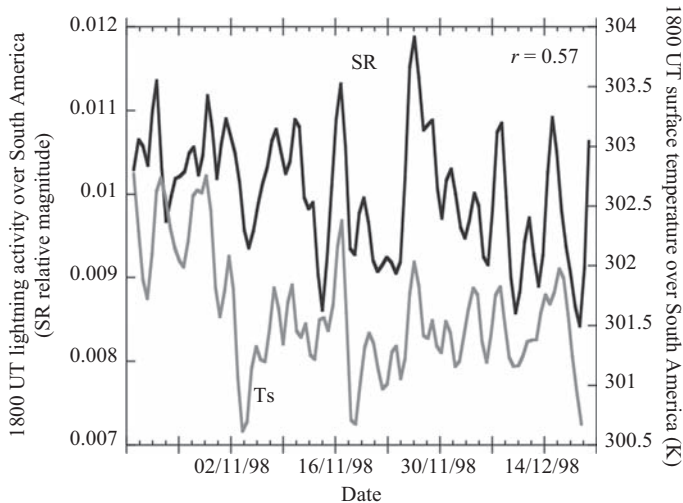


**Figure 15.8** Relative amplitude of the 8 Hz SR signal at 1800 UT every day, arriving from South America, but detected in Israel (black), compared with the spatially averaged 1800 UT tropical land surface temperatures over South America (grey)

direct effects as a greenhouse gas, as well as indirect effect through interaction with clouds, aerosols and tropospheric chemistry. UTWV has a much greater impact on global warming than water vapour in the lower atmosphere (Hansen *et al.*, 1984), but whether this impact is a positive, or a negative feedback is still debated (Lindzen, 1990; Rind *et al.*, 1991; Del Genio *et al.*, 1994; Sun and Held, 1996; Rind, 1998). The main challenge in addressing this question is the difficulty in monitoring UTWV globally over long timescales. Price (2000) and Price and Asfur (2006) showed that changes in the UTWV can be monitored from records of the SR. Figure 15.9 shows an example of the connection between daily SR amplitudes and UTWV over Africa, the largest source of lightning and thunderstorms on the planet. It should be noted that the UTWV curve has been shifted one day to show the agreement between the curves. However, the lightning activity peaks one day before the peak in the UTWV.

In addition to climate change, the SR has also been shown to be linked to the natural climate oscillation El Nino/Southern Oscillation (ENSO) that changes the Earth's climate every few year (Satori and Zieger, 1999; Satori *et al.*, 2009). During ENSO years the convection, and hence the lightning activity, shifts position relative to the fixed SR stations. Therefore, changes in SR parameters can be used to monitor the natural ENSO cycle, and the shifts in convection that occur during these events.

The above results show that two of the most important parameters of global climate change – surface temperature and UTWV – can be monitored via observations of the SR, utilizing its relation to worldwide thunderstorm activity. In addition, the SRs may also help us understand important feedback effects in the climate system, such as the water vapour feedback in the upper troposphere. One of the great advantages of this method is the availability of long-term calibrated data sets that can provide past and future records of global lightning variations on Earth.

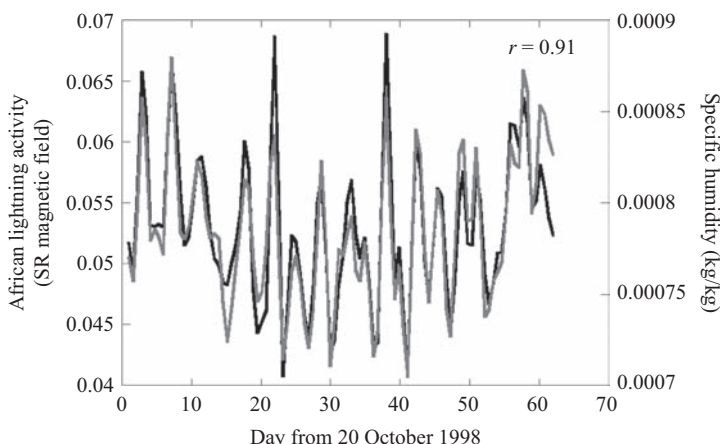


*Figure 15.9 Daily SR 8 Hz magnetic field records (black) and upper tropospheric water vapour (grey) over tropical Africa (from Price and Asfur, 2006)*

## 15.7 SR in transient luminous events (TLE) research

It is now believed that many of the SR transients (Q-bursts) are related to TLEs, spectacular optical flashes in the upper atmosphere above active thunderstorms. The existence of TLEs was theoretically predicted by Wilson (1924), but the official discovery came with the first image captured above a thundercloud by Franz *et al.* (1990). In the last 20 years, there has been an extensive hunt for TLEs using photography from ground stations, aircrafts, satellites and space shuttles, leading to TLE documentation in different geographical locations all over the world (Boeck and Vaughan, 1990; Sentman and Wescott, 1993; Lyons, 1994; Boeck *et al.*, 1995; Heavner *et al.*, 1995; Sentman, 1996; Dowden and Rodger, 1997; Fukunishi *et al.*, 1999; Hardman *et al.*, 2000; Su *et al.*, 2002; Yair *et al.*, 2003; Neubert *et al.*, 2005; Chen *et al.*, 2008).

TLEs can be classified into two main classes: sprites and elves (Williams, 2001), although there are also blue jets, gigantic jets, halos and trolls. Both elves and sprites are short-lived luminous events associated with active thunderstorms. Elves are dim doughnut-shaped glows of red light with a radius of a few hundred kilometres, lasting typically  $\sim 1$  ms, and occurring at altitudes of  $\sim 90\text{--}100$  km, located above the parent lightning discharge. Elves are produced by the electromagnetic pulse of the lightning, with the intensity of elves related to the lightning peak current (Barrington-Leigh and Inan, 1999). Sprites are also red in colour (due to the excitation of atmospheric nitrogen molecules (Pasko *et al.*, 1995)), while being a lot brighter than elves. Sprites have a much longer lifetime of tens of milliseconds, and occur at lower altitudes in the atmosphere (40–90 km). Unlike the uniform featureless elves, sprites can be very varied in shapes, structure and size, with widths ranging to 50–100 km horizontally. Sprites are produced by the quasi-static electric field induced above thunderstorms immediately after large cloud-to-ground (CG) lightning (Pasko *et al.*, 1997). In the case of sprites, the brightness appears to be related to the charge removed by the lightning, and not the peak current (Takahashi *et al.*, 2010). Since the SR transients are dominated by large charge moments, irrelevant to peak currents, the SR are better suited for studying sprites than elves (Williams *et al.*, 2007a).

The physical mechanisms responsible for sprites and elves initiation are independent of the polarity of the lightning flash (Pasko *et al.*, 1995; Bell *et al.*, 1995; Milikh *et al.*, 1995; Roussel-Dupré and Gurevich, 1996; Pasko *et al.*, 1997; Valdivia *et al.*, 1997); however, the vast majority of sprites are initiated by positive CG flashes (Reising *et al.*, 1996; Boccippio *et al.*, 1995; Williams *et al.*, 2007b). These powerful positive flashes emit strong electromagnetic energy in the ELF range, indicative of continuing currents lasting over timescales of at least a few milliseconds (Reising *et al.*, 1996), and thus can be detected in the SR band. Boccippio *et al.* (1995) suggested that sprites are produced by positive CG occurring in the stratiform region of a thunderstorm system, and are accompanied by large-amplitude transient pulses ('Q-burst') in the SR band. Recent observations (Boccippio *et al.*, 1995; Huang *et al.*, 1999; Hobara *et al.*, 2001; Price *et al.*, 2002;

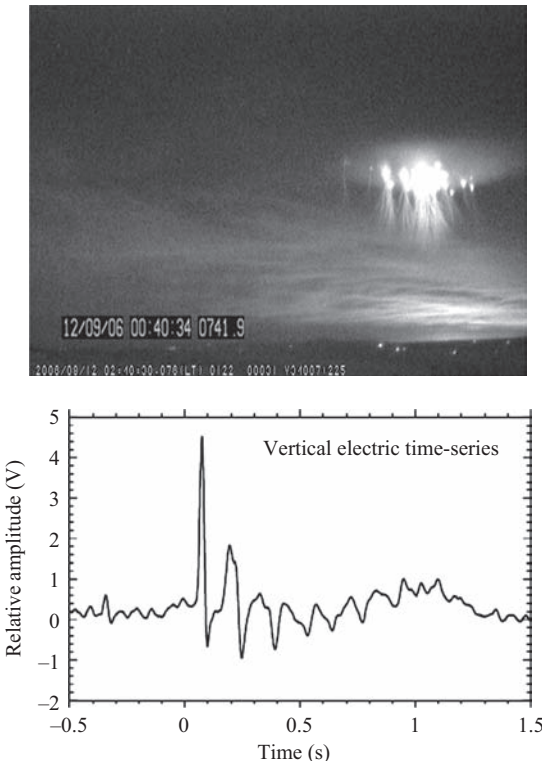


*Figure 15.10* A sprite observed by the ILAN team (Ganot *et al.*, 2007) together with a typical ELF transient, showing clearly the 8 peaks per second (8 Hz) in the vertical electric field (Price *et al.*, 2002)

Sato *et al.*, 2003; Price *et al.*, 2004) reveal that occurrences of sprites and transient SR are highly correlated (Figure 15.10).

SR records can be used to estimate the magnitude of the charge removed from CG (Cummer and Inan, 1997; Bell *et al.*, 1996), which appears to be one of the crucial parameters in determining which lightning discharge can produce sprites. A method of charge moment estimation of sprite-inducing CG discharges from SR data was developed by Huang *et al.* (1999), who showed that the charge moments of sprite-inducing CG discharges range from 200 to 2000 Ckm. Hu *et al.* (2002) suggested a sprite initiation probability as a function of charge moments of positive CG discharges, and hence the charge moment estimation derived from SR data can possibly enable us to estimate the global occurrence rate of sprites. However, it should be noted that not all sprites produce strong ELF transients (Greenberg *et al.*, 2007, 2009).

Since sprites are rather rare, occurring at rate of only a few per minute (while regular lightning occurs at a rate of 50–100 flashes per second around the globe) SR techniques appear to be one of the most convenient and low-cost tools for continuous TLE monitoring.

## 15.8 SR in extraterrestrial lightning research

Existence of SRs depends generally on two factors – presence of a substantial ionosphere with electric conductivity increasing with height from low values near the surface (or a high-conductivity layer, in case of gaseous planets) to form an ELF waveguide and a source of excitation of electromagnetic waves in the ELF range. In the Solar System, there are a number of candidates for SR detection: Venus, Mars, Jupiter, Saturn and its moon Titan (Yair *et al.*, 2008).

The speculations that lightning occurs on Venus first arose about 30 years ago. The strongest evidence for lightning on Venus comes from the impulsive electromagnetic waves seen by the Venera 11 and 12 landers (Ksanfomaliti, 1979; Ksanfomaliti, 1983a, 1983b; Ksanfomaliti, 1985) and the Pioneer Venus Orbiter (Taylor *et al.*, 1979; Scarf and Russell, 1983). On Mars lightning activity has not been detected, but charge separation and lightning strokes are considered possible in the Martian dust storms (Eden and Vonnegut, 1973; Melnik and Parrot, 1998; Farrell *et al.*, 1999; Renno *et al.*, 2003). Jupiter and Saturn are the only planet where lightning activity is well established. Existence of lightning on Jupiter was predicted by Bar-Nun (1975) and it is supported by data from Galileo, Voyagers 1 and 2, Pioneers 10 and 11 and Cassini (Little *et al.*, 1999; Desch *et al.*, 2002). Recently lightning on Saturn has also been confirmed by measurements from the Cassini spacecraft (Fischer *et al.*, 2007a; Fischer *et al.*, 2011). Although no lightning was observed during Voyager flybys of Titan in 1980 and 1981, it was long suggested that lightning dischargers do take place on this moon of Saturn (Tokano *et al.*, 2001; Lammer *et al.*, 2001). However, recent data from Cassini/Huygens seems to indicate that there is no lightning activity on Titan (Fischer *et al.*, 2007b; Fischer and Gurnett, 2011).

Modelling of SR parameters on the planets and moons of the Solar System is complicated by the lack of knowledge of the waveguide parameters. SR frequencies depend on the structure of the lower part of the ionosphere, which is not sufficiently studied. On Jupiter and Saturn, the situation is yet more complicated. Little is known about the electrical parameters of the interior of Jupiter and Saturn. Even the question of what should serve as the lower waveguide boundary is a non-trivial one in the case of these gaseous planets. To our best knowledge, there are no works dedicated to SR on Saturn. Till date there was only one attempt to model SRs on Jupiter – in the work by Sentman (1990). Sentman's calculations yielded resonant frequencies of  $\sim 0.76$ , 1.35 and 1.93 Hz with quality factors of roughly 7, predicting sharp, pronounced peaks.

The situation with other planets is a little better. SRs on Venus were studied by Nickolaenko and Rabinowicz (1982), Pechony and Price (2004), Yang *et al.* (2006) and Simões *et al.* (2008). All studies, based on different conductivity profiles and with different models, yielded very close resonant frequencies: around 9, 16 and 23 Hz. The quality factors, though, differ substantially: Nickolaenko and Rabinowicz obtained Q-factors of  $\sim 5$  while Pechony and Price acquired Q $\sim 10$ . Such a difference – by a factor of two – was predicted by Nickolaenko and Rabinowicz for more sophisticated ionosphere representations.

Martian global resonances were modelled by Sukhorukov (1991), Pechony and Price (2004), Molina-Cuberos *et al.* (2006) and Yang *et al.* (2006). The results of the studies are somewhat different. Sukhorukov obtained the resonant frequencies at about 13, 25 and 37 Hz with Q-factors around 3.5. The frequencies calculated by Pechony and Price are lower: 8.6, 16.3 and 24.4 Hz, with Q-factors of  $\sim 2.4$ . The disparity can probably be explained by the different models of Martian lower ionosphere used in the two studies. Nevertheless, the low quality factors obtained in both studies show that pronounced sharp peaks at resonance frequencies should not be expected for the Martian ELF waveguide. Significantly, different results were obtained by Molina-Cuberos *et al.* (2006), where several ionosphere models were used. The first resonance occurred at 11–12 Hz (depending on ionosphere model), the second and third resonances interfered to form a single peak at 21–25 Hz and the fourth, fifth and sixth modes produced a very smooth-shaped peak at around 60 Hz.

The ionosphere of Titan is perhaps the most thoroughly modelled today. The recent interest in the largest satellite of Saturn is associated with the Cassini/Huygens Mission and the expectations of finding evidence of lightning activity on Titan. Consequently, SR on Titan received more attention than resonances on other celestial bodies. The resonant frequencies obtained for various ionospheric conductivity profiles tested in studies by Besser *et al.* (2002), Morente *et al.* (2003), Molina-Cuberos *et al.* (2004) and Navarro *et al.* (2007) range (for realistic models) from 11.0 to 15.0 Hz for the first mode, 21.2–27.8 Hz for the second and 35.6–41.6 for the third. Unfortunately, the quality factors were not calculated in these studies. Comparable results were obtained by other authors: resonant frequencies of 19.9, 35.8 and 51.8 Hz with Q-factors of 1–3 were obtained by Nickolaenko *et al.* (2003), and 11.8, 22.5 and 34.1 Hz with Q-factors of  $\sim 2$  by Pechony and Price (2004). The low Q-factors acquired in these two studies show that the expected peaks, should lightning activity be found on Titan, are rather wide. After the Huygens probe entered Titan's atmosphere in 2005, a heated debate evolved over the existence of SR signals in the observed data (Fischer *et al.*, 2007b; Simoes *et al.*, 2007; Morente *et al.*, 2008).

Today there is no possibility to validate SR parameters calculated for other planets and moons. The values of the resonance frequencies and quality factors are very dependent on the ionospheric profile models. The accuracy of the latter is limited, and a deeper knowledge of planetary ionospheres would allow more precise predictions of SR parameters. On the other hand, experimental evaluation of SR parameters can aid in the elaboration of the effective model of the ionospheric conductivity profile and contribute substantially to the knowledge of lower ionospheres on planets of the Solar System.

## 15.9 Summary

Being a global phenomenon, SRs have numerous applications in lightning research. Background SR records can serve as a convenient and a low-cost tool for global lightning activity monitoring. The SR can provide a global geoelectric index for monitoring climate changes. It provides one of the few tools that, through

variations in global lightning activity, can provide continuous and long-term monitoring of such important global climate change parameters as tropical land surface temperature and tropical UTWV.

SR transients (Q-bursts) can be used to geolocate intense lightning strikes anywhere on the planet. These large-amplitude pulses are apparently related to the occurrence of sprites and elves above thunderstorms, and therefore TLEs can be studied using SR observations. An additional application of SR is extraterrestrial lightning research. SRs may be used to detect and, if necessary, monitor lightning activity on the planets and moons of the Solar System.

There are still many open questions in SR research: importance of the day-night variation in the ionosphere conductivity profile (Pechony *et al.*, 2007; Satori *et al.*, 2007), influence of the latitudinal changes in the Earth magnetic field, impacts of cosmic, solar and geomagnetic disturbances (Price and Mushtak, 2001; Williams and Satori, 2007); polar cap absorption, accuracy of source geolocation and the determination of the spatial lightning distribution from the background records (Greenberg and Price, 2004; Price *et al.*, 2004; Shvets and Nickolaenko, 2011). Despite these open problems, SR is one of the most promising tools in a variety of fields related to lightning electromagnetics.

## Acknowledgements

I would like to thank all of my graduate students and researchers who have been involved in our SR studies over the years, and who have contributed to the results in this chapter: Dr Mustafa Asfur, Dr Olga Pechony, Dr Eran Greenberg, Dr Michael Finkelstein, Dr Alex Melnikov, Mr David Shtibelman and Mr Boris Starobinets.

## References

- Angell, J. K. (1986), On the variation in period and amplitude of the quasi-biennial oscillation in the equatorial stratosphere, 1951–85, *Mon. Weather Rev.*, 114(11), 2272–2278
- Balser, M. and C. Wagner (1960a), Measurement of the spectrum of radio noise from 50 to 100 c/s, *J. Res. NBS*, 64D, 415–418
- Balser, M. and C. Wagner (1960b), Observations of earth-ionosphere cavity resonances, *Nature*, 188, 638–641
- Balser, M. and C. Wagner (1962a), Diurnal power variations of the earth-ionosphere cavity modes and their relationship to worldwide thunderstorm activity, *J. Geophys. Res.*, 67, 619–625
- Balser, M. and C. Wagner (1962b), On frequency variations of the earth-ionosphere cavity modes, *J. Geophys. Res.*, 67, 4081–4083
- Balser, M. and C. Wagner (1963), Effect of a high-altitude nuclear detonation on the earth-ionosphere cavity, *J. Geophys. Res.*, 68, 4115–4118
- Bar-Nun, A. (1975), Thunderstorms on Jupiter, *Icarus*, 24, 86–94

- Barrington-Leigh, C. P. and U. S. Inan (1999), Elves triggered by positive and negative lightning discharges, *Geophys. Res. Lett.*, 26, 683–686
- Bell, T. F., V. P. Pasko, U. S. Inan (1995), Runaway electrons as a source of red sprites in the mesosphere, *Geophys. Res. Lett.*, 22, 2127
- Bell, T. F., S. C. Reising, U. S. Inan (1996), Continuing currents determined from broadband ELF/VLF magnetic fields radiated by positive cloud-to-ground discharges associated with red sprites, *EOS Supplement*, 77, F61 (abstract)
- Belyaev, G. G., A. Yu. Schekotov, A. V. Shvets, A. P. Nickolaenko (1999), Schumann resonances observed using Poynting vector spectra. *J. Atmos. Sol-Terr. Phys.*, 61, 751–763
- Besser, B. P. (2007), Synopsis of the historical development of Schumann resonances, *Radio Sci.*, 42, RS2S02, doi:10.1029/2006RS003495
- Besser, B. P., K. Schwingenschuh, I. Jernej, H. U. Eichelberger, H. I. M. Lichtenegger, M. Fulchignoni, G. J. Molina-Cuberos, J. A. Morente, J. A. Porti, A. Salinas (2002), Schumann resonances as indicators for lighting on Titan, *Proceedings of the Second European Workshop on Exo/Astrobiology, Graz, Australia*, 16–19 Sep. 2002, (ESA SP-518, November 2002)
- Bliokh, P. V., A. P. Nickolaenko, Yu. F. Filippov (1980), *Schumann Resonances in the Earth-Ionosphere Cavity*, D. Ll. Jones, ed., Peter Peregrinus, Oxford
- Boccippio, D. J., E. R. Williams, S. J. Heckman, W. A. Lyons, I. T. Baker, R. Boldi (1995), Sprites, ELF transients, and positive ground strokes, *Science*, 269, 1088–1091
- Boccippio, D. J., C. Wong, E. Williams, R. Boldi, H. J. Christian, S. J. Goodman (1998), Global validation of single-station Schumann resonance lightning location, *J. Atmos. Terr. Phys.*, 60, 701–712
- Boeck, W. L. and O. H. Vaughan Jr. (1990), Lightning observations from the STS-32 space shuttle mission, *EOS Trans. AGU*, 71, 1241
- Boeck, W. L., O. H. Vaughan Jr., R. J. Blakeslee, B. Vonnegut, M. Brook, J. McKune (1995), Observations of lightning in the stratosphere, *J. Geophys. Res.*, 100, 1465–1475
- Burke, C. P. and D. Ll. Jones (1992), An experimental investigation of ELF attenuation rates in the Earth-ionosphere duct, *J. Atmos. Terr. Phys.*, 54, 243–254
- Burke, C. P. and D. Ll. Jones (1995), Global radiolocation in the lower ELF frequency band, *J. Geophys. Res.*, 100(D12), 26,263–26,272
- Chen, A. B., et al. (2008), Global distributions and occurrence rates of transient luminous events, *J. Geophys. Res.*, 113, A08306, doi:10.1029/2008JA013101
- Christian, H. J., R. J. Blakeslee, D. J. Boccippio, W. L. Boeck, D. E. Buechler, K. T. Driscoll, S. J. Goodman, J. M. Hall, W. J. Koshak, D. M. Mach, M. F. Stewart (2003), Global frequency and distribution of lightning as observed from space by the Optical Transient Detector, *J. Geophys. Res.*, 108(D1), 4005
- Clayton, M. and C. Polk (1977), Diurnal validation and absolute intensity of worldwide lightning activity, in *Electrical Processes in Atmospheres*, H. Dolezalek and R. Reiter, eds., pp. 440–449, Steinkopff, Darmstadt, Germany

- Cummer, S. A. and U. S. Inan (1997), Measurement of charge transfer in sprite-producing lightning using ELF radio atmospherics, *Geophys. Res. Lett.*, 24, 1731
- Del Genio, A. D., W. Kovari Jr., N. S. Yao (1994), Climatic implications of the seasonal variations of upper troposphere water vapour, *Geophys. Res. Lett.*, 21, 2701–2704
- Desch, S. J., W. J. Borucki, C. T. Russell, A. Bar-Nun (2002), Progress in planetary lighting, *Rep. Prog. Phys.*, 65, 955–997
- Dowden, R. L. and C. J. Rodger (1997), Decay of a vertical plasma column: A model to explain VLF sprites, *Geophys. Res. Lett.*, 24, 2765–2768
- Eden, H. F. and B. Vonnegut (1973), Electrical breakdown caused by dust motion in low-pressure atmospheres: consideration for Mars, *Science*, 180, 962
- Farrell, W. F., M. L. Kaiser, M. D. Desch, J. G. Houser, S. A. Cummer, D. M. Wilt, G. A. Landis (1999), Detecting electrical activity from Martian dust storms, *J. Geophys. Res.*, 104, 3795
- Fischer, G., et al. (2007a), Analysis of a giant lightning storm on Saturn, *Icarus*, 190, 528–544
- Fischer, G., D. A. Gurnett, W. S. Kurth, W. M. Farrell, M. L. Kaiser, P. Zarka (2007b), Nondetection of Titan lightning radio emissions with Cassini/RPWS after 35 close Titan flybys, *Geophys. Res. Lett.*, 34, L22104, doi:10.1029/2007GL031668
- Fischer, G., and D. A. Gurnett (2011), The search for Titan lightning radio emissions, *Geophys. Res. Lett.*, 38, L08206, doi:10.1029/2011GL047313
- Fischer, G., et al. (2011), A giant thunderstorm on Saturn, *Nature*, 475, 75–77, doi:10.1038/nature10205
- Franz, R. C., R. J. Nemzek, J. R. Winckler (1990), Television image of a large upward electrical discharge above a thunderstorm system, *Science*, 249, 48
- Fraser-Smith, A. C. and P. R. Bannister (1998), Reception of ELF signals at antipodal distance, *Radio Sci.*, 33(1), 83–88, doi:10.1029/97RS01948
- Fukunishi, H., Y. Takahashi, A. Uchida, M. Sera, K. Adachi, R. Miyasato (1999), Occurrences of sprites and elves above the Sea of Japan near Hokuriku in winter, *Eos Trans. AGU*, 80(46), Fall Meet. Suppl., F217
- Fullekrug, M. and A. C. Fraser-Smith (1997), Global lightning and climate variability inferred from ELF magnetic field variations, *Geophys. Res. Lett.*, 24, 2411–2414
- Galejs, J. (1972), *Terrestrial Propagation of Long Electromagnetic Waves*, Pergamon Press, New York
- Ganot, M., Y. Yair, C. Price, B. Ziv, Y. Sherez, E. Greenberg, A. Devir, R. Yaniv (2007), First detection of transient luminous events associated with winter thunderstorms in the eastern Mediterranean, *Geophys. Res. Lett.*, 34, L12801, doi:10.1029/2007GL029258
- Gendrin, R. and R. Stefant (1962a), Effet de l'explosion thermonucleaire a tres haute altitude du 9 juillet 1962 sur la resonance de la cavite Terre-ionosphere: Resultats experimentaux, *C.R. Acad. Sci. Paris*, 255, 2273–2275

- Gendrin, R. and R. Stefant (1962b), Effet de l'explosion thermonucleaire à très haute altitude du 9 juillet 1962 sur la résonance de la cavité Terre-ionosphère: Interprétation, *C.R. Acad. Sci. Paris*, 255, 2493–2495
- Greenberg, E. and C. Price, (2004), A global lightning location algorithm based on the electromagnetic signature in the Schumann resonance band, *J. Geophys. Res.*, 109, D21111, doi:10.1029/2004JD004845
- Greenberg, E. and C. Price (2007), Diurnal variations of ELF transients and background noise in the Schumann resonance band, *Radio Sci.*, 42, RS2S08, doi:10.1029/2006RS003477
- Greenberg, E., C. Price, Y. Yair, M. Ganot, J. Bór, G. Sátori (2007), ELF transients associated with sprites and elves in eastern Mediterranean winter thunderstorms, *J. Atmos. Solar-Terr. Physics*, 69, 1569–1586
- Greenberg, E., C. Price, Y. Yair, C. Haldoupis, O. Chanrion, T. Neubert (2009), On the ELF charge moment change, VLF bursts and subionospheric perturbations associated with sprites, *J. Atmos. Terr.-Solar Phys.*, doi:10.1016/j.jastp.2009.05.005
- Greifinger, C. and Ph. Greifinger (1978), Approximate method for determining ELF eigenvalues in the Earth-ionosphere waveguide, *Radio Sci.*, 13, 831–837
- Hansen, J., A. Lacis, D. Rind, G. Russel, P. Stone, I. Fung, R. Ruedy, J. Lerner (1984), Climate sensitivity: Analysis of feedback mechanisms, in *Climate Processes and Climate Sensitivity*, J. E. Hansen and T. Takahashi, eds., AGU Geophys. Monograph 29, pp. 130–163. American Geophysical Union, Washington, D.C.
- Hardman, S. F., R. L. Dowden, J. B. Brundell, J. L. Blahr, Z. I. Kawasaki, C. J. Rodger (2000), Sprites observation in the northern territory of Australia, *J. Geophys. Res.* 105, 4689
- Haung, H. G., E. Williams, R. Boldi, S. Heckman, W. Lyons, M. Taylor, T. Nelson, C. Wong (1999), Criteria for sprites and elves based on Schumann resonance observations, *J. Geophys. Res.*, 104, 16,943–16,964
- Heavner, M. J., D. L. Hampton, D. D. Sentman, E. M. Wescott (1995), Sprites over Central and South America (abstract), *Eos Trans. AGU*, 76(46), Fall Meet. Suppl., 115
- Heckman, S. J., E. Williams, B. Boldi (1998), Total global lightning inferred from Schumann resonance measurements, *J. Geophys. Res.*, 103(D24), 31775–31779
- Hobara, Y., N. Iwasaki, T. Hayashida, M. Hayakawa, K. Ohta, H. Fukunishi (2001), Interrelation between ELF transients and ionospheric disturbances in association with sprites and elves, *Geophys. Res. Lett.*, 28, 935–938
- Holzer, R. E. (1958), World thunderstorm activity and extremely low frequency spherics, in *Recent Advances in Atmospheric Electricity*, L. G. Smith, ed. pp. 599–602, Pergamon Press, New York
- Hu, W., S. A. Cummer, W. A. Lyons, T. E. Nelson (2002), Lightning charge moment changes for the initiation of sprites, *Geophys. Res. Lett.*, 29(8), 1279, doi:10.1029/2001GL014593

- Huang, E., E. Williams, R. Boldi, S. Heckman, W. Lyons, M. Taylor, T. Nelson, C. Wong (1999), Criteria for sprites and elves based on Schumann resonance observations, *J. Geophys. Res.-Atmos.*, 104(D14), 16943
- Hynninen, E. M. and Yu. P. Galyuck (1972), 'The field of a vertical electric dipole over the spherical Earth's surface below the vertically inhomogeneous ionosphere', (in Russian), The Problems of Diffraction and Wave Propagation, 11, 109–115
- Ishaq, M. and D. L. Jones (1977) Method of obtaining radiowave propagation parameters for the Earth–ionosphere duct at ELF, *Electron. Lett.*, 13, 254–255
- Jones, D. Ll. (1974a), The calculations of the Q-factors and frequencies of Earth–ionosphere cavity resonances for a two-layer ionosphere model, *J. Geophys. Res.*, 69, 4037–14041
- Jones, D. Ll. (1974b), *ELF-VLF radio wave propagation*, J. A. Holtet, ed., D. Reidel Publishing Company, Dordrecht, 207
- Jones, D. Ll. (1967), Schumann resonances and ELF propagation for inhomogeneous, isotropic ionosphere profiles, *J. Atmos. Terr. Phys.*, 29, 1037–1044
- Jones, D. Ll. and C. P. Burke (1992), An experimental investigation of ELF attenuation rates in the Earth–ionosphere cavity, *J. Atmos. Terr. Phys.*, 54, 243
- Jones, P. D., T. M. L. Wigley, P. B. Wright (1986), Global Temperature-Variations between 1861 and 1984, *Nature*, 322, 430–434
- Kemp, D. T. and D. Ll. Jones (1971), A new technique for the analysis of transient ELF electromagnetic disturbances within the Earth–ionosphere cavity, *J. Atmos. Terr. Phys.*, 33, 567–572
- Ksanfomaliti, L. V. (1979), Lightning in the cloud layer of Venus, (in Russian), *Kosmicheske Issledovaniya*, 17(5), 747–762
- Ksanfomaliti, L. V. (1983a), Electrical activity of the atmosphere of Venus. I. Measurements on descending probes, (in Russian), *Kosmicheske Issledovaniya*, 21(2), 279–296
- Ksanfomaliti, L. V. (1983b), Electrical activity of the atmosphere of Venus. II. Satellite measurements, (in Russian), *Kosmicheske Issledovaniya*, 21(4), 619–633
- Ksanfomaliti, L. V. (1985), *Planet Venus*, (in Russian), Nauka, Moscow
- Lammer, H., T. Tokano, G. Fischer, W. Stumptner, G. J. Molina-Cuberos, K. Schwingenschuh, H. O. Rucher (2001), Lightning activity of Titan: can Cassini/Huygens detect it?, *Planet. Space Sci.*, 49, 561–574
- Lindzen, R. S. (1990), Some coolness concerning global warming, *Bull. Am. Meteorol. Soc.* 71, 288–299
- Little, B., C. D. Anger, A. P. Ingersoll, A. R. Vasavada, D. A. Senske, H. H. Breneman, W. J. Borucki, The Galileo SSI Team (1999), Galileo images of lightning on Jupiter, *Icarus*, 142, 306–323
- Lyons, W. A. (1994), Characteristics of luminous structures in the stratosphere above thunderstorms as imaged by low-light video, *Geophys. Res. Lett.*, 21, 875–878

- Madden, T. and W. Thompson (1965), Low-frequency electromagnetic oscillations of the Earth-ionosphere cavity, *Rev. Geophys.*, 3(2), 211
- Melnik, O. and M. Parrot (1998), Electrostatic discharge in Martian dust storms, *J. Geophys. Res.*, 103(A12), 29107–29117
- Milikh, G. M., K. Papadopoulos, C. L. Chang (1995), On the physics of high altitude lightning, *Geophys. Res. Lett.*, 22, 85
- Molina-Cuberos, G. J., J. A. Morente, B. P. Besser, J. Porti, H. Lichtenegger, K. Schwingenschuh, A. Salinas, J. Margineda (2006), Schumann resonances as a tool to study the lower ionosphere of Mars, *Radio Sci.*, 41, RS1003, doi:10.1029/2004RS003187
- Molina-Cuberos, G. J., J. Porti, B. P. Besser, J. A. Morente, J. Margineda, H. I. M. Lichtenegger, A. Salinas, K. Schwingenschuh, H. U. Eichelberger (2004), Shumann resonances and electromagnetic transparency in the atmosphere of Titan, *Adv. Space Res.*, 33, 2309–2313
- Morente, J. A., G. J. Molina-Cuberos, J. A. Porti, K. Schwingenschuh, B. P. Besser (2003), A study of the propagation of electromagnetic waves in Titan's atmosphere with the TLM numerical method, *Icarus*, 162, 374–384
- Morente, J. A., J. A. Porti, A. Salinas, E. A. Navarro (2008), Evidence of electrical activity on Tital drawn from the Schumann resonances sent by Huygens probe, *Icarus*, 195, 802–811
- Mushtak, V. C. and E. R. Williams (2002), ELF propagation parameters for uniform models of the Earth-ionosphere waveguide, *J. Atmos. Sol-Terr. Phys.*, 64, 1989–2001
- Mushtak, V. C. and E. R. Williams (2009), An improved Lorentzian technique for evaluating resonance characteristics of the Earth-ionosphere cavity, *Atmos. Res.*, 91, 188–193
- Nakamura, T., M. Sekiguchi, Y. Hobara, M. Hayakawa (2010), A comparison of different source location methods for ELF transients by using the parent lightning discharges with known positions, *J. Geophys. Res.*, 115, A00E39, doi:10.1029/2009JA014992
- Navarro, E. A., A. Soriano, J. A. Morente, J. A. Portí (2007), A finite difference time domain model for the Titan ionosphere Schumann resonances, *Radio Sci.*, 42, RS2S04, doi:10.1029/2006RS003490
- Neubert, T., T. H. Allin, E. Blanc, T. Farges, C. Haldoupis, A. Mika, S. Soula, L. Knutsson, O. van der Velde, R. A. Marshall, U. S. Inan, G. Sátori, J. Bór, A. Hughes, A. Collier, S. Laursen, Ib. L. Rasmussen (2005), Co-ordinated observations of transient luminous events during the EuroSprite2003 campaign, *J. Atmos. Sol-Terr. Phys.*, 67, 807–820
- Nickolaenko, A. P. (1997), Modern aspects of Schumann resonance studies, *J. Atmos. Sol-Terr. Phys.*, 59, 806–816
- Nickolaenko, A. P., B. P. Besser, K. Schwingenschuh (2003), Model computations of Schumann resonance on Titan, *Planet. Space Sci.*, 51(13), 853–862
- Nickolaenko, A. P. and M. Hayakawa (2002), *Resonances in the Earth-Ionosphere Cavity*, Kluwer Academic Publishers, Dordrecht-Boston-London

- Nickolaenko, A. P., M. Hayakawa, Y. Hobara (1996), Temporal variations of the global lightning activity deduced from the Schumann resonance data, *J. Atmos. Terr. Phys.*, 58, 1699–1709
- Nickolaenko, A. P. and L. M. Rabinowicz (1982), On the possibility of existence of global electromagnetic resonances on the planets of Solar system, *Space Res.*, 20, 82–89
- Nickolaenko, A. P. and L. M. Rabinowicz (1987), On the applicability of extremely low frequency global resonances in the studies of lightning activity at Venus, *Space Res.*, 25, 301–308
- Nickolaenko, A. P. and L. M. Rabinowicz (1995) Study of the annual changes of global lightning distribution and frequency variations of the first Schumann resonance mode, *J. Atmos. Sol-Terr. Phys.*, 57(11), 1345–1348
- Nickolaenko, A. P., G. Satori, B. Zieger, L. M. Rabinowicz, L. G. Kudintseva (1998), Parameters of global thunderstorm activity deduced from the long-term Schumann resonance records, *J. Atmos. Sol-Terr. Phys.*, 60(3), 387–399
- Nickolaenko, A. P., M. Hayakawa, Y. Hobara (2010), Q-bursts: Natural ELF radio transients, *Surv. Geophys.*, 31, 409–425
- Ogawa, T., Y. Tanka, T. Miura, M. Yasuhara (1966), Observations of natural ELF electromagnetic noises by using the ball antennas, *J. Geomagn. Geoelectr.*, 18, 443–454
- Pasko, V. P., U. S. Inan, Y. N. Taranenko, T. F. Bell (1995), Heating, ionization and upward discharges in the mesosphere due to intense quasi-electrostatic thundercloud fields, *Geophys. Res. Lett.*, 22, 365–368
- Pasko, V. P., U. S. Inan, T. F. Bell, Y. N. Taranenko (1997), Sprites produced by quasi-electrostatic heating and ionization in the lower ionosphere, *J. Geophys. Res.*, 102, 4529–4561
- Pechony, O. and C. Price (2004), Schumann resonance parameters calculated with a partially uniform knee model on Earth, Venus, Mars, and Titan, *Radio Sci.*, 39(5), RS5007, doi:10.1029/2004RS003056
- Pechony, O., C. Price, A. P. Nickolaenko (2007), Relative importance of the day-night asymmetry in Schumann resonance amplitude records, *Radio Sci.*, 42, RS2S06, doi:10.1029/2006RS003456
- Polk, C. (1968), Relation of ELF noise and Schumann resonances to thunderstorm activity, in *Planetary Electrodynamics*, 2, 55–83, H. Volland, ed., CRC Press, Boca Ration, Florida
- Polk, C. and F. Fitchen (1962), Schumann resonances of the earth-ionosphere cavity – extremely low frequency reception at Kingston, R.I., *J. Res. NBS*, 66D, 313–318
- Price, C. (1993), Global surface temperatures and the atmospheric global circuit, *Geophys. Res. Lett.*, 20, 1363–1366
- Price, C., E. Greenberg, Y. Yair, G. Sátori, J. Bór, H. Fukunishi, M. Sato, P. Israelevich, M. Moalem, A. Devir, Z. Levin, J. H. Joseph, I. Mayo, B. Ziv, A. Sternlieb (2004), Ground-based detection of TLE-producing intense lightning during the MEIDEX mission on board the Space Shuttle Columbia, *Geophys. Res. Lett.*, 31, L20107, doi:10.1029/2004GL020711

- Price, C. and D. Rind (1990), The effect of global warming on lightning frequencies, in *Proceedings of the AMS 16<sup>th</sup> Conf. on Severe Local Storms Conf. on Atmos. Electr.*, Kananaskis Park, Alberta, Canada, 748–751
- Price, C. (2000), Evidence for a link between global lightning activity and upper tropospheric water vapor, *Nature*, 406, 290–293
- Price, C. and M. Asfur (2006), Can lightning observations be used as an indicator of upper-tropospheric water-vapor variability, *Bull. Am. Met. Soc.*, doi:10.1175/BAMS-87-3-xxx, in press
- Price, C., M. Asfur, W. Lyons, T. Nelson (2002), An improved ELF/VLF method for globally geolocating sprite-produced lightning, *Geophys. Res. Lett.*, 29(3), 1.1–1.4
- Price, C., E. Greenberg, Y. Yair, G. Sátori, J. Bór, H. Fukunishi, M. Sato, P. Israelevich, M. Moalem, A. Devir, Z. Levin, J. H. Joseph, I. Mayo, B. Ziv, A. Sternlieb (2004), Ground-based detection of TLE-producing intense lightning during the MEIDEX mission on board the Space Shuttle Columbia, *Geophys. Res. Lett.*, 31, L20107, doi:10.1029/2004GL020711
- Price, C. and A. Melnikov (2004), Diurnal, seasonal and inter-annual variations of the Schumann resonance parameters, *J. Atmos. Sol-Terr. Phys.*, 66(13–14), 1179
- Price, C. and V. Mushtak (2001), The impact of the August 27, 1998,  $\gamma$ -ray burst on the Schumann resonances, *J. Atmos. Sol-Terr. Phys.*, 63, 1043–1047
- Price, C. and D. Rind (1994), Possible implications of global climate change on global lightning distributions and frequencies, *J. Geophys. Res.*, 99, 10823–10831
- Raemer, H. R. (1961), On the extremely low frequency spectrum of the earth-ionosphere cavity response to electrical storms, *J. Geophys. Res.*, 66, 1580–1583
- Rafalsky, V. A., A. V. Shvets, M. Hayakawa (1995), One-site distance-finding technique for locating lightning discharges, *J. Atmos. Sol-Terr. Phys.*, 57(11), 1255–1261
- Reising, S. C., U. S. Inan, T. F. Bell, W. A. Lyons (1996), Evidence for continuing current in sprite-producing cloud-to-ground lightning, *Geophys. Res. Lett.*, 23, 3639–3642
- Renno, N. O., A. Wong, S. K. Atreya, I. de Pater, M. Roos-Serote (2003), Electrical discharges and broadband radio emission by Martian dust devils and dust storms, *Geophys. Res. Lett.*, 30(22), 2140
- Rind, D. (1998), Just add water vapor, *Science*, 28, 1152–1153
- Rind, D., E. W. Chiou, W. Chu, J. Larsen, S. Oltmans, J. Lerner, M. P. McCormick, L. McMaster (1991), Positive water vapor feedback in climate models confirmed by satellite data, *Nature*, 349, 500–502
- Roussel-Dupré, R. and A. V. Gurevich (1996), On runaway breakdown and upward propagating lightning, *J. Geophys. Res.*, 101, 2297–2311
- Rycroft, M. J. (1963), *Low frequency disturbances of natural origin of the electric and magnetic fields of the earth*, Ph.D. thesis, University of Cambridge
- Sato, M. and H. Fukunishi (2003), Global sprite occurrence locations and rates derived from triangulation of transient Schumann resonance events, *Geophys. Res. Lett.*, 30(16), 1859, doi:10.1029/2003GL017291

- Sato, M., H. Fukunishi, M. Kikuchi, H. Yamagishi, W. A. Lyons (2003), Validation of sprite-inducing cloud-to-ground lightning based on ELF observations at Syowa station in Antarctica, *J. Atmos. Sol-Terr. Phys.*, 65, 607–614
- Satori, G., J. Szendroi, J. Vero, (1996), Monitoring Schumann resonances—I. Methodology. *J. Atmos. Terr. Phy.*, 58, 1475–1481
- Sátori, G. and B. Zieger (1999), El Niño-related meridional oscillation of global lightning activity. *Geophys. Res. Lett.*, 26, 1365–1368
- Satori, G., E. R. Williams, I. Lemperger (2009), Variability of global lightning activity on the ENSO time scale, *Atmos. Res.*, 91, 500–507
- Satori, G., M. Neska, E. Williams, J. Szendroi (2007), Signatures of the day-night asymmetry of the Earth-ionosphere cavity in high time resolution Schumann resonance records, *Radio Sci.*, 42, RS2S10, doi:10.1029/2006RS003483
- Scarf, F. L. and C. T. Russell (1983), Lightning measurements from the Pioneer Venus Orbiter, *Geophys. Res. Lett.*, 10(12), 1192–1195
- Schmidt, C. T. (1993), Detection of distant lightning strikes from one location using Schumann resonances, M.Ph. thesis, Mich. Technol. Univ., Houghton
- Schumann, W. O. (1952a), Über die strahlungsgesetzen Eigenschwingungen einer leitenden Kugel, die von einer Luftsicht und einer Ionosphärenhülle umgeben ist, *Zeitschrift und Naturforschung*, 7a, 149–154
- Schumann, W. O. (1952b), Über die Dämpfung der elektromagnetischen Eigenschwingungen des Systems Erde – Luft – Ionosphäre, *Zeitschrift und Naturforschung*, 7a, 250–252
- Schumann, W. O. (1952c), Über die Ausbreitung sehr langer elektrischer Wellen um die Signale des Blitzes, *Nuovo Cimento*, 9, 1116–1138
- Schumann, W. O. and H. König (1954), Über die Beobachtung von Atmospherics bei geringsten Frequenzen, *Naturwiss.*, 41, 183–184
- Sentman, D. D. (1987), Magnetic elliptical polarization of Schumann resonances, *Radio Sci.*, 22, 595–606
- Sentman, D. D. (1990), Electrical conductivity of Jupiter's Shallow interior and the formation of a resonant planetary-ionosphere cavity, *ICARUS*, 88, 73–86
- Sentman, D. D. (1996), Observations of red sprites and blue jets, *Paper presented at 25th General Assembly, Union Radio Science International*, Lille, France, July 1996
- Sentman, D. D. and B. J. Fraser (1991), Simultaneous observation of Schumann resonances in California and Australia: evidence for intensity modulation by local height of the D region, *J. Geophys. Res.*, 96(9), 15973–15984
- Sentman, D. D. and E. M. Wescott (1993), Observations of upper atmosphere optical flashes recorded from an aircraft, *Geophys. Res. Lett.*, 20, 2857–2860
- Shvets, A. and M. Hayakawa (2011), Global lightning activity on the basis of inversions of natural ELF electromagnetic data observed at multiple stations around the world, *Surv. Geophys.*, 32, 705–732
- Shvets, A. V. (1999), Distance estimation to the world thunderstorm centers by measurement of the Schumann resonance background. *XXVI General Assembly URSI, University of Toronto*, Toronto, Ont., Canada, August 13–21, 1999, Abstracts, p. 297

- Shvets, A. V. (2001), A technique for reconstruction of global lightning distance profile from background Schumann resonance signal, *J. Atmos. Sol-Terr. Phys.*, 63, 1061–1074
- Shvets, A. V., M. Hayakawa, M. Sekiguchi, Y. Ando (2009), Reconstruction of the global lightning distribution from ELF electromagnetic background signals, *J. Atmos. Solar Terr. Phys.*, 71, 1405–1412
- Simões, F., et al. (2007), A new numerical model for the simulation of ELF wave propagation and the computation of eigenmodes in the atmosphere of Titan: Did Huygens observe any Schuman resonance? *Planet. Space Sci.*, 55, 1978–1989
- Simões, F., et al. (2008), Electromagnetic wave propagation in the surface-ionosphere cavity of Venus, *J. Geophys. Res.*, 113, E07007, doi:10.1029/2007JE003045
- Su, H. T., R. R. Hsu, A. B. C. Chen, Y. J. Lee, L. C. Lee (2002), Observation of sprites over the Asian continent and over oceans around Taiwan, *Geophys. Res. Lett.*, 29(4), 1044, doi:10.1029/2001GL013737
- Sukhorukov, A. I. (1991), On the Schumann resonances on Mars, *Planet. Space Sci.*, 39(12), 1673–1676
- Sun, D. Z. and I. M. Held (1996), A comparison of modeled and observed relationships between interannual variations of water vapor and temperature, *J. Clim.*, 9, 665–675
- Takahashi, Y., et al. (2010), Absolute optical energy of sprites and its relationship to charge moment of parent lightning discharge based on measurement by ISUAL/AP, *J. Geophys. Res.*, 115, A00E55, doi:10.1029/2009JA014814
- Taylor, W. W. L., F. L. Scarf, C. T. Russell, L. H. Brace (1979), Evidence for lightning on Venus, *Nature*, 279, 614–616
- Tesla, N. (1905), The transmission of electrical energy without wires as a means of furthering world peace, *Electrical World Engineer*, January 7, 21–24
- Tokano, T., G. J. Molina-Cuberos, H. Lammer, W. Stumptner (2001) Modeling of thunderclouds and lightning on Titan, *Planer. Space Sci.*, 49, 539–560
- Valdavia, J. A., G. Milikh, K. Papadopoulos (1997), Red sprites: Lightning as a fractal antenna, *Geophys. Res. Lett.*, 24(24), 3169–3172
- Volland, H. (1984), *Atmospheric Electrodynamics*, Springer-Verlag, Berlin, 205p.
- Wait, J. R. (1962), *Electromagnetic Waves in Stratified Media*, Pergamon Press
- Wait, J. R. (1974a), Historical background and introduction to the special issue on extremely low frequency (ELF) communication, *IEEE Trans. Commun.*, 22(4), 353–354
- Wait, J. R. (1977), Propagation of ELF electromagnetic waves and project Sanguine/Seafarer, *IEEE J. Oceanic Eng.*, 2(2), 161–172
- Williams, E. R. (1992), The Schumann resonance: a global tropical thermometer, *Science*, 256, 1184–1186
- Williams, E. R. (2001), Sprites, elves, and glow discharge tubes, *Physics Today* 41, 41–47
- Williams, E. R. (2005), Lightning and climate: a review, *Atmos. Res.*, 76, 272–287

- Williams, E., E. Downes, R. Boldi, W. Lyons, S. Heckman (2007a), Polarity asymmetry of sprite-producing lightning: A paradox?, *Radio Sci.*, 42, RS2S17, doi:10.1029/2006RS003488.
- Williams, E. R., V. C. Mushtak, R. Boldi, R. L. Dowden, Z.-I. Kawasaki (2007b), Sprite lightning heard round the world by Schumann resonance methods, *Radio Sci.*, 42, RS2S20, doi:10.1029/2006RS003498
- Wilson, C. T. R. (1924), The electric field of a thundercloud and some of its effects, *Proc. Phys. Soc. London*, 37, 32D–37D, doi:10.1088/1478-7814/37/1/314
- Yair, Y., C. Price, Z. Levin, J. Joseph, P. Israelevitch, A. Devir, M. Moalem, B. Ziv, M. Asfur (2003), Sprite observations from the space shuttle during the Mediterranean Israeli Dust Experiment (MEIDEX), *J. Atmos. Sol-Terr. Phys.*, 65, 635–642
- Yair, Y., G. Fischer, F. Simoes, N. Renno, P. Zarka (2008), Updated review of planetary atmospheric electricity, *Space Sci. Rev.*, 137, 29–49, doi:10.1007/s11214-008-9349-9
- Yamashita, M. (1967), Propagation of ELF radio waves to great distances below the unisotropic ionosphere, *J. Atmos. Terr. Phys.*, 29, 937–948
- Yamashita, M. (1968), The propagation characteristics of ELF radio waves to great distances below the horizontally stratified ionosphere, *J. Atmos. Terr. Phys.*, 30, 1943–1953
- Yang, H., V. P. Pasko, Y. Yair (2006), Three-dimensional finite difference time domain modeling of the Schumann resonance parameters on Titan, Venus, and Mars, *Radio Sci.*, 41, RS2S03, doi:10.1029/2005RS003431
- Yang, H., V. P. Pasko, G. Sátori (2009), Seasonal variations of global lightning activity extracted from Schumann resonances using a genetic algorithm method, *J. Geophys. Res.*, 114, D01103, doi:10.1029/2008JD009961
- Yano, M., Y. Ida, Y. Hobara, M. Hayakawa, A. P. Nickolaenko (2010), Reception of ELF transmitter signals at Moshiri, Japan, and their propagation characteristics, *Radio Sci.*, 45, RS1009, doi:10.1029/2009RS004224
- Yatsevich, E. I., A. V. Shvets, L. M. Rabinowicz, A. P. Nickolaenko, G. G. Belyaev, A. Yu. Schekotov (2005), Results of comparing Schumann resonance observations with a model of the single world thunderstorm center, *Izvestia Vuzov, Radiophysics*, 48(4), 283–298. English translation is published in *Radiophysics and Quantum Electronics*



---

## *Chapter 16*

# **Lightning effects in the mesosphere and ionosphere**

*M. Hayakawa<sup>1</sup>, Y. Hobara<sup>2</sup> and T. Suzuki<sup>3</sup>*

---

### **16.1 Introduction**

During over a century before the first scientific recordings in the 1990s, there were reports of visually observed lightning-like channels (see the monograph by Rakov and Uman (2003)). The first recording of luminous phenomena above thunderstorm cloud tops was serendipitously obtained in 1989 by Franz *et al.* (1990) while testing a new low-light video system. Since 1990 there has been considerable progress in identifying, characterizing and modelling the variety of luminous optical phenomena that occur in the clear air above thunderstorms.

Three general types of transient luminous events (TLEs) have been so far observed: (1) sprites (red sprites), (2) blue jets (and blue starters) and (3) elves. The locations and structure of those three types of TLEs are illustrated in Figure 16.1. Blue starters and blue jets propagate upward from the top of the cloud, generally at a height of 20 km or less up to an altitude of 40 km in the form of blue, cone-shaped structures as in Figure 16.1. Blue starters propagate upward less than 10 km, and jets up to 20 km. Blue starters and jets are probably variations of the same phenomena. Next, red sprites in Figure 16.1 are most spectacular luminous effects at the heights of 40~90 km. They often have faint bluish tendrils extending downward from 50 km or so to altitudes as low as 20 km. Red sprites exhibit a wide diversity of forms and features (e.g. carrots, columns, etc.) and generally occur in possible association with the large positive ground flashes as in Figure 16.1. Elves are the optical phenomena taking place in the lower ionosphere, which can spread laterally over 300 km. It is thought that these elves are due to lightning-induced electromagnetic effect. It appears from ground-based observations that TLEs occur over most regions of the globe (in temperate and tropical areas, over the ocean and over the land). To date TLEs have been successfully detected in North America, in

<sup>1</sup>The University of Electro-Communications (UEC), Advanced Wireless Communications Research Center, 1-5-1 Chofugaoka, Chofu Tokyo 182-8585, Japan

<sup>2</sup>UEC, Graduate School of Informatics and Engineering, Chofu Tokyo, Japan

<sup>3</sup>Japan Air Self-Defence Force, Fuchu Tokyo, Japan

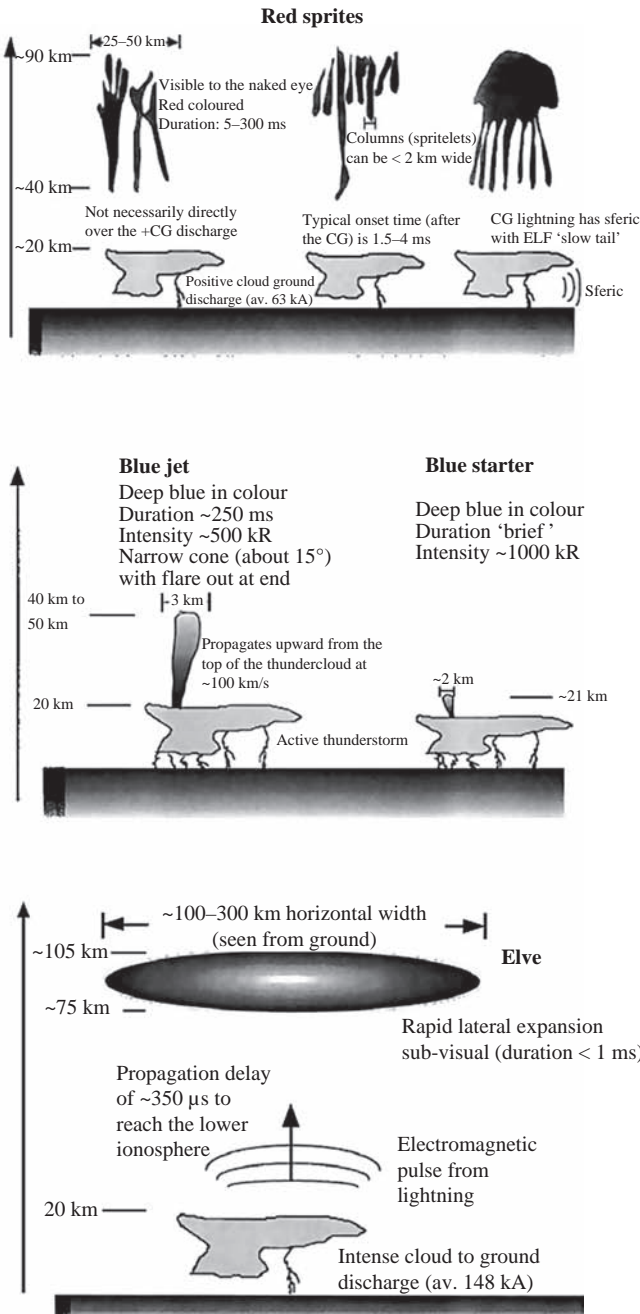


*Figure 16.1 Different types of TLEs including red sprites, blue jets and elves in association with a lightning discharge below [adapted from Rodger (1999)]*

the Caribbean region, in Australia, over winter storms in Japan, on the Asian continent, etc.

There have already been published several excellent reviews on these TLEs: e.g. Williams (2001), Rakov and Uman (2003), Pasko (2006), Lyons (2006), Rycroft (2006) and Williams and Yair (2006) for the observations on TLEs and their associated lightning discharges, and Rowland (1998), Sukhorukov and Stubbe (1998), Wescott *et al.* (1998a) and Pasko (2006) for the theories and modelling on different kinds of TLEs; please consult any of these for further detailed descriptions. Of course, as is easily imagined, each review has its own taste based on the interest and choice of its authors. In this chapter we try to pay more attention only to the fundamental parts of observations and theories of different TLEs. Finally, we would like to indicate several essentially important, but unsolved, problems of sprites. During this process, we want to emphasize the important role of Japanese winter sprites and the associated parent lightning in the general understanding of sprite problems.

## 16.2 General phenomenology of TLEs

### 16.2.1 Phenomenology of sprites

Sprites (colour is red, so that sometimes called red sprites) are large luminous discharges, which appear in the altitude range of ~40 to 90 km above large thunderstorms mainly following intense positive cloud-to-ground (CG) lightning discharges (Sentman *et al.*, 1995; Boccippio *et al.*, 1995). The duration of sprites is in a range from 5 to 300 ms and their optical emission intensity is up to 100 kR with the maximum value of 600 kR.

Various terms have been used to describe the diversity of forms of, and features within, sprites as observed primarily on standard frame rate (16.7 ms field), low-light-intensity video. A typical one is a ‘carrot’ sprite, which is characterized by a relatively bright ‘head’ region of red colour, with a red glow or wispy structures (‘hair’) that extend above the head upward to as high as 95 km, and bluish tendrils below the head often extending reaching cloud anvil tops near 20 km, as illustrated in Figure 16.1 (Sentman *et al.*, 1995). The spatial width of carrots is on the order of 25–50 km. An alternative fundamental form is the so-called ‘columniform’ (or simply column) sprites (Wescott *et al.*, 1998b), which are vertically oriented cylinders that do not show any tendrils or hair-like structures. The vertical length of these columniform sprites is about 10 km in height and their diameter is less than 1 km. They often tend to appear as a group.

Recent telescopic imaging of sprites at standard video rates revealed an amazing variety of generally vertical fine structure with transverse spatial scales ranging from tens to a few hundreds of metres (Gerken *et al.*, 2000; Gerken and Inan, 2003). First high-speed (1 ms) telescopic imaging of sprites has been reported indicating that streamer-like formations in sprites rarely persist for more than 1–2 ms (Marshall and Inan, 2005). It has also recently been demonstrated that sprites often exhibit a sharp altitude transition between the upper diffuse and the lower

highly structured regions (Stenbaek-Nielsen *et al.*, 2000). Many sprites are observed with an amorphous diffuse glow at their tops, the so-called sprite halo (Barrington-Leigh *et al.*, 2001).

The remote sensing of sprites-producing lightning discharges using ELF (extremely low frequency) waves and by utilizing a known charge moment change threshold for sprite initiation provide an estimate of the global occurrence rate of sprites  $\sim 720$  events/day on average (Sato and Fukunishi, 2003). However, it is known that sprites are not always associated with ELF transients (Price *et al.*, 2004), and estimates by other authors indicate that 80% of ELF signatures produced by positive lightning are related to sprites (Füllekrug and Reising, 1998), but only 20% of all sprites are associated with ELF transients, which leads to an estimate of  $\sim 5$  sprite events/min or 7200 events/day globally (Füllekrug and Constable, 2000).

Spectral measurements of sprites show that the first positive band of nitrogen produces the observed red sprites (Mende *et al.*, 1995; Hampton *et al.*, 1996).

The sprites are known to be closely associated with large-scale thunderstorms (so-called mesoscale convective systems (MCSs)) (Lyons, 2006), though they are infrequently triggered by exceptionally small thunderstorms (Hayakawa *et al.*, 2004, 2005). Sprites tend not to occur until the storm has approached its mature stage and developed a considerable stratiform precipitation region. The MCS stratiform area usually reaches a minimum of  $(10\text{--}20) \times 10^3 \text{ km}^2$  before significant sprite activity can be expected.

Peak current of the sprite parent lightning is only a poor indicator of the sprite potential (Lyons, 2006), but another quantity, so-called charge moment change ( $Q_{ds}$ ), is found to be a good indicator of sprite initiation (Huang *et al.*, 1999; Hobara *et al.*, 2001; Williams *et al.*, 2007), which can be estimated experimentally from the ELF observations. At 600 C km, there is a 10% of sprite initiation, reaching to 90% by 1000 C km. Also, there seems to exist a lowest threshold of 200~300 C km for sprite initiation for the Japanese winter sprites on the Japan Sea side (Hayakawa *et al.*, 2004).

### *16.2.2 Phenomenology of blue jets*

Blue jets develop upwards from cloud tops to terminal altitude of about 40 km at speeds of the order of 100 km/s and are characterized from blue jets by a blue conical (with angular cone of  $\sim 15^\circ$ ) shape (Wescott *et al.*, 1995, 1998a). Blue starters can be distinguished from blue jets by a much lower terminal altitude. They propagate upward from the cloud top (17–18 km) to a maximum altitude of 25.5 km (Wescott *et al.*, 1996, 2001). Several ground-based video recordings of blue jets, which also electrically connect a thundercloud with the lower ionosphere, have recently been reported (Pasko *et al.*, 2002; Su *et al.*, 2003). This type of events is now termed ‘gigantic jets’ (Su *et al.*, 2003). Recent photographic observations of blue jets at close range have clearly shown the small-scale streamer structure of blue jets similar to that reported for sprites (Wescott *et al.*, 2001; Pasko *et al.*, 2002).

The duration of blue jets is considerably longer than that of sprites, and is of the order of 250 ms. Their intensity is also larger than that of sprites, which is of the

order of 500 kR. Blue starters are considered to be the initial-phase phenomena of blue jets.

Unfortunately there have been published very few papers on the detailed characteristics of blue jets, but an early report (Wescott *et al.*, 1995) indicated that 56 blue jets were observed during a period of 22 min, but only 4 sprites were detected. Unlike the sprites that are predominantly related with positive lightning discharge, it seems that blue jets have no definite polarity dependence.

### 16.2.3 Phenomenology of elves

Boeck *et al.* (1992) reported video observations from the space shuttle of a case of transient brightening in the airglow layer over a tropical oceanic thunderstorm, and the region of enhanced luminosity is 10–20 km thick at the height of ~95 km and about 500 km in the apparent horizontal extent. Such transient luminosity effects were later named ‘elves’. The first time-resolved and spatially resolved documentation of the phenomena was reported by Fukunishi *et al.* (1996), who employed high-speed multi-channel photometers and image-intensified CCD cameras because elves are difficult to detect using conventional video systems as they persist only for a single field in such video systems.

These optical emissions named ‘elves’ (emissions of light and VLF perturbations due to EMP sources) are diffuse optical flashes with a duration of less than 1 ms, occurring at 75–105 km altitude just after the onset of CG lightning discharges, but preceding the onset of sprites. An elve is a rapidly expanding toroidal disc and the expanded disc can attain a diameter of 400 km or even larger. The time lag between a return stroke and the onset of luminosity of the elve is that of the propagation speed of light. The luminosity of elves is found to range from 1 to 10 MR, suggesting that the lower ionosphere is significantly heated by elves.

Subsequent measurements of elves (Barrington-Leigh and Inan, 1999; Barrington-Leigh *et al.*, 2001) showed that both positive and negative return strokes were observed to produce elves, unlike the case of sprites mainly induced by positive lightning discharges. Elves seem to be associated with a significant percentage of negative strokes. Typically these have higher peak currents than those for sprites, indicative of the more impulsive nature of the CG lightning source. Typical charge moment changes of parent lightning of elves seem to approach those for sprites, though data are required to determine if any threshold may be systematically lower or not.

## 16.3 General consideration of physical mechanisms and modellings

This section is mainly based on the excellent review by Rowland (1998). Three sources of field energy have been identified that can transmit power to these upper atmosphere phenomena like TLEs. There is an electrostatic field from the initial charges in the thunderstorm prior to the discharge. Then, there is the electromagnetic pulse (EMP) from the propagation of the return stroke as an electromagnetic antenna

and the quasi-electrostatic (QE) fields due to the currents moving charges following the return stroke. To connect this energy to the neutral atmosphere, two fundamental mechanisms have been proposed. The first is thermal heating by low energy (less than a few eV) electrons, and this is expanded later to include thermal breakdown. The other mechanism is through accelerating MeV electrons driving a runaway breakdown. The basic physics underlying the different models proposed so far falls into these categories. Table 16.1 is the summary on the general consensus of the possible mechanisms for different TLEs like elves, sprites and jets.

### 16.3.1 High-altitude electric fields induced by a lightning discharge

The fundamental question related to TLEs lies in the estimation of electric field strengths by a lightning storm in the higher altitudes. A lightning storm can generate electric fields above the thunderstorm during the slow build-up of charges before the discharge, through the time-varying currents associated with the return stroke, and by the redistribution of charge by the currents. The return stroke drives the radiation fields while the continuing flow of the current forms the QE, near-field radiation.

The initial charges in the cloud build up over time scales of seconds or longer. Because of this, the atmospheric conductivity shields these charges so that there are only strong fields inside or near the cloud. The EMP has a much shorter time scale (0.1 ms) and the conductivity is not large enough to affect the fields until they reach the ionosphere. The QE fields change on the time scale of milliseconds so that they are weakly shielded by the atmosphere.

The return stroke can be modelled as a uniform line charge and current moving along  $z$  (vertical axis) at a constant speed  $v = \beta c$  ( $c$ , velocity of the light),

$$I(\rho, z, t) = \beta c Q_z(\rho, z, t) = I_0 \delta(\rho) H(z) H(t - z/\beta c) \quad (16.1)$$

Here  $I$  is the current in the return stroke ( $I_0$ , amplitude),  $\beta = v/c$  is the normalized velocity,  $Q_z$  is the distributed charge,  $\rho$  measures distance from the discharge axis,  $\delta$  is the Dirac delta function, and  $H$  is the Heaviside function. To conserve charge, an additional charge is placed at the origin:

$$Q(\rho, z, t) = -I_0 \delta(\rho) \delta(z) H(t) \quad (16.2)$$

*Table 16.1 The different combinations of electric field and possible mechanisms for the general explanation of sprites, elves and jets*

	Thermal	Runaway
EMP	Elves	
QE field	Sprites	Sprites, blue jets
Initial cloud charge	Blue jets	

If the return stroke propagates at a normalized speed of  $\beta = 0.5$ , it takes  $\tau_p = 70 \mu\text{s}$  to travel a tortuous channel of 10 km long. This time  $\tau_p$  determines the typical duration of the EMP that is emitted by the return stroke. This is seen in the observed frequency spectrum that drops off above 10 kHz.

### 16.3.1.1 Electromagnetic pulse

By using (16.1) and (16.2), we can estimate the corresponding vector and scalar potentials, which enable us to obtain the electromagnetic fields (electric and magnetic fields). In the far (radiation) field the electric field  $E$  is transverse (Le Vine and Willet, 1992; Fernsler and Rowland, 1996), where  $\theta$  is the angle from the discharge axis and  $r = (\rho^2 + z^2)^{1/2}$  is the distance from the discharge origin.

$$E_\theta = \frac{\beta I_0}{rc} \frac{\sin \theta}{1 - \beta \cos \theta} \quad (16.3)$$

The model has a constant  $\partial I / \partial t$ , so that  $E_\theta$  has a constant amplitude during the pulse time  $\tau_p$ . The field is found to be no longer than due to a conventional dipole (for which  $\beta = 0$ ).

We must also include the image currents and charges, and can treat the Earth as a perfect conductor. For a vertical discharge (negative-to-ground) the return stroke propagates upward from the ground, and consequently the image ground field can be obtained by letting  $I_0 \rightarrow -I_0$  and  $\theta \rightarrow \theta - \pi$  in (16.3). The sum of the source and image fields gives the total radiation field as follows (Krider, 1992):

$$E_\theta = \frac{2\beta I_0}{rc} \frac{\sin \theta}{1 - \beta^2 \cos^2 \theta} \quad (16.4)$$

$$= \frac{2\beta I_0}{rc} \frac{\sin 2\theta}{1 - \beta^2 \cos^2 \theta} \quad (16.5)$$

where  $z = r \cos \theta$ . For a constant  $r$  from the origin (with  $\beta < 0.7$ ), the field peaks on the Earth's surface at  $\theta = \pi/2$ . For a constant altitude  $z = h$ , the field peaks instead at

$$\theta_{max} = 0.5 \cos^{-1} \left[ \frac{\beta^2}{2 - \beta^2} \right] \quad (16.6)$$

with respect to the vertical. For  $\beta = 0$ , which is a standard dipole,  $\theta_{max} = 45^\circ$ . For  $\beta = 0.5$ ,  $\theta_{max} = 40^\circ$ . For a vertical discharge, the EMP will be maximum in a ring around the discharge. The radius of the ring will be roughly equal to  $h$ , though relativistic effects will tend to reduce the radius. The maximum field intensity will be given by

$$E_{max}(h) = 30 \frac{\beta \gamma I_0 \text{ (kA)}}{h \text{ (km)}} \quad (16.7)$$

where  $\gamma = (1 - \beta^2)^{-1/2}$  is the relativistic Lorentz factor and  $E$  is given in the unit of V/m. The field has a null above the discharge. In these computations we have thus far ignored the interaction of the EMP with the ionosphere (such as reflection).

For a horizontal discharge, the current and the EMP are rotated by  $90^\circ$ . The ground image current flows in the opposite direction so that for low altitude discharges (i.e.  $h_d \ll z_d/\beta$ , where  $h_d$  is the height of the discharge and  $z_d$  is its length), the two fields approximately cancel. If the discharge height is large,  $h_d > z_d/\beta$ , the two fields separate. For the vertical discharge the ground image charge doubles the strength, while for the horizontal case the duration is doubled. For an observer at a height  $h = h_d + r \sin \theta$  above the charge, the field peaks at an angle

$$\theta_{max} = \cos^{-1} \left[ \frac{\beta\gamma}{\gamma + 1} \right] \quad (16.8)$$

with respect to the horizontal. For a simple dipole, the maximum field is centred above the discharge. For  $\beta = 0.5$ , the peak is moved by  $15^\circ$ . At  $h = 80$  km, this is a 20 km displacement. The first peak is given by

$$E_{max} = \left[ \frac{\gamma}{\gamma + 1} \right] \frac{2\beta I_0}{(h - h_d)c} \quad (16.9)$$

The second negative pulse has a maximum given by (16.9) with  $(h - h_d)$  replaced by  $(h + h_d)$ .

We have discussed the simplest case, either a vertical or a horizontal discharge and its associated EMP fields. However, the real situation is expected to be much more complex than these simple geometries. Kudintseva *et al.* (2010) have computed the space-time distribution of the pulsed electric field in the middle atmosphere above a positive gamma-shaped lightning stroke commonly observed often in the sprite situation. The channel of such a discharge contains a vertical and a horizontal section, and they have included the reflections from the ground and ionosphere, as well. The obtained waveform is found to resemble the so-called M component of the lightning. The non-stationary fine structure appears in the spatial distribution of electric field, which persists for 2 ms or even more and exceeds the runaway electron threshold.

### 16.3.1.2 Quasi-electrostatic fields

The current associated with the return stroke will build charge differences inside the thunderstorm or between the cloud and the ground. If the current is large enough and continues long enough, the QE fields can become stronger than the EMP field.

In the absence of shielding, the QE field from a vertical current is given by  $\mathbf{E} = -\nabla\phi$ , where

$$\phi = I_0 t \left[ \frac{1}{\sqrt{\rho^2 + (z - z_d)}} + \frac{1}{\sqrt{\rho^2 + z^2}} \right] \quad (16.10)$$

This can be reduced to

$$\phi = \frac{Q(t)z_d}{r^2} \cos \theta \quad (16.11)$$

for discharge lengths  $z_d \ll r = \sqrt{(\rho^2 + z^2)}$ . Here  $Q(t) = I_0 t$  is the charge transferred, and time retardation is neglected because of the long charging time. In this case the far fields are the dipole fields.

$$E_\rho = \frac{2Q(t)z_d}{r^3} \cos \theta \quad (16.12)$$

and

$$E_\theta = \frac{Q(t)z_d}{r^3} \sin \theta \quad (16.13)$$

The strongest fields are directly above the current channel and are vertical. For a vertical discharge, the EMP is weakest above the discharge, where the QE field is strongest above the discharge. The ground image charges double the field strength. For a horizontal current, the ground image charges produce a pair of opposing dipoles (a quadrupole) that reduces the far fields. If  $z_d > h$ , the pair will be separated and this cancellation will be reduced. This will form two vertical-discharge QE fields of equal but opposite strength at each end of the horizontal current channel.

For the EMP, the field strength is determined by  $\beta I_0$ , while it is  $Qz_d$  for the QE field (this will be called later charge moment, Qds). Figure 16.2 illustrates the EMP and QE fields from computer simulations (Rowland *et al.*, 1996) for (1) a horizontal and (2) a vertical discharge. This computation used a simpler model of the return stroke as a spatially uniform, time-varying line of current so that  $\beta = 0$ . In this figure  $z$  is the vertical direction and  $x$  the horizontal direction. The discharge is centred at  $x = 0$  and is 6 km long. The figure shows the fields 300  $\mu$ s following the start of the discharge. The EMP is a dipole ring propagating from the discharge. For the horizontal discharge, the EMP is strongest above the discharge. On the other hand, for the vertical case of common use, the EMP has a null above the discharge. The QE fields are the spikes located near the discharge. For the vertical case, the QE fields are stronger and are directly above the discharge.

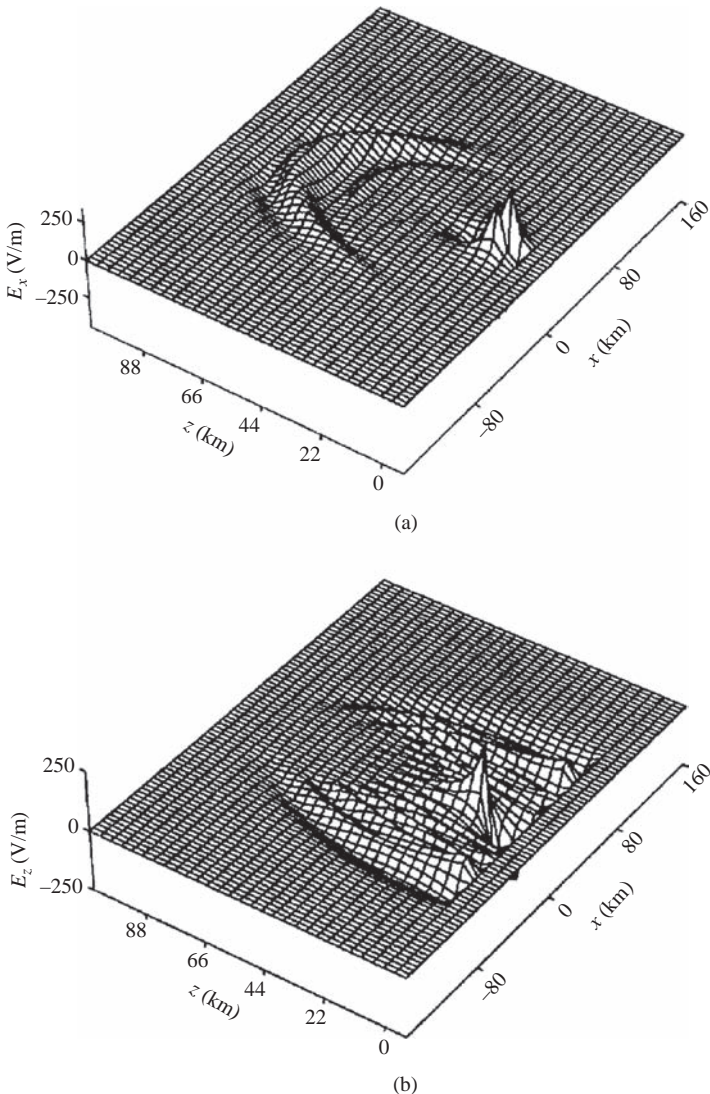


*Figure 16.2* Computer simulation results on the EMP and QE fields.

(a) A horizontal and (b) a vertical discharge. The large ring is due to the EMP fields, and the QE field dominates near the discharge ( $x = 0$ ) [after Rowland (1998)]

### 16.3.2 Heating of the ionosphere and neutral atmosphere

The electric fields accelerate the ambient electrons in the atmosphere. In this section we review how these electrons can excite the neutral atmosphere, leading to the generation of TLEs. If the electrons are sufficiently accelerated, breakdown can occur, increasing the ambient plasma density and optical emissions. Two processes

have been proposed to explain the heating. Both involve collisions between accelerated electrons to energies where they can collisionally excite or ionize the neutrals while the bulk of the electrons remains at a few eV. Gurevich *et al.* (1992) and Roussel-Dupré *et al.* (1994) developed a model of runaway breakdown for triggering lightning discharges. This method starts with a high-energy electron in the runaway regime and accelerates it to MeV energies. If this electron generates more runaway electrons when it collides with a neutral, then the number of runaways can grow spatially, and then breakdown is possible.

The collision between an electron and an atom changes with electron incident energy. When the electron velocity is low such that it has less than the excitation energy of the atom, the collision will be elastic. The electron will see a hard sphere and the collision cross-section drops, increasing its velocity. There can be an exchange of energy between the free electrons and the bound atomic electrons. As the velocity ( $v$ ) goes up, the time of the interaction goes as  $v^{-1}$ . The maximum energy loss  $\sim (\Delta v)^2 \sim [(Et)^2 \sim [(q/b^2)(b/v)]^2 \sim (q/bv)^2]$ , where  $\Delta v$  is the change in velocity,  $E$  is the transverse electric field,  $t$  is the interaction time,  $q$  is the electron charge and  $b$  is the distance of closest approach. So, as the electron is accelerated, the cross-section drops and the mean free path goes up. If the field is strong enough so that the electron gains more energy between collisions than it loses, the electron can be continuously accelerated and runaway occurs. At higher energies (>MeV), the cross-section increases due to relativistic focusing of the transverse fields and because the particle can penetrate closer to the atom allowing large scattering. A good review of runaways and references to the original literature is provided in Jackson (1975).

The models use several different approaches to calculate the thermal heating and ionization. Presently, the models use a Boltzmann code or experimental swarm data to determine the heating and ionization, and to calculate the airglow emissions.

## 16.4 Physical mechanism of sprites

### 16.4.1 Thermal ionization and QE mechanism

The possibility of large-scale gas discharge events above thunderclouds, which we currently know as sprite phenomenon, was first predicted in 1925 by the Nobel Prize winner C. T. R. Wilson (Wilson, 1925). He first recognized that the relation between the thundercloud electric field, which decreases with altitude  $r$  as  $\sim r^{-3}$ , as estimated in (16.12) and (16.13) and shown in Figure 16.3, and the critical breakdown field  $E_k$ , which falls more rapidly (being proportional to the exponentially decreasing atmospheric density), leads to the result that ‘there will be a height above which the electric field intensity due to the cloud exceeds the sparking limit’ (Wilson, 1925). It should be noted that due to the finite atmospheric conductivity above thunderclouds the dipole field configuration shown in Figure 16.3 is realized at mesospheric altitudes only during very transient time periods  $\sim 1$  to 10 ms, following intense lightning discharges, in part defining similarly transient nature of the observed sprite phenomenon (e.g. Pasko *et al.* (1997) and references therein).

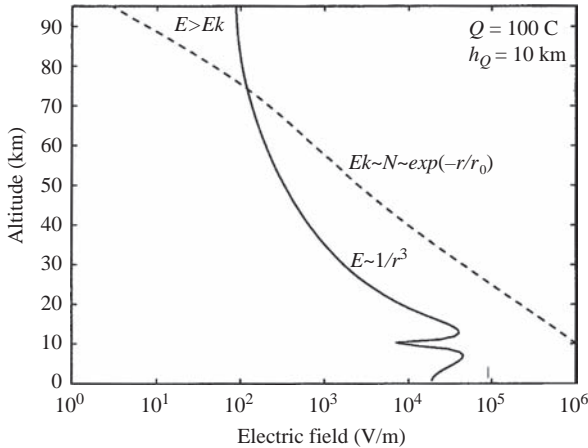


Figure 16.3 Physical mechanism of sprites by Wilson (1925) [after Pasko (2006)]

The mechanism of the penetration of the thundercloud electric fields to the higher-altitude regions is illustrated in Figure 16.4, which is already discussed in Section 16.3.1.2. This QE mechanism was initially proposed by Pasko *et al.* (1996), and is presently well accepted. As the thundercloud charges build up slowly before a lightning discharge, high-altitude regions are shielded from the QE fields of the thundercloud charges by the space charge induced in the conducting atmosphere at the lower altitudes. The appearance of this shielding charge is a consequence of the finite vertical conductivity gradient of the atmosphere above the thundercloud. When one of the thundercloud charges (e.g. the positive one as shown in Figure 16.4) is quickly removed by a lightning discharge, the remaining charges of opposite sign above the thundercloud produce a large QE field that appears at all altitudes above the thundercloud, and endures for a time equal to approximately the local relaxation time  $\tau_\sigma$  ( $\tau_\sigma = \varepsilon_0/\sigma$ , where  $\sigma$  is the local conductivity and  $\varepsilon_0$  is the permittivity of free space) at each altitude. These temporarily existing electric fields lead to the heating of ambient electrons and the generation of ionization changes and optical emissions known as sprite phenomena. Figure 16.5 illustrates the above-discussed scenario by showing model calculations of the vertical component of the electric field at altitudes 50, 60, 70 and 80 km directly above a positive lightning discharge removing 200 C of charge from altitude 10 km in 1 ms (Pasko *et al.*, 1997). During a very transient time period  $\sim 1$  ms, mostly defined by atmospheric conductivity profile, the electric field can reach values on the order of the critical breakdown threshold field  $E_k$  at mesospheric/lower ionospheric altitudes. The QE approximation employed here is valid for relatively slow source variations with time scales  $> 0.5$  ms (Pasko *et al.*, 1999).

It should be emphasized that the simplified schematics shown in Figure 16.4 is used to discuss the physical concept of penetration of large electric field transients to mesospheric altitudes and by no means reflects the complexity of charge

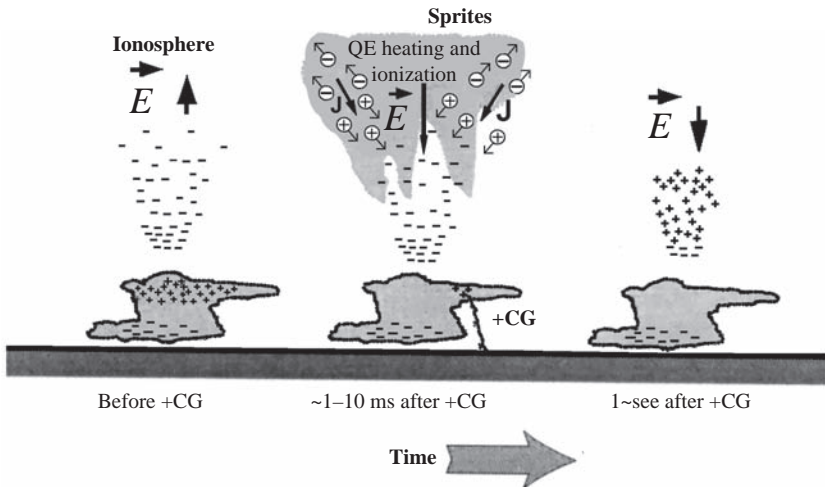


Figure 16.4 Illustration of the mechanism of penetration of large electric fields to mesospheric altitude [after Pasko *et al.*, 1997]

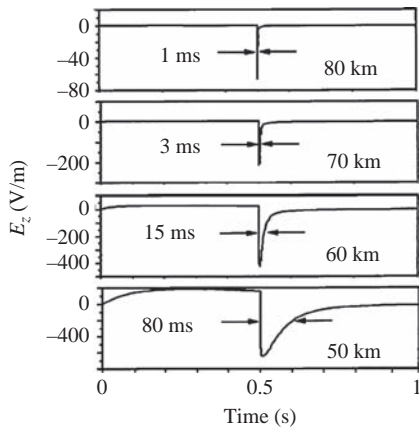


Figure 16.5 Time dynamics of the vertical component of the electric field at selected altitudes directly above a positive CG lightning discharge [after Pasko *et al.*, 1997]

distributions in the thundercloud, which sometimes involve up to six charge layers in the vertical direction (Marshall and Rust, 1993; Shepherd *et al.*, 1996), each of the charge centres can be viewed as generating its own polarization charge in and above the thundercloud, and the resultant configuration of the electric field and charge density can be obtained by using the principle of superposition. This consideration is helpful in visualization of the fact that the electric field appearing at

mesospheric altitudes after the charge removal by CG lightning discharge is defined mostly by the absolute value and altitude of the removed charge and is essentially independent of the complexity of the charge configuration in the cloud. The charge removal can also be viewed as the ‘placement’ of an identical charge of opposite sign. The initial field above the cloud is simply the free space field due to the ‘newly placed’ charge and its image in the ground, which is assumed to be perfectly conducting. The most recent observations indicate that most of the charge responsible for production of sprites can be lowered from relatively low altitudes 2–5 km, with an average height 4.1 km for one particular storm studied in Lyons *et al.* (2003). The charge moment change  $Qh_Q$  (i.e. charge removed by lightning  $Q$  times the altitude from which it was removed  $h_Q$ ) represents the key parameter that is used in the current sprite literature to measure the strength of lightning in terms of sprite production potential (Cummer *et al.*, 1998; Hu *et al.*, 2002; Cummer, 2003). One of the major unsolved problems in current sprite research, which is also directly evident from Figure 16.3, depicting the field created by a charge moment  $Qh_Q = 1000$  C km, is the observed initiation of sprites at altitudes 70–80 km by very weak lightning discharges with charge moment changes as small as 120 C km (Hu *et al.* (2002) and references therein). Several theories have been advanced to explain these observations, which include localized inhomogeneities created by small conducting particles of meteoric origin (Zabotin and Wright, 2001), the formation of upwardly concave ionization regions near the lower ionospheric boundary associated with sprite halos (Barrington-Leigh *et al.*, 2001), and so on. The problem of initiation of sprite streamers in low applied electric fields is one of unsolved problems in current TLE research (Pasko, 2006).

It is considered that this QE theory has been successful in explaining the general characteristics of sprites (e.g. altitude range, time delay of a few milliseconds from the onset of a lightning discharge, occurrence of a sprite above the thunderstorm, etc.). However, the sprite morphology and sprite altitude structure in particular, appear to be quite complex, and will be discussed later in Section 16.6.

#### *16.4.2 Runaway mechanism*

The general idea of breakdown process that starts with relativistic runaway electrons has been already described in Section 16.3.2, and it has been applied also to sprites. Early review on this mechanism was provided by Rowland (1998).

We now consider further the issue of conventional breakdown in the previous section versus breakdown initiated by runaway electrons. Pasko *et al.* (1997) reviewed the available experimental data on sprites and presented a detailed update of their QE model. They did allow that both the conventional breakdown mechanism and the runaway mechanism might operate simultaneously in sprite formation.

Yukhimuk *et al.* (1998) reviewed the runaway electron mechanism of sprite production, which they claim is the only reasonable mechanism for the generation of blue tendrils. They assumed that a relatively large positive charge is removed from the cloud top producing a QE electric field above the cloud. Energetic

electrons, in the MeV range, from cosmic ray interactions with the atmosphere are accelerated in this field producing ions and additional electrons as a result of collisions. If the electric field is strong enough, the number of high-energy electrons grows exponentially, creating a relativistic electron beam with a mean energy of the order of 1 MeV and runaway breakdown. The relativistic electron beam in turn produces secondary electrons of low energy, of order 1 eV, whose population also grows exponentially in time and whose mean energy, in the eV range, is determined by the local electric field and the rate of collision of these electrons with air molecules. The secondaries behave in a mode similar to the conventional breakdown discussed earlier. Yukhimuk *et al.* (1998) assumed that a positive cloud charge of 150–200 C at about 12 km altitude is removed in a time between 1 and 10 ms. Their simulations suggest that optical emissions from red sprites consist of two components: (1) a short-term emission (0.3–2 ms) visible at altitude from 40 to 77 km with significant blue radiation near the base of the emission region, this radiation being due to both runaway electrons and secondary electrons at all altitudes but the lower-altitude blue emissions being due primarily to the electron beam dissipation and (2) a long-term emission (2–10 ms), visible at altitudes above 66 km and primarily red, due to the secondary electrons.

Roussel-Dupré *et al.* (1998) presented a similar runaway-electron model for sprite production that starts with 200 C of positive charge neutralized at 11.5 km altitude. They found blue emission from 40 to 50 km and red from 50 to 77 km. Radio frequency pulses of 300 µs duration and 20–75 V/m amplitude are predicted by the model to occur 50 km from the sprite at 80 km altitude. They suggested that these pulses, produced as a result of sprite formation, may be responsible for elves and in any case should be sufficient to cause breakdown and heating of the lower ionosphere, all, of course, assuming that the runaway model is correct. Roussel-Dupré *et al.* stated that their sprite simulations yielded results in good agreement with both the amplitude and temporal signatures of the measured gamma- and X-ray fluxes above 40 keV of Fishman *et al.* (1994).

The model of runaway-electron effects in the region between cloud tops and the ionosphere published through 1998 (Lehtinen *et al.*, 1997; Taranenko and Roussel-Dupré, 1996; Yukhimuk *et al.*, 1998; Roussel-Dupré *et al.*, 1998) used the results of the runaway avalanche model of Roussel-Dupré *et al.* (1994), which has been found to contain errors (Symbalisty *et al.*, 1998). Apparently, more adequate calculations that do not contain these errors have been published by Yukhimuk *et al.* (1999) and Lehtinen *et al.* (1999). Yukhimuk *et al.* (1999) stated that the new calculations of the temporal evolution of sprite optical emissions are in better agreement with ground-based optical observations than the earlier calculations. In particular, the maximum duration of the detectable optical emissions in the new studies has a value greater than one TV camera field, 16.7 ms, whereas before it was less.

Characteristics of the electron runaway process in air that may be applicable to the sprite models are found in the work of Gurevich *et al.* (1992), Roussel-Dupré *et al.* (1994), Roussel-Dupré and Gurevich (1996) and Taranenko and Roussel-Dupré (1996), although as noted above, there are errors in some of this work.

In conclusion, the relative importance of runaway breakdown mechanism and the conventional breakdown in the previous section requires further future studies.

## 16.5 Elves and sprites

Most of the observed features of elves are found to be consistent with models in which the optical emission is produced as a result of the heating of electrons in the lower ionosphere by the EMP from lightning discharges (Nickolaenko and Hayakawa, 1995; Inan *et al.*, 1996). Optical emissions and significant changes in levels of ionization result from the acceleration of electrons by the electric radiation field associated with lightning as discussed in Section 16.3.1.

Fernsler and Rowland (1996) studied the formation of both elves and sprites based on a theory and simulations in which the model was fully electromagnetic, and the lightning discharge was accurately modelled with a moving line of charge. They were successful in identifying elves with the EMP breakdown. Based upon their analytic model, they calculate a minimum current for EMP breakdown by a vertical discharge (50 kA) and a horizontal discharge (30 kA). These thresholds are in good agreement with earlier simulation results (Rowland *et al.*, 1996), and for the QE breakdown, the minimum charge moment change was 150–300 C km. The charge moment ( $Qz_d$ ) is the product of the thundercloud charge and the separation between the charges ( $z_d$ ), and it is this product that determines the strength of the QE field (16.12 and 16.13). Therefore, the height of the upper charge is just as important as  $Q$  for determining the QE field as in Section 16.3.1.2. As we have noted, some of the differences between different QE models are due to the upper charge being at different altitudes. Because the velocity of the return stroke can be greater than  $0.5c$ , relativistic effects modify the EMP radiation pattern and the shape of the elves as shown in Section 16.3.1.1. For vertical discharges, the ring diameter becomes smaller, going from 90 km down to 50 km, while the maximum ionization is shifted from directly overhead by 20–50 km for horizontal discharges. Fernsler and Rowland (1996) also set a vertical range for elves from 70 to 95 km. The ionospheric conductivity limits sprites to a maximum altitude of 80–85 km, which is also the altitude for the minimum dipole strength for breakdown.

At lower altitudes, much larger values of  $Qz_d$  appear to be needed. Fernsler and Rowland (1996) pointed out that a field enhancement could allow the sprite to move to lower altitudes with a smaller  $Qz_d$ . The sprite itself will become narrower as it goes to lower altitudes. It can then split further into narrow branching tendrils that allow even further enhancement of the field for a given  $Qz_d$ . Experimentally, this enhancement has been measured in the range of 10–30. With no enhancement to reach breakdown at 50 km requires 8000 C km, but with a factor of 10 enhancement this is reduced to 800 C km.

Fernsler and Rowland (1996) showed the first simulations forming both elves and sprites. In agreement with the theoretical model, the elves are formed first due to the EMP. As the current continues, a sprite is formed a few km lower than the elves and then moves to lower altitudes.

Cho and Rycroft (1998) compared simulations from an electrostatic (ES) and an electromagnetic (EM) two-dimensional code. The breakdown model is thermal. The ionization, collision and optical emission rates are based upon experimental data, for which plots are provided. They showed that the EM code produced both the elves and the sprite, while the ES code produced only the sprite. They looked at the time-dependent  $E$  fields, electron density and optical emission. The code is written in the cylindrical coordinates ( $\rho, z$ ), but they converted the emissions to ( $x, y$ ) geometry and time averaged over 16 ms for comparison with the video observations. They studied how the pulse shape and the location of the discharge affected the optical emissions. As shown by Fernsler and Rowland (1996), moving the top charge to higher altitudes increases the electric field and hence the ionization and the emissions from the sprite. They showed that keeping  $Q$  the same but shortening the discharge led to higher emissions that were dominated by the elves. For the longest pulse, the sprite dominated. By shortening the discharge time while keeping  $Q$  the same,  $\beta I$  is increased. This enhances the EMP field, which in turn enhances the elves. Reducing  $\beta I$  but keeping  $Qz_d$  constant means that the sprite, which depends upon  $Qz_d$ , will start to dominate.

For the one discharge case where they show the electron density, the elves showed an increase in electron density of roughly 100 above ambient at 80 km. They used the same electron density as the night-time model used by Rowland *et al.* (1996). The pulse shapes are different, which, especially because of reflection, can significantly change by (<2) the number of 3-foldings. The maximum ionization shows very good agreement with the values of Rowland *et al.* (1996), not the lower values of Sukhorukov *et al.* (1996).

### 16.5.1 Blue jets

Fernsler and Rowland (1996) noted that blue jets could be upward travelling examples of the streamers and leaders that normally are observed below lightning storms. These streamers propagate through the same field enhancement process used to model the sprites and sprite tendrils. They pointed out that the observed velocity was consistent and that the radial spreading was expected with the reduced gas density. Unlike the normal step leaders, blue jets travel in straight lines and their scaled width appears to be larger. They pointed out that field enhancement has never been fully simulated in long discharges in weak fields.

Pasko *et al.* (1996) developed a model of blue jets based upon positive charge streamers. The basic concept is that the QE field exceeds threshold at the top of the cloud providing seed ionization. Current flows towards the head so that the field increases. The field can build until further breakdown occurs at the head of the streamer. The head moves forward and the process continues. This is the same process that was used to describe the formation of tendrils below sprites. The formation of a relatively thin region of higher conductivity acts to focus the field and to raise it above breakdown. For jets, the breakdown moves up, and tendrils move down. The model by Pasko *et al.* (1996) is two dimensional ( $\rho, z$ ) with only QE field, and breakdown is thermal. The possible effect of runaways is discussed.

Typical charges of 300–400 C are used, with the upper charge being located at 20 km. They claim that, based upon the simulations of Vitello *et al.* (1994) behind the head of the streamer, the conductivity remains constant. In their ionization model, below breakdown, attachment is not included. This keeps the electron density and the conductivity from dropping behind the head. They obtain good agreement with the velocity and shape of the blue jet. The velocity was determined by the electric field staying at breakdown values. The maximum height was determined by the time dependence of  $Q$  or at what altitude the jet's conductivity matches that of the ambient atmosphere. When the conductivities match, the jet can no longer focus the field. They note that the calculated optical emissions are higher than observations.

Sukhorukov *et al.* (1996) also presented a model of blue jets based upon ionization breakdown waves. In their model, the streamer is negative at head and the QE field is pointed down. The Pasko *et al.* (1996) model has a positive head and  $E$  is pointed up, while the Sukhorukov *et al.* (1996) model requires an intracloud (IC) discharge of the right polarity or a positive-to-ground discharge. The charge needed to trigger the blue jet is in the 350 C range. The velocity of the blue jet is determined by the electron velocity when the ambient  $E$  field is at breakdown. This velocity depends on the ratio of the breakdown field to the collision rate. Since both of these quantities depend on the neutral density, the velocity is constant with altitude. The values for the speed of the blue jet are in good agreement with observations. In agreement with the runaway model of Roussel-Durp  and Gurevich (1996), the vertical field normalized to the breakdown field has a minimum between 40 and 60 km. If this ratio falls far enough below 1, the blue jets will stop. If  $Q$  is even smaller, then the terminal altitude could be much lower, explaining blue starters (Wescott *et al.*, 1995). Both they and Pasko *et al.* (1996) also point out that when the conductivity at the front matches the ambient conductivity the blue jet will stop.

## 16.6 Unsolved problems

Among the three basic types of TLEs, elves are found to be most completely understood because most of the observed features of elves are consistent with the model in which the optical output is produced by the EMP of a lightning discharge, as in Table 16.1. Next, as for blue jets, there are only a limited number of observational results so that we need further acquisition of data. However, the phenomenon itself is rather simple, and it is likely that the ‘streamer’/thermal model may be the most plausible mechanism of blue jets.

Finally, we have to mention again that red sprites are much richer in different underlying physical processes than the former two types of TLEs (elves and blue jets). A lot of observational results on sprites have been accumulated not only in the continental summer but also in Japanese winter, but there remain several important, but unsolved, problems only for sprites. Initially, red sprites are very often observed in summer in the continents, in possible association with huge thunderstorms like MCS. However, there have been found very few exceptions that even small

thunderstorms can trigger sprites. In this sense we would like to emphasize the important role of Japanese winter sprites in the general understanding of sprites problems; especially in offering a hint to several important, but unsolved, problems of sprites. That is, winter thunderstorms in Japan are different from the conventional summer-time counterparts mostly in their dynamical evolution and vertical extent. Developing in a colder atmosphere, they tend to exhibit weaker updrafts and a lower cloud top, nonetheless maintaining the existence of the mixed-phase region that is essential for charge separation. We will try to show our latest results on the Japanese winter sprite results in order to understand the unsolved sprite problems. We do believe that the general characteristics of sprite are well explained in terms of the QE theory in Section 16.4.1, but we want to point out that there are several underlying processes to be answered and that they might be essential in the sprite mechanism.

### 16.6.1 Polarity problem

Polarity of lightning ground flashes casual to sprites is the most fundamental issue to answer, but it is not completely resolved (Williams *et al.*, 2007). This problem has been extensively studied by Williams *et al.* (2007), and we will follow closely their argument. Detailed comparisons in numerous studies have shown that the lightning type casual to sprites is almost inevitably the positive ground flash, and remarkably few observations associate sprites with negative polarity ground flashes. The most notable study is that of Barrington-Leigh and Inan (1999), in which two (and possibly three) sprites are convincingly linked with negative flashes documented by the National Lightning Detection Network (NLDN). There are some others, but substantially less convincing.

The lightning charge moment ( $Q_{ds}$ ) is the quantity of interest in assessing the initiation of sprites (and halos) in the mesosphere. The critical charge moment depends on the height of initiation of the sprite (or halo), but generally values exceeding a few hundred C km are needed. The determination of the vertical charge moment of lightning flashes by single-station ELF methods is now widely recognized (Nickolaenko and Hayakawa, 2002). The determination of the polarity of the charge transferred to ground (and hence the polarity of the charge moment change) with the ELF method is highly reliable and is based on thousands of event comparisons. Figure 16.6 is the bipolar distribution of  $Q_{ds}$  for hundreds of thousands of lightning flash located in Africa (as an example) as measured from Rhode Island, USA (Williams *et al.*, 2007). This figure indicates the well-known prevalence of negative ground flashes over positive ground flashes, by a typical 10 to 1 margin. As the  $Q_{ds}$  increases further beyond the threshold value for sprites, one enters the important tails of the distribution. Here the polarity prevalence reverses, and positive begins to dominate. It is important to note, however, that substantial numbers of events are found above the nominal sprites initiation threshold ('supercritical' events) for both negative and positive polarity. This result is much the same in different land regions. The key finding here is that roughly 10% of all lightning flashes globally believed capable of making sprites are negative in

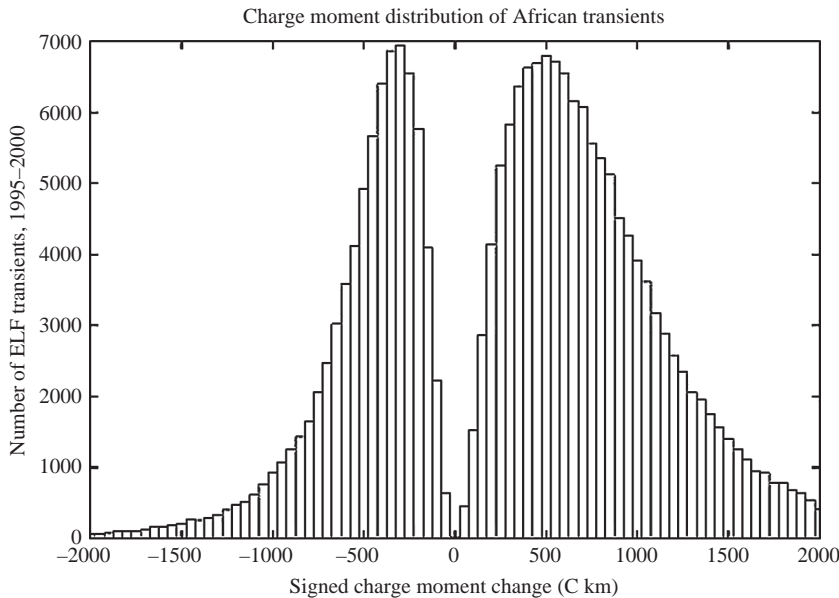


*Figure 16.6 Bipolar charge moment distributions for hundreds of thousands of lightning flashes located in Africa as detected at Rhode Island, USA [after Williams et al. (2007)]*

polarity. However, this statistic stands in sharp contrast with the 0.1% of sprites linked with negative lightning.

One additional distinction can be drawn between positive and negative flashes on the basis of the ELF observations, and this distinction may ultimately aid in the resolution of the paradox. The slope of the frequency spectrum of current moment is a measure of the impulsiveness of the flash. When the duration of the lightning current is short in comparison to the time required for light to circle the Earth ( $\sim 130$  ms), then the flash is impulsive and the current moment spectrum is flat with frequency (i.e. ‘white’). When a persistent current flows, the spectral slope becomes negative (i.e. the spectrum ‘reddens’). Figure 16.7 compares the least squares fit slopes of the current moment spectra for a large number of lightning flashes worldwide, as again recorded in Rhode Island. The negative flashes are found to have a clear tendency for mean spectrum close to ‘white’ (zero slope), whereas the positive flashes show a significant tendency for negative slopes. This ELF evidence for more persistent currents in positive is consistent with the general knowledge for ordinary lightning that return strokes in positive flashes are almost inevitably followed by continuing current, whereas negative flashes are often characterized by discrete strokes without continuing current.

The quantitative contrast between sprite observations and the ELF-observed populations of charge moment change presents a paradox. This polarity asymmetry of sprites is pronounced, and Williams *et al.* (2007) have suggested explanations in

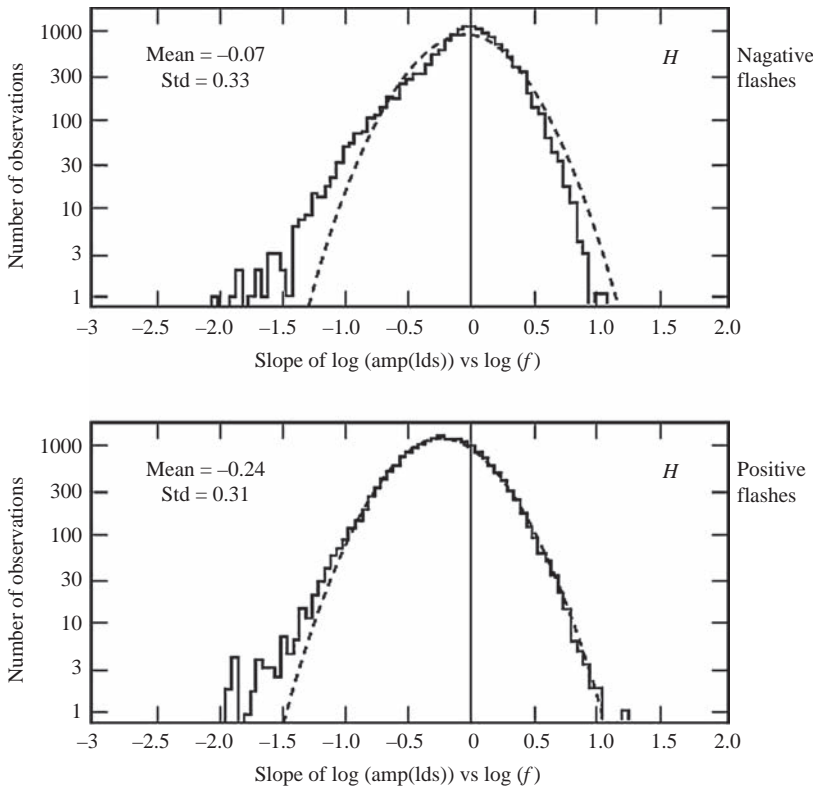


*Figure 16.7 Distributions of least squares slope for negative and positive current moment spectra for a large number of supercritical lightning flashes [after Williams *et al.* (2007)]*

different kinds of polarity asymmetry, including (1) polarity asymmetry in charge moments, (2) polarity asymmetry in sprite detectability, (3) polarity asymmetry in the threshold for streamer propagation, (4) polarity asymmetry in an electron runaway mechanism, (5) polarity asymmetry of the global electrical circuit, and (6) polarity asymmetry in the forcing of sprites (and halos) by lightning. The detailed discussions have been given in Williams *et al.* (2007), but, as their conclusion, there seems to be no definite answer to this paradox, which still requires further study in future as well.

### 16.6.2 Morphological changes of sprites

In the case of summer continental sprites, a majority of them are known to be ‘carrots’, and ‘column’ sprites are a minority. It seems that there have been published no detailed statistical treatments of this morphological study for

summer continental studies. Here we present our study on the morphological properties of Japanese winter sprites not only in the Hokuriku area (Japan Sea side) but also in the Pacific Ocean (off-Chiba area) (Myokei *et al.*, 2009). This information would be of use in discussing the mechanism of having different shapes of sprites. The observation has been performed in three winter (November–May) periods of 2004/5, 2006/7 and 2007/8, and the observation is made continuously in the LT (local time) interval from 18:00 to 5:00. The sprite capture is performed every 33 ms on the conventional video, so that if we find anything (any kind of sprites) in one frame, this is counted as ‘ONE’ event. Unlike the summer sprites as in the United States, it is extremely rare for us to have sprites on the successive frames in our Japanese winter sprites. One frame contains one column, but sometimes there are several columns in the frame (these are all ‘ONE’ event). The definitions of three different types, namely columns, carrots and intermediate, are defined as follows: When we observe only one type of sprites (e.g. only column sprites (either single or multiple)), we define these as column sprites. The same is true for carrots. The term of intermediate indicates that any intermediate type is observed such as V-shaped sprite or a combination of different types (e.g. coexistence of columns and carrots) in one frame. The total number of events of sprites is 60 during the winter of 2004/5, 67 for 2006/7 and 61 for 2007/8, and we use 188 events as a total.

In order to obtain the information in the upper atmosphere close to the time when one sprite event is observed, we have examined the data obtained at Wajima Meteorological Observatory (geographic coordinates: 37.39° N, 136.90° E) belonging to Japan Meteorological Agency, where they measure the vertical profile of temperature by means of a radiosonde twice a day (UT (universal time)=0 and 12 h; correspondingly LT=9 and 21 h). When we observe one event at a particular LT on a specific day, we use the height profiles of temperature at two LTs (LT=9 and 21 h on the day if the sprite observation is before 21 h, but LT=21 h on the same day and LT=9 h on the next day if the sprite is observed after 21 h). Then, we interpolate the height of  $-10^{\circ}\text{C}$  by using the above two values at LT=21 and 9 h and also the LT when a sprite event is observed.

By using the data on the height of  $-10^{\circ}\text{C}$  when a sprite event is observed, we have plotted the occurrence number of sprites (carrots, columns and intermediate) as a function of the height of  $-10^{\circ}\text{C}$  in Figure 16.8. This figure is based on the events during the three winter periods of 2004/5, 2006/7 and 2007/8, and the most important finding from Figure 16.8 can be summarized as follows:

1. The occurrence of sprites is mainly concentrated in a range of height of  $-10^{\circ}\text{C}$  from 1200 m to mainly 3000 m (though very few events of  $-10^{\circ}\text{C}$  are observed at 4400 km).
2. There are two characteristic height ranges in the sprite occurrence: the height range below 1800 m and that above 1800 m. This might suggest that 1800 m is a kind of boundary between two characteristic height regions.
3. In the lower height range below 1800 m, the number of sprites is not so much, and the main part of sprite morphology is column (about 71% (10/14)).

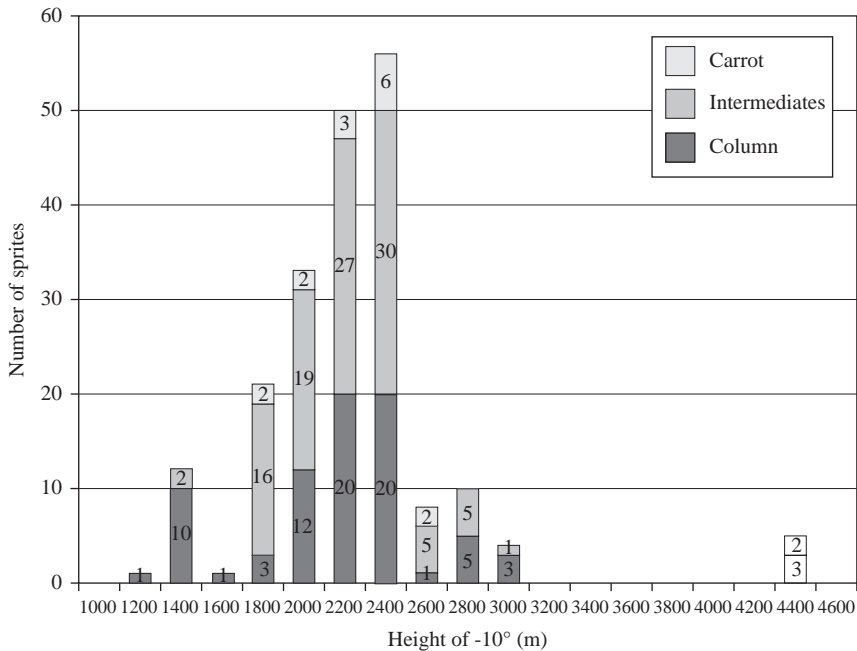


Figure 16.8 Occurrence histogram of carrots, intermediate and columns as a function of the height of  $-10^{\circ}\text{C}$ . The numerical value in each block indicates the number of events [after Myokei *et al.* (2009)]

4. Just above 1800 m, the occurrence of sprites is found to be very frequent, but it tends to decrease in the upper height range of 2600–3000 m.
5. Above 1800 m (up to 3000 m), the morphological characteristics of winter sprites become very complicated in such a way that the more complex structure like carrots or intermediate type becomes more frequent in addition to column sprites. The percentage occurrence is as follows: 8% for carrot type (15/182), 57% for intermediate type (103/182) and 35% for column type (64/182).
6. Sprites are not observed at heights higher than 3000 m, with exceptionally very few events at 4400 m.

The type of sprites may be dependent on many factors, including not only the parent flash but also mesospheric temperature and conductivity profiles, ionospheric height, etc. However, a recent study based on the computer simulation by Asano *et al.* (2008) and the discussion in Sections 16.3.1 and 16.3.2 have indicated the primary importance of cloud charge height in the initiation and morphology of sprites. We have used the height of  $-10^{\circ}\text{C}$  isotherms as the first approximation of cloud charge height. We do not know the exact location of the positive charge reservoir necessary for the generation of winter sprites in the Hokuriku region. Anyway, the altitude of  $-10^{\circ}\text{C}$  is known to be, at least, that of negative charge

accumulation (Takahashi, 1978), together with the small positive charges. Though it is found that some (of course, not all) IC discharges may produce sprites (van der Velde *et al.*, 2006), this fact weakens the above argument.

As is seen in Figure 16.8, sprites (either carrots or columns) are observed when the height of  $-10^{\circ}\text{C}$  lies in a range from 1200 to 3000 m as summarized in points (1)–(4). There is an additional important finding regarding the sprite shapes. That is, when the height of  $-10^{\circ}\text{C}$  is lower than 1800 m, the simple structure of columns seems to be dominant (point (5)). Moreover, more spectacular shapes (like carrots) tend to happen in addition to column sprites when the height of  $-10^{\circ}\text{C}$  becomes relatively higher such as 1800–3000 m (point (5)). One more point seen from Figure 16.8 is that there are approximately no sprites when the height of  $-10^{\circ}\text{C}$  is above 3000 up to 4000 m. This might suggest that this height region is not suitable for generating lightning itself. There are, at least, four types of weather systems producing lightning in the Hokuriku area (Rakov and Uman, 2003). In the mid-winter, a typical one is that trains of convective clouds are formed in Siberia. In the case when the tropospheric instability caused by the advection is intense enough, some of the clouds develop into thunderclouds over the Japan Sea coast. It is not well understood whether the parent lightning originates from the upper (tilted) positive charge centre or from the lower stratiform region (Williams and Yair, 2006). However, Hayakawa *et al.* (2004) and Suzuki *et al.* (2006) have found in the climatic approach that the reservoir of positive charge resides within the stratiform region.

Another important point to mention is the morphological difference between sprites on the Japan Sea side and those on the Pacific Ocean. Figure 16.9 illustrates the percentage occurrence of different kinds of sprites in both regions. In the Hokuriku area, the percentage of the simplest columns is 68% and that for carrots is 16%, whereas the corresponding percentage is 62% for columns and 28% for carrots.

The morphological properties of Japanese winter sprites are compared to those of summer sprites. As summarized, the dominant shape of Japanese winter sprites is confirmed to be columns with the occurrence probability of above 60% not only in the Hokuriku area but also in the Pacific Ocean. However, the occurrence property of carrots is found to be remarkably different in the two regions; i.e. much more frequent in the Pacific Ocean than in the Hokuriku area. Though so many papers have been published on summer sprites in the continents as summarized in Williams *et al.* (2007), it seems that the occurrence percentage of carrots, columns, etc. for summer sprites in the continents is not well documented. But it seems that carrots are much more popular than columns for the continental summer. For example, van der Velde *et al.* (2006) indicated that two-thirds are carrots, even though they had a small sample of 15 events. A morphological difference of predominance of columns is very peculiar to winter sprites in Japan (either in the Japan Sea or in the Pacific Ocean).

### *16.6.3 Lateral shift of a sprite from its parent lightning*

It is known that a sprite does not always take place above its parent lightning, and there exists a remarkable displacement of a sprite from its parent lightning of the

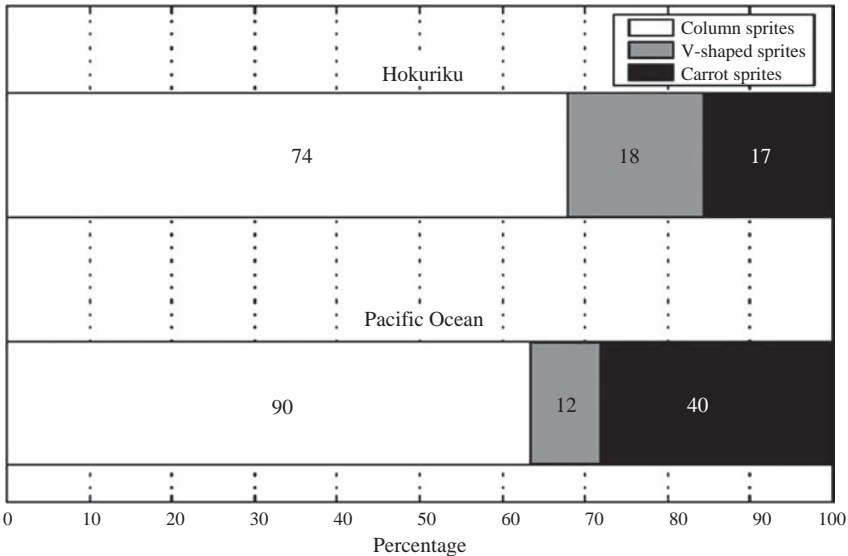


*Figure 16.9 Morphology of optical sprites observed in the Hokuriku (top) and the Pacific Ocean (bottom). The shapes of sprites are classified into three categories: columns, V-shaped and carrots [after Matsudo et al. (2009)]*

order of  $\sim 50$  km (Lyons, 1996), which is poorly understood. The QE mechanism predicts that a sprite should take place above its parent lightning discharge if it is a vertical channel as discussed in Section 16.3.1.2. It is general to attribute the lateral shift of sprites to the geometry and electrical structure of the sprite-producing lightning discharge. Of course, it is possible to explain such a lateral shift in terms of a complicated lightning geometry including the horizontal channel as discussed in Section 16.3.1 and also in Cho and Rycroft (2001), Asano *et al.* (2009a) and Kudintseva *et al.* (2010).

An alternative explanation may be possible in terms of the effect of EMP field of a lightning discharge (Cho and Rycroft, 2001; Asano *et al.*, 2009b). The oblique propagation and its lateral shift of the maximum electric field is easily expected in the estimation of electric fields in Section 16.3.

Future coordinated measurement will enable us to distinguish which mechanism for the lateral shift is more plausible (either the lightning geometry or the lightning electric field (QE and/or EMP fields)).

#### 16.6.4 Time delay effect

As the general characteristics, summer sprites taking place very often in the continents and associated with MCSs are found to be rather simple to understand. They are mainly carrot sprites, and they occur within 10 ms after the occurrence of a parent lightning discharge (Huang *et al.*, 1999). These characteristics are found to

be satisfactorily accounted for in terms of the QE theory initially proposed by Pasko *et al.* (1996).

As concerned with the problem of the time delay of sprites behind their parent lightning, some exceptions of extremely large delays of the order of 100 ms are observed even for the summer continental sprites (Bell *et al.*, 1998), and the mechanism for this phenomenon is poorly understood. Furthermore, the information on the Japanese winter sprites seems to be of extreme importance in understanding this large delay times. Here we present our latest results on this topic on the basis of observations in Japanese winters (not only in the Hokuriku area (Japan Sea side) but also in the Pacific Ocean) (Matsudo *et al.*, 2009). Another important finding is that the time delay may be dependent on the morphology of sprites as discussed in Section 16.6.2. Though we have observed about 200 TLEs during three winter seasons discussed in Section 16.6.2, we have used 30 events for Japan Sea sprites and 23 events for Pacific Ocean sprites because the time stamp by GPS is superimposed on the video recording only for the two cameras from the four.

We have calculated the time delay between ELF peak time and sprite emission. Figure 16.10(a) shows the obtained occurrence histogram of time delay of winter sprites in the Hokuriku area with a bin of 30 ms, and Figure 16.10(b) shows the corresponding results for the Pacific Ocean sprites. We can summarize the following points from Figure 16.10 and Matsudo *et al.* (2007, 2009).

- (i) We have found that there are ELF transients with positive polarity in the vertical electric field for all of sprite events in both the Hokuriku and the Pacific Ocean areas. This lends further support to our previous report by Hobara *et al.* (2001, 2006), Hayakawa *et al.* (2004) and Matsudo *et al.* (2007)
- (ii) It is revealed that there are clearly visible differences of time delay characteristics between Hokuriku and Pacific Ocean sprites in winter. Hokuriku sprites take place 90 ms (as average) after their parent lightning flashes, while sprites in the Pacific Ocean occur 43 ms after their parent lightning flashes.
- (iii) As a result of comparison of time delay from a parent lightning flash in dependence with sprite shape (morphology), columns and carrots occur, on average, 80 and 100 ms after their parent lightning flashes in the Hokuriku area, respectively. However, in the Pacific Ocean area, both columns and carrots occur ~40 ms after their parent lightning flashes. Thus, it is estimated that there are noticeable differences of initiation of sprites between carrots and columns in the Hokuriku area, in contrast to Pacific Ocean sprites.

Here, we compare our observational results on time delay with previous works for summer sprites in the continents (Huang *et al.*, 1999; van der Velde *et al.*, 2006). Without paying any attention to different shapes of sprites and with paying particular attention to the comparison between sprites and elves, Huang *et al.* (1999) obtained that the average delay time of summer sprites from their parent lightning flashes in the United States is 0–30 ms (as the result of 245 sprites (but the histogram of the delay time seems to be produced with less than 245 events) observed during one night; 24 July 1996). Recently, van der Velde *et al.* (2006) have estimated the time delay of columns to be less than 30 ms, while the delay of

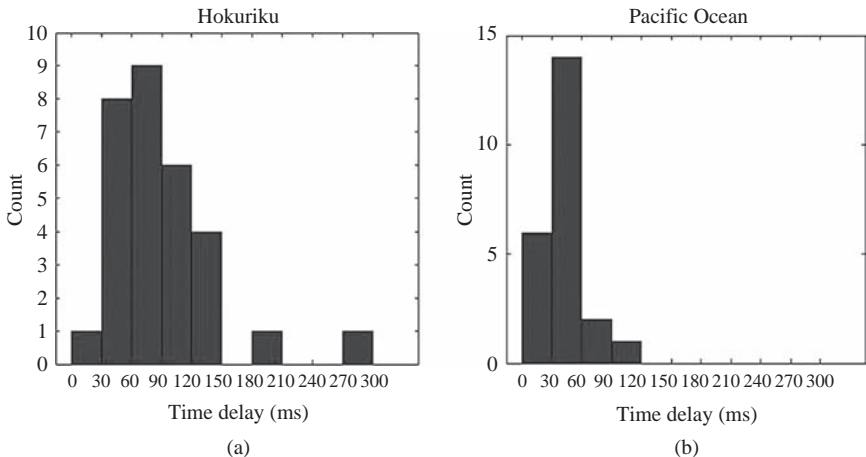


Figure 16.10 (a) Occurrence histogram of time delay of sprites from ELF lightning to sprites around the Hokuriku area observed from Shimizu, Japan. The time delay is given with a bin of 30 ms. (b) Same as (a), but for the Pacific Ocean area [after Matsudo *et al.* (2009)]

carrots lies in a range from 25 to 75 ms, even though the event number was not enough (as the result of 15 summer sprites in France observed during one night; 23–24 July 2003). These results for summer sprites are now compared with our findings as points (ii) and (iii). Extremely large time delay ( $\sim 90$  ms as an average) for the Hokuriku area seems to be completely distinct from the corresponding time delay characteristics for continental summer sprites. However, the comparison of time delay of carrots and columns in the Hokuriku area indicates a smaller value for columns and larger values for carrots; this general tendency in dependence on sprite morphology seems to be consistent with the result by van der Velde *et al.* (2006). On the other hand, the time delay of  $\sim 40$  ms for Pacific Ocean sprites (not much difference between carrots and columns) is likely to be relatively close to the result by van der Velde *et al.* (2006).

The morphological difference of sprites in the Hokuriku area (Japan Sea side) and in the Pacific Ocean, and also the difference in time delay characteristics, is closely related with significant difference in the lightning discharge properties of parent thunderclouds in the two regions. Takahashi *et al.* (2003) have examined the relationship between the cloud-top height and sprite occurrence. They have found that the top of sprite-producing thunderstorm in the Hokuriku area was 4.2–6.5 km, while the top of sprite-producing thunderstorm in the Pacific Ocean was 5–7 km. Thus, the top of winter thunderstorms in the Pacific Ocean is significantly higher than that in the Hokuriku area, and a little smaller than summer ones. In this sense, the cloud structure in the Pacific Ocean is likely to be comparatively similar to summer continental lightning. This might be one reason for the similarity of time delay of Pacific Ocean sprites with that of summer continental ones as mentioned earlier.

As for Hokuriku lightning, several papers have been published, giving us some more details on their meteorological and electrical characteristics. Michimoto (1993) and Kitagawa and Michimoto (1994) studied the charge distribution in winter active convective clouds in the Hokuriku area of Japan (the Japan Sea side). They indicated that the duration of both dipole and tripole structures is suggested to be very short (less than 10 min) because the graupel particles carrying the main negative and the lower positive charges do not stay for a long time in the clouds and fall rapidly. The duration of the remained cloud lasts relatively long. Thus, the positive charge will predominate in the cloud. This individuality is peculiar to Japanese winter lightning, and considerably distinct from summer lightning. As compared with a considerable number of works on Hokuriku lightning, no paper has been published that deals with the specific meteorological/electrical properties of lightning discharges in the Pacific Ocean. However, it seems that lightning discharges in the Pacific Ocean are more alike to the conventional summer ones in the United States.

The possible difference in the electrical properties of lightning in the Japan Sea side and on the Pacific Ocean side is already confirmed by other observations such as lightning-induced ionospheric perturbations (so-called Trimpis) by Otsuyama *et al.* (2004). They have shown that the Trimpis are more easily triggered in the Japan Sea than in the Pacific Ocean, though the detailed mechanism on the difference is poorly understood.

Recently, two important papers have been published on the initiation of sprites, especially relating to the time delay effects. Based on the EM (not ES) computer code, Asano *et al.* (2009b) have indicated that the fast rise time of a return stroke is also essential to enhance the initiation of sprites, suggesting an important role of high-frequency (a few kHz to a few MHz) electromagnetic effect (like M components). Independently, Yashunin *et al.* (2007) have considered the effect of the radiation field of lightning flushes in addition to the QE field (corresponding to return stroke), and their conclusion is that electromagnetic fields (like M components) would enhance the initiation of sprites. Seemingly to support these theoretical works, several papers have been recently published on the observational fact of high-frequency components (fast varying) in association with sprite occurrences/morphology (Ohkubo *et al.*, 2005; van der Velde *et al.*, 2006; Suzuki *et al.*, 2006), though they have not suggested any mechanism on how high-frequency components might be involved in sprite occurrence.

As a possible hint on how high-frequency current is involved in sprite initiation, Asano *et al.* (2009b) have performed EM code computer simulations on the initiation of sprites, in which they have assumed a return stroke with continuing current, together with M components ( $\approx$  a few kHz) being superimposed. The presence of M components is found to drastically change the initiation and enhance the luminosity of sprites, so that they have shown that the time delay effect of sprites is closely related to the occurrence of M components. Therefore, we hypothesize that M components in continuing current would give an answer to very long-delayed sprites as found for Japanese winter sprites.

### 16.6.5 Fine structure of sprites

Macroscopic structure and morphological characteristics of sprites are relatively well investigated and well understood. However, recent studies have indicated the presence of small-scale fine structures in sprites. Recent telescopic imaging of sprites even at standard video rates (i.e. with the time resolution of 16 ms) revealed an amazing variety of generally vertical fine structure with transverse spatial scales ranging from tens to a few hundreds of metres (Gerken *et al.*, 2000; Gerken and Inan, 2003, 2005). First high-speed (1 ms) telescope imaging of sprites has been reported indicating that streamer-like formations in sprites rarely persist for more than 1–2 ms (Marshall and Inan, 2005). Also, recently, it has been documented that some sprites exhibit a sharp transition between the upper diffuse and the lower highly structured regions (Stenbaek-Nielsen *et al.*, 2000; Pasko and Stenbaek-Nielsen, 2002; Gerken and Inan, 2003, 2005). Many sprites are observed with an amorphous diffuse glow at their tops (the so-called sprite halo) (Barrington-Leigh *et al.*, 2001; Wescott *et al.*, 2001; Miyasato *et al.*, 2002; Gerken and Inan, 2003).

Pasko *et al.* (1998) proposed a theory indicating that sprite structure (fine structures of sprites) as a function of altitude should exhibit a transition from essentially non-structured diffuse glow at altitudes  $\geq 85$  km to the highly structured streamer region at altitudes  $\leq 75$  km (as shown in Figure 16.11). It is proposed that the vertical structuring in sprites is created due to interplay of three physical time scales: (1) the dissociative attachment time scale  $\tau_a$  (which is defined by the maximum net attachment coefficient as  $1/(v_a - v_i)_{max}$ , where  $v_i$  and  $v_a$  are the ionization and attachment coefficients, respectively); (2) the ambient dielectric relaxation time scale  $\tau_\sigma = \epsilon_0/\sigma$ ; (3) the time scale for the development of an individual electron avalanche into a streamer  $t_s$ . This time is an effective time over which the electron avalanche generates a space charge field comparable in magnitude to the externally applied field. The interplay between these three parameters creates three unique altitude regions as illustrated in Figure 16.11: (1) the diffuse region ( $\tau_\sigma < \tau_a$ ,  $\tau_\sigma < t_s$ ) characterized by simple volumetric multiplication of electrons (Townsend electron multiplication mechanism); (2) the transition region ( $\tau_\sigma > \tau_a$ ,  $\tau_\sigma < \sim t_s$ ) characterized by strong attachment of ambient electrons before the onset of the electrical breakdown and (3) the streamer region ( $\tau_\sigma > \tau_a$ ,  $\tau_\sigma > t_s$ ) also characterized by the strong attachment as well as by individual electron avalanches evolving into streamers. The upper and the lower boundaries of the transition region shown in Figure 16.11 represent an estimate of the altitude range in which the actual transition between the diffuse and streamer regions is expected to occur. The upper boundary may shift downward under conditions of an impulsive lightning discharge that generates substantial electron density (i.e. conductivity) enhancement associated with the sprite halo at the initial stage of sprite formation (Barrington-Leigh *et al.*, 2001). The lower boundary may shift upward due to streamers originating at lower altitudes but propagating upward towards the lower ionosphere (Stanley *et al.*, 1999). Barrington-Leigh *et al.* (2001) demonstrated a very close agreement of model optical emissions and high-speed video observations and for the first time identified sprite halos as being produced entirely by QE

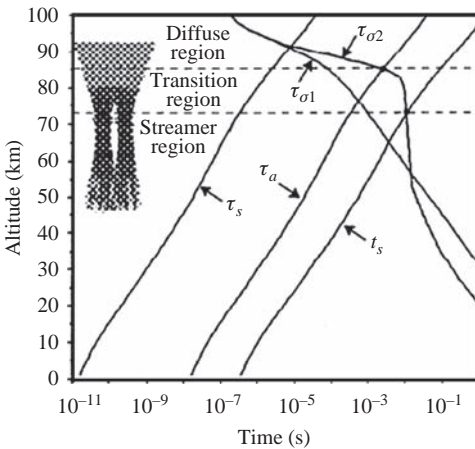


*Figure 16.11 The altitude distribution of different time scales characterizing the vertical structuring of optical emissions in sprites [after Pasko et al. (1998)]*

thundercloud fields. Sprites indeed often exhibit sprite halos that appear as relatively amorphous non-structured glow at sprite tops and that convert to highly structured regions at lower altitudes (Stanley *et al.*, 1999; Gerken *et al.*, 2000, and references therein). This vertical structure in sprites is apparent in recent high-speed video images of Stenbaek-Nielsen *et al.* (2000) and also was reported during telescopic observations of sprites by Gerken and Inan (2003, 2005). Further discussion can be found in Pasko (2006).

The appearance of these fine structures in sprites is of great importance in sprite problem. It has been interpreted in terms of positive and negative streamer coronas what are considered as scaled analogues of small-scale streamers, which exist at high atmospheric pressures at ground level (Pasko *et al.*, 1998). However, there remain a lot of questions to be investigated in future.

Unlike the above physical modelling, a completely new type of mathematical sprite structure has been proposed by Hayakawa *et al.* (2007) based on the cellular automaton concept. A large-scale model of sprites based on the phenomenological percolation-like probabilistic approach is developed to model streamer discharges in sprites. This kind of new attempts would be of use in understanding the fine structures of sprites, which should be pursued as well.

## References

- Asano, T., Hayakawa, M., Cho, M. and Suzuki, T., Computer simulations on the initiation and morphological difference of Japan winter and summer sprites, *J. Geophys. Res.*, 113, A02308, doi:10.1029/2007JA012528, 2008

- Asano, T., Suzuki, T., Hayakawa, M. and Cho, M. G., Three-dimensional EM computer simulation on sprite initiation above a horizontal lightning discharge, *J. Atmos. Solar-Terr. Phys.*, 71, 983–990, 2009a
- Asano, T., Suzuki, T., Hiraki, Y., Mareev, E., Cho, M. G. and Hayakawa, M., Computer simulations on sprite initiation for realistic lightning models with higher-frequency surges, *J. Geophys. Res.*, 114, A02310, doi: 10.1029/2008JA013651, 2009b
- Barrington-Leigh, C. P. and Inan, U. S., Elves triggered by positive and negative lightning discharges, *Geophys. Res. Lett.*, 26, 683–686, 1999
- Barrington-Leigh, C. P., Inan, U. S. and Stanley, M., Identification of sprites and elves with intensified video and broadband array photometry, *J. Geophys. Res.*, 106(A2), 1741–1750, doi: 10.1029/2000JA000073, 2001
- Bell, T. F., Reising, S. C. and Inan, U. S., Intense continuing currents following positive cloud-to-ground lightning associated with red sprites, *Geophys. Res. Lett.*, 25, 1285–1288, 1998
- Boccippio, D. J., Williams, E. R., Heckman, S. J., Lyons, W. A., Baker, I. T. and Boldi, R., Sprites, ELF transients, and positive ground strokes, *Science*, 269, 1088–1091, 1995
- Boeck, W. L., Vaughan Jr., O. H., Blakeslee, R., Vonnegut, B. and Brook, M., Lightning induced brightening in the airglow layer, *Geophys. Res. Lett.*, 19, 99–102, 1992
- Cho, M. and Rycroft, M. J., Computer simulation of the electric field structure and optical emission from cloud top to the ionosphere, *J. Atmos. Solar-Terr. Phys.*, 60, 871–888, 1998
- Cho, M. and Rycroft, M. J., Non-uniform ionization of the upper atmosphere due to the electromagnetic pulse from a horizontal lightning discharge, *J. Atmos. Solar-Terr. Phys.*, 63, 559–580, 2001
- Cummer, S. A., Current moment in sprite-producing lightning, *J. Atmos. Solar-Terr. Phys.*, 65, 499–508, doi:10.1016/S1364-6826(02)00318-8, 2003
- Cummer, S. A., Inan, U. S., Bell, T. F. and Barrington-Leigh, C. P., ELF radiation produced by electrical currents in sprites, *Geophys. Res. Lett.*, 25, 1281–1285, 1998
- Fernsler, R. F. and Rowland H. L., Models of lightning-produced sprites and elves, *J. Geophys. Res.*, 101, D23, 29653–29662, 1996
- Fishman, G. J., Bhat, P. N., Mallozzi, R., Horack, J. M., Koshut, T., Kouveliotou, C., et al., Discovery of intense gamma-ray flashes of atmospheric origin, *Science*, 264, 1313–1316, 1994
- Franz, R. C., Nemzek, R. J. and Winckler, J. R., Television image of a large upward electrical discharge above a thunderstorm system, *Science*, 249, 48–51, 1990
- Fukunishi, H., Takahashi, Y., Kubota, M., Sakanoi, K., Inan, U. S. and Lyons, W. A., Elves: lightning-induced transient luminous events in the lower ionosphere, *Geophys. Res. Lett.*, 23(16), 2157–2160, 1996
- Füllekrug, M. and Constable, S., Global triangulation of intense lightning discharges, *Geophys. Res. Lett.*, 27, 333–336, 2000

- Füllekrug, M. and Reising, S. C., Excitation of Earth-ionosphere cavity resonances by sprite-associated lightning flashes, *Geophys. Res. Lett.*, 25, 4145–4148, 1998
- Gerken, E. A. and Inan, U. S., Observations of decameter-scale morphologies in sprites, *J. Atmos. Solar-Terr. Phys.*, 65, 567–572, doi:10.1016/S1364-6826(02)00333-4, 2003
- Gerken, E. A. and Inan, U. S., Streamers and diffuse glow observed in upper atmospheric electrical discharges, *IEEE Trans. Plasma Sci.*, 33(2), 282–283, 2005
- Gerken, E. A., Inan, U. S. and Barrington-Leigh, C. P., Telescopic imaging of sprites, *Geophys. Res. Lett.*, 27, 2637–2640, 2000
- Gurevich, A. V., Milikh, G. M. and Roussel-Dupré, R., Runaway electron mechanism of air breakdown and preconditioning during a thunderstorm, *Phys. Lett. A*, 165, 463–468, 1992
- Hampton, D. L., Heavner, M. J., Wescott, E. M. and Sentman, D. D., Optical spectral characteristics of sprites, *Geophys. Res. Lett.*, 23, 89–93, 1996
- Hayakawa, M., Iudin, D. I., Mareev, E. A. and Trakhtengerts, V. Y., Cellular automaton modeling of mesospheric optical emissions: sprites, *Phys. Plasmas*, 14(4), 042902 1–6, 2007
- Hayakawa, M., Nakamura, T., Hobara, Y. and Williams, E., Observations of sprites over the Sea of Japan and conditions for lightning-induced sprites in winter, *J. Geophys. Res.*, 109, 1312, doi:10.1029/2003JA009905, 2004
- Hayakawa, M., Nakamura, T., Iudin, D., Michimoto, K., Suzuki, T., Hanada, T., et al., On the structure of thunderstorms leading to the generation of sprites and elves: fractal analysis, *J. Geophys. Res.*, 110, D06104, doi:10.1029/2004JD004545, 2005
- Hobara, Y., Hayakawa, M., Williams, E., Boldi, R. and Downes, E., Location and electrical properties of sprite-producing lightning from a single ELF site, in M. Füllekrug, et al. (ed.), *Sprites, Elves and Intense Lightning Discharges*, NATO Science Series, Dordrecht, 211–229, 2006
- Hobara, Y., Iwasaki, N., Hayashida, T., Hayakawa, M., Ohta, K. and Fukunishi, H., Interrelation between ELF transients and ionospheric disturbances in association with sprites and elves, *Geophys. Res. Lett.*, 28(5), 935–938, doi:10.1029/2000GL003795, 2001
- Hu, W. Y., Cummer, S. A. and Lyons, W. A., Lightning charge moment changes for the initiation of sprites, *Geophys. Res. Lett.*, 29(8), 1279, doi:10.1029/2001GL014593, 2002
- Huang, E., Williams, E., Boldi, R., Heckman, S., Lyons, W., Taylor, M., et al., Criteria for sprites and elves based on Schumann resonance observations, *J. Geophys. Res.*, 104, 16943–16964, 1999
- Inan, U. S., Sampson, W. A. and Taraneko, Y. N., Space-time structure of optical flashes and ionization changes produced by lightning-EMP, *Geophys. Res. Lett.*, 23, 1017–1020, 1996
- Jackson, J. D., *Classical Electrodynamics*, Wiley & Sons, New York, 1975
- Kitagawa, N. and Michimoto, K., Meteorological and electrical aspects of winter thunderclouds, *J. Geophys. Res.*, 99(D5), 10713–10721, 1994

- Krider, E. P., On the electromagnetic fields, Poynting vector, and peak power radiated by lightning return strokes, *J. Geophys. Res.*, 97, D14, 15913–15917, 1992
- Kudintseva, I. G., Nickolaenko A. P. and Hayakawa M., Transient electric field in the mesosphere above a  $\Gamma$ -shape lightning stroke, *Surv. Geophys.*, 31, 427–448, 2010
- Lehtinen, N. G., Bell, T. F., Pasko, V. P. and Inan, U.S., Two dimensional model of runaway electron beams driven by quasi-electrostatic thundercloud fields, *Geophys. Res. Lett.*, 242639–242642, 1997
- Lehtinen, N. G., Inan, U. S. and Bell, T. F., Monte Carlo simulation of runaway MeV electron breakdown with application to red sprites and terrestrial gamma ray flashes, *J. Geophys. Res.*, 104, 24699–24712, 1999
- Le Vine, D. M. and Willett J. C., Comment on the transmission-line model for computing radiation from lightning, *J. Geophys. Res.*, 97, D2, 2601–2610, 1992
- Lyons, W. A., Sprite observations above the U.S. high plains in relation to their parent thunderstorm system, *J. Geophys. Res.*, 101, 29641–29652, 1996
- Lyons, W. A., The meteorology of transient luminous events – An introduction and overview, in M. Füllekrug, *et al.* (ed.), *Sprites, Elves and Intense Lightning Discharges*, NATO Science Series, Dordrecht, 19–44, 2006
- Lyons, W. A., Nelson, T. E., Williams, E. R., Cummer, S. A. and Stanley, M. A., Characteristics of sprite-producing positive cloud-to-ground lightning during the 19 July 2000 STEPS mesoscale convective systems, *Mon. Weather Rev.*, 131, 2417–2427, 2003
- Marshall, R. A. and Inan, U. S., High-speed telescopic imaging of sprites, *Geophys. Res. Lett.*, 32(L05804), doi:10.1029/2004GL021988, 2005
- Marshall, T. C. and Rust, W. D., Two types of vertical electrical structures in stratiform precipitation regions of mesoscale convective systems, *Bull. Amer. Met. Soc.*, 74, 2159–2170, 1993
- Matsudo, Y., Suzuki, T., Hayakawa, M., Yamashita, K., Ando, Y., Michimoto, K., *et al.*, Characteristics of Japanese winter sprites and their parent lightning as estimated by VHF lightning and ELF transients, *J. Atmos. Solar-Terr. Phys.*, 69, 1431–1446, 2007
- Matsudo, Y., Suzuki, T., Michimoto, K., Myokei, K. and Hayakawa, M., Comparison of time delays of sprites induced by winter lightning flashes in the Japan Sea with those in the Pacific Ocean, *J. Atmos. Solar-Terr. Phys.*, 71, 101–111, 2009
- Mende, S. B., Rairden, R. L., Swenson, G. R. and Lyons, W. A., Sprite spectra: N<sub>2</sub>1PG band identification, *Geophys. Res. Lett.*, 22, 2633–2637, 1995
- Michimoto, K., A study of radar echoes and their relation to lightning discharge of thunderclouds in the Hokuriku district, II. Observation and analysis of “single-flash” thundercloud in mid-winter, *J. Meteor. Soc. Japan*, 71, 195–204, 1993
- Miyasato, R., Taylor, M. J., Fukunishi, H. and Stenbaek-Nielsen, H. C., Statistical characteristics of sprite halo events using coincident photometric and imaging data, *Geophys. Res. Lett.*, 29(21), 2033, doi:10.1029/2001GL014480, 2002
- Myokei, K., Matsudo, Y., Asano, T., Suzuki, T., Hobara, Y., Michimoto, K., *et al.*, A study of the morphology of winter sprites in the Hokuriku area of Japan

- in relation to cloud charge height, *J. Atmos. Solar-Terr. Phys.*, 71, 597–602, 2009
- Nickolaenko, A. P. and Hayakawa, M., Heating of the lower ionosphere electrons by electromagnetic radiation of lightning discharges, *Geophys. Res. Lett.*, 22, 3015–3018, 1995
- Nickolaenko, A. P. and Hayakawa, M., *Resonances in the Earth-Ionosphere Cavity*, Kluwer Academic Publisher, Dordrecht, 2002
- Ohkubo, A., Fukunishi, H., Takahashi, Y. and Adachi, T., VLF/ELF sferic evidence for in-cloud discharge acting preceding sprites, *Geophys. Res. Lett.*, 32, L04812, doi:10.1029/2004 GL 021943, 2005
- Otsuyama, T., Manabe, J., Hayakawa, M. and Nishimura, M., Characteristics of subionospheric VLF perturbations associated with winter lightning around Japan, *Geophys. Res. Lett.*, 31, L04117, doi:10.1029/2003 GL0/9064, 2004
- Pasko, V. P., Theoretical modeling of sprites and jets, in M. Füllekrug, *et al.* (ed.), *Sprites, Elves and Intense Lightning Discharges*, NATO Science Series, Dordrecht, 253–311, 2006
- Pasko, V. P. and Stenbaek-Nielsen, H. C., Diffuse and streamer regions of sprites, *Geophys. Res. Lett.*, 29(A10), 1440, doi:10.1029/2001GL014241, 2002
- Pasko, V. P., Inan, U. S. and Bell, T. F., Sprites as luminous columns of ionization produced by quasi-electrostatic thundercloud fields, *Geophys. Res. Lett.*, 23, 649–652, 1996
- Pasko, V. P., Inan, U. S. and Bell, T. F., Spatial structure of sprites, *Geophys. Res. Lett.*, 25, 2123–2126, 1998
- Pasko, V. P., Inan, U. S. and Bell, T. F., Mesospheric electric field transients due to tropospheric lightning discharges, *Geophys. Res. Lett.*, 26, 1247–1250, 1999
- Pasko, V. P., Inan, U. S., Bell, T. F. and Taranenko, Y. N., Sprites produced by quasi-electrostatic heating and ionization in the lower ionosphere, *J. Geophys. Res.*, 102, 4529–4561, 1997
- Pasko, V. P., Stanley, M. A., Mathews, J. D., Inan, U. S. and Wood, T. G., Electrical discharge from a thundercloud top to the lower ionosphere, *Nature*, 416, 152–154, 2002
- Price, C., Greenberg, E., Yair, Y., Satori, G., Bor, J., Fukunishi, H., *et al.*, Ground-based detection of TLE-producing intense lightning during the MEIDEX mission on board the Space Shuttle Columbia, *Geophys. Res. Lett.*, 31(20), L20107, doi:10.1029/2004GL020711, 2004
- Rakov, V. A. and Uman, M. A., *Lightning: Physics and Effects*, Cambridge University Press, Cambridge. Chapter 14 (4/0-506), Cambridge UK, 2003
- Rodger, C., Red sprites, upward lightning and VLF perturbations, *Rev. Geophys.*, 37, 317–336, 1999
- Roussel-Dupré, R. and Gurevich, A. V., On runaway breakdown and upward propagating discharges, *J. Geophys. Res.*, 101, 2297–2311, 1996
- Roussel-Dupré, R., Gurevich, A. V., Tunnell, T. and Milikh, G. M., Kinetic-theory of runaway air breakdown, *Phys. Rev. E*, 49, 2257–2271, 1994

- Roussel-Dupré, R., Symbalisty, E., Taranenko, Y. and Yukhimuk, V., Simulations of high-altitude discharges initiated by runaway breakdown, *J. Atmos. Solar-Terr. Phys.*, 60, 917–940, 1998
- Rowland, H. L., Theories and simulations of elves, sprites and blue jets, *J. Atmos. Solar-Terr. Phys.*, 60, 831–844, 1998
- Rowland, H. L., Fernsler, R. F. and Bernhardt, P. A., Breakdown of the neutral atmosphere in the D region due to lightning-driven electromagnetic pulses, *J. Geophys. Res.*, 101, 7935–7945, 1996
- Rycroft, M. J., Introduction to the physics of sprites, elves and intense lightning discharges, in M. Füllekrug, *et al.* (ed.), *Sprites, Elves and Intense Lightning Discharges*, NATO Science Series, Dordrecht, 1–18, 2006
- Sato, M. and Fukunishi, H., Global sprite occurrence locations and rates derived from triangulation of transient Schumann resonance events, *Geophys. Res. Lett.*, 30(16), 1859, doi: 10.1029/2003GL017291, 2003
- Sentman, D. D., Wescott, E. M., Osborne, D. L., Hampton, D. L. and Heavner, M. J., Preliminary results from the Sprites94 campaign: red sprites, *Geophys. Res. Lett.*, 22, 1205–1208, 1995
- Shepherd, T. R., Rust, W. D. and Marshall, T. C., Electric fields and charges near 0° in stratiform clouds, *Mon. Weather Rev.*, 124, 919–938, 1996
- Stanley, M., Krehbiel, P., Brook, M., Moore, C., Rison, W. and Abrahams, B., High speed video of initial sprite development, *Geophys. Res. Lett.*, 26, 3201–3204, 1999
- Stenbaek-Nielsen, H. C., Moudry, D. R., Wescott, E. M., Sentman, D. D. and Sao-Sabbas F. T., Sprites and possible mesospheric effects, *Geophys. Res. Lett.*, 27, 3827–3832, 2000
- Su, H. T., Hsu, R. R., Chen, A. B., Wang, Y. C., Hsiao, W. S., Lai, W. C., *et al.*, Gigantic jets between a thundercloud and the ionosphere, *Nature*, 423, 974–976, 2003
- Sukhorukov, A. I. and Stubbe, P., Problems of blue jet theories, *J. Atmos. Solar-Terr. Phys.*, 60, 725–732, 1998
- Sukhorukov, A. I., Rubenchik, E. A. and Stubbe, P., Simulation of strong lightning pulse penetration into the lower ionosphere, *Geophys. Res. Lett.*, 23, 2911–2914, 1996
- Suzuki, T., Hayakawa, M., Matsudo, Y. and Michimoto, K., How do winter thundercloud systems generate sprite-inducing lightning in the Hokuriku area of Japan? *Geophys. Res. Lett.*, 33, L10806, doi: 10.1029/2005GL025433, 2006
- Symbalisty, E. M. D., Roussel-Dupré, R. A. and Yukhimuk, V. A., Finite volume solution of the relativistic Boltzmann equation for electron avalanche studies, *IEEE Trans. Plasma Sci.*, 26, 1575–1582, 1998
- Takahashi, T., Riming electrification as a charge generation mechanism in thunderstorms, *J. Atmos. Sci.*, 35, 1536–1548, 1978
- Takahashi, Y., Miyasato, R., Adachi, T., Sera, M., Uchida, A. and Fukunishi, H., Activities of sprites and elves in winter season, Japan, *J. Atmos. Solar-Terr. Phys.*, 65, 551–560, 2003

- Taranenko, Y. N. and Roussel-Dupré, R., High altitude discharges and gamma ray flashes: a manifestation of runaway air breakdown, *Geophys. Res. Lett.*, 23, 571–574, 1996
- van der Velde, O. A., Mika, A., Soula, S., Haldoupis, C., Neubert, T. and Inan, U. S., Observations of the relationship between sprite morphology and in-cloud lightning process, *J. Geophys. Res.*, 111, D15203, doi: 10.1029/2005JD 006879, 2006
- Vitello, P. A., Penetrante, B. M. and Bardsley, J. N., Simulation of negative-streamer dynamics in nitrogen, *Phys. Rev. E*, 49, 5574–5598, 1994
- Wescott, E. M., Sentman, D., Osborne, D., Hampton, D. and Heavner, M., Preliminary results from the Sprites94 aircraft campaign: 2. Blue jets, *Geophys. Res. Lett.*, 22, 1209–1212, 1995
- Wescott, E. M., Sentman, D. D., Heavner, M. J., Hampton, D. L., Osborne, D. L. and Vaughan Jr., O. H., Blue starters: brief upward discharges from an intense Arkansas thunderstorm, *Geophys. Res. Lett.*, 23, 2153–2156, 1996
- Wescott, E. M., Sentman, D. D., Heavner, M. J. Hampton, D. L. and Vaughan Jr., O. H., Blue jets: their relationship to lightning and very large hailfall, and their physical mechanisms for the brightness and ionization of blue starters and blue jets, *J. Geophys. Res.*, 106, 21549–21554, 1998a
- Wescott, E. M., Sentman, D. D., Heavner, M. J. Hampton, D. L., Lyons, W. A. and Nelson, T., Observations of ‘columniform’ sprites, *J. Atmos. Solar-Terr. Phys.*, 60, 733–740, 1998b
- Wescott, E. M., Sentman, D. D., Stenbaek-Nielsen, H. C., Huet, P., Heavner, M. J. and Moudry, D. R., New evidence for the brightness and ionization of blue starters and blue jets, *J. Geophys. Res.*, 106, 21549–21554, 2001
- Williams, E. R., Sprites, elves and glow discharge tubes, *Phys. Today*, 54, 41–47, 2001
- Williams, E. R. and Yair, T., The microphysical and electrical properties of sprite-producing thunderstorms, in M. Füllekrug, *et al.* (ed.), *Sprites, Elves and Intense Lightning Discharges*, NATO Science Series, Dordrecht, 57–83, 2006
- Williams, E., Downes, E., Boldi, R., Lyons, W. and Heckman, S., Polarity asymmetry of sprite-producing lightning: a paradox? *Radio Sci.*, 42, RS2517, doi: 10.1029/2006RS003488, 2007
- Wilson, C. T. R., The electric field of a thundercloud and some of its effects, *Proc. Phys. Soc. London*, 37, 32D–37D, 1925
- Yashunin, A. A., Mareev, E. A. and Rakov, V. A., Are lightning M components capable of initiating sprites and sprite halos? *J. Geophys. Res.*, 112, D10109, doi:10.1029-2006JD007631, 2007
- Yukhimuk, V., Roussel-Dupré, R. A. and Symbalisty, E. M. D., On the temporal evolution of red sprites: runaway theory versus data, *Geophys. Res. Lett.*, 26, 679–682, 1999
- Yukhimuk, V., Roussel-Dupré, R. A., Symbalisty, E. M. D. and Taranenko, Y., Optical characteristics of red sprites produced by runaway air breakdown, *J. Geophys. Res.*, 103, 11473–11482, 1998
- Zabotin, N. A. and Wright, J. W., Role of meteoric dust in sprite formation, *Geophys. Res. Lett.*, 28(13), doi:10. 1029/2000GL012699, 2001

---

## *Chapter 17*

# The effects of lightning on the ionosphere/magnetosphere

*Y. Hobara<sup>1,3</sup> and M. Hayakawa<sup>2,3</sup>*

---

### **17.1 Introduction**

The phenomena and effects of lightning discharges are discussed in other chapters of this monograph, and hence this chapter will deal with the effect of lightning onto the upper atmosphere such as the ionosphere and magnetosphere. There are a few possible effects of lightning on the ionosphere/magnetosphere, but we restrict our attention to the following two phenomena: (1) lightning-induced whistlers and (2) ionospheric Alfvén resonators (IARs). The former well-known whistlers are defined generally by signals in the extremely low frequency (ELF) and very low frequency (VLF) bands of causative lightning discharges that travel through the ionospheric/magnetospheric plasma along the Earth's magnetic field. Then, there have been already published a few good reviews on the topic of whistlers (Helliwell, 1965; Park, 1982; Hayakawa, 1995; Rakov and Uman, 2003). On the other hand, the latter phenomena (IARs) are a rather new effect even for space physicists, and hence the generation mechanism itself of IARs is not completely understood. At any rate IARs are characterized by the resonance phenomena in the frequency range below the conventional Schumann resonance. Their morphological characteristics and their interpretation in terms of lightning discharges are presented in this chapter.

### **17.2 Lightning-induced whistlers in the ionosphere/magnetosphere**

#### *17.2.1 General description of whistlers*

We present the brief history of whistlers. Barkhausen (1919) is generally credited with the discovery of whistlers. He observed whistling tones on German army radio receivers that were used to eavesdrop on Allied army telephone conversations and

<sup>1</sup>The University of Electro-Communications (UEC), Graduate School of Informatics and Engineering, 1-5-1 Chofugaoka, Chofu Tokyo, 182-8585, Japan

<sup>2</sup>UEC, Advanced Wireless Communications Research Center, Chofu Tokyo, Japan

<sup>3</sup>UEC, Earth Environment Research Station, Chofu Tokyo, Japan

concluded that they were not the noise inside the receiver but due to the origin outside the receiver. Additional observations of whistlers and related VLF/ELF noises (recently called VLF/ELF emissions) were published by Burton and Boardman (1933). There were very few additional significant developments in the understanding of whistlers until the landmark work of Storey (1953). With taking into account the earlier theoretical work by Eckersley (1931, 1935) on the wave propagation in an anisotropic plasma, Storey concluded that the whistlers observed at one location are originated in lightning discharges in the opposite hemisphere and then propagated in the magnetosphere along the Earth's magnetic field lines to the hemisphere of the observer. Additionally, he suggested that, in order to explain the observed dispersion, the electron density a few Earth radii away, in the remote part of the propagation path, must be of order of hundreds of electrons per cubic centimetres, providing the first evidence that plasma was present far beyond the ionospheric F layer. Hence, the use of whistlers opened a new era for space physics. There is a sizable literature on whistles, including Helliwell (1965), Walker (1976), Hayakawa and Tanaka (1978), Park (1982), Al'pert (1990), Hayakawa and Ohta (1992) and Hayakawa (1995).

Whistlers are electromagnetic signals with a frequency spectrum in the range from approximately 100 Hz to over 10 kHz, which are originated in lightning discharges in the atmosphere, penetrate into the ionosphere and then propagate in the magnetosphere approximately along the Earth's magnetic field lines to the opposite hemisphere. Here the waves again traverse the ionosphere, this time in the downward direction and are observable in the conjugate point on the Earth's surface. The main frequency range of whistlers is ELF and VLF, which are less than the local electron plasma frequency and the local gyrofrequency (the definition of these characteristic frequencies is given later), and this frequency range is called 'whistler-mode' branch. Propagation along the Earth's magnetic field is made possible by trapping waves in field-aligned density irregularities (the so-called ducts), so that these whistlers are named ducted whistlers as in Figure 17.1(a) and (c). The physics of the whistler-mode propagation is such that the higher frequencies in the signal travel faster than lower ones and hence the higher frequencies arrive at an observing point on the Earth's surface in the conjugate point, earlier than the lower frequencies. This is the reason why we observe a descending tone as shown in Figure 17.1(b). If the whistler electromagnetic signal is converted into an audio signal, the audio signal will sound like a whistle, and this is the reason why we call it a whistler. A less commonly observed type of whistlers is the so-called 'nose' whistler as shown in Figure 17.2, for which there is a minimum propagation time, corresponding to a maximum propagation speed, at one 'nose' frequency, the frequencies below and above that value travelling slower and arriving increasingly later. The more commonly observed whistler as in Figure 17.1(b) represents simply the lower frequency fraction of the nose whistler as shown in Figure 17.2(a). Apparently, only a small fraction of lightning flashes produces ducted whistlers, but probably a major of flashes produce electromagnetic signals that propagate through the ionosphere and then propagate in the magnetosphere both across and along the magnetic field lines as 'non-ducted' whistlers, travelling in the magnetosphere until their energy is dissipated as shown in Figure 17.1(d).

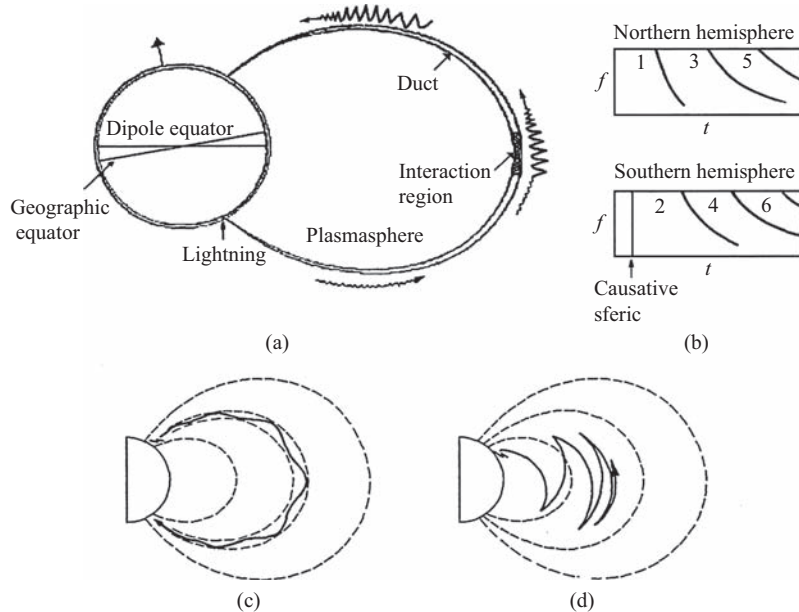


**Figure 17.1** (a) Typical path of a ducted whistler within the plasmasphere, shown together with the waveform of the ducted whistler signal before, during and after its interaction with cyclotron-resonant electrons in the magnetospheric equatorial region. (b) Frequency versus time curves (dynamic spectra) for a whistler traversing a path that echoes from hemisphere to hemisphere along a geomagnetic field as observed at conjugate points in the northern and southern hemispheres. The causative sferic is also indicated: it was produced by a lightning discharge in the southern hemisphere. Potential ray paths (solid lines) for ducted (c) and non-ducted (d) whistler-mode propagation in the magnetosphere [adapted from Rakov and Uman (2003)]

It follows that non-ducted whistlers can only be observed on board satellites in the magnetosphere and not on the Earth's surface. Diagrams showing idealized paths taken by ducted and non-ducted whistlers are presented in Figure 17.1(c) and (d). An idealized time-domain whistler spectrum is shown in Figure 17.3(a) and idealized plots of frequency versus time in Figure 17.3(b). The square root of inverse frequency versus time is plotted in Figure 17.3(c).

### 17.2.2 Theoretical background

#### 17.2.2.1 Characterization of the ionosphere and magnetosphere

The ionosphere is composed of plasmas (electrons and ions) and is a complex structure made up of three major layers (D, E and F regions) as in Figure 17.4 for temperate latitudes near sunspot maximum. The lowest layer, the D region extends in

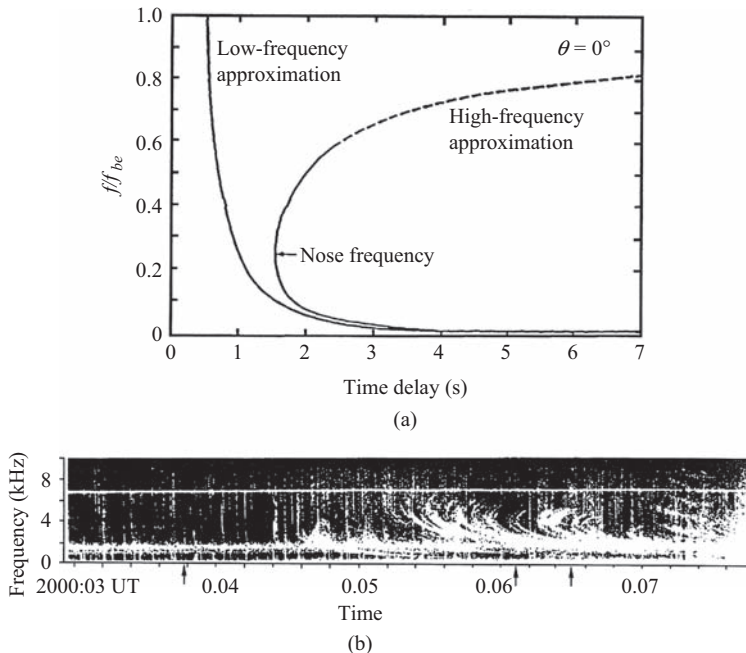


*Figure 17.2 (a)* Normalized frequency versus time delay for longitudinal propagation ( $\theta = 0^\circ$ ) over a path of length  $c/B_0$ . *(b)* An example of observed spectrograms of nose whistlers. The left-hand arrow indicates the causative sferic for the two whistler groups indicated by the right-hand two arrows [adapted from Hayakawa (1995)]

height from approximately 40 to 90 km. Its typical electron density is of the order of  $10^9 \text{ m}^{-3}$  ( $10^3 \text{ cm}^{-3}$ ) at day and diminished to a negligible value after sunset. The E region extends between approximately 90 and 160 km. The electron density in this region typically has a value above  $10^{11} \text{ m}^{-3}$  ( $10^5 \text{ cm}^{-3}$ ) in the daytime, but it is about two orders of magnitude lower. Above the E region is the F region, which extends to a height of 1000 km or so. The peak (maximum) F region electron density has an average value of approximately  $2 \times 10^{12} \text{ m}^{-3}$  ( $2 \times 10^6 \text{ cm}^{-3}$ ) during the day and  $2 \times 10^{11} \text{ m}^{-3}$  ( $2 \times 10^5 \text{ cm}^{-3}$ ) at night. As shown in Figure 17.4, the ionospheric electron density varies over four orders of magnitude.

Above the F region of the ionosphere, at heights over approximately 1000 km, is called the ‘magnetosphere’, where the motions of plasmas (electrons and ions) are strongly influenced by the Earth’s magnetic field. The inner part of the magnetosphere is called the plasmasphere. It extends outward by four or five Earth’s radii to the plasmapause, where the plasma density decreases abruptly.

### 17.2.2.2 General equations

We give a general theoretical overview of the interaction of electromagnetic waves with the charged particles of the ionosphere and magnetosphere. We consider an

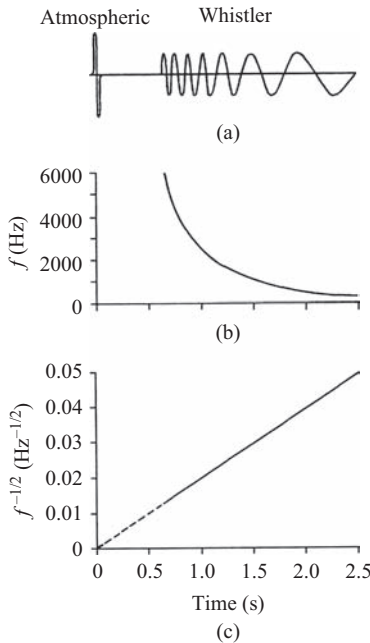


Figure 17.3 Idealized time-domain waveform and frequency content of a ducted whistler as a function of time. (a) The waveform; each cycle represents 400 Hz on the original; (b) The actual frequency  $f$  versus time  $t$ ; (c)  $f^{-1/2}$  versus  $t$  [adapted from Helliwell (1965)]

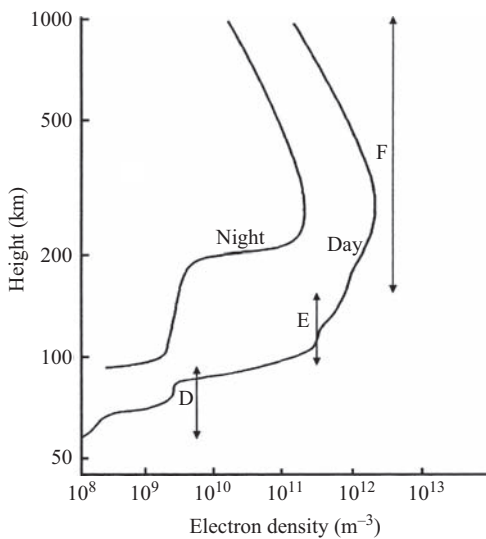


Figure 17.4 Idealized ionization profiles of the Earth's ionosphere at temperate latitudes near sunspot maximum [adapted from Yeh and Liu (1972)]

electron having electric charge  $-e$  ( $e > 0$ ) and mass  $m$  that moves with velocity  $\mathbf{v}$ . Only the motion of electrons can be considered because the mass of electrons is significantly lighter than that of ions (e.g. mass of protons is approximately 2000 times heavier than that of electrons). The electrons are influenced by the wave electric and magnetic fields as well as the DC Earth's magnetic field ( $\mathbf{B}_0$ ) during the propagation of electromagnetic waves and the currents generated by the electrons regenerate the electromagnetic waves. For electrons the equation of motion in the Cartesian coordinate is given by

$$m \frac{d\mathbf{v}}{dt} = -e(\mathbf{E} + \mathbf{v} \times (\mathbf{B}_0 + \mathbf{B})) \quad (17.1)$$

The electromagnetic electric and magnetic field vectors are  $\mathbf{E}$  and  $\mathbf{B}$  and the ambient Earth's magnetic field is  $\mathbf{B}_0 = B_0 \mathbf{a}_z$  ( $\mathbf{a}_z$  is the unit vector directed towards positive  $z$  direction). Here collisions between electrons and heavy neutral particles are ignored. We are also justified in neglecting the force on the electron from the time-varying magnetic field ( $\mathbf{v} \times \mathbf{B}$ ). The force due to the time-varying magnetic field is generally negligible in comparison with the force due to the electric field, since the ratio of these forces is roughly  $v/c$  and  $v/c \ll 1$  where  $c$  is the speed of light. By assuming the time dependence of  $e^{j\omega t}$  ( $\omega$  is angular frequency and  $j = \sqrt{-1}$ ) the equation of motion of electrons will be as follows:

$$j\omega \begin{bmatrix} v_x \\ v_y \\ v_z \end{bmatrix} = -\frac{e}{m} \begin{bmatrix} E_x \\ E_y \\ E_z \end{bmatrix} - \frac{eB_0}{m} \begin{bmatrix} v_y \\ -v_x \\ 0 \end{bmatrix} \quad (17.2)$$

Then we obtain the three components of electron velocities driven by the wave electric field and ambient Earth's magnetic field as follows:

$$\begin{aligned} v_x &= -\frac{e j \omega}{m} \frac{E_x - \omega_H E_y}{\omega_H^2 - \omega^2} \\ v_y &= -\frac{e}{m} \frac{\omega_H E_x + j \omega E_y}{\omega_H^2 - \omega^2} \\ v_z &= -\frac{e}{m j \omega} \frac{E_z}{\omega_H} \end{aligned} \quad (17.3)$$

where  $\omega_H$  is the electron angular gyrofrequency given by  $\omega_H (= 2\pi f_H) = eB_0/m$ , which is easily calculated by the form  $f_H(\text{Hz}) = 28B_0(\text{nT})$ . This gyrofrequency means the angular frequency at which the electron makes circular orbits in a plane perpendicular to the Earth's magnetic field. The current density is given by

$$\mathbf{J} = -N e \mathbf{v} \quad (17.4)$$

where  $N$  is the electron density. Each component of this current is shown by using (17.4).

$$\begin{aligned} J_x &= \frac{Ne^2}{m} \frac{j\omega E_x - \omega_H E_y}{\omega_H^2 - \omega^2} \\ J_y &= \frac{Ne^2}{m} \frac{\omega_H E_x + j\omega E_y}{\omega_H^2 - \omega^2} \\ J_z &= \frac{Ne^2}{m} \frac{E_z}{j\omega} \end{aligned} \quad (17.5)$$

Then the conductivity tensor  $\langle\sigma\rangle$  is given by

$$\begin{aligned} \sigma_{xx} &= \frac{\frac{Ne^2}{m} j\omega}{\omega_H^2 - \omega^2} = \sigma_{yy} \\ \sigma_{xy} &= -\frac{\frac{Ne^2}{m} \omega_H}{\omega_H^2 - \omega^2} = -\sigma_{yx} \\ \sigma_{zz} &= \frac{\frac{Ne^2}{m}}{j\omega} \\ \sigma_{xz} = \sigma_{zx} = \sigma_{yz} = \sigma_{zy} &= 0 \end{aligned} \quad (17.6)$$

and the dielectric tensor  $\langle\varepsilon\rangle$  is also given by using  $\langle\varepsilon\rangle = \varepsilon_0 \langle I \rangle - j \langle \sigma \rangle / \omega$

$$\begin{aligned} \varepsilon_{xx} = \varepsilon_{yy} &= \varepsilon_0 \left( 1 + \frac{\omega_p^2}{\omega_H^2 - \omega^2} \right) \\ \varepsilon_{xy} = -\varepsilon_{yx} &= j\varepsilon_0 \frac{\omega_p^2 \omega_H}{\omega(\omega_H^2 - \omega^2)} \\ \varepsilon_{zz} &= \varepsilon_0 \left( 1 - \frac{\omega_p^2}{\omega^2} \right) \\ \varepsilon_{xz} = \varepsilon_{zx} = \varepsilon_{yz} = \varepsilon_{zy} &= 0 \end{aligned} \quad (17.7)$$

where  $\langle I \rangle$  is a unit tensor and the electron plasma frequency is defined by  $\omega_p^2 (= (2\pi f_p)^2) = Ne^2/m\varepsilon_0$  ( $\varepsilon_0$ , dielectric constant of free space) ( $f_p$ (kHz) =  $9\sqrt{N}(\text{cm}^{-3})$ )

Consider now Maxwell's equations for the case of time-harmonic electromagnetic fields that vary in space as

$$\exp[j(\omega t - \mathbf{k} \cdot \mathbf{r})] \quad (17.8)$$

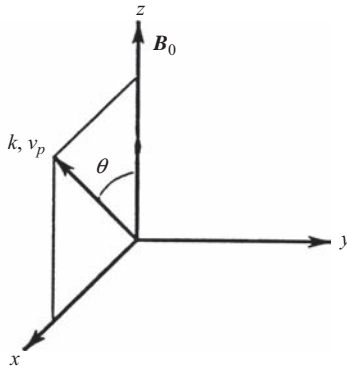


Figure 17.5 Coordinate system for the wave propagation. The Earth's magnetic field  $\mathbf{B}_0$  is in the  $z$  direction and the wave propagation ( $\mathbf{k}$ ) is in the  $x$ - $z$  plane and makes an angle  $\theta$  with  $\mathbf{B}_0$

Here we have used the time dependence assumed previously and now include a spatial variation specified by the term of  $-j \mathbf{k} \cdot \mathbf{r}$ , where  $\mathbf{k}$  is the propagation vector (or wave normal direction) (its direction is the direction of wave propagation and its magnitude  $k$  equals  $2\pi$  divided by the wavelength) and  $\mathbf{r}$  is a position vector. Figure 17.5 is the coordinate system of our propagation study, in which the static Earth's magnetic field  $\mathbf{B}_0$  is already assumed to be in the  $z$  axis and the wave propagation ( $\mathbf{k}$ ) is assumed to be in the  $x$ - $z$  plane and to make an angle ( $\theta$ ) with  $\mathbf{B}_0$ .

For an electromagnetic wave with temporal and spatial variation given by (17.8), we can write Maxwell's equations as ( $\mu_0$ , magnetic permeability of free space)

$$-jk \times \mathbf{E} = -j\omega \mu_0 \mathbf{H} \quad (17.9)$$

$$-jk \times \mathbf{H} = j\omega \mathbf{D} \quad (17.10)$$

Combining the above two equations yields to

$$\mathbf{k} \times (\mathbf{k} \times \mathbf{E}) + \omega^2 \mu_0 \langle \epsilon \rangle \mathbf{E} = 0 \quad (17.11)$$

This equation is the so-called wave equation of electromagnetic waves in the anisotropic plasma with the presence of  $\mathbf{B}_0$ . Equation (17.11) is decomposed into the  $(x, y, z)$  components as follows:

$$\begin{bmatrix} k^2 \cos^2 \theta - \omega^2 \mu_0 \epsilon_{xx} & -\omega^2 \mu_0 \epsilon_{xy} & -k^2 \sin \theta \cos \theta \\ \omega^2 \mu_0 \epsilon_{xy} & k^2 - \omega^2 \mu_0 \epsilon_{xx} & 0 \\ -k^2 \sin \theta \cos \theta & 0 & k^2 \sin^2 \theta - \omega^2 \mu_0 \epsilon_{zz} \end{bmatrix} \begin{bmatrix} E_x \\ E_y \\ E_z \end{bmatrix} = 0 \quad (17.12)$$

The solution to any equation of this form (i.e. in order to have a non-trivial solution ( $\mathbf{E}$ )) is found by setting to zero the determinant of the matrix in (17.12).

This result is inserted in (17.12), which can be solved for the wave electric field. Once both the electric field and the propagation direction are known, the wave magnetic field can be calculated from (17.9).

The phase velocity  $v_p$  and group velocity  $v_g$  can be expressed by a vector representation as

$$\begin{aligned} v_p &= \frac{\omega}{\mathbf{k}} = \frac{\omega}{k^2} \mathbf{k} \\ v_g &= \frac{\partial \omega}{\partial \mathbf{k}} \end{aligned} \quad (17.13)$$

On one hand, the phase velocity  $v_p$  is defined as the direction normal to the wave front, so that it is easily understood as being parallel to  $\mathbf{k}$ . On the other hand, the group velocity  $v_g$  is defined as the direction of electromagnetic wave energy (ray direction) and the most interesting peculiarity of the anisotropic plasma is that  $v_g$  is not parallel to  $v_p$  for the general oblique propagation (Please consult Helliwell (1965) and Park (1982) and Hayakawa (1995) for further details.). Only when  $\theta = 0$ , the direction of  $v_g$  is parallel to  $v_p$  and the value of  $v_g$  is easily given by  $v_g = \partial(n\omega)/\partial\omega$  ( $n$ : refractive index).

### 17.2.2.3 Special cases of longitudinal and perpendicular propagation and general oblique propagation

By using (17.12), we study first the special cases of propagation, i.e. (1) longitudinal propagation ( $\theta = 0$ ) and (2) transverse propagation ( $\theta = \pi/2$ ). The introduction and details of the following plasma waves are found in the books by Stix (1962), Allis *et al.* (1963), Ginzburg (1970), Budden (1988), Al'pert (1990), Parks (1991), Nicholson (1991), Walker (1993) and Kivelson and Russel (1995).

#### 1. Longitudinal propagation

This longitudinal propagation means that the propagation vector ( $\mathbf{k}$ ) is parallel to the Earth's magnetic field ( $\mathbf{B}_0$ ); i.e.  $\theta = 0$ . Putting  $\theta = 0$  in (17.12) yields the following wave equation.

$$\begin{bmatrix} k^2 - \omega^2 \mu_0 \epsilon_{xx} & -\omega^2 \mu_0 \epsilon_{xy} \\ \omega^2 \mu_0 \epsilon_{xy} & k^2 - \omega^2 \mu_0 \epsilon_{xx} \end{bmatrix} \begin{bmatrix} E_x \\ E_y \end{bmatrix} = 0 \quad (17.14)$$

$$(\epsilon_{zz}) E_z = 0 \quad (17.15)$$

Since (17.15) represents only the plasma oscillation ( $\omega = \omega_p$ ), we do not discuss this oscillation further. The presence of non-trivial solution of  $E_x$  and  $E_y$  in (17.14) requires the determinant of the coefficients in (17.14) equals to zero. This leads to the following:

$$[k^2 - \omega^2 \mu_0 (\epsilon_{xx} - j\epsilon_{xy})] [k^2 - \omega^2 \mu_0 (\epsilon_{xx} + j\epsilon_{xy})] = 0 \quad (17.16)$$

Equation (17.16) is found to yield the following two mode waves.

(i) Right-handed polarized wave

Taking the first term on the left-hand side of (17.16) being zero, the following dispersion relation is obtained:

$$n^2 = \frac{k^2 c^2}{\omega^2} = 1 + \frac{\omega_p^2}{\omega(\omega_H - \omega)} = R \quad (17.17)$$

where  $n$  is called refractive index, and this wave is right-handed circularly polarized as shown below. The rotation of wave electric field is exactly the same as the gyration of electrons in the Earth's magnetic field.

$$j \frac{E_x}{E_y} = -1 \quad (17.18)$$

This wave mode is the so-called 'whistler' mode when the wave frequency is below  $\omega_H$ .

(ii) Left-handed polarized wave

Similarly taking the second term on the left-hand side of (17.16) being zero, the dispersion relation for this wave is

$$n^2 = \frac{k^2 c^2}{\omega^2} = 1 - \frac{\omega_p^2}{\omega(\omega_H + \omega)} = L \quad (17.19)$$

and this wave is found to be left-handed circularly polarized as is evidenced by the following relation:

$$j \frac{E_x}{E_y} = 1 \quad (17.20)$$

## 2. Transverse propagation

We now consider the transverse propagation characterized by  $\theta = \pi/2$ ; i.e. propagation direction ( $\mathbf{k}$ ) is perpendicular to  $\mathbf{B}_0$ . In this case, the wave equation (17.12) becomes

$$\begin{bmatrix} -\omega^2 \mu_0 \epsilon_{xx} & -\omega^2 \mu_0 \epsilon_{xy} \\ \omega^2 \mu_0 \epsilon_{xy} & k^2 - \omega^2 \mu_0 \epsilon_{xx} \end{bmatrix} \begin{bmatrix} E_x \\ E_y \end{bmatrix} = 0 \quad (17.21)$$

$$(k^2 - \omega^2 \mu_0 \epsilon_{zz}) E_z = 0 \quad (17.22)$$

That is, there exist two mode waves as follows.

(i) Ordinary wave (O wave) ( $\mathbf{k} \perp \mathbf{B}_0$  and  $\mathbf{E} \parallel \mathbf{B}_0$ )

The wave mode obtained by (17.22) is characterized by its electric field being parallel to  $\mathbf{B}_0$  ( $E_z \neq 0$ ) with  $E_x = E_y = 0$ . By setting the first term of

the left-hand side of (17.22) to zero, we obtain the following dispersion relation for the ordinary mode:

$$n^2 = 1 - \frac{\omega_p^2}{\omega^2} = P \quad (17.23)$$

This wave is linearly polarized and (17.23) is identical to the dispersion relation of the plasma oscillation with no effect of the Earth's magnetic field (17.15). This is the reason why we use the terminology of 'ordinary' wave.

- (ii) Extraordinary wave (X wave) ( $\mathbf{k} \perp \mathbf{B}_0$  and  $\mathbf{E} \perp \mathbf{B}_0$ )

In order to have non-trivial solutions ( $E_x \neq 0, E_y \neq 0$ ) in (17.21), the determinant of the matrix on the left-hand side of (17.21) is set to zero. This leads to the following dispersion relation:

$$n^2 = \frac{\epsilon_{xx}^2 + \epsilon_{xy}^2}{\epsilon_{xx}} = \frac{2RL}{R + L} \quad (17.24)$$

The wave polarization of this extraordinary wave is estimated from (17.21) as

$$\frac{E_x}{E_y} = -\frac{\epsilon_{xy}}{\epsilon_{xx}} = -j \frac{\omega_p^2 \omega_H}{\omega(\omega_p^2 + \omega_H^2 - \omega^2)} \quad (17.25)$$

so that the wave electric field is elliptically polarized in the  $xy$  plane.

### 3. Cut-offs and resonances

A cut-off is defined as a frequency at which the value  $k^2$  goes to zero (or  $n^2 \rightarrow 0$ ), so that these cut-off frequencies can be obtained by setting the refractive index  $n^2 \rightarrow 0$  (or  $k^2 \rightarrow 0$ ). Hence we expect that the wavelength and phase velocity become infinity. When the wave propagates through the plasma with a spatial gradient of refractive index including  $n^2 = 0$ , the wave is reflected at the point of a cut-off.

The cut-off frequencies can be easily estimated by setting  $n^2 \rightarrow 0$  in the dispersion relation for each mode. The cut-off frequencies for the longitudinal propagation can be obtained from (17.17) and (17.19).

$$\omega_R = \frac{\omega_H}{2} + \sqrt{\omega_p^2 + \frac{\omega_H^2}{4}} \quad (17.26)$$

$$\omega_L = -\frac{\omega_H}{2} + \sqrt{\omega_p^2 + \frac{\omega_H^2}{4}} \quad (17.27)$$

Similarly the cut-off frequencies for the transverse propagation are obtained from (17.23) and (17.24). For the extraordinary wave, the cut-off frequencies occur when  $n^2 \rightarrow 0$  (or  $R = 0$  or  $L = 0$ ), so that they are identical to those for the

longitudinal propagation,  $\omega_R$  and  $\omega_L$ . For the ordinary wave, the cut-off frequency is expected from  $n^2 = P = 0$ ; that is,  $\omega_p$ .

Next we explain the resonance. Resonance is defined at a frequency at which  $n^2 = \infty$  ( $k^2 \rightarrow \infty$ ). When the wave approaches a resonance condition,  $k^2$  goes to infinity so that the phase velocity becomes zero, then the wave is mainly dissipated due to the significant interaction with plasma.

The resonance frequencies for the longitudinal propagation are obtained when the denominator of (17.17) and (17.19) vanishes. That is, the right-handed polarized ( $R$ ) mode exhibits a resonance at  $\omega = \omega_{Hi}$ , and at this frequency the wave electric field continuously accelerates electrons because the wave field is in phase with the gyro-motion of electrons. This resonance is called electron cyclotron resonance. Similarly the left-handed polarized ( $L$ ) mode is found to have a resonance at  $\omega = \omega_{Hi}$  (ion gyrofrequency). Though in our former equations we have only considered the motion of electrons, the motion of ions becomes important when the frequency becomes smaller than  $\omega_{Hi}$  and it is very easy for us to take into account the effect of ions.

The resonance for the transverse propagation can be obtained exactly in the same way as above. The ordinary wave has no resonance because the denominator of (17.23) may not vanish except  $\omega = 0$ . On the other hand, the extraordinary wave ((17.24)) exhibits a resonance at a particular frequency of  $\omega_{UHR}$  (upper hybrid resonance frequency), so that the wave electromagnetic energy is converted to the upper hybrid oscillation. The similar hybrid resonance is observed as well at  $\omega_{LHR}$ .

#### 4. Oblique propagation

We have discussed two representative cases of propagation, that is, longitudinal and transverse, and these gave us a lot of useful ideas on the propagation characteristics of electromagnetic waves in the anisotropic plasma. Here, the dispersion relation of the waves propagating obliquely to  $\mathbf{B}_0$  is obtained by solving the following equation by setting the determinant of the coefficients of  $\mathbf{E}$  in (17.12) to zero.

$$An^4 - Bn^2 + C = 0 \quad (17.28)$$

$$\begin{aligned} A &= \epsilon_{xx}\sin^2\theta + \epsilon_{zz}\cos^2\theta \\ B &= (\epsilon_{xx}^2 + \epsilon_{xy}^2)\sin^2\theta + \epsilon_{xx}\epsilon_{zz}(1 + \cos^2\theta) \\ C &= \epsilon_{zz}(\epsilon_{xx}^2 + \epsilon_{zy}^2) \end{aligned} \quad (17.29)$$

$$\begin{aligned} A &= S\sin^2\theta + P\cos^2\theta \\ B &= RL\sin^2\theta + PS(1 + \cos^2\theta) \\ C &= PRL \end{aligned} \quad (17.30)$$

$$S = \frac{1}{2}(R + L), D = \frac{1}{2}(R - L) \quad (17.31)$$

Equation (17.28) gives us the presence of two characteristic modes in the plasma at any frequency as

$$n^2 = \frac{B \pm \sqrt{B^2 - 4AC}}{2A} \quad (17.32)$$

The dispersion relation ( $\omega$ - $k$  diagram) of different modes in the plasma is illustrated in Figure 17.6 for different  $\theta$  values. In the figure, the longitudinal propagation ( $\theta=0$ ) is indicated by  $\parallel$ , while the transverse propagation ( $\theta=\pi/2$ ) by  $\perp$ . Shaded regions correspond to the oblique propagation. The plasma condition of  $\omega_p > \omega_H$  (the situation nearly almost in all regions in the magnetosphere) is assumed in Figure 17.6, and Figure 17.6 indicates the presence of three frequency branches as follows.

(i) Free space waves ( $\omega > \omega_p, \omega_H$ )

This plasma wave branch is called quasi-free-space mode. There are the extraordinary mode ( $R$ - $X$  and  $Z$  mode) and ordinary mode ( $L$ - $O$ ), but this branch is not so interesting in our chapter, so that we do not go into the details of this branch. Please look at the books by Parks (1991) and Kivelson and Russel (1995) for further details and the corresponding wave phenomena including the  $Z$  mode in the magnetosphere.

(ii) Whistler-mode branch ( $\omega_{Hi} < \omega < \omega_H$ )

This is the so-called ‘whistler-mode’ branch, which is of our main interest for this chapter. In this frequency range we have only this whistler mode because another  $L$  wave is evanescent (i.e. non-propagating) ( $n^2 = L < 0$  in this frequency). This whistler mode wave has a right-handed polarization and tends to propagate along  $\mathbf{B}_0$ . This is discussed later in some details.

(iii) Alfvén wave branch ( $\omega < \omega_{Hi}$ )

This frequency range is Alfvén wave branch, and there exist two characteristic modes (i.e. Alfvén wave and modified Alfvén wave). Alfvén wave is considered to be the counterpart of whistler mode in the sense that it is left-handed polarized and its ray direction tends to be very parallel to  $\mathbf{B}_0$ . Modified Alfvén wave is considered to be the lower frequency part of the whistler branch. The Alfvén wave is responsible for IARs to be discussed in the next section.

#### 17.2.2.4 Whistler propagation, dispersion relation and the use of whistlers as a diagnostic tool of magnetospheric plasma

Many important properties of whistlers can be explained by using the theory outlined in sections 17.2.2.2 and 17.2.2.3. To understand how the electromagnetic waves from lightning propagate into the ionosphere, we first examine the application of Snell’s law to the boundary between the free space and ionosphere:

$$\sin \theta_i = n_i \sin \theta_t \quad (17.33)$$

where  $n_i$  is the refractive index of the ionosphere and that of free space is taken as unity. And  $\theta_i$  is the incidence angle measured from the vertical downward and  $\theta_t$  is the transmitted angle in the ionosphere measured from the vertical upward.

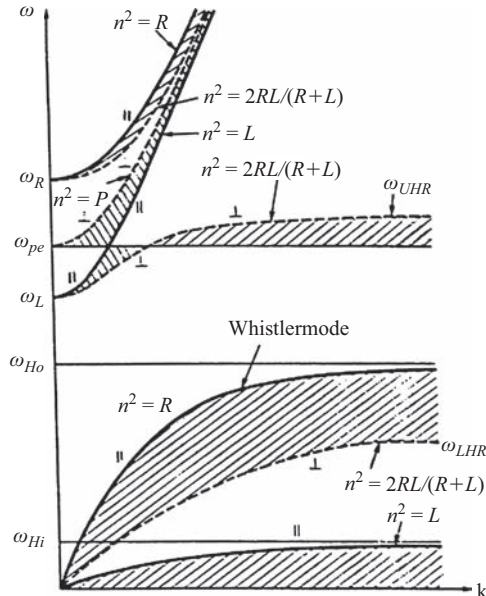


*Figure 17.6 Dispersion curve in the form of  $\omega$ - $k$  diagram for an electron–ion plasma for the case of  $\omega_p = 2\omega_H$ .  $\parallel$  and  $\perp$  mean the longitudinal ( $\theta = 0$ ) and transverse propagation ( $\theta = \pi/2$ ) and the dispersion curve for oblique propagation must lay in the shaded area.  $\omega_R$  and  $\omega_L$  are the cut-off frequencies of right- and left-handed polarized mode waves. While  $\omega_{UHR}$  and  $\omega_{LHR}$  are the upper and lower hybrid resonance frequencies,  $n^2 = R$  and  $n^2 = L$  for  $\theta = 0$  indicate the right- and left-handed circularly polarized waves, respectively*

We show that  $n_i \gg 1$  and hence  $\theta_t$  in the ionosphere must be nearly zero; that is, essentially vertical for any incidence angle ( $\theta_i$ ) of the wave in free space impinging on the boundary. We now derive  $n_i$  for the expected case, a wave in the ionosphere/magnetosphere propagating along the magnetic field (e.g. ducted wave ( $\theta = 0$ ) and trapped by a field-aligned plasma column (duct)). Using (17.17), we can have the whistler-mode refractive index to good approximation as

$$n_i^2 = \frac{\omega_p^2}{\omega(\omega_H - \omega)} \quad (17.34)$$

This refractive index exceeds much that of free space. For example, at the ionospheric F region, where the electron density is near  $10^6 \text{ cm}^{-3}$ ,  $n_i$  is close to 100 at the frequencies near 5 kHz. After the whistler enters the magnetosphere, propagates along the magnetic field line and reaches the conjugate hemisphere on the ionosphere, the reverse interface situation happens. Shell's law can also be involved to show that if the wave normal direction is inside a relatively narrow angle around the vertical (this is called transmission cone), then it can traverse the

ionosphere and hence be detected on the ground. When the wave is ducted and also we consider the high-to-middle latitudes where the Earth's magnetic field is close to the vertical, this condition is easily satisfied. However, if not (e.g. at low latitudes), then the wave will be reflected (totally reflected) back into the magnetosphere.

Once the whistler wave is propagating along a magnetic field line, the time of propagation  $T(\omega)$  from the source to the receiver can be computed from a knowledge of the group velocity of the wave.

$$T(\omega) = \int_{path} \frac{ds}{v_g} \quad (17.35)$$

In the case of  $\theta=0$ ,  $v_g$  is easily estimated by  $v_g=\partial(n\omega)/(\partial\omega)$  and when  $\omega \ll \omega_H$  (the so-called low-frequency approximation in Figure 17.2(a)), (17.35) becomes

$$T(\omega) = \frac{1}{2c} \int_{path} \frac{\omega_p}{\sqrt{\omega\omega_H}} ds \quad (17.36)$$

We can define the dispersion  $D$  as

$$D = T(f)f^{1/2} = \frac{c}{2\sqrt{2\pi}} \int \frac{\omega_p}{\sqrt{\omega_H}} ds \quad (17.37)$$

which is independent of the wave frequency  $f$  and which can be determined only by the plasma conditions. This equation is known as the Eckersley dispersion law and is valid at frequencies far below the nose frequency. The fact that the dispersion  $D$  is independent of frequency is illustrated in Figure 17.3(c).

By using the more general equation (17.17) for a given path, the integral in (17.35) enables us to deduce a nose frequency  $f_n$  for which the propagation time is a minimum. For a homogeneous plasma, the nose frequency  $f_n=f_H/4$ , where  $\omega_H=2\pi f_H$ . The ionosphere does not contribute much to the observed time delays; the most important contribution is expected at the highest part of the path (equatorial plane) of the magnetosphere. So that, the latitudinal distribution of  $D$  enables us to deduce the electron density profile of the magnetospheric plasma, equatorial density versus path latitude (Park, 1982; Sazhin *et al.*, 1992) and the behaviour of plasmapause (Carpenter and Park, 1973; Corcuff, 1975).

## 17.3 IAR

### 17.3.1 Brief history and general introduction

Different kinds of resonance phenomena are known to exist in the near-Earth environment. From the higher frequency there is a transverse resonance in the Earth-ionosphere waveguide of lightning discharges in the ELF and VLF range (known as cut-off of tweek sferics) (e.g. Al'pert, 1974; Hayakawa *et al.*, 1994; Nickolaenko and Hayakawa, 2002). When we go to the lower frequency down to ELF range, we know

the presence of longitudinal resonance in the Earth–ionosphere waveguide due to lightning discharges, which is known as Schumann resonance (Nickolaenko and Hayakawa, 2002). Its fundamental frequencies are 8, 14, 20 Hz, etc. and recently the observation of the Schumann resonance intensity is found to serve as a kind of global thermometer (e.g. Williams, 1992; Nickolaenko and Hayakawa, 2002).

At the frequency below the Schumann resonance region, there is an additional resonance phenomenon called ‘IAR’, which is the topic of this section. Polyakov (1976) and Polyakov and Rapoport (1981) predicted theoretically the existence of such Alfvén quasi-resonances in the ionosphere, and the IAR plays an important role in the understanding of the physical phenomena in the coupled magnetosphere–ionosphere system (e.g. Trakhtengertz and Feldstein, 1991; Lysak, 1991; Pokhotelov *et al.*, 2000, 2001; Trakhtengertz *et al.*, 2000a, 2000b; Demekhov *et al.*, 2000a, 2000b). The fundamental idea of this IAR is that there is the presence of IAR due to the two regions of sharp boundary where the Alfvén velocity  $v_A = B_0^2/\mu_0 n_i m_i$  changes abruptly ( $B_0$  is the Earth’s magnetic field intensity, and  $m_i$  and  $n_i$  are the ion mass and density). One is the lowest ionosphere (D/E layer) and the other is the height of 500 to 1000 km. The resonance frequencies are found to range from 1 to 5 Hz and IAR appears as a fingerprint structure. However, the generation mechanism of this IAR is not yet agreed at the moment. As you imagine, there are two possibilities, that is, (1) magnetospheric origin; any noise in the upper magnetosphere or (2) lightning origin; that is, the effect of lightning discharges in the atmosphere. No matter whether the origin of IAR is either magnetospheric or lightning, the mode responsible for this IAR is left-handed polarized Alfvén mode as discussed in the previous section.

IAR was discovered at a middle-latitude station (Nizhni Novgorod, Russia) and at a high-latitude station (Kilpisjarvi, Finland) by Belyaev *et al.* (1987, 1990, 1999). Recently experimental evidence for the existence of IAR at high latitudes was confirmed by Demekhov *et al.* (2000a) by using the data at Kilpisjarvi observatory ( $L = 6$  corresponding to the geomagnetic latitude of  $66^\circ$ ). Yahnin *et al.* (2003) have studied diurnal and seasonal variations of spectral resonance structure (SRS) occurrence rate based on continuous observations for more than four years at a high-latitude station, Sodankylä ( $L = 5.2$ , geomagnetic latitude of  $64^\circ$ ). They have found a clear tendency of decrease in both the resonant frequencies and difference  $\Delta F$  from the minimum to maximum solar activity. The high-resolution measurements of IAR signatures during half a year were made also at a low-latitude station in Crete ( $L = 1.3$ , geomagnetic latitude of  $28^\circ$ ) by Bösinger *et al.* (2002).

In the present section the statistical properties of the SRS of IAR are presented on the basis of our results of continuous observations for more than two years at a mid-latitude observatory at Karimshino (Kamchatka, Russia;  $L = 2.1$ , geomagnetic latitude of  $46^\circ$ ) (Molchanov *et al.*, 2004; Hayakawa *et al.*, 2004), to be compared with the corresponding results at high ( $L = 5.2$ ) and low ( $L = 1.3$ ) latitudes. Because the latitudinal effect of peculiarities of IAR seems to be the most important factor to elucidate the generation mechanism of IAR, just like the latitudinal dependence of whistler occurrence rate. The details of the following characteristics are found in Hayakawa *et al.* (2004).

### 17.3.2 Observations and data processing

The continuous registration of the ultra-low frequency (ULF) magnetic field variations at the geophysical observatory, Karimshino started in June 2000. The observatory is located in Karimshino (geographic coordinates: 52.94°N, 158.25°E) at a distance of approximately 50 km from Petropavlovsk-Kamchatsky (see the details in Uyeda *et al.* (2002) and Gladych *et al.* (2002)). Three axial induction magnetometers are used to measure geomagnetic field variations in the frequency range 0.003–40 Hz. The sensitivity threshold is better than  $20 \text{ pT}/\sqrt{\text{Hz}}$  at a frequency of 0.01 Hz, and it corresponds to  $0.02 \text{ pT}/\sqrt{\text{Hz}}$  at the frequencies above 10 Hz. Sampling rate per channel is 150 sp/s and sampling resolution is 24 bit. The accuracy of absolute and relative (between channels) timing of digital data is 5 ms and better than 10  $\mu\text{s}$ , respectively.

Because of relatively high crust conductivity in the region of observations the vertical magnetic signal amplitude is low in comparison with the horizontal one. The amplitude of the vertical component in the frequency range 1–3 Hz is comparable with the sensor sensitivity. Thus, the resonant structures cannot be detected for the vertical component with the equipment used. The technique and results of the signal analysis for two horizontal components are presented below.

The signal spectra were calculated with the Welch's method in the range 0.1–5 Hz with the frequency resolution 0.05 Hz in the time window 30 min and many parameters of resonance structures were estimated. An example of the evolution of night-time dynamic frequency spectra is shown in Figure 17.7 for about one week from 12 to 18 September 2000. The bottom three panels illustrate the dynamic spectra for the three magnetic field components ( $H$ ,  $D$  and  $Z$ ), respectively. The second panel indicates the coherency between the two magnetic components  $H$  and  $D$  and the third panel indicates the wave polarization by using the two horizontal magnetic field components. The top panel indicates the temporal evolution of  $K_p$  index (geomagnetic activity) for comparison. Figure 17.8 is another type of presentation of Figure 17.7 in the form of spectral power density versus wave frequency for the two horizontal components  $D$  (in thick line) and  $H$  (in thin line). The local time is changed from LT = 19 h to LT = 06 h on a particular day of 13/14 September 2000. We can recognize from this figure the IAR spectra with typical resonance (fingerprint) structures especially in the local time interval from LT = 21 h to 01 h, but weak (not so conspicuous) resonance structures are also seen at other LTs.

We can notice from Figures 17.7 and 17.8 that we can find very clear resonance structures on the horizontal magnetic field components ( $H$  and  $D$ ). However, when we use the polarization spectrum, it is much easier for us to identify such resonance structures, which is clearly recognized in the 2nd top panel of Figure 17.7, when we compare it with the corresponding amplitude dynamic spectra (e.g. the 2nd panel from the bottom in Figure 17.7). The wave is found to be left-handed polarized.

The algorithm of automatic SRS detection and calculation of its main parameters have been described below. Various parameters obtained from the analysis of the spectra are as follows:

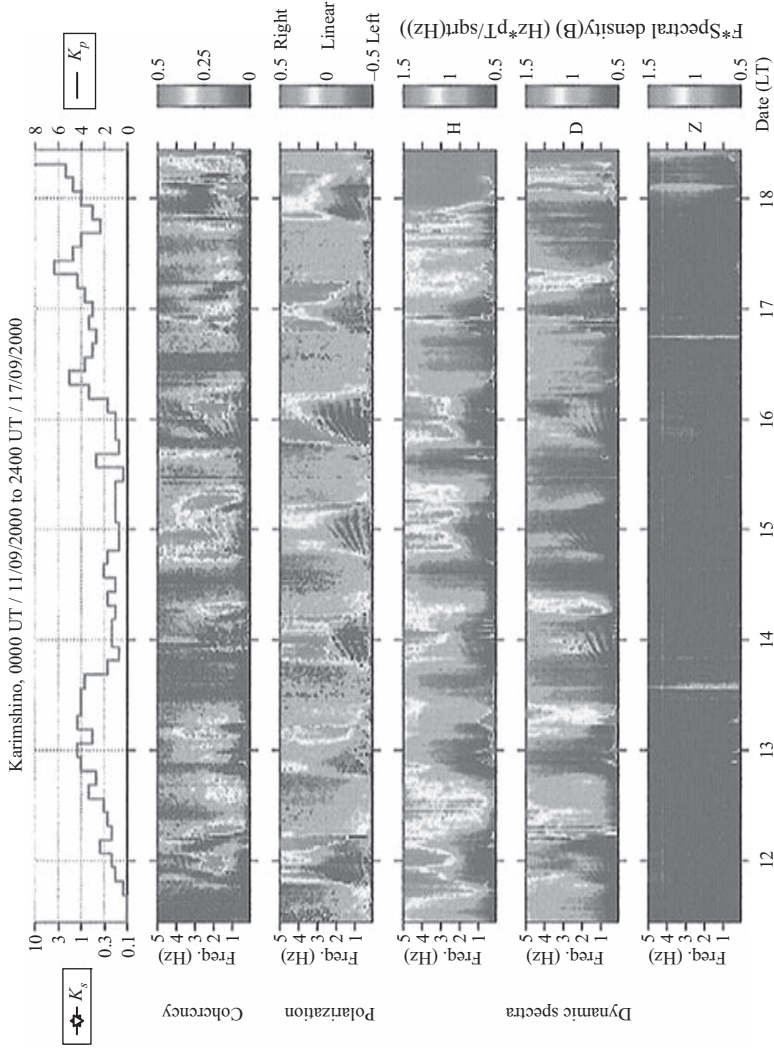


Figure 17.7 An example of daily evolution of SRS of IAR for about one week from 12 to 18 September, 2000. Date is given in LT (UT+12 h). The top panel indicates the  $K_p$  index, the second one, the coherency between the horizontal magnetic field components, the third, wave polarization by means of the horizontal magnetic field components, and the last three panels the dynamic spectra for  $H$ ,  $D$  and  $Z$  components. The values are indicated in colour

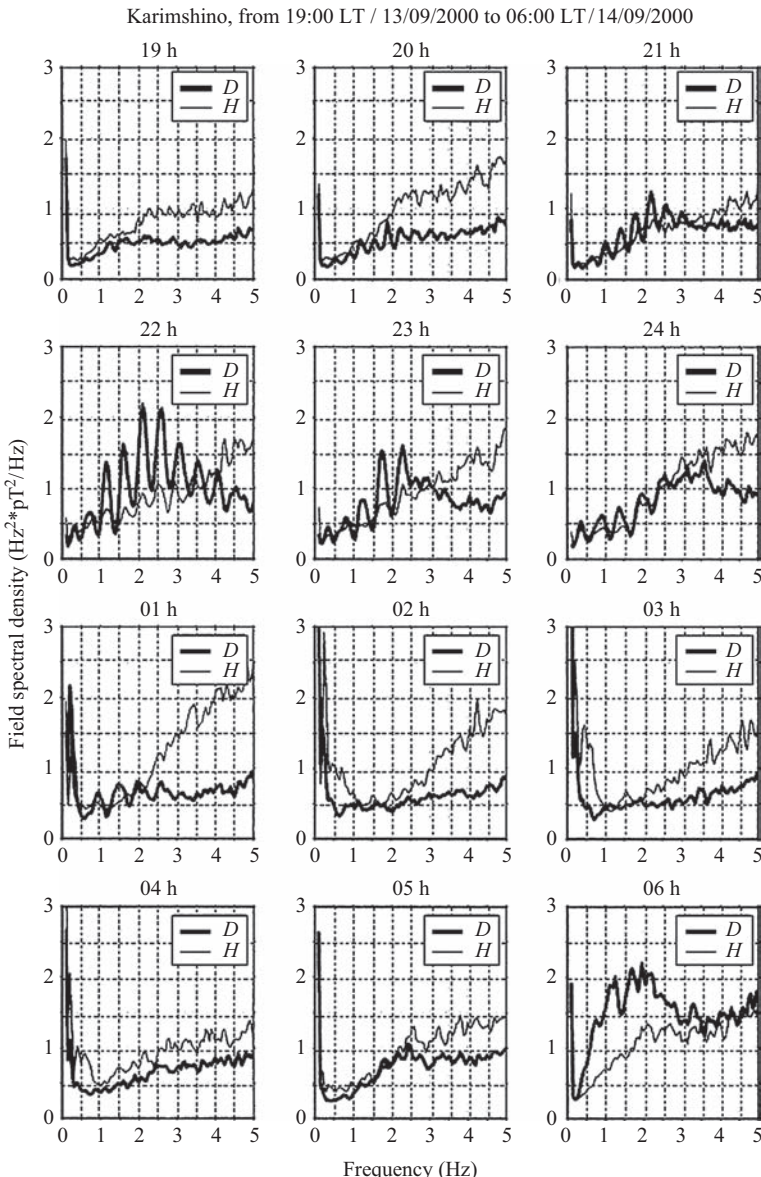


Figure 17.8 An example of temporal evolution of dynamic spectra of IARs on a particular day (13/14 September, 2000). LT = 19 h to 06 h.

- Averaged frequency difference  $\Delta F$ ,
- Intensity of the resonance signal,
- ‘Quality’ parameter  $Q$  of the resonance structure.

The algorithm of data analysis is schematically shown in Figure 17.9. The SRS with the frequency difference  $\Delta F$  is given in the top panel (a). Its 5th order polynomial approximation is shown with a dashed line as a trend. The difference between the raw spectrum and its approximation (trend) (hereafter, we call it spectral density variation) is given in the middle panel (b). The total power can be estimated as a sum of the resonant power and the background power approximately corresponding to the curve going through the minima of spectra in Figure 17.9(a). The intensity of the resonant signal is numerically estimated as the mean of the absolute value of spectral density variation. The relative inaccuracy of this approximation is low. Both spectra of the total signal and its resonant part have several approximately equidistant maxima. The average distance between the maxima is estimated with a help of Fourier transform of the spectrum of the resonant signal. This spectrum is shown in Figure 17.9(c) as a function of frequency. Its maximum corresponds to the averaged frequency difference between the SRS maxima. We define the ‘quality’  $Q$  of the resonant structure as the ratio of this maximal frequency to the half-width of the maximum  $\delta f$  using the formal similarity with the parameters of damping oscillations. A resonance structure by definition exists if at least two maxima are found in the spectrum, that is,  $Q > 1$ . This allows us to exclude a possibility of false IAR detection caused by some other effects like Pc1 geomagnetic pulsations.

### 17.3.3 Seasonal and diurnal variations of the SRS parameters

The IAR occurrence rate (occurrence probability) is defined as the ratio of number of night-time (21 h–03 h LT) intervals with our having observed SRS IAR to the total number of intervals, and this is plotted in Figure 17.10 (upper panel). The average frequency difference between adjacent spectral maxima is shown in Figure 17.10 (bottom panel). The top of each grey rectangle means the average  $\Delta F$  for a certain month, and the range of the dark rectangle indicates the error bar of estimation. When only one event was registered during a month, the frequency difference is not shown because of a big error in estimation. The seasonal variation averaged over all periods of observations of the IAR occurrence rate, frequency difference  $\Delta F$  and intensity are shown in Figure 17.11 from the top to the bottom. It is seen from the figures that during all the periods of observations the probability of IAR occurrence is maximal in autumn–winter and it vanishes in spring–early summer. A clear maximum of  $\Delta F$  is also observed in winter in the 2nd panel of Figure 17.11. The bottom panel of Figure 17.11 shows a broad maximum, so that we can suggest that the IAR power density depends relatively weakly on the season. So, the seasonal variations of the two quantities of IAR power and SRS IAR occurrence rate seem to be in anti-correlation with each other.

The diurnal variation of IAR occurrence rate for the four seasons is shown in Figure 17.12 (winter, spring, summer and autumn, from top to the bottom). In winter and autumn when the occurrence rate is maximal there is a clear pre-midnight maximum. Besides, in winter a secondary weaker maximum is found at early morning (04 h–06 h LT). Only few events were registered in spring, so that no estimates can be made for them. The IAR occurrence rate in summer seems to be shifted to the post-midnight hours.

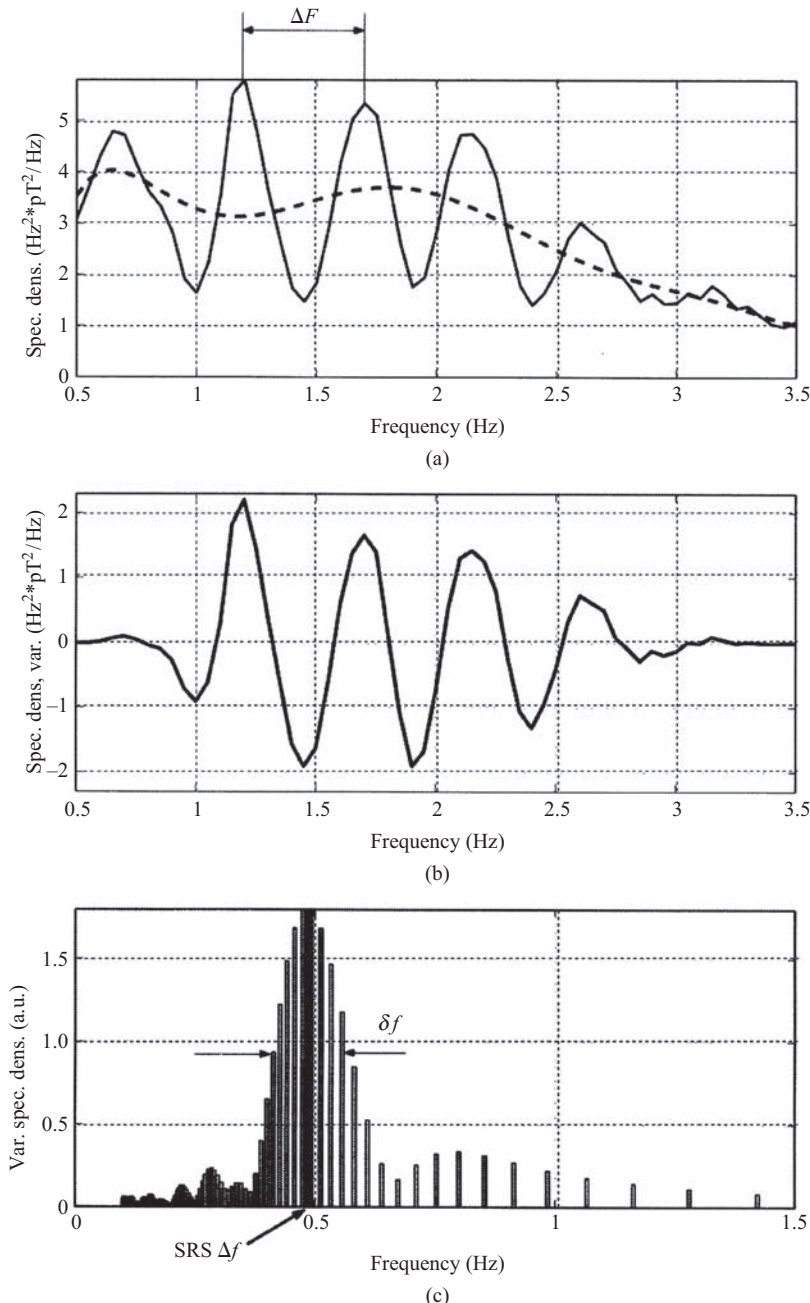


Figure 17.9 The method of SRS identification and determination of the SRS parameters. (a) SRS (in solid line) and its trend (in dashed line), (b) SRS difference and (c) Spectrum of the SRS difference. Its maximum location is the averaged  $\Delta f$  in the SRS. SRS exists if the distribution is narrow banded, that is, quality  $Q > 1$

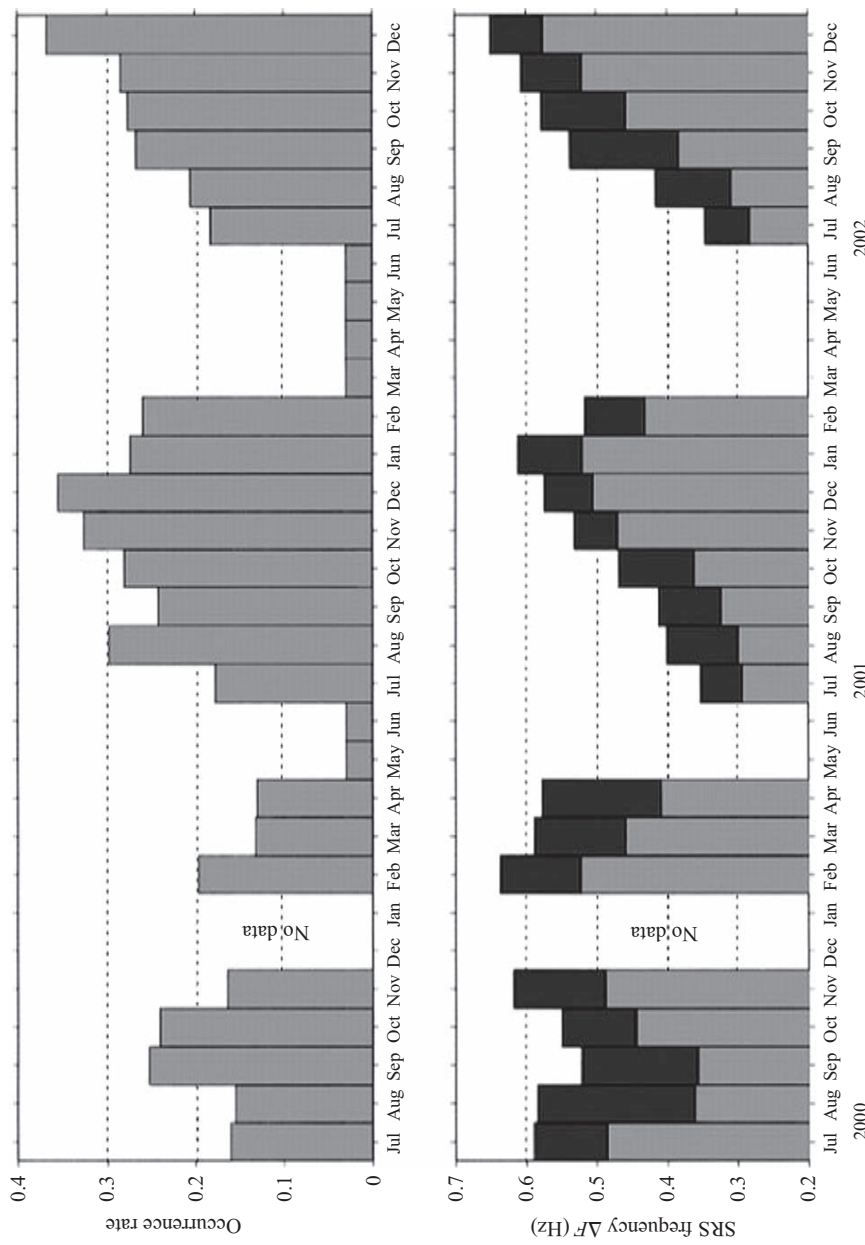


Figure 17.10 The temporal evolution of monthly IAR occurrence rate (probability) during all the observation period from July 2000 to December 2002 (top panel). The bottom, the corresponding temporal variation of  $\Delta F$  during the same period. The top of each grey rectangle indicates  $\Delta F$  and the range of dark rectangle means the error bar

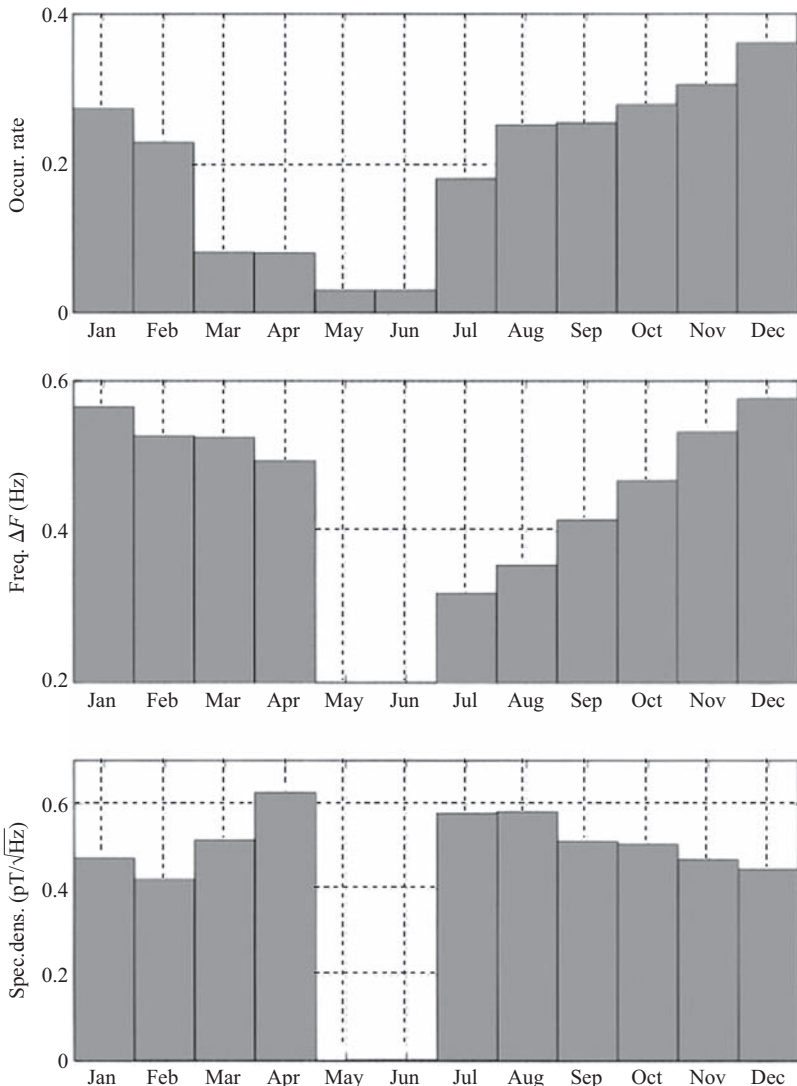


Figure 17.11 Seasonal behaviour of the occurrence rate (probability) (top),  $\Delta F$  (middle) and power spectrum density (bottom) averaged over the observation period

#### 17.3.4 SRS IAR and geomagnetic activity

SRS IAR occurrence rate at middle latitudes as well as at high latitudes (Yahnnin *et al.*, 2003) is found to increase with the decrease in geomagnetic activity. This observational result is confirmed by our statistical analysis. Correlation coefficients

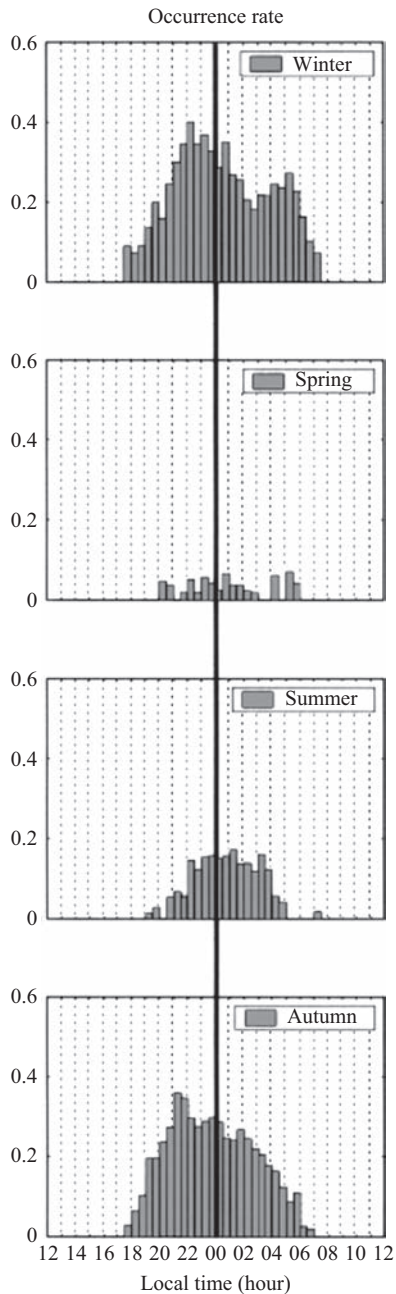


Figure 17.12 Diurnal variation (or local time dependence) of the IAR occurrence rate for different seasons (winter, spring, summer and autumn, from top to the bottom)

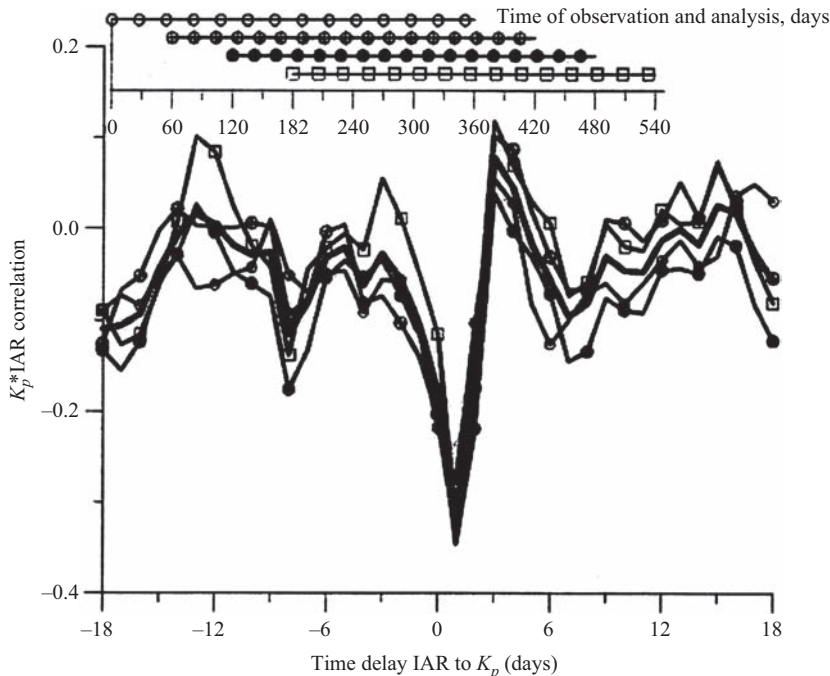


Figure 17.13 Correlation coefficients of the IAR occurrence rate with the  $K_p$  index for different one-year periods (shown above). All the correlation coefficients are negative for time delay of 0–1 day

of SRS occurrence rate with the  $K_p$  index of global magnetic activity for different one-year intervals are shown in Figure 17.13 (days with data gaps and the last three months, April–June 2002 (see seasonal dependence) were excluded from the analysis). The stable and reliable negative correlation of IAR with  $K_p$  is seen from the figure and it may be possible that SRS IARs are masked under disturbed geomagnetic conditions by the high background activity.

### 17.3.5 Summary of observations at middle latitudes

We characterize SRS by the fundamental frequency and averaged  $\Delta F$ . The parameter  $Q$  characterizing the ‘quality’ of the SRS has been introduced. It is controlled by the IAR quality and the ratio of the amplitude of resonant signal to the background noise. If the resonance ‘quality’ parameter exceeds some threshold value, we can detect any SRS IAR. We have found that the seasonal variation of the IAR occurrence rate is estimated based on the above detection criterion. The seasonal variation is strong: in spring–early summer only few SRS IAR events are registered, whereas the occurrence rate is found to strongly grow in autumn–winter.

The main results of this observation can be summarized as follows:

1. Statistical properties of the IAR structures are analysed for two-and-a-half years of observations. IAR structures occur during approximately one-quarter of the observation period (250 nights). There is an evident seasonal variation in the occurrence rate with the maximum in the autumn–winter period and almost a complete absence of IAR structures at the spring–early summer time.
2. The occurrence maximum in the diurnal variation is found at the LT of 21–23 h, and almost all the IAR structures are observed at local night-time.
3. The averaged  $\Delta F$  is approximately 0.2–0.5 Hz in the summer–autumn period, but it increases up to 0.5–0.7 Hz in the winter time.
4. IARs are mostly polarized along the azimuthal direction ( $D$  component) and the diurnal variations in the two horizontal components are sometimes not identical.
5. IAR is found to be left-handed polarized (i.e. Alfvén mode waves).
6. There is anti-correlation of the IAR occurrence rate and  $K_p$  index of the global geomagnetic activity.

We compare the present experimental findings from the long-term observation at our middle latitude ( $L=2.1$ ) station with the previous observations at a high latitude ( $L=5.2$ ) (Yahnin *et al.*, 2003) and at a low latitude ( $L=1.3$ ) (Bösinger *et al.*, 2002). The observation by Yahnin *et al.* (2003) was based on an extremely long-term observation of about five years, whereas the observation by Bösinger *et al.* (2002) was performed only for half a year. When we think about the generation mechanism of IAR, the latitudinal dependence of different characteristics of IAR would be of essential importance. Several results have been reported on the basis of shorter database (Belyaev *et al.*, 1987, 1990) at middle latitude ( $L=2.65$ ), but this section has provided the first results of middle latitude IAR characteristics by using the sufficiently long-term observation. In contrast to the previous results at high and middle latitudes, point (1) in our summary suggests that IAR structures occur for approximately one-quarter of the observation periods (250 nights). This means that the IAR phenomena are not so rare, but that they are rather regular phenomena. This point seems to be close to and be consistent with the conclusion by Bösinger *et al.* (2002, 2004) at low latitude.

According to the common view, the main source of the IAR excitation is the activity of the global thunderstorm centres. However, this activity seems to depend on the season only weakly (Nickolaenko and Hayakawa, 2002) and the observed strong seasonal variation of IAR occurrence rate seems to be unexplainable only by this assumption.

### *17.3.6 Former generation mechanisms of IAR*

Here we review the former mechanisms of IAR. In an early study of IAR, Polyakov (1976) and Polyakov and Rapoport (1981) assumed that variations of natural ionospheric currents can serve as a source for the excitation of the resonance cavity. In later works, Belyaev *et al.* (1987, 1990) developed a model for the IAR

excitation due to electromagnetic emission stemming from global thunderstorm activity. The later stochastic model of the global thunderstorm activity developed by Surkov *et al.* (2005) has indicated that the predicted magnitude of the IAR power spectrum at middle latitudes is essentially lower than that typically measured on ground-based stations. This demands the search for other mechanisms for IAR excitation at middle and high latitudes. Trakhtengertz and Feldstein (1981, 1984, 1987, 1991) proposed a mechanism of the IAR excitation at high latitudes due to an instability of laminar magnetospheric convection that causes formation of a turbulent Alfvén boundary layer near the upper wall of the IAR. Owing to that the intensive small-scale Alfvén waves can get trapped in the F region, thereby exciting the resonator. The IAR interaction with the magnetospheric convective flow termed the feedback instability can serve as the basic mechanism of IAR at high latitudes where the convection electric fields can reach quite strong values (Lysak, 1991, 1993, 1999; Lysak and Song, 2002; Pokhotelov *et al.*, 2001). Recently, Surkov *et al.* (2004) and Molchanov *et al.* (2004) have suggested that the neutral wind at the altitudes of the E layer could play an important role in the IAR studies. As shown above, the different generation mechanisms of the IAR have been proposed, but it seems likely which hypothesis will prevail and also it seems that the mechanism may depend on the latitude (Fedorov *et al.*, 2006). So, here we present one latest paper by Surkov *et al.* (2006) indicating a possible link of IAR at middle latitudes to nearby lightning discharges.

### 17.3.7 Excitation of IAR by nearby thunderstorms

We think the fact that the low frequencies determine the near field of the lightning discharge, while the high frequencies make a main contribution to the far-field spectrum. On the other hand, the quasi-static field falls off faster with distance than the wave field, which means that in the ULF frequency range the discharge spectrum from nearby lightning is more intense than that of more distant discharges (Surkov *et al.*, 2006). This is the basic idea of trying to correlate IARs to nearby lightning.

As it is seen from the examples shown in Figure 17.7, there are many impulses that can be associated with thunderstorm activity, and only some of these impulses are accompanied by the sharp impulses in the frequency range of 0.25–4 Hz. The former are thus assumed to be a result from the nearby lightning discharges. In order to estimate the number of lightning discharges per unit time we chose the signal discrimination level as 5 pT. Total number of the impulses,  $\Delta N$ , with amplitude that is greater than this level, increases with time as shown in Figure 17.14. The lines 1 and 2 correspond to the frequency filters 6–20 and 0.25–4 Hz, accordingly. Averaging over an interval of 1 h results in a mean occurrence rate of the impulses of about  $v_1 = 0.144 \text{ s}^{-1}$  and  $v_2 = 0.023 \text{ s}^{-1}$ , which is typical for the night-time conditions at Karimshino station. Note that approximately 2000 thunderstorms operate simultaneously in the whole world producing the total current of about 1800–2000 A (Nickolaenko and Hayakawa, 2002). Taking into account that the lightning discharge usually brings the charge 20–30 C, one can find that the mean occurrence rate of the lightning discharges  $v = 60\text{--}100 \text{ s}^{-1}$ . Hence a thunderstorm

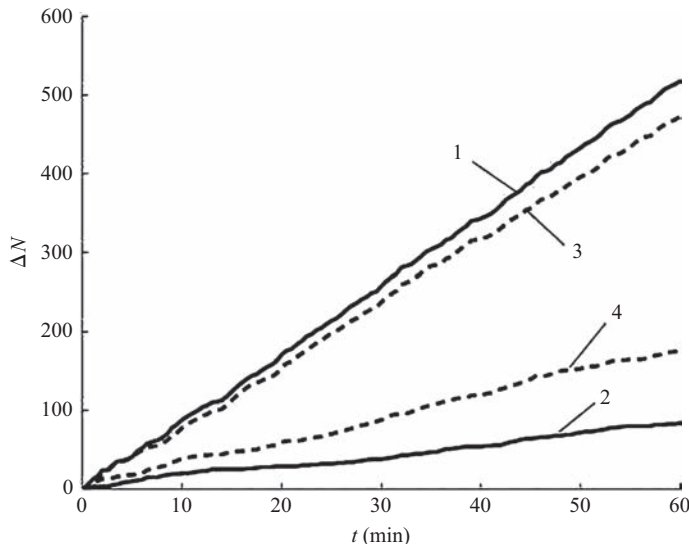


*Figure 17.14 Time variations of the sum of magnetic impulses. The threshold level for the impulse amplitude is 5 pT. The lines 1 and 2 correspond to the frequency channels 6–20 and 0.25–4 Hz, accordingly. The impulses of solely H component (6–20 Hz) are shown with dash lines 3, while D component is shown with dash line 4*

typically produces the rate number of about  $0.03\text{--}0.05 \text{ s}^{-1}$ , which is close to  $\nu_2$ . From here we may assume that one nearby thunderstorm and 3–6 remote ones make a major contribution to the rate number shown in Figure 17.14. Concerning the signals of remote thunderstorms, it should be noted that the intensity of the *H* component is larger than that of the *D* component. The impulses of the *H* component (6–20 Hz) that are displayed in Figure 17.14 with dashed line 3 occur more frequently than in the *D* component shown with dashed line 4. On the other hand, in the frequency range of 0.25–4 Hz the occurrence rate numbers of both components are very close to each other.

Most of the intense signals that can be associated with a nearby thunderstorm have a bipolar structure. It appears that the first impulse in the signals is due to the primary wave radiated by the return stroke. The interval between positive and negative impulses is typically approximately 2 s. One may assume that such a shape of the signal results from Alfvén wave reflection from the gradient in Alfvén velocity at the upper boundary of the resonance cavity. If the typical size of the resonance cavity is 500–1000 km, the arrival time of the reflected Alfvén wave is estimated as 2 s, which is close to the signal duration. The signal occasionally contains three distinct impulses at least. This implies the possibility for multiple wave reflections from the IAR upper boundary.

Let  $N$  be the number of nearby thunderstorm centres simultaneously operating around the ground-based recording station. A local coordinate system has the  $x$  axis

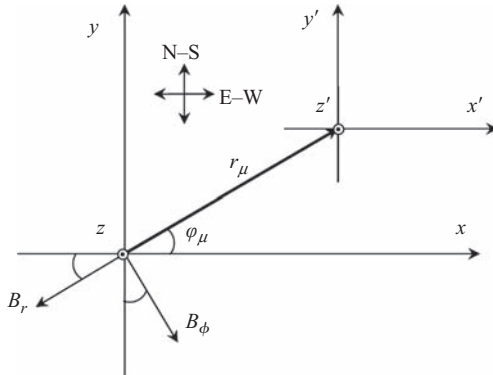


Figure 17.15 A schematic drawing of reference and local coordinate systems. There,  $z$  and  $z'$  axes are 'out of paper'.  $B_r$  and  $B_\varphi$  are the components of magnetic variations due to thunderstorm located at  $\mathbf{r} = \mathbf{r}_\mu$

eastward, the  $y$  axis to the north and  $z$  axis vertically upward. Since we are interested in solely nearby thunderstorms, a plane-stratified model of the medium is used. Let  $r_\mu$  and  $\varphi_\mu$  be the polar coordinates of the thunderstorm epicentre, where  $\mu = 1, 2, \dots, N$  as shown in Figure 17.15. A typical size of the thunderstorm is assumed to be smaller than the distance from the recording station. In what follows we ignore the lightning discharge distribution inside a thunderstorm area. This implies that all the lightning discharges related to the same thunderstorm must have the same coordinates; that is, the coordinates of a given thunderstorm.

Now we also introduce a reference frame  $x', y'$  and  $z'$  fixed to the thunderstorm with number  $\mu$ . Let  $\mathbf{B}(\mathbf{r}_\mu, t - t_{n\mu})$  be the magnetic field due to the lightning discharge happened at the accidental moment  $t_{n\mu}$ , where  $n_\mu = 1, 2, \dots$  is number of the lightning discharges. It is usually the case that the lightning discharges are vertical and transfer a negative electric charge to the ground (Uman and Krider, 1982; Uman, 1987). If we use a cylindrical coordinate system in which the lightning discharge is in the direction of the polar  $z'$  axis, the magnetic field  $\mathbf{B}$  is independent of azimuthal angle  $\varphi$ . According to Belyaev *et al.* (1990), only radial component  $B_r$  among two horizontal ones contains the resonance factor, which dominates the IAR resonance properties. In the Cartesian reference frame fixed to the ground-recording station, the horizontal magnetic field can be expressed through the radial and azimuthal components as follows:

$$\begin{aligned} B_x &= B_\varphi \sin \varphi_\mu - B_r \cos \varphi_\mu \\ B_y &= -B_\varphi \cos \varphi_\mu - B_r \sin \varphi_\mu \end{aligned} \quad (17.38)$$

On the ground  $z = z' = 0$  the components  $B_r$  and  $B_\varphi$  are random values, which depend on  $r_\mu$  and  $t - t_{n\mu}$ .

Far from the lightning discharge the electromagnetic field of the lightning discharge can be characterized by the current moment of the discharge  $m(t) = I(t)$

$I(t)$ , where  $I(t)$  is the current produced by the median return strokes of lightning and  $l(t)$  denotes the lightning channel length. According to Surkov *et al.* (2004), we approximate the actual current moments with the function  $m(t) = MF(t)$ , where the magnitude  $M$  of the current moment is assumed to be a random value, whereas  $F(t)$  is a universal function of time. Hence the horizontal magnetic field of the single lightning discharge can be written as

$$B_{r,\varphi}(r_\mu, t - t_{n\mu}) = M_{n\mu} G_{r,\varphi}(r_\mu, t - t_{n\mu}) \quad (17.39)$$

where the functions  $G_{r,\varphi}$  is supposed to be equal to zero as  $t < t_{n\mu}$ . These functions are derived from Maxwell's equations, which should be supplemented by proper boundary conditions at the ground and the atmosphere-ionosphere boundary.

The net magnetic perturbation at the ground-recording station is a random quantity  $\mathbf{B}_{ran}$  that equals the sum of the magnetic perturbations caused by separate lightning discharges. The net horizontal field of all the thunderstorms located around the station is then

$$\mathbf{B}_{ran}(t) = \sum_{\mu=1}^N \mathbf{B}_\mu(t), \quad \mathbf{B}_\mu(t) = \sum_{n\mu} M_{n\mu} \hat{\mathbf{A}}_\mu \mathbf{G}_{n\mu} \quad (17.40)$$

where  $\mathbf{B}_\mu$  is the horizontal magnetic field due to the thunderstorm with number  $\mu$ , the matrix  $\hat{\mathbf{A}}_\mu$  and the vector  $\mathbf{G}_{n\mu}$  are given by

$$\hat{\mathbf{A}}_\mu = \begin{pmatrix} -\cos \varphi_\mu & \sin \varphi_\mu \\ -\sin \varphi_\mu & -\cos \varphi_\mu \end{pmatrix} \quad (17.41)$$

and

$$\mathbf{G}_{n\mu} = \begin{pmatrix} G_r(r_\mu, t - t_{n\mu}) \\ G_\varphi(r_\mu, t - t_{n\mu}) \end{pmatrix} \quad (17.42)$$

We now turn to the modelling of a single lightning discharge. A typical lightning discharge consists of several return strokes. According to Jones (1970), Uman and Krider (1982) and Uman (1987), the current produced by the median return stroke of lightning is modelled as

$$I(t) = \sum_{m=1}^4 I_m \exp(-\omega_m t) \quad (17.43)$$

where  $\omega_m$  are inverse time constants and the amplitudes  $I_m$  of individual currents term must satisfy the condition  $\sum_{m=1}^4 I_m = 0$ . The vertical current channel grows upward with the velocity  $dl/dt = V_0 \exp(-\Omega t)$ , where  $V_0 = 8 \times 10^7$  m/s is the current wave velocity at the ground level and  $\Omega$  is the relaxation time parameter whence it follows that the final channel length is  $l_1 = V_0/\Omega$ . The current moment of the single return stroke

$m_1(t) = I(t)l(t)$  can be written as (see, e.g. Nickolaenko and Hayakawa, 1998, 1999, 2002)

$$m_1(t) = l_1[1 - \exp(-\Omega t)] \sum_{m=1}^4 I_m \exp(-\omega_m t) \quad (17.44)$$

It is usually the case that the lightning discharge contains  $n = 2-6$  return strokes. More frequently, there are 3 return strokes with characteristic duration of about 100 ms. The mean interval between them is of the order of  $t_0 = 40$  ms. Following Jones (1970), we assume that the final length of the return stroke increases with its number  $n$  as  $l_n = l_1 + (n - 1) \Delta l$ , where  $l_1 = 4$  km and  $\Delta l = 1$  km. The current relaxation time parameter  $\Omega_n$  is related to the channel length  $l_n$  as follows:

$$\Omega_n^{-1} = \frac{l_n}{V_0} = \Omega_1^{-1} + \frac{\Delta l}{V_0}(n - 1) \quad (17.45)$$

where  $\Omega_1 = V_0/l_1 = 2 \times 10^4$  s $^{-1}$ . The net magnetic moment of the multiple discharge can be written as  $m(t) = MF(t)$ , where  $M = l_1|I_1|$  is the ‘magnitude’ of the magnetic moment while the dimensionless function  $F(t)$  describes the shape of the multiple discharge

$$F(t) = \sum_{n=1}^{n_0} \frac{l_n}{l_1} [1 - \exp(-\Omega_n t'_n)] \cdot \eta(t'_n) \sum_{m=1}^4 \frac{I_m}{|I_1|} \exp(-\omega_m t'_n) \quad (17.46)$$

where  $t'_n = t - (n - 1)t_0$  and  $\eta(x)$  denotes the step-function, that is,  $\eta = 1$  if  $x \geq 0$  and  $\eta = 0$  if  $x < 0$ . In this model all the current impulses have the same shape while the increase in the lightning channel length results in gradual enhancement of the electric current moment. To simplify the problem, we assume now that the lightning discharge contains  $n_0 = 3$  return strokes. Taking the typical parameters for the models of the return strokes (see, e.g. Berger *et al.*, 1975; Nickolaenko and Hayakawa, 1998, 1999, 2002; Visacro *et al.*, 2004)  $I_{1-4} = -28.45, 23.0, 5.0, 0.45$  (in kA) and  $\omega_{1-4} = 6.0 \times 10^5, 3.0 \times 10^4, 2.0 \times 10^3, 147.0$  (in s $^{-1}$ ), one can estimate the typical magnitude of the magnetic moment as  $M = 170$  kA km. The spectrum of the function  $F(t)$  is

$$F(\omega) = \frac{\Omega_1}{2\pi} \sum_{n=1}^{n_0} \sum_{m=1}^4 \frac{I_m}{|I_1|} \frac{\exp[j\omega t_0(n - 1)]}{(\omega_m - j\omega)(\Omega_n + \omega_m - j\omega)} \quad (17.47)$$

Here we study electromagnetic field spectrum of the lightning discharge in the upper atmosphere, and we approximate the actual conductivity distribution with the plane-stratified model (Surkov *et al.*, 2004) that is a reasonable approximation to the variation of the conductivity with altitude. Figure 17.16 illustrates a schematic medium model. The ground  $z \leq 0$  is considered to be a uniform conductor with constant conductivity  $\sigma_g$ . The vertical lightning discharge has appeared in the atmosphere at the altitude  $z = h$  above the ground at the moment  $t = 0$ . When considering far distances, the actual lightning discharge can be replaced with the

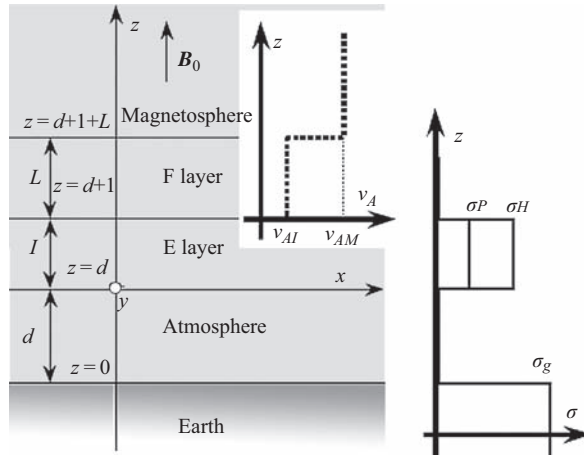


Figure 17.16 A schematic drawing of a stratified medium model. The plots of the Alfvén velocity and the ionosphere/ground conductivities are shown in the right panel

vertical lumped electric current moment  $m(t)$  located at the  $z$  axis at the altitude  $z = h$ . Since a lightning discharge transfers the negative electric charge to the ground, the vector of current moment is therefore vertically upward. The atmospheric slab  $0 < z < d$  is supposed to be an insulator. The ionospheric plasma  $z > d$  is immersed in the constant Earth's magnetic field  $\mathbf{B}_0$ . The actual profile of the Hall and Pedersen conductivities strongly varies with altitude. The plasma conductivity peak lies inside the ionospheric E layer, which is considered in the thin-slab approximation. This condition is not so burdensome on account of smallness of the typical wave number  $k$  allowing for the condition  $kl \ll 1$ , where  $l$  denotes the characteristic width of the E layer. In the model, the region above the E layer (i.e. F layer and magnetosphere) is supposed to be the area consisting solely of cold collision-less plasma. The IAR formation in this region is due to the plasma density fall off with altitude, which makes the Alfvén velocity,  $v_A$ , rapidly increase upward. The ionospheric resonance cavity is bounded from below by the conductive E layer and from above by the region where the gradient of the Alfvén velocity reaches a peak, which makes it possible to have reflection of the Alfvén wave from the upper space. The typical vertical scale of the resonance cavity is  $L \approx 10^3$  km.

It should be noted that the same resonance cavity can serve as a waveguide for the magnetosonic/compressional mode (modified Alfvén wave in the previous section) (e.g. Greifinger and Greifinger, 1968). According to Pokhotelov *et al.* (2000), we use a suitably idealized model of the resonance cavity that describes the Alfvén velocity in terms of a piece-wise function so that  $v_A = v_{AI}$  within the resonance cavity ( $d < z < d + l + L$ ) and  $v_A = v_{AM}$  in the outer magnetosphere ( $z > d + l + L$ ), where  $v_{AI}$  and  $v_{AM}$  ( $v_{AM} \gg v_{AI}$ ) are constant quantities referring to the ionosphere (I) and magnetosphere (M), respectively. The geomagnetic field  $\mathbf{B}_0$  is supposed to be vertically upward. A more accurate model that takes into account

the dip angle of the local geomagnetic field gives rise to very complicated equations (Surkov, 1996; Surkov *et al.*, 1997; Fedorov *et al.*, 1999). For simplicity we adopt the model of the vertical geomagnetic field in order to avoid the complexities connected with magnetic field inclination.

On account of axial symmetry of the field produced by the vertical current moment, the cylindrical coordinates  $z$ ,  $r$  and  $\varphi$  are used. In this case all the quantities are free of  $\varphi$  so that  $\partial/\partial\varphi = 0$ . In the atmosphere the primary field of the current moment contains only three components,  $E_r$ ,  $E_z$  and  $B_\varphi$  termed as TM mode. When the electromagnetic wave of the TM mode penetrates into the ionosphere, it produces excitation of the TE mode, that is,  $E_\varphi$ ,  $B_r$  and  $B_z$  due to the mode coupling via Hall conductivity in the ionosphere. The shear and compressional Alfvén waves can get trapped in the F layer of the ionosphere, thereby exciting the IAR. Low-frequency resonant oscillations are leaking back into the atmosphere so that all the components of the electromagnetic field, which are TM and TE modes, can be detected on the ground.

In the framework of the model, we note that the spectra of the electromagnetic perturbations due to a solitary lightning discharge have been obtained by Surkov *et al.* (2004, 2005). The reader is referred to those works for details about derivation of the formulae. Let  $\Sigma_w = 1/(\mu_0 v_{AI})$  be the Alfvén parallel conductance,  $\alpha_p = \Sigma_p/\Sigma_w$  and  $\alpha_H = \Sigma_H/\Sigma_w$  stand for the dimensionless height-integrated Pedersen and Hall conductivities, respectively, and  $x_0 = \omega L/v_{AI}$  be dimensionless frequency. The Fourier transforms of the magnetic perturbation  $\delta B_r$  and  $\delta B_\varphi$  on the ground level  $z = 0$  can be written as follows:

$$\delta B_r(r, \omega) = Mg_r(r, \omega) \quad (17.48)$$

$$\delta B_\varphi(r, \omega) = Mg_\varphi(r, \omega) \quad (17.49)$$

The mathematical derivations of  $g_r(r, \omega)$  and  $g_\varphi(r, \omega)$  are rather complicated, so that we want to avoid these. Please look at our original paper by Surkov *et al.* (2006) for further details of electromagnetic fields in each region and the application of boundary conditions to each boundary.

A model calculation of the lightning-generated spectra of the resonance component  $\delta B_r$  for the typical night-time parameters of the mid-latitude ionosphere is given in Figure 17.17. The discharge contains three cloud-to-ground return strokes. The numerical parameters of the lightning discharge used in making this plot are given above. The numerical values for the various magnetospheric, ionospheric and other parameters are  $v_{AI} = 500$  km/s,  $v_{AM} = 5 \times 10^3$  km/s,  $L = 500$  km,  $d = 100$  km,  $l = 40$  km,  $z = 0$ ,  $\sigma_g = 2 \times 10^{-3}$  S/m,  $\Sigma_p = 0.2 \Omega^{-1}$  and  $\Sigma_H = 0.3 \Omega^{-1}$  (night-time conditions). In this figure the lines 1–4 correspond to the distances  $r = 100$ , 300, 1000 and 10,000 km, respectively. It is obvious from Figure 17.17 that the spectra exhibit distinct resonance structures in such a way that the resonance frequencies are close to the IAR eigen frequencies as observed. Owing to the symmetry of the problem the radial component of the magnetic perturbation must tend to zero when  $r \rightarrow 0$ . The calculations have shown that the spectrum magnitude reaches a peak at the distance of about 300 km.

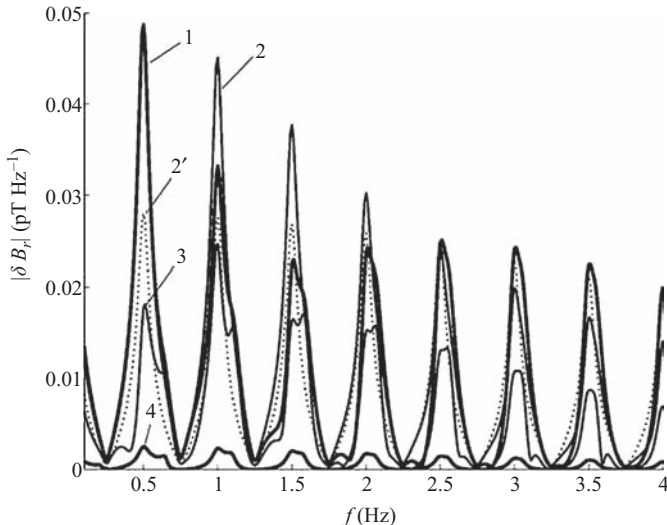


*Figure 17.17* A model calculation of the night-time IAR spectra excited by a solitary cloud-to-ground lightning discharge. The radial/resonant component  $B_r$  on the ground is shown with lines 1–4, which correspond to the distances  $r = 100, 300, 1000$  and  $10,000$  km, respectively. The approximate analytical solution at distance  $r = 300$  km is shown with dotted line 2'

Surkov *et al.* (2006) have further considered the random magnetic variations produced by the cloud-to-ground lightning discharges treated as a stochastic process. The obtained frequency spectra are found to be close to the observations. The theoretical consideration by Surkov *et al.* (2006) can be summarized as follows:

1. The model computations of the power spectra are in favour of the nearby thunderstorms as a possible cause for the IAR excitation at middle latitudes.
2. The solitary cloud-to-ground lightning discharges in the neighbourhood of the ground station may result in the impulse IAR excitation, which is capable of producing observable SRS signature on the ground.
3. The random lightning discharges in the range of  $1000\text{--}2000$  km make a main contribution to the mid-latitude IAR power spectrum since the predicted resonant frequencies and peaks are practically consistent with those observed.

## 17.4 Summary of lightning effects onto the ionosphere/magnetosphere

This chapter is concerned with two major effects of lightning discharges on the upper atmosphere of the ionospheric/magnetospheric plasma. The first is an

extremely known phenomenon: whistler. This whistler signal is originated in the VLF/ELF part of the causative lightning discharge and it propagates in the ionosphere/magnetosphere. General characteristics and general theory of whistlers are presented, and finally we have presented the use of this lightning-induced whistler as the diagnosis of magnetospheric plasma density.

The second is IAR, which has a relatively short history. This IAR is known to take place in the frequency range below the famous Schumann resonance and the eigen frequencies are in a range from 1 to approximately 5 Hz. The frequency spectra of IARs are just like fingerprint structure. Theoretically, this IAR was predicted around 1980, but it is only recently that several workers have paid extensive attention to this IAR. The characteristic IAR eigen frequencies can be roughly estimated as  $f_{rn} \sim nv_A/(2L)$  where  $n = 1, 2, \dots$  (mode number) and  $L$  is the length of field line piece within the resonance cavity. Two hypotheses are proposed as the possible candidate as the exciter of this IAR: (1) magnetospheric effect and (2) lightning in the atmosphere. Probably the most important information to distinguish between the above hypotheses will be the latitudinal dependence of the occurrence rate of IAR. In this chapter, we have presented our recent paper to suggest a possible link of this IAR to nearby lightning activity.

## References

- Allis, W. A., S. J. Buchsbaum and A. Bers, *Waves in Anisotropic Plasmas*, MIT Press, Massachusetts, 1963
- Al'pert, Ya. L., *Propagation of Radio Waves in the Ionosphere*, Plenum Press, New York, 1974
- Al'pert, Ya. L., *Space Plasma*, Cambridge University Press, Cambridge, 1990
- Barkhausen, H., Zwei mit Hilfe der neuen Verstärker entdeckte Erscheinungen, *Physik A*, 20, 401, 1919
- Belyaev, P. P., S. V. Polyakov, V. O. Rapoport and V. Y. Trakhtengertz, Discovery of the resonance spectrum structure of atmospheric electromagnetic noise background in the range of short-period geomagnetic pulsations, *Dokl. Akad. Nauk SSSR*, 297, 840–846, 1987
- Belyaev, P. P., S. V. Polyakov, V. O. Rapoport and V. Y. Trakhtengertz, The ionospheric Alfvén resonator, *J. Atmos. Terr. Phys.*, 52, 781–788, 1990
- Belyaev, P. P., T. Bösinger, S. V. Isaev and J. Kangas, First evidence at high latitudes for the ionospheric Alfvén resonator, *J. Geophys. Res.*, 104, 4305–4317, 1999
- Berger, K., R. B. Anderson and H. Kröninger, Parameters of lightning flashes, *Electra*, 41, 23–27, 1975
- Bösinger, T., C. Haldoupis, P. P. Belyaev, M. N. Yakunin, N. V. Semenova, A. G. Demekhov, *et al.*, Spectral properties of the ionospheric Alfvén resonator observed at a low-latitude station ( $L = 1.3$ ), *J. Geophys. Res.*, 107(A10), 1281, doi:10.1029/2001JA005076, 2002

- Bösinger, T., A. G. Demekhov and V. Y. Trakhtengertz, Fine structure in ionospheric Alfvén resonator spectra observed at low latitude, *Geophys. Res. Lett.*, 31, L18802, doi:10.1029/2004GL020777, 2004
- Budden, K. G., *The Propagation of Radio Waves*, Cambridge University Press, Cambridge, 1988
- Burton, E. T. and E. M. Boardman, Audio-frequency atmospherics, *Proc. Inst. Radio Eng.*, 21, 1476, 1933
- Carpenter, D. L. and C. G. Park, On what ionospheric workers should know about the plasmapause-plasmasphere?, *Rev. Geophys. Space. Res.*, 81, 2728–2736, 1973
- Corcuff, Y., Probing the plasmapause by whistlers, *Ann. Geophys.*, 31, 53–67, 1975
- Demekhov, A. G., V. Yu. Trakhtengertz and T. Bösinger, Pc 1 waves and ionospheric Alfvén resonator: Generation or filtration?, *Geophys. Res. Lett.*, 27, 3805–3808, 2000a
- Demekhov, A. G., P. P. Belyaev, J. Manninen, T. Turunen and J. Kangas, Modeling the diurnal evolution of the resonance spectral structure of the atmospheric noise background in the PC 1 frequency range, *J. Atmos. Solar-Terr. Phys.*, 62, 257–265, 2000b
- Eckersley, T. L., 1929–1930 developments in the study of radio wave propagation, *Marconi Rev.*, 5, 1, 1931
- Eckersley, T. L., Musical atmospherics, *Nature*, 135, 104–105, 1935
- Fedorov, E., V. Pilipenko, V. Surkov, D. R. K. Rao and K. Yumoto, Ionospheric propagation of magnetohydrodynamic disturbances from the equatorial electrojet, *J. Geophys. Res.*, 104, 4329–4336, 1999
- Fedorov, E., A. Schekotov, O. Molchanov, M. Hayakawa and V. Gladyshev, An energy source for the mid-latitude IAR: World thunderstorm centers, nearby discharges or neutral wind fluctuations?, *Phys. Chem. Earth*, 31, 462–468, 2006
- Ginzburg, V. L., *The Propagation of Electromagnetic Waves in Plasmas*, Permagon Press, Oxford, 1970
- Gladyshev, V., L. Baransky, A. Schekotov, E. Fedorov, O. Pokhotelov, S. Andreevsky, et al., *Some Preliminary Results of Seismo-Electromagnetic Research at Complex Geophysical Observatory, Kamchatka, in Seismo Electromagnetics: Lithosphere–Atmosphere–Ionosphere Coupling*, Ed. by M. Hayakawa and O. A. Molchanov, Terra Scientific Publishing Company, Tokyo, 421–432, 2002
- Greifinger, C. and S. Greifinger, Theory of hydromagnetic propagation in the ionospheric waveguide, *J. Geophys. Res.*, 73, 7473–7490, 1968
- Hayakawa, M., Whistlers, in *Handbook of Atmospheric Electrodynamics*, Vol. 2, Ed. by H. Volland, CRC Press, Boca Raton Florida, 155–193, 1995
- Hayakawa, M. and K. Ohta, The propagation of low-altitude whistlers: A review, *Planet. Space Sci.*, 40, 1339–1351, 1992
- Hayakawa, M., K. Ohta and K. Baba, Wave characteristics of the tweek atmospherics deduced from the direction finding measurement and theoretical interpretation, *J. Geophys. Res.*, 99, 10733–10743, 1994

- Hayakawa, M., O. A. Molchanov, A. P. Nickolaenko, Yu. Schekotov and E. Fedorov, Observation of ionospheric Alfvén resonance at a middle latitude station, *Adv. Polar Upper Atmos. Res., Nat'l Inst. Polar Res.*, Tokyo, 18, 65–76, 2004
- Hayakawa, M. and Y. Tanaka, On the propagation of low-latitude whistlers, *Rev. Geophys. Space Phys.*, 16, 111–123, 1978
- Helliwell, R. A., *Whistlers and Related Ionospheric Phenomena*, Stanford University Press, Stanford, CA, 1965
- Jones, D. L., Electromagnetic radiation from multiple return stroke of lightning, *J. Atmos. Terr. Phys.*, 32, 1077–1093, 1970
- Kivelson, M. G. and C. T. Russell, *An Introduction to Space Physics*, Cambridge University Press, Cambridge, UK, 1995
- Lysak, R. L., Feedback instability of the ionospheric resonator cavity, *J. Geophys. Res.*, 96, 1553–1568, 1991
- Lysak, R. L., Generalized model of the ionospheric Alfvén resonator, in *Auroral Plasma Dynamics, Geophys. Monogr. Ser.*, Vol. 80, Ed. by R. L. Lysak, AGU, Washington, D. C., 121, 1993
- Lysak, R. L., Propagation of Alfvén waves through the ionosphere: Dependence on ionospheric parameters, *J. Geophys. Res.*, 104, 10017–10030, 1999
- Lysak, R. L. and Y. Song, Energetics of the ionospheric feedback interaction, *J. Geophys. Res.*, 107(A8), 1160, doi:10.1029/2001JA000308, 2002
- Molchanov, O. A., A. Y. Schekotov, E. N. Fedorov and M. Hayakawa, Ionospheric Alfvén resonance at middle latitudes: Results of observations at Kamchatka, *Phys. Chem. Earth*, 29, 649–655, 2004
- Nickolaenko, A. P. and M. Hayakawa, Electric fields produced by lightning discharges, *J. Geophys. Res.*, 103, 17175–17189, 1998
- Nickolaenko, A. P. and M. Hayakawa, A model for causative discharge of ELF-transients, *J. Atmos. Electr.*, 19, 11–24, 1999
- Nickolaenko, A. P. and M. Hayakawa, *Resonances in the Earth-Ionosphere Cavity*, Kluwer Academic Publishers, Dordrecht, 2002
- Nicholson, D. R., *Introduction to Plasma Theory*, Krieger Publishing Company, Florida, 1991
- Park, C. G., Whistlers, in *Handbook of Atmosphericics*, Vol. 2, Ed. by H. Volland, CRC Press, Boca Raton Florida, 21–79, 1982
- Parks, G. K., *Physics of Space Plasma: An introduction*, Addison-Wesley, Massachusetts, 1991
- Polyakov, S. V., On the properties of the ionospheric Alfvén resonator, KAPG Symposium on Solar-Terrestrial Physics, Vol. 3, Moscow, Nauka, 72–73, 1976
- Polyakov, S. V. and V. O. Rapoport, The ionospheric Alfvén resonator, *Geomagn. Aeron.*, 21, 610–614, 1981
- Pokhotelov, O. A., D. Pokhotelov, A. Strelkov, V. Khruschev and M. Parrot, Dispersive ionospheric Alfvén resonator, *J. Geophys. Res.*, 105, 7737–7746, 2000
- Pokhotelov, O. A., V. Khruschev, M. Parrot, S. Senchenkov and V. P. Pavlenko, Ionospheric Alfvén resonator revisited: Feedback instability, *J. Geophys. Res.*, 106, 25813–25823, 2001

- Rakov, V. A. and M. A. Uman, *Lightning: Physics and Effects*, Cambridge University Press, Cambridge, 2003
- Sazhin, S. S., M. Hayakawa and K. Bullough, Whistler diagnostics of magnetospheric parameters: A review, *Ann. Geophys.*, 10, 293–308, 1992
- Stix, T. H., *The Theory of Plasma Waves*, McGraw-Hill, New York, 1962
- Storey, L. R. O., An investigation of whistling atmospherics, *Phil. Trans. Roy. Soc.*, A246, 113–141, 1953
- Surkov, V. V., Front structure of the Alfvén wave radiated into the magnetosphere due to excitation of the ionospheric E layer, *J. Geophys. Res.*, 101, 15403–15409, 1996
- Surkov, V. V., E. N. Fedorov, V. A. Pilipenko and D. R. I. Rao, Ionospheric propagation of geomagnetic perturbations caused by equatorial electrojet, *Geomagn. Aeron.*, 37, 792–796, 1997
- Surkov, V. V., O. A. Pokhotelov, M. Parrot, E. N. Fedorov and M. Hayakawa, Excitation of the ionospheric resonance cavity by neutral winds at middle latitudes, *Ann. Geophys.*, 22, 2877–2889, 2004
- Surkov, V. V., O. A. Molchanov, M. Hayakawa and E. N. Fedorov, Excitation of the ionospheric resonance cavity by thunderstorms, *J. Geophys. Res.*, 110, A04308, doi:10.1029/2004JA010850, 2005
- Surkov, V. V., M. Hayakawa, A. Y. Schekotov, E. N. Fedorov and O. A. Molchanov, Ionospheric Alfvén resonator excitation due to nearby thunderstorms, *J. Geophys. Res.*, 111, A1303, doi:10.1029/2005JA011320, 2006
- Trakhtengertz, V. Y. and A. Y. Feldstein, Effect of the nonuniform Alfvén velocity profile on stratification of magnetospheric convection, *Geomagn. Aeron.*, 21, 711, 1981
- Trakhtengertz, V. Y. and A. Y. Feldstein, Quiet auroral arcs: Ionospheric effect of magnetospheric convection stratification, *Planet. Space Sci.*, 32, 127–134, 1984
- Trakhtengertz, V. Y. and A. Y. Feldstein, About excitation of small-scale electromagnetic perturbations in ionospheric Alfvén resonator, *Geomagn. Aeron.*, 27, 315, 1987
- Trakhtengertz, V. Y. and A. Y. Feldstein, Turbulent Alfvén boundary layer in the polar ionosphere: 1. Excitation conditions and energetics, *J. Geophys. Res.*, 96, 19363–19374, 1991
- Trakhtengertz, V., A. G. Demekhov, S. V. Polyakov and V. O. Rapoport, A mechanism of PC 1 pearl formation based on the Alfvén sweep maser, *J. Atmos. Solar-Terr. Phys.*, 62, 231–238, 2000a
- Trakhtengertz, V. Yu., P. P. Belyaev, S. V. Polyyakov, A. G. Demekhov and T. Bösinger, Excitation of Alfvén waves and vortices in the ionospheric Alfvén resonator by modulated powerful radio waves, *J. Atmos. Solar-Terr. Phys.*, 62, 267–276, 2000b
- Uman, M. A., *The Lightning Discharge*, Elsevier, New York, 1987
- Uman, M. A. and E. P. Krider, A review of natural lightnings: Experimental data and modeling, *IEEE Trans. Electromagn. Compat.*, 24, 79–112, 1982
- Uyeda, S., T. Nagao, K. Hattori, Y. Noda, M. Hayakawa, K. Miyaki, et al., Russian-Japanese complex geophysical observatory in Kamchatka for monitoring of

- phenomena connected with seismic activity, in *Seismo Electromagnetics: Lithosphere—Atmosphere—Ionosphere Coupling*, Ed. by M. Hayakawa and O. A. Molchanov, Terra Scientific Publishing Company, Tokyo, 413–419, 2002
- Visacro, S., A. Soares Jr., M. A. O. Schroeder, L. C. L. Cherchigola and V. J. de Sousa, Statistical analysis of lightning current parameters: Measurements at Morro do Cachimbo Station, *J. Geophys. Res.*, 109, D01105, doi:10.1029/2003JD003662, 2004
- Walker, A. D. M., The theory of whistler propagation, *Rev. Geophys. Space Phys.*, 30, 411–421, 1976
- Walker, A. D. M., *Plasma Waves in the Magnetosphere*, Springer-Verlag, Berlin, 1993
- Williams, E. R., The Schumann resonance: A global tropical thermometer, *Science*, 256, 1184–1187, 1992
- Yahnin, A. G., N. V. Semenova, A. A. Ostapenko, J. Kangas, J. Manninen and T. Turunen, Morphology of the spectral resonance structure of the electromagnetic background noise in the range of 0.1–4 Hz at  $L = 5.2$ , *Ann. Geophys.*, 21, 779–786, 2003
- Yeh, K. C. and C. H. Liu, *Theory of Ionospheric Waves*, Academic Press, New York, 1972



---

## *Chapter 18*

# **Interaction of lightning-generated electromagnetic fields with overhead and underground cables**

*Carlo Alberto Nucci<sup>1</sup>, Farhad Rachidi<sup>2</sup> and  
Marcos Rubinstein<sup>3</sup>*

---

## **18.1 Introduction**

The problem of lightning protection of overhead and buried power lines has been reconsidered in recent years due to the proliferation of sensitive loads and the increasing demand by customers for good quality in the power supply [1]. Overvoltages originated by lightning are a major cause of flashovers and disturbances. Additionally, lightning-originated surges can also damage, depending on their amplitude and energy content, the power components connected to these networks as well as the relevant electronic devices.

The evaluation of lightning-induced voltages requires the knowledge of the electromagnetic field change along the considered line. This electromagnetic field is generally determined assuming that the lightning return stroke channel is a straight vertical antenna above a conducting plane. Some studies have attempted to take into account the channel tortuosity and inclination in the computation of electromagnetic fields (e.g. [2–6]). The spatial and temporal distribution of the current along the channel is specified using a return stroke model.

The problem of return stroke modelling and electromagnetic field computation is beyond the scope of this chapter. It is, however, worth mentioning that

- Four classes of lightning return stroke models have been defined by Rakov and Uman [7]: (1) The gas dynamic models, (2) electromagnetic models, (3) distributed-circuit models and (4) engineering models. Outputs of the electromagnetic, distributed-circuit and engineering models can be directly used for the computation of electromagnetic fields. A review on recent work on these three types of models can be found in Reference 8.

<sup>1</sup>University of Bologna, Bologna, Italy

<sup>2</sup>Swiss Federal Institute of Technology (EPFL), Lausanne, Switzerland

<sup>3</sup>University of Applied Sciences Western Switzerland HES-SO, Yverdon, Switzerland

- Three different approaches are more frequently adopted to compute the electromagnetic fields, both above and below the earth surface: (1) Numerical solution of the exact equations through dedicated algorithms, (2) numerical solution of the Maxwell's equations using numerical methods, such as the finite-difference time-domain (FDTD) technique or the method of moments (MoM) and (3) use of simplified equations. These approaches have been recently reviewed by Rakov and Rachidi [8].

In this chapter, we present the general theory describing the interaction of an impinging electromagnetic field with transmission lines, with particular reference to lightning-induced voltages.

The chapter is organized as follows. Section 18.2 contains a brief presentation of the transmission line theory and a discussion of its underlying assumptions. Section 18.3 presents the field-to-overhead transmission line models that have been proposed to describe the coupling of electromagnetic fields to transmission lines. In that section, the derived equations are then extended to deal with the presence of losses and multiple conductors, and expressions for the line parameters, including the ground impedance and admittance are presented. Solution methods in the frequency domain and in the time domain are also presented. In addition, application examples of lightning-induced voltages are presented, with special emphasis on the effects of ground losses. Section 18.4 presents a theoretical framework for modelling the electromagnetic field interaction with a buried cable. Expressions for the line parameters are given and solution methods in the frequency and the time domains are presented. Examples of lightning-induced currents and a comparison with experimental data obtained using triggered lightning are also included in that section. General conclusions are given in Section 18.5.

## 18.2 Transmission line theory

The problem of an external electromagnetic field coupling to an overhead line can be solved using a number of approaches. One such approach makes use of antenna theory, a general methodology based on Maxwell's equations\* [9]. When electrically long lines are involved, however, the antenna theory approach requires prohibitively long computational times and high computer resources. On the other hand, the less resource hungry quasi-static approximation [9], in which propagation is neglected and coupling is described by means of lumped elements, can be adopted only when the overall dimensions of the circuit are smaller than the minimum significant wavelength of the electromagnetic field. For many practical cases, however, this condition is not satisfied. As an example, let us consider the case of power lines illuminated by a lightning electromagnetic pulse (LEMP). Power networks extend, in general, over distances of several kilometres, much larger than the minimum wavelengths associated with LEMP. Indeed, significant portions of the frequency

\*Different methods based on this approach generally assume that the wire's cross-section is smaller than the minimum significant wavelength (thin-wire approximation).

spectrum of LEMP extend to frequencies up to of a few megahertz and beyond, which corresponds to minimum wavelengths of about 100 m or less (e.g. [10]).

A third approach is known as transmission line (TL) theory. The main assumptions for this approach are [11] as follows:

1. Propagation occurs along the line axis.
2. The sum of the line currents at any cross-section of the line is zero. In other words, the ground – the reference conductor – is the return path for the currents in the  $n$  overhead conductors.
3. The response of the line to the coupled electromagnetic fields is quasi-transverse electromagnetic (quasi-TEM) or, in other words, the electromagnetic field produced by the electric charges and currents along the line is confined in the transverse plane and perpendicular to the line axis.

If the cross-sectional dimensions of the line are electrically small, propagation can indeed be assumed to occur essentially along the line axis only and the first assumption can be considered to be a good approximation.

Furthermore, the second condition is satisfied if the ground plane exhibits infinite conductivity since, in that case, the currents and voltages can be obtained making use of the method of images, which guarantees currents of equal amplitude and opposite direction in the ground.

The condition that the response of the line is quasi-TEM is satisfied only up to a threshold frequency above which higher-order modes begin to appear [9]. For some cases, such as infinite parallel plates or coaxial lines, it is possible to derive an exact expression for the cut-off frequency below which only the TEM mode exists [12]. For other line structures (i.e. multiple conductors above a ground plane), the TEM mode response is generally satisfied as long as the line cross-section is electrically small [12].

Under these conditions, the line can be represented by a distributed-parameter structure along its axis.

For uniform transmission lines with electrically small cross-sectional dimensions (not exceeding about one tenth of the minimum significant wavelength of the exciting electromagnetic field), a number of theoretical and experimental studies have shown a fairly good agreement between results obtained using the transmission line approximation and results obtained by means of either antenna theory or experiments (see, e.g., [1, 13]). A detailed discussion of the validity of the basic assumptions of the transmission line theory is beyond the scope of this chapter. However, it is worth noting that, by assuming that the sum of all the currents is equal to zero, we are considering only ‘transmission line mode’ currents and neglecting the so-called antenna-mode currents [9]. If we wish to compute the load responses of the line, this assumption is adequate, because the antenna-mode current response is small near the ends of the line. Along the line, however, and even for electrically small line cross-sections, the presence of antenna-mode currents implies that the sum of the currents at a cross-section is not necessarily equal to zero [9, 12]. However, the quasi-symmetry due to the ground plane, if present, results in a very small contribution of antenna-mode currents and, consequently, the predominant mode on the line will be transmission line [9].

## 18.3 Electromagnetic field interaction with overhead lines

### 18.3.1 Single-wire line above a perfectly conducting ground

We will consider first the case of a lossless, single-wire line above a perfectly conducting ground. This simple case will allow us to introduce various field-to-transmission line coupling models and to discuss a number of concepts essential to the understanding of the electromagnetic field coupling phenomenon. Later in this chapter, we will cover the cases of lossy and multiconductor lines. The transmission line is defined by its geometrical parameters (wire radius  $a$  and height above ground  $h$ ) and its terminations  $Z_A$  and  $Z_B$ , as illustrated in Figure 18.1, where the line is illuminated by an external electromagnetic field. The problem of interest is the calculation of the induced voltages and currents along the line and at the terminations.

The external exciting electric and magnetic fields  $\vec{E}^e$  and  $\vec{B}^e$  are defined as the sum of the incident fields,  $\vec{E}^i$  and  $\vec{B}^i$ , and the ground-reflected fields,  $\vec{E}^r$  and  $\vec{B}^r$ , determined in absence of the line conductor. The total fields  $\vec{E}$  and  $\vec{B}$  at a given point in space are hence given by the sum of the excitation fields and the scattered fields from the line, the latter being denoted as  $\vec{E}^s$  and  $\vec{B}^s$ . The scattered fields are created by the currents and charges induced on the line conductor and in the ground.

Three seemingly different but completely equivalent approaches have been proposed to describe the coupling of electromagnetic fields to transmission lines. In what follows, we will present each one of them in turn. For a step-by-step derivation of the equations, see Reference 11.

### 18.3.2 Taylor, Satterwhite and Harrison model

The field-to-transmission line coupling equations as derived by Taylor, Satterwhite and Harrison [14] are given by

$$\frac{dV(x)}{dx} + j\omega L'I(x) = -j\omega \int_0^h B_y^e(x, z) dz \quad (18.1)$$

$$\frac{dI(x)}{dx} + j\omega C'V(x) = -j\omega C' \int_0^h E_z^e(x, z) dz \quad (18.2)$$

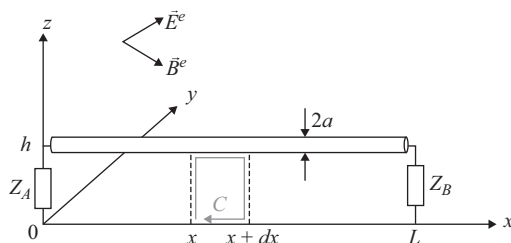


Figure 18.1 Geometry of the problem

where  $L'$  and  $C'$  are the per-unit-length line inductance and capacitance of the line, related to each other through  $\epsilon_0\mu_0 = L'C'$ .

For a line of finite length, such as the one represented in Figure 18.1, the boundary conditions for the load currents and voltages must be enforced. They are simply given by

$$V(0) = -Z_A I(0) \quad (18.3)$$

$$V(L) = Z_B I(L) \quad (18.4)$$

Note that, unlike the classical telegrapher's equations in which no external excitation is considered, the presence of an external field results in forcing functions expressed in terms of the exciting magnetic flux and electric field in both Telegrapher's equations.

Equations (18.1) and (18.2) are commonly referred to as the Taylor *et al.* model. They can be represented using an equivalent circuit, as shown in Figure 18.2. The forcing functions (source terms) in (18.1) and (18.2) are included as a set of distributed series voltage and parallel current sources along the line.

### 18.3.3 Agrawal, Price and Gurbaxani model

An equivalent formulation of the field-to-transmission line coupling equations was proposed in 1980 by Agrawal, Price and Gurbaxani [15]. This model is commonly referred to as the Agrawal *et al.* model.

The basis for the derivation of the Agrawal *et al.* model can be described as follows: The excitation fields produce a line response that is TEM. This response is expressed in terms of a scattered voltage  $V_s(x)$ , which is defined in terms of the line integral of the scattered electric field from the ground to the line. The total voltage can be obtained from the scattered voltage through

$$V(x) = V^s(x) + V^e(x) = V^s(x) - \int_0^h E_z^e(x, z) dz \quad (18.5)$$

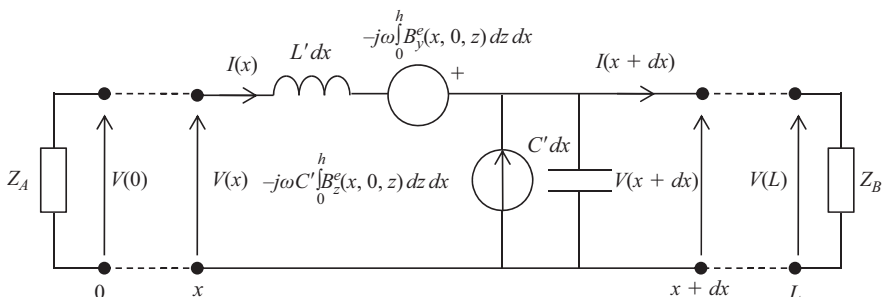


Figure 18.2 Equivalent circuit of a lossless single-wire overhead line excited by an electromagnetic field. Taylor *et al.* model

The field-to-transmission line coupling equations as derived by Agrawal *et al.* [15] are given by

$$\frac{dV^s(x)}{dx} + j\omega L'I(x) = E_x^e(x, h) \quad (18.6)$$

$$\frac{dI(x)}{dx} + j\omega C'V^s(x) = 0 \quad (18.7)$$

Note that, in this model, only one source term is present (in the first equation) and it is simply expressed in terms of the exciting electric field tangential to the line conductor  $E_x^e(x, h)$ .

The boundary conditions in terms of the scattered voltage and the total current as used in (18.6) and (18.7) are given by

$$V^s(0) = -Z_A I(0) + \int_0^h E_z^e(0, z) dz \quad (18.8)$$

$$V^s(L) = Z_B I(L) + \int_0^h E_z^e(L, z) dz \quad (18.9)$$

The equivalent circuit representation of this model ((18.6)–(18.9)) is shown in Figure 18.3. For this model, the forcing function (the exciting electric field tangential to the line conductor) is represented by distributed voltage sources along the line. In accordance with boundary conditions (18.8) and (18.9), two lumped voltage sources (equal to the line integral of the exciting vertical electric field) are inserted at the line terminations.

It is also interesting to note that this model involves only electric field components of the exciting field and the exciting magnetic field does not appear explicitly as a source term in the coupling equations. As we will see in the next section where we present the Rachidi model [16], it is also possible to represent the coupling model in terms of magnetic fields only.

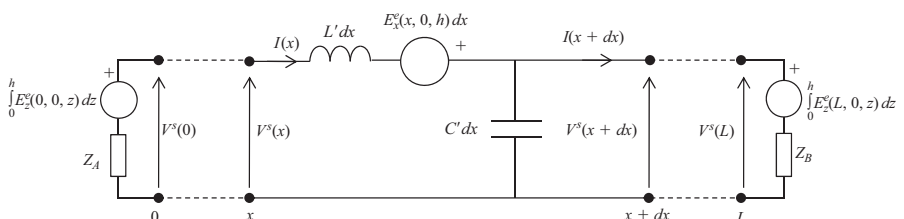


*Figure 18.3 Equivalent circuit of a lossless single-wire overhead line excited by an electromagnetic field. Agrawal *et al.* model*

### 18.3.4 Rachidi model

Another form of the coupling equations, equivalent to the Agrawal *et al.* and to the Taylor *et al.* models, has been derived by Rachidi [16]. In this model, only the exciting magnetic field components appear explicitly as forcing functions in the equations:

$$\frac{dV(x)}{dx} + j\omega L' I^s(x) = 0 \quad (18.10)$$

$$\frac{dI^s(x)}{dx} + j\omega C' V(x) = \frac{1}{L'} \int_0^h \frac{\partial B_x^e(x, z)}{\partial y} dz \quad (18.11)$$

in which  $I^s(x)$  is the so-called scattered current related to the total current by

$$I(x) = I^s(x) + I^e(x) \quad (18.12)$$

where the excitation current  $I^e(x)$  is defined as

$$I^e(x) = -\frac{1}{L'} \int_0^h B_y^e(x, z) dz \quad (18.13)$$

The boundary conditions corresponding to this formulation are

$$I^s(0) = -\frac{V(0)}{Z_A} + \frac{1}{L'} \int_0^h B_y^e(0, z) dz \quad (18.14)$$

$$I^s(L) = \frac{V(L)}{Z_B} + \frac{1}{L'} \int_0^h B_y^e(L, z) dz \quad (18.15)$$

The equivalent circuit corresponding to the above equivalent set of coupling equations is shown in Figure 18.4. Note that the equivalent circuit associated with the Rachidi model could be seen as the dual circuit – in the sense of electrical network theory – of the one corresponding to the Agrawal *et al.* model (Figure 18.3).

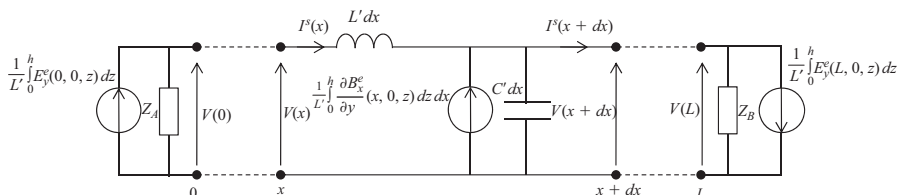


Figure 18.4 Equivalent circuit of a lossless single-wire overhead line excited by an electromagnetic field. Rachidi model

### 18.3.5 Inclusion of losses

In the calculation of lightning-induced voltages, losses are, in principle, to be taken into account both in the wire and in the ground. Losses due to the finite ground conductivity are the most important ones, and they affect both the electromagnetic field and the surge propagation along the line [17].

Let us make reference to the same geometry of Figure 18.3, and let us now take into account losses both in the wire and in the ground plane. The wire conductivity and relative permittivity are  $\sigma_w$  and  $\epsilon_{rw}$ , respectively, and the ground, assumed to be homogeneous, is characterized by its conductivity  $\sigma_g$  and its relative permittivity  $\epsilon_{rg}$ . The Agrawal *et al.* coupling equations extended to the present case of a wire above an imperfectly conducting ground can be written as (for a step-by-step derivation see Reference 9)

$$\frac{dV^s(x)}{dx} + Z'I(x) = E_x^e(x, 0, h) \quad (18.16)$$

$$\frac{dI(x)}{dx} + Y'V^s(x) = 0 \quad (18.17)$$

where  $Z'$  and  $Y'$  are the longitudinal and transverse per-unit-length impedance and admittance, respectively, given by [9, 17]

$$Z' = j\omega L' + Z'_w + Z'_g \quad (18.18)$$

$$Y' = \frac{(G' + j\omega C')Y'_g}{G' + j\omega C' + Y'_g} \quad (18.19)$$

in which

- $L'$ ,  $C'$  and  $G'$  are the per-unit-length longitudinal inductance, transverse capacitance and transverse conductance, respectively, calculated for a lossless wire above a perfectly conducting ground:

$$L' = \frac{\mu_0}{2\pi} \cosh^{-1}\left(\frac{h}{a}\right) \cong \frac{\mu_0}{2\pi} \ln\left(\frac{2h}{a}\right) \quad \text{for } h \gg a \quad (18.20)$$

$$C' = \frac{2\pi\epsilon_0}{\cosh^{-1}(h/a)} \cong \frac{2\pi\epsilon_0}{\ln(2h/a)} \quad \text{for } h \gg a \quad (18.21)$$

$$G' = \frac{\sigma_{air}}{\epsilon_0} C' \quad (18.22)$$

- $Z'_w$  is the per-unit-length internal impedance of the wire; assuming a round wire and an axial symmetry for the current, the following expression can be derived for the wire internal impedance (e.g. [18]):

$$Z'_w = \frac{\gamma_w I_0(\gamma_w a)}{2\pi a \sigma_w I_1(\gamma_w a)} \quad (18.23)$$

where  $\gamma_w = \sqrt{j\omega\mu_0(\sigma_w + j\omega\varepsilon_0\varepsilon_{rw})}$  is the propagation constant in the wire and  $I_0$  and  $I_1$  are the modified Bessel functions of zero and first order, respectively;

- $Z'_g$  is the per-unit-length ground impedance, which is defined as [19, 20]

$$Z'_g = \frac{j\omega \int_{-\infty}^h B_y^s(x, z) dx}{I} - j\omega L' \quad (18.24)$$

where  $B_y^s$  is the  $y$ -component of the scattered magnetic induction field.

Sunde [21] derived a general expression for the ground impedance that is given by

$$Z'_g = \frac{j\omega\mu_0}{\pi} \int_0^\infty \frac{e^{-2hx}}{\sqrt{x^2 + \gamma_g^2} + x} dx \quad (18.25)$$

where  $\gamma_g = \sqrt{j\omega\mu_0(\sigma_g + j\omega\varepsilon_0\varepsilon_{rg})}$  is the propagation constant in the ground.

The general expression (18.25) is not suitable for a numerical evaluation since it involves an integral over an infinitely long interval. Several approximations for the ground impedance of a single-wire line have been proposed in the literature (see Reference 17 for a survey). One of the simplest and most accurate was proposed by Sunde himself and is given by the following logarithmic function

$$Z'_g \cong \frac{j\omega\mu_0}{2\pi} \ln \left( \frac{1 + \gamma_g h}{\gamma_g h} \right) \quad (18.26)$$

It has been shown [17] that the above logarithmic expression represents an excellent approximation to the general expression (18.25) over the frequency range of interest.

Finally,  $Y'_g$  is the so-called ground admittance, given by [9]

$$Y'_g \cong \frac{\gamma_g^2}{Z'_g} \quad (18.27)$$

For typical overhead power lines, the effects of the ground admittance and the wire impedance are negligible compared to the effect of the ground impedance and the line inductance, and can be disregarded in the computation [1, 19].<sup>†</sup>

### 18.3.6 Multiconductor lines

The field-to-transmission line coupling equations for the case of a multiwire system along the  $x$ -axis above an imperfectly conducting ground (see Figure 18.5) are given by [9, 1, 22]

$$\frac{d}{dx} [V_i^s(x)] + j\omega [L'_{ij}] [I_i(x)] + [Z'_{gij}] [I_i(x)] = [E_x^e(x, 0, h_i)] \quad (18.28)$$

<sup>†</sup> Note that for buried cables, the effect of the ground admittance is no longer negligible [23].

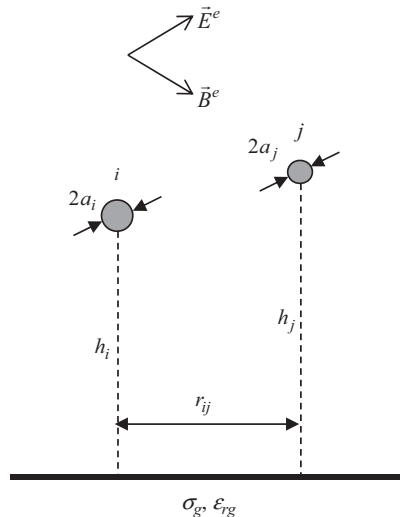


*Figure 18.5 Cross-sectional geometry of a multiconductor line above a conducting ground plane in the presence of an external electromagnetic field*

$$\frac{d}{dx} [I_i(x)] + \left[ G'_{ij} \right] [V_i^s(x)] + j\omega \left[ C'_{ij} \right] [V_i^s(x)] = [0] \quad (18.29)$$

in which

- $[V_i^s(x)]$  and  $[I_i(x)]$  are frequency-domain vectors of the scattered voltage and the current along the line;
- $[E_x^e(x, h_i)]$  is the vector of the exciting electric field tangential to the line conductors;
- $[0]$  is the zero-matrix (all elements are equal to zero);
- $[L'_{ij}]$  is the per-unit-length line inductance matrix. When the distances between conductors are much larger than their radii, the general expression for the mutual inductance between two conductors  $i$  and  $j$  is given by [9]

$$L'_{ij} = \frac{\mu_0}{2\pi} \ln \left( \frac{r_{ij}^2 + (h_i + h_j)^2}{r_{ij}^2 + (h_i - h_j)^2} \right) \quad (18.30)$$

The self-inductance for conductor  $i$  is given by

$$L'_{ii} = \frac{\mu_0}{2\pi} \ln \left( \frac{2h_i}{r_{ii}} \right) \quad (18.31)$$

$[C'_{ij}]$  is the per-unit-length line capacitance matrix. It can be evaluated directly from the inductance matrix using the following expression [9]

$$[C'_{ij}] = \epsilon_0 \mu_0 [L'_{ij}]^{-1} \quad (18.32)$$

$[G'_{ij}]$  is the per-unit-length transverse conductance matrix. The transverse conductance matrix elements can be evaluated starting from either the capacitance matrix or the inductance matrix using the following relations

$$\left[ G'_{ij} \right] = \frac{\sigma_{air}}{\epsilon_0} \left[ C'_{ij} \right] = \sigma_{air} \mu_0 [L'_{ij}]^{-1} \quad (18.33)$$

In most practical cases, the transverse conductance matrix elements  $G'_{ij}$  are negligible in comparison with  $j\omega C'_{ij}$  [12] and can therefore be neglected in the computation.

Finally,  $[Z'_{gij}]$  is the ground impedance matrix. The general expression for the mutual ground impedance between two conductors  $i$  and  $j$  derived by Sunde is given by [21]

$$Z'_{gij} = \frac{j\omega \mu_0}{\pi} \int_0^\infty \frac{e^{-(h_i+h_j)x}}{\sqrt{x^2 + \gamma_g^2} + x} \cos(r_{ij}x) dx \quad (18.34)$$

In a similar way as for the case of a single-wire line, an accurate logarithmic approximation has been proposed by Rachidi *et al.* [22] that is given by

$$Z'_{gij} \cong \frac{j\omega \mu_0}{4\pi} \ln \left[ \frac{\left( 1 + \gamma_g \left( \frac{h_i + h_j}{2} \right) \right)^2 + \left( \gamma_g \frac{r_{ij}}{2} \right)^2}{\left( \gamma_g \frac{h_i + h_j}{2} \right)^2 + \left( \gamma_g \frac{r_{ij}}{2} \right)^2} \right] \quad (18.35)$$

Note that in (18.28) and (18.29), the terms corresponding to the wire impedance and the so-called ground admittance have been neglected. This approximation is valid for typical overhead power lines [17].

The boundary conditions for the two line terminations are given by

$$[V_i^s(0)] = -[Z_A][I_i(0)] + \left[ \int_0^{h_i} E_z^e(0, 0, z) dz \right] \quad (18.36)$$

$$[V_i^s(L)] = [Z_B][I_i(L)] + \left[ \int_0^{h_i} E_z^e(L, 0, z) dz \right] \quad (18.37)$$

in which  $[Z_A]$  and  $[Z_B]$  are the impedance matrices at the two line terminations.

The line coupling equations can be solved using Green's functions to obtain closed-form solutions in the frequency domain, as we will see in Section 12.3.8, or in the time domain using the FDTD technique.

### 18.3.7 Coupling to complex networks

In order to take into account the presence of power system components, line discontinuities and complex system topologies, the LEMP-to-transmission line coupling model has been linked with appropriate circuit solver software taking advantage of the large available library of power system components (e.g. [13, 23–33]). The developed models for the calculation of LEMP-caused transients in overhead power lines have been experimentally validated using reduced-scale set-ups with LEMP and NEMP (nuclear electromagnetic pulse) simulators, and full-scale set-ups illuminated by fields from rocket-triggered lightning (see Reference 13 for a review).

### 18.3.8 Frequency-domain solutions

As mentioned in Section 12.3.6, the field-to-transmission line coupling equations, together with the boundary conditions, can be solved in the frequency domain using Green's functions, which represent the solutions for line current and voltage due to a point voltage and/or current source [9]. In this section, we will present the solutions, using the Agrawal *et al.* model for the case of a single-conductor line. Similar solutions can be found for the case of a multiconductor line (see, e.g., References 9, 12).

Considering a voltage source of unit amplitude at a location  $x_s$  along the line, the Green's functions for the current and the voltage along the line read, respectively [9],

$$G_I(x; x_s) = \frac{e^{-\gamma L}}{2Z_c(1 - \rho_1\rho_2 e^{-2\gamma L})} (e^{-\gamma(x_s - L)} - \rho^2 e^{\gamma(x_s - L)}) (e^{\gamma x_s} - \rho_1 e^{-\gamma x_s}) \quad (18.38)$$

$$G_V(x; x_s) = \frac{\delta e^{-\gamma L}}{2(1 - \rho_1\rho_2 e^{-2\gamma L})} (e^{-\gamma(x_s - L)} + \delta\rho_2 e^{\gamma(x_s - L)}) (e^{\gamma x_s} - \delta\rho_1 e^{-\gamma x_s}) \quad (18.39)$$

where

- $x_{<}$  represents the smaller of  $x$  or  $x_s$ , and  $x_{>}$  represents the larger of  $x$  or  $x_s$ .
- $-\delta = 1$  for  $x > x_s$  and  $\delta = -1$  for  $x < x_s$ .
- $\gamma = \sqrt{Z'/Y'}$  is the complex propagation constant along the transmission line,
- $Z_c = \sqrt{Z'/Y'}$  is the line's characteristic impedance.
- $\rho_1$  and  $\rho_2$  are the voltage reflection coefficients at the loads of the transmission line given by

$$\rho_1 = \frac{Z_A - Z_c}{Z_A + Z_c} \quad \rho_2 = \frac{Z_B - Z_c}{Z_B + Z_c} \quad (18.40)$$

The solutions for the total line current  $I(x)$  and scattered voltage  $V^s(x)$  can be written as the following integrals of the Green's functions [9]

$$I(x) = \int_0^L G_I(x; x_s) V'_s dx_s + G_I(x; 0) \int_0^h E_z^e(0, 0, z) dz - G_I(x; L) \int_0^h E_z^e(L, 0, z) dz \quad (18.41)$$

$$V^s(x) = \int_0^L G_V(x; x_s) V'_s dx_s + G_V(x; 0) \int_0^h E_z^e(0, 0, z) dz - G_V(x; L) \int_0^h E_z^e(L, 0, z) dz \quad (18.42)$$

Note that the second and the third terms on the right hand side of (18.41) and (18.42) are due to the contribution of equivalent lumped sources at the line ends (see Figure 18.4).

The total voltage can be determined from the scattered voltage by adding the contribution from the exciting field as

$$V(x) = V^s(x) - \int_0^h E_z^e(x, 0, z) dz \quad (18.43)$$

If we are interested in the transmission line response at its terminal loads, the solutions can be expressed in a compact way by using the so-called BLT (Baum, Liu, Tesche) equations [9]

$$\begin{bmatrix} I(0) \\ I(L) \end{bmatrix} = 1/Z_c \begin{bmatrix} 1 - \rho_1 & 0 \\ 0 & 1 - \rho_2 \end{bmatrix} \begin{bmatrix} -\rho_1 & e^{\gamma L} \\ e^{\gamma L} & -\rho_2 \end{bmatrix}^{-1} \begin{bmatrix} S_1 \\ S_2 \end{bmatrix} \quad (18.44)$$

$$\begin{bmatrix} V(0) \\ V(L) \end{bmatrix} = \begin{bmatrix} 1 + \rho_1 & 0 \\ 0 & 1 + \rho_2 \end{bmatrix} \begin{bmatrix} -\rho_1 & e^{\gamma L} \\ e^{\gamma L} & -\rho_2 \end{bmatrix}^{-1} \begin{bmatrix} S_1 \\ S_2 \end{bmatrix} \quad (18.45)$$

where the source vector is given by

$$\begin{bmatrix} S_1 \\ S_2 \end{bmatrix} = \begin{pmatrix} \frac{1}{2} \int_0^L e^{\gamma x_s} E_x^e(x_s, 0, h) dx_s + \frac{1}{2} \int_0^h E_z^e(0, 0, z) dz - \frac{e^{\gamma L}}{2} \int_0^h E_z^e(L, 0, z) dz \\ -\frac{1}{2} \int_0^L e^{\gamma(L-x_s)} E_x^e(x_s, 0, h) dx_s - \frac{e^{\gamma L}}{2} \int_0^h E_z^e(0, 0, z) dz + \frac{1}{2} \int_0^h E_z^e(L, 0, z) dz \end{pmatrix} \quad (18.46)$$

Note that in the BLT equations, the solutions are directly given for the total voltage and not for the scattered voltage.

For an arbitrary excitation field, the integrals in (18.46) cannot be carried out analytically. However, for the special case of a plane wave excitation field, the integrations can be performed analytically and closed-form expressions can be obtained for the load responses. General solutions for vertical and horizontal field polarizations are given in Reference 9.

### 18.3.9 Time-domain solutions

A time-domain representation of the field-to-transmission line coupling equations allows the straightforward treatment of nonlinear phenomena as well as the variation in the line topology [1]. On the other hand, frequency-dependent parameters, such as the ground impedance, need to be represented using convolution integrals.

The field-to-transmission line coupling equations (18.44) and (18.45) can be converted into the time domain to obtain the following expressions [11, 22]

$$\frac{\partial}{\partial x} [v_i^s(x, t)] + [L'_{ij}] \frac{\partial}{\partial t} [i_i(x, t)] + [\xi'_{ij}] \otimes \frac{\partial}{\partial t} [i_i(x, t)] = [E_x^e(x, y=0, z=h_i, t)] \quad (18.47)$$

$$\frac{\partial}{\partial x} [i_i(x, t)] + [G'_{ij}] \frac{\partial}{\partial t} [v_i^s(x, t)] + [C'_{ij}] \frac{\partial}{\partial t} [v_i^s(x, t)] = 0 \quad (18.48)$$

in which  $\otimes$  denotes convolution product and the matrix  $[\xi'_{ij}]$  is called the transient ground resistance matrix; its elements are defined as

$$[\xi'_{ij}] = F^{-1}\{[Z'_{gij}]/j\omega\} \quad (18.49)$$

The inverse Fourier transforms of the boundary conditions written, for simplicity, for resistive terminal loads read

$$[v_i^s(x, t)] = -[R_A][i_i(0, t)] + \left[ \int_0^{h_i} E_z^e(x=0, y=0, z, t) \right] \quad (18.50)$$

$$[v_i^s(L, t)] = -[R_B][i_i(L, t)] + \left[ \int_0^{h_i} E_z^e(x=L, y=0, z, t) \right] \quad (18.51)$$

where  $[R_A]$  and  $[R_B]$  are the matrices of the resistive loads at the two line terminals.

The general expression for the ground impedance matrix terms in the frequency domain does not have an analytical inverse Fourier transform. Thus, the elements of the transient ground resistance matrix in the time domain have to be, in general, determined using a numerical inverse Fourier transform algorithm. However, analytical expressions have been derived by Rachidi *et al.* [34] and Araneo and Celozzi [35] that have been shown to be reasonable approximations to the

numerical values obtained using an inverse FFT. More discussion on the validity of the approximate analytical expressions can be found in Reference 36.

One of the most popular approaches to solve the coupling equations in the time domain is the FDTD technique (e.g. [37]). Such a technique was already used by Agrawal *et al.* [15] where partial time and space derivatives were approximated using a first-order FDTD scheme. In Reference 38, instead, the use of a second-order FDTD scheme based on the Lax–Wendroff algorithm [39, 40] was proposed. The second-order FDTD scheme shows much better stability compared to its first-order counterpart, especially when analysing complex systems involving nonlinearities [38, 41].

The second-order discretized solutions for the line current and scattered voltage are given by Paolone *et al.* [13]

$$\begin{aligned} [v_i]_k^{n+1} = & [v_i]_k^n - \Delta t [C_{ij}']^{-1} \left( \frac{[i_i]_{k+1}^n - [i_i]_{k-1}^n}{2\Delta x} \right) + -\frac{\Delta t^2}{2} [[L_{ij}'][C_{ij}']]^{-1} \\ & \left( \frac{[E_{xi}]_{k+1}^n - [E_{xi}]_{k-1}^n}{2\Delta x} - \frac{[v_i]_{k+1}^n + [v_i]_{k-1}^n - 2[v_i]_k^n}{\Delta x^2} \right) \\ & + \frac{\Delta t^2}{2} [[L_{ij}'][C_{ij}']]^{-1} \left( \frac{[v'_{gi}]_{k+1}^n - [v'_{gi}]_{k-1}^n}{2\Delta x} \right) \end{aligned} \quad (18.52)$$

$$\begin{aligned} [i_i]_k^{n+1} = & [i_i]_k^n - \Delta t [L_{ij}']^{-1} \left( \frac{[v_i]_{k+1}^n - [v_i]_{k-1}^n}{2\Delta x} - [E_{xi}]_k^n + [v'_{gi}]_k^n \right) \\ & + \frac{\Delta t^2}{2} [[C_{ij}'][L_{ij}']]^{-1} \left( \frac{[i_i]_{k+1}^n + [i_i]_{k-1}^n - 2[i_i]_k^n}{\Delta x^2} \right) \\ & + \frac{\Delta t^2}{2} [[C_{ij}'][L_{ij}']]^{-1} \left( [C_{ij}'] \frac{[E_{xi}]_k^{n+1} - [E_{xi}]_k^{n-1}}{2\Delta t} \right) \\ & - \frac{\Delta t^2}{2} [[C_{ij}'][L_{ij}']]^{-1} \left( [C_{ij}'] \frac{[v'_{gi}]_k^n - [v'_{gi}]_k^{n-1}}{\Delta t} \right) \end{aligned} \quad (18.53)$$

where

- $\Delta x$  is the spatial integration step;
- $\Delta t$  is the time integration step;
- $k = 0, 1, 2, \dots, k_{max}$  is the spatial discretization index ( $k_{max} = (L/\Delta x) + 1$ , where  $L$  is the line length);
- $n = 0, 1, 2, \dots, n_{max}$  is the time discretization index;
- $[v_i]_k^{n+1}$  is the vector of the scattered voltages corresponding to the spatial and time discretization indexes  $k$  and  $n + 1$ , respectively;
- $[i_i]_k^{n+1}$  is the vector of the conductors currents corresponding to the spatial and time discretization indexes  $k$  and  $n + 1$ , respectively;

- $[E_{xi}]_k^{n+1}$  is the vector of the exciting horizontal electric field along the wires corresponding to the spatial and time discretization indexes  $k$  and  $n + 1$ , respectively;
- $[v'_{gi}]_k^n = \sum_{h=0}^n [\xi'_{gij}]_k^{n-h} \left( \frac{[i]_n^k - [i]_{n-1}^k}{\Delta t} \right)$ .

### 18.3.10 Application to lightning-induced voltages

Ground losses are generally associated with attenuation and dispersion of propagating surges along transmission lines. This is indeed the case when the travelling voltage and current waves are originated from lumped excitation sources located at specific points along the line.

However, the situation is different when the travelling waves are originated from distributed voltage and/or current sources along the line, representing the interaction of an external electromagnetic field with the line. Indeed, it has been shown that line losses due to the ground finite conductivity (e.g. [17, 42–44]) or the corona phenomenon (e.g. [45]) could result in important enhancement of the induced voltages and currents.

The aim of this section is to illustrate the complex effects of ground losses in field-to-transmission line interaction, and to emphasize that such effects could result in important enhancement of voltages induced by external fields, as opposed to direct overvoltages.

#### 18.3.10.1 Effect of Ground Losses on Overvoltages Due to a Direct Strike

Let us consider a 20-km long, 7.5-m high overhead line above a perfectly conducting ground. We shall present the overvoltages due to a direct strike to the line, calculated at different observation points along the line, as shown in Figure 18.6. The lightning current has a peak value of 4 kA and a maximum time derivative of 2 kA/ $\mu$ s.

Figure 18.7 shows the computed voltages calculated taking into account ground losses. The adopted ground parameters in the simulations are  $\sigma_g = 0.001$  S/m and  $\epsilon_r = 10$ , and the expression for the ground transient resistance is the one proposed in Reference 34. As expected, it can be seen that the resulting voltage wave experiences the typical dispersion as it travels away from the strike point.

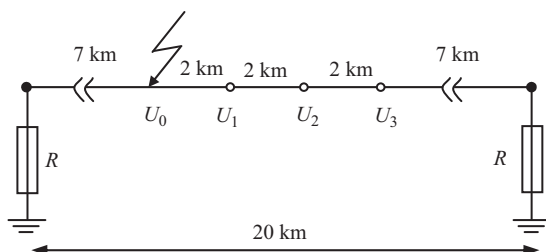
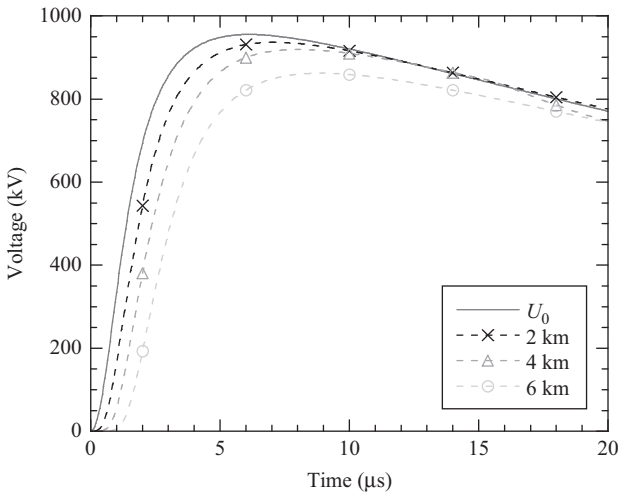


Figure 18.6 Direct lightning overvoltages along an overhead line



*Figure 18.7 Effect of ground losses on travelling voltages along the line, due to a direct lightning strike [adapted from Reference 46]. The curves at 2, 4 and 6 km correspond, respectively, to the observation points  $U_1$ ,  $U_2$  and  $U_3$  in Figure 18.6*

It is important to mention that for direct lightning strikes, the effect of ground losses is far less significant than the effect of corona. In Figure 18.8, the voltages calculated taking into account the corona effect (and omitting the effect of ground losses) are shown. The simple corona model adopted for the purpose of interest, in other words the dependence of the dynamic capacitance as a function of the voltage, is taken from Nucci *et al.* [45].

It can be seen that the travelling waves exhibit the typical distortion and attenuation associated with corona effect. A comparison between the results of Figures 18.7 and 18.8 shows, additionally, that the overvoltages are more significantly affected by the corona effect, rather than by the ground losses.

In the simulations presented in Figures 18.7 and 18.8, we assumed the magnitude of the overvoltages is below the lightning impulse withstand voltage of the line. In most of the cases, however, the surge propagating from the point of strike along the line is altered by flashovers occurring between the strike location and the point of interest. Practically, all flashovers to ground occur at the poles, as on overhead distribution lines, the weakest insulation is generally at a pole structure rather than between conductors through air [47]. Figure 18.9 shows a typical overvoltage (evaluated by calculations) due to a direct lightning strike of 30 kA current amplitude. The calculations have been performed using the Electromagnetic Transient Program (EMTP) [48] for a single-wire line with no ground wires. The line is composed of eight spans (nine poles) of 200 m length each with a characteristic impedance of 440  $\Omega$ . Each pole, 8-m high, is modelled as a transmission line with a characteristic impedance of 300  $\Omega$ . The footing DC resistance

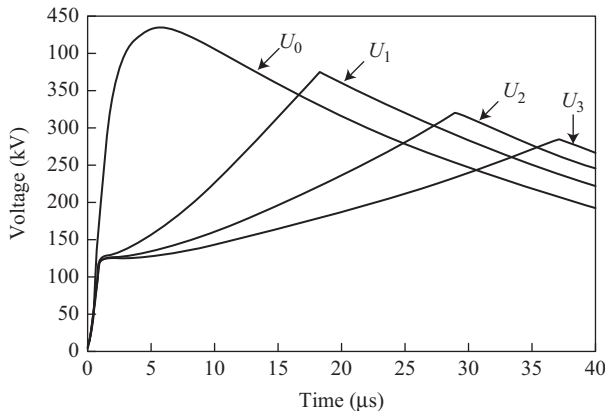


*Figure 18.8* Influence of corona on travelling voltages along the line, due to a direct lightning strike [adapted from Reference 45]. The curves labelled  $U_0$ ,  $U_1$ ,  $U_2$  and  $U_3$  correspond, respectively, to the curves labelled  $U_0$ , 2, 4 and 6 km in Figure 18.7 and to the observation points labelled  $U_0$ ,  $U_1$ ,  $U_2$  and  $U_3$  in Figure 18.6

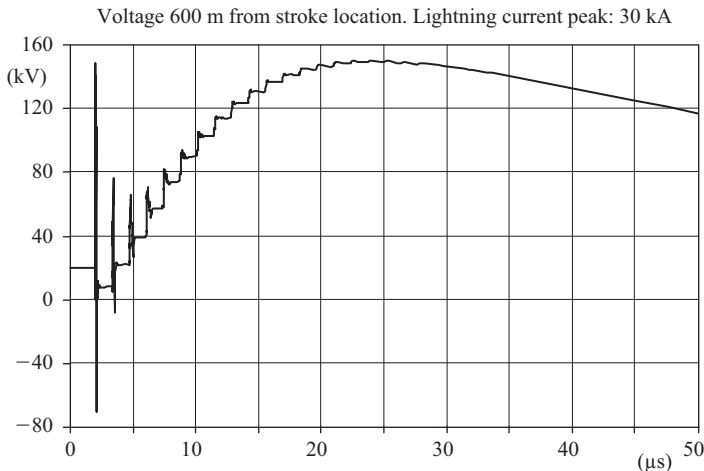


*Figure 18.9* Example of a typical lightning overvoltage due to a direct strike to the MV line [adapted from Reference 47, computations performed by T. Henriksen]

was assumed to be nonlinear (current-dependent), with  $30 \Omega$  at zero current. The insulator flashover voltage was fixed at 150 kV. The voltage is calculated 600 m from the stroke location. The example shows the general characteristics of the direct lightning overvoltage that presents a few very short spikes followed by an impulse voltage with a smoother shape [47].

### 18.3.10.2 Effect of Ground Losses on Induced O vervoltages

We will now consider a single-wire overhead line matched at both ends, and illuminated by the electromagnetic field radiated by a nearby lightning return stroke. The computations are carried out by means of the LIOV code (see Reference 1 for a detailed description of models used in the code).

The wire is at a height of 10 m above a ground plane characterized by a ground conductivity  $\sigma_g = 0.001 \text{ S/m}$  and a relative permittivity  $\epsilon_r = 10$ . The return stroke current has a peak value of 12 kA and a maximum time derivative of  $40 \text{ kA}/\mu\text{s}$  (typical of subsequent return strokes).

Figure 18.10 presents the voltage induced along a 2.8-km line for a return stroke located in the vicinity of the left-end terminal. This configuration has been chosen because it is similar to an event recorded by De La Rosa *et al.*, on an experimental line in Mexico [49]. The voltages reported in Figure 18.10 are calculated assuming (i) the ground as perfectly conducting; and (ii) considering the finitely conducting ground.

The computed results show that the voltages calculated taking into account ground losses exhibit significantly larger amplitudes than those calculated assuming a perfectly conducting ground. Also, the voltages exhibit an inversion of polarity as the observation point moves towards the far end of the line.

The reason why, for the examined case, ground losses can result in an amplitude enhancement has been discussed thoroughly in a few papers [1, 44, 50]. In summary, it can be said that the finite conductivity of the ground does not significantly affect the vertical electric field amplitude and waveshape, but acts in modifying the horizontal electric field waveshape and, in particular, it results in this field component's polarity reversal [17, 51, 52]. This inversion of polarity is more pronounced for larger distances and for larger values of ground resistivity, as shown in Figure 18.11.

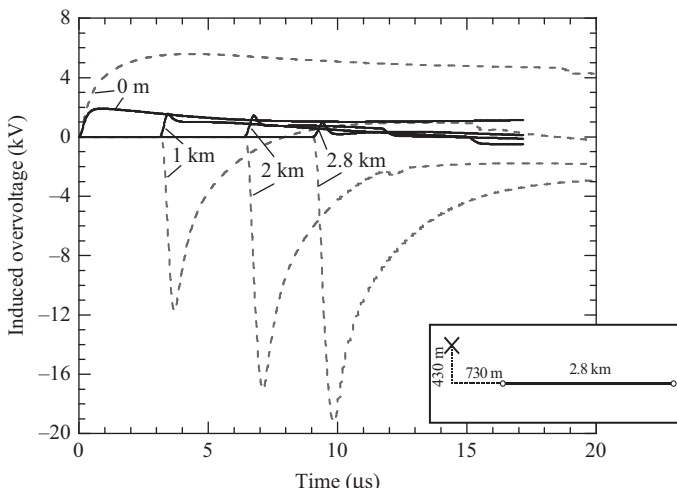
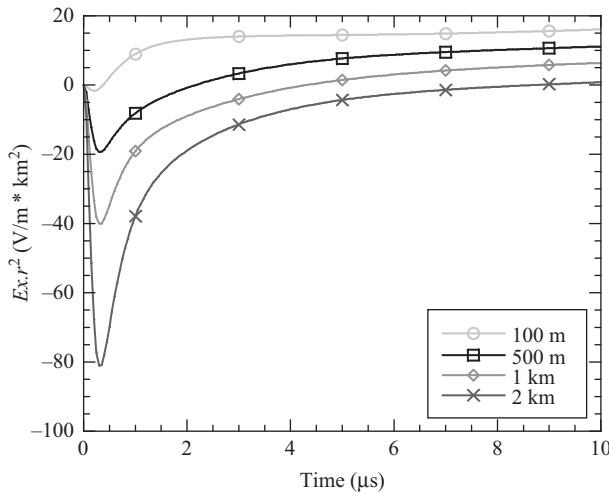


Figure 18.10 Lightning-induced voltages along the line. Solid line: perfect ground; dashed line: lossy ground [adapted from Reference 46]



*Figure 18.11 Radial electric field at four distances from the stroke location calculated with the Cooray–Rubinstein formula [51, 52]. Ground conductivity 0.001 S/m, ground relative permittivity 10. Observation point: at 10 m above ground. For illustrative purpose, the values are multiplied by the square of the distance from the stroke location [adapted from Reference 44]*

Figure 18.10 also shows that the voltage induced at farther distances along the line from the strike location exhibits larger amplitudes than that close to lightning. Experimental data obtained by De La Rosa and co-workers [49] support this theoretical finding, since for an event similar to the one presented in Figure 18.10, they observed line flashover occurring at the far end of the line and not at the close one.

Additional experimental data supporting the enhancement of the induced voltage due to the finite ground conductivity were presented by Ishii *et al.* [42, 53]. An example is shown in Figure 18.12 where the induced voltage measured on an experimental reduced-scale line is compared with computation results. As it can be seen from the figure, the induced voltage magnitude for a ground conductivity of 0.06 S/m is about twice as large as the induced voltage computed assuming a perfectly conducting ground.

It is important to bear in mind, however, that for different stroke locations and observation points along the line, ground losses also could result in an attenuation of the induced voltages (see References 1, 19). For this reason, statistical evaluations are of utmost importance when the assessment of the lightning performance of distribution lines is pursued [54, 55].

As we have seen in the previous subsection, lightning overvoltages due to a direct strike are essentially determined by the corona effect. For the case of induced voltages by a nearby lightning strike, corona effect needs to be taken into account

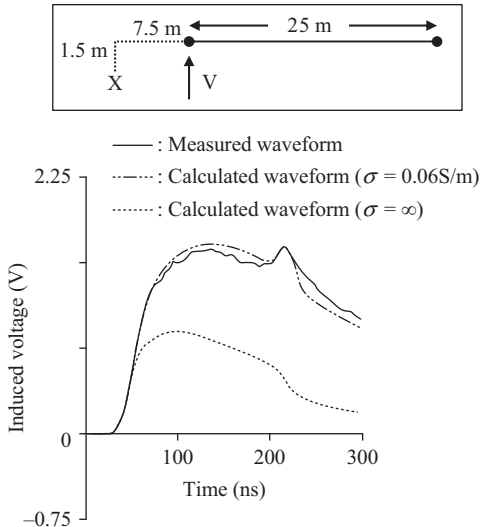


Figure 18.12 Lightning-induced voltage on an experimental reduced-scale line. Comparison between measured waveforms and computations [adapted from Reference 53]

only for particularly severe excitation conditions (very close impact point and/or large return stroke current peaks) [45]. In this case, Nucci *et al.* [45] have shown that the corona effect would result in an enhancement of the induced voltage magnitudes, as opposed to the typical attenuation observed in the case of direct strikes. This enhancement can be explained, theoretically, by considering that the increase in the line capacitance produced by corona results in a decrease of the propagation speed of the various surges induced by lightning. This reduction in the propagation speed makes it possible for the total induced voltage – which results from all the contributions of the various induced surges – to reach larger magnitudes (see Reference 45 for a more detailed explanation).

As an example, Figure 18.13 shows the lightning-induced voltages on a 1-km long, 7.5-m high, single-conductor overhead line, taking into account the corona effect [45, 56].

## 18.4 Electromagnetic field interaction with buried cables

### 18.4.1 Field-to-buried cables coupling equations

Consider a horizontal buried cable of length  $L$  (cylindrical conductor with an insulated jacket) located along the  $x$ -axis at depth  $d$ . Assuming that the vertical component of electric field can be neglected below the ground surface [57], voltages and

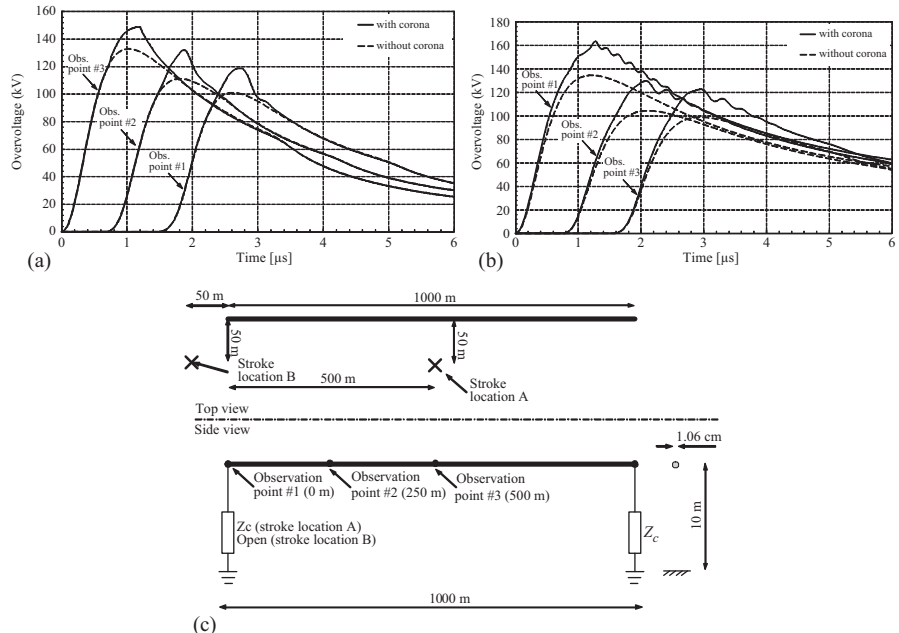


*Figure 18.13* Voltage induced by a nearby lightning at three observation points along a 1-km overhead line in the presence of corona. Solid lines: taking into account corona; dotted lines: disregarding corona. Ground: perfectly conducting. Stroke location: (a) stroke location A of Figure 18.13c; stroke location B of Figure 18.13c [adapted from Reference 56]

currents along the cable induced by a nearby lightning can be calculated using the field-to-transmission line equations expressed in the frequency domain [58, 59]

$$\frac{dV(x)}{dx} + Z'I(x) = E_x^e(x, z = -d) \quad (18.54)$$

$$\frac{dI(x)}{dx} + Y'V(x) = 0 \quad (18.55)$$

where the longitudinal impedance is

$$Z' = j\omega L' + Z'_w + Z'_g \quad (18.56)$$

and the transversal admittance is

$$Y' = \frac{(G' + j\omega C') \cdot Y'_g}{(G' + j\omega C') + Y'_g} \quad (18.57)$$

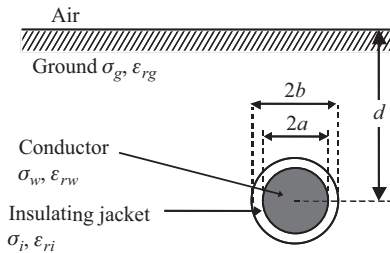


Figure 18.14 Geometry of the buried cable (cylindrical conductor of radius  $a$  with an insulating jacket)

in which (see Figure 18.14 for the geometrical parameters)

- $L'$  and  $C'$  are, respectively, the per-unit-length longitudinal inductance and transverse capacitance of the cable:

$$L' = \frac{\mu_0}{2\pi} \ln\left(\frac{b}{a}\right) \quad (18.58)$$

$$C' = \frac{2\pi\epsilon_0\epsilon_{ri}}{\ln(b/a)} \quad (18.59)$$

- $G'$  is the per-unit-length transverse conductance of the cable:

$$G' = \frac{\sigma_i}{\epsilon_0\epsilon_{ri}} C' \quad (18.60)$$

- $Z'_w$  is the per-unit-length internal impedance of the conductor (wire). Assuming an axial symmetry for the current, the following expression can be adopted [18]:

$$Z'_w = \frac{\gamma_w I_0(\gamma_w a)}{2\pi a \sigma_w I_1(\gamma_w a)} \quad (18.61)$$

where  $\gamma_w = \sqrt{j\omega\mu_0(\sigma_w + j\omega\epsilon_0\epsilon_{rw})}$  is the propagation constant in the wire and the  $\epsilon_{rw}$  relative permittivity of the wire.

- $Z'_g$  and  $Y'_g$  are the per-unit-length ground impedance and ground admittance, respectively. These two quantities are related through the following expression [9]:

$$Y'_g \cong \frac{\gamma_g^2}{Z'_g} \quad (18.62)$$

where  $\gamma_g$  is the propagation constant in the ground, which can be expressed as  $\gamma_g = \sqrt{j\omega\mu_0(\sigma_g + j\omega\epsilon_0\epsilon_{rg})}$ .

Several expressions have been proposed in the literature for the ground impedance (see Reference 60 for a review).

Most of the approximate formulas neglect the contribution of the displacement current and therefore predict values for the ground impedance that tend to infinity at higher frequencies. This corresponds in the time domain to a singularity of the ground transient resistance at  $t=0$ . A logarithmic approximation has been proposed by Petrache *et al.* [60] that, unlike most of the considered approximations, has an asymptotic behaviour at high frequencies. This expression reads

$$Z'_g = \frac{j\omega\mu_0}{2\pi} \ln\left(\frac{1 + \gamma_g b}{\gamma_g b}\right) \quad (18.63)$$

Petrache *et al.* [60] have also shown that, within the frequency range of interest, the wire impedance can be neglected, due to its small contribution to the overall longitudinal impedance of the line. The ground admittance, however, can play an important role at high frequencies (1 MHz or so) especially in the case of poor ground conductivity. The ground admittance needs to be taken into account in the calculation of lightning-induced currents and voltages on buried cables. This is in contrast with the case of overhead lines in which its contribution is generally negligible even in the MHz range.

#### 18.4.2 Frequency-domain solutions

In a similar way to the case of overhead lines (Section 18.2.8), the field-to-buried wire lines can be solved using Green's functions. For an arbitrary incident field exciting the cable (the vertical electric field component underground is neglected), the solution for the cable current and voltage at an arbitrary position  $x$  on the cable can be written as the following integrals of the Green's functions [9, 60]

$$I(x) = \int_0^L G_I(x, x_s) V'_s dx_s \quad (18.64)$$

$$V(x) = \int_0^L G_V(x, x_s) V'_s dx_s \quad (18.65)$$

Where  $G_I$  and  $G_V$  represent the Green's function for the cable current and voltage, respectively, which are given by [9]

$$G_I(x, x_s) = \begin{cases} \frac{e^{-\gamma L}}{2Z_c(1 - \rho_1\rho_2 e^{-2\gamma L})} \left[ e^{-\gamma(x_s - L)} - \rho_2 e^{\gamma(x_s - L)} \right] (e^{\gamma x} - \rho_1 e^{-\gamma x}) & \text{for } x < x_s \\ \frac{e^{-\gamma L}}{2Z_c(1 - \rho_1\rho_2 e^{-2\gamma L})} \left[ e^{-\gamma(x - L)} - \rho_2 e^{\gamma(x - L)} \right] (e^{\gamma x_s} - \rho_1 e^{-\gamma x_s}) & \text{for } x > x_s \end{cases} \quad (18.66)$$

$$G_V(x, x_s) = \begin{cases} \frac{-e^{-\gamma L}}{2(1 - \rho_1\rho_2 e^{-2\gamma L})} \left[ e^{-\gamma(x_s - L)} - \rho_2 e^{\gamma(x_s - L)} \right] (e^{\gamma x} + \rho_1 e^{-\gamma x}) & \text{for } x < x_s \\ \frac{e^{-\gamma L}}{2(1 - \rho_1\rho_2 e^{-2\gamma L})} \left[ e^{-\gamma(x - L)} + \rho_2 e^{\gamma(x - L)} \right] (e^{\gamma x_s} - \rho_1 e^{-\gamma x_s}) & \text{for } x > x_s \end{cases} \quad (18.67)$$

where  $\gamma = \sqrt{Z'Y'}$  is the line complex propagation constant along the cable and  $Z_c = \sqrt{Z'/Y'}$  is the line characteristic impedance.

A frequency-domain solution is particularly useful when one is interested in calculating the inner response of a shielded cable [61], which involves the cable transfer function, a highly frequency-dependent quantity.

### 18.4.3 Time-domain solutions

The field-to-transmission line coupling equations (18.54) and (18.55) can be converted into the time domain to obtain the following expressions:

$$\frac{\partial v(x, t)}{\partial x} + L' \frac{\partial i(x, t)}{\partial t} + \xi'_g(t) \otimes \frac{\partial i(x, t)}{\partial t} = E_x^e(x, d, t) \quad (18.68)$$

$$\frac{\partial i(x, t)}{\partial x} + C' \frac{\partial v(x, t)}{\partial t} + \eta'_g(t) \otimes \frac{\partial i(x, t)}{\partial t} = 0 \quad (18.69)$$

where

$\xi'_g(t)$  is the transient ground resistance defined as the inverse Fourier transform of  $\frac{Z'_g}{j\omega}$ ;

$\otimes$  denotes convolution product;

$\eta'_g(t)$  represents the transient ground conductance defined as the inverse Fourier transform of  $\frac{Y'_{add}}{j\omega}$ , where  $Y'_{add}$  is defined by

$$Y'_{add} = -\frac{(j\omega C')^2}{j\omega C' + Y'_g} \quad (18.70)$$

The general expression for the ground impedance in the frequency domain does not have an analytical inverse Fourier transform. However, an analytical expression for the ground transient resistance in the time domain is proposed in Reference 60 which is shown to be sufficiently accurate and nonsingular. The ground transient conductance has to be determined using a numerical inverse Fourier transform. A time-domain solution of field-to-buried cable coupling equations using the point-centred FDTD method can be found in Reference 60.

### 18.4.4 Lightning-induced disturbances in a buried cable

Paolone *et al.* [62] and Petrache *et al.* [61] presented experimental results obtained at the International Center for Lightning Research and Testing (ICLRT) at Camp Blanding, Florida during the summers of 2002 and 2003. Currents induced by triggered and natural lightning events were measured at the terminations of a buried power cable, in the cable shield and in the inner cable conductor.

Figure 18.15 illustrates the positions (stroke locations) for which experimental data were recorded.

A comparison between the measured currents in the cable shield at the IS2 termination and those predicted by simulations is presented in Figure 18.16 [62]. Figure 18.17 presents the measured and simulated currents in the inner conductor of

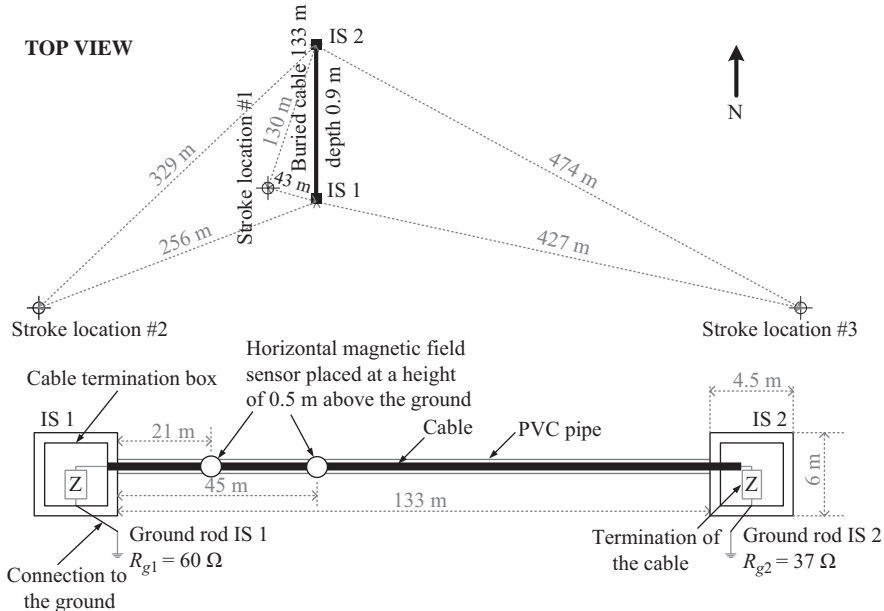


Figure 18.15 Positions of the triggered lightning strokes (top) and buried cable experimental set-up (bottom). The cable shield is connected to the ground rods at IS 1 and IS 2 [adapted from Reference 62]

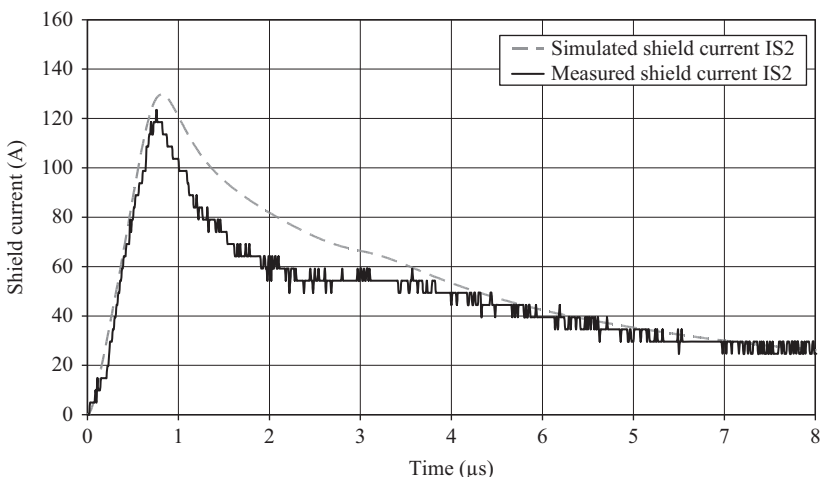
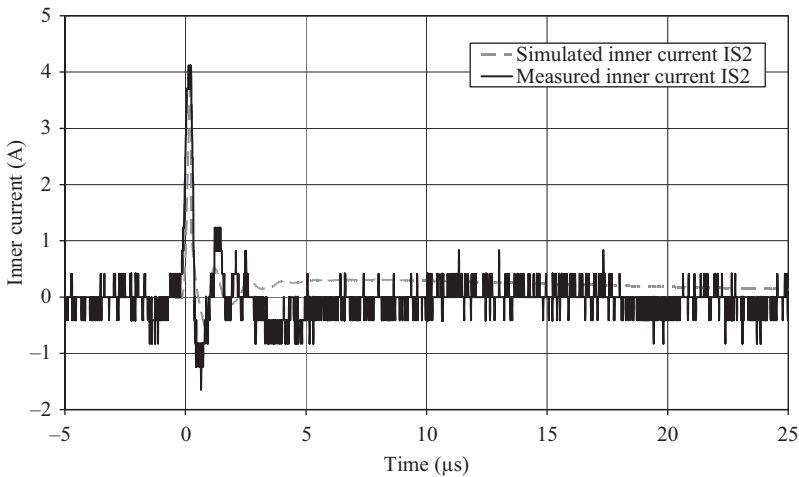


Figure 18.16 Comparison between experimental and simulation results for the lightning-induced current in the shield of the experimental cable for the first return stroke of a single-stroke flash recorded on 18 August 2002; strike location no. 1 [adapted from Reference 62]



*Figure 18.17 Experimental data and simulation results for the lightning-induced currents in the inner conductor of the experimental cable for the flash recorded on 18 August 2002; strike location no. 1 [adapted from Reference 61]*

the buried shielded cable. The coupling to the inner conductor was evaluated using the concept of cable transfer impedance. It can be seen that the simulation results are in good agreement with experimental data.

## 18.5 Conclusions

In this chapter, we discussed the Transmission Line (TL) theory and its application to the problem of lightning electromagnetic field coupling to transmission lines.

After a short discussion on the underlying assumptions of the transmission line theory, we described seemingly different but completely equivalent approaches that have been proposed to describe the coupling of electromagnetic fields to transmission lines.

The field-to-transmission line coupling equations were then extended to deal with the presence of losses and multiple conductors and expressions for the line parameters, including the ground impedance and admittance were presented. The time-domain representation of the field-to-transmission line coupling equations, which allows for a straightforward treatment of nonlinear phenomena as well as the variation in the line topology, was also described. Solution methods in the frequency domain and in the time domain were given and application examples with reference to lightning-induced voltages were presented and discussed.

Specifically, the effect of ground losses was illustrated and discussed. When the travelling voltage and current waves are originated from lumped excitation sources located at a specific location along a transmission line (direct lightning strike), both the corona phenomenon and ground losses result in an attenuation and

dispersion of propagating surges along transmission lines. However, when distributed sources representing the action of the electromagnetic field from a nearby lightning illuminating the line are present, ground losses and the corona phenomenon could result in important enhancement of the induced voltage magnitude.

Finally, we reviewed the theory of electromagnetic field coupling to a buried cable. Solution methods in the frequency and the time domain were also presented. Examples of lightning-induced currents and comparison with experimental data were presented.

## Acknowledgements

The material presented in this chapter is mainly the results of a joint Italo-Swiss research cooperation carried out during the last two decades involving Alberto Borghetti, Silvia Guerreri, Michel Ianoz, Carlo Mazzetti, Mario Paolone and Emanuel Petrache. Their contribution and support are gratefully acknowledged. The authors wish to express their gratitude to V.A. Rakov, F.M. Tesche and M.A. Uman for their precious cooperation throughout these years.

## References

1. C. Nucci and F. Rachidi, ‘Interaction of electromagnetic fields generated by lightning with overhead electrical networks’, in *The Lightning Flash*, V. Cooray, Ed., London: IEE, 2003, pp. 425–478
2. D. M. Le Vine and R. Meneghini, ‘Simulation of radiation from lightning return strokes: the effects of tortuosity’, *Radio Science*, vol. 13, pp. 801–809, 1978
3. D. M. Le Vine and R. Meneghini, ‘Electromagnetic fields radiated from a lightning return stroke: application of an exact solution to Maxwell’s equations’, *Journal of Geophysical Research*, vol. 83, pp. 2377–2384, 1978
4. A. Sakakibara, ‘Calculation of induced voltages on overhead lines caused by inclined lightning strikes’, *IEEE Transactions on Power Delivery*, vol. 4, pp. 683–693, 1989
5. S. C. Wu and W. T. Hsiao, ‘Characterization of induced voltages on overhead power lines caused by lightning strokes with arbitrary configurations’, in *International Conference on Systems, Man, and Cybernetics*, 1994, pp. 2706–2710
6. R. Moini, S. H. H. Sadeghi, B. Kordi and F. Rachidi, ‘An antenna-theory approach for modeling inclined lightning return stroke channels’, *Electric Power Systems Research*, vol. 76, pp. 945–952, 2006
7. V. A. Rakov and M. A. Uman, ‘Review and evaluation of lightning return stroke models including some aspects of their application’, *IEEE Transactions on Electromagnetic Compatibility*, vol. 40, pp. 403–426, 1998

8. V. A. Rakov and F. Rachidi, 'Overview of recent progress in lightning research and lightning protection', *IEEE Transactions on Electromagnetic Compatibility*, vol. 51, pp. 428–442, 2009
9. F. M. Tesche, M. Ianoz and T. Karlsson, *EMC Analysis Methods and Computational Models*. New York: Wiley Interscience, 1997
10. V. Cooray, *The Lightning Flash*. United Kingdom: IEE, 2003
11. C. A. Nucci, F. Rachidi and A. Rubinstein, 'Derivation of telegrapher's equations and field-to-transmission line interaction', in *Electromagnetic Field Interaction with Transmission Lines: From Classical Theory to HF Radiation Effects*, F. Rachidi and S. Tkachenko, Eds., Southampton: WIT Press, 2008
12. C. R. Paul, *Analysis of Multiconductor Transmission Lines*. New York: Wiley, 1994
13. M. Paolone, F. Rachidi, A. Borghetti, C. A. Nucci, M. Rubinstein, V. A. Rakov and M. A. Uman, 'Lightning electromagnetic field coupling to overhead lines: theory, numerical simulations and experimental validation', *IEEE Transactions on Electromagnetic Compatibility*, vol. 51, pp. 532–547, 2009
14. C. D. Taylor, R. S. Satterwhite and C. W. Harrison, 'The response of a terminated two-wire transmission line excited by a nonuniform electromagnetic field', *IEEE Transactions on Antennas and Propagation*, vol. AP-13, pp. 987–989, 1965
15. A. K. Agrawal, H. J. Price and S. H. Gurbaxani, 'Transient response of multiconductor transmission lines excited by a nonuniform electromagnetic field', *IEEE Transactions on Electromagnetic Compatibility*, vol. 22, pp. 119–129, May 1980
16. F. Rachidi, 'Formulation of the field-to-transmission line coupling equations in terms of magnetic excitation fields', *IEEE Transactions on Electromagnetic Compatibility*, vol. 35, pp. 404–407, 1993
17. F. Rachidi, C. A. Nucci, M. Ianoz and C. Mazzetti, 'Influence of a lossy ground on lightning-induced voltages on overhead lines', *IEEE Transactions on Electromagnetic Compatibility*, vol. 38, pp. 250–263, 1996
18. S. Ramo, J. R. Whinnery and T. van Duzer, *Fields and Waves in Communication Electronics*, 3rd ed. New York: Wiley, 1994
19. F. Rachidi, C. A. Nucci, M. Ianoz and C. Mazzetti, 'Importance of losses in the determination of lightning-induced voltages on overhead lines', *EMC '96 ROMA. International Symposium on Electromagnetic Compatibility. Univ. Rome 'La Sapienza', Rome, Italy*, vol. 2, 1996
20. F. M. Tesche, 'Comparison of the transmission line and scattering models for computing the HEMP response of overhead cables', *IEEE Transactions on Electromagnetic Compatibility*, vol. 34, May 1992
21. E. D. Sunde, *Earth Conduction Effects in Transmission Systems*. New York: Dover Publication, 1968, p. 112
22. F. Rachidi, C. A. Nucci and M. Ianoz, 'Transient analysis of multiconductor lines above a lossy ground', *IEEE Transactions on Power Delivery*, vol. 14, pp. 294–302, 1999

23. C. A. Nucci, V. Bardazzi, R. Iorio, A. Mansoldo and A. Porrino, ‘A code for the calculation of lightning-induced overvoltages and its interface with the Electromagnetic Transient program’, in *22nd International Conference on Lightning Protection (ICLP)*, Budapest, Hungary, 1994, R 3b-05
24. D. Orzan, P. Baraton, M. Ianoz and F. Rachidi, ‘Comparaison entre deux approches pour traiter le couplage entre un champ EM et des réseaux de lignes’, in *8ème Colloque International sur la Compatibilité Electromagnétique*, Lille, France, 1996
25. D. Orzan, ‘Couplage externe et interne entre un champ électromagnétique et un réseau de lignes multifilaires (Ph.D. thesis)’, Ph.D., Ecole Polytechnique Federale de Lausanne, Lausanne, Switzerland, 1998
26. H. K. Hoidalen, ‘Lightning-induced overvoltages in low-voltage systems (Ph.D. thesis)’, Norwegian University of Science and Technology, 1997
27. H. K. Hoidalen, ‘Calculation of lightning-induced overvoltages using MODELS’, *International Conference on Power Systems Transients. Tech. Univ. Budapest*, Budapest, Hungary, 1999
28. H. K. Hoidalen, ‘Analytical formulation of lightning-induced voltages on multiconductor overhead lines above lossy ground’, *IEEE Transactions on Electromagnetic Compatibility*, vol. 45, pp. 92–100, 2003
29. H. K. Hoidalen, ‘Calculation of lightning-induced voltages in MODELS including lossy ground effects’, in *International Conference on Power System Transient IPST 2003*, New Orleans, USA, 2003
30. E. Perez, A. Delgadillo, D. Urrutia and H. Torres, ‘Optimizing the Surge Arresters Location for Improving Lightning Induced Voltage Performance of Distribution Network’, presented at the IEEE PES General Meeting, Tampa, Florida, 2007
31. A. Borghetti, A. Gutierrez, C. A. Nucci, M. Paolone, E. Petracche and F. Rachidi, ‘Lightning-induced voltages on complex distribution systems: models, advanced software tools and experimental validation’, *Journal of Electrostatics*, vol. 60, pp. 163–174, 2004
32. F. Napolitano, A. Borghetti, C. A. Nucci, M. Paolone, F. Rachidi and J. Mahserejian, ‘An advanced interface between the liov code and the EMTP-RV’, in *29th International Conference on Lightning Protection (ICLP)*, Uppsala, Sweden, 2008
33. R. Montano, N. Theethayi and V. Cooray, ‘An efficient implementation of the Agrawal *et al.* model for lightning-induced voltage calculations using circuit simulation software’, *IEEE Transactions on Circuits and Systems-I: Regular Papers*, vol. 55, pp. 2959–2965, 2008
34. F. Rachidi, S. Loyka, C. A. Nucci and M. Ianoz, ‘A new expression for the ground transient resistance matrix elements of multiconductor overhead transmission lines’, *Electric Power System Research Journal*, vol. 65, pp. 41–46, 2003
35. R. Araneo and S. Cellozi, ‘Direct time domain analysis of transmission lines above a lossy ground’, *IEE Proc. Science & Measurement Technology*, vol. 148, pp. 73–79, 2001

36. N. Theethayi and R. Thottappillil, ‘Surge propagation and crosstalk in multi-conductor transmission lines above ground’, in *Electromagnetic Field Interaction with Transmission Lines. From Classical Theory to HF Radiation Effects*, F. Rachidi and S. Tkachenko, Eds., United Kingdom: WIT Press, 2008
37. A. Taflove, *Computational Electrodynamics: The Finite Difference Time Domain Method*. USA: Artech House, 1995
38. M. Paolone, C. A. Nucci and F. Rachidi, ‘A new finite difference time domain scheme for the evaluation of lightning induced overvoltages on multi-conductor overhead lines’, in *5th International Conference on Power System Transients*, Rio de Janeiro, 2001
39. P. D. Lax and B. Wendroff, ‘System of conservations laws’, *Communications on Pure & Applied Mathematics*, vol. 13, pp. 217–237, 1960
40. S. R. Omick and S. P. Castillo, ‘A new finite difference time-domain algorithm for the accurate modeling of wide-band electromagnetic phenomena’, *IEEE Transactions on Electromagnetic Compatibility*, vol. 35, pp. 215–222, 1993
41. M. Paolone, ‘Modeling of lightning-induced voltages on distribution networks for the solution of power quality problems, and relevant implementation in a transient program Ph.D. thesis’, Department of Electrical Engineering, University of Bologna, Bologna, Italy, 2001
42. M. Ishii, K. Michishita, Y. Hongo and S. Ogume, ‘Lightning-induced voltage on an overhead wire dependent on ground conductivity’, *IEEE Transactions on Power Delivery*, vol. 9, pp. 109–118, 1994
43. V. F. Hermosillo and V. Cooray, ‘Calculation of fault rates of overhead power distribution lines due to lightning induced voltages including the effect of ground conductivity’, *IEEE Transactions on Electromagnetic Compatibility*, vol. 37, pp. 392–399, August 1995
44. S. Guerrieri, C. A. Nucci and F. Rachidi, ‘Influence of the ground resistivity on the polarity and intensity of lightning induced voltages’, in *10th International Symposium on High Voltage Engineering*, Montreal, Canada, 1997
45. C. A. Nucci, S. Guerrieri, M. T. Correia de Barros and F. Rachidi, ‘Influence of corona on the voltages induced by nearby lightning on overhead distribution lines’, *IEEE Transactions on Power Delivery*, vol. 15, pp. 1265–1273, 2000
46. F. Rachidi, C. A. Nucci, S. Guerrieri and M. T. Correia de Barros, ‘On the amplitude enhancement of voltages induced by external EM fields on transmission lines due to ground losses and corona phenomenon’, in *IEEE International Symposium on Electromagnetic Compatibility*, Montreal, Canada, 2001
47. ‘CIGRE-CIRED JWG C4.4.02: Protection of MV and LV Networks against Lightning. Part I: Common Topics’, *CIGRE Technical Brochure No 287*, 2006
48. H. W. Dommel, *Electromagnetic Transient Program Reference Manual (EMTP Theory Book)*, Bonneville Power Administration, Portland, OR August 1986
49. F. De la Rosa, R. Valdivia, H. Pérez and J. Loza, ‘Discussion about the inducing effects of lightning in an experimental power distribution line in Mexico’, *IEEE Transactions on Power Delivery*, vol. 3, pp. 1080–1089, 1988

50. P. Chowdhuri, V. Cooray, M. T. Correia de Barros, M. Darveniza, F. De la Rosa, G. Diendorfer, F. Heidler, M. Ishii, W. Janischewskyj, T. Kawamura, C. Mazzetti, C.A. Nucci (Responsible Member), P. Pettersson, F. Rachidi, V. A. Rakov, M. Rubinstein, T. Short, V. Shostak, L. Thione, M. A. Uman and S. Yokoyama, ‘Lightning induced voltages on overhead power lines. Part III: sensitivity Analysis’, *Electra*, vol. 222, pp. 27–30, 2005
51. V. Cooray, ‘Lightning-induced overvoltages in power lines: validity of various approximations made in overvoltage calculations’, in *22nd International Conference on Lightning Protection*, Budapest, Hungary, 1994
52. M. Rubinstein, ‘An approximate formula for the calculation of the horizontal electric field from lightning at close, intermediate, and long range’, *IEEE Transactions on Electromagnetic Compatibility*, vol. 38, pp. 531–535, 1996
53. M. Ishii, K. Michishita and Y. Hongo, ‘Verification of coupling model for calculation of induced lightning voltages’, in *CIGRE International Colloquium on Insulation Coordination*, Toronto, Canada, 1997
54. A. Borghetti, C. A. Nucci and M. Paolone, ‘An improved procedure for the assessment of overhead line indirect lightning performance and its comparison with the IEEE Std. 1410 Method’, *IEEE Transactions on Power Delivery*, vol. 22, pp. 684–692, January 2007
55. A. Borghetti, C. A. Nucci and M. Paolone, ‘Indirect-lightning performance of overhead distribution networks with complex topology’, *IEEE Transactions on Power Delivery*, vol. 24, pp. 2206–2213, 2009
56. G. Dragan, G. Florea, C. A. Nucci and M. Paolone, ‘On the influence of corona on lightning-induced overvoltages’, in *30th International Conference on Lightning Protection*, Cagliari, Italy, 2010
57. V. Cooray, ‘Horizontal fields generated by return strokes’, *Radio Science*, vol. 27, pp. 529–537, 1992
58. A. Galvan and V. Cooray, ‘Lightning induced voltages on bare and insulated buried cables’, in *13th Zurich International Symposium on Electromagnetic Compatibility*, Zurich, Switzerland, 1999, pp. 191–196
59. E. F. Vance, *Coupling with Shielded Cables*. New York: Wiley, 1978
60. E. Petrache, F. Rachidi, M. Paolone, C. Nucci, V. A. Rakov and M. A. Uman, ‘Lightning-Induced Voltages on Buried Cables’, Part I: theory’, *IEEE Transactions on Electromagnetic Compatibility*, vol. 47, pp. 498–508, August 2005
61. E. Petrache, M. Paolone, F. Rachidi, C. A. Nucci, V. A. Rakov, M. A. Uman, D. Jordan, K. Rambo, J. Jerauld, M. Nyffeler and J. Schoene, ‘Lightning-induced currents in buried coaxial cables: a frequency-domain approach and its validation using rocket-triggered lightning’, *Journal of Electrostatics*, vol. 65, pp. 322–328, 2007
62. M. Paolone, E. Petrache, F. Rachidi, C. A. Nucci, V. A. Rakov, M. A. Uman, D. Jordan, K. Rambo, J. Jerauld, M. Nyffeler and J. Schoene, ‘Lightning-induced voltages on buried cables. Part II: experiment and model validation’, *IEEE Transactions on Electromagnetic Compatibility*, vol. 47, pp. 509–520, 2005

---

## *Chapter 19*

# **Scale models and their application to the study of lightning transients in power systems**

*Alexandre Piantini<sup>1</sup> and Jorge M. Janiszewski<sup>1</sup>*

---

## **19.1 Introduction**

The reliability of a power system bears on its ability to supply continuous and uninterrupted energy without significant momentary disturbances. However, power lines are often located in areas of high ground flash densities, being therefore prone to lightning-caused faults.

For most overhead power transmission lines, lightning is the primary cause of unscheduled interruptions, which may result from either shielding failure or back-flashover. The first situation occurs when the lightning stroke bypasses the overhead ground wire and terminates directly on a phase conductor. If the stroke current is larger than a certain value, the resultant voltages across the insulator strings will exceed the line critical impulse flashover voltage (CFO) and lead to flashover. Even if lightning strikes the tower or an overhead ground wire, depending on parameters such as the stroke current magnitude and front time, line CFO, tower impedance and footing resistance, the voltages across the insulators may be high enough to cause a flashover. In such a situation it is called back-flashover, as it results from a lightning stroke to part of the network that is normally at ground potential.

Concerning distribution networks, failures of power equipment, especially transformers and pin insulators, are frequently observed, particularly when lines cross rural areas and are consequently more exposed to direct strikes. Lightning overvoltages on distribution lines may be originated either from direct strikes or by induction due to nearby flashes. Although the former are much more severe, the latter are usually responsible for a greater number of line flashovers and supply interruptions on systems with rated voltage 15 kV or less, due to their higher frequency of occurrence and low line insulation withstand capability. The generation mechanisms of these two kinds of overvoltages are completely different and both of them must be correctly computed for the evaluation of the lightning performance of a given distribution network.

Investigations on lightning transients on power systems can be carried out through the use of the following methods: measurements on real, full-scale power

<sup>1</sup>University of São Paulo, Brazil

lines; rocket-triggered lightning; digital simulations and scale models. The first provides direct data about overvoltages caused by natural lightning [1–15], but a complete analysis can only be made if the lightning strike point, stroke current waveform and propagation velocity, soil resistivity, high-frequency behaviour of power line equipment (e.g. transformers) and line parameters such as the grounding interval and ground resistance at each point are known. Besides, a long time is required to obtain a statistically relevant amount of data.

On the other hand, the rocket-triggered lightning technique allows for simultaneous measurements of overvoltages and the most important lightning parameters, constituting a notable tool for the study of the interaction of lightning with various objects and systems [16–23]. The results obtained from the experiments carried out at the International Center for Lightning Research and Testing (ICLRT) in Camp Blanding, Florida, USA, have contributed significantly to a better understanding of the lightning phenomenon and to the characterization of stroke parameters. However, owing to the costs associated with the implementation of such system (area, launch control, experimental lines, measuring equipment, etc.), as well as to the high degree of personnel specialization required, there are just a few research centres in operation around the world.

Once the physical principles that dominate the induction phenomenon are understood, the assessment of the overvoltages and of the line lightning performance can be achieved by means of computer simulations. Elaborate models and numerical codes, capable of describing the transient behaviour of realistic line configurations in a rather accurate way, have been developed in recent years, such as the Electromagnetic Transients Program (EMTP) [24]. Nonetheless, there are situations of high complexity level which cannot be simulated with the existing versions of such codes.

The scale model technique enables tests to be performed under controlled conditions and allows for the simulation of a wide variety of situations. Once the system is implemented, a significant amount of data can be obtained in a relatively short time. The technique is widespread in the fields of civil and mechanical engineering. In electrical engineering, models have been employed to study, for instance, transient voltages in transformers [25], the radiation patterns of antennas [26], electric fields in substations or close to overhead lines [27–30], direct strikes to power transmission lines [31–34], lightning strikes in the vicinity of power distribution networks [35–48] and overvoltages in wind turbine generator systems resulting from direct lightning strikes [49, 50]. Scale models of electrical systems have been an important tool to predict power system transients after different types of perturbations. These are flexible tools that can be advantageous for the validation of theoretical models as well as for the analysis of the lightning electromagnetic pulse (LEMP) response of complex electric power networks.

This chapter presents, initially, the theory of scale models. Then, methods for simulating the electromagnetic environment, as well as various power system components, namely overhead lines, transformers and surge arresters are described, and details are given on the reduced system implemented at the University of São Paulo, Brazil. The last part of the chapter is dedicated to the application of the

technique for the evaluation of lightning transients, with emphasis on the analysis of lightning-induced voltages on overhead power distribution lines. The versatility of the scale model technique is demonstrated and examples are presented that illustrate its usefulness in the analysis of complex phenomena, either for enabling the evaluation of situations that are not worthwhile to be treated theoretically or for giving adequate support for the validation of theoretical models and relevant computer codes.

## 19.2 Basis of scale modelling

A scale model of a certain electromagnetic system depends on the definition of the numerical relationships between the values of the quantities in the model and in the full-scale system. The scale factors can be derived by applying Maxwell's equations to the real system and the reduced scale model and, then, by relating the quantities of interest in both systems.

Considering the equations for the curls of the electric ( $E$ ) and magnetic ( $H$ ) fields

$$\nabla \times \bar{H} = \sigma \bar{E} + \varepsilon \frac{\partial \bar{E}}{\partial t} \quad (19.1)$$

and

$$\nabla \times \bar{E} = -\mu \frac{\partial \bar{H}}{\partial t} \quad (19.2)$$

in a given medium with conductivity  $\sigma$ , permittivity  $\varepsilon$  and permeability  $\mu$ , the scale factors for length ( $p$ ), time ( $\gamma$ ), electric field ( $\alpha$ ) and magnetic field ( $\beta$ ) can be defined as

$$\left\{ \begin{array}{l} p = \frac{x_m}{x} = \frac{y_m}{y} = \frac{z_m}{z} \quad \gamma = \frac{t_m}{t} \\ \alpha = \frac{E_m}{E} \quad \beta = \frac{H_m}{H} \end{array} \right. \quad (19.3)$$

where  $x, y$  and  $z$  refer to the coordinate system,  $t$  represents the time and subscript  $m$  refers to scale model variables. In the scale model, the fields are described by

$$\left\{ \begin{array}{l} \nabla_m \times \bar{H}_m = \sigma_m \bar{E}_m + \varepsilon_m \frac{\partial \bar{E}_m}{\partial t_m} \\ \nabla_m \times \bar{E}_m = -\mu_m \frac{\partial \bar{H}_m}{\partial t_m} \end{array} \right. \quad (19.4)$$

$$\left. \left\{ \begin{array}{l} \nabla_m \times \bar{H}_m = \sigma_m \bar{E}_m + \varepsilon_m \frac{\partial \bar{E}_m}{\partial t_m} \\ \nabla_m \times \bar{E}_m = -\mu_m \frac{\partial \bar{H}_m}{\partial t_m} \end{array} \right. \right. \quad (19.5)$$

with

$$\bar{H}_m = \bar{H}_m(x_m, y_m, z_m, t_m), \quad \bar{E}_m = \bar{E}_m(x_m, y_m, z_m, t_m)$$

and  $\sigma_m$ ,  $\varepsilon_m$  and  $\mu_m$  representing the characteristics of the scale model medium.

In (19.4) and (19.5), the symbol  $\nabla_m$  stands for differentiations with respect to the model coordinates. It can be shown that the scale factor for the curl operator is  $1/p$ . Thus,

$$\nabla_m \times \bar{\mathbf{H}}_m = \frac{1}{p} \nabla \times \bar{\mathbf{H}}_m = \frac{\beta}{p} \nabla \times \bar{\mathbf{H}} \quad (19.6)$$

Analogously

$$\nabla_m \times \bar{\mathbf{E}}_m = \frac{\alpha}{p} \nabla \times \bar{\mathbf{E}} \quad (19.7)$$

Differentiating  $E_m$  and  $H_m$  with respect to time leads to

$$\frac{\partial \bar{\mathbf{E}}_m}{\partial t_m} = \frac{\alpha}{\gamma} \frac{\partial \bar{\mathbf{E}}}{\partial t} \quad (19.8)$$

and

$$\frac{\partial \bar{\mathbf{H}}_m}{\partial t_m} = \frac{\beta}{\gamma} \frac{\partial \bar{\mathbf{H}}}{\partial t} \quad (19.9)$$

Substituting (19.6) to (19.9) into (19.4) and (19.5) results in

$$\frac{\beta}{p} \nabla \times \bar{\mathbf{H}} = \sigma_m \alpha \bar{\mathbf{E}} + \frac{\alpha}{\gamma} \varepsilon_m \frac{\partial \bar{\mathbf{E}}}{\partial t} \quad (19.10)$$

and

$$\frac{\alpha}{p} \nabla \times \bar{\mathbf{E}} = -\mu_m \frac{\beta}{\gamma} \frac{\partial \bar{\mathbf{H}}}{\partial t} \quad (19.11)$$

In order to represent correctly the real system by the model, (19.10), (19.11) and (19.1), (19.2) must be equivalent. Thus,

$$\begin{cases} \varepsilon_m = \frac{\gamma\beta}{p\alpha} \varepsilon \\ \mu_m = \frac{\alpha\gamma}{p\beta} \mu \\ \sigma_m = \frac{\beta}{p\alpha} \sigma \end{cases} \quad (19.12)$$

From the above definitions, the scale factor of any electromagnetic quantity can be determined. If air is the medium in both systems, the following conditions must prevail:

$$\begin{cases} \varepsilon_m = \varepsilon \rightarrow \frac{\gamma\beta}{p\alpha} = 1 \\ \mu_m = \mu \rightarrow \frac{\alpha\gamma}{p\beta} = 1 \end{cases} \quad (19.13)$$

Then,

$$\alpha = \beta, \quad \gamma = p, \quad \sigma_m = \frac{\sigma}{p} \quad (19.14)$$

i.e. the scale factor for conductivity must be the inverse of that of length. Clearly, the last condition is not satisfied, as air is the medium for both systems. However, considering that air is a good insulator, the error resulting in not taking its conductivity into account can be neglected.

The scale factors for the quantities of interest, considering the general case and the special one, when the medium (air) is the same for both systems, are reported in Table 19.1. The results show that if  $p$  and either  $\alpha$  or  $\beta$  are known, the scale factors for all quantities can be determined. On the other hand, if only  $p$  and the ratio between  $\alpha$  and  $\beta$  are known, then only some of the quantities can be directly related.

*Table 19.1 Scale factors: ratios between the values of the quantities in the model and in the full-scale system [35, 41]*

Quantity	General case	Special case: same medium (air) for both systems
Length	$p$	$p$
Time	$\gamma$	$p$
Electric field	$\alpha$	$\alpha$
Magnetic field	$\beta$	$\alpha$
Resistance	$\alpha/\beta$	1
Capacitance	$\beta \cdot \gamma / \alpha$	$p$
Inductance	$\alpha \cdot \gamma / \beta$	$p$
Impedance	$\alpha/\beta$	1
Propagation velocity	$p/\gamma$	1
Frequency	$1/\gamma$	$1/p$
Conductivity	$\beta/(p \cdot \alpha)$	$1/p$
Voltage	$\alpha \cdot p$	$\alpha \cdot p$
Current	$\beta \cdot p$	$\beta \cdot p$

### 19.3 Simulation of the electromagnetic environment

The choice of the length scale factor  $p$  depends on the available area for the installation of the facility and on the features of the available generation and measuring systems. A very low scale factor allows for the simulation of longer lines and stroke channels in laboratories of smaller dimensions. This procedure, however, implies the need of measuring systems with larger bandwidths.

This section describes the requirements for simulating the electromagnetic environment and for modelling some important power system components. The information given here refers mostly to the 1:50 scale model implemented at the University of São Paulo for the investigation of lightning transients in overhead

*Table 19.2 Scale factors relevant to the system implemented at the University of São Paulo [41]*

Quantity	Scale factor
Length	1:50
Time	1:50
Electric field	1:360
Magnetic field	1:360
Resistance	1:1
Capacitance	1:50
Inductance	1:50
Impedance	1:1
Propagation velocity	1:1
Frequency	50:1
Conductivity	50:1
Voltage	1:18,000
Current	1:18,000

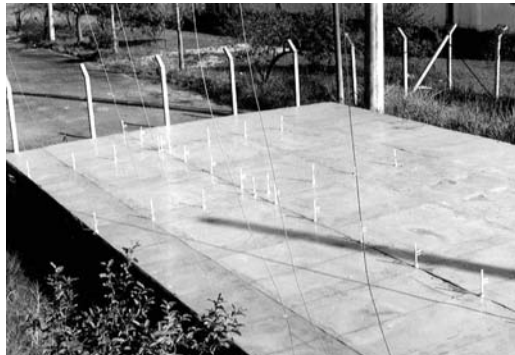


*Figure 19.1 General view of the scale model; generation and measuring systems located below the ground plane*

power lines. The scale factors relevant to the electrical quantities of this system are reported in Table 19.2, whereas a general view of the experimental facility, showing the ground plane and a typical configuration of an urban distribution system with a main feeder and some laterals, is presented in Figure 19.1.

### 19.3.1 Return stroke channel

Among the various stages of a lightning discharge, it is usually during the return stroke phase that the major problems concerning lightning overvoltages arise. In this phase the lightning current may reach peak values, at ground level, from few kA to more than 100 kA. The return stroke front propagation velocity along the channel decreases with height and falls in the range of about 6–87% of that of light

in free space [51], although even higher values were reported in Reference 52 within the lowest 500 m of the lightning channel.

Several physical and mathematical models have been proposed for the return stroke [53–57]. In reduced scale experiments related to the analysis of overvoltages on power lines caused by either direct or nearby lightning events, the lightning channel is usually represented by means of a transmission line [31, 32, 34–46, 48]. Nevertheless, other methods are sometimes used. For instance, the tests carried out in Reference 33 to evaluate the voltages across insulator strings as a result of direct strikes to transmission lines were performed using a repetitive pulse generator to apply current surges directly to the tower or to one end of the overhead ground wire. In Reference 47, the assessment of the influence of shield wires on lightning-induced voltages on overhead lines was made using a pulse generator, from which pulse voltages were applied to a metal mesh suspended in the air and located in the vicinity of a distribution line model.

In References 35 and 41, the return stroke channel was simulated by a copper conductor wound on an insulating rod in such a way that the propagation velocity of the current along the channel was about 11% of that of light in free space. Owing to local restrictions, the stroke channel model, which is shown in Figure 19.2, was limited to a length of 12 m. The number of turns was approximately 323 per metre of rod length and the diameters of the copper conductor and insulating rod were 0.7 mm and 25.4 mm, respectively.

The propagation velocity along the return stroke channel model (r.s.m.) and the surge impedance of the simulated channel ( $Z_0$ ) were experimentally determined from the analysis of reflected voltages resulting from the application of a step signal at one end, leaving the other one open. The value obtained for  $Z_0$  was  $2.2 \text{ k}\Omega$ . In order to eliminate reflections, a non-inductive resistor  $R = 2.2 \text{ k}\Omega$  was then



Figure 19.2 Return stroke channel model

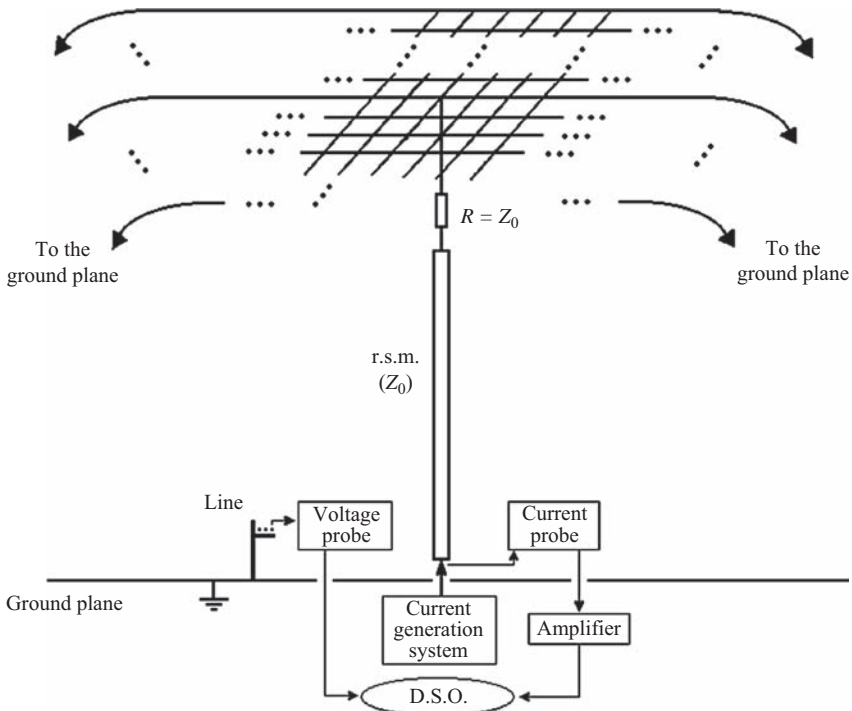


*Figure 19.3 Schematic diagram of the experimental set up [35]*

connected between the top of the stroke channel model and the mesh of conductors providing the return path for the injected current, as shown in Figure 19.3. The return conductors, some of which can be seen in Figure 19.1, were separated by a distance of approximately 1 m. Therefore, for the relevant frequencies of the r.s.m. current spectrum, the return conductors can be reasonably assumed to represent a conducting surface involving the system, so that the electromagnetic field in the region under analysis is established by the current along the r.s.m. As pointed out in Reference 35, although the r.s.m. was not intended to provide an accurate simulation of the lightning channel, for points relatively far from it the current can be assumed to propagate upwards with the determined velocity so that the radiated electromagnetic field can be calculated with good accuracy.

As air is the medium for both systems and therefore the scale factors for time and length are equal, currents with very short rise times are needed to simulate typical lightning currents. For a scale model with  $p = 1:50$ , the front time of the simulated stroke current must be about some tens of nanoseconds (e.g. 40 ns for a typical first stroke front time of 2  $\mu$ s). Moreover, the current amplitude must be of the order of at least a few amperes in order to enable the simulation of surge arresters. As the channel surge impedance  $Z_0$  is relatively high, it would not be possible to obtain currents with the desired characteristics with the use of a

capacitor. Therefore, a high-voltage cable, 280 m long, charged by a d.c. voltage source was used to generate such a current [35, 41, 45]. Once the desired voltage was reached, the cable was connected to the r.s.m. through a high-speed switch. As the circuit impedance was predominantly resistive, this technique allowed the generation of currents with the desired, relatively short, front times.

The current injected into the r.s.m. was measured at ground level by a current probe associated with an amplifier. The measuring system bandwidth was from d.c. to 50 MHz and its rise time was shorter than 7 ns. For the measurements reported in Reference 35, digital storage oscilloscopes (DSO) with sampling rates of either 500 MS/s or 1 GS/s (single-shot bandwidths of 200 MHz and 250 MHz, respectively) were used.

### 19.3.2 Ground

The ground resistivity depends on the type of soil and on various factors such as soil granulometry, degree of compactness, quantity and kind of dissolved salts, stratification, water content and temperature. It varies widely and, depending on the condition, may assume values lower than  $100 \Omega\text{.m}$  or greater than  $10,000 \Omega\text{.m}$ .

With a few exceptions [48], in scale model experiments the ground is usually assumed as a perfectly conducting plane and simulated by means of copper or aluminium sheets [31–47]. In Reference 58, Rachidi *et al.* show that the approximation of a perfectly conducting ground is in general reasonable for the calculation of both the azimuthal magnetic field and the vertical component of the electric field for distances between the lightning stroke location and the observation point shorter than about 1 km, although the time derivatives of both fields may be significantly affected by the propagation effects, as pointed out by Cooray [59, 60]. On the other hand, the earth resistivity has a remarkable effect on the horizontal electric field [58, 61–66], and, by extension, on the lightning-induced voltages. Several investigations have been carried out about the influence of a lossy ground on lightning-induced voltages on overhead lines [9, 48, 58, 61, 67–70] and, according to Nucci [61], the assumption of a perfectly conducting ground is reasonable for distribution systems located above a soil with resistivity lower than about  $100 \Omega\text{.m}$ .

In References 35 and 41, the whole scale model was placed above a conducting plane realized by means of interconnected aluminium plates covering an area of  $28 \times 9 \text{ m}^2$ , which is equivalent to  $1400 \times 450 \text{ m}^2$  on a full-scale basis.

### 19.3.3 Overhead lines

Although the choice of a scale factor for length  $p$  requires the use of materials with conductivities  $1/p$  times (thus, higher than) those of the materials of the actual system, in reduced scale experiments copper wires are usually used for simulating the line conductors, as the inherent errors can be reasonably neglected.

In References 35 and 41, the scale model was used to simulate typical 15-kV distribution lines. The conductors were simulated by means of copper wires with an overall length of 28 m and diameter of 0.4 mm. They were mounted on polyvinyl



*Figure 19.4 Model of a single-phase distribution line*

chloride (PVC) structures spaced 60 cm and with such a form that allowed the representation of different network configurations. The adopted dimensions represent a full-scale system of 1.4-km overall length with 2.0-cm conductors diameter and spacing of 30 m between adjacent poles. The line was composed of either a single or four conductors (three phases plus neutral). One of test configurations corresponding to a single-phase line is illustrated in Figure 19.4. The three-phase line had a main feeder and various laterals, and the phase and neutral conductors were placed at heights of 20 cm and 16 cm above ground, corresponding to 10 m and 8 m, respectively.

#### 19.3.4 Transformers

A transformer can be viewed as a complex network of capacitances, resistances, self-inductances and mutual inductances, and the knowledge of its response when subject to lightning and switching surges is of great importance for designing and development. In Reference 25, an electromagnetic model was developed to evaluate transient voltages in transformer windings. The model, which represented an important advance in the field of transient analysis in transformers, consisted of two parts of different scale factors: an equivalent circuit of capacitances and a geometrical model for the self and mutual inductances, even if non-linear. The voltages measured at different points of real transformers and their respective models were in very good agreement, and the accuracy of the model was considered entirely adequate for design purposes. The electromagnetic model is flexible, all points of interest are readily available and measurements can be made easily and rapidly.

However, when the reproduction of the transformer's internal characteristics is not aimed at and only its response as a power system component is required, much simpler models can be used. For instance, in the investigation on lightning-induced

voltages on medium voltage (MV) networks carried out in References 35 and 41, the distribution transformers were represented, in the scale model, by capacitors of 10 pF (corresponding to 0.5 nF on a full-scale basis) connected between each phase conductor and the neutral. This capacitance value was inferred from measurements, as function of frequency, of the input impedance ( $Z_t$ ) of a typical three-phase, 30 kVA, 13.8 kV–220/127 V, delta-grounded wye connected distribution transformer. The measurements were performed with the three terminals of the MV side short-circuited, assuming the differential mode of induced voltage to be negligible. This is indeed a very reasonable assumption, as the distance from the stroke location to the line is in general much larger than the distance between the line conductors, and therefore, the voltages induced on the phase conductors are practically equal.

Through a signal generator, voltages of constant amplitude and variable frequency were applied to the MV terminals and simultaneous measurements were made of the applied voltage and of the currents injected into each terminal. The input impedances were obtained from those measurements for 50 different frequencies in the range of 2 kHz to 1 MHz. As no significant differences were found among the values relative to the three terminals, the impedance corresponding to the middle terminal was taken as representative of the transformer. For a transformer with its primary winding delta connected and short-circuited terminals, there is no current flow through the primary winding and thus  $Z_t$  is practically independent of the load connected to the secondary. This was confirmed by tests carried out considering three conditions for the low-voltage (LV) terminals: open, short-circuited and connected to resistors of  $1.6\ \Omega$  representing the transformer nominal load.

Although the evaluation of voltages transferred to the transformer secondary demands a more detailed representation, this simple model is perfectly suitable for studies concerned with lightning transients on MV networks, for which only the simulation of the transformer input impedance seen from the primary side is required. This impedance has in general a predominantly capacitive behaviour, as illustrated in Figure 19.5 for a three-phase distribution transformer, similar to the

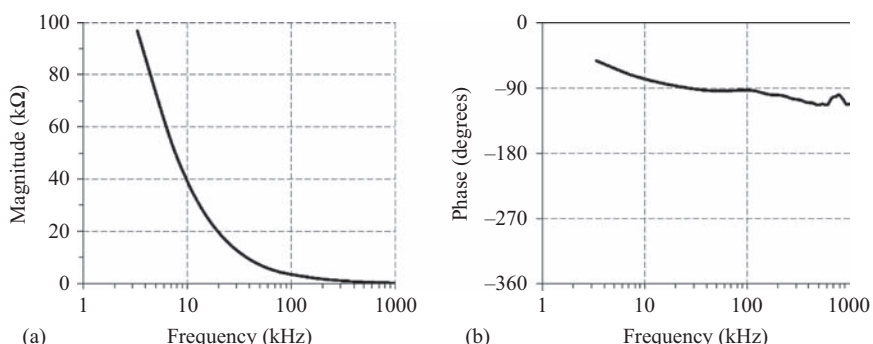


*Figure 19.5 Input impedance  $Z_t$  (per phase) of a typical three-phase, 30 kVA, 13.8 kV–220/127 V, delta-grounded wye connected distribution transformer: (a) Magnitude; (b) phase*

one considered in References 35 and 41, also rated 30 kVA and delta-grounded wye connected.

### 19.3.5 Surge arresters

Several investigations have been carried out on the effectiveness of surge arresters in mitigating lightning overvoltages and improving the lightning performance of power lines [1, 11, 35–37, 40–42, 71–73]. In Reference 41, a model was developed to enable an experimental study of the effect of surge arresters on lightning-induced voltages on overhead lines. The main motivation for developing such a model was related to the non-existence, at that time, of a complete set of data involving measurements of lightning-induced voltages on lines with surge arresters. As induced voltages are influenced by several parameters [36, 41, 66, 74, 75], the use of data obtained under controlled conditions is essential to validate theoretical models and their relevant codes.

The arrester models were designed to reproduce the non-linear *VI* characteristics (residual voltage vs. discharge current) of surge arresters commonly used in distribution systems, what was accomplished by a combination of diodes and resistors. For the model validation, tests were performed on nine distribution arresters (six SiC and three ZnO) with rated voltage and current of 12 kV and 5 kA, respectively.

The *VI* characteristic is in general obtained by applying the standard current (8/20  $\mu$ s waveform) to the arrester and measuring the peak value of the voltage at its terminals. However, instead of the peak value, in Reference 41, the *VI* characteristics were obtained considering the voltage values corresponding to the instant at which the current reaches its maximum, as the usual measuring techniques do not eliminate the circuit inductance effects and, therefore, the obtained peak values are larger than the real ones. This discrepancy increases for faster front time currents, and in Reference 76 it is recommended to take the value of the voltage at the current peak point, especially for front times shorter than about 4  $\mu$ s.

As in the case of nearby strokes the currents through the arresters hardly ever reach values higher than 1 kA [41, 77], the similarity between the behaviours of the model and the actual arresters was verified also for relatively low currents. An appropriate circuit with components selected to produce the standard current waveform, taking into account the time scale factor, was used to test the model and the actual arresters. Based on the analysis of the test results, the scale factor 1:18,000 was adopted for voltage and current and, as a consequence, the scale factor for electric and magnetic fields ( $\alpha$ ) was determined as 1:360. Therefore, the quantities of the model could be related to the full-scale system by applying the relationships shown in Table 19.1, as presented in Table 19.2.

Figure 19.6 shows the dynamic *VI* characteristics, i.e. the curves relating instantaneous values of voltages and currents, for the model and for the distribution arresters. The *VI* characteristics obtained by combining all the test results are presented in Figure 19.7. As the scatter among the results relative to surge arresters of the same type (ZnO or SiC) was small, the results corresponding to each type were grouped. It can be readily seen that the surge arrester model represents relatively

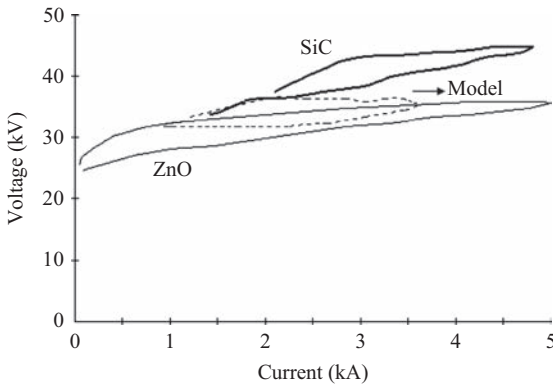


Figure 19.6 Dynamic VI characteristics for the model (scale factor 1:18,000 for voltage and current) and for actual SiC and ZnO surge arresters [adapted from References 35 and 41]

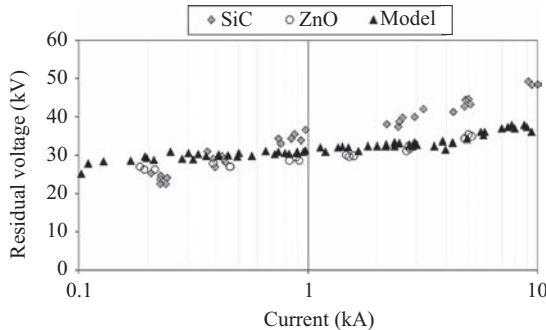
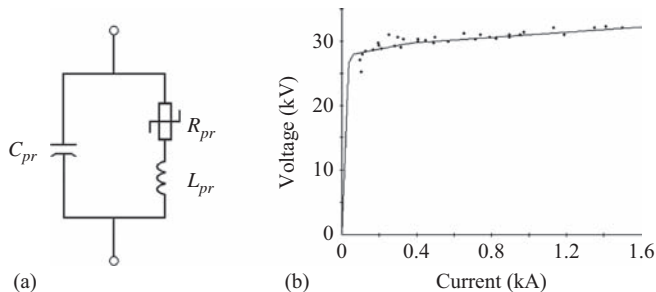


Figure 19.7 VI characteristics for the model (scale factor 1:18,000 for voltage and current) and actual SiC and ZnO surge arresters [adapted from References 35 and 41]

well the behaviour of the actual arresters within the range of the current peak values considered.

The equivalent circuit of the surge arrester model is composed of a resistance  $R_{pr}$  in series with an inductance  $L_{pr}$ , both in parallel with a capacitance  $C_{pr}$ , as shown in Figure 19.8(a). The behaviour of the non-linear resistance  $R_{pr}$  is presented in Figure 19.8(b). The inductance  $L_{pr}$  and the capacitance  $C_{pr}$  were introduced to represent more accurately the model transient behaviour. In particular, the inductance stands for the increase on the residual voltage for currents with short front times, whereas the capacitance is associated with the voltage wavefront.

Several preliminary simulations indicated that the circuit shown in Figure 19.8 represents relatively well the arrester model when the values of  $L_{pr}$  and  $C_{pr}$  are, respectively, 0.02  $\mu\text{H}$  and 270 pF (corresponding to 1.0  $\mu\text{H}$  and 13.5 nF on a



*Figure 19.8 Surge arrester model equivalent circuit: (a) electric circuit; (b) characteristic of the non-linear resistor  $R_{pr}$  [adapted from References 35 and 41]*

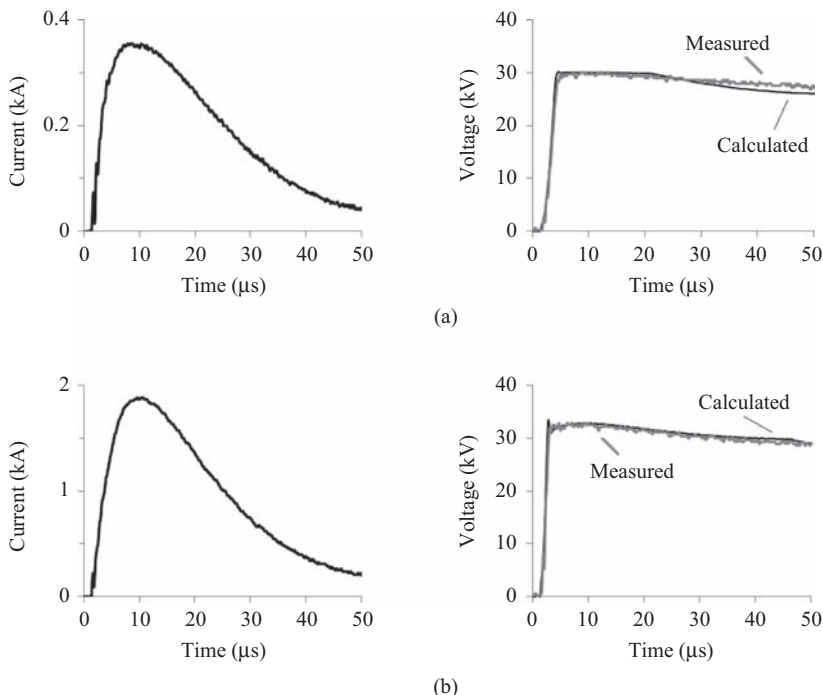


*Figure 19.9 Currents injected into the surge arrester model and corresponding measured and calculated residual voltages (all scales referred to the full-scale system): (a) applied current: 0.36 kA; (b) applied current: 1.89 kA [adapted from References 35 and 41]*

full-scale basis). Figure 19.9 presents some examples of comparisons between calculations, performed using the equivalent circuit, and relevant measurements for current amplitudes of 20 mA and 105 mA (corresponding to 0.36 kA and 1.89 kA). The associated residual voltages were, respectively, 1.67 V and 1.83 V (30 kV and 33 kV on a full-scale basis). A very close agreement was reached in all comparisons, thus validating the arrester model equivalent circuit.

### 19.3.6 Buildings

Urban overhead distribution networks are characterized not only by a high density of transformers, surge arresters and laterals, but also by the presence of buildings in their vicinity. The presence of nearby tall structures limits the line exposure to direct lightning strokes, but on the other hand, lightning flashes may occur very close to the line and, therefore, overvoltages of high magnitudes may be induced even in the case of stroke currents of moderate intensity [39]. The induced overvoltages are affected by the electromagnetic field distortion caused by neighbouring buildings, and the computation of lightning surges under such condition is extremely complex and cannot be done with the existing versions of the most advanced codes, e.g. the so-called lightning-induced overvoltage (LIOV) EMTP code [78, 79].

According to Table 19.1, if the medium is the same for the model and the full-scale system, the conductivity scale factor is the reciprocal of length scale factor. This means that, for the system described in References 35 and 39, buildings should be made of materials 50 times more conductive than those of full-scale constructions. In References 35 and 39, grounded aluminium structures were used for simulating the buildings and analysing their effect on lightning-induced voltages on overhead lines. However, as aluminium is characterized by an electrical conductivity greater than 50 times those of the materials used in real structures, in actual situations the effect of the structures will be less significant than that observed in the tests [35, 39, 41].

One of the test configurations considered in Reference 41, corresponding to structures 15 m high, is presented in Figure 19.10, where one of the return conductors shown in Figure 19.3 can also be seen at the left side of the picture. In this particular case, the r.s.m., which can be seen in the centre of the figure, was only 20 m from the closest lateral, simulating a direct strike to a nearby structure. The distances between the buildings and the main feeder, referred to the full-scale system, are indicated in Figure 19.11.

## 19.4 Evaluation of lightning surges in power lines

In this section, a number of examples are given which illustrate the application of the scale model technique in studies concerning lightning transients in power transmission and distribution systems. Surges originating from both direct and



*Figure 19.10 Scale model for the study of the effect of nearby buildings on lightning-induced voltages on overhead distribution lines [adapted from Reference 41]*

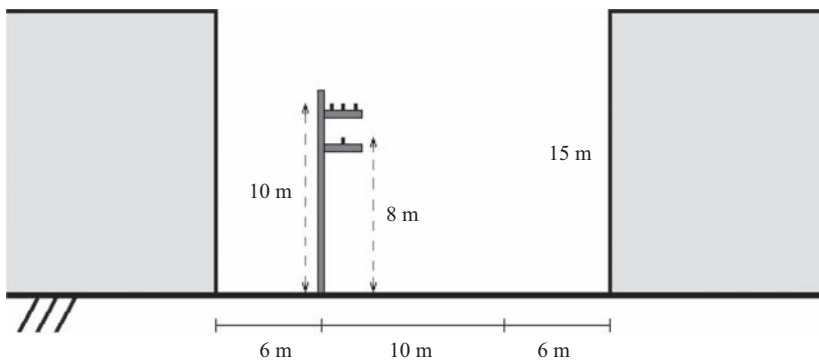


*Figure 19.11 Distances between buildings and main feeder corresponding to the test configuration shown in Figure 19.10 (dimensions referred to the full-scale system)*

indirect strokes can be investigated through this procedure. The examples presented here concern investigations aiming at

- evaluating the influences of various parameters on lightning overvoltages;
- validating theoretical models and relevant computer codes for voltage calculations;
- analysing the characteristics of lightning-induced voltages considering highly complex situations such as the case of overhead power distribution networks located in urban areas, with buildings in their vicinity.

### 19.4.1 Surges associated with direct strokes

Owing to their impulse withstand capability, much higher than those of distribution networks, transmission lines are not affected by nearby flashes, and their lightning performance is determined by their response to direct strokes. Most of the studies conducted on this topic make use of sophisticated numerical codes such as the EMTP [24], capable of describing the transient behaviour of power systems in a rather accurate way. Nowadays scale models are rarely used in this context, but in the past they were a popular tool for investigating the influence of various parameters on the overvoltages appearing across the insulators as a consequence of direct strikes to transmission lines. At that time, besides oversimplified concepts of the response of a system when struck by lightning, the level of knowledge of the characteristics of the lightning parameters was much less than today, and therefore discrepancies between the number of line outages predicted by the existing methodologies and those actually observed in the field motivated the search for better tools for evaluating the lightning performance of transmission lines.

An unexplained large number of outages on the 345-kV Ohio Valley Electric Corporation system motivated a study on several of the factors that influence the line lightning outage rate [34]. By making use of a 1:250 scale model, the authors simulated two spans of a transmission line and discussed the charge distribution along the downward leader channel and the build-up of charges on the phase conductors and ground wire due to the electric and magnetic fields produced around the channel of an approaching downward-moving leader. Measurements of the capacitance of the simulated channel and of the charges on the line conductors were performed. The shielding effects of other conductors and upward leaders from the ground wire were also discussed. The results showed that the voltage produced by the released bound charges on the line conductors may be neglected in comparison with the voltage associated with the current injected into the struck point.

The lightning performance of a 345-kV transmission line was also investigated in Reference 32. A 1:25 scale model, representing a line section composed of two spans, was built using an exact model for the centre tower and equivalent cylindrical structures for the two adjacent towers. The conductors were suspended from the tower at their proper heights by model string insulators and allowed to sag between towers a realistic amount. A network of resistors was placed at each end of the model to provide terminations between conductors and between conductors and ground in order to extend the apparent length of the model and to prevent reflections of travelling waves. The ground plane was formed by an aluminium sheet about 1.5 m wide, which extended the full length of the line. The stroke channel was modelled by a spiral of wire suspended vertically above the tower in such a way that it had an effective surge impedance of  $1150 \Omega$  and a return stroke velocity of about 18% that of light in free space ( $c$ ). Currents having front times as short as  $0.002 \mu\text{s}$ , corresponding to full-scale values of  $0.05 \mu\text{s}$ , were obtained. The voltages that resulted across the insulators when an approximate step function of current was delivered into the tower top were measured without ground wires and with one or two ground wires installed. Parameters such as current propagation velocity and

tower footing resistance were varied. Measurements were performed also on a 1:50 model, which allowed for the simulation of stroke currents with full-scale front times of 1–5  $\mu\text{s}$ .

In studies involving direct lightning strikes to transmission lines, the string insulator voltages are usually discussed in terms of transfer impedances between stroke current and insulator voltages, or volts per ampere of stroke current. The transfer impedance is defined as the ratio of instantaneous values of insulator voltage and stroke current. For currents with very short front times – as for example the case considered in Reference 32 – if the transfer impedance is plotted as a function of time, the resulting curve is a close approximation to the response of the system to a true step function of current.

Measurements performed in Reference 32 with stroke current front times corresponding to 0.05  $\mu\text{s}$  and 0.30  $\mu\text{s}$  in the full-scale system showed that the transfer impedance associated with the longer front time was lower, indicating that reflections from the lower portions of the tower had been able to reduce the overall tower impedance before the current wave reached its crest. For both current front times, the voltages that resulted at the top, middle and bottom insulators when the current was delivered into the tower top were measured for the system without ground wires and with one or two ground wires installed. The experiments showed that two ground wires reduce the insulator voltages substantially more than what one ground wire does. For the shorter current front time, the ratio of the transfer impedances corresponding to the case of one ground wire and of no ground wire was approximately 0.5 for the three insulators. With two ground wires, the ratios with respect to the case of system without ground wire were about 0.36, 0.30 and 0.37 for the top, middle and bottom insulators, respectively. For the longer current front time and system with one ground wire, the ratio is about 0.56 for the three insulators. Similar experiments were carried out in Reference 31 using a 1:60 scale model representing a 380-kV transmission line with only the top conductor. For a stroke current front time, on a full-scale basis, less than 0.1  $\mu\text{s}$ , the measured ratios of the transfer impedances corresponding to one or two ground wires with respect to the case of no ground wire were 0.6 and 0.43, respectively.

The effects of the channel impedance and of the stroke current propagation velocity ( $v$ ) were examined in Reference 32 by measuring the voltage across the top insulator for three different channel models. Two of them were helical lines; one with a characteristic velocity of about  $0.18 c$  and an impedance of  $1150 \Omega$ , and the other with a characteristic velocity of  $0.32 c$  and an impedance of  $750 \Omega$ . The third channel model was simply a length of wire suspended above the tower. Its characteristic velocity was the same as the speed of light and its impedance was about  $500 \Omega$ . The results showed that the effects of different stroke velocities and channel impedances on the shapes of the transfer impedance curves are small, as illustrated in Figure 19.12. The same conclusion was obtained in Reference 31.

Evaluations of the influence of the tower footing resistance on the transfer impedance, considering the presence of one overhead ground wire, were carried out in References 31 and 32. Three situations were considered in Reference 31 regarding the value of the footing resistance:  $0 \Omega$  (tower grounded solidly),  $75 \Omega$

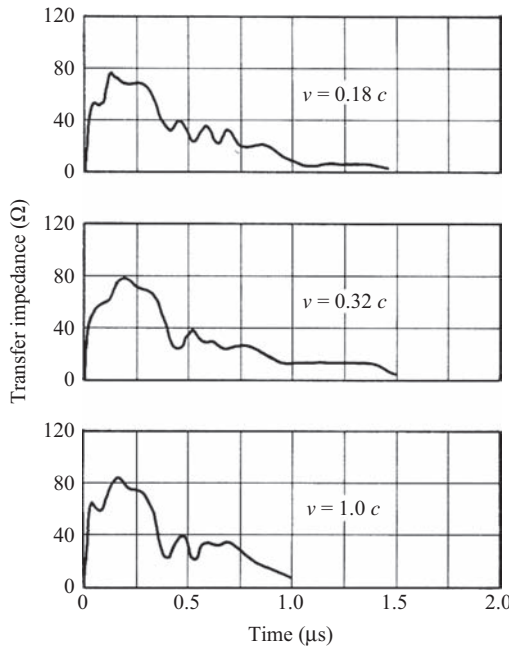


*Figure 19.12 Transfer impedance for top insulator as function of stroke current propagation velocity; time scale referred to the full-scale system [adapted from Reference 32]*

and  $220 \Omega$ . The stroke current front time, on a full-scale basis, was less than  $0.1 \mu s$ . In Reference 32, the response of the system was measured considering the following situations: tower grounded solidly, grounded through  $82 \Omega$  ( $330 \Omega$  at each leg), and isolated. The stroke current front time, on a full-scale basis, was  $0.05 \mu s$  and the voltage was measured at the top insulator. As expected, both studies showed that, due to the time delay for the arrival of the reflections originated at the tower bottom, the initial portion of the waveforms was not affected. After a current wave had been reflected back from the tower base, the transfer impedance and insulator voltage assumed a value depending on the parallel resistance of the footing resistance and ground wire surge impedances. The transfer impedances corresponding to the three arrangements considered in Reference 31 are presented in Figure 19.13.

The study conducted in Reference 31 included also an evaluation of the influence of the tower representation, and therefore tests were performed considering three different tower models: an exact scale reproduction, a combination of a cylinder and a cone, and a cylinder. Very similar transfer impedances were obtained in the tests corresponding to the three tower representations.

An analysis of the effects of the surge response of a tower and its conductors and of the severity of the stroke current waveform required to produce flashover

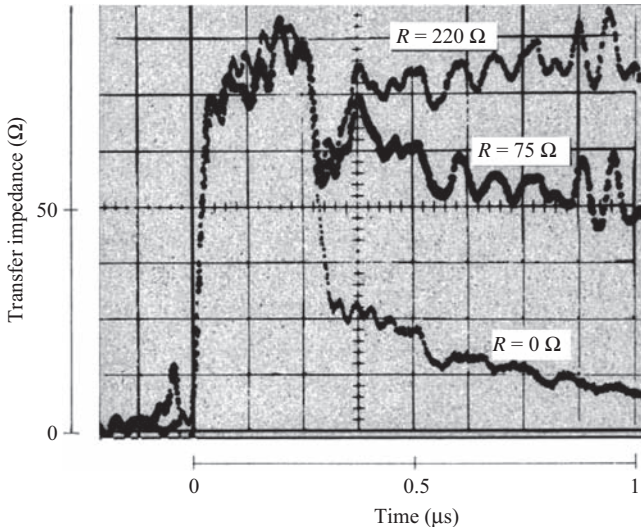


*Figure 19.13 Transfer impedance for different values of the tower footing resistance ( $R$ ); time scale referred to the full-scale system [adapted from Reference 31]*

voltages across the suspension insulators was carried out in Reference 33 through the use of a 1:28 scale model. A series of tests was made using a miniature representation of an actual 51 m high transmission tower and its associated conductors. Lightning strokes to the tower and to the overhead ground wire were simulated making use of a repetitive surge generator. The applied surges had exponentially rising fronts and essentially flat tails. The slope of the wavefront was varied and the resulting voltage across the insulator of the model tower was measured. The results were presented in terms of either the initial or the effective (determined from the 10% and 90% points on the current waveform) stroke current rates of rise required to cause insulator flashovers for the cases of systems without ground wire, with one ground wire and with two ground wires.

#### 19.4.2 Surges associated with indirect strokes

Overvoltages induced by nearby strokes are an important source of disturbance in telecommunications systems and are usually among the main causes of voltage sags and short interruptions on electric power supply distribution networks. The surge magnitudes and waveforms vary widely depending on the system configuration and on the lightning stroke parameters. A number of coupling models have been proposed in the literature to model the phenomenon [80–83] and modified or extended to enable the analysis of more practical situations [58, 61, 62, 66, 68, 84–90]. Such models require, apart from a few very simple cases, a computer code for the calculation of induced surges.

### 19.4.2.1 Validation of theoretical models

In comparison with transients caused by direct strikes to power lines, those associated with nearby strokes are more complicated to calculate. There are many parameters involved in the induction mechanism and, moreover, some of the approaches for computing lightning-induced voltages lead to significantly divergent results. Comparisons among the most popular coupling models are presented in References [85, 91–96], as well as the analyses of the reasons for the observed discrepancies. An example that illustrates the situation is shown in Figure 19.14, in which an induced voltage waveform recorded by Yokoyama *et al.* [12] is compared with simulations performed using the models by Chowdhuri [81], Rusck [82] and Liew and Mar [83].

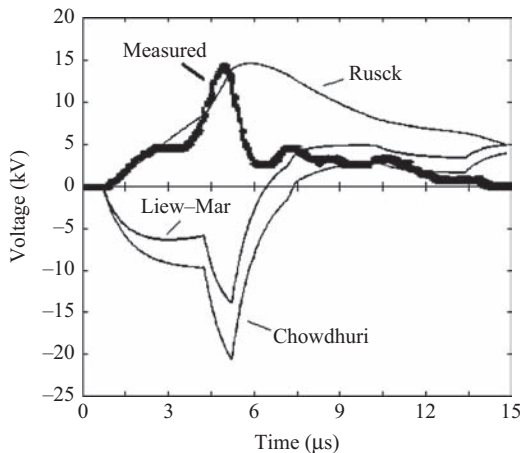


*Figure 19.14 Comparison between a measured induced voltage obtained by Yokoyama *et al.* [12] and the calculations according to the models by Chowdhuri [81], Rusck [82] and Liew and Mar [83] [adapted from Reference 85]*

The experimental research developed by Yokoyama *et al.* [6, 8, 12] was the first in which lightning currents and the associated induced voltages were recorded simultaneously. The voltages were measured on a 10-m high, 820-m long, unenergized overhead line. The line was L-shaped, matched at both ends and located at a distance of 200 m from a 200 m high tower. The stroke currents on the top of the tower and the corresponding voltages on the line were recorded simultaneously. Details of the experimental set up and of the measuring systems are presented in Reference 12, but it is relevant to mention that owing to the characteristics of the optical-electrical converter used for the voltage measurements, the recorded voltage waveforms presented a faster decay than the original ones [8]. As the stroke current propagation velocity was not measured, a constant value of 30% of that of light in free space was assumed for the calculations presented in Figure 19.14. Other assumptions concern the soil, which was assumed as a perfectly conducting

plane, and the stroke channel, which was considered vertical, without branches and 3 km long. The current distribution along the channel was calculated according to the transmission line (TL) model [97].

The results presented in Figure 19.14 indicate that it is vital to utilize, for the estimation of the lightning performance of a given line, a method – and the respective computer code – whose validity has been demonstrated from comparisons with experimental results obtained under controlled conditions.

The reduced scale system developed in Reference 41 has been used to validate two methods, namely the extended Rusck model (ERM) [41, 85, 87, 88, 98] and the LIOV-EMTP [78, 79, 99]. The former is an extension to the Rusck model in the sense that, unlike the original model, its features allow for taking into account situations of practical interest such as the case of a line with various sections of different directions, the presence of a multi-grounded neutral or shield wire and the presence of equipment such as transformers and surge arresters. The incidence of lightning flashes to nearby elevated objects and the occurrence of upward leaders can also be considered [84].

The LIOV-EMTP is a code based on two already existing computer programmes, the LIOV program – developed in the framework of an international collaboration involving the University of Bologna, the Swiss Federal Institute of Technology of Lausanne, and the University of Rome [62] and the EMTP [24]. This programme allows for the calculation of the voltages induced by lightning return strokes on homogeneous, multi-conductor, lossy overhead lines using the Agrawal *et al.* coupling model [80].

The comparisons between theoretical and experimental results presented in this section involve overhead distribution lines either protected or not against lightning. The voltages were measured through high-impedance probes with capacitance of 13 pF (corresponding to 0.65 nF on a full-scale basis) and bandwidth from d.c. to 100 MHz. The digital storage oscilloscopes had sampling rates of 500 MS/s and 1 GS/s and single-shot bandwidths of 200 MHz and 250 MHz, respectively.

### *Line without protection*

As the comparisons presented in this subsection concern very simple line configurations, where surge arresters and other sources of non-linearities are not present and therefore the voltages are directly proportional to the currents, the voltages and currents presented in the figures are not referred to the full-scale system. Correlation can, however, be done by applying the scale factors shown in Table 19.2. In the text, reference to the full-scale system is provided in parentheses.

A comparison between measured and calculated induced voltages is depicted in Figure 19.15. The computation, carried out using the ERM, refers to a 5.4 m (270 m) long straight single-phase line matched at both terminations. The lightning channel was 1.4 m (70 m) from the line and the stroke current could be approximated by a triangular waveform with amplitude of 2.78 A (50 kA), front time of 40 ns (2  $\mu$ s) and time to half-value of 1.7  $\mu$ s (85  $\mu$ s). A good agreement is found

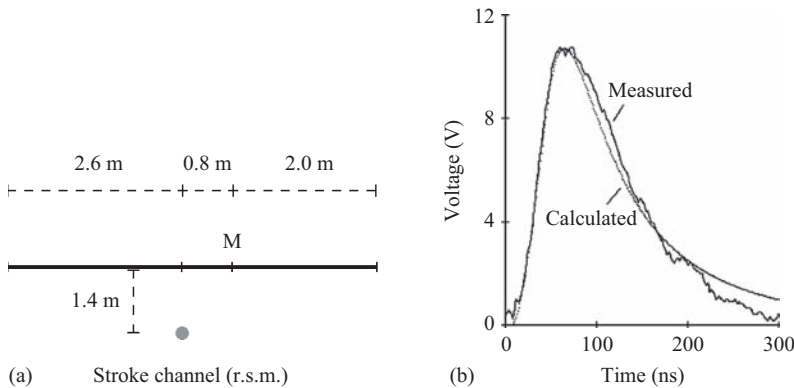


Figure 19.15 Measured and calculated (using the ERM) induced voltages. Stroke current with peak value of 50 kA, front time of 2  $\mu$ s and time to half-value of 85  $\mu$ s. M: measuring point. (a) Line topology (top view); (b) induced voltages [adapted from Reference 100]

between the results derived from numerical simulation and experiment, in terms of both the voltage magnitudes and waveforms.

Figures 19.16 to 19.18 present comparisons between measured and calculated induced voltages corresponding to three different currents injected into the r.s.m. The single-phase straight line (henceforth referred to as ‘reference line’) was 28 m (1.4 km) long, matched at both ends, 1.4 m (70 m) from the r.s.m., and its terminations were equidistant from the stroke location. The copper conductor was supported by PVC poles spaced every 60 cm (30 m), and its diameter was 0.4 mm (2 cm) – the influence of the wire cross section on the induced voltages is not significant for the typical range normally used [98]. The conductor height was 20 cm

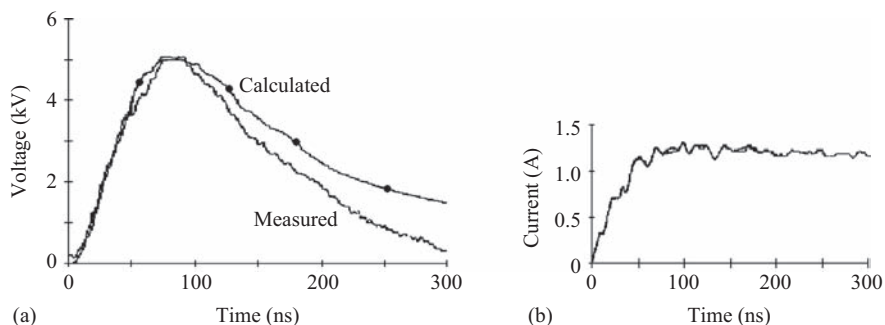
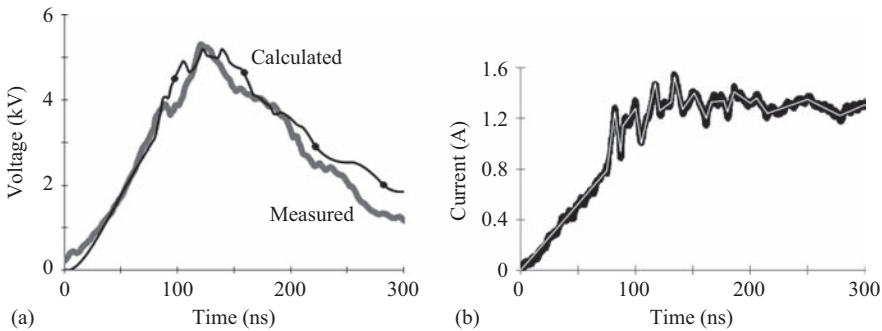
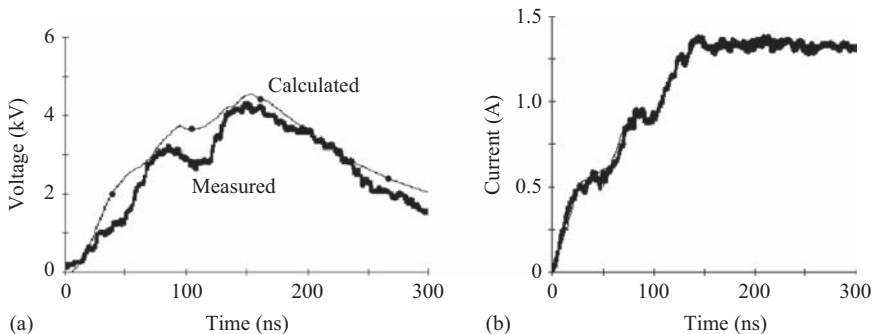


Figure 19.16 Measured and calculated (using the ERM) induced voltages – Case MOD-1: (a) induced voltages; (b) measured current and straight line approximation superimposed



*Figure 19.17 Measured and calculated (using the ERM) induced voltages – Case MOD-2: (a) induced voltages; (b) measured current and straight line approximation superimposed*



*Figure 19.18 Measured and calculated (using the ERM) induced voltages – Case MOD-3: (a) induced voltages; (b) measured current and straight line approximation superimposed*

(10 m) and its measured surge impedance was  $455 \Omega$ . The calculations were performed with the recorded current waveforms approximated by straight lines, which in the figures are shown superimposed to the measured currents.

Comparisons between measured and calculated induced voltages considering lines with different terminations are presented in Figures 19.19 to 19.21. The voltages were measured simultaneously on the reference line and on a second line (henceforth referred to as ‘test line’), placed symmetrically with respect to the lightning channel model. The configurations were exactly the same, except for the terminations – the reference line was matched at both ends, whereas the test line was terminated in different ways. An impulse current with amplitude of 1.1 A (19.8 kA) and front time of 60 ns (3  $\mu$ s) was injected into the r.s.m. and the voltages induced on both lines were recorded simultaneously. In all the tests the current amplitude remained practically constant for the time window of interest.

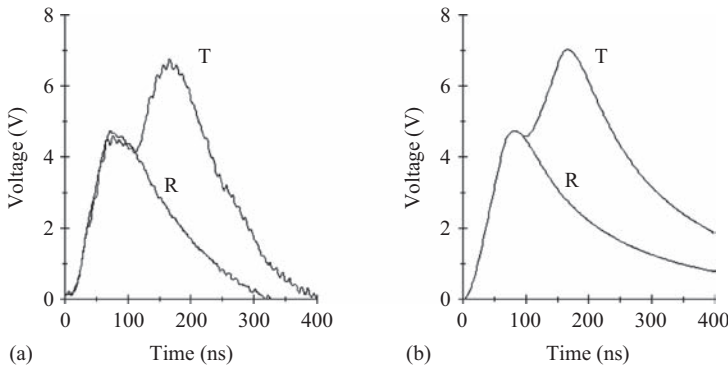


Figure 19.19 Measured and calculated (using the ERM) induced voltages [98]. Reference line (R): matched at both ends; test line (T): one end matched and the other open. (a) Measured voltages; (b) calculated voltages

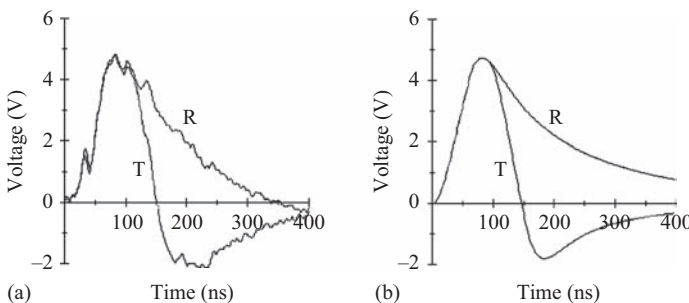
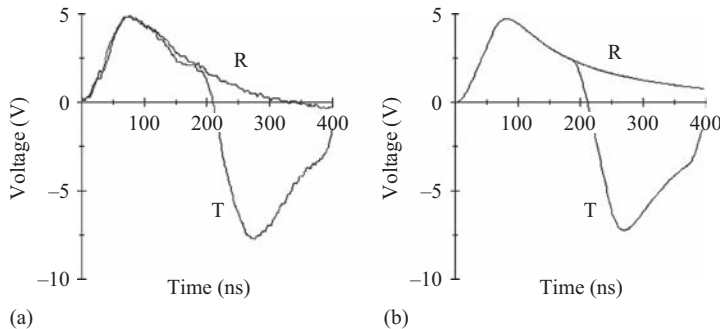


Figure 19.20 Measured and calculated (using the ERM) induced voltages [98]. Reference line (R): matched at both ends; test line (T): one end matched and the other short-circuited. (a) Measured voltages; (b) calculated voltages

### *Line with a shield wire or surge arresters*

The most effective methods of improving the lightning performance of distribution lines are the increase of the insulation withstand capability, the use of shield wires and the application of surge arresters.

Independently of its position, a neutral or a shield wire tends to reduce the magnitude of the induced voltages due to the electromagnetic coupling with the phase conductors. By its turn, the application of line surge arresters can significantly reduce the magnitudes of lightning-induced voltages provided that the arrester spacing is not too large. In both cases the degree of voltage reduction depends on several line and lightning parameters, such as the distance between



**Figure 19.21** Measured and calculated (using the ERM) induced voltages [98]. Reference line (R): matched at both ends; test line (T): one end open and the other short-circuited. (a) Measured voltages; (b) calculated voltages

adjacent grounding points, the value of the ground resistance, the stroke current steepness and the position of the stroke location with respect to the line and the observation point.

The examples presented in this subsection concern realistic line configurations, representative of actual rural distribution lines. Thus, for convenience, the values of all the parameters are referred to the full-scale system. The conversion to the values actually recorded in the scale model experiments can be made by applying the scale factors indicated in Table 19.2.

A comparison between measured and calculated voltages on a line with a shield wire is presented in Figure 19.22. In this case the test line had two conductors, phase and shield wires, respectively, at the heights  $h = 10$  m and  $h_g = 9$  m. The horizontal distance between the conductors was 0.75 m. The voltages were

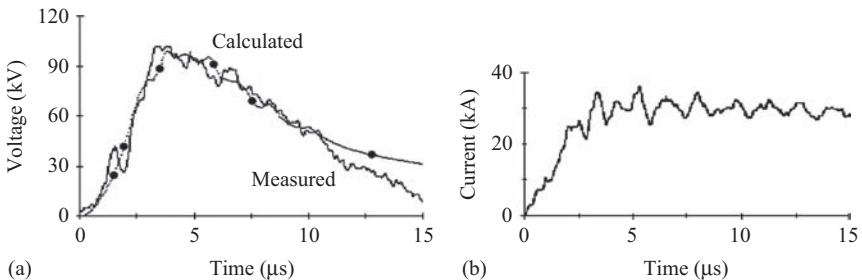


**Figure 19.22** Measured and calculated (using the ERM) phase-to-ground induced voltages at the point closest to the stroke location for the line configuration shown in Figure 19.23(a) [98].  $I = 36$  kA;  $t_f = 3.1$   $\mu$ s,  $d = 70$  m;  $h = 10$  m,  $h_g = 9$  m,  $x_g = 450$  m,  $R_g = 0$   $\Omega$ , r.s.m. in front of a grounding point. (a) Induced voltages; (b) measured current

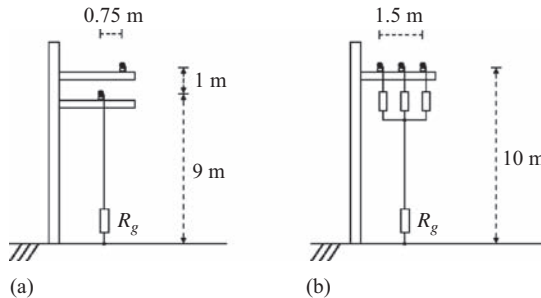


Figure 19.23 Configurations of the test line for the comparisons shown in Figures 19.22 and 19.24: (a) with a shield wire ( $h_g = 9 \text{ m}$ ); (b) with surge arresters

obtained at the point of the line closest to the stroke location and the values of the parameters were current magnitude  $I = 36 \text{ kA}$ , current front time  $t_f = 3.1 \mu\text{s}$ , distance between the r.s.m. and the line  $d = 70 \text{ m}$ , distance between adjacent grounding points  $x_g = 450 \text{ m}$  and ground resistance  $R_g = 0 \Omega$ . The stroke location was in front of a grounding point and equidistant from the line terminations. This test configuration is depicted in Figure 19.23(a), whereas Figure 19.23(b) shows one of the configurations used for the evaluation of the effect of surge arresters.

Figure 19.24 presents a comparison between measured and calculated voltages for the case of surge arresters added on all the three phases of the test line, which in this configuration had no shield wire. The distance between adjacent conductors was 0.75 m. The observation point was in front of the r.s.m. and the values of the parameters, referred to the full-scale system, were  $I = 54 \text{ kA}$ ,  $t_f = 3.2 \mu\text{s}$ ,  $x_g = 450 \text{ m}$  and  $R_g = 200 \Omega$ . The stroke location was equidistant from two sets of surge arresters.

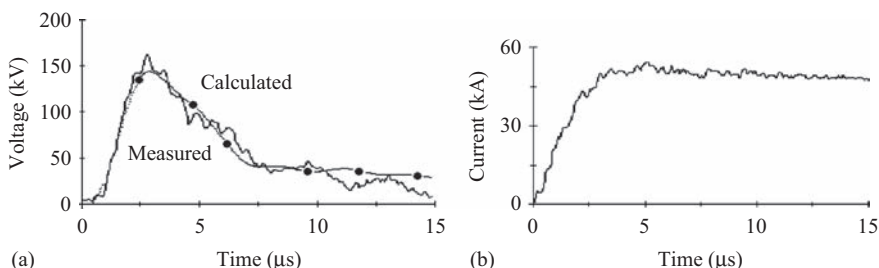
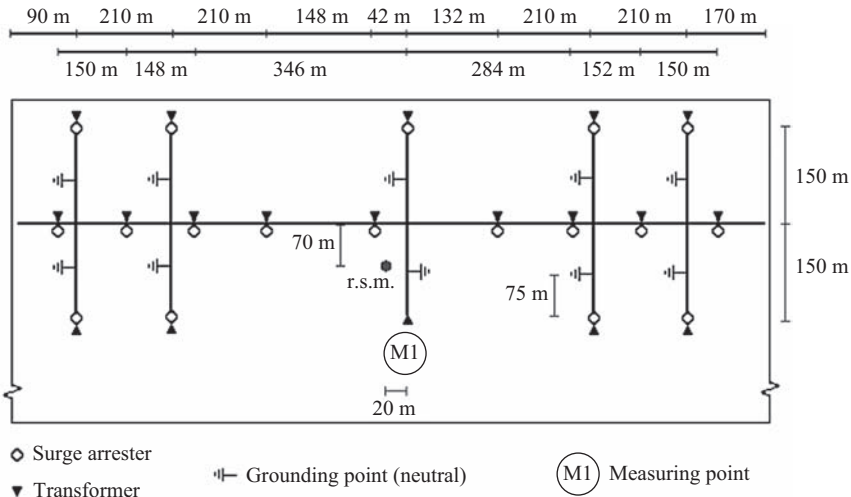


Figure 19.24 Measured and calculated (using the ERM) phase-to-ground induced voltages at the point closest to the stroke location for the line configuration shown in Figure 19.23(b) [98].  $I = 54 \text{ kA}$ ;  $t_f = 3.2 \mu\text{s}$ ,  $d = 70 \text{ m}$ ;  $h = 10 \text{ m}$ ,  $x_g = 450 \text{ m}$ ,  $R_g = 200 \Omega$ , r.s.m. equidistant from two sets of surge arresters. (a) Induced voltages; (b) measured current



*Figure 19.25 Network configuration for the comparison shown in Figure 19.26 [adapted from Reference 35]*

Figure 19.25 presents a configuration more representative of urban distribution networks, in which the main feeder has various laterals. The line was three phase and the heights of the phase and neutral conductors were 10 m and 8 m, respectively. The distance between adjacent phases was 0.75 m and the main feeder was matched at both ends. Each transformer was represented by capacitors connected between each phase and the neutral. However, as the value of the simulated transformer input capacitance (0.5 nF) was similar to the value of the voltage probe capacitance (0.65 nF), at the measuring point the capacitor was replaced with the voltage probe.

The neutral was grounded at every transformer and also at the middle of the laterals through ground resistances of  $50 \Omega$ . At the measuring point, however,  $R_g$  was zero and therefore the neutral-to-ground voltage was related only to the inductive voltage drop across the down conductor. Owing to the low value of the down conductor inductance (estimated of the order of tens of  $\mu\text{H}$ ), such a voltage was negligible compared with the voltage across the capacitances and therefore the differences between phase-to-ground and phase-to-neutral voltages were negligible, as confirmed by simulations.

Figure 19.26, which corresponds to case 1 [35], depicts a comparison between the measured and calculated induced voltages at node M1 indicated in Figure 19.25 for a stroke current with peak value of 34 kA, front time equal to 2  $\mu\text{s}$  and time to half-value equal to 85  $\mu\text{s}$ . The measurement and simulation regard the phase conductor closest to the stroke location.

Comparisons were also made for the system configuration presented in Figure 19.27. The voltages shown in Figure 19.28 (case 2.1 [35]) refer to a stroke

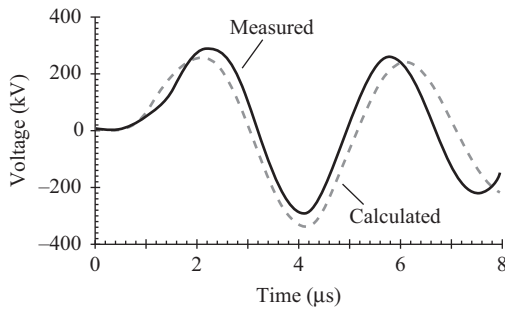


Figure 19.26 Measured and calculated (using the LIOV-EMTP) induced voltages at point M1 of Figure 19.25 (case 1 [35]).  $I = 34 \text{ kA}$ ,  $t_f = 2 \mu\text{s}$

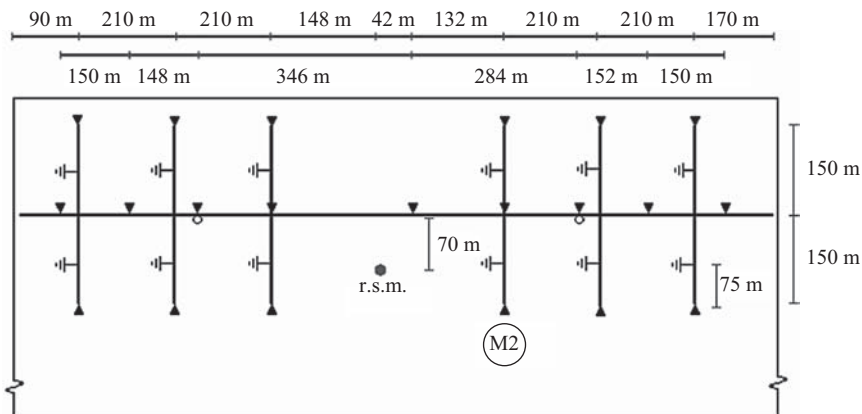


Figure 19.27 Network configuration for the comparison shown in Figure 19.28. Meaning of the symbols is the same as in Figure 19.25 [adapted from Reference 35]

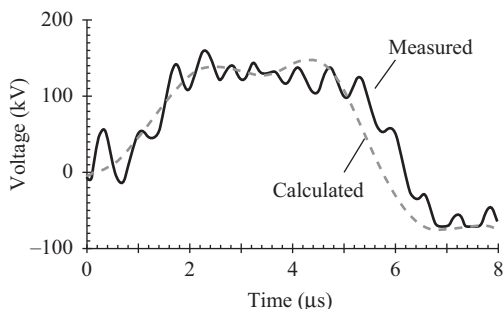


Figure 19.28 Measured and calculated (using the LIOV-EMTP) induced voltages at point M2 of Figure 19.27 (case 2.1 [35]).  $I = 70 \text{ kA}$ ,  $t_f = 2 \mu\text{s}$

current with the same previous waveform but with a peak value equal to 70 kA. The calculation was performed considering a simplified configuration with two conductors (middle phase and neutral). Despite the higher stroke current magnitude in relation to case 1 (70 kA against 34 kA), the corresponding induced voltage peak values are lower (roughly 150 kV against 300 kV), mostly because the distance between the stroke location and the closest line section (70 m) is larger than that corresponding to case 1 (20 m). Moreover, in case 1 the measuring point is located at the terminal of the lateral closest to the stroke location, while in case 2.1 the stroke location is closest to the main feeder. The combination of the above-mentioned conditions has a significant effect on the induced voltages.

The comparison presented in Figure 19.29 concerns the same network configuration of Figure 19.27 except with regard to the location of the surge arresters, which in this case were placed only at the transformer at the end of the lateral where the voltage was measured, i.e. point M2. The stroke current peak value was 34 kA and the waveform was the same as that of the previous cases.

The results obtained with the ERM and the LIOV-EMTP show a good agreement between measured and calculated induced voltages. Possible reasons for discrepancies between measurements and simulations, for all cases, can be addressed to

- measuring errors: the overall uncertainty of the measuring system used in the tests was less than  $\pm 5\%$ ;
- slight deviations of the stroke current from the waveform considered in the calculations;
- representation of the surge arrester model by means of its equivalent circuit;
- high-frequency oscillations associated with noise or switching of the current generation system (both of random nature);
- variation of the current propagation velocity, its distortion and attenuation as it progresses upwards along the r.s.m. Some superimposed high-frequency

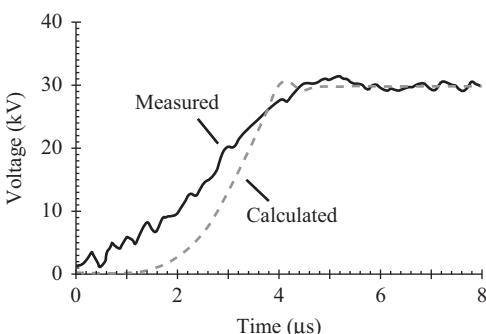


Figure 19.29 *Measured and calculated (using the LIOV-EMTP) induced voltages at point M2 of Figure 19.27, but with surge arresters placed only at point M2 (case 2.2 [35]).  $I = 34 \text{ kA}$ ,  $t_f = 2 \mu\text{s}$*

oscillations, probably related to the reasons (b) and (d) above, are particularly evident on the measured voltage shown in Figure 19.28. As, however, they are not caused by reflections (and hence not associated with the line configuration) and as an idealized current waveform was considered for the calculations, these oscillations are never present in the calculated voltages.

Nevertheless, the disagreements between measurements and computer simulations were relatively low and the experimental validation of the proposed models, performed for realistic line configurations, can be considered satisfactory.

#### 19.4.2.2 Analysis of complex situations

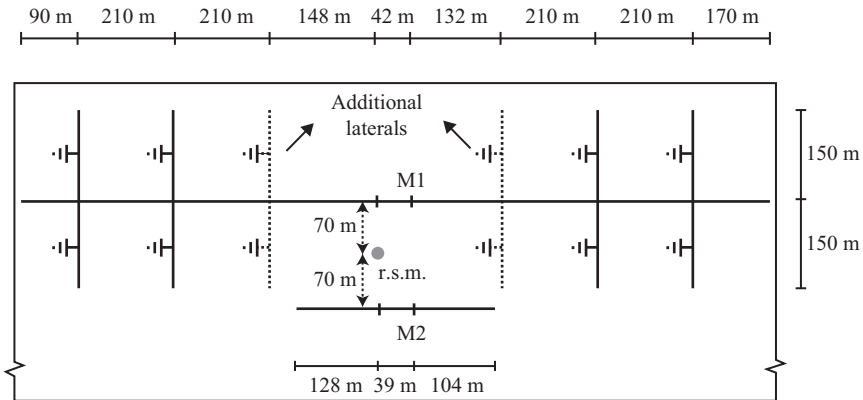
Another important application of the scale model technique is related to the analysis of the lightning performance of electrical systems located within a complex electromagnetic environment, for which the implementation of the relevant theoretical models is not yet available. Such a kind of situation occurs, for example, in the case of urban distribution systems. The difficulty, in this case, is related mainly to the computation of the effect of structures in the vicinity of the line on the inducing electromagnetic field, as well as, to a lesser degree, to the large number of laterals, transformers and surge arresters that characterize an urban power distribution system. This subsection illustrates the application of scale models to the investigation of the behaviour of lightning-induced voltages on urban distribution networks.

##### *Influence of line laterals*

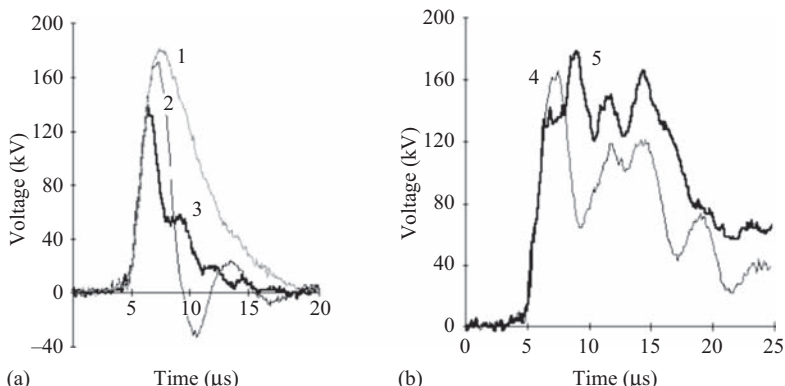
Each intersection point of the main feeder with the laterals represents a line discontinuity, since a surge that arrives at one of these points ‘sees’ an impedance that is smaller than the line surge impedance. The polarity of the reflected voltage will be opposite to that corresponding to the incident one. On the other hand, the transmitted voltage, although of the same polarity, will have smaller amplitude than the incident one. Therefore, the voltages induced on points of the line that are close to a lateral tend, in general, to reach smaller magnitudes than those that would be reached in the absence of the lateral. This is the case when the distance between the lateral and the observation point is small enough so that the effect of the reflection is ‘felt’ before the voltage reaches its maximum.

Figure 19.30 presents one of the test configurations used in Reference 38, which consisted of two lines placed at a distance of 70 m from the r.s.m. The shorter line was single-phase, straight and with both ends matched, while the other had four conductor and was branched. The main feeder of the branched line was matched at both ends; the laterals were either matched or open ended. In this configuration the lines had neither arresters nor transformers. The value of the ground resistances was  $50 \Omega$  except at the measuring point, where it was zero. The voltages shown in Figure 19.31 illustrate the influence of the line laterals on the induced voltages for the case of a stroke current with amplitude of 46 kA, front time of 2  $\mu$ s and time to half-value of 85  $\mu$ s.

The induced surges are affected not only by the presence of the laterals but also by their termination conditions. The voltage magnitudes tend to decrease either in



*Figure 19.30 Test configuration for the analysis of the influence of the line laterals on lightning-induced voltages. Meaning of the symbols is the same as in Figure 19.25 [adapted from Reference 38]*



*Figure 19.31 Induced voltages at points M1 and M2 of the lines shown in Figure 19.30.  $I = 46 \text{ kA}$ ,  $t_f = 2 \mu\text{s}$ . Curve 1: point M2; curves 2 and 4: point M1, line without the additional laterals; curves 3 and 5: point M1, line with the additional laterals. (a) Matched laterals; (b) open-ended laterals [adapted from Reference 38]*

the case of long (or matched) laterals or when they are terminated with surge arresters. The shorter the distance between the measuring point and the nearest lateral, the greater the voltage reduction, as can be readily seen in Figure 19.31(a). On the other hand, if the laterals are open ended, the induced voltage may increase as the distance between the measuring point and the nearest lateral becomes shorter, as shown in Figure 19.31(b).

The voltages corresponding to the case of open-ended laterals tend to be greater than those relative to long (or matched) laterals; the difference tends to increase as the observation point approaches a line branch. For instance, although notable differences are observed between the wavetails of voltages 2 (ends of all laterals matched) and 4 (ends of all laterals open), measured at a distance of 342 m from the nearest lateral, their peak values are about the same. On the other hand, a difference of about 30% is observed between the magnitudes of curves 3 (ends of all laterals matched) and 5 (ends of all laterals open), which were measured at a shorter distance (132 m) from the nearest lateral.

### *Influence of buildings*

The presence of nearby structures causes reduction of the lightning electromagnetic field around the overhead distribution line and, as a result, the induced voltages are affected. Figure 19.32 depicts two test configurations adopted in an investigation of the impact, on the lightning-induced voltages, of the presence of buildings of different heights ( $h_b$ ) in the vicinity of the distribution network. Aluminium structures connected to the ground were used to simulate the buildings, as illustrated in Figure 19.10 for the case of  $h_b = 15$  m. The parameters  $s_e$  and  $s_d$  indicated in Figure 19.32 represent the distances between the measuring point (M) and the closest set of surge arresters located on its left and right sides, respectively. The same distance between the line and the stroke location, equal to 20 m, was adopted in all the tests, although, especially for the case of  $h_b = 0$  m, a lightning stroke so close to the line is an unlikely event, unless it hits an elevated object like a tree, a mast or another structure protruding above the line itself.

Figure 19.33 shows the measured induced voltages at the transformer of the main feeder located in front of the lightning strike point for the three buildings' heights considered, namely 0 m, 5 m and 15 m. The stroke current magnitude was 34 kA and, in order to illustrate the effects of the presence of surge arresters, two situations were considered regarding the distances  $s_e$  and  $s_d$ . It can be clearly noted that the buildings provoke a reduction in the electromagnetic field around the line and, consequently, the induced voltages may be substantially affected. This reduction is more significant in the case of higher structures, which provide a more effective shielding of the line against the inducing field.

The influence of the distance between the observation point and the arresters on the induced voltages tends to decrease as the building height increases. For  $h_b = 0$  m (no buildings around the line), the ratio between the crest values of the induced voltages for the two cases considered ( $s_e = s_d = 75$  m and  $s_e = 148$  m,  $s_d = 174$  m) is approximately 0.54. For  $h_b = 5$  m the ratio is 0.57, while for  $h_b = 15$  m the ratio is 0.96. This can be explained by the fact that, for  $h_b = 0$  m, the difference on the induced voltages is due only to the different distances between the transformer and the nearest sets of arresters. This influence is very significant, especially for discharges close to the line. On the other hand, the amplitude of the total electromagnetic field near the line diminishes as the buildings' heights increase, as a consequence of the shielding, that becomes more effective. Therefore, in the test conditions, for  $h_b = 15$  m, the induced

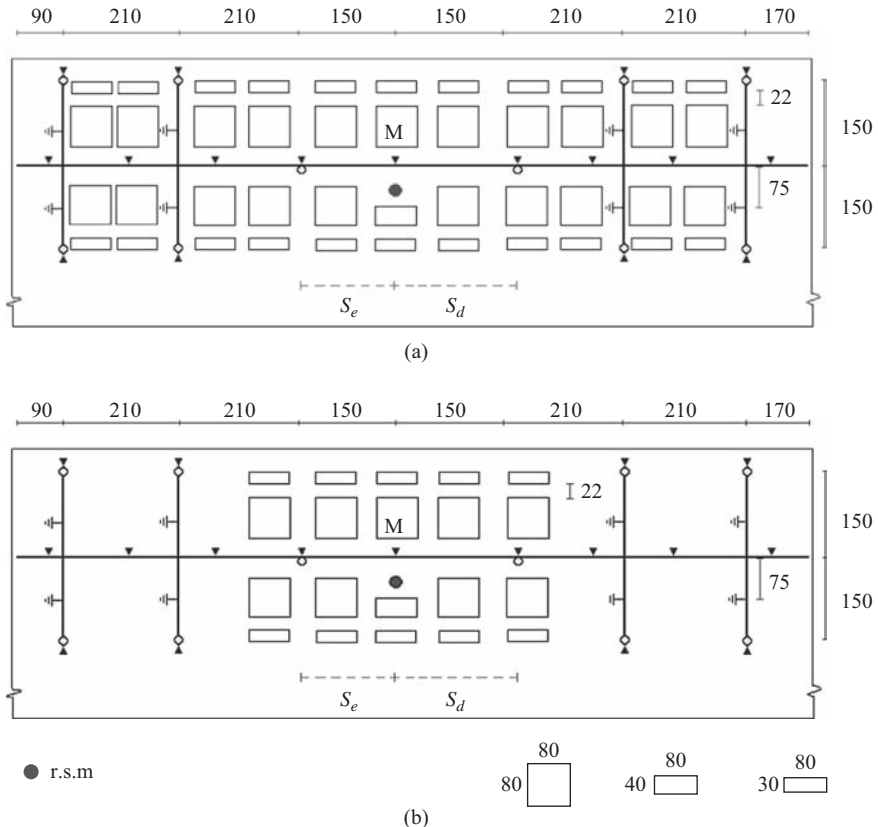


*Figure 19.32 Test configurations (top view). Distance of 20 m between line and stroke location. Squares and rectangles denote blocks with structures of different heights ( $h_b$ ). All dimensions in metres. Meaning of the symbols is the same as in Figure 19.25. (a)  $h_b = 5$  m; (b)  $h_b = 15$  m*

voltages are more influenced by the presence of buildings than by the distance between the measuring point and the arresters.

The results shown in Figure 19.33, even that corresponding to the case of  $h_b = 0$  m, differ from those illustrated in Figures 19.26 and 19.29, which were obtained for the same lightning current. The induced voltage magnitude of Figure 19.26 (around 300 kV) is greater because the measuring point is located at the end of a lateral where the transformer is not protected with surge arresters. On the other hand, the voltages presented in Figure 19.29 were obtained with surge arresters placed at the measuring point and therefore they are lower than those shown in Figure 19.33, which refer to measurements performed in the main feeder, close to the stroke location.

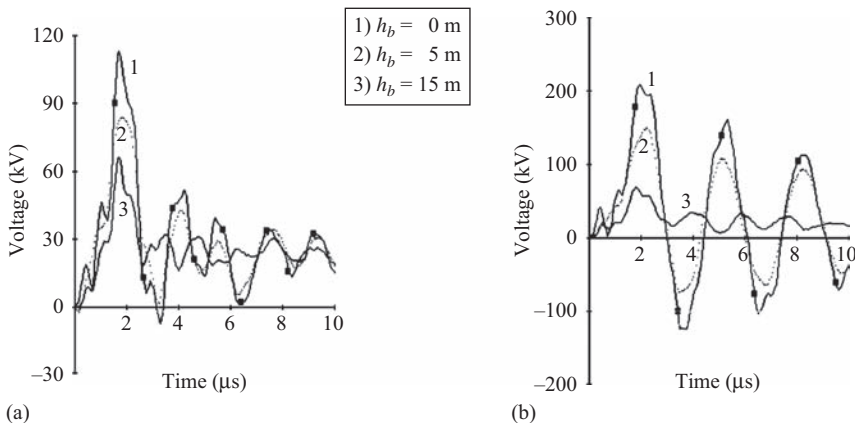


Figure 19.33 Measured induced voltages for different buildings' heights (test configurations indicated in Figure 19.32) and different distances between the observation point and the closest set of arresters.  $I = 34$  kA,  $t_f = 2 \mu\text{s}$ . (a)  $s_e = 75$  m,  $s_d = 75$  m; (b)  $s_e = 148$  m,  $s_d = 174$  m [adapted from Reference 39]

Another test configuration considered in Reference 39, in which the measurements were performed at the transformer located at the end of the closest lateral to the stroke location, is depicted in Figure 19.34. The distances from the r.s.m. to the main feeder and to the closest lateral were 70 m and 20 m, respectively. Except the transformer at which the voltages were measured, all the transformers

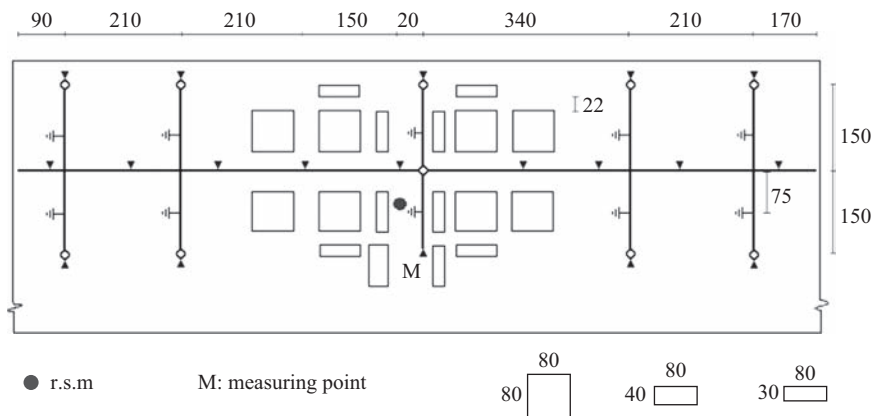
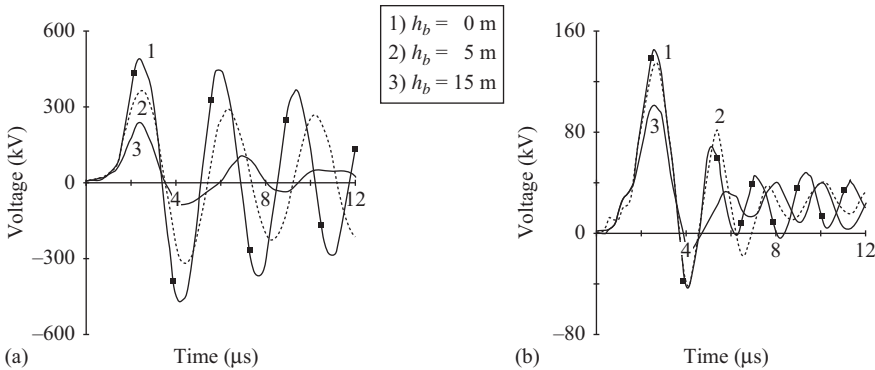


Figure 19.34 Test configuration (top view) for  $h_b = 15$  m and  $s_r = 150$  m. Distances of the stroke location to the main feeder and to the closest lateral equal to 70 m and 20 m, respectively. Squares and rectangles denote blocks with structures of different heights. All dimensions in metres. Meaning of the symbols is the same as in Figure 19.25



*Figure 19.35 Measured induced voltages for different buildings' heights and different distances  $s_r$  between the observation point and the closest set of arresters (Figure 19.34 corresponds to the case of  $h_b = 15$  m and  $s_r = 150$  m).  $I = 50$  kA,  $t_f = 2$  μs. (a)  $s_r = 150$  m; (b)  $s_r = 75$  m [adapted from Reference 39]*

located at the ends of laterals were protected by surge arresters. Figure 19.34 is for  $h_b = 15$  m and distance of 150 m between the measuring point and closest set of surge arresters ( $s_r$ ), but tests were performed also for the cases of  $h_b = 0$  m,  $h_b = 5$  m and  $s_r = 75$  m. Figure 19.35 presents the induced voltages for a stroke current magnitude of 50 kA and the various test conditions.

The voltage magnitudes diminish as the buildings' heights increase, and this effect becomes more evident as the distance  $s_r$  increases. For  $s_r = 150$  m, the ratio between the crest values of the voltages relative to  $h_b = 15$  m and  $h_b = 0$  m,  $U_{15}/U_0$ , is approximately 0.48, whereas in the case corresponding to  $s_r = 75$  m, the ratio is about 0.70. If  $s_r = 0$  m, the phase-to-ground voltages at the transformer terminals will be given by the sum of the arrester residual voltages and the voltage drop on the grounding conductor. As the dependence of these voltages upon the buildings' heights is very little, the ratio  $U_{15}/U_0$  will be close to unity. Thus, the ratio diminishes (i.e. the influence of the buildings increase) as  $s_r$  increases.

As shown in Figures 19.33 and 19.35, the presence of buildings close to distribution networks reduces the lightning electromagnetic field and, consequently, the induced voltages. On the other hand, high structures may attract lightning flashes close to the line and, therefore, voltages of large amplitudes can be induced. It is important to mention, though, that the effect of the buildings observed in the tests is somehow overestimated. The reason is that a perfect model would require the structures to be simulated by using materials having conductivity 50 times greater than those of full-scale constructions, as the scale factor for conductivity is the inverse of that for length – see Table 19.2. However, the models were actually constructed using aluminium, whose conductivity is larger than this value, and therefore, those results should be analysed under a qualitative perspective or taken as superior limits, as pointed out in References 35, 38, 39 and 41.

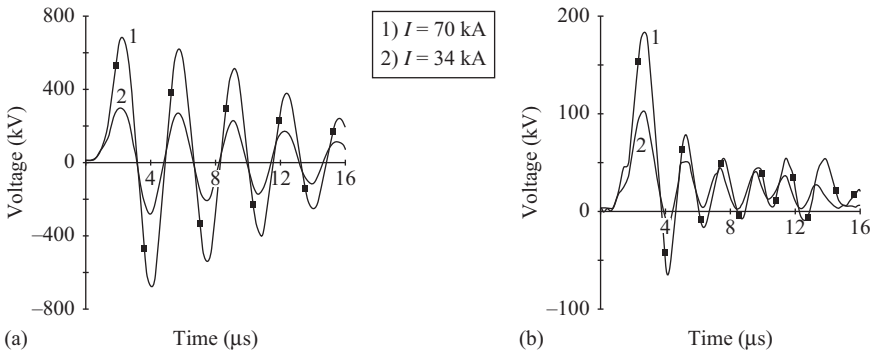


*Figure 19.36 Measured induced voltages for different stroke current peak values and different distances  $s_r$  between the observation point and the closest set of arresters (test configuration indicated in Figure 19.34, but with  $h_b = 0\text{ m}$ ).  $t_f = 2\text{ }\mu\text{s}$ . (a)  $s_r = 150\text{ m}$ ; (b)  $s_r = 75\text{ m}$  [adapted from Reference 39]*

The induced voltages have a strong dependence on the stroke current magnitude, and this is illustrated in Figure 19.36, which presents the measured voltages for stroke current magnitudes of 34 kA and 70 kA and the test configuration shown in Figure 19.34, but without the presence of buildings around the line. The variation of the peak voltages was almost linear in the test conditions, a behaviour that can be explained by the relatively high value of the ground resistance ( $50\text{ }\Omega$ ), the short front time of the stroke current ( $2\text{ }\mu\text{s}$ ) and the distance  $s_r$  between the surge arresters and the measuring point. A decrease in the value of the ground resistance or in the distance  $s_r$  would tend to increase the system non-linearity. A slower stroke current or a greater distance between the stroke location and the distribution line would have a similar effect, as in this case the voltage peak would be reached in a longer time and therefore the effect of the arresters would be larger.

As suggested by the voltage peak values observed in Figures 19.35(a) and 19.36(a), the obtained results interestingly show that in some exceptional cases, namely for strokes in the very close vicinity of the line and for stroke currents with high amplitude and time-variation rate, surge arresters may not prevent an insulation flashover from occurring, especially if they are installed at some distance (e.g. 150 m) from the closest point to the lightning channel.

## 19.5 Conclusions

The scale model technique is a very powerful and versatile tool for the analysis of the interaction of lightning with electric power lines and well complements other methods such as rocket-triggered lightning and experiments with full-scale systems. It enables the simulation of a wide variety of situations, and, moreover, tests

can be carried out under controlled conditions. After the system implementation, a substantial amount of data can be obtained in a relatively short time.

An important application of scale models concerns the validation of theoretical models of complex phenomena and their relevant codes. They can also be very useful in the evaluation of the influence of the line configuration and of various lightning parameters on the magnitudes and waveforms of overvoltages, which can be assessed with satisfactory accuracy. In this chapter, the usefulness of the method was illustrated by its application for the validation of the ERM and LIOV-EMTP predictions, as well as for the investigation of the behaviour of lightning transients on overhead power transmission and distribution lines subjected to direct and indirect strokes. The technique is particularly suitable for the analysis of situations that are either too complex or not worthwhile to be treated theoretically, as e.g. the case of lightning-induced voltages on urban power distribution networks surrounded by nearby buildings.

## Acknowledgements

Special thanks are due to Prof. C. A. Nucci, Prof. A. Borghetti and Dr. M. Paolone for the valuable discussions and for providing the simulation results obtained with the LIOV-EMTP code.

## References

- PIANTINI, A., DE CARVALHO, T. O., SILVA NETO, A., JANISZEWSKI, J. M., ALTAFIM, R. A. C. and NOGUEIRA, A. L. T.: 'A system for simultaneous measurements of lightning induced voltages on lines with and without arresters', Proceedings of the 27th International Conference on Lightning Protection (ICLP), Avignon, **1**, Sep. 2004, pp. 297–302
- MICHISHITA, K., ISHII, M., ASAOKAWA, A., YOKOYAMA, S. and KAMI, K.: 'Voltage induced on a test distribution line by negative winter lightning strokes to a tall structure', *IEEE Transactions on Electromagnetic Compatibility*, 2003, **45**, (1), pp. 135–140
- FERNANDEZ, M. I., RAKOV, V. A. and UMAN, M. A.: 'Transient currents and voltages in a power distribution system due to natural lightning', Proceedings of the 24th International Conference on Lightning Protection (ICLP), Birmingham, Sep. 1998, pp. 622–629
- DE LA ROSA, F., PÉREZ, H. and GALVÁN, A.: 'Lightning-induced voltage measurements in an experimental power distribution line in Mexico', Proceedings of the 22nd International Conference on Lightning Protection (ICLP), Budapest, Sep. 1994, pp. R 6b-09/1–6
- GEORGIADIS, N., RUBINSTEIN, M., UMAN, M. A., MEDELJUS, P. J. and THOMSON, E. M.: 'Lightning-induced voltages at both ends of a 448 m power-distribution line', *IEEE Transactions on Electromagnetic Compatibility*, 1992, **34**, (4), pp. 451–460

6. YOKOYAMA, S., MIYAKE, K. and FUKUI, S.: 'Advanced observations of lightning induced voltage on power distribution lines (II)', *IEEE Transactions on Power Delivery*, 1989, **4**, (4), pp. 2196–2203
7. RUBINSTEIN, M., TZENG, A. Y., UMAN, M. A., MEDELJUS, P. J. and THOMSON, E. M.: 'An experimental test of a theory of lightning – induced voltages on an overhead wire', *IEEE Transactions on Electromagnetic Compatibility*, 1989, **31**, (4), pp. 376–383
8. YOKOYAMA, S., MIYAKE, K., MITANI, H. and YAMAZAKI, N.: 'Advanced observations of lightning induced voltage on power distribution lines', *IEEE Transactions on Power Delivery*, 1986, **1**, (2), pp. 129–139
9. COORAY, V. and DE LA ROSA, F.: 'Shapes and amplitudes of the initial peaks of lightning-induced voltage in power lines over finitely conducting earth: theory and comparison with experiment', *IEEE Transactions on Antennas and Propagation*, 1986, **34**, (1), pp. 88–92
10. MASTER, M. J., UMAN, M. A., BEASLEY, W. and DARVENIZA, M.: 'Lightning induced voltages on power lines: experiment', *IEEE Transactions on Power Apparatus and Systems*, 1984, **103**, (9), pp. 2519–2529
11. ERIKSSON, A. J., PENMAN, C. L. and MEAL, D. V.: 'A review of five years' lightning research on an 11 kV test – line', Proceedings of the International Conference on Lightning and Power Systems, IEE, London, 1984, pp. 62–66
12. YOKOYAMA, S., MIYAKE, K., MITANI, H. and TAKANISHI, A.: 'Simultaneous measurement of lightning induced voltages with associated stroke currents', *IEEE Transactions on Power Apparatus and Systems*, 1983, **102**, (8), pp. 2420–2427
13. ERIKSSON, A. J., STRINGFELLOW, M. F. and MEAL, D. V.: 'Lightning – induced overvoltages on overhead distribution lines', *IEEE Transactions on Power Apparatus and Systems*, 1982, **101**, (4), pp. 960–968
14. PERRY, F. R., WEBSTER, G. H., BAGULEY, P. W.: 'The measurement of lightning voltages and currents in Nigeria: part 2, 1938–1939', *Journal of I.E.E. – Part II: Power Engineering*, 1942, **89**, (9), pp. 185–203
15. PERRY, F. R.: 'The measurement of lightning voltages and currents in South Africa and Nigeria: 1935 to 1937', *Journal of I.E.E. – Part II: Power Engineering*, 1941, **88**, (2), pp. 69–87
16. DECARLO, B. A., RAKOV, V. A., JERAULD, J., SCHNETZER, G. H., SCHOENE, J., UMAN, M. A., *et al.*: 'Triggered-lightning testing of the protective system of a residential building: 2004 and 2005 results', Proceedings of the 28th International Conference on Lightning Protection (ICLP), Kanazawa, Sep. 2006, pp. 628–633
17. BEJLERI, M., RAKOV, V. A., UMAN, M. A., RAMBO, K. J., MATA, C. T. and FERNANDEZ, M. I.: 'Triggered lightning testing of an airport runway lighting system', *IEEE Transactions on Electromagnetic Compatibility*, 2004, **46**, (1), pp. 96–101
18. RAKOV, V. A. and UMAN, M. A. (eds.): 'Artificial initiation (triggering) of lightning by ground-based activity', in *Lightning: Physics and Effects* (Cambridge University Press, Cambridge, 2003), Chapter 7, pp. 265–307

19. RAKOV, V. A., UMAN, M. A., FERNANDEZ, M. I., MATA, C. T., RAMBO, K. J., STAPLETON, M. V., *et al.*: 'Direct lightning strikes to the lightning protective system of a residential building: triggered-lightning experiments', *IEEE Transactions on Power Delivery*, 2002, **17**, (2), pp. 575–586
20. RAKOV, V. A.: 'Rocket-triggered lightning experiments at Camp Blanding, Florida', Proceedings of the 5th International Symposium on Lightning Protection (SIPDA), São Paulo, May 1999, pp. 375–388
21. BARKER, P. P., SHORT, T. A., EYBERT-BERARD, A. R. and BERLANDIS, J. P.: 'Induced voltage measurements on an experimental distribution line during nearby rocket triggered lightning flashes', *IEEE Transactions on Power Delivery*, 1996, **11**, (2), pp. 980–995
22. RUBINSTEIN, M., UMAN, M. A., MEDELIUS, P. J. and THOMSON, E. M.: 'Measurements of the voltage induced on an overhead power line 20 m from triggered lightning', *IEEE Transactions on Electromagnetic Compatibility*, 1994, **36**, (2), pp. 134–140
23. CLEMENT, M. and MICHAUD, J.: 'Overvoltages on the low voltage distribution networks. Origins and characteristics. Consequences upon the construction of Electricite de France networks', Proceedings of the 12th International Conference on Electricity Distribution (CIRED), Birmingham, 1993, pp. 2.16.1–2.16.6
24. DOMMEL, H. W.: *Electromagnetic Transients Program Reference Manual (EMTP Theory Book)* (The University of British Columbia, Vancouver, 1986)
25. ABETTI, P. A.: 'Transformer models for the determination of transient voltages', *AIEE Transactions*, 1953, **72**, (2), pp. 468–480
26. SINCLAIR, G.: 'Theory of models of electromagnetic systems', *Proceedings of the I. R. E.*, 1948, **36**, (11), pp. 1364–1370
27. SEBO, S. A., DEVORE, R. V., CALDECOTT, R. and WUHAN J. H.: 'Design and RF operation of scale model of Dickinson + 400 kV HVDC converter station', *IEEE Transactions on Power Apparatus and Systems*, 1985, **PAS-104**, (7), pp. 1930–1936
28. SEBO, S. A., CALDECOTT, R. and KASTEN, D. G.: 'Model study of HVDC electric field effects', *IEEE Transactions on Power Apparatus and Systems*, 1982, **101**, (6), pp. 1743–1756
29. SEBO, S. A. and CALDECOTT, R.: 'Scale model studies of AC substation electric fields', *IEEE Transactions on Power Apparatus and Systems*, 1979, **PAS-98**, (3), pp. 926–939
30. CONSA, R. P. and RENÉ, J. G.: 'Air model for the study of electrostatic induction by transmission lines', *IEEE Transactions on Power Apparatus and Systems*, 1968, **PAS-87**, (4), pp. 1002–1010
31. GARBAGNATI, E. and LO PIPARO, G. B.: 'Modelli geometrici per la determinazione della risposta al fulmine di un sostegno di linea aerea', *L'Eletrotecnica*, 1970, **57**, (8), pp. 439–448
32. FISHER, F. A., ANDERSON, J. G. and HAGENGUTH, J. H.: 'Determination of lightning response of transmission lines by means of geometrical models', *AIEE Transactions on Power Apparatus and Systems*, 1960, **78**, pp. 1725–1736

33. JOHNSON, I. B. and SCHULTZ, A. J.: 'Analytical studies on lightning phenomena involving towers, insulator strings, and transmission lines', *AIEE Transactions*, 1958, **76**, pp. 1310–1314
34. HAGENGUTH, J. H. and ANDERSON, J. G.: 'Factors affecting the lightning performance of transmission lines', *AIEE Transactions*, 1958, **76**, pp. 1379–1392
35. PIANTINI, A., JANISZEWSKI, J. M., BORGHETTI, A., NUCCI, C. A. and PAOLONE, M.: 'A scale model for the study of the LEMP response of complex power distribution networks', *IEEE Transactions on Power Delivery*, 2007, **22**, (1), pp. 710–720
36. PIANTINI, A. and JANISZEWSKI, J. M.: 'The effectiveness of surge arresters on the mitigation of lightning induced voltages on distribution lines', *Journal of Lightning Research*, 2007, **2**, pp. 34–52
37. PIANTINI, A. and JANISZEWSKI, J. M.: 'Protection of distribution lines against indirect lightning strokes through the use of surge arresters', CIGRE Surge Arrester Tutorial, Rio de Janeiro, Apr. 2005
38. PIANTINI, A. and JANISZEWSKI, J. M.: 'Lightning induced voltages on distribution transformers: the effects of line laterals and nearby buildings', Proceedings of the 6th International Symposium on Lightning Protection (SIPDA), Santos, Nov. 2001, pp. 77–82
39. PIANTINI, A. and JANISZEWSKI, J. M.: 'Lightning induced voltages on distribution lines close to buildings', Proceedings of the 25th International Conference on Lightning Protection (ICLP), Rhodes, **B**, Sep. 2000, pp. 558–563
40. NUCCI, C. A., BORGHETTI, A., PIANTINI, A. and JANISZEWSKI, J. M.: 'Lightning-induced voltages on distribution overhead lines: comparison between experimental results from a reduced-scale model and most recent approaches', Proceedings of the 24th International Conference on Lightning Protection (ICLP), Birmingham, **1**, Sep. 1998, pp. 314–320
41. PIANTINI, A.: 'Lightning induced voltages on overhead rural and urban lines, considering different protection alternatives – theoretical and experimental modelling and calculation of the number of supply interruptions' (in Portuguese). PhD Thesis, Dept. of Electrical Engineering, University of São Paulo, Feb. 1997
42. PIANTINI, A. and JANISZEWSKI, J. M.: 'Use of surge arresters for protection of overhead lines against nearby lightning', Proceedings of the 10th International Symposium on High Voltage Engineering (ISH), Montreal, **5**, Aug. 1997, pp. 213–216
43. PAULINO, J. O. S., BOAVENTURA, W. C. and LOPES, I. J. S.: 'Lightning induced voltage on distribution lines with shield wires: digital simulations and reduced model measurements', Proceedings of the 9th International Symposium on High Voltage Engineering (ISH), Graz, 1995, pp. 6718/1–4
44. PIANTINI, A. and JANISZEWSKI, J. M.: 'Lightning induced voltages on overhead lines: the effect of ground wires', Proceedings of the 22nd International Conference on Lightning Protection (ICLP), Budapest, Sep. 1994, pp. R3b/1–R3b/5

45. PIANTINI, A. and JANISZEWSKI, J. M.: 'An Experimental study of lightning induced voltages by means of a scale model', Proceedings of the 21st International Conference on Lightning Protection (ICLP), Berlin, Sep. 1992, pp. 195–199
46. YOKOYAMA, S.: 'Calculation of lightning – induced voltages on overhead multiconductor systems', *IEEE Transactions on Power Apparatus and Systems*, 1984, **103**, (1), pp. 100–108
47. YOKOYAMA, S.: 'Experimental analysis of earth wires for induced lightning surges', *IEE Proceedings – C*, 1980, **127**, (1), pp. 33–40
48. ISHII, M., MICHISHITA, K. and HONGO, Y.: 'Experimental study of lightning-induced voltage on an overhead wire over lossy ground', *IEEE Transactions on Electromagnetic Compatibility*, 1999, **41**, (1), pp. 39–45
49. YAMAMOTO, K., NODA, T., YOKOYAMA, S. and AMETANI, A.: 'Experimental and analytical studies of lightning overvoltages in wind turbine generation systems', Proceedings of the International Conference on Power Systems Transients (IPST), Lyon, June 2007
50. YAMAMOTO, K., NODA, T., YOKOYAMA, S. and AMETANI, A.: 'An experimental study of lightning overvoltages in wind turbine generation systems using a reduced-size model', *Electrical Engineering in Japan*, 2007, **158**, (4), pp. 22–30
51. RAKOV, V. A.: 'Lightning parameters important for lightning protection', Proceedings of the 6th International Symposium on Lightning Protection (SIPDA), Santos, Nov. 2001, pp. 393–412
52. MACH, D. M. and RUST, W. D.: 'Photoelectric return-stroke velocity and peak current estimates in natural and triggered lightning', *Journal of Geophysical Research*, 1989, **94**, pp. 13,237–247
53. NUCCI, C. A.: 'Lightning induced voltages on overhead power lines. Part I: Return-stroke current models with specified channel-base current for the evaluation of the return-stroke electromagnetic fields', *Electra*, 1995, (161), pp. 74–102
54. THOTTAPPILLIL, R., RAKOV, V. A. and UMAN, M.: 'Distribution of charge along the lightning channel: Relation to remote electric and magnetic fields and to return stroke models', *Journal of Geophysical Research*, 1997, **102**, pp. 6887–7006
55. RAKOV, V. A. and UMAN, M. A.: 'Review and evaluation of lightning return stroke models including some aspects of their applications', *IEEE Transactions on Electromagnetic Compatibility*, 1998, **40**, (4), pp. 403–426
56. GOMES, C. and COORAY, V.: 'Concepts of lightning return stroke models', *IEEE Transactions on Electromagnetic Compatibility*, 2000, **42**, (1), pp. 82–96
57. RAKOV, V. A.: 'Engineering models of the lightning return stroke', Proceedings of the 7th International Symposium on Lightning Protection (SIPDA), Curitiba, Nov. 2003, pp. 511–530

58. RACHIDI, F., NUCCI, C. A., IANOZ, M. and MAZZETTI, C.: 'Influence of a lossy ground on lightning-induced voltages on overhead lines', *IEEE Transactions on Electromagnetic Compatibility*, 1996, **38**, (3), pp. 250–264
59. COORAY, V.: 'On the validity of several approximate theories used in quantifying the propagation effects on lightning generated electromagnetic fields', Proceedings of the 8th International Symposium on Lightning Protection (SIPDA), São Paulo, Nov. 2005, pp. 112–119
60. COORAY, V.: 'Propagation effects due to finitely conducting ground on lightning generated magnetic fields evaluated using Sommerfeld's integrals', Proceedings of the 9th International Symposium on Lightning Protection (SIPDA), Foz do Iguaçu, Nov. 2007, pp. 151–150
61. NUCCI, C. A.: 'Lightning-induced voltages on distribution systems: influence of ground resistivity and system topology', Proceedings of the 8th International Symposium on Lightning Protection (SIPDA), São Paulo, Nov. 2005, pp. 761–773
62. NUCCI, C. A., RACHIDI, F., IANOZ, M. and MAZZETTI, C.: 'Lightning-induced overvoltages on overhead lines', *IEEE Transactions on Electromagnetic Compatibility*, 1993, **35**, (1), pp. 75–86
63. ROMERO, F. and PIANTINI, A.: 'Evaluation of lightning horizontal electric fields over a finitely conducting ground', Proceedings of the 9th International Symposium on Lightning Protection (SIPDA), Foz do Iguaçu, Nov. 2007, pp. 145–150
64. BARBOSA, C. F. and PAULINO, J. O. S.: 'An approximate time-domain formula for the calculation of the horizontal electric field from lightning', *IEEE Transactions on Electromagnetic Compatibility*, 2007, **49**, (3), pp. 593–601
65. SHOORY, A., MOINI, R., SADEGHI, S. H. H. and RAKOV, V. A.: 'Analysis of lightning-radiated electromagnetic fields in the vicinity of lossy ground', *IEEE Transactions on Electromagnetic Compatibility*, 2005, **47**, (1), pp. 131–145
66. NUCCI, C. A. and RACHIDI, F.: 'Interaction of electromagnetic fields with electrical networks generated by lightning', in COORAY, V. (ed.): *The Lightning Flash* (IEE Power Engineering Series, London, **34**, 2003), Chapter 8, pp. 425–478
67. ISHII, M., MICHISHITA, K., HONGO, Y. and OGUME, S.: 'Lightning-induced voltage on an overhead wire dependent on ground conductivity', *IEEE Transactions on Power Delivery*, 1994, **9**, (1), pp. 109–118
68. RACHIDI, F., NUCCI, C. A. and IANOZ, M.: 'Transient analysis of multi-conductor lines above a lossy ground', *IEEE Transactions on Power Delivery*, 1999, **14**, (1), pp. 294–302
69. BORGHETTI, A. and NUCCI, C. A.: 'Frequency distribution of lightning-induced voltages on an overhead line above a lossy ground', Proceedings of the 5th International Symposium on Lightning Protection (SIPDA), São Paulo, May 1999, pp. 229–233

70. HOIDALEN, H. K., SLETBAK, J. and HENRIKSEN, T.: 'Ground effects on induced voltages from nearby lightning', *IEEE Transactions on Electromagnetic Compatibility*, 1997, **39**, pp. 269–278
71. NUCCI, C. A. and RACHIDI, F.: 'Lightning protection of medium voltage lines', in COORAY, V. (ed.): *Lightning Protection* (IET Power and Energy Series, London, **58**, 2010), Chapter 13, pp. 635–680
72. PAOLONE, M., NUCCI, C. A., PETRACHE, E. and RACHIDI, F.: 'Mitigation of lightning-induced overvoltages in medium voltage distribution lines by means of periodical grounding of shielding wires and of surge arresters: modeling and experimental validation', *IEEE Transactions on Power Delivery*, 2004, **19**, (1), pp. 423–431
73. YOKOYAMA, S.: 'Lightning protection of MV overhead distribution lines', Proceedings of the 7th International Symposium on Lightning Protection (SIPDA), São Paulo, Nov. 2003, pp. 485–507
74. NUCCI, C. A.: 'Lightning-induced voltages on overhead power lines. Part III: Sensitivity analysis', *Electra*, 2005, (222) pp. 27–30
75. PIANTINI, A.: 'Lightning protection of low-voltage networks', in COORAY, V. (ed.): *Lightning Protection* (IET Power and Energy Series, London, **58**, 2010), Chapter 12, pp. 553–634
76. LAT, V. and CARR, J.: 'Application guide for surge arresters on distribution systems', Canadian Electrical Association, Toronto, 1988
77. YOKOYAMA, S.: 'Distribution surge arrester behavior due to lightning induced voltages', *IEEE Transactions on Power Delivery*, 1986, **1**, (1), pp. 171–178
78. BORGHETTI, A., GUTIERREZ, A., NUCCI, C. A., PAOLONE, M., PETRACHE, E. and RACHIDI, F.: 'Lightning-induced voltages on complex distribution systems: models, advanced software tools and experimental validation', *Journal of Electrostatics*, 2004, **60**, pp. 163–174
79. NUCCI, C. A., BARDAZZI, V., IORIO, R., MANSOLDO, A. and PORRINO, A.: 'A code for the calculation of lightning-induced overvoltages and its interface with the Electromagnetic Transient program', Proceedings of the 22nd International Conference on Lightning Protection (ICLP), Budapest, Sep. 1994, pp. 19–23
80. AGRAWAL, A. K., PRICE, H. J. and GURBAXANI, S. H.: 'Transient response of a multiconductor transmission line excited by a nonuniform electromagnetic field', *IEEE Transactions on Electromagnetic Compatibility*, 1980, **EMC-22**, (2), pp. 119–129
81. CHOWDHURI, P.: 'Analysis of lightning – induced voltages on overhead lines', *IEEE Transactions on Power Delivery*, 1989, **4**, (1), pp. 479–492
82. RUSCK, S.: 'Induced lightning over-voltages on power-transmission lines with special reference to the over-voltage protection of low-voltage networks', Transactions of the Royal Institute of Technology, Stockholm, 1958, (120)
83. LIEW, A. C. and MAR, S. C.: 'Extension of the Chowdhuri – gross model for lightning induced voltage on overhead lines', *IEEE Transactions on Power Systems*, 1986, **1**, (2), pp. 240–247

84. PIANTINI, A. and JANISZEWSKI, J. M.: 'The influence of the upward leader on lightning induced voltages', Proceedings of the 23rd International Conference on Lightning Protection (ICLP), Florence, Sep. 1996, pp. 352–357
85. PIANTINI, A. and JANISZEWSKI, J. M.: 'Induced voltages on distribution lines due to lightning discharges on nearby metallic structures', *IEEE Transactions on Magnetics*, 1998, **34**, (5), pp. 2799–2802
86. HOIDALEN, H. K.: 'Analytical formulation of lightning-induced voltages on multiconductor overhead lines above lossy ground', *IEEE Transactions on Electromagnetic Compatibility*, 2003, **45**, (1), pp. 92–100
87. PIANTINI, A. and JANISZEWSKI, J. M.: 'An improved model for lightning induced voltages calculations', Proceedings of the IEEE/PES Transmission & Distribution Conference and Exposition: Latin America, São Paulo, Nov. 2004, pp. 554–559
88. PIANTINI, A. and JANISZEWSKI, J. M.: 'The Extended Rusck Model for calculating lightning induced voltages on overhead lines', Proceedings of the 7th International Symposium on Lightning Protection (SIPDA), Curitiba, Nov. 2003, pp. 151–155
89. DARVENIZA, M.: 'A practical extension of Rusck's formula for maximum lightning-induced voltages that accounts for ground resistivity', *IEEE Transactions on Power Delivery*, 2007, **22**, (1), pp. 605–612
90. REN, H. M., ZHOU, B. H., RAKOV, V. A., SHI, L. H., GAO, C. and YANG, J. H.: 'Analysis of lightning-induced voltages on overhead lines using a 2-D FDTD method and Agrawal coupling model', *IEEE Transactions on Electromagnetic Compatibility*, 2008, **50**, (3), pp. 651–659
91. BABA, Y. and RAKOV, V. A.: 'Voltages induced on an overhead wire by lightning strikes to a nearby tall grounded object', *IEEE Transactions on Electromagnetic Compatibility*, 2006, **48**, (1), pp. 212–224
92. MICHISHITA, K. and ISHII, M.: 'Theoretical comparison of Agrawal's and Rusck's field-to-line coupling models for calculation of lightning-induced voltage on an overhead wire', *IEE Transactions of Japan*, 1997, **117**, (9), pp. 1315–1316
93. PIANTINI, A. and JANISZEWSKI, J. M.: 'Analysis of three different theories for computation of induced voltages on distribution lines due to nearby lightning', Proceedings of the International Conference on Electricity Distribution, Buenos Aires, Dec. 1996, pp. session 1/127–132
94. NUCCI, C. A.: 'Lightning-induced voltages on overhead power lines. Part II: Coupling models for the evaluation of the induced voltages', *Electra*, 1995, (162), pp. 121–145
95. NUCCI, C. A., RACHIDI, F., IANOZ, M. and MAZZETTI, C.: 'Comparison of two coupling models for lightning-induced overvoltage calculations', *IEEE Transactions on Power Delivery*, 1995, **10**, (1), pp. 330–339
96. COORAY, V.: 'Calculating lightning-induced overvoltages in power lines: a comparison of two coupling models', *IEEE Transactions on Electromagnetic Compatibility*, 1994, **36**, (3), pp. 179–182

97. UMAN, M. A. and MCLAIN, D. K.: ‘Magnetic field of the lightning return stroke’, *Journal of Geophysical Research*, 1969, **74**, pp. 6899–6910
98. PIANTINI, A. and JANISZEWSKI, J. M.: ‘Lightning-induced voltages on overhead lines – application of the Extended Rusck Model’, *IEEE Transactions on Electromagnetic Compatibility*, 2009, **51**, (3), pp. 548–558
99. PAOLONE, M., RACHIDI, F., BORGHETTI, A., NUCCI, C. A., RUBINSTEIN, M., RAKOV, V. A., *et al.*: ‘Lightning electromagnetic field coupling to overhead lines: theory, numerical simulations and experimental validation’, *IEEE Transactions on Electromagnetic Compatibility*, 2009, **51**, (3), pp. 532–547
100. PIANTINI, A., JANISZEWSKI, J. M. and BRAZ, C. P.: ‘Utilization of reduced models for the analysis of lightning induced overvoltages on overhead lines’, Proceedings of the International Conference on High Voltage Engineering and Application, New Orleans, Oct. 2010

---

# *Chapter 20*

## **Attachment of lightning flashes to grounded structures**

*Vernon Cooray<sup>1</sup>*

---

### **20.1 Introduction**

A grounded structure can interact with a lightning flash in two different ways. It can interact with either a downward or an upward lightning flash. The initiation of a downward lightning flash takes place in the cloud, whereas in the case of upward lightning flash, the point of initiation is usually at the tip of a tall structure. In other words, upward lightning flashes are created by the grounded structure itself. In this chapter, a brief description of various models used to study the lightning attachment is given together with some of their predictions. A portion of the material presented here is published previously in References 1 and 2.

First, let us consider the events associated with the attachment of a downward negative lightning flash (i.e. a lightning flash that transports negative charges to ground) with a grounded structure. Experimental investigations show that a downward lightning flash is initiated by a column of charge called the stepped leader that travels from cloud to ground in a stepped manner. As the stepped leader approaches the ground, the electric field at ground level increases steadily. The electric field at the pointed tips of a grounded structure, which is immersed in this background electric field, may reach values that are several times to several tens of times the magnitude of the background electric field produced by the stepped leader due to field enhancement. When the electric field at the tip of a structure reaches a critical value of about  $3.0 \times 10^6$  V/m, electron avalanches will be generated from the tip. As the background electric field and hence the local electric field at the tip intensifies, the ionization taking place at the tip becomes more vigorous leading to an increase in the number of charged particles in the head of the electron avalanches. When this number reaches a value around  $10^8$  to  $10^9$ , electron avalanches will be transformed to a streamer discharge [3, 4] (see also Chapter 3). This conversion of electron avalanches to a streamer, or the streamer inception, is called avalanche to streamer transition. Once the conditions necessary for streamer inception are satisfied, several streamer bursts will be issued from the point under consideration. These streamer bursts are generated from a common stem and if

<sup>1</sup>Uppsala University, Uppsala, Sweden

the charge in the streamer burst is larger than about  $1 \mu\text{C}$ , the streamer stem will be thermalized leading to the creation of a leader [3]. This transition is called streamer to leader transition. This leader, created by the action of the electric field generated by the stepped leader, is called a connecting leader. Once inception, a connecting leader starts to grow towards the down-coming stepped leader. This growth of the connecting leader is mediated by streamer bursts generated at its tip. The charge associated with each streamer burst depends on the background electric field and the potential gradient of the connecting leader channel. The potential gradient of the connecting leader channel (which is positively charged in this case) can be obtained by appealing to the thermodynamic model of the positive leaders as described by Gallimberti [3]. Each streamer burst extends the leader by a small amount. For example, if the charge in a streamer burst is  $Q$ , then the amount of elongation of the positive leader is given by  $Q/q_l$ , where  $q_l$  is the amount of charge necessary to thermalize a unit length of the leader channel. For positive leaders, this is equal to about  $40\text{--}60 \mu\text{C/m}$ . Indeed, both the down-coming stepped leader and the upward-moving connecting leader moves with the aid of streamer bursts that generate enough charge to thermalize a section of the leader. As the positive leader approaches the negative one, the average potential gradient between the two leader tips continues to increase, and when it reaches a value equal to  $500 \text{ kV/m}$ , all conditions necessary for the final connection are satisfied making the final connection imminent. This condition is called the final jump condition. Once the connection is made, the resulting rapid neutralization of the stepped leader charge leads to the generation of a return stroke. The point of attachment of the downward flash on the structure is the point of initiation of the connecting leader that made the final connection with the stepped leader.

Now, let us consider the upward lightning flashes initiated by tall grounded structures. Upward lightning flashes are initiated by the tall structures themselves due to the enhancement, caused by the geometry of the structure, of the background electric field generated by the thundercloud. As the electric field generated by the thundercloud increases and once all the stages that have been described above, namely, initiation of avalanches, initiation of streamers and initiation of a leader, had been completed, an upward-moving leader will be initiated from a field-enhanced tip of a tall grounded structure. Once initiated, the conditions necessary for its propagation are identical to that of the connecting leader described in the previous section except for the fact that here the background electric field remains more or less constant whereas in the previous case it was increasing with time as the stepped leader approaches the structure. Once the leader initiated from the structure reaches the charge centre in the cloud, dart leaders will follow this channel to ground initiating subsequent return strokes.

For a lightning attachment model to be self-consistent, it should take into account all the processes mentioned above. However, due to the difficulties associated with including all these processes into a lightning striking model, engineers have constructed empirical models that can be applied easily in practice. In the next section, some of the models utilized to analyse the problem of lightning attachment are described. However, before proceeding further, let us describe the meaning of the striking distance as applied in lightning protection studies.

## 20.2 Striking distance

Since the striking distance is a man-made parameter, it is first necessary to define what is meant by the term striking distance. According to the definition of this parameter by Golde [5], the striking distance is the separation between the tip of the stepped leader and the tip of a grounded structure when a stable (i.e. continuously propagating) upward connecting leader is established from the tip of the grounded structure. However, one can see immediately that this definition will lead to ambiguous situations in practice. For example, as a stepped leader approaches the ground, several stable connecting leaders could be established either by several points on the same structure or by points in several structures. In this case the above definition cannot be used to define the striking distance uniquely. Another situation where this definition may cause difficulties is when one tries to analyse lightning strikes to a flat ground. In this case the final attachment may take place without the origin of a connecting leader in a conventional sense. However, one can get out of this ambiguous situation by redefining the striking distance as follows. It could be defined as *the separation between the tip of the structure, where a connecting leader is generated, and the tip of the stepped leader when the final jump condition is established between the connecting leader and the stepped leader*. This is illustrated in Figure 20.1. With this definition, a striking distance is associated only with a connecting leader that successfully intercepts the down-coming

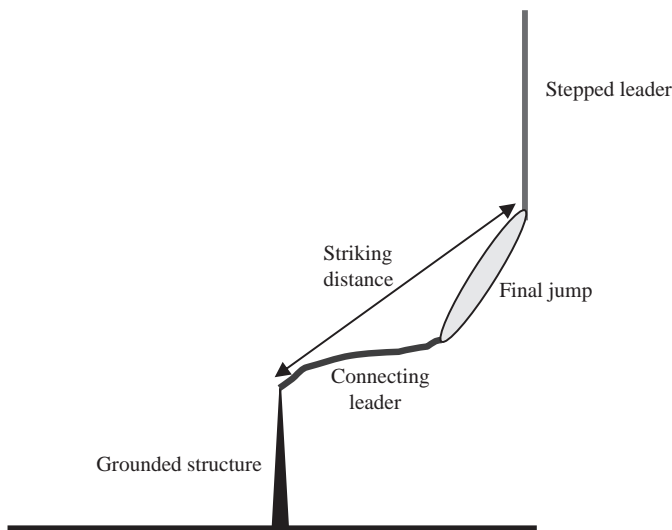


Figure 20.1 The striking distance is defined in the figure as the separation between the tip of the structure, where a connecting leader is generated, and the tip of the stepped leader when the final jump condition is established between the connecting leader and the stepped leader

stepped leader. It could also be applied without any ambiguity in situations where a connecting leader, in the conventional sense, is absent (or is very short) during a lightning strike.

One of the most simple and user-friendly lightning strike models is the electrogeometrical model (EGM). According to EGM, the attachment between the stepped leader and the grounded structure takes place when the final jump condition (defined in the next section) is established between the tip of the stepped leader and the grounded structure. EGM does not envisage the presence of a connecting leader. In this chapter, the critical distance between the tip of the stepped leader and the grounded structure when the final jump condition is established between them is referred to as EGM striking distance. This is the striking distance in the absence of a connecting leader. Thus, the striking distance as defined in the previous section reduces to EGM striking distance when the connecting leader is absent or negligibly short.

The final jump condition, borrowed from the jargon of laboratory long sparks, is defined as the instant when the streamers generated from the leader channel reaches the grounded electrode. Since the streamers maintain a constant potential gradient, one can assume that the final jump condition is reached when the average potential gradient between the leader tip and the grounded structure becomes equal to the potential gradient of streamer channels. Now consider a strike of a negative downward flash to flat ground. If the ground is completely flat then the final jump condition is reached when the average electric field between the leader tip and the ground reaches a value 1–2 MV/m. This is the critical electric field necessary for negative streamer propagation. However, in practice, a completely flat ground does not exist and even on the surface of an ocean the turbulence created during thunderstorms may result in the formation of waves that may act as temporary protrusions. In such cases, positive streamers could be generated from small protrusions on ground or on the ocean surface. If the breakdown is mediated purely by positive streamers, then it is reasonable to use an average potential gradient of 500 kV/m, the critical electric field necessary for the propagation of positive streamers, during the final jump. Golde [5] suggested using 500 kV/m for negative ground flashes and 300 kV/m for positive ground flashes. On the other hand, based on the breakdown voltage as a function of gap length of long sparks, Armstrong and Whitehead [6] assumed that the average potential gradient,  $E_{ave}$  (voltage divided by the gap length, V/m), during the final jump is given by

$$E_{ave} = \frac{7.55 \times 10^5}{r^{0.166}} \quad (20.1)$$

In the above equation,  $r$  is the gap length (in m). As one can observe from the above equation, this average potential gradient depends on the gap length and it decreases with increasing gap length.

In the case of encounter between the connecting leader and the stepped leader, the final jump condition is reached when the potential gradient between the two leader tips is equal to the specified critical potential gradient. With the definition

given earlier, the striking distance in the absence of a connecting leader from a grounded structure is equal to the separation between the tip of the structure and the tip of the stepped leader when the average potential gradient between them reaches the specified critical value. With increasing length of the connecting leader, the striking distance increases.

In order to apply this concept of striking distance, it is necessary to know when and where from the structure a connecting leader is incepted. There are several theories that can be utilized to find this information and some of the important ones are summarized below.

## 20.3 Leader inception models

### 20.3.1 Critical radius and critical streamer length concepts

Laboratory experiments conducted with rod–plane gaps in air show that for a given gap length the breakdown voltage remained the same with increasing electrode radius until a critical radius is reached [7, 8]. Further increase of the radius led to an increase of the breakdown voltage. The radius at which the breakdown voltage starts to increase is named the critical radius. The critical radius is the minimum radius of a spherical electrode in a given gap length that will produce leader inception immediately with the inception of streamers. The critical radius increases initially with gap length but reaches a more or less asymptotic value of about 38 cm for large gap lengths. Experiments conducted with inverted geometries gave values in the range of 10–28 cm [9].

The critical radius concept is commonly applied in lightning research in the evaluation of the background electric field necessary for the generation of a continuous leader from a point on a grounded structure. This is done by assuming that a leader is incepted from a point when the electric field at a distance of critical radius from the point reaches breakdown value in air.

Experiments also show that the length of the streamers at the critical radius is about 3 m [7]. In other words, the length of the streamers should exceed this critical value before the inception of a leader. Akyuz and Cooray [10] have used the critical streamer length as the criterion, instead of the critical radius, in evaluating the inception of connecting leaders. Based on the results of Chernov *et al.* [11], Petrov and Waters [12] assumed that the streamer initiated from a given point on a structure must extend to a critical length of 0.7 m, before an upward leader is initiated from that point. In a model developed by Bazelyan and Raizer [13], it is assumed that the unstable leader inception takes place when the potential drop between the electrode tip and a point about 1 m from it is equal to a critical value that is assumed to be approximately equal to 400 kV. Since 400 kV/m is approximately equal to the potential gradient of positive streamers, this criterion implies that the inception of a leader takes place when the streamers extend to a length of about 1 m. According to them, for the continuous propagation of the leader, the difference between the potential of the leader tip and the potential produced by the external field at the location of the leader tip should increase continuously.

One advantage of the critical streamer length criterion over the critical radius criterion is that it can be easily implemented in any complicated structure that one may encounter in practice.

It is important to point out, however, that the critical radius and critical streamer length concepts are derived from breakdown characteristics of long rod-plane gaps under the application of switching impulses of critical time to crest. In the case of lightning attachment, the temporal variation of the electric field generated at the grounded structure by a down-coming stepped leader is very different to that of an electric field generated by a switching impulse. For this reason, the validity of such concepts in the case of lightning flashes is still a topic of discussion.

### *20.3.2 Rizk's generalized leader inception equation*

Based on the results from laboratory, Rizk [14] has constructed a theory to evaluate the inception of leaders from grounded structures. According to this theory, the ambient potential  $U$  (potential in the absence of the structure) required to incept an upward connecting leader from a horizontal wire is given by

$$U = \frac{2247}{1 + (5.15 - 5.49\ln(a))/h\ln(h/2a)} \quad (20.2)$$

where  $h$  is the height in metres,  $a$  is the radius of the wire in metres and  $U$  is in kV. For a vertical tower, it is given by

$$U = \frac{1556}{1 + 3.89/h} \quad (20.3)$$

where  $h$  is the height of the tower in metres.

Note that these results are based on laboratory data pertinent to switching impulses, and the assessment of their validity in the case of electric fields generated by stepped leaders may require further research efforts. Recently, Rizk [15] has established theory that allows evaluation of leader inception from any structure.

### *20.3.3 Lalande's stabilization field equation*

Lalande [16] used a physical model for the leader propagation in long gaps proposed by Goelian *et al.* [17] and combined it with the thermo-hydrodynamic model of the leader channel proposed by Gallimberti [3] in order to compute the leader inception condition. In constructing the model, it is also assumed that the ratio of the leader velocity to leader current remains constant during the development of the leader. Based on this analysis, the background electric field necessary to initiate leaders from grounded structures was estimated as

$$E_0 \geq \frac{240}{1 + h/10} + 12 \text{ [kV/m]} \quad (20.4)$$

where  $h$  is the height of the structure in metres. In a later study, however, Lalande *et al.* [18] proposed the following equation, which is different from the above, for the stabilization electric field:

$$E_0 \geq \frac{306.7}{1 + h/6.1} + \frac{21.6}{1 + h/132.7} \text{ [kV/m]} \quad (20.5)$$

Unfortunately, details as to the modifications necessary both in physics and in mathematics to change the results from (20.4) to (20.5) were not given in Reference 18.

#### 20.3.4 Leader inception model of Becerra and Cooray (SLIM)

Utilizing the same physics as developed by Gallimberti [3], Becerra and Cooray [19, 20] introduced a model to evaluate the inception of connecting leaders. The model can be applied to any grounded structure including conductors and towers of power transmission and distribution lines. The main steps that are included in the model are the following:

1. Formation of a streamer discharge (streamer inception) at the tip of a grounded object.
2. Transformation of the stem of the streamer into thermalized leader channel (unstable leader inception).
3. Extension of the positive leader and its self-sustained propagation (stable leader inception).

In the model, the streamer inception is evaluated using the well-known streamer inception criterion [3], while the transition from streamer to leader is assumed to take place if the total charge in a streamer burst is equal to or larger than about  $1 \mu\text{C}$  [3]. The condition for self-propagation of the leader, i.e. stable leader inception, is assumed to be satisfied if the leader continues to accelerate in the background electric field at least for a distance of a few metres. In addition, this model not only predicts the conditions under which leaders are inception but it provides the current and speed of the upward-moving leaders. A detailed description of the procedure proposed by Becerra and Cooray to evaluate the leader inception can be found in [19, 20] (see also Chapter 3).

In the above section we have described some of the important leader inception models. However, inception of a connecting leader itself does not guarantee lightning attachment. It is necessary for the connecting leader to propagate and make the final connection with the stepped leader. There are several models that attempt to simulate this process and they are called leader progression models. Now, let us summarize several of these models.

## 20.4 Leader progression and attachment models

For a complete description of the attachment of a leader to grounded structures both the inception of a connecting leader and its subsequent propagation and final

connection to the downward stepped leader have to be analysed. The leader progression models attempt to simulate the dynamics associated with this process. Five models that, in contrast to EGM, take into account the formation of an upward leader exist today and they were introduced by Eriksson [21], Dellera and Garbagnati [22], Rizk [23], Becerra and Cooray [24] and Vargas and Torres [25–27]. Only for some of them, however, the dynamic progress of downward and upward leader is explicitly represented, as it will be illustrated in what follows. For ease of reference, refer to these five models as A, B, C, D and E, respectively. Basic features of these models are schematically depicted in Figure 20.2. Note that the description given here for the model C is based on Reference [23]. In a recent paper, the model was updated and improved by Rizk [15].

- In models A, C and D, the downward stepped leader is assumed to take a straight path to ground without branches, while in B the path is determined step by step by the solution of subsequent electrostatic problems, in which the boundary conditions are represented essentially by the downward and upward leaders. In E, the downward leader channel may also be tortuous and branched, and the channel geometry is based on the statistical characterizations of natural lightning channels as reported by Hill [28, 29] and Idone and Orville [30].
- The charge distribution on the downward stepped leader channel is assumed to decrease upwards in models A, C, D and E. In B, the charge per unit length has

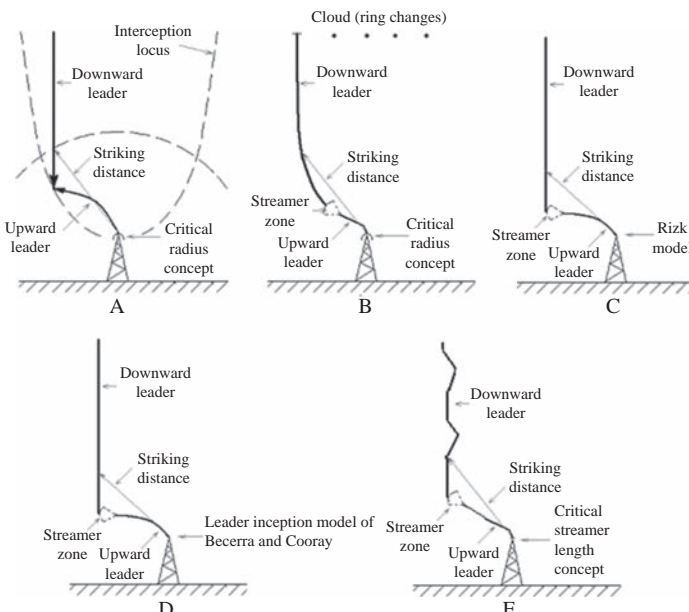


*Figure 20.2 Schematics of the leader propagation models A, B, C, D and E. [adapted from Reference 1]. The indicated striking distance follows Golde [5] definition*

two different values: one in the vicinity (last tens of metres) of the leader tip, which is uncorrelated to the amplitude of the lightning current and assumed equal to  $100 \mu\text{C/m}$ , and the other one, the magnitude of which varies with the prospective return stroke current, along the rest of the leader channel. In D, the variation of the charge per unit length of the stepped leader is approximated by an analytical expression extracted by Cooray *et al.* [31] by analysing the charge brought to ground by first return strokes within the first  $100 \mu\text{s}$ . In E, the charge distribution along the downward stepped leader, including main channel and branches, is estimated by an electrostatic model of the lightning leader channel and the thundercloud [26].

- As the downward leader propagates towards the ground, the conditions at the surface of the grounded structure are evaluated continuously to find the time of leader inception. The criterion for upward connecting leader inception used is either critical radius concept (A and B), Rizk's generalized equation (C), Becerra and Cooray procedure (D) or Vargas and Torres criteria (E). The latter considers a streamer inception electric field assumption and the critical streamer length concept [26]. It is worth noticing that models A, B and C are only applicable to horizontal wires and vertical earthed structures [see the comment made on model C at the beginning of this section], whereas models D and E can be applied to any grounded structure, including complex buildings. Recently, the procedure to apply models B and C to any grounded structure is illustrated in references 32 and 15 respectively.
- In models A, C, D and E, the downward stepped leader path is considered unaffected by the presence of upward connecting leaders. In models A, C and D, the connecting leader travels in space in such a way that it will find the closest path for the connection with the stepped leader. In model B, both leaders propagate in the direction of the maximum electric field that exists along an equipotential line that is located at the outer boundary of the streamer region. The same criterion is applied in model E to simulate the propagation of the connecting leader.
- The ratio between the speed of propagation of the downward stepped leader and the upward-moving stepped leader is assumed to be either 1 or 4. However, in model D, the velocity of the upward leader is evaluated from first principles.
- In model A, the final attachment of the two leaders takes place when two tips of the leader channel meet each other. In model B, the final jump condition is reached when the streamer systems from the two leaders meet each other. In C, D and E, the final jump condition is reached when the average electric field between the two leader tips is  $500 \text{ kV/m}$ .

Recently, Mazur *et al.* [33] introduced a model to describe the propagation of negative stepped leaders. They utilized the model to estimate the striking distance of lightning flashes. In the model, the direction of a new leader step is taken to be the direction in which the length of the negative streamers issued by the negative leader head is longest. The direction of the positive leader is given by the direction of the maximum electric field at the tip of the positive leader immediately outside

the boundary region with an electric field of 3 MV/m. They also assumed that the striking distance is equal to the length of the final step of the stepped leader. The length of the final leader step was estimated by dividing the leader potential by the electric field of the negative streamer zone. Based on their simulations, it was claimed that the connecting leader does not play a significant role in determining the striking distance.

When considering the complexity of the lightning phenomena, it will always be necessary to make a large number of assumptions and simplifications in order to formulate a usable lightning strike model. However, the creation of leader progression models has been a major step forward and they are capable of predicting several phenomena observed in the field. Moreover, the models seem to be well suited for sensitivity analysis where the effects of various parameters on the efficiency of lightning protection procedures are being studied by changing one parameter at a time. It is important to stress here that self-consistent leader progression models can also be utilized to compliment the simple engineering models that are being used in practice.

## **20.5 The potential of the stepped leader channel and the striking distance**

The potential of the leader channel cannot be measured directly but has to be inferred from other experimental data or theory.

### *20.5.1 Armstrong and Whitehead [6]*

Armstrong and Whitehead [6] appealed to the return stroke model of Wagner [34] to obtain the potential of the leader channel as a function of the prospective return stroke current. According to the model of Wagner, the potential of the leader channel is given by the equation

$$V = 3.7 \times 10^6 I_p^{2/3} \quad (20.6)$$

In the above equation, the voltage,  $V$ , is in volts and the peak return stroke current,  $I_p$ , in kA.

### *20.5.2 Leader potential extracted from the charge neutralized by the return stroke*

How the potential of the stepped leader channel can be extracted from the charge dissipated by the first 100  $\mu$ s of the return stroke channel as measured by Cooray *et al.* [31] is illustrated below. The description given is identical to the procedure used by Cooray and Rakov [35] to extract the stepped leader potential from the same data.

Cooray *et al.* [31] analysed the negative first return stroke currents measured by Berger and Vogelsanger [36, 37] at Monte San Salvatore to find out whether there is any relationship between the peak current and the charge brought to ground during the first 100  $\mu$ s. They reasoned that the time interval of 100  $\mu$ s is

representative of the time for the return stroke front to reach the charge centre in the cloud and therefore the charge brought to ground during this time is a result of the neutralization of the section of the leader channel located below the charge centre. They found that there is a strong correlation between the two parameters. Figure 20.3 shows the results obtained by Cooray *et al.* [31]. The relationship between the two parameters can be represented by the equation

$$Q = 0.061 I_p \quad (20.7)$$

where  $I_p$  is the first return stroke peak current in kA and  $Q$  is the charge, in Coulombs, transported to ground by the return stroke during the first 100  $\mu$ s. Cooray *et al.* [31] extended their analysis further to obtain the distribution of the linear charge density along the leader channel as a function of return stroke peak current. The procedure adopted by Cooray *et al.* [31] to extract the leader charge distribution corresponding to a given prospective return stroke peak current is the following. First, they assumed that the stepped leader channel can be represented by a vertical, finitely conducting channel with a given potential gradient. The length of the channel was selected by Cooray *et al.* [31] to be 4 km, a representative value for the height of the charge centre from the measuring station used by Berger and Vogelsanger [36, 37]. Second, they assumed that, since the negative charge region extends more in a horizontal direction than vertical, as far as the distribution of the charge along the leader channel is concerned, the effects of the charges in the cloud can be represented by a conducting plane charged to a given potential.

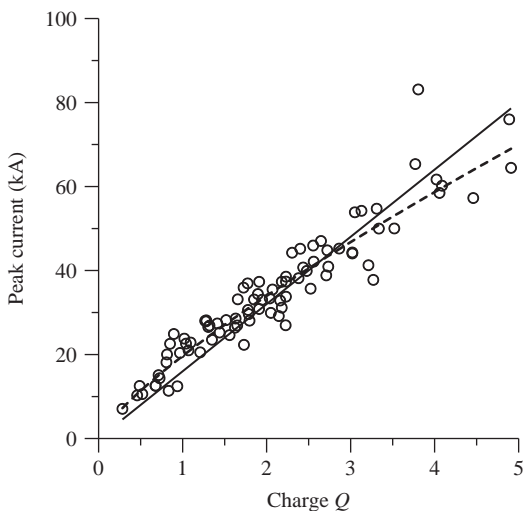


Figure 20.3 The charge dissipated by first return strokes in the first 100  $\mu$ s into the stroke (circular points). The first return stroke current waveforms used in the study are from Berger and Vogelsanger [36] and Berger [37]. The solid line shows the linear fit to the data and the dashed line the power fit [from Reference 31]

This assumption led to a uniform electric field below the cloud. Third, they assumed that the charge brought to ground during the return stroke is the sum of positive charge necessary to neutralize the negative charge on the leader channel and the additional positive charge induced on the leader channel due to the presence of the background electric field caused by the remaining negative charge in the cloud. Once these assumptions are made, the analysis is carried out as follows. First, from the observed relationship between the return stroke peak current and the charge, as depicted in Figure 20.3, the charge corresponding to a given peak return stroke current is obtained. Second, the background electric field was adjusted so that the estimated total charge deposited in the leader channel by the return stroke is equal to this charge. The resulting distribution of the charge along the leader channel is the one corresponding to the prospective return stroke current selected. Since the background electric field corresponding to a given charge is known (or estimated), the leader tip potential as a function of this charge can be estimated. This potential can be expressed as a function of return stroke peak current with the aid of (20.7). The resulting relationship between the potential of the tip of the stepped leader and the peak return stroke current is given by

$$V = 3 \times 10^6 I_p^{0.813} \quad (20.8)$$

where  $I_p$  is the first return stroke peak current in kA and  $V$  is the potential of the tip of the fully extended stepped leader channel in volts. Note that the potential gradient of the thermalized leader channel is about 1–2 kV/m, and the potential of the leader channel increases (by about 1–2 kV/m) as one moves along the channel towards the cloud.

It is important to point out here that the stepped leader tip potential obtained by Cooray and Rakov [35] using an identical analysis is different from the one given by (20.8). The reason for this difference is that Cooray and Rakov [35] fitted a power curve instead of a line (as done by Cooray *et al.* [31]) to the data in Figure 20.3. The best-fit curve used by Cooray and Rakov [35] is also depicted in Figure 20.3 for comparison. However, the linear charge distribution of the stepped leader channel as derived by Cooray *et al.* [31] is based on a linear fit to the data, and for this reason it is appropriate to use the leader potential given by (20.8) together with the charge distribution derived by Cooray *et al.* [31].

### 20.5.3 Striking distance based on the leader tip potential

In calculating the striking distance it is necessary to know the potential of the stepped leader channel because the final jump condition is defined according to the average potential gradient across the gap between the connecting leader and the stepped leader channel or in the absence of a connecting leader, between the structure and the tip of the stepped leader.

Now, if the connecting leader is short or absent, then the striking distance,  $S$ , is given by  $S = V/E_s$ . We define this as the EGM striking distance appropriate to the given potential and denote it by  $S_{egm}$ . In this expression,  $E_s$  is the average electric

field between the stepped leader tip and the grounded structure when the final jump condition is reached. Thus, the EGM striking distance according to the study of Armstrong and Whitehead [6] becomes (combining (20.1) and (20.6))

$$R_{egm} = 6.7I_p^{0.8} \quad (20.9)$$

On the other hand, if one uses the leader potential given by (20.8) and assumes that the average potential gradient at final jump is equal to 500 kV/m, the EGM striking distance as a function of return stroke peak current becomes

$$R_{egm} = 6.0I_p^{0.813} \quad (20.10)$$

Note that the similarity between the two equations, i.e. (20.9) and (20.10), is a mere coincidence. In the above estimation it is assumed that the potential gradient in the final jump zone is equal to  $5 \times 10^5$  V/m. On the other hand if the ground is assumed to be completely flat then the final jump condition is reached when the negative streamers of the stepped leader reach the ground. This happens when the average potential gradient between the leader tip and the ground is equal to  $(1-2) \times 10^6$  V/m, the potential gradient of negative streamers. If an average value of  $1.5 \times 10^6$  V/m is used, the striking distance of a negative stepped leader to completely flat ground becomes

$$S = 2I_p^{0.813} \quad (20.11)$$

This expression is approximately equal to the expression for the striking distance to flat ground obtained by Cooray *et al.* [31]. The slight difference between this equation and the one derived by Cooray *et al.* [31] is due to the fact that the estimation given here is based on the exact charge distribution of the stepped leader channel as estimated in the analysis whereas in Cooray *et al.* [31] an approximate analytical expression for the same charge distribution is used to estimate the average potential gradient between the leader tip and the ground. Note also that in the section where the striking distance is calculated in Cooray *et al.* [31], the potential gradient of the negative streamer zone is given as  $5 \times 10^5$  V/m by mistake.

## 20.6 Comparison of EGM against SLIM

Cooray [1] and Cooray and Becerra [2] compared the results predicted by the advanced model introduced by Becerra and Cooray [19, 20, 24] (called self-consistent leader inception and propagation model, SLIM) with the predictions of EGM. In the calculation presented by Cooray and Becerra [2], the leader tip potential is represented by the equation derived by Cooray and Rakov [35]. However, here the potential based on the linear fit to the measured data of Cooray *et al.* [31] will be used i.e. equation (20.8). The reason for this choice is the following. In SLIM the

electric field generated by the leader is calculated using an analytical expression for the leader charge derived by Cooray *et al.* [31]. This analytical expression is derived by Cooray *et al.* [31] from a linear fit to the measured data. Thus it is appropriate to use the potential given by equation (20.8) in calculating the final jump condition in SLIM. Moreover, in the study conducted by Cooray and Becerra [2], what was calculated is the attractive radius of vertical and horizontal conductors. The parameter under study here is the striking distance.

The definition of the striking distance that will be used is given in Section 20.2. The structure studied here is a vertical structure of cylindrical shape. The tip of the structure is a hemisphere with a radius equal to the radius of the cylindrical section. In the calculation, the radius of the structure is assumed to be 0.1 m. Calculations are performed for vertical conductor heights varying from 5 m up to 100 m. For a given conductor, the striking distance radius is evaluated for prospective return stroke peak currents of 5–90 kA. In the calculation it is assumed that the stepped leader approaches vertical structure directly overhead. It is important to mention here that the calculated striking distance depends also on the final jump condition used in the analysis. Here, it is assumed that the final jump condition is reached when the average potential gradient between the tips of the connecting leader and the stepped leader is equal to 500 kV/m.

Before proceeding further, let us consider the EGM. As mentioned previously, according to the EGM a stepped leader will terminate at a point on a structure if the potential gradient between the tip of the stepped leader and the point on the structure reaches a critical value. Here it is assumed that this critical potential gradient is 500 kV/m. Recall that according to SLIM the final attachment of the stepped leader to the structure takes place when the potential gradient between the tip of the connecting leader and the tip of the stepped leader reaches 500 kV/m. Since EGM neglects the presence of a connecting leader, for a given leader potential EGM provides a lower limit to the striking distance. As the length of the connecting leader increases, the striking distance increases. Thus, the striking distance obtained by SLIM will be longer than the striking distance predicted by EGM. Of course this is true as long as the same critical criterion (i.e. same average potential gradient across the gap) is used for the final jump condition. For example, in attractive radii calculations presented by Cooray and Becerra [38], it was assumed that the potential gradient at every point in the gap should exceed 500 kV/m before the final jump condition is reached. This condition is more restrictive than the final jump condition based on the average potential gradient of 500 kV/m across the gap. Figure 20.4 illustrates how the striking distance varies as the height of the structure is increased. For comparison purposes, the EGM striking distance (i.e. (20.10)) is also depicted in each diagram. Analytical expressions for the variation of striking distance as a function of peak current for different heights are tabulated in Table 20.1.

Note, from the data given in Figure 20.4, that the difference between the striking distances calculated using SLIM and EGM increases with increasing structure height. For a given height, the difference is less for smaller currents than for the larger ones. However, for structure heights less than about 30 m, the differences in the striking distances are negligible for practical purposes even for peak return stroke currents as large as 90 kA. For peak return stroke currents less than about 16 kA, the difference between SLIM and EGM is less than about 30% for structure heights less than about 50 m.

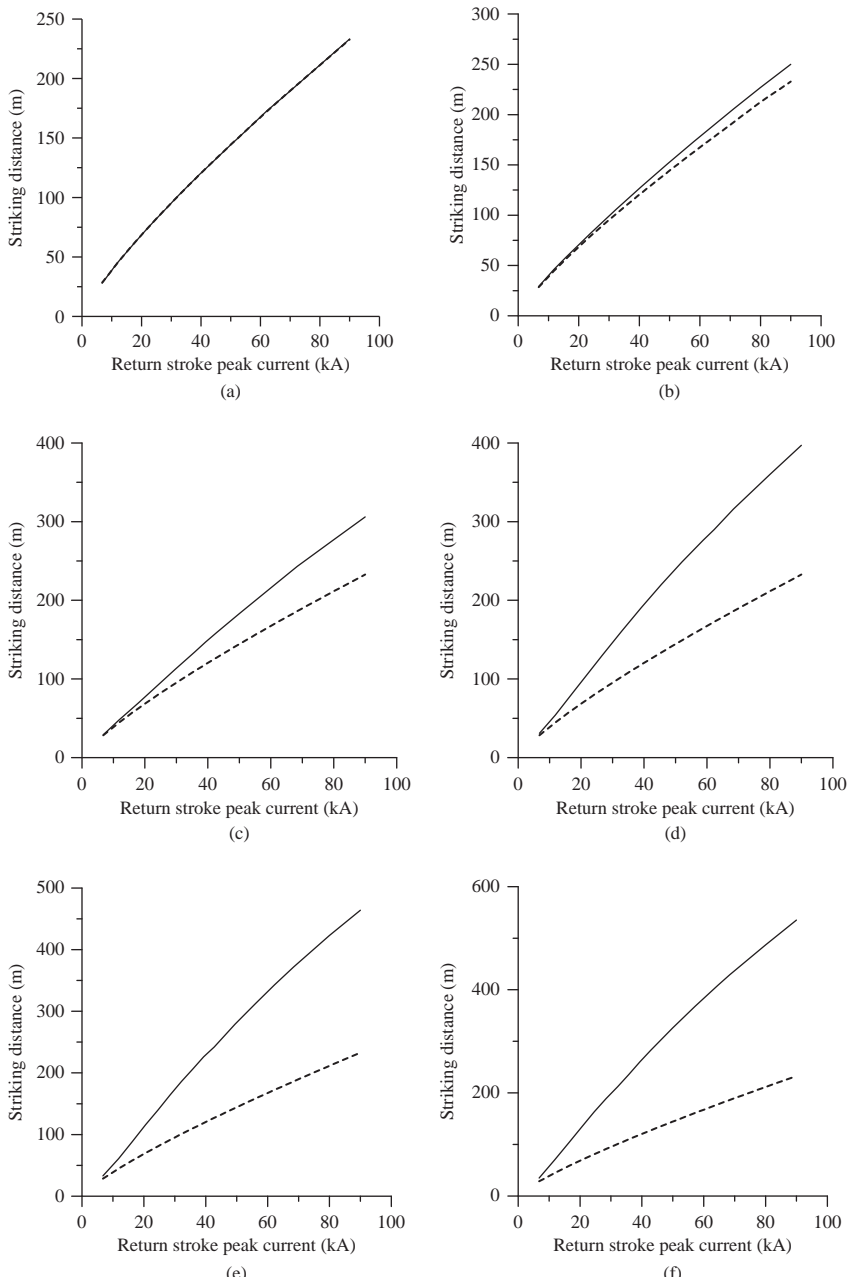


Figure 20.4 The striking distance of vertical structures (cylindrical in shape) of different heights evaluated from the model of Becerra and Cooray [19, 20, 24] (solid line). The dashed lines correspond to the striking distance that one would obtain if the presence of the connecting leader is neglected (i.e. from the EGM). Results are shown for structure heights of (a) 10 m, (b) 20 m, (c) 30 m, (d) 50 m, (e) 70 m and (f) 100 m

*Table 20.1 Analytical expressions for the striking distance as a function of peak return stroke current,  $I_p$ , for different structure heights*

Height (m)	$S = aI_p^b$		$S = a_q + b_qI_p + c_qI_p^2$		
	$a$	$b$	$a_q$	$b_q$	$c_q$
10	6.0	0.813	10.378	2.979	$5.75 \times 10^{-3}$
20	5.824	0.835	9.595	3.129	$5.15 \times 10^{-3}$
30	4.953	0.920	1.97	3.911	$5.85 \times 10^{-3}$
40	4.8	0.966	-4.142	4.765	$8.61 \times 10^{-3}$
50	4.835	0.993	-8.315	5.497	$11.08 \times 10^{-3}$
60	5.017	1.006	-10.743	6.101	$13.35 \times 10^{-3}$
70	5.106	1.021	-14.04	6.667	$15.04 \times 10^{-3}$
80	5.271	1.028	-15.662	7.107	$16.26 \times 10^{-3}$
90	5.299	1.039	-17.528	7.480	$17.24 \times 10^{-3}$
100	5.497	1.039	-18.409	7.795	$18.33 \times 10^{-3}$

Coefficients for both power and quadratic fits are tabulated. In the case of EGM, the striking distance is given by  $S = 6I_p^{0.813}$  or  $S = 10.38 + 2.98I_p + .006I_p^2$ . The striking distance is given in metres and the peak return stroke current in kA. The quadratic function fits the data better than the power function.

## 20.7 Points where more investigations are needed

It is important to note here first that, since the knowledge concerning the detailed mechanism of the lightning flash and the relevant physics is not available, it is difficult and sometimes even impossible to justify the assumptions that are being made in developing lightning strike models. In creating a model one has to achieve a balance between the correct model and the correct physics. One can simplify the model very much and get the physics correctly but such a procedure does not help because the model will be very far from the reality. On the other hand, one can make the model complicated but at the same time one has to downplay the physics of the problem because the exact physics of the complicated processes taking place during a lightning flash is not known. Whatever the case, when considering the complexity of the lightning phenomena, it will always be necessary to make several assumptions and simplifications in order to formulate a usable lightning strike model. Some of these assumptions may not be easy to justify because of our limited knowledge on the physics of the process under consideration. Let us consider the points where more research is needed to justify or falsify the assumptions made in developing lightning strike models.

### 20.7.1 Orientation of the stepped leader

In the leader progression models, two assumptions are made concerning the path of propagation of the stepped leader. In the model of Dellera and Garbagnati [22, 39], it is assumed that the leaders travel along the maximum electric field direction. Consequence of this assumption is that the path of the stepped leader is influenced by the grounded structures and by the connecting leaders. This is the case since these structures can modify the magnitude and direction of the electric field experienced by the stepped leader. In the models of Rizk [23] and Becerra and

Cooray [19, 20, 24], it is assumed that the path of propagation of the stepped leader is not influenced both by the grounded structures and by the connecting leader until the final jump condition is reached. Of course the first assumption makes some physical sense but it is not that clear how this assumption should be applied in practice. It is difficult, if not impossible, to determine the direction of the maximum electric field ahead of the leader channel due to following reasons: The space in front of the leader channel is occupied by streamer discharges that supply the current necessary for the propagation of the leader. The electric field configuration in front of the leader channel is determined by the spatial distribution of the space charge of the streamer system, which, due to the random nature of the electrical discharges, is not uniform. Thus, the exact distribution of the electric field in space in front of the leader cannot be determined with certainty. Moreover, the direction of the stem of the streamer system, which becomes the new leader segment, may to some extent be controlled by the space charge lying ahead of it. This space charge reduces the electric field at the stem and therefore the direction of the next section of the leader channel may lie in a direction away from the main concentration of the space charge. The situation is even more complicated in the case of negative stepped leaders. In this case, the high electric field at the outer edge of the negative streamer system leads to the creation of a space stem. Subsequently, this space stem is converted to a space leader. The space leader extends in two directions, one tip moving towards the tip of the stepped leader and the other away from it. When the two leaders meet (i.e. space leader and the stepped leader) the space leader becomes the next step of the stepped leader. Thus, the location of the space stem with respect to the tip of the leader channel will decide the direction of the next leader step. The theory available at present cannot be used to predict the exact location of the space stem with respect to the electric field configuration. Thus, the exact direction of the new step of the leader (or its current direction of propagation) is not a parameter that can be predicted easily. Indeed it is this random nature of the discharge that causes the leader channel to take a tortuous path. It is important to note, however, that Mazur *et al.* [33] assumed that the direction of a new leader step (and hence the direction of propagation of the stepped leader) coincides with the direction in which the length of the negative streamers issued by the negative stepped leader is longest.

The next problem is our lack of knowledge concerning the external electric field necessary to divert the direction of propagation of a stepped leader channel. The engine that drives the leaders is the streamer bursts created in front of the leader channel, and the direction of propagation of the streamers is controlled mainly by the electric field produced by the already thermalized leader channel. The background electric field necessary for the propagation of negative streamers is about 1 to 2 MV/m and it is reasonable to assume that in order to divert the direction of the negative streamer bursts the background electric field may reach values comparable to this value. If this is correct, then the background electric field produced at the head of the negative stepped leader channel by the grounded structures or the connecting leader has to reach values comparable to 1–2 MV/m to divert the path of the stepped leader channel. This can happen only when the grounded structure or the connecting leader has approached the down-coming stepped leader almost to the

point of final jump distance. This, to some extent, justifies the assumption that the stepped leader path is not influenced by the grounded structure or the connecting leader until the final jump condition is reached. Of course, in reality, the situation could lie somewhere in between these two extreme scenarios.

One clear example of a time-resolved stepped leader that propagated without being much influenced by the connecting leader is shown in Figure 15 of Berger [40]. In this example, the connecting leader issued from the tower propagated first upwards for a distance of about 10–20 m and then turned towards the down-coming stepped leader and met it at point A (marked in Figure 15 of Berger [40]), which is at a height of about 40–50 m from the tip of the tower. More time-resolved photographs similar to this are needed to investigate how the electric fields created by structures and connecting leaders can influence the path of negative stepped leaders.

### *20.7.2 The orientation of the connecting leader*

In some of the leader propagation models, it is assumed that the positive connecting leader always travel towards the tip of the down-coming negative stepped leader. The discussion made above concerning the direction of propagation of negative leaders is also applicable to the positive leader. However, one difference is that the background electric field necessary for the propagation of positive streamers is about 450–500 kV/m and this is considerably less than the background electric field necessary for the propagation of negative streamers. It is reasonable to assume, therefore, that the background electric field necessary to influence the propagation of positive leaders is less than the ones required to influence the negative stepped leaders. Thus, the influence of the negative stepped leader on the path of the positive connecting leader is more pronounced than the influence of the positive connecting leader on the path of the negative stepped leader. However, in SLIM, for example, it is assumed that the connecting leader from the very beginning of its initiation travels towards the negative stepped leader tip. The reality lies again somewhere in between. Initially, the positive connecting leader may travel without much influence from the negative stepped leader but it may turn towards it when the background electric field produced by the negative stepped leader is large enough to influence the direction of the movement of streamers located ahead of the positive leader. Actually, the photograph referred to in the previous section shows that the positive leader initially travelled vertically upwards without much influence from the negative leader but later turned towards the negative stepped leader. However, the independent upward movement of the connecting leader may take place only when the stepped leader tip is far from the grounded structure. Fortunately, during that time the orientation of the tip of the negative leader with respect to the structure is also close to the vertical making the above assumption reasonable. Detailed analysis of time-resolved pictures of lightning strikes could shed more light on this problem.

### *20.7.3 The connection between the leader potential and the return stroke current*

One of the fundamental assumptions in lightning protection studies is the existence of a relationship between the potential of the stepped leader and the prospective

peak return stroke current. Once this relationship is known, one can extract from it the other engineering parameters such as the striking distance. The existence of such a relationship is in agreement with physical considerations because the charge that will be stored on the down-coming leader channel is related to its potential and the resulting return stroke current, which, in turn, is governed by this charge. The final jump condition between the connecting leader (or the grounded structure) and the stepped leader is reached when the average potential gradient between the tips of the two leaders (or between the grounded structure and the tip of the stepped leader) is equal to the critical electric field necessary for positive streamer propagation. Thus, the main parameter that influences the final jump condition is the potential of the stepped leader channel.

Here and in the study conducted by Cooray and Rakov [35], the potential of the stepped leader channel is evaluated first by theoretically analysing the charge on the stepped leader channel as a function of its potential and then connecting this charge to the charge brought to ground by the return strokes over the first 100  $\mu\text{s}$  of the discharge in the current waveforms measured by Berger and Vogelsanger [36] and Berger [37]. The detailed procedure of the analysis and the assumptions involved were discussed by Cooray *et al.* [31]. The validity of the assumptions made in the analysis was tested by Cooray *et al.* [31] at least for the subsequent return strokes by checking whether the derived relationship between the charge and the current could provide a fit to the experimentally observed relationship between the magnitude of the close electric fields and the return stroke peak current. Recently, Mazur and Ruhnke [41] attempted to obtain the leader potential from the remote measurements of the electric field change produced by the stepped leader and connecting this derived potential to the return stroke current estimated from the lightning location systems. Unfortunately, they could not find a strong relationship between the derived leader potential and the return stroke current. The various assumptions made in simulating the leader channel together with the fact that the currents used in the analysis were not measured but were estimates from the direction finding systems may have influenced to some extent the obtained results.

More studies should be conducted to get more accurate values of leader potential because, as shown in this chapter, it is the most important parameter in lightning attachment. The experimental data show that the mechanism of the negative leader is similar to that of laboratory sparks. If this is the case, then the step length is approximately equal to the extension of the streamer region. The extension of the streamer region is a measure of the potential of the leader channel. Thus, by measuring the average step length as a function of return stroke current one may be able to derive an expression for the variation of leader potential with return stroke current. For example, Figure 20.5 depicts the length of the leader step as a function of prospective return stroke current calculated using the leader charge distribution extracted by Cooray *et al.* [31]. In the calculation it is assumed that the space stem is created at the edge of the streamer region. The estimated leader step lengths correspond to leaders at a height of 300 m from ground level. Note that the estimated leader step lengths for typical return stroke currents are considerably smaller than the typical value of 50 m estimated in classical studies.

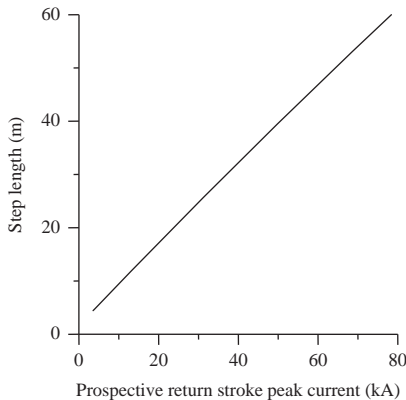


*Figure 20.5 The length of the leader step as a function of prospective return stroke current calculated using the leader charge distribution extracted by Cooray et al. [31]. In the calculation it is assumed that the space stem is created at the edge of the streamer region*

#### 20.7.4 Inclination of the leader channel

Almost all the studies reported so far in the literature have assumed the leader channel to propagate vertically downwards. However, to establish the full picture of lightning strikes, it is necessary to complement these studies using inclined leader channels. Such analysis also requires information concerning how to represent the charge distribution along inclined stepped leader channels. Future studies should also be directed to address such issues.

#### 20.7.5 Main assumptions of SLIM

In constructing SLIM, several assumptions and approximations are made especially in calculating the streamer charge. First, it was assumed that the corona region is conical in shape. This is based on some of the experimental evidence available in the literature [19, 20, 24]. However, more studies are needed to establish the correct shape of the streamer region. In calculating the streamer charge it was assumed that as the streamers grow from the head of the leader the background potential is changed only in the streamer region while the potential distribution ahead of the streamer region is unaffected. In reality, as the streamers extend forward they will also modify the potential distribution ahead of them. Future studies should address this issue. Moreover, in calculating the streamer charge it was assumed that the area associated with the region in a potential-distance diagram between the line representing the potential of the streamer region (denoted by a straight line) and the background potential is proportional to the streamer charge. In future studies, this assumption should be relaxed and the streamer charge should be calculated from first principles. The first attempt in this direction was made recently by Arevalo *et al.* [42].

Recently, based on a back-of-the-envelope calculation, Rizk [15] concluded that SLIM is incapable of predicting the correct inception voltage of a 10-m long gap experiments conducted by Les Renardières Group. Interestingly, SLIM had already been tested against the data from the same long gap experiment referred to in Rizk [15] by Becerra and Cooray [20] and a good agreement was found between the predicted and experimentally observed leader inception and breakdown voltages.

## 20.8 Concluding remarks

The main conclusion that can be extracted from the work presented in the chapter is that the connecting leader does not play a significant role in the case of lightning attachment to normal (i.e. short) structures. For structures shorter than about 30 m, one can use EGM without significant errors. However, it is important to stress here that this difference may still play an important role when two conductors are competing with each other to get attached to a down-coming stepped leader. In such cases, the predictions of EGM and SLIM so as to the point of attachment may differ from each other.

Note also that in the comparison between lightning strike models, the same leader charge distribution and leader potential should be used in all models. It is only then the concepts and predictions of different models could be tested against each other. This is a point worth keeping in mind because there are many lightning strike models in the literature, each based on a different leader charge distribution or leader potential.

## References

1. Cooray, V., A review of simulation procedures utilized to study the attachment of lightning flashes to grounded structures, Prepared on behalf of the CIGRE working group C4.405, *Electra*, 257, pp. 48–55, 2011
2. Cooray, V. and M. Becerra, Attractive radii of vertical and horizontal conductors evaluated using a self consistent leader inception and propagation model – SLIM, *Atmos. Res.*, 2011, Accepted for publication in *Atmos. Res.*, Available online in *Science Direct* since August, 2011
3. Gallimberti, I., The mechanism of long spark formation, *J. Physique Coll.*, 40, C7, suppl. 7, pp. 193–250, 1972
4. Bazelyan, E. M. and Y. P. Raizer, *Spark Discharge*, CRC Press, New York, 1977
5. Golde, R. H., *Lightning Protection*, Edward Arnold, London, 1973
6. Armstrong, H. R. and E. R. Whitehead, Field and analytical studies of transmission line shielding, *IEEE Trans.*, PAS-87, (1), pp. 270–279, 1968
7. Les Renardières Group, Research on long air gap discharges—1973 results, *Electra* 35, pp. 47–155, 1974
8. Carrara, G. and L. Thione, Switching surge strength of large air gaps: a physical approach, *IEEE Trans.*, PAS-95, (2), pp. 512–524, March/April, 1976
9. Bernardi, M., L. Dellera, E. Garbagnati, G. Sartorio, Leader progression model of lightning: Updating of the model on the basis of recent tests results, Proc. 23rd Int. Conf. Lightning Protection (ICLP), Florence, Italy, September, 1996

10. Akyuz, M. and V. Cooray, The Franklin lightning conductor: conditions necessary for the initiation of a connecting leader, *J. Electrostat.*, 51–52, pp. 319–325, 2001
11. Chernov, E. N., A. V. Lupeiko, N. I. Petrov, Investigation of spark discharge in long air gaps using Pockel's device, Proc. 7th Int. Symp. High Voltage Eng., Dresden, pp. 141–144, 1991
12. Petrov, N. I. and R. T. Waters, Determination of the striking distance of lightning to earthed structures, *Proc. R. Soc. A*, 450, pp. 589–601, 1995
13. Bazelyan, E. M. and Y. P. Raizer, *Lightning Physics and Lightning Protection*, Institute of Physics, Bristol, 2000
14. Rizk, F., A model for switching impulse leader inception and breakdown of long air-gaps, *IEEE Trans. Power Delivery*, 4, (1), pp. 596–603, 1989
15. Rizk, F., Modeling of lightning exposure of buildings and massive structures, *IEEE Trans. Power Delivery*, 24, (4), pp. 1987–1998, 2009
16. Lalande, P., Study of the lightning stroke conditions on a grounded structure, Doctoral thesis, Office National d'Etudes et de Recherches Aérospatiales ONERA, France, 1996
17. Goelian, N., P. Lalande, A. Bondiou-Clergerie, G. L. Bacchigia, A. Gazzani, I. Gallimberti, A simplified model for the simulation of positive-spark development in long air gaps, *J. Phys. D: Appl. Phys.*, 30, pp. 2441–2452, 1997
18. Lalande, P., A. Bondiou-Clergerie, G. Bacchigia, I. Gallimberti, Observations and modeling of lightning leaders, *C.R. Physique*, 3, pp. 1375–1392, 2002
19. Becerra, M. and V. Cooray, A simplified physical model to determine the lightning upward connecting leader inception, *IEEE Trans. Power Delivery*, 21, (2), pp. 897–908, 2006
20. Becerra, M. and V. Cooray, Time dependent evaluation of the lightning upward connecting leader inception, *J. Phys. D: Appl. Phys.*, 39, pp. 4695–4702, 2006
21. Eriksson, A. J., An improved electrogeometric model for transmission line shielding analysis, *IEEE Trans.*, PWDR-2, pp. 871–877, 1987
22. Dellera, L. and E. Garbagnati, Lightning strike simulation by means of the Leader Progression Model: II. Exposure and shielding failure evaluation of overhead lines with assessment of application graphs, *IEEE Trans. Power Delivery*, PWDR-5, pp. 2023–2029, 1990
23. Rizk, F., Modeling of lightning incidence to tall structures. Part I: Theory, *IEEE Trans. Power Delivery*, PWDR-9, pp. 162–171, 1994
24. Becerra, M. and V. Cooray, A self-consistent upward leader propagation model, *J. Phys. D: Appl. Phys.*, 39, pp. 3708–3715, 2006
25. Vargas, M., Novel integral model of the lightning discharge channel and its attachment to grounded structures, Doctoral thesis, Faculty of Engineering, National University of Colombia, Bogotá D.C., Colombia, 2006
26. Vargas, M. and H. Torres, On the development of a lightning leader model for tortuous or branched channels – Part I: Model description, *J. Electrostat.*, 66, (9+10), October, ISSN: 0304-3886, pp. 482–488, 2008
27. Vargas, M. and H. Torres, On the development of a lightning leader model for tortuous or branched channels – Part II: Model results, *J. Electrostat.*, 66, (9+10), October, ISSN: 0304-3886, pp. 489–495, 2008

28. Hill, R. D., Analysis of irregular paths of lightning channels, *J. Geophys. Res.*, 73, (6), pp. 1897–1906, 1968
29. Hill, R. D., Tortuosity of lightning, *Atmos. Res.*, 22, (3), pp. 217–233, 1988
30. Idone, V. and R. Orville, Channel tortuosity variation in Florida triggered lightning, *Geophys. Res. Lett.*, 15, (7), pp. 645–648, 1988
31. Cooray, V., V. Rakov, N. Theethayi, The lightning striking distance – revisited, *J. Electrostat.*, 65, (5,6), pp. 296–306, 2007
32. Borghetti, A., F. Napolitano, C. A. Nucci, M. Paolone, M. Bernardi, Numerical solution of the leader progression model by means of the finite element method, Proc. 30th Int. Confer. Lightning Protection, Cagliari, Italy, 2010
33. Mazur, V., L. Ruhnke, A. Bondiou-Clergerie, P. Lalande, Computer simulation of a downward negative stepped leader and its interaction with a grounded structure, *J. Geophys. Res.*, 105, (D17), pp. 22361–22369, 2000
34. Wagner, C. F., Relation between stroke current and velocity of the return stroke, *IEEE Trans.*, PAS-82, pp. 609–617, 1963
35. Cooray, V. and V. Rakov, On the upper and lower limit of peak current of first return strokes in negative lightning flashes, Accepted for publication, *Atmos. Res.*, Available online in *Science Direct* since August, 2011
36. Berger, K. and E. Vogelsanger, Measurement and results of lightning records at Monte San Salvatore from 1955–1963 (in German), *Bull. Schweiz. Elektrotech.*, 56, pp. 2–22, 1965
37. Berger, K., Methods and results of lightning records at Monte San Salvatore from 1963–1971 (in German), *Bull. Schweiz. Elektrotech. Ver.*, 63, pp. 1403–1422, 1972
38. Cooray, V. and M. Becerra, Attachment of lightning flashes to grounded structures, in Cooray, V. (ed.), *Lightning Protection*, The IET, London, 2009
39. Dellera, L. and E. Garbagnati, Lightning simulation by means of the leader progression model, I. Description of the model and evaluation of exposure of free standing structure, *IEEE Trans. Power Delivery*, 5, (4), pp. 20009–20017, 1990a
40. Berger, K., The Earth flash, in Golde, R. H., (ed.), *Lightning*, vol. 1, Academic Press, London, UK, 1977
41. Mazur, V. and L. H. Rhunke, Determining the striking distance of lightning through its relationship to leader potential, *J. Geophys. Res.*, 108, p. 4409, doi:1029/2002JD003047, 2003
42. Arevalo, L., V. Cooray, D. Wu, Laboratory long gaps simulation considering a variable corona region, Proc. Int. Confer. Lightning Protection (ICLP), Cagliari, Italy, 2010



---

## *Chapter 21*

# **On the NO<sub>x</sub> generation in corona, streamer and low-pressure electrical discharges\***

*Vernon Cooray<sup>1</sup>, Marley Becerra<sup>1</sup> and Mahbubur Rahman<sup>2</sup>*

---

### **21.1 Introduction**

An assessment of the global distribution of nitrogen oxides (NO<sub>x</sub>) is required for a satisfactory description of tropospheric chemistry and in the evaluation of the global impact of increasing anthropogenic emissions of NO<sub>x</sub> [1]. In the mathematical models utilized for this purpose, it is necessary to have the natural as well as man-made sources of NO<sub>x</sub> in the atmosphere as inputs. Thunderstorms are a main natural source of NO<sub>x</sub> in the atmosphere and it may be the dominant source of NO<sub>x</sub> in the troposphere in equatorial and tropical South Pacific [2].

In quantifying the production of NO<sub>x</sub> by thunderstorms, scientists have until recently concentrated on the lightning return strokes neglecting all other processes associated with thunderstorms [3]. This view is gradually changing as the theories and experimental data show that not only the return strokes in ground flashes but other discharge events in ground and cloud flashes, such as continuing currents, are also contributing significantly to the NO<sub>x</sub> emissions [4]. For example, the study conducted by Rahman *et al.* [4] shows that the contribution by continuing currents to the NO<sub>x</sub> production in lightning flashes is comparable, if not overwhelm, to the contribution by return strokes. However, the physics behind the process that makes continuing currents as efficient as return strokes in producing NO<sub>x</sub> is still unknown.

Based on the ionization process that leads to the production of free electrons, electrical discharges taking place in the atmosphere can be divided into two types, namely, ‘cold’ and ‘hot’ electrical discharges. In cold electrical discharges, free electrons are produced solely by the collisions between energetic electrons and atoms. In these discharges the electron temperature may reach several tens of thousands of degrees whereas the gas and ion temperature remains close to ambient temperature. Corona discharges, streamer discharges and Townsend-type electrical

\*This material was published previously by the same authors in *Open Atmospheric Science Journal*, vol. 2, pp. 176–180, 2008. It is reproduced here by permission from the journal.

<sup>1</sup>Uppsala University, Uppsala, Sweden

<sup>2</sup>School of Engineering, Royal Institute of Technology, KTH, Stockholm, Sweden

discharges taking place at low pressure are several examples of cold discharges taking place in the atmosphere. In hot electrical discharges, the gas and ion temperature can also reach several tens of thousands of degrees and the main mechanism in the discharge that generates free electrons is the thermal ionization. In these discharges, ions and neutral atoms are heated to such high temperatures through a process called thermalization that facilitates the transfer of energy from free electrons to neutrals via ions [5]. This transfer of energy from electrons to neutrals causes the temperature of the neutrals to go up. This increase in the temperature of the neutrals leads to production of copious amount of electrons by the energetic collisions between neutral particles (i.e. thermal ionization). Several examples of hot discharge processes taking place in the atmosphere are return strokes, leaders, M components and continuing currents.

In addition to hot discharges mentioned above, an active thundercloud also produces cold discharges in the form of corona and streamer discharges. However, in quantification of  $\text{NO}_x$  produced by thunderstorms, scientists neglect the contribution of the cold discharge processes. Moreover, the recent discovery of thunderstorm-created ionization processes in the stratosphere and mesosphere, known as sprites, blue jets and elves, also poses a question as to the effects of these ionization processes on the chemistry of the upper atmosphere. These ionization processes can also be categorized under ‘cold’ discharges because the pressure at which these discharges take place does not support thermal ionization, making electron impacts the main source of ionization. Indeed, there is a need today to develop procedures to quantify the  $\text{NO}_x$  production in cold discharges.

The effects of solar proton events in the  $\text{NO}_x$  production in the upper atmosphere and the effect of  $\text{NO}_x$  on the chemical balance of the stratosphere were a major concern of the atmospheric scientists since the discovery of the importance of  $\text{NO}_x$  in ozone production and destruction [6]. In quantifying the  $\text{NO}_x$  production from these events, scientists utilized the connection between the ionizing events in the atmosphere and the number of resulting  $\text{NO}_x$  molecules. To facilitate further discussion, let us denote the number of  $\text{NO}_x$  molecules produced per ionizing event in the atmosphere by the parameter  $k$ . The theoretical work of Nicolet [7] set the value of  $k$  close to unity, whereas the investigations of Jackman *et al.* [8] predicted that at altitudes larger than about 80 km,  $k$  is about 1.5 and for low altitude it is about 1.2–1.3. These results have been used extensively to study the  $\text{NO}_x$  production by cosmic rays and solar radiation impinging on the Earth’s atmosphere. Recently, Rahman *et al.* [9] investigated the validity of this theoretical calculation by studying the  $\text{NO}_x$  production in air by alpha particles emitted by a radioactive source. The results of this study confirmed these theoretical predictions fixing the value of  $k$  to about 1.0. Since the main source of ionization during proton impacts are high energetic secondary electrons, it is reasonable to assume that the number of  $\text{NO}_x$  molecules produced in discharge processes in which electrons are the main source of ionization is approximately equal to the number of ion pairs produced in the discharge. This hypothesis is tested in this chapter using the data obtained from corona discharges and then it is utilized to quantify the  $\text{NO}_x$  production in low-pressure discharges and streamer discharges.

## 21.2 Testing the theory using corona discharges

The working hypothesis of this chapter is that in cold electrical discharges, the total number of  $\text{NO}_x$  molecules generated by the discharge is  $k$  times the total number of ion pairs produced in the discharge. Let us test this hypothesis by using the experimental data on corona discharges.

In a recent study, Rehbein and Cooray [10] conducted an experiment to quantify the  $\text{NO}_x$  production in corona discharges. In the study, a corona discharge is maintained in a coaxial geometry and the discharge voltage and the current are measured simultaneously with the concentration of  $\text{NO}_x$  produced in the discharge chamber. If one neglects the ionization loss processes (i.e. attachment and recombination), the steady state current gives the rate of production of electrons and hence the rate of occurrence of ionizing events in the discharge. Since the total  $\text{NO}_x$  production in the discharge over a given time interval is known, the data can be used to quantify the number of  $\text{NO}_x$  molecules produced per ion pair. The results of this calculation gave  $k = 0.6$  for negative corona and  $k = 1.0$  for positive corona. Even though the  $\text{NO}_x$  generating efficiency per ion pair is lower in negative corona than in positive corona, this result confirms that the number of  $\text{NO}_x$  molecules produced in the discharge is approximately equal to the number of ionization events.

## 21.3 $\text{NO}_x$ generation in electron avalanches and its relationship to energy dissipation

Consider a single electron accelerating in a background electric field of strength  $E$ . The number of ionizations caused by the electron in moving a unit length per unit is equal to the Townsend's primary ionization coefficient  $\alpha(p, E)$ , which is a function of pressure  $p$  and the electric field  $E$ . Assuming that one ionization event corresponds to  $k$  number of  $\text{NO}_x$  molecules, the total number of  $\text{NO}_x$  molecules  $N_{ul}$  produced by the ionization processes as the electron moves a unit length is given by

$$N_{ul} = k\alpha(p, E) \quad (21.1)$$

Now, the energy dissipated as the electron moves a unit length in the background electric field is given by  $eE$ , where  $e$  is the electronic charge. Thus, the number of  $\text{NO}_x$  molecules produced per unit energy,  $N_{ue}$ , is given by

$$N_{ue} = \frac{k\alpha(p, E)}{eE} \quad (21.2)$$

Since  $\alpha/p$  is a function of the reduced electric field  $E/p$  alone, the above equation predicts that  $N_{ue}$  is only a function of  $E/p$ . Figure 21.1 shows how the value of  $N_{ue}$  varies as a function of  $E/p$ . First note that the  $\text{NO}_x$  production efficiency increases with increasing  $E/p$ . This also shows that for a given pressure, the  $\text{NO}_x$  production per unit energy is not unique but depends also on the applied electric field. Consequently, in any experiment that is designed to obtain the  $\text{NO}_x$  production

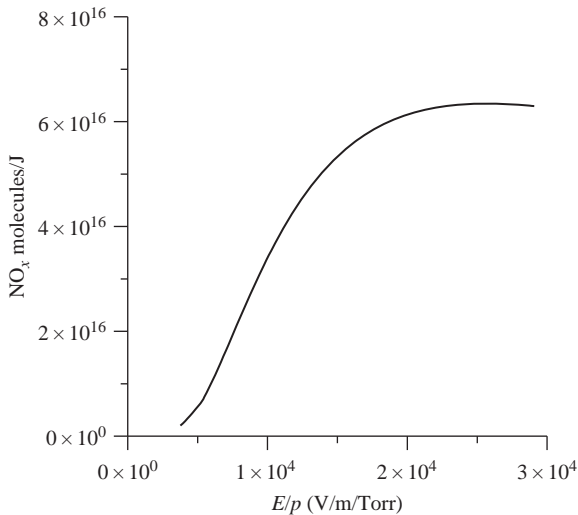


Figure 21.1  $NO_x$  production per unit energy  $N_{ue}$  as a function of  $E/p$  in electron avalanches

efficiency of cold electrical discharges, it is necessary to utilize voltage impulses in which the reduced electric field  $E/p$  remains the same.

## 21.4 $NO_x$ production in streamer discharges

As an electron avalanche propagates towards the anode of a discharge gap, low mobile positive space charge accumulates at the avalanche head. When the avalanche reaches the anode, the electrons will be absorbed into it leaving behind the net positive space charge. Due to the recombination of positive ions and electrons, the avalanche head is a strong source of high energetic photons. These photons will create other avalanches in the vicinity of the positive space charge. If the number of positive ions in the avalanche head is larger than a critical value, the electric field created by the space charge becomes comparable to the background electric field and the secondary avalanches created by the photons will be attracted towards the positive space charge. The electrons in the secondary avalanches will be neutralized by the positive space charge of the primary avalanche, leaving behind a new positive space charge, little bit closer to the cathode. The process repeats itself and the positive space charge head travels towards the cathode as a consequence [11]. This discharge that travels towards the cathode from the anode is called a positive streamer. At atmospheric pressure, the total number of ions in the streamer head,  $\omega$ , is about  $10^8$  and the radius of the streamer head,  $R_s$ , is about  $100\text{ }\mu\text{m}$  [12]. The streamer needs a background field of about  $5\text{--}10\text{ kV/cm}$ , depending on polarity for continuous propagation. Consider a streamer moving in a uniform electric field of strength  $E$ . In order for the streamer to move a unit length in this electric field,

the total number of ionizing events taking place in the vicinity of the streamer head is about  $\omega/2R_s$  and the total number of  $\text{NO}_x$  molecules created by the streamer in moving a unit length,  $N_s$ , is

$$N_s = \frac{k\omega}{2R_s} \quad (21.3)$$

On the other hand, the amount of energy dissipated by the streamer channel in moving the unit distance is  $Ee\omega$ . Thus, the production efficiency of  $\text{NO}_x$  in streamer discharges,  $P_{\text{NO}_x}$ , in molecules/J is

$$P_{\text{NO}_x} = \frac{k}{2eER_s} \quad (21.4)$$

Substituting  $k = 1$ ,  $R_s = 10^{-4}$  m and  $E = 5 \times 10^5$  V/m (for positive streamers), we find that the streamer will make about  $6 \times 10^{16}$   $\text{NO}_x$  molecules/J.

In a recent study, Cooray and Rahman [13] conducted an experiment in coaxial geometry to measure the  $\text{NO}_x$  production efficiency of streamer discharges. Let us consider the cylindrical coaxial geometry. Assume that the peak voltage applied to the central conductor of the coaxial system is  $V$ . This voltage will create an electric field in the cylinder, which has its highest value at the surface of the conductor and then decreases inversely with increasing radial distance. Consider a streamer discharge initiated close to the inner electrode and moving in this electric field. Assume that the streamer discharge will propagate to a distance where the background electric field reaches  $E_s$ , the critical electric field necessary for streamer propagation. If the applied voltage is  $V$ , then the charge that will be induced on a unit length of the inner conductor of the coaxial arrangement is given by

$$Q = \frac{2\pi\varepsilon_0 V}{\ln(b/a)} \quad (21.5)$$

where  $a$  and  $b$  are the radii of the inner and outer conductors. The electric field at a radial distance  $r$  from the inner conductor is then given by

$$E_r = \frac{V}{r\ln(b/a)} \quad (21.6)$$

Since the streamers propagate to a distance where the background electric field is  $E_s$ , the length of the streamers,  $l_s$ , in the coaxial arrangement is given by

$$l_s = \frac{V}{\ln(b/a)E_s} - a \quad (21.7)$$

Then the number of ionizing events,  $N_s$ , generated during the propagation of the streamer is given by

$$N_s = \frac{\omega l_s}{2R_s} \quad (21.8)$$

On the other hand, the energy released by the movement of the streamer head in the gap,  $U_s$ , is given by

$$U_s = e\omega \frac{V}{\ln(b/a)} \ln(l_s/a) \quad (21.9)$$

Thus, the number of  $\text{NO}_x$  molecules produced per unit energy,  $N_{ue}$ , is given by

$$N_{ue} = \frac{k}{2E_s R_s \ln(l_s/a)} \quad (21.10)$$

For the experimental conditions reported in [13], i.e.  $a = 0.001$  m,  $b = 0.15$  m and  $V = 83 \times 10^3$  V, the calculated production efficiency is about  $1.6 \times 10^{16}$  molecules/J. The measurements produced  $1-2 \times 10^{16}$  molecules/J.

## 21.5 Discussion and conclusions

Studies on the  $\text{NO}_x$  production in the atmosphere by proton impacts show that the number of  $\text{NO}_x$  molecules created is almost equal to the number of ion pairs created during the impact. By comparing theory with available experimental data it is shown in this chapter that this result is also valid for electrical discharges in which electron impacts are the main source of ionization. Based on this observation, the  $\text{NO}_x$  production in electrical discharges where the electron production depends solely on the impact of electrons with neutral atoms is evaluated. The types of electrical discharges considered in this chapter are the corona discharges, electrical discharges at low pressure and streamer discharges.

In a corona discharge associated with current amplitude  $I$ , the rate of occurrence of ionizing events (neglecting attachment and recombination) is  $I/e$ , where  $e$  is the electronic charge. This is equal to  $6.25 \times 10^{18}I$ . Thus, the number of  $\text{NO}_x$  molecules produced per second in the discharge is given by  $6.25 \times 10^{18}kI$  in which the value of  $k$  depends on polarity (i.e.  $k \approx 1$  for positive polarity and  $k \approx 0.6$  for negative). It is of interest to note that this equation can be utilized to estimate the global production of  $\text{NO}_x$  by ground corona associated with thunderstorms. Various studies estimate that the global corona current associated with ground corona is about 1–2 kA [14]. Substituting this value in the above equation and using  $k = 1.0$  for positive corona, the number of  $\text{NO}_x$  molecules produced globally by ground corona per second is estimated to be about  $(6-12) \times 10^{21}$ . This is equivalent to an annual production of 0.01 Tg (N). During thunderstorms, it is not only at ground level that corona discharges are initiated. The thunderstorm itself is a large source of corona discharges. For example, in a thundercloud, charges may disperse from regions of high concentration to low concentration through corona discharges and the same could be the vehicle that transports the charges induced in conducting channels during neutralization events in to the bulk of the cloud. The theory as presented in this chapter could be applied to obtain the  $\text{NO}_x$  production from these

processes once the magnitude of the currents associated with these processes are known.

Let us consider the results presented in Figure 21.1. These results are obtained using several assumptions. First, it is assumed that the electron generating mechanism in the discharge is the impact ionization due to energetic electrons. Second, it is assumed that the background electric field is uniform in the region in which the discharge is taking place. However, the calculation procedure can be modified rather easily to take into account the effect of non-uniform electric fields. Third, it is assumed that the space charge accumulated in space during the discharge will not distort the electric field locally. Due to these assumptions, the results as given in Figure 21.1 are valid for ‘Townsend’s like’ low-pressure electrical discharges where the space charge effects can be neglected. On the other hand, the data given in Figure 21.1 can be utilized to study the  $\text{NO}_x$  production in any cold discharge with space charge distortions provided that the quantity  $E$  is replaced by the effective electric field in which the electron avalanches are generated.

An example of a cold discharge in which the space charge effects cannot be neglected is a streamer discharge. In streamers the electron avalanches are initiated in the electric field of the streamer head that is much stronger than the background electric field in which streamers are propagating. In evaluating the  $\text{NO}_x$  production of streamer discharges in this chapter, instead of evaluating the  $\text{NO}_x$  production in each individual avalanche taking place at the streamer head, a simpler but an equivalent procedure based on the known mechanism of the streamer is utilized. In a streamer discharge, electron avalanches are generated in a specially varying electric field. The maximum value of the field, which is about  $2 \times 10^7$  to  $4 \times 10^7 \text{ V/m}$ , occurs at the head of the streamer (assuming  $10^8$  ions located within a radius of about  $50\text{--}100 \mu\text{m}$ ) and it decreases to about  $3 \times 10^6 \text{ V/m}$  at a distance of about  $200 \mu\text{m}$  from the head. Recall that our analysis gave about  $2 \times 10^{16} \text{ NO}_x \text{ molecules/J}$  for streamer discharges moving in a background electric field of about  $5 \times 10^5 \text{ V/m}$ . Comparison of this  $\text{NO}_x$  production efficiency with the data given in Figure 21.1 indicates that in streamer discharges the electron avalanches are generated in an effective electric field of about  $5 \times 10^6 \text{ V/m}$ .

Streamer discharges occurring in the atmosphere are associated mainly with the lightning leaders in ground flashes and cloud flashes. Actually, the propagation of the leader is mediated by streamer bursts emanating from the tip of the leader. They may also originate during the neutralization of these leaders by return strokes. Cooray *et al.* [15] utilized the theory as developed in this chapter to study the  $\text{NO}_x$  production by streamers in lightning leaders.

The experimental observations indicate that the space charge effects cannot be neglected in upper atmospheric discharges known as sprites even though these discharges are taking place at considerably low atmospheric pressures. For example, observations indicate that sprites give rise to streamer-like structures. Therefore, the electric field in which the avalanches are growing during the development of sprites may be considerably higher than the background electric field generated by the thunderclouds. However, if the dimension and the ion concentration in these

streamer heads are known, an analysis similar to that utilized in this chapter to study the NO<sub>x</sub> production in streamer discharges at atmospheric pressure could be used to evaluate the NO<sub>x</sub> production in streamers in sprites. On the other hand, the elves are not associated with streamers and the results presented in Figure 21.1 could be applied directly if the background electric field that drives them is estimated.

The reason for the development of streamers in sprites, even though they are taking place at considerably low atmospheric pressure, is the large dimensions involved with the region of ionization associated with these electrical discharges. This allows the accumulation of space charge over large volumes affecting the local electric field. On the other hand, laboratory discharges generated at the same pressures would not have streamer-type discharges because the special dimensions are not large enough in laboratory discharges to support them. The results presented in Figure 21.1 would be applicable directly in low-pressure laboratory discharges. In a study conducted recently by Peterson *et al.* [16], NO<sub>x</sub> generated by laboratory discharges at different pressures were measured, and based on the results an estimation was made on how the NO<sub>x</sub> production efficiency in molecules/J varies as a function of pressure. Based on the results the authors predicted that the NO<sub>x</sub> production efficiency increases with decreasing pressure. Unfortunately, in that study the applied voltage is not given and therefore it is difficult to find out whether the voltage applied at different pressures is such that the  $E/p$  ratio is the same at different pressures. As shown in the present chapter, the NO<sub>x</sub> production efficiency in these discharges depends on the ratio  $E/p$  and any change in this ratio when one moves from one pressure to another will also affect the NO<sub>x</sub> production.

## References

1. Crutzen, P. J., The influence of nitrogen oxides on the atmospheric ozone content, *Quart. J. R. Met. Soc.*, vol. 96, 320–325, 1970
2. Gallardo, L. and H. Rodhe, Oxidized nitrogen in the remote pacific: the role of electrical discharge over oceans, *J. Atmos. Chem.*, vol. 26, 147–168, 1997
3. Chameides, W. L., The role of lightning in the chemistry of the atmosphere, in *The Earth's Electrical Environment*, National Academy Press, Washington D. C., 1986
4. Rahman, M., V. Cooray, V. A. Rakov, M. A. Uman, P. Liyanage, B. A. DeCarlo, *et al.*, Measurements of NO<sub>x</sub> produced by rocket-triggered lightning, *Geophys. Res. Lett.*, vol. 34, L03816, doi:10.1029/2006GL027956, 2007
5. Orville, R. E., Lightning spectroscopy, in R. H. Golde (ed.), *Lightning, Volume 1, Physics of Lightning*, Academic Press, London, 1977
6. Crutzen, P. J., Atmospheric interactions-homogeneous gas reactions of C, N and S containing compounds, in B. Bolin and R. B. Cook, (eds.), *The Major Bio-geochemical Cycles and Their Interactions*, SCOPE, Paris, 1983

7. Nicolet, M., On the production of nitric oxide by cosmic rays in the mesosphere and stratosphere, *Planet. Space Sci.*, vol. 23, 637–649, 1975
8. Jackman, C. H., H. S. Porter and J. E. Frederick, Upper limits on production rate of NO per ion pair, *Nature*, vol. 280, 170, 1979
9. Rahman, M., V. Cooray, G. Possnert and J. Nyberg, An experimental quantification of the  $NO_x$  production efficiency of energetic particles in air, *J. Atmos. Solar-Terr. Phys.*, vol. 68(11), 1215–1218, 2006
10. Rehbein, N. and V. Cooray,  $NO_x$  production in spark and corona discharges, *J. Electrostat.*, vol. 51–52, 333–339, 2001
11. Cooray, V., Mechanism of electrical discharges, in V. Cooray (ed.), *The Lightning Flash*, The Institution of Electrical Engineers, London, 2003
12. Van Veldhuizen, E. M. and W. R. Rutgers, Pulsed positive corona streamer propagation and branching, *J. Phys. D: Appl. Phys.*, vol. 35, 2169–2179, 2002
13. Cooray, V. and M. Rahman, Efficiencies for production of  $NO_x$  and  $O_3$  by streamer discharges in air at atmospheric pressure, *J. Electrostatics*, vol. 63, 977–983, 2005
14. Roble, R. G. and I. Tzur, The global atmospheric-electrical circuit, in *The Earth's Electrical Environment*, National Academy Press, Washington, D. C., 1986
15. Cooray, V., M. Rahman and V. Rakov, NOx production in lightning flashes, Proceedings of International Conference on Atmospheric Electricity, Beijing, 2007
16. Peterson, H., M. Bailey, J. Hallett and W. Beasley,  $NO_x$  production in laboratory simulated blue jets and sprite discharges, 12th Conference on Cloud Physics, P2.13, Madison, WI, 2006



---

## *Chapter 22*

# **On the NO<sub>x</sub> production by laboratory electrical discharges and lightning\***

*Vernon Cooray<sup>1</sup>, Mahbubur Rahman<sup>1</sup> and Vladimir Rakov<sup>2</sup>*

---

## **22.1 Introduction**

An assessment of the global distribution of nitrogen oxides is required for an adequate description of tropospheric chemistry and in the evaluation of the global impact of increasing anthropogenic emissions of NO<sub>x</sub> [1]. In the mathematical models utilized for this purpose, one needs to specify as inputs the natural as well as man-made sources of nitrogen oxides in the atmosphere. Lightning is one of the main natural sources of nitrogen oxides in the atmosphere, and it may be the dominant source of nitrogen oxides in the troposphere in equatorial and tropical South Pacific regions [2]. Thus, an accurate quantification of nitrogen oxide production by thunderstorms is necessary for further development of the chemical models of the troposphere and in the evaluation of the effects of the man-made nitrogen emissions in the terrestrial atmosphere.

Because of the difficulty of making direct measurements of NO<sub>x</sub> produced by natural lightning flashes, researchers have employed indirect methods to quantify the global production of NO<sub>x</sub> [3–12]. Because of a large number of uncertainties involved in these methods, the estimates of global NO<sub>x</sub> production by lightning flashes available in the literature vary by two orders of magnitude, from 1 to 100 Tg(N) per year. In estimating lightning produced NO<sub>x</sub> by indirect methods scientists have usually utilized the following two procedures: (1) A laboratory measurement of the number of NO<sub>x</sub> molecules per unit energy for a laboratory spark is made and the result is extrapolated to lightning by multiplying this measured value by estimated energy of lightning event. (2) A ground-based NO<sub>x</sub> measurement is made in the vicinity of a natural lightning flash and from it the source strength is estimated by making suitable assumptions concerning the fluid dynamics of the NO<sub>x</sub> flow from the source to the measurement point.

\*This material was published previously by the same authors in *Journal of Atmospheric and Solar-Terrestrial Physics*, vol. 71, pp. 1877–1889, 2009. It is reproduced here by permission from the journal.

<sup>1</sup>Uppsala University, Uppsala, Sweden

<sup>2</sup>Department of Electrical and Computer Engineering, University of Florida, Gainesville, Florida, USA

In studies of  $\text{NO}_x$  production by lightning flashes, only return stroke is assumed to be the  $\text{NO}_x$  source and the effects, if any, of leaders, continuing currents,  $M$  components, and  $K$  processes are neglected. Many studies have excluded cloud flashes from  $\text{NO}_x$  estimates assuming their contribution to be insignificant. Recent direct measurements of  $\text{NO}_x$  produced by triggered lightning flashes [13] show, however, that it is not only the return stroke in ground flashes but also other slow processes such as continuing currents are significantly contributing to the  $\text{NO}_x$  production. This calls for a more thorough investigation of the problem including different processes in both ground and cloud flashes. In this chapter we describe how this could be achieved. First, we quantify the  $\text{NO}_x$  production by different discharge processes of lightning flashes such as return strokes, leaders, continuing currents, and  $M$  components and subsequently this information is utilized to quantify  $\text{NO}_x$  production by a typical lightning flash containing all these elements. The results are used to obtain a global estimate of the lightning produced  $\text{NO}_x$ . While performing this analysis, we will also attempt to provide answers to the following important questions related to the quantification of  $\text{NO}_x$  emission by lightning flashes: (a) Is the energy of discharge the correct scaling factor to extrapolate  $\text{NO}_x$  emission from laboratory discharges to lightning flashes? (b) Does the shape of discharge current waveform influence the  $\text{NO}_x$  emission? (c) What are the relative contributions from leaders, return strokes, continuing currents,  $M$  components and  $K$  processes to the  $\text{NO}_x$  production by lightning flashes? (d) Can one neglect the cloud flashes in evaluating the global  $\text{NO}_x$  production?

## 22.2 $\text{NO}_x$ production by laboratory sparks

In order to evaluate  $\text{NO}_x$  production from electrical discharges or sparks it is necessary to estimate the amount of air heated to a given temperature in the discharge. This requires information concerning the dimension of the hot core of electrical discharges and how it will change for different current waveforms. Therefore, let us first investigate how the hot core of the electrical sparks varies as a function of its current.

### 22.2.1 Radius of spark channels

According to Braginskii [14], the radius of spark channel at time  $t$ ,  $r(t)$ , as a function of current is given by

$$r(t) = k \rho_o^{-1/6} i^{1/3} t^{1/2} \quad (22.1)$$

where  $r(t)$  is in m,  $t$  is in microseconds,  $i$  is the instantaneous current in the spark channel in kA,  $k$  is a constant and  $\rho_o$  is the air density at atmospheric pressure ( $1.29 \times 10^{-3}$  g/cm<sup>3</sup>). In deriving this expression, Braginskii assumed that the current increases linearly with time. However, the current in sparks decays after reaching the peak value, and Braginskii noted that the value of constant  $k$  (originally set to  $0.93 \times 10^{-3}$ ) may have to be changed if the equation is to predict the time

variation in channel radius of sparks. Cooray and Rahman [15] have made a comparison of the results predicted by (22.1) with the constant suggested by Braginskii [14] with the experimental data published by Flowers [16] and Higham and Meek [17] and found that it overestimates the radius of spark channels. Table 22.1 gives channel radii observed in the experiment and constants  $k$  in (22.1) that give the best fit to the experimental data. Based on this comparison, Cooray and Rahman [15] estimated that  $k = (0.328 \pm 0.05) \times 10^{-3}$ . Recently, Perera *et al.* [18] analysed the diameter of spark channels of length 30 cm using a photographic technique and the maximum channel diameter is obtained as a function of spark peak current for both positive and negative polarities. Perera *et al.* [18] compared the measured maximum channel diameter with the one obtained from (22.1) using the current waveform measured in the discharge as input. The results of that study confirm that the Braginskii's original constant overestimates the channel diameter, whereas the constant suggested by Cooray and Rahman [15] (i.e.  $0.328 \times 10^{-3}$ ) provides a reasonable fit to the data. Based on these experimental validations, the value of the constant suggested by Cooray and Rahman [15] is used in the analysis presented here.

Lightning currents were directly measured on tall towers and at the triggered lightning channel base (e.g. Berger [19]; Fisher *et al.* [20]). Mathematical expressions to describe the waveform of typical first and subsequent return-stroke currents recorded by Berger [19] are found in CIGRE Study Committee 33 Report [21] and Nucci *et al.* [22]. First let us utilize the typical current waveforms found in the above references to study how the radii of the first and subsequent return strokes vary as a function of peak current. Figure 22.1 shows how the maximum radius of the channel given by (22.1) varies as a function of peak current for first and subsequent return strokes. Note that the radius of a typical first return stroke (with a peak current of 30 kA) is about 2 cm and that of a typical subsequent stroke (peak current 12 kA) is about 1 cm. These values are in agreement with the radii of return-stroke channels estimated in photographic studies as summarized by Orville [23].

Table 22.1 Measured spark radii and values of  $k$  in (22.1) giving the best fit to data

Reference	Peak current (kA)	Rise time ( $\mu\text{s}$ )	Decay time ( $\mu\text{s}$ )	$r(t_m)$ (cm)	$t_m$ ( $\mu\text{s}$ )	Value of $k$ giving the best fit ( $\times 10^{-3}$ )
Flowers, 1943	17	8	60	0.8	8	0.37
	18	6	60	0.7	6	0.35
	22	3.3	60	0.615	3.3	0.41
	26	8	60	0.9	8	0.35
Higham and Meek, 1950	0.185		20	0.19	12	0.259
	0.250		20	0.145	12	0.254
	0.500		10	0.225	12	0.34
	0.400		10	0.195	12	0.32
	0.300		10	0.16	9	0.31

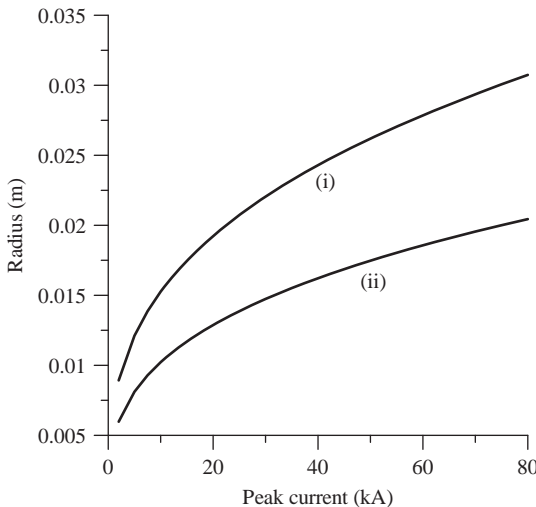


*Figure 22.1* The maximum radius of the channel as given by (22.1) as a function of peak current for first (i) and subsequent (ii) return strokes. In these calculations, the typical current wave-shapes for first and subsequent return strokes found in the literature were used

### 22.2.2 The volume of air heated in a spark channel and its internal energy

Detailed studies of the temporal variation in temperature and pressure of lightning discharges and long laboratory sparks show that the channel temperature reaches a peak of about 25,000–30,000 K and the channel pressure is of the order of 10 atm in a few microseconds after the commencement of current flow through the channel [24–26]. Then the channel plasma cools down mostly due to the channel expansion, loss of heat due to radiation and engulfing cold air from outer zones. This phase may last for about few tens of microseconds. At the end of this phase, the channel temperature reduces to a value of about 15,000 K and the pressure inside the channel attains the atmospheric pressure clamping down the pressure driven expansion of the channel. Experimental data that support this scenario are provided, both for laboratory sparks and for lightning flashes, by Orville [24, 25, 27] and Orville *et al.* [26]. Another experimental observation that supports this scenario is the following. The experimental data obtained by Orville [24] on the temperature of the lightning stepped leader channel show that at the formation of the step the channel temperature increases to about 25,000 to 30,000 K. Subsequently, the temperature decreases to about 15,000 K and remains at that level until the channel is retraced by the return stroke. The theoretical calculations of Paxton *et al.* [28], Hill [29] and Plooster [30] also indicate that by the time the pressure inside the spark channel reduces to the atmospheric pressure the average temperature in the channel is close to 20,000–15,000 K. After the pressure equilibrium is reached, the cooling

of the channel takes place mainly due to the entrainment of cold air across the channel boundaries into the hot core of the channel effectively reducing the diameter of the hot core [31]. Similarly, (22.1) predicts that the spark channel expands initially with time and its maximum radius is attained in a few microseconds to a few tens of microseconds, depending on the peak and the duration of current. After this, the radius of the hot channel decreases, while the channel resistance starts to increase with time. Based on the experimental and theoretical data [24, 25, 26, 28, 29, 30], we assume in our analysis that the pressure in the channel at the time of maximum radius is close to atmospheric pressure and that the average temperature of the hot air in the channel at this time is close to 15,000 K. In reality, the channel temperature is not uniform across the cross-section of the channel. But the theoretical calculations of Paxton *et al.* [28] and Hill [32] indicate that after a few tens of microseconds the radial temperature distribution is relatively flat with a sharp decrease to ambient temperature at the channel boundaries. This justifies the use of an average value to describe the channel temperature. Further, the temperature of 15,000 K estimated by Orville [27] when the channel was close to pressure equilibrium is the average temperature across the channel justifying our selection of 15,000 K as the average temperature. Thus, we assume that in a cylindrical spark channel the volume of air,  $V$ , heated to a temperature of about 15,000 K is given by

$$V = l\pi r_{max}^2 \quad (22.2)$$

where  $l$  is the length of the spark and  $r_{max}$  is the maximum radius of the spark channel given by (22.1) with  $k = 0.328 \times 10^{-3}$ .

### 22.2.3 $NO_x$ production in spark channels

It is believed that in an electrical discharge mainly NO is being produced through a series of high temperature reactions, which is confirmed by different laboratory experiments. Depending on the presence of excess  $O_2$  and  $O_3$  and the residence time, the experimentally found  $NO/NO_x$  ratios vary significantly. However, the total number of molecules of  $NO_x$  ( $NO + NO_2$ ) produced by a discharge is equal to the total number of NO molecules produced in the discharge, which is calculated in this section.

As mentioned previously, a procedure outlined by Borucki and Chameides [33] has been adopted to quantify the number of NO molecules that will be ‘fixed’ as the discharge channel cools down to ambient temperature. The amount of NO produced by a discharge via high temperature reactions is determined by the freeze-out temperature,  $T_f$ . This temperature is defined as follows: Let us denote by  $\tau_{NO}(T)$  the time required by NO to reach thermodynamic equilibrium at a given temperature,  $T$ . The freeze-out temperature is defined in such a way that  $\tau_{NO}(T_f) = \tau_T(T_f)$  where  $\tau_T(T)$  is the characteristic cooling time of the heated gas. When  $T > T_f$  then  $\tau_{NO}(T) < \tau_T(T)$  and the chemical reactions are fast enough to keep NO in thermodynamic equilibrium. If  $T < T_f$  then  $\tau_{NO}(T) > \tau_T(T)$  and chemical reactions are too slow to adjust to the rapidly decreasing temperature. In this case, the amount of NO at  $T_f$  in the

mixture is frozen out. Thus, if  $N$  is the number of air molecules heated above  $T_f$ , the number of NO molecules generated by the process,  $M_{\text{NO}}$ , is given by

$$M_{\text{NO}} = Nf(T_f) \quad (22.3)$$

where  $f(T_f)$  is the fraction of NO molecules in the gas at temperature  $T_f$  [33, 34].

The value of  $T_f$  depends on the cooling rate of the gas in the discharge. For lightning-like discharges,  $T_f$  and corresponding  $f(T_f)$  were estimated to be around 2660 K and 0.029 respectively [33, 34]. These values have been used in the calculations presented here. In order to evaluate  $M_{\text{NO}}$  it is necessary to evaluate  $N$ , the number of molecules heated above  $T_f$ , which can be found from the following equation:

$$N = V * \left( \frac{E_h}{E_f} \right) * N_o * \left( \frac{T_o}{T_f} \right) \quad (22.4)$$

where  $V$  is the volume of hot air in the discharge channel given by (22.2),  $E_h$  and  $E_f$  are the internal energy of air per unit volume at the temperatures  $T_h$  and  $T_f$ , respectively,  $T_o$  is the standard temperature and  $N_o$  is the number of molecules per unit volume at standard temperature and pressure. In the calculations, we have assumed that  $T_h = 15,000$  K,  $T_f = 2660$  K,  $T_o = 273$  K and  $N_o = 2.69 \times 10^{25} \text{ m}^{-3}$ . In deriving (22.4) we have assumed that, as the channel cools after reaching the pressure equilibrium due to the entrainment of cold ambient air into the discharge channel, not much of the energy escapes the channel as radiation. Moreover, in the derivation we have neglected the production of NO, if any, by the shock wave generated by the discharge. Both these assumptions are supported by the calculations of Hill *et al.* [31]. The number of NO molecules produced by the discharge is then given by

$$M_{\text{NO}} = f(T_f) * V * \left( \frac{E_h}{E_d} \right) * N_o * \left( \frac{T_0}{T_f} \right) \quad (22.5)$$

The values of  $E_h$  and  $E_f$  are calculated using the set of equations given by Plooester [30, 35] describing the variation in internal energy of air as a function of temperature and pressure. Since the radii of spark channels and hence the amount of air heated to a given temperature depends not only on the peak current but also on the temporal variation of the current, the amount of  $\text{NO}_x$  produced by a spark depends both on the peak current and the current waveshape. Thus, if the current waveform in the discharge channel is known, then (22.1) to (22.5) can be used to evaluate the number of NO molecules produced by the discharge.

#### 22.2.4 Efficiency of $\text{NO}_x$ production in sparks with different current wave-shapes

Let us now check the validity of (22.5) by comparing its predictions with the available experimental data. The efficiency of  $\text{NO}_x$  production by electrical discharges is evaluated in the references [33, 36–41]. Unfortunately, only in a few cases the current waveform associated with the electric discharges used in the experiment is

given. These are the studies conducted by Wang *et al.* [40], Rehbein and Cooray [39] and Rahman *et al.* [41]. The current waveform associated with the sparks analysed by Wang *et al.* [40] has a rise time of 30  $\mu\text{s}$  and a decay time (time taken by the current to decay to 1/2 of its peak value) of 400  $\mu\text{s}$ . The current waveform associated with the sparks in the experiment conducted by Rehbein and Cooray ([39]; the current waveforms are given in Reference 42) was oscillatory with a frequency of 2.8 MHz and decay time of 2  $\mu\text{s}$ . The current waveform in the spark experiments conducted by Rahman *et al.* [41] had a rise time of about 0.3  $\mu\text{s}$  and a decay time of about 25  $\mu\text{s}$ . The  $\text{NO}_x$  production per unit length by these discharges is evaluated using the equations presented in the previous section and the results, together with the experimental data, are shown in Figure 22.2. First note that there is a reasonable agreement between the experimental data and the theory. Second, note how the  $\text{NO}_x$  production depends on the wave-shape of current. For a given peak current, a current with a longer duration gives rise to more  $\text{NO}_x$  than a current with a shorter duration. The reason for this is that the volume of the discharge channel increases with increasing the duration of current waveform. Since the volume of the discharge

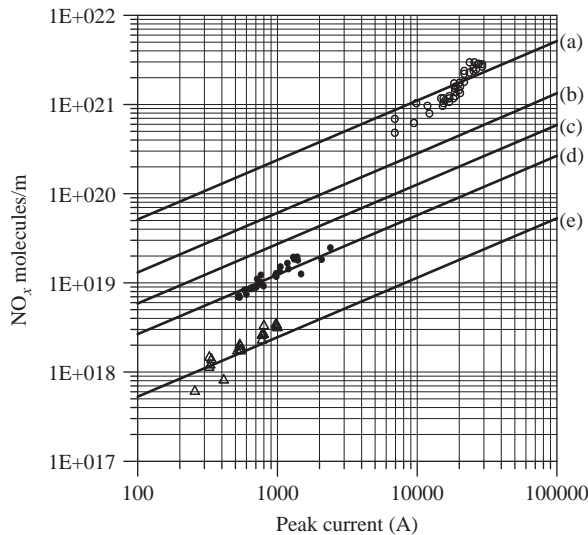


*Figure 22.2*  $\text{NO}_x$  production efficiency of laboratory sparks and lightning return strokes as a function of peak current. (a) Theoretical prediction based on the current waveform of the study conducted by Wang *et al.* [40], (b) prediction based on the typical first return-stroke current waveform, (c) prediction based on the typical subsequent return-stroke current waveform, (d) prediction based on the current waveform in the sparks studied by Rahman *et al.* [41] and (e) prediction based on the current waveform in the sparks studied by Rehbein and Cooray [39]). The experimental data corresponding to different studies (Rehbein and Cooray: hollow triangles; Wang *et al.*: hollow circles; Rahman *et al.*: solid circles) are also shown in the figure

channel is a measure of the internal energy retained in the discharge channel, in long-duration currents more energy goes into the internal energy of the discharge than in short-duration currents. As the internal energy of the discharge increases the mass of air that is being heated beyond the  $\text{NO}_x$  freeze-out temperature also increases leading to a higher  $\text{NO}_x$  production. To the best of our knowledge, this is the first time that the dependence of  $\text{NO}_x$  production on the shape of the current waveform flowing in the discharge channel is explicitly recognized.

### 22.2.5 $\text{NO}_x$ production in sparks as a function of energy

In order to calculate the energy dissipated in the discharge channel, we will employ again the spark discharge channel model of Braginskii [14]. Two simplifying assumptions made in developing this model are as follows: (a) The conductivity of the channel is uniform across the channel cross-section. (b) The conductivity of the channel does not vary as a function of time. With these assumptions, the energy dissipated in the discharge channel is given by

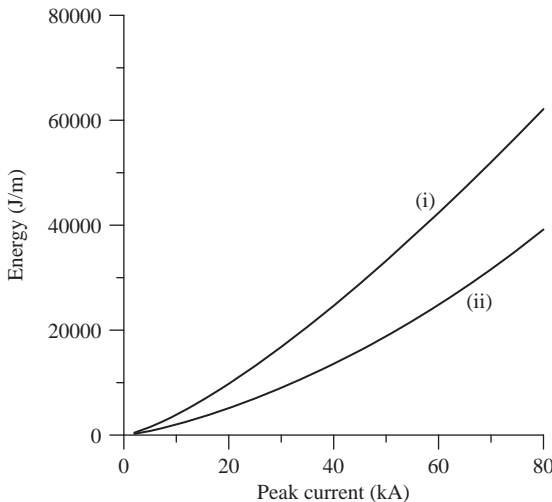
$$U = l \int_0^{\infty} \frac{i^2(t)}{\pi r(t)^2 \sigma} dt \quad (22.6)$$

where  $\sigma$  is the effective conductivity of the spark channel,  $r(t)$  is the radius of the channel at time  $t$  (given by (22.1)) and  $l$  is the length of the channel. Braginskii [14] recommended the use of  $\sim 10^4$  S/m as the effective conductivity of the channel.

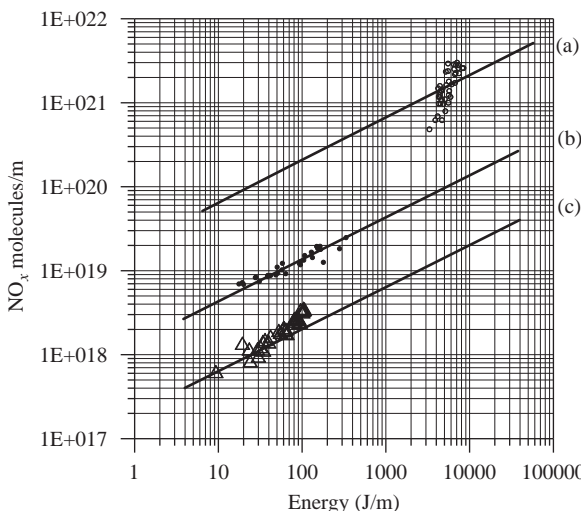
In order to test the validity of this equation, the energy in the sparks studied by Rahman *et al.* [41] was evaluated by integrating the product of voltage and current waveforms. For 35 current waveforms, the total energy calculated from the above equation agrees within 15%, when the value of  $\sigma$  is assumed to be  $0.65 \times 10^4$  S/m. Paxton *et al.* [28] studied the development of lightning channel taking into account the detailed physics of the complex electrohydrodynamic and thermodynamic processes. The current waveform used by Paxton *et al.* had a linear rise to peak followed by an exponential decay. The peak value, rise time and decay time of the current waveform used by Paxton *et al.* were 20 kA, 5  $\mu\text{s}$ , and 50  $\mu\text{s}$  respectively. The calculated total energy dissipation in the discharge up to 50  $\mu\text{s}$  was about 5 kJ/m. Equation (22.6) for the same current predicts the same energy dissipation when  $\sigma = 10^4$  S/m. These comparisons suggest that (22.6) can give a reasonable value for the total energy dissipated in the discharge for values of  $\sigma$  ranging from  $0.65 \times 10^4$  to  $10^4$  S/m. In the calculations to follow, we will use  $\sigma = 0.8 \times 10^4$  S/m.

Figure 22.3 depicts the energy dissipation per unit length in electrical discharges having current signatures similar to those of typical first and subsequent strokes, as a function of peak current. According to Figure 22.3, typical first (30 kA) and subsequent (12 kA) return strokes will dissipate about 20 and 2.5 kJ/m, respectively, in channel sections close to ground.

In Figure 22.4, the calculated yield of  $\text{NO}_x$  as a function of the energy dissipated in the discharge is depicted for current waveforms corresponding to the experiments



*Figure 22.3 The energy dissipation per unit length in (i) first return strokes and (ii) subsequent return strokes as a function of peak current*



*Figure 22.4 NO<sub>x</sub> production efficiency of laboratory sparks and lightning return strokes as a function of the energy dissipated in the discharge. (a) Theoretical prediction based on the current waveform of the study conducted by Wang et al. [40], (b) prediction based on the current waveform in the sparks studied by Rahman et al. [41] and (c) prediction based on the current waveform in the sparks studied by Rehbein and Cooray [39]). The experimental data corresponding to different studies (Rehbein and Cooray: hollow triangles; Wang et al.: hollow circles; Rahman et al.: solid circles) are also shown in the figure*

conducted by Wang *et al.* [40], Rehbein and Cooray [39] and Rahman *et al.* [41]. For comparison purposes the experimental data are also shown in the same diagram. It is important to note that the experimental evaluation of the energy dissipated in spark channels is not trivial. Errors may result from the measurement of voltage across the spark channel either due to inductances in the circuit or due to the response characteristics of high-voltage dividers. Moreover, for large currents the discharge channel transverse diameters may reach several centimetres and in the case of short gaps (about 3 cm), as in the case of Wang *et al.* [40] study, the electrode effects may influence the total energy measured. Nevertheless, as one can see in Figure 22.4, there is a reasonable agreement between the theory and the experiment. One important conclusion that can be made from the results of this analysis is that the energy dissipated in the discharge cannot be used as a scaling factor in extrapolating laboratory data to lightning. The reason for this is that for a given energy the NO<sub>x</sub> production efficiency of a spark depends on the waveform of the discharge current.

### **22.3 NO<sub>x</sub> production in discharges containing long-duration currents**

Currents having relatively long durations ranging from several milliseconds to hundreds of milliseconds are associated with different lightning processes. One such process is the stepped leader. A stepped leader may carry currents of tens to hundreds of amperes with durations of some tens of milliseconds. Long-duration currents initiated by return strokes and flowing along the channel to ground are known as continuing currents. Discharge processes taking place inside the cloud can also generate long-duration currents.

The theory presented in Section 22.2.3 cannot be applied to calculation of NO<sub>x</sub> production in channels carrying long-duration currents. When the current duration is long, ample time is available for the mixing of cold air into the discharge channel while the current is still flowing in the channel. Thus, the energy dissipated in the channel is continuously being utilized to heat cold air coming into the channel. At the same time hot air leaving the channel as it cools down creates NO<sub>x</sub> in gas volumes adjacent to the discharge channel. In the case of long-duration current, this turbulent mixing of cold air into the channel and hot air leaving it has to be taken into account in the calculation of NO<sub>x</sub> production. This prevents us from using the procedure for calculating the NO<sub>x</sub> production in spark channels, described in Section 22.2.3. Recent measurements conducted by Rahman *et al.* [13] show that the NO<sub>x</sub> production by steady currents in rocket-triggered lightning is proportional to the charge transferred along the channel. According to their measurements, the NO<sub>x</sub> production efficiency of long-duration currents is equal to about  $2 \times 10^{20}$  molecules/m/C.

### **22.4 NO<sub>x</sub> production in streamer discharges**

The propagation of leaders in long laboratory sparks and lightning is facilitated by streamer discharges taking place at the forward moving leader tip. Streamer

discharges may also be responsible for the leakage of charge from the hot leader channel core, which is at extremely high potential, into the corona sheath. The air temperature in a streamer is close to the ambient temperature, whereas the electron temperature can be several tens of thousands of degrees Kelvin. The collision between energetic electrons and neutral molecules leads to the dissociation of  $\text{N}_2$  and  $\text{O}_2$  in the streamer discharges and the resulting chemistry gives rise to both  $\text{NO}_x$  and  $\text{O}_3$ . However, the theory developed for the  $\text{NO}_x$  generation in hot sparks cannot be utilized here, because the  $\text{NO}_x$  production process is not controlled by temperature variation. Recently, Cooray *et al.* [43, see chapter 21] demonstrated that a theory developed for studying  $\text{NO}_x$  production by solar proton events [1, 44] could be utilized to calculate the  $\text{NO}_x$  production from corona and streamer discharges. According to this theory, the  $\text{NO}_x$  production rate is approximately equal to the rate of production of ion pairs during the proton impact. Since the bulk of ionization in such events is produced by secondary electron impacts, Cooray *et al.* [43] applied the same concept to study the  $\text{NO}_x$  production in low pressure gas discharges, corona discharges and streamer discharges in which the source of ionization is the electron impacts. Let us assume that the radius of the streamer channel is  $R_s$  and the number of charge particles at the streamer head is  $N_{\text{head}}$ . Since the number of ionizing events created by a streamer in moving a unit length is equal to  $N_{\text{head}}/2R_s$ , according to Cooray *et al.* [43], the number of  $\text{NO}_x$  molecules produced by a streamer in propagating a unit distance is given by  $kN_{\text{head}}/2R_s$ , where  $k$  is the number of  $\text{NO}_x$  molecules generated per ionizing event. Using experimental data for corona Cooray *et al.* [43] demonstrated that  $k \approx 1$  for positive polarity and  $k \approx 0.6$  for negative polarity.

## 22.5 $\text{NO}_x$ production in ground lightning flashes

Having outlined the procedure to evaluate the efficiency of  $\text{NO}_x$  production in sparks, continuing currents and streamer discharges we are now in a position to incorporate them all into a single model that can be used for evaluating the  $\text{NO}_x$  production by lightning flashes.

### 22.5.1 *The model of a ground lightning flash*

As summarized by Cooray [45], a ground flash is initiated by an electrical breakdown process in the cloud that is called *the preliminary breakdown*. This process leads to the creation of a column of charge *called the stepped leader* that extends from cloud to ground in a stepped manner. On its way towards the ground a stepped leader may give rise to several branches. Once the connection of the stepped leader to ground is made, a nearly ground-potential wave and the associated luminosity wave travel along the leader channel towards the cloud at a speed comparable to that of light. This wave is called the *return stroke*. Although the current signature associated with the return stroke proper tends to have duration of a few hundred microseconds, the return-stroke current may not go to zero within this time, and a

low-level current may continue to flow for tens to hundreds of milliseconds. Such long-duration currents are called *continuing currents*. Continuing current longer than 40 ms tends to follow subsequent (as opposed to first) strokes, described below. The arrival of the first return-stroke front at the cloud end of the return-stroke channel leads to a change of potential in the vicinity of this point. This change in potential may initiate a positive discharge that travels away from the upper end of the return-stroke channel (the so-called *J*-process). When a fresh discharge is created in the previously ionized channel, the process that follows depends on the conditions along the channel. If the channel carries a continuing current, there will be a wave that travels towards the ground and produces a reflection there. This process is called the *M* component. If the channel carries essentially no current, the downward-moving wave may take the form of *dart leader* that travels towards the ground and produces a return stroke there. Such return stroke is called the *subsequent return stroke*. Processes similar to those occurring after the first return strokes may also take place after subsequent return strokes. Unsuccessful dart leaders and other transient processes involving in-cloud channels are referred to as *K* changes.

In evaluating the  $\text{NO}_x$  production by a ground flash, one has to consider all these processes. In the present study, an attempt is made to include the various lightning processes in the estimation of the global  $\text{NO}_x$  production by ground flashes. In this evaluation, a ground flash is represented by the following model. The geometry of the lightning channel consists of a vertical section of height  $H$  and a horizontal section of length  $L$ . The horizontal channel that is located in the cloud consists of  $n$  branches of equal lengths. Each branch is created by a leader discharge and during its creation the leader current is confined to that particular branch, i.e. it does not flow along other branches. In lightning flashes giving rise to continuing currents, the source is confined to a single branch, i.e. the current passes through a branch and follows the vertical channel to ground. Processes to be taken into account are the leaders, return strokes, continuing currents and *M* components in the vertical channel section and leaders and *K* changes in the horizontal channel sections. A cloud flash is represented by two networks of horizontal channels, one in the positive charge region and the other in the negative, connected to each other by a vertical channel. The geometry of the horizontal channels is identical to the one assumed for ground flashes.

## 22.5.2 $\text{NO}_x$ production in different processes in ground flashes

### 22.5.2.1 Leaders

#### *Corona sheath*

A leader channel consists of a hot core surrounded by a corona sheath. The corona sheath is created through the action of streamer discharges, and the charge deposited in the corona sheath by the streamers is supplied by the current flowing in the hot core. Both these processes (i.e. streamer discharges and current flow along the core of the leader) have to be considered in evaluating the  $\text{NO}_x$  production by leader discharges. In this section, we will concentrate on the former.

According to bidirectional leader concept, the vertical channel of a negative ground flash is forged by negative stepped leaders and the channels in the cloud are created by positive leaders moving away from the point of origin of the flash. In the analysis to follow, we assume that the magnitude of the charge deposited per unit length of the leader channel is the same on both vertical and horizontal channels. Let us denote this by  $\rho$ . We also assume that most of this charge resides in the corona sheath and the transport of this charge into the corona sheath is mediated by streamers. Since most of the charge of the streamer is located at the head of the streamer [46], the number of streamers,  $N_s$ , per unit length of the leader channel is

$$N_s = \frac{\rho}{eN_{\text{head}}} \quad (22.7)$$

where  $N_{\text{head}}$  is the charge on the head of the streamer channel. Applying the Gauss law over a cylindrical surface encompassing the whole corona sheath, one obtains the radius of the corona sheath of a positive leader,  $R_{c+}$ , as

$$R_{c+} = \frac{\rho}{(2\pi\epsilon_0 E_{s+})} \quad (22.8)$$

where  $E_{s+}$  is the critical background electric field necessary for the propagation of positive streamers. Note that in writing down the above equation, we assume that all the charge in the corona sheath is located inside the radius  $R_{c+}$  and the electric field at this outer edge of the corona sheath is equal to  $E_{s+}$ . If the electric field in the streamer region remains constant at this critical electric field, in order to satisfy the boundary conditions in coaxial geometry the volume charge density in the streamer region should decrease inversely with radius. Since most of the streamer charge is located at its head, this condition requires the number of streamers moving out from the central conductor to decrease linearly with radial distance. In other words the number of streamers having a given length  $l$  is two times the number of streamers of length  $2l$  provided that  $2l < R_{c+}$ . Thus, streamers travel, on average, a distance of  $R_{c+}/2$  in creating the corona sheath. Using the expression for the number of  $\text{NO}_x$  molecules generated by a single streamer in moving a unit length derived previously, we find the number of  $\text{NO}_x$  molecules created by positive streamers per unit length of positive leader channel,  $\eta_{\text{str}+}$ , as

$$\eta_{\text{str}+} = \frac{k_+ \rho^2}{8\pi\epsilon_0 e E_{s+} R_s} \quad (22.9)$$

where  $k_+$  is the number of  $\text{NO}_x$  molecules generated per ionizing event in positive discharges. Similarly, the number of  $\text{NO}_x$  molecules generated by negative streamers per unit length of the negative leader channel is given by

$$\eta_{\text{str}-} = \frac{k_- \rho^2}{8\pi\epsilon_0 e E_{s-} R_s} \quad (22.10)$$

where the parameters have the same definition as in previous equation but corresponding to negative streamers. Thus, the total number of  $\text{NO}_x$  molecules generated by corona sheath of the leaders in the whole ground flash is given by

$$\text{NO}_{x-\text{leadersheath}} = \eta_{\text{str}-} H + \eta_{\text{str}+} L \quad (22.11)$$

The charge per unit length of lightning stepped leaders is expected to be in the range of 0.0005–0.001 C/m. In the calculations, we assumed that  $\rho = 0.0005$  C/m. The values of  $E_{s+}$  and  $E_{s-}$  are equal to 500 kV/m and 1 MV/m respectively [47]. We assume that  $N = 10^8$  [46]. We also assumed that the values of  $k_- = 0.6$  and  $k_+ = 1.0$  are independent of pressure. Recall that  $k_-$  and  $k_+$  refer to the number of  $\text{NO}_x$  molecules created by an ionizing event. The assumption is based on the study of Jackman *et al.* [48] whose theoretical calculations predict that  $\text{NO}_x$  molecules per ionizing events does not change significantly with increasing altitude and hence with pressure. We have also assumed that the values of  $E_{s+}$  and  $E_{s-}$  do not vary with pressure. In reality, they decrease linearly with pressure but that effect is somewhat compensated by the increase in the size of the streamer head with decreasing pressure. Substituting these values in (22.9), we obtain  $\eta_{\text{str}+} \approx 2 \times 10^{20}$  for  $\rho = 0.0005$  C/m.

#### *$\text{NO}_x$ production in the hot core of the leader*

The average speed of propagation of lightning stepped leaders is about  $2 \times 10^5$  m/s and to supply a charge per unit length equal to 0.0005 C/m the current flowing along the hot core should be about 100 A. As the leader progresses, this current will continue to flow in any given channel section as long as the conditions are suitable for the continuous propagation of the leader head. Let us represent the current flowing along the stepped leader channel by  $I_{ls}$ . If the charge density along the leader channel is constant and equal to  $\rho$  then  $I_{ls} = v\rho$  where  $v$  is the speed of propagation of the head of the leader channel. Let  $\eta_{lea}$  be the number of  $\text{NO}_x$  molecules generated per unit length per unit charge by the current flowing in the core of the leader channel. Thus, the number of  $\text{NO}_x$  molecules generated by a unit length of the leader channel due to this current is  $\eta_{lea} I_{ls} \tau_d$ , where  $\tau_d$  is the time over which a current of amplitude  $I_{ls}$  flows along the core of the channel section. Consider the vertical channel of length  $H$ . In a channel element of length  $dz$  located at a height  $(H - z)$  above ground level the duration of this current is  $(H - z)/v_s$ , where  $v_s$  is the speed of progression of the leader head. Note that this time is equal to the time needed for the leader head to travel the distance from the channel element to the ground. The total number of  $\text{NO}_x$  molecules generated in the channel element by the core current after correction for the pressure is  $\eta_{lea} I_{ls} (H - z) e^{-(H-z)/\lambda_p} dz/v_s$ . The total contribution from the vertical channel section can be obtained by integration of this expression from 0 to  $H$ . In constructing the above equation, we have assumed that the atmospheric pressure decreases exponentially with height with a decay height constant  $\lambda_p$  and the efficiency of  $\text{NO}_x$  production by hot discharges decreases linearly with pressure [49, 50].

The evaluation of the contribution to the  $\text{NO}_x$  production from non-vertical in-cloud channels is more complicated. The channel system inside the cloud may consist of many branches and at a given time only a few of these branches may be developing [51–53], and hence the core current is active only along those branches at that time. Thus, one problem in evaluating the  $\text{NO}_x$  production in the core of the non-vertical in-cloud channel is the difficulty of knowing the length of the channel sections in which the current is flowing at a given time. Consider that the non-vertical in-cloud channels comprise  $n$  identical branches connected to the top of the vertical channel. We presume that these channels in the cloud are also created by processes similar to that of lightning leaders observed in ground flashes, and therefore, their current and speed of development are also identical to those of these leaders. As mentioned in Section 22.5.1, we assume that the core current will flow in each branch only when that particular branch is being formed. In reality, core current may pass from an active branch to a previously formed branch thus increasing the total length of the channel sections supporting a core current at a given time. Consider the development of a horizontal channel section inside the cloud. Let us direct the coordinate  $x$  along the channel section. Consider an element  $dx$  on this channel located at a distance  $x$  from the origin of the section. In this element, the current flows for a duration of  $(l - x)/v_s$  where  $v_s$  is the speed of development of the channel and  $l$  is the length of the channel. Thus, the number of  $\text{NO}_x$  molecules produced in this channel element is  $\eta_{\text{lea}} I_{ls}^{-H/\lambda_p} (l - x) dx / v_s$ . The total  $\text{NO}_x$  production in the channel section can be obtained by integrating the above expression from 0 to  $l$ . The result of this integration is  $\eta_{\text{lea}} I_{ls} l^2 e^{-H/\lambda_p} / 2v_s$ . Since we have assumed that there are  $n$  identical branches and the total length of the horizontal channels is  $L$  the number of  $\text{NO}_x$  molecules produced by the current flowing through the core of the channels inside the cloud is given by  $\eta_{\text{lea}} I_{ls} L^2 e^{-H/\lambda_p} / 2v_s n$ . A similar procedure can be used to evaluate the  $\text{NO}_x$  production along the vertical section of the leader channel, but the mathematics is slightly more complicated due to the fact that the pressure varies along the channel. After applying the mathematics, one can show that the total number of  $\text{NO}_x$  molecules produced by the core current in the stepped leader channel of the ground flash (including the branches in the cloud) is

$$\begin{aligned} NO_{x-sl-core} = & \frac{\eta_{\text{lea}} I_{ls}}{v_s} \left( \lambda_p^2 - \lambda_p e^{-H/\lambda_p} [H + \lambda_p] \right) \\ & + \frac{\eta_{\text{lea}} I_{ls}}{2v_s n} L^2 e^{-H/\lambda_p} \end{aligned} \quad (22.12a)$$

Using the same procedure the number of  $\text{NO}_x$  molecules produced in the dart leader channel core can be written as

$$NO_{x-dl-core} = \frac{\eta_{\text{lea}} I_{ld}}{v_d} \left( \lambda_p^2 - \lambda_p e^{-H/\lambda_p} [H + \lambda_p] \right) \quad (22.12b)$$

where  $I_{dl}$  is the current in the dart leader and  $v_d$  the speed of dart leaders. To evaluate this equation, it is necessary to have values for  $\eta_{\text{lea}}$ ,  $n$ ,  $v_s$ ,  $I_{ls}$ ,  $v_d$  and  $I_{ld}$ . As

pointed out in Section 22.3, the efficiency of  $\text{NO}_x$  production by long-duration currents is about  $2 \times 10^{20}$  molecules/m/C. We assume that this is also true for the currents flowing along the leaders channels, i.e.  $\eta_{lea} = 2 \times 10^{20}$  molecules/m/C. This assumption is justified because, like continuing currents, leaders also support currents with amplitudes on the order of hundred amperes or more for durations of many milliseconds depending on the time of travel. The channel structure inside the cloud, as revealed from interferometric studies, can be approximated by a few large channels connected to the main channel [51, 52]. Thus, the value of  $n$  may lie in the range of, say, 3–10. Optical observations of the stepped leaders and the interferometric studies show that the speed of development of stepped leader channels in virgin air,  $v_s$ , is about  $2 \times 10^5$  m/s [51, 54]. Measurements conducted with both natural and triggered lightning show that the speed of dart leaders,  $v_d$ , is about  $10^7$  m/s [55–57]. The currents in either the stepped leaders or dart leaders cannot be measured directly. But, inferences based on electric field measurements show that stepped and dart leaders are associated with currents of the order of 100 A and 1 kA [58–60], respectively.

### 22.5.2.2 Return strokes

In assessing the  $\text{NO}_x$  production by first and subsequent strokes, we make the following assumptions. (a) The shape of the current waveform at the channel base of the first and subsequent return strokes are similar to the typical waveforms constructed by CIGRE Study Committee 33 [21] and Nucci *et al.* [22]. (b) The return-stroke peak current decreases linearly along the vertical section of the channel and reducing to zero amplitude at the cloud end of the vertical channel. (c) The return-stroke channel is vertical from ground level to the height of the charge centre,  $H$ . With these assumptions, the  $\text{NO}_x$  produced by the first return stroke after correcting for the decrease in pressure with height is

$$\text{NO}_{x-fr} = \eta_{fr} \lambda_p \left[ 1 - \frac{\lambda_p}{H} + \frac{\lambda_p}{H} e^{-H/\lambda_p} \right] \quad (22.13)$$

where  $\eta_{fr}$  is the number of  $\text{NO}_x$  molecules produced by a unit length of the discharge at atmospheric pressure having a current identical to that of a typical first return stroke. In the calculation, we assume that the peak current of a typical first return stroke is 30 kA. Note that, as depicted by curve b in Figure 22.2,  $\text{NO}_x$  production depends on the peak current of the first return stroke. From this figure we estimate that  $\eta_{fr} = 5.9 \times 10^{20}$  molecules/m. Similarly, the number of  $\text{NO}_x$  molecules generated by a subsequent return stroke is given by

$$\text{NO}_{x-sr} = \eta_{sr} \lambda_p \left[ 1 - \frac{\lambda_p}{H} + \frac{\lambda_p}{H} e^{-H/\lambda_p} \right] \quad (22.14)$$

where  $\eta_{sr}$  is the number of  $\text{NO}_x$  molecules produced by a unit length of the discharge at atmospheric pressure having a current identical to that of a typical subsequent return stroke. In the calculation, we assume that the peak current of a

typical subsequent return stroke is 12 kA. Note again that, as depicted by curve c in Figure 22.2,  $\text{NO}_x$  production also depends on the peak current of the subsequent return stroke. From this figure, we estimate that  $\eta_{sr} = 1.4 \times 10^{20}$  molecules/m.

The use of return-stroke current instead of the energy dissipated in return strokes as an input parameter in quantifying  $\text{NO}_x$  production in return strokes, as done above, has at least one important advantage. The energy dissipated in lightning flashes cannot be measured directly but has to be inferred by indirect methods leading to large inaccuracies in the estimated  $\text{NO}_x$  production. On the other hand, the current at the channel base of ground flashes can be measured and a large amount of data on this parameter is available in the literature.

In deriving (22.13) and (22.14), it has been assumed that the return-stroke peak current decreases with height. The experimental observations show that the luminosity of both first and subsequent return strokes decreases with height indicating that the return-stroke current peak also decreases with height [54, 61]. Of course, since the exact nature of how the return-stroke peak current decreases with height is not known, one has a freedom to select any other form of decay for the peak current than the linear decay assumed in the calculation. However, the expression describing a linear decay with current amplitude decreasing to zero at cloud level involves only one parameter, i.e. height of the vertical channel, and it also specifies the boundary conditions for the current at the cloud end of the channel. Moreover, the linear decay has been shown to produce electric fields at both far and close distances that are similar to those measured when used in return-stroke models [62, 63].

### 22.5.2.3 $M$ components and $K$ processes

As pointed out earlier, the development or extension of the lightning channels located inside the cloud is mediated by leaders. As these leaders develop, the changes in the potential at the extremities of the leader may cause  $K$  processes that travel along the channel reducing the potential differences. The interferometric observations indicate that it is usual to have a few  $K$  processes in the developing stage of a given channel section [51, 52]. Thus, if  $\eta_k$  is the number of  $\text{NO}_x$  molecules produced per unit length of the channel by a  $K$  process, then the total number of  $\text{NO}_x$  molecules generated by  $K$  processes during the development of the channels inside the cloud after correction for the pressure is  $\eta_k n_k L e^{-H/\lambda_p}$ . In this expression,  $n_k$  is the number of  $K$  changes taking place in the development of a particular branch. In writing down the above expression, we have also assumed that the current associated with a given  $K$  change occurring during the development of a given branch travels only along that branch. In the calculations to be conducted later, we assume that  $n_k = 3$ . Thus, the total number of  $K$  changes per flash is equal to  $n n_k$ , where  $n$  is the number of branches in the channel. In a lightning flash with five branches in the cloud, the total number of  $K$  changes would be 15. If these  $K$  changes end up in a channel carrying a continuing current to ground, then the resulting current will propagate to ground as an  $M$  component. The number of  $\text{NO}_x$  molecules produced in the vertical channel by the  $M$  components after correction for the pressure is given by  $n_m \eta_m \lambda_p (1 - e^{-H/\lambda_p})$ , where  $n_m$  is the number of  $M$  components travelling along the vertical channel of a typical ground flash. It is also

assumed that the  $\text{NO}_x$  production efficiency of a typical  $K$  change is identical to that of a typical  $M$  component, i.e.  $\eta_k = \eta_m$ . This assumption is not unreasonable since, as mentioned above, they share a common origin and therefore they probably have similar currents. The total number of  $\text{NO}_x$  molecules generated by  $K$  changes and  $M$  components after the pressure correction is

$$\text{NO}_{x-m} = \left[ n_m \eta_m \lambda_p (1 - e^{-H/\lambda_p}) + n_k \eta_k L e^{-H/\lambda_p} \right] \quad (22.15)$$

Now, let us evaluate the magnitude of  $\eta_m$ . A typical  $M$  component current has a more or less symmetric bell-shaped waveform with a rise time of about 400  $\mu\text{s}$  and a peak of about 160 A [64]. Calculations done with such a current waveform show that  $\eta_m = 2 \times 10^{20}$ . Thus,  $\eta_k$  is also equal to  $2 \times 10^{20}$ .  $M$  components travel along the vertical channel carrying continuing currents. In a typical ground flash having a continuing current,  $M$  component may outnumber the number of return strokes by 1 to 4. Therefore, a typical ground flash containing continuing currents may support about 16  $M$  components along the vertical channel. In making the above statement, we have assumed that a typical ground flash contains four return strokes. On the other hand, the percentage of ground flashes containing long (longer than 40 ms) continuing currents is about 30–50% [65, 66]. This fixes the value of  $n_m$  to about 5.

#### 22.5.2.4 Continuing currents

In the model under consideration, we assume that the continuing currents are flowing only through the vertical section of the ground flash. Of course, they also flow along horizontal channels, but our knowledge at present on how continuing current is distributed in channels in the cloud is rather meagre. In this case, the total number of  $\text{NO}_x$  molecules generated by these continuing currents in a ground flash after pressure correction is given by

$$\text{NO}_{x-cv} = \left[ k_c \eta_{con} I_{con} \tau_c \lambda_p (1 - e^{-H/\lambda_p}) \right] \quad (22.16)$$

where  $\eta_{con}$  is the number of  $\text{NO}_x$  molecules produced per Coulomb by a unit length of the discharge channel carrying continuing current,  $I_{con}$  is the magnitude of continuing current,  $\tau_c$  is the typical duration of continuing current and  $k_c$  is the fraction of ground flashes that support continuing currents. In the calculations we assumed that  $\eta_{con} = 2 \times 10^{20}$  molecules/m/C (see Section 22.3). According to experimental data, about 30–50% of the lightning flashes contain continuing currents and the amplitude and the duration of a typical continuing current are about 100 A and 100 ms respectively [65, 66]. Thus,  $k_c = 0.3$  and  $\tau_c = 0.1$  s.

The exact nature of the source that drives continuing current along the vertical channel is not known. Most likely the source is the development and the charge transfer along the upper channel sections. Since we have taken this activity into account in Section 22.5.2.1 under leaders, it is reasonable to consider only the vertical channel here.

### 22.5.2.5 $\text{NO}_x$ production in a typical negative ground flash

One can sum the contributions to the  $\text{NO}_x$  production from different processes taking place in a ground flash as done in the following equation:

$$\begin{aligned}
 \text{NO}_{x-\text{ground}} = & \eta_{\text{str}-}H + \eta_{\text{str}+}L + \frac{\eta_{\text{lea}}I_{ls}}{v_s} \left( \lambda_p^2 - \lambda_p e^{-H/\lambda_p} [H + \lambda_p] \right) \\
 & + \frac{\eta_{\text{lea}}I_{ls}}{2v_sn} L^2 e^{-H/\lambda_p} + \eta_{\text{fr}}\lambda_p \left[ 1 - \frac{\lambda_p}{H} + \frac{\lambda_p}{H} e^{-H/\lambda_p} \right] \\
 & + \frac{n_s\eta_{\text{lea}}I_{ld}}{v_d} \left( \lambda_p^2 - \lambda_p e^{-H/\lambda_p} [H + \lambda_p] \right) \\
 & + \eta_{\text{sr}}n_s\lambda_p \left[ 1 - \frac{\lambda_p}{H} + \frac{\lambda_p}{H} e^{-H/\lambda_p} \right] + n_m\eta_m\lambda_p (1 - e^{-H/\lambda_p}) \\
 & + n_k\eta_k L e^{-H/\lambda_p} + k_c\eta_{con}I_{con}\tau_c\lambda_p (1 - e^{-H/\lambda_p})
 \end{aligned} \tag{22.17}$$

We made an attempt above to specify numerical values for the constants that appear in this equation. One has to admit, of course, that our knowledge on the numerical values of different parameters is not complete and more work has to be done before the above equation could be applied with confidence. However, this equation provides a foundation on which the procedure to estimate  $\text{NO}_x$  production in lightning flashes could be built as one obtains more information concerning the parameters. In Appendix 1, we have summarized our current knowledge on each of the parameters that appear in (22.17).

Note that since  $M$  components are discharges propagating in channels carrying continuing currents, one may wonder whether the contribution from  $M$  components to the  $\text{NO}_x$  production is already taken into account in the production of  $\text{NO}_x$  by continuing currents. The reason why we have included both contributions (i.e. continuing currents and  $M$  components) in the above equation is the following. The lightning channel becomes more luminous when  $M$  components are travelling through it. This shows that they cause additional atomic excitation and ionization because the channel becomes luminous while they propagate along it. Furthermore, the optical observations show that during the propagation of the  $M$  components the diameter of the channel through which a continuing current is already propagating gradually increases from about 0.5 cm to about 3 cm [67]. Moreover,  $M$  components were also observed to produce thunder [68]. Thus, it is reasonable to assume that the  $M$  component will enhance the  $\text{NO}_x$  production beyond the  $\text{NO}_x$  production level of the continuing current during its passage through the channel. This justifies adding the contribution of the  $M$  components to that of the continuing current. The same reasoning applies to the addition of the contribution from  $K$  processes to the  $\text{NO}_x$  yield from the leader currents flowing through the hot core of the developing leaders.

Now, let us illustrate the use of (22.17). In Figure 22.5, we have depicted the contributions from leaders (separated into contribution from streamers in the corona sheath and current flow along the core), return strokes,  $M$  components,  $K$  processes and continuing currents as a function of the horizontal channel length  $L$ . First, note that the contributions from return strokes and the continuing currents do

not vary with increasing length of the horizontal channels because these currents are assumed to propagate only along the vertical channel. Second observe that the return strokes produce the least contribution to the  $\text{NO}_x$  production, whereas the largest contribution is made by leaders with the current flowing along the core being the main contributor. More than 90% of the contribution to the  $\text{NO}_x$  production is coming from leaders,  $M$  components and  $K$  processes. Leaders alone contribute about 50% to the  $\text{NO}_x$  production. Note that these observations are true also for horizontal channel lengths as short as 10 km. On the other hand, in the literature, the return stroke is often assumed to be the  $\text{NO}_x$  source in ground flashes. Our study shows that this assumption is incorrect. Using VHF lightning channel mapping technique, Laroche *et al.* [69] observed that the mean total channel length in over 20,000 cloud and ground flashes is 45 km. Taking this length as a typical value the results presented in Figure 22.5 show that an average ground flash with four return strokes will generate about  $4 \times 10^{25}$   $\text{NO}_x$  molecules per flash.

## 22.6 $\text{NO}_x$ production by cloud flashes

Cloud flashes normally occur between the main negative and upper positive charge regions of the cloud. Much of the information available today on the mechanism of the cloud flash is based on electric field measurements. Also Proctor [70–72],

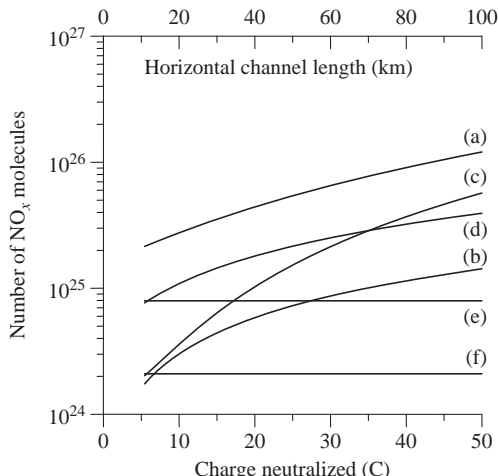


*Figure 22.5 The number of  $\text{NO}_x$  molecules produced by different processes associated with a ground flash as a function of horizontal channel length. (a) Total, (b) streamers in corona sheaths, (c) core current in leaders, (d)  $M$  components and  $K$  changes, (e) continuing currents and (f) return strokes (four strokes). The vertical channel length is assumed to be 5 km and the number of main branches in the cloud is assumed to be 5*

Shao *et al.* [51] and Shao and Krehbiel [52] made important discoveries utilizing VHF radio imaging techniques. Based on this information, Cooray [45] summarized the activities during a cloud flash as follows (see also [65]).

The cloud flash commences with a movement of negative leader discharge from the negative charge region towards the positive one in a more or less vertical direction. The vertical channel develops within the first 10 to 20 ms from the beginning of the flash. This channel is a few kilometres in length and it developed with a speed of about  $2.0 \times 10^5$  m/s. Even after the vertical channel was formed, one could detect an increase in the electrostatic field indicative of negative charge transfer to the upper levels along the vertical channel.

The main activity after the development of the vertical channel is the horizontal extension of the channels in the upper level (i.e. the channels in the positive charge region). These horizontal extensions of the upper level channels are correlated to the brief breakdowns at the lower levels, followed by discharges propagating from the lower level to the upper level along the vertical channel. Thus, the upper level breakdown events are probably initiated by the electric field changes caused by the transfer of charge from the lower levels. For about 20 to 140 ms of the cloud flash, repeated breakdowns occur between the lower and upper levels along the vertical channel. These discharges transported negative charge to the upper levels. Breakdown events of this type can be categorized as *K* changes. In general, the vertical channels through which these discharges propagate do not generate any radiation in the VHF range, which indicates that they are conducting. This is so because, in general, conducting channels do not generate VHF radiation as discharges propagate along them. Occasionally, however, a discharge makes the vertical channel visible at VHF and then the speed of propagation can be observed to be about  $(5-70) \times 10^6$  m/s, typical of *K* changes. This active stage of the discharge may continue to about 200 ms.

In the latter part of this active stage (140–200 ms), significant extensions of the lower level channels (i.e. the channel in the negative charge region) take place, but they occur retrogressively. That is, successive discharges, or *K* changes, often start just beyond the outer extremities of the existing channels and then move into and along these channels, thereby extending them further. These *K* changes transport negative charge from successively longer distances to the origin of the flash, and sometimes even to the upper level of the cloud flash as inferred from VHF emissions from the vertical channel. Sometimes, these *K* changes give rise to discharges that start at the origin of the flash and move away from it towards the origin of the *K* changes. Such discharges can be interpreted as positive recoil events that transport positive charge away from the flash origin and towards the point of initiation of the *K* change. At the final part of the discharge, the vertical channel and the upper level channels were cut off from the lower level channels. This is probably caused by the decrease in the conductivity of the vertical channel. The above description shows that a cloud flash can be described as an electrical activity that collects the charge from the main negative charge centre and redistribute it in the positive charge centre after transporting it along a more or less vertical channel. The recent observations based on three-dimensional interferometry also confirm the basic features of cloud flashes.

described above [73–76]. It is important to mention here that, since positive discharges do not radiate efficiently in HF and VHF, the channels created by positive discharges could be detected only when negative recoil discharges travelling along them. Thus, the channel structure of lightning flashes inside the cloud available today may not be complete.

Let us assume that the total length of the channels in the negative charge centre is equal to that in the positive charge centres. Denote this length by  $L$ . Assume further that these channels are oriented in a horizontal direction. The electrical activity taking place in the negative and positive charge centres during a cloud flash are not very different from the electrical activity taking place in the negative charge centre in the case of a ground flash (i.e. creation and extension of channels by leaders and intermittent occurrence of  $K$  changes). Taking into account the fact that the atmospheric pressure is different at the heights where negative and positive charges are located in a cloud, we can describe the  $\text{NO}_x$  production by a cloud flash by the following equation.

$$\begin{aligned} \text{NO}_{x-\text{cloud}} = & \eta_{\text{str+}}L + \eta_{\text{str-}}L + \frac{\eta_{\text{lea}}}{2vn} I_{\text{lea}} L^2 e^{-H_n/\lambda_p} + \frac{\eta_{\text{lea}}}{2vn} I_{\text{lea}} L^2 e^{-H_p/\lambda_p} \\ & k_c \eta_{\text{con}} I_{\text{con}} \tau_c \lambda_p [e^{-H_n/\lambda_p} - e^{-H_p/\lambda_p}] + n_k \eta_k L e^{-H_n/\lambda_p} + n_k \eta_k L e^{-H_p/\lambda_p} \\ & + n_m \eta_m \lambda_p [e^{-H_n/\lambda_p} - e^{-H_p/\lambda_p}] \end{aligned} \quad (22.18)$$

where  $H_n$  is the height of the negative charge centre and  $H_p$  is the height of the positive charge centre. We assume that  $H_p = 10$  km. In writing down the above equation, it was assumed that the percentage of cloud flashes supporting continuing currents and the number of M components in a cloud flash are identical to those of ground flashes. The results obtained for different values of  $L$  are shown in Figure 22.6. In many studies dealing with the global production of  $\text{NO}_x$  the assumption is made that the cloud flashes do not contribute significantly to the  $\text{NO}_x$  production in thunderstorms. This assumption was challenged previously by Gallardo and Cooray [77]. There are also field measurements showing the importance of cloud flashes in  $\text{NO}_x$  production. For example, airborne measurements of Dye *et al.* [78] show that  $\text{NO}_x$  from a storm that produced exclusively cloud discharges was comparable to other observations, where both cloud and ground discharges are occurring. Further, the modelling of airborne  $\text{NO}_x$  measurements by DeCaria *et al.* [9, 79] show that intracloud lightning (or the intracloud part of the ground flashes) was the dominant source of  $\text{NO}_x$  for the thunderstorms investigated in the study. The results presented in Figure 22.6 show that for a given channel length both the ground flash and the cloud flash generate more or less equal number of  $\text{NO}_x$  molecules.

## 22.7 Global production of $\text{NO}_x$ by lightning flashes

The results presented above can be used to evaluate the global production of  $\text{NO}_x$  by lightning flashes if the flash rate of the lightning flashes is known. In the analysis,

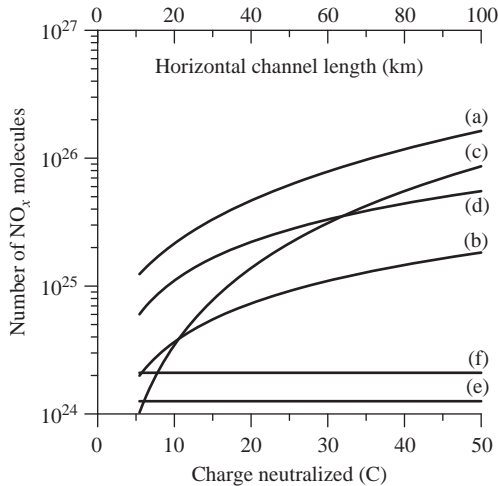


*Figure 22.6 The number of  $\text{NO}_x$  molecules produced by different processes associated with a cloud flash as a function of horizontal channel length. (a) Total, (b) streamers in corona sheaths, (c) core current in leaders, (d) K changes, (e) continuing currents and (f) M components. The vertical channel length is assumed to be 5 km long and the number of main branches in the cloud is assumed to be 5*

we have not treated positive flashes separately but indirectly assumed that the  $\text{NO}_x$  production from a typical positive flash is similar to that of a typical negative flash. In the literature, the flash rate is assumed to lie in the range of 40–300 flashes/s [80, 81]. In the results to be presented, we assumed a global lightning flash rate of 100/s. There is no reason to separate the flash rate into ground and cloud flashes because both types of flashes produced more or less the same amounts of  $\text{NO}_x$ . In Figure 22.7, we have depicted the annual  $\text{NO}_x$  production by lightning flashes as a function of the horizontal channel length. If one assumes an average total channel length of 45 km for a lightning flash, the global  $\text{NO}_x$  production by lightning flashes will be about 4 Tg(N)/year. One has to understand that the global lightning flash frequency is not a constant and it may vary from one year to another. Moreover the number 100 flashes/s is based on thunderstorm observations and satellite data suggest values in the range of 40–60 flashes/s. But, of course, this estimation too depends on the detection threshold level of the satellite and the possible screening of light by cloud cover. The important point however is that the  $\text{NO}_x$  production rate is proportional to the global lightning flash frequency. The number 4 Tg(N)/year is based on 100 flashes/s and if it varies between 40 and 300 flashes/s, the global  $\text{NO}_x$  production rate will also vary between 2 and 12 Tg(N)/year. Lee *et al.* [82] studied the various sources and sinks of  $\text{NO}_x$  in the atmosphere and concluded that the contribution from lightning should be in the range of 4–8 Tg(N)/year. Our results agree with this prediction. The present global estimates of  $\text{NO}_x$  based on theoretical and laboratory studies vary between 1 and about

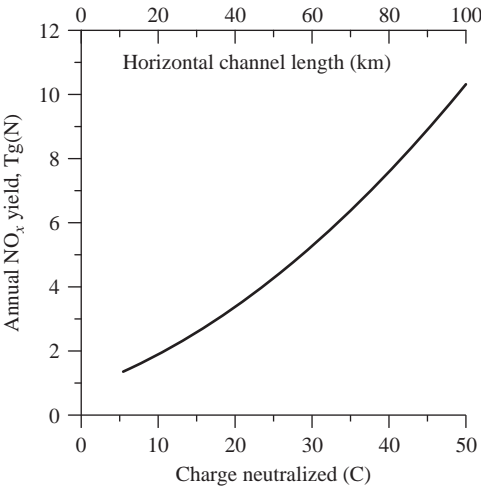


*Figure 22.7 Annual production of NO<sub>x</sub> by lightning flashes as a function of horizontal channel length. The flash rate is assumed to be 100/s, the vertical channel length in ground flashes is assumed to be 5 km and the number of main branches in the cloud is assumed to be 5*

100 Tg(N)/year. The two orders of magnitude variation in this estimate are due to the different results obtained for the NO<sub>x</sub> production efficiency of laboratory discharges and the different values assumed for the energy dissipation in lightning flashes. As pointed out previously, the variation in the efficiency of NO<sub>x</sub> production in laboratory discharges is probably due to the differences in the current waveforms associated with these discharges. The energy dissipation in lightning flashes is a parameter that cannot be measured directly and therefore is not a good scaling quantity in NO<sub>x</sub> studies. Our estimate is free from both these drawbacks. Another interesting point of our study is the observation that most of the NO<sub>x</sub> production in lightning flashes is due to cloud flashes or the cloud portion of ground flashes. Thus, the injection of NO<sub>x</sub> by thunderstorms into the atmosphere takes place primarily at a height of 5–10 km. The theoretical studies conducted by Gallardo and Rodhe [2] show that in order to account for the nitrate deposition in the remote marine regions, the strength of the NO<sub>x</sub> source due to lightning should be about 5 Tg(N)/year and the source should be located at the cloud height. Our study confirms this inference.

## 22.8 Conclusions

The results presented in this chapter show that the NO<sub>x</sub> production efficiency of electrical discharges depends not only on the energy dissipated in the discharge but also on the shape of the current waveform. This provides an explanation for the different values of NO<sub>x</sub> molecules/J obtained by different researchers in different experiments. Thus, energy dissipated in a discharge is not suitable as the scaling

quantity for extrapolating the laboratory data to lightning flashes. In this chapter, we present a theory that can be used to evaluate the  $\text{NO}_x$  production in electrical discharges, if the discharge current is known. The results obtained are compared with the available experimental data and a good agreement is found between theory and experiment. The study shows that the primary contribution to  $\text{NO}_x$  from thunderstorms is coming from the electrical activity inside the cloud, with only a small fraction being contributed by return strokes. Using the proposed theory, we estimated the global  $\text{NO}_x$  production by lightning flashes taking into account different lightning processes such as leaders, return strokes,  $M$  components,  $K$  changes and continuing currents. The results show that the efficiency of  $\text{NO}_x$  production in ground flashes and cloud flashes are similar and for an average total channel length of 45 km the global production of  $\text{NO}_x$  by lightning flashes, based on lightning flash frequency of 100 flashes/s, is about 4 Tg(N)/year.

## Appendix 1

---

- $\eta_{str}$  – The number of  $\text{NO}_x$  molecules generated in the corona sheath during the creation of a leader channel. The current estimate is  $2 \times 10^{20}$  molecules/m.
- $\eta_{con}$  – The number of  $\text{NO}_x$  molecules generated per unit length per unit charge by a continuing current. The best estimate is  $2.0 \times 10^{20}$  molecules/m/C.
- $\eta_{lea}$  – The number of  $\text{NO}_x$  molecules generated per unit length per unit charge by the leader current flowing through the channel core. The best estimate is  $2.0 \times 10^{20}$  molecules/m/C.
- $\lambda_P$  – The decay height constant for the atmospheric pressure. This is equal to 8500 m.
- $H$  – The height of the negative charge centre. The value used in the calculations is 5000 m.
- $H_p$  – The height of the positive charge centre. The value used in the calculation is 10,000 m.
- $L$  – The total length of the horizontal sections in the cloud. Current estimates place it somewhere between 30 and 50 km.
- $\eta_{fr}$  – The number of  $\text{NO}_x$  molecules generated per unit length in a discharge channel carrying a current waveform similar to that of a typical first return stroke. The best estimate is  $5.9 \times 10^{20}$  molecules/m.
- $\eta_{sr}$  – The number of  $\text{NO}_x$  molecules generated per unit length in a discharge channel carrying a current waveform similar to that of a typical subsequent return stroke. The best estimate is  $1.4 \times 10^{20}$  molecules/m.
- $n_s$  – The number of subsequent return strokes in a typical ground flash. The best estimate is 3.
- $\eta_m$  – The number of  $\text{NO}_x$  molecules generated per unit length in a discharge channel carrying a current waveform similar to that of  $M$  component. The best estimate is  $2.0 \times 10^{20}$  molecules/m.
- $\eta_k$  – The number of  $\text{NO}_x$  molecules generated per unit length by a  $K$  change. It is assumed that  $\eta_k = \eta_m$ .
- $n_k$  – The average number of  $K$  changes taking place during the development of a given channel branch in the cloud. It is assumed to be 3.
- $n_m$  – The average number of  $M$  components in a typical ground flash. The best estimate is 5. This number is based on the fact that a ground flash with a continuing current can support about 16  $M$  components and about 30% of the ground flashes contain continuing currents.

- $k_c$  – The fraction of ground flashes containing continuing currents. The best estimate is 0.3.
- $\tau_c$  – The average duration of continuing current. The best estimate is 100 ms. This figure is actually valid for long continuing currents.
- $I_{con}$  – Magnitude of typical continuing current. The best estimate is 100 A.
- $I_{ls}$  – Magnitude of typical stepped leader current. The best estimate is 100 A.
- $I_{ld}$  – Magnitude of typical dart leader current. The best estimate is 1 kA.
- $v_s$  – The average speed of development of lightning leader channels in virgin air inside the cloud. The best estimate is  $2 \times 10^5$  m/s.
- $v_d$  – The average speed of dart leaders. The best estimate is  $10^7$  m/s.
- $n$  – The number of major branches inside the channel. The available VHF interferometric images show that it may vary from about 3 to 10. It is assumed to be 5.
- 

## References

1. Crutzen, P. J., The influence of nitrogen oxides on the atmospheric ozone content, *Quart. J. R. Met. Soc.*, vol. 96, pp. 320–325, 1970
2. Gallardo, L. and H. Rodhe, Oxidized nitrogen in the remote pacific: the role of electrical discharges over the oceans, *J. Atmos. Chem.*, vol. 26, pp. 147–168, 1997
3. Tuck, A. F., Production of nitrogen oxides by lightning discharges, *Quart. J. R. Met. Soc.*, vol. 102, pp. 749–755, 1976
4. Noxon, J. F., Atmospheric nitrogen fixation by lightning, *Geophys. Res. Lett.*, vol. 3, no. 8, pp. 463–465, 1976
5. Chameides, W. L., D. H. Stedman, R. R. Dickerson, D. W. Rusch and R. J. Cicerone, NOx production in lightning, *J. Atmos. Sci.*, vol. 34, pp. 143–149, 1977
6. Drapcho, D. L., D. Sisterson and R. Kumar, Nitrogen fixation by lightning activity in a thunderstorm, *Atmos. Environ.*, vol. 17, no. 4, pp. 729–734, 1983
7. Franzblau, E. and C. J. Popp, Nitrogen oxides produced from lightning, *J. Geophys. Res.*, vol. 94(D8), pp. 11089–11104, 1989
8. Stith, J., J. Dye, B. Ridley, P. Laroche, E. Defer, K. Baumann, G. Hübner, R. Zerr and M. Venticinque, NO signatures from lightning flashes, *J. Geophys. Res.*, vol. 104, pp. 16081–16089, 1999
9. DeCaria, A. J., K. E. Pickering, G. L. Stenchikov and L. E. Ott, Lightning-generated NOX and its impact on tropospheric ozone production: A three-dimensional modeling study of a stratosphere-Troposphere Experiment: Radiation, Aerosols and Ozone (STERAO-A) thunderstorm, *J. Geophys. Res.*, vol. 110, no. D14303, doi: 10.1029/2004JD005556, 2005
10. Cook, D. R., Y. P. Liaw, D. L. Sisterson and N. L. Miller, Production of nitrogen oxides by a large spark generator, *J. Geophys. Res.*, vol. 105, no. D6, pp. 7103–7110, 2000
11. Huntrieser, H., C. Feigl, H. Schlager, F. Schröder, C. Gerbig, P. van Velthoven, F. Flatøy, C. Théry, A. Petzold and U. Schumann, Airborne measurements of NOX, tracer species, and small particles during the European

- Lightning Nitrogen Oxides Experiment, *J. Geophys. Res.*, vol. 107, p. 4113, doi: 10.1029/2000JD000209, 2002
- 12. Zhou, Y., S. Soula, V. Pont and X. Qie, NO<sub>x</sub> ground concentration at a station at high altitude in relation to cloud-t-ground lightning flashes, *Atmos. Res.*, vol. 75, pp. 47–69, 2005
  - 13. Rahman, M., V. Cooray, V. A. Rakov, M. A. Uman, P. Liyanage, B. A. DeCarlo, J. Jerauld and R. C. Olsen, Measurements of NOX produced by rocket-triggered lightning, *Geophys. Res. Lett.*, vol. 34, no. L03816, doi:10.1029/2006GL027956, 2007
  - 14. Braginskii, S. I., Theory of the development of a spark channel, *Sov. Phys.-JEPT*, vol. 34, pp. 1068–1074, 1958
  - 15. Cooray, V. and M. Rahman, On the relationship between discharge current, energy dissipation and NO<sub>x</sub> production in spark discharges. Proc. International Conference on Lightning and Static Electricity, Seattle, Washington, 2005
  - 16. Flowers, J. L., The channel of the spark discharge, *Phys. Rev.*, vol. 64, pp. 225–239, 1943
  - 17. Higman, J. B. and J. M. Meek, The expansion of gaseous spark channels, *Proc. Phys. Soc.*, LXIII, 9-B, pp. 649–663, 1950
  - 18. Perera, C., M. Fernando, P. Liyanage, M. Rahman and V. Cooray, Correlation between current and channel diameter of long laboratory sparks, Proc. 29th International Conference on Lightning Protection, Uppsala, Sweden, 2008
  - 19. Berger, K., Methods and results of lightning records at Monte San Salvatore from 1963–1971 (in German), *Bull. Schweiz. Elektrotech.* ver., 63, pp. 21403–21422, 1972
  - 20. Fisher, R. J., G. H. Schnetzer, R. Thottappillil, V. A. Rakov, M. A. Uman and J. D. Goldberg, Parameters of triggered lightning flashes in Florida and Alabama, *J. Geophys. Res.*, vol. 98, no. 22, pp. 887–22, 902, 1993
  - 21. CIGRE, paper 63, report of the working group 01 (lightning) of study committee 33, 1991
  - 22. Nucci, C. A., G. Diendorfer, M. A. Uman, F. Rachidi, M. Ianoz and C. Mazzetti, Lightning return stroke current models with specified channel base current: A review and comparison, *J. Geophys. Res.*, vol. 95, pp. 20395–20408, 1990
  - 23. Orville, R. E., Quantitative analysis of a lightning return stroke for diameter and luminosity changes as a function of space and time, *J. Geophys. Res.*, vol. 79, pp. 4059–4067, 1977a
  - 24. Orville, R. E., Spectrum of the lightning stepped leader, *J. Geophys. Res.*, vol. 73, pp. 6999–7008, 1968a
  - 25. Orville, R., A high speed time resolved spectroscopy study of the lightning return stroke, Part I, Part II and Part III, *J. Atmos. Sci.*, vol. 25, pp. 827–856, 1968b
  - 26. Orville, R., M. A. Uman and A. M. Sletten, Temperature and electron density in long air sparks, *J. Appl. Phys.*, vol. 38, pp. 895–896, 1967
  - 27. Orville, R. E., *Lightning Spectroscopy. Lightning. Volume 1. Physics of Lightning*, R. H. Golde ed., Academic Press, London, 1977b

28. Paxton, A. H., R. L. Gardner and L. Baker, Lightning return stroke: A numerical calculation of the optical radiation, *Phys. Fluids*, vol. 29, p. 2736, 1986
29. Hill, R. D., Channel heating in return stroke lightning, *J. Geophys. Res.*, vol. 76, pp. 637–645, 1971
30. Ploooster, M. N., Numerical model of the return stroke of the lightning discharge, *Phys. Fluids*, vol. 14, pp. 2124–2133, 1971
31. Hill, R. D., R. G. Rinker, and H. Dale Wilson, Atmospheric nitrogen fixation by lightning, *J. Atmos. Sci.*, vol. 37, pp. 179–192, 1980
32. Hill, R. D., On the production of nitric oxide by lightning, *Geophys. Res. Letts.*, vol. 6, no. 12, pp. 945–947, 1979
33. Borucki, W. J. and W. L. Chameides, Lightning: Estimates of the rates of energy dissipation and nitrogen fixation, *Rev. Geophys.*, vol. 22, no. 4, pp. 363–372, 1984
34. Chameides, W. L., The role of lightning in the chemistry of the atmosphere, in *The Earth's Electrical Environment*, National Academic Press, Washington, 1986
35. Ploooster, M. N., Shock-waves from line sources. Numerical solutions and experimental measurements. *Phys. Fluids*, vol. 13, pp. 2665–2675, 1970
36. Chameides, W. L., The implications of CO production in electrical discharges, *Geophys. Res. Lett.*, vol. 6, pp. 287–290, 1979
37. Levine, J. S., R. S. Rogowski, G. L. Gregory, W. E. Howell and J. Fishman, Simultaneous measurements of NO<sub>x</sub>, NO, and O<sub>3</sub> production in a laboratory discharge: Atmospheric implications, *Geophys. Res. Lett.*, vol. 8, no. 4, pp. 357–360, 1981
38. Peyroux, R. and R-M. Lapeyre, Gaseous products created by electrical discharges in the atmosphere and condensation nuclei resulting from gaseous phase reactions, *Atmos. Environ.*, vol. 16, no. 5, pp. 959–968, 1982
39. Rehbein, N. and V. Cooray, NO<sub>x</sub> production in spark and corona discharges, *J. Electrostatics*, vol. 51–52, pp. 333–339, 2001
40. Wang, Y., A. W. DeSilva, G. C. Goldenbaum and R. R. Dickerson, Nitric oxide production by simulated lightning: Dependence on current, energy and pressure, *J. Geophys. Res.*, vol. 103, no. D15, pp. 19149–19159, 1998
41. Rahman, M., V. Cooray, R. Montano and P. Liyanage, NO<sub>x</sub> production in laboratory discharges, Proc. 29th International Conference on Lightning Protection, Uppsala, Sweden, 2008
42. Rehbein, N., Experimental studies on nitrogen oxide production from spark discharges in air, Internal Report, Institute of High Voltage Research, Uppsala University, 1999
43. Cooray, V., M. Becerra and M. Rahman, On the NO<sub>x</sub> generation in corona, streamer and low pressure electrical discharges, Accepted to be published in *Open Access Atmos. Sci. J.* 2008
44. Nicolet, M. On the production of nitric oxide by cosmic rays in the mesosphere and stratosphere, *Planet. Space Sci.*, vol. 23, pp. 637–649, 1975
45. Cooray, V., The mechanism of the lightning flash, in *The Lightning Flash*, ed. V. Cooray, pp. 127–239, Institute of Electrical Engineers, UK, 2003

46. Gallimberti, I., The mechanism of long spark formation, *J. Phys.*, vol. 40, suppl. 7, pp. 193–250, 1979
47. Les Renardières Group, Research on long air gaps discharges at Les Renardières, *Electra*, vol. 35, pp. 49–156, 1974
48. Jackman, C. H., H. S. Porter and J. E. Frederick, Upper limits on production rate of NO per ion pair, *Nature*, vol. 280, p. 170, 1979
49. Zipf, E. C. and S. S. Prasad, Evidence for new sources of NOx in the lower atmosphere, *Science*, vol. 279, pp. 211–213, 1998
50. Rahman, M. and V. Cooray, A study of NOx production in air heated by laser discharges: Effects of energy, wavelength, multiple discharges and pressure, *Optic. Laser Tech.*, vol. 40, pp. 208–214, 2008
51. Shao, X. M., P. R. Krehbiel, R. J. Thomas and W. Rison, Radio interferometric observation of cloud to ground lightning phenomena in Florida, *J. Geophys. Res.*, vol. 100, pp. 2749–2783, 1995
52. Shao, X. M. and P. R. Krehbiel, The spatial and temporal development of intracloud lightning, *J. Geophys. Res.*, vol. 101, pp. 26641–26668, 1996
53. Thomas, R. J., P. R. Krehbiel, W. Rison, S. J. Hunyady, W. P. Winn, T. Hamlin and J. Harlin, Accuracy of the Lightning Mapping Array, *J. Geophys. Res.*, vol. 109, no. D14207, doi:10.1029/2004JD004549, 2004
54. Schonland, B. F. J., The lightning discharge, in *Handbuch der Physik*, vol. 23, pp. 576–628, Springer, New York, 1956
55. Schonland, B.F.J., D. J. Malan and H. Collens, Progressive lightning, 2, *Proc. R. Soc. London, Ser. A*, vol. 152, pp. 595–625, 1935
56. Orville, R. E. and V. P. Idone, Lightning leader characteristics in the Thunderstorm Research International Program (TRIP), *J. Geophys. Res.*, vol. 87, no. C13, pp. 11,177–11,192, December 20, 1982
57. Wang D., N. Takagi and T. Watanabe, V. A. Rakov, and M. A. Uman, Observed leader and return-stroke propagation characteristics in the bottom 400 in of a rocket-triggered lightning channel, *J. Geophys. Res.*, vol. 104, no. D12, pp. 14,369–14,376, June 27, 1999
58. Idone, V. P. and R. E. Orville, Correlated peak relative light intensity and peak current in triggered lightning subsequent strokes, vol. 90, pp. 6159–6164, 1985
59. Cooray, V., P. Idone. and R.E. Orville, Velocity of a self-propagating discharge as a function of current parameters with special attention to return strokes and dart leaders, papers presented at the 1989 International Conference on Lightning and Static Electricity, pp. 1A.3.1–1A.3.9, University of Bath, England, September 26–28, 1989
60. Kodali, V., V. A. Rakov, M. A. Uman, K. J. Rambo, G. H. Schnetzer, J. Schoene and J. Jerauld, Triggered-lightning properties inferred from measured currents and very close electric fields, *Atmos. Res.*, vol. 76, no. 1–4, pp. 355–376, 2005
61. Jordan, D. M. and M. A. Uman, Variation in lightning intensity with height and time from subsequent lightning return strokes, *J. Geophys. Res.*, vol. 88, pp. 6555–6562, 1983
62. Rakov, V. A. and A. A. Dulzon, Calculated electromagnetic fields of lightning return stroke, *Tech Elektrodinam.*, vol. 1, pp. 87–89, 1987

63. Thottappillil, R., V. A. Rakov and M. A. Uman, Distribution of charge along the lightning channel: Relation to remote electric and magnetic fields and to return-stroke models, *J. Geophys. Res.*, vol. 102, pp. 6987–7006, 1997
64. Thottappillil, R., J. D. Goldberg, V. A. Rakov, M. A. Uman, R. J. Fisher and G. H. Schnetzer, Properties of M components from currents measured at triggered lightning channel base, *J. Geophys. Res.*, vol. 100, pp. 25711–25720, 1995
65. Rakov, V. and M. Uman, *Lightning Physics and Effects*, Cambridge University Press, Cambridge, UK, 2003
66. Saba, M. M. F., O. Pinto Jr. and M. G. Ballarotti, Relation between lightning return stroke peak current and following continuing current, *Geophys. Res. Lett.*, vol. 33, pp. l23807, doi:10.1029/2006gl027455, 2006
67. Idone, V. P., The luminous development of Florida triggered lightning, *Res. Lett. Atmos. Electr.*, vol. 12, pp. 23–28, 1992
68. Rakov, V. A., M. A. Uman, K. J. Rambo, G. H. Schnetzer and M. Miki, Triggered-Lightning Experiments Conducted in 2000 at Camp Blanding, Florida, (Abstract), *Eos Trans. Suppl., AGU*, vol. 81, no. 48, Nov. 28, p. F90, 2000
69. Laroche, P., E. Defer, P. Blanchet and C. Thery, Evaluation of NO<sub>x</sub> produced by storms based on 3D VHF lightning mapping, ICAE 99 – 11th Int. Conf. On Atmospheric Electricity, Huntsville, AL(USA), June 07–11, 1999
70. Proctor, D. E., Lightning flash with high origins, *J. Geophys. Res.*, vol. 102, pp. 1693–1706, 1997
71. Proctor, D. E., VHF radio pictures of cloud flashes, *J. Geophys. Res.*, vol. 86, pp. 4041–4071, 1981
72. Proctor, D. E., Regions where lightning flashes began, *J. Geophys. Res.*, vol. 96, pp. 5099–5112, 1991
73. Lojou, J. Y. and K. L. Cummins, On the representation of two- and three-dimensional total lightning information. Conf. on Meteorological Applications of Lightning Data, San Diego, Cal., Amer. Meteor. Soc., paper 2.4 (2005)
74. Lojou, J. Y., M. J. Murphy, R. L. Holle and N. W. S. Dimetriades, Nowcasting of thunderstorms using VHF measurements, in Lightning: Principles, Instruments and Applications, eds. D. Betz, U. Schumann and P. Laroche, Springer, the Netherlands, 2008.
75. Coleman, L. M., T. C. Marshall, M. Stolzenburg, T. Hamlin, P. R. Krehbiel, W. Rison and R. J. Thomas, Effects of charge and electrostatic potential on lightning propagation. *J. Geophys. Res.*, vol. 108, p. 4298, doi: 10.1029/2002JD002718, 2003
76. Morimoto, T., Z. Kawasaki and T. Ushio, Lightning observations and consideration of positive charge distribution inside thunderclouds using VHF broadband digital interferometry, *Atmos. Res.*, vol. 76, no. 1–4, pp. 445–454, 2005
77. Gallardo, L. and V. Cooray, Could cloud-to-cloud discharges be as effective as cloud-to-ground discharges in producing NO<sub>x</sub>?, *Tellus, Ser B*, vol. 48, pp. 641–651, 1996

78. Dye, J. E., *et al.*, An overview of the Stratospheric – Tropospheric Experiment: Radiation, Aerosols and Ozone (STERAO) – Deep convection experiment with results for the July 10, 1996 storm, *J. Geophys. Res.*, vol. 105, pp. 10023–10045, 2000
79. DeCaria, A. J., E. Pickering, G. L. Stenchikov, J. R. Scala, J. L. Stith, J. E. Dye, B. A. Ridley and P. Laroche, A cloud scale model study of lightning-generated NO<sub>x</sub> in an individual thunderstorm during STERAO-A, *J. Geophys. Res.*, vol. 105, pp. 11601–11616, 2000
80. Turman, B. N. and B. C. Edgar, Global lightning distribution at dawn and dusk, *J. Geophys. Res.*, vol. 87, pp. 1191–1206, 1982
81. Christian, H. J., R. J. Blakeslee, D. J. Boccippio, W. L. Boeck, D. E. Buechler, K. T. Driscoll, S. J. Goodman, J. M. Hall, W. J. Koshak, D. M. Mach and M. F. Stewart, Global frequency and distribution of lightning as observed from space by the Optical Transient Detector, *J. Geophys. Res.*, vol. 108, no. D1, p. 4005, doi:10.1029/2002JD002347, 2003
82. Lee, D. S., I. Köhler, E. Grobler, F. Rohrer, R. Sausen, L. Gallardo-Klenner, J. G. J. Olivier, F. J. Dentener and A. F. Bouwman, Estimation of global NO<sub>x</sub> emissions and their uncertainties, *Atmos. Environ.*, vol. 31, pp. 1735–1749, 1997



---

## *Chapter 23*

# **High energetic radiation from thunderstorms and lightning**

*Joseph R. Dwyer<sup>1</sup> and Hamid K. Rassoul<sup>1</sup>*

---

### **23.1 Introduction**

Because air typically has a non-zero conductivity, when strong electric fields are applied in our atmosphere, electrical currents will flow in a manner that discharges the field. Without additional charges being supplied, the field will eventually disappear. Exactly how the field is discharged depends upon the magnitude and geometry of the applied electric field, the temperature, the density and humidity of the air, the recombination rate of ions, the flux of ionizing radiation and the presence of metal electrodes or other objects in the air such as ice or water particles. The most common and familiar form of electrical discharge in air involves the production of low-energy (few eV) electrons through the collision of electrons with air atoms. Specifically, as free electrons move in an applied electric field, they may gain enough energy to liberate other electrons by impact ionization of air atoms. These new electrons may then do the same, creating even more free electrons and so on. If new free electrons are created at a rate faster than the rate at which electrons are lost through attachment to air and recombination with ions, then the number of free electrons will grow exponentially with time, resulting in an avalanche of electrons that moves opposite the direction of the electric field vector (due to the electron's negative charge). This avalanche growth occurs at a threshold of approximately 3 million V/m at sea level, called the conventional breakdown field (Raether, 1964). Below the conventional breakdown field, according to this scenario, few free electrons are generated. Above the conventional breakdown field, the number of free electrons and hence the conductivity grows rapidly. As a result, it is difficult to maintain an electric field above the convention breakdown field. Often times, the air responds by generating a spark, a hot channel that carries most of the current. Lightning also involves electrical currents flowing along hot channels. How these hot channels form is not completely clear, but it is generally believed that at some place and time the electric field in air had to exceed the conventional breakdown

<sup>1</sup>Department of Physics and Space Sciences, Florida Institute of Technology, Melbourne, FL 32901, USA

field (Rakov and Uman, 2003). One of the biggest puzzles in the atmospheric sciences involves understanding the conditions that occur when lightning initiates. Specifically, how and where do the large electric fields form that initiate lightning.

The reason that lightning initiation is so puzzling is that decades of *in situ* measurements of thundercloud electric fields have failed to find electric fields near the conventional breakdown field (MacGorman and Rust, 1998). The conventional breakdown field, in fact, decreases with air density and can be written as  $E_b \cong 3.0 \times 10^6 \text{ V/m} \times n$ , where  $n$  is the density of air relative to that at sea level. Even taking into account the reduced density of air at thundercloud altitudes, the measured thundercloud fields still appear to be too low by about a factor of 10. It is possible that the presence of hydrometeors (e.g. rain or hail) inside thunderclouds assists in the initiation of lightning by locally enhancing the fields near their surfaces, thereby allowing electron avalanches to form and somehow resulting in a hot channel. However, exactly how this might occur in reality has not yet been fully worked out and so is an active area of research.

Another interesting and perhaps related puzzle is the observed emissions of x-rays and gamma-rays from thunderclouds and lightning. Many independent observations show that lightning emits bright bursts of x-rays up to a few MeV in energy and thunderclouds emit gamma-ray flashes up to many tens of MeV. However, the conventional breakdown process that we described above involves only low-energy electrons with little more than 10 eV or so of kinetic energy. As a result, conventional breakdown should not produce any high-energy radiation, certainly not MeV gamma-rays. Even the hot lightning channel only reaches approximately 30,000 K, much too cold to make even soft x-rays, and billions of degrees too cold to produce the observed gamma-rays thermally (Uman, 2001). As a result, there must be other processes at work to generate the high-energy emissions. In this chapter, we shall discuss these processes and how they may be applicable to thunderstorms, lightning and laboratory sparks.

## 23.2 Observations

We shall begin with a brief overview of the measurements of energetic radiation produced in our atmosphere. In Section 23.2, we shall introduce the mechanisms that may explain this radiation. Our purpose here is not to provide a comprehensive review of all observations and experiments in this field. Instead, we wish to provide the reader with some of the key measurements that highlight the basic processes involved. In particular, we shall not discuss many of the early observations made over the last 70 years. Instead, we refer the interested reader to Suszynsky, Roussel-Dupré and Shaw (1996), which provides a useful review.

It has been known for about 100 years that high-energy radiation exists in our atmosphere. Although some of this radiation comes from radioactive decays from elements such as radon, most comes from galactic cosmic rays impinging on our atmosphere from space (Hillas, 1972). At sea level, most of these energetic particles are secondary muons and electrons with a flux of a few hundred per square

metre per second. At thundercloud altitudes, the flux is about 100 times higher and most of the charged particles are electrons and positrons. The flux of these cosmic rays varies somewhat depending upon the solar cycle, solar activity and the geographic location. Furthermore, the natural background rate of energetic radiation may increase when it rains or snows due to the washout of atmospheric radioactive particles produced by radon decays (Foote and Frick, 2001). All of these fluctuations, however, are relatively modest and are well understood.

In 1994, BATSE, onboard the Compton Gamma-Ray observatory (CGRO), observed intense millisecond-long bursts of gamma-rays emanating from the earth's atmosphere (Fishman *et al.*, 1994). These bursts, which were named terrestrial gamma-ray flashes (TGFs), were later found to be produced by thunderstorms at altitudes below 21 km (Cummer *et al.*, 2005; Dwyer and Smith, 2005; Carlson *et al.*, 2007). The only viable mechanism for generating such gamma-rays is bremsstrahlung interactions of energetic electrons with air. Specifically, when an MeV electron collides with an atomic nucleus, the rapid acceleration of the electron in the coulomb field of the nucleus causes an energetic photon to be emitted. Monte Carlo computer simulations that take into account the propagation of gamma-rays through the atmosphere, including Compton scattering, photoelectric absorption and pair-production, showed that there must be about  $10^{17}$  high-energy (MeV) electrons present inside or just above the thundercloud in order to generate the number of gamma-rays measured  $>600$  km away in space. This is a very large number of energetic electrons. Considering that they were produced in less than 1 ms, the duration of the TGF, the fluence (number per square metre) of the energetic electrons must have been at least 10 billion times higher than the fluence of the cosmic-ray particles that were passing through the thundercloud. If an aircraft were struck by such a TGF at the source, the radiation dose received by individuals inside the aircraft could be significant (Dwyer *et al.*, 2010). In fact, TGFs are so bright that spacecrafts designed to measure powerful x-ray and gamma-ray bursts from the sun and astrophysical sources often experience large dead-times (i.e. saturation) during TGFs (Grefenstette *et al.*, 2008; Gjesteland *et al.*, 2010).

Later it was found that a subset of the observed TGFs were actually high-energy electron beams generated by Compton scattering and pair-production from the TGF gamma-rays in the upper atmosphere (Dwyer *et al.*, 2008; Cohen *et al.*, 2010). These terrestrial electron beams (TEBs), which follow the geomagnetic field line in the inner magnetosphere, may be observed thousands of kilometres away and sometimes contain large numbers of positrons (Briggs *et al.*, 2011), illustrating some of the interesting phenomena associated with TGFs.

Currently, TGFs are thought to be produced inside thunderclouds during the initial stage of upward positive intra-cloud (IC) lightning (Inan *et al.*, 1996; Stanley *et al.*, 2006; Lu *et al.*, 2010; Shao *et al.*, 2010; Connaughton *et al.*, 2010; Lu *et al.*, Cummer *et al.*, 2011). How lightning is related to TGF production is not clear, nor is it well understood why some lightning produces TGFs and many others do not (Splitt *et al.*, 2010; Smith *et al.*, 2011).

In addition to the spacecraft observations, x-rays and gamma-rays have been found to be emitted by thunderclouds using both *in situ* and ground-based

observations (Shaw, 1967; Whitmore, 1979; Parks *et al.*, 1981; McCarthy and Parks, 1985; Eack *et al.*, 1996a, 1996b; Brunetti *et al.*, 2000; Tsuchiya *et al.*, 2007; Chilingarian *et al.*, 2010, 2011). These emissions often take the form of ‘surges’ or ‘glows’ that can last seconds to minutes. Many of these observations show energy spectra similar to TGFs, which extend into the multi-MeV range, indicating similar source mechanisms. However, the flux of these gamma-rays is generally many orders of magnitude lower than the flux of gamma-rays in TGFs. Two events that did have TGF-like fluxes were a ground-based observation of a TGF-like burst seen at sea level in Florida (Dwyer *et al.*, 2004a) and an observation of a TGF by the ADELE instrument onboard an NCAR-NSF Gulfstream-V aircraft (Smith *et al.*, 2011). Both of these events appeared to be very similar to the TGFs observed from space.

Another source of energetic radiation in our atmosphere is associated with lightning leaders (Moore *et al.*, 2001; Dwyer *et al.*, 2003). Indeed, x-rays are now routinely measured from natural cloud-to-ground and rocket-and-wire-triggered lightning. In a series of experiments beginning in 2002 at the University of Florida/Florida Tech International Center for Lightning Research and Testing (ICLRT) at Camp Blanding, FL, it was found that lightning produces significant x-ray emission up to about an MeV during the stepped-leader phase of natural lightning and during the dart-leader phase of natural and rocket-and-wire-triggered lightning, with the most intense emission often detected immediately before the return stroke during the attachment process (Dwyer *et al.*, 2004; Dwyer *et al.*, 2005a; Howard *et al.*, 2008; Saleh *et al.*, 2009; Howard *et al.*, 2010). The x-rays are usually observed to arrive in short ( $<1\ \mu\text{s}$ ) bursts in coincidence with the step formation of the stepped-leaders and dart-stepped leaders.

Long laboratory sparks in air at 1 atmosphere pressure also have been found to emit x-rays, with characteristics very similar to those found in lightning discharges (Dwyer *et al.*, 2005b; Dwyer *et al.*, 2008; Rahman *et al.*, 2008; Nguyen, van Deursen and Ebert, 2008; March and Montanyà, 2010; March and Montanyà, 2011). However, unlike the TGFs and some thundercloud emissions, the energy spectra of x-rays from lightning and laboratory sparks only extend up to an MeV or so, indicating a different mechanism for the production of the runaway electrons (Dwyer, 2004).

We note that in this chapter and often in the literature the names ‘x-ray’ and ‘gamma-ray’ are used interchangeably. Technically, all of the energetic photons under consideration here are x-rays, since they are emitted by energetic electrons via the bremsstrahlung process. The name ‘gamma-ray’ is sometimes reserved for photons emitted during nuclear processes. However, we instead follow the astrophysics convention of calling the photons in the MeV range gamma-rays and photons in the keV range x-rays, regardless of the mechanism that produced them (in astrophysics this is not always known). A confusing exception occurs when discussing TGFs: all of the TGF photons are usually called gamma-rays, even the lower-energy ones in the keV range, since the TGFs were first observed by a gamma-ray experiment.

Finally, we wish to point out that there exists a growing body of literature on the production and detection of neutrons from thunderclouds and lightning. It is possible that these neutrons are a natural by-product of the energetic processes

discussed in this chapter. However, more work is needed on this topic. We shall refer the interested reader to the review paper by Milikh and Roussel-Dupré (2010) and the references therein regarding neutrons.

### 23.3 Runaway electrons

In 1925, C. T. R. Wilson showed that for sufficiently strong electric fields, electrons could gain large energies from the field (Wilson, 1925). Specifically, when the rate that an electron gains energy from the field exceeds the rate at which it loses energy, predominately through ionization energy losses, then the electron will gain energy and is said to ‘run away.’ The electric field at which this happens is about  $2.8 \times 10^5 \text{ V/m} \times n$ , where  $n$  is the density of air with respect to that at sea level. This field is about a factor of 10 below the conventional breakdown field and is comparable to maximum fields seen inside thunderclouds. This is illustrated in Figure 23.1, which shows that rate of energy loss of an energetic electron moving in air (effective frictional force). The plot also shows that rate of energy gain from a strong electric field (horizontal line). As can be seen, when the electrons have energies above a threshold,  $K_{th}$ , then they may run away. However, below  $K_{th}$ , they will lose energy and so will not run away. Therefore, in order to generate a runaway electron, an energetic ‘seed’ electron with energy above  $K_{th}$  must be provided from an external source. An exception to this rule occurs when the electric field is increased above the critical field,  $E_c$ , above the energy loss curve for all kinetic energies. In this case, all free electrons may run away, and, in particular, the thermal population created at low energies may run away. This mechanism is usually called ‘cold runaway’ or sometimes ‘thermal runaway,’ and does not require any external seed particles (Gurevich, 1961; Moss *et al.*, 1996). As we will discuss below, cold runaway may be important for lightning leader x-ray emissions.

According to Wilson’s original work, the energetic seeds that result in runaway electrons are all provided by external sources such as cosmic rays. Therefore, for each atmospheric cosmic-ray electron that arrives, at most one runaway electron may be generated. Although a runaway electron may gain energy and travel farther than the seed particle that it came from, this mechanism will not produce large fluxes of runaway electrons, especially the large fluxes known to be associated with TGFs. On the other hand, it is possible for cold runaway to provide the energetic seeds, which subsequently experience additional energy gain via Wilson’s mechanism. This combination could potentially explain TGFs, as will be discussed below.

In 1992, Gurevich, Milikh and Roussel-Dupré showed that when Møller scattering (electron–electron elastic scattering) is included, the runaway electrons described by Wilson will also undergo avalanche multiplication, resulting in a large number of relativistic runaway electrons for each energetic seed electron injected into the high-field region (Gurevich *et al.*, 1992). Interestingly, based upon Wilson’s research notes, Williams (2010) argued that Wilson was aware of runaway electron avalanche multiplication, referring to it as a ‘snowball effect.’ This

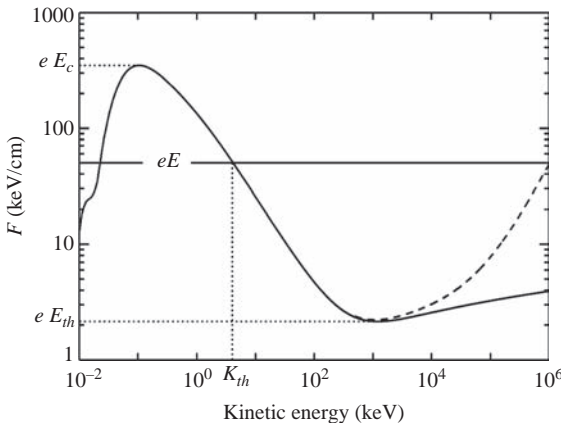


*Figure 23.1* The effective frictional force experienced by a free electron moving through air at STP as a function of kinetic energy. The solid curve is due to inelastic scattering of the electron by air molecules, and the dashed curve indicates the effects of bremsstrahlung emission. The horizontal line shows the electric force from a  $5.0 \times 10^6$  V/m electric field. Runaway electrons occur for kinetic energies greater than the threshold energy,  $K > K_{th}$ . In the figure,  $E_c$  is the critical electric field strength for which low-energy thermal electrons will run away, and  $E_{th}$  is the minimum field needed to produce relativistic runaway electrons [from Dwyer (2004)]

avalanche mechanism is commonly referred to as the relativistic runaway electron avalanche (RREA) mechanism (Babich *et al.*, 1998, 2001). In addition, a hypothesized electrical breakdown of air generated by RREAs has been named ‘runaway breakdown’ (Gurevich and Zybin, 2001). Specifically, several authors have claimed that a RREA acting on cosmic rays results in a large enough conductivity increase to result in an electrical breakdown. Recently, Dwyer and Babich (2011) have challenged these conductivity calculations and argued against the use of the term ‘runaway breakdown,’ since RREA is not really an electrical breakdown as the term is usually used.

In 2003, Dwyer introduced a new mechanism that involves positive feedback effects from positrons and energetic photons. In this mechanism, illustrated in Figure 23.2, avalanches of runaway electrons emit bremsstrahlung x-rays that may either Compton backscatter or pair-produce in air. If the backscattered photons propagate to the start of the avalanche region and produce other runaway electrons, either via Compton scattering or photoelectric absorption, then a secondary avalanche is created. Alternatively, the positrons created by pair-production often turn around in the ambient electric field and run away in the opposite direction of the electrons. The positrons are relativistic, allowing them to travel for many hundreds of metres before annihilating. If these positrons propagate to the start of the avalanche region they can produce additional runaway electrons via hard elastic

scattering with atomic electrons in the air (i.e. Bhabha scattering), thereby producing secondary avalanches. These secondary avalanches can in turn emit more x-rays than Compton scatter or pair-produce, resulting in more feedback and more avalanches. This positive feedback effect allows the runaway discharge to become self-sustaining, no longer requiring an external source of energetic seed electrons. As a result of this positive feedback, the number of runaway electron avalanches increases exponentially on a timescale measured in microseconds.

The two principal feedback mechanisms, which shall be referred to as x-ray feedback (also called gamma-ray or photon feedback) and positron feedback, were originally described by Dwyer (2003), who also used a Monte Carlo simulation to calculate the electric field thresholds necessary for feedback to be important (also see Babich *et al.*, 2005). In addition, second-order feedback effects can occur such as feedback from bremsstrahlung x-rays emitted from the backward-propagating positrons, and feedback from the 511 keV gamma-rays emitted by the annihilating positrons (Dwyer, 2007). To distinguish the feedback mechanisms described here, which involve high-energy particles, from the low-energy feedback mechanisms occurring in ordinary Townsend gas discharges, these feedback mechanisms, described above are jointly referred to as relativistic feedback (RF) (Dwyer, 2007).

Because the discharge currents generated by RF grow exponentially on very short timescales, the electric field will be discharged very quickly, regardless of the charging currents. As a result, RF describes a new internal state of the system, a self-sustained discharge that does not rely upon externally supplied particles. Once RF starts, the electric field will always at least partially discharge, and so this may be considered a novel form of electrical breakdown. Indeed, Dwyer (2003) showed that large electric fields are highly unstable due to RF, sometimes referred to as the Dwyer instability. RF is important both because it may naturally explain very large fluxes of energetic electrons and gamma-rays, and because it also severely limits the electric field regimes in which alternative mechanisms (i.e. runaway breakdown) may operate.

Table 23.1 summarizes the three mechanisms that produce relativistic runaway electrons as discussed above. The table includes the new feature in each mechanism that is added to the previous mechanism, and includes the increase in the number of energetic electrons that results. For Wilson's runaway electrons, the previous mechanism is the ambient atmospheric cosmic rays. The time for the electric field to discharge due to the increase in conductivity from ionization is also listed. In addition, cold runaway is important in that it provides seed particles for Wilson's runaway electrons and RREA and so is treated as a fourth runaway electron generating mechanism.

## 23.4 Monte Carlo simulations

Monte Carlo simulations are a useful tool for modeling runaway electron physics, including the production and propagation of x-rays and gamma-rays and the

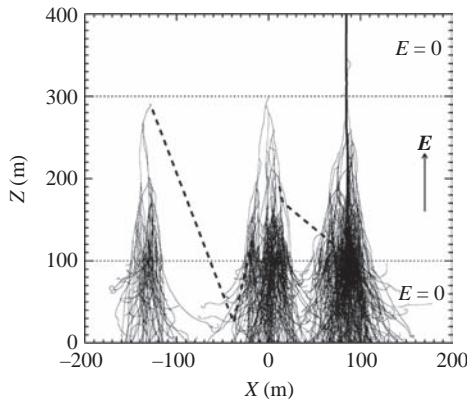


**Figure 23.2** The RF mechanism. Partial results of the Monte Carlo simulation are shown. The light tracks are the runaway electrons, the dashed lines are the x-rays and the dark track is a positron. The entire avalanche is initiated by one, 1 MeV, seed electron injected at the top centre of the volume. The horizontal dotted lines show the boundaries of the electric field volume ( $E = 1000 \text{ kV/m}$ ). For clarity, only a small fraction of the runaway electrons and x-rays produced by the avalanche are plotted. The avalanches on the left and right illustrate the x-ray feedback and positron feedback mechanisms, respectively [from Dwyer (2003)]

positron and x-ray feedback mechanisms. Monte Carlo codes are used to extract many of the fundamental quantities that describe runaway electrons, including avalanche lengths and times, lateral and longitudinal diffusion coefficients for the runaway electrons, positron production rates and feedback rates. For any given electric and magnetic field configuration, including time-varying fields, Monte Carlo simulations can accurately calculate the production of all of the energetic particles that result. These calculations have been successfully compared with TGF observations to determine properties of the TGFs. On the other hand, because Monte Carlo codes are only capable of simulating a limited number of energetic particles (e.g. up to a million or so), these simulations are not well suited to model changes in the electric field that results from the ionization caused by the energetic particles. In other words, Monte Carlo simulations usually do not describe the electric and magnetic fields self-consistently. Instead, the field must be prescribed externally. In order to simulate the changes to the field that result from the runaway discharge, the runaway electrons are usually modeled using a separate transport code that simulates the propagation of the particles as a whole, not modeling every individual particle. The Monte Carlo simulations, in this case, are useful for providing the parameters used by the transport code, such as diffusion coefficients, runaway avalanche propagation speeds and avalanche times (Dwyer, 2005).

Table 23.1 Mechanisms for generating relativistic runaway electrons

Name	Reference	New feature	Increase in energetic electrons	Discharge time
Runaway electron	Wilson (1925)	Electron energy gain from electric field	$\times 1$	~ hours
Relativistic runaway electron avalanche (RREA)	Gurevich <i>et al.</i> (1992)	Møller scattering	Up to $\times 10^5$	~ 10 s
Relativistic feedback	Dwyer (2003)	Backward-propagating runaway positrons and Compton scattered x-rays	Up to $\times 10^{13}$	< 1 ms

One productive Monte Carlo code was developed at Florida Tech in 2002 by J. R. Dwyer (Dwyer, 2003, 2004, 2005, 2007, 2008, 2009, 2010; Coleman and Dwyer, 2006; Saleh *et al.*, 2009; Dwyer and Babich, 2011). This Monte Carlo simulation of relativistic runaway electron avalanches is capable of modeling the development and propagation of runaway electron avalanches in any gaseous medium for both spatially and time-varying electric and magnetic fields. This simulation includes, in an accurate form, all the important interactions involving runaway electrons, positrons, x-rays and gamma-rays. These interactions include energy losses through ionization and atomic excitation, bremsstrahlung and Møller scattering. The simulation fully models elastic scattering using a shielded-Coulomb potential and includes bremsstrahlung production of x-rays and gamma-rays and the subsequent propagation of the photons, including photoelectric absorption, Rayleigh scattering, Compton scattering and pair-production. In addition, the simulation includes positron propagation (and annihilation) and the generation of energetic seed electrons via Bhabha scattering of positrons and via Compton scattering and photoelectric absorption of energetic photons.

In practice, the Monte Carlo code propagates the electrons and positrons in successive small time steps. During each step, the forces acting on the particles from the electric and magnetic fields plus the effective frictional force from the ionization energy loss and atomic excitations are found. The relativistic equations of motion are then solved using a 4th order Runge–Kutta method. During each time step, the probability of interactions such as electron–electron elastic scattering, elastic scattering with the atomic nuclei, and bremsstrahlung interactions, are calculated from the relevant cross-sections. A random number generator is then used to determine if the particles actually undergo each interaction for that time step based upon these probabilities. If an interaction does occur, the interaction cross-section and relativistic kinematics are used to calculate the momentum and energy changes that result from the interaction and the production of either secondary electrons or bremsstrahlung photons. These secondary particles are then added to

the Monte Carlo and simulated along with the original particles. For electrons and positrons, we are often only interested in the particles that are involved in the runaway electron avalanches and so electrons below the threshold energy  $K_{th}$  are usually discarded to save computational time.

Because Monte Carlo simulations include all of the relevant physics in their calculations, a description of the important runaway electron physics describes the ingredients of Monte Carlo code as well. For electrons moving through air with kinetic energies above a few hundred eV, most of the energy loss goes into ionizing the air, with a smaller amount going into atomic excitations. The ionization/atomic excitation energy losses per unit length along the path of the energetic particle are well described by the famous Bethe equation (Bethe and Ashkin, 1953)

$$F_b(\varepsilon') \equiv -\frac{d\varepsilon'}{dx} = \frac{2\pi N_{air} Z r_e^2 m c^2}{\beta'^2} \times \left[ \ln\left(\frac{m^2 c^4 (\gamma'^2 - 1)(\gamma' - 1)}{I^2}\right) - \left(1 + \frac{2}{\gamma'} - \frac{1}{\gamma'^2}\right) \ln 2 + \frac{1}{\gamma'^2} + \frac{(\gamma' - 1)^2}{8\gamma'^2} - \delta_{den}(\gamma') \right] \quad (23.1)$$

where  $N_{air}$  is the number density of the gas atoms ( $N_{air} = 5.39 \times 10^{25} \text{ m}^{-3}$  for air at sea level);  $Z$  is the average atomic number of the gas atoms ( $Z = 7.26$  for air);  $r_e = 2.818 \times 10^{-15} \text{ m}$  is the classical electron radius;  $mc^2 = 511 \text{ keV}$  is the rest energy of an electron;  $\beta' = \nu'/c$ , and  $\gamma' = 1/\sqrt{1 - \beta'^2}$  is the Lorentz factor of the energetic electron;  $I$  is the effective ionization potential (e.g.  $I = 85.7 \text{ eV}$  for air) and  $\delta_{den}$  is a small correction due to the density effect. Equation 23.1 is accurate above a few hundred eV and agrees with the curve in Figure 23.1 for these energies.

As the energetic electrons move through air, some of the secondary electrons are produced with substantial energies. The production of secondary electrons is described by Møller scattering (electron–electron elastic scattering), given by the cross-section (Berestetskii *et al.*, 1982)

$$\frac{d\sigma_{Moller}}{d\varepsilon} = \frac{2\pi r_e^2 m c^2}{\beta'^2} \left[ \frac{(\gamma' - 1)^2 m^2 c^4}{\varepsilon^2 (mc^2(\gamma' - 1) - \varepsilon)^2} - \frac{(2\gamma'^2 + 2\gamma' - 1)}{\varepsilon (mc^2(\gamma' - 1) - \varepsilon) \gamma'^2} + \frac{1}{m^2 c^4 \gamma'^2} \right] \quad (23.2)$$

where  $\varepsilon$  is the kinetic energy of the scattered atomic electron and  $\beta'$  and  $\gamma'$  are the speed divided by  $c$  and Lorentz factor of the incident electron.

Because the energy losses from Møller scattering are explicitly modeled in the Monte Carlo simulation, these losses should not also be included in the ionization

energy loss  $F_b$ . Following Lehtinen *et al.* (1999), this is remedied by subtracting the quantity

$$\begin{aligned} F_{\text{Moller}} &= N_{\text{air}} Z \int_{\varepsilon_{\min}}^{mc^2(\gamma' - 1)/2} \varepsilon \frac{d\sigma_{\text{Moller}}}{d\varepsilon} d\varepsilon \\ &= \frac{2\pi N_{\text{air}} Z r_e^2 mc^2}{\beta'^2} \left[ \ln\left(\frac{mc^2(\gamma' - 1)}{2\varepsilon_{\min}}\right) + 1 - \frac{\varepsilon_{\min}}{(mc^2(\gamma' - 1) - \varepsilon_{\min})} \right. \\ &\quad \left. - \left(1 + \frac{2}{\gamma'} - \frac{1}{\gamma'^2}\right) \ln\left(\frac{2(mc^2(\gamma' - 1) - \varepsilon_{\min})}{mc^2(\gamma' - 1)}\right) + \frac{(\gamma' - 1)^2}{8\gamma'^2} - \frac{\varepsilon_{\min}^2}{2m^2c^4\gamma'^2} \right] \end{aligned} \quad (23.3)$$

from the energy loss rate (23.1) when calculating the effective frictional force (energy loss rate):

$$F_{\text{eff}} = F_b - F_{\text{Moller}} \quad (23.4)$$

In (23.3), the upper limit of the integration comes from the maximum energy for an indistinguishable secondary electron during the scattering process.

When photons are emitted via bremsstrahlung, the photon propagation involves four principle interactions: photoelectric absorption, Compton Scattering, pair-production and Rayleigh scattering. At high energies, Compton scattering is well described by the famous Klein–Nishina formula. At intermediate energies, coherent scattering becomes important and tabulated values are used. Tabulated values for the cross-sections for photoelectric absorption and pair-production are also used. Rayleigh scattering is calculated using the standard cross-sections for this process. In all cases, when secondary electrons or positrons are created from the basic interactions described above, their emission angle is calculated using the kinematics of the interaction and the new electrons and positrons are then added to the simulation.

The positrons created via pair-production are simulated by the Monte Carlo in a manner similar to the simulation of the runaway electrons. The ionization energy loss equation is modified slightly and the Møller scatter cross-section is replaced with the Bhabha scattering cross-section. In practice, the propagation of the runaway positrons looks very similar to that of electrons, with the exception that avalanches of runaway positions are not produced like the avalanches of electrons. On the other hand, the positions generate energetic secondary electrons that spawn new runaway electron avalanches; this is the positron feedback process. As positrons are propagated, the annihilation cross-section is used to determine if the positrons annihilate with atomic electrons. The runaway positrons are very energetic, reaching many tens of MeV and so the annihilation cross-section for the positrons is small, allowing the positrons to travel on the order of a kilometre at sea level before annihilating. When the positrons do annihilate, the two annihilation gamma-rays are added to the simulation.

In the Monte Carlo simulations described above, elastic scattering of the runaway electrons (and runaway positrons) with atoms with atomic number  $Z$  are calculated using the shielded-Coulomb potential

$$V(r) = \frac{Ze}{4\pi \varepsilon_0 r} \exp(-r/a) \quad (23.5)$$

where in this equation  $r$  is the spherical radius. This potential is an approximate expression for the potential derived from the Thomas–Fermi model of the atom when  $a = 183.8\lambda Z^{-1/3}$  (Mott and Massey, 1965), where  $\lambda$  is the Compton wavelength. As already discussed, elastic scattering of the runaway electrons with the individual atomic electrons (Møller scattering) is also included in the simulation.

As derived in Dwyer (2007), the elastic scattering differential cross-section per solid angle is given by

$$\frac{d\sigma}{d\Omega} = \frac{1}{4} \left( \frac{Zr_e}{\beta^2 \gamma} \right)^2 \cdot \frac{(1 - \beta^2 \sin^2(\theta/2))}{(\sin^2(\theta/2) + \hbar^2/4p^2a^2)^2} \quad (23.6)$$

where all the symbols have their usual meaning. The Monte Carlo simulation fully models the runaway electron propagation by allowing electrons and positrons to scatter according to this cross-section. Accurately modeling this elastic scattering is very important, because it results in the electrons being scattered off the electric field lines, affecting the rate of energy gain, and it causes spatial diffusion of the runaway electrons as the avalanche propagates. The latter reduces the maximum conductivity produced by a runaway electron avalanche, affecting models of lightning initiation (Dwyer, 2010).

## 23.5 Energy spectrum

An important characteristic of runaway electron avalanches is their steady-state energy spectrum. After runaway electron avalanches move more than a few avalanche lengths, the energy spectrum approaches a steady-state configuration. Although the number of runaway electrons grows exponentially, as the avalanche continues, the overall shape of the energy spectrum does not change. The reason is that as individual electrons gain energy, they always create new lower-energy electrons via Møller scattering, resulting in an exponential energy spectrum.

The runaway electron energy distribution (spectrum) in an avalanche may be described by the approximate equation

$$\frac{f_{re}}{\tau_{re}} = -\frac{d}{d\varepsilon} (b(\varepsilon)f_{re}) + N_{air}Z \int_{\varepsilon}^{\infty} \frac{d\sigma_{Moller}}{d\varepsilon'} v' f_{re} d\varepsilon' \quad (23.7)$$

where  $b(\varepsilon) = d\varepsilon/dt$  is the average rate of change of the energy of the electrons;  $f(\varepsilon, t) = dN/d\varepsilon$  is the number of electrons per unit energy (Ginzburg and

Syrovatskii, 1964); and  $\tau_{re}$  is the runaway electron avalanche time. The first term on the right side describes the rate of change in the number of electrons due to energy loss or gain. The second term on the right describes the creation of new electrons due to Møller scattering.

Although runaway electrons may propagate for energies above  $K_{th}$  (see Figure 23.1), in practice, many electrons that have energies only slightly above this threshold do not run away due to scattering processes. Instead, we may define the boundary energy,  $\varepsilon_b$ , at which point as many electrons gain energy as lose energy. This boundary energy is usually a few times larger than  $K_{th}$ , found from Figure 23.1 (Dwyer and Babich, 2011). Starting with (23.7), for  $\varepsilon \gg \varepsilon_b$ , the electrons runaway in a direction opposite the applied electric field vector, resulting in a field-aligned beam. Therefore,  $b(\varepsilon) \approx v(eE - F_b)$ . For relativistic electrons,  $F_b(\varepsilon) = F_d \approx 276 \text{ keV}/m \times n$ , and  $v = 0.89c$ , where  $F_d$  is the average energy loss rate, which is approximately constant for relativistic particles. If we consider energies that are high enough above  $\varepsilon_b$  so that most of the new electrons are injected below that energy, then (23.7) becomes

$$\frac{f_{re}}{\lambda} = -(eE - F_d) \frac{df_{re}}{d\varepsilon} \quad (23.8)$$

where  $\lambda = v\tau_{re}$ . The solution to this equation is

$$f_{re} = f_0 \exp\left(\frac{-\varepsilon}{(eE - F_d)\lambda}\right) \quad (23.9)$$

Monte Carlo simulations (Dwyer, 2003) show that the avalanche length may be written approximately as

$$\lambda \approx \frac{7.3 \text{ MeV}}{eE - F_d} \quad (23.10)$$

Substituting this in (23.9) gives

$$f_{re} = f_0 \exp\left(\frac{-\varepsilon}{7.3 \text{ MeV}}\right) \quad (23.11)$$

independent of the electric field or the density of air. In contrast, the energy spectrum from the runaway electrons for the cold runaway electron mechanism does not possess any specific shape and may extend up to much smaller energies (e.g. a few 100 keV), depending upon the nature of the electric field. As a result, the observation of an x-ray (gamma-ray) spectrum that only extends into the 100 keV range, which is typical for lightning and laboratory sparks, is a strong indication that cold runaway and not RREA is most important in the production of the runaway electrons.

### 23.6 RREA parameters from Monte Carlo simulations

From Monte Carlo simulations, the avalanche threshold field in air,  $E_{th}$ , at a number density,  $n$ , is  $284 \text{ kV/m} \times n$  for air, where  $n$  is the number density of air molecules with respect to the sea level value  $n_0 = 2.69 \times 10^{25} \text{ m}^{-3}$ . The avalanche (e-folding) length is well fit by the empirical relation,

$$\lambda = \frac{7300 \text{ kV}}{[E - (276 \text{ kV/m}) \times n]} \quad (23.12)$$

valid over the range  $(300\text{--}3000 \text{ kV/m}) \times n$ , where the electric field,  $E$ , is measured in kV/m.

The fluence [electrons/m<sup>2</sup>] of runaway electrons in an avalanche passing through a plane, perpendicular to the avalanche direction ( $z$ -direction) can be written approximately as

$$\Phi_{re}(r, z) = \frac{1}{4\pi (D_\perp/v) (z - z_o)} \exp\left(\frac{(z - z_o)}{\lambda} - \frac{r^2}{4(D_\perp/v) (z - z_o)}\right) S(z - z_o) \quad (23.13)$$

where  $r$  in this case is the cylindrical radius  $r^2 = (x - x_0)^2 + (y - y_0)^2$  and  $S$  is the step function. The sea level values of the lateral diffusion coefficient,  $D_\perp/v$ , as a function of electric field strength, are found by Monte Carlo simulations and are well described by the empirical formula (Dwyer, 2010):

$$\frac{D_\perp}{v} = (5.86 \times 10^4) E^{-1.79} \text{ (m)} \quad (23.14)$$

The diffusion of the runaway electrons in the longitudinal direction along the avalanche can be similarly described (Dwyer, 2010) and the longitudinal diffusion coefficient is found to be

$$\frac{D_{||}}{v} = (3.80 \times 10^3) E^{-1.57} \text{ (m)} \quad (23.15)$$

In (23.14) and (23.15),  $E$  is in units of kV/m and  $D_\perp/v$  and  $D_{||}/v$  are in metres. To calculate the diffusion coefficients,  $D_\perp$  and  $D_{||}$ ,  $D_\perp/v$  and  $D_{||}/v$  should be multiplied by the avalanche speed presented in Coleman and Dwyer (2006) or by the approximate value  $v = 0.89c$ . Because runaway electron avalanches follow the similarity rule with reduced atmospheric density, (23.14) and (23.15) may be used to find the values at other air densities by converting the actual  $E$  to the sea level equivalent field, and then scaling  $D/v$  by  $1/n$ .

### 23.7 Relativistic feedback

In the Monte Carlo simulations, RF is recorded by keeping track of the electrons and photons that pass through the plane midway between the top and bottom of the

avalanche region. The initial runaway electrons and photons are labelled as first generation particles. Any secondary electrons, photons or positrons, regardless of the production mechanisms, carry the same generation number as the runaway electrons that led to the production of the new particles. Once an electron passes through the mid-plane, moving in the direction opposite the electric field vector, its generation number is increased by 1. The feedback factor,  $\gamma$ , is defined to be the ratio of the number of runaway electrons with generation number  $N + 1$ , passing through the mid-plane, divided by number of runaway electrons with generation number  $N$ , passing through the mid-plane. (Note that  $\gamma$  in this case is not the Lorentz factor, which shares the same symbol.) Looked at another way, the feedback factor is the number of new seed electrons that are created per initial seed electron. The feedback factor is analogous to the second Townsend coefficient for low-energy discharges.

The feedback factor describes the rate at which new avalanches are generated. It is important not to confuse this rate with the rate that positrons or x-rays contribute to the runaway electron growth in a given avalanche. For example, there may be only one electron-positron pair created for every 1000 runaway electrons in an avalanche, making a negligible contribution to the development of an individual avalanche. However, just one such positron is needed to generate an entirely new avalanche, resulting in a dramatic increase in the number of runaway electrons through the production of an ever increasing number of new secondary avalanches. As a result, the review paper by Milikh and Roussel-Dupre (2010) came to an erroneous conclusion about the applicability of RF (see Dwyer and Rassoul, 2011).

Dwyer (2007) calculated the flux of runaway electrons from RF and compared this flux with results of the standard RREA model. Let  $S_0$  be the flux of energetic seed particles that run away, e.g. the flux due to atmospheric cosmic-ray particles and radioactive decays. Depending upon the altitude and the geographic location,  $S_0$  is in the range  $100\text{--}10,000 \text{ m}^{-2} \text{ s}^{-1}$ . If no feedback were occurring, then according to the RREA model, the flux of runaway electrons at the end of the avalanche region would be

$$F_{RREA} = S_0 \exp(\xi), \quad \text{where } \xi = \int_0^L \frac{dz}{\lambda} \quad (23.16)$$

In (23.16),  $\xi$  is the number of e-folding lengths and is equal to  $L/\lambda$  for a uniform field.

When RF is considered, then the runaway electron flux at time  $t$  is the sum of all the feedback generations up until that time. For the case  $t \gg \tau_{fb}$ , where  $\tau_{fb}$  is the time required for one feedback cycle,

$$F_{RF} = \begin{cases} \frac{S_0 \exp(\xi) \exp(t/\tau')}{(\gamma - 1)}, & \gamma > 1 \\ S_0 \left( \frac{t}{\tau_{fb}} \right) \exp(\xi), & \gamma = 1 \\ \frac{S_0 \exp(\xi)}{(1 - \gamma)}, & \gamma < 1 \end{cases} \quad (23.17)$$

where

$$\tau' \equiv \frac{\tau_{fb}}{\ln(\gamma)} \quad (23.18)$$

is the e-folding time to increase the flux of runaway electrons due to feedback (assuming  $\gamma > 1$ ). Note that for  $\gamma > 1$  and a uniform electric field, (23.17) is proportional to  $\gamma^{t/\tau} \exp(L/\lambda)$ , which is the same as (23.2) in Dwyer (2003). Furthermore, for the case  $\gamma \ll 1$ , i.e. very little feedback,  $F_{RF}$  approaches the standard result for the RREA model given by (23.16).

It should be noted that RF also operates when  $\gamma < 1$ , as can be seen in (23.17). In this case, the discharge does not become self-sustaining. However, the effect of the feedback can dramatically increase the number of runaway electrons produced per seed particle injected as  $\gamma$  approaches 1.

On the other hand, for  $\gamma > 1$ , the discharge becomes self-sustaining and increases exponentially with time. Comparing (23.16) and (23.17) (for  $\gamma > 1$ ), the ratio of the runaway electron flux from RF to that from the RREA model is then

$$\frac{F_{RF}}{F_{RREA}} \approx \frac{\exp(t/\tau')}{(\gamma - 1)} \quad (23.19)$$

Equation 23.19 is also the ratio of x-rays emitted by the two mechanisms, since the x-ray emission is proportional to the flux of runaway electrons. Detailed calculations show that the ratio given by (23.19) can reach trillions.

The calculations of the feedback factor,  $\gamma$ , are complicated and depend upon the details of the electric field geometry. The threshold value for feedback to become self-sustaining ( $\gamma = 1$ ) has been found for several shapes of the electric field region and is presented in Figure 23.3.

## 23.8 Theory and observations

Several conclusions can be drawn from the currently available observations of x-rays and gamma-rays from thunderclouds and lightning:

1. The energy spectra from lightning and laboratory sparks are too soft, i.e. are too low in energy, to be consistent with RREA production. The fluxes are also too high to be explained by standard RREA seeded by background radiation (Dwyer 2004). Although RF could account for the fluxes, this mechanism does not seem likely for lightning and is not possible for laboratory sparks given the low voltages involved. This leaves so-called cold runaway electron production in the strong electric fields associated with the streamer heads or leader tips as the most likely mechanism (Dwyer, 2004; Moss *et al.*, 2006). It is possible that these energetic electrons experience some additional energy gain in the electric fields as described by the Wilson runaway electron mechanism. However, to date there has been no evidence that RREA multiplication, as

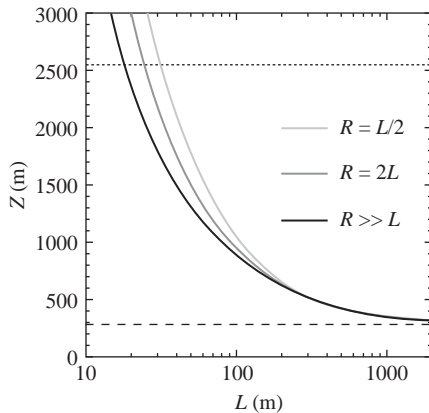


**Figure 23.3** The maximum static electric field strength achievable in air versus the length of the electric field region for the cases  $R = L/2$ ,  $R = 2L$  and  $R \gg L$ . These lines satisfy the condition that the feedback factor  $\gamma = 1$ . The dotted line shows the conventional breakdown threshold and the dashed line shows the runaway avalanche threshold. For electric field configurations on the upper right side of the figure, the field is highly unstable and will quickly discharge until it drops below the feedback threshold, moving to the lower left side of the figure. [Figure from Dwyer (2007)]

described by Gurevich *et al.* (1992), plays any role in the energetic radiation from lightning or sparks.

2. The gamma-ray surges and glows seen from thunderclouds are consistent with RREA and perhaps in some cases just Wilson runaway acting on the ambient cosmic-ray background. As thunderclouds charge and the electric field grows, the feedback threshold may be approached. This will result in a growing discharge current from the runaway electrons and their resulting ionization that may eventually balance the charging current in the thundercloud. In such cases, a near-steady-state glow of gamma-rays may result. However, it is not clear at this time if feedback effects are important for describing the observed gamma-ray emissions that last seconds to minutes.
3. Dwyer (2008) showed that the flux of RREAs acting on cosmic rays cannot explain TGFs. It was also shown that based upon the timing and fluxes, extensive cosmic-ray air showers seeding RREAs cannot explain TGFs. Recent measurements of the lightning associated with TGFs show that TGFs occur during the early stages of normal +IC lightning and that little charge is transferred at the time that the TGF begins. This makes models that involve runaway electron production above the thunderstorms in fields caused by the lightning discharge very unlikely. Dwyer (2008) argued that this leaves only two viable hypotheses: TGFs are caused by RF or TGFs are caused by cold runaway seeding RREAs. Both explanations may involve lightning. For feedback, the

- charge moment change from an upward-propagating lightning may drive the system over the feedback threshold, resulting in a self-sustained production of runaway electrons and a very rapid burst of gamma-rays (Dwyer, 2012). Alternatively, the lightning leader may emit runaway electrons similar to that seen near the ground. Using the luminosity of runaway electrons measured from triggered lightning of about  $10^{17}$  electrons per second (Salah *et al.*, 2009), with an additional RREA multiplication of  $10^4$  (consistent with the feedback limit), in  $10^{-4}$  s (the duration of a TGF)  $10^{17}$  runaway electrons would result, with the correct 7 MeV energy spectrum. More work is required in order to determine which mechanism (if either) is involved in production of TGFs. At this time, it is not clear if models involving RREA can explain the recent energy spectrum measured by the AGILE spacecraft, which followed a power law up to 100 MeV (Tavani *et al.*, 2011). As discussed above, the RREA spectrum is exponential and so does not appear to be consistent with these new observations.
4. Lightning initiation: The idea that runaway electron avalanches seeded by extensive cosmic-ray air showers may initiate lightning has gained considerable popularity in recent years (Gurevich *et al.*, 1999). However, using the diffusion coefficients calculated by Dwyer (2010) along with the avalanche multiplication limit from x-ray and positron feedback (Dwyer, 2003, 2007), it is found that even  $10^{17}$  eV cosmic-ray air showers do not produce high enough conductivities to significantly alter the electric field inside a thundercloud. As a result, at present, no compelling theoretical argument exists to suggest that cosmic-ray extensive air showers initiate lightning.
  5. Narrow bipolar events and radio pulses: Several authors have calculated the radio frequency emissions produced by extensive air showers initiating RREA. An interesting question is whether or not radio frequency pulses produced by air shower/runaway electron avalanches can account for narrow bipolar events (NBEs), as has been suggested by others (Gurevich *et al.*, 2002; Gurevich and Zybin, 2004). Narrow bipolar events are large ( $\sim 1$  to 10 V/m at 100 km) radio frequency pulses with rise times typically on the order of 1 microsec (Rakov and Uman, 2003). Dwyer *et al.* (2009) calculated the size of these radio frequency pulses and found them to be too small to explain NBEs. Dwyer and Babich (2011) also calculated the conductivity resulting from runaway electron avalanches and found that previous estimates were at least an order of magnitude too large, which raises serious questions about the size of the radio frequency pulses calculated by other authors.

## 23.9 Summary

Great progress has been made in the last 10 years both measuring the energetic radiation from thunderclouds and lightning, and developing theory and models to explain these emissions. To date, four basic mechanisms have been used to describe the production of runaway electrons and the resulting energetic radiation: Wilson runaway electrons; RREA, RF and cold runaway. Although all four share some

features and some underlying physics, their behaviour and the regimes of applicability are sufficiently different that it is useful to treat them independently when describing the production of energetic radiation in our atmosphere. Discharges involving runaway electrons also behave very differently from conventional discharges that involve only low-energy electrons. Because runaway electrons may be involved in thundercloud and lightning processes, understanding these interesting and novel kinds of electrical discharges is an important part of atmospheric physics.

## Acknowledgements

This work has been supported in part by the NSF grant ATM 0607885 and by DARPA grant HR0011-1-10-1-0061. Any opinions, findings, and conclusions or recommendations expressed in this material are those of the author(s) and do not necessarily reflect the views of the National Science Foundation.

## References

- Babich, L. P., I. M. Kutsyk, E. N. Donskoy and A. Yu. Kudryavtsev, New data on space and time scales of a relativistic runaway electron avalanche for thunderstorms environment: Monte Carlo calculations, *Phys. Lett. A*, vol. 245, pp. 460–470, 1998
- Babich, L.P., E. N. Donskoy, I. M. Kutsyk, , A. Yu. Kudryavtsev, R. A. Roussel-Dupré, B. N. Shamraev, and E.M.D. Symbalisty, Comparison of relativistic runaway electron avalanche rates obtained from Monte Carlo simulations and kinetic equation solution, *IEEE Trans. on Plasma Sci.*, vol. 29, no. 3, pp. 430–438, 2001
- Babich, L. P., E. N. Donskoy, I. M. Kutsyk and R. A. Roussel-Dupré, The feedback mechanism of runaway air breakdown, *Geophys. Res. Lett.*, vol. 32, CiteID L09809, doi:10.1029/2004GL021744, 2005
- Berestetskii, V. B., E. M. Lifshitz and L. P. Pitaevskii, *Quantum Electrodynamics*, Pergamon Press, Oxford, 1982
- Bethe H. and J. Ashkin, Transport of radiation through the matter, In: *Experimental Nuclear Physics*, E. Segre (Ed.), John Wiley, New York, vol. 1, Part 2, 1953
- Briggs, M. S., V. Connaughton, C. Wilson-Hodge, R. D. Preece, G. J. Fishman, R. M. Kippen, *et al.*, Electron-positron beams from terrestrial lightning observed with Fermi GBM, *Geophys. Res. Lett.*, vol. 38, no. 2, CiteID L02808, 2011
- Brunetti, M., S. Cecchini, M. Galli, G. Giovannini and A. Pagliarin, Gamma-ray bursts of atmospheric origin in the MeV energy range, *Geophys. Res. Lett.*, vol. 27, pp. 1599–1602, 2000
- Carlson, B., N. Lehtinen and U. Inan, Constraints on terrestrial gamma-ray flash production derived from satellite observations, *Geophys. Res. Lett.*, vol. 34, no. 8, CiteID L08809, 2007
- Chilingarian, A., A. Daryan, K. Arakelyan, A. Hovhannisyan, B. Mailyan, L. Melkumyan, G. Hovsepyan, S. Chilingaryan, A. Reymers and L. Vanyan,

- Ground-based observations of thunderstorm-correlated fluxes of high-energy electrons, gamma rays, and neutrons, *Phys. Rev. D*, vol. 82, no. 4, id. 043009, 2010
- Chilingarian, A., G. Hovsepyan and A. Hovhannisyan, Particle bursts from thunderclouds: Natural particle accelerators above our heads, *Phys. Rev. D*, vol. 83, no. 6, id. 062001, 2011
- Cohen, M. B., U. S. Inan, R. K. Said, M. S. Briggs, G. J. Fishman, V. Connaughton and S. A. Cummer, A lightning discharge producing a beam of relativistic electrons into space, *Geophys. Res. Lett.*, vol. 37, no. 18, CiteID L18806, 2010
- Coleman, L. M. and J. R. Dwyer, The propagation speed of runaway electron avalanches, *Geophys. Res. Lett.*, vol. 33, CiteID L11810, doi:10.1029/2006GL025863, 2006
- Connaughton, V., M. S. Briggs, R. H. Holzworth, M. L. Hutchins, G. J. Fishman, C. A. Wilson-Hodge, *et al.*, Associations between Fermi Gamma-ray Burst Monitor terrestrial gamma ray flashes and sferics from the World Wide Lightning Location Network, *J. Geophys. Res.*, vol. 115, no. A12, CiteID A12307, 2010
- Cummer, S. A., Y. Zhai, W. Hu, D. M. Smith, L. I. Lopez and M. A. Stanley, Measurements and implications of the relationship between lightning and terrestrial gamma ray flashes, *Geophys. Res. Lett.*, vol. 32, L08811, doi:10.1029/2005GL022778, 2005
- Cummer, S. A., G. Lu, M. S. Briggs, V. Connaughton, S. Xiong, G. J. Fishman, J. R. Dwyer, The lightning-TGF relationship on microsecond timescales, *Geophys. Res. Lett.*, 38, CiteID L14810, 2011
- Dwyer, J. R., A fundamental limit on electric fields in air, *Geophys. Res. Lett.*, vol. 30, p. 2055, 2003
- Dwyer, J. R., Implications of x-ray emission from lightning, *Geophys. Res. Lett.*, vol. 31, CiteID L12102, doi:10.1029/2004GL019795, 2004
- Dwyer, J. R., The initiation of lightning by runaway air breakdown, *Geophys. Res. Lett.*, vol. 32, CiteID L20808, doi:10.1029/2005GL023975, 2005
- Dwyer, J. R., Relativistic breakdown in planetary atmospheres, *Phys. Plasmas*, vol. 14, no. 4, pp. 042901-1–042901-17, 2007
- Dwyer, J. R., The source mechanisms of Terrestrial Gamma-ray Flashes (TGFs), *J. Geophys. Res.*, vol. 113, no. D10, CiteID D10103, 2008
- Dwyer, J. R., *Energetic Radiation and Lightning, Lightning: Principles, Instruments and Applications*, H. D. Betz, U. Schumann, P. Laroche (Eds.), Springer, 2009
- Dwyer, J. R., Diffusion of relativistic runaway electrons and implications for lightning initiation, *J. Geophys. Res.*, vol. 115, CiteID A00E14, 2010
- Dwyer, J. R., M. A. Uman, H. K. Rassoul, M. Al-Dayeh, E. L. Caraway, J. Jerauld, *et al.*, Energetic radiation produced during rocket-triggered lightning, *Science*, vol. 299, pp. 694–697, 2003
- Dwyer J. R., M. A. Uman, H. K. Rassoul, V. A. Rakov, M. Al-Dayeh, E. L. Caraway, *et al.*, Measurements of x-ray emission from rocket-triggered lightning, *Geophys. Res. Lett.*, vol. 31, CiteID L05118, doi:10.1029/2003GL018770, 2004

- Dwyer, J. R., M. A. Uman, H. K. Rassoul, V. A. Rakov, M. Al-Dayeh, E. L. Caraway, *et al.*, X-ray bursts associated with leader steps in cloud-to-ground lightning, *Geophys. Res. Lett.*, vol. 32, CiteID L01803, doi:10.1029/2004GL021782, 2005a
- Dwyer, J. R., H. K. Rassoul, Z. Saleh, M. A. Uman, J. Jerauld and J. A. Plumer, X-ray bursts produced by laboratory sparks in air, *Geophys. Res. Lett.*, vol. 32, CiteID L20809, doi:10.1029/2005GL024027, 2005b
- Dwyer, J. R., Z. Saleh, H. K. Rassoul, D. Concha, M. Rahman, V. Cooray, J. Jerauld, M. A. Uman, and V. A. Rakov, A study of x-ray emission from laboratory sparks in air at atmospheric pressure, *J. Geophys. Res.*, vol. 113, no. D23, CiteID D23207, 2008
- Dwyer, J. R., B. W. Grefenstette and D. M. Smith, High-energy electron beams launched into space by thunderstorms, *Geophys. Res. Lett.*, vol. 35, CiteID L02815, doi:10.1029/2007GL032430, 2008
- Dwyer, J. R., D. M. Smith, M. A. Uman, Z. Saleh, B. Grefenstette, B. Hazelton, *et al.*, Estimation of the fluence of high-energy electron bursts produced by thunderclouds and the resulting radiation doses received in aircraft, *J. Geophys. Res.*, doi:10.1029/2009JD012039, 2010
- Dwyer, J. R., M. A. Uman and H. K. Rassoul, The remote measurement of thunderstorm electrostatic fields, *J. Geophys. Res.*, vol. 114, no. D09208, doi:10.1029/2008JD011386, 2009
- Dwyer, J. R., and L. Babich, Low-energy electron production by relativistic runaway electron avalanches in air, *J. Geophys. Res.*, 116, doi:10.1029/2011JA016494, 2011
- Dwyer, J. R., The relativistic feedback discharge model of terrestrial gamma ray flashes, *J. Geophys. Res.*, 117, A02308, doi:10.1029/2011JA017160, 2012
- Dwyer, J. R., and H. K. Rassoul, Comment on “Runaway breakdown and electrical discharges in thunderstorms,” by G. Milikh and R. Roussel-Dupré, *J. Geophys. Res.*, 116, A08312, doi:10.1029/2011JA016670, 2011
- Eack, K. B., W. H. Beasley, W. D. Rust, T. C. Marshall and M. Stolzenburg, Initial results from simultaneous observation of X rays and electric fields in a thunderstorm, *J. Geophys. Res.*, vol. 101, no. D23, pp. 29,637–29,640, 1996a
- Eack, K. B., W. H. Beasley, W. D. Rust, T. C. Marshall and M. Stolzenburg, X-ray pulses observed above a mesoscale convective system, *Geophys. Res. Lett.*, vol. 23, no. 21, pp. 2915–2918, 1996b
- Foote, R. S. and N. E. Frick, Time variations of natural gamma radiation, *Environ. Geosci.*, vol. 8, no. 2, pp. 130–139, 2001
- Fishman, G. J., P. N. Bhat, R. Mallozzi, J. M. Horack, T. Koshut, C. Kouveliotou, *et al.*, Discovery of intense gamma-ray flashes of atmospheric origin, *Science*, vol. 264, p. 1313, 1994
- Ginzburg, V. L. and S. I. Syrovatskii, *The Origin of Cosmic Rays*, Pergamon, London, 1964
- Gjesteland, T., N. Østgaard, P. H. Connell, J. Stadsnes and G. J. Fishman, Effects of dead time losses on terrestrial gamma ray flash measurements with the burst

- and transient source experiment, *J. Geophys. Res.*, vol. 115, no. 3, CiteID A00E21, 2010
- Grefenstette, B. W., D. M. Smith, J. R. Dwyer and G. J. Fishman, Time evolution of terrestrial gamma ray flashes, *Geophys. Res. Lett.*, vol. 35, no. 6, CiteID L06802, 2008
- Gurevich, A. V., On the theory of runaway electrons, *Soviet Phys. JETP*, vol. 12, no. 5, pp. 904–912, 1961
- Gurevich, A. V., G. M. Milikh and R. A. Roussel-Dupré, Runaway electron mechanism of air breakdown and preconditioning during a thunderstorm, *Phys. Lett. A*, vol. 165, p. 463, 1992
- Gurevich, A. V., K. P. Zybin and R. A. Roussel-Dupré, Lightning initiation by simultaneous effect of runaway breakdown and cosmic ray showers, *Phys. Lett. A*, vol. 254, pp. 79–87, 1999
- Gurevich, A. V. and K. P. Zybin, Runaway breakdown and electric discharges in thunderstorms, *Physics-Uspokhi*, vol. 44, p. 1119, 2001
- Gurevich, A. V., L. M. Duncan, Yu. V. Medvedev and K. P. Zybin, Radio emission due to simultaneous effect of runaway breakdown and extensive atmospheric showers, *Phys. Lett. A*, vol. 301, pp. 320–326, 2002
- Gurevich, A. V. and K. P. Zybin, High energy cosmic ray particles and the most powerful discharges in thunderstorm atmosphere, *Phys. Lett. A*, vol. 329, no. 4–5, pp. 341–347, 2004
- Hillas, A. M., *Cosmic Rays*, Pergamon, Oxford, 1972
- Howard, J., M. A. Uman, J. R. Dwyer, D. Hill, C. Biagi, Z. Saleh, J. Jerauld and H. K. Rassoul, Co-location of lightning leader x-ray and electric field change sources, *Geophys. Res. Lett.*, vol. 35, no. 13, CiteID L13817, 2008
- Howard, J., M. Uman, C. Biagi, D. Hill, J. Jerauld, V. A. Rakov, *et al.*, RF and x-ray source locations during the lightning attachment process, *J. Geophys. Res.*, doi:10.1029/2009JD012055, 2010
- Inan, S. U., S. C. Reising, G. J. Fishman and J. M. Horack, On the association of terrestrial gamma-ray bursts with lightning and implications for sprites, *Geophys. Res. Lett.*, vol. 23, pp. 1017–1020, 1996
- Lehtinen, N. G., T. F. Bell and U. S. Inan, Monte Carlo simulation of runaway MeV electron breakdown with application to red sprites and terrestrial gamma ray flashes, *J. Geophys. Res.*, vol. 104, pp. 24699–24712, 1999
- Lu, G., R. J. Blakeslee, J. Li, D. M. Smith, X-M Shao, E. W. McCaul, *et al.*, Lightning mapping observation of a terrestrial gamma-ray flash, *Geophys. Res. Lett.*, vol. 37, no. 11, CiteID L11806, 2010
- Lu, G., S. A. Cummer, J. Li, F. Han, D. M. Smith and B. W. Grefenstette, Characteristics of broadband lightning emissions associated with terrestrial gamma ray flashes, *J. Geophys. Res.*, vol. 116, no. A3, CiteID A03316, 2011
- MacGorman, D. R. and W. D. Rust, *The Electrical Nature of Storms*, Oxford University Press, New York, 1998
- March, V. and J. Montanyà, Influence of the voltage-time derivative in X-ray emission from laboratory sparks, *Geophys. Res. Lett.*, vol. 37, no. 19, CiteID L19801, 2010

- March, V. and J. Montanyà, X-rays from laboratory sparks in air: The role of the cathode in the production of runaway electrons, *Geophys. Res. Lett.*, vol. 38, no. 4, CiteID L04803, 2011
- McCarthy, M. and G. K. Parks, Further observations of x-rays inside thunderstorms, *Geophys. Res. Lett.*, vol. 12, pp. 393–396, 1985
- Milikh, G. and R. Roussel-Dupré, Runaway breakdown and electrical discharges in thunderstorms, *J. Geophys. Res.*, doi:10.1029/2009JA014818, 2010
- Moore, C. B., K. B. Eack, G. D. Aulich and W. Rison, Energetic radiation associated with lightning stepped-leaders, *Geophys. Res. Lett.*, vol. 28, pp. 2141–2144, 2001
- Moss, G. D., V. P. Pasko, N. Liu and G. Veronis, Monte Carlo model for analysis of thermal runaway electrons in streamer tips in transient luminous events and streamer zones of lightning leaders, *J. Geophys. Res.*, vol. 111, no. A2, CiteID A02307, 2006
- Mott, N. F. and H. S. W. Massey, *The Theory of Atomic Collisions*, 3rd Edition, Oxford University Press, London, 1965
- Nguyen, C. V., A. P. J. van Deursen and U. Ebert, Multiple x-ray bursts from long discharges in air, *J. Phys. D: Appl. Phys.*, vol. 41, p. 234012, 2008
- Parks, G. K., B. H. Mauk, R. Spiger and J. Chin, X-ray enhancements detected during thunderstorm and lightning activities, *Geophys. Res. Lett.*, vol. 8, pp. 1176–1179, 1981
- Raether, H., *Electron Avalanches and Breakdown in Gases*, Butterworth & Co. Ltd., Washington D.C., 1964
- Rahman, M., V. Cooray, N. A. Ahmad, J. Nyberg, V. A. Rakov and S. Sharma, X rays from 80-cm long sparks in air, *Geophys. Res. Lett.*, vol. 35, L06805, doi:10.1029/2007GL032678, 2008
- Rakov, V. A. and M. A. Uman, *Lightning Physics and Effects*, Cambridge University Press, 2003
- Saleh, Z., J. Dwyer, J. Howard, M. Uman, M. Bakhtiari, D. Concha, *et al.*, Properties of the x-ray emission from rocket-triggered lightning as measured by the Thunderstorm Energetic Radiation Array (TERA), *J. Geophys. Res.*, vol. 114, D17, doi:10.1029/2008JD011618, 2009
- Shaw, G. E., Background cosmic count increases associated with thunderstorms, *J. Geophys. Res.*, vol. 72, pp. 4623–4626, 1967
- Shao, X.-M., T. Hamlin and D. M. Smith, A closer examination of terrestrial gamma-ray flash-related lightning processes, *J. Geophys. Res.*, vol. 115, no. 9, CiteID A00E30, 2010
- Smith, D. M., J. R. Dwyer, B. J. Hazelton, B. W. Grefenstette, G. F. M. Martinez-McKinney, Z. Y. Zhang, *et al.*, The rarity of terrestrial gamma-ray flashes, *Geophys. Res. Lett.*, vol. 38, no. 8, CiteID L08807, 2011
- Splitter, M. E., S. M. Lazarus, D. Barnes, J. R. Dwyer, H. K. Rassoul, D. M. Smith, *et al.*, Thunderstorm characteristics associated with RHESSI identified terrestrial gamma-ray flashes, *J. Geophys. Res.*, doi:10.1029/2009JA014622, 2010
- Stanley, M. A., X.-M. Shao, D. M. Smith, L. I. Lopez, M. B. Pongratz, J. D. Harlin, M. Stock, and A. Regan, Link between terrestrial gamma-ray flashes and

- intra-cloud lightning discharges, *Geophys. Res. Lett.*, vol. 33, no. 6, CiteID L06803, 2006
- Suszczynsky, D. M., R. Roussel-Dupre and G. Shaw, Ground-based search for X rays generated by thunderstorms and lightning, *J. Geophys. Res.*, vol. 101, no. 23, p. 505, 1996
- Tavani, M., J. R. Dwyer and H. K. Rassoul, Terrestrial Gamma-Ray flashes as powerful particle accelerators, *Phys. Rev. Lett.*, vol. 106, no. 1, id. 018501, 2011
- Tsuchiya, H., T. Enoto, S. Yamada, T. Yuasa, M. Kawaharada, T. Kitaguchi, Detection of high-energy gamma rays from winter thunderstorms, *Phys. Rev. Lett.*, vol. 99, p. 165002, 2007
- Uman, M. A., *The Lightning Discharge*, Dover Publications Inc., Mineola, New York, 2001
- Whitmire, D. P., Search for high-energy radiation near lightning strokes, *Lett. Nuovo Cimento*, vol. 26, no. 16, pp. 497–501, 1979
- Williams, E. R., The origin and context of C. T. R. Wilson's ideas on electron runaway in thunderclouds, *J. Geophys. Res.*, vol. 115, A00E50, doi:10.1029/2009JA014581, 2010
- Wilson, C. T. R., The acceleration of beta-particles in strong electric fields such as those of thunder-clouds, *Proc. Cambridge Phil. Soc.*, vol. 22, pp. 534–538, 1925

---

## *Chapter 24*

# **Excitation of visual sensory experiences by electromagnetic fields of lightning**

*Vernon Cooray<sup>1</sup> and Gerald Cooray<sup>2</sup>*

---

### **24.1 Introduction**

Lightning flashes can interact with a human in six different ways [1–3]. These are through direct strikes, side flashes, ground currents, shock waves, connecting leaders and electromagnetic fields. A direct strike results when the lightning channel terminates on the person's body. In this case, there is a direct current injection from the lightning flash into the body as a result of which the person generally may experience cardiac and/or respiratory arrests; about 20% of the victims die as a result. A side flash happens when the human is located close to an object struck by lightning. The potential gradient created by the current flow along the object may give rise to a discharge between the object and the human. A portion of the lightning current will flow along this discharge path and pass through the body. Depending on the path along which the current travels through the body, the injuries could be similar to that of a direct strike. Someone standing close to the point at which lightning strikes could be injured by ground currents as the current flowing through the ground short-circuits its path by passing into the body from one leg and flowing out from the other. Since the current path is not directly through the brain or the heart, the injuries tend to be less severe than those caused by a direct strike. Injuries can also arise from shock waves created by the lightning channel. During a lightning strike, the channel temperature can rise to about 25,000 K and the channel pressure can increase to several atmospheres. The rapid expansion of heated air creates a shock wave that can injure a person located close to a lightning strike. Someone standing in the vicinity of a lightning strike could also be injured by an aborted connecting leader. Connecting leaders are initiated from grounded objects, including humans, under the influence of the electric field generated by the down-coming stepped leader. The resultant electric field is concentrated on sharp points and on the tips of grounded objects, increasing the electric field at these points to several times the background electric field. In the case of a person standing, the maximum field enhancement would take place on the

<sup>1</sup>Uppsala University, Uppsala, Sweden

<sup>2</sup>Department of Clinical Neuroscience, Karolinska Institute, Stockholm, Sweden

top of the head. The electric field continues to grow as the stepped leader approaches the ground, and when the electric field at the tip of an object exceeds a critical value, a corona discharge (known in the popular literature as St. Elmo's fire) is initiated from it. This corona discharge continues to grow as the stepped leader approaches the ground and when the charge associated with it reaches a critical level, a thermalized electrical discharge travelling from the tip towards the down-coming stepped leader is formed. Several objects, including humans, in the vicinity of a lightning channel may launch connecting leaders, but only one of them will succeed in joining with the stepped leader. The object that initiated the 'successful' connecting leader will receive a direct strike. As the electric field collapses during the lightning strike, the connecting leaders issued by other objects will be aborted, but the current generated by these aborted leaders could be large enough to cause injury especially if it happened to be created from a person's head. When the person is located at a sufficiently large distance where the electric field is not large enough to launch a connecting leader, a corona discharge may still be issued from the person's head.

The electric current passing through the body during a direct strike or during the launch of a connecting leader can be large enough to cause either cardiac arrest or a respiratory arrest, or both. If, however, someone is located at a distance large enough to ensure that they will not be affected by direct strikes, connecting leaders or ground currents, the person can still be affected by the lightning-generated electromagnetic fields and the corona currents generated from the body.

In this chapter, we will consider the possible interactions, either direct or indirect, of the lightning-generated electromagnetic fields with the brain or the visual system of humans to induce visual sensations. Some of these visual sensations are known as phosphenes in the medical literature. Since some of these visual sensations could be misinterpreted as ball lightning, this subject is of interest for lightning researchers due to the still unsolved problem of the origin of ball lightning.

## 24.2 Features of ball lightning

Ball lightning has been seen and described since antiquity and recorded in many places around the globe. Because ball lightning has not been produced in the laboratory and the authenticity of the available photographs is questionable, the properties of ball lightning have to be extracted from eyewitness records. Observed properties of ball lightning have been summarized in several books [4–6], in which it is described as being spherical in shape, although other shapes such as teardrops or ovals have also been reported. In rare occasions, ball lightning shaped like rods has also been observed. The diameter of ball lightning is usually 10–40 cm but occasionally ball lightning as large as 1 m has been reported. The lifetime of ball lightning is reported to be about a few seconds, but occasionally ball lightning with a duration of as long as one minute has been observed. Ball lightning may manifest in different colours such as red, red-yellow, yellow, white, green and purple. In some cases, the intensity of ball lightning may increase with time and becomes a dazzling white before it disappears explosively. The structure of the ball lightning may vary from one report to another. Sometimes a

solid core surrounded by a translucent envelope is reported; in other cases it is a rotating structure or a structure that emits spark-like phenomena. Most ball lightning phenomena are said to move horizontally; however, descriptions including motionlessness, a zig-zag movement or moving from a cloud towards the ground can also be found. The speed of movement is reported to be walking speed, i.e. about 1–2 m/s, and ball lightning that moves against the wind has also been reported. Some reports describe sharp or acrid odours and 10% of the observers report sounds associated with the manifestation. The ball may disappear silently or explosively. However, in many cases in which the ball exploded in the vicinity of different objects, no movement of objects or damage to them has been reported.

Ball lightning is usually observed during thunderstorms, but a significant number of sightings have also been reported during fine weather without any connection to thunderstorms or lightning. They are also been reported under stressful natural conditions, such as tornadoes, storms and earthquakes. Most of the ball lightning has been sighted indoors, and in one case it was observed inside a commercial aircraft. Ball lightning has also been reported by sailors under stormy conditions but without any lightning. According to observations, balls of lightning can enter or depart from closed rooms, and pass through solid walls and closed windows without any apparent change in its structure and without causing any damage.

## **24.3 Alternative explanations**

There is a wide variety of theories on ball lightning, but so far none of them is able to explain all of the observed features. The great difficulty of encompassing all observed features of ball lightning into a single theory makes it highly probable that many observations and experiences that have no connection to ball lightning are also categorized as ball lightning experiences. If visual sensations are generated by lightning electromagnetic fields, some of these could also be misinterpreted as a ball lightning observation.

So far scientists have identified four pathways that could give rise to visual stimulations, with features similar to ball lightning reports, through the interaction of lightning electromagnetic fields with the visual system or the brain. These are (i) interaction of the magnetic field with the retina or the visual cortex to generate phosphenes, (ii) interaction of the magnetic field or the intermittent light of lightning flashes with the visual system or the brain to induce occipital seizures that accompany visual hallucinations similar to the features documented in ball lightning reports, (iii) interaction of the high energetic radiation with the retina to induce phosphenes and (iv) stimulation of the brain or the visual system by electric currents of corona discharges caused by the close electric field. Let us consider these alternatives one at a time.

### *24.3.1 Visual sensations produced by the magnetic fields generated by lightning*

A phosphene is a visual sensation that is characterized by perceiving luminous phenomena without light entering the eye. Normal visual perception is created by

the conversion of light falling on the retina into electrical signals by photoreceptors and subsequent interpretation of this signal by the occipital brain. Phosphenes are created when such electrical signals are created by other means in the absence of light stimuli. Phosphenes can be induced by direct stimulation of the retina or the optical nerve, either by mechanical, magnetic or electrical means. Phosphenes are created by the interaction of low frequency magnetic fields with the retina or the visual cortex as the time-varying magnetic fields generate currents that disrupt their normal electrical activity.

The occurrence of phosphenes during the interaction of magnetic fields with the brain has been documented in the medical literature related to transcranial magnetic stimulation (TMS) studies. In TMS investigations, time-varying magnetic fields are applied repeatedly to the brain using circular coils located on the head [7]. In clinical studies, TMS has provided a noninvasive means of evaluating distinct excitatory and inhibitory functions of the human cerebral cortex [8, 9]. A pulse of duration 0.2–0.5 ms repeated three to five times at a frequency of 25 Hz has been shown to induce phosphenes [10]. A single pulse TMS can create a phosphene of a maximum of 50–100 ms duration [11]. Induction of phosphenes by stimulating the visual cortex would require an induced electric field of magnitude 20–50 V/m [10]. It is of interest to note, e.g. that Bernhardt [12] has estimated that the critical current density in the brain necessary to perturb normal biological functions is about  $1 \text{ A/m}^2$ . For a brain conductivity of about  $0.1 \text{ S/m}$  [13], this translates to about  $10 \text{ V/m}$ . This electric field strength is approximately of the same magnitude as the induced electric field values necessary to stimulate cortical phosphenes in TMS studies.

Peer and Kendl [14] concluded that the magnetic fields generated by lightning within about 100 m of a lightning strike are large enough to generate magnetic phosphenes through interaction with the visual cortex. A revised analysis conducted by Peer *et al.* [15] showed that for stronger-than-average currents cortical phosphenes stimulation can be induced only by lightning striking within a few metres. In the case of lightning flashes at medium distances (about 50 m), only the initial peak, whose width is about 10 to 20  $\mu\text{s}$ , of the magnetic field derivative of rather high current derivatives ( $dI/dt > 100 \text{ kA } \mu\text{s}^{-1}$ ) could exceed the phosphenes threshold. Taking into account that these pulses are shorter than established axion excitation periods and since the retinal phosphene stimulation threshold is much lower than cortical stimulation they suggested that retinal phosphenes stimulation is the most probable for lightning electromagnetic fields.

#### *24.3.2 Visual sensations produced by the epileptic seizures of the occipital lobe*

Cooray and Cooray [16] pointed out that the visual hallucinations produced during the partial epileptic seizures of the occipital lobe are similar to the features of ball lightning observations. They suggested the possibility of either the magnetic field or the intermittent light from the lightning flashes could trigger these seizures establishing the connection between them with thunderstorms and lightning. The following description is based on their study.

An epileptic seizure is an event caused by abnormal, excessive, hypersynchronous discharges from an aggregate of neurons in the brain. The results of this activity can vary from dramatic convulsive activity to experiential phenomena. Epilepsy describes a condition in which a person has recurrent seizures owing to a chronic, underlying process. Its prevalence has been estimated at 5 to 10 persons per 1000 worldwide [17]. A few per cent of all epilepsies have been described as being of occipital origin. Visual hallucinations sometimes occur as a result of a seizure in the occipital, temporo-occipital or temporal lobes of the brain [18–20]. Elementary visual hallucinations as perceived and drawn by eight patients with occipital epilepsy are shown in Figure 24.1. Visual hallucinations in the form of luminous objects, that are either circular or ball like, are not uncommon [18, 19]. In particular luminous balls of different colours, red, yellow, blue and green, moving horizontally from the periphery of the vision to the centre have been described that may appear to be rotating or spinning. Sometimes, the ball may also appear to have a solid structure surrounded by a thin glow or, in other cases, it appears to generate spark-like phenomena. When the ball is moving towards the centre of the vision it may increase in intensity and, when it reaches the centre, it can 'explode' illuminating the whole field of vision [18]. During the hallucinations, the vision is obscured only in the area occupied by the apparent object. The hallucinations may last for 5–30 s and, rarely, up to a minute. Occipital seizures may spread into other regions of the brain giving auditory, olfactory and sensory sensations. These sensations can take the form of buzzing sounds, the smell of burning rubber, pain with thermal sensation, especially in the arms and the face, and numbness and a tingling sensation.

In some cases, people may experience only one or a few seizures during their lifetime and may not be aware of the reason for the experience. This is specially the case with idiopathic occipital epilepsy, a benign condition affecting predominantly children [21]. Children affected with this condition will often experience only one or a few seizures. Otherwise being in good health, those concerned may categorize their experience as ball lightning encounters. If, as described above, the seizure

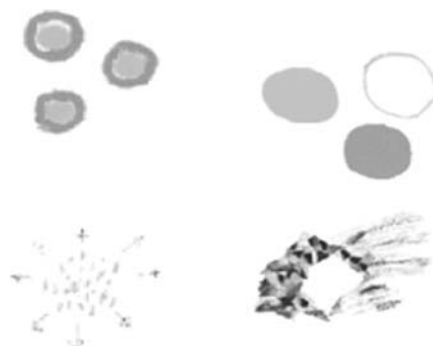


Figure 24.1 Elementary visual hallucinations as perceived and drawn by patients with occipital epilepsy [19]

affected other sensory regions, the resulting experience may appear to have been an electrical effect (the smell of burning, sensation of heat, tingling feeling, etc.) of the ball lightning. Epileptic seizures are a common and important medical problem, with about one in ten persons experiencing at least one seizure at some point in their life. Thus, some of the ball lightning encounters presented in the literature could very well be associated with the experiences of persons who have had an epileptic seizure with visual hallucinations. It is of interest to note that some of the ball lightning observations occur without any association to thunderstorms and such experiences could also be explained by epileptic seizures of the occipital lobe.

#### 24.3.2.1 Possible association with thunderstorms

Cooray and Cooray [16, 22] suggested two mechanisms that could trigger partial occipital seizures during thunderstorms. These are the strong magnetic fields produced by near by lightning flashes and the intermittent light produced by lightning flashes. Let us consider these two possibilities separately.

##### *Magnetic fields of return strokes*

Over the last few decades, scientists have been considering the safety issues related to the medical use of time-varying magnetic fields [23, 24]. From a combination of theory and experiment, they have come up with threshold levels for the magnetic time derivatives necessary for nerve and cardiac stimulation [24]. Figure 24.2 shows the rate of change of a magnetic field applied in the form of a ramp required

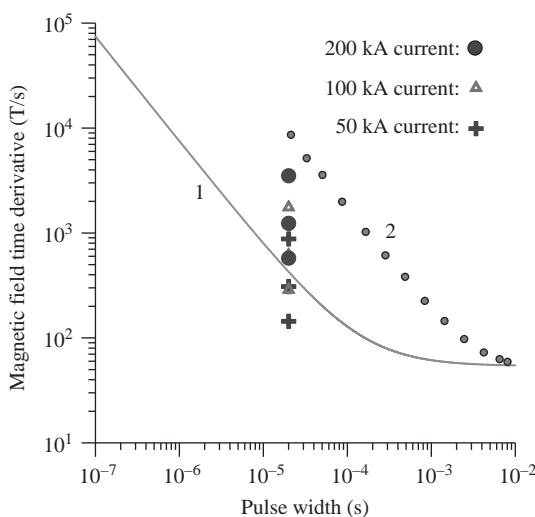


*Figure 24.2 The rate of change of magnetic field applied in the form of a ramp required to excite the nerves (curve 1) and induce cardiac stimulation (curve 2) [23, 24]. On the same figure, the peak magnetic field derivative for lightning flashes 10, 5 and 2 m from the channel is also depicted for currents of 50, 100 and 200 kA*

to excite nerves and to induce cardiac stimulation. In this graph, the horizontal axis gives the duration of the ramp and the vertical one the rate of change of the magnetic field. The curve for the cardiac stimulation corresponds to the most sensitive population percentile, while the nerve stimulation corresponds to the mean population. Usually, the safe level for magnetic fields in MRI is set to be about three times less than the one corresponding to the nerve stimulation [23].

In order to study whether the magnetic field of a close lightning strike could stimulate nerves in the brain, Cooray and Cooray [16] calculated the time derivative of magnetic fields of lightning flashes with different currents located at different distances and compared the results with the threshold magnetic field time derivatives necessary to stimulate nerves in the brain. In the calculations, the transmission line model is used together with a return stroke speed of  $1.5 \times 10^8$  m/s (see Chapter 7). The current at the channel base of the return stroke was represented by the following waveform that has been adopted in lightning protection standards:

$$i = \frac{I}{k} \cdot \frac{(t/\tau_1)^{10}}{1 + (t/\tau_1)^{10}} \cdot \exp(-t/\tau_2) \quad (24.1)$$

where  $I$  gives the peak current and  $\tau_1 = 19.0$   $\mu$ s,  $\tau_2 = 485$   $\mu$ s and  $k = 0.93$ . Calculations were conducted for peak currents of 50, 100 and 200 kA. Since the full width of the lightning-generated magnetic field derivative evaluated in the study is about 20  $\mu$ s, Cooray and Cooray [16] superimposed the peak values of these magnetic field time derivatives in Figure 24.2 at 20  $\mu$ s pulse width. First note that the magnetic field derivative of a strong lightning flash striking close to a person could not induce cardiac stimulation. This is in agreement with the conclusions made by Andrew's *et al.* [25]. On the other hand, observe that, depending on the distance to the current path, the peak values of magnetic time derivatives exceed the values required for nerve stimulation. Recall, too, that the curve for nerve stimulation corresponds to the mean for the population, whilst the most sensitive percentile may lie about factor two below this [23, 24]. The results show that a person located within a few metres of the path of a lightning current could be exposed to a magnetic field derivative that is large enough to stimulate neurons in the brain. This, together with the observed fact that intracranial magnetic stimulation, where the brain is exposed to strong magnetic field derivatives, can cause seizures in epileptic patients [9], makes a strong case for the nonzero probability of a close lightning flash triggering an epileptic seizure of the occipital lobe.

Cooray and Cooray [16] also pointed out that the striking distance, i.e. the distance of attraction, of lightning flashes supporting large currents is larger than several tens of metres and the chances that lightning flashes of this magnitude will strike ground within 10 m of a human standing on open ground is rather small. In such cases, the lightning flash would terminate on the human. However, they pointed out that there are several situations in which a person could be exposed to the magnetic fields generated by strong lightning flashes striking within 10 m. One such example is a person standing within 10 m of a tree or a high object struck by

lightning. A similar scenario could also occur, e.g. when lightning strikes a protected building. The current of the lightning flash flows along the down conductors of the lightning protection system and the person could be standing within metres of such a conductor during a lightning strike. Thus, the probability that a human could be exposed to the magnetic field generated by a strong lightning flash within 10 m is not negligible, according to Cooray and Cooray [16].

### *Effect of intermittent light*

In a letter to the editor of the *Journal of Neurology, Neurosurgery and Psychiatry*, Cooray and Cooray [22] suggested that the intermittent light produced by lightning flashes could also be a possible trigger for the epileptic seizures. An epileptic seizure could be triggered in a person having a lower seizure threshold upon exposure to certain visual stimuli. The nature of the stimuli that can trigger a seizure may vary from one person to another. The visual trigger for a seizure is generally intermittent such as flashing lights or rapidly changing images. The clinical data available at present confirm that the frequency of the flashing lights that induce epileptic seizures lie in the range 5–30 pulses/s [26]. Interestingly, lightning flashes also emit light pulses with a frequency that lies in the above range. A lightning flash is a composite event containing many high current events called return strokes. Each of these return strokes generates a strong light pulse since it heats the lightning channel to temperatures higher than 25,000°C. A typical lightning flash may contain up to about three to five return strokes, but in some cases the number of return strokes can exceed 20 [27]. The time interval between each event is about 50 ms on average, and, therefore, the light emitted by a lightning flash would pulsate at a frequency of about 20 pulses/s. Now, in severe thunderstorms, the lightning flashing rate can exceed 60 lightning flashes/min and in extreme cases it may increase to 500 flashes/min [27]. With the light from each lightning flash pulsating at a frequency of 20 pulses/s and with more than 60 such flashes taking place in a minute, the light generated by such thunderstorms might be responsible for provoking a seizure, especially when the ambient light level is low (e.g. night time when the flashes are more obvious against the dark background), in a person who is sensitive to pulsating light.

Interestingly, Ferrie *et al.* [28] show that light pulses can trigger partial epileptic seizures of the occipital lobe. As described previously, the work done by Panayiotopoulos *et al.* [19] shows that such seizures can induce visual hallucinations with the victim remaining in a conscious state throughout the seizure.

## **24.4 Visual effects produced by energetic radiation**

Cooray *et al.* [29] suggested that the energetic radiation generated by thunderstorms and lightning could induce phosphenes in a person located in the vicinity of thunderstorms and lightning. The following description is adapted from their study.

Energetic radiation produced by radium can give rise to phosphenes was first noted by Diesel in 1899 [as referred to in 30]. A resurge of studies related to the

creation of phosphenes by energetic radiation took place after the reports of light flashes observed in space by Apollo astronauts. It was first reported by Buzz Aldrin after Apollo 11 flight to the moon in 1969. Actually the possibility of visual effects caused by energetic radiation in space was first predicted by Tobias in 1934 [31]. Based on a 29 questionnaire distributed to 98 astronauts, 47 out of 58 who responded had experienced phosphenes (so-called light flashes at the time) at least in some space flights but not necessarily in all the flights. They were mostly noted just before going to sleep when the eye is adapted to the darkness. However, some have experienced them during daytime. The shapes of the phosphenes were either stripe, comet shaped, single dot, several dots or blobs. The colours were mostly white, but some had yellow, orange, blue, green and red. Schematic drawings of phosphenes observed by astronauts on Apollo flights are shown in Figure 24.3 [32]. Majority of the astronauts had perceived some kind of motion to the phosphenes. Most of the time, they were moving horizontally and sometimes diagonally, but never vertical. Experiments conducted in subsequent space missions have confirmed that the phosphenes are created by the passage of energetic particles through the visual system. The apparent motion of the phosphenes observed had to be

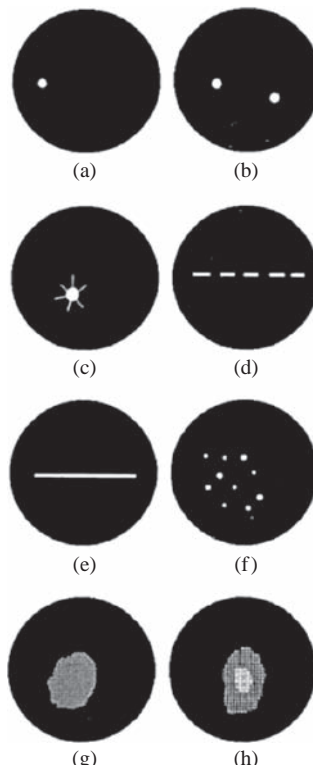


Figure 24.3 Schematic diagrams of the phosphenes observed by astronauts in Apollo missions [adapted from Reference 32]

physiological because the flight time of the energetic particles through the optical system was on the order of nanoseconds.

The observations of Apollo astronauts and subsequently the astronauts in the Skylab had motivated some scientists to expose themselves to low-energy particle beams to study the occurrence of phosphenes. Other experiments were conducted using cosmic rays. These experiments managed to reproduce what the astronauts have experienced. Phosphenes were seen by human volunteers from neutron generators at energies of 3, 8, 14 and 300 MeV as well as from Cf-252 at around 1 MeV [as summarized in Reference 33]. Phosphenes have been also observed after exposure to low doses of X-rays. In another study, 10 cancer patients whose eyes were therapeutically irradiated with 6–18 MeV electrons reported phosphenes. Nine reported seeing blue phosphenes while one reported white.

Studies conducted in space show that the probability of phosphene induction by energetic particles depends on their Linear Energy Transfer (LET) in tissue. The threshold LET necessary for the creation of phosphenes is about 10 MeV/cm and the probability increases to about 5% at 50 MeV/cm [34].

Based on this experimental data that confirm the induction of phosphenes in humans by energetic radiation, Cooray *et al.* [29] suggested the possibility of induction of phosphenes in humans located in the vicinity of lightning flashes. They showed that the energy dissipation by energetic radiation in the eye of a person located in the vicinity of lightning strikes exceeds the phosphene threshold. Let us consider their analysis now.

#### *24.4.1 Induction of phosphenes by the energetic radiation of lightning and thunderstorms*

X-rays and gamma rays have been found to be emitted by thunderclouds using both in situ and ground-based observations [35–42]. X-rays are now routinely measured from natural and rocket-triggered lightning flashes [43–47]. Large bursts of gamma rays, called terrestrial gamma-ray flashes, have been observed to emanate from thunderclouds by several spacecrafts [48–50]. The source of the high-energy radiation is the acceleration of electrons to relativistic energies by the electric fields of thunderclouds or lightning flashes. Cooray *et al.* [29] pointed out that the energetic radiation generated by thunderstorms and lightning is strong enough to generate phosphenes in a person located in the vicinity of lightning flashes. According to Cooray *et al.* [29], there are four scenarios that are of interest in connection with phosphenes stimulations. Following is a description of the four scenarios adapted from the work of Cooray *et al.* [29].

##### **24.4.1.1 Energetic electrons generated by leader steps**

X-ray bursts have been observed within several hundred metres of stepped leaders, dart stepped leaders and dart leaders. Dwyer *et al.* [45] measured X-ray energies up to 250 keV, but later Saleh *et al.* [51] measured a triggered lightning flash with X-ray energies extending up to about 1 MeV. From the measured energy spectrum of the X-ray photons, Saleh *et al.* [51] have estimated that a dart leader step should

produce about  $10^{17}$  energetic electrons per second with an average energy of about 1 MeV. Assuming that the radius of the electron beam is about 1 m, Dwyer *et al.* [52] have estimated the fluence of the electrons in the vicinity of the source to be  $3 \times 10^6$  electrons/cm<sup>2</sup>. This will decrease to  $3 \times 10^4$  electrons/cm<sup>2</sup> if the radius is assumed to be 10 m. Dwyer *et al.* [52] considered  $r = 10$  m to be a reasonable upper limit because this corresponds to the length of one dart leader step near to the ground.

Cooray *et al.* [29] calculated the fluence of electrons that will be injected through the roof of a building by a subsequent return stroke during a direct lightning strike and showed that for an input fluence (at the roof) of  $3 \times 10^6$  electrons/cm<sup>2</sup> the energy dissipated in the eye of a person located inside the building is about 3 MeV/cm. This calculation is based on the assumption that the spatial distribution of the electrons is isotropic. In reality, the electrons could be beamed and consequently the energy dissipation could be higher. Cooray *et al.* [29] also pointed out that in the case of first return strokes the electrons can be further accelerated in the electric field of the final jump region and, consequently, the energy dissipation in the eye tissue by a first return stroke could be higher. These energy dissipation values are beyond the limits necessary for phosphene generation.

#### **24.4.1.2 X-ray bursts from lightning**

Saleh *et al.* [51] estimated the average energy of X-ray photons emitted by the dart leader step to be a couple of hundred kiloelectron volts. The peak X-ray luminosity was estimated to be  $4 \times 10^{15}$  photons/s. Since the duration of the last dart leader step is about a microsecond, the total number of photons generated by a leader step is about  $4 \times 10^9$ . Assuming that the radius of the X-ray beam is about 1 m, the fluence of the X-rays in the vicinity of the source is about  $10^5$  photons/cm<sup>2</sup>. This will decrease to  $10^3$  photons/cm<sup>2</sup> if the radius is assumed to be 10 m.

Conducting an analysis similar to the one conducted for electrons, Cooray *et al.* [29] estimated that for a person located inside a building the energy dissipation in the eye by this radiation would be 9 MeV/cm to 125 MeV/cm depending on whether the incident fluence is  $10^3$  photons/cm<sup>2</sup> or  $10^5$  photons/cm<sup>2</sup>. These energy dissipation levels are beyond the threshold energies necessary for phosphenes stimulation.

#### **24.4.1.3 Terrestrial gamma rays**

Terrestrial gamma ray flashes are intense bursts of X-rays and gamma rays lasting a few milliseconds or less. Until recently, it had been assumed, based on theoretical calculations, that the energy of the flashes follows a power law spectra with a cut-off near 10 MeV [53–55]. Recently, Tavani *et al.* [56] found that the spectrum extends up to 100 MeV without exponential attenuation. The energy content of this extra high-energy component was about 10% of the total energy. In 2004, Dwyer *et al.* [41] observed a gamma ray flash with energies as high as 10 MeV at ground level generated during a lightning flash. The fluence of the photons in the flash which occurred at a height of about 8 km with energies up to about 10 MeV was about 1 photon/cm<sup>2</sup>. Analysing this data, Cooray *et al.* [29] showed that a similar

burst from a 5 km height cloud would dissipate about 250 MeV/cm in eye tissue that again is beyond the phosphenes threshold.

#### **24.4.1.4 Possible effects inside airplanes**

Cooray *et al.* [29] pointed out that another situation where humans could be exposed directly to bursts of energetic electrons and neutrons could arise if an airplane in flight were to intercept the source region of an ongoing terrestrial gamma ray flash. In such an encounter, the passengers would be exposed to a burst of electrons of fluence  $5 \times 10^8$  electrons/cm<sup>2</sup> having energies of the order of 10 MeV or more and delivered in less than 1 ms inside an aircraft. These electrons could also dissipate energies much beyond the phosphenes threshold in the eye.

#### *24.4.2 Concluding remarks concerning the possibility of phosphenes stimulation by energetic radiation of lightning and thunderstorms*

The information presented by Cooray *et al.* [29] shows conclusively that the energetic radiation produced by thunderstorms and lightning flashes could dissipate enough energy inside the human body to stimulate phosphenes in the visual system. Since the appearance of these phosphenes is similar to ball lightning, they suggested that some of the ball lightning observations could indeed be phosphenes generated by the interaction of this radiation with the visual system.

### **24.5 Stimulation of phosphenes by Corona currents**

Recently, Cooray *et al.* [57] demonstrated that the corona current generated from a persons head could be strong enough to excite phosphenes. As mentioned in the introduction, if a person stands within the striking distance of lightning flash, he or she will be exposed to a direct strike. However, as the distance between the person and the lightning flash increases, he would be exposed to an aborted connecting leader rather than receive a direct strike [58]. As the distance between the human and the lightning channel increases further, the background electric field generated by the down-coming stepped leader may decrease to such a level that only a corona burst is issued from the person's head, without a connecting leader. Based on a model identical to the one that was used previously to estimate currents in an aborted leader by Becerra and Cooray [58], Cooray *et al.* [57] estimated the magnitude and duration of the corona current from a head of a person under those circumstances.

Figure 24.4 shows the results obtained by Cooray *et al.* [57] for the growth of the corona current generated from a head as a function of time as the stepped leader approaches the ground. Cooray *et al.* [57] hypothesized that, since the skin resistance and the resistivity of the cranium are rather high, a considerable portion of this current will flow through the brain. Assuming that the conductivity of both the grey and white matter is about 0.1 S/m [13], Cooray *et al.* [57] evaluated the electric

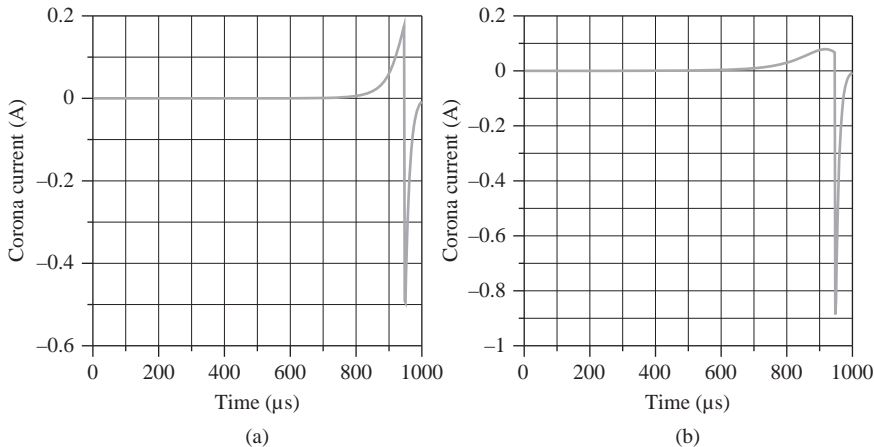


Figure 24.4 *Corona current generated from a person's head at certain distance from the lightning channel (a) 30 kA current at a distance of 40 m from the person. (b) 75 kA current at a distance of 90 m from the person. The speed of the down-coming stepped leader is  $5 \times 10^5$  m/s [adapted from Reference 57]*

field generated by the corona current in the brain using the relationship  $J = \sigma E$ , where  $J$  is the current density,  $E$  is the electric field and  $\sigma$  the conductivity. Assuming that the electric field in the brain tissue necessary to generate phosphene is about 20 V/m (based on TMS studies), the distance over which phosphenes could be generated by corona currents is evaluated as a function of return stroke peak current. The results are presented in Figure 24.5. In this figure, the region marked 1 shows the area within which a human will be exposed to a direct strike. In region 2, a human will be exposed to an aborted connecting leader. These regions were previously calculated and published by Becerra and Cooray [58]. In region 3, the amplitude of the corona current generated from a person's head is large enough to generate phosphene.

Cooray *et al.* [57] also pointed out that electric fields large enough to generate corona discharges may also appear inside houses during direct strikes if the house is made of insulating materials such as wood. A person located in such a house could be exposed to rather high electric fields capable of generating a corona discharge from the head during direct lightning strikes to the house. In such cases, visual perceptions similar to phosphene could occur indoors.

## 24.6 Concluding remarks

It is important to stress here that none of the authors of the papers [14–16, 22, 29] and [57] claimed that ball lightning is nothing but a visual sensation produced by the direct or indirect interaction of the electromagnetic fields of near by lightning flashes. However, their work shows the possibility that some of the ball

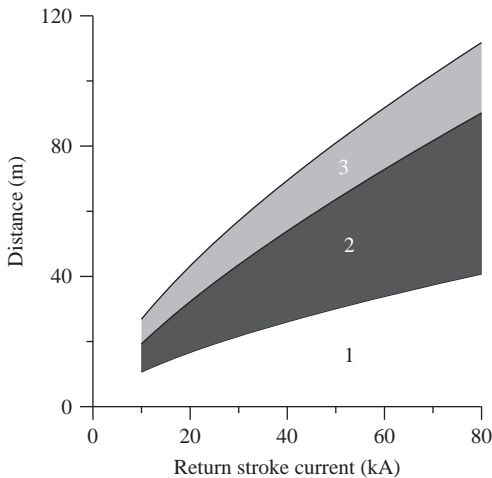


*Figure 24.5* The distance from a stepped leader within which a human will experience a direct strike (region 1), an aborted connecting leader (region 2) and a corona discharge large enough to excite cortical phosphenes (region 3) as a function of the prospective return stroke current associated with a stepped leader. Regions 1 and 2 were calculated previously by Becerra and Cooray [58]

lightning reports could be contaminated by the phosphene experiences caused by lightning electromagnetic fields. Their results may also help to separate the real physical facts of ball lightning from lightning electromagnetic effects on the brain paving the way for the future progress in the ball lightning research.

## References

1. Andrews, C. J., M. A. Cooper, M. Darveniza and D. Mackerras (Eds.), *Lightning injuries: Electrical, medical and legal aspects*, CRC Press, FL, 1992
2. Anderson, R. B., Does a fifth mechanism exist to explain lightning injuries, *IEEE Eng. Med. Biol.*, Jan–Feb, vol. 20, pp. 105–113, 2001
3. Cooray, V., C. Cooray and C.J. Andrews, Lightning caused injuries in humans, *J. Electrostat.*, vol. 65, no. 5–6, pp. 386–394, May 2007
4. Singer, S., *The Nature of Ball Lightning*, Plenum Press, New York, 1971
5. Barry, J. D., *Ball Lightning and Bead Lightning*, Plenum Press, New York, 1980
6. Stenhoff, M., *Ball Lightning – An Unsolved Problem in Atmospheric Physics*, Plenum Press, New York, 1999
7. Walsh, V. and A. Cowey, Nature reviews, *Neuroscience*, vol. 1, pp. 73–80, 2000
8. Currà, A., N. Modugno, M. Inghilleri, M. Manfredi, M. Hallett and A. Berardelli, Transcranial magnetic stimulation techniques in clinical investigation, *Neurology*, vol. 59, pp. 1851–1859, 2002

9. Tassinari, C. A., M. Cincotta, G. Zaccara and R. Michelucci, Transcranial magnetic stimulation and epilepsy, *Clin. Neurophysiol.*, vol. 114, pp. 777–798, 2003
10. Marg, E., Magneto-stimulation of vision: direct non invasive stimulation of the retina and the visual brain, *Optom. Vis. Sci.*, vol. 68, pp. 427–440, 1991
11. Marg, E. and D. Rudiak, Phosphenes induced by magnetic stimulation over the occipital brain: description and probable site of stimulation, *Optom. Vis. Sci.*, vol. 71, pp. 301–311, 1994
12. Bernhardt, J., The direct influence of electromagnetic fields on nerve and muscle cells of man within the frequency range 1 Hz to 30 MHz, *Radiat. Environ. Biophys.*, vol. 16, p. 309, 1979
13. Gabriel, C., A. Peyman and E. H. Grant, Electrical conductivity of tissue below 1 MHz, *Phys. Med. Biol.*, vol. 54, pp. 4863–4878, 2009
14. Peer, J. and A. Kendl, Transcranial stimulability of phosphenes by long lightning electromagnetic pulse, *Phys. Lett.*, vol. A 374, pp. 2932–2935, 2010
15. Peer, J., V. Cooray, G. Cooray and A. Kendl, Erratum and addendum to Transcranial stimulability of phosphenes by long lightning electromagnetic pulse, *Phys. Lett.*, vol. A 374, p. 2932, 2010
16. Cooray, G. and V. Cooray, Could some ball lightning observations be optical hallucinations caused by epileptic seizures?, *Open Atmos. Sci. J.*, vol. 2, pp. 101–105, 2008
17. Harrison, T. R. (Ed.), *Principles of Internal medicine*, 14th ed., McGraw-Hill, New York, 1998
18. Blom, S. T. Tomson and C-E Westerberg, Epilepsy, in *Neurology*, Edited by S-M Aquilonius and J. Fagius, Liber, Stockholm, 2000
19. Panayiotopoulos, C. P., Elementary visual hallucinations, blindness, and headache in idiopathic occipital epilepsy: differentiation from migraine, *J. Neurol. Neurosurg. Psychiatry*, vol. 66, pp. 536–540, 1999
20. Bien, C. G., F. D. Benninger and H. Urbach, Localizing value of epileptic visual auras, *Brain*, vol. 123, pp. 244–253, 2000
21. Taylor, I., I. E. Scheffer and S. F. Berkovic, Occipital epilepsies: identification of specific and newly recognized syndromes, *Brain*, vol. 126, pp. 753–769, 2003
22. Cooray, V. and G. Cooray, Could the intermittent light generated by lightning flashes trigger epileptic seizures?, Letter to the Editor, *J. Neurol. Neurosurg. Psychiatry*, <http://jnnp.bmjjournals.org/letters?first-index=31&hits=10>, 2010
23. Reilly, J. P., Peripheral nerve stimulation by induced electric currents: exposure to time-varying magnetic fields, *Med. Biol. Eng. Comput.*, vol. 27, pp. 101–110, 1989
24. Schaefer, D. J., J. D. Bourland and J. A. Nyenhuis, Review of patient safety in time-varying gradient fields, *J. Magn. Reson. Imaging*, vol. 12, pp. 20–29, 2000
25. Andrews, C., M. A. Cooper, T. Kotsos, N. Kitagawa and D. Mackerras, Magnetic effect of lightning strokes on the human heart, *J. Lightning Research*, vol. 1, pp. 158–165, 2007
26. Harding, G.F.A. and P. M. Jeavons, *Photosensitive Epilepsy*, 2nd ed., MacKeith Press, London, 1994

27. Rakov, A. A. and M. A. Uman, *Lightning: Physics and effects*, Cambridge University Press, Cambridge, 2003
28. Ferrie, C. D., P. De Marco, R. A. Grunewald, S Giannakodimos and C P Panayiotopoulos, Video game induced seizures, *J. Neurol. Neurosurg. Psychiatry*, vol. 57, pp. 925–931, 1994
29. Cooray, V., G. Cooray and J. Dwyer, On the possibility of phosphenes being generated by the energetic radiation from lightning flashes and thunderstorms, Submitted for *Phys. Lett. A*, 2011 [A summary of the work is also presented at International Symposium of Lightning Protection (SIPDA), Fortaleza, Brazil, 2011, under the title ‘Some of the ball lightning observations could be visual sensations produced by energetic radiation of thunderstorms and lightning’]
30. Lipetz, L. E., The X-ray and radium phosphenes, *Br. J. Ophthalmol.*, vol. 39, pp. 577–598, 1955
31. Tobias, C. A., *Radiation hazards in high altitude aviation*, *Aviation Med.*, vol. 23, p. 345, 1952
32. Akatov, Yu., V. Arkhangelsky, V. Petrov, K. Truckhanov, S. Adveev, Yu. Ozerov, *et al.*, Biomedical aspects of light flashes observed by astronauts during space flights. In *Proceedings of 6th European symposium on life sciences research in space*, Trondheim, Norway, June 16–20, ESA SP-390, 1996
33. Steidley, K. D., The radiation phosphene, *Vision Res.*, vol. 30, pp. 1139–1143, 1990
34. Fuglesang, C., Using the human eye to image space radiation or the history and status of the light flash phenomena, *Nucl. Instr. Meth. Phys. Res. A*, vol. 580, pp. 861–865
35. Shaw, G. E., Background cosmic count increases associated with thunderstorms, *J. Geophys. Res.*, vol. 72, pp. 4623–4626, doi:10.1029/JZ072i018p04623, 1967
36. Parks, G. K., B. H. Mauk, R. Spiger and J. Chin, X-ray enhancements detected during thunderstorm and lightning activities, *Geophys. Res. Lett.*, vol. 8, pp. 1176–1179, doi:10.1029/GL008i011p01176, 1981
37. McCarthy, M. and G. K. Parks, Further observations of X-rays inside thunderstorms, *Geophys. Res. Lett.*, vol. 12, pp. 393–396, doi:10.1029/GL012i006p00393, 1985
38. Eack, K. B., W. H. Beasley, W. D. Rust, T. C. Marshall and M. Stolzenburg, X-ray pulses observed above a mesoscale convection system, *Geophys. Res. Lett.*, vol. 23, pp. 2915–2918, doi:10.1029/96GL02570, 1996
39. Brunetti, M., S. Cecchini, M. Galli, G. Giovannini and A. Pagliarin, Gamma-ray bursts of atmospheric origin in the MeV energy range, *Geophys. Res. Lett.*, vol. 27, pp. 1599–1602, doi:10.1029/2000GL003750, 2000
40. Chubenko, A. P., V. P. Antonova, S. Y. Kryukov, V. V. Piskal, M. O. Ptitsyn, A. L. Shepetov, L. I. Vildanova, K. P. Zybin and A. V. Gurevich, Intense X-ray emission bursts during thunderstorms, *Phys. Lett. A*, vol. 275, pp. 90–100, doi:10.1016/S0375-9601(00)00502-8, 2000

41. Dwyer, J. R., H. K. Rassoul, M. Al-Dayeh, L. Caraway, B. Wright, A. Chrest, M. A. Uman, V. A. Rakov, K. J. Rambo, D. M. Jordan, J. Jerauld and C. Smyth, A ground level gamma-ray burst observed in association with rocket-triggered lightning, *Geophys. Res. Lett.*, vol. 31, L05119, doi: 10.1029/2003GL018771, 2004
42. Tsuchiya, H., T. Enoto, S. Yamada, T. Yuassa, M. Kawaharada, T. Kitaguchi, M. Kokukbun, H. Kato, M. Okano, S. Nakamura and K. Makishima, Detection of high-energy gamma rays from winter thunderstorms, *Phys. Rev. Lett.*, vol. 99, 165002, doi:10.1103/PhysRevLett.99.165002, 2007
43. Moore, C. B., K. B. Eack, G. D. Aulich and W. Rison, Energetic radiation associated with lightning stepped-leaders, *Geophys. Res. Lett.*, vol. 28, pp. 2141–2144, doi:10.1029/2001GL013140, 2001
44. Dwyer, J. R., M. A. Uman, H. K. Rassoul, M. Al-Dayeh, L. Caraway, J. Jerauld, V. A. Rakov, D. M. Jordan, K. J. Rambo, V. Corbin and B. Wright, Energetic radiation produced during rocket triggered lightning, *Science*, vol. 299, pp. 694–697, doi:10.1126/science.1078940, 2003
45. Dwyer, J. R., H. K. Rassoul, M. Al-Dayeh, L. Caraway, B. Wright, A. Chrest, M. A. Uman, V. A. Rakov, K. J. Rambo, D. M. Jordan, J. Jerauld and C. Smyth, Measurements of X-ray emission from rocket triggered lightning, *Geophys. Res. Lett.*, vol. 31, L05118, doi:10.1029/2003GL018770, 2004
46. Dwyer, J. R., H. K. Rassoul, M. Al-Dayeh, L. Caraway, A. Chrest, B. Wright, E. Kozak, J. Jerauld, M. A. Umna, V. A. Rakov, D. M. Jordan, K. J. Rambo, X-ray bursts associated with leader steps in cloud-to-ground lightning, *Geophys. Res. Lett.*, vol. 32, L01803, doi:10.1029/2004GL021782, 2005
47. Howard, J., M. A. Uman, J. R. Dwyer, D. Hill, C. Biagi, Z. Saleh, J. Jerauld and H. K. Rassoul, Co-location of lightning leader X-ray and electric field change sources, *Geophys. Res. Lett.*, vol. 35, L13817, doi:10.1029/2008GL034134, 2008
48. Fishman, G. J., *et al.*, Discovery of intense gamma-ray flashes of atmospheric origin, *Science*, vol. 264, pp. 1313–1316, doi:10.1126/science.264.5163.1313, 1994
49. Smith, D. M., L. I. Lopez, R. P. Lin and C. P. Barrington-Leigh, Terrestrial gamma-ray flashes observed up to 20 MeV, *Science*, vol. 307, pp. 1085–1088, 2005
50. Cohen, M. B., U. S. Inan and G. R. Fishman , Terrestrial gamma ray flashes observed aboard compton gamma ray observatory/burst and transient source experiment and ELF/VLF radio atmospherics, *J. Geophys. Res.*, vol. 111, D24109, doi:10.11029/2005JD006987, 2006
51. Saleh, Z., J. Dwyer, H. Rassoul, M. Bakhtiari, M. Uman, J. Howard, D. Concha, M. Stapleton and D. Hill, Properties of the X-ray emission from rocket-triggered lightning as measured by the Thunderstorm Energetic Radiation Array, *J. Geophys. Res.*, vol. 114, D17210, doi:10.1029/2008JD011618, 2009
52. Dwyer, J. R., D. M. Smith, M. A. Uman, Z. Saleh, B. Grefenstette and H. K. Rassoul, Estimation of the fluence of high-energy electron bursts

- produced by thunderclouds and resulting radiation doses received in aircraft, *J. Geophys. Res.*, vol. 115, D09206, doi:10.1029/2009JD012039, 2010
- 53. Dwyer, J. R. and D. M. Smith, A comparison between Monte Carlo simulations of runaway breakdown and terrestrial gamma-ray flash observations, *Geophys. Res. Lett.*, vol. 32, L22804, doi:10.1029/2005GL023848, 2005
  - 54. Lehtinen, N. G., T. F. Bell and U. S. Inan, Monte Carlo simulation of runaway MeV electron breakdown with application to red sprites and terrestrial gamma ray flashes, *J. Geophys. Res.*, vol. 104, pp. 24699, 1999
  - 55. Dwyer, J. R., Source mechanisms of terrestrial gamma-ray flashes, *J. Geophys. Res.*, vol. 113, D10103, doi:10.1029/2007JD009248, 2008
  - 56. Tavani, M., *et al.*, Terrestrial gamma-ray flashes as powerful particle accelerators, *Phys. Rev. Lett.*, vol. 106, p. 018501, 2011
  - 57. Cooray, V., G. Cooray and M. Becerra, Corona currents generated from a person's head in the vicinity of lightning strikes — Stimulation of phosphenes, 7<sup>th</sup> Asia-Pacific International Conference on Lightning, Chengdu, China, 2011
  - 58. Becerra, M. and V. Cooray, On the interaction of lightning upward connecting positive leaders with humans, *IEEE Trans. Electromagn. Compat.*, vol. 51, no. 4, pp. 1001–1008, 2009

---

## *Chapter 25*

# **Modelling lightning strikes to tall towers**

*Farhad Rachidi<sup>1</sup> and Marcos Rubinstein<sup>2</sup>*

---

## **25.1 Introduction**

In this chapter, we present a review of recent progress in the modelling of lightning strikes to tall structures. Since some tall structures are struck by lightning several tens of time per year, they can be used as ground-truth to measure and calibrate the location accuracy of lightning location systems. In addition, knowledge of the transient processes in tall objects when they are subjected to a lightning strike allows us to use them to calibrate the lightning return-stroke currents reported by lightning detection and location systems. Tall objects constitute also a primary source of data from which channel-base lightning current statistics are obtained. These statistics are in turn used to improve the design of lightning protection devices and systems.

This chapter is organized as follows: Section 25.2 presents a review of the extension of lightning return-stroke models to include the presence of an elevated strike object. Section 25.3 deals with the computational methods for the evaluation of the electromagnetic fields generated by lightning strikes to tall structures. A review of available data on lightning currents from lightning to tall structures is presented in Section 25.4. Finally, a summary is given in Section 25.5.

## **25.2 Modelling lightning strikes to tall structures**

The presence of an elevated strike object has been included in two classes of return-stroke models, namely the engineering models and the electromagnetic or antenna theory (AT) models, as defined by Rakov and Uman [1]. In the engineering return-stroke models, the spatial and temporal distribution of the channel current is specified based on observed characteristics such as channel-base current, return-stroke speed and remote electromagnetic fields. The presence of an elevated strike object in such models has been considered by assuming the object as a uniform, lossless transmission line [2]. In AT models [3–6], the strike object and the lightning channel are represented using thin wires. Maxwell’s equations are numerically solved using

<sup>1</sup>Swiss Federal Institute of Technology (EPFL), Lausanne, Switzerland

<sup>2</sup>University of Applied Sciences, Western Switzerland HES-SO, Yverdon, Switzerland

usually the method of moments (MoM) [7] to find the current distribution along the lightning channel, from which the radiated electromagnetic fields can be computed. Besides the electromagnetic and engineering model classes, the so-called *hybrid electromagnetic (HEM)/circuit theory* model could be considered as a third class based on a combination of the electromagnetic approach and circuit theory [8, 9]. Each of the model classes will be presented in turn in the next few sections.

### 25.2.1 Engineering models

To analyse the interaction of lightning with tall strike objects, some of the engineering return-stroke models, initially developed for the case of return strokes initiated at ground, have been extended to take into account the presence of a vertically extended strike object [10–24]. In some of these models, it is assumed that a current pulse  $i_0(t)$  associated with the return-stroke process is injected at the lightning attachment point, both into the strike object and into the lightning channel [11, 12, 14–21]. The upward-moving wave propagates along the channel at the return-stroke speed  $v$  as specified by the return-stroke model. The downward-moving wave propagates at the speed of light along the strike object, assumed to be a lossless, uniform transmission line characterized by constant non-zero reflection coefficients at its top and its bottom. As noted in Reference 13, the assumption of two identical current waves injected into the lightning channel and into the strike object implies that their characteristic impedances are equal to each other. If the impedance of the channel is considered to be time-invariant, this assumption appears to compromise the self-consistency of the models in that there is no impedance discontinuity at the tower top at the time of lightning attachment to the tower, but there is one when the reflections from ground arrive at the tower top.

#### 25.2.1.1 Extension of engineering models based on a distributed source representation

Rachidi *et al.* [2] presented an extension of the so-called engineering return-stroke models, taking into account the presence of a vertically extended strike object, which does not employ the assumption that identical current pulses are launched both upwards and downward from the object top. The extension is based on a distributed source representation of the return-stroke channel [25, 26], which allows for more general and straightforward formulations of these models than the traditional representations, which imply a lumped current source at the bottom of the channel.

The general equations for the spatial-temporal distribution of the current along the lightning channel and along the strike object derived in Reference 2 are

$$\begin{aligned} i(z', t) = & \left[ P(z' - h) i_0 \left( h, t - \frac{z' - h}{v^*} \right) - \rho_t i_0 \left( h, t - \frac{z' - h}{c} \right) \right. \\ & \left. + (1 - \rho_t)(1 + \rho_t) \sum_{n=0}^{\infty} \rho_g^{n+1} \rho_t^n i_0 \left( h, t - \frac{h + z'}{c} - \frac{2nh}{c} \right) \right] u \left( t - \frac{z' - h}{v} \right) \end{aligned} \quad (25.1)$$

for  $h < z' < H_0$

$$\begin{aligned} i(z', t) = (1 - \rho_t) \sum_{n=0}^{\infty} & \left[ \rho_t^n \rho_g^n i_0 \left( h, t - \frac{h-z'}{c} - \frac{2nh}{c} \right) \right. \\ & \left. + \rho_t^n \rho_g^{n+1} i_0 \left( h, t - \frac{h+z'}{c} - \frac{2nh}{c} \right) \right] \end{aligned} \quad (25.2)$$

for  $0 \leq z' \leq h$

where  $h$  is the height of the tower,  $\rho_t$  and  $\rho_g$  are the top and bottom current reflection coefficients for upward and downward propagating waves, respectively, given by

$$\rho_t = \frac{Z_t - Z_{ch}}{Z_t + Z_{ch}} \quad (25.3)$$

$$\rho_g = \frac{Z_t - Z_g}{Z_t + Z_g} \quad (25.4)$$

$H_0$  is the total height of the extending return-stroke channel,  $c$  is the speed of light,  $P(z')$  is a model-dependent attenuation function,  $u(t)$  the Heaviside unit-step function,  $v$  is the return-stroke front speed, and  $v^*$  is the current wave speed. Expressions for  $P(z')$  and  $v^*$  for some of the most commonly used return-stroke models are summarized in Table 25.1, in which  $\lambda$  is the attenuation height for the modified transmission line with exponential decay (MTLE) model and  $H_{tot}$  is the total height of the lightning channel.

Equations (25.1) and (25.2) are based on the concept of ‘undisturbed current’  $i_0(t)$ , which represents the ‘ideal’ current that would be measured at the tower top if the current reflection coefficients at both of its extremities were equal to zero.

It is assumed that the current reflection coefficients  $\rho_t$  and  $\rho_g$  are constant. In addition, any upward-connecting leader and any reflections at the return-stroke wavefront [19] are disregarded.

Table 25.1  $P(z')$  and  $v^*$  for different return-stroke models [adapted from Reference 1]

Model	$P(z')$	$v^*$
BG	1	$\infty$
TCS	1	$-c$
TL	1	$v$
MTLL	$1-z'/H_{tot}$	$v$
MTLE	$\exp(-z'/\lambda)$	$v$

More recently, an extension of the engineering models was proposed by Mosaddeghi *et al.* [27] that takes into account the presence of possible reflections at the return-stroke wavefront and a return-stroke initiation above the structure due to an upward-connecting leader. Based on the approach proposed by Shostak *et al.* [19], Mosaddeghi *et al.* derived closed-form iterative solutions for the current distribution along the channel and the strike object. Mosaddeghi *et al.* [27] used their enhanced model to obtain simulations for the magnetic fields and compared them with experimental waveforms associated with lightning strikes to the CN Tower (553 m). They showed that taking into account the reflections at the return-stroke wavefront results in a better agreement regarding the typical features of the magnetic fields [27].

### **25.2.1.2 Extension of engineering models based on a lumped series voltage source**

Baba and Rakov [24, 28] proposed an alternative approach to the distributed source representation by Rachidi *et al.* [2] using a lumped series voltage source at the junction point between the channel and the strike object. They showed that such a representation ensures appropriate boundary conditions at the attachment point and is equivalent to the distributed source representation [28]. In their representation, Baba and Rakov expressed the spatial–temporal distribution of the current along the strike object and along the channel in terms of the short-circuit current  $i_{sc}(t)$ , which is related to the undisturbed current through

$$i_{sc}(t) = 2i_0(t) \quad (25.5)$$

Furthermore, in Reference 28, Baba and Rakov considered in their expressions a different speed  $v_{ref}$  for the upward propagating current waves reflected from the ground and then transmitted into the lightning channel.

Note that an equivalent representation in terms of the so-called reference current – the current that would flow through the return-stroke channel in the absence of the elevated struck object – has also been proposed by Shighara and Piantini [29].

### **25.2.1.3 On the representation of the elevated strike object**

In all engineering models, the elevated strike object is modelled as an ideal transmission line. To include the structural discontinuities of the elevated strike object, several transmission line sections in cascade have also been considered [14, 30]. The transmission line representation of the elevated strike object has been shown to yield reasonable results in comparison with experimental data. However, the waveforms of experimentally measured current data associated with lightning to tall structures are affected by other, less-easily controlled factors such as the variability of lightning channel impedance and possible reflections at the return-stroke wavefront [31]. In Reference 32, Bermudez *et al.* presented an experimental validation of the transmission line representation of an elevated object struck by lightning. The experimental results were obtained using a reduced-scale model and

injected signals with narrow pulse widths (down to 500 ps). The validation was performed using a reduced-scale structure representing the Toronto CN Tower in Canada. Two models consisting, respectively, of a single section uniform transmission line and a three-section uniform transmission line were considered for the comparison. It was shown that the three-section model was able to accurately reproduce the obtained experimental data. The overall agreement between the single-section model and the experimental results was also satisfactory for the early-time response, although some differences appeared for later times.

More recently, finite difference time domain (FDTD) simulations performed by Baba and Rakov [33] and confirmed by Shoory *et al.* [34] suggest that the waveguide properties of a biconical antenna (representing a tower) depend on the direction of propagation. In particular, while the current pulses suffer no attenuation as they travel from the tower apex to its base, the attenuation is significant when they propagate from the base to the apex [33]. This finding might render questionable the validity of reflection coefficients at ground level inferred from the measurements of current at the top of the tower.

### 25.2.1.4 Current distribution along the channel as predicted by engineering models

Pavanello *et al.* [35] compared the spatial–temporal distribution of the current predicted by engineering models (based on the distributed source representation), employing an undisturbed current  $i_0(t)$ , given by

$$i_0(h, t) = \frac{I_{01}}{\eta} \frac{(t/\tau_1)^2}{1 + (t/\tau_1)^2} e^{(-t/\tau_2)} + I_{02}(e^{-t/\tau_3} - e^{-t/\tau_4}) \quad (25.6)$$

This undisturbed current is shown in Figure 25.1, where the values of the parameters chosen are  $I_{01} = 9.9$  kA,  $\eta = 0.845$ ,  $\tau_1 = 0.072$   $\mu$ s,  $\tau_2 = 5.0$   $\mu$ s,  $I_{02} = 7.5$  kA,  $\tau_3 = 100.0$   $\mu$ s,  $\tau_4 = 6.0$   $\mu$ s. These values correspond to the channel-base current adopted in Reference 36 to compare ground-initiated lightning return-stroke models. Starting from the same undisturbed current, the spatial–temporal distributions of the current along the channel and along the strike object were calculated for each model (see Figure 25.1).

In the calculation, the elevated strike object was assumed to have a height  $h = 168$  m, corresponding to the Peissenberg Tower in Germany, and the reflection coefficients were set, respectively, to  $\rho_t = -0.53$  and  $\rho_g = 0.7$  [37].

Figure 25.2 shows the current distribution along the tower and along the channel, at different time instants ( $t = 1, 2, \dots, 10$   $\mu$ s), predicted by each model.

It can be seen that [35]

- In accordance with Equation (25.2), the current distribution along the tower (the lower part of each figure, for heights up to the 168 m height of the tower) is independent of the model.
- The Bruce-Golde (BG) and traveling current source (TCS) models exhibit a strong discontinuity at the return-stroke wavefront, inherent in these models [1].

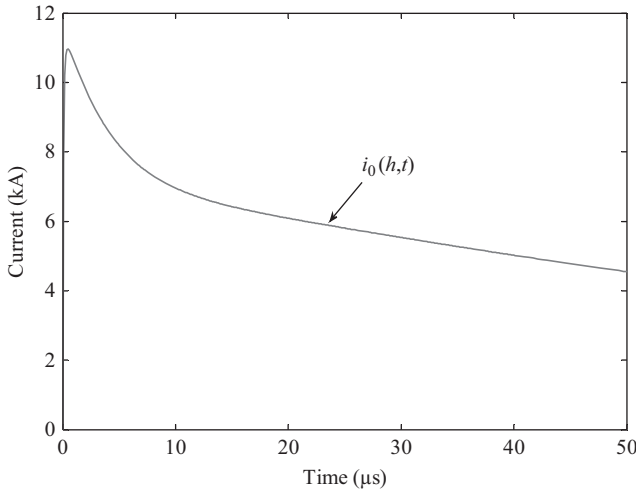


Figure 25.1 Undisturbed current [adapted from Reference 35]

- Although not clearly visible due to the vertical scale of Figure 25.2, the return-stroke wavefront for the transmission line (TL), modified transmission line with linear decay (MTLL) and MTLE models also exhibits a discontinuity at the front. This discontinuity arises from the fact that the current injected into the tower at its top is reflected back and forth at its top and bottom ends, and portions of this current are transmitted into the channel; these transmitted pulses, which are assumed to travel at the speed of light, catch up with the return-stroke wavefront travelling at a lower speed, but not allowed to propagate into the leader channel above the return-stroke front [38].

Figure 25.3 shows the waveforms of current evaluated at the top (168 m) and the base of the tower (0 m). The effects of the multiple reflections at the tower extremities are clearly visible in the waveforms. It can also be seen that the current at the tower base has a higher peak value due to the contribution from the reflected wave at ground level [35].

### 25.2.1.5 Determination of reflection coefficients at the top and the bottom of the strike object

Engineering models require that the reflection coefficients at the top and bottom of the strike object be known. In most of the studies, those coefficients are assumed to be constant and frequency-independent. The values of the reflection coefficients have been inferred by several authors from a limited experimental set of current waveforms found in the literature [39–41]. The knowledge of the reflection coefficients is also required to extract the ‘primary’ (or undisturbed) current exempt from the disturbances introduced by the transient processes along the tower.

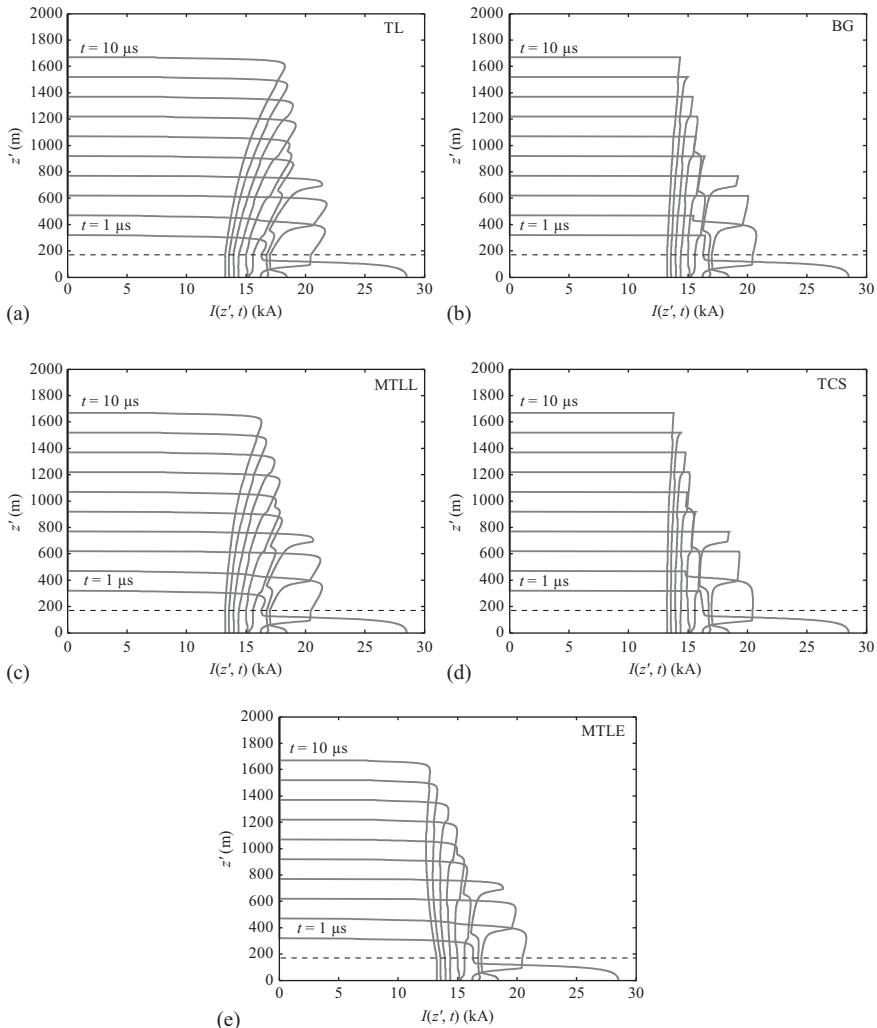


*Figure 25.2 Current as a function of height  $z'$  at ten instants of time,  $t = 1, 2, \dots, 10 \mu\text{s}$ , for five models starting from the same undisturbed current (shown in Figure 25.1). (a) TL model, (b) BG model, (c) MTL model, (d) TCS model and (e) MTLE model. The horizontal dashed line indicates the height of the tower (168 m) [adapted from Reference 35]*

Guerrieri *et al.* [12] proposed a formula, corrected by Rachidi *et al.* [2], to extract the undisturbed current. The formula involves an infinite summation in the time domain, assuming that the reflection coefficients are constant and known. Gavric [42] proposed an iterative method based on the Electromagnetic Transient Program (EMTP)

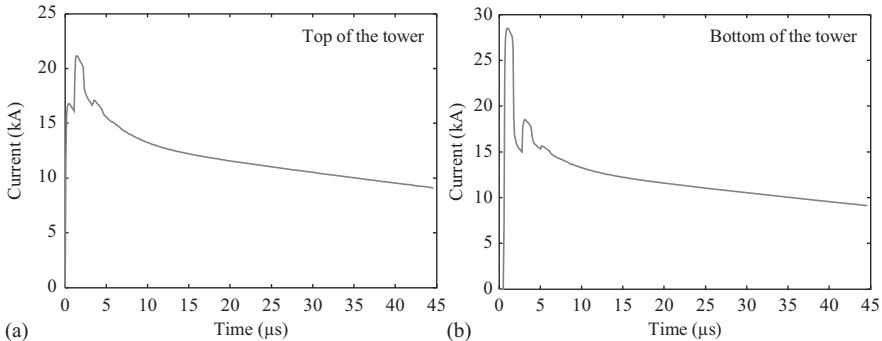


*Figure 25.3 Current at the top (a) and at the bottom (b) of a 168-m tower [adapted from Reference 35]*

to remove superimposed reflections caused by a strike tower from digitally recorded lightning flash currents. Janischewskyj *et al.* [43] derived reflection coefficients at the CN Tower in Toronto and stated that the values depend on the initial rise time of the measured current, although the limited number of points in their plots render the drawing of conclusions difficult. A dependence on the risetime would suggest that at least one of the reflection coefficients is a function of the frequency. They also proposed a method to extract the reflection coefficients from the measured current waveform. However, their method is applicable only assuming a simplified current waveform (double ramp) and neglecting any frequency dependence for the reflection coefficients. The last consideration was relaxed in a first approximation by Bermudez *et al.* [22]. They derived a frequency-domain counterpart of expressions (25.1) and (25.2) which include the frequency dependence of reflection coefficients. They also derived an expression to calculate the reflection coefficient as a function of frequency at the bottom of the lightning strike object from two currents measured at different heights along the strike object.

Interestingly, Bermudez *et al.* [22] showed that, if the current and its time derivative overlap with reflections at the top or bottom of the strike object, it is impossible to derive the reflection coefficient at the top of the strike object exactly regardless of the number of simultaneous current measurements and they proposed an extrapolation method to estimate this reflection coefficient. They applied their proposed methodology to experimental data obtained on Peissenberg Tower (Germany) consisting of lightning currents measured at two heights and obtained results that suggest that the reflection coefficient at ground level can be considered as practically constant in the frequency range 100 to 800 kHz [22].

### 25.2.2 Electromagnetic models

Electromagnetic models have been widely employed by lightning researchers for investigating lightning strikes to tall structures. An AT-type model was first

proposed by Podgorski and Landt [3, 44] in 1985 and it was applied to analyse lightning strikes to the CN Tower. In AT-type models [4–6, 45], the elevated strike object is represented using thin wires and the ground is generally assumed to be perfectly conducting. More recently, the finite conductivity of the ground and the buried grounding structure of the tower have been included in the analysis [46, 47]. The lightning return-stroke channel is modelled as a vertical wire antenna and the lightning return-stroke current is injected by a voltage source at the tip of the tower. The current distribution along the channel and along the tower is found by solving an electric field integral equation [6].

### 25.2.3 Hybrid electromagnetic model

The so-called hybrid electromagnetic model [8, 9] is a combination of electromagnetic and circuit theory models. In this model, the electric scalar and magnetic vector potentials are employed to take into account electromagnetic coupling, which is represented in terms of circuit quantities, voltages and currents.

## 25.3 Electromagnetic field computation

In contrast with electromagnetic models for which electromagnetic fields are computed simultaneously with the distribution of the current along the radiating structure (strike object and lightning channel), the use of engineering models, which specify the spatial-temporal distribution of the current along the channel and the struck object, require the evaluation of the associated electromagnetic fields. The calculation procedure essentially depends on the electromagnetic properties of the ground. When the ground can be assumed to be a perfectly conducting plane, image theory can be adopted for the evaluation of the electromagnetic fields. For distances not exceeding a few kilometres, the perfect ground assumption is considered to be a reasonable approximation for the vertical component of the electric field and for the azimuthal component of the magnetic field [48, 49]. Indeed, even for a finitely conducting ground, contributions of the source dipole and of its image (see Figure 25.4) to these field components add constructively and, consequently, relatively small variations in the image field due to the finite ground conductivity will have little effect on the total field. However, the horizontal (radial) component of the electric field radiated by lightning is appreciably affected by the finite ground conductivity. Indeed, for this field component, the effects of the two contributions subtract, and small changes in the image field may lead to appreciable changes in the total horizontal field. Although the intensity of the horizontal field component is generally much smaller than that of the vertical field, within the context of certain field-to-transmission line coupling models [50], this component plays an important role and, thus, its calculation requires the use of rigorous expressions or at least reasonable approximations.

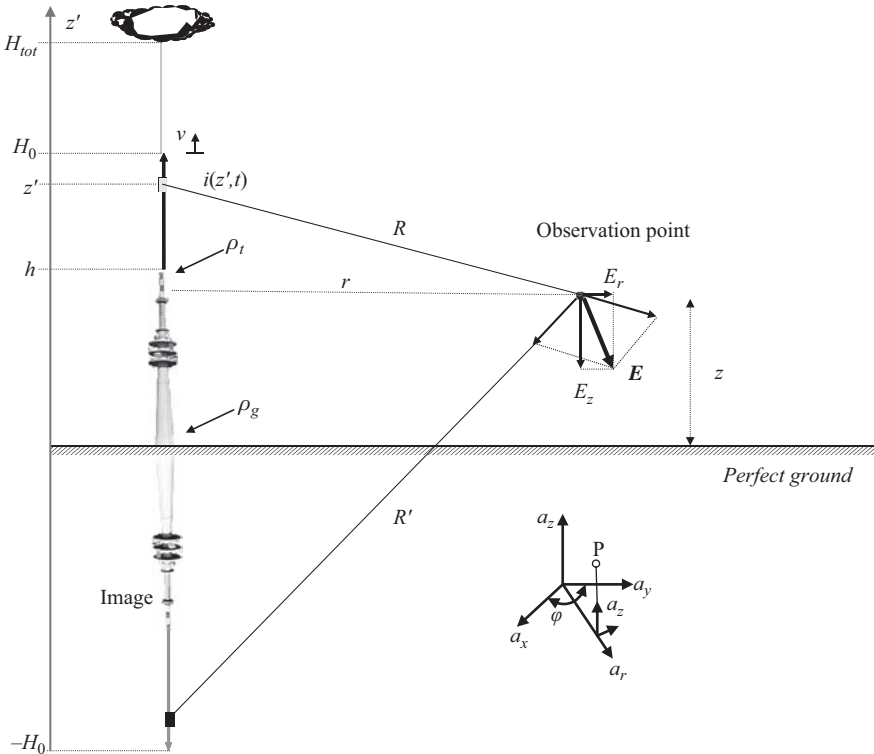


*Figure 25.4* Adopted geometry for field computation [after Reference 51]

### 25.3.1 Electromagnetic field expressions for a perfectly conducting ground

With reference to (25.1), the current at a height  $z'$  along the lightning channel results from the contribution of a series of time-delayed current components. The first one, moving upward at a constant speed  $v$ , represents the return-stroke wavefront that progressively turns on the distributed current sources [2] by way of which the channel is modelled.

Assuming that no current flow is possible above this return-stroke wavefront, the current distribution is abruptly interrupted at this front [38, 51] as discussed further in the next paragraph. This is mathematically expressed by the Heaviside function present in (25.2).

All other contributions resulting from multiple reflections at the two ends of the tall structure are supposed to travel at the speed of light. Because of their higher speed, they catch up with the return-stroke wavefront providing a non-zero contribution that leads to a discontinuity mentioned in the previous paragraph if no current is admitted above the front. Notice that this truncation already produces a discontinuity at time  $t = 0^+$  since the contribution of the very first distributed

current source in the channel is reflected from the tower top and propagates upward at the speed of light [38].

The current discontinuity may only occur if there is accumulation of charge at the wavefront. This has led some researchers to suggest that the abrupt halt in the current may be unlikely or inconceivable from a physical point of view. Regardless of the physical merits of the assumption, the discontinuity must still be considered in the analysis for the sake of consistency with the adopted engineering models.

The electromagnetic field contributions from an elemental dipole of current  $i(z', t)$  of length  $dz'$  located along the vertical axis at  $z'$  (see Figure 25.4) are calculated with the usual expressions valid for a perfectly conducting ground [52]:

$$dE_z(r, z, z', t) = \frac{dz'}{4\pi\epsilon_0} \left[ \frac{2(z - z')^2 - r^2}{R^5} \int_{R/c}^t i(z', \tau - R/c) d\tau + \frac{2(z - z')^2 - r^2}{cR^4} i(z', t - R/c) - \frac{r^2}{c^2 R^3} \frac{\partial i(z', t - R/c)}{\partial t} \right] \quad (25.7)$$

$$dE_r(r, z, z', t) = \frac{dz'}{4\pi\epsilon_0} \left[ \frac{3r(z - z')}{R^5} \int_{R/c}^t i(z', \tau - R/c) d\tau + \frac{3r(z - z')}{cR^4} i(z', t - R/c) + \frac{r(z - z')}{c^2 R^3} \frac{\partial i(z', t - R/c)}{\partial t} \right] \quad (25.8)$$

$$dH_\phi(r, z, z', t) = \frac{dz'}{4\pi} \left[ \frac{r}{R^3} (z', t - R/c) + \frac{r}{cR^2} \frac{\partial i(z', t - R/c)}{\partial t} \right] \quad (25.9)$$

in which

- $r$  and  $z$  are the cylindrical coordinates of the observation point,
- $R$  is the distance between the dipole and the observation point,  

$$R = \sqrt{r^2 + (z' - z)^2},$$
- $i(z', t)$  is the dipole current,
- $c$  is the speed of light and
- $\epsilon_0$  is the permittivity of free space.

The total electromagnetic fields are calculated by integrating the above equations along the tower channel and its image, assuming a perfectly conducting ground.

In the presence of a current discontinuity, the radiation term, namely the last term in each equation, which is proportional to the current time-derivative, introduces a singularity that needs to be treated separately [52–57].

### 25.3.1.1 Turn-on term

The complete expression of the electromagnetic field is obtained by integrating (25.7) through (25.9) along  $z'$  from ground level to the wavefront and then by adding the corrective turn-on term across the discontinuity in  $H$ , expressed as

$$\int_H f(z', z, r) \frac{\partial i(z', t - R/c)}{\partial t} dz' \quad (25.10)$$

where  $f(z', z, r)$  can be  $r^2/c^2 R^3$ ,  $r(z-z')/c^2 R^3$  or  $r/cR^2$ , depending on which component of the field is being calculated [38].

The reason why an additional turn-on term must be introduced in the field equations is that the presence of the Heaviside function in (2.1) cannot be disregarded when the time-derivative of the current is calculated. Its derivative, namely, a delta function, multiplied by the amplitude of the current at the wavefront, needs to be added to the radiation term. In the case in which the current distribution presents no discontinuity at the return-stroke wavefront, this turn-on term contribution vanishes. The discontinuity can be treated considering a continuous current wavefront of length  $\Delta z''$  that reaches the level  $I_{\text{front}}$  linearly in a time  $\Delta t$ , and expressing the radiation integral across  $H$  taking the limit when the front duration tends to zero [52].

The final expressions for the turn-on term fields, in which the apparent front speed appears as the reciprocal of the term between brackets, are given by [38]:

$$H_{\Phi/\text{turn-on}} = \frac{I_{\text{front}}(H) \cdot r}{4\pi c R^2} \cdot \frac{1}{[(1/v) - ((z - H)/cR)]} + \frac{I_{\text{front}}(H') \cdot r}{4\pi c R'^2} \cdot \frac{1}{[(1/v) - ((z - H')/cR')]} \quad (25.11)$$

$$E_{r/\text{turn-on}} = \frac{I_{\text{front}}(H) \cdot r \cdot (z - H)}{4\pi \epsilon_0 c^2 R^3} \cdot \frac{1}{[(1/v) - ((z - H)/cR)]} - \frac{I_{\text{front}}(H') \cdot r \cdot (z - H')}{4\pi \epsilon_0 c^2 R'^3} \cdot \frac{1}{[(1/v) - ((z - H')/cR')]} \quad (25.12)$$

$$E_{r/\text{turn-on}} = - \frac{I_{\text{front}}(H) \cdot r^2}{4\pi \epsilon_0 c^2 R^3} \cdot \frac{1}{[(1/v) - ((z - H)/cR)]} - \frac{I_{\text{front}}(H') \cdot r^2}{4\pi \epsilon_0 c^2 R'^3} \cdot \frac{1}{[(1/v) - ((z - H')/cR')]} \quad (25.13)$$

In (25.11)–(25.13), the two terms on the right-hand side represent the turn-on term due to the discontinuity at the wavefront and at its image, respectively.

The general expression for the current at the wavefront is simply obtained from (25.1), in which the time variable  $t$  appears implicitly through  $H$  [38]:

$$\begin{aligned}
 I_{front}(H) = & P(H-h)i_0\left(h, \frac{H-h}{v} + \frac{1}{c}\sqrt{r^2 + (H-z)^2} - \frac{H-h}{v^*}\right) \\
 & - \rho_t i_0\left(h, \frac{H-h}{v} + \frac{1}{c}\sqrt{r^2 + (H-z)^2} - \frac{H-h}{c}\right) \\
 & + (1-\rho_t)(1+\rho_t)\sum_{n=0}^{\infty} \rho_g^{n+1} \rho_t^n \\
 & \times i_0\left(h, \frac{H-h}{v} + \frac{1}{c}\sqrt{r^2 + (H-z)^2} - \frac{H+h}{c} - \frac{2nh}{c}\right)
 \end{aligned} \quad (25.14)$$

It is worth observing that the first term on the right-hand side of (25.14) is non-zero only for the BG and TCS models, and it corresponds to the inherent discontinuity predicted by these two models. As a consequence of this, the turn-on term has the same expression for the TL, MTLL and MTLE models [38].

The contribution of the turn-on term to the total field depends on many factors, such as the height of the tower, the reflection coefficients at its extremities, the return-stroke speed and the position of the observation point (distance and elevation). Pavanello *et al.* [38] found that the contribution of the turn-on term to the total electric and magnetic fields is negligible at close distances (below 100 m) and increases rapidly to reach an asymptotic value of about 12% at a distance of 5 km and beyond. At these distances, the field peak is essentially due to the radiation term.

### 25.3.1.2 Comparison between different engineering models

Pavanello *et al.* [35] compared five engineering models\* (BG, TCS, TL, MTLL and MTLE) employing the same undisturbed current  $i_0(t)$  presented in Figure 25.1. The elevated strike object was assumed to have a height  $h = 168$  m, corresponding to the Peissenberg Tower in Germany.

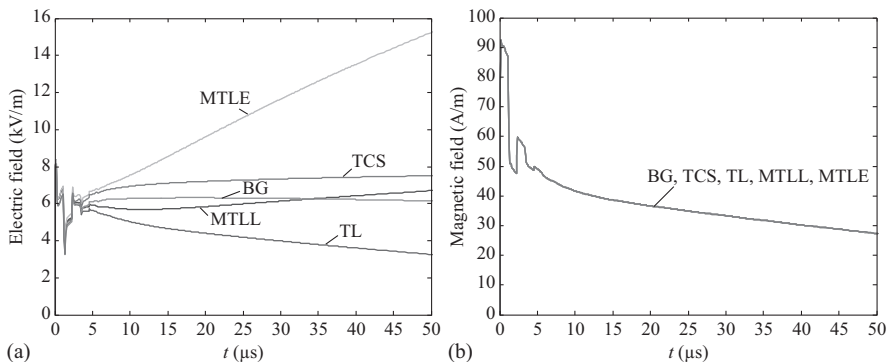
The reflection coefficients are set, respectively, to  $\rho_t = -0.53$  and  $\rho_g = 0.7$  [37].

Figure 25.5 presents electric and magnetic fields calculated at a distance of 50 m from the tower base [35]. At this distance, the electric field is dominated (for late times, after the initial fast transition) by its electrostatic term. The model-predicted electric fields are very similar for the first 5  $\mu$ s, beyond which the BG, TCS and MTLL models predict the flattening of the field, typically observed at close distances, while the TL model predicts a field decay. The late-time E-field predicted by the MTLE model exhibits a ramp, as in the case of a ground-initiated return stroke [35]. Note, however, that a judicious choice of the attenuation factor would result in the flattening of the late-time E-field at close range [58].

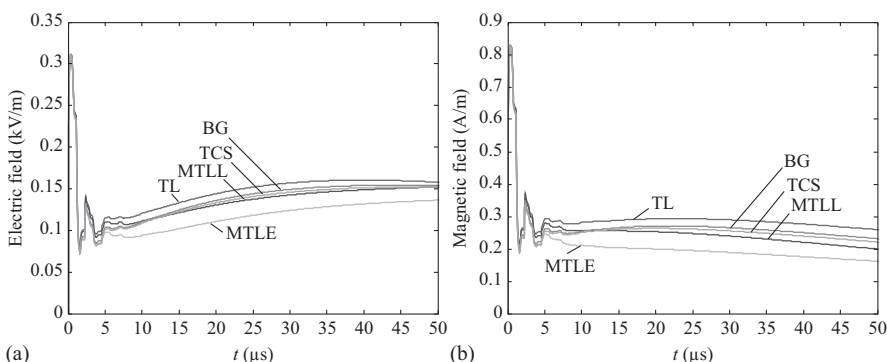
\*Extended using the distributed source approach.

Figure 25.5(b) shows that the predicted magnetic field is nearly model independent. At this distance, the magnetic field is dominated by its induction term, and its waveshape is similar to the current at the base of the tower shown in Figure 25.3(b).

Figure 25.6 presents calculated electric and magnetic fields at a distance of 5 km [35]. The electric and magnetic field waveshapes for the first 5  $\mu$ s are dominated by the radiation term and, hence, they are very similar. No significant differences are found between the various models in this early-time region.



*Figure 25.5 Electric (a) and magnetic (b) fields calculated at a distance of 50 m from a lightning return stroke to a 168-m tower [adapted from Reference 35]*



*Figure 25.6 Electric (a) and magnetic (b) fields calculated at a distance of 5 km from a lightning return stroke to a 168-m tower [adapted from Reference 35]*

The differences between the model predictions become more pronounced at late times,  $t > 5 \mu\text{s}$  or so, although they are unremarkable. Note that all the models predict flattening of the electric field at later times at a value that is significantly smaller than the initial peak, in contrast with calculated electric fields for ground-initiated return strokes (see, e.g. [36]).

The electric and magnetic fields at a distance of 100 km are plotted in Figure 25.7 [35]. At this distance, the fields are essentially radiation fields, and electric and magnetic fields have the same waveshape. The fields associated with ground-initiated return strokes at such distances exhibit a zero-crossing that is only reproduced by the MTLE and MTLL models [1, 36]. As seen in Figure 25.7, for the considered case of a 168-m tower-initiated return stroke, none of the models predicts a zero-crossing. The absence of zero-crossing, in particular for the MTLE and MTLL models, can be explained by the contribution of the turn-on term [38].

As mentioned in Section 25.2.1.1, Mosaddeghi *et al.* [27] proposed a revision of the engineering models for return strokes to tall structures that takes into account the presence of possible reflections at the return-stroke wavefront and a return-stroke initiation above the structure due to an upward-connecting leader. Simulation results for the magnetic fields obtained using the new model were compared with experimental waveforms associated with lightning strikes to the CN Tower (553 m). It was shown that taking into account the reflections at the return-stroke wavefront results in better reproducing the fine structure of the magnetic field waveforms, including the double peak, the early narrow undershoot and the far-field zero-crossing (see Figure 25.8). The results also suggest that the typical double-peak response of the radiated fields from tall structures might be due to the combined effect of upward-connecting leaders and reflections at the return-stroke wavefront.

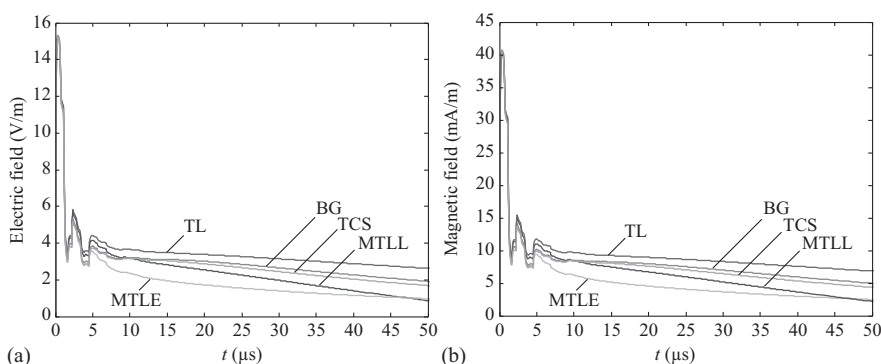
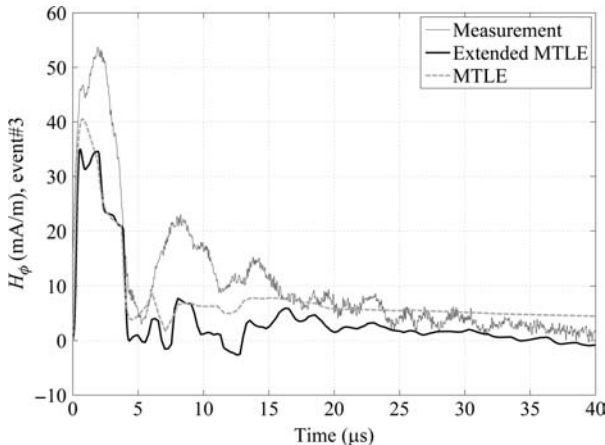


Figure 25.7 Electric (a) and magnetic (b) fields calculated at a distance of 100 km from a lightning return stroke to a 168-m tower [adapted from Reference 35]



*Figure 25.8 Comparison of simulated azimuthal magnetic fields at 50.9 km using the original MTLE model and the extended version of Mosaddeghi et al. with the measured waveform [adapted from Reference 27]*

### 25.3.1.3 Effect of the tower

Based on theoretical modelling and experimental observations, it is well established that the presence of a tower could result in a substantial increase (a factor of 3 or so) of the electric and magnetic field peaks and their derivatives [16, 23, 24] for observation points located at distances exceeding the height of the tower.

Interestingly, the effect of the tower at distances of about the height of the tower or less could result in a significant decrease of the electric field [24, 59–61].

### 25.3.2 Electromagnetic field computation for a finitely conducting ground

Assuming the lightning channel as a lossless vertical antenna above a finitely conducting ground, the associated electromagnetic fields could be basically calculated using three different approaches: (1) use of dedicated algorithms, (2) use of simplified approaches and (3) use of numerical methods (MoM or FDTD) [62].

#### 25.3.2.1 Dedicated algorithms

The exact solution of Maxwell equations due to a vertical dipole located above a finitely conducting ground as discussed in [63] result in the so-called Sommerfeld integral equations. The high oscillatory nature of the Sommerfeld integrals makes it difficult to evaluate the resulting expressions numerically. Some efforts have been recently made to find an algorithm to carry out the required numerical integrations efficiently. A dedicated algorithm [64–67] has been developed by Delfino and

co-workers that could be applied to both air-ground expressions generated by a lightning discharge.

### 25.3.2.2 Simplified approaches

*Cooray–Rubinstein and Barbosa et al. formulae (above-ground horizontal electric field)*

Several studies have shown that the Cooray–Rubinstein formula [68, 69] yields a satisfactory approximation of the above-ground horizontal electric field at close (100 m), intermediate (some kilometres) and far (tens of kilometres) distances [49, 68]. In the Cooray–Rubinstein formula, the horizontal electric field at a given height,  $h$ , is expressed as the sum of two terms. The first term is the horizontal electric field for a perfectly conducting ground and the second term accounts for the effect of a finitely conducting ground. This formula reads

$$E_r(z = h, r) = E_{rp}(z = h, r) - H_{qp}(z = 0, r) \frac{\sqrt{\mu_0}}{\sqrt{\epsilon + \sigma/j\omega}} \quad (25.15)$$

where  $E_{rp}$  is the radial electric field calculated at the height,  $h$ , and  $H_{qp}$  the azimuthal magnetic field computed at the ground level, both computed assuming the ground to be a perfect conductor.

Delfino *et al.* [66] showed that only for very low conductivities does the Cooray–Rubinstein formula exhibit some deviations from the reference one, but it still gives a conservative estimate of the radial field component since it behaves as an upper bound for the exact curve. General limits of validity of the Cooray–Rubinstein approximation were theoretically examined by Wait [70]. Shoory *et al.* [71] presented a general equation for the horizontal electric field, from which the Cooray–Rubinstein formula can be derived as a special case. Cooray [26] further proposed a simple modification of (25.15) that provides a better early-time response. Barbosa and Paulino [72] proposed an approximate time-domain formula for the horizontal electric field whose range of validity was stated to be equivalent to that of the Cooray–Rubinstein formula (which is in the frequency domain). Caligaris *et al.* [73] mathematically derived the time-domain counterpart of the Cooray–Rubinstein formula.

*Cooray formula (underground electric fields)*

Use of modern underground power and communication systems over the past few years has resulted in increasing attention to the study of penetrating lightning electromagnetic fields into a finitely conducting ground. The direct use of equations for radiated electromagnetic fields inside the ground [63] from a simple dipole, as for the case of above-ground fields, can be very costly in terms of computation time. In Reference 74, Cooray proposed a simplified formula for the evaluation of underground vertical and horizontal electric fields from lightning. The accuracy of Cooray's simplified expression has been further evaluated by Petrache *et al.* [75] by taking as a reference the exact solutions published by Degauque and Zeddam [76]. Petrache *et al.* reported a good agreement between the

exact and predicted horizontal electric field penetrating the ground at distances as close as 100 m [75]. The predictions of the Cooray's formula were found to be in good agreement with exact solutions for large values of the ground conductivity (about 0.01 S/m) [64]. For poor ground conductivities (0.001 S/m or so), Cooray's expression yields less satisfactory results, especially for the late time response [64].

### **25.3.2.3 Numerical methods**

#### *Finite difference time domain technique*

Compared with traditional approaches for the evaluation of electromagnetic fields in the vicinity of the lightning channel, the FDTD method has the advantage of being easily implemented in computer codes [77] and, further, the finite ground conductivity is taken into account in a straightforward way. The one-dimensional FDTD method has been widely applied to the analysis of the induced overvoltages on overhead transmission lines by nearby lightning return strokes [78]. It is only recently that the method has also been applied to the analysis of lightning electromagnetic fields. Sartori and Cardoso [79] have proposed a hybrid method based partially on the FDTD technique for the near electric field calculation. The magnetic field was first determined analytically, assuming the spatial-temporal distribution of the current in each radiating dipole to be a step function. In 2004, Yang and Zhou [80] also used FDTD to compute electromagnetic fields in the vicinity of a return stroke. Their FDTD approach has been used as a reference to test the validity of the quasi-image method and the Cooray–Rubinstein formula.

More recently, Mimouni *et al.* [81, 82] calculated the underground electric and magnetic fields for strikes to both flat ground and tall towers, using engineering return-stroke models and the FDTD method. Figures 25.9 and 25.10 show simulation results obtained by Mimouni *et al.* for the evaluation of the underground horizontal electric field, which have been compared with those of Delfino *et al.* [67] as well as the results obtained using the Cooray simplified formula [74].

It can be seen that the FDTD results are in excellent agreement with the exact evaluation of Delfino *et al.* [67]. The comparisons also show that the results obtained using the Cooray formula are in general in good agreement with more exact solutions, although some discrepancies can be observed for late-time response of the field and for poor ground conductivities.

Baba and Rakov [33, 83] also used the FDTD method to study the mechanisms of current wave propagation along vertical conductors [83], to reproduce small-scale experiments [33] and to study the enhancement of electromagnetic fields measured on the top of buildings [84].

#### *Method of moments*

The MoM has also been extensively applied to compute electromagnetic fields radiated by a lightning discharge, within the so-called AT models, which belong to the class known as electromagnetic models and in which the return-stroke channel is represented using thin wires [4–6, 44–46, 71, 85]. Most of the MoM solutions are implemented in the frequency domain, which allows taking into account the presence of a lossy ground in a straightforward way.

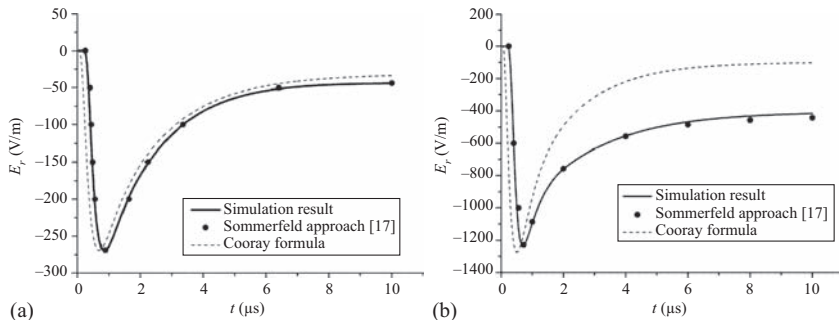


Figure 25.9 Underground radial electric field ( $r = 50$  m, depth  $d = 5$  m) for (a)  $\sigma = 0.01$  S/m and (b)  $\sigma = 0.001$  S/m lossy ground, compared with Sommerfeld approach and Cooray formula [adapted from Reference 81]

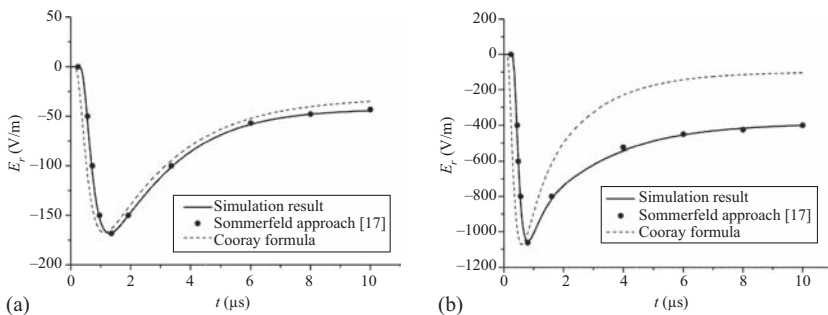


Figure 25.10 Underground radial electric field ( $r = 50$  m, depth  $d = 10$  m) for (a)  $\sigma = 0.01$  S/m and (b)  $\sigma = 0.001$  S/m lossy ground, compared with Sommerfeld approach and Cooray formula [adapted from Reference 81]

## 25.4 Review of lightning current data and associated electromagnetic fields

Tall structures, such as telecommunication towers, transmission line towers, buildings and chimneys have been instrumented to measure lightning current characteristics using sensors with varying degrees of sophistication. The very first lightning current measurements with a purposely installed sensor appear to have been made by Pockels on Mount Cimone in Italy, by observing the magnetization of basalt pieces placed near a lightning rod on an observation tower [86]. Based on the same principle, Foust and Kuehni [87] and Foust and Gardner [88] developed a sensor called a magnetic link that measures the peak current by determining the

remnant magnetization on strips of the appropriate type of magnetic material. Foust and Gardner's magnetic link sensor measures only the highest current in a flash. Wagner and McCann [89] made an improved instrument, called a fulchronograph, which uses a number of strips attached to the edge of a wheel. As the wheel spins, the magnetic strips pass successively close to coils through which the current to be measured flows and, thus, different levels are recorded on different strips, providing a crude indication of the change of the current with time.

These relatively inexpensive sensors, especially the magnetic links, have been used extensively in Germany, Poland, Czechoslovakia and Russia and other countries [90–94].

Although knowledge of the peak current is important, appropriate protection of current electric and electronic systems requires more detailed information about the waveshapes of the currents.

Measurements of the lightning current as a function of time were made by McEachron [95] starting in 1937 on the 443-m tall Empire State Building using oscilloscopes to measure lightning currents at a height of 389 m, on top of the building but below its final spire. Since then, a number of towers have been instrumented to capture lightning currents. Without being exhaustive, but including both active and inactive measurement stations, towers are located in Austria, Brazil, Canada, Colombia, Germany, Italy, Japan, Russia, Spain, South Africa and Switzerland, and, with at least two more tower instrumentation projects in the works as of the writing of this text, one in Serbia and Montenegro, and one in China.

In the following section, we will present a representative selection of experimental lightning current data and electromagnetic fields from them.

#### *25.4.1 Experimental data*

Experimental data on lightning return-stroke currents to towers can be classified into two categories: (1) data obtained using short instrumented towers (less than 100 m effective height) and (2) data obtained using tall instrumented towers (taller than 100 m effective height). We will discuss the difference between effective and actual height later.

Tall objects measuring less than 100 m or so are believed to be struck essentially by downward lightning, which initiates in the cloud with a downward leader discharge that connects to a relatively short upward-connecting discharge that is initiated by enhancement of the electric field near the top of the tall object as the downward leader approaches. For towers taller than 500 m or so, essentially all lightning flashes are initiated by an upward leader from the tall object. Contrary to downward lightning, upward flashes are considered to be initiated by the tall objects since they would not be initiated if the object were not present. Towers between 100 m and 500 m experience a combination of both types of flashes.

The currents from downward and upward lightning differ in a number of points. Figure 25.11 illustrates a typical upward current record.

As seen in Figure 25.11, upward lightning begins with an initial continuous current (ICC), whose initiation is associated with the start of the upward leader.

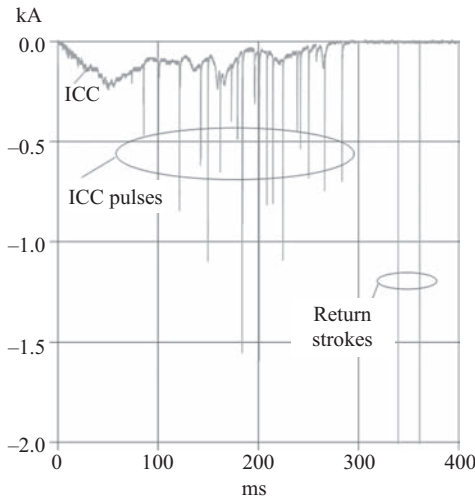


Figure 25.11 Typical upward lightning current [adapted from Reference 96]

The ICC has a typical amplitude of a few hundred amperes and a duration of a few hundred milliseconds. It may exhibit superimposed pulses currently called ICC pulses (in the past called  $\alpha$ -pulses), exhibiting amplitudes lower than 2 kA. Once the ICC has ceased to flow, one or more return-stroke pulses may appear. Return-stroke pulses are generally larger than ICC pulses, have shorter risetimes and may be followed by a continuing current similar to the ICC. Currents in downward lightning striking grounded objects do not exhibit the initial ICC part. Instead, they are characterized by the presence of a first return-stroke current that follows a downward stepped leader. This first return stroke may be followed by subsequent leader-return strokes.

It is important to note that the 100-m height limit for the appearance of upward lightning does not refer to the actual height of the tall object but to its effective height, which takes into account the enhancement of the electric field on the object due, for instance, to a mountain on which the object may be built. Since there is, at present, no accurate way of estimating theoretically the effective height of a tower, empirical methods are employed (by the ratio of upward to downward flashes or the increase in the number of flashes to a tower with respect to the surrounding terrain). In the following sections, we use the actual physical heights of the towers.

#### 25.4.2 Data from short towers

The most widely referenced and most comprehensive dataset to date on lightning return-stroke currents measured on short instrumented towers was presented by Berger and co-workers. The measurements were made on two 70-m tall towers including the steel needle that acts as a lightning rod, built on Mount San Salvatore in Lugano. Mount San Salvatore has a height of 640 m above the level of the adjacent Lake Lugano and it is 914 m above sea level.

The towers were instrumented using resistive shunt sensors at their tops and the currents were recorded using cathode-ray oscilloscopes installed in 1958. On each tower, two different shunts were used in series, one with a resistance of  $0.05\ \Omega$  for currents in the 1 to 200 kA range and the other with a  $0.8\ \Omega$  resistance used for currents from 50 A to 24 kA [97]. Four channels were used with two time deflections with a resolution of  $0.5\ \mu\text{s}$  [98].

About 15% of the measurements reported by Berger and co-workers were due to downward-moving stepped leaders. Most discharges to the towers were initiated by upward-moving stepped leaders of both polarities.

### 25.4.3 Summary of Berger's data

Figures 25.12 and 25.13 show a compilation of measurements, performed by Berger and co-workers, for lightning initiated by downward-moving leaders.

The waveforms in Figure 25.12 correspond to the average of 88 normalized first return-stroke waveforms and 76 normalized subsequent return-stroke waveforms. They are presented in two time scales, with the label 'A' corresponding to a

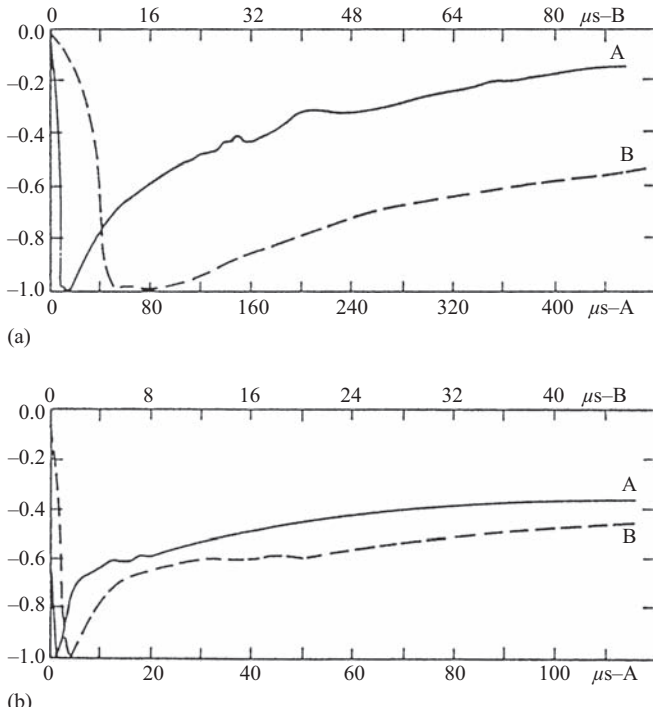


*Figure 25.12* Typical, normalized negative return-stroke current waveshapes: (a) first return stroke, (b) subsequent return stroke [adapted from Reference 99]

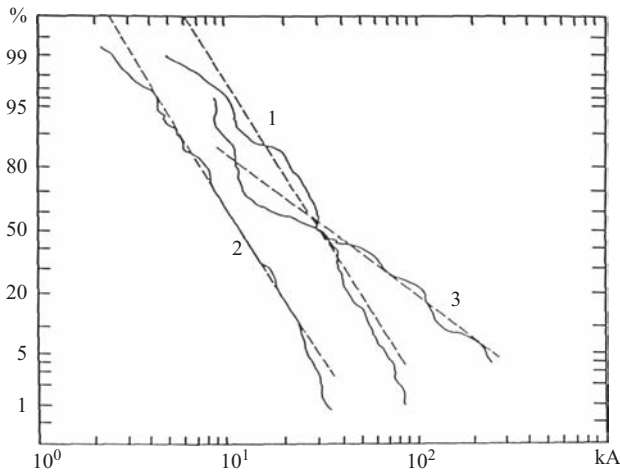


*Figure 25.13 Cumulative statistical distributions of return-stroke current peak (solid-line curves) and their log-normal approximations (slanted dashed lines) for (1) negative first strokes, (2) negative subsequent strokes and (3) positive first strokes as reported by Berger et al. [99]. The vertical scale gives the percentage of peak currents exceeding a given value on the horizontal axis [adapted from Reference 99]*

large scale going up to 100  $\mu$ s and ‘B’ to a shorter time scale of 40  $\mu$ s (dashed lines). In Figure 25.12, it is possible to observe that the average subsequent stroke current exhibits a faster risetime than that of the average subsequent stroke.

In Figure 25.13, the peak current distribution is presented for negative first return strokes, negative subsequent return strokes and positive return strokes. The dashed, slanted lines represent a log-normal distribution fit to the experimental data for all three cases [100]. The value of the peak current distribution at 50% is around 30 kA for first return strokes, both negative and positive. The corresponding value for negative subsequent strokes is close to 12 kA. Most positive flashes are single stroke.

Table 25.2 contains parameters of negative as well as positive lightning. There is a controversy concerning the front duration and the maximum rate of rise,  $di/dt$ , in Berger’s data. Indeed, the instrumentation used by Berger and co-workers had a limited frequency bandwidth, which may have introduced inaccuracies in their experimental observations.

#### 25.4.4 Other data obtained using short towers ( $\leq 100$ m)

Other short instrumented towers have been used around the world to measure lightning return-stroke parameters.

*Table 25.2 Lightning current parameters for downward flashes [adapted from Reference 99]*

Parameter	Units	Sample size	Percent exceeding tabulated value		
			95%	50%	5%
<b>Peak current (minimum 2 kA)</b>					
Negative first strokes	kA	101	14	30	80
Negative subsequent strokes	kA	135	4.6	12	30
Positive first strokes	kA	26	4.6	35	250
<b>Charge (total charge)</b>					
Negative first strokes	C	93	1.1	5.2	24
Negative subsequent strokes	C	122	0.2	1.4	11
Complete negative flash	C	94	1.3	7.5	40
<b>Impulse charge</b>					
Negative first strokes	C	90	1.1	4.5	20
Negative subsequent strokes	C	117	0.22	0.95	4.0
Positive first strokes	C	25	2.0	16	150
<b>Front duration (2 kA to peak)</b>					
Negative first strokes	μs	89	1.8	5.5	18
Negative subsequent strokes	μs	118	0.22	1.1	4.5
Positive first strokes	μs	19	3.5	22	200
<b>Maximum <math>di/dt</math></b>					
Negative first strokes	kA/μs	92	5.5	12	32
Negative subsequent strokes	kA/μs	122	12	40	120
Positive first strokes	kA/μs	21	0.20	2.4	32
<b>Stroke duration (2 kA to half value)</b>					
Negative first strokes	μs	90	30	75	200
Negative subsequent strokes	μs	115	6.5	32	140
Positive first strokes	μs	16	25	230	2000
<b>Integral (<math>i^2 dt</math>)</b>					
Negative first strokes	A <sup>2</sup> s	91	$6.0 \times 10^3$	$5.5 \times 10^4$	$5.5 \times 10^5$
Negative subsequent strokes	A <sup>2</sup> s	88	$5.5 \times 10^2$	$6.0 \times 10^3$	$5.2 \times 10^4$
Positive first strokes	A <sup>2</sup> s	26	$2.5 \times 10^4$	$6.5 \times 10^3$	$1.5 \times 10^7$
<b>Time interval</b>					
Between negative strokes	ms	133	7	33	150
<b>Flash duration</b>					
Negative (including single stroke flashes)	ms	94	0.15	13	1100
Negative (excluding single stroke flashes)	ms	39	31	180	900
Positive (only single flashes)	ms	24	14	85	500

Garbagnati, Dellera, Lo Pipero and co-workers measured currents at the top of two 40-m television towers in the 1970s using, as Berger and co-workers did, resistive shunts, located at the top of the towers, and oscilloscopes. The towers were located on the top of two mountains, each about 900 m above sea level [98, 100, 101]. One of the towers was located in the north of Italy, not far from Mount Berger's

towers in San Salvatore, and the other tower was located in central Italy. Table 25.3 summarizes the results of the Italian group for downward flashes.

Eriksson and co-workers measured lightning currents on a 60-m tall tower located above a relatively flat ground in South Africa in the 1970s. The tower was insulated from ground and the lightning current was measured at the bottom via a current transformer and a Rogowski coil. More than 50% of the flashes they measured were initiated by downward, negatively charged stepped leaders. All of the flashes recorded lowered negative charge to the ground. The 10% to 90% risetimes of the measured currents had a median value of 0.6 µs, significantly shorter than the risetimes observed on other towers. Table 25.4 shows values reported by Anderson and Eriksson in 1980.

Other data have been obtained using short towers in Japan [103], in Austria [96, 104, 105] and in Colombia [106–108].

The Gaisberg Tower in Austria is located near the city of Salzburg. The tower is 100 m tall and it sits on top of the Gaisberg Mountain, whose summit is at 1287 m above sea level and 800 m above the surrounding terrain.

The current is measured at the base of the air terminal installed on the top of the tower using a shunt resistor of 0.25 mΩ. Two separate channels with different

*Table 25.3 Return-stroke current parameters measured by Garbagnati and co-workers in Italy for discharges lowering negative charge to ground [adapted from References 100, 101]*

Parameter	Downward	
	First strokes	Subsequent strokes
Sample size	42	33
Peak value (kA)	33	18
Maximum rate of rise (kA/µs)	14	33
Time to crest (µs) – (3 kA to peak)	9	1.1
Time to half value (µs)	56	28
Impulse charge (C) – (to end of impulse of 500 µs)	2.8	1.4

*Table 25.4 Return-stroke current parameters measured by Eriksson and co-workers in South Africa for natural subsequent strokes lowering negative charge to ground [adapted from Reference 102]*

Parameter	Subsequent natural strokes		
	95%	50%	5%
Sample size	114		
Peak value (kA)	4.9	12	29
10–90% average of current steepness (kA/µs)	3.3	15	72
10–90% time duration (µs)	0.1	0.6	2.8

gains are used to transmit and record the data from the Gaisberg Tower: One of them, whose saturation level is 2 kA (positive and negative) is used to record the small, slow ICC. The other is set for a saturation level of plus or minus 40 kA to record pulses and return strokes.

Diendorfer *et al.* [96] analysed currents from strikes to the Gaisberg Tower recorded from 2000 to 2007. The authors reported that the incidence of lightning to the tower is essentially independent of the season, even though an active thunderstorm season exists in Austria during the summer. The average number of flashes per year recorded during the 8-year study period was somewhat higher than 60. Overall, 93% of the flashes were negative (all strokes lowered negative charge to ground), 4% were positive (all the strokes lowered positive charge to ground) and 3% of the records showed bipolar current waveforms.

Based on the presence or absence of an ICC, Diendorfer *et al.* concluded that at least 99% of all flashes to the Gaisberg Tower were upward initiated for the studied period. Of those, 30% of the negative flashes exhibited at least one return stroke, the average number of strokes being 4.4. The interstroke interval for the analysed flashes had a geometric mean of 17.3 ms. Of the remaining 70% of upward-initiated negative flashes, 22% consisted of an ICC with superimposed pulses greater than 2 kA and 48% had no superimposed current pulses with peak currents greater than 2 kA.

#### *25.4.5 Data from tall towers*

Lightning return-stroke currents measured on the 540-m tall Ostankino Tower in Moscow represent the first measurements of currents performed simultaneously at three different heights along a tower. The three current sensors were installed at 533, 272 and 47 m above ground level as reported by [109]. The lightning return-stroke current observations present different waveshapes at the three observation points (Figure 25.14). The differences are presumably due to reflections produced at the tower discontinuities during the initial lightning current propagation to ground.

From the three waveshapes presented in Figure 25.14, we can see that the largest ‘absolute peak’ amplitude appears at the lower observation point (about 22 kA). This suggests that, at the point of discontinuity between the bottom of the tower and the grounding impedance, there is a positive reflection of current that adds to the initial return-stroke current. This positive reflection from the bottom is clearly discernible at the other two locations after a few microseconds of propagation delay. The fact that the peak amplitude of the current measured at 533 m (8 kA) is smaller than the peak amplitude at 272 m (10 kA) indicates that a negative reflection coefficient can be associated with the top of the tower. This coefficient represents the discontinuity between the tower and the ‘equivalent’ impedance of the lightning channel.

Rakov [109] reports a median peak value for currents measured at 47 and 533 m of 18 and 9 kA, respectively. He suggests that the effective grounding impedance of the tower is much smaller than its characteristic impedance and

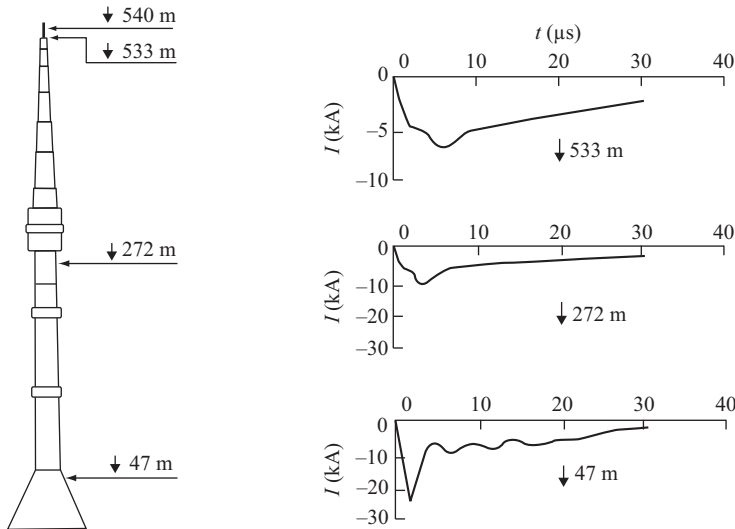


Figure 25.14 Sample of return-stroke current waveshape of upward negative lightning, recorded at three different locations in the Ostankino Tower in Moscow [adapted from Reference 109]

that this is appreciably lower than the equivalent impedance of the lightning channel.

Studies on lightning striking the CN Tower (553-m high) in Toronto, Canada, have been performed and reported by the ‘CN Tower Lightning Studies Group (CNTLSG)’ since 1978 [43, 110, 111]. The lightning return-stroke current derivatives striking the CN Tower are measured by two inductive Rogowski coils located at 509 and 474 m height. A photograph of the CN Tower in Toronto is shown in Figure 25.15.

A lightning return-stroke current measured on the CN Tower in 1999 is presented in Figure 25.16. Lightning return-stroke currents and current derivatives observed at the CN Tower have been found to exhibit multiple reflections produced at the tower discontinuities. The observed currents and current derivatives are therefore ‘contaminated’ by these reflections.

The waveshapes of the currents in Figure 25.16 exhibit a positive reflection arriving around 3.6 ms after the first current maximum. This propagation time corresponds to a round-trip time from the tower top to ground, confirming that this reflection was produced at the lower discontinuity level between the tower bottom and the grounding impedance. The positive value of the reflection implies a positive ground reflection coefficient. The observed positive reflection is less pronounced for the sensor located closer to the top of the tower. This is similar to the observations at the Ostankino Tower, suggesting a negative top reflection coefficient.

However, comparing the waveshapes for the observed currents in Figures 25.14 and 25.16, we can see that the currents observed on the CN Tower exhibit a more complex structure than those of the Ostankino Tower. This is probably due to the architecture of the CN Tower, which presents a number of features that act as discontinuities to the current (see Figure 25.15), as suggested by Shostak [20].

A more complete study of reflections produced in the CN Tower data was recently presented by Shostak and co-workers (see [19, 30, 31, 113, 114]).

The 168-m tall Peissenberg Tower located near Munich in Germany, on a ridge 250 m above the surrounding open ground and 950 m above sea level, was used first from 1978 until 1999 to study lightning currents and their associated electromagnetic fields [37]. From 1978 to 1999, the tower had two current measurement systems installed, respectively, at approximately 167 m and 13 m. The systems were able to measure return-stroke currents and their derivatives. During the time of exploitation of the tower, only one stroke of a downward negative flash was recorded by the system. The majority of the strokes recorded at the Peissenberg Tower were produced by upward flashes, with negative or positive polarity. Figure 25.17(a) shows a photograph of the Peissenberg Tower and Figure 25.17(b) presents waveforms of return-stroke currents measured simultaneously at the bottom



Figure 25.15 A picture of the CN Tower in Toronto

and top of the tower in which the ‘contamination’ of the current by multiple reflections is clearly distinguishable.

The current waveshapes in Figure 25.17(b) exhibit a higher peak value for the current observed at the bottom of the tower.

A 250-m-tall telecommunication tower was instrumented by Montandon and Beyeler in St. Chrischona, near Basel, in Switzerland, with two current loop antennas at 248 and 175 m, and an additional current probe at the top. The tower was located at the summit of a hill 500 m above sea level. The two current derivative systems and the current probe were used over a period of 5 years to record

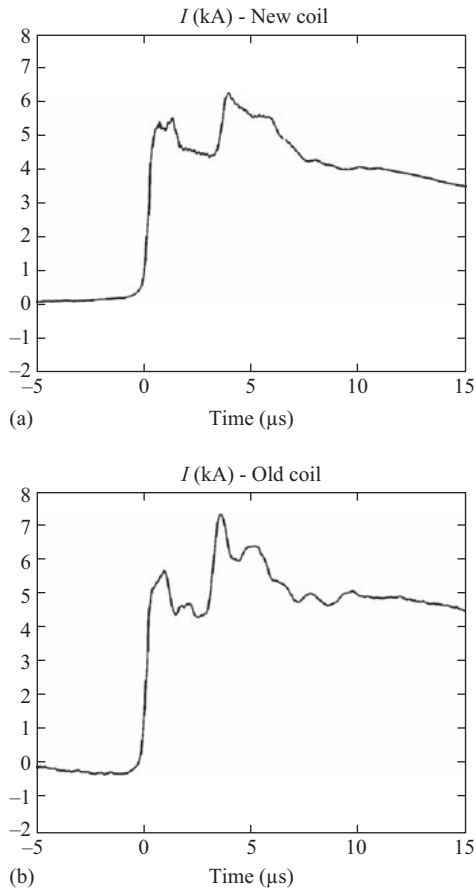
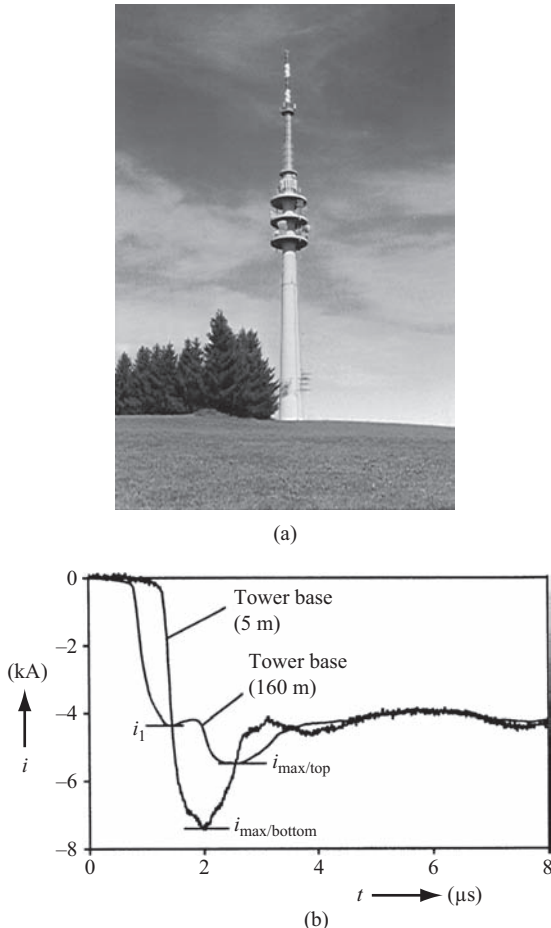


Figure 25.16 Sample of a lightning return-stroke current observed at (a) 509 and (b) 474 m height at the CN Tower in Toronto [adapted from Reference 112]



*Figure 25.17 (a) Peissenberg Tower and (b) comparison of a lightning return-stroke current recorded at the Peissenberg Tower top and bottom [adapted from Reference 37]*

lightning return-stroke current waveshapes impacting the tower [115, 116]. Figure 25.18 shows the location of the measurement systems on the tower.

The 200-m high Fukui Tower in Japan was also used to measure lightning return-stroke currents and their associated electromagnetic fields at the Fukui thermal power plant on the coast of the Sea of Japan. Two coaxial shunt resistors ( $2 \text{ m}\Omega$ ,  $10 \text{ m}\Omega$ ) were installed at the top of the tower [21]. It was found that the measured current was affected by reflected waves at the ground and at the top of the tower. Figure 25.19 presents a schematic representation of

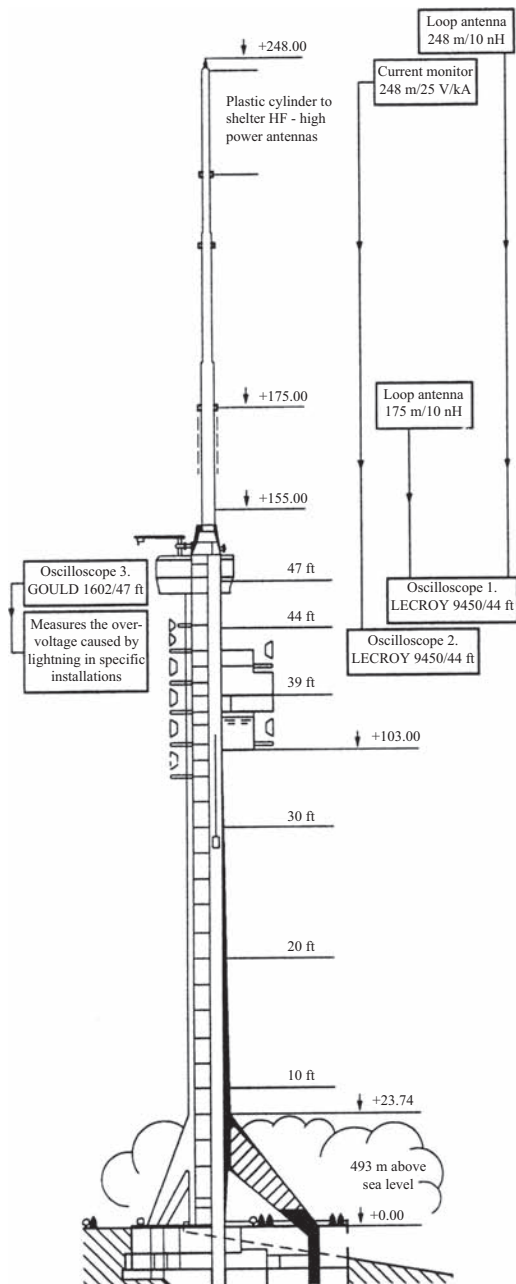


Figure 25.18 Position of the lightning measurement equipment in the tower St. Chrischona, Switzerland [adapted from Reference 116]

the installation of the Fukui Tower and the electromagnetic field recording system.

A study conducted using data from EUCLID (European Cooperation for Lightning Detection) over a three and half year time period starting in January 1998 showed that a telecommunication tower near Saint Gallen, in the Northeastern part of Switzerland, is struck by lightning more than any other tower in that country, with an average number of direct hits of more than 100 per year.

The Säntis Tower is 125 m tall and it sits on top of the 2505-m mount Säntis (see Figure 25.20).

The tower was instrumented and put and the measurement system was put in operation in June 2010, with Rogowski coils and wideband B-dot sensors installed to measure the current at 24 m and 82 m AGL [117, 118].

Table 25.5 summarizes statistical results for the current peak and risetime obtained using various instrumented towers around the world.

## 25.5 Summary

In this chapter, the recent progress in our understanding of the transient processes that take place when lightning strikes tall structures was presented. The extension

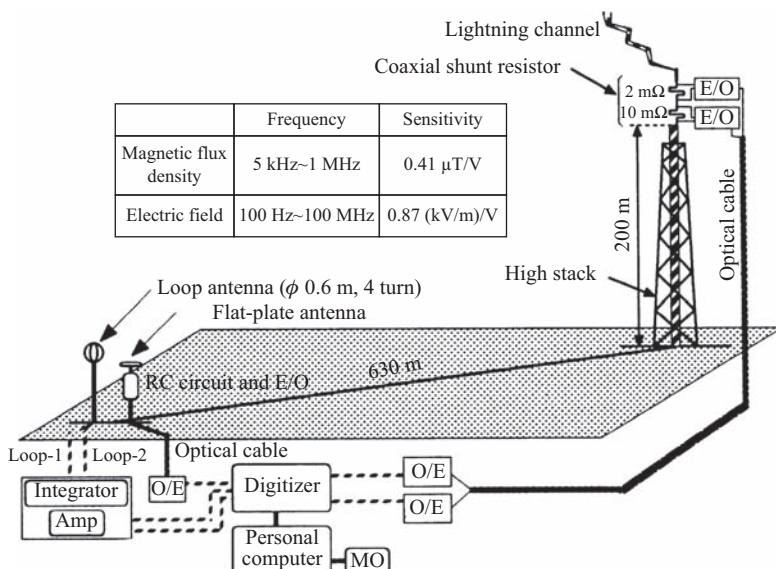


*Figure 25.19 Configuration of lightning stroke current and electromagnetic field observation systems at the Fukui thermal power plant [adapted from Reference 21]*



Figure 25.20 Photograph of the Säntis telecommunication tower in Northeastern Switzerland

of lightning return-stroke models to include the presence of these strike structures was given, including the engineering, electromagnetic and hybrid model classes. The computational methods commonly used to calculate the electromagnetic fields generated by lightning strikes to tall structures were presented, both for the idealized case of a perfectly conducting ground, and for a lossy ground. For the latter, in addition to standard FDTD and MoM numerical methods and dedicated algorithms for the evaluation of Sommerfeld's integrals, simplified, approximate approaches were presented. Finally, the available data on lightning current and its associated electromagnetic fields was reviewed.

A review of available data on lightning current and associated electromagnetic fields is presented in Section 25.4, where the dataset of Berger and co-workers was presented in detail and an overview was given of some of the instrumented towers around the world, including the most recent lightning current and electromagnetic field results.

*Table 25.5 Comparison of return-stroke current peaks in downward and upward flashes measured in instrumented towers, and rocket triggered lightning effectively transporting negative charge to ground*

Location	Height (m)	Location	Sample size	$I_{\text{peak}}^{(50\%)}$ (kA)	Risetime (μs)	Sensor location
<b>CN Tower – Toronto (1992–2001) [112, 119]</b>						
Upward flashes	553	Canada	387	5.06 <sup>a</sup> 7.19 <sup>b</sup>	0.64 <sup>c</sup>	Top (474 m)
<b>Ostankino Tower – Moscow (1984) [109]</b>						
Negative upward flashes at 533 m	540	Russia	58	9	–	533 m
Negative upward flashes at 47 m			76	18	–	47 m
<b>Empire State Building – USA (1952) [109]</b>						
Upward flashes	410	USA	84	10	–	Top
<b>Fukui thermal power plant (1989–1994) [120]</b>						
Upward flashes type A (strong luminosity)	200	Japan	22	33 (23.5 <sup>d</sup> )	1–2 <sup>d</sup>	Top
Upward flashes type B (low luminosity)			33	3.4		
<b>Peissenberg Tower – Germany (1992/1998) [37]</b>						
Negative upward flashes, ICC pulses <sup>e</sup>	168	Peissenberg at 167 m	89	3.63 <sup>b</sup>	–	Top
Negative upward flashes, return-stroke pulses <sup>e</sup>			68	7.97 <sup>b</sup>	–	
<b>Japan Transmission Towers (1994/1997) [103]</b>						
Negative downward flashes, 1st stroke at top	40–140	Japan	36	39	4.5 <sup>f</sup>	Top
<b>Gaisberg Tower (Austria) [121]</b>						
Downward negative, first strokes				14 <sup>g</sup>	–	
Downward negative, subsequent strokes	100	Austria		2.91 <sup>g</sup>	–	Top

Table 25.5 (Continued)

Location	Height (m)	Location	Sample size	$I_{\text{peak}}(50\%)(\text{kA})$	Risetime ( $\mu\text{s}$ )	Sensor location
Upward negative, ICC pulses <sup>e</sup>				2.94 <sup>g</sup>		
Upward negative, return-stroke pulses <sup>e</sup>				8.57 <sup>g</sup>		
<b>Mount Saint Salvatore</b>						
<b>Tower-CH [99]</b>						
Negative downward flashes, 1st stroke	70–90	Switzerland	101	30	5.5 <sup>h</sup>	Top
Negative downward flashes, 2nd stroke			135	12	1.1 <sup>h</sup>	
Upward flashes			70	10	—	
<b>South Africa Tower (1980) [102, 122]</b>						
Negative downward flashes	60	South Africa	114	12 <sup>b</sup>	0.6 <sup>i</sup>	Bottom
<b>Morro do Cachimbo Tower – Brazil [123]</b>						
Negative downward strokes, 1st stroke	60	Brazil	31	40.4 <sup>a</sup> 45.3 <sup>b</sup>	5.6 <sup>i</sup>	Bottom
Negative downward strokes, subsequent stroke			59	16.3 <sup>b</sup>	0.7 <sup>i</sup>	
<b>Italy Towers [100, 101]</b>						
Negative downward flashes, 1st stroke			42	33	9 <sup>j</sup>	
Negative downward flashes, 2nd stroke	40	Italy	33	18	1.1 <sup>j</sup>	Top
Negative upward flashes, 1st stroke			61	7	4 <sup>j</sup>	
Negative upward flashes, 2nd stroke			142	8	1.3 <sup>j</sup>	

<sup>a</sup>First peak of the current.<sup>b</sup>Absolute peak of the current.<sup>c</sup>Risetime to wavefront peak.<sup>d</sup>Values reported by Reference 21.<sup>e</sup> $\alpha$ -components: ICC pulses (sometimes known as  $\alpha$ -components or  $\alpha$ -pulses) are superimposed on the ICC. Return-stroke pulses (also known as  $\beta$ -components or  $\beta$ -pulses) are pulses following a period of no current in the channel.<sup>f</sup>The time resolution of the system was 100 ns [103].<sup>g</sup>1 kA threshold.<sup>h</sup>Front duration defined as the time interval between the 2 kA point on the front and the first peak, the time resolution of the system was 0.5  $\mu\text{s}$ .<sup>i</sup>Time interval between instants corresponding to 10% and 90% of first current peak.<sup>j</sup>Time to crest defined between 3 kA to peak.

## References

1. Rakov, V.A. and M.A. Uman, Review and evaluation of lightning return stroke models including some aspects of their application, *IEEE Transactions on Electromagnetic Compatibility*, 1998;**40**(4):403–26
2. Rachidi, F., V.A. Rakov, C.A. Nucci and J.L. Bermudez, The effect of vertically-extended strike object on the distribution of current along the lightning channel, *Journal of Geophysical Research*, 2002;**107**(D23):4699
3. Podgorski, A.S. and J.A. Landt, Numerical analysis of the lightning-CN tower interaction, in 6th Symposium and Technical Exhibition on Electromagnetic Compatibility, Zurich, Switzerland, 1985
4. Heidler, F. and T. Zundl, Influence of tall towers on the return stroke current, Presented at Aerospace and Ground Conference on Lightning and Static Electricity, Williamsburg, VA, 1995
5. Baba, Y. and M. Ishii, Numerical electromagnetic field analysis of lightning current in tall structures, *IEEE Transactions on Power Delivery*, 2001;**16**(2): 324–8
6. Kordi, B., R. Moini, W. Janischewskyj, A. Hussein, V. Shostak and V.A. Rakov, Application of the antenna theory model to a tall tower struck by lightning, *Journal of Geophysical Research*, 2003;**108**(D17), doi:10.1029/2003JD003398
7. Harrington, R.F., *Field Computation by Moment Methods*, New York: IEEE & Wiley, 1993
8. Visacro, S. and F.H. Silveira, Evaluation of lightning current distribution along the lightning discharge channel by a hybrid electromagnetic model, *Journal of Electrostatics*, 2004;**60**:111–120
9. Silveira, F.H., S. Visacro and A.R. De Conti, Lightning effects on the vicinity of elevated structures, in International Conference on Lightning Protection, Avignon, France, 2004
10. Zundl, T., Lightning current and LEMP calculations compared to measurements gained at the Peissenberg tower, in 22nd International Conference on Lightning Protection, Budapest, Hungary, 1994
11. Guerrieri, S., F. Heidler, C.A. Nucci, F. Rachidi and M. Rubinstein, Extension of two return stroke models to consider the influence of elevated strike objects on the lightning return stroke current and the radiated electromagnetic field: comparison with experimental results. EMC '96 ROMA. International Symposium on Electromagnetic Compatibility. Univ. Rome 'La Sapienza', Rome, Italy, vol. 2, 1996
12. Guerrieri, S., C.A. Nucci, F. Rachidi and M. Rubinstein, On the influence of elevated strike objects on directly measured and indirectly estimated lightning currents, *IEEE Transactions on Power Delivery*, 1998;**13**(4):1543–55
13. Guerrieri, S., E.P. Krider and C.A. Nucci, Effects of traveling-waves of current on the initial response of a tall Franklin Rod, in International Conference on Lightning Protection, Rhode, Greece, 2000

14. Rusan, I., W. Janischewskyj, A.M. Hussein and J.-S. Chang, Comparison of measured and computed electromagnetic fields radiated from lightning strikes to the Toronto CN tower, in 23rd International Conference on Lightning Protection, Florence, 1996
15. Motoyama, H., W. Janischewskyj, A.M. Hussein, R. Rusan, W.A. Chisholm and J.S. Chang, Electromagnetic field radiation model for lightning strokes to tall structures, *IEEE Transactions on Power Delivery*, 1996; **11**(3):1624–32
16. Rachidi, F., W. Janischewskyj, A.M. Hussein, C.A. Nucci, S. Guerrieri, B. Kordi, *et al.*, Current and electromagnetic field associated with lightning return strokes to tall towers, *IEEE Transactions on Electromagnetic Compatibility*, 2001; **43**(3):356–67
17. Janischewskyj, W., V. Shostak and A.M. Hussein, Comparison of lightning electromagnetic field characteristics of first and subsequent return strokes to a tall tower 1. Magnetic field, in 24th International Conference on Lightning Protection, Birmingham, UK, 1998
18. Janischewskyj, W., V. Shostak and A.M. Hussein, Lightning electric field characteristics of first and subsequent return strokes to a tall tower, *11th International Symposium on High Voltage Engineering*, 1999, vol. 467, no. 5, pp. 270–74
19. Shostak, V., W. Janischewskyj, A. Hussein and B. Kordi, Electromagnetic fields of lightning strikes to a tall tower: a model that accounts for upward-connecting discharges, in 25th International Conference on Lightning Protection, Rhodes, Greece, 2000
20. Shostak, V., W. Janischewskyj, A.M. Hussein, J.S. Chang and B. Kordi, Return-stroke current modeling of lightning striking a tall tower accounting for reflections within the growing channel and for upward-connecting discharges, in 11th International Conference on Atmospheric Electricity, Guntersville, AL, 1999
21. Goshima, H., A. Asakawa, T. Shindo, H. Motoyama, A. Wada and S. Yokoyama, Characteristics of electromagnetic fields due to winter lightning stroke current to a high stack, *Transactions of the Institute of Electrical Engineers of Japan, Part B*, 2000; **120**(1):44–9
22. Bermudez, J.L., M. Rubinstein, F. Rachidi, F. Heidler and M. Paolone, Determination of reflection coefficients at the top and bottom of elevated strike objects struck by lightning, *Journal of Geophysical Research*, 2003; **108**(D14):4413, doi: 10.1029/2002JD002973
23. Bermudez, J.L., F. Rachidi, W. Janischewskyj, V. Shostak, M. Rubinstein, D. Pavanello, *et al.*, Far-field – current relationship based on the TL model for lightning return strokes to elevated strike objects, *IEEE Transactions on Electromagnetic Compatibility*, 2005; **47**(1):146–59
24. Baba, Y. and V.A. Rakov, Lightning electromagnetic environment in the presence of a tall grounded strike object, *Journal of Geophysical Research*, 2005; **110**, doi: 10.1029/2004JD005505
25. Rachidi, F. and C.A. Nucci, On the Master, Uman, Lin, Standler and the modified transmission line lightning return stroke current models, *Journal of Geophysical Research*, 1990; **95**(D12):20389–94

26. Cooray, G.V., On the concepts used in return stroke models applied in engineering practice, *IEEE Transactions on Electromagnetic Compatibility*, 2002;**45**(1):101–8
27. Mosaddeghi, A., F. Rachidi, M. Rubinstein, F. Napolitano, D. Pavanello, V. Shostak, *et al.*, Radiated fields from lightning strikes to tall structures: Effect of upward connecting leader and reflections at the return stroke wavefront, *IEEE Transactions on Electromagnetic Compatibility*, 2011;**53**(2):437–45
28. Baba, Y. and V.A. Rakov, On the use of lumped sources in lightning return stroke models, *Journal of Geophysical Research*, 2005;**110**, doi: 10.1029/2004JD005202
29. Shigihara, M. and A. Piantini, Estimation of lightning currents from measurements performed on elevated objects, in 28th International Conference on Lightning Protection, Kanazawa, Japan, 2006
30. Shostak, V., W. Janischewskyj, A. Hussein, J.S. Chang, F. Rachidi and J.L. Bermudez, Modeling of the electromagnetic field associated with lightning return strokes to a complex tall tower, in 26th International Conference on Lightning Protection, Cracow, Poland, 2002
31. Shostak, V., W. Janischewskyj and A.M. Hussein, Expanding the modified transmission line model to account for reflections within the continuously growing lightning return stroke channel, *IEEE Power Engineering Society Summer Meeting*. Piscataway, NJ: Cat. IEEE, 2000
32. Bermudez, J.L., F. Rachidi, W.A. Chisholm, M. Rubinstein, W. Janischewskyj, A.M. Hussein, *et al.*, On the use of transmission line theory to represent a nonuniform vertically-extended object struck by lightning, in 2003 IEEE Symposium on Electromagnetic Compatibility (EMC), Boston, MA, 2003
33. Baba, Y. and V.A. Rakov, On the interpretation of ground reflections observed in small-scale experiments simulating lightning strikes to towers, *IEEE Transactions on Electromagnetic Compatibility*, 2005;**47**(3):533–42
34. Shoory, A., F. Vega, F. Rachidi and M. Rubinstein, On the propagation of current pulses along tall structures struck by lightning, in 2010 Asia-Pacific Symposium on Electromagnetic Compatibility, Beijing, China, 2010
35. Pavanello, D., F. Rachidi, V.A. Rakov, C. Nucci and J.L. Bermudez, Return stroke current profiles and electromagnetic fields associated with lightning strikes to tall towers: Comparison of engineering models, in International Conference on Lightning Protection, Avignon, France, 2004
36. Nucci, C.A., G. Diendorfer, M. Uman, F. Rachidi, M. Ianoz and C. Mazzetti, Lightning return stroke current models with specified channel-base current: a review and comparison, *Journal of Geophysical Research*, 1990;**95**(D12): 20395–408
37. Heidler, F., J. Wiesinger and W. Zischank, Lightning currents measured at a telecommunication tower from 1992 to 1998, in 14th International Zurich Symposium on Electromagnetic Compatibility, Zurich, Switzerland, 2001
38. Pavanello, D., F. Rachidi, J.L. Bermudez, M. Rubinstein and C.A. Nucci, Electromagnetic field radiated by lightning to tall towers: Treatment of the

- discontinuity at the return stroke waveform, *Journal of Geophysical Research*, 2004;109(D06114), doi: 10.1029/2003JD004185
- 39. Beierl, O., Front shape parameters of negative subsequent strokes measured at the Peissenberg Tower, in 21st International Conference on Lightning Protection, Berlin, Germany, 1992
  - 40. Montandon, E. and B. Beyeler, The lightning measuring equipment on the Swiss PTT telecommunications tower at St. Chrischona, Switzerland, in 22nd International Conference on Lightning Protection, Budapest, Hungary, 1994
  - 41. Willett, J.C., V.P. Idone, R.E. Orville, C. Leteinturier, A. Eybert-Berard, L. Barret, *et al.*, An experimental test of the "Transmission-Line Model" of electromagnetic radiation from triggered lightning return strokes, *Journal of Geophysical Research*, 1988;93(D4):3867–78
  - 42. Gavric, M.R., Iterative method for waveshape restoration of directly measured lightning flash currents, *IEE Proceedings Generation, Transmission and Distribution*, 2002;149(1):66–70
  - 43. Janischewskyj, W., V. Shostak, J. Barratt, A.M. Hussein, I. Rusan and J.S. Chang, Collection and use of lightning return stroke parameters taking into account characteristics of the struck object, in 23rd International Conference on Lightning Protection, Florence, Italy, 1996
  - 44. Podgorski, A.S. and J.A. Landt, Three dimensional time domain modelling of lightning, *IEEE Transactions on Power Delivery*, 1987;PWRD-2(3):931–8
  - 45. Moini, R., V.A. Rakov, M.A. Uman and B. Kordi, An antenna theory model for the lightning return stroke, in 12th International Zurich Symposium on Electromagnetic Compatibility, Zurich, Switzerland, 1997
  - 46. Petrache, E., F. Rachidi, D. Pavanello, W. Janischewskyj, A.M. Hussein, M. Rubinstein, *et al.*, Lightning strikes to elevated structures: Influence of grounding conditions on currents and electromagnetic fields, in IEEE International Symposium on Electromagnetic Compatibility, Chicago, IL, 2005
  - 47. Petrache, E., F. Rachidi, D. Pavanello, W. Janischewskyj, M. Rubinstein, W.A. Chisholm, *et al.*, Influence of the finite ground conductivity on the transient response to lightning of a tower and its grounding, in 28th General Assembly of International Union of Radio Science (URSI), New Delhi, India, 2005
  - 48. Rubinstein, M., An approximate formula for the calculation of the horizontal electric field from lightning at close, intermediate, and long range, *IEEE Transactions on Electromagnetic Compatibility*, 1996;38(3):531–5
  - 49. Rachidi, F., C.A. Nucci, M. Ianoz and C. Mazzetti, Influence of a lossy ground on lightning-induced voltages on overhead lines, *IEEE Transactions on Electromagnetic Compatibility*, 1996;38(3):250–63
  - 50. Agrawal, A.K., H.J. Price and S.H. Gurbaxani, Transient response of multi-conductor transmission lines excited by a nonuniform electromagnetic field, in IEEE International Symposium Digest, Antennas and Propagation, New York, NY, 1980
  - 51. Pavanello, D., F. Rachidi, M. Rubinstein, J.L. Bermudez and C.A. Nucci, On the calculation of electromagnetic fields radiated by lightning to tall

- structures, in International Conference on Lightning Protection, Avignon, France, 2004
- 52. Rubinstein, M. and M.A. Uman, Transient electric and magnetic fields associated with establishing a finite electrostatic dipole, revisited, *IEEE Transactions on Electromagnetic Compatibility*, 1991;33(4):312–20
  - 53. Rubinstein, M. and M.A. Uman, On the radiation field turn-on term associated with traveling current discontinuities in lightning, *Journal of Geophysical Research*, 1990;95(D4):3711–13
  - 54. Le Vine, D.M. and J.C. Willett, Comment on the transmission line model for computing radiation from lightning, *Journal of Geophysical Research*, 1992;97:2601–610
  - 55. Thottappillil, R. and V.A. Rakov, On different approaches to calculating lightning electric fields, *Journal of Geophysical Research*, 2001;106: 14191–205
  - 56. Thottappillil, R., V.A. Rakov and M.A. Uman, Distribution of charge along the lightning channel: relation to remote electric and magnetic fields and to return-stroke models, *Journal of Geophysical Research*, 1997;102(D6):6987–7006
  - 57. Thottappillil, R., M.A. Uman and V.A. Rakov, Treatment of retardation effects in calculating the radiated electromagnetic fields from the lightning discharge, *Journal of Geophysical Research*, 1998;103(D8):9003–13
  - 58. Cooray, V., V.A. Rakov, C.A. Nucci, F. Rachidi and R. Montano, On the constraints imposed by the close electric field signature on the equivalent corona current in lightning return stroke models, in International Conference on Lightning Protection, Avignon, France, 2004
  - 59. Pavanello, D., F. Rachidi, M. Rubinstein, N. Theethayi and R. Thottappillil, Electromagnetic environment in the immediate vicinity of a tower struck by lightning, in EUROEM'2004, Magdeburg, Germany, 2004
  - 60. Miyazaki, S. and M. Ishii, Influence of elevated stricken object on lightning return-stroke current and associated fields, in International Conference on Lightning Protection, Avignon, France, 2004
  - 61. Mosaddeghi, A., A. Shoory, F. Rachidi, G. Diendorfer, H. Pichler, D. Pavanello, *et al.*, Lightning electromagnetic fields at very close distances associated with lightning strikes to the Gaisberg Tower, *Journal of the Geophysical Research*, 2010;115(D17101), doi: 10.1029/2009JD013754
  - 62. Rakov, V.A. and F. Rachidi, Overview of recent progress in lightning research and lightning protection, *IEEE Transactions on Electromagnetic Compatibility*, 2009;51(3):428–42
  - 63. Baños, A., *Dipole Radiation in the Presence of a Conducting Half-Space*. Oxford: Pergamon Press, 1966
  - 64. Delfino, F., R. Procopio, F. Rachidi and C.A. Nucci, An algorithm for the exact evaluation of the underground lightning electromagnetic fields, *IEEE Transactions on Electromagnetic Compatibility*, 2007;49(2):401–11
  - 65. Delfino, F., R. Procopio and M. Rossi, Lightning return stroke current radiation in presence of a conducting ground: 1. Theory and numerical

- evaluation of the electromagnetic fields, *Journal of Geophysical Research*, 2008;113(D05110), doi: 10.1029/2007JD008553
- 66. Delfino, F., R. Procopio, M. Rossi, F. Rachidi and C.A. Nucci, Lightning return stroke current radiation in presence of a conducting ground: 2. Validity assessment of simplified approaches, *Journal of Geophysical Research*, 2008;113(D05111), doi: 10.1029/2007JD008567
  - 67. Delfino, F., R. Procopio, M. Rossi, F. Rachidi and C.A. Nucci, Evaluation of underground lightning electromagnetic fields, in International Symposium on Electromagnetic Compatibility EMC EUROPE 2006, Barcelona, Spain, 2006
  - 68. Rubinstein, M., An approximate formula for the calculation of the horizontal electric field from lightning at close, intermediate, and long range, *IEEE Transactions on Electromagnetic Compatibility*, 1996;38:531–5
  - 69. Cooray, V., Horizontal fields generated by return strokes, *Radio Science*, 1992;27(4):529–37
  - 70. Wait, J.R., Concerning the horizontal electric field of lightning, *IEEE Transactions on Electromagnetic Compatibility*, 1997;39(2):186
  - 71. Shoory, A., R. Moini, S.H.H. Sadeghi and V.A. Rakov, Analysis of lightning-radiated electromagnetic fields in the vicinity of lossy ground, *IEEE Transactions on Electromagnetic Compatibility*, 2005;47(1):131–45
  - 72. Barbosa, C.F. and J.O.S. Paulino, An approximate time-domain formula for the calculation of the horizontal electric field from lightning, *IEEE Transactions on Electromagnetic Compatibility*, 2007;49(3):593–601
  - 73. Caligaris, C., F. Delfino and R. Procopio, Cooray-Rubinstein formula for the evaluation of lightning radial electric fields: Derivation and implementation in the time domain, *IEEE Transactions on Electromagnetic Compatibility*, 2008;50(1):194–7
  - 74. Cooray, V., Underground electromagnetic fields generated by the return strokes of lightning flashes; *IEEE Transactions on Electromagnetic Compatibility*, 2001;43(1):75–84
  - 75. Petrache, E., F. Rachidi, M. Paolone, C. Nucci, V.A. Rakov and M.A. Uman, Lightning-induced voltages on buried cables, Part I: Theory, *IEEE Transactions on Electromagnetic Compatibility*, 2005;47(3):498
  - 76. Degauque, P. and A. Zeddam, Remarks on the transmission-line approach to determining the current induced on above-ground cables, *IEEE Transactions on Electromagnetic Compatibility*, 1988;30(1):77–80
  - 77. Tirkas, P.A., C.A. Balanis, M.P. Purchine and G.C. Barber, Finite-difference time-domain method for electromagnetic radiation, interference, and interaction with complex structures, *IEEE Transactions on Electromagnetic Compatibility*, 1993;35(2):192–203
  - 78. Paolone, M., C.A. Nucci and F. Rachidi, A new finite difference time domain scheme for the evaluation of lightning induced overvoltages on multi-conductor overhead lines, in 5th International Conference on Power System Transients, Rio de Janeiro, Brazil, 2001

79. Sartori, C.A.F. and J.R. Cardoso, An analytical-FDTD method for near LEMP calculation, *IEEE Transactions on Magnetics*, 2000;36(4):1631–4
80. Yang, C. and B. Zhou, Calculation methods of electromagnetic fields very close to lightning, *IEEE Transactions on Electromagnetic Compatibility*, 2004;46(1):133–41
81. Mimouni, A., F. Rachidi and Z. Azzouz, Electromagnetic environment in the immediate vicinity of a lightning return stroke, *Journal of Lightning Research*, 2007;2:64–75
82. Mimouni, A., F. Rachidi and Z. Azzouz, A finite-difference time-domain approach for the evaluation of electromagnetic fields radiated by lightning to tall structures, *Journal of Electrostatics*, 2008;866:504–13
83. Baba, Y. and V.A. Rakov, On the mechanism of attenuation of current waves propagating along a vertical perfectly conducting wire above ground: application to lightning, *IEEE Transactions on Electromagnetic Compatibility*, 2005;47(3):521–32
84. Baba, Y. and V.A. Rakov, Electromagnetic fields at the top of a tall building associated with nearby lightning return strokes, *IEEE Transactions on Electromagnetic Compatibility*, 2007;49(3):632–43
85. Moini, R., B. Kordi, G.Z. Rafi and V.A. Rakov, A new lightning return stroke model based on antenna theory, *Journal of Geophysical Research*, 2000; 105(D24):29693–702
86. Pockels, F., Über die Blitzentladungen erreicht Strömstärke, in *Physikalische Zeitschrift*, 1900;2:306–7
87. Foust, C.M. and H.P. Kuehni, The surge crest ammeter, *General Electric Review*, 1932;35:5
88. Foust, C.M. and G.F. Gardner, A new surge-crest ammeter, *General Electric Review*, 1934;37:324
89. Wagner, C.F., and G.D. McCann, New instruments for recording lightning currents, *Transactions of the American Institute of Electrical Engineers*, 1940;59(12):1061–68
90. Grünewald, H., Die Messung von Blitzstromstärken an Blitzableitern und Freileitungsmasten, *Elektrotechnische Zeitschrift*, 1934;22:4
91. Zaduk, H., Neuere Ergebnisse der Blitzstromstärkemessungen an Hochspannungsleitungen, *Elektrotechnische Zeitschrift*, 1935;17:5
92. Popolansky, F., Lightning current measurement on high objects in Chechoslovakia, in 20th International Conference on Lightning Protection, Interlaken, Switzerland, 1990
93. Kulikow, D., Blitzströme, in 14th International Conference on Lightning Protection, Danzig, 1978
94. Miladowska, K., Vergleichung der Blitzresultate von hohen Schornsteinen und den Zählern, in 14th International Conference on Lightning Protection, Danzig, 1978
95. McEachron, K.B., Lightning to the Empire State Building, *Journal of Franklin Institute*, 1939;227:149–217

96. Diendorfer, G., H. Pichler and M. Mair, Some parameters of negative upward-initiated lightning to the Gaisberg Tower (2000–2007), *IEEE Transactions on Electromagnetic Compatibility*, 2009;51(3):443–52
97. Uman, M.A., *Lightning*. New York: McGraw-Hill, 1984
98. Golde, R.H., *Lightning*, vol. 1. London: Academic Press, 1977, p. 496
99. Berger, K., R.B. Anderson and H. Kroninger, Parameters of lightning flashes, *Electra*, 1975;41:23–37
100. Uman, M.A., *The Lightning Discharge*, vol. 39. Florida: Academic Press, Inc., 1987, p. 377
101. Cortina, R., E. Garbagnati, W. Serravalli, L. Dellera, A. Pigini and L. Thione, Quelques aspects de l'évaluation des performances des réseaux électriques vis-à-vis de la foudre, in CIGRE, Paris, 1980
102. Fisher, R.J., G.H. Schnetzer, R. Thottappillil, V.A. Rakov, M.A. Uman and J.D. Goldberg, Parameters of triggered-lightning flashes in Florida and Alabama, *Journal of Geophysical Research*, 1993;98(D12):22887–902
103. Narita, T., T. Yamada, A. Mochizuki, E. Zaima and M. Ishii, Observation of current waveshapes of lightning strokes on transmission towers, *IEEE Transactions on Power Delivery*, 2000;15(1):429–35
104. Diendorfer, G., M. Mair and W. Schulz, Detailed brightness versus lightning current amplitude correlation of flashes to the Gaisberg tower, in 26th International Conference on Lightning Protection, Cracow, Poland, 2002
105. Diendorfer, G., M. Mair, W. Schulz and W. Hadrian, Lightning current measurements in Austria-experimental setup and first results, in 25th International Conference on Lightning Protection, Rhodes, Greece, 2000
106. Torres, H., *Experimental station “Ilyapa” to measure directly lightning parameters in tropical zone*, Available from <http://www.paas.unal.edu.co/investigacion> [Accessed September 2000]
107. Torres, H., O. Trujillo, F. Amortegui, F. Herrera, G. Pinzon, C. Quintana, et al., Experimental station to measure directly lightning parameters in tropical zone, *11th International Symposium on High Voltage Engineering*, 1999, vol. 467, no. 5, pp. 177–80
108. Torres, H., O. Trujillo, F. Amortegui, G. Pinzon, C. Quintana, D. Gonzalez, et al., Design, construction and calibration of three devices to measure directly lightning parameters, *11th International Symposium on High Voltage Engineering*, 1999, vol. 2, pp. 430–3, London, UK
109. Rakov, V.A., Transient response of a tall object to lightning, *IEEE Transactions on Electromagnetic Compatibility*, 2001;43(4):654–61
110. Janischewskyj, W., J.S. Chang, A.M. Hussein, V. Shostak, I. Rusan and Y. Chen, Parameters of CN Tower lightning during severe and non-severe thunderstorms, in 10th International Conference on Atmospheric Electricity, Osaka, Japan, 1996
111. Hussein, A.M., W. Janischewskyj, J.S. Chang, V. Shostak, W.A. Chisholm, P. Dzurevych, et al., Simultaneous measurement of lightning parameters for

- strokes to the Toronto Canadian National Tower, *Journal of Geophysical Research*, 1995;100(D5):8853–61
- 112. Hussein, A., W. Janischewskyj, M. Milewski, V. Shostak, J.S. Chang and W.A. Chisholm, Return-stroke current waveform parameters of lightning to the CN Tower (1992–2001), in 26th International Conference on Lightning Protection, Cracow, Poland, 2002
  - 113. Shostak, V., Modeling of return stroke current for lightning events at a complex tall structure, in 2001 International Workshop on Electromagnetic Radiation from Lightning to Tall Structures, Toronto, Canada, 2001
  - 114. Shostak, V., W. Janischewskyj, A.M. Hussein and B. Kordi, Characteristics of return stroke current and electromagnetic field waveforms observed in multistroke lightning flashes to a tall tower, *11th International Symposium on High Voltage Engineering*, vol. 2, pp. 389–92, London, UK, 1999
  - 115. Montandon, E. and B. Beyeler, Lightning induced voltages on electrical installations on a Swiss ptt instrumented tower in St. Chrischona, Switzerland, in 22nd International Conference on Lightning Protection, Budapest, Hungary, 1994
  - 116. Montandon, E. and B. Beyeler, The lightning measuring equipment on the Swiss PTT Telecommunications Tower at St. Chrischona, Switzerland, in 22nd International Conference on Lightning Protection, Budapest, Hungary, 1994
  - 117. Rubinstein, A., C. Romero, M. Paolone, F. Rachidi, M. Rubinstein, P. Zweiacker, *et al.*, Lightning measurement station on Mount Säntis in Switzerland, in 10th International Symposium on Lightning Protection (SIPDA), Curitiba, Brazil, 2009
  - 118. Romero, C., A. Rubinstein, M. Paolone, F. Rachidi, M. Rubinstein, P. Zweiacker, *et al.*, Instrumentation of the Säntis Tower in Switzerland for lightning current measurements, *International Journal of Plasma Environmental Science & Technology*, 2010;4(1):79–85
  - 119. Hussein, A.M., W. Janischewskyj, M. Milewski, V. Shostak, F. Rachidi and J.S. Chang, Comparison of current characteristics of lightning strokes measured at the CN tower and at other elevated objects, *IEEE International Symposium on Electromagnetic Compatibility*, 2003;2:495–500
  - 120. Asakawa, A., K. Miyake, S. Yokoyama, T. Shindo, T. Yokota and T. Sakai, Two types of lightning discharges to a high stack on the coast of the sea of Japan in winter, *IEEE Transactions on Power Delivery*, 1997;12(3):1222–31
  - 121. Pichler, H., G. Diendorfer and M. Mair, Statistics of lightning current parameters measured at the Gaisberg Tower, in 18th International Lightning Detection Conference, Helsinki, Finland, 2004
  - 122. Rakov, V.A., Lightning discharges triggered using rocket-and-wire techniques, in Research Signpost (ed.), *Recent Research Development on Geophysics*. Research Signpost: India, 1999, pp. 141–71
  - 123. Schroeder, M.A.O., A.J. Soarez, S. Visacro, L.C.L. Cherchiglia and V.J. Souza, Lightning current statistical analysis: Measurements of Morro do Cachimbo Station – Brazil, in 26th International Conference on Lightning Protection, Cracow, Poland, 2002

---

# Index

---

Page numbers followed by *f* and *t* denotes a figure and table respectively.

- accelerating charges, electromagnetic fields from, 55–65  
accretion, 143  
active region, 74  
adaptive mesh refinement (AMR), 118  
advection, 171  
  forms, 157  
  scalar, 158  
aggregation, 143  
AGILE spacecraft, 848  
Agrawal, Price and Gurbaxani model, 691–2  
air  
  azimuthal magnetic field in, 430–1  
  electromagnetic field in, evaluation of soil stratification and, 557–61  
  heated volume of, in electrical spark channel, 802–3  
horizontal electric field in, 431–2  
non-thermal electrical discharges, numerical simulations:  
  *see* electrical discharges, non-thermal  
temperature in streamer, 809  
vertical electric field in, 430  
aircraft penetrating thunderstorms, 226, 226*f*  
aircraft-triggered lightning, 194  
Alfvén wave branch, 659  
'altitude-triggered lightning,' 211  
Ampere's law, 24  
  Maxwell's modification of, 33–4  
AMR: *see* adaptive mesh refinement (AMR)  
AMR sensors: *see* anisotropic magnetoresistive (AMR) sensors  
anelastic form, cloud models and, 147  
angular frequency, defined, 31  
anisotropic magnetoresistive (AMR) sensors  
magnetic field measurements using, 578  
antenna-mode currents, 689  
antennas  
  ball, 587  
  crossed loop: *see* crossed loop antennas  
  electric field components measurement and, 574–5  
  equivalent circuit of, 570*f*  
  measurement of magnetic field and, 577*f*  
  plate/whip: *see* plate/whip antenna  
  rise time constant/decay time constant of, 572*f*, 573*f*  
antenna theory (AT) models, of lightning return-stroke, 232, 315–82, 688  
frequency-domain, 349–50  
  numerical results, 372–81  
general formulation, 318–27  
  frequency-domain, 323–7, 325*f*  
  time-domain, 319–23, 321*f*  
with non-linear loading  
  numerical results, 364–72

- numerical results
  - current profiles, 350–2, 351*f*–352*f*
  - electromagnetic fields, 353–6, 354*f*, 355*f*, 357*f*
  - line charge density, 352–3, 353*f*
- numerical treatment, 327–38
  - frequency-domain formulation, 331–4, 331*f*, 332*f*
  - lossy half-space problem, 335–8, 335*f*
  - MOM, 327–8
  - time-domain formulation, 328–31
- overview, 317
- time-domain, 317, 339–41, 339*f*–340*f*
  - with inductive loading, 341–5, 342*f*, 344*f*, 345*f*
  - with non-linear loading, 346–9, 348*f*, 349*f*
- arc resistance equation (Toepler), 412
- AT: *see* antenna theory (AT) models
- ATIL-F: *see* AT model with fixed inductive loading (ATIL-F)
- ATIL model
  - ATIL-F, 317–18, 345, 346
  - ATIL-V, 344, 345
  - numerical results
    - current dispersion, 358*f*, 359
    - current profiles, 356–9
    - current wave propagation speed, 359–60, 361*f*
    - electromagnetic fields, 360, 362*f*, 363*f*, 364
  - ATIL model with variable inductive loading (ATIL-V), 344, 345
  - ATIL-V: *see* ATIL model with variable inductive loading (ATIL-V)
  - AT model with fixed inductive loading (ATIL-F), 317–18, 345, 346
  - atmosphere, discharge processes in: *see* discharge processes, in atmosphere
- attachment coefficient, 68
- attenuation
  - of current wave in absence of ohmic losses, 266–8, 267*f*
  - electromagnetic fields by current pulse propagating with/without, 57–60, 58*f*, 60–5
- attenuation function, 438, 476*f*, 488
  - for dipole, at ground level, 464–6
  - Wait's simplified expressions for, 471–3
- expression, above homogeneous ground, 489
- inverse Fourier transformation of, 466
- mixed-path ground, 502
- of two-layer horizontally stratified ground, 493
- avalanche, electron: *see* electron avalanches
- average length of a grid mesh ( $L_{moy}$ ), 179
- axial symmetry, 104, 487, 504, 679
- axisymmetric model, 141, 142, 147, 149, 150, 177
- azimuthal magnetic field, 487, 532–3, 535, 557
  - in air/underground, 430–1
  - above homogeneous ground, 490–1
  - simulations results, 498, 499
  - at surface/depths below ground, 461
  - above two-layer horizontally stratified ground, 499*f*, 500*f*
  - vs. vertical electric, model-predicted, 280–3, 281*f*, 282*f*, 284*f*, 285*f*
- ball antenna, vertical electric field, 587*f*
- ball lightning, features of, 856
- Bannister's approximation
  - for electric/magnetic field over finitely conducting ground, 438–40

- Norton's *vs.*, 439–40  
 Barbosa and Paulino expression  
   for horizontal electric field,  
     456–8  
 Bessel function, 335, 429, 431–2,  
     460, 461, 462, 516, 520,  
     527, 550  
 Bethe equation, 840  
 BG: *see* Bruce-Golde (BG) model  
 Bhabha scattering, 837, 839, 841  
 bidirectional leaders, 199, 200, 200f,  
     202, 203f, 205, 206, 206f, 207,  
     207f, 811  
 bin parameterizations, 145  
 bin/spectral microphysics, 143, 145  
   disadvantages of, 145–6  
 Biot–Savarts law, 22–3, 23f  
 BLT (Baum, Liu, Tesche) equations,  
     699  
 blue starters/jets, 611, 612, 627–8, 790  
   duration of, 614  
   phenomenology of, 614–15  
 boundary conditions  
   in corona model, 103–4, 104f  
   electrostatic, 17–19, 18f  
   for scalar potential ( $\phi$ ), 155  
   for static magnetic fields,  
     25–6, 25f  
 breakdown streamers, 75  
 breakeven electric field, 175  
 Bruce-Golde (BG) model, 877, 885  
 buffer amplifier system  
   electronic circuit of, 570f  
 buildings  
   heights, and induced voltages,  
     753f, 754f  
   lightning-induced voltages and,  
     751–5  
   in scale model experiments, 733, 734  
 bulk microphysics, 143–5  
   disadvantages of, 145–6  
 buried cables  
   electromagnetic field interaction  
     with, 707–13  
   geometry of, 709  
 lightning-induced disturbances in,  
     711–13, 712f–713f  
   *see also* field-to-buried wire lines  
 capacitance, channel  
   of transmission line, 399–400, 401f  
 ‘carrot’ sprite, 613, 631, 632  
   occurrence histogram of, 633f  
 Cartesian coordinates, 2, 3f  
   curl of vector field in, 7  
 case studies  
   negative streamer in weak  
     homogeneous background  
       fields, 130–4, 131f, 132f, 133f  
   positive corona between coaxial  
     cylinders, 107–12, 109f,  
     110f, 112f  
   positive streamer in weak  
     homogeneous background  
       field, 124–30, 127f, 128f,  
       129f, 130f  
   rod–plane electrode system,  
     positive corona in, 112–16,  
     113f, 114f, 115f, 116f  
 CD models: *see* current dissipation  
   models (CD models)  
 CFO: *see* critical impulse flashover  
   voltage (CFO)  
 CG: *see* cloud-to-ground (CG)  
   lightning  
 CG models: *see* current generation  
   models (CG models)  
 CGRO: *see* Compton Gamma-Ray  
   observatory (CGRO)  
 channel base current, 236  
   return stroke, 433, 495, 535–6  
 channel currents, transmission line  
   models  
   non-uniform channel  
     lossless, 414–16, 415f  
     lossy, 416–17, 417f  
       lossy, with corona, 418–19, 418f  
 channel instability, concept of, 209  
 channel parameters, transmission  
   line models

- calculation of, 398–414
- capacitance, 399–400, 401*f*
- corona, effect of, 401–9
- inductance, 399–400, 401*f*
- leader channel, 398
- resistance, 409–14
- return stroke channel, 399
- charge
  - continuity equations for, 156–8
  - density, rate of change in, 165–6
  - estimation, 176
  - structure and lightning type, 182–6, 183*f*, 184*f*, 185*f*
- charged particles
  - force on, 29
  - in gas
    - generation of, 88–9
    - losses of, 89–90
- charge mixing ratio, 156
- charge moment ( $Q_{ds}$ ), lightning, 629
- charging processes, in cloud models:
  - see* cloud models, charging processes in
- Chen's analytical equation, 265–6, 266*f*
- current distributions comparison
  - along vertical perfectly conducting wire and, 294, 295*f*, 296*f*
- circuit theory model: *see* hybrid electromagnetic (HEM) model
- cloud charges, lightning discharges and, 205–8, 206*f*, 207*f*
- cloud flashes, nitrogen oxides production by, 818–20
- cloud ice, change in charge density and, 166
- cloud models, charging processes in, 139–86
  - applications, 180–6
    - charge structure and lightning type, 182–6, 183*f*, 184*f*, 185*f*
    - ion and inductive mechanisms, 180–1
- non-inductive graupel–ice sensitivity, 181
- challenges, 186
- electrical processes,
  - parameterization of: *see* parameterization, of electrical processes
- electrification modelling, 149–53
- lightning parameterizations: *see* lightning, parameterizations
- model descriptors, 140–8
  - categorizations, other, 147–8
  - electrification processes, categories of, 146–7
  - microphysics and: *see* microphysics
  - terminology, 140–2
- overview, 139–40
- cloud-to-ground (CG) lightning, 152, 182, 184, 186, 201–3, 595, 596
- bidirectional, bipolar lightning
  - 'tree' in negative, 201–2, 202*f*
  - dart/dart-stepped negative leaders in, 203
- IC leaders, development of, 206–8, 206*f*, 207*f*
- multi-stroke negative, 201, 201*f*
- negative: *see* negative CG flashes
- positive: *see* positive CG flashes
  - recoil leaders and, 211, 212
  - as stochastic process, 680
- CNTLSG: *see* CN Tower Lightning Studies Group (CNTLSG)
- CN Tower, 899, 900, 900*f*, 901*f*, 906*f*
  - electromagnetic models applications, 300, 302
- CN Tower Lightning Studies Group (CNTLSG), 899
- coalescence, 143
- coaxial cylinders, positive corona between (case study), 107–12, 109*f*, 110*f*, 112*f*
- cold cloud models, 143
- cold electrical discharges, 789, 791
- cold runaway, 835

- collection efficiency, 161, 166  
 collision efficiency, 161–2  
 collision kernel, 165  
 ‘columniform’ sprites, 613, 631, 632  
     occurrence histogram of, 633f  
 Compton backscatter, 836, 837  
 Compton Gamma-Ray observatory (CGRO), 833  
 Compton scattering, 833, 841  
 Comsol Multiphysics, 96, 97–107  
 conducting media  
     Maxwell’s equations and plane waves in, 43–4  
     re-distribution of excess charge in, 22  
 conduction currents, 492  
 conductivity, 542  
     equivalent, of multi-section ground, 470–1  
     finitely conducting ground, 428  
 ground, 521  
     as function of frequency, 546f  
 plasma, 678  
 profiles, 479f  
 scale factor for, 723  
 soil, 476  
     on frequency, 543–5  
 connecting leaders, 855  
     defined, 766  
 inception models: *see* leader inception models  
     orientation of, 782  
     and stepped leader, 768–9  
 conservation of charge, 20–1, 156  
 conservative field, 12  
 constants, in corona model, 98–9, 99f  
 ‘contamination’ of current, 899, 901  
 continuing current, 810, 816  
     discharges, 203  
     as indicator of developing leader, 203–4, 204f  
     in upward positive leaders, 216  
 continuity equations  
     for charge, 156–8  
     for free ions, 171  
     ‘convective’ charging hypothesis, 152  
     ‘convective flux,’ for electrons, 103–4, 104f  
 convective mechanism, 180–1  
 conventional breakdown field, 831–2  
 Cooperative Convective Precipitation Experiment, 150  
 Cooray, Rakov and Montano model, of CG, 248–9  
 Cooray and Rakov model of CG, 248  
     combination of CD and CP models, 252–3  
 Cooray model of CG, 242–4, 247  
 Cooray-Rubinstein (CR) formula, 338, 535  
     electromagnetic field computation and, 889  
     for horizontal electric field, 491–2  
     radial electric field, calculation, 537f, 538f–539f  
     underground electromagnetic field and, 537, 540–2  
 Cooray’s formula  
     electromagnetic field computation and, 889–90  
 coordinate systems, electromagnetic theory in, 2, 3f  
 Cartesian coordinates: *see* Cartesian coordinates  
 cylindrical coordinates: *see* cylindrical coordinates  
 spherical coordinates: *see* spherical coordinates  
 corona  
     on channel parameters, calculation, 401–9  
     leader channel, 402–6, 402f, 404f  
     return stroke channel, 402–6, 402f, 404f  
     transmission line equations, 407–9  
 currents, 237–8  
     fast, 238

- phosphenes, simulation, 866–7, 867*f*
- slow, 238
- decay time constant, 237, 238
- discharges, 75–6, 789–90, 791
  - glow corona/Hermitian glow, 75
  - Hermitian sheath, 75
  - negative space charge region in, 76
  - onset streamers and, 75
  - Trichel pulses, 76
- model
  - boundary conditions for, 103–4, 104*f*
  - coefficients, calculating, 98–9, 100*f*
  - computer implementation of, 97–107
  - constants in, 98, 99*f*
  - convection–diffusion, settings for, 102, 103*f*
  - convection-diffusion equation, stabilization method for, 106, 107*f*
  - field dependencies of ionization and attachment coefficients, 101, 101*f*
  - field-dependent characteristics of electrons in air, 101–2, 102*f*
  - integration coupling variables, for discharge current, 99, 100, 100*f*, 101
  - Poisson’s equation, settings for, 102, 103*f*
  - solver parameters, choosing, 105–6, 105*f*
  - non-uniform channel with, lossy, 418–19, 418*f*
  - positive
    - between coaxial cylinders (case study), 107–12, 109*f*, 110*f*, 112*f*
    - in rod–plane electrode system (case study), 112–16, 113*f*, 114*f*, 115*f*, 116*f*
  - sheath, NO<sub>x</sub> production and, 810–12
  - simulations, in air, 96–7
  - streamers, formation, 195
  - cosmic rays, 171
  - Coulomb’s law, 10–11, 10*f*, 11*f*
  - CP models: *see* Current propagation models (CP models)
  - CR formula: *see* Cooray-Rubinstein (CR) formula
  - critical impulse flashover voltage (CFO), 719
  - critical radius, 769–70
  - critical streamer length, 769–70
  - crossed loop antennas
    - equivalent circuit of, 576*f*
    - and magnetic field measurement, 576–8
  - crossing field, 128–9
  - cumulative ionization, 67
  - curl of vector field, 7
    - line integral and, 8
  - current cut-off, in lightning flash development, 208–12, 208*f*
  - branching of developing leader, 209
  - channel instability in, 209
  - field screening, 209–10, 210*f*
  - recoil leaders and, 211–12
  - self-screening, 209
  - current dispersion
    - ATIL model and, 358*f*, 359
  - current dissipation models (CD models), 249–53
  - Cooray and Rakov model, 252–3
  - features, 250, 250*f*
  - general description, 249–51
  - generalization/conversion of any model to, 255–6
  - mathematical background, 251–2
  - modified transmission line models and, 256–7
  - current distributions
    - electromagnetic models

- along vertical perfectly conducting wire, 265–8, 266f, 287–90, 288f, 289f, 294, 295f, 296f  
 for different channel representation, 277–9, 278f, 280f  
 electric vs. magnetic fields with measurements, 280–3, 281f, 282f, 284f, 285f  
*see also* electromagnetic models of lightning return strokes prediction, engineering models and, 877–8, 879f, 880f vector potential of, 27–8, 27f  
 current element electromagnetic fields of, 48–51, 49f magnetic field by, 22–3, 23f vector potential and, 28–9, 29f, 48  
 current generation models (CG models), 236–49 basic concept, 236–8 Cooray, Rakov and Montano model, 248–9 Cooray and Rakov model, 248 Cooray model, 242–4, 247 Diendorfer and Uman model: *see* Diendorfer–Uman (DU) model generalization/conversion of any model to, 253–5 Heidler model, 241–2 Hubert model, 242 mathematical background, 238–40 *Ib(t)* given  $\rho(z)$ ,  $\tau(z)$  and  $v(z)$ , 238–9  $\rho(z)$ , given *Ib(t)*,  $\tau(z)$  and  $v(z)$ , 240  $\tau(z)$ , given *Ib(t)*,  $\rho(z)$  and  $v(z)$ , 239–40  $v(z)$ , given *Ib(t)*,  $\rho(z)$  and  $\tau(z)$ , 240 Wagner model, 241  
 current peak AT model with non-linear loading, 365–6, 366f  
 current profiles ATIL model, 356–9 frequency-domain AT model, 372–3, 372f, 373f AT models, 350–2, 351f–352f with non-linear loading, 364–5, 365f  
 current propagation models (CP models), 232–6 basic concept, 232–4 channel base current, 236 Cooray and Rakov model, 252–3 features, 235t general description, 234, 236 return stroke speed, 236  
 current pulse, propagating: *see* propagating current pulse  
 current rise time AT model with non-linear loading, 365–6, 367f  
 current wave attenuation in absence of ohmic losses, 266–8, 267f  
 current wave propagation speed ATIL model, 359–60, 361f AT model with non-linear loading, 372  
 cut-off frequency, 657–8 cylindrical coordinates, 2, 3f curl of vector field in, 7 divergence and Laplacian in, 6 gradient of scalar function in, 5  
 dark discharge, 91  
 dart leaders, 810 electrostatic charge representation of, 224f M-event, electrostatic model of, 222–4, 223f, 224f, 225f nature of, 196–8, 201  
 dedicated algorithms electromagnetic field computation and, 888–9  
 Diendorfer–Uman (DU) model, 316 return stroke model, 244–5

- first modification by Thottappillil *et al.*, 245–6
- second modification by Thottappillil and Uman, 246–7
- difference of time-of-arrival (DTOA), 198–9, 199*f*
- diffusivity, 172
- digital storage oscilloscopes (DSO), 727
- dipole
  - attenuation function for, at ground level, 464–6
  - over finitely conducting ground electromagnetic fields, expressions for, 430–2
  - vector potential, expressions for, 428–9, 428*f*
- radiations
  - in free space, 520*f*
  - over conducting ground, 518*f*
  - in subsoil, 533*f*
- Dirac delta function, 237, 257, 517, 519, 540, 573
- direct lightning strikes/strokes, 855
  - on ground lossess, 702–4
  - surges in power lines and, 735–8
- discharge plasma
  - charge carriers in, densities, 90
- discharge processes, in atmosphere, 67–84
  - corona discharges, 75–6
  - electron avalanche, 68–70, 69*f*
  - leader discharges: *see* leaders, discharges
  - low-pressure electrical, 77
  - overview, 67–8
  - streamer discharges: *see* streamer discharges
  - thermalization/heating of air by, 76–7
- discharge-type transmission line models, 392, 393–5, 393*f*
- dispersion curve, 660*f*
- displacement current density, 33–4
- ‘distributed capacitance’ conditions, 104
- distributed-circuit models, 263–4, 316
  - see also* transmission line models
- distributed source representation engineering models, extension of, 874–6, 875*t*
- distribution networks
  - lightning overvoltages and, 719
  - divergence of vector field, 6–7
    - flux and, 9
  - divergence theorem, 9
  - downward negative lightning flash, 765
- drift-diffusion equations, solving, 118
- drift/fluid-diffusion model, 92–6
- drift velocity, 20
- DRIVER, routine, 124, 124*f*
- DSO: *see* digital storage oscilloscopes (DSO)
- DTOA: *see* difference of time-of-arrival (DTOA)
- DU: *see* Diendorfer–Uman (DU) model
- Dwyer instability, 837
- Earth, magnetic field, 648, 652
- Earth-ionosphere waveguide, 584, 662
  - wave propagation in, 585
- effective liquid water content (EW), 161–2
- EFIE: *see* electric field integral equation (EFIE)
- EGM: *see* electrogeometrical model (EGM)
- elastic scattering, in Monte Carlo simulations, 842
- electrical discharges,
  - low-pressure, 77
- electrical discharges, non-thermal
  - electrophysical processes, in gaseous medium: *see* electrophysical processes, in gaseous medium
- gas discharge

- plasma, hydrodynamic  
description of, 92–6  
problems, solving, 96–116  
numerical simulations of, 87–134  
overview, 87  
streamer discharges, simulations  
of: *see* streamer discharges,  
simulations of
- electrical sparks  
channels  
air heated in, volume of, 802–3  
current waveform associated  
with, 805  
 $\text{NO}_x$  production in, 803–8 *see*  
*also* nitrogen oxides ( $\text{NO}_x$ )  
radius of, 800–2, 801*t*, 802*f*
- electric charge  
conservation of, 20–1  
re-distribution of excess, 22
- electric currents, 19–20
- electric dipole, 48–51, 49*f*
- electric field integral equation  
(EFIE), 317
- electric fields  
amplitude of, 479*f*  
calculations, 153–6, 154*f*  
configuration, leader channel  
and, 781  
different combinations of, 616*t*
- electrodynamics, time-varying: *see*  
electrodynamics  
energy density of, 29–30  
of first three SR modes, 586, 586*f*  
generated by lightning flash,  
477*f*, 478*f*
- horizontal component of  
above two-layer horizontally  
stratified ground, 499*f*, 500*f*  
in air/underground, 431–2  
calculation of, 448–56, 488  
at ground level, 458*f*, 498*f*  
simulations results of, 498, 499  
at surface/depths below ground,  
461–4  
at surface for first stroke, 459*f*
- large, penetration of, 623*f*  
measurement, plate/whip antenna  
and, 568–74
- mill: *see* field mill
- over finitely conducting ground,  
calculation procedures,  
438–64
- Norton/Bannister's  
approximations, 438–40
- of plane waves, 39
- radial component of, 530, 534,  
557–61, 558*f*, 559*f*, 560*f*  
calculation, using CR formula,  
537, 538–9
- from return strokes, calculation  
of, 433
- signature, of lightning return  
stroke, 468*f*, 469*f*
- spectra as function of SOD, 586*f*
- static, 10–19  
boundary conditions,  
electrostatic, 17–19, 18*f*  
conservative field and, 12  
Coulomb's law, 10–11, 10*f*, 11*f*  
Gauss's law, 13–14  
images, concept of, 16–17, 17*f*  
Poisson and Laplace equations,  
15–16  
scalar potential, electric,  
14–15, 15*f*
- three components measurements,  
574–5
- time derivative, 481*f*
- underground, calculation  
time domain expressions to,  
458–64
- vertical component of, 527–30,  
534, 557  
above homogeneous ground,  
490–1  
above two-layer horizontally  
stratified ground, 499*f*, 500*f*  
in air/underground, 430  
at ground level, 435*f*, 441*f*, 474*f*,  
475*f*, 497*f*, 504*f*

- measurement, field mill and, 567–8
- peak/rise times of, 497*t*, 507*t*
- propagation effects on, 434
- simulations results of, 498, 499
- at surface/depths below ground, 459–60
- at surface of mixed-path ground, 467*f*
- time derivative of, 435, 436, 436*f*, 440*f*, 444*f*, 446*f*
- time dynamics of, 623*f*
- electric radiation fields, propagating
  - current pulse and
  - due to attenuation of current, 62–3
  - with non-uniform velocity and
  - with attenuation, 61
  - with uniform velocity and without attenuation, 58
  - due to variation of current velocity, 64
- electric scalar potential, 14–15, 15*f*
- electrification modelling
  - evolution of, 149
  - history of, 149–53
- electrification processes, categories of, 146–7
- electrodynamics
  - time-varying electric and magnetic fields, 30–5
  - displacement current density, 33–4
  - energy density in magnetic field, 34–5, 34*f*
  - Faraday’s law, 31–2
  - Maxwell’s modification of Ampere’s law, 33–4
- electrogeometrical model (EGM), 768
  - vs. SLIM, 777–80
- electromagnetic (EM) code, 627
  - rise time of return stroke and, 638
- electromagnetic fields
  - above lossy half-space, frequency-domain AT model, 374–81, 376*f*, 377*t*, 378*f*–380*f*
  - from accelerating charges, 55–65
  - amplitude of, 476, 479
  - ATIL model and, 360, 362*f*, 363*f*, 364
  - characteristics of, 427
  - computation
    - approaches for, 688
    - lightning strikes to tall towers and, 881–91, 882*f*, 886*f*–888*f*, 891*f*
  - of current element, 48–51, 49*f*
  - of dipole, over finitely conducting ground, 430–2
  - frequency-domain AT model and, 373–4, 374*f*
  - interaction with buried cables, 707–13
  - interaction with overhead lines, 690–707
    - Agrawal, Price and Gurbaxani model, 691–2
    - frequency-domain solutions, 698–700
    - inclusion of losses, 694–5
    - LEMP-to-transmission line coupling model, 698
    - multiconductor lines, 695–8
    - Rachidi model, 693
    - single-wire transmission line, 690
    - Taylor/Satterwhite/Harrison model, 690–1
    - time-domain solutions, 700–2
  - lightning, calculation of
    - above homogeneous lossy ground, 489–92
    - above horizontally stratified ground, 493–500
    - above perfect ground, 486–8
    - above vertically stratified ground, 500–5
  - electrical parameters of soil and, 542–8
  - ground parameters and, 516–33
  - soil stratification and, 548–61

- lightning-radiated, propagation of over two-layer vertically stratified ground, 502*f*
- of lightning return stroke, 51–3, 52*f*
- AT models and, 353–6, 354*f*, 355*f*, 357*f*
- AT model with non-linear loading, 367–71, 368*f*–371*f*
- of moving charge, 55–6, 55*f*
- overground, 517–33, 535–7
- Green's functions theory and:  
*see* Green functions
- lightning return stroke, derivation of, 522–3
- numerical simulation of, 545–8
- radial component of electric field, 530–1
- Sommerfeld's integrals, evaluation of, 523–7
- vertical component of electric field, 527–30
- by propagating current pulse: *see* propagating current pulse
- of return strokes, 432, 548*t*
- transmission line models, 419–21, 420*f*
- underground, 533–5, 537, 540–2
- numerical simulation of, 545–8
- visual sensations of, 855–68
- see also* visual sensations, electromagnetic fields
- electromagnetic models of lightning
- return strokes, 232, 316–17, 728
- applications, 294–305
- flat ground, 295–300, 299*f*
- free-standing tall object, 300–4, 301*f*, 303*f*, 304*f*
- overhead power transmission lines, 304–5
- papers on, 297*t*
- wire-mesh-like structures, 305
- channel representation, 268
- current distributions
- comparison of different, 277–9, 278*f*, 280*f*
- model-predicted electric and magnetic fields comparison, 280–3, 281*f*, 282*f*, 284*f*, 285*f*
- papers on, 270*t*–272*t*
- perfectly conducting/resistive wire in air above ground (type 1), 269
- two wires having additional distributed shunt capacitance in air (type 6), 276–7
- wire coated by dielectric material in air above ground (type 4), 276
- wire coated by fictitious material having high relative permittivity and permeability in air above ground (type 5), 276
- wire embedded in dielectric (other than air) above ground (type 3), 274–5
- wire loaded by additional distributed series inductance in air above ground (type 2), 269, 273–4
- Chen's analytical equation, 265–6
- current distribution along vertical perfectly conducting wire above ground, 265–6, 266*f*
- current wave attenuation in absence of ohmic losses, 266–8, 267*f*
- excitations used in, 283–90
- charged vertical conducting wire closing at its bottom end with specified circuit, 286
- current distributions comparison along vertical perfectly conducting wire, 287–90, 288*f*, 289*f*
- lumped current source, 287
- lumped voltage source, 287
- papers on, 286*t*

- features, 268–9
- lightning strikes to tall towers, 880–1
- Maxwell's equations and, 263, 264, 290, 292, 315–16, 390, 415
- AT models, 317
  - see also* antenna theory (AT)
  - models, of lightning return-stroke
- numerical procedures, 290–4
  - current distributions comparison
    - along vertical perfectly conducting wire, and Chen's analytical equation, 294, 295*f*, 296*f*
- FDTD method, 292–3, 293*f*
- MoM in frequency domain, 292
- MoM in time domain, 290–2, 291*f*
  - papers on, 291*t*
- overview, 263–5
- electromagnetic pulse (EMP), 615, 617–18
  - computer simulation results
    - on, 620*f*
  - for horizontal discharge, 618
  - for vertical discharge, 617–18
- electromagnetic theory
  - basic concepts of, 1–53
  - coordinate systems: *see* coordinate systems
  - electric dipole, 48–51, 49*f*
  - electric fields: *see* electric fields
  - electrodynamics: *see* electrodynamics
  - electromagnetic fields, of lightning return stroke, 51–3, 52*f*
  - energy density, of electric field, 29–30
  - laws of electricity, summary of, 35–6
  - magnetic fields: *see* magnetic fields
  - Maxwell's equations and plane waves, 42–5
- Maxwell's prediction of electromagnetic waves, 37–8
- nomenclature, 1–2
- plane wave solution: *see* plane waves
- retarded potentials, 46–8
- vectors in: *see* vectors
- wave equation, 36–7
- electromagnetic transient program (EMTP), 703–4, 720, 879
- electromagnetic waves
  - Maxwell's prediction of, 37–8
  - plane, 39
- electromotive force (emf), changing magnetic field and, 32
- electron avalanches, 68–70, 69*f*
  - concept of, 90–2
  - nitrogen oxides production in, 791–2
  - streamer discharge from, 70–4, 71*f*, 73*f*
  - to streamer transition, 765
- electrons
  - heating of ionosphere and neutral atmosphere, 620–1
  - ionosphere/magnetosphere, electromagnetic waves interaction with, 650, 652–5
  - runaway: *see* runaway electrons
- electrophysical processes, in gaseous medium, 87–92
- charged species
  - carriers in discharge plasma, densities of, 90
  - generation of, 88–9
  - losses of, 89–90
- electron avalanche and streamer, 90–2
- electrostatic boundary conditions, 17–19, 18*f*
- electrostatic (ES) code, 627
- elevated strike object
  - engineering models on, 876–7
- ELF: *see* extremely low frequency (ELF)

- El Niño/Southern Oscillation (ENSO), 594
- elves, 595, 611, 612, 790  
phenomenology of, 615  
and sprites, 626–7
- EM code: *see* electromagnetic (EM) code
- EMP: *see* electromagnetic pulse (EMP)
- Empire State Building, 892, 906*f*
- EMTP: *see* electromagnetic transient program (EMTP)
- energetic radiation  
phosphenes, induction of, 864–6  
visual sensations by, 862–6, 863*f*
- energy, in electrical sparks channel, 806–8
- energy density  
of electric field, 29–30  
in magnetic field, 34–5, 34*f*
- energy spectrum, in runaway electrons, 842–3
- engineering models, 316  
comparison, electromagnetic field computation, 885–8, 886*f*, 887*f*, 888*f*
- lightning strikes to tall towers, 874–80  
current distribution, prediction of, 877–8, 879*f*, 880*f*
- distributed source  
representation, extension on, 874–6, 875*t*
- lumped series voltage source, extension on, 876
- reflection coefficients at top and bottom of strike object, 878–80
- on representation of elevated strike object, 876–7
- for return stroke, 263
- CD type model, generalization/conversion to, 255–6
- CG type model, generalization/conversion to, 253–5
- current dissipation models, 249–53
- current generation models, 236–49
- current propagation models, 232–6  
development of, 232, 233*f*  
ground conductivity, effects of, 257–9, 258*f*  
input parameters, 232, 236  
overview, 232
- ENSO: *see* El Niño/Southern Oscillation (ENSO)
- epileptic seizures, of occipital lobe, 858–60, 859*f*  
*see also* occipital lobe, epileptic seizures of
- equivalent circuit  
of crossed loop antennas, 576
- ERM: *see* extended Rusck model (ERM)
- ES code: *see* electrostatic (ES) code
- EUCLID: *see* European Cooperation for Lightning Detection (EUCLID)
- Eulerian models, 148
- European Cooperation for Lightning Detection (EUCLID), 904
- EW: *see* effective liquid water content (EW)
- extended Rusck model (ERM), 740, 748
- extraterrestrial lightning  
research, SR in, 597–8
- extremely low frequency (ELF)  
sprites and, 614  
SR and, 583–4  
transient recorded at Mitzpe Ramon, 592  
transmitters, 583–4
- fair-weather state, 172  
defined, 171  
positive and negative ion fluxes in, 171

- Faraday's law, 31–2  
 far fields, 50  
 FCT: *see* flux-corrected transport (FCT)  
 FDTD: *see* finite-difference time-domain (FDTD) technique  
 feedback factor, 845–6, 847f  
 'field choking' effect, 209  
 field mill  
     advantage of, 568  
     principle of, 568f  
     vertical electric field measurement and, 567–8  
     *vs.* plate/whip antenna, 572–3  
 field-to-buried wire lines  
     coupling equations, 707–10, 708f, 709f  
     frequency-domain solutions, 710–11  
     time-domain solutions, 711  
 field-to-transmission line coupling  
     equations  
     by Agrawal/Price/Gurbaxani, 691–2  
     frequency domain representation of, 698–700  
     inclusion of losses, 694–5  
     multiwire system and, 695–8  
     by Taylor, Satterwhite and Harrison, 690–1  
     time-domain representation of, 700–2  
 final jump condition, 768–9  
 finite-difference time-domain (FDTD) technique, 277, 278f, 279, 280f, 292–3, 293f, 294, 298, 300, 302, 304, 414, 493, 688, 701, 877, 890  
 electromagnetic field computation and, 890  
 simulations, 496f, 505f  
     horizontally stratified ground, 495–6  
     vertically stratified ground, 504–5  
 finitely conducting ground  
     electric/magnetic fields over, calculation procedures, 438–64  
     Norton/Bannister's approximations, 438–40  
     electromagnetic fields of dipole over, expressions for, 430–2  
     vector potential of dipole over, expressions for, 428–9  
 first return stroke  
     horizontal electric field, 450f, 452f, 454f, 456f, 540f, 541f  
     NO<sub>x</sub> production by, 814–15  
     parameters of, 434t  
 Fitzgerald, George F., 583  
 flash, 315  
 flat ground, electromagnetic models  
     applications, 295–300, 299f  
 fluid/drift-diffusion model, 92–6  
 flux-corrected transport (FCT), 119–20  
 flux-correction/flux-limiting, 119–20  
 flux forms, 157  
 fluxgate magnetometer, 578  
 flux-limiting/flux-correction, 119–20  
 flux of vector field, 8–9  
     divergence and, 9  
 FORTRAN, 120, 123  
 Franklin, Benjamin, 193  
 free-space wave number, 490  
 free-standing tall object  
     electromagnetic models  
         applications, 300–4, 301f, 303f, 304f  
 frequency-domain AT model, 349–50  
     numerical results  
         current profiles, 372–3, 372f, 373f  
         electromagnetic fields, 373–4, 374f  
         electromagnetic fields above lossy half-space, 374–81, 376f, 377t, 378f–380f  
 Fukui chimney  
     electromagnetic models  
         applications, 300, 301f, 302

- Fukui thermal power plant, 902, 904f, 906t  
 Fukui Tower, 902, 904, 904t  
 fulchronograph, 892  
 full simulation model, 140, 147, 148  
 fully compressible, cloud models, 147
- Gaisberg Tower, 897, 898, 906t  
 Gamma function, 529  
 gamma-rays, 832, 833, 834  
     bursts, 833  
     feedback, 837  
     observations, from thunderclouds  
         and lightning, 846–8  
 gas discharge  
     computer modelling of, 92–6  
     plasma, hydrodynamic description  
         of, 92–6  
     problems, solving, 96–116  
         Comsol Multiphysics for: *see*  
             Comsol Multiphysics  
         corona models: *see* corona  
 gas dynamic models, 263, 316, 410  
 gaseous medium  
     electrophysical processes in, 87–92  
         charge carriers in discharge  
             plasma, densities of, 90  
         charged species, generation of,  
             88–9  
         charged species, losses of, 89–90  
         electron avalanche and  
             streamer, 90–2  
 Gauss's law, 13–14, 811  
     for magnetic fields, 23  
 geometry function, definitions of,  
     123t  
 'gigantic jets,' 614  
 global lightning activity  
     SR and, 584, 588–92  
         background observations,  
             588–91  
         transient measurements, 591–2  
 global warming  
     SR as research tool for, 592–4  
     UTWV on, 594
- glow corona, 75  
 Godunov's method, 118  
 gradient of scalar function, 5–6  
 graupel-ice collision mechanism,  
     non-inductive: *see* non-  
         inductive graupel-ice collision  
         mechanism  
 graupel-ice sensitivity,  
     non-inductive, 181  
 Green functions, 516  
     defined, 518  
     derivation, 549–53  
         for overground electromagnetic  
             field, 518–22  
     frequency-domain solutions and,  
         698–700  
     integrals of, 710  
     lightning electromagnetic field  
         and, 522–3, 553  
         overview of, 517–18  
 Grenet–Vonnegut mechanism, 180–1  
 ground conductivity, 521  
     as function of frequency, 546f  
     on return stroke current, 257–9,  
         258f  
 ground currents, 855  
 grounded structure  
     interaction with lightning flash,  
         765–85  
     inception models: *see* leader  
         inception models  
         overview, 765–6  
         striking distance, 767–9  
 ground flash  
     negative, NO<sub>x</sub> production in,  
         817–18  
         *see also* lightning flash  
 ground losses  
     direct lightning overvoltages  
         effects on, 702–4  
         on travelling voltages, 703  
 ground parameters  
     constant, and calculation of  
         lightning electromagnetic  
             field, 516–33

- electrical, and calculation of lightning electromagnetic field, 542–8
- ground permittivity, as function of frequency, 547*f*
- group velocity, 655
  
- Hall effect sensors, 578
- Hankel transform, 526–7, 526*f*
- Heidler CG model, 241–2
- Heidler’s functions
  - parameters, and channel-base current waveshape, 536*t*
- Helmholtz equations, 519, 520, 550
- HEM: *see* hybrid electromagnetic (HEM) model
- Hermitian glow, 75
- Hermitian sheath, 75
- Heaviside step function, 571
  - derivative of, 573
- HMC1022 sensor, Honeywell’s, 578
  - electronic circuit for, 579*f*
- Hokuriku region, sprites in, 633–4, 635*f*, 637, 638
- homogeneous background fields, weak (case studies)
  - negative streamer in, 130–4, 131*f*, 132*f*, 133*f*
  - positive streamer in, 124–30, 127*f*, 128*f*, 129*f*, 130*f*
- homogeneous lossy ground electromagnetic fields
  - approximations above, 489–92, 489*f*
  - surface impedance of, 490
- Honeywell’s HMC1022 sensor, 578
  - electronic circuit for, 579*f*
- horizontal electric field, 487
  - above two-layer horizontally stratified ground, 499*f*, 500*f*
  - in air/underground, 431–2
  - calculation of, 448–56, 488
    - Barbosa/Paulino expression, 456–8
    - CR formula and, 491–2
- quasi-static expression for, 449
- surface impedance expression, 449
- first stroke, at ground level, 450*f*, 452*f*, 454*f*, 456*f*
  - at ground level, 458*f*, 498*f*
  - simulations results of, 498, 499
  - subsequent stroke, at ground level, 451*f*, 452, 453*f*, 455*f*, 457*f*
  - at surface/depths below ground, 461–4
  - at surface for first stroke, 459*f*
- underground
  - first stroke, 463*f*, 464*f*, 540*f*, 541*f*
  - subsequent stroke, 541*f*, 542*f*
- horizontally stratified ground
  - electromagnetic fields above, 493–500
  - propagation effects over, 471–81, 472*f*
  - on radiation fields, 473–81
  - simulation domain of FDTD technique, 495–6
- two-layer
  - attenuation function of, 493
  - surface impedance of, 494
- hot electrical discharges, 790
  - NO<sub>x</sub> production and, 812–14
- Hubert CG model, 242
- hybrid electromagnetic (HEM) model, 264–5, 300, 415, 874
- lightning strikes to tall towers, 881
  
- IAR: *see* ionospheric Alfvén resonator (IAR)
- IC: *see* intracloud (IC) flashes
- ICC: *see* initial continuous current (ICC)
- ice multiplication, 143
- ice–particle interactions, for thunderstorm electrification, 149
- ICLRT: *see* International center for lightning research and testing (ICLRT)

- ‘ideal fields,’ 522, 552
- images, concept of, 16–17, 17*f*
- inception models, leader: *see* leader inception models
- indirect strokes
  - lightning surges in power lines and, 738–55
- induced voltages
  - comparisons, 739*f*
  - for different buildings’ heights, 753
  - measured/calculated, 740–3, 741*f*, 742*f*, 743*f*, 744*f*, 747
- inductance, channel
  - of transmission line, 399–400, 401*f*
- induction coils, 587
- induction field, 50
- inductive charging mechanism, 146, 146*f*, 167–70
- inductive parameterization, 150, 168
- initial continuous current (ICC), 892–3, 893*f*
- intermediate sprites, 632
  - occurrence histogram of, 633*f*
- intermittent light
  - occipital seizures and, 862
- International center for lightning research and testing (ICLRT), 834
- intracloud (IC) flashes, 198–201
  - CG leaders, development of, 206–8, 206*f*, 207*f*
  - development of bipolar lightning ‘tree’ in, 200, 200*f*
- DTOA technique: *see* difference of time-of-arrival (DTOA)
- initial stage of, 200
- inverted, 201
- lightning radiation map of, 199–200, 199*f*
- negative leaders in, 199–200
- positive leaders in, 199–200
- recoil leaders in, 211, 212
- intrinsic impedance of vacuum (free space), 41
- inverse exponential (IE) distribution, 167
- inverse Fourier transform, 432, 700–1
  - of attenuation function, 466
  - of ideal term, 527, 530–1, 532
  - vertical electric field calculation and, 443
- inverted IC flashes, 201
- ion and inductive mechanisms, 180–1
- ion generation rate, 172
- ionic recombination coefficient, 172
- ionization coefficient, effective, 68
- ionosphere
  - characterization of, 649–50, 650*f*
  - electrons, electromagnetic waves interaction and, 650, 652–5
  - heating of, 620–1
- IAR: *see* ionospheric Alfvén resonator (IAR)
  - layers of, 649–50
  - lightning effects in, 611–40, 647–80
    - see also* transient luminous event (TLE)
  - lightning-induced whistlers in, 647–61
    - overview of, 647–9
    - theoretical background, 649–61
  - of Titan, SR on, 598
- ionospheric Alfvén resonator (IAR), 647, 661–80
  - correlation coefficients of, 671*f*
  - defined, 662
  - dynamic spectra of, 665*f*
  - excitation of, thunderstorms and, 673–80, 674*f*, 675*f*, 678*f*
  - former generation mechanisms of, 672–3
  - history of, 661–2
  - observations/data processing, 663–6
  - occurrence rate, 666, 668–9
    - diurnal variation of, 666, 670*f*
    - spectra, night-time, 680*f*
  - spectral resonance structure: *see* spectral resonance structure (SRS), IAR

- temporal evolution of, 668*f*
- isotropic media
- Maxwell's equations and plane waves in, 43–4
- Italy Towers, 907*t*
- ITPACK 2C, 121, 121*f*
- Japan Transmission Towers, 906*t*
- Journal of Neurology, Neurosurgery and Psychiatry*, 862
- J*-process, 810
- Kasimir, Heinz, 194
- kinematic model, 140–1, 148, 150–1
- Kirchhoff's laws, 390
- K* processes, 815–16
- Lagrangian models, 148
- Lalande's stabilization field equation, 770–1
- Laplace equation, 15–16
- Laplace transform, 460, 580
- Laplace variable, 570, 580
- Laplacian of scalar function, 6
- Laplacian of vector field, 6
- large-scale model, of sprites, 640
- leader channel, 398
  - corona, effect of, 402–6, 402*f*, 404*f*
- leader inception models
  - of Becerra/Cooray, 771
  - critical radius concept, 769–70
  - critical streamer length concept, 769–70
- Lalande's stabilization field equation, 770–1
- Rizk's generalized leader inception equation, 770
- leader progression/attachment model, 771–4
  - schematics of, 772*f*
- leaders
  - branching of, 209
  - continuing current as indicator of developing, 203–4, 204*f*
  - discharges, 77–9, 78*f*, 80*f*
- defined, 78
- negative, development of, 79, 80*f*
- pilot system in, 79
- positive leader discharges: *see* positive leaders, discharges
- space leader, 79
- space stem, 79
- initiation, 195
- polarity, 194
- LEMP: *see* lightning electromagnetic pulse (LEMP)
- Lenz's law, 32
- lightning
  - channel, 428
  - vertical, 486*f*
- current data
  - Berger's data, 894–5, 894*f*–895*f*, 896*t*
  - experimental data, 892–3, 893*f*
  - experimental data, classification, 892
  - from short towers, 893–4, 895–8, 897*t*
  - from tall towers, 898–904, 899*f*, 900*f*–905*f*, 906*t*–907*t*
- effects in mesosphere/ionosphere, 611–40
- electromagnetic field, calculation of above homogeneous lossy ground, 489–92
  - above perfect ground, 486–9
  - above vertically stratified ground, 500–5
- electrical parameters of soil and, 542–8
- ground parameters and, 516–33
  - soil stratification and, 548–61
- location problem, 592
- as natural source of nitrogen oxides, 799
- overhead power transmission lines and, 719
- overvoltages, distribution networks and, 719

- parameterizations, 151, 152, 174–9, 174*f*  
 pseudo-fractal lightning, 179  
 stochastic lightning model, 176–8, 177*f*  
 radiation map, interpretation of, 200–1, 200*f*  
 over conducting ground, 522*f*  
 over multilayered ground, 549*f*  
 return stroke, electromagnetic fields of, 51–3, 52*f*  
 spatial distribution, SR and, 588–9  
 surges, in power lines direct strokes and, 735–8 evaluation of, 733–55 indirect strokes and, 738–55 thunderstorms and, energetic radiation from, 831–48 energy spectrum, 842–3 Monte Carlo simulations: *see* Monte Carlo simulations observations, 832–5 overview, 831–2 RF: *see* relativistic feedback (RF)  
 runaway electrons: *see* runaway electrons theory and observations, 846–8 x-rays/gamma-rays, observations of, 846–8 type, charge structure and, 182–6, 183*f*, 184*f*, 185*f*  
 lightning electromagnetic pulse (LEMP), 688–9 lightning flash bipolar charge moment distributions for, 630*f* development: *see* lightning flash development downward negative, 765 electromagnetics of: *see* electromagnetic theory interaction with grounded structure, 765–85 inception models: *see* leader inception models overview, 765–6 striking distance, 767–9 model of, 809–10 NO<sub>x</sub> production in, 809–18 continuing currents, 816 corona sheath and, 810–12 global, 820–2 hot electrical discharges and, 812–14 K processes, 815–16 M components, 815–16 overview, 809–10 return strokes, 814–15 upward, 766 lightning flash development, 193–227 cloud and lightning parameters, 205–8, 206*f*, 207*f* composition, 196–203 CG flashes: *see* cloud-to-ground (CG) lightning IC flashes: *see* intracloud (IC) flashes ‘recoil streamers’ and dart leaders, nature of, 196–8, 197*f*, 198*f* continuing current as indicator of developing leader, 203–4, 204*f* current cut-off in: *see* current cut-off definitions and attributes of, 194–6 M-component, 218–20, 220*f* M-events, electrostatic model of: *see* M-events, electrostatic model of overview, 193–4 positive CG flashes: *see* positive CG flashes spider lightning, 204–5, 205*f* upward lightning: *see* upward lightning Lightning Imaging Sensor (LIS), 592 lightning-induced overvoltage (LIOV)-EMTP code, 733, 740, 748

- lightning-induced whistlers
  - in ionosphere/magnetosphere, 647–61
  - overview of, 647–9
  - theoretical background, 649–61
  - ionosphere/magnetosphere characterization, 649–50, 650*f*
- lightning return-stroke models
  - categories, 232, 263
  - distributed-circuit models, 316
  - electromagnetic models, 316–17
    - Maxwell's equations and, 315–16
    - AT models of, 315–82
    - see also* antenna theory (AT)
    - models, of lightning return-stroke
    - see also* electromagnetic models of lightning return strokes
  - engineering models, 316
    - see also* engineering models, for return stroke
  - features, 231–2
  - overview, 231–2
  - physical models, 316
  - transmission line models: *see* transmission line models of lightning return stroke
- lightning storm, 616
- lightning strikes to tall towers, 873–907
  - data: *see* lightning, current data
  - electromagnetic field computation, 881–91
    - for finitely conducting ground, 888–91, 891*f*
    - for perfectly conducting ground, 882–8, 882*f*, 886*f*–888*f*
  - electromagnetic models, 880–1
  - engineering models, 874–80
    - see also* engineering models
  - hybrid electromagnetic model, 881
- lightning surges, in power lines
  - direct strokes and, 735–8
  - evaluation of, 733–55
  - indirect strokes and, 738–55
- linear dielectric media
  - Maxwell's equations and plane waves in, 43–4
- linear system solver, 105–6
- line charge density
  - AT models and, 352–3, 353*f*
- line integral, of vector field
  - curl and, 8
- line laterals, influence of, 749–51, 750*f*
- liquid (cloud) water content (LWC), 160, 161
- LIS: *see* Lightning Imaging Sensor (LIS)
- longitudinal propagation, 655–6
- Lorentz force, 29
- Lorentz Gauge, 47
- lossless non-uniform channel
  - current calculation, 414–16, 415*f*
- lossy ground
  - layers of, 549
  - lightning electromagnetic field calculation, 548–61
    - with frequency-dependent electrical parameters, 542–8
  - lossy half-space problem, 335–8, 335*f*
  - lossy non-uniform channel, current calculation, 416–17, 417*f*
    - with corona, 418–19, 418*f*
  - lumped current source, 287
  - lumped-excitation transmission line models, 392, 395–8, 396*f*
  - lumped series voltage source engineering models, extension of, 876
  - lumped voltage source, 287
  - LWC: *see* liquid (cloud) water content (LWC)
  - MacCormack's method, 118
  - magnetic fields
    - amplitude of, 437*f*
    - azimuthal component of, 532–3, 535, 557
      - above homogeneous ground, 490–1

- above two-layer horizontally stratified ground, 499*f*, 500*f*  
in air/underground, 430–1  
simulations results of, 498, 499  
at surface/depths below ground, 461  
of Earth, 648  
electrodynamics, time-varying: *see* electrodynamics  
energy density in, 34–5, 34*f*  
of first three SR modes, 586, 586*f*  
mean error/standard deviation, 442*t*  
measurement  
AMR sensors and, 578  
antennas and, 577*f*  
crossed loop antennas and, 576–8  
occipital seizures and, 860–2, 860*f*  
over finitely conducting ground, calculation procedures, 438–64  
Norton/Bannister's approximations, 438–40  
peak time derivatives of, 439  
of plane waves, 39–41  
propagation effects on, 434, 437  
raw data, 589*f*  
static, 19–29  
    Ampères law, 24  
    Biot–Savarts law, 22–3, 23*f*  
    boundary conditions for, 25–6, 25*f*  
    charged particle, force on, 29  
    by current element, 22–3, 23*f*  
    electric charge, conservation of: *see* electric charge  
    by electric current, 19–20  
    Gauss's law for, 23  
    vector potential and: *see* vector potential  
    visual sensations by, 857–8  
magnetic link, 891–2  
magnetic media
- Maxwell's equations and plane waves in, 43–4  
magnetic radiation fields, propagating current pulse and due to attenuation of current, 63 due to variation of current velocity, 64–5  
with non-uniform velocity and with attenuation, 62  
with uniform velocity and without attenuation, 59  
magnetic velocity field, propagating current pulse and current pulse, generated by  
    with non-uniform velocity and with attenuation, 62  
    with uniform velocity and without attenuation, 59–60  
magnetosphere  
characterization of, 649–50, 650*f*  
electrons, and electromagnetic waves interaction, 650, 652–5  
IAR: *see* ionospheric Alfvén resonator (IAR)  
lightning effects in, 647–80  
lightning-induced whistlers in, 647–61  
    overview of, 647–9  
theoretical background, 649–61  
Marshall–Palmer distribution, 144  
Maxwell's equations, 35–6, 585  
electromagnetic models and, 263, 264, 290, 292, 315–16, 390, 415  
plane waves and  
    in conducting media, 43–4  
    in isotropic media, 43–4  
    in linear dielectric media, 43–4  
    in magnetic media, 43–4  
    in vacuum, 42–3  
scale factors and, 721  
Maxwell's modification of Ampere's law, 33–4  
Maxwell's prediction of electromagnetic waves, 37–8

- M-component, 218–20, 220*f*, 810, 815–16
- MCS: *see* mesoscale convective system (MCS)
- mean impact cosine, 168–9
- mean separation probability, 168–9
- medium voltage (MV) networks, 729
- Meso-NH model, 152
- mesoscale convective system (MCS), 614
- mesosphere
  - lightning effects in, 611–40
    - see also* transient luminous event (TLE)
- method of moments (MoM), 264, 317, 688
  - electromagnetic field computation and, 890
  - in frequency domain, 292
  - numerical treatment, 327–8
  - in time domain, 290–2, 291*f*
- method of weighted residuals: *see* method of moments (MoM)
- M-events, 219
  - electrostatic model of, 221–6, 221*f*, 223*f*, 224*f*, 225*f*
  - aircraft penetrating thunderstorms, 226, 226*f*
  - principles, 221–6
- microphysics, 142–6
  - bin/spectral: *see* bin/spectral microphysics
  - bulk: *see* bulk microphysics
- minimal crossing field, 129
- mini-return strokes, 196
- Mitzpe Ramon (MR), 590
  - ELF transient recorded at, 592*f*
- mixed-phase models, 143
- mixing coefficient, 157
- mixing ratios, 142
- Model Navigator window
  - application modes in, choosing, 97–8, 98*f*
- modified transmission line models
  - CD models and, 256–7
  - modified transmission line model
    - with exponential current decay (MTLE), 234, 433, 495
    - with height, 316
  - modified transmission line model
    - with linear current decay (MTLL), 234, 875, 875*t*, 878
    - with height, 316
  - MoM: *see* method of moments (MoM)
  - moments, of distribution, 144, 145
  - Monte Carlo simulations, 833, 837–42
    - Compton scattering in, 840
    - elastic scattering in, 842
    - Rayleigh scattering in, 840
    - of RREA, 839
    - parameters, 844
  - Morro do Cachimbo Tower, 907*t*
  - Mount Saint Salvatore Tower, 907*t*
  - moving charge, electromagnetic fields of, 55–6, 55*f*
  - MR: *see* Mitzpe Ramon (MR)
  - MTLE: *see* modified transmission line model with exponential current decay (MTLE)
  - MTLL: *see* modified transmission line model with linear current decay (MTLL)
  - MUDPACK, 123
  - multiconductor transmission lines, 695–8
    - cross-sectional geometry of, 696*f*
  - MV networks: *see* medium voltage (MV) networks
  - nabla operator, operations of, 5–8
  - curl of vector field, 7
  - divergence of vector field, 6–7
  - gradient of scalar function, 5–6
  - Narrowband measurements, 578, 580, 580*f*
  - narrow bipolar events (NBE), 848
  - National Lightning Detection Network (NLDN), 629

- NBE: *see* narrow bipolar events (NBE)
- NEC-2: *see* Numerical Electromagnetic Code (NEC-2)
- NEC-4 code, 298, 303, 305
- negative CG flashes, 212–15, 213*f*
- negative leaders, 194, 195, 195*f*  
discharges, 79, 80*f*  
in IC development, 199–200  
upward, 215–16, 216*f*
- negative space charge region, 76
- negative streamers, 72, 73*f*
- NEMP: *see* nuclear electromagnetic pulse (NEMP)
- neutralization, 176, 196, 242–3, 254, 255, 257
- nitrogen oxides ( $\text{NO}_x$ )  
freeze-out temperature, 803, 806  
global distribution of, 789  
global production, by lightning flashes, 820–2  
ground-based measurement, 799  
lightning as natural source of, 799  
lightning production of, 153  
molecules production  
  cloud flash and, 821*f*  
  ground flash and, 818*f*
- production  
  annual, by lightning flashes, 822*f*  
  by cloud flashes, 818–20  
  in corona discharges, 791  
  corona sheath and, 810–12  
  efficiency, 805*f*, 807*f*  
  by electrical discharges or sparks: *see* electrical sparks  
  by electrical discharges/sparks, 800–8  
  in electron avalanches, 791–2  
  hot electrical discharges and, 812–14  
  in lightning flash, 809–18 *see also* lightning flash  
  in negative ground flash, 817–18
- from non-vertical in-cloud channel, 813
- per unit energy, 792*f*
- by return stroke, 800, 814–15
- in streamer discharges, 792–4, 808–9
- solar proton events in, 790
- thunderstorms as natural source of, 789, 799
- NLDN: *see* National Lightning Detection Network (NLDN)
- ‘non-ducted’ whistlers, 648–9
- non-inductive charging process, 146, 147*f*
- non-inductive graupel-ice collision mechanism, 158–67  
general formulation, 165–7  
parameterized laboratory results, 158–65, 159*f*, 159*t*, 161*t*, 162*f*
- non-inductive graupel-ice sensitivity, 181
- non-inductive parameterization, 150
- non-thermal electrical discharges, in air: *see* electrical discharges, non-thermal
- non-vertical in-cloud channel  
  nitrogen oxides production from, 813
- ‘normal fluxes,’ for charge carriers, 104
- Norton’s approximations  
  to calculate electric/magnetic field over finitely conducting ground, 438–40  
  vs. Bannister’s, 439–40
- Norton surface wave (NSW), 338
- ‘nose’ whistler, 648
- NPW model, 176, 178
- NSW: *see* Norton surface wave (NSW)
- nuclear electromagnetic pulse (NEMP), 698
- nucleation, defined, 143
- number concentration collection rate integral, 166–7

- numerical distance, 490, 493  
 Numerical Electromagnetic Code (NEC-2), 294, 298, 300, 302, 305, 317
- oblique propagation, 658–9  
 occipital lobe, epileptic seizures of visual sensations by, 858–60, 859f effect of intermittent light, 862 magnetic fields of return strokes, 860–2, 860f
- one-and-one-half dimensional model, 151
- one-dimensional cloud models, 141
- ‘ONE’ event, 632
- onset streamers, 75
- optical-electrical converter, 739
- Optical Transient Detector (OTD), 592
- oscilloscopes, 892
- Ostankino Tower, 898, 899–900, 906t
- OTD: *see* Optical Transient Detector (OTD)
- overground electromagnetic field, 517–33, 535–7 azimuthal component of magnetic field, 532–3
- Green’s functions theory and: *see* Green functions lightning return stroke, derivation of, 522–3 numerical simulation of, 545–8 radial component of electric field, 530–1
- Sommerfeld’s integrals, evaluation of, 523–7
- stratified soil and, 557–61
- vertical component of electric field, 527–30
- overhead lines electromagnetic field interaction with, 690–707
- Agrawal/Price/Gurbaxani model, 691–2
- frequency-domain solutions, 698–700 inclusion of losses, 694–5 LEMP-to-transmission line coupling model, 698 multiconductor lines, 695–8 Rachidi model, 693 single-wire transmission line, 690 Taylor/Satterwhite/Harrison model, 690–1 time-domain solutions, 700–2
- electromagnetic models applications, 304–5 lightning and, 719 in scale model experiments, 727–8, 728f single-wire, equivalent circuit of, 691f, 692f
- overvoltages ground lossess effects on, direct lightning and, 702–4, 702f–704f induced, effect of ground losses on, 705–7, 705f–707f
- Pacific Ocean sprites in, 632, 634, 635, 636, 637
- parameterization, of electrical processes, 153–7
- continuity equations, for charge, 156–8
- electric field, calculating, 153–6, 154f
- inductive charging mechanism: *see* inductive charging mechanism non-inductive, 158–65, 159f, 159t, 161t, 162f
- graupel–ice collision mechanism: *see* non-inductive graupel–ice collision mechanism of Helsdon and Farley, 158, 159t of Saunders, 161–2, 161t
- small ion processes, 170–3, 172t

- parameterizations, 139
  - of electrical processes: *see* parameterization, of electrical processes
- lightning: *see* lightning, parameterizations
- PARDISO, 106
- partial differential equations (PDE), 94
- particle tracing models, 148
- PDE: *see* partial differential equations (PDE)
- PEC: *see* perfect conductor (PEC)
- Peek's formula, 111, 405
- Peissenberg Tower, 900, 902*f*, 906*t*
- perfect conductor (PEC), 557
  - ground as, 525
- permittivity, 542
  - ground
    - as function of frequency, 547*f*
    - soil, on frequency, 543–5
- phase velocity, 655
- phosphenes
  - by corona currents, 866–7, 867*f*
  - induction by energetic radiation, 864–6
    - energetic electrons generated by leader steps, 864–5
    - inside airplanes, 866
    - terrestrial gamma rays, 865–6
    - x-ray bursts from lightning, 865
- photoionization, 118
- photon feedback, 837
- physical models, 316
- pilot system, 79
- plane waves, 39–42
  - electric field of, 39
  - energy transported by, 41–2
  - magnetic field of, 39–41
- Maxwell's equations and
  - in conducting media, 43–4
  - in isotropic media, 43–4
  - in linear dielectric media, 43–4
  - in magnetic media, 43–4
  - in vacuum, 42–3
- Poyntings theorem, 41–2
- plasmasphere, 650
- plate/whip antenna, 568–74, 569*f*
  - decay time constant of, 571, 572
  - and electric field derivative measurement, 573–4
- electronic circuitry, 569, 570
- equivalent circuit of, 569*f*
- field mill *vs.*, 572–3
- output of, 573
- physical configuration of, 568, 569
- rise time constant of, 571, 572
- POISSON, routine, 124, 124*f*
- Poisson's equation, 15–16, 95
  - methods for solving, 120–2
- polarity
  - asymmetry, of sprites, 630–1
  - problem of, sprites and, 629–31
- polyvinyl chloride (PVC) structures, 727–8
- positive CG flashes, 203, 212–15, 213*f*, 214*f*
- positive leaders, 194–5, 195*f*
  - discharges
    - mathematical modelling of, 79, 81–4, 82*f*, 83*f*
    - mechanism of, 78, 78*f*
  - in IC development, 199–200
  - upward, 215, 215*f*, 217*f*
    - continuing current in, 216
    - M-components in, 219
- positive streamer, 71–2, 71*f*
- positron feedback, 837
- Poyntings theorem
  - plane waves and, 41–2
- preliminary breakdown, 809
- 'primary' current, 878
- propagating current pulse, electromagnetic fields by, 55–65
  - with non-uniform velocity and
    - with attenuation, 60–5
  - electric radiation field and, 61
  - magnetic radiation field and, 62
  - magnetic velocity field and, 62

- static fields and, 61
- velocity fields and, 61–2
- radiation and velocity field of, 56–7, 56*f*
- with uniform velocity and without attenuation, 57–60, 58*f*
- electric radiation field and, 58
- magnetic radiation fields and, 59
- magnetic velocity field and, 59–60
- static fields and, 58
- velocity fields by, 59
- propagation: *see* wave propagation
- proportionality, constant of, 160
- pseudo-fractal lightning, 179
- PVC structures: *see* polyvinyl chloride (PVC) structures
  
- Q-bursts, 591–2
  - see also* transient luminous event (TLE)
- QE fields: *see* quasi-electrostatic (QE) fields
- quasi-electrostatic (QE) fields, 616, 618–21, 627, 635
  - computer simulation results on, 620*f*
  - and sprites, 621–4
- quasi-free-space mode, 659
- quasi-static approximation
  - for horizontal electric field calculation, 449
  - vs. surface impedance expression, 449–56
- quasi-TEM: *see* quasi-transverse electromagnetic (quasi-TEM)
- quasi-transverse electromagnetic (quasi-TEM), 689
  
- Rachidi model, 693
- radial electric field, 530, 534, 557–61
  - calculation, using CR formula, 537, 538–9
- radiated fields
  - horizontally stratified ground effects on, 473–81
- vertically stratified ground effects on, 466–71
  - equivalent conductivity, 470–1
  - principle of reciprocity, 468–70
  - sea gain, 466–8
- radiation
  - energetic, from thunderstorms and lightning: *see* lightning, thunderstorms and field, 50
  - of propagating current pulse, 56–7, 56*f*
  - lightning radiation map of IC flash, 199–200, 199*f*
- RAR: *see* rime accretion rate (RAR)
- rate of photoionization, 94
- Rayleigh scattering, 841
- reciprocity, principle of
  - and propagation effects, 468–70
- recoil leaders, 197–8, 197*f*, 198*f*, 200
  - current cut-off and, 211–12
  - in IC flashes, 211
- recoil streamers, nature of, 196–8, 197*f*, 198*f*
- recombination coefficient, 89–90
- red sprites: *see* sprites
- reference current, 876
- ‘reference line,’ 741
- reflection coefficient, 551, 554–7
  - absolute value of, 556–7
  - for first layer depth, 556*f*, 557*f*
  - physical properties of, 555
- reflection coefficients, of strike object engineering models, 878–80
- refractive index, 656, 659, 660
- relativistic feedback (RF), 837, 844–6, 847*f*
  - feedback factor in, 845–6
- relativistic runaway electron avalanche (RREA), 836, 837, 839*f*
  - flux of, 847
  - Monte Carlo simulation of, 839 parameters, 844
- relaxation time, of conductor, 22

- resistance, channel  
 of transmission line, 409–14  
 computation, 412–14, 413*f*  
 strong-shock approximation,  
 411–12  
 Toepler's arc resistance  
 equation, 412  
 resonance frequency, 658  
 retarded potentials, 46–8  
 return-stroke channel (RSC),  
 315, 399  
 corona, effect of, 402–6, 402*f*, 404*f*  
 models, 724–7, 725*f*, 726*f*  
 lightning: *see* lightning  
 return-stroke models  
 MTLE of, 495  
 propagation velocity, 725  
 return strokes, 68, 616  
 in CG flashes, 196, 199, 201  
 channel-base current, 433, 535–6  
 current, leader potential and,  
 782–4  
 defined, 809  
 electric field signature, 468*f*, 469*f*  
 electromagnetic fields, 432  
 characteristics of, 427  
 first: *see* first return stroke  
 front, 237  
 M-event, electrostatic model of,  
 222–4, 223*f*, 224*f*, 225*f*  
 modelling, 433–4, 616  
 classes of, 687  
 NO<sub>x</sub> production by, 814–15  
 overground electromagnetic field,  
 derivation of, 522–3  
 phase, measured characteristics  
 of, 315  
 scale model for: *see* return-stroke  
 channel (RSC), models  
 speed, 236, 237, 238  
 stepped leader potential, 774–6  
 subsequent: *see* subsequent return  
 stroke  
 RF: *see* relativistic feedback (RF)  
 Riemann surface, 523
- rime accretion rate (RAR),  
 163–4, 163*f*  
 riming, 143  
 Rizk's generalized leader inception  
 equation, 770  
 rocket-triggered lightning  
 technique, 720  
 rod-plane electrode system, positive  
 corona in (case study),  
 112–16, 113*f*, 114*f*, 115*f*, 116*f*  
 Rogowski coil, 897, 899, 904  
 Romberg method, 531  
 RREA: *see* relativistic runaway  
 electron avalanche (RREA)  
 RSC: *see* return-stroke channel  
 (RSC)  
 RSSI solver, 121, 121*f*  
 runaway breakdown, 836  
 runaway electrons, 175, 835–7, 836*f*  
 avalanches of, 836–7, 838*f*  
 cold/thermal runaway, 835  
 energy spectrum in, 842–3  
 feedback mechanisms, 837  
 mechanism, 624–6  
 model, 624–6  
 characteristics of, 625–6  
 Monte Carlo simulations: *see*  
 Monte Carlo simulations  
 relativistic, mechanisms for  
 generating, 836, 837, 839*t*  
 snowball effect, 835–6
- Sântis Tower, 904, 905*f*  
 Sato's equation, 95  
 scalar potential  
 boundary conditions for, 155  
 electric, 14–15, 15*f*  
 Poisson solvers for,  
 numerical, 155  
 retarded potentials, 46–8  
 scalar product, of vectors, 2, 3–4  
 scale model  
 basis of, 721–3  
 general view of, 724*f*  
 overview of, 720–1

- and simulation of electromagnetic environment, 723–33
- buildings, 733, 734
- ground, 727
- overhead lines, 727–8
- return stroke channel, 724–7
- surge arresters, 730–3, 731*f*, 732*f*
- transformers, 728–30
- at University of São Paulo, 723–4
- Schumann resonances (SR), 583–98, 662
  - amplitude, 590*f*, 593*f*
  - as climate research tool, 592–4
  - defined, 583
  - in extraterrestrial lightning research, 597–8
  - features of, 590
  - first three modes, electric/magnetic fields of, 586
  - and global lightning activity, 584, 588–92
    - background observations, 588–91
    - transient measurements, 591–2
  - history of, 583–4
  - on ionosphere of Titan, 598
  - mean diurnal/seasonal variations in, 591*f*
  - measurements, 587–8
  - theoretical background, 584–6
    - in TLE research, 595–6
  - screening effect, field, 209–10, 210*f*
  - sedimentation, 157
  - self-consistent leader inception and propagation model (SLIM), 782
    - assumptions of, 784–5
    - EGM *vs.*, 777–80
  - self-screening, 209
  - sensors
    - AMR, 578
    - Hall effect, 578
    - and SR measurement, 587–8
    - three-dimensional electric field, 574–5, 574*f*
  - shock waves, 855
  - short towers
    - lightning current data from, 893–4, 895–8, 897*t*
  - side flash, 855
  - single-moment schemes, 144
  - single-phase straight line, 741
  - single-station SR methodology and lightning location problem, 592
  - single-wire transmission line, 690
  - slab-symmetric model, 141, 142
  - SLIM: *see* self-consistent leader inception and propagation model (SLIM)
  - small ion processes, 170–3, 172*t*
  - Snell’s law, 659
  - ‘snowball effect,’ 835–6
  - SOD: *see* source-observer distance (SOD)
  - soil
    - electrical parameters, and lightning electromagnetic field calculation, 542–8
    - properties of, 557
  - soil conductivity, 476
  - soil moisture, content in, 475–6
  - soil stratification
    - and lightning electromagnetic fields, 548–61
    - overground electromagnetic field and, 557–61
  - solar proton events
    - in nitrogen oxides, 790
  - Solar System
    - lightning research on, SR and, 597–8
  - Sommerfeld’s integrals, 489
    - defined, 523
    - evaluation of, 515, 517, 523–7
      - branch points, 523–5
      - $\sigma$ -dependent term, 525–7, 525*f*, 526*f*
  - Green functions and, 516
  - integration path for, 524*f*

- inverse Fourier transform and, 527
- source charge leader model, 193–4, 196, 203
- source-observer distance (SOD), 585, 586
- South Africa Tower, 907*t*
- space leader, 79, 195
- space stem, 79
- S91 parameterization, 181, 182, 186
- spatial dimension, to model, 141
- spectral parameterization, 145
- spectral resonance structure (SRS), IAR, 662, 666
  - daily evolution of, 664*f*
  - geomagnetic activity and, 669–71
  - occurrence rate, correlation coefficients of, 669, 671
  - parameters
    - identification/determination of, 667*f*
    - variations of, 666–9
  - spherical coordinates, 2, 3*f*
    - curl of vector field in, 7
    - divergence and Laplacian in, 6
    - gradient of scalar function in, 6
  - spider lightning, 204–5, 205*f*
  - ‘split explicit’ method, 147
  - SPOOLEs, 105–6
  - sprite halo, 614, 640
  - sprites, 595, 611, 612, 628–9, 790
    - displacement from parent lightning, 634–5
    - duration of, 613
    - elves and, 626–7
    - fine structure of, 639–40
    - in Hokuriku region, 633–4, 635, 638
    - large-scale model of, 640
    - morphological changes of, 631–4
      - in Hokuriku area/Pacific Ocean, 637
    - observed by ILAN team, 596*f*
    - optical emissions in, 640*f*
    - in Pacific Ocean, 632, 634, 635, 636, 637
  - phenomenology of, 613–14
  - physical mechanism of, 621–6, 622*f*
  - runaway mechanism, 624–6
  - thermal ionization/QE mechanism, 621–4
  - polarity problem, 629–31
  - telescopic imaging of, 613
  - time delay effect, 635–8, 637*f*
  - SP98 simulation, 182, 183, 184, 186
  - SR: *see* Schumann resonances (SR)
  - SRS, IAR: *see* spectral resonance structure (SRS), IAR
  - static fields, 50
    - propagating current pulse and charge deposited along channel by current pulse, 63–4
    - with non-uniform velocity and with attenuation, 61
    - with uniform velocity and without attenuation, 58
  - static magnetic field: *see* magnetic fields, static
  - static term, 529
  - stepped leaders, 201, 765, 767, 809
    - channel inclination of, 784
    - potential of, striking distance and, 774–7
    - connecting leader and, 768–9
  - inception models: *see* leader inception models
  - orientation of, 780–2
  - speed of propagation of, 812
  - stochastic lightning model, 176–8, 177*f*
  - stokes theorem, 10
  - storm
    - charges in, 157–8
    - decaying stage of, 205
    - mature stage of, 205
  - streamer discharges, 70–4, 71*f*, 73*f*
    - active region and, 74
    - advancement of, 724
    - from avalanche, 70–4, 71*f*, 73*f*

- concept of, 90–2
- mid gap streamer, 72
- negative streamers
  - cathode-directed, 72, 73*f*
  - mechanism of, 72, 73*f*
- $\text{NO}_x$  production in, 792–4, 808–9
- positive streamers, 72
  - anode-directed, 71–2, 71*f*
  - mechanism of, 71–2, 71*f*
  - neutralization process in, 72
- simulations of, 116–34, 121*f*, 122*f*
  - algorithm for solving coupled equations, flow chart of, 123–4, 124*f*
- AMR, 118
- FCT: *see* flux-corrected transport (FCT)
- geometry function, definitions of, 123*t*
- ITPACK 2C, 121, 121*f*
- MUDPACK, 123
- negative streamer in weak homogeneous background fields (case study), 130–4, 131*f*, 132*f*, 133*f*
- photoionization in, 118
- Poisson's equation, methods for solving, 120–2
- positive streamer in weak homogeneous background field (case study), 124–30, 127*f*, 128*f*, 129*f*, 130*f*
- RSSI solver, 121, 121*f*
- streamer-leader transition process, 194–5, 195*f*
- streamer stem, 77
- streamer to leader transition, 766
- striking distance, 767–9, 767*f*
  - analytical expressions for, 780
  - defined, 767
  - and leader tip potential, 776–7
  - potential of stepped leader channel and, 774–7
  - of vertical structures, 779
- strong-shock approximation, 411–12
- 'subdomain settings,' 102–3
- subsequent return stroke, 495, 810
  - horizontal electric field, 451*f*, 453*f*, 455*f*, 457*f*
- $\text{NO}_x$  production by, 814–15
  - parameters of, 434*t*
- supercell storms, 151
- superposition, principle of, 11
- surface impedance expression for horizontal electric field calculation, 449
- quasi-static approximation *vs.*, 449–56
- surge arresters, 743–9
  - currents injected into, 732
  - equivalent circuit of, 731, 732
  - in scale model experiments, 730–3, 731*f*, 732*f*
- Takahashi (TAK) charging diagram, 159–60, 159*f*
- Taylor/Satterwhite/Harrison model, 690–1, 690*f*
- TCS: *see* traveling current source (TCS) models
- TEB: *see* terrestrial electron beams (TEB)
- telegrapher's equations, 263, 390, 391, 407
- TEM: *see* transverse electromagnetic (TEM) field structure
- terrestrial electron beams (TEB), 833
- terrestrial gamma-ray flashes (TGF), 833–4
- terrestrial gamma rays
  - phosphenes and, 865–6
- 'test line,' 742
  - configurations of, 745*f*
- TGF: *see* terrestrial gamma-ray flashes (TGF)
- thermal ionization
  - and sprites, 621–4
- thermalization/heating, 194
  - of air by discharge, 76–7
  - low-pressure discharges and, 77

- thermal runaway, 835  
 thin-wire time-domain (TWTD)  
   code, 269, 291, 294, 298, 300,  
   304, 317  
 three-dimensional cloud models, 141  
 three-moment schemes, 144  
 thundercloud, 790  
 thunderstorms  
   aircraft penetrating, 226, 226*f*  
   excitation of IAR and, 673–80  
   lightning and, energetic radiation  
     from: *see* lightning,  
     thunderstorms and  
   model, of Wilson-Simpson, 205  
   as natural source of nitrogen  
     oxides, 789, 799  
 time constant  
   integration, 576  
   rise/decay, of plate/whip antenna,  
     571, 572  
 time delay effect, of sprites, 635–8  
 time dependent, cloud models, 147  
 time-domain AT models, 317, 339–41,  
   339*f*–340*f*  
   with inductive loading, 341–, 342*f*,  
     344*f*, 345*f*  
   with non-linear loading, 346–9,  
     348*f*, 349*t*  
 time-domain functions, 540  
   for underground electric fields,  
     458–64  
 time-harmonic electromagnetic fields  
   Maxwell's equations for, 653–4  
 time variation  
   in electric and magnetic fields, 30–5  
 Titan, ionosphere of  
   SR on, 598  
 TL: *see* transmission line (TL),  
   model  
 TLE: *see* transient luminous event  
   (TLE)  
 TL theory: *see* transmission line  
   (TL), theory  
 Toepler's arc resistance  
   equation, 412  
 towers  
   in electromagnetic field  
     computation, 888  
   short, lightning current data from,  
     893–4, 895–8, 897*t*  
 tall  
   lightning current data, 898–904,  
     899*f*, 900*f*–905*f*, 906*t*–907*t*  
   lightning strikes to, 873–907*see*  
     *also* lightning strikes to tall  
     towers  
 Townsend's discharge, 91  
 Townsend's first ionization  
   coefficient, 68  
 Townsend's ionization coefficient,  
   88–9  
 transformers, in scale model  
   experiments, 728–30  
 transient ground resistance  
   matrix, 700  
 transient luminous event  
   (TLE), 584  
   heating of ionosphere/neutral  
     atmosphere and, 620–1  
   phenomenology of, 613–15  
   physical mechanisms/modellings,  
     615–21  
   EMP, 617–18  
   QE fields, 618–21  
   SR in, 595–6  
   types of, 595, 611–13, 612*f*  
     *see also* blue starters/jets; elves;  
     sprites  
 transmission cone, 660  
 transmission line equations  
   corona, effect of, 407–9  
 transmission line models of lightning  
   return stroke, 232, 234  
 channel currents, 414–19  
   lossless non-uniform channel,  
     414–16, 415*f*  
   lossy non-uniform channel,  
     416–17, 417*f*  
   lossy non-uniform channel with  
     corona, 418–19, 418*f*

- channel parameters per-unit-length, calculation of, 398–414
- corona, effect of, 401–9
- inductance and capacitance, 399–400, 401*f*
- leader channel, 398
- resistance, 409–14
- return stroke channel, 399
- discharge-type, 392, 393–5, 393*f*
- electromagnetic fields, predicted, 419–21, 420*f*
- lumped-excitation, 392, 395–8, 396*f*
- overview, 389–98
- transmission line (TL)
  - model, 316
  - theory, 688–9, 740
- TRANSPORT, routine, 124, 124*f*
- transverse electromagnetic (TEM) field structure, 263, 390
- transverse propagation, 656–7
  - resonance for, 658
- traveling current source (TCS)
  - models, 316, 877, 885
- Trichel pulses, 76
- turbulent mixing, 157, 171
- turn-on term
  - electromagnetic field computation and, 884–5
- two-dimensional cloud models, 141
- TWTD code: *see* thin-wire time-domain (TWTD) code
  
- ULF: *see* ultra-low frequency (ULF)
- ultra-low frequency (ULF), 663
- UMFPACK, 105
- underground electric fields
  - Cooray's formula and, 889–90
  - underground electromagnetic field, 533–5
    - CR formula and, 537, 540–2
    - numerical simulation of, 545–8
  - underground transmission lines: *see* buried cables
  
- undisturbed current, 875
- University of São Paulo scale model implemented at, 723–4
- upper tropospheric water vapour (UTWV), 593–4
- upward lightning, 215–18, 218*f*, 219*f*
  - negative leader, 215–16, 216*f*
  - non-branching positive leader, 217–18, 217*f*
  - positive leader, 215–16, 215*f*
    - M-components in, 219
    - non-branching, 216–17, 217*f*
- urban distribution networks configuration of, 746
- UTWV: *see* upper tropospheric water vapour (UTWV)
  
- vacuum, Maxwell's equations and
  - plane waves in, 42–3
- vector field, 5
  - curl of, 7
  - line integral and, 8
  - divergence, nabla operator and, 6–7
  - flux, through surface, 8–9
  - divergence and, 9
- vector identities, 8
- vector potential, 26–9
  - of current distribution, 27–8, 27*f*
  - due to current element, 28–9, 29*f*
  - of current element, 48
  - retarded potentials, 46–8
  - spatial distribution, 519, 552
- vectors, in electromagnetic theory, 2, 3–10
  - in Coulombs law, 10–11, 10*f*, 11*f*
  - divergence theorem, 9
  - magnitude of, 2
  - nabla operator, operations of: *see* nabla operator, operations of
- scalar product of, 2, 3–4
- stokes theorem, 10
- vector field: *see* vector field
- vector identities, 8
- vector product of two, 4

- velocity  
 non-uniform, electromagnetic fields by current pulse propagating with, 60–5  
 uniform, electromagnetic fields by current pulse propagating with, 57–60, 58*f*
- velocity fields  
 of propagating current pulse, 56–7, 56*f*  
 with non-uniform velocity and with attenuation, 61–2  
 with uniform velocity and without attenuation, 59
- vertical electric field, 487, 527–30, 534, 557  
 above homogeneous ground, 490–1  
 above two-layer horizontally stratified ground, 499*f*, 500*f*  
 in air/underground, 430  
 ball antenna, 587*f*  
 calculation, inverse Fourier transformation and, 443  
 at ground level, 435*f*, 438, 441*f*, 474*f*, 475*f*, 497*f*, 504*f*  
 measurement, field mill and, 567–8  
 Norton's vs. Bannister's expressions for, 439–40  
 over finitely conducting ground, 440–8  
 peak/rise times of, 497*t*, 507*t*  
 propagation effects on, 434  
 simulations results of, 498, 499  
 at surface/depths below ground, 459–60  
 at surface of mixed-path ground, 467*f*  
 time derivative of, 435, 436, 436*f*, 440*f*, 444*f*, 446*f*  
 time-domain simulation results of, 503, 504  
 time dynamics of, 623*f*  
 vs. azimuthal magnetic fields with measurements, 280–3, 281*f*, 282*f*, 284*f*, 285*f*
- vertically stratified ground  
 effects on radiation fields, 466–71  
 equivalent conductivity, 470–1  
 principle of reciprocity, 468–70  
 sea gain, 466–8  
 electromagnetic fields above, 500–5  
 electromagnetic fields from lightning over, 466  
 propagation over, 466–71  
 simulation domain of FDTD technique, 504–5
- very low frequency (VLF), 647
- VHF-UHF band, 199
- VI* characteristic, 730, 731
- visual sensations, electromagnetic fields, 855–68  
 ball lightning, features of, 856  
 by energetic radiation, 862–6, 863*f*  
 phosphenes, induction of, 864–6  
 by epileptic seizures of occipital lobe, 858–60, 859*f*  
 association with thunderstorms, 860–2, 860*f*  
 by magnetic fields, 857–8  
 phosphenes stimulation by corona currents, 866–7, 867*f*
- VLF: *see* very low frequency (VLF)
- Wagner CG model, 241
- Wajima Meteorological Observatory, 632
- warm cloud models, 143
- water substance category  
 continuity equation for the charge on, 156
- wave equation, 36–7  
 of electromagnetic waves, 654
- wave propagation  
 analysis over horizontally stratified ground, 472*f*  
 coordinate system for, 654*f*  
 cut-off/resonance frequencies, 657–8  
 in Earth-ionosphere cavity, 585

- effect on return-stroke channel, 434–7
- longitudinal, 655–6
- oblique, 658–9
- over stratified ground
  - horizontal: *see* horizontally stratified ground
  - vertical: *see* vertically stratified ground
- transverse, 656–7
- whistlers, 659–61
- whip antenna: *see* plate/whip antenna
- ‘whistler-mode’ branch, 648, 656, 659
- whistlers
  - defined, 648
  - description of, 647–9
  - frequency range of, 648
  - lightning-induced: *see* lightning-induced whistlers
  - ‘non-ducted,’ 648–9
  - ‘nose,’ 648
  - propagation, 659–61
  - ‘wildfire’ technique, 175
- Wilson, C. T. R., 621
- wind fields, changes in, 148
- wire-mesh-like structures
  - electromagnetic models
    - applications, 305
- wire(s), in electromagnetic models
  - charged vertical conducting, closing at its bottom end with a specified circuit, 286
  - coated by dielectric material in air above ground, 276
- fictitious material having high relative permittivity and permeability in air above ground, 276
- embedded in dielectric (other than air) above ground, 274–5
- excitation, current distributions
  - comparison along vertical perfectly conducting, 287–90, 288*f*, 289*f*
- having additional distributed shunt capacitance in air, 276–7
- loaded by additional distributed series inductance in air above ground, 269, 273–4
- perfectly conducting/resistive, in air above ground (type 1), 269
- WZ model, 178
  
- x-ray bursts
  - phosphenes and, 865
- x-rays, 832, 833, 834
  - bursts, 832, 833
  - feedback, 837
  - observations, from thunderclouds and lightning, 846–8
- Zenneck surface wave (ZSW), 338
- ‘zero charge/symmetry,’ 104
- zero-dimensional cloud models, 141
- zero-net-charge leader, bidirectional, 202, 202*f*
- ZSW: *see* Zenneck surface wave (ZSW)



# Lightning Electromagnetics

Lightning research is an interdisciplinary subject where several branches of engineering and physics converge. *Lightning Electromagnetics* is a book that caters for the needs of both physicists and engineers. It provides:

- The physicist with information on how to simulate: the charge generation in thunderclouds, different discharge processes in air that ultimately lead to a lightning flash, and the mechanism through which energetic radiation in the form of X-rays and Gamma rays are produced by lightning flashes.
- The power engineer with several numerical tools to study the interaction of lightning flashes with power transmission and distribution systems.
- The telecommunication engineer with numerical procedures with which to calculate the electromagnetic fields generated by lightning flashes and their interactions with overhead and underground telecommunication systems.
- The electromagnetic specialist with the basic theory necessary to simulate the propagation of lightning electromagnetic fields over the surface of the Earth.
- The atmospheric scientist with numerical procedures to quantify interactions between lightning flashes and the Earth's atmosphere, including the production of NOx by lightning flashes occurring in the atmosphere.

This book also contains a chapter on the stimulation of visual phenomena in humans by electromagnetic fields of lightning flashes, which is essential reading for those who are interested in ball lightning.

**Vernon Cooray** is a leading professor of lightning research at Uppsala University. He has published more than 270 scientific articles on lightning and electrical discharges. Two other books edited by him on this subject, *The Lightning Flash* and *Lightning Protection*, were published in 2003 and 2009, respectively, by the IET, London.

ISBN 978-1-84919-215-6

A standard 1D barcode representing the ISBN number 978-1-84919-215-6.

9

The Institution of Engineering and Technology  
[www.theiet.org](http://www.theiet.org)  
978-1-84919-215-6